frontiers | Research Topics

State-of-the-art laser spectroscopy and its applications: Volume II

Edited by
Yufei Ma, Qun Hao and Karol Krzempek

Published in
Frontiers in Physics

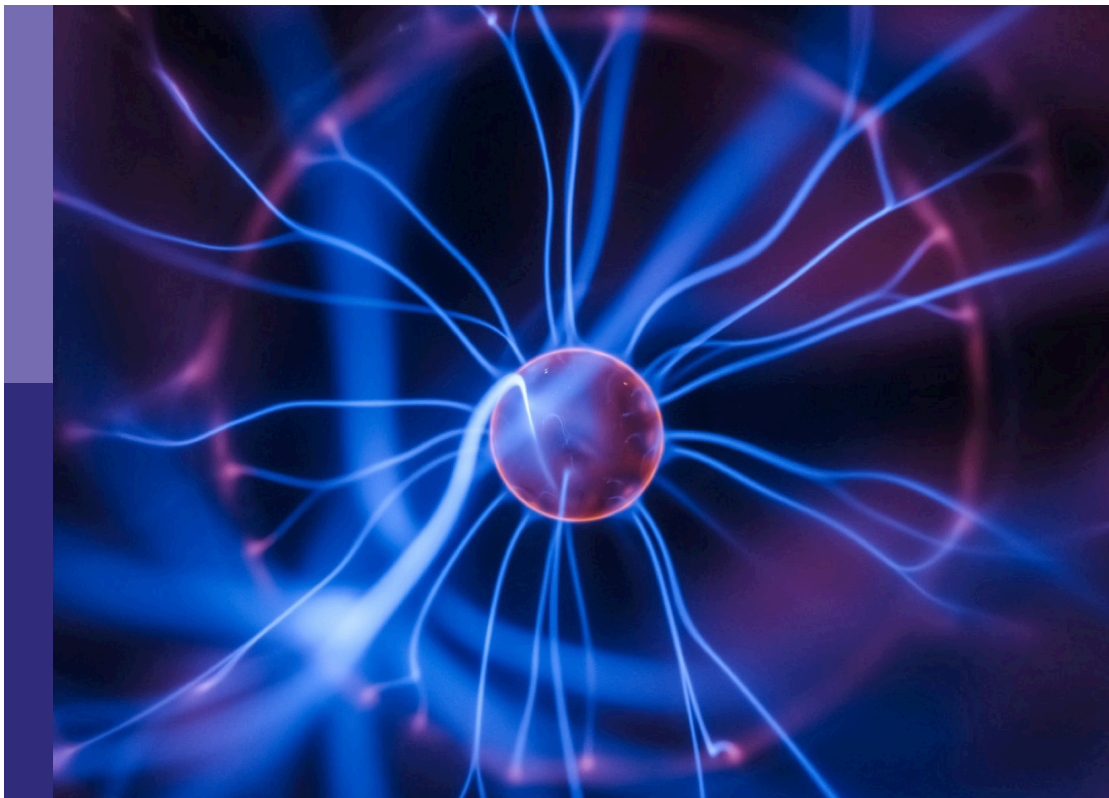

ISSN 1664-8714
ISBN 978-2-83251-412-2
DOI 10.3389/978-2-83251-412-2

About Frontiers

Frontiers is more than just an open access publisher of scholarly articles: it is a pioneering approach to the world of academia, radically improving the way scholarly research is managed. The grand vision of Frontiers is a world where all people have an equal opportunity to seek, share and generate knowledge. Frontiers provides immediate and permanent online open access to all its publications, but this alone is not enough to realize our grand goals.

Frontiers journal series

The Frontiers journal series is a multi-tier and interdisciplinary set of open-access, online journals, promising a paradigm shift from the current review, selection and dissemination processes in academic publishing. All Frontiers journals are driven by researchers for researchers; therefore, they constitute a service to the scholarly community. At the same time, the *Frontiers journal series* operates on a revolutionary invention, the tiered publishing system, initially addressing specific communities of scholars, and gradually climbing up to broader public understanding, thus serving the interests of the lay society, too.

Dedication to quality

Each Frontiers article is a landmark of the highest quality, thanks to genuinely collaborative interactions between authors and review editors, who include some of the world's best academicians. Research must be certified by peers before entering a stream of knowledge that may eventually reach the public - and shape society; therefore, Frontiers only applies the most rigorous and unbiased reviews. Frontiers revolutionizes research publishing by freely delivering the most outstanding research, evaluated with no bias from both the academic and social point of view. By applying the most advanced information technologies, Frontiers is catapulting scholarly publishing into a new generation.

What are Frontiers Research Topics?

Frontiers Research Topics are very popular trademarks of the *Frontiers journals series*: they are collections of at least ten articles, all centered on a particular subject. With their unique mix of varied contributions from Original Research to Review Articles, Frontiers Research Topics unify the most influential researchers, the latest key findings and historical advances in a hot research area.

Find out more on how to host your own Frontiers Research Topic or contribute to one as an author by contacting the Frontiers editorial office: frontiersin.org/about/contact

State-of-the-art laser spectroscopy and its applications: Volume II

Topic editors

Yufei Ma — Harbin Institute of Technology, China

Qun Hao — Beijing Institute of Technology, China

Karol Krzempek — Wrocław University of Science and Technology, Poland

Citation

Ma, Y., Hao, Q., Krzempek, K., eds. (2023). *State-of-the-art laser spectroscopy and its applications: Volume II*. Lausanne: Frontiers Media SA. doi: 10.3389/978-2-83251-412-2

Table of contents

frontiers in Physics

ORIGINAL RESEARCH
published: 29 November 2021
doi: 10.3389/fphy.2021.785540

Pulsatile Flow Measurement by a Speckle Triangle Assessment

Yuan Yuan[1], *Yong Bi*[1], *Xiao Cao Gao*[1,2] *and Wei Nan Gao*[1]*

[1]*Center of Applied Laser, Technical Institute of Physics and Chemistry, Chinese Academy of Sciences, Beijing, China,* [2]*University of Chinese Academy of Sciences, Beijing, China*

The blood flow in the coronary artery (CA) is pulsatile and much higher than that measured in the brain, retina, and skin before. Its quantitative measurement is medically significant in the coronary artery bypass grafting (CABG). Here, to the best of our knowledge, we first detect the pulsatile flow using the laser speckle contrast imaging technique. Since the factors influencing the flow rate in the CA are complex, we developed a comprehensive model, a speckle triangle assessment (STA), to assess the characteristics of the flow: the speckle flow index (SFI), mean flow index (MFI), and pulsatility index (PI). The phantom experiment was performed and found that our customized setup possessed high dynamic range of the velocity measurement with good sensitivity. It also indicated that the pulsatile flow estimated by the speckle triangle assessment is promising to obtain a more accurate assessment of a coronary artery's patency in the CABG.

Keywords: pulsatile flow measurement, laser speckle, speckle triangle assessment, speckle flow index, pulsatile index

OPEN ACCESS

Edited by:
Yufei Ma,
Harbin Institute of Technology, China

Reviewed by:
Qiang Liu,
Tsinghua University, Beijing, China
Jin Yu,
Aerospace Information Research Institute (CAS), China

***Correspondence:**
Wei Nan Gao
wngao@mail.ipc.ac.cn

Specialty section:
This article was submitted to Optics and Photonics, a section of the journal Frontiers in Physics

Received: *29 September 2021*
Accepted: *26 October 2021*
Published: *29 November 2021*

Citation:
Yuan Y, Bi Y, Gao XC and Gao WN (2021) Pulsatile Flow Measurement by a Speckle Triangle Assessment. Front. Phys. 9:785540. doi: 10.3389/fphy.2021.785540

INTRODUCTION

The heart works like a pump, performing the alternating activities of contraction and relaxation to provide energy for the blood circulation. Unfortunately, the gradually increasing coronary heart disease has been severely threatening the normal blood circulation. Medically, the coronary artery bypass grafting (CABG) is the main method for the treatment of severe coronary heart disease [1–3], where the accurate blood flow monitoring of the coronary artery before and after CABG is significant.

For the blood flow quantitative measurement, laser speckle blood flow imaging (LSBFI) as a minimally invasive full-field imaging technique has attracted extensive attention. A number of methods have been used to measure the blood flow including laser speckle contrast imaging (LSCI) [4–7], multi-exposure speckle imaging (MESI) [8, 9], dynamic light scattering imaging (DLSI) [10], time varied illumination laser speckle contrast imaging (TVI–LSCI) [11], and dynamic light scattering laser speckle contrast imaging (DLS–LSCI) [12]. These methods were performed in relatively small vessels, such as the cerebrum, the retina, and the skin. Furthermore, since those vessels are elastic and the vessels are far from the beating heart, the blood flow velocity is nearly steady.

However, the blood flow of the coronary artery (CA) is significantly different from the small vessels measured before. First, the inner diameter is much larger. Second, the flow rate is much higher. Third, the flow speed of the CA, as the secondary artery, is pulsatile. In CABG, there are multiple factors that can affect the blood flow velocity. Physiological factors like spasm in the graft or native coronary, mean arterial pressure, and run-off in the myocardium will affect the flow velocity. The size of the vessels and a patient's weight are also factors that will affect the flow rate. Technical problems such as thrombus formation, twist or kinks of the graft, or air bubbles, and misapplied

stitches will reduce the flow. Medically, all the factors are summarized to a triangle assessment model: mean flow (MF), pulsatile index (PI), and diastolic filling percentage (DF) using the transit time flow measurement (TTFM) technology [13]. Nevertheless, TTFM is limited to measure the graft other than the CA. In addition, TTFM cannot map the spatial distribution of the blood flow velocity. Since LSCI has been widely attempted in many clinical and biomedical applications during recent years [14–16], the LSCI technology is promising to detect the flow of the CA and has not been reported. In this study, to obtain a more accurate assessment of the pulsatile flow of the CA, we developed a speckle triangle assessment using the LSCI model: the speckle flow index (SFI), mean flow index (MFI), and pulsatility index (PI). The phantom experiment is performed. First, the system parameter and the scattering type of the sample were determined. Second, the measurable dynamic range and the sensitivity of velocity measurement were calibrated and improved. Finally, the three parameters were calculated by analyzing the dynamic speckle patterns to synthetically assess the different pulsatile flows.

PRINCIPLES

Laser speckle contrast imaging (LSCI) maps the two-dimensional blood flow rapid changes based on analyzing speckle contrast linked to the electric field autocorrelation time of the fluctuating speckle. The speckle contrast changes in accordance with the movement of the scatters, and it is larger at smaller velocities, and vice versa. Theoretically, the speckle contrast (K) is characterized by the standard deviation of intensity normalized with the mean intensity given as follows:

$$\boldsymbol{K = \frac{\sigma_I}{\langle I \rangle}}, \tag{1}$$

where σ_I is the standard deviation and $<I>$ is the average of the speckle intensity. Assuming that the static scattering component is completely removed, the speckle decorrelation time τ_c can be derived in the following way [17, 18]:

$$\boldsymbol{K = \left(\beta \int_0^T \frac{2\exp\left(-2\left(\frac{t}{t_c}\right)^n \right)\left(1-\frac{t}{T}\right)}{T} dt \right)^{1/2}} \tag{2}$$

where K is the speckle contrast, T is the exposure time, and the constant β is a normalization factor depending on the speckle size, pixel size, the source, and additional factors of the experimental setup. The inverse correlation time ($1/\tau_c$) is considered to be proportional to the speed of the moving particles (such as red blood cells). Hereby we term the T/τ_c as *speckle flow index* (SFI) to represent the flow velocity.

For the coronary artery (CA), factors influencing the blood flow are complex: the artery pressure, the size of the vessel, the quality of the coronary bed, and so on. Looking at only the flow velocity may not be enough. It is necessary to "see the whole picture." Here, we evaluated three parameters to assess the blood flow: *speckle flow index* (SFI), *mean flow* index (MFI), and *pulsatility index* (PI).

When the dynamic SFI distribution is averaged, the *mean flow* index (*MFI*) can be obtained. In addition, the *pulsatility index*, or PI, is defined as the difference between the maximum (SFI_{max}) and minimum flow (SFI_{min}) divided by the mean flow (*MFI*). A large difference between the maximum and minimum flow will lead to a high PI value. The expression is given as follows:

$$\boldsymbol{PI = \frac{SFI_{max} - SFI_{min}}{MFI}}. \tag{3}$$

The details on the derivation process are illustrated in **Figure 1A**: First, we convert the raw speckle images to speckle contrast images using **Eq. 1**. Second, we compute the β and the dynamic scattering type n by the dynamic light scattering imaging technique. Third, we substitute the β and n to **Eq. 2**, and the inverse correlation time (T/τ_c) is solved to represent the flow velocity. Eventually, we assess the flow with the SFI, MFI, and PI.

EXPERIMENTAL SETUP

We implemented a phantom experiment with the 1% concentration intralipid fluid in **Figure 1B**. A laser diode (λ = 785 nm) was placed on a mount with a thermoelectric cooling stage (LDM56, Thorlabs, United States). The laser spot was collimated and expanded, illuminating on a microfluidic device. The scattered speckle was recorded by the customized imaging system, which consists of an objective lens (5X, Nikon, Japan), tube lens (TTL200, Thorlabs, United States), and a high-speed camera (Mikrotron, German). Besides, a polarizer and filter were assembled to increase the contrast. In addition, the high-speed camera combined with an image acquisition card (KAYA Instrument, Israel) was used to record the dynamic scattering light. A customized software along with the data acquisition card DAQ (NI USB–6251) was written to control the timing of the step motor (Zolix, KA050, China) and synchronize it with image acquisition. The speckle size was larger than the camera pixel size [19, 20]. The CCD's exposure time was set to 26 μs with a frame rate of 2000 Hz.

The 1% concentration intralipid fluid was pumped by the step motor (**Figure 1C**) whose movement undergoes the acceleration stage and then the deceleration stage with different peak velocities. The microfluidic device is shown in **Figure 1D**. Its cross section is rectangular (50 mm × 5 mm × 0.4 mm). The dimensions were adopted to mimic the coronary artery (cross-sectional area 2 mm^2), which is usually chosen for bypass in the CABG.

RESULTS AND DISCUSSION

High Dynamic Range and Sensitivity of the Velocity Measurements

When the laser speckle contrast imaging (LSCI) technique is used to quantify the flow velocity, the range and the sensitivity of the flow speed estimation have been shown to depend on many experimental parameters such as the coherence factor β, exposure time, the static scattering, light intensity, and the camera noise [8, 21, 22]. For the phantom experiment, the

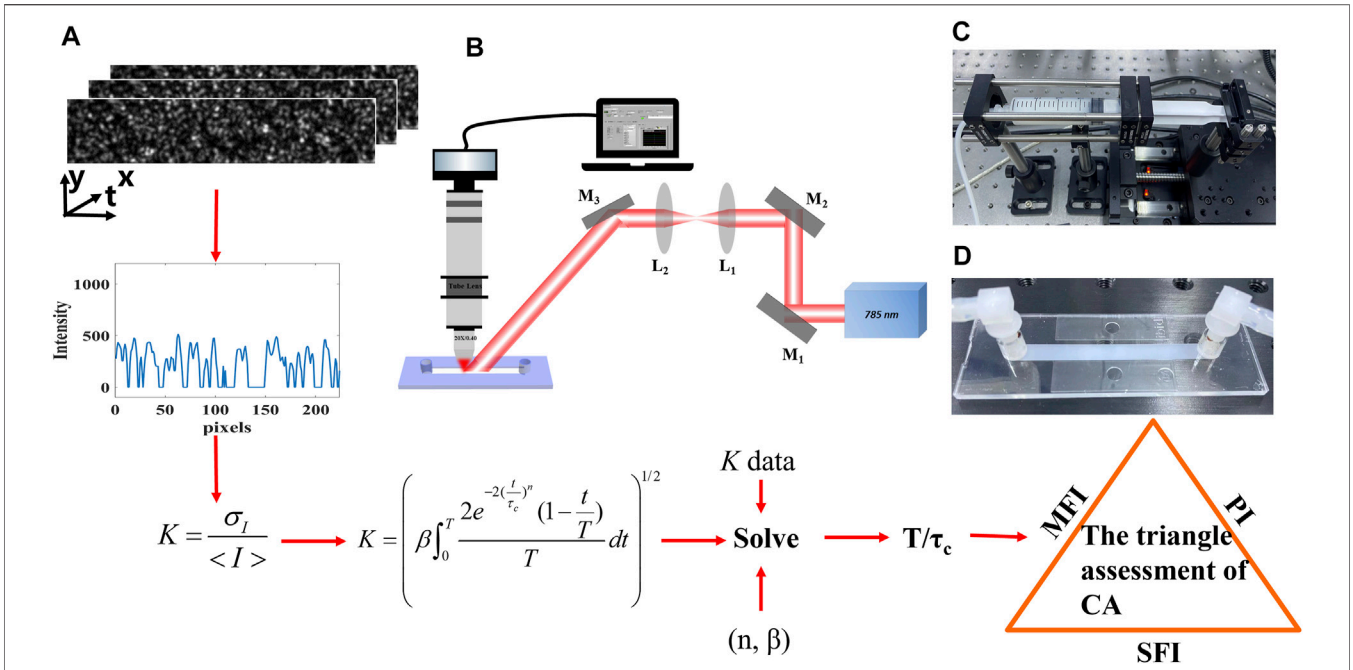

FIGURE 1 | Schematic of the experiment. **(A)** Flowchart of the model and derivation process. **(B)** Diagram of the illuminating and imaging system. M, mirror; L, lens. **(C)** Step motor. **(D)** Microfluidic device.

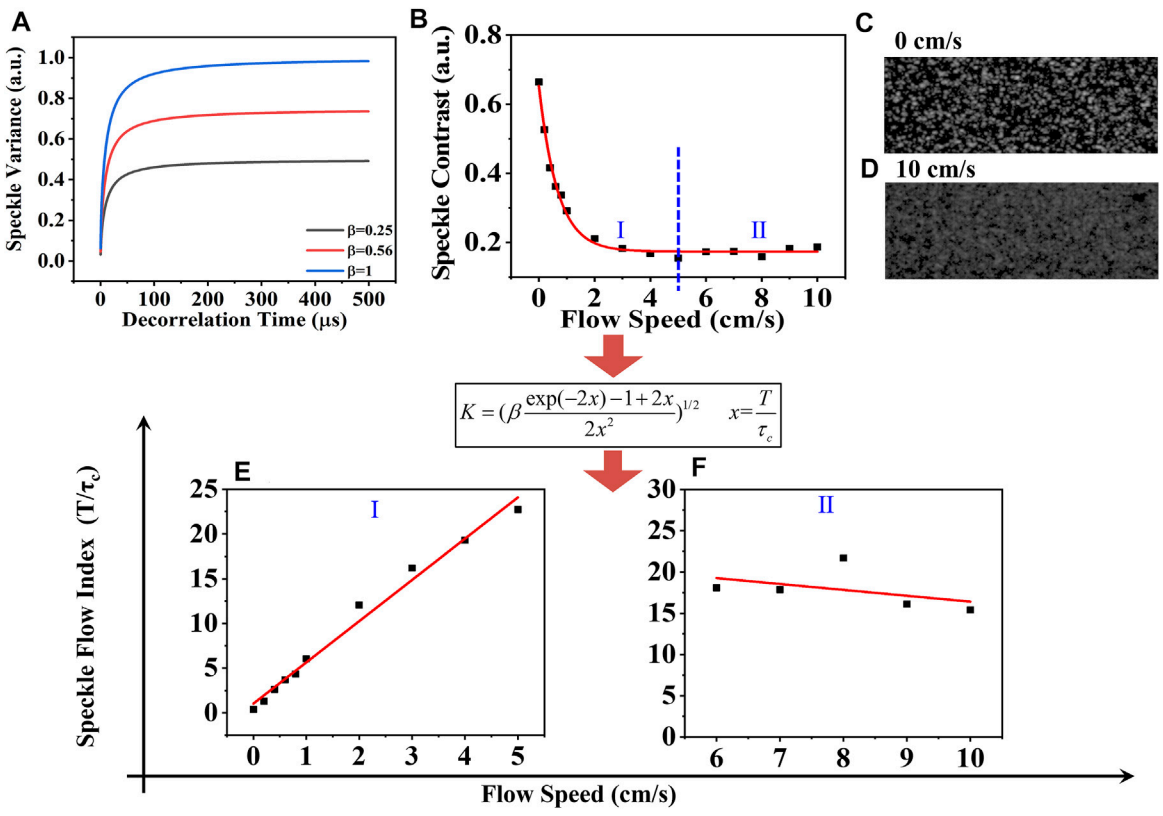

FIGURE 2 | (A) Speckle contrast as a function of the decorrelation time τ_c by **Eq. 2**. **(B)** Speckle contrast varies with the different flow velocities. **(C)** and **(D)** Speckle patterns at 0 cm/s and 10 cm/s. The relationship between the SFI and the actual velocity in the range from **(E)** 0 cm/s to 5 cm/s and **(F)** 5 cm/s to 10 cm/s. Black squares represent experimental data, and red solid lines represent fitting curve.

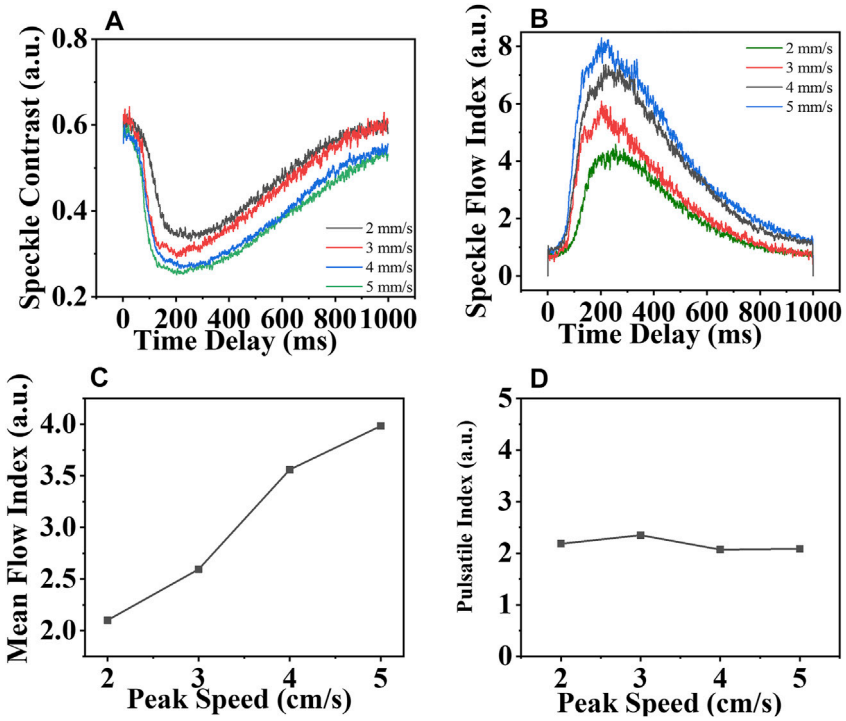

FIGURE 3 | (A) Speckle contrast and **(B)** Speckle flow index vary with time; **(C)** mean flow index and **(D)** pulsatile index varies with the pulsatile velocity whose peak velocity increases from 2 cm/s to 5 cm/s.

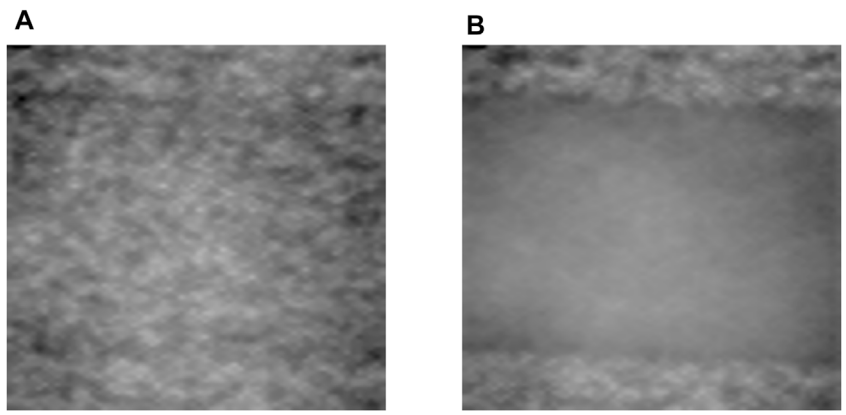

FIGURE 4 | Speckle image scattered from the sample with flow rates at **(A)** 0 cm/s and **(B)** 5 cm/s.

static scattering component was removed from the surface of the microfluidic device. Besides, since light absorption is much lower than the tissue, the intensity on the imaging plane is higher than the camera noise, and thus, a high signal-to-noise ratio can be obtained. Therefore, the effects of the light intensity and camera noise are ignored here. We focus on the first two factors.

In **Figure 2A**, we theoretically show speckle contrast K versus the speckle decorrelation time τ_c for different β values. There is a rapid increase in all three curves when τ_c is small. When β is equal to one, speckle contrast approaches 1, which means the maximum velocity range estimation can be measured with β equal to one. When β becomes smaller to 0.56 and 0.25, speckle contrast approaches 0.74 and 0.43, respectively, with a decreased measurable range. Therefore, the coherence factor β determines the range of the flow speed estimation. The β value of the setup can be obtained using two methods: Firstl, according to **Eq. 2**, when x tends to zero, the spatial speckle variance K will tend to β, so β can be obtained by computing the local speckle contrast in the corresponding spatial windows [21, 22]. Second, it can be

calculated as a fitting parameter with the dynamic scattering light imaging (DSLI) technique [10]. Here, the parameter β of our setup was determined to be 0.56 using the DSLI method in our previous work [12].

To further validate the measurable velocity range with our experimental setup, the varying flow velocity from 0 cm/s to 10 cm/s was separately driven by the step motor. The increasing step was first set to be 0.1 cm/s from 0 cm/s to 1 cm/s and then 1 cm/s from 1 cm/s to 10 cm/s. Because a long exposure time decreases the speckle contrast signal resulting in a low SNR, the exposure time here is set to be 26 μs. **Figure 2B** shows that the speckle contrast K decreased from 0.68 to 0.15 with the increasing velocity from 0 cm/s to 5 cm/s, termed as Ⅰ, and eventually fluctuated around 0.17 with further increasing velocity, termed as Ⅱ. The black squares represent the experimental data. The red line is the fitting curve, $K = 0.48e^{(-v/0.67)} + 0.17$. The speckle patterns at 0 cm/s and 10 cm/s are shown in **Figures 2C, D**.

Afterward, we computed the speckle flow index (SFI: T/τ_c) using **Eq. 2**. In **Figures 2E,F**, we show the relationship between the SFI and the actual velocity. The black squares correspond to the experimental data. The red line is the fitting curve. In part Ⅰ, one can observe the linear response range as the velocity increases from 0 cm/s to 5 cm/s, during which the fitting function is $SFI = 1.03 + 4.61v$. It was found that the sensitivity of the velocity measurements remained nearly constant. While in part Ⅱ, the SFI slightly decreased with the increasing velocity. This is because the scattered light from the static scattering medium under the microfluidic device always affects the relative flow speed estimation. Another possible reason is that the spatial correlation between the pixels exists, that is, the speckle size is larger than one pixel size, which is necessary for obtaining a larger coherent parameter β to measure lower flow velocity. A trade-off is needed here. Therefore, the maximum speed that could be obtained was greatly improved to be 5 cm/s with our setup. Although the range and the sensitivity decrease with velocity due to the presence of noise, this is the highest dynamic range of flow speed measurement, to the best of our knowledge.. Afterward, the following experiment with the velocity from 0 cm/s to 5 cm/s can be conducted.

Pulsatile Flow Measurement by a Speckle Triangle Assessment

To accurately mimic the characteristics of the pulsatile flow velocity, the step motor was programmed to drive the sample, with which the image acquisition was strictly synchronized. The peak velocities varied from 2 cm/s to 5 cm/s in the step of one. As shown in **Figure 3A**, due to the characteristics of the flow velocity, the speckle contrast decreased initially and then showed an increasing trend with time, which was termed as "time delay." Using the speckle contrast data, the pulsatile SFI (T/τ_c) was obtained using **Eq. 2** in **Figure 3B**; first rising up and then slowing down, which mimicked the characteristics of the diastolic blood flow of the coronary artery. Because the diastolic filling percentage (DF%) cannot be measured without the electrocardiogram (ECG) connected to the system in this phantom experiment, the SFI is obtained instead. Once the speckle triangle assessment is conducted with the ECG, the SFI estimation can be easily converted to DF%. Afterward, the mean flow index, MFI, was calculated, as shown in **Figure 3C**. The MFI increased with the velocity linearly. Similar to the SFI estimation, MFI is not only an indication of a compromised CA but also part of the flow information. Eventually, in **Figure 3D**, the pulsatile index (PI) was obtained using **Eq. 3**. despite the different SFI profiles and the increasing MFI, the PI remained constant at 2.17 ± 0.13. Normally, the PI value is less than 5.0 [13]. Higher or lower PI indicates the possible error in CABG, which introduces one to correct it. We contended that the blood flow changes in the physiology characterized by the speckle triangle assessment would take on more comprehensive information about the flow velocity of the CA than the MFI estimation before.

More than the quantitative assessment for the flow velocity, the LSCI technology can image the spatial distribution of the flow speed. We replaced the microscopic imaging system with an f–50 mm imaging lens for a larger viewing field. **Figure 4** shows the speckle image when the sample is flowing at 0 cm/s and 5 cm/s. It is obvious that the higher flow speed produced less speckle, making the outline of the vessel clear. That indicates the two-dimension flow distribution of the CA in CABG is possible. Because the blood vessels are covered by the tissue (static scattering component), we would further obtain the dynamic SFI map with the pulsatile speed cycle under different static scattering in our next work.

CONCLUSION

In conclusion, we presented a new model, to the best of our knowledge, speckle triangle assessment (STA), to comprehensively account for the characteristics of pulsatile flow velocity to mimic the coronary artery (CA). The calculation of the STA model is based on the laser speckle contrast imaging (LSCI) technology. The coherent parameter β of our customized speckle imaging instrument was first calibrated and measured, which enables the velocity measurements not only to be more sensitive to the velocity changes (0.1 cm/s) but also to be of much higher dynamic range (up to 5 cm/s). Coupled with the ability to discriminate flows in the pulsatile mode, the STA model, speckle flow index (SFI), mean flow index (MFI), and pulsatile index (PI) were separately computed, among which SFI helped to obtain the diastolic filling percentage (DF%) when the electrocardiogram (ECG) was connected; the MFI was used to quantify the dynamic flow speed, and the PI value was used to check possible technical errors in CABG. We contended that the STA model would enable us to obtain a more comprehensive estimation of the pulsatile flow for further animal CABG experiment, and that would be compatible with the future embedded speckle blood flow device. In addition, this customized setup can be applied to ghost imaging [23, 24] and ghost cytometry [25] in biological engineering.

DATA AVAILABILITY STATEMENT

The original contributions presented in the study are included in the article/Supplementary Material; further inquiries can be directed to the corresponding author.

AUTHOR CONTRIBUTIONS

YY was responsible for article conception, model building, code implementation, and writing; YB was responsible for guidance and model construction; XG was responsible for constructing the optical path and help take some data; and WG, corresponding author, was responsible for guidance and revision work.

FUNDING

The Special Project of Central Government Guiding Local Science and Technology Development in Beijing 2020 (Z20111000430000); Key-Area Research and Development Program of Guangdong Province (2019B010926001); and National Key Research and Development Program of China (2016YFb0402000).

REFERENCES

1. Uva MS, Neumann FJ, Ahlsson A, Alfonso F, Banning AP, Benedetto U, et al. ESC Scientific Document Group, "Guidelines on Myocardial Revascularization". *Eur Heart J* (2018) 25:4–90. doi:10.1093/eurheartj/ehy394
2. Hillis LD, SmithSmith PK, Anderson JL, Bittl JA, Bridges CR, Byrne JG, et al. 2011 ACCF/AHA Guideline for Coronary Artery Bypass Graft Surgery. A Report of the American College of Cardiology Foundation/American Heart Association Task Force on Practice Guidelines. Developed in Collaboration with the American Association for Thoracic Surgery, Society of Cardiovascular Anesthesiologists, and Society of Thoracic Surgeons. *J Am Coll Cardiol* (2011) 58(23):e123–210. doi:10.1016/j.jacc.2011.08.009
3. Paluszkiewicz L, Kwinecki P, Jemielity M, Szyszka A, Dyszkiewicz W, Cieśliński A. Myocardial Perfusion Correlates with Improvement of Systolic Function of the Left Ventricle after CABG. Dobutamine Echocardiography and Tc-99m-MIBI SPECT Study. *Eur J Cardiothorac Surg* (2002) 21(1):32–5. doi:10.1016/s1010-7940(01)01078-8
4. Goodman JW. *Speckle Phenomena in Optics: Theory and Application*. Roberts and Company Publishers. United states. (2007).
5. Duncan DD, Kirkpatrick SJ, Wang RK. Statistics of Local Speckle Contrast. *J Opt Soc Am A* (2008) 25:9–15. doi:10.1364/josaa.25.000009
6. Dunn AK, Bolay H, Moskowitz MA, Boas DA. Dynamic Imaging of Cerebral Blood Flow Using Laser Speckle. *J Cereb Blood Flow Metab* (2001) 21:195–201. doi:10.1097/00004647-200103000-00002
7. Le TM, Paul JS, Al-Nashash H, Tan A, Luft AR, Sheu FS, et al. New Insights into Image Processing of Cortical Blood Flow Monitors Using Laser Speckle Imaging. *IEEE Trans Med Imaging* (2007) 26:833–42. doi:10.1109/tmi.2007.892643
8. Parthasarathy AB, Tom WJ, Gopal A, Zhang X, Dunn AK. Robust Flow Measurement with Multi-Exposure Speckle Imaging. *Opt Express* (20081989) 16(3):1975. doi:10.1364/oe.16.001975
9. Kazmi SMS, Balial S, Dunn AK. Optimization of Camera Exposure Durations for Multi-Exposure Speckle Imaging of the Microcirculation. *Biomed Opt Express* (2014) 5(7):2157–71. doi:10.1364/boe.5.002157
10. Postnov DD, Tang J, Sefik Evren E, Erdener SE, Kılıç K, Boas DA. Dynamic Light Scattering Imaging. *Sci Adv* (2020) 6:eabc4628. doi:10.1126/sciadv.abc4628
11. Siket M, Jánoki I, Demeter K, Földesy MP, Peter F. Time Varied Illumination Laser Speckle Contrast Imaging. *Opt Lett* (2021) 46(4):713. doi:10.1364/ol.413767
12. Yuan Y, Bi Y, Gao XC, Sun MY, Gao WN. High-dynamic-range Blood Flow Rate Measurement in a Large-Diameter Vessel. *Appl Opt* (2021) 60(23):6837–42. doi:10.1364/ao.432846
13. Kieser TM, Teresa M. Graft Quality Verification in Coronary Artery Bypass Graft Surgery: How, when and Why? *Curr Opin Cardiol* (2017) 32:722–36. doi:10.1097/HCO.0000000000000452
14. Hecht N, Müller M-M, Sandow N, Pinczolits A, Vajkoczy P, Woitzik J. Infarct Prediction by Intraoperative Laser Speckle Imaging in Patients with Malignant Hemispheric Stroke. *J Cereb Blood Flow Metab* (2016) 36:1022–32. doi:10.1177/0271678x15612487
15. Ringkamp M, Wooten M, Carson BS, Lim M, Hartke T, Guarnieri M. Laser Speckle Imaging to Improve Clinical Outcomes for Patients with Trigeminal Neuralgia Undergoing Radiofrequency Thermocoagulation. *Jns* (2016) 124:422–8. doi:10.3171/2015.1.jns14408
16. Milstein DMJ, Ince C, Gisbertz SS, Boateng KB, Geerts BF, Hollmann MW, et al. Laser Speckle Contrast Imaging Identifies Ischemic Areas on Gastric Tube Reconstructions Following Esophagectomy. *Medicine* (2016) 95:e3875. doi:10.1097/md.0000000000003875
17. Boas DA, Dunn AK. Laser Speckle Contrast Imaging in Biomedical Optics. *J Biomed Opt* (2010) 15(1):011109. doi:10.1117/1.3285504
18. Bandyopadhyay R, Gittings AS, Suh SS, Dixon PK, Durian DJ. Speckle-visibility Spectroscopy: A Tool to Study Time-Varying Dynamics. *Rev Scientific Instr* (2005) 76:093110. doi:10.1063/1.2037987
19. Kirkpatrick SJ, Duncan DD, Wells-Gray EM. Detrimental Effects of Speckle-Pixel Size Matching in Laser Speckle Contrast Imaging. *Opt Lett* (2008) 33:2886–8. doi:10.1364/ol.33.002886
20. Yuan Y, Bi Y, Sun MY, WangWang DZ, WangWang DD, Gao WN, et al. Speckle Evaluation in Laser Display: From Speckle Contrast to Speckle Influence Degree. *Opt Commun* (2020) 454:124405. doi:10.1016/j.optcom.2019.124405
21. Wang Y, Wen D, Chen X, Huang Q, Chen M, Lu J, et al. Improving the Estimation of Flow Speed for Laser Speckle Imaging with Single Exposure Time. *Opt Lett* (2017) 42:57. doi:10.1364/ol.42.000057
22. Wang Y, Lv W, Chen X, Lu J, Li P. Improving the Sensitivity of Velocity Measurements in Laser Speckle Contrast Imaging Using a Noise Correction Method. *Opt Lett* (2017) 42:4655. doi:10.1364/ol.42.004655
23. Yu Hang H, Zhang AX, Fei Li M, Huan YY, Quan BG, Zhang Li D. Ling an Wu and Li Ming Chen, "High-Resolution Sub-sampling Incoherent X–ray Imaging with a Single-Pixel Detector". *APL Photon* (2020) 5:056102.
24. He Y-H, Wu L-A, Chen L-M, Wang B-B. Tabletop X-ray Ghost Imaging with Ultra-low Radiation. *Optica* (2018) 5(4):374. doi:10.1364/optica.5.000374
25. Ota S, Horisaki R, Kawamura Y, Ugawa M, Sato I, Hashimoto K, et al. Ghost Cytometry. *Science* (2018) 360:1246–51. doi:10.1126/science.aan0096

Conflict of Interest: The authors declare that the research was conducted in the absence of any commercial or financial relationships that could be construed as a potential conflict of interest.

Publisher's Note: All claims expressed in this article are solely those of the authors and do not necessarily represent those of their affiliated organizations, or those of the publisher, the editors, and the reviewers. Any product that may be evaluated in this article, or claim that may be made by its manufacturer, is not guaranteed or endorsed by the publisher.

frontiers in Physics

ORIGINAL RESEARCH
published: 21 December 2021
doi: 10.3389/fphy.2021.809049

Recent Progress and Development Trend of Self-Sweeping Fiber Laser

Zhenzhong Zuo[1,2], *Kaile Wang*[1,2], *Haowei Chen*[1,2,3], *Baole Lu*[1,2,3]* *and Jintao Bai*[1,2,3]*

[1]State Key Laboratory of Energy Photon-Technology in Western China, Shaanxi Engineering Technology Research Center for Solid State Lasers and Application, Northwest University, Xi'an, China, [2]Institute of Photonics and Photon-Technology, Northwest University, Xi'an, China, [3]International Collaborative Center on Photoelectric Technology and Nano Functional Materials, Provincial Key Laboratory of Photo-Electronic Technology, Northwest University, Xi'an, China

Since 2011, when Kir'yanov et al. first reported a new wavelength self-sweeping ytterbium-doped fiber laser that does not rely on any tuning element but only on the dynamic induced grating generated in the gain fiber by the standing wave resonator structure, the self-sweeping effect based on fiber waveguides has been extensively studied, leading to great progress in fundamental physics and other applications of self-sweeping fiber lasers. Different doped fiber lasers have not only achieved the self-sweeping effect, but also observed new phenomena such as anomalous self-sweeping and continuous pulses. Due to their remarkable spectral and pulsed characteristics, self-sweeping fiber lasers have been widely used in spectral detection, fiber sensing and short pulse synthesis. In this paper, we will introduce the classification of different doped self-sweeping fiber lasers, summarize their different implementations, and introduce their self-sweeping laws, pulse characteristics, recent progress of applications and future development prospects.

Keywords: fiber laser, self-sweeping effect, wavelength tunable, spectral characteristics, pulse dynamic

OPEN ACCESS

Edited by:
Yufei Ma,
Harbin Institute of Technology, China

Reviewed by:
Pavel Honzatko,
Institute of Radio Engineering and Electronics (ASCR), Czechia
Bo Guo,
Harbin Engineering University, China

***Correspondence:**
Baole Lu
lubaole1123@163.com
Jintao Bai
baijt@nwu.edu.cn

Specialty section:
This article was submitted to Optics and Photonics, a section of the journal Frontiers in Physics

Received: *04 November 2021*
Accepted: *30 November 2021*
Published: *21 December 2021*

Citation:
Zuo Z, Wang K, Chen H, Lu B and Bai J (2021) Recent Progress and Development Trend of Self-Sweeping Fiber Laser. Front. Phys. 9:809049. doi: 10.3389/fphy.2021.809049

INTRODUCTION

Tunable fiber lasers are valuable for optical communication, optical sensing, and spectral synthesis due to their flexible wavelength tuning properties [1–5]. Among them, swept-frequency lasers with periodic wavelength variation using an optical filter with an electric driver are widely used in fiber optic sensing, biomedicine, and spectral detection. However, the development of swept-frequency fiber lasers is limited by the influence of swept-frequency devices [6–8] and the output performance of the lasers themselves, and in recent years, a new swept-frequency fiber laser based on the self-sweeping effect has attracted a lot of attention from researchers. The self-sweeping effect refers to the spontaneous, stable and periodic tuning process of the laser output wavelength in a certain spectral range, and does not require any complex tunable devices or electric drives. It is attributed to the spatial hole-burning (SHB) effect of the gain fiber in the standing wave field [9], which forms a periodic light intensity distribution, and then the particle number inversion causes a refractive index change, which induces a grating-like structure along the gain fiber, i.e., a "gain grating and a phase grating" [10–12], where the dynamic change in the net gain of the grating resulted in a shift of the spectrum. The self-sweeping effect was first reported in 1962 [13], where a periodic shift in wavelength was observed in a ruby laser. Half a century later, based on the excellent waveguide medium of optical fiber, Ref.[14] in Russia successfully observed the self-sweeping effect in an ytterbium-doped fiber laser and named it as self-sweeping fiber laser.

Since the formal report on self-sweeping ytterbium-doped fiber lasers in 2011, they have undergone rapid development in the past decade. So far, based on the typical Fabry-Perot (F-P) linear resonator structure, the self-sweeping effect has been observed in different doped fiber lasers

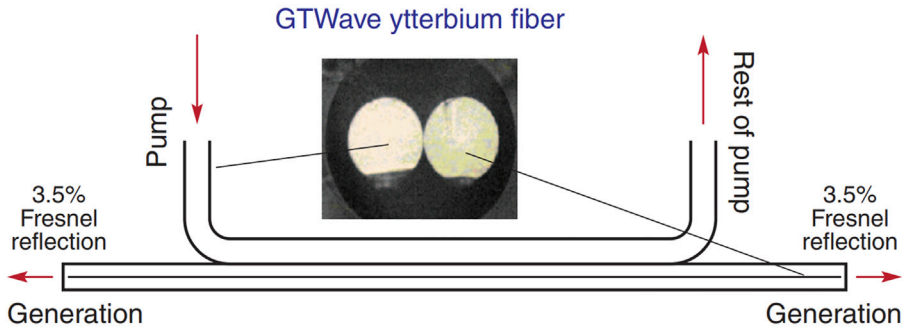

FIGURE 1 | Experimental setup of Yb-doped fiber laser generating self-sweeping effect for the first time [14]. (Inset) A cross-sectional view of a GT-Wave fiber.

such as ytterbium, erbium, thulium, thulium-holmium, bismuth, holmium and neodymium. In addition, self-sweeping ranges up to 45 nm have been obtained in ytterbium-doped fiber lasers by temperature-controlled Lyot filters; single-frequency self-sweeping fiber lasers have been achieved by limiting the intracavity longitudinal mode number by adjusting the resonator length; and normal as well as reverse self-sweeping effects have been defined according to the wavelength shift direction in hybrid self-sweeping fiber lasers. Later, both bi-directional and unidirectional fiber ring resonator structures were used to realize self-sweeping fiber lasers, while the time-domain dynamics evolved from the pulsed state to the continuous wave state. The rapid development of self-sweeping fiber lasers has promoted their applications in various research fields such as spectral detection and analysis, pulsed coherent synthesis, and optical sensing, and has become one of the research hotspots for fiber lasers.

Combined with the research work of our team in self-sweeping fiber laser, this paper summarizes the research status and latest application progress of self-sweeping fiber laser at home and abroad from four aspects: doped fiber types, pulse intensity dynamics, basic law of self-sweeping and application of self-sweeping fiber laser, and looks forward to its future development direction.

DIVERSELY DOPED SELF-SWEEPING FIBER LASERS

Ytterbium-Doped Self-Sweeping Fiber Laser

Linear Resonator

In 2011, the Russian Kir'yanov' research group [14] obtained the first ytterbium-doped self-sweeping fiber laser using the F-P linear resonator structure. The principle of this experimental setup is shown in **Figure 1**. The gain medium of the laser is a special section of GT-Wave ytterbium-doped fiber with the presence of two core channels for the transmission of pump light and signal light, respectively. The pump light is pumped into the ytterbium-doped fiber to produce an excited amplified spontaneous emission (ASE) spectrum into the other channel of the fiber. The resonant cavity of the laser consists of two flat tangent ports of the fiber providing 3.5% Fresnel reflection on the left and right side, and the interference of the standing wave field inside the resonator forms a SHB effect producing a dynamic grating-induced self-sweeping effect.

The tuning of the output spectrum in the range of 1,081 nm–1087 nm was observed at pump powers of 1.4, 1.7, 2.0, 2.3, 2.6, and 2.9 W, respectively. When the pump power is increased from 1.4 to 2.6 W, the self-sweeping spectral range gradually increases to 7 nm, but further increasing the pump power, the stable self-sweeping spectrum is replaced by a random chaotic spectrum due to the presence of a very pronounced stimulated Raman scattering (SRS) signal at higher pump power that destroys the conditions for the stable generation of the self-sweeping effect.

Following the report by Kir'yanov's group, the self-sweeping effect in a typical F-P linear resonator structure was also achieved in ytterbium-doped fiber laser by Lobach's group [15] at Novosibirsk University, Russia, in 2011, with the experimental setup shown in **Figure 2A**, where the high reflectance mirror is formed by the fiber loop mirror (FLM), while the output mirror is formed by the Fresnel reflection from a perpendicularly cleaved fiber facet. The polarization controller (PC) is adjusted for a self-sweeping range up to 16 nm (1,062 nm–1078 nm) and a self-sweeping rate range of 0.5 nm/s-16 nm/s, as shown in **Figure 2B**. After replacing the FLM with a fiber bragg grating (FBG) with a central wavelength of 1,066 nm, the maximum self-sweeping range is reduced to 0.1 nm due to the bandwidth limitation of the FBG. However, due to the significant emission loss of the laser in **Figure 2A**, this greatly affects the stability of the self-sweeping phenomenon. To solve this problem, in 2012 they [16] used an all-fiber structure and obtained a stable self-sweeping range of about 8–10 nm, where the self-sweeping range was up to 16 nm under specific PC modulation. In addition, the linewidth of the self-sweeping fiber laser was very narrow, about 0.3 pm, which was much smaller than the 0.1 nm linewidth obtained by Ref.[14]. In 2013, Ref. [17] extended the self-sweeping band to 1,087 nm–1094 nm with a slow self-sweeping rate of 0.24 nm/s.

Based on the experiments of Lobach et al. in 2013, Peterka's team [18] from the Czech Academy of Sciences obtained the self-sweeping effect near the 1,080 nm band by adjusting the current and shell temperature of the intracavity laser diode (LD) in the self-sweeping range of 2 nm/s-6 nm/s, which can reach 7 nm when the

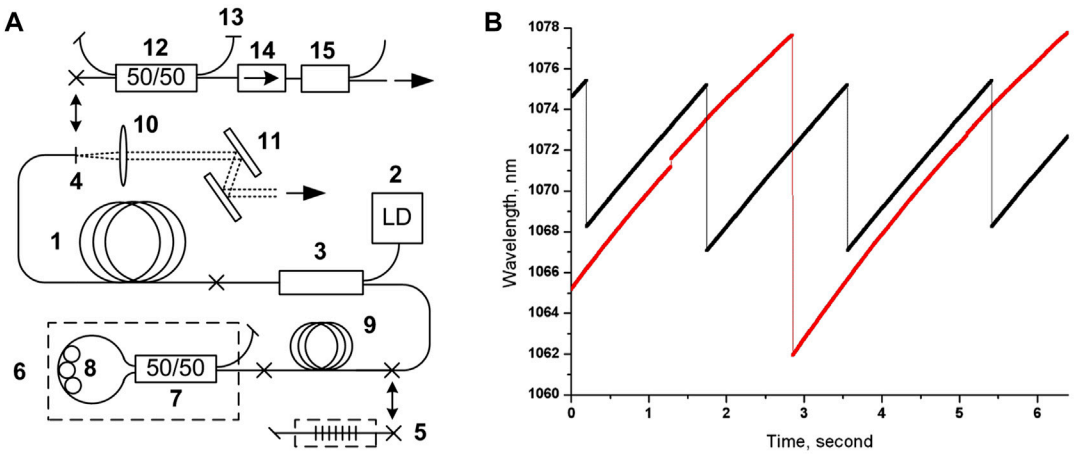

FIGURE 2 | (A) The experimental setup of a typical F-P cavity Yb-doped self-sweeping fiber laser [15] (1 Yb-doped fiber; 2 Laser diode; 3 Pump combiner; 4 Cleaved; 5 Fiber bragg grating; 6 Fiber loop mirror; 7 50/50 coupler; 8 Polarization controller; 9 Single-mode fiber; 10 Aspherical lens; 11 Dichromatic mirror; 12 50/50 coupler; 13 Cleaved; 14 Isolator; 15 Coupler); **(B)** FLM cavity spectral dynamic (Red-black curve corresponding to different modulations of PC).

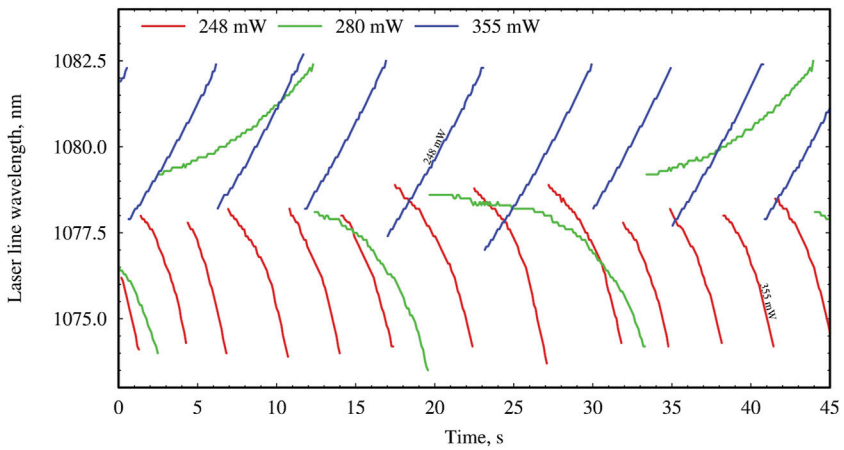

FIGURE 3 | Three spectral dynamics observed by Yb-doped self-sweeping fiber laser in 2017 [22]. Normal self-sweeping (blue curve); Mixed self-sweeping (green curve); Reverse self-sweeping (red curve).

LD shell temperature is 35°C. In 2016, the Lobach's team [19] obtained a self-sweeping in a wavelength range of up to 18 nm with a central wavelength adjustable from 1,025 nm to 1,070 nm by varying the length of the gain fiber. The self-sweeping range can be tuned to below 30 nm by simultaneously varying the resonator loss and pump power. In addition, the maximum self-sweeping range can be up to 18 nm by adjusting the temperature of the gain fiber or the pump source, respectively. In the same year, the group [20] achieved a self-sweeping range of 1,058–1076 nm with a self-sweeping rate of 0.8 nm/s and an output power greater than 50 mW for an ytterbium-doped self-sweeping fiber laser. In 2017, they [21] obtained a self-swept spectral tuning of 1,050–1070 nm at a pump power of 2 W with a self-sweeping rate of about 1 nm/s and increased the average and peak output power to about 100 and 400 mW.

In 2017, Ref. [22] achieved the first reverse self-sweeping effect of an ytterbium-doped fiber laser. In this experiment, the wavelength sweeping direction was divided into two categories, the normal self-sweeping direction, which refers to the shift of the output wavelength from short to long wavelengths, and the reverse self-sweeping direction, which refers to the shift of the output wavelength from long to short wavelengths. The ytterbium-doped fiber laser has three types of self-sweeping output spectral dynamics with pump power: normal self-sweeping (blue curve in **Figure 3**), reverse self-sweeping (red curve in **Figure 3**) and hybrid self-sweeping (unstable state where both normal and reverse self-sweeping exist, green curve in **Figure 3**). The normal self-sweeping range was 2.5–6.6 nm with a sweeping rate of 0.3 nm/s-6.6 nm/s, and the reverse self-scan range was 4.3–5.3 nm with a rate of 0.5–1.7 nm/s.

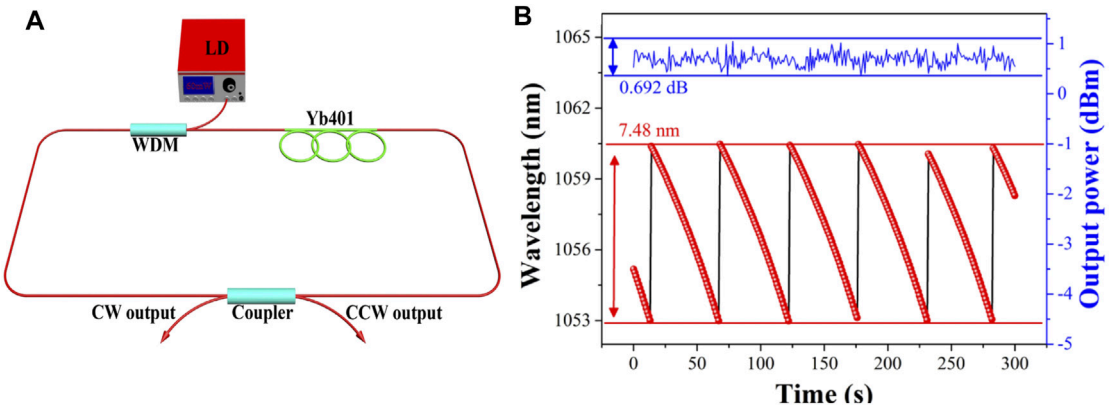

FIGURE 4 | (A) Experimental setup of all-polarization-maintaining bidirectional ring resonator Yb-doped self-sweeping fiber laser [25]; **(B)** Self-sweeping spectral dynamics and output power stability at pump power of 65 mW.

Bidirectional Fiber Ring Resonator

In 2018, Sze Yun Set's group [23] at the University of Tokyo, Japan, achieved the first bidirectional fiber ring resonator self-sweeping fiber laser using thulium-doped fiber as the gain medium. In 2019, our group [24] achieved the reverse self-sweeping effect near the 1.037 μm band in a bidirectional fiber ring resonator ytterbium-doped fiber laser with a single-mode structure. The laser achieved a self-scan range of 2.75 nm (1,038.98–1036.23 nm) with an average self-sweeping rate of 0.38 nm/s for output spectral tuning at a pump power of 60 mW. The output power in the stable self-sweeping state fluctuates by about 2 dB due to the influence of the external environment and the gain difference in the self-sweeping range.

Due to the narrow self-sweeping range generated by the single-mode structured bi-directional resonator ytterbium-doped self-sweeping fiber laser and the high output fluctuations due to the external environment, it is difficult to observe the full characteristics of the self-sweeping effect. To solve this problem, in 2020, our group [25] used an all-polarization-maintaining resonator structure and two different coupling ratios (50/50 and 10/90) of the output coupler to achieve a comparative analysis of the self-sweeping effect, and the experimental setup is shown in **Figure 4A**. In the experiments, the self-scan range obtained with the output coupler of 50/50 coupling ratio was 7.48 nm at a pump power of 65 mW (red line in **Figure 4B**), the output power fluctuation was about 0.692 dB (blue line in **Figure 4B**), and the self-sweeping rate ranged from 7.8 nm/min to 9.48 nm/min. When the output coupler of 10/90 was used in the resonator, the self-sweeping rate and the pump power range could be effectively reduced to as low as 0.016 nm/min. The reason for this reduction is that the microsecond pulses generated by the latter are often spaced at larger intervals.

Based on previous experiments, a bidirectional resonator ytterbium-doped self-sweeping fiber laser based on intracavity loss tuning brought by bending the fiber circle was investigated by our group [26] in 2021. The self-sweeping was obtained over intervals in the range 4–8 nm with a sweeping rate of 0.19–0.43 nm/s while the central wavelength was adjusted in a range of 1,055.6 nm–1034.6 nm by varying the bending loss. This experiment shows that the self-sweeping rate increases as the diameter of the bent fiber circle decreases, and the self-sweeping range tends to be further towards shorter wavelengths. This simple wavelength tuning method not only saves cost, but also helps to improve the sweeping performance of the self-sweeping fiber laser and expand its application in the field of spectral detection.

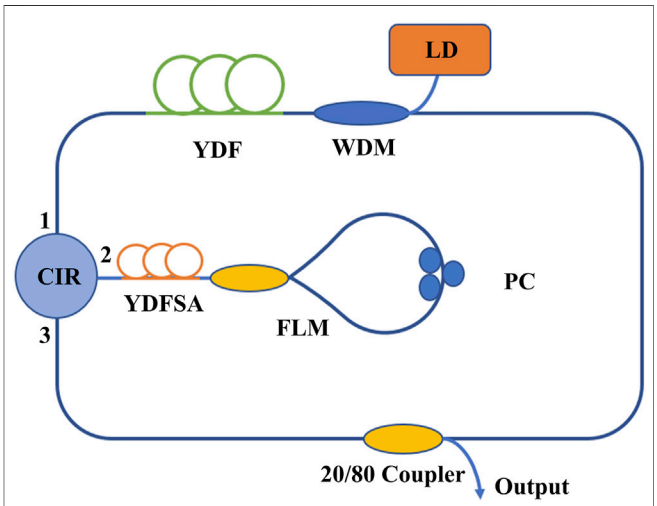

FIGURE 5 | Experimental setup of Yb-doped self-sweeping fiber laser with unidirectional ring cavity based on a fiber saturable absorber [28].

Unidirectional Fiber Ring Resonator

From the self-sweeping fiber lasers reported in recent years, it is known that the self-sweeping effect depends on the dynamic grating formed by the standing wave field in the resonator, whether in a linear resonator or a bidirectional fiber ring resonator structure, and based on this principle, we can try to

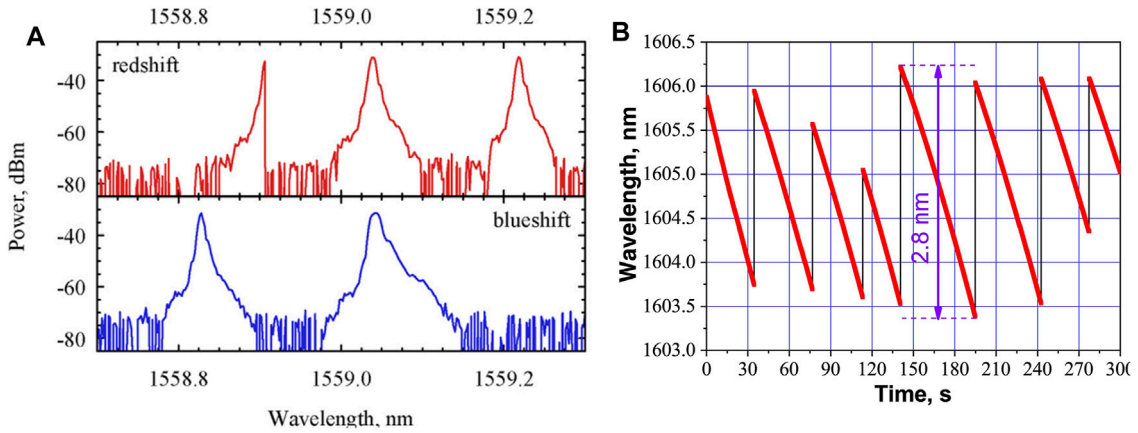

FIGURE 6 | Self-sweeping spectrum dynamics of Er-doped self-sweeping fiber laser. **(A)** Wavelength red-shift and blue-shift self-sweeping [29]; **(B)** Reverse self-sweeping [30].

form a dynamic grating in the fiber saturable absorber [27] to realize the self-sweeping effect.

In 2021, our group [28] introduced a 1.8 m-long section of ytterbium-doped fiber as a fiber saturable absorber into the laser resonator through a circulator (CIR), and the experimental setup is shown in **Figure 5**. The ytterbium-doped fiber absorbs light in two directions to form a standing wave, forming a position-dependent periodic refractive index change, i.e., a grating, which in turn produces a normal self-sweeping effect. Also because of its filtering effect, as a tracking filter, the appearance of the laser's central output wavelength is also very dependent on it. The experiment obtained a self-sweeping spectral tuning of 1.5–4.85 nm with a self-sweeping rate of 0.145–0.284 nm/s. This work both extends the application of fiber saturable absorbers and provides a new direction for the research of self-sweeping fiber lasers.

Erbium-Doped Self-Sweeping Fiber Laser

Based on a typical F-P linear resonator structure, an erbium-doped self-sweeping fiber laser was first reported by Peterka's group [29] in 2018, where mean wavelength was adjusted by a tunable filter in a range 1.54–1.57 μm. A 30 cm section of thulium-doped fiber was fused in the resonator as a passive Q-tuned switch, but the fiber did not achieve huge pulses like saturable absorbers, which exhibited a lower saturation intensity than expected by Peterka et al. Only the concomitant effect of self-sweeping-self-pulse effect-was achieved. Since the signal optical power in the thulium-doped fiber is very small and the inversion of the excited collective number of thulium ions is negligible, Peterka et al. suggest that the SHB effect may not occur in the thulium-doped fiber as in the erbium-doped fiber to form a dynamic grating to generate self-sweeping. The red and blue shifts of wavelengths were observed by the conditioning PC, as shown in **Figure 6A**. The self-sweeping ranges were 0.37 and 0.43 nm, respectively, and the average self-sweeping rates were 2.85 nm/s and 1.48 nm/s, respectively. In 2020, Lobach's group [30] implemented an erbium-doped self-sweeping fiber laser in the 1,605 nm band and extended the self-sweeping range to 2.8 nm, as shown in **Figure 6B**.

Thulium-Doped Self-Sweeping Fiber Laser

Linear Resonator

In 2018, the Lobach research group [31] achieved a stable self-sweeping phenomenon in the 1.92 μm band for the first time using a thulium-doped fiber as a laser gain medium with a self-sweeping range of 21.5 nm and even 26 nm at some moments. They also reported [32] a hybrid thulium-doped self-sweeping fiber laser in 2019. This laser obtained three self-sweeping spectral dynamics in the presence of pump power: reverse self-sweeping (**Figures 7A,B**), wavelength stop state (**Figure 7C**, the wavelength can be stopped at any value in the 1912–1923 nm range) and normal self-sweeping (**Figures 7D,E**). The results show that any wavelength output in a specific spectral range of about 10 nm can be obtained by appropriately varying the pump power, which may contribute to the development and practical application of self-sweeping fiber lasers.

Bidirectional Fiber Ring Resonator

In 2018, a bidirectional fiber ring resonator thulium-doped self-sweeping fiber laser was first proposed by Sze Yun Set's team at the University of Tokyo, Japan [23], and its experimental principle is shown in **Figure 8**. In the absence of any direction-selective elements such as optical isolators in the laser resonator, the ASE spectrum generated by a pumped thulium-doped fiber amplified by an erbium-doped optical amplifier (EDFA) propagates CW and CCW along the resonator shape, creating a standing wave field in the thulium-doped fiber, generating a SHB effect and generating a dynamic grating for self-sweeping. The laser achieved reverse self-sweeping near the 1970 nm band in the output spectral range from 10 to 15 nm. In 2019, the research group [33] added PC to the resonator and obtained the bi-directional self-sweeping effect in the 1.95 μm band by twisting the PC. This experiment showed that adjusting the PC could control the self-sweeping rate, and

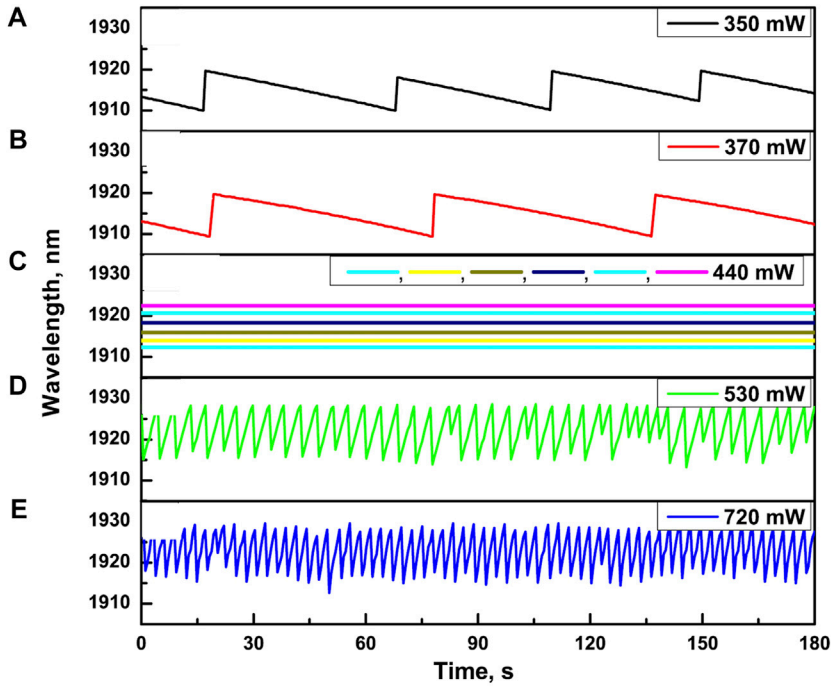

FIGURE 7 | Self-sweeping spectrum dynamics of hybrid Tm-doped self-sweeping fiber laser [32]. **(A)**, **(B)** Reverse self-sweeping; **(C)** Wavelength stop state; **(D)**, **(E)** Normal self-sweeping.

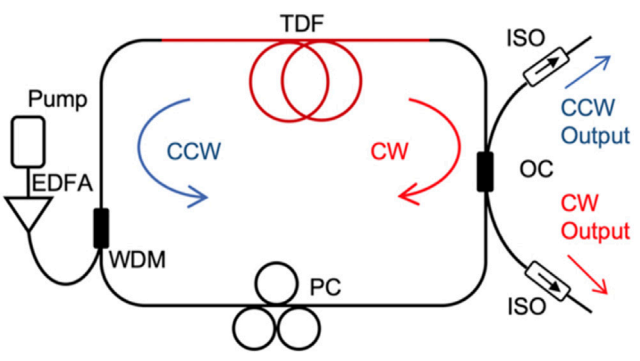

FIGURE 8 | Experimental setup of bidirectional Tm-doped self-sweeping fiber laser [23].

even it could be adjusted to zero to obtain a fixed wavelength output.

Other Doped Self-Sweeping Fiber Lasers

So far, self-sweeping effect has been observed not only in the most typical three bands of ytterbium-doped, erbium-doped, and thulium-doped fiber lasers, but also in different bands based on typical F-P linear cavities using other doped fibers as gain media.

In 2013, Pu Zhou's group at the National University of Defense Technology [34] first achieved the self-sweeping effect of thulium-holmium co-doped fiber lasers in the 1.9 μm band with a self-sweeping range between 4 and 17 nm and a self-sweeping rate between 0.4 nm/s and 1.5 nm/s. In 2015, Ref. [35] first investigated bismuth-doped self-sweeping fiber lasers in the 1,460 nm central wavelength band obtained a maximum self-sweeping range of 10 nm with a self-sweeping rate of 0.75 nm/s. In 2017, Peterka's group achieved and extended the self-sweeping band of holmium-doped self-sweeping fiber laser to about 2.1 μm for the first time, obtaining self-sweeping ranges of about 4 nm [36] and 6 nm [37].

In 2021, Ref. [38] found that holmium-doped fibers are unstable in the self-sweeping state due to large pump absorption and large quantum defects between the pump and laser radiation that make the fiber heating uneven. Then they solved the fiber heating problem by using full bias-preserving elements and gaining fiber water cooling to obtain stable operation of the holmium-doped self-sweeping fiber laser. The laser achieves a stable self-scan of 10 nm in the 2.1 μm band with a self-sweeping rate of 2–8 nm/s and an average output power of more than 200 mW. The sweeping range does not exceed 7 nm (2,108–2101 nm) when the 7 m passive fiber is removed, or the maximum spectral range can be reduced to 7 nm by shortening the gain fiber to 0.8 m. The first neodymium-doped self-sweeping fiber laser was realized by Lobach's group [39] in 2019. Two sections of bias-preserving fiber with lengths of 21 and 33 cm were fused in the resonator as Lyot filters for additional spectral selection. The laser obtained the self-sweeping effect near the 1.06 and 0.93 μm bands, respectively. The self-scan spectra was tuned up to 1.8 nm and the self-sweeping rate was up to 9 nm/s.

TABLE 1 | Summary of parametric studies of various doped self-sweeping fiber lasers.

Resonator gain media	Sweeping direction	Wavelength range (nm)	Sweeping range (nm)	Sweeping rate (nm/s)	References
Linear (YDF)	Normal	1,081–1,087	7 (maximum)	——	[14]
Linear (YDF)	Normal	1,062–1,078	0.1–16	0.5–16	[15]
Linear (YDF)	Normal	1,028–1,080	30 (maximum)	——	[19]
Linear (YDF)	Normal	1,076–1,083	2.5–6.8	0.3–6.6	[22]
	Reverse	1,073–1,079	4.3–5.3	0.5–1.7	
Ring resonator (YDF)	Reverse	1,060.468–1,052.984	~7.48	0.158–0.13	[25]
		1,070.448–1,066.026	——	0.0018–0.0002	
Ring resonator (YDF)	Reverse	1,055.6–1,034.6	——	0.19–0.43	[26]
Ring resonator (YDF)	Reverse	——	1.5–4.85	0.145–0.284	[28]
Linear (EDF)	Normal	1,540–1,570	0.37	~2.85	[29]
	Reverse		0.43	~1.48	
Linear (EDF)	Reverse	1,605	0.7–2.8	0.05 (mimimum)	[30]
Linear (TDF)	Normal	1920	26 (maximum)	——	[31]
	Reverse				
	Wavelength stopping				
Ring resonator (TDF)	Reverse	1950	~15	~0.2	[33]
Linear (THDF)	Normal	1900	4–17	0.4–1.5	[34]
Linear (BDF)	Normal	1,460	~10	~0.75	[35]
Linear (HDF)	Normal	2,100	~10	2–8	[38]
Linear (NDF)	Normal	1,060	1.8 (maximum)	9 (mimimum)	[39]
		930	~0.2	——	

Table 1 summarizes the research results of the self-sweeping fiber lasers presented in *Diversely Doped Self-Sweeping Fiber Lasers*, and provides a comparative analysis of their self-sweeping range, self-sweeping rate, and self-sweeping direction. As can be seen from the table, the reported research results cover the self-scan band from near 1 μm to near 2.1 μm, and the resonator structure involves both linear and ring resonators.

PULSE TYPE OF SELF-SWEEPING FIBER LASER

The pulse intensity dynamics of the self-sweeping effect is one of the distinguishing features of self-sweeping fiber lasers. Based on the reported self-sweeping literature, it is known that fiber lasers generate self-sweeping by forming dynamic gain or phase gratings in the gain fiber. Since there are few longitudinal modes in the laser output, the pulse sequence is modulated in an inter-mode beat frequency manner [40] and is associated with relaxation oscillations, which cause self-pulse effects [41] and exhibit microsecond pulse sequences. Currently, a variety of microsecond pulse sequences have been observed in doped self-sweeping fiber lasers, which can be broadly classified into the following four categories: typical microsecond pulse sequences, discontinuous pulse sequences, quasi-continuous pulse sequences, and novel pulse sequences.

Typical Microsecond Pulse Sequence

Microsecond pulse sequences are typical pulse intensity time domain dynamics of self-sweeping fiber lasers. Most of the doped (ytterbium-doped, thulium-doped, holmium-doped, thulium-holmium co-doped) self-sweeping fiber lasers are obtained with irregular microsecond pulse sequences, as shown in **Figure 9A**. Significant beat frequency modulation is observed after amplification of each pulse, as shown in the inset in **Figure 9A**. By limiting the number of longitudinal modes in the resonator by adjusting the laser resonator length, a single-frequency self-sweeping fiber laser can be obtained. Compared with a self-sweeping fiber laser operating with multiple longitudinal modes, the microsecond pulse sequence obtained from a single-frequency self-sweeping fiber laser has a more pronounced periodic, regular nature. **Figure 9B** shows a typical microsecond pulse sequence of a single-frequency self-sweeping fiber laser [39]. **Figure 9C** shows its radio frequency spectrum (RF), which consists mainly of two peaks corresponding to the main (frequency near 0 MHz) mode and the nearest neighbor (frequency of 7.8 MHz) mode, respectively. In the RF spectrum, the intensity of the nearest neighbor mode is 10 dB smaller than that of the main mode. Based on these results, the researchers concluded that each pulse actually consists of a single longitudinal mode, which was also confirmed by using the delayed self-heterodyne method [42].

Discontinuous Pulse Sequence

In 2020, our group [25] observed the reverse self-sweeping effect in a bidirectional fiber ring resonator ytterbium-doped self-sweeping fiber laser, in which an ultra-slow self-sweeping operation was achieved with a 10/90 coupling ratio coupler in the resonator and a discontinuous pulse sequence was observed. **Figure 10A** shows the pulse intensity signal in the 30 ms range recorded at a pump power of 32 mW, and a group of pulses can be observed near 1 ms. The pulse intensity signal shows that the pulse signal is discontinuous under the ultra-slow self-scan operation. When this set of pulses is amplified, the average pulse repetition frequency of the microsecond pulse sequence

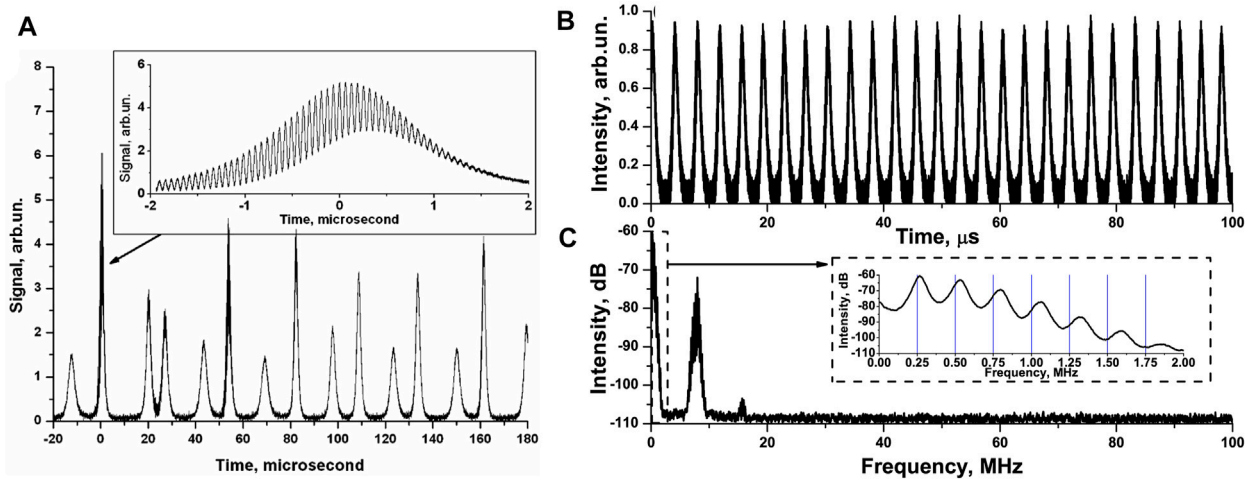

FIGURE 9 | (A) Typical irregular microsecond pulse sequences [15] (Inset) Beat modulation; **(B)** Typical single-frequency pulse sequences [39]; **(C)** RF spectrum of single-frequency self-sweeping fiber laser [39].

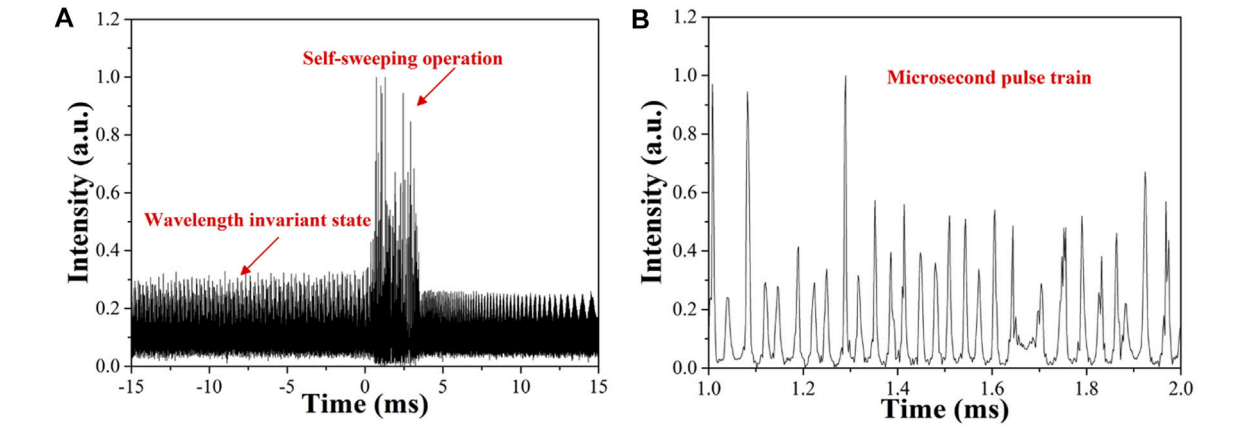

FIGURE 10 | Pulse intensity dynamics under ultra-slow self-sweeping operation [25]. **(A)** Discontinuous pulse signal within 30 ms; **(B)** A continuous microsecond pulse sequence in a magnified view within 1 ms

is 28 kHz. At this point, the microsecond pulse signal in **Figure 10B** can be considered to represent the normal self-scan operation, and the rest of the pulse signals can be considered as wavelength-invariant states. Super-slow self-scan is also caused by large intervals (hundreds or tens of milliseconds) of microsecond pulse sets.

Quasi-Continuous Pulse Sequence

In 2020, Lobach's group [30] observed a novel pulse time domain dynamic in an erbium-doped self-sweeping fiber laser that obtained a continuous wave output with periodic bursts of intensity instead of the near-zero power microsecond pulse sequence between pulses of other self-sweeping fiber lasers, as shown in **Figure 11A**. This new pulse intensity dynamic consists of a pure sinusoidal waveform (**Figure 11B**) and a periodic pulse train (**Figure 11C**), and Fourier analysis of the pulse signal shows that the pulse train consists of two longitudinal modes with an intermodal beat frequency modulation of 7.1 MHz, which manifests as a single peak in the RF spectrogram (**Figure 11D**). During the pulse generation, an additional peak at a multiplicative frequency appears in the RF spectrum (**Figure 11E**). On the other hand, the zero-level intensity at the sinusoidal minimum (**Figure 11B**) proves that the amplitudes of the individual modes are approximately equal. In addition, the average power magnitude over 1 μs is essentially the same (red line in **Figure 11A**), which is in marked contrast to the microsecond pulse sequences generated in other current self-sweeping fiber lasers.

Novel Pulse Sequences

In 2021, our group [28] observed a new sequence of self-pulse signals, similar to spike pulses, in a single-frequency ytterbium-doped self-sweeping fiber laser based on a fiber saturable absorber, as shown in **Figure 12A**. The laser hops over modes of the

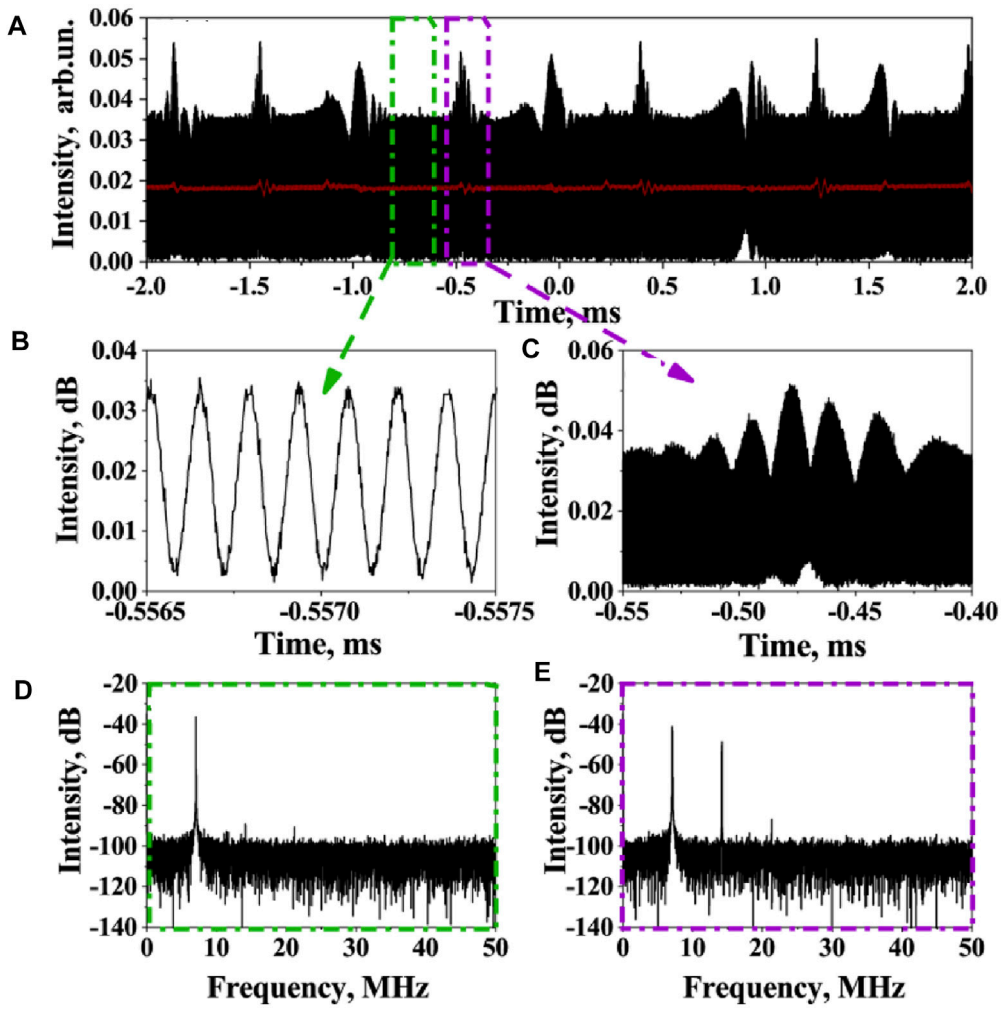

FIGURE 11 | Er-doped self-sweeping fiber laser [30]. **(A)** Overall pulse intensity dynamics; **(B)** Pure sinusoidal waveform intensity dynamics; **(C)** Periodic pulse string; **(D)** Left rectangular RF spectrum; **(E)** Right rectangular RF spectrum.

resonator. Time intervals of the single frequency operation are separated by short time intervals when the laser generates two neighbor lines (and old one and a new one) resulting in the sinusoidal beat signal. **Figures 12B,C** show the sinusoidal beat frequency modulation detail of 28.57 MHz and a single beat frequency signal duration of 37.17 μs, respectively, as shown by the RF spectrum of the fiber laser in the inset of **Figure 12C**, which shows that the laser outputs two longitudinal modes during the duration. Moreover, it is clear that there are attenuation fluctuations at the dynamic end of the intensity, which we correspond with the simulation of the photon density variation of the fiber laser in **Figure 12D**.

THE BASIC LAWS OF THE SELF-SWEEPING FIBER LASER

The unique spectral dynamics as well as the pulse dynamics of the self-sweeping effect have been the focus of researchers since it was studied in the ytterbium-doped fiber laser in 2011. Under extensive experimental observations, researchers have demonstrated the dependence of the fundamental laws of self-sweeping such as self-sweeping range, average pulse repetition frequency and self-sweeping rate on pump power.

Variation of Self-Sweeping Range

From present reports, it is known that the variation of the output spectra of various doped self-sweeping fiber lasers with pump power or output power is roughly consistent. **Figure 13A** shows the variation of the self-sweeping range with output power for a typical self-sweeping fiber laser in a stable self-sweeping state [39], and its variation law with output power is similar to a parabolic function or e-exponential function. With the increase of pump power or output power, the self-sweeping range will gradually increase, and after reaching the maximum value, it will gradually decrease and then slowly disappear due to the interference of nonlinear effects such as the excited stimulated Brillouin scattering (SBS) effect [43] and SRS effect in the resonator.

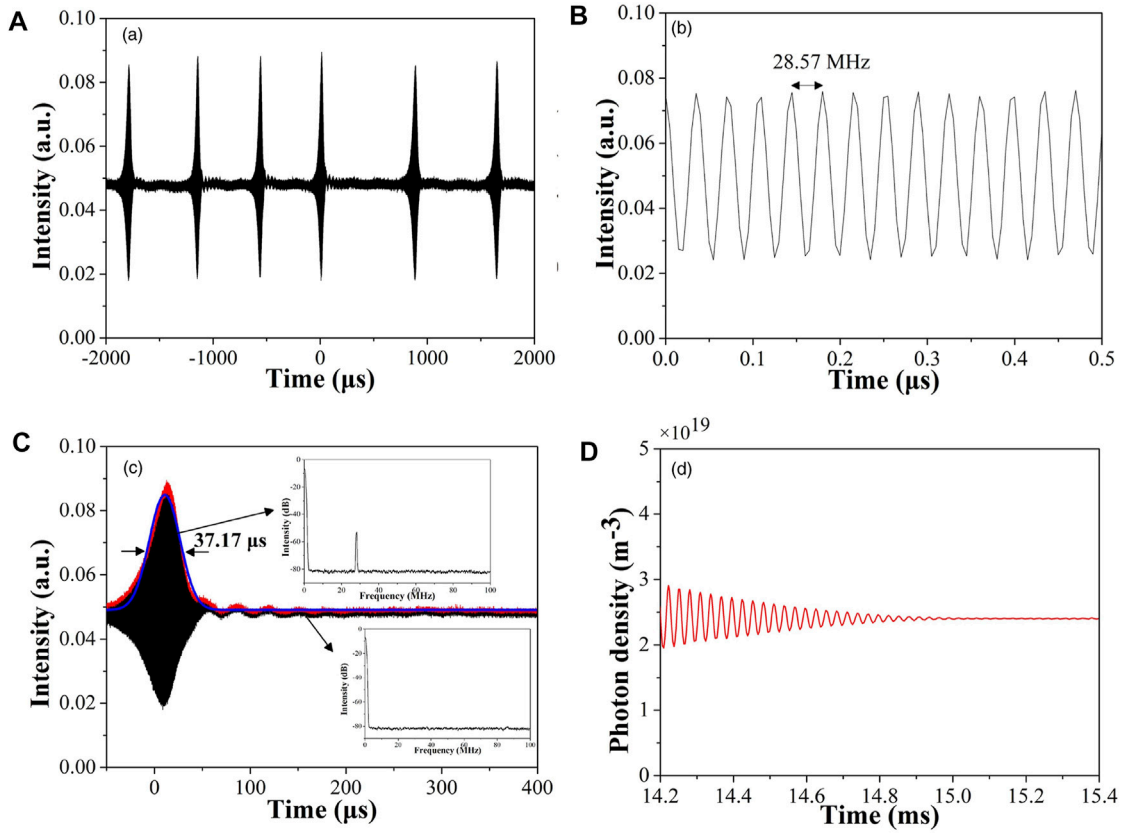

FIGURE 12 | Yb-doped self-sweeping fiber laser [28]. **(A)** Pulse intensity dynamics; **(B)** Pulse detail expansion; **(C)** Dynamic intensity of single pulse (inset) RF spectrum of pulse and continuous wave, **(D)** Simulated changes in photon density.

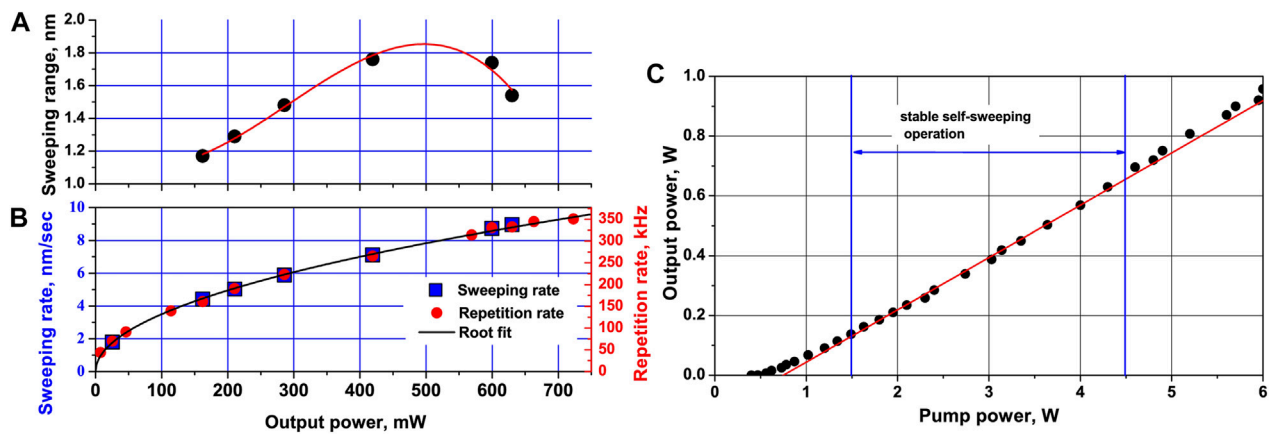

FIGURE 13 | Typical self-sweeping fiber laser [39] **(A)** Sweeping spectral range changes; **(B)** Variation of average pulse repetition frequency and sweeping rate; **(C)** Output slope efficiency.

Variation of Average Pulse Repetition Frequency

Figure 13B demonstrates that the average pulse repetition frequency of a typical self-sweeping fiber laser shows a specific pattern with pump power, i.e., the average pulse repetition frequency increases with increasing output power. Based on a large number of experimental studies, the researchers concluded that the average pulse repetition frequency is linearly related to the squared output power [39], following the Equation:

$$\Delta v = a\sqrt{P} \quad (1)$$

Where: Δv is the average pulse repetition frequency; a is the scale factor; P is the output power.

From the reported self-sweeping literature, it is clear that the relationship between the average pulse repetition frequency and output power follows **Eq. 1**, regardless of whether it is a typical microsecond pulse sequence, a discontinuous pulse signal, a quasi-continuous pulse signal or a novel pulse signal.

Variation of Self-Sweeping Rate

The self-sweeping rate depends on the speed of dynamic grating generation and removal in the gain medium, a grating generation and removal process represents a self-sweeping cycle, if the self-this cycle is shortened, then the self-sweeping rate will naturally become faster. The relationship between the self-sweeping rate and the variation of pump power or output power satisfies the following equation:

$$V = b\sqrt{P} \quad (2)$$

Where: V is the self-sweeping rate; b is the scale factor; P is the output power.

This equation is in clear agreement with **Eq. 1** for the variation of the average pulse repetition frequency with pump power or output power. This indicates that the self-sweeping rate is consistent with the average pulse repetition frequency, i.e., both increase with the increase of pump power or output power. **Figure 13B** shows a graph of the variation of the self-sweeping rate with output power for a typical self-sweeping fiber laser [39], following **Eq. 2** above.

Pump Power Range of Self-Sweeping Effect

Based on the reported self-sweeping fiber laser, it is known that the self-sweeping effect does not generally occur directly at the laser threshold, but is generated and continues to operate for a period of time at some power range above the laser threshold. **Figure 13C** shows the output slope efficiency of a typical self-sweeping fiber laser [39], where the self-sweeping effect can be seen to occur between 1.5 and 4.5 W above the pump power threshold. The reason for its appearance only in a certain power range and its disappearance after a certain period of time is that the stable conditions for the formation of self-sweeping are destroyed by nonlinear effects such as SBS effect and SRS effect in the resonator.

APPLICATIONS OF THE SELF-SWEEPING FIBER LASER

Spectral Detection

The laser output wavelength with stable periodic spontaneous tuning is a distinctive feature of the self-sweeping fiber laser, and the detection by high-resolution interferometry shows that the jump interval of the self-sweeping fiber laser wavelength is very narrow. Therefore, the self-sweeping fiber laser can be used for the spectral detection of wide and narrow band FBGs as well as bandpass filters and other filter devices.

In 2013, Lobach's group [17] conducted the first study related to the application of self-sweeping fiber lasers. This experiment used an ytterbium doped self-sweeping fiber laser to measure the reflection spectrum of a π-phase-shifted grating [44]. The reflectance spectra of the phase-shifted grating in the wider and narrower band ranges measured using this method are in good agreement with the reflectance spectra from standard measurements. This experiment demonstrates that the accuracy of the self-sweeping fiber laser is reliable for narrow-band and broad-band reflection spectra detection. Later, in 2018, the group [31] used a thulium-doped self-sweeping fiber laser as a light source to measure the absorption spectra of water molecules in air. **Figure 14** shows that the experimentally measured absorption spectra of water molecules in air agree well with the actual absorption spectra. Where the small differences observed between experiments and simulations around the intensity maximum (about 1) are related to the weak power modulation of the self-sweeping fiber laser.

The holmium doped self-sweeping fiber laser near the 2.06 μm band studied by the group [45] in 2020 can be used for the spectral detection and analysis of $^{12}CO_2$ and $^{13}CO_2$ isotopes. The holmium-doped self-sweeping fiber laser near the 2.1 μm band studied by the group [38] in 2021 has absorption lines in the spectral region of N_2O and can be used for its spectral detection. All these works show that self-sweeping fiber lasers are more reliable for spectral detection applications.

Short-Pulse Synthesis

A new technique for short pulse synthesis in the Fourier domain was reported by Lobach's group [46] in 2015, as shown in **Figure 15**. The synthesis method differs from the conventional intracavity mode-locking of multimode lasers [47, 48], Fourier-domain mode-locking of tunable lasers [49], Fourier synthesis of multiple independent sources [50, 51], and line-by-line processing [52]. This new technique uses a single-frequency ytterbium-doped self-sweeping fiber laser instead of multiple independent sources to extract a single resonator mode as an entire time series and to perform coherent synthesis in an external circumferential resonator. This experiment allows the combination of 20 single-mode pulses to achieve the synthesis of different waveforms, but the disadvantage is that the pulse intensity fluctuations of the self-sweeping fiber laser can cause mode-limitation.

Optical Fiber Sensing

Due to the lack of reflection sensitivity of fiber optic sensor devices designed based on self-sweeping light sources, the use of such devices for any sensing application is limited, and this problem is now generally solved by using FBGs with externally induced modulation of refractive index to increase the reflection signal strength. In 2016, the team of Lobach [20] designed a fiber optic sensing interrogator using an ytterbium-doped self-sweeping fiber laser, which was successfully tested on a sensing line consisting of six FBG sensors, achieving an accuracy estimate of ~600 MHz (2 pm) spectral measurements, comparable to actual measurement instruments. In addition, the device has a higher spectral resolution and higher peak output power than comparable devices, which means that multiple sensor sub-lines can operate simultaneously. In 2020, the group [53] realized the application of a frequency

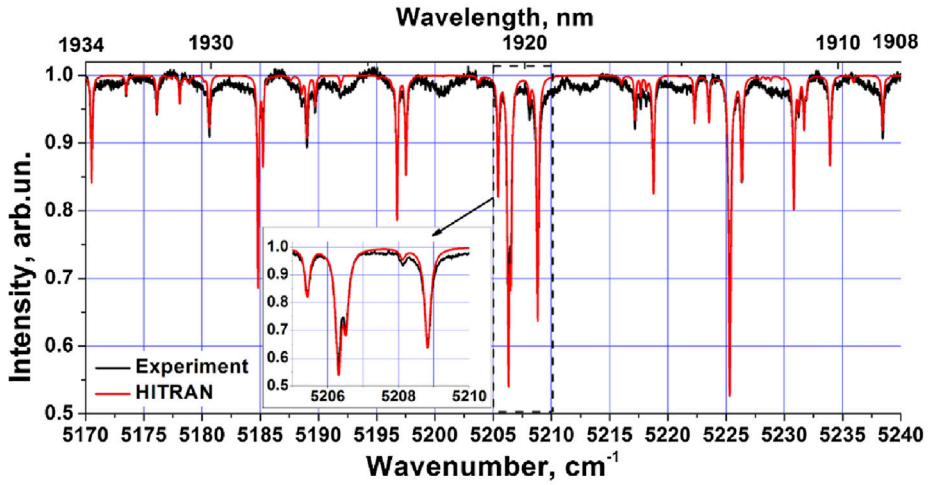

FIGURE 14 | Measurement of absorption spectra of water molecules by Tm-doped self-sweeping fiber laser [31].

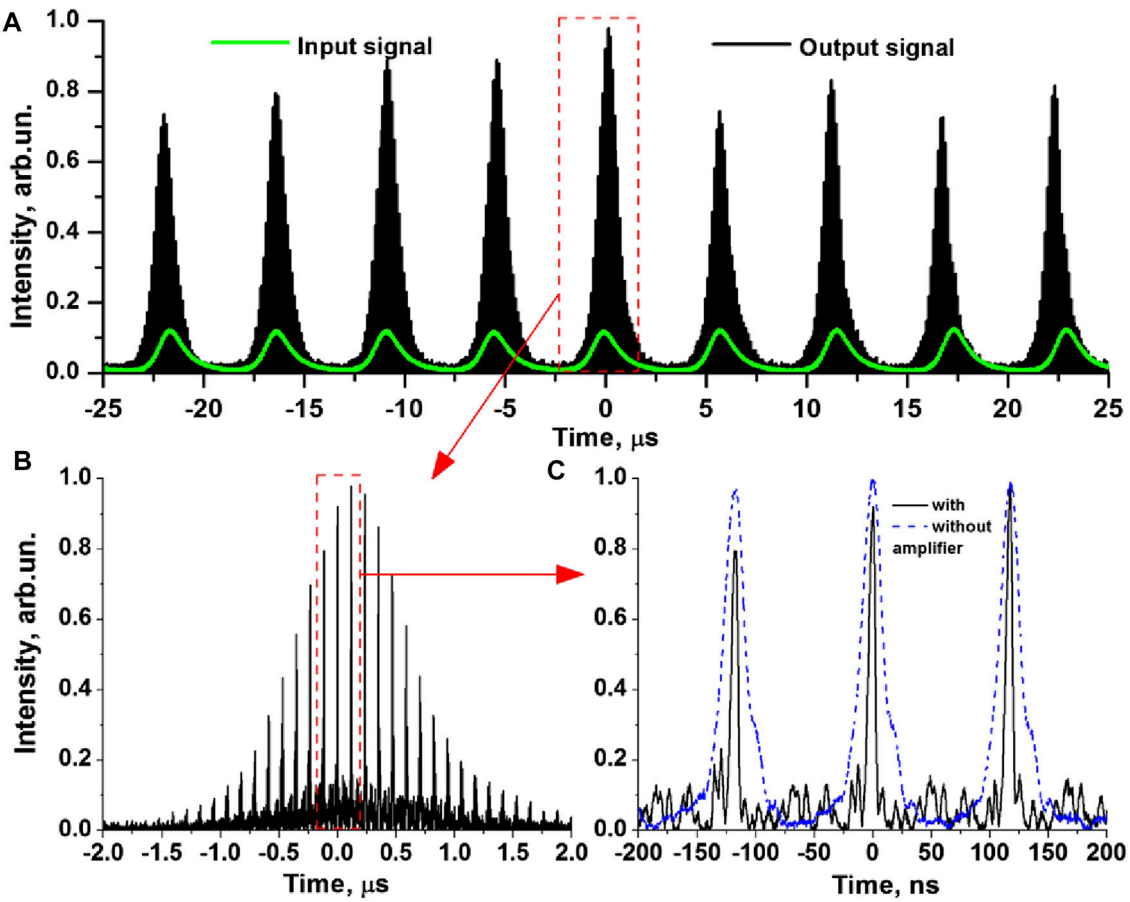

FIGURE 15 | (A) Output synthesis pulse [46]; **(B)** Envelope of synthesis pulse; **(C)** Single pulse.

domain reflectometer based on a self-sweeping laser for sensing. As shown in **Figure 16**, a sensing line was fused to one interferometer arm of the Mach-Zehnder interferometer, and a set of FBG arrays were used on the sensing line, which consisted of one reference FBG (1,064 nm) of a Bragg wavelength inside the sweeping range of the laser and 28 equidistant FBGs (1,092 nm) of Bragg

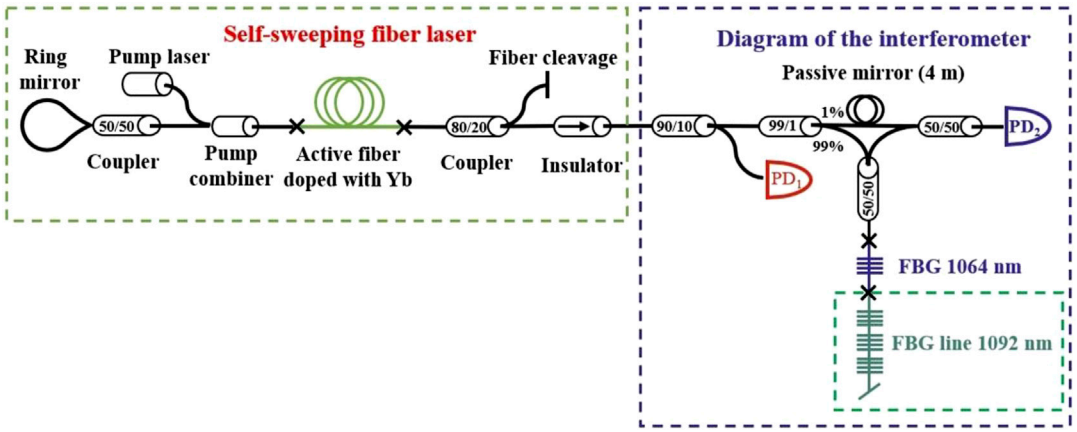

FIGURE 16 | The experimental device of the frequency-domain reflectometer consisting of a self-sweeping laser and a Mach–Zehnder interferometer: (PD1, PD2) photodiodes [53].

wavelength outside (but close to) the sweeping range. Each time domain pulse generated by this self-sweeping fiber laser corresponds to a specific frequency in the spectral region. The frequency change interval is 5.5 MHz in one scan cycle, and the pulses are equally spaced in the frequency domain. The longitudinal distribution of the reflected signal on the fiber was obtained by analyzing the interferometric reflection signal dependent on the optical frequency or the number of pulses by means of the fast Fourier transform. Each peak on the reflection map corresponds to an FBG reflection signal, and since the FBG in the 1,064 nm band is in the self-sweeping tuning range, its reflection signal has a higher amplitude compared to the FBG at 1,092 nm, which is not in the tuning range. The reflection spectra of individual FBGs can be obtained by selectively analyzing a region through Fourier inversion. Since the reflection spectrum of the 1,092 nm FBG has a narrower peak, a temperature change can be more clearly observed in the peak shift values, so this approach may be useful for temperature measurements. In fact, tunable lasers using special devices have sweeping ranges of more than 100 nm and sweeping rates of up to a million nanometers per second [54]. Also, sensor systems for practical applications usually require a sweeping range of 40 nm and a sweeping rate of no less than 10 nm/s, which is not yet met by sensor systems using self-sweeping light sources, which achieve a suboptimal spectral range. Most fiber grating sensors on the market operate in the 1.5 μm spectral range, while erbium-doped self-sweeping fiber lasers operating near 1.5 μm have a small sweeping range of 2.8 nm, which greatly limits their practical applications.

Now that a decade has passed since the development of the self-sweeping fiber laser, many practical applications are still waiting to be explored by researchers. We believe that in addition to spectral detection, short pulse synthesis and fiber sensing, there are more potential applications for self-sweeping fiber lasers in fiber optic communication and coherent synthesis. With further research on self-sweeping fiber lasers, they will be more widely used and their development will continue to open up a new chapter.

SUMMARY AND OUTLOOK

This paper reviews the research progress of various doped self-sweeping fiber lasers in the last decade, including the spectral range, fundamental laws, dynamic types of pulse intensity, and recent application progress of self-sweeping fiber lasers. The currently reported self-sweeping fiber lasers are capable of generating autonomous wavelength tuning in different spectral ranges between 1 and 2.1 μm, and related application studies are also conducted in spectral detection and analysis, and optical sensing applications. However, the current research on self-sweeping fiber lasers is still at the initial stage, and the principle of the self-sweeping effect needs to be explained more comprehensively and profoundly. Establishing a theoretical model to predict the specific behavioral dynamics of self-sweeping considering all influencing factors is the direction researchers need to work on. Among them, precise observation of small wavelength drifts and expansion of more wavelength bands and wider self-sweeping range are also the goals pursued by researchers. In the application of self-sweeping fiber laser, firstly, the laser needs to be packaged and miniaturized for practical application, and secondly, considering that the self-sweeping fiber laser is influenced by the environment and resonator loss, the temperature and resonator loss control module needs to be added to stabilize the self-scanning range, and the spectral selection device needs to be added to reduce the boundary fluctuation of the scanning area, and the self-sweeping range needs to be artificially regulated. The current applications of self-sweeping fiber lasers are mainly in the field of spectroscopy, and a lot of research needs to be done to expand the field of fiber sensing and communication.

DATA AVAILABILITY STATEMENT

The original contributions presented in the study are included in the article/Supplementary Material, further inquiries can be directed to the corresponding authors.

AUTHOR CONTRIBUTIONS

ZZ and BL finished writing the whole article. KW is responsible for part of the work. HC and JB is responsible for article modification.

FUNDING

National Natural Science Foundation of China (61905193); Key R&D project of Shaanxi Province-International Science and Technology Cooperation Programme (2020KW-018).

REFERENCES

1. Villatoro J, Monzon-Hernandez D. Low-cost Optical Fiber Refractive-index Sensor Based on Core Diameter Mismatch. *J Lightwave Technol* (2006) 24(3): 1409–13. doi:10.1109/JLT.2005.863246
2. Xia T-H, Zhang AP, Gu B, Zhu J-J. Fiber-optic Refractive-index Sensors Based on Transmissive and Reflective Thin-Core Fiber Modal Interferometers. *Opt Commun* (2010) 283(10):2136–9. doi:10.1016/j.optcom.2010.01.031
3. Qiao S, Ma Y, He Y, Patimisco P, Sampaolo A, Spagnolo V. Ppt Level Carbon Monoxide Detection Based on Light-Induced Thermoelastic Spectroscopy Exploring Custom Quartz Tuning forks and a Mid-infrared QCL. *Opt Express* (2021) 29(16):25100–8. doi:10.1364/OE.434128
4. Lang Z, Qiao S, He Y, Ma Y. Quartz Tuning fork-based Demodulation of an Acoustic Signal Induced by Photo-Thermo-Elastic Energy Conversion. *Photoacoustics* (2021) 22:100272. doi:10.1016/j.pacs.2021.100272
5. Dong B, Wei L, Zhou D-P, Liu W-K, Lit JWY. Core-offset Small-Core-Diameter Dispersion Compensation Fiber Interferometer and its Applications in Fiber Sensors. *Appl Opt* (2009) 48(23):4577–81. doi:10.1364/AO.48.004577
6. Yang Z, Wu X, Ouyang D, Sun H, Ruan S. Analysis of Performance Improvement in a Swept Source for Optical Coherence Tomography Applications. *Jpn J Appl Phys* (2020) 59(3):030904. doi:10.35848/1347-4065/ab7216
7. Fukushima K, Bui QH, Nakaya K, Soares MG, Wada A, Tanaka S. EDF Ring Laser Using Cascaded-Chirped Long Period Fiber Grating for Temperature Measurement. *Opt Express* (2020) 28(9):13081–90. doi:10.1364/OE.389235
8. Woodward RI, Majewski MR, Hudson DD, Jackson SD. Swept-wavelength Mid-infrared Fiber Laser for Real-Time Ammonia Gas Sensing. *APL Photon* (2019) 4(2):020801. doi:10.1063/1.5065415
9. Sarmani AR, Sheih S-J, Mahamd Adikan FR, Mahdi AM. Spectral Hole Burning Effects Initiated by Uniform Signal Intensities in a Gain-Flattened EDFA. *Chin Opt Lett*(2011) 9(2):020603–6. doi:10.3788/COL201109.020603
10. Peterka P, Honzátko P, Koška P, Todorov F, Aubrecht J, Podrazký O. Reflectivity of Transient Bragg Reflection Gratings in Fiber Laser with Laser-Wavelength Self-Sweeping: Erratum. *Opt Express* (2016) 24(14): 16221. doi:10.1364/oe.24.016221
11. Peterka P, Honzátko P, Koška P, Todorov F, Aubrecht J, Podrazký O. Reflectivity of Transient Bragg Reflection Gratings in Fiber Laser with Laser-Wavelength Self-Sweeping. *Opt Express* (2014) 22(24):30024. doi:10.1364/OE.22.030024
12. Peterka P, Koska P, Ctyroky J. Reflectivity of Superimposed Bragg Gratings Induced by Longitudinal Mode Instabilities in Fiber Lasers. *IEEE J Select Top Quan Electron.* (2018) 24:1–8. doi:10.1109/JSTQE.2018.2806084
13. Hughes TP, Young KM. Mode Sequences in Ruby Laser Emission. *Nature* (1962) 196(4852):332–4. doi:10.1038/196332a0
14. Kir'yanov AV, Il'ichev NN. Self-induced Laser Line Sweeping in an Ytterbium Fiber Laser with Non-resonant Fabry-Perot Cavity. *Laser Phys Lett* (2011) 8(4): 305–12. doi:10.1002/lapl.201010138
15. Lobach IA, Kablukov SI, Podivilov EV, Babin SA. Broad-range Self-Sweeping of a Narrow-Line Self-Pulsing Yb-Doped Fiber Laser. *Opt Express* (2011) 19(18):17632–40. doi:10.1364/OE.19.017632
16. Lobach IA, Babin SI, Podivilov EV, Kablukov SA. All-fiber Broad-Range Self-Sweeping Yb-Doped Fiber Laser. *Proc SPIE-The Int Soc Opt Eng* (2012) 8237: 30. doi:10.1117/12.906660
17. Lobach IA, Kablukov SI. Application of a Self-Sweeping Yb-Doped Fiber Laser for High-Resolution Characterization of Phase-Shifted FBGs. *J Lightwave Technol* (2013) 31(18):2982–7. doi:10.1109/JLT.2013.2278177
18. Navratil P, Peterka P, Kubecek V, Kalli K, Kanka J, Mendez A. Effect of Pump Wavelength on Self-Induced Laser Line Sweeping in Yb-Doped Fiber Laser. *Micro-structured Specialty Opt Fibres* (2013) 8775:87750D. doi:10.1117/12.2017471
19. Lobach IA, Yu Tkachenko A, Kablukov SI. Optimization and Control of the Sweeping Range in an Yb-Doped Self-Sweeping Fiber Laser. *Laser Phys Lett* (2016) 13(4):045104. doi:10.1088/1612-2011/13/4/045104
20. Tkachenko AY, Lobach IA, Guskov LN. Fiber Sensor Interrogator Based on Self-Sweeping Fiber Laser. Proceeding of the 2016 17th International Conference of Young Specialists on Micro/Nanotechnologies and Electron Devices (EDM), 30 June-4 July 2016, Erlagol, Russia, IEEE (2016) 348–51. doi:10.1109/EDM.2016.7538756
21. Tkachenko AY, Lobach IA, Kablukov SI. All-fiber Brillouin Optical Spectrum Analyzer Based on Self-Sweeping Fiber Laser. *Opt Express* (2017) 25(15): 17600. doi:10.1364/OE.25.017600
22. Navratil P, Peterka P, Honzatko P, Kubecek V. Reverse Spontaneous Laser Line Sweeping in Ytterbium Fiber Laser. *Laser Phys Lett* (2017) 14(3):035102. doi:10.1088/1612-202X/aa548d
23. Jiang H, Lei J, Set SY, Yamashita S. Spontaneous Laser Line Sweeping in Tm Doped Fiber Laser. *Laser Congress 2018 (ASSL)* (2018) 34. doi:10.1364/ASSL.2018.AM6A.34
24. Wang K, Wen Z, Lu B, Qi X, Bai J. Wavelength Self-Sweeping Yb-Doped Bi-directional Fiber Ring Laser[C]. Proceeding of the Eleventh International Conference on Information Optics and Photonics (CIOP 2019); Xi'an, China (2019). doi:10.1117/12.2548390
25. Wang K, Wen Z, Chen H, Qi X, Lu B, Bai J. Observation of Reverse Self-Sweeping Effect in an All-Polarization-Maintaining Bidirectional Ytterbium-Doped Fiber Laser. *Opt Express* (2020) 28(9):13913–20. doi:10.1364/OE.392903
26. Wang K, Wen Z, Chen H, Lu B, Bai J. Wavelength-flexible All-Polarization-Maintaining Self-Sweeping Fiber Laser Based on Intracavity Loss Tuning. *Chin Opt Lett* (2021) 19(4):041401. doi:10.3788/COL202119.041401
27. Stepanov S, Fotiadi A, Mégret P. Effective Recording of Dynamic Phase Gratings in Yb-Doped Fibers with Saturable Absorption at 1064nm. *Opt Express* (2007) 15(14):8832–7. doi:10.1364/OE.15.008832
28. Wen Z, Wang K, Chen H, Lu B, Bai J. Self-sweeping Ytterbium-Doped Fiber Laser Based on a Fiber Saturable Absorber. *Appl Phys Express* (2020) 14(1): 012005. doi:10.35848/1882-0786/abd37d
29. Navratil P, Peterka P, Vojtisek P, Kasik I, Aubrecht J, Honzatko P. Self-swept Erbium Fiber Laser Around 1.56 μm. *Opto-Electronics Rev* (2018) 26(1):29–34. doi:10.1016/j.opelre.2017.11.004
30. Kashirina EK, Lobach IA, Kablukov SI. Dual-longitudinal-mode CW Self-Sweeping Operation in Er-Doped Fiber Laser. *Opt Lett* (2020) 45(24):6659–62. doi:10.1364/OL.412781
31. Budarnykh AE, Vladimirskaya AD, Lobach IA, Kablukov SI. Broad-range Self-Sweeping Single-Frequency Linearly Polarized Tm-Doped Fiber Laser. *Opt Lett* (2018) 43(21):5307–10. doi:10.1364/OL.43.005307
32. Budarnykh AE, Lobach IA, Kablukov SI. Self-sweeping Tm-Doped Fiber Laser with Wavelength Stopping. *Laser Phys Lett* (2019) 16(2):025108. doi:10.1088/1612-202X/aaf804
33. Jiang H, Zhao Z, Jin L, Set SY, Yamashita S. Self-wavelength-sweeping in a Bi-directional Thulium-Doped Fiber Ring Laser. *Appl Phys Express* (2019) 12(4): 042006. doi:10.7567/1882-0786/ab071e
34. Wang X, Zhou P, Wang X, Xiao H, Si L. Tm-Ho Co-doped All-Fiber Brand-Range Self-Sweeping Laser Around 19 μm. *Opt Express* (2013) 21(14):16290. doi:10.1364/OE.21.016290
35. Lobach IA, Kablukov SI, Melkumov MA, Khopin VF, Babin SA, Dianov EM. Single-frequency Bismuth-Doped Fiber Laser with Quasi-Continuous Self-Sweeping. *Opt Express* (2015) 23(19):24833–42. doi:10.1364/OE.23.024833
36. Aubrecht J, Peterka P, Koška P, Podrazký O, Todorov F, Honzátko P. Self-swept Holmium Fiber Laser Near 2100 Nm. *Opt Express* (2017) 25(4):4120–5. doi:10.1364/oe.25.004120

37. Aubrecht J, Peterka P, Koška P, Honzátko P, Jelínek M, Kamrádek M. Spontaneous Laser-Line Sweeping in Ho-Doped Fiber Laser. *Fiber Lasers XIV: Tech Syst* (2017) 10083:100831V. doi:10.1117/12.2249486
38. Vladimirskaya AD, Kamynin VA, Lobach IA, Kablukov SI. Robust Operation of Linearly Polarized Broad-Range Self-Sweeping Ho-Doped Fiber Laser. *Laser Phys Lett* (2021) 18(7):075101. doi:10.1088/1612-202X/ac0154
39. Kashirina EK, Lobach IA, Kablukov SI. Single-frequency Self-Sweeping Nd-Doped Fiber Laser. *Opt Lett* (2019) 44(9):2252. doi:10.1364/OL.44.002252
40. Fernandez Casares S, Balle S, Menendez-Valdes P. Mode Beating and Spontaneous Emission Noise Effects in a Variable-Waveguide Model for the Dynamics of Gain-Guided Semiconductor Laser Arrays. *IEEE J Quan Electron.* (1994) 30(11):2449–57. doi:10.1109/3.333695
41. Guan W, Marciante JR. Complete Elimination of Self-Pulsations in Dual-Clad Ytterbium-Doped Fiber Lasers at All Pumping Levels. *Opt Lett* (2009) 34(6):815–7. doi:10.1364/OL.34.000815
42. Ludvigsen H, Tossavainen M, Kaivola M. Laser Linewidth Measurements Using Self-Homodyne Detection with Short Delay[J]. *Opt Commun* (1998) 155(1-3):180–6. doi:10.1016/S0030-4018(98)00355-1
43. Kobyakov A, Sauer M, Chowdhury D. Stimulated Brillouin Scattering in Optical Fibers. *Adv Opt Photon* (2010) 2(1):1–59. doi:10.1364/AOP.2.000001
44. Malara P, Campanella CE, De Leonardis F, Giorgini A, Avino S, Passaro VMN. Enhanced Spectral Response of π-phase Shifted Fiber Bragg Gratings in Closed-Loop Configuration. *Opt Lett* (2015) 40(9):2124–6. doi:10.1364/OL.40.002124
45. Vladimirskaya AD, Skvorsov MI, Wolf AA, Kaminin VA, Lobach IA, Kablukov SI. Ho-doped Fiber Laser with Wavelength Self-Sweeping Near 2.06 μm for CO2 Spectroscopy[C]. Proceeding of the International Conference Laser Optics (ICLO); Nov. 2020; St. Petersburg, Russia. IEEE (2020). doi:10.1109/iclo48556.2020.9285573
46. Lobach IA, Kablukov SI, Podivilov EV, Fotiadi AA, Babin SA. Fourier Synthesis with Single-Mode Pulses from a Multimode Laser. *Opt Lett* (2015) 40(15):3671–4. doi:10.1364/ol.40.003671
47. Song Y-W, Morimune K, Set SY, Yamashita S. Polarization Insensitive All-Fiber Mode-Lockers Functioned by Carbon Nanotubes Deposited onto Tapered Fibers. *Appl Phys Lett* (2007) 90(2):021101. doi:10.1063/1.2431445
48. Song Y-W, Yamashita S, Goh CS, Set SY. Carbon Nanotube Mode Lockers with Enhanced Nonlinearity via Evanescent Field Interaction in D-Shaped Fibers. *Opt Lett* (2007) 32(2):148–50. doi:10.1364/OL.32.000148
49. Todor S, Biedermann B, Wieser W, Huber R, Jirauschek C. Instantaneous Lineshape Analysis of Fourier Domain Mode-Locked Lasers. *Opt Express* (2011) 19(9):8802. doi:10.1364/OE.19.008802
50. Hyodo M, Abedin KS, Onodera N. Generation of Arbitrary Optical Waveforms by Fourier Synthesis Using Three Continuous-Wave Semiconductor Lasers. *Electron Lett* (2000) 36(3):224–5. doi:10.1049/el:20000212
51. Hyodo M, Onodera N, Abedin KS. Fourier Synthesis of 96-GHz Optical-Pulse Trains by Phase Locking of Three Continuous-Wave Semiconductor Lasers. *Opt Lett* (1999) 24(5):303. doi:10.1364/OL.24.000303
52. Zhao C, Deng W, Yan Y, Yao X. Progressive Line Processing of Kernel RX Anomaly Detection Algorithm for Hyperspectral Imagery. *Sensors* (2017) 17(8):1815. doi:10.3390/s17081815
53. Tkachenko AY, Smolyaninov NN, Skvortsov MI, Lobach IA, Kablukov SI. A Coherent Optical Frequency-Domain Reflectometer Based on a Self-Sweeping Fiber Laser for Sensing Applications. *Instrum Exp Tech* (2020) 63(4):532–7. doi:10.1134/S0020441220040338
54. Yamashita S, Takubo Y. Wide and Fast Wavelength-Swept Fiber Lasers Based on Dispersion Tuning and Their Application to Optical Coherence Tomography. *Photonic Sens* (2013) 3(4):320–31. doi:10.1007/s13320-013-0129-0

Conflict of Interest: The authors declare that the research was conducted in the absence of any commercial or financial relationships that could be construed as a potential conflict of interest.

Publisher's Note: All claims expressed in this article are solely those of the authors and do not necessarily represent those of their affiliated organizations, or those of the publisher, the editors and the reviewers. Any product that may be evaluated in this article, or claim that may be made by its manufacturer, is not guaranteed or endorsed by the publisher.

frontiers in Physics

ORIGINAL RESEARCH
published: 23 December 2021
doi: 10.3389/fphy.2021.786357

Bright Soliton and Bright–Dark Soliton Pair in an Er-Doped Fiber Laser Mode-Locked Based on In_2Se_3 Saturable Absorber

Qin Wei [1,2†], Xile Han [3†], Huanian Zhang [1,4], Chonghui Li [5,6], Chao Zhang [1] and Baoyuan Man [1]**

[1]School of Physics and Electronics, Shandong Normal University, Jinan, China, [2]Shandong University of Traditional Chinese Medicine, Jinan China, [3]Institute of Photonics Technology, Jinan University, Guangzhou, China, [4]School of Physics and Optoelectronic Engineering, Shandong University of Technology, Zibo, China, [5]Shandong Key Laboratory of Biophysics, Institute of Biophysics, Dezhou University, Dezhou, China, [6]Institute for Integrative Nanosciences, IFW Dresden, Dresden, Germany

The output power in ultrafast fiber lasers is usually limited due to the lack of a versatile saturable absorber with high damage threshold and large modulation depth. Here we proposed a more efficient strategy to improve the output energy of erbium-doped fiber laser based on indium selenide (In_2Se_3) prepared by using the physical vapor deposition (PVD) method. Finally, stable mode-locked bright pulses and triple-wavelength dark–bright pulse pair generation were obtained successfully by adjusting the polarization state. The average output power and pulse energy were 172.4 mW/101 nJ and 171.3 mW/100 nJ, which are significantly improved compared with the previous work. These data demonstrate that the PVD-In_2Se_3 can be a feasible nonlinear photonic material for high-power fiber lasers, which will pave a fresh avenue for the high-power fiber laser.

Keywords: Indium selenide (In_2Se_3), saturable absorber(SA), physical vapor deposition, mode-locked fiber lasers, soliton

OPEN ACCESS

Edited by:
Yufei Ma,
Harbin Institute of Technology, China

Reviewed by:
Ahmed Al-Masoodi,
American University of Kuwait, Kuwait
Xingliang Li,
Hebei Normal University, China

***Correspondence:**
Chao Zhang
czsdnu@126.com
Baoyuan Man
byman@sdnu.edu.cn

†These authors have contributed equally to this work

Specialty section:
This article was submitted to Optics and Photonics, a section of the journal Frontiers in Physics

Received: *30 September 2021*
Accepted: *24 November 2021*
Published: *23 December 2021*

Citation:
Wei Q, Han X, Zhang H, Li C, Zhang C and Man B (2021) Bright Soliton and Bright–Dark Soliton Pair in an Er-Doped Fiber Laser Mode-Locked Based on In_2Se_3 Saturable Absorber. Front. Phys. 9:786357. doi: 10.3389/fphy.2021.786357

INTRODUCTION

Recently, ultra-fast mode-locked fiber lasers with the virtues of miniaturization, good stability, and beam quality have attracted great attention due to promising applications in industrial manufacturing, biomedicine, defense, optical imaging, and nonlinear optical conversion [1–14]. Especially when studying various nonlinear phenomena, high-power mode-locked fiber lasers often serve as ideal platforms and powerful experimental tools. As the key nonlinear optical element in the passively mode-locked laser, excellent saturable absorbers (SAs) have always been the goal of scientific researchers [15]. At present, various types of two-dimensional (2D) materials were widely employed as passive SAs in mode-locked fiber lasers [16–35]. As a novel two-dimensional layered material, transition metal dichalcogenides (TMDs MoS_2, WS_2, $MoSe_2$, and WSe_2) [19–23] show layer-number-dependent bandgap properties and exhibit a huge potential in nanoelectronics, optical sensor, optoelectronics, and other fields. However, due to the limited carrier mobility of a single layer, its wide application was restricted. Recently, topological insulators (Bi_2Se_3, Bi_2Te_3, and Sb_2Te_3) [24–26] with large modulation depth and excellent optical nonlinearity have aroused great interest in laser photonics. Additionally, black phosphorus with an adjustable direct band gap is widely used in intermediate infrared optoelectronic materials [30–32]. Due to the high nonlinear optical response and the fast recovery time, the ZnO is considered to be an ideal SA [35]. Regretfully, the output power of fiber

lasers based on various broadband SAs was limited to tens of milliwatts due to a low laser damage threshold. Therefore, it is of vital importance to improve the output power of ultrafast fiber lasers.

Most recently, In_2Se_3 with crystalline polymorphism and diverse electronic properties has attracted extensive attention [36–41], which is beneficial to many laser photonic applications. In ultrafast photonic applications, Yan *et al.* fabricated α-In_2Se_3 as SA by magnetron sputtering deposition method and then inserted SA into erbium-doped fiber laser. They finally obtained soliton pulses with maximum average power and single pulse energy of 83.2 mW and 2.03 nJ for erbium-doped fiber laser (EDFL), respectively [42]. Although scientists have conducted extensive research on In_2Se_3, few have been done on nonlinear optical properties to be used as SA for high-power operations.

Generally, 2D In_2Se_3 nanostructures can be prepared by using the mechanical exfoliation (ME) method [29]. However, the size and the thickness of In_2Se_3 nanosheets obtained by the ME method are uncontrollable, and this leads to further limiting the optical response. Additionally, the chemical vapor deposition (CVD) and the physical vapor deposition (PVD) methods were also successfully employed for fabricating In_2Se_3 nanoflakes [43, 44]. Compared with other methods, the PVD method could accurately control the thickness of In_2Se_3 nanoflakes. The PVD-In_2Se_3 exhibits high crystallinity that is beneficial to improve the laser damage threshold. Moreover, the PVD method could achieve highly uniform large-area films, which could further improve the nonlinear optical properties of SA.

In this paper, few-layered In_2Se_3 nanoflakes were successfully fabricated with the PVD method, which showed a high laser damage threshold and excellent nonlinear saturable absorption characteristics. We estimated that the damage threshold of this proposed SA reached up to 50 mJ/cm^2 at the highest pump power in our experiment. The modulation depth of 19% and the saturable intensity of 7.9 MW/ cm^2 are obtained. Stable mode-locked bright pulses and triple-wavelength dark–bright pulses were obtained successfully in our EDFL. The experimental results indicate that In_2Se_3 is a potential SA in the large-energy mode-locked fiber laser application and also demonstrate that the PVD method can be an excellent way for studying high-performance SAs.

FABRICATION AND CHARACTERIZATION OF IN_2SE_3 SA

High-quality In_2Se_3 nanoflakes were prepared by the PVD method, which was similar to our previous reports [45]. The few-layered In_2Se_3 nanoflakes were synthesized on monolayer fluorophlogopite mica (FM˜20 μm) substrate *via* van der Waals epitaxy. The In_2Se_3 power (99.99%) used for evaporation source had been placed in the center of the horizontal tube furnace (OTL1200). A piece of FM substrate was placed downstream, about 12 cm away from the powder source, for sample growth. Under argon (Ar) gas of 50 sccm, the In_2Se_3 powder was heated to 750°C. After growth, keeping the Ar flow unchanged, we let the tubular furnace naturally cool down to ambient temperature. In addition, the PVD-In_2Se_3 nanoflakes were transferred to the facet of a fiber connector for fabricating In_2Se_3-based SA, which enhanced the laser damage threshold under high-power conditions.

The performance of the sample materials is also very important. The In_2Se_3 nanosheets were characterized, and data results are shown in **Figure 1**. **Figures 1A,B** indicate that In_2Se_3 nanoflakes have a multi-layered structure. It can be clearly observed that most of the nanoflakes have asymmetric hexagonal and irregular truncated trigonal morphology, which grow along the horizontal direction. However, due to the limitation of the heating rate of the tube furnace, the homogeneity of the deposited nanoflakes was weakened. Most of the nanoflakes show uniform thickness across the lateral dimension. From the inset of **Figure 1A**, the stoichiometric ratio of Se (51.43%) and In (34.80%) was about 3:2. The Raman result is displayed in **Figure 1C**. Apparently, three peaks at˜107,˜172, and ˜205 cm^{-1} are considered to be done by A_1 (LO + TO), A_1 (TO), and A_1 (LO) phonon modes of In_2Se_3 [42], which evidently prove that we successfully synthesized the In_2Se_3 nanoflakes [43, 44]. Diffraction peaks including (004), (006), (106), (0010), (1115), and (1118) were detected, as shown in **Figure 1D**. Compared with bulk In_2Se_3, the intensity of (006) peak is relatively higher and shows that the In_2Se_3 nanoflakes exhibit a well-layered structure. This further indicates that the In_2Se_3 nanoflakes grown with the PVD method have good uniformity and high crystallinity.

The linear absorption property is shown in **Figure 2A**. The In_2Se_3 SA has a higher transmission of 93% at 1,560 nm. As can be seen from **Figure 2A**, the linear transmission exhibits some fluctuation fringes. This phenomenon may be attributed to the interference due to the thickness of the sample. Moreover, through a power-dependent transmission technique, the nonlinear absorption properties of the In_2Se_3 SA were measured, and the experimental setup is the same as that in our previous work [46]. The final result is depicted in **Figure 2B**, where the modulation depth of 19% and the saturable intensity of 7.9 MW/ cm^2 are estimated. Due to the good uniformity of the In_2Se_3 nanoflakes, the In_2Se_3 SA exhibits a high modulation depth [47]. It has been demonstrated that SAs with a large modulation depth is beneficial to generate mode-locked ultrafast pulses with a larger single-pulse energy [48]. Therefore, In_2Se_3 prepared by the PVD method was regarded as an excellent SA to realize high-power and large-energy pulse generation.

EXPERIMENTAL SETUP

The typical experimental arrangements of the proposed PVD-In_2Se_3 EDFL are shown in **Figure 3**. Two laser diodes (LD, 976 nm) were used as a pump source, and the final highest output power was 1,838 mW. Two wavelength division multiplexer couplers were employed to couple the pump laser into the ring cavity. The highly erbium-doped fiber served as the gain medium. Meanwhile, a polarization-insensitive isolator (PI-ISO) retained the unidirectional laser operation in the ring cavity, and two polarization controllers (PCs) were connected into the laser cavity to be used to control the polarization state of the laser cavity. A 40:60 optical coupler was used to collect the output laser beam. Additionally, in order to improve the output stability of the cavity and adjust the net dispersion value in the cavity to achieve the various soliton phenomena more easily, a single-

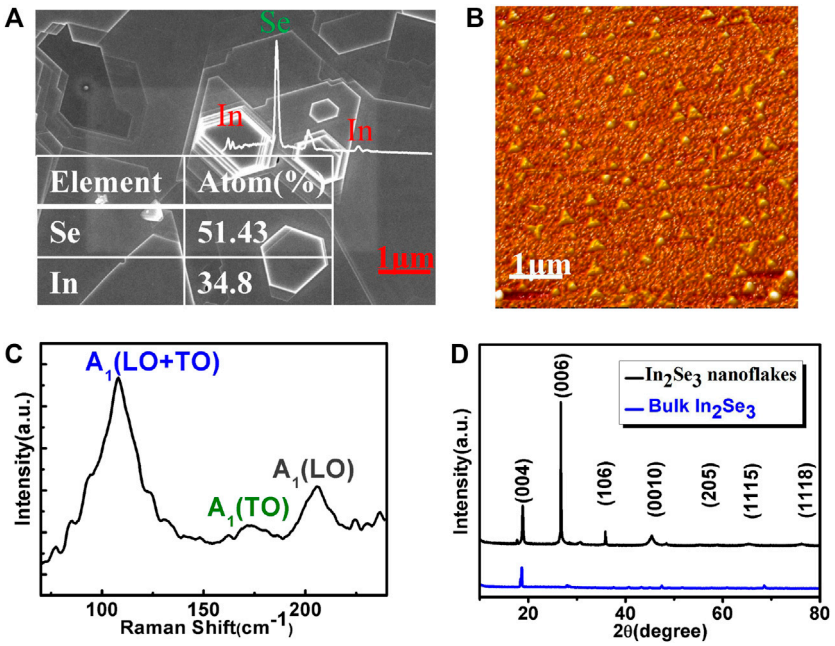

FIGURE 1 | (A) SEM image of the prepared In_2Se_3 nanoflakes (inset: energy-dispersive X-ray spectroscopy of the sample). **(B)** Atomic force microscopy image of In_2Se_3 nanoflakes. **(C)** Raman spectrum of the prepared In_2Se_3 nanoflakes. **(D)** XRD analysis of the In_2Se_3 nanoflakes.

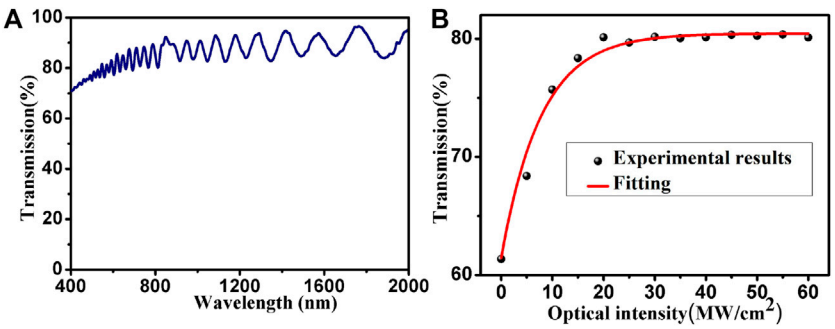

FIGURE 2 | (A) Linear transmission spectrum of In_2Se_3-FM. **(B)** The nonlinear saturable absorption curve of the In_2Se_3.

mode fiber was inserted between SA and PI-ISO in the ring laser cavity. The whole length of the proposed laser cavity is about 119 m, and the total net dispersion in the cavity is calculated as being about -2.61 ps^2.

EXPERIMENTAL RESULTS AND DISCUSSIONS

As is known to all, owing to the Kerr effect, self-mode-locked or Q-switching often occurs in the ring fiber laser cavity. Therefore, at the beginning of the experiment, we inserted a pure FM substrate without a saturated absorber into the ring laser cavity and inspected if Q-switched or self-mode-locked operations were not observed, which showed that the pure FM substrate did not produce a Kerr effect and a saturated absorption effect in the ring laser cavity. Then, we connected the In_2Se_3 SA to the EDFL system and obtained mode-locked operations. The insertion loss of the proposed cavity was calculated as 0.95 dB. Thus, the relatively large insertion loss and the high output coupling ratio caused the laser threshold to be relatively high. By maintaining the pump power at 1,838 mW for 5 or 6 h (maybe a little short), a stable mode-locked output can always be obtained, which showed that PVD-In_2Se_3 SA had a high

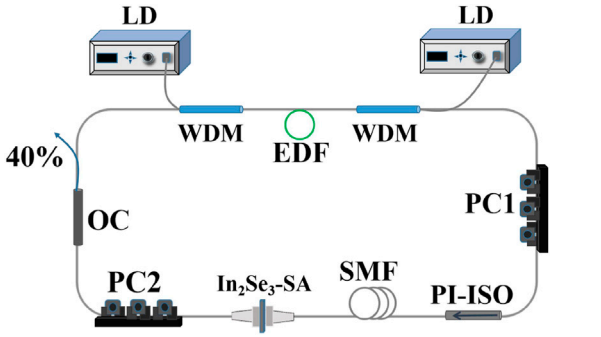

FIGURE 3 | Experimental schematic of the mode-locked erbium-doped fiber laser.

stability. What is more, no material damage was found. It can be proved that the laser damage threshold of the prepared In_2Se_3 SA was relatively high. In general, within the mode-locked laser cavity, the balance between various nonlinear optical effects, the total laser gain and loss, and the net dispersion value of the cavity contributed to the formation of different soliton generations. Bright pulses and dark–bright pulses were observed successfully by adjusting the PCs in this proposed cavity. We will discuss the two mode-locked operations in detail.

Bright Pulses

The bright pulses can be obtained easily by adjusting the PCs upon the pump power to 313 mW. Here we mainly discussed the bright pulse output characteristics, where the pump power is set as 1,838 mW, as shown in **Figure 4**. **Figure 4A** shows an oscilloscope trace of a single bright pulse with the full-width at half-maximum of 15.3 ns, which can be attributed to the large net dispersion. The inset of **Figure 4A** illustrates the pulse train with 1.718 MHz fundamental frequency, corresponding to a period of 582.8 ns, which demonstrates a stable mode-locked state. **Figure 4B** shows the optical spectrum of the dual-wavelength bright pulse with the central wavelength located at 1,559.436 and 1,560.974 nm, which is similar to the previous report [49]. However, we have not observed Kelly sidebands in the spectrum, thus proving that the EDFL operation mode was not a conventional soliton regime. The large dispersion in the experiment is one of the causes of the disappearance of the Kelly sideband [50]. Additionally, the stability issue of the passively mode-locked is an important parameter limiting the practical application of the laser. **Figure 4C** exhibits the radiofrequency (RF) spectrum of the dual-wavelength bright pulse. The peak of the fundamental frequency locates at 1.718 MHz with a signal-to-noise ratio (SNR) of 42 dB, which further indicates the relative stability of bright pulse. The average output power and single pulse energy under a different pump power are recorded in **Figure 4D**. In the case of pump power setting at 1,838 mW, the average output power was measured to be 172.4 mW and single pulse energy was 101 nJ. The high output power generation could be explained by the following aspects: (1) differently from the 2D materials prepared by other methods, such as ME and CVD, PVD-In_2Se_3 exhibits uniform thickness and high crystallinity of nanosheets and (2) PVD-In_2Se_3 SA displays excellent nonlinear optical properties—for example, larger modulation depth. In general, the lasers that operate in a negative dispersion cavity would generate conventional soliton. Limited by a soliton area theorem, the pulse energy would not

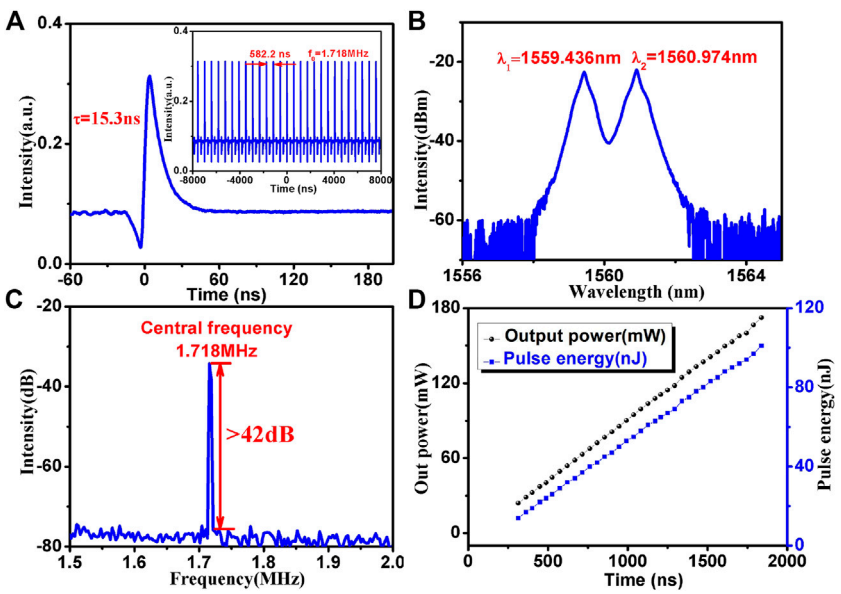

FIGURE 4 | (A) Single pulse of the bright pulse (inset: typical pulse train). **(B)** The output optical spectrum. **(C)** RF spectrum. **(D)** Pulse energy and average output power *versus* pump power.

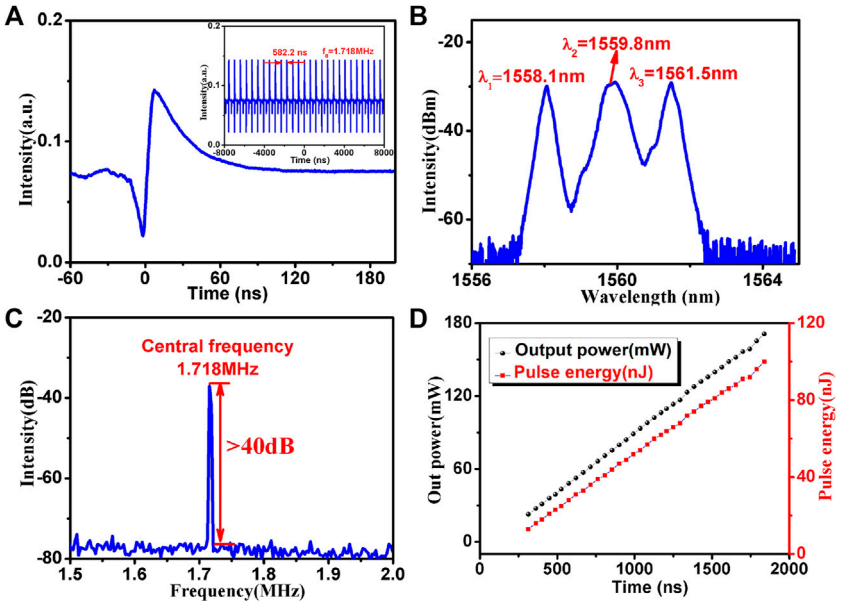

FIGURE 5 | (A) Single pulse profile of the dark-bright pulse and the inset shows the typical pulse train. **(B)** Output spectrum. **(C)** Radiofrequency spectrum. **(D)** Average output power and pulse energy.

survive above 0.1 nJ. However, according to previous reports, Yan *et al.* and Wang *et al.* achieved a soliton pulse with a single pulse energy of 2.03, 2.14, and 128.3 nJ in a negative dispersion cavity, respectively [42, 48, 50]. In our experiment, although the single pulse energy reached up to 101 nJ, but the peak power remained almost immutable due to pulse broadening caused by the large dispersion. In addition, it is well known that mode-locked lasers could operate in different soliton states under the interaction of dispersion, nonlinearity, gain, and loss. In the experiment, due to the lack of an autocorrelator, the soliton state cannot be measured. However, since the pulse obtained in our experiment was not a traditional soliton pulse, according to previous reports [51, 52], the displayed value of the oscilloscope was the real value of the pulse width. Obviously, compared with the previous work, the highest average output power was obtained and was very competitive among the reported fiber lasers based on In_2Se_3 SA in our work. The experiment results demonstrated that PVD-In_2Se_3 SA had prominent advantages in obtaining stable pulse generation with high output power.

Dark–Bright Pulse Pairs

`By further controlling the PCs, we can observe the stable dark–bright pulse pairs with 1,838 mW pump power. **Figure 5** depicts a dark–bright pulse mode locking state of the proposed fiber laser. The corresponding single dark–bright pulse pair is shown in **Figure 5A**. The depth of the dark pulse and that of the bright pulse are nearly equal in a uniform continuous wave background. The inset in **Figure 5A** shows a typical dark–bright pulse pair train with a fundamental frequency of 1.718 MHz. As can be seen from **Figure 5B**, a triple-wavelength dark–bright pulse pair can also be achieved, and spectral centers were located at 1,558.1, 1,559.8, and 1,561.5 nm, with wavelength spacing per laser wavelength of 1.7 nm, respectively. In addition, no Kelly sidebands were observed in the spectrum, similar to previous reports [53, 54]. **Figure 5C** presents the RF spectrum of the dark–bright pulse pair with a SNR of 40 dB, which indicates that a relatively stable mode-locked operation was achieved. As shown in **Figure 5D**, the maximum average output power was 171.3 mW under the pump power of 1,838 mW, corresponding to the optical conversion efficiency of 9.32%. The largest energy of the dark–bright pulse is calculated to be about 100 nJ, which is the total pulse energy of the dark–bright pulses. Other researchers had done a similar work [55, 56]. As is known, the formation of the dark–bright pulse pairs may resulted in the cross-phase modulation effect [57]. In our opinion, the formation of a dark–bright pulse pair is not only owing to the cross-phase modulation [58, 59] but also due to the interaction of the nonlinear refractivity of In_2Se_3 nanoflakes with high nonlinear effects that resulted in high-power laser cavity. Moreover, when the pump power increases, triple-wavelength mode-locked pulse generated benefits from a combination of the high nonlinearity of In_2Se_3 nanoflakes and the spectral filtering effect in laser cavity. Regrettably, owing to the lack of a tunable filter, the polarization

characteristics of the dark–bright pulse pair were not further analyzed. In addition, no pulse pairs were observed despite adjusting the PCs when the In_2Se_3-FM SA was taken away. It can be confirmed that In_2Se_3 SA is an effective saturable absorber for stable passively mode-locked operation.

CONCLUSION

In summary, due to variations in birefringence and high nonlinearity of the laser cavity, a multiwavelength output can be generated. Finally, we successfully obtained two stable soliton pulses with average output power of 172.4 and 171.3 mW and single pulse energy of 101 and 100 nJ, respectively, in a passively mode-locked EDFL using PVD-In_2Se_3 as the saturable absorber. Besides this, a triple-wavelength dark–bright pulse pair operation with highest output power and maximum pulse energy was also first observed. All in all, the type of pulse laser based on few-layer bismuthene will provide a new reference resource for obtaining a large-energy, high-power output in the mode-locked fiber lasers and its application in optical fiber communication, spectral analysis, and pump probe experiment.

DATA AVAILABILITY STATEMENT

The raw data supporting the conclusions of this article will be made available by the authors without undue reservation.

AUTHOR CONTRIBUTIONS

CZ and BM contributed to conception and design of the study. HZ and CL performed the analysis. QW wrote the first draft of the manuscript. XH wrote sections of the manuscript. All authors contributed to manuscript revision and read and approved the submitted version.

FUNDING

This study was supported by the National Natural Science Foundation of China (11974222, 11774208, and 11804200) and a Project of Shandong Province Higher Educational Science and Technology Program (J18KZ011).

REFERENCES

1. Guo S, Zhang Y, Ge Y, Zhang S, Zeng H, Zhang H. 2D V-V Binary Materials: Status and Challenges. *Adv Mater* (2019) 31:1902352. doi:10.1002/adma.201902352
2. Jiang X, Zhang L, Liu S, Zhang Y, He Z, Li W, et al. Ultrathin Metal-Organic Framework: An Emerging Broadband Nonlinear Optical Material for Ultrafast Photonics. *Adv Opt Mater* (2018) 6:1800561. doi:10.1002/adom.201800561
3. Xu Y, Shi Z, Shi X, Zhang K, Zhang H. Recent Progress in Black Phosphorus and Black-Phosphorus-Analogue Materials: Properties, Synthesis and Applications. *Nanoscale* (2019) 11:14491–527. doi:10.1039/c9nr04348a
4. Lu J, Zhang K, Liu XF, Zhang H, Sum TC, Castro Neto AH, et al. Order-disorder Transition in a Two-Dimensional boron-carbon-nitride alloy. *Nat Commun* (2013) 4:2681–7. doi:10.1038/ncomms3681
5. Xie H, Li Z, Sun Z, Shao J, Yu X-F, Guo Z, et al. Metabolizable Ultrathin Bi2Se3Nanosheets in Imaging-Guided Photothermal Therapy. *Small* (2016) 12:4136–45. doi:10.1002/smll.201601050
6. Lu L, Tang X, Cao R, Wu L, Li Z, Jing G, et al. Broadband Nonlinear Optical Response in Few-Layer Antimonene and Antimonene Quantum Dots: A Promising Optical Kerr media with Enhanced Stability. *Adv Opt Mater* (2017) 5:1700301. doi:10.1002/adom.201700301
7. Li X, Zhang S, Liu J, Yang Z. Using Reverse Saturable Absorption to Boost Broadband Noise-like Pulses. *J Lightwave Technol* (2020) 38(14): 3769–74. doi:10.1109/jlt.2020.2977272
8. Zhang H, Bao Q, Tang D, Zhao L, Loh K. Large Energy Soliton Erbium-Doped Fiber Laser with a Graphene-Polymer Composite Mode Locker. *Appl Phys Lett* (2009) 95:141103. doi:10.1063/1.3244206
9. Li G, Ma K, Jiao Y, Jiang Q, Zhang X, Zhang Z, et al. Performance Enhancement of DFBL Based Near-infrared CH 4 Telemetry System Using a Focus Tunable Lens. *Microw Opt Technol Lett* (2021) 63: 1147–51. doi:10.1002/mop.32733
10. Yu J, Li C, Qiu X, Chen H, Zhang W. Defect Measurement Using the Laser Ultrasonic Technique Based on Power Spectral Density Analysis and Wavelet Packet Energy. *Microw Opt Technol Lett* (2021) 63:2079–84. doi:10.1002/mop.32888
11. Feng W, Qu Y, Gao Y, Ma Y. Advances in Fiber-based Quartz Enhanced Photoacoustic Spectroscopy for Trace Gas Sensing. *Microw Opt Technol Lett* (2021) 63:2031–9. doi:10.1002/mop.32841
12. Lang Z, Qiao S, He Y, Ma Y. Quartz Tuning fork-based Demodulation of an Acoustic Signal Induced by Photo-Thermo-Elastic Energy Conversion. *Photoacoustics.* (2021) 22:100272. doi:10.1016/j.pacs.2021.100272
13. Ma Y, Hu Y, Qiao S, He Y, Tittel FK. Trace Gas Sensing Based on Multi-Quartz-Enhanced Photothermal Spectroscopy. *Photoacoustics.* (2020) 20: 100206. doi:10.1016/j.pacs.2020.100206
14. Qiao S, Ma Y, He Y, Patimisco P, Sampaolo A, Spagnolo V. Ppt Level Carbon Monoxide Detection Based on Light-Induced Thermoelastic Spectroscopy Exploring Custom Quartz Tuning forks and a Mid-infrared QCL. *Opt Express* (2021) 29:25100–8. doi:10.1364/OE.434128
15. Jiang T, Yin K, Wang C, You J, Ouyang H, Miao R, et al. Ultrafast Fiber Lasers Mode-Locked by Two-Dimensional Materials: Review and prospect. *Photon Res* (2020) 8(1):78–90. doi:10.1364/prj.8.000078
16. Guo B, Xiao QL, Wang SH, Zhang H. 2D Layered Materials: Synthesis, Nonlinear Optical Properties, and Device Applications. *Laser Photon Rev* (2019) 13(12):1800327. doi:10.1002/lpor.201800327
17. Pawliszewska M, Martynkien T, Przewłoka A, Sotor J. Dispersion-managed Ho-Doped Fiber Laser Mode-Locked with a Graphene Saturable Absorber. *Opt Lett* (2018) 43(1):38–41. doi:10.1364/ol.43.000038
18. Lau KY, Abu Bakar MH, Muhammad FD, Latif AA, Omar MF, Yusoff Z, et al. Dual-wavelength, Mode-Locked Erbium-Doped Fiber Laser Employing a Graphene/polymethyl-Methacrylate Saturable Absorber. *Opt Express* (2018) 26(10):12790–800. doi:10.1364/oe.26.012790
19. Khazaeizhad R, Kassani SH, Jeong H, Yeom D-I, Oh K. Mode-locking of Er-Doped Fiber Laser Using a Multilayer MoS_2 Thin Film as a Saturable Absorber in Both Anomalous and normal Dispersion Regimes. *Opt Express* (2014) 22(19):23732–42. doi:10.1364/oe.22.023732
20. Yang HR, Liu XM. WS_2-Clad Microfiber Saturable Absorber for High-Energy Rectangular Pulse Fiber Laser. *IEEE J Sel Top Quan Electron.* (2018) 24(3): 0900807. doi:10.1109/jstqe.2017.2757142
21. Du J, Wang Q, Jiang G, Xu C, Zhao C, Xiang Y, et al. Ytterbium-doped Fiber Laser Passively Mode Locked by Few-Layer Molybdenum Disulfide (MoS2) Saturable Absorber Functioned with Evanescent Field Interaction. *Sci Rep* (2014) 4:6346. doi:10.1038/srep06346
22. Mao D, She X, Du B, Yang D, Zhang W, Song K, et al. Erbium-doped Fiber Laser Passively Mode Locked with Few-Layer WSe2/MoSe2 Nanosheets. *Sci Rep* (2016) 6:23583. doi:10.1038/srep23583
23. Luo Z, Li Y, Zhong M, Huang Y, Wan X, Peng J, et al. Nonlinear Optical Absorption of Few-Layer Molybdenum Diselenide (MoSe2) for Passively Mode-Locked Soliton Fiber Laser. *Photon Res.* (2015) 3:79–86. doi:10.1364/prj.3.000a79

24. Liu H, Zheng X-W, Liu M, Zhao N, Luo A-P, Luo Z-C, et al. Femtosecond Pulse Generation from a Topological Insulator Mode-Locked Fiber Laser. *Opt Express* (2014) 22(6):6868–73. doi:10.1364/oe.22.006868
25. Lee J, Koo J, Jhon YM, Lee JH. A Femtosecond Pulse Erbium Fiber Laser Incorporating a Saturable Absorber Based on Bulk-Structured Bi_2Te_3 Topological Insulator. *Opt Express* (2014) 22(5):6165–73. doi:10.1364/oe.22.006165
26. Sotor J, Sobon G, Macherzynski W, Abramski KM. Harmonically Mode-Locked Er-Doped Fiber Laser Based on a Sb2Te3topological Insulator Saturable Absorber. *Laser Phys Lett* (2014) 11(5):055102. doi:10.1088/1612-2011/11/5/055102
27. Guo B, Wang S-H, Wu Z-X, Wang Z-X, Wang D-H, Huang H, et al. Sub-200 Fs Soliton Mode-Locked Fiber Laser Based on Bismuthene Saturable Absorber. *Opt Express* (2018) 26(18):22750–60. doi:10.1364/oe.26.022750
28. Song Y, Liang Z, Jiang X, Chen Y, Li Z, Lu L, et al. Few-layer Antimonene Decorated Microfiber: Ultra-short Pulse Generation and All-Optical Thresholding with Enhanced Long Term Stability. *2d Mater* (2017) 4: 045010. doi:10.1088/2053-1583/aa87c1
29. Li P, Chen Y, Yang T, Wang Z, Lin H, Xu Y, et al. Two-Dimensional CH3NH3PbI3 Perovskite Nanosheets for Ultrafast Pulsed Fiber Lasers. *ACS Appl Mater Inter* (2017) 9:12759–65. doi:10.1021/acsami.7b01709
30. Sotor J, Sobon G, Kowalczyk M, Macherzynski W, Paletko P, Abramski KM. Ultrafast Thulium-Doped Fiber Laser Mode Locked with Black Phosphorus. *Opt Lett* (2015) 40(16):3885–8. doi:10.1364/ol.40.003885
31. Luo Z-C, Liu M, Guo Z-N, Jiang X-F, Luo A-P, Zhao C-J, et al. Microfiber-based Few-Layer Black Phosphorus Saturable Absorber for Ultra-fast Fiber Laser. *Opt Express* (2015) 23(15):20030–9. doi:10.1364/oe.23.020030
32. Al-Masoodi AHH, Yasin M, Ahmed MHM, Latiff AA, Arof H, Harun SW. Mode-locked Ytterbium-Doped Fiber Laser Using Mechanically Exfoliated Black Phosphorus as Saturable Absorber. *Optik* (2017) 147:52–8. doi:10.1016/j.ijleo.2017.08.038
33. Bao Q, Zhang H, Wang Y, Ni Z, Yan Y, Shen ZX, et al. Atomic-Layer Graphene as a Saturable Absorber for Ultrafast Pulsed Lasers. *Adv Funct Mater* (2009) 19(19):3077–83. doi:10.1002/adfm.200901007
34. Zheng Z, Zhao C, Lu S, Chen Y, Li Y, Zhang H, et al. Microwave and Optical Saturable Absorption in Graphene. *Opt Express* (2012) 20(21):23201–14. doi:10.1364/oe.20.023201
35. Alani IAM, Lokman MQ, Ahmed MHM, Al-Masoodi AHH, Latiff AA, Harun SW. A Few-Picosecond and High-Peak-Power Passively Mode-Locked Erbium-Doped Fibre Laser Based on Zinc Oxide Polyvinyl Alcohol Film Saturable Absorber. *Laser Phys* (2018) 28:075105. doi:10.1088/1555-6611/aabd24
36. Mafi E, Soudi A, Gu Y. Electronically Driven Amorphization in Phase-Change In2Se3 Nanowires. *J Phys Chem C* (2012) 116:22539–44. doi:10.1021/jp305696w
37. Li QL, Li Y, Gao J, Wang SD, Sun XH. High Performance Single In2Se3 Nanowire Photodetector. *Appl Phys Lett* (2011) 99:243105. doi:10.1063/1.3669513
38. Jacobs-Gedrim RB, Shanmugam M, Jain N, Durcan CA, Murphy MT, Murray TM, et al. Extraordinary Photoresponse in Two-Dimensional In2Se3 Nanosheets. *ACS Nano* (2014) 8(1):514–21. doi:10.1021/nn405037s
39. Popović S, Tonejc A, Gržeta-Plenković B, Čelustka B, Trojko R. Revised and New crystal Data for Indium Selenides. *J Appl Crystallogr* (1979) 12:416–20. doi:10.1107/s0021889879012863
40. Quereda J, Biele R, Rubio-Bollinger G, Agraït N, D'Agosta R, Castellanos-Gomez A. Strong Quantum Confinement Effect in the Optical Properties of Ultrathin α-In2Se3. *Adv Opt Mater* (2016) 4(12):1939–43. doi:10.1002/adom.201600365
41. Zhou J, Zeng Q, Lv D, Sun L, Niu L, Fu W, et al. Controlled Synthesis of High-Quality Monolayered α-In2Se3 via Physical Vapor Deposition. *Nano Lett* (2015) 15(10):6400–5. doi:10.1021/acs.nanolett.5b01590
42. Yan P, Jiang Z, Chen H, Yin J, Lai J, Wang J, et al. α-In2Se3 Wideband Optical Modulator for Pulsed Fiber Lasers. *Opt Lett* (2018) 43(18):4417–20. doi:10.1364/ol.43.004417
43. Feng W, Zheng W, Gao F, Chen X, Liu G, Hasan T, et al. Sensitive Electronic-Skin Strain Sensor Array Based on the Patterned Two-Dimensional α-In2Se3. *Chem Mater* (2016) 28(12):4278–83. doi:10.1021/acs.chemmater.6b01073
44. Zhou Y, Wu D, Zhu Y, Cho Y, He Q, Yang X, et al. Out-of-Plane Piezoelectricity and Ferroelectricity in Layered α-In2Se3 Nanoflakes. *Nano Lett* (2017) 17(9):5508–13. doi:10.1021/acs.nanolett.7b02198
45. Han XL, Zhang HN, Jiang SZ, Zhang C, Li DW, Guo QX, et al. Improved Laser Damage Threshold of In_2Se_3 Saturable Absorber by PVD for High-Power Mode-Locked Er-Doped Fiber Laser. *Nanomaterials* (2020) 9:1216.
46. Ming N, Tao S, Yang W, Chen Q, Sun R, Wang C, et al. Mode-locked Er-Doped Fiber Laser Based on PbS/CdS Core/shell Quantum Dots as Saturable Absorber. *Opt Express* (2018) 26(7):9017–26. doi:10.1364/oe.26.009017
47. Fu X, Qian J, Qiao X, Tan P, Peng Z. Nonlinear Saturable Absorption of Vertically Stood WS_2 Nanoplates. *Opt Lett* (2014) 39(22):6450–3. doi:10.1364/ol.39.006450
48. Wang J, Jiang Z, Chen H, Li J, Yin J, Wang J, et al. High Energy Soliton Pulse Generation by a Magnetron-Sputtering-Deposition-Grown MoTe2 Saturable Absorber. *Photon Res* (2018) 6(6):535–41. doi:10.1364/prj.6.000535
49. Guo B, Yao Y, Xiao J-J, Wang R-L, Zhang J-Y. Topological Insulator-Assisted Dual-Wavelength Fiber Laser Delivering Versatile Pulse Patterns. *IEEE J Select Top Quan Electron.* (2016) 22(2):8–15. doi:10.1109/jstqe.2015.2426951
50. Yan P, Chen H, Yin J, Xu Z, Li J, Jiang Z, et al. Large-area Tungsten Disulfide for Ultrafast Photonics. *Nanoscale* (2017) 9(5):1871–7. doi:10.1039/c6nr09183k
51. Fu S, Shang X, Zhang F, Xing F, Man Z, Zhang W, et al. Ferromagnetic Insulator Cr2Ge2Te6 as a Modulator for Generating Near-Infrared Bright-Dark Soliton Pairs. *Appl Opt* (2019) 58(33):9217–23. doi:10.1364/ao.58.009217
52. Zhao R, Wang M, Zheng Y, Xu N, Liu D, Li D. Generation of Dark-Bright-Bright Solitons in Er-Doped Fiber Laser Based on Ferromagnetic Insulator Cr2Ge2Te6. *Infrared Phys Tech* (2020) 109:103417. doi:10.1016/j.infrared.2020.103417
53. Gao J, Hu FM, Huo XD, Gao P. Bright-dark Pair in Passively Mode-Locked Fiber Laser Based on Graphene. *Laser Phys* (2014) 24(8):085104. doi:10.1088/1054-660x/24/8/085104
54. Guo B, Yao Y, Tian J-J, Zhao Y-F, Liu S, Li M, et al. Observation of Bright-Dark Soliton Pair in a Fiber Laser with Topological Insulator. *IEEE Photon Technol Lett* (2015) 27(7):701–4. doi:10.1109/lpt.2015.2390212
55. Zhao L, Xu NN, Zhao R, Shang XX, Liu XY, Zhang ZD, et al. Generation of Single-,dual-Wavelength Mode-Locked Operations Based on $ZrSe_2$ as Saturable Absorber in an Er-Doped Fiber Laser. *INFRARED PHYS TECHN* (2021) 116:103775. doi:10.1016/j.infrared.2021.103775
56. Ma P, Li J, Zhang H, Yang Z. Preparation of High-Damage Threshold WS2 Modulator and its Application for Generating High-Power Large-Energy Bright-Dark Solitons. *Infrared Phys Tech* (2020) 105:103257. doi:10.1016/j.infrared.2020.103257
57. Zhao R, Li G, Zhang B, He J. Multi-wavelength Bright-Dark Pulse Pair Fiber Laser Based on Rhenium Disulfide. *Opt Express* (2018) 26(5):5819–26. doi:10.1364/oe.26.005819
58. Ning Q-Y, Wang S-K, Luo A-P, Lin Z-B, Luo Z-C, Xu W-C. Bright-Dark Pulse Pair in a Figure-Eight Dispersion-Managed Passively Mode-Locked Fiber Laser. *IEEE Photon J.* (2012) 4(5):1647–52. doi:10.1109/jphot.2012.2212878
59. Lisak M, Höök A, Anderson D. Symbiotic Solitary-Wave Pairs Sustained by Cross-phase Modulation in Optical Fibers. *J Opt Soc Am B* (1990) 7(5):810–4. doi:10.1364/josab.7.000810

Conflict of Interest: The authors declare that the research was conducted in the absence of any commercial or financial relationships that could be construed as a potential conflict of interest.

Publisher's Note: All claims expressed in this article are solely those of the authors and do not necessarily represent those of their affiliated organizations or those of the publisher, the editors, and the reviewers. Any product that may be evaluated in this article or claim that may be made by its manufacturer is not guaranteed or endorsed by the publisher.

frontiers in Physics

ORIGINAL RESEARCH
published: 03 January 2022
doi: 10.3389/fphy.2021.786443

Research on Calibration Method of Infrared Temperature Measurement System Near Room Temperature Field

*Shuanglong Cui and Jian Xing**

College of Information and Computer Engineering, Northeast Forestry University, Harbin, China

The calibration accuracy of the infrared temperature measurement system near room temperature field is easily affected by the calibration environment. In this paper, an equivalent blackbody calibration method is proposed for this problem. In this method, the target radiation and ambient radiation superimposed in calibration data are separated by two calibration functions at different ambient temperatures, and an equivalent blackbody calibration function is constructed. The experimental verification of the proposed method is carried out, and the results show that the proposed method has a better calibration effect for the surface blackbody than the commonly used environmental compensation methods. This method can effectively improve the calibration accuracy of infrared temperature measurement system near room temperature field, and further improve the infrared temperature measurement theory.

Keywords: infrared temperature measurement, calibration method, equivalent blackbody, ambient temperature, calibration near room temperature field

OPEN ACCESS

Edited by:
Yufei Ma,
Harbin Institute of Technology, China

Reviewed by:
Changyong Cao,
National Oceanic and Atmospheric Administration (NOAA), United States
Guohui Mei,
Northeastern University, China

***Correspondence:**
Jian Xing
xingniat@sina.com

Specialty section:
This article was submitted to Optics and Photonics, a section of the journal Frontiers in Physics

Received: *30 September 2021*
Accepted: *12 November 2021*
Published: *03 January 2022*

Citation:
Cui S and Xing J (2022) Research on Calibration Method of Infrared Temperature Measurement System Near Room Temperature Field. Front. Phys. 9:786443. doi: 10.3389/fphy.2021.786443

1 INTRODUCTION

The spectral detection technology has the advantages of fast response, high sensitivity, and high resistance to electromagnetic noise [1], including TDLAS [2], CARS [3], QEPAS [4], QEPTS [5], THz [6], photoacoustic spectrum [7], infrared temperature measurement technology [8] and et al. Among them, infrared temperature measurement technology is widely used for non-contact temperature measurement in military, industrial, agricultural, biological, and other fields. Calibration is very important for infrared temperature measurement technology. The infrared radiation detection equipment needs to be calibrated regularly to ensure the measurement accuracy, and many scholars are constantly studying the calibration methods [9, 10]. Fluke has set up a new IR calibration laboratory with radiometric traceability for this reason [11]. For low-temperature infrared calibration, Kimball BA began the research of low-temperature infrared calibration in 1984 [13]. In 2004, NIST held calibration and intercomparison of infrared radiometers [12]. The ambient impact of some blackbodies used in the laboratory had been calibrated by the National Institute of Standards and Technology (NIST) Thermal-infrared Transfer Radiometer (TXR), and the blackbodies calibration results can be used for subsequent ambient compensation. In 2011, Barry T et al presents a self-calibration technique for the removal of measurement errors caused by thermal gradients in thermopile-based infrared thermometry [14, 15]. In 2012, Dai Y et al developed a surface blackbody for low-temperature infrared calibration, and calculated the ambient compensation value required when using this blackbody for calibration [16]. In 2020, Zhang Z Q et al explained the compensation method that takes into account the calibration error introduced by the blackbody emissivity and ambient temperature, and illustrated the difference of calibration curves before and after compensation with examples [17].

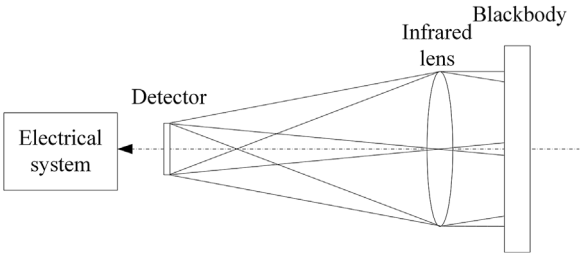

FIGURE 1 | Schematic diagram of calibration principle of infrared temperature measurement system.

The calibration experiment of the infrared temperature measurement system is usually carried out in laboratory with a surface blackbody [18]. If the target temperature is close to the ambient temperature, or even lower than the ambient temperature, the calibration accuracy is easily affected by the ambient. For this problem, the method given in the reference [12, 17] can generally be used for compensation, but sometimes the effect is not good because the given emissivity is inaccurate or the compensation model does not match the experiment.

In this paper, this problem is studied. The ambient influence is removed by comparing two calibration functions under different ambient temperatures. And the equivalent blackbody calibration function is obtained.

2 PRINCIPLE OF INFRARED CALIBRATION AND TEMPERATURE MEASUREMENT

It is necessary to calibrate the infrared temperature measurement system to establish the quantitative relationship between the input radiation intensity and the output signal of the infrared detector before use. In this paper, a refrigerating photoelectric detector is used in the infrared temperature measurement system [19], and the output signal of the detector has a linear relationship with the irradiance from the infrared source [20]. When the target is a blackbody, the calibration function is shown as **Eq. 1**.

$$V = kf(T) + b \tag{1}$$

Where V is the output voltage of detector, k system response factor, including parameters such as lens transmittance, amplifier gain, lens area, field of view area, distance between target and instrument, b system bias, $f(T)$ is calculated according to **Eq. 2** [21].

$$L = \int_{\lambda_1}^{\lambda_2} R_\lambda L_{\lambda B}(T) d\lambda = \int_{\lambda_1}^{\lambda_2} R_\lambda \cdot \frac{c_1}{\pi\lambda^5} \cdot \frac{1}{e^{c_2/\lambda T} - 1} d\lambda = f(T) \tag{2}$$

Where λ_2 and λ_1 are the upper and lower limits of the spectral response of the detector, R_λ the wavelength function of thermometer [22], $L_{\lambda B}(T)$ the blackbody radiation exitance at T temperature, and c_1 and c_2 the first and second Plank's radiation constants.

The calibration principle schematic diagram of the infrared temperature measurement system is shown in **Figure 1** [23]. The blackbody radiation emission needs to cover the entire field of view of the calibrated infrared temperature measurement system. By changing the temperature of the blackbody, the response of the detector at the corresponding temperature can be obtained. The calibration coefficients of **Eq. 1** are determined through least square fitting the band radiation response $f(T)$ versus the detector response at different temperatures [24].

When calibration results are used to measure the temperature of a grey body target (with constant emissivity ε), focusing the thermometer on it, the target radiation exitance L is calculated from the output voltage with **Eq. 1**. And after compensating for environmental interference, the target temperature T is calculated inverting **Eq. 2**. So the following **Eq. 3** is obtained [25]:

$$T = f^{-1}\left[\frac{\frac{V-b}{k} - (1-\varepsilon) f(T_{\text{amb}})}{\varepsilon}\right] \tag{3}$$

Where T_{amb} is the ambient temperature (which behaves as a blackbody being a cavity).

3 CALIBRATION METHOD PRINCIPLE OF INFRARED TEMPERATURE MEASUREMENT SYSTEM NEAR ROOM TEMPERATURE FIELD

For the infrared temperature measurement system which is easily affected by the environment near room temperature field, the calibration coefficients are different due to different calibration environments. Set the standard calibration function after removing ambient influence as **Eq. 4**.

$$V = kf\left(T_{\text{obj}}\right) + b \tag{4}$$

The calibration function **Eq. 5** can be obtained by calibrating with an ambient temperature of T_{amb1}.

$$V_1 = k_1 f\left(T_{\text{obj}}\right) + b_1 \tag{5}$$

The calibration function **Eq. 6** can be obtained by calibrating with an ambient temperature of T_{amb2}.

$$V_2 = k_2 f\left(T_{\text{obj}}\right) + b_2 \tag{6}$$

Eq. 7 can be obtained by constructing **Eq. 4** as the addition of target radiation and ambient radiation.

$$V = k\left[\varepsilon f\left(T_{\text{obj}}\right) + (1-\varepsilon) f(T_{\text{amb}})\right] + b \tag{7}$$

When the target temperature is the same as the ambient temperature, **Eq. 7** is the same as **Eq. 4**. **Eq. 8** can be obtained by further decomposing **Eq. 7**.

$$V = k\varepsilon f\left(T_{\text{obj}}\right) + k(1-\varepsilon) f(T_{\text{amb}}) + b \tag{8}$$

It can be seen from **Eq. 8** that the effects of ambient temperatures T_{amb1} and T_{amb2} are included in coefficients b_1

and b_2 during laboratory calibration. **Eq. 9** can be obtained by combining **Eq. 8** with **Eq. 5**.

$$\begin{cases} k\varepsilon = k_1 \\ k(1-\varepsilon)f(T_{amb1}) + b = b_1 \end{cases} \tag{9}$$

Eq. 10 can be obtained by combining **Eq. 8** with **Eq. 6**.

$$\begin{cases} k\varepsilon = k_2 \\ k(1-\varepsilon)f(T_{amb2}) + b = b_2 \end{cases} \tag{10}$$

From **Eq. 9** and **Eq. 10**, we can see that in theory $k_1=k_2=k\varepsilon$. In the actual experiment, only $k_1\approx k_2$ can be achieved, and $k\varepsilon\approx(k_1+k_2)/2$ can be used in the calculation. New calibration coefficients k and b can be obtained by substituting $k\varepsilon\approx(k_1+k_2)/2$ back to **Eq. 9** and **Eq. 10**.

$$\begin{cases} k = \dfrac{\frac{k_1+k_2}{2}\left[f(T_{amb2}) - f(T_{amb1})\right] + (b_2 - b_1)}{f(T_{amb2}) - f(T_{amb1})} \\ b = b_1 - kf(T_{amb1}) + \dfrac{k_1+k_2}{2}f(T_{amb1}) = b_2 - kf(T_{amb2}) \\ \quad + \dfrac{k_1+k_2}{2}f(T_{amb2}) \end{cases} \tag{11}$$

In this way, the equivalent blackbody calibration function with the target temperature equivalent blackbody radiation as a variable can be obtained.

4 CALIBRATION METHOD VERIFICATION EXPERIMENT OF INFRARED TEMPERATURE MEASUREMENT SYSTEM NEAR ROOM TEMPERATURE FIELD

In order to verify the calibration method proposed in this paper, calibration experiments were carried out in two environments with different temperatures. The calibration functions are used to measure the target which is equal to the ambient temperature (the ambient temperature has little influence according to **Eq. 7**). The validity of the proposed calibration method can be verified by observing the measurement deviation. A temperature-controllable calibration environment is formed with a high and low-temperature test chamber.

4.1 Apparatus for Verification Experiment

In order to complete the verification experiment of the proposed calibration method, the infrared temperature measuring system and the small surface blackbody were disassembled to reduce their volume. They can be conveniently placed in the high and low temperature test chamber. The main experimental devices of the verification experiment include: the disassembled infrared temperature measurement system, the high and low temperature test chamber, and the disassembled small surface blackbody.

Since the minimum working temperature of the surface blackbody used in the experiment is −10°C, and the maximum working temperature of the disassembled infrared detector module is 40°C, the verification experiment is carried out in the range of −10°C–40°C. The schematic diagram and photos of calibration method verification experiment are shown in **Figure 2**.

4.2 Results of Verification Experiment

1) Calibration Function Fitting

The selected calibration ambient temperature is expected to be close to the conventional laboratory ambient temperature. The high and low temperature test chamber used in this experiment has better stability during refrigeration, so two temperatures lower than room temperature, 10°C and 15°C, are selected. After setting up the experimental environment as shown in **Figure 2**, set the temperature of the high and low temperature test chamber to 10°C. The calibration experiment was carried out at this ambient temperature. The blackbody temperature varied from −10°C to 40°C, and the change step was 10°C. The detector output at the corresponding temperature were recorded. Then adjust the temperature of the high and low temperature test chamber to 15°C, and perform the calibration experiment again. The summary of calibration experimental data is shown in **Table 1**.

According to the calibration data, the calibration function at 10°C is obtained as shown in **Eq. 12**. The fitting correlation coefficient is 0.9981, and the linearity is good.

$$V_1 = 0.0403f\left(T_{obj}\right) - 1.5996 \tag{12}$$

According to the calibration data, the calibration function at 15°C is obtained as shown in **Eq. 13**. The fitting correlation coefficient is 0.9982, and the linearity is good.

$$V_2 = 0.0402f\left(T_{obj}\right) - 1.5811 \tag{13}$$

According to the method described in Refs. [12, 17], the calibration function obtained at a fixed ambient temperature is compensated, and the calibration function after compensation is shown as **Eq. 14**.

$$V = 0.0424f\left(T_{obj}\right) - 1.6216 \tag{14}$$

According to **Eq. 11**, **Eq. 12**, and **Eq. 13**, the coefficients of the equivalent blackbody calibration function are calculated, and the calibration function is shown as **Eq. 15**.

$$V = 0.0510f\left(T_{obj}\right) - 1.7868 \tag{15}$$

2) Measurement Verification

An experimental scene without ambient influence is formed by adjusting the set temperature of the high and low temperature experiment chamber and the surface blackbody simultaneously, and making the two temperatures equal. The temperature increased from −10°C to 40°C. Temperature inversion on the data collected in the experiment is carried out with **Eq. 13**, **Eq. 14**, and **Eq. 15**. Summarize the deviation results into a table, as shown in **Table 2**.

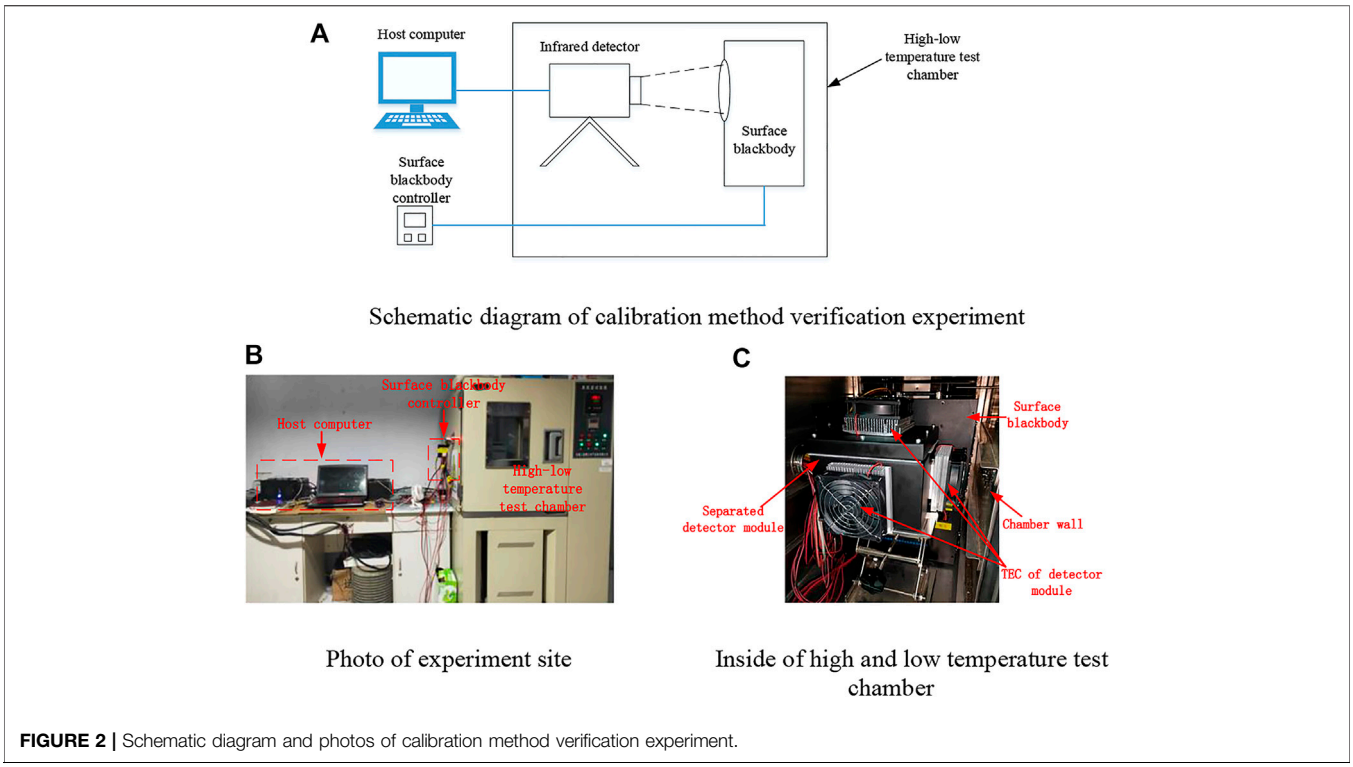

FIGURE 2 | Schematic diagram and photos of calibration method verification experiment.

TABLE 1 | Calibration experimental data of infrared temperature measurement system.

Serial number	Target temperature	Output at ambient temperature 10°C	Output at ambient temperature 15°C
1	−10.0°C	−1.1146 V	−1.0970 V
2	0.0°C	−1.0145 V	−0.9953 V
3	10.0°C	−0.9033 V	−0.8857 V
4	20.0°C	−0.7714 V	−0.7533 V
5	30.0°C	−0.6129 V	−0.5954 V
6	40.0°C	−0.4307 V	−0.4126 V

TABLE 2 | Verification experiment when environmental temperature equal to target temperature.

Serial number	Target temperature	Results of Eq. 13	Results of Eq. 14	Results of Eq. 15
1	−10.0°C	−6.6°C	−4.6°C	1.8°C
2	0.0°C	−4.3°C	−3.1°C	0.7°C
3	10.0°C	−1.9°C	−1.8°C	−0.7°C
4	20.0°C	0.8°C	0.5°C	−0.9°C
5	30.0°C	3.6°C	2.8°C	−0.5°C
6	40.0°C	6.5°C	5.1°C	0.6°C

The effectiveness of the calibration method proposed in this paper can be seen from the experimental results in **Table 2**. The equivalent blackbody calibration function **Eq. 15** has the best data inversion result, with the maximum error of ±1.8°C and the average absolute value error of 0.9°C. The maximum error of calibration function obtained by direct calibrating is ±6.6°C, and the average absolute error is 4.0°C. The maximum error of the calibration function after conventional ambient compensation is ±5.1°C, and the average absolute value error is 3.0°C.

According **Table 2**, the measured result is lower than the actual temperature with the conventional calibration function when the target temperature is lower than the calibration ambient temperature. This is because when calibration is carried out in this case, the total radiation received by the infrared temperature measuring equipment will be higher than the blackbody radiation

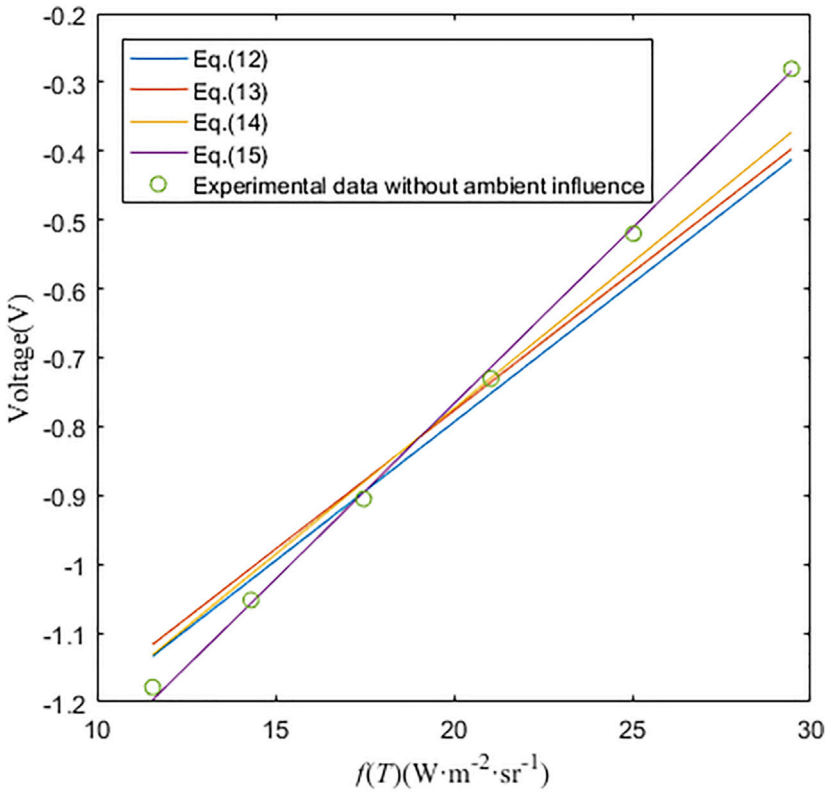

FIGURE 3 | Calibration functions and experimental data without environmental interference.

at the target temperature. When the target temperature is higher than the ambient temperature, on the contrary, the experimental measurement result is higher than the actual temperature. Because the error caused by the ambient temperature is far greater than that caused by the nonlinearity and random noise of calibration data, the signs of errors obtained by the conventional calibration method show obvious regularity with the calibration ambient temperature as the dividing line. The method proposed in this paper has largely eliminated the influence of calibration ambient temperature, so the error distribution is symmetrical, which is mainly caused by the nonlinearity of calibration data.

The experimental results show that the ambient temperature has a great influence on the infrared calibration near room temperature field in the laboratory, and the maximum error can reach ±6.6°C when using the direct calibration function in the verification experiment. Conventional environmental temperature compensation methods can reduce the environmental impact, but sometimes the effect is not ideal. The maximum measurement error is reduced from ±6.6°C to ±5.1°C in the experiment. The equivalent blackbody calibration method can more effectively remove the environmental interference in the infrared calibration, and the maximum measurement error is reduced from ±6.6°C to ±1.8°C in the experiment.

The calibration curves **Eq. 12**, **Eq. 13**, **Eq. 14**, **Eq. 15**, and the data without environmental interference measured in the verification experiment are plotted as shown in **Figure 3**.

It can be seen from **Figure 3** that the calibration functions **Eq. 12** and **Eq. 13** obtained by calibrating at different ambient temperatures are basically parallel, that is, the slope is basically fixed. According to Ref. [17], after environmental temperature compensation, the slope of the calibration curve increases, and calibration curve is closer to the experimental data. It is indicated that the compensation has a certain effect, but the effect is not satisfactory. The equivalent blackbody calibration function basically coincides with the experimental data without environmental interference, which shows the effectiveness of the method.

5 CONCLUSION

During the calibration of the infrared temperature measurement system near room temperature field, the target temperature is close to the ambient temperature, or even lower than the ambient temperature. The calibration accuracy is easily affected by the ambient. In this paper, an equivalent blackbody calibration method is proposed to solve this problem. The calibration method can be used for the calibration of large aperture infrared radiation equipment with a surface blackbody. It is studied to solve the inadaptability of the ambient compensation method in the Refs. [12, 17]. In this method, the target radiation and ambient radiation superimposed in calibration data are separated by two calibration functions at different ambient

temperatures, and an equivalent blackbody calibration function is constructed. The experimental verification of the proposed method shows that the maximum measurement error is reduced from ±6.6°C to ±1.8°C. Compared with the calibration function after conventional ambient compensation, the result of the equivalent blackbody calibration function is more satisfying.

DATA AVAILABILITY STATEMENT

The original contributions presented in the study are included in the article/supplementary material, further inquiries can be directed to the corresponding author.

AUTHOR CONTRIBUTIONS

SC: Methodology, Software, Validation, Formal analysis, Writing—Original Draft, Project administration; JX: Conceptualization, Resources, Writing—Reviewing and Editing, Supervision, Funding acquisition.

FUNDING

This work was supported by the National Natural Science Foundation of China (No. 61975028).

REFERENCES

1. Lang Z, Qiao S, He Y, Ma Y. Quartz Tuning fork-based Demodulation of an Acoustic Signal Induced by Photo-Thermo-Elastic Energy Conversion. *Photoacoustics* (2021) 22:100272. doi:10.1016/j.pacs.2021.100272
2. Qiao S, Ma Y, He Y, Patimisco P, Sampaolo A, Spagnolo V. Ppt Level Carbon Monoxide Detection Based on Light-Induced Thermoelastic Spectroscopy Exploring Custom Quartz Tuning forks and a Mid-infrared QCL. *Opt Express* (2021) 29(16):25100–8. doi:10.1364/OE.434128
3. Isobe K, Suda A, Tanaka M, Hashimoto H, Kannari F, Kawano H, et al. Single-pulse Coherent Anti-stokes Raman Scattering Microscopy Employing an Octave Spanning Pulse. *Opt Express* (2009) 17(14):11259–66. doi:10.1364/OE.17.011259
4. Ma Y, Lewicki R, Razeghi M, Tittel FK. QEPAS Based Ppb-Level Detection of CO and N_2O Using a High Power CW DFB-QCL. *Opt Express* (2013) 21(1): 1008. doi:10.1364/OE.21.001008
5. Ma Y, He Y, Tong Y, Yu X, Tittel FK. Quartz-tuning-fork Enhanced Photothermal Spectroscopy for Ultra-high Sensitive Trace Gas Detection. *Opt Express* (2018) 26(24):32103–10. doi:10.1364/OE.26.032103
6. Jepsen PU, Cooke DG, Koch M. Terahertz Spectroscopy and Imaging - Modern Techniques and Applications. *Laser Photon Rev* (2010) 5:124–66. doi:10.1002/lpor.201000011
7. Ma Y, Hu Y, Qiao S, He Y, Tittel FK. Trace Gas Sensing Based on Multi-Quartz-Enhanced Photothermal Spectroscopy. *Photoacoustics* (2020) 20: 100206. doi:10.1016/j.pacs.2020.100206
8. Zhang Y-c., Chen Y-m., Luo C. A Method for Improving Temperature Measurement Precision on the Uncooled Infrared thermal Imager. *Measurement* (2015) 74:64–9. doi:10.1016/j.measurement.2015.07.016
9. Choi T, Cao C, Blonski S, Wang W, Uprety S, Shao X. NOAA-20 VIIRS Reflective Solar Band Postlaunch Calibration Updates Two Years In-Orbit. *IEEE Trans Geosci Remote Sensing* (2020) 58(99):7633–42. doi:10.1109/TGRS.2020.2982764
10. Chen Y, Iturbide-Sanchez F, Tremblay D, Tobin D, Strow L, Wang L, et al. Reprocessing of Suomi NPP CrIS Sensor Data Records to Improve the Radiometric and Spectral Long-Term Accuracy and Stability. *IEEE Trans Geosci Remote Sensing* (2021)(99) 1–14. doi:10.1109/TGRS.2021.3060639
11. Liebmann F. Infrared Calibration Development at Fluke Corporation Hart Scientific Division. *Thermosense XXX* (2008) 693906, 2008 . International Society for Optics and Photonics. doi:10.1117/12.781510
12. Rice JP, Butler JJ, Johnson BC, Minnett PJ, Maillet KA, Nightingale TJ, et al. The Miami2001 Infrared Radiometer Calibration and Intercomparison. Part I: Laboratory Characterization of Blackbody Targets. *J Atmos Oceanic Technol* (2004) 21(2):258–67. doi:10.1175/1520-0426(2004)021<0258:tmirca>2.0.co;2
13. Kimball BA, Mitchell ST. Low-temperature Calibration of Infrared Thermometers. *J Atmos Oceanic Technol* (1984) 1:379–82. doi:10.1175/1520-0426(1984)001<0379:ltcoit>2.0.co;2
14. Barry T, Fuller G, Hayatleh K, Lidgey J. Self-Calibrating Infrared Thermometer for Low-Temperature Measurement. *IEEE Trans Instrum Meas* (2011) 60: 2047–52. doi:10.1109/TIM.2011.2113123
15. Barry T, Fuller G, Hayatleh K. Infrared Temperature Measurement for Remote Monitoring in Cold Climates. *Meas Sci Technol* (2012) 23:114001. doi:10.1088/0957-0233/23/11/114001
16. Dai Y, Liu Z, Mao H, Zhang Y, Xiang L, Sandy T. Study on the Calibration Method for the Measurement of Low-Temperature Radiation Responsivity of IR Camera. *Int Soc Opt Photon* (2012) 84172F. doi:10.1117/12.977819
17. Zhang ZQ, Wang P, Yu XD, Zhang J, Li T. Study on High Accuracy Temperature Measurement Technology of Infrared thermal Imager. *Chin J Scientific Instrument* (2020) 10–8. doi:10.19650/j.cnki.cjsi.J2006177
18. Zhang H, Hui Z. *Design and Experimental Test of a Novel Surface Blackbody with Honeycombs*. IEEE (2010). p. 361–4.
19. Vigo System SA (2017). PVMI-2TE. Available at: https://vigo.com.pl/produkty/pvmi-2te/ [Accessed December 15, 2017].
20. Svensson T, Renhorn I, Broberg P. A Study of the Radiometric Calibration of Spectral Bands in the Mid-wave Infrared (MWIR) Spectral Range 1.5-5 μm. *Infrared Imaging Syst Des Anal Model Test* (2009) XX:73000. doi:10.1117/12.818442
21. Yang L. Calculation and Error Analysis of Temperature Measurement Using Thermal Imager. *Infrared Tech* (1999) 20–4. CNKI:SUN:HWJS.0.1999-04-005.
22. Coppa P, Ruffino G, Spena A. Pyrometer Wavelength Function: its Determination and Error Analysis. *High temp.-High Press* (1988) 20:479–90.
23. Sun ZY, Wang M, Chang ST. Effect and Correction of Environmental Temperature on Infrared Radiation Measurement Precision. *Laser & Infrared* (2014) 522–7. CNKI:SUN:JGHW.0.2014-05-011.
24. Yang CY, Zhang JP, Cao LH. Infrared Radiation Measurement Based on Real-Time Correction. *J Infrared Millimeter Waves* (2011) 284–8. CNKI:SUN:HWYH.0.2011-03-022.
25. Cui S, Sun B, Sun X. A Method for Improving Temperature Measurement Accuracy on an Infrared Thermometer for the Ambient Temperature Field. *Rev Scientific Instr* (2020) 91:054903. doi:10.1063/1.5121214

Conflict of Interest: The authors declare that the research was conducted in the absence of any commercial or financial relationships that could be construed as a potential conflict of interest.

Publisher's Note: All claims expressed in this article are solely those of the authors and do not necessarily represent those of their affiliated organizations, or those of the publisher, the editors and the reviewers. Any product that may be evaluated in this article, or claim that may be made by its manufacturer, is not guaranteed or endorsed by the publisher.

frontiers in Physics

ORIGINAL RESEARCH
published: 21 January 2022
doi: 10.3389/fphy.2021.796549

An Elliptical-Core Few-Mode Fiber with Low Loss and Low Crosstalk for the MIMO-FREE Applications

Yan Gao[1†], Yanlei Li[1†], Xin Li[1], Hongjun Zheng[1], Chenglin Bai[1], Weisheng Hu[2], Hengying Xu[1], Qiuhuan Dong[1], Huadong Xing[1], Yingqun Su[1], Yingxin Yin[1], Chongqi Wei[1] and Baiqiang Zhao[1]*

[1]*Shandong Provincial Key Laboratory of Optical Communication Science and Technology, School of Physics Science and Information Engineering, Liaocheng University, Liaocheng, China,* [2]*State Key Laboratory of Advanced Optical Communication Systems Networks, School of Electronic Information and Electrical Engineering, Shanghai Jiao Tong University, Shanghai, China*

In this invited paper, a novel elliptical-core few-mode fiber (EFMF) with low loss and low Crosstalk is proposed for multiple input multiple output free (MIMO-FREE) applications. The EFMF, which adopts pure silica elliptical core with a step refractive index profile and trench refractive index, can be used in MIMO-FREE operation. The result using a full-vector finite element method shows that the proposed EFMF breaks the mode degeneracy and achieves modes maintaining function. The EFMF performs five non-degenerate modes operations with the modes LP01, LP11a, LP11b, LP21b, and LP21a for the MIMO-FREE applications. The mode crosstalk of the EFMF is effectively reduced using the optimized ellipticity and the large effective refractive index difference between the modes. If the data rate or capacity is conventionally set to a multiple of 2, the transmission system can be upgraded using the EFMF with four modes operations where the effective refractive index difference between any two modes is more than 2×10^{-3}. A pure silica core is employed to effectively reduce intrinsic loss. The low bending loss is realized by using the trench refractive index at the cladding. The EFMF can be applied to the good transmission of mode division multiplexing in MIMO-FREE applications while eliminating the difficulty and complexity of the MIMO digital signal processing.

Keywords: mode division multiplexing, elliptical-core few-mode fiber, multiple-input multiple-output free applications, pure silica, low loss, low crosstalk, large effective refractive index difference

OPEN ACCESS

Edited by:
Yufei Ma,
Harbin Institute of Technology, China

Reviewed by:
Dong Mao,
Northwestern Polytechnical University, China
Guijun Hu,
Jilin University, China

****Correspondence:***
Hongjun Zheng
hjzheng@yahoo.com

[†]These authors have contributed equally to this work

Specialty section:
This article was submitted to Optics and Photonics, a section of the journal Frontiers in Physics

Received: *17 October 2021*
Accepted: *27 December 2021*
Published: *21 January 2022*

Citation:
Gao Y, Li Y, Li X, Zheng H, Bai C, Hu W, Xu H, Dong Q, Xing H, Su Y, Yin Y, Wei C and Zhao B (2022) An Elliptical-Core Few-Mode Fiber with Low Loss and Low Crosstalk for the MIMO-FREE Applications. Front. Phys. 9:796549. doi: 10.3389/fphy.2021.796549

INTRODUCTION

With the increasing development of various communication services such as cloud computing, big data, and short video, users have an increasing demand for data transmission capacity or transmission spectral efficiency. The single-mode fiber transmission system has been unable to meet the needs of more and more communication services, because the communication capacity of the single-mode optical fiber has approached the non-linear Shannon limit [1]. The method of mode division multiplexing based on few-mode fibers, which can exponentially increase the transmission capacity or spectral efficiency to meet the demand for unabated growth of data traffic, has attracted wide attention and become a research focus in the field of fiber communication. The research of mode division multiplexing is mainly focused on few-mode fiber (FMF) [2–9], few-mode (de) multiplexer [5–7, 10, 11], few-mode erbium-doped fiber amplifier [12, 13], few-mode fiber transmission system [5–7, 14, 15], etc.

The researches on the few-mode (de)multiplexer, few-mode erbium-doped fiber amplifier, and few-mode fiber transmission system all focus on the main line of the few-mode fiber. The few-mode fiber is the carrier of information transmission in the mode division multiplexing system. Mode division multiplexing based on the few-mode fiber has become one of the research focuses of the next-generation optical communication technology. We will discuss the few-mode fiber in this article. The few-mode fiber generally adopts a circular core with a typical graded refractive index and step refractive index distribution [4]. The mode division multiplexing transmission system based on this kind of few-mode fiber is constantly refreshing the experimental record of spectral efficiency. For instance, the mode division multiplexing transmission based on the three-mode few-mode fiber is proposed [16]. A net capacity of 280 Tbps (93.34 Tbps per mode) and a total spectral efficiency of 29.4 bit/s/Hz are achieved over 30 km few-mode fiber by using 381 WDM channels, three spatial modes, PDM-64QAM modulation format, appropriate mode delay, and 6 × 6 MIMO processing. A mode division multiplexing transmission system based on a weakly coupled 10-mode few-mode fiber is proposed [17]. A capacity record of 257 Tbps and a total spectral efficiency of 30.5 bit/s/Hz are realized over 48 km few-mode fiber by using 336 WDM channels, 10 spatial modes, DP-QPSK modulation format, appropriate mode delay, and 2 × 2 and 4 × 4 partial MIMO processing. In the study mentioned in reference [18], the mode division multiplexing transmission over six-mode graded index few-mode fiber is proposed, where a net capacity of 138 Tbps and the spectral efficiency of 34.91 bit/s/Hz are realized on the loop over 59 km few-mode fiber by using 120 WDM channels, 12 spatial and polarization modes, PDM-16QAM modulation format, appropriate mode delay, and 12 × 12 MIMO processing. It is proposed that a transmission capacity of 266.1 Tbps and a spectral efficiency of 36.7 bit/s/Hz are realized over 90.4 km few-mode fiber by using 580 WDM channels, 19-core 6 spatial modes, DP-64QAM modulation format, appropriate mode delay, and 12 × 12 MIMO processing [19]. The mode division multiplexing transmission based on weakly coupled 10-mode step index few-mode fiber is proposed in the study mentioned in reference [20]. The transmission system with a capacity of 402.7 Tbps and spectrum efficiency of 39.7 bit/s/Hz is realized over 48 km few-mode fiber by using 747 WDM channels, 10 spatial and polarization modes, PS-PDM-16QAM modulation format, appropriate mode delay, and four 4 × 4 MIMO and two 2 × 2 MIMO processing. In the study mentioned in reference [21], mode division multiplexing transmission based on the few-mode fiber with 38 cores and 3 spatial modes is proposed. The net capacity of 10.66 Pbps (93.5 Tbps per mode) and average spectral efficiency of 1158.7 bit/s/Hz are realized over 13 km few-mode fiber by using 368 WDM channels, 138 cores three spatial modes, 64QAM and 256QAM modulation formats, appropriate mode delay, and 6 × 6 MIMO processing.

Although the spectral efficiency of the few-mode fiber transmission system is increased, the circular-core few-mode fiber used in the aforementioned mode division multiplexing system has the problems of mode degeneracy and inter-mode crosstalk. In these circular-core few-mode fibers, linear polarization (LP) modes can be divided into two categories, one is circular symmetrical mode denoted as the LP0m mode, and the other is non-circular symmetrical mode denoted as the LP1m (l > 0) mode. Non-circular symmetric modes have twofold degeneracy such as even mode LP11a and odd mode LP11b. If twofold degeneracy modes such as the modes LP11a and LP11b are used as the two channels of mode division multiplexing at the same time, it is necessary to use appropriate mode delay and 4 × 4 MIMO-DSP receiver to deal with mode degeneracy and polarization diversity, or appropriate mode delay and larger matrix MIMO-DSP receiver to handle more inter-mode crosstalk and mode degeneracy at the same time [16–21]. Mode degeneracy and mode crosstalk need to be handled by using the MIMO-DSP method. The more the modes, the more rapidly the amount of data calculation and complexity increase, which leads to serious problems such as huge power consumption and high cost of short-distance data communication systems [22–24]. In order to solve the aforementioned problems due to mode degeneracy and mode crosstalk in circular-core few-mode fiber, we propose an EFMF with low loss and low crosstalk to break the mode degeneracy and achieve mode maintaining function for the MIMO-FREE applications. The EFMF uses a pure silica core with step refractive index and a trench refractive index profile. The research results show that the EFMF breaks the mode degeneracy and realizes five non-degenerate modes operations including the mode LP01, LP11a, LP11b, LP21b, and LP21a. The EFMF has the advantages of low loss, low crosstalk, and low bending loss, which are obviously better than those in the studies mentioned in Refs. [25–29]. Obviously, our proposed EFMF not only has important applications of MIMO-FREE in the optical communication field, but also can be widely used in the pulse transmission systems [30, 31], high-speed transmission systems [32, 33], sensor systems [34], and fiber laser systems [35, 36]. For example, our proposed EFMF can be applied to the fiber lasers in the reference [36] which can produce two-color laser pulses with narrower linewidth and a higher extinction ratio.

THE DESIGN STRATEGY, TOPOLOGY DIAGRAM, AND THEORETICAL MODEL OF EFMF

The Main Design Strategy of EFMF

The main purpose of our proposed EFMF is to break the mode degeneracy and realize a mode maintaining function with low crosstalk and low loss for the MIMO-FREE applications, which can effectively solve the serious problems of large delay, large computation, high complexity, huge power consumption, and high cost induced by the MIMO-DSP method in a short-distance communication system based on the conventional circular-core FMF.

These parameters of our proposed EFMF are obtained on the basis of the previous references. First, considering that the radius of the standard single-mode fiber core is about 5 μm in the studies mentioned in Refs. [4, 7] and our proposed fiber core has the major and minor axis radius, we adopt a minor axis radius of

4.6 μm, which is slightly smaller than that of a single-mode fiber. A major axis radius of 6.9 μm and the ellipticity ρ of 1.5 of our proposed EFMF are optimized by that the effective refractive index difference between the modes is as large as possible and the effective area is approximately equal to that of the standard single-mode fiber. This main discussion is described in detail in the section "3.3 Variations of the effective refractive index differences with the ellipticity" in this article.

In this way, that our proposed EFMF breaks the mode degeneracy and realizes the mode-maintaining function with low crosstalk and low loss for the MIMO-FREE applications is achieved by using the optimized ellipticity, a large effective refractive index difference between the modes and pure silica core method. In the case of achieving our goal, other transmission characteristics of our proposed EFMF are also approximately optimized due to the correlation of various parameters, such as effective refractive index difference, effective area, non linear effect, and bending loss. In order to further reduce the bending loss, we use the trench refractive index at the cladding to achieve the lower bending loss.

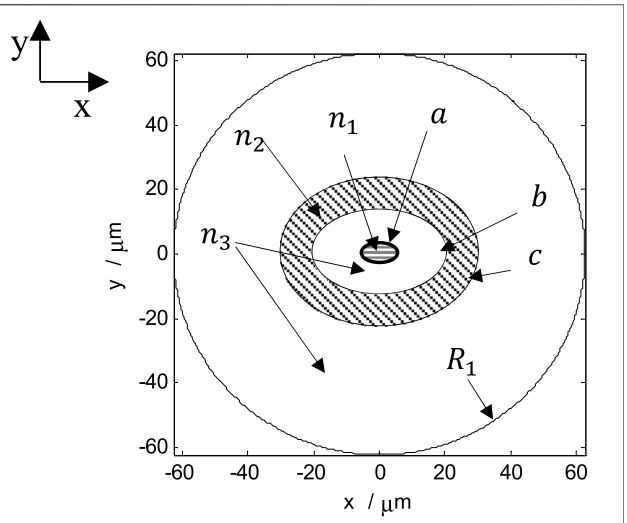

FIGURE 1 | Cross section of the EFMF.

Design Idea of Bending Loss and Cutoff Mode

The bending loss of our proposed EFMF decreases with an increase of the trench width and bending radius R, as shown in **Figure 8A** in *The Variations of the Bending Losses*. However, the trench depth, trench width, and the spacing between the trench and the fiber core, which are comprehensively determined from the studies mentioned in the Refs. [4, 7, 8], are sufficient for our proposed EFMF. For example, a trench width of 10 μm is comprehensively determined from the studies mentioned in the Refs. [4, 7, 8], which is sufficient for our proposed EFMF. This is just an example to show the effect of trench on the bending loss. Of course, we can continue to further optimize the trench. However, too much discussion of the bending loss seems to deviate from our main purpose, so we will not discuss the effect of trench depth and spacing between the trench and the fiber core on the bending loss.

Considering that the span of a practical optical communication application is generally 80 km, the launch power is 0 dBm, and the actual background noise of detection devices such as optical spectrum analyzer is about -60 dBm in general, that one mode transmits over a span of 80 km with the fiber loss of 7.5×10^{-4} dB/m (i.e., 0.75 dB/km) results in the total fiber loss of 60 dB (60 dB = 0.75 dB/km × 80 km), where the mode will be cutoff and submerged in the background noise due to the mode received power of −60 dBm [37].

There are two evaluation criteria to determine which mode is the cutoff mode and which one is the transmission mode in a fiber [37]. The first criterion is that the fiber loss of a cutoff mode can be higher than the initial threshold value of 7.5×10^{-4} dB/m (i.e., 0.75 dB/km) for practical optical transmission applications [37]. Here, we can take the fiber loss higher than 7.5×10^{-2} dB/m at a bending radius of 14 cm used for single mode fibera as a strict evaluation criterion of the cutoff mode, which is hundred times the evaluation standard value of the cutoff mode, as described in the study mentioned in reference [37] for practical application. The second criterion is that the fiber loss of the transmission mode should be smaller than the initial threshold value of 7.5×10^{-4} dB/m (i.e., 0.0141 dB/100 turns) [37]. Here, we can take the fiber loss lower than 7.5×10^{-6} dB/m at a bending radius of 30 mm as a strict evaluation criterion of the transmission mode, which is one percent of the evaluation standard value of the transmission mode, as described in the study mentioned in reference [37] for practical optical transmission application.

For our proposed EFMF, the fiber loss includes the intrinsic loss and bending loss. If we take the intrinsic loss of 0.16 dB/km in the C band for calculation, the initial threshold value of bending loss in the evaluation criterion is 0.59 dB/km (0.75 dB/km −0.16 dB/km = 0.59 dB/km, i.e., 5.9×10^{-4} dB/m). Here, we can take the bending loss higher than 5.9×10^{-2} dB/m as a strict evaluation criterion of the cutoff mode, which is hundred times the initial threshold value of bending loss of 5.9×10^{-4} dB/m. We can take the bending loss lower than 5.9×10^{-6} dB/m as a strict evaluation criterion of the transmission mode, which is one percent of the initial threshold value of 5.9×10^{-4} dB/m. For our proposed EFMF, the bending loss of the mode LP02 is about 1 dB/m, which is much higher than 5.9×10^{-2} dB/m at the bending radius of 14 cm, and the bending losses of the modes LP01, LP11a, LP11b, LP21b, and LP21a are all much less than 5.9×10^{-6} dB/m at a bending radius of 30 mm where those of the higher order modes LP21b and LP21a are about 10^{-12}–10^{-11} dB/m. According to the two strict criteria from the study mentioned in reference [37], it shows that the modes LP01, LP11a, LP11b, LP21b, and LP21a are the transmission modes in our proposed EFMF, and the mode LP02 is the cutoff mode. Meanwhile, that the lower cutoff wavelength of our proposed EFMF is 1.5 μm and the upper one is 1.8 μm is given in the section "3.9 Cutoff wavelength" in this article.

Topology Diagram and Theoretical Model of EFMF

Figure 1 shows the cross section of the EFMF. The EFMF consists of a pure silica elliptical core with a large refractive index, a trench refractive region, and a cladding. The central coordinate of the core is (0, 0). The shadow area with the horizontal line is the elliptical core of the EFMF, where the major axis radius is a_x = 6.9 μm, the minor axis radius is a_y = 4.6 μm, and the ellipticity is $\rho = a_x/a_y = 1.5$. The shaded elliptical ring with the lower diagonal line is the region of trench refractive index, where the major axis radius of the inner ellipse is b_x = 15 μm, the minor axis radius is b_y = 10 μm, and those of the outer ellipse are, respectively, c_x = 30 μm and c_y = 20 μm. The rest of the white part is the cladding, and its outer cladding radius is R_1 = 62.5 μm. The refractive indexes of the pure silica core, the trench refractive index region, and the cladding are n_1 = 1.4440, n_2 = 1.4262, and n_3 = 1.4303, respectively.

We solve the electromagnetic field equation to obtain the electric field vector and the complex effective index using the full-vector finite element method (FEM), and then, the effective refractive index difference of the spatial modes is calculated. Some important parameters such as dispersion, differential mode group delay (DMGD), effective area, non linear coefficient, bending loss, and intrinsic loss are obtained by studying and designing the MATLAB program.

Fiber dispersion is a kind of important physical characteristic that causes transmission signal distortion, which is composed of material dispersion and waveguide dispersion. The dispersion is shown as the variation of refractive index n(ω) with frequency, which can be calculated by using the Sellmeier equation, and the material dispersion can be obtained from the following equation [7, 8, 38, 39]:

$$n^2(\boldsymbol{\omega}) = 1 + \sum_{j=1}^{m} \frac{B_j \cdot \omega_j^2}{\omega_j^2 - \omega^2}, \tag{1}$$

where $\omega_j{}^2$ is the resonant frequency and B_j is the strength of *j*th resonance. For silica materials, the corresponding parameters are as follows: m = 3, B_1 = 0.6961663, B_2 = 0.4079426, B_3 = 0.8974794, λ_1 = 0.0684043 μm, λ_2 = 0.1162414 μm, λ_3 = 9.896161 μm, $\lambda_j = 2\pi c/\omega_j$, and C is the speed of light in vacuum. The waveguide dispersion can be obtained from the following equation [7, 8, 38, 39]:

$$D = -\frac{\lambda}{C}\frac{d^2 n}{d\lambda^2}, \tag{2}$$

where n is the refractive index, C is the speed of light in vacuum, and λ is the wavelength of incident light. DMGD can be obtained from the following equation [38, 39]:

$$DMGD = \frac{n_{eff_{nm}} - n_{eff_{01}}}{C} - \frac{\lambda}{C}\left(\frac{\partial n_{eff_{nm}}}{\partial \lambda} - \frac{\partial n_{eff_{01}}}{\partial \lambda}\right), \tag{3}$$

where $n_{eff_{nm}}$ is the effective refractive index of LP_{nm} mode, and $n_{eff_{01}}$ is the effective refractive index of the mode LP01. The effective area of optical fiber is defined as [7, 38, 39] follows:

$$A_{eff} = \frac{\left(\iint_{-\infty}^{\infty} \left|F(x,y)\right|^2 dxdy\right)^2}{\iint_{-\infty}^{\infty} \left|F(x,y)\right|^4 dxdy}, \tag{4}$$

and the non linear coefficient is given by the following equation:

$$\gamma = \frac{n_2 \omega_0}{C A_{eff}} \tag{5}$$

where n_2 is the non linear refractive index coefficient. ω_0 is the central angular frequency of the pulse. The intrinsic loss (α_{total}) of our proposed EFMF consists of infrared absorption loss (α_{IR}) and Rayleigh scattering loss (α_R) [40].

$$\alpha_{total} = \alpha_R + \alpha_{IR} \tag{6}$$

The Rayleigh scattering loss of optical fiber can be obtained by [40] the following equation:

$$\alpha_{R\_SI\_Pure\_silica} = \frac{1}{\lambda^4}\left(A_0 \frac{\iint P_{core}(r,\theta) r dr d\theta}{\iint P_{core}(r,\theta) r dr d\theta + \iint P_{clad}(r,\theta) r dr d\theta} + A_F \frac{\iint P_{clad}(r,\theta) r dr d\theta}{\iint P_{core}(r,\theta) r dr d\theta + \iint P_{clad}(r,\theta) r dr d\theta}\right) \tag{7}$$

for pure silica core

$$\alpha_{R\_SI\_Ge} = \frac{1}{\lambda^4}\left(A_{Ge} \frac{\iint P_{core}(r,\theta) r dr d\theta}{\iint P_{core}(r,\theta) r dr d\theta + \iint P_{clad}(r,\theta) r dr d\theta} + A_0 \frac{\iint P_{clad}(r,\theta) r dr d\theta}{\iint P_{core}(r,\theta) r dr d\theta + \iint P_{clad}(r,\theta) r dr d\theta}\right) \tag{8}$$

for GeO_2-doped silica core.where $P_{core}(r,\theta)$ and $P_{clad}(r,\theta)$ are the mode intensity profiles in the core and the cladding, respectively. A_0 = 0.71 (dB/km) (μm^4) is the Rayleigh scattering loss coefficient of pure silica fiber. $A_F = A_0(1 + 41|\Delta|)$, $A_{Ge} = A_0(1 + 44|\Delta|)$, Δ is the relative refractive index difference. The infrared absorption loss can be calculated by the following formula [40]:

$$\alpha_{IR} = B\exp\left(-\frac{b}{\lambda}\right) \tag{9}$$

The B and b of different materials are different.

$$B = 6 \times 10^{11}\ \text{dB/km},\ b = 48\ \mu\text{m} \tag{10}$$

for pure silica core and

$$B = 7.81 \times 10^{11}\ \text{dB/km},\ b = 48.48\ \mu\text{m} \tag{11}$$

for GeO_2-doped silica core.

The bending loss is defined as [41]follow:

$$\frac{20}{\ln 10}\frac{2\pi}{\lambda} Im(\text{neff}) \tag{12}$$

where Im(neff) is the imaginary part of the effective refractive index.

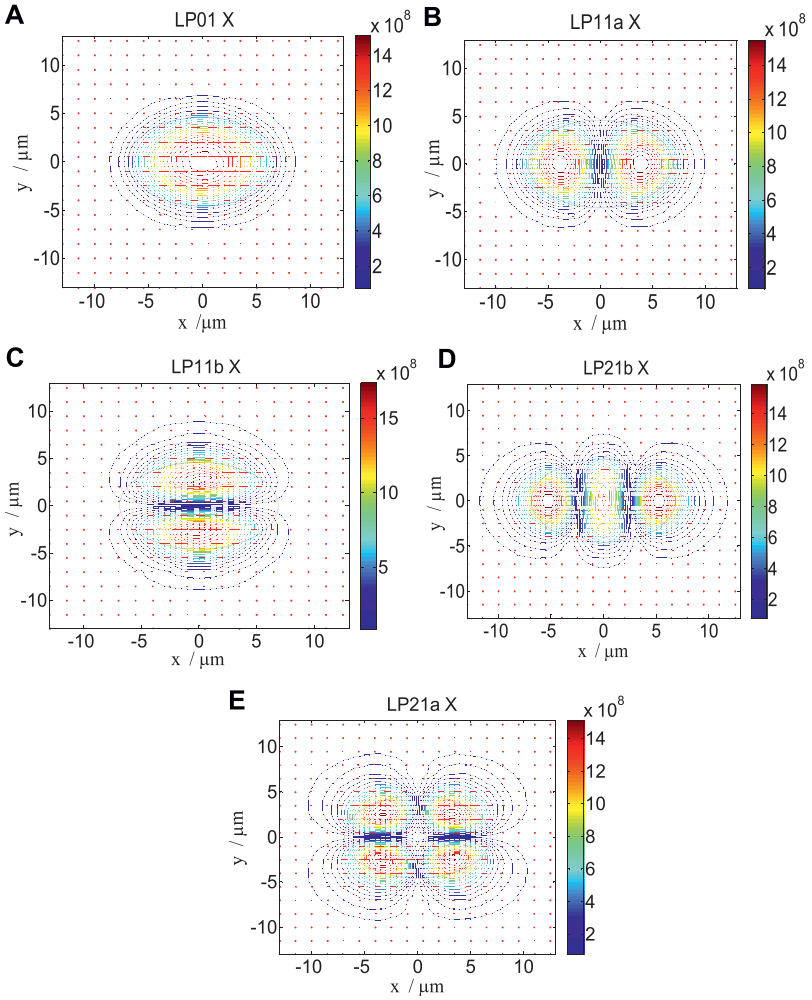

FIGURE 2 | Electric field distribution of five non-degenerate modes LP01 **(A)**, LP11a **(B)**, LP11b **(C)**, LP21b **(D)**, and LP21a **(E)** of our proposed EFMF.

CHARACTERISTICS OF OUR PROPOSED EFMF

Electric Field Distribution

Figure 2 shows the X polarization electric field distribution of five non-degenerate modes LP01 (A), LP11a (B), LP11b (C), LP21b (D), and LP21a (E) of our proposed EFMF when the input wavelength is 1.55 μm. We use the notations LP01, LP11a, LP11b, LP21b, and LP21a for the involved modes of the EFMF, due to their mode profiles being similar to those of traditional circular core few-mode fiber (CFMF). Although the mode profile of LP21b in the traditional CFMF shrinks into a profile with three lobes for the EFMF, we still use the notation of LP21b to indicate the corresponding relationship with that of traditional CFMF for ease of comparison investigation. According to the description of the mode-maintaining function of the FMF in the studies mentioned in reference [27, 28], our proposed EFMF obviously performs mode-maintaining operation with five non-degenerate modes LP01, LP11a, LP11b, LP21b, and LP21a.

Variations of Effective Refractive Indexes of Spatial Modes

Figure 3 shows the variations of the effective refractive indexes of the five spatial modes with the input wavelength λ. The solid lines with squares, stars, diamonds, circles, and triangles represent the variations of the effective refractive indexes of the modes LP01, LP11a, LP11b, LP21b, and LP21a, respectively. It can be seen from **Figure 3** that the effective refractive indexes of the five modes decrease with the increase of input light wavelength, and the variations of effective refractive indexes with the input wavelength are slow.

The variation of the effective refractive index of the mode LP01 with the input wavelength is the slowest. The variation of the mode LP21a is the fastest, and that of the modes LP11a, LP11b,

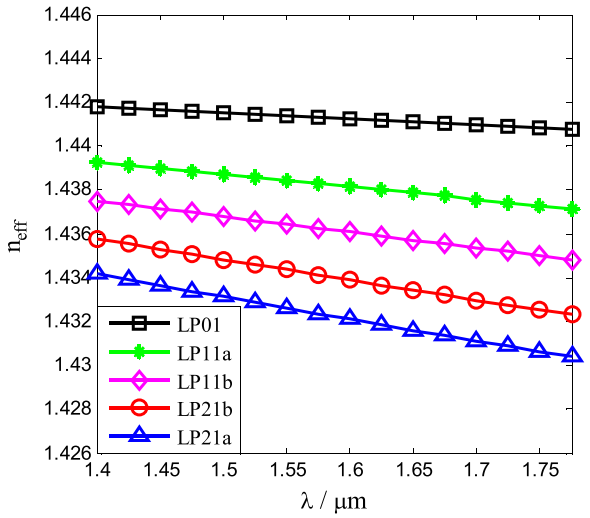

FIGURE 3 | Variations of the effective refractive indexes with the input light wavelength. The solid lines with squares, stars, diamonds, circles, and triangles represent the effective refractive indexes of the modes LP01, LP11a, LP11b, LP21b, and LP21a, respectively.

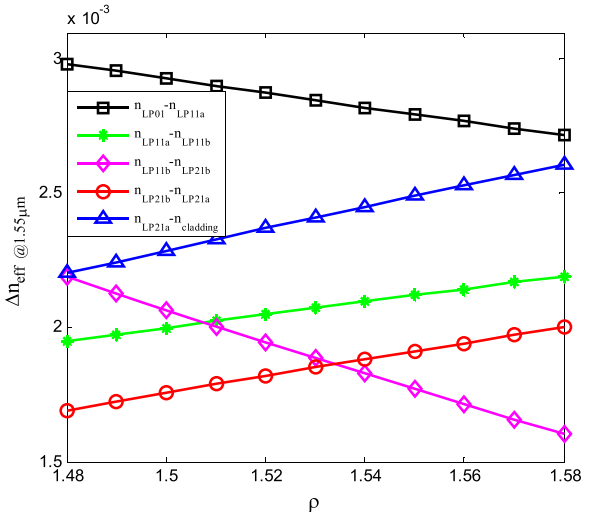

FIGURE 4 | Variations of effective refractive index differences with the ellipticity. The solid lines with squares, stars, diamonds, circles, and triangles represent the effective refractive index differences between the modes LP01 and LP11a, LP11a and LP11b, LP11b and LP21b, LP21b and LP21a, and LP21a and cladding, respectively.

and LP21b gradually increases in turn. For a given input wavelength, the effective index n_{eff} of the mode LP01 is the largest, that of the mode LP21a is the smallest, and the effective refractive indexes of the modes LP11a, LP11b, and LP21b decrease in turn. When the input wavelength is 1.55 μm, the effective refractive indexes of the modes LP01, LP11a, LP11b, LP21b, and LP21a are 1.4414, 1.4384, 1.4364, 1.4344, and 1.4326, respectively.

Variations of the Effective Refractive Index Differences With the Ellipticity

Figure 4 shows the variations of the effective refractive index differences with the ellipticity ρ at the input wavelength of 1.55 μm. The solid lines with squares, stars, diamonds, circles, and triangles represent the variations of the effective refractive index differences between the modes LP01 and LP11a, LP11a and LP11b, LP11b and LP21b, LP21b and LP21a, and LP21a and cladding, respectively. It can be seen from **Figure 4** that the effective refractive index differences between the modes LP01 and LP11a, and LP11b and LP21b decrease with the increase of the ellipticity. However, the effective refractive index differences between the modes LP11a and LP11b, LP21b and LP21a, and LP21a and cladding increase with the increase of the ellipticity. When the ellipticity ρ is about 1.53, a large effective refractive index difference between the modes can be obtained. However, in order to reduce the fabrication error and facilitate the implementation of our proposed EFMF, $\rho = 1.5$ is selected as the ellipticity of the elliptical core in this study, which makes the effective refractive index differences between the modes larger and reduces the coupling between the modes.

When the input wavelength is 1.55 μm and the ellipticity is $\rho = 1.5$, the effective refractive index difference between the modes LP01 and LP11a is 3.0×10^{-3}, and those between the modes LP11a and LP11b, LP11b and LP21b, LP21b and LP21a, and LP21a and cladding are, respectively, 2.0×10^{-3}, 2.1×10^{-3}, 1.8×10^{-3}, and 2.3×10^{-3}. If the data rate or capacity is conventionally set to a multiple of 2, the EFMF transmission system can be upgraded using four non-degenerate modes operation with the modes LP01, LP11a, LP11b, and LP21b, where the effective refractive index difference between any two modes is more than 2.0×10^{-3}. The index difference between the modes LP11a and LP11b is 2.0×10^{-3} in this study, which is 122% larger than that (9×10^{-4}) in the study mentioned in reference [28], and is about 67% larger than that in the study mentioned in reference [27]. In order to minimize mode coupling, the low crosstalk criterion that the effective refractive index difference between any two modes is greater than 0.5×10^{-3} (preferably >1.0×10^{-3}) is proposed in the study mentioned in reference [42]. The low crosstalk between the non-degenerate modes of our proposed EFMF is achieved because the effective refractive index difference between the modes is more obviously greater than the low crosstalk criterion by using the ellipticity $\rho = 1.5$.

Variations of the Mode Dispersions

Variations of the mode dispersions with the input wavelength λ are shown in **Figure 5**. **Figures 5A–E** show the dispersions of the modes LP01, LP11a, LP11b, LP21b, and LP21a, respectively. The solid lines with circles, stars, and triangles represent the material dispersion D_M, waveguide dispersion D_W, and total dispersion D_T of each mode, respectively. From **Figure 5A**, the waveguide dispersion of the mode LP01 is small, and its variation with the input wavelength is approximately flat in the wavelength range from 1.30 to 1.74 μm. The total dispersion of the mode LP01 increases gradually from 23.79 ps/(nm·km) to 25.93 ps/

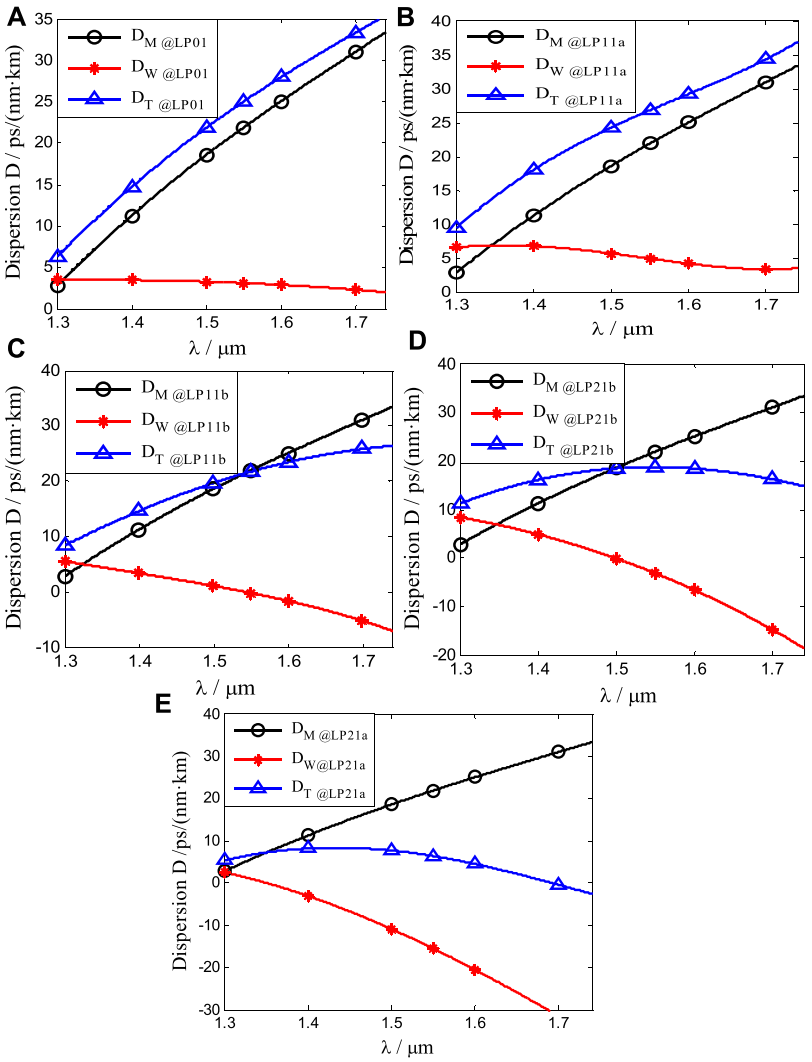

FIGURE 5 | Dispersions of the modes LP01 **(A)**, LP11a **(B)**, LP11b **(C)**, LP21b **(D)**, and LP21a **(E)** vary with the input wavelength. The solid lines with circles, stars, and triangles represent the material dispersion D_M, waveguide dispersion D_W, and total dispersion D_T of each mode.

(nm·km) in the C-band (1.53–1.565 μm). The total dispersion is 25.02 ps/(nm·km) at 1.55 μm.

From **Figure 5B**, the waveguide dispersion of the mode LP11a decreases gradually, and the total dispersion of the mode LP11a increases gradually in the wavelength range from 1.40 to 1.74 μm. The total dispersion is 26.83 ps/(nm·km) at 1.55 μm.

The waveguide dispersion of the mode LP11b decreases gradually from 5.54 ps/(nm·km) to −7.05 ps/(nm·km) in **Figure 5C**. The total dispersion of this mode increases gradually in the wavelength range from 1.30 to 1.74 μm, and the increasing rate decreases gradually. The total dispersion is 21.70 ps/(nm·km) at 1.55 μm, and the waveguide dispersion is about 0 at 1.542 μm.

It can be seen from **Figure 5D** that the waveguide dispersion of the mode LP21b decreases linearly in the wavelength range from 1.30 to 1.74 μm. With the increase of input wavelength, the total dispersion of the mode LP21b is flat in the wavelength range from 1.40 to 1.74 μm. The total dispersion is 18.74 ps/(nm·km) at 1.55 μm.

It can be seen from **Figure 5E** that the waveguide dispersion of the mode LP21a decreases in the wavelength range from 1.30 to 1.74 μm. The total dispersion increases gradually from 5.34 ps/(nm·km) to 8.38 ps/(nm·km) in the wavelength range from 1.30 to 1.438 μm. The total dispersion gradually decreases from 8.38 ps/(nm·km) to −2.59 ps/(nm·km) in the wavelength range from 1.438 to 1.74 μm. The total dispersion of the mode LP21a is flattened in the wavelength range from 1.30 to 1.60 μm. The total dispersion is 6.39 ps/(nm·km) at 1.55 μm.

Variations of Effective Mode Field Area and Non-Linear Coefficient

Figure 6 shows variations of the effective mode field area A_{eff}(A) and the non-linear coefficient γ(B) with the incident wavelength.

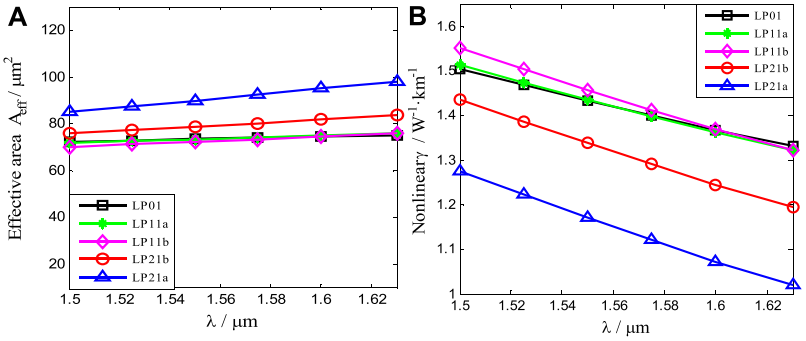

FIGURE 6 | Variations of the effective mode field area A_{eff} **(A)** and the non-linear coefficient γ **(B)** with input wavelength. The solid lines with squares, stars, diamonds, circles, and triangles in Figure (A) represent the effective areas of the modes LP01, LP11a, LP11b, LP21b, and LP21a, respectively. The solid lines with squares, stars, diamonds, circles, and triangles in Figure (B) represent the non-linear coefficients of the modes LP01, LP11a, LP11b, LP21b, and LP21a, respectively.

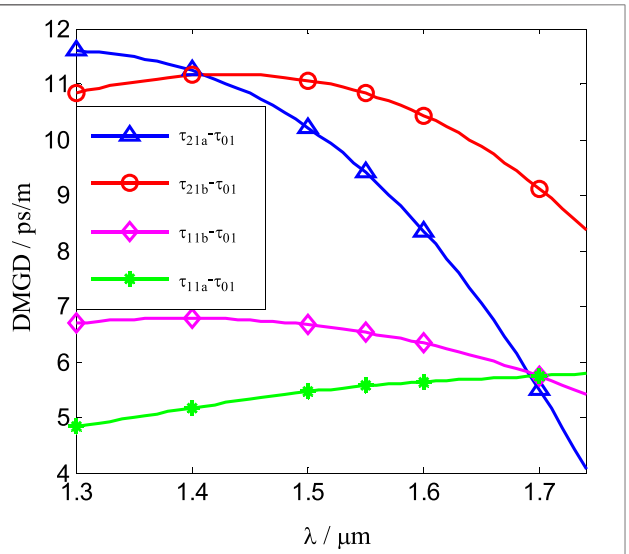

FIGURE 7 | Variations of the DMGDs with input wavelength. The solid lines with stars, diamonds, circles, and triangles represent the DMGDs of the modes LP11a, LP11b, LP21b, and LP21a, respectively.

The solid lines with squares, stars, diamonds, circles, and triangles represent the variations of the modes LP01, LP11a, LP11b, LP21b, and LP21a, respectively. As can be seen from **Figure 6A**, the effective areas of the five non-degenerate modes increase with the increase of input wavelength. For a given input wavelength, the effective area of the mode LP21a is the largest, and those of other four modes are approximately equal to those of the standard single-mode fiber and slightly less than that of the mode LP21a. When the wavelength is 1.55 μm, the effective areas of the modes LP01, LP11a, LP11b, LP21b, and LP21a are, respectively, 73.47, 73.40, 72.31, 78.76, and 89.96 μm^2, which are close to the effective area of 80 μm^2 of the standard single-mode fiber.

The non-linear coefficients of the five modes all decrease with the increase of input wavelength from **Figure 6B**. At a given input wavelength, the non-linear coefficient of the mode LP21a is the smallest, which is slightly less than that of other four modes.

Variations of the DMGDs

Figure 7 shows variations of the DMGDs with the input wavelength. The solid lines with stars, diamonds, circles, and triangles represent the DMGDs of the modes LP11a, LP11b, LP21b, and LP21a, respectively. The difference of the DMGDs of the four modes is slightly large.

The DMGD of the mode LP11a, which is gradually increased with the increase in the input wavelength, is the most minimum in the wavelength range from 1.30 to 1.68 μm among all DMGDs. The DMGD of the LP21a mode, which is slightly larger than that of the mode LP21b, is much larger than that of the mode LP11b from 1.30 to 1.40 μm. The DMGDs of the modes LP11b, LP21b, and LP21a are all decreased with the input wavelength from 1.40 to 1.68 μm, where the decrease rate of the mode LP21a is the largest, and that of the mode LP11b is the lowest. When the wavelength is 1.55 μm, the DMGDs of the modes LP11a, LP11b, LP21b, and LP21a are, respectively, 5.56, 6.53, 10.82, and 9.40 ps/m.

Variations of the Bending Losses

The bending loss of our proposed EFMF is calculated according to the method of the study mentioned in reference [41]. In order to obtain low bending loss, a trench refractive index region is added to the cladding. Because the bending losses of the modes LP01, LP11a, and LP11b are much smaller than those of the modes LP21b and LP21a, only the bending losses of the modes LP21b and LP21a are studied in this study. **Figure 8** shows the variations of the bending losses of the modes LP21a and LP21b.

Figure 8A shows the effects of different trench widths on bending loss at 1.55 μm. The solid and dashed lines show the variations of bending losses for the trench width of 10 and 5 μm, respectively. The lines with squares and asterisks represent the variations of bending losses for the modes LP21a and LP21b, respectively. It can be seen from Figure (A) that the bending losses of the modes LP21a and LP21b decrease with the increase of the bending radius R and the trench width.

When the trench width increases from 5 to 10 μm, corresponding to the given bending radius, the bending losses of the modes LP21a and LP21b with trench width of 5 μm are significantly larger than those of the modes LP21a and LP21b

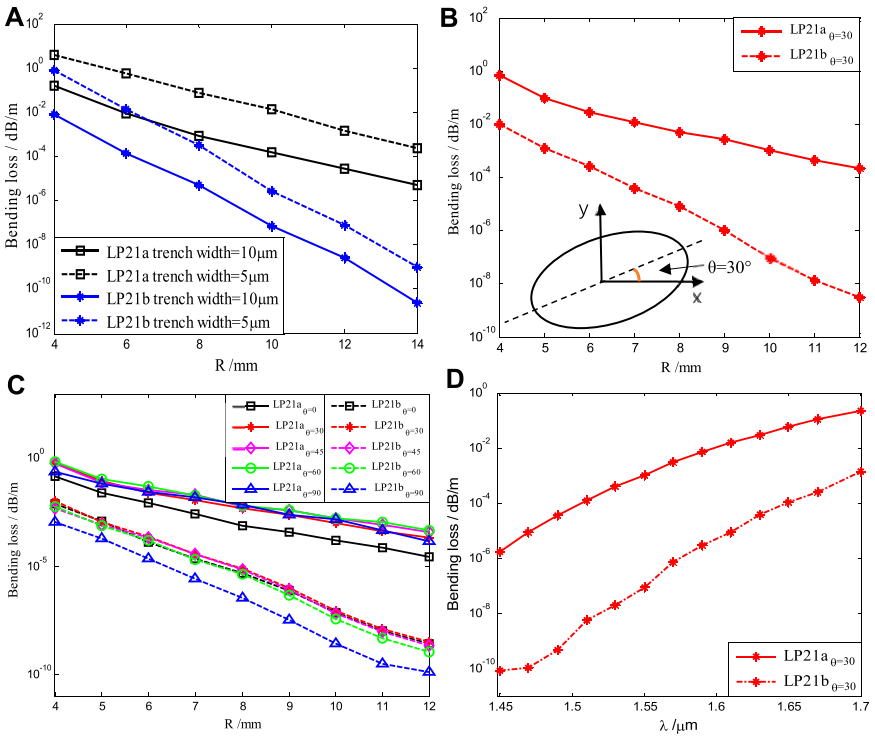

FIGURE 8 | When the light wavelength is 1.55 μm, effect of different trench widths on bending loss **(A)**, bending losses of the modes LP21a and LP21b for θ = 30° **(B)**, bending losses of the modes LP21a and LP21b for θ = 0°, 30°, 45°, 60°, 90° **(C)**. Variations of bending losses with the input wavelength for θ = 30° and R = 10 mm **(D)**.

with trench width of 10 μm. For the same trench width, the bending loss of the modes LP21a decreases with the increase of R, the variation rate of the modes LP21a with R is less than that of the mode LP21b, and the bending loss of the modes LP21a is larger than that of the mode LP21b for a given R. For R = 10 mm, the bending losses of the modes LP21a and LP21b with trench width of 5 μm are 1.30×10^{-2} and 7.56×10^{-6} dB/m, respectively, and the bending losses of the modes LP21a and LP21b with trench width of 10 μm are 1.58×10^{-4} and 7.34×10^{-8} dB/m, respectively. The trench width of 10 μm is comprehensively determined from the studies mentioned in Refs. [4, 7, 8], which is sufficient for our proposed EFMF.

The illustration in **Figure 8B** shows that θ is defined as the angle between the major axis direction of the elliptical core and the bending direction x. The bending losses of the modes LP21a and LP21b are for θ = 30°(B), and those of the modes LP21a and LP21b are for θ= 0°, 30°, 45°, 60°, and 90°, respectively (C). The solid and dashed lines with stars in **Figure 8B** represent the bending losses of the modes LP21a and LP21b, respectively. The solid lines with squares, stars, diamonds, circles, and triangles in **Figure 8C** correspond to the bending losses of the mode LP21a for θ = 0°, 30°, 45°, 60°, and 90°, respectively. The dashed lines with squares, stars, diamonds, circles, and triangles in **Figure 8C** are those of the mode LP21b.

It can be seen from **Figure 8B** that the bending losses of the modes LP21a and LP21b decrease with the increase of the bending radius for θ = 30°. The decreasing rate of bending loss of the mode LP21a is obviously less than that of the mode LP21b. Corresponding to the given bending radius, the bending loss of the mode LP21a is greater than that of the mode LP21b. When the bending radius of the fiber is 5 mm, the bending losses of the mode LP21a and LP21b are, respectively, 9.28×10^{-2} and 1.20×10^{-3} dB/m. This variation is related to the fact that the refractive index difference between LP21b and cladding is greater than that between LP21a and cladding. As a result, the energy of the mode LP21a is more easily transferred to the cladding than that of the mode LP21b; thus, the bending loss of the mode LP21a is larger.

It can be seen from **Figure 8C** that the bending losses of the modes LP21a and LP21b decrease with the increase of the bending radius, where the decrease rates are similar to those of **Figure 8B**. When θ varies from 0° to 90°, the bending loss of the mode LP21a is larger than that of the mode LP21b for a given bending radius. The bending losses of the mode LP21a for θ = 30°, 45°, 60°, and 90°, which are approximately equal, are obviously larger than that of the mode LP21a for θ = 0°. The bending losses of the mode LP21b for θ = 0°, 30°, 45°, and 60°, which are approximately equal, are obviously larger than that of the mode LP21b for θ = 90°.

When the bending radius of the fiber is 10 mm and θ equals to 0°, 30°, 45°, 60°, and 90°, the bending losses of the mode LP21a are 1.58×10^{-4}, 1.00×10^{-3}, 1.70×10^{-3}, 1.70×10^{-3}, and 1.50×10^{-3} dB/m, respectively, and those of the modes LP21b are 7.34×10^{-8}, 8.87×10^{-8}, 6.84×10^{-8}, 3.80×10^{-8}, and 2.64×10^{-9} dB/m, respectively. Our results agree with the bending loss characteristics and satisfy the condition of mode robustness in

the study mentioned in reference [43], which shows that the non-degenerate modes of our proposed EFMF have good mode robustness.

For R = 12 mm and θ = 0°, 30°, 45°, 60°, and 90°, the bending losses of the mode LP21b are 2.64×10^{-9}, 3.13×10^{-9}, 2.28×10^{-9},1.08×10^{-9}, and 1.26×10^{-10} dB/m, respectively, and those of the mode LP21a are 2.74×10^{-5}, 2.18×10^{-4}, 3.89×10^{-4}, 4.89×10^{-4}, and 1.52×10^{-4} dB/m, respectively. However, optical fiber is generally wound on a standard size reel with a 25 cm flange diameter or a straight optical cable in transmission applications [44]. In this way, the bending radius of the optical fiber on the spool is more than 125 mm. The large bending radius results in a very small bending loss, which shows that the bending loss of our proposed EFMF is very small and is suitable for the application of optical fiber transmission system.

Since the bending losses for θ = 30° can show the basic characteristics of our proposed EFMF from the previous discussion, we give variations of bending losses with the input wavelength, as shown in **Figure 8D** for θ = 30° and R = 10 mm. The solid and dashed lines with stars in **Figure 8D** represent the variations of the bending losses of the modes LP21a and LP21b with the input wavelength, respectively. As can be seen from **Figure 8D**, the bending losses of the two modes increase with the increase of the input wavelength. The bending losses of the two modes are less than 2.20×10^{-1} dB/m, and the bending loss of the mode LP21a is larger than that of the mode LP21b. At the wavelength of 1.55 μm, the bending losses of the modes LP21a and LP21b are 1.00×10^{-3} and 8.88×10^{-8} dB/m, respectively. Our results are consistent with the bending loss characteristics of the study mentioned in reference [43], which shows that the non-degenerate modes of our proposed EFMF have good mode robustness.

The refractive index of the transmission medium is decreased with the increase of wavelength on the basis of the Sellmeier equation [7, 8]. For a given mode and bending radius, the effective refractive index of the mode also decreases with the increase of wavelength and is closer to the refractive index of the cladding, according to the well-known coordinate transformation formula in the case of the fiber bending [41]. It implies that the energy of the mode is more easily transmitted to the cladding and leaked out with the increase of wavelength. That is to say, the bending loss is increased with the increase of wavelength. However, the bending loss of our proposed fiber wound on the conventional fiber spool is very low, which can be widely used in the practical MIMO-FREE applications.

Intrinsic Loss of Our Proposed EFMF

The intrinsic loss of our proposed EFMF is calculated according to the method in detail in the study mentioned in reference [40]. The trench of the EFMF is ignored in the calculation of the intrinsic loss. The reasons are as follows: The optical power of the mode in our proposed EFMF is mainly concentrated in the fiber core, while the optical power in the trench is so small that it can be ignored. So, the contribution of the trench to the intrinsic loss can be neglected. The trench of our proposed EFMF is not taken into account for the calculation of intrinsic loss.

Figure 9 shows the variations of the intrinsic losses of our proposed EFMF with pure silica core (A) and the conventional FMF with elliptical GeO_2-doped core (B) with the input wavelength. The illustrations in **Figure 9** show the variations of refractive index profiles with the radius. The solid lines with squares, stars, real dots, circles, and triangles represent the intrinsic losses of the modes LP01, LP11a, LP11b, LP21b, and LP21a with the incident wavelengths, respectively. As can be seen from **Figure 9A**, the intrinsic loss of the low-order mode is lower than that of the higher order mode of our proposed EFMF. The intrinsic losses of the modes LP01, LP11a, LP11b, LP21b, and LP21a reach the lowest when the input wavelength is 1.53 μm, and the intrinsic losses are 0.1458, 0.1481, 0.1512, 0.1525, and 0.1564 dB/km, respectively. When the wavelength is less than 1.53 μm, the intrinsic losses of the modes increase with the decrease of the wavelength, which are mainly due to the losses caused by the Rayleigh scattering. When the wavelength is greater than 1.53 μm, the intrinsic losses increase with the increase of the wavelength, which are mainly due to the increase of the infrared absorption losses with the increase of the wavelength. In the whole C-band, the intrinsic losses of the five non-degenerate modes of our proposed EFMF are low, which are all less than 0.1595 dB/km. And the intrinsic loss differences between the modes are very small, which is beneficial to signal transmission and detection. From **Figure 9B**, we can see the variations of the intrinsic losses of the modes LP01, LP11a, LP11b, LP21b, and LP21a of the conventional FMF with elliptical GeO_2-doped core. The intrinsic loss of the low-order mode is larger than that of the higher order mode. The lowest intrinsic losses of the modes LP01, LP11a, LP11b, LP21b, and LP21a at 1.55 μm are, respectively, 0.1926, 0.1903, 0.1871, 0.1856, and 0.1815 dB/km, which are 31.65, 28.06, 23.42, 21.31, and 15.75% larger than those of the five modes of our proposed EFMF in **Figure 9A**. The variations of intrinsic losses with the input wavelength are similar to those of our proposed EFMF.

By comparing **Figure 9A** with (B), the intrinsic losses of the two types of optical fibers vary similarly with the input wavelength. However, the intrinsic losses of our proposed EFMF are lower than those of the conventional FMF with an elliptical GeO_2-doped core. The intrinsic losses of the modes LP01, LP11a, LP11b, LP21b, and LP21a of our proposed EFMF are increased in turn for a given wavelength, while those of the conventional FMF with elliptical GeO_2-doped core are on the contrary. In the conventional FMF with elliptical GeO_2-doped core, the intrinsic loss factor of the fiber core is larger than that of the cladding. Therefore, the more concentrated the core energy of GeO_2-doped fiber is, the greater the loss is, and the intrinsic losses of the modes LP21a, LP21b, LP11b, LP11a, and LP01 increase in turn. In our proposed EFMF, the intrinsic loss factor of the fiber core is less than that of the cladding. The more the energy is concentrated in the core, the smaller the loss, which leads to the decrease of the intrinsic loss of the modes LP21a, LP21b, LP11b, LP11a, and LP01 in turn.

Cutoff Wavelength

When the refractive index distribution and radius of optical fibers are given, the input wavelength determines the number of

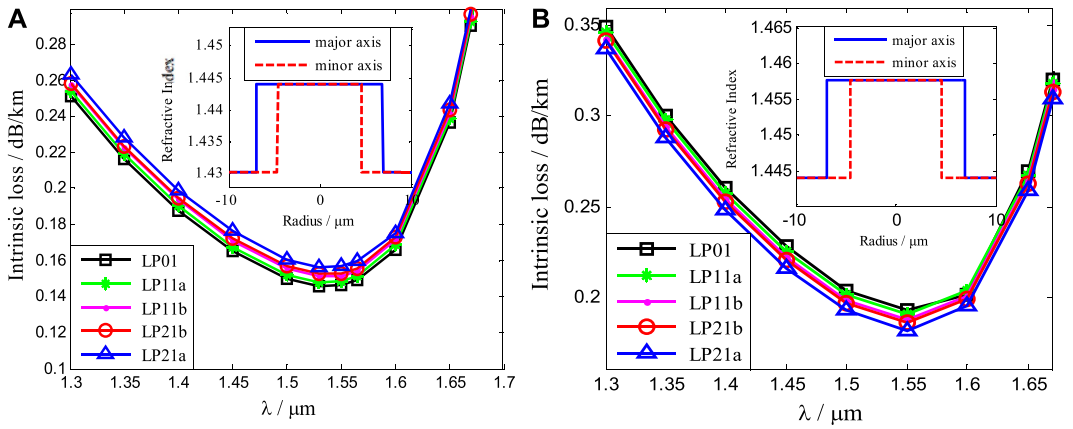

FIGURE 9 | Variations of intrinsic losses of our proposed EFMF with pure silica core **(A)** and the conventional FMF with elliptical GeO_2-doped core **(B)** with the incident wavelength.

propagation modes in optical fibers. When the wavelength is very short, the number of optical fiber modes increases; when the wavelength is very long, the number of optical fiber modes will decrease. The cutoff wavelength of the few-mode fiber includes the upper cutoff wavelength and the lower cutoff wavelength. The new mode is added in the few-mode fiber below the lower cutoff wavelength. The fiber mode obviously attenuates when the cutoff wavelength is higher than the upper cutoff wavelength. The cutoff wavelength of our proposed EFMF can be obtained by numerical calculation. When the wavelength is 1.5 μm, other modes appear in our proposed EFMF, so the lower cutoff wavelength of the EFMF is 1.5 μm. When the wavelength is 1.8 μm, the mode LP21a in the EFMF attenuates, and the wavelengths of the modes LP01, LP11a, LP11b, and LP21b are very long, so the upper cutoff wavelength of the EFMF is 1.8 μm. In addition, the cutoff wavelength can be shifted by appropriately setting the fiber parameters.

FABRICATION METHOD OF OUR PROPOSED EFMF

Our proposed EFMF in this study can be fabricated by using the existing mature "prefabricated rod drawing process" method. A 7.94 km elliptical core three-mode fiber was successfully fabricated using a method of traditional plasma chemical vapor deposition (PCVD) method, as in the study mentioned in reference [28]. Compared with other methods, the PCVD process has the following advantages: First, the PCVD does not use hydrogen–oxygen flame heating, but uses microwave as the heat source. For microwave plasma, there is no electrode pollution and high energy, which is the advantage of the optical fiber preform deposition process. Second, the deposition efficiency is high. Finally, the greatest advantage of the PCVD is that it can produce a very complex optical waveguide structure prefabricated rod. Therefore, the elliptical core few-mode fiber we proposed can obviously be fabricated by the traditional PCVD method.

First of all, the preform of the circular core is prepared by the PCVD. In the PCVD process [45–47], the gas raw material (SiC_{14} and O_2) is fed into the F-doped high-purity silica glass tube and then immediately enters the electric field region of the microwave resonator. In the high-frequency resonant cavity, these mixed gases are excited, ionized, and maintained the glow discharge to form a non-isothermal plasma, which reciprocate along the tube line to realize the deposition process. Neutral molecules of various raw materials are ionized into charged particles (electrons, positive ions, negative ions) and uncharged particles (gas atoms, molecules, excited atoms, metastable atoms, etc.). In the mixture, silicon and oxygen form the compound SiO_2 (pure silica). A layer of the pure silica was deposited on the inner surface of the F-doped silica glass tube by diffusion. When all the layers are deposited, the temperature is increased to collapse the tube into a glass rod, which is what we call a circular-core prefabricated rod.

Second, an elliptical core preform can be fabricated from the circular-core prefabricated rod using the method described in the references [28, 48, 49]. The circular-core prefabricated rod was symmetrically grinded on both sides to form two flat and parallel surfaces along its longitudinal axis. Then, the prefabricated rod is heated to eliminate the flat surfaces due to surface tension and the flow of material, forming a new preform with an elliptical core and a circular cladding. At the end of this process, the original circular core becomes an elliptical one. The ellipticity can be controlled by the grinded volume of the cladding, and the diameter can be managed by the temperature and tension during the drawing process. Finally, this new preform can be drawn to our proposed EFMF for the MIMO-FREE applications.

DISCUSSION AND CONCLUSION

The results using a full-vector finite-element method show that our proposed EFMF breaks the mode degeneracy and

achieves the mode-maintaining function, which can be employed in the MIMO-FREE applications. If the EFMF transmission system is upgraded using the four–non-degenerate modes operations, the effective refractive index difference between any two modes is more than 2.0×10^{-3} in our study. It shows that our proposed EFMF performs lower crosstalk.

The effective area, non-linear coefficient, and dispersion of some modes in our proposed fiber are slightly larger than those of the standard single-mode fiber, and those of other modes are smaller than those of the standard single-mode fiber. On the whole, these characteristics are suitable for MIMO-FREE applications.

The bending losses of the modes decrease with the increase of the bending radius, and the bending losses of the modes increase with the increase of wavelength. However, the bending losses of our proposed fiber wound on the conventional fiber spool are very low, which is appropriate in the practical MIMO-FREE applications. Our results are consistent with the bending losses characteristics of the study mentioned in the reference [43], which show that the non-degenerate modes of our proposed EFMF have good mode robustness.

The intrinsic losses of the modes increase with the decrease of the wavelength in the short wavelength region, which are mainly due to the losses caused by the Rayleigh scattering. The intrinsic losses increase with the increase of the wavelength in the long-wavelength region, which are mainly due to the increase of the infrared absorption losses. In the whole C-band, the intrinsic losses of our proposed EFMF are as low as 0.1595 dB/km, which are much lower than those of the conventional FMF with elliptical GeO_2-doped core. So, our proposed EFMF is more suitable for optical transmission.

In conclusion, we propose a novel EFMF with low loss and low crosstalk, which breaks the mode degeneracy and performs the application of MIMO-FREE mode division multiplexing. The mode crosstalk of the EFMF is effectively reduced using the optimized ellipticity and the large effective refractive index difference between the modes. A pure silica core is employed to effectively reduce intrinsic loss. The low bending loss is realized by using the trench refractive index at the cladding. Our method solves the serious problems of large time delay, large computation, high complexity, huge power consumption, and high cost induced by the MIMO-DSP method in a short-distance communication system based on the conventional circular-core FMF, which is a new idea for further research on the MIMO-FREE mode division multiplexing in the future. Of course, our proposed EFMF can be applied in fiber lasers and other fields.

DATA AVAILABILITY STATEMENT

The raw data supporting the conclusions of this article will be made available by the authors, without undue reservation.

AUTHOR CONTRIBUTIONS

YG contributed to data curation, formal analysis, validation, writing–original draft, and software. YL helped with data curation, formal analysis, validation, writing–original draft, and software. XL assisted with conceptualization, project administration, supervision, writing–review editing, funding acquisition, investigation, and methodology. HZ contributed to conceptualization, project administration, supervision, writing–review editing, funding acquisition, investigation, and methodology. CB helped with conceptualization, supervision, funding acquisition, investigation, and methodology. WH involved in conceptualization, supervision, funding acquisition, investigation, and methodology. HyX assisted with conceptualization, supervision, funding acquisition, investigation, and methodology. QD contributed to data curation, validation, and software. HdX helped with data curation, validation, and software. YS involved in data curation, validation, and software. YY contributed to data curation, validation, software. CW: data curation, validation, and software. BZ helped with data curation, validation, and software.

FUNDING

This work is supported in part by the National Natural Science Foundation of China (grant nos: 61671227 and 61431009), the Shandong Provincial Natural Science Foundation (ZR2020MF012, ZR2011FM015), and the Taishan Scholar Research Fund of Shandong Province.

REFERENCES

1. Ellis AD, Jian Zhao J, Cotter D. Approaching the Non-linear Shannon Limit. *J Lightwave Technol* (2010) 28:423–33. doi:10.1109/JLT.2009.2030693
2. Miyamoto Y, Shibahara K, Mizuno T, Kobayashi T. Mode-Division Multiplexing Systems for High-Capacity Optical Transport Network. In: Optical Fiber Communication Conference. San Diego, California United States; OSA Technical Digest(Optical Society of America,2019),paper M2I.3 (2019). doi:10.1364/OFC.2019.M2I.3
3. Liang X, Li W-L, Wood WA, Downie JD, Hurley JE, Ng'oma A. Transmission of Wireless Signals Using Space Division Multiplexing in Few Mode Fibers. *Opt Express* (2018) 26:20507–18. doi:10.1364/OE.26.020507
4. Sillard P, Bigot-Astruc M, Molin D. Few-Mode Fibers for Mode-Division-Multiplexed Systems. *J Lightwave Technol* (2014) 32(16):2824–9. doi:10.1109/JLT.2014.2312845
5. Richardson DJ, Fini JM, Nelson LE. Space-division Multiplexing in Optical Fibres. *Nat Photon* (2013) 7(5):354–62. doi:10.1038/nphoton.2013.94
6. Li G, Bai N, Zhao N, Xia C. Space-division Multiplexing: the Next Frontier in Optical Communication. *Adv Opt Photon* (2014) 6(4):413–87. doi:10.1364/AOP.6.000413
7. Zheng H, Li X, Bai C. *Transmission of Chirped Pulse in Optical Fiber*. Beijing: Science Press (2018). p. 1–184.

8. Li Y, Wang X, Zheng H, Li X, Bai C, Hu W, et al. A Novel Six-Core Few-Mode Fiber with Low Loss and Low Crosstalk. *Opt Fiber Technol* (2020) 57:102211. doi:10.1016/j.yofte.2020.102211
9. Wang X, Zheng H, Li X, Liu Y, Yu R, Bai C, et al. Recent Progresses on Few Mode Fibers for Mode-Division Multiplexing System. *J Liaocheng Univ (Nat Sci Ed* (2019) 32(2):69–79. doi:10.19728/j.issn1672-6634.2019.02.011
10. Liu Y, Dong Q, Zheng H, Li X, Bai C, Hu W, et al. Research on a Novel Mode Division Multiplexer with Low Crosstalk, Low Loss and Few Mode Ring-Core Transmission Channel. *Opt Commun* (2020) 469:125778–189. doi:10.1016/j.optcom.2020.125778
11. Dong Q, Liu Y, Zheng H, Li X, Bai C, Hu W, et al. Research on mode (de) multiplexing technology for mode-division multiplexing system. *J Liaocheng Univ (Nat Sci Ed* (2020) 33(2):50–67. doi:10.19728/j.issn1672-6634.2020.02.008
12. Bai N, Ip E, Luo Y, Peng G-D, Wang T, Li G. Experimental Study on Multimode Fiber Amplifier Using Modal Reconfigurable Pump. In: Optical Fiber Communication Conference. Los Angeles, California United States: OSA Technical Digest (Optical Society of America,2012),paper OW1D.3 (2012). doi:10.1364/OFC.2012.OW1D.3
13. Jung Y, Lim EL, Kang Q, May-Smith TC, Wong NHL, Standish R, et al. Cladding Pumped Few-Mode EDFA for Mode Division Multiplexed Transmission. *Opt Express* (2014) 22(23):29008–13. doi:10.1364/OE.22.029008
14. Wen H, Zheng H, Mo Q, Velázquez-Benítez AM, Xia C, Huang B, et al. Few-mode Fibre-Optic Microwave Photonic Links. *Light Sci Appl* (2017) 6(8): e17021. doi:10.1038/lsa.2017.21
15. Gao Y, Li Y, Xing H, Li X, Zheng H, Bai C, et al. Research on Mode Division Multiplexing Optical Transmission. *J Liaocheng Univ (Nat Sci Ed* (2022) 35(1):30–56. doi:10.19728/j.issn1672-6634.2021040006(in Chinese)
16. Rademacher G, Luís RS, Puttnam BJ, Ryf R, Furukawa H, Maruyama R, et al. 93.34Tbit/s/mode (280Tbit/s) Transmission in a 3-Mode Graded-Index Few-Mode Fiber. In: Optical Fiber Communication Conference. San Diego, California United States: OSA Technical Digest (online) (Optical Society of America,2018) (2018). doi:10.1364/OFC.2018.W4C.3
17. Soma D, Beppu S, Wakayama Y, Igarashi K, Tsuritani T, Morita I, et al. 257-Tbit/s Weakly Coupled 10-Mode C + L-Band WDM Transmission. *J Lightwave Technol* (2018) 36(6):1375–81. doi:10.1109/jlt.2018.2792484
18. van Weerdenburg J, Ryf R, Alvarado-Zacarias JC, Alvarez-Aguirre RA, Fontaine NK, Chen H, et al. 138-Tb/s Mode- and Wavelength-Multiplexed Transmission over Six-Mode Graded-Index Fiber. *J Lightwave Technol* (2018) 36:1369–74. doi:10.1109/JLT.2018.2791100
19. Wakayama Y, Soma D, Beppu S, Sumita S, Igarashi K, Tsuritani T. 266.1-Tbit/s Transmission over 90.4-km 6-Mode Fiber with Inline Dual C+L-Band 6-Mode EDFA. *J Lightwave Technol* (2019) 37:404–10. doi:10.1109/JLT.2018.2876730
20. Beppu S, Soma D, Sumita S, Wakayama Y, Takahashi H, Tsuritani T, et al. 402.7-Tb/s MDM-WDM Transmission over Weakly Coupled 10-Mode Fiber Using Rate-Adaptive PS-16QAM Signals. *J Lightwave Technol* (2022) 38(10):2835–41. doi:10.1109/JLT.2020.2979195
21. Rademacher G, Puttnam BJ, Luís RS, Sakaguchi J, Klaus W, Eriksson TA, et al. 10.66 Peta-Bit/s Transmission over a 38-Core-Three-Mode Fiber. In: Optical Fiber Communication Conference. San Diego, California United States: OSA Technical Digest (Optical Society of America,2020),paper Th3H.1 (2020). doi:10.1364/OFC.2020.Th3H.1
22. Hu T, Li J, Ge D, Wu Z, Tian Y, Shen L, et al. Weakly-coupled 4-mode Step-index FMF and Demonstration of IM/DD MDM Transmission. *Opt Express* (2018) 26:8356–63. doi:10.1364/OE.26.008356
23. Wang L, Nejad RM, Corsi A, Lin J, Messaddeq Y, Rusch LA, et al. MIMO-free Transmission over Six Vector Modes in a Polarization Maintaining Elliptical Ring Core Fiber. In: Optical Fiber Communication Conference. Los Angeles, California United States: OSA Technical Digest (online) (Optical Society of America,2017),paper Tu2J.2 (2017). doi:10.1364/OFC.2017.Tu2J.2
24. Hong K, Yeom J, Jang C, Hong J, Lee B. Full-color Lens-Array Holographic Optical Element for Three-Dimensional Optical See-Through Augmented Reality. *Opt Lett* (2014) 39:127–30. doi:10.1364/OL.39.000127
25. Wang L, LaRochelle S. Design of Eight-Mode Polarization-Maintaining Few-Mode Fiber for Multiple-Input Multiple-output-free Spatial Division Multiplexing. *Opt Lett* (2015) 40:5846–9. doi:10.1364/OL.40.005846
26. Corsi A, Ho Chang J, Wang R, Wang L, Ann Rusch L, LaRochelle S. Highly Elliptical Core Fiber with Stress-Induced Birefringence for Mode Multiplexing. *Opt Lett* (2020) 45:2822–5. doi:10.1364/OL.387751
27. Milione G, Ip E, Ji P, Huang Y, Wang T, Li M, et al. MIMO-less Space Division Multiplexing with Elliptical Core Optical Fibers. In: Optical Fiber Communication Conference. Los Angeles, California United States: OSA Technical Digest (online) (Optical Society of America, 2017), paper Tu2J.1 (2017). doi:10.1364/OFC.2017.Tu2J.1
28. Liang J, Mo Q, Fu S, Tang M, Shum P, Liu D. Design and Fabrication of Elliptical-Core Few-Mode Fiber for MIMO-Less Data Transmission. *Opt Lett* (2016) 41:3058–61. doi:10.1364/OL.41.003058
29. Yu D, Mo Q, Hong Z, Fu S, Sima C, Tang M, et al. Temperature-insensitive Fiber Twist Sensor Based on Elliptical-Core Few-Mode Fiber. *Opt Lett* (2016) 41:4617–20. doi:10.1364/OL.41.004617
30. Zheng H, Liu S, Wu C, Yu H, Li X, Wang W, et al. Experimental Study on Pulse Propagation Characteristics at normal Dispersion Region in Dispersion Flatted Fibers. *Opt Laser Technol* (2012) 44(4):763–6. doi:10.1016/j.optlastec.2011.11.033
31. Zheng H, Wu C, Wang Z, Yu H, Liu S, Li X. Propagation Characteristics of Chirped Soliton in Periodic Distributed Amplification Systems with Variable Coefficients. *OPTIK* (2012) 123(9):818–22. doi:10.1016/j.ijleo.2011.06.045
32. Zheng H, Li X, Liu S, Hu W, Bai C. Generation and Transmission of a High-Bit-Rate Optical Millimeter Wave with an Unrepeated Long Single-Span Using Equalization Amplification. *Opt Commun* (2015) 356:599–606. doi:10.1016/j.optcom.2015.08.062
33. Wang X, Zheng H, Zhu L, Li X, Bai C, Hu W, et al. A Long Single-Span Dispersion-decreasing-like Fiber Transmission System. *Opt Laser Technol* (2019) 116:338–44. doi:10.1016/j.optlastec.2019.03.046
34. Qiao S, Ma Y, He Y, Patimisco P, Sampaolo A, Spagnolo V. Ppt Level Carbon Monoxide Detection Based on Light-Induced Thermoelastic Spectroscopy Exploring Custom Quartz Tuning forks and a Mid-infrared QCL. *Opt Express* (2021) 29(16):25100–8. doi:10.1364/OE.434128
35. Zheng H, Wu C, Liu S, Li X. Experimental Observation of Lasering Behavior in Wavelength-Switchable Fiber Laser with Arrayed Waveguide Grating. *OPTIK* (2012) 123(8):715–9. doi:10.1016/j.ijleo.2011.06.030
36. Zhang H, Zheng Y, Mao D, Zeng C, Du Y, Zhao J. Morphology-controllable Ultrafast Fiber Lasers Based on Intracavity Manipulation of Transverse Modes. *Phys Rev Appl* (2021) 16(3):034045. doi:10.1103/PhysRevApplied.16.034045
37. Zheng Hongjun 郑., Wu Chongqing 吴., Wang Jian 王., Wang Zhi 王., Liu Shanliang 刘., Li Xin 黎.. A Novel Single-Polarization Single-Mode Photonic Crystal Fiber with Two Arrays of Four Lines of Semiminor-Axis-Decreasing Elliptical Air-Holes. 光学学报 (2011) 31(8):0806003. doi:10.3788/AOS201131.0806003
38. Agrawal G. *Introduction Nonlinear Fiber Optics*. 5th ed.. Academic Press (2013). p. 1–25. doi:10.1016/b978-0-12-397023-7.00001-2
39. Yu R-y., Zheng H-j., Li X, Bai C-l., Hu W-s.. A Novel Three-Ring-Core Few-Mode Fiber with Large Effective Area and Low Nonlinear Coefficient. *Optoelectron Lett* (2018) 14(1):30–5. doi:10.1007/s11801-018-7200-4
40. Liu Y, Yang Z, Zhao J, Zhang L, Li Z, Li G. Intrinsic Loss of Few-Mode Fibers. *Opt Express* (2018) 26:2107–16. doi:10.1364/OE.26.002107
41. Schulze C, Lorenz A, Flamm D, Hartung A, Schröter S, Bartelt H, et al. Mode Resolved bend Loss in Few-Mode Optical Fibers. *Opt Express* (2013) 21: 3170–81. doi:10.1364/OE.21.003170
42. Sillard P. Few-Mode Fibers for Space Division Multiplexing. In: Optical Fiber Communication Conference. California United States: Anaheim (2016). doi:10.1364/OFC.2016.Th1J.1
43. Han J, Gao G, Zhao Y, Hou S. Bend Performance Analysis of Few-Mode Fibers with High Modal Multiplicity Factors. *J Lightwave Technol* (2017) 35:2526–34. doi:10.1109/JLT.2017.2696983
44. Yaman F, Bai N, Huang YK, Huang MF, Zhu B, Wang T, et al. 10 X 112Gb/s PDM-QPSK Transmission over 5032 km in Few-Mode Fibers. *Opt Express* (2010) 18:21342–9. doi:10.1364/OE.18.021342

45. Deng D, Luo H, Wang Y, Xiong J, Wang S. The Preparation of Low-Loss Optical Fiber with Microwave Plasma Activated Chemical Vapor Deposition Process. *J Commun* (1982) 3(1):33–8.
46. Geittner P, Küppers D, Lydtin H. Low-loss Optical Fibers Prepared by Plasma-activated Chemical Vapor Deposition (CVD). *Appl Phys Lett* (1976) 28:645–6. doi:10.1063/1.88608
47. Lydtin H. Update on Fiber Manufacture by PCVD. In: Optical Fiber Communication Conference. New OrleansLouisiana United States: OSA Technical Digest Series (Optical Society of America, 1984), paper TuM1 (1984). doi:10.1364/OFC.1984.TuM1
48. Jung Y, Han SR, Kim S, Paek UC, Oh K. Versatile Control of Geometric Birefringence in Elliptical Hollow Optical Fiber. *Opt Lett* (2006) 31:2681–3. doi:10.1364/OL.31.002681
49. Corsi A, Chang J, Wang R, Wang L, Rusch LA, LaRochelle S. Highly Elliptical Core Fiber with Stress-induced Birefringence for Mode Multiplexing. *Opt Lett* (2020) 45:2822–2825. doi:10.1364/OL.387751

Conflict of Interest: The authors declare that the research was conducted in the absence of any commercial or financial relationships that could be construed as a potential conflict of interest.

frontiers in Physics

REVIEW
published: 27 January 2022
doi: 10.3389/fphy.2022.821528

Application of Molecular Emissions in Laser-Induced Breakdown Spectroscopy: A Review

Fanghao Xu[1,2], *Shixiang Ma*[1], *Chunjiang Zhao*[1] *and Daming Dong*[1]*

[1]National Research Center of Intelligent Equipment for Agriculture, Beijing Academy of Agriculture and Forestry Sciences, Beijing, China, [2]College of Mechanical and Electrical Engineering, Gansu Agricultural University, Lanzhou, China

Laser-induced breakdown spectroscopy (LIBS) with advantages of rapid, *in situ*, and little sample pretreatment has been used in various fields. However, LIBS technology remains challenging in the detection of halogens, isotopes, and samples with similar elements. Therefore, molecular emission was proposed to improve the detection ability of LIBS. In this review, we introduced molecular emissions formed by organic elements, oxidizable elements, and halogens. Then, molecular emission in different experiment parameters, such as the acquisition window, laser characters (laser energy, laser wavelength, and pulse duration), and ambient atmospheres, were discussed. In the end, we highlight the application of molecular emissions on element content determination, material type classification, and combustion and explosion process monitoring.

Keywords: laser-induced breakdown spectroscopy, molecular emissions, isotope, halogen, energetic samples, plastic samples, biomedical samples, process monitoring

OPEN ACCESS

Edited by:
Yufei Ma,
Harbin Institute of Technology, China

Reviewed by:
Minchao Cui,
Northwestern Polytechnical University, China
Anmin Chen,
Jilin University, China

****Correspondence:***
Daming Dong
damingdong@hotmail.com

Specialty section:
This article was submitted to Optics and Photonics, a section of the journal Frontiers in Physics

Received: *24 November 2021*
Accepted: *04 January 2022*
Published: *27 January 2022*

Citation:
Xu F, Ma S, Zhao C and Dong D (2022) Application of Molecular Emissions in Laser-Induced Breakdown Spectroscopy: A Review. Front. Phys. 10:821528. doi: 10.3389/fphy.2022.821528

1 INTRODUCTION

Laser-induced breakdown spectroscopy (LIBS) is an ideal spectroscopic technique for material component analysis. The advantages of a rapid, *in situ*, real-time and remote analysis, and simple sample preparation [1–3] extend LIBS to detection in various environments, such as the space [4, 5], ocean [6, 7], nuclear reactors [8, 9], mines [10, 11], and in the metallurgical [12, 13] and industrial fields [14, 15]. These studies are based on the atomic emissions in the spectra. However, atomic emissions still have several drawbacks, including 1) the matrix effect [16,] and self-absorption [17, 18] blocking accuracy for quantitation and 2) its unsuitability for the classification of matters with similar elemental compositions. To overcome these drawbacks, researchers have focused on molecular emission in recent years [19]. Moreover, molecular emission can monitor burning and exploding processes.

In recent years, molecular emission was mentioned in LIBS reviews of specific targets, such as organics [20], explosives [21], and combustion [22]. The formation mechanism and experimental parameters for molecular emission were not discussed. The purpose of this review was to summarize the application of laser-induced molecular emission in quantitative classification and process monitoring. To make the molecular emission application well-founded, we summarized the molecular emission formation and how the experimental parameters influenced molecular emissions before the application. And, the framework of this review is shown in **Figure 1**.

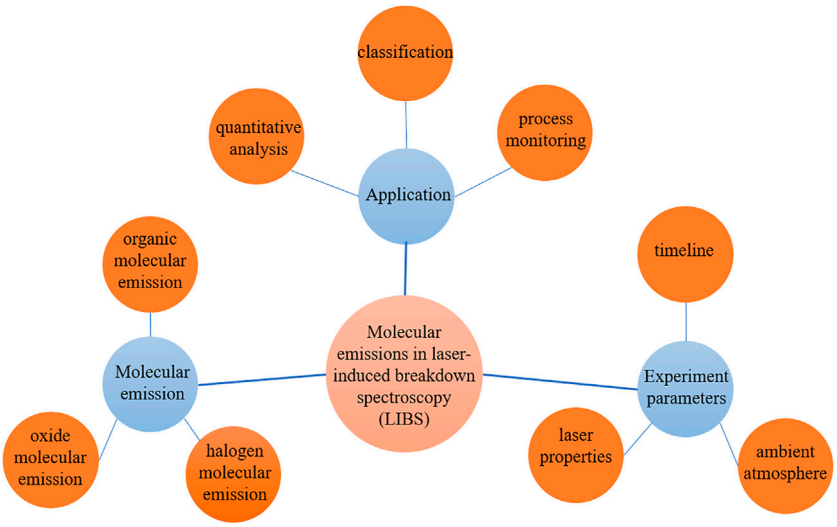

FIGURE 1 | Framework of this review.

2 MOLECULAR EMISSIONS IN LIBS

The characteristic molecular emission line radiates from the plasma induced by high irradiance (typically about 10^{10} W/cm^2) and short pulse duration (typically <10 ns) laser, which is the same condition as that for atomic and ionic emissions. Different from the atomic and ionic emissions, however, there are two routes for molecular emissions: 1) recombination of the atomic and ionic species in the plasma and/or 2) direct emission by the molecular fragments separate from the matrix. For recombination routes, the species in the plasma contain molecular fragments and atomic and ionic species induced from the sample and surroundings, and the process can be described as plasma chemistry [20].

The molecular emission can be divided into organic element molecular emissions, oxide molecular emissions, and halogen element molecular emissions by the composition of the molecular radical. The band system and formation routes are listed in **Table 1**.

Organic Element Molecular Emissions

Carbon (C), hydrogen (H), nitrogen (N), and oxygen (O) are the main organic elements and can combine to form diatomic molecular radicals, such as CN (cyanogen), C_2 (carbon dimer), CH (methylidyne), OH (hydroxyl) and NH (amidogen), and so on.

CN molecular emissions can easily occur during laser ablation of carbonic matter in the air. This mainly comes from the recombination of the carbon and nitrogen atoms in the plasma [23].

C_2 molecular emissions can also occur from the carbonic matter. However, they always require the presence of a carbon–carbon bond (C-C) or carbon–carbon double bond (C=C) in the matrix. This mainly comes from molecular fragments [24].

CH molecular emissions are common from the core of the combustion zone. CH emission can be directly released and formed by carbon and hydrogen species [25].

OH molecular emission can radiate from plasma that includes high amount of H and O species. Such as laser ablation materials containing high mount water (H_2O) and hydroxide radical. And the OH molecular emission is generally low [26].

NH molecular emissions can radiate from the plasma with nitrogen and hydrogen species. These molecular emissions are commonly released in high hydrogen (H) content materials induced by laser in the air and occur more commonly in the femtosecond-induced plasma [27].

Oxide Molecular Emissions

Metals and non-metals induced by lasers can combine with O to form oxide molecular emissions, such as aluminum monoxide (AlO), strontium monoxide (SrO), carbon monoxide (CO), boron monoxide (BO), and silicon monoxide (SiO).

AlO molecular emission can occur when aluminum alloy undergoes laser ablation in ambient air [28], combining Al and O in the plasma. SrO, CO, BO, and SiO molecular emissions are similar to the AlO molecular emission.

Halogen Molecular Emissions

Halogen is difficult to detect in LIBS due to the weak emission, which overlaps with the matrix, and because of their ultraviolet spectral region. The emissions of diatomic molecules of halogens, such as fluorine (F), chlorine (Cl), bromine (Br), and iodine (I), combined with alkali earth elements substantially increases the sensitivity for halogen detection. Alkali earth-halogen molecular emissions mainly recombined in the plasma [29].

TABLE 1 | Molecular emissions used in this review.

Species	Formation path	Wavelength (nm)	Transition
CN	Formation C + N → CN C + N_2 → CN + N C_2 + N → CN + C	421.6 (0–1), 419.7 (1–2), 418.1 (2–3), 416.8 (3–4), 415.6 (4–5), 415.2 (5–6)	$B^2\Sigma^+ \rightarrow X^2\Sigma^+$ Δυ = -1
	C_2 + N_2 → 2CN Consumption CN + O → CO + N CN + O → CO + N Fragmentation: Samples contain carbon–nitrogen bonds (C-N).	388.32 (0–0), 387.12 (1–1), 386.14 (2–2), 385.44 (3–3), 385.03 (4–4) 359.0 (1–0), 358.6 (2–1), 358.4 (3–2)	$B^2\Sigma^+ \rightarrow X^2\Sigma^+$ Δυ = 0 $B^2\Sigma^+ \rightarrow X^2\Sigma^+$ Δυ = +1
C_2	Formation: CN + C → C_2 +N C + C → C_2 Consumption: C_2 + O_2 → 2CO Fragmentation:. Samples contain carbon–carbon bonds (C-C) and carbon–carbon double bonds (C=C)	619.1 (0–2), 612.2 (1–3), 606.0 (2–4), 600.5 (3–5), 595.9 (4–6), 592.3 (5–7) 563.48, 558.51, 554.05, 545.22, 544.61 516.52 (0–0), 512.87 (1–1) 473.66, 471.5, 469.67, 467.82 438.2	$d^3\Pi_g \rightarrow a^3\Pi_u$ Δυ = -2 $d^3\Pi_g \rightarrow a^3\Pi_u$ Δυ = -1 $d^3\Pi_g \rightarrow a^3\Pi_u$ Δυ = 0 $d^3\Pi_g \rightarrow a^3\Pi_u$ Δυ = +1 $d^3\Pi_g \rightarrow a^3\Pi_u$ Δυ = +2
CH	Formation: C_2 + OH → CO + CH C_2H + O → CO + CH	418.1 (2–3), 419.7 (1–2), 421.6 (0–1), 431.5 (0–0)	$A^2\Delta \rightarrow X^2\pi$ Δυ = 0
OH	plasma containing H_2O.	306.4, 306.8, 307.8, 309.0, 308.2, 309.6	$A^2\Sigma^+ \rightarrow X^2\Pi_r$ Δυ = 0
NH	From H content materials and N_2.	336.3, 337.4	$A^3p_i \rightarrow X^3\Sigma^-$
AlO	Al + O → AlO Al + CO_2 → AlO + CO	483–491	$B^2\Sigma^+ - X^2\Sigma^+$ Δυ = 0
SrO	Combine from Sr and O.	640–650, 651–662, 676–685	/
CO	Combine from C and O.	395.36, 519.82	/
BO	Combine from C and O.	255.14 (0–2), 258.80 (1–3)	$B^2\Sigma^+ \rightarrow X^2\Sigma^+$
SiO	Combine from Si and O.	248.68 (0–2)	$A^1\Pi \rightarrow X^1\Sigma^+$
CaF	Combine from Ca and F.	590–610 535	$A^2\Pi \rightarrow X^2\Sigma$ $B^2\Sigma \rightarrow X^2\Sigma$
CaCl	Combine from Ca and Cl.	593.4, 621.2	/
SrCl	Combine from Sr and Cl.	619–628, 630–637, 668–675	/
CaBr	Combine from Ca and Br.	vicinity 630	$A^2\Pi \rightarrow X^2\Sigma$
CaOH	From $CaCl_2$ and NaCl aqueous solution.	632 554	$A^2\Pi \rightarrow X^2\Sigma^+$ $B^2\Sigma^+ \rightarrow X^2\Sigma^+$

3 EXPERIMENTAL PARAMETERS FOR MOLECULAR EMISSION

The same matters can radiate different molecular emissions due to the fact that plasma chemistry can be strongly influenced by experimental parameters [30], such as the timeline, laser characteristics (laser energy, pulse duration, and laser wavelength), and ambient air, which are the main influence factors. And, most studies were about CN and C_2 molecular emissions. The CN emission is obtained by recombination, while the C_2 emission is principally fragmented directly from the matrix. In this part, we will discuss the influence though CN and C_2 molecular emissions. The formation route of CN and C_2 molecular emissions is shown in **Figure 2**.

Timeline of Molecular Emission

Spectral lines emitted from the plasma are changed continuously because of the electron density and temperature decrease during the expansion. Over the duration of the plasma's persistence, the prevailing emitting species changes from ions to atoms, and to molecules in the ns LIB spectrum [31]. Furthermore, the lifetimes of the molecular emissions from the laser-induced plasma are much longer and later than the ionic and atomic emissions [32]. The molecular

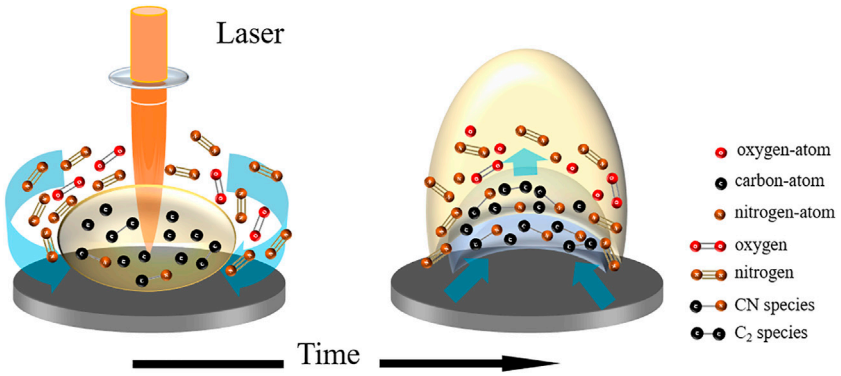

FIGURE 2 | Formation routes of CN and C_2 molecular emissions. Laser ablate sample, atomizing carbon-atom and nitrogen-atom, fragmenting CN and C_2 species from the sample, and atomizing nitrogen-atom and oxygen-atom from ambient gas. Species from the sample and surroundings combining new molecular species in the plasma.

emission signal acquisition windows are in delay time 0.5–5 μs and gate width 0.5–1 F06Ds in experiments, generally [33–35]. For CN molecular emissions, Fernandez-Bravo et al. [30] obtained precise time-resolved CN emissions. The results showed that CN emissions exhibited large behavior differences among organic compounds.

Laser Characteristics for Molecular Emission

In the LIBS system, the laser used to ablate the sample can be described by three characteristics: laser energy, pulse duration, and laser wavelength. As mentioned before that molecular species is produced at the timeline where the plasma temperature is low, the excitation of the molecular emission can be enhanced by reducing the heating effect of the laser with the materials.

When the laser energy reaches the ablation threshold of the material and vaporized it, the remaining energy is used to excite the vaporized materials to the upper state, and then the plasma is generated. Serrano et al. [36] showed that with a laser energy of increasing strength, greater energy will be used to atomize the material after reaching the ablation threshold, resulting in less molecular species in the plasma. And, they represented the atomization by the intensity ratio of CN/C_2. Thus, to achieve more molecular fragments in the plume, it is helpful to have the laser energy close to the sample ablation threshold.

The other two characteristics, pulse duration and laser wavelength, depend on the native properties of lasers. Research studies have indicated that a shorter pulse duration and ultraviolet (UV) wavelength of the laser pulse can improve the spectral quality of molecular emission.

For the duration of the laser pulse, Junjuri et al. [37] concluded that femtosecond (fs) lasers are more suitable for the excitation of molecular emission than nanosecond (ns) lasers owing to shorter interacting time between the laser and materials. Rao et al. [33] showed that fs lasers can induce molecular emission earlier than ns counterparts, and the emission intensity can be stronger [38]. The reused **Figure 3** shows that CN and C_2 molecular emissions in ns and fs laser–induced spectra [34]. The intensity of ionic and atomic emissions is higher in the ns laser–induced spectrum, but molecular emissions are higher in the fs laser–induced spectrum. De Lucia et al. [39] discovered that the fs laser can reduce the disturbance due to inducing less species from the ambient atmosphere. Further, Shaik et al. [40] concluded that fs lasers can introduce less substrate interferences in molecular emissions.

For the wavelength of the laser pulse, the most commonly used wavelengths are the infrared (IR) laser pulses (1,064 nm) and the second harmonic, visible (Vis) laser pulses (532 nm) of the Nd:YAG laser. The short wavelength can interact with the sample more efficiently. Baudelet et al. ablated organic materials with UV pulses (266 nm) delivered by a quadrupled Nd:YAG laser, comparing the plasmas induced by the 4 ns IR laser with energy from 1–5 mJ [41]. The results demonstrated that ns UV pulses with a low fluence can produce native molecular fragments efficiently and a minimized recombination with ambient air [42]. The middle-infrared (M-IR) laser pulse (10.591 μm, 3.16 J) is also used in molecular emission studies [43, 44].

Ambient Atmospheres for Molecular Emission

The N and O atoms in the air (approximately 80% N_2 and 20% O_2) are also excited by the laser and participate in the plasma chemistry. To make more accurate use of molecular emission, it is necessary to study the atmosphere condition. Mousavi et al. [23] studied the molecular emissions of CN and C_2 in ambient nitrogen (N_2), air, oxygen (O_2), and argon (Ar) atmospheres by the ns laser pulse. The results showed that the intensity of the CN and C_2 molecular emissions decreased owing to the increased O_2 content. In the N_2 environment, the CN molecular emission intensity increased owing to the recombination of C and N. In the inert gas, Ar atmosphere, the vibrational temperatures of both CN and C_2 had the highest values. Researchers have also studied CN and C_2 in helium (He) and carbon dioxide (CO_2) atmospheres [45, 46].

In addition, molecular emission is influenced by different pressures of the surrounding atmosphere. Delgado et al. [47]

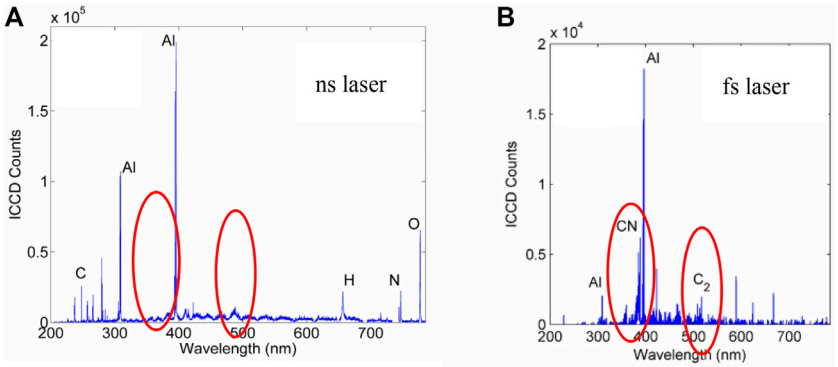

FIGURE 3 | (A) Nanosecond LIBS signal obtained from TNT on an aluminum substrate. The detection gate delay and width values were 1 and 2 μs, respectively. **(B)** Femtosecond LIBS signal obtained from TNT on an aluminum substrate, over the complete detection wavelength range. The detection gate delay and width values were 100 ns and 1 μs, respectively [34].

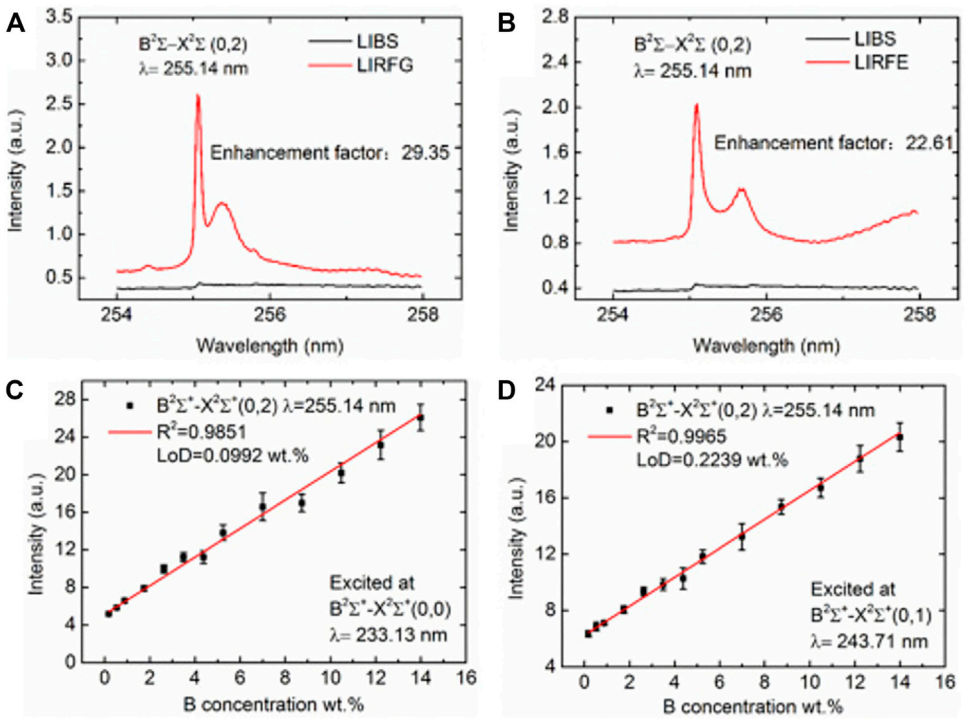

FIGURE 4 | Spectral comparisons of **(A)** LIBS and LIRFG and **(B)** LIBS and LIRFE. Calibration curves of BO in **(C)** LIRFG and **(D)** LIRFE. [50].

investigated the molecular emissions at high vacuum ($<10^{-1}$ mbar) to high pressure (1,000 mbar). The results showed that emissions were dominated by ionic and atomic emissions at high vacuum. The C_2 and CN emissions increased rapidly when the pressure was increased in the range between 10–100 mbar. While the pressure surpassed 100 mbar, the C_2 and CN emissions decreased. The authors attributed this observation to there being less species collision in the plasma at a low pressure, leading to less reaction in the plasma.

4 APPLICATION OF MOLECULAR EMISSION

Quantitative Analysis by Molecular Emission

LIBS analysis through atomic and ionic emissions provides insufficient results when the self-absorption appearance and/or disturbed by other elements. In this part, we will discuss the role of molecular emissions in quantitative analysis [48].

4.1.1 Molecular Emission for Quantitative Analysis

Ionic and atomic emissions are rarely used for the quantitative analysis of high-content samples because of the strong self-absorption effect. The molecular emission from LIBS can be a promising solution. Zhu et al. [49] collected the BO molecular emissions from a mixture of H_3BO_3 and $C_6H_{12}O_6{\cdot}H_2O$ in the powder form. The root mean square error of prediction (RMSEP) and the mean prediction error (MPE) for the genetic algorithm and partial least square regression combination model (GA-PLSR) were 0.8667 wt.% and 10.9685% by BO molecular emissions, respectively. There was much better linearity in the molecular emission than the atomic emission of B I (249.68, 249.77, 208.88, and 208.96 nm), owing to the much lower self-absorption effect. However, the intensity of molecular emissions is much lower, which means that there is still room for further improvement in the calibration of the molecular emission. Guo et al. [50] assisted LIBS with laser-induced radical fluorescence (LIBS-LIRF) to establish calibration of BO molecular emissions. The results showed that the enhancement factors are 29.35 for vibrational ground state excitation (LIRFG) and 22.61 for vibrational excited state excitation separately (LIRFE). The LIRFG had better sensitivity, with a limit of detection (LoD) of 0.0993 wt.%, while the LIRFE was more accurate, with a root mean square error of cross validation (RMSECV) of 0.2514 wt.%. The enhancement factors and quantitative results are shown in **Figure 4**. Zhang et al. [51] used LIBS assisted with laser-induced molecular fluorescence (LIBS-LIMF) to establish the calibration of the silicon content by silicon monoxide (SiO) molecular emission in micro-alloyed steel. The determination coefficient R^2 = 0.988, LoD = 187 μg/g, and RMSECV of 0.046 wt.%. In addition, CaOH emission can be used to detect the Ca content in underwater conditions. The results showed a LoD = 2.46 ppm with good linearity in a range from 5 to 2000 ppm [52].

4.1.2 Molecular Isotopic Emission for Quantitative Analysis

LIBS has been used in nuclear isotope safeguard inspection [8, 9, 53], but the tiny shifts between the isotopic atomic or ionic emissions can only be detected by high-resolution detectors and/or in low-pressure environments. Laser ablation molecular isotopic spectrometry (LAMIS) has been proposed as an efficient isotope detection method owing to the larger isotopic shifts. For example, the boron isotopic (^{11}B–^{10}B) shift in atomic emission is 2 picometer (pm). However, for ^{10}BO and ^{11}BO, the isotopic shifts extend from 0.74 nm to 5–8 nm. A partial least square (PLS) regression was used to further analyze the isotopic abundance approximately from 1 to 100% content of ^{11}B, R^2 = 0.9993 [54]. Furthermore, researchers at the Lawrence Berkeley National Laboratory detected the isotopes of hydrogen (H), boron (B), carbon (C), and oxygen (O) with LAMIS in reference [55]. Mao et al. [56] performed the isotopic analysis of solid Sr-containing samples (^{86}Sr, ^{87}Sr, and ^{88}Sr) in ambient air at normal pressure. The results showed that the radial spectra of SrO and strontium fluoride (SrF) molecular emissions provided a well-resolved spectrogram for the naturally occurring Sr isotopes. Chirinos et al. [57] detected ^{13}C from a graphite sample at a distance of 36 m by fs filaments - laser ablation molecular isotopic spectrometry (F-2-LAMIS) with a standardless quantification approach. The authors concluded that F-2-LAMIS can be a method to remote sense isotopes in the field.

In addition, the second laser enhance technology has been used in LAMIS. Brown et al. [58] utilized middle-infrared (Mid-IR) laser pulses (10.6 μm) for the second pulse, referred to as double-pulse LAMIS (DP-LAMIS) to determine the relative abundance of ^{11}B and ^{10}B. The results showed R^2 > 0.960 and LoD <2.3%. Akpovo et al. [59] combined LIBS and molecular laser-induced fluorescence (MLIF) to selectively enhance the BO molecular emission (253–271 nm). The LoD was 1.88% by PLS regression, which was better than the single pulse result of 2.45%.

4.1.3 Halogen Molecular Emission for Quantitative Analysis

The emission of halogen elements (such as F, Cl, Br, and I) is weak in LIBS because they require a high excitation energy and cannot reach a good quantitative accuracy. Alkali earth-halogen molecular emission can be another choice to detect the halogen elements.

Dietz et al. [60] quantified the Cl content, a harmful element present in cement-based materials, by calcium-monochloride (CaCl) molecular emission. The results showed an LoD = 0.075 wt.%, which was below the critical threshold of 0.2 wt.% of chlorides related to the cement in reinforced concrete. Álvarez et al. [61] investigated the fluorite (CaF_2) mass-content from 2.3 to 60% by calcium fluoride (CaF) molecular emissions in powdered ore samples. Further, CaF molecular emission was used to studied Cu matrix samples containing different F concentrations (between 50 and 600 μg/g) with variable amounts of Ca in the copper ore [62]. The results showed good linear relationships between the CaF molecular emission and F content. This methodology was extended in Ca-free samples by nebulizing a Ca-containing solution on the surface to form CaF molecular emission [63]. The LoD was 50 μg/g, similar to the Ca-containing samples. For other researchers, Tang et al. [64] used strontium fluoride (SrF) molecular emissions to detect the fluorine (F) content. The results showed that LoD = 5 ppm, R2 = 0.9933, and RMSECV = 0.0049 wt.%. In water condition [65], LoDs of F and Cl elements detected by CaF and CaCl molecular emissions were 0.38 mg/L and 1.03 mg/L, respectively. In addition, Br and I amounts were studied by molecular emission [66].

Classification by Molecular Emission

There are many research studies on classification analysis based on molecular emission. We summarized the research studies on the energetic materials, plastics, and biomedical samples.

4.1.4 Energetic Sample Classification

The direct chemical detection of energetic materials and explosives in real time is a particularly challenging problem. LIBS is a suitable technology to detect energetic materials. The first research study on explosives was reported by the U.S. Army Research Laboratory. De Lucia et al. [67] observed that the laser-produced plasma did not initiate any of the energetic materials and could be used to identify explosives. The C_2 molecular

emission and the H, O, and N emission intensity ratios were the necessary parameters to identify the explosive [68]. In addition, the relationship between the various kinds of explosives and plasma emission could be established by the ratio of the atomic/molecular emission intensities and the CN and C_2 molecular emission decay rates with time [39]. Furthermore, the double pulse could improve the discrimination of explosives by decreasing the contributions of atmospheric N_2 and O_2 to the LIBS signal in the remote and on-line ways [69]. Partial least square discriminant analysis (PLS-DA) was used for distinguishing explosives at 50 m. The results showed that the correct classification rate was 80%, and the false positive rate remained at 7.8% [70].

For other research studies, Moros et al. [71] imported the original intensities of the most relevant emission signals (C:CN:C_2:H:N:O) to different machine learning classifiers. False positive and false negative rates better than 5% were achieved. Yang et al. [72] captured three commonly used explosives (RDX, HMX, and PETN) molecular emissions in the long-wave infrared region (LWIR; range from 5.6 to 10 μm). The results showed that molecular emission signatures in the LWIR region could rapidly identify the different explosives.

Other energetic materials, such as solid propellants and petroleum, can also be studied by molecular emission. Solid propellants chemical aging is one of the most important problems for assessing the shelf-life of chemical propellants. Farhadian et al. [73] investigated and compared the CN and AlO molecular emissions of different kinds of solid propellants. The intensity ratios of the molecular emissions (CN, C_2, and AlO) were also considered [74]. El-Hussein et al. [75] studied the different grades of petroleum crude oil by C2 and CN molecular emission. The results showed that the C_2 and CN molecular emissions were related to the American Petroleum Institute (API) gravity values of the various oil samples with the possibility of identifying the API gravity values of unknown oil samples.

4.1.5 Plastic Sample Classification

LIBS technology is not affected by the plastic shape and surface contaminants and can be used in online, rapid detection in industrial applications. The intensity ratio of molecular emission can be used to complete the identification of different types of plastics without an algorithm model. Anzano et al. [76] studied four kinds of plastic samples. The ratios of C_2/C could be used to classify those plastic samples. Barbier et al. [46] investigated plastic samples in the He atmosphere. The results showed that the plot of C_2/He against CN/He was sufficient to identify the four groups of plastics employed in this study.

Researchers combine emission intensity ratios with statistical and stoichiometric methods to plastic samples. Banaee et al. [77] studied six plastic samples by ratios of the emission lines and molecular bands were analyzed by k-nearest neighbors (KNN) and soft independent modeling of class analogy (SIMCA). The results showed the average classification accuracies of 98% for KNN and 92% for SIMCA. Further, Banaee et al. [78] input the ratios of the CN and C_2 molecular emissions, and the atomic emissions of C, N, Cl, O, and H were discriminated by discriminant function analysis (DFA) with the accuracy of 99%. Junjuri et al. [37] used an fs laser to enhance the effect of distinguishing the plastics by the principal component analysis (PCA) and artificial neural network (ANN), and the discriminant accuracy was 100%.

4.1.6 Biomedical Samples Classification

The development of reliable sensors to detect biological residuals is important for security terrorist activity and is a high priority for the military and homeland security. Gottfried et al. [79] collected the molecular emission of CN, C_2, and CaOH from bacterial residues in the aluminum substrate, and the intensity and ratio of the emission were each input into the PLS-DA model. The results showed that the intensity/ratio models were able to correctly identify more types of residues in the presence of interferents. Baudelet et al. [80, 81] collected the CN molecular emission from the native CN band in *Escherichia coli* by the fs laser, and the emissions could be used to identify the bacterium [81]. In a low- pressure CO_2 atmosphere, Delgado et al. [45] analyzed adenine, glycine, pyrene, and urea mixed with carbons. The results indicated LIBS with a potential for exploring life in the space environment. Yang et al. [82] detected the solid pharmaceutical tablet of Tylenol and buffering in the ultraviolet/ visible/ NIR (UVN) range (200–1,100 nm) and LWIR (Longwave infrared) range (5.6–10 μm), respectively. The molecular emissions were highly specific and could distinguish between tablets.

Process Monitoring

Molecular emission can identify intermediate chemical species among the combustion and explosive explosions *in situ*, which is helpful to understand the process. In this section, we summarized molecular emission research in combustion and explosion.

Molecular emissions of combustion intermediates can indicate the flame's structure and burning quality. Ghezelbash et al. [25] investigated the CH, CH*, C_2, and CO molecular emissions in different areas in the laminar diffusion of methanol, ethanol, and n-propanol alcohol flames. The strong molecular emissions of CH and CH* were from the blue zones (with low combustion quality). Kotzagianni et al. [83] demonstrated that the CN molecular emissions at 388.3 nm can be used to study the radial and axial variation within the flames. Li et al. [84] concluded that the femtosecond filament-induced spectrum contained rich information about the CN, CH, and C_2 molecular emissions from the combustion intermediates of the butane flame.

The explosive ignited by the laser is similar to optical breakdown, and the molecular emissions that radiated from the process can be used to study it. Rao et al. [33] induced seven explosive molecules utilizing fs and ns lasers in the air and argon atmosphere. They observed the intensity ratio of CN/C_2 emission increase with an increasing percentage of O atoms, indicating the oxygen balance of explosive molecules. They further concluded that the ratio of atomization/fragmentation could indicate the explosive properties. A similar research by Kalam et al. [85] found the ratios of (CN + C_2)/(C + H + N + O) correlated well with the detonation parameters, namely, oxygen balance, velocity of detonation, detonation pressure, and chemical energy. It supported the understanding and improvement of the discrimination procedures for such hazardous materials. In addition, aluminum powder was added to molecular explosives to study its chemistry at high temperatures. Gottfried et al. [86] ablated cyclotrimethylenetrinitramine (RDX) mixed with aluminum power at (0:1, 1:1, 2:1, and 4:1). The results showed

that Al could combine with O to generate AlO molecular emission, which reduced the oxidation reaction of the explosive and reduced the adequacy of the reaction.

5 CONCLUSION AND PROSPECTS

In this review, we overviewed experiment parameters and the application of molecular emissions. The results showed molecular emission is emitted from a time of low electron temperature and density in the plasma. The intensity is strong when the laser energy is close to the ablation threshold and UV laser wavelength (266 nm) in the ns laser system. In the counterparts, the fs laser can produce more abundant molecular emissions owing to less heating effect. The UV laser is economic and maintainable compared with the fs laser. We consider the UV laser maybe a better choice for molecular emission analysis. In addition, the ambient atmosphere should be considered in molecular emissions, such as N and O species in air surroundings. For the quantitative study, molecular emissions, including isotopic and halogen molecules, can detect a wider range of matter content. For the classification study, molecular emission can distinguish matters with similar elements, such as energetic materials, plastics, and biomedical samples. Furthermore, researchers studied the combustion process and characteristics of explosives and the degrees of explosion *in situ* and in real time.

Molecular emission is a kind of useful spectral line in LIBS; the study can further focus on detection of halogens, isotopes, and organic samples in the field. However, the complex radiation process confined the application LIBS. To apply laser-induced molecular emission in the field, it is necessary to study the molecular formation mechanism and optimize the parameters of the experimental system, reducing the disturbance of the ambient.

AUTHOR CONTRIBUTIONS

FX helped with the writing and editing of the original draft. FX and SM helped organize the draft. CZ carried out the investigation. DD contributed to investigation, methodology, and conceptualization.

FUNDING

This research was financially supported by the Distinguished Young Scientists Program of Beijing Natural Science Foundation (JQ19023) and the Distinguished Scientist Development Program of the Beijing Academy of Agriculture and Forestry Sciences (JKZX201904). This review also funded by National & Local Joint Engineering Laboratory For Agricultural Internet of Things (PT2021-06).

REFERENCES

1. Fortes FJ, Moros J, Lucena P, Cabalín LM, Laserna JJ. Laser-induced Breakdown Spectroscopy. *Anal Chem* (2013) 85:640–69. doi:10.1021/ac303220r
2. Fernández-Menéndez LJ, Méndez-López C, Alvarez-Llamas C, González-Gago C, Pisonero J, Bordel N. Spatio-temporal Distribution of Atomic and Molecular Excited Species in Laser-Induced Breakdown Spectroscopy: Potential Implications on the Determination of Halogens. *Spectrochimica Acta B: At Spectrosc* (2020) 168:105848. doi:10.1016/j.sab.2020.105848
3. Grégoire S, Motto-Ros V, Ma QL, Lei WQ, Wang XC, Pelascini F, et al. Correlation between Native Bonds in a Polymeric Material and Molecular Emissions from the Laser-Induced Plasma Observed with Space and Time Resolved Imaging. *Spectrochimica Acta Part B: At Spectrosc* (2012) 74-75:31–7. doi:10.1016/j.sab.2012.07.020
4. Wan X, Li CH, Wang HP, Xu WM, Jia JJ, Xin YJ, et al. Design, Function, and Implementation of China's First LIBS Instrument (MarSCoDe) on the Zhurong Mars Rover. *At Spectrosc.* (2021) 42:294–8. doi:10.46770/as.2021.608
5. Wiens RC, Maurice S, Barraclough B, Saccoccio M, Barkley WC, Bell JF, et al. The ChemCam Instrument Suite on the Mars Science Laboratory (MSL) Rover: Body Unit and Combined System Tests. *Space Sci Rev* (2012) 170:167–227. doi:10.1007/s11214-012-9902-4
6. Guirado S, Fortes FJ, Lazic V, Laserna JJ. Chemical Analysis of Archeological Materials in Submarine Environments Using Laser-Induced Breakdown Spectroscopy. On-Site Trials in the Mediterranean Sea. *Spectrochimica Acta Part B: At Spectrosc* (2012) 74-75:137–43. doi:10.1016/j.sab.2012.06.032
7. Michel APM, Lawrence-Snyder M, Angel SM, Chave AD. Laser-induced Breakdown Spectroscopy of Bulk Aqueous Solutions at Oceanic Pressures: Evaluation of Key Measurement Parameters. *Appl Opt* (2007) 46:2507–15. doi:10.1364/Ao.46.002507
8. Singh M, Sarkar A, Banerjee J, Bhagat RK. Analysis of Simulated High Burnup Nuclear Fuel by Laser Induced Breakdown Spectroscopy. *Spectrochimica Acta Part B: At Spectrosc* (2017) 132:1–7. doi:10.1016/j.sab.2017.03.012
9. Doucet FR, Lithgow G, Kosierb R, Bouchard P, Sabsabi M. Determination of Isotope Ratios Using Laser-Induced Breakdown Spectroscopy in Ambient Air at Atmospheric Pressure for Nuclear Forensics. *J Anal At. Spectrom* (2011) 26:536–41. doi:10.1039/c0ja00199f
10. Balaram V. Rare Earth Elements: A Review of Applications, Occurrence, Exploration, Analysis, Recycling, and Environmental Impact. *Geosci Front* (2019) 10:1285–303. doi:10.1016/j.gsf.2018.12.005
11. Rifai K, Laflamme M, Constantin M, Vidal F, Sabsabi M, Blouin A, et al. Analysis of Gold in Rock Samples Using Laser-Induced Breakdown Spectroscopy: Matrix and Heterogeneity Effects. *Spectrochimica Acta Part B: At Spectrosc* (2017) 134:33–41. doi:10.1016/j.sab.2017.06.004
12. Dong F-Z, Chen X-L, Wang Q, Sun L-X, Yu H-B, Liang Y-X, et al. Recent Progress on the Application of LIBS for Metallurgical Online Analysis in China. *Front Phys* (2012) 7:679–89. doi:10.1007/s11467-012-0263-y
13. Hudson SW, Craparo J, De Saro R, Apelian D. Applications of Laser-Induced Breakdown Spectroscopy (LIBS) in Molten Metal Processing. *Metall Materi Trans B* (2017) 48:2731–42. doi:10.1007/s11663-017-1032-7
14. Lopez-Moreno C, Amponsah-Manager K, Smith BW, Gornushkin IB, Omenetto N, Palanco S, et al. Quantitative Analysis of Low-alloy Steel by Microchip Laser Induced Breakdown Spectroscopy. *J Anal At. Spectrom* (2005) 20:552–6. doi:10.1039/b419173k
15. Noll R, Fricke-Begemann C, Connemann S, Meinhardt C, Sturm V. LIBS Analyses for Industrial Applications - an Overview of Developments from 2014 to 2018. *J Anal At. Spectrom* (2018) 33:945–56. doi:10.1039/c8ja00076j
16. Sallé B, Cremers DA, Maurice S, Wiens RC. Laser-induced Breakdown Spectroscopy for Space Exploration Applications: Influence of the Ambient Pressure on the Calibration Curves Prepared from Soil and clay Samples. *Spectrochimica Acta Part B: At Spectrosc* (2005) 60:479–90. doi:10.1016/j.sab.2005.02.009
17. Bulajic D, Corsi M, Cristoforetti G, Legnaioli S, Palleschi V, Salvetti A, et al. A Procedure for Correcting Self-Absorption in Calibration Free-Laser Induced Breakdown Spectroscopy. *Spectrochimica Acta Part B: At Spectrosc* (2002) 57:339–53. doi:10.1016/S0584-8547(01)00398-6

18. El Sherbini AM, El Sherbini TM, Hegazy H, Cristoforetti G, Legnaioli S, Palleschi V, et al. Evaluation of Self-Absorption Coefficients of Aluminum Emission Lines in Laser-Induced Breakdown Spectroscopy Measurements. *Spectrochimica Acta Part B: At Spectrosc* (2005) 60:1573–9. doi:10.1016/j.sab.2005.10.011
19. Dong M, Mao X, Gonzalez JJ, Lu J, Russo RE. Time-resolved LIBS of Atomic and Molecular Carbon from Coal in Air, Argon and Helium. *J Anal At. Spectrom* (2012) 27:2066–75. doi:10.1039/c2ja30222e
20. Moros J, Laserna J. Laser-induced Breakdown Spectroscopy (LIBS) of Organic Compounds: A Review. *Appl Spectrosc* (2019) 73:963–1011. doi:10.1177/0003702819853252
21. Gottfried JL, De Lucia FC, Jr., Munson CA, Miziolek AW. Laser-induced Breakdown Spectroscopy for Detection of Explosives Residues: A Review of Recent Advances, Challenges, and Future Prospects. *Anal Bioanal Chem* (2009) 395:283–300. doi:10.1007/s00216-009-2802-0
22. Li B, Zhang D, Liu J, Tian Y, Gao Q, Li Z. A Review of Femtosecond Laser-Induced Emission Techniques for Combustion and Flow Field Diagnostics. *Appl Sci* (2019) 9:1906. doi:10.3390/app9091906
23. Mousavi SJ, Hemati Farsani M, Darbani SMR, Mousaviazar A, Soltanolkotabi M, Eslami Majd A. CN and C_2 Vibrational Spectra Analysis in Molecular LIBS of Organic Materials. *Appl Phys B* (2016) 122:106. doi:10.1007/s00340-016-6371-6
24. Harilal SS, Issac RC, Bindhu CV, Nampoori VPN, Vallabhan CPG. Spatial Analysis of Band Emission from Laser Produced Plasma. *Plasma Sourc Sci. Technol.* (1997) 6:317–22. doi:10.1088/0963-0252/6/3/008
25. Ghezelbash M, Majd AE, Darbani SMR, Mousavi SJ, Ghasemi A, Tehrani MK. Spatial Investigation of Plasma Emission from Laminar Diffusion Methanol, Ethanol, and N-Propanol Alcohol Flames Using LIBS Method. *Appl Phys B* (2017) 123:36. doi:10.1007/s00340-016-6615-5
26. Wilson WE. A Critical Review of the Gas-phase Reaction Kinetics of the Hydroxyl Radical. *J Phys Chem Reference Data* (1972) 1:535–73. doi:10.1063/1.3253102
27. Serrano J, Moros J, Laserna JJ. Exploring the Formation Routes of Diatomic Hydrogenated Radicals Using Femtosecond Laser-Induced Breakdown Spectroscopy of Deuterated Molecular Solids. *J Anal At. Spectrom* (2015) 30:2343–52. doi:10.1039/c5ja00192g
28. Wang Q, Chen A, Xu W, Zhang D, Wang Y, Li S, et al. Effect of Lens Focusing Distance on AlO Molecular Emission from Femtosecond Laser-Induced Aluminum Plasma in Air. *Opt Laser Tech* (2020) 122:105862. doi:10.1016/j.optlastec.2019.105862
29. Nagli L, Gaft M, Raichlin Y. Halogen Detection with Molecular Laser Induced Fluorescence. *Spectrochimica Acta Part B: At Spectrosc* (2020) 166:105813. doi:10.1016/j.sab.2020.105813
30. Fernández-Bravo Á, Delgado T, Lucena P, Laserna JJ. Vibrational Emission Analysis of the CN Molecules in Laser-Induced Breakdown Spectroscopy of Organic Compounds. *Spectrochimica Acta Part B: At Spectrosc* (2013) 89:77–83. doi:10.1016/j.sab.2013.08.004
31. Harilal SS, Brumfield BE, Cannon BD, Phillips MC. Shock Wave Mediated Plume Chemistry for Molecular Formation in Laser Ablation Plasmas. *Anal Chem* (2016) 88:2296–302. doi:10.1021/acs.analchem.5b04136
32. Zhao YL, Lai GD, Li GG, Shang YL, Shi JC. Identifying $C_2H_4N_4$ Structural Isomers Using Fs-Laser Induced Breakdown Spectroscopy. *Analyst* (2020) 145:7372–9. doi:10.1039/d0an01593h
33. Rao EN, Mathi P, Kalam SA, Sreedhar S, Singh AK, Jagatap BN, et al. Femtosecond and Nanosecond LIBS Studies of Nitroimidazoles: Correlation between Molecular Structure and LIBS Data. *J Anal At. Spectrom* (2016) 31:737–50. doi:10.1039/c5ja00445d
34. Dikmelik Y, McEnnis C, Spicer JB. Femtosecond and Nanosecond Laser-Induced Breakdown Spectroscopy of Trinitrotoluene. *Opt Express* (2008) 16:5332–7. doi:10.1364/oe.16.005332
35. Sunku S, Gundawar MK, Myakalwar AK, Kiran PP, Tewari SP, Rao SV. Femtosecond and Nanosecond Laser Induced Breakdown Spectroscopic Studies of NTO, HMX, and RDX. *Spectrochimica Acta Part B: At Spectrosc* (2013) 79-80:31–8. doi:10.1016/j.sab.2012.11.002
36. Serrano J, Moros J, Laserna JJ. Sensing Signatures Mediated by Chemical Structure of Molecular Solids in Laser-Induced Plasmas. *Anal Chem* (2015) 87:2794–801. doi:10.1021/acs.analchem.5b00212
37. Junjuri R, Gundawar MK. Femtosecond Laser-Induced Breakdown Spectroscopy Studies for the Identification of Plastics. *J Anal At. Spectrom* (2019) 34:1683–92. doi:10.1039/c9ja00102f
38. Harilal SS, Yeak J, Brumfield BE, Suter JD, Phillips MC. Dynamics of Molecular Emission Features from Nanosecond, Femtosecond Laser and Filament Ablation Plasmas. *J Anal At. Spectrom* (2016) 31:1192–7. doi:10.1039/c6ja00036c
39. De Lucia FC, Jr., Gottfried JL. Influence of Molecular Structure on the Laser-Induced Plasma Emission of the Explosive RDX and Organic Polymers. *J Phys Chem A* (2013) 117:9555–63. doi:10.1021/jp312236h
40. Shaik AK, Epuru NR, Syed H, Byram C, Soma VR. Femtosecond Laser Induced Breakdown Spectroscopy Based Standoff Detection of Explosives and Discrimination Using Principal Component Analysis. *Opt Express* (2018) 26:8069–83. doi:10.1364/OE.26.008069
41. Baudelet M, Boueri M, Yu J, Mao SS, Piscitelli V, Mao X, et al. Time-resolved Ultraviolet Laser-Induced Breakdown Spectroscopy for Organic Material Analysis. *Spectrochimica Acta Part B: At Spectrosc* (2007) 62:1329–34. doi:10.1016/j.sab.2007.10.043
42. Boueri M, Baudelet M, Yu J, Mao X, Mao SS, Russo R. Early Stage Expansion and Time-Resolved Spectral Emission of Laser-Induced Plasma from Polymer. *Appl Surf Sci* (2009) 255:9566–71. doi:10.1016/j.apsusc.2009.04.088
43. Camacho JJ, Diaz L, Martinez-Ramirez S, Caceres JO. Time- and Space-Resolved Spectroscopic Characterization of Laser-Induced Swine Muscle Tissue Plasma. *Spectrochimica Acta Part B: At Spectrosc* (2015) 111:92–101. doi:10.1016/j.sab.2015.07.008
44. Moncayo S, Marín-Roldán A, Manzoor S, Camacho JJ, Motto-Ros V, Caceres JO. Time-resolved Study of the Plasma Produced from Animal Muscle Tissue Using a Nd:YAG Laser. *J Anal At. Spectrom* (2018) 33:1884–91. doi:10.1039/c8ja00258d
45. Delgado T, García-Gómez L, Cabalín LM, Laserna JJ. Detectability and Discrimination of Biomarker Organic Precursors in a Low Pressure CO_2 Atmosphere by LIBS. *J Anal At. Spectrom* (2020) 35:1947–55. doi:10.1039/d0ja00167h
46. Barbier S, Perrier S, Freyermuth P, Perrin D, Gallard B, Gilon N. Plastic Identification Based on Molecular and Elemental Information from Laser Induced Breakdown Spectra: a Comparison of Plasma Conditions in View of Efficient Sorting. *Spectrochimica Acta Part B: At Spectrosc* (2013) 88:167–73. doi:10.1016/j.sab.2013.06.007
47. Delgado T, Vadillo JM, Laserna JJ. Primary and Recombined Emitting Species in Laser-Induced Plasmas of Organic Explosives in Controlled Atmospheres. *J Anal At. Spectrom* (2014) 29:1675–85. doi:10.1039/c4ja00157e
48. Rother A-S, Dietz T, Kohns P, Ankerhold G. Molecular Laser-Induced Breakdown Spectroscopy for Elemental Analysis. *Tm-Technisches Messen.* (2017) 84:23–31. doi:10.1515/teme-2016-0032
49. Zhu Z, Li J, Guo Y, Cheng X, Tang Y, Guo L, et al. Accuracy Improvement of boron by Molecular Emission with a Genetic Algorithm and Partial Least Squares Regression Model in Laser-Induced Breakdown Spectroscopy. *J Anal At. Spectrom* (2018) 33:205–9. doi:10.1039/c7ja00356k
50. Guo LB, Zhu ZH, Li JM, Tang Y, Tang SS, Hao ZQ, et al. Determination of boron with Molecular Emission Using Laser-Induced Breakdown Spectroscopy Combined with Laser-Induced Radical Fluorescence. *Opt Express* (2018) 26:2634–42. doi:10.1364/oe.26.002634
51. Zhang W, Zhou R, Liu K, Li Q, Tang Z, Zhu C, et al. Silicon Determination in Steel with Molecular Emission Using Laser-Induced Breakdown Spectroscopy Combined with Laser-Induced Molecular Fluorescence. *J Anal At. Spectrom* (2021) 36:375–9. doi:10.1039/d0ja00427h
52. Tian Y, Hou S, Wang L, Duan X, Xue B, Lu Y, et al. CaOH Molecular Emissions in Underwater Laser-Induced Breakdown Spectroscopy: Spatial-Temporal Characteristics and Analytical Performances. *Anal Chem* (2019) 91:13970–7. doi:10.1021/acs.analchem.9b03513
53. Choi S-U, Han S-C, Lee J-Y, Yun J-I. Isotope Analysis of Iron on Structural Materials of Nuclear Power Plants Using Double-Pulse Laser Ablation Molecular Isotopic Spectrometry. *J Anal At. Spectrom* (2021) 36:1287–96. doi:10.1039/d1ja00097g
54. Mao X, Bol'shakov AA, Perry DL, Sorkhabi O, Russo RE. Laser Ablation Molecular Isotopic Spectrometry: Parameter Influence on boron Isotope Measurements. *Spectrochimica Acta Part B: At Spectrosc* (2011) 66:604–9. doi:10.1016/j.sab.2011.06.007
55. Russo RE, Bol'shakov AA, Mao X, McKay CP, Perry DL, Sorkhabi O. Laser Ablation Molecular Isotopic Spectrometry. *Spectrochimica Acta Part B: At Spectrosc* (2011) 66:99–104. doi:10.1016/j.sab.2011.01.007

56. Mao X, Bol'shakov AA, Choi I, McKay CP, Perry DL, Sorkhabi O, et al. Laser Ablation Molecular Isotopic Spectrometry: Strontium and its Isotopes. *Spectrochimica Acta Part B: At Spectrosc* (2011) 66:767–75. doi:10.1016/j.sab.2011.12.002
57. Chirinos J, Spiliotis A, Mao X, Chan GC-Y, Russo RE, Zorba V. Remote Isotope Detection and Quantification Using Femtosecond Filament-Laser Ablation Molecular Isotopic Spectrometry. *Spectrochimica Acta Part B: At Spectrosc* (2021) 179:106117. doi:10.1016/j.sab.2021.106117
58. Brown S, Ford A, Akpovo CA, Johnson L. Mid-IR Enhanced Laser Ablation Molecular Isotopic Spectrometry. *Spectrochimica Acta Part B: At Spectrosc* (2016) 122:178–87. doi:10.1016/j.sab.2016.07.005
59. Akpovo CA, Helms L, Profeta LTM, Johnson L. Multivariate Determination of 10B Isotopic Ratio by Laser-Induced Breakdown Spectroscopy Using Multiple BO Molecular Emissions. *Spectrochimica Acta Part B: At Spectrosc* (2019) 162:105710. doi:10.1016/j.sab.2019.105710
60. Dietz T, Klose J, Kohns P, Ankerhold G. Quantitative Determination of Chlorides by Molecular Laser-Induced Breakdown Spectroscopy. *Spectrochimica Acta Part B: At Spectrosc* (2019) 152:59–67. doi:10.1016/j.sab.2018.12.009
61. Álvarez C, Pisonero J, Bordel N. Quantification of Fluorite Mass-Content in Powdered Ores Using a Laser-Induced Breakdown Spectroscopy Method Based on the Detection of Minor Elements and CaF Molecular Bands. *Spectrochimica Acta Part B: At Spectrosc* (2014) 100:123–8. doi:10.1016/j.sab.2014.07.024
62. Alvarez-Llamas C, Pisonero J, Bordel N. Quantification of Fluorine Traces in Solid Samples Using CaF Molecular Emission Bands in Atmospheric Air Laser-Induced Breakdown Spectroscopy. *Spectrochimica Acta Part B: At Spectrosc* (2016) 123:157–62. doi:10.1016/j.sab.2016.08.006
63. Alvarez-Llamas C, Pisonero J, Bordel N. A Novel Approach for Quantitative LIBS Fluorine Analysis Using CaF Emission in Calcium-free Samples. *J Anal At. Spectrom* (2017) 32:162–6. doi:10.1039/c6ja00386a
64. Tang Z, Zhou R, Hao Z, Zhang W, Li Q, Zeng Q, et al. Determination of Fluorine in Copper Ore Using Laser-Induced Breakdown Spectroscopy Assisted by the SrF Molecular Emission Band. *J Anal At. Spectrom* (2020) 35:754–61. doi:10.1039/c9ja00407f
65. Tang Z, Hao Z, Zhou R, Li Q, Liu K, Zhang W, et al. Sensitive Analysis of Fluorine and Chlorine Elements in Water Solution Using Laser-Induced Breakdown Spectroscopy Assisted with Molecular Synthesis. *Talanta* (2021) 224:121784. doi:10.1016/j.talanta.2020.121784
66. Gaft M, Nagli L, Raichlin Y, Pelascini F, Panzer G, Ros VM. Laser-induced Breakdown Spectroscopy of Br and I Molecules with Alkali-Earth Elements. *Spectrochimica Acta Part B: At Spectrosc* (2019) 157:47–52. doi:10.1016/j.sab.2019.05.003
67. De Lucia FC, Harmon RS, McNesby KL, Winkel RJ, Miziolek AW. Laser-induced Breakdown Spectroscopy Analysis of Energetic Materials. *Appl Opt* (2003) 42:6148–52. doi:10.1364/ao.42.006148
68. López-Moreno C, Palanco S, Javier Laserna J, DeLucia Jr F, Miziolek AW, Rose J, et al. Test of a Stand-Off Laser-Induced Breakdown Spectroscopy Sensor for the Detection of Explosive Residues on Solid Surfaces. *J Anal At. Spectrom* (2006) 21:55–60. doi:10.1039/b508055j
69. De Lucia FC, Jr., Gottfried JL, Munson CA, Miziolek AW. Double Pulse Laser-Induced Breakdown Spectroscopy of Explosives: Initial Study towards Improved Discrimination. *Spectrochimica Acta Part B: At Spectrosc* (2007) 62:1399–404. doi:10.1016/j.sab.2007.10.036
70. De Lucia, Jr. FC, Jr., Gottfried JL, Munson CA, Miziolek AW. Multivariate Analysis of Standoff Laser-Induced Breakdown Spectroscopy Spectra for Classification of Explosive-Containing Residues. *Appl Opt* (2008) 47:G112–G121. doi:10.1364/ao.47.00g112
71. Moros J, Serrano J, Sánchez C, Macías J, Laserna JJ. New Chemometrics in Laser-Induced Breakdown Spectroscopy for Recognizing Explosive Residues. *J Anal At. Spectrom* (2012) 27:2111–22. doi:10.1039/c2ja30230f
72. Yang CS-C, Jin F, Trivedi SB, Brown EE, Hommerich U, Tripathi A, et al. Long-wave Infrared (LWIR) Molecular Laser-Induced Breakdown Spectroscopy (LIBS) Emissions of Thin Solid Explosive Powder Films Deposited on Aluminum Substrates. *Appl Spectrosc* (2017) 71:728–34. doi:10.1177/0003702817696089
73. Farhadian AH, Tehrani MK, Keshavarz MH, Karimi M, Darbani SMR, Rezayi AH. A Novel Approach for Investigation of Chemical Aging in Composite Propellants through Laser-Induced Breakdown Spectroscopy (LIBS). *J Therm Anal Calorim* (2015) 124:279–86. doi:10.1007/s10973-015-5116-9
74. Farhadian AH, Tehrani MK, Keshavarz MH, Karimi M, Reza Darbani SM. Relationship between the Results of Laser-Induced Breakdown Spectroscopy and Dynamical Mechanical Analysis in Composite Solid Propellants during Their Aging. *Appl Opt* (2016) 55:4362–9. doi:10.1364/ao.55.004362
75. El-Hussein A, Marzouk A, Harith MA. Discriminating Crude Oil Grades Using Laser-Induced Breakdown Spectroscopy. *Spectrochimica Acta Part B: At Spectrosc* (2015) 113:93–9. doi:10.1016/j.sab.2015.09.002
76. Anzano J, Lasheras R-J, Bonilla B, Casas J. Classification of Polymers by Determining of C1:C2:CN:H:N:O Ratios by Laser-Induced Plasma Spectroscopy (LIPS). *Polym Test* (2008) 27:705–10. doi:10.1016/j.polymertesting.2008.05.012
77. Costa VC, Aquino FWB, Paranhos CM, Pereira-Filho ER. Identification and Classification of Polymer E-Waste Using Laser-Induced Breakdown Spectroscopy (LIBS) and Chemometric Tools. *Polym Test* (2017) 59:390–5. doi:10.1016/j.polymertesting.2017.02.017
78. Banaee M, Tavassoli SH. Discrimination of Polymers by Laser Induced Breakdown Spectroscopy Together with the DFA Method. *Polym Test* (2012) 31:759–64. doi:10.1016/j.polymertesting.2012.04.010
79. Gottfried JL. Discrimination of Biological and Chemical Threat Simulants in Residue Mixtures on Multiple Substrates. *Anal Bioanal Chem* (2011) 400:3289–301. doi:10.1007/s00216-011-4746-4
80. Baudelet M, Guyon L, Yu J, Wolf J-P, Amodeo T, Fréjafon E, et al. Spectral Signature of Native CN Bonds for Bacterium Detection and Identification Using Femtosecond Laser-Induced Breakdown Spectroscopy. *Appl Phys Lett* (2006) 88:063901. doi:10.1063/1.2170437
81. Baudelet M, Guyon L, Yu J, Wolf J-P, Amodeo T, Fréjafon E, et al. Femtosecond Time-Resolved Laser-Induced Breakdown Spectroscopy for Detection and Identification of Bacteria: A Comparison to the Nanosecond Regime. *J Appl Phys* (2006) 99:084701. doi:10.1063/1.2187107
82. Yang CSC, Jin F, Swaminathan SR, Patel S, Ramer ED, Trivedi SB, et al. Comprehensive Study of Solid Pharmaceutical Tablets in Visible, Near Infrared (NIR), and Longwave Infrared (LWIR) Spectral Regions Using a Rapid Simultaneous Ultraviolet/visible/NIR (UVN) + LWIR Laser-Induced Breakdown Spectroscopy Linear Arrays Detection System and a Fast Acousto-Optic Tunable Filter NIR Spectrometer. *Opt Express* (2017) 25:26885–97. doi:10.1364/oe.25.026885
83. Kotzagianni M, Kakkava E, Couris S. Laser-induced Breakdown Spectroscopy (LIBS) for the Measurement of Spatial Structures and Fuel Distribution in Flames. *Appl Spectrosc* (2016) 70:627–34. doi:10.1177/0003702816631296
84. Li S, Li Y, Shi Z, Sui L, Li H, Li Q, et al. Fluorescence Emission Induced by the Femtosecond Filament Transmitting through the Butane/air Flame. *Spectrochimica Acta A: Mol Biomol Spectrosc* (2018) 189:32–6. doi:10.1016/j.saa.2017.08.006
85. Kalam SA, Murthy NL, Mathi P, Kommu N, Singh AK, Rao SV. Correlation of Molecular, Atomic Emissions with Detonation Parameters in Femtosecond and Nanosecond LIBS Plasma of High Energy Materials. *J Anal At. Spectrom* (2017) 32:1535–46. doi:10.1039/c7ja00136c
86. Gottfried JL. Laser-induced Plasma Chemistry of the Explosive RDX with Various Metallic Nanoparticles. *Appl Opt* (2012) 51:B13–B21. doi:10.1364/Ao.51.000b13

Conflict of Interest: The authors declare that the research was conducted in the absence of any commercial or financial relationships that could be construed as a potential conflict of interest.

frontiers in Physics

ORIGINAL RESEARCH
published: 31 January 2022
doi: 10.3389/fphy.2021.815343

A Comprehensive Comparison and Analysis of Several Intensity Modulations Based on the Underwater Photon-Counting Communication System

Xiaotian Han[1,2], Peng Li[1], Chang Chang[1], Duorui Gao[1], Dongquan Zhang[1], Peixuan Liao[1], Wei Wang[1] and Xiaoping Xie[1,2]**

[1]State Key Laboratory of Transient Optics and Photonics, Xi'an Insitute of Optics and Precision Mechanics, Chinese Academy of Science, Xi'an, China, [2]School of Future Technology, University of Chinese Academy of Science, Beijing, China

Underwater wireless optical communication is facing absorption, scattering problems, which, in principle, can be greatly resolved by underwater photon-counting communication (UPCC) technology that exhibits high-sensitivity communication characteristics in long-range underwater wireless optical communication. Recent studies on UPCC are mainly focused on a single intensity modulation such as on–off keying (OOK) and pulse position modulation (PPM) technologies, and the comprehensive analysis of communication performance combing OOK modulation and digital pulse modulations remains a lack. To this, by using a UPCC system based on a single-photon avalanche diode, we reveal the communication performances of OOK, PPM, differential pulse interval modulation (DPIM), differential pulse position modulation (DPPM), and dual-header pulse interval modulation, and find that (1) the PPM has the longest transmission distance at the same bit error ratio when $M > 2$, but the lowest communication rate under identical modulation bandwidth and average transmit power; and (2) the DPPM and DPIM perform the optimum communication performance at the fixed communication rate when $M = 8$. We thus conclude that the DPPM and DPIM have advantages of low modulation bandwidth and long time slot time compared with PPM, indicating the significance of reducing the difficulty of signal synchronization and the complexity of the underwater photon-counting system accordingly.

Keywords: underwater wireless optical communication (UWOC), intensity modulation (IM), direct detection (DD), digital pulse modulation, photon counting, channel model

OPEN ACCESS

Edited by:
Yufei Ma,
Harbin Institute of Technology, China

Reviewed by:
Heping Zeng,
East China Normal University, China
Shuangyi Yan,
University of Bristol, United Kingdom

****Correspondence:***
Wei Wang
wangwei2012@opt.ac.cn
Xiaoping Xie
xxp@opt.ac.cn

Specialty section:
This article was submitted to Optics and Photonics, a section of the journal Frontiers in Physics

Received: *15 November 2021*
Accepted: *14 December 2021*
Published: *31 January 2022*

Citation:
Han X, Li P, Chang C, Gao D, Zhang D, Liao P, Wang W and Xie X (2022) A Comprehensive Comparison and Analysis of Several Intensity Modulations Based on the Underwater Photon-Counting Communication System. Front. Phys. 9:815343. doi: 10.3389/fphy.2021.815343

INTRODUCTION

Lasers, since their invention, have been widely used in the fields of sensing [1], communication [2], and measurement [3] because of their special characteristics such as high directionality, high brightness, monochromaticity, and good coherence. Especially in recent years, with the increase in comprehensive ocean observations in scientific, industrial, and military activities, building efficient, flexible, and reliable marine environmental sensing networks is becoming urgent and important [4].

In fact, any sensors need to be linked to each other in some way of communication, so there is great interest around how to communicate between marine mobile sensing devices in a high-speed and reliable way [5]. For underwater wireless communication, the existing communication methods mainly include hydroacoustic communication, microwave communication, optical communication, and so on [6]. Underwater wireless optical communication (UWOC) is a technology that uses the blue/green light in the visible spectrum as the information carrier for signal transmission in water [7] and has the advantages of high data transmission rate, low latency, high bandwidth, low power consumption, and so on, compared with the hydroacoustic communication and microwave communication [8]. However, achieving long-range, high-speed underwater wireless optical transmission still faces challenges due to the existence of severe water attenuation and the bandwidth limitations of blue–green wavelength devices [9]. This makes high-speed signal modulation and demodulation techniques and high-sensitivity reception techniques an important research topic in the field of UWOC. Currently, the main modulation methods include intensity modulation (IM) [10], nonlinear frequency conversion [11], subcarrier modulation [12], higher-order modulation, signal multiplexing [13], and so on. The nonlinear frequency conversion technique can generate high-speed blue–green light signals with the help of mature 1,064-nm high-power devices, but the coherence of the optical signal is demanded in the frequency doubling process that high-energy consumption is needed because of the low electro-optical conversion efficiency. Although subcarrier modulation, higher-order modulation, and signal multiplexing techniques can significantly increase the data transmission rate of the system, they require high water quality and system stability and are applicable only to the laboratory technology research stage; the adaptability of these modulation techniques to the underwater channel needs further verification. In practical engineering applications, the IM techniques represented by on–off keying (OOK) are still the preferred choice. However, the high requirements for transmitting optical power for long-range underwater communications make OOK modulation unsuitable for applications on energy-limited underwater platforms. Thus, it is necessary to study the channel suitability of IM techniques with high-power utilization efficiency for underwater channels.

High-energy utilization modulation technologies represented by pulse position modulation (PPM) and high-sensitivity reception technology represented by photon-counting have become hot topics to improve power efficiency and achieve long-distance transmission. Theoretically, Hiskett et al. [14] first proposed to apply the photon-counting reception technology into underwater communication. Mao et al. [15] formulated the output characteristics of the single-photon avalanche diode (SPAD) as an ideal Poisson model and investigated the communication performance of long-range underwater photon-counting communication (UPCC) system applied with OOK modulation. Wang [16] established a long-distance underwater visible light communication system with a two-term exponential channel model and a SPAD receiver, and the arrived link distance in pure seawater can be extended to 500 m by proposing the SPAD detection algorithm. Sarbazi et al. [17] investigated the bit error performance of the receiver based on SPAD array with OOK modulation in various array sizes, dead time, and background count rate. Experimentally, Rao et al. [18] demonstrated a multirate UPCC system at data rates up to 10.416 Mbps over a 9.1-m tap water channel. Hu et al. [19] achieved a PMT-based UPCC system using a 256-PPM; the length of channel and communication sensitivity are 120 m and 3.32 bits/photon in Jerlov II water. Chen et al. [20] used a 520-nm laser diode modulation to generate the OOK signal, whereas a high-sensitivity silicon photomultiplier was used at the receiver side to achieve an attenuation length of more than 14 at a communication rate of 20 Mbps.

By and large, in the reported research articles about UPCC systems, the research and analysis are based on a single IM such as OOK or PPM. It is well known that the OOK is one of the simplest IM techniques with high bandwidth utilization, but low power utilization makes the signal transmission distance limited. For PPM, the high-power utilization makes the signal transmission distance much higher, but low bandwidth utilization leads to a short bit duration, making it difficult for signal synchronization. Furthermore, digital pulse modulation techniques including differential pulse position modulation (DPPM), differential pulse interval modulation (DPIM), and dual-header pulse interval modulation (DH-PIM), combining both bandwidth utilization and power utilization, are expected to be a good alternative modulation technique for UPCC system in some application scenarios. Therefore, a comparative analysis of the communication performance of OOK modulation and various digital pulse modulations is not only important for optimizing the performance of the UPCC system, but also an important guide for the design of communication systems. Of course, as far as modulations are concerned, similar comparisons have been made by numerous researchers, but mostly based on positive–intrinsic–negative (PIN) and avalanche photodiode (APD) receivers. However, single-photon detector-based receivers differ from conventional PIN and APD-based receivers in terms of the statistical model of the signal output [21]. Therefore, it is significant to compare the performance of multiple IM schemes based on the photon counting receiver model.

In this article, an underwater photon counting system is built based on IM and direct detection (IM/DD) photon counting reception technique. First, this article introduces the bit-symbol mapping principles of OOK, PPM, DPPM, DPIM, and DH-PIM; the seawater channel model; the statistical model of the output of the SPAD under the influence of dead time; and the minimum error judgment criterion to obtain the expressions for the bit error ratio (BER) calculation. Second, the performance parameters of a commonly used UWOC system and a commercially available SPAD detector are selected to analyze and compare the communication performance of different IM methods in a pure seawater channel. For one thing, the article compares the variation of BER with a transmission distance of communication system for different modulation schemes when modulation bandwidth is fixed. For another thing, the same analysis is done under a fixed communication rate. Finally, the simulation results are shown and discussed.

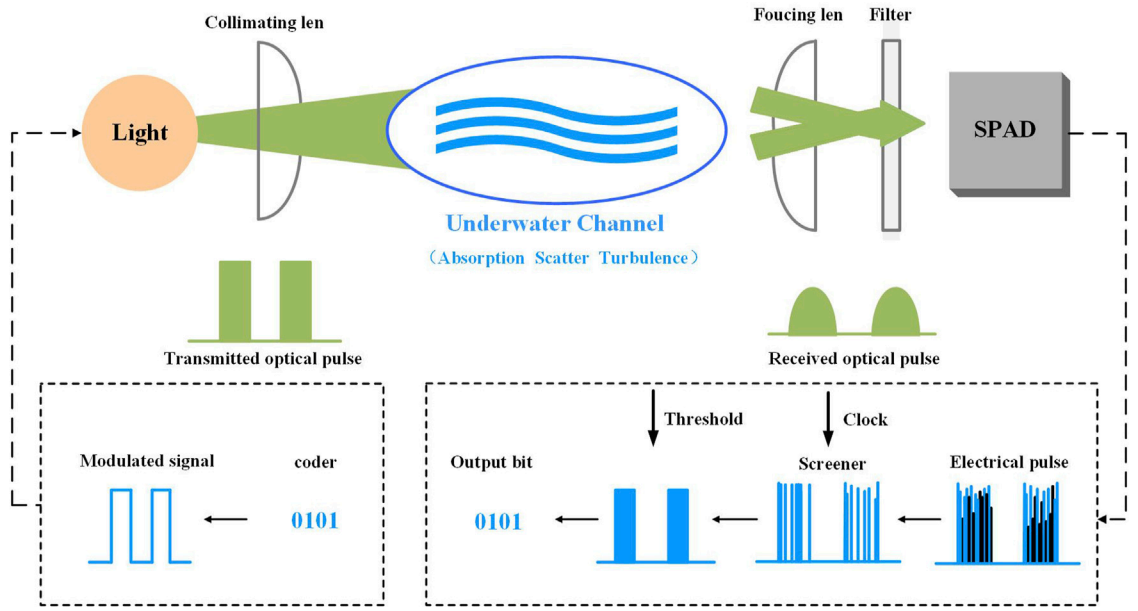

FIGURE 1 | The conceptual diagram of underwater photon-counting communication (UPCC) system. The system consists of two parts: intensity modulation and direct detection photon-counting receiver. The information bits are encoded and modulated into an optical signal; the optical signal is transmitted through the underwater channel, and only a few photons are received. The photons are then received by a single-photon avalanche diode (SPAD) and converted into electrical pulses that are synchronized, counted, and demodulated to recover the original bits.

UPCC SYSTEM MODELING

The system architecture of UPCC, as shown in **Figure 1**, is composed of two parts: IM and DD photon-counting receiver. As demonstrated in **Figure 1**, the source bit is encoded and modulated into the optical carrier; the optical signal is transmitted through the underwater channel and degraded by the absorption, scattering, and turbulence effects of the medium. At the receiver, the photon-counting receiver that uses a SPAD working in counting mode is used to receive and process single-photon signals. When the receiver works, the SPAD detects the weak photon signal to generate a single electrical pulse signal, and a large number of noise pulses are introduced due to SPAD dark counts and background noise. For these reasons, a screener is used to extract useful information by rejecting noisy count pulses regarding the synchronous clock. Finally, the count module counts the signal pulses within a certain period, and counted signal pulses are used to restore the initial code stream signal by comparing it with the threshold value. In addition, to increase the reliability of data transmission, communication systems often use channel coding and equalization, and so on. It should be noted that it is assumed that the UPCC system has been clock synchronized at both the transceiver side in this study.

The Modulation Schemes for OOK and Digital Pulse Modulations

In the UPCC system with IM/DD, OOK and PPM are the commonly used IM schemes. Compared with OOK modulation, PPM has higher power utilization efficiency but lower bandwidth utilization [22], which is often used in photon-counting communication systems to improve sensitivity. To optimize the bandwidth utilization of PPM, many digital pulse modulation schemes have been developed, such as DPPM, DPIM, DPIM, and DH-PIM. OOK modulation uses one optical pulse to represent a 1-bit signal, whereas digital pulse modulations decompose a signal symbol into multiple time slots; the position of the optical pulse within a symbol is used to represent multiple bits, with the remaining slots being empty. DPPM removes the redundant time slots that exist in PPM. For DPIM, each symbol begins with a slot-duration pulse, followed by a series of empty data slots, the number of which depends on the decimal value of the encoded M-bit data stream. To mitigate intersymbol interference degradation of the signal, a guard slot consisting of one or more empty slots is added after the pulse. Compared with PPM, DPPM, and DPIM, DH-PIM not only removes the redundant time slots that follow the pulse in the PPM and but also reduces the average symbol length compared with DPIM. The time-domain waveforms of OOK and several digital pulse modulation schemes are shown in **Figure 2** [23]. As shown in the figure, to have the same data throughout as OOK, the slot duration time T_s of digital pulse modulation is shorter than the OOK bit duration time T_b.

For IMs, the digital signal is loaded into the carrier wave by modulating the intensity and position of a light wave. The biggest difference between these modulations is the number of slots in a single symbol, which influences directly the transmit optical power per ON slot. The more slots, the higher transmit optical power per ON slot when the average optical transmit power keeps fixed; the relation between the mean transmit power

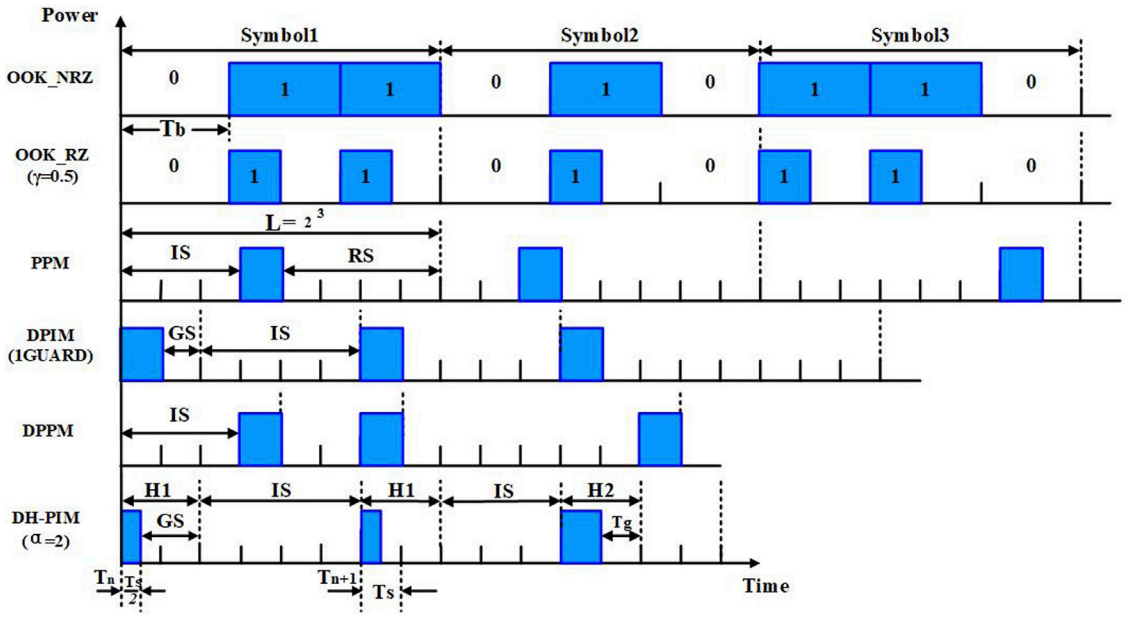

FIGURE 2 | Time waveforms for OOK, DPIM, PPM, DPIM, DPPM, DH_PIM (α = 2). NRZ non–return-to-zero, RZ return-to-zero, IS information slots, RS redundant slots, GS guard slots; the time-domain waveform reflects the bit mapping relationships for the several intensity modulations. The presence or absence of an optical pulse is used to represent 1 bit of data in OOK modulation, and the duration time of the optical pulse is equal to 1-bit duration, whereas the duration of the optical pulse of OOK-RZ modulation is less than the duration of a single bit. When the duty ratio is 0.5, the light pulse duration of OOK-RZ modulation is half of the single bit duration. For PPM, The slot position of the optical pulse, corresponding to the decimal value of the M-bit input data, represents the information bit. DPIM and DPIM remove the redundant time slot after the optical pulse compared with PPM, whereas DH-PIM not only removes the redundant time slot after the PPM optical pulse but also reduces the number of time slots within a single symbol compared with DPIM.

TABLE 1 | The modulation orders and the communication rates for different modulation schemes under a given B and M [23].

Modulation schemes	Modulation order (L or $\bar{L}$)	Rates (R_b)
PPM	2^M	$MB/2^M$
DPIM(1GUARD)	$(2^M + 3)/2$	$2MB/(2^M + 3)$
DPPM	$(2^M + 1)/2$	$2MB/(2^M + 1)$
DH-PIM	$(2^{M-1} + 2\alpha + 1)/2$	$2MB/(2^{M-1} + 2\alpha + 1)$

per symbol and optical power per ON slot can be expressed as $P_{ON} = LP_{average}$, where $P_{average}$ is the average optical of a symbol, and L is the length of a single symbol or usually named the modulation order. For OOK_NRZ and OOK_RZ, L is equal to 2 and 4, respectively. For the PPM, $L = 2^M$ [24]. For DPPM, DPIM, and DH-PIM, different symbols have different numbers of time slots, so the symbol length is represented by the average symbol length, and the average symbol length $\bar{L}$ can be found in [23]. The modulation orders and the communication rates for different modulation schemes under a given modulation bandwidth ($B = 1/T_s$) are listed in **Table 1**.

Underwater Channel Model

The absorption and scattering of the light by the seawater will cause the attenuation of the energy of the optical signal, especially when the turbidity of seawater is high; the signal quality will also deteriorate. The extinction coefficient $c(\lambda)$ of seawater on light, which is determined by the absorption coefficient $a(\lambda)$ and scattering coefficient $b(\lambda)$ of seawater, can be expressed by the formula [25]:

$$c(\lambda) = a(\lambda) + b(\lambda) \tag{1}$$

In the formula, the units of the three parameters are m^{-1}. The energy loss factor $L(\lambda, z)$, decided by the light beam transmission distance z (m) and the wavelength λ (nm) of light, can be given by the following equation [26].

$$L(\lambda, z) = e^{c(\lambda)z} \tag{2}$$

The coefficients $a(\lambda)$, $b(\lambda)$, and $c(\lambda)$ for Petzold seawater types are presented in **Table 2** at the wavelength of 532 nm, which are taken from [27].

Many channel models of UWOC can be obtained from [25, 28–31]. When an optical beam is transmitting in the pure seawater and clear seawater, the temporal spread of the optical pulse can be neglected. Geometric Beer's Law (GBL) can be applied to these two water types to calculate the geometric attenuation since the beam spreading and alignment error [32]. In this article, we consider the line-of-sight communication link model. In this scenario, the light beam is directed from a transmitter into a receiver; both telescope gain and loss are taken into account, the optical signal reaching the receiver is obtained by [25]:

TABLE 2 | Absorption, scattering, and extinction coefficient for the Pure seawater and three Petzold water types.

Water type	Pure seawater	Clear seawater	Coastal seawater	Harbor seater
a (m^{-1})	0.0405	0.114	0.179	0.266
b (m^{-1})	0.0025	0.037	0.219	1.824
c (m^{-1})	0.043	0.151	0.298	2.190

$$P_R = \begin{cases} P_{ON}\eta_T\eta_R L\left(\lambda, \frac{d}{\cos\theta}\right) \frac{A_{Rec}\cos\theta}{2\pi d^2(1-\cos\theta_0)} & \theta_0 \\ P_{ON}\eta_T\eta_R L\left(\lambda, \frac{d}{\cos\theta}\right) \frac{A_{Rec}\cos\theta}{\pi(d\tan\theta_0)^2} & \theta_0 \ll \pi/20 \end{cases} \tag{3}$$

where P_{ON} is the transmitted-light power per slot, η_T is the optical efficiency of the transmitter, η_R is the efficiency of the receiver, d is the perpendicular distance between the transmitter and receiver plane, and θ is the angle between the perpendicular to the receiver plane and the transmitter-receiver trajectory, also known as the angle of inclination between transmitter and receiver. A_{Rec} is the receiver aperture area, and θ_0 is the optical beam divergence angle (half-angle transmit beam width) [25].

Underwater Turbulence Model

In the practical application of UWOC, considering aperture average effect, received optical power under the influence of underwater optical turbulence can be represented by log-normal distribution from weak to strong turbulence condition, which has been validated by a large number of field experiments. The probability density function (PDF) $f(I)$ for the underwater channel can be expressed by the log-normal function [33]:

$$f(I) = \frac{1}{P\sigma\sqrt{2\pi}}\exp\left(-\frac{\left(\ln(I/I_0)+\sigma^2/2\right)^2}{2\sigma^2}\right) \tag{4}$$

where I_0 is the mean received light energy in the time interval $[0, T_s]$. For plane-wave, the scintillation index (S.I), σ, can be expressed as [34]:

$$\sigma^2 = \exp\left(\frac{0.49\sigma_r^2}{\left(1+1.11\sigma_r^{12/5}\right)^{7/6}} + \frac{0.51\sigma_r^2}{\left(1+0.69\sigma_r^{12/5}\right)^{5/6}}\right) - 1 \tag{5}$$

where σ_r^2 is the Rytov variance; the classical Kolmogorov spectrum model can be given [35]:

$$\sigma_r^2 = 44.76\varepsilon^{2/3}\overline{\left(\frac{\partial T}{\partial z}\right)^2}\left(\frac{2\pi}{\lambda_{light}}\right)^{7/6} z^{11/6} N^{-1} \tag{6}$$

where ε is the turbulence kinetic energy dissipation rate, $\partial T/\partial z$ is the temperature gradient, λ_{light} is the optical wavelength, z is the transmitting distance of the light beam, and N represents the buoyancy frequency.

SPAD Photon-Counting Receiver Model

When the UWOC works, assume the average signal photon rate reaching the front end of the detector is the constant λ_s, the average background photon-counting rate is the constant λ_b, and the dark count rate of SPAD is the constant λ_d. Of course, the other parameters including afterpulsing and timing-jitter, crosstalk, and fill-factor should also be considered, but in this article, we neglect these influences. Thus, the SPAD's photoelectron count model can be given:

$$\lambda = \begin{cases} \eta\lambda_s + \eta\lambda_b + \lambda_d & \text{signal} \\ \eta\lambda_b + \lambda_d & \text{no}-\text{signal} \end{cases} \tag{7}$$

where η is the photon detection efficiency of SPAD, the average photon arrival rate λ_s, and λ_b is related to the received optical power P_R of signal and background P_b; the relational expression is given as:

$$\lambda_s = \frac{\eta P_R}{h\nu} \tag{8}$$

$$\lambda_b = \frac{\eta P_b}{h\nu} \tag{9}$$

where h is the Planck constant, and ν is the frequency of the single photon.

We assume the sampling rate of SPAD is very high compared with the dead time so that the counting losses due to finite sampling rate can be negligible. If the dead time of SPAD is the constant τ, the maximum number of photons recorded by SPAD during the slot interval time $[0, T_s]$ can be expressed as $k_{max} = [T_s/\tau] + 1$, where $[x]$ is the maximum that is smaller than x. The PDF of counting k photons in a timing period $[0, T_s]$ is given [36]:

$$p(k,\lambda,T_s) = \begin{cases} \frac{\lambda^i(T_s-(k+1)\tau)^i}{i!}\exp(-\lambda(T_s-(k+1)\tau)) & \\ \quad -\sum_{i=0}^{k-1}\frac{\lambda^i(T_s-k\tau)^i}{i!}\exp(-\lambda(T_s-k\tau)), & k < k_{max} \\ 0, & k \geq k_{max} \end{cases} \tag{10}$$

Bit Error Ratio Calculation

For OOK modulation, based on the principle of threshold test, the bit error ratio (BER) can be given as [37]:

$$P_{OOK} = \frac{1}{2} - \frac{1}{2}\sum_{k=0}^{k_{th}}\left[\int_0^{\infty} p(k,\lambda_{sn},T_s)f(I)dI - p(k,\lambda_n,T_s)\right] \tag{11}$$

where k_{th} is the optimum decision threshold of the number of photons in the interval time $[0, T_s]$, which can be obtained by the following decision principle of the threshold.

For PPM, DPIM, DMMP, and DH-PIM symbol, the symbol error ratio (SER) for a continuous output L-order digital pulse modulation signal is [38] :

$$P_{SER} = 1 - \left[1 - \frac{1}{L}\sum_{k=0}^{k_{th}}\int_{0}^{\infty} p(m, \lambda_{sn}, T_s) f(I) dI - \frac{L-1}{L}\sum_{k=k_{th}}^{\infty} p(k, \lambda_n, T_s)\right]^L \quad (12)$$

The SER can be converted into BER by:

$$P_{BER} = \frac{LP_{SER}}{2(L-1)}$$

Based on the principle of minimum error probability [39], by solving the following **Eq. 13**, we can get the optimum threshold k_{th}.

$$\frac{\int_0^{\infty} p(k, \lambda_{sn}, T_s) f(I) dI}{p(k, \lambda_n, T_s)} = \frac{P(0)}{P(1)} \quad (13)$$

where $P(0)$ and $P(1)$ are a prior probability of time slot detection.

NUMERICAL RESULTS AND DISCUSSION

In this research, with the assumption of negligible delay spread, based on the GBL model and SPAD photon-counting receiver model, we establish the relationship between the BER and attenuation length on the underwater wireless UPCC system in the pure seawater. The effect of M on various IM schemes is also investigated. The parameters of the UWOC system are listed in **Table 3**. In the following discussion, the specifications of the SPCM20A from Thorlabs [40] have been applied to this simulation. The values of other parameters characterize the classical channel of the UWOC system. According to [41], the attenuation length, which is defined as the multiple of the transmission distance and attenuation coefficient, is used to represent the link transmission distance to remove the ambiguity of distance and various water conditions. In addition, with the assumption of negligible slot time delay spread, the degradation of signal bandwidth and the intersymbol caused by channel transmission can be ignored. Therefore, the mathematical relationship between data rate and modulation bandwidth in **Table 1** [23] can be used in this article.

On the one hand, BERs for OOK, PPM, DPIM, DPPM, and DH-PIM as the function of attenuation length when $T_s = 15\tau$ (modulation bandwidth $B = 1.9$ Mbps) are given in **Figure 3**. The forward-error-correction (FEC) limit of 3.8×10^{-3}, a commonly used BER at some of the reported UWOC systems [42–44], and some FEC codes providing reliable communication with an overhead of approximately 7% [45], is regarded as a criterion for evaluation in this article. As shown in **Figure 3**, BERs of all modulation schemes rise with the increment of attenuation length. At the FEC limit, the OOK system can arrive the maximum attenuation length for $M = 2$, and the attenuation length that the DH_PIM system can achieve its minimum. For the fixed modulation bandwidth and average transmit power, to achieve the same BER, the UPCC system for all digital pulse modulation schemes transmits over a shorter distance than the OOK_RZ modulation system when $M = 2$. The longer the transmission distance, the higher the power utilization is. Thus, the DPIM with a guard slot has higher power utilization than DPPM, and the power utilization of PPM is the highest. As bit resolution improves, when $M = 4, 6, 8$, the power utilizations of DH-PIM ($\alpha \leq 4$), DPPM, DPIM (1GUARD), and PPM have higher power utilization than OOK modulation, and the power utilization of DPPM and DPIM(1GUARD) tends to keep consistent. When the modulation bandwidth and average transmit power are certain, it should be noted that the communication distance that can be achieved by OOK modulation at a given BER does not change with M.

TABLE 3 | Parameters of UPCC system.

Parameter	Symbol	Value
The wavelength of lighter (nm)	λ	532
Extinction coefficient (m^{-1})	c	0.045
Divergence angle (rad)	λ_0	0.1745
Average transmit power (W)	P_T	1.0
Transmitter inclination angle (rad)	θ	0
Photon efficiency of the transmitter	η_T	0.9
The optical efficiency of the receiver	η_R	0.9
Receiver aperture (mm)	D	350
Photon detection effeciency@532 nm	η	35%
Deadtime (ns)	τ	35
Dark count rate (counts/sec)	λ_d	60
Background photon count (counts/slot)	λ_b	0.01
Average turbulence kinetic energy (m^2s^{-3})	ε	3×10^{-10}
temperature gradient (°C m^{-1})	$\partial T/\partial z$	7.94×10^{-6}
Average buoyancy frequency(s^{-1})	$\langle N \rangle$	2.9×10^{-4}

DH-PIM is one of the digital pulse modulations. Compared with PPM and PIM, DH_PIM not only removes the redundant time slots that follow the pulse in the PPM but also reduces the average symbol length compared with PIM [46]. In DH-PIM, the nth symbol starts with a header duration and follows with a sequence of d_n empty slots, the header duration consists of a header pulse H_n and a guard band G_n, and the value of d_n is the decimal value of modulated binary codeword within a symbol. If the value of $d_n \in \{0, 1, \cdots, 2^{M-1}\}$, H_1 will be as header pulse; otherwise, the header pulse will be H_1. The duration time of the header H_1 and H_2 is $0.5\alpha T_s$ and αT_s, respectively; each header pulse is followed by a guard band $G_n \in \{(0.5\alpha + 1)T_s, T_s\}$; the number of empty slots is equal to the decimal value of modulated binary codeword and the decimal value of complement of the modulated binary word. In this modulation, the header pulse plays dual roles of symbol initial and time reference for preceding and succeeding symbol. For the value, α, which is an adjustment factor, the average symbol length $\bar{L}$ of DH_PIM will be changed by adjusting α When α is reduced, the reduction of average symbol length improves transmission throughput. By analysis, we can conclude that with increasing the α, the BER becomes bigger gradually when the system transmits the same attenuation length, or when BER is a constant, the smaller the adjustment factor α, the bigger the attenuation length.

As the results of the above analysis, increasing the value of the M for the same modulation bandwidth significantly improves the power utilization of the digital pulse

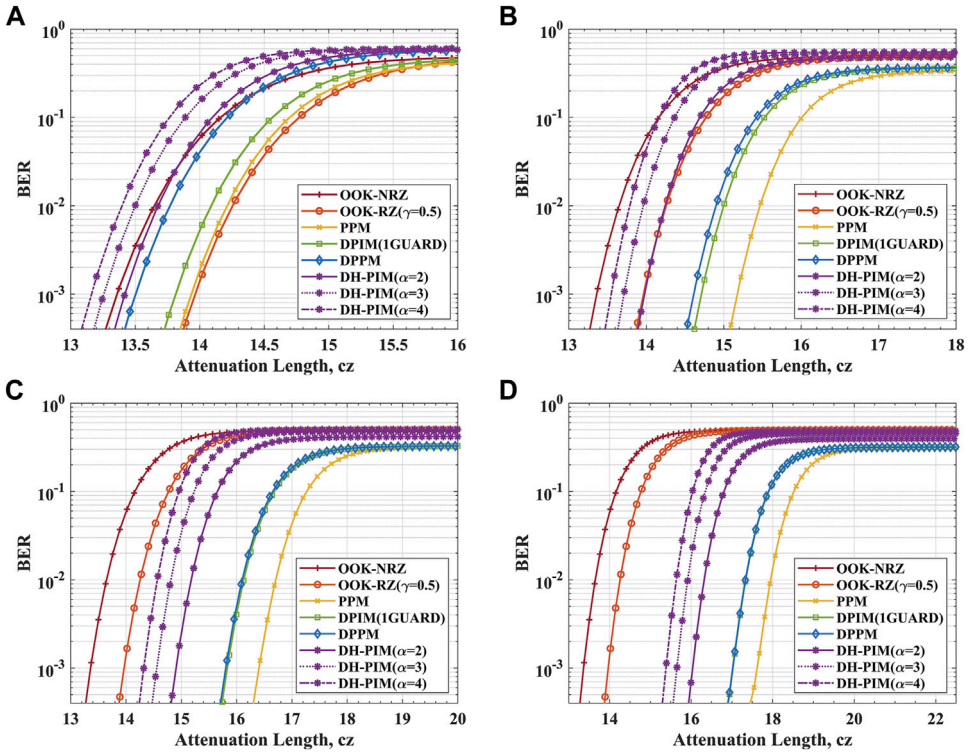

FIGURE 3 | The BER against the attenuation length for UPCC system in the pure seawater channel when $T_s = 15\tau$. The communication performance of UPCC systems under several modulation schemes when **(A)** $M = 2$ and **(B)** $M = 4$, **(C)** $M = 6$, **(D)** M = 8, respectively.

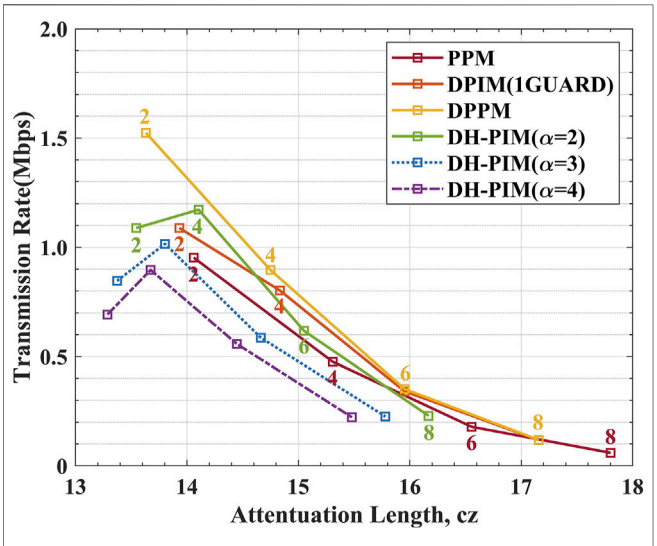

FIGURE 4 | The rate versus the attenuation length for BER is 3.8×10^{-3}. The numbers marked on the curve indicate the values of *M*.

modulation so that the attenuation length of the system increases. However, *M* is related to the bandwidth utilization, which decides the transmission rate of a communication system. The higher transmission rate means the higher bandwidth utilization for the same *M*. We limit the BER simulation results to below the FEC limit; the transmission rates and attenuation lengths of a system for DH-PIM, PPM, DPPM, and DPIM under the different *M* are shown in **Figure 4**. This figure clearly shows the trade-off between transmission rate and attenuation length. For PPM, DPIM, and DPPM systems, the attenuation length increases with *M*, but the transmission rate decreases accordingly. This is because for digital pulse modulation schemes, when the modulation bandwidth is fixed, the power utilization is proportional to the value of *M*, and the bandwidth utilization is inversely proportional to *M*. For DPIM with a guard slot, the transmission rate and attenuation length of the system are almost the same for $M = 6$ and $M = 8$. Comparing the performance of DPIM with a guard slot and PPM, the system for the PPM scheme can achieve a longer transmission length, but the transmission rate is lower than the DPIM system at a certain value of *M*. For DH-PIM, the bandwidth utilization efficiency is the highest of all digital pulse modulations, and it is evident that there is the highest point of transmission rate for DH-PIM when $M = 4$.

On the other hand, to do a fair comparison between the different IM schemes, the communication performance of the UPCC system under the various IM schemes is compared when the data rate and average transmit optical power are fixed. As shown in **Figure 5**, setting the bit rate to 50 Kbps, the value of *M* is 2, 4, 6, 8 in sequence. When $M = 2$ and BER is the

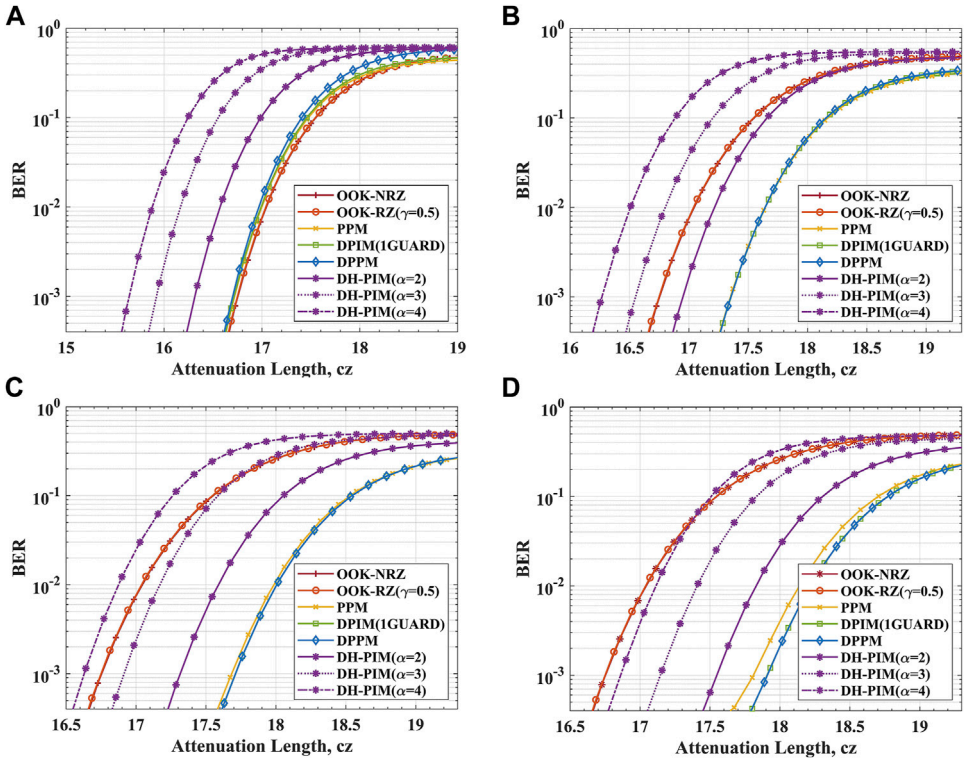

FIGURE 5 | The BER against the attenuation length for UPCC system in the pure seawater channel when the bit rate is 50 Kbps. The communication performance of UPCC systems under several modulation schemes when **(A)** M = 2 and **(B)** M = 4, **(C)** M = 6, **(D)** M = 8, respectively.

FEC limit, the minimum attenuation length that DH-PIM (α = 4) can transmit is approximately 15.74 and the maximum attenuation length that OOK-RZ can transmit is approximately 16.90. Similarly, when M = 4, the attenuation lengths of DH-PIM (α = 4) and OOK-RZ are 16.38 and 16.90, respectively. When M is 6 and 8 separately, the attenuation lengths of DH-PIM (α = 4) and OOK (OOK-NRZ and OOK-RZ) can arrive at 16.73 and 16.90, and 16.99 and 16.90. We can conclude that the performance of the OOK keeps constant, but the other system performances do not improve much with the increase in M. For digital pulse modulation schemes, the power utilization is proportional to the value of M, and the bandwidth utilization is inversely proportional to M. The power utilization is improved, and the bandwidth utilization is decreased with the increase in M. When the transmission rate keeps fixed, an increasing M affects both the bandwidth utilization and the power utilization of the system, which makes the performance of the system with digital pulse modulations not improve much. But, for OOK, the power utilization and the bandwidth utilization keep constant with the increase in M; the performances of the OOK as M increases have no changes. Compared with digital pulse modulation schemes, OOK has poor power utilization efficiency, but good bandwidth utilization efficiency compensates for this disadvantage. Therefore, when M = 2, the performance of the UPCC system with OOK is much better than the other systems in the overall comparison. As M increases, digital pulse modulations can transmit a longer attenuation length than OOK modulation. Except for DH-PIM, the digital pulse modulations can transmit a longer attenuation length than OOK modulation for $M > 2$. Various modulation schemes, including DPIM (1GUARD), DPPM, and PPM, tend to transmit the same distance at the same rate when M = 4 and M = 6. However, with the increase in the value of M, the DPPM and DPIM (1GUARD) display a more excellent communication performance compared with DH-PIM and PPM schemes when M = 8.

CONCLUSION

In this article, a UPCC system model based on IM and DD photon counting reception techniques is built. The article compares the variation of BER with a transmission distance of communication system for OOK, PPM, DPIM, DPPM, and DH-PIM under the same modulation bandwidth. From our analysis, we conclude that the PPM has the longest transmission distance at the same BER when $M > 2$, but the lowest communication rate. Transmission distance gets farther, and the communication rate gets lower as M increases. In addition, the same analysis is done under a fixed communication rate. It is concluded that the DPPM and DPIM have the optimum communication performance at

the same communication rate when $M = 8$. As the modulation bandwidth is lower and the time slot time is longer for DPPM and DPIM than PPM when the communication rate is the same, long slot time will help reduce the difficulty of signal synchronization and hence the complexity of the underwater photon counting system. The simulation and analysis in this article are based on published theoretical models, and the results concluded can be referenced for real transmission communication.

DATA AVAILABILITY STATEMENT

The original contributions presented in the study are included in the article/supplementary material, further inquiries can be directed to the corresponding authors.

AUTHOR CONTRIBUTIONS

XX, WW, and XH conceived the idea of the study; XH and PL analyzed the data, interpreted the results, and wrote the article; all authors discussed the results and revised the manuscript.

FUNDING

Program Name: Deep-sea Omni-directional High-speed Long-distance Optical. (Strategic Pioneer Science and Technology Special Project of Chinese Academy of Sciences(Class A)) Funder: Chinese Academy of Sciences Grant number: XDA22030203 Program Name: Ministry of Science and Technology Key R&D Program. Grant number: 2018YFC0307904.

REFERENCES

1. Qiao S, Ma Y, He Y, Patimisco P, Sampaolo A, Spagnolo V. Ppt Level Carbon Monoxide Detection Based on Light-Induced Thermoelastic Spectroscopy Exploring Custom Quartz Tuning forks and a Mid-infrared QCL. *Opt Express* (2021) 29(16):25100–8. doi:10.1364/OE.434128
2. Gao D, Xie Z, Ma R, Wang W, Bai Z, Jia S, et al. Analysis of the Current Situation and Trends in the Development of Satellite Laser Communications (Invited). *J Photon* (2021) 50(04):9–29. doi:10.3788/gzxb20215004.0406001
3. Lang Z, Qiao S, He Y, Ma Y. Quartz Tuning fork-based Demodulation of an Acoustic Signal Induced by Photo-Thermo-Elastic Energy Conversion. *Photoacoustics* (2021) 22:100272. doi:10.1016/j.pacs.2021.100272
4. Ali MF, Jayakody DNK, Chursin YA, Affes S, Dmitry S. Recent Advances and Future Directions on Underwater Wireless Communications. *Arch Computat Methods Eng* (2020) 27(5):1379–412. doi:10.1007/s11831-019-09354-8
5. Kodama T, Arai K, Nagata K, Nakamura K, Hanawa M. Underwater Wireless Optical Access Network with OFDM/SBMA System: Concept and Demonstration. In: Proceeding of the 2019 24th OptoElectronics and Communications Conference (OECC) and 2019 International Conference on Photonics in Switching and Computing (PSC); 2019 July 7-11; Fukuoka, Japan. IEEE (2019). p. 18957302. doi:10.23919/ps.2019.8817754
6. Ooi BS, Kong M, Ng TK. Underwater Wireless Optical Communications: Opportunity, Challenges and Future Prospects Commentary on "Recent Progress in and Perspectives of Underwater Wireless Optical Communication". *Prog Quan Electronics* (2020) 73:100275. doi:10.1016/j.pquantelec.2020.100275
7. Duntley SQ. Light in the Sea*. *J Opt Soc Am* (1963) 53(2):214–33. doi:10.1093/icb/26.2.38910.1364/josa.53.000214
8. Sun X, Kang CH, Kong M, Alkhazragi O, Guo Y, Ouhssain M, et al. A Review on Practical Considerations and Solutions in Underwater Wireless Optical Communication. *J Lightwave Technol* (2020) 38(2):421–31. doi:10.1109/jlt.2019.2960131
9. Saeed N, Celik A, Al-Naffouri TY, Alouini M-S. Underwater Optical Wireless Communications, Networking, and Localization: A Survey. *Ad Hoc Networks* (2019) 94:101935. doi:10.1016/j.adhoc.2019.101935
10. Matthews W, Ahmed Z, Ali W, Collins S. A 3.45 Gigabits/s SiPM-Based OOK VLC Receiver. *IEEE Photon Technol Lett* (2021) 33(10):487–90. doi:10.1109/LPT.2021.3069802
11. Hanson F, Radic S. High Bandwidth Underwater Optical Communication. *Appl Opt* (2008) 47(2):277–83. doi:10.1364/AO.47.000277
12. Du J, Wang Y, Fei C, Chen R, Zhang G, Hong X, et al. Experimental Demonstration of 50-M/5-Gbps Underwater Optical Wireless Communication with Low-Complexity Chaotic Encryption. *Opt Express* (2021) 29(2):783–96. doi:10.1364/OE.416117
13. Tsai W-S, Lu H-H, Wu H-W, Tu S-C, Huang Y-C, Xie J-Y, et al. 500 Gb/s PAM4 FSO-UWOC Convergent System with a R/G/B Five-Wavelength Polarization-Multiplexing Scheme. *IEEE Access* (2020) 8:16913–21. doi:10.1109/ACCESS.2020.2967856
14. Hiskett PA, Struthers RA, Tatton R, Lamb R. A Photon-Counting Optical Communication System for Underwater Data Transfer. In: Proceeding of the Electro-Optical Remote Sensing, Photonic Technologies, and Applications VI; 2021 Nov. 19; Edinburgh, United Kingdom. Edinburgh, UK: International Society for Optics and Photonics (2012). p. 854214. doi:10.1117/12.974938
15. Mao T, Wang Z, Wang Q. Receiver Design for SPAD-Based VLC Systems under Poisson-Gaussian Mixed Noise Model. *Opt Express* (2017) 25(2):799–809. doi:10.1364/OE.25.000799
16. Wang C, Yu H-Y, Zhu Y-J. A Long Distance Underwater Visible Light Communication System with Single Photon Avalanche Diode. *IEEE Photon J.* (2016) 8(5):1–11. doi:10.1109/JPHOT.2016.2602330
17. Sarbazi E, Safari M, Haas H. The Bit Error Performance and Information Transfer Rate of SPAD Array Optical Receivers. *IEEE Trans Commun* (2020) 68(9):5689–705. doi:10.1109/TCOMM.2020.2993374
18. Rao HG, DeVoe CE, Fletcher AS, Gaschits ID, Hakimi F, Hamilton SA. A Burst-Mode Photon Counting Receiver with Automatic Channel Estimation and Bit Rate Detection. In: SPIE Proceedings Free-Space Laser Communication and Atmospheric Propagation XXVIII; 2016 April 13; San Franciso, California, United States. San Franciso, CA: SPIE (2016). p. 9739. International Society for Optics and Photonics. doi:10.1117/12.2222885
19. Hu S, Mi L, Zhou T, Chen W. 3588 Attenuation Lengths and 332 Bits/photon Underwater Optical Wireless Communication Based on Photon-Counting Receiver with 256-PPM. *Opt Express* (2018) 26(17):21685–99. doi:10.1364/oe.26.021685
20. Chen Z, Tang X, Sun C, Li Z, Shi W, Wang H, et al. Experimental Demonstration of over 14 AL Underwater Wireless Optical Communication. *IEEE Photon Technol Lett* (2021) 33(4):173–6. doi:10.1109/LPT.2020.3048786
21. Gabriel C, Khalighi M-A, Bourennane S, Léon P, Rigaud V. Investigation of Suitable Modulation Techniques for Underwater Wireless Optical Communication. In: Proceeding of the 2012 International Workshop on Optical Wireless Communications (IWOW); 2012 Oct. 22-22; Pisa, Italy. IEEE (2012). p. 113–4. doi:10.1109/IWOW.2012.6349691
22. Wang X, Wang Y, Yao Z, Chen X, Zhu X, Zhang X. Timing Offset Estimation of PPM Signal for Deep Space Optical Communications. In: *Signal and Information Processing, Networking and Computers: Proceedings of the 6th International Conference on Signal and Information Processing, Networking and Computers (ICSINC)*. Xi'an China: Springer Nature (2020). p. 444–52. doi:10.1007/978-981-15-4163-6_53
23. Ghassemlooy Z, Popoola W, Rajbhandari S. *Optical Wireless Communications: System and Channel Modelling with Matlab®*. New York, USA: CRC Press (2019). p. 204–309.
24. Sato K, Asatani K. Speckle Noise Reduction in Fiber Optic Analog Video Transmission Using Semiconductor Laser Diodes. *IEEE Trans Commun* (1981) 29(7):1017–24. doi:10.1109/TCOM.1981.1095084

25. Gabriel C, Khalighi M, Bourennane S, Leon P, Rigaud V. Channel Modeling for Underwater Optical Communication. In: Proceeding of the 2011 IEEE GLOBECOM Workshops (GC Wkshps); 5-9 Dec. 2011; Houston, Tx USA. IEEE (2011). p. 6162571. doi:10.1109/GLOCOMW.2011.6162571
26. Arnon S, Kedar D. Non-line-of-sight Underwater Optical Wireless Communication Network. *J Opt Soc Am A* (2009) 26(3):530–9. doi:10.1364/JOSAA.26.000530
27. Cochenour BM, Mullen LJ, Laux AE. Characterization of the Beam-Spread Function for Underwater Wireless Optical Communications Links. *IEEE J Oceanic Eng* (2008) 33(4):513–21. doi:10.1109/JOE.2008.2005341
28. Tang S, Dong Y, Zhang X. Impulse Response Modeling for Underwater Wireless Optical Communication Links. *IEEE Trans Commun* (2014) 62(1):226–34. doi:10.1109/TCOMM.2013.120713.130199
29. Akhoundi F, Salehi JA, Tashakori A. Cellular Underwater Wireless Optical CDMA Network: Performance Analysis and Implementation Concepts. *IEEE Trans Commun* (2015) 63:882–91. doi:10.1109/TCOMM.2015.2400441
30. Zhang H, Dong Y. Impulse Response Modeling for General Underwater Wireless Optical MIMO Links. *IEEE Commun Mag* (2016) 54:56–61. doi:10.1109/MCOM.2016.7402261
31. Li Y, Leeson MS, Li X. Impulse Response Modeling for Underwater Optical Wireless Channels. *Appl Opt* (2018) 57(17):4815–23. doi:10.1364/AO.57.004815
32. Huang J, Wen G, Dai J, Zhang L, Wang J. Channel Model and Performance Analysis of Long-Range Deep Sea Wireless Photon-Counting Communication. *Opt Commun* (2020) 473:125989. doi:10.1016/j.optcom.2020.125989
33. Andrews LC, Phillips RL, Hopen CY. *Laser Beam Scintillation with Applications*. Bellingham, Washington USA: SPIE press (2001). p. 112–5.
34. Cheng X, Qu F, Yang L. Single Carrier FDMA over Underwater Acoustic Channels. In: Proceeding of the 2011 6th International ICST Conference on Communications and Networking in China (CHINACOM); 17-19 Aug. 2011; Harbin. IEEE (2011). p. 6158311.
35. Weng Y, Guo Y, Alkhazragi O, Ng TK, Guo J-H, Ooi BS. Impact of Turbulent-Flow-Induced Scintillation on Deep-Ocean Wireless Optical Communication. *J Lightwave Technol* (2019) 37(19):5083–90. doi:10.1109/JLT.2019.2928465
36. Sarbazi E, Safari M, Haas H. Statistical Modeling of Single-Photon Avalanche Diode Receivers for Optical Wireless Communications. *IEEE Trans Commun* (2018) 66(9):4043–58. doi:10.1109/TCOMM.2018.2822815
37. Popoola W, Ghassemlooy Z, Awan MS, Leitgeb E. *Atmospheric Channel Effects on Terrestrial Free Space Optical Communication Links3rd International Conference on Computers and Artificial Intelligence (ECAI 2009)*. Pites ti: Citeseer (2009).
38. Hemmati H. *Deep Space Optical Communications*. California: John Wiley & Sons (2006). p. 253–5.
39. Kay SM. *Fundamentals of Statistical Signal Processing. Detection Theory, Volume Ii*. New York: Printice Hall PTR (1998). p. 435–7.
40. Thorlabs. *V21 Catalog* (2011). Available at: https://www.thorlabs.com/NewGroupPage9_PF.cfm?ObjectGr oup_ID=5255 (Accessed September 15, 2021).
41. Zhang L, Tang X, Sun C, Chen Z, Li Z, Wang H, et al. Over 10 Attenuation Length Gigabits Per Second Underwater Wireless Optical Communication Using a Silicon Photomultiplier (SiPM) Based Receiver. *Opt Express* (2020) 28(17):24968–80. doi:10.1364/OE.397942
42. Wang J, Lu C, Li S, Xu Z. 100 M/500 Mbps Underwater Optical Wireless Communication Using an NRZ-OOK Modulated 520 Nm Laser Diode. *Opt Express* (2019) 27(9):12171–81. doi:10.1364/OE.27.012171
43. Tang X, Kumar R, Sun C, Zhang L, Chen Z, Jiang R, et al. Towards Underwater Coherent Optical Wireless Communications Using a Simplified Detection Scheme. *Opt Express* (2021) 29(13):19340–51. doi:10.1364/OE.426820
44. Fei C, Hong X, Zhang G, Du J, Gong Y, Evans J, et al. 166 Gbps Data Rate for Underwater Wireless Optical Transmission with Single Laser Diode Achieved with Discrete Multi-Tone and post Nonlinear Equalization. *Opt Express* (2018) 26(26):34060–9. doi:10.1364/OE.26.034060
45. ITU. ITU-T Fecfhb-rDss (ITU, 2004) (2021). Available: http://www.itu.int/rec/T-REC-G.97 5.1-200402-I/en (Accessed December 15, 2021).
46. Aldibbiat NM, Ghassemlooy Z, McLaughlin R. Indoor Optical Wireless Systems Employing Dual Header Pulse Interval Modulation (DH-PIM). *Int J Commun Syst* (2005) 18(3):285–305. doi:10.1002/dac.704

Conflict of Interest: The authors declare that the research was conducted in the absence of any commercial or financial relationships that could be construed as a potential conflict of interest.

frontiers in Physics

REVIEW
published: 01 February 2022
doi: 10.3389/fphy.2022.821057

A Review on Laser-Induced Breakdown Spectroscopy in Different Cancers Diagnosis and Classification

Muhammad Nouman Khan[1,2], Qianqian Wang[1,2], Bushra Sana Idrees[1,2], Wenting Xiangli[1,2], Geer Teng[1,2], Xutai Cui[1,2], Zhifang Zhao[1,2], Kai Wei[1,2] and Muhammad Abrar[3]*

[1]School of Optics and Photonics, Beijing Institute of Technology, Beijing, China, [2]Key Laboratory of Photonic Information Technology, Ministry of Industry and Information Technology, Beijing Institute of Technology, Beijing, China, [3]Departement of Physics, Hazara University, Manshera, Pakistan

Due to the new demonstrations of Laser-induced breakdown spectroscopy (LIBS) applicability in a surprisingly wide variety of applications, the use of LIBS as a medical diagnostic tool is steadily gaining momentum. Especially in different cancer diseases, LIBS has the potential to become a fast and valuable analytical tool. We addressed LIBS equipment and quantitative analytical procedures, and signal enhancement techniques for improving element detection. For detailed aspects of applications, we reviewed the recent progress of LIBS in different cancer diseases diagnoses by using different tissues and medical fluid as samples. To fulfill the high demands in the medical industry and overcome the severe tissue sample problem, it is proposed that the chemometric and signal amplification techniques for quantitative analysis should be employed, and robust and effective LIBS devices should be developed. This overview of the different cancers by LIBS is meant to summarize the research performed to date and suggest some suitable advanced chemometrics techniques and effective LIBS devices, if successfully implemented, would be significantly beneficial to the medical field in the future.

Keywords: laser-induced breakdown spectroscopy, cancer, detection, tissue, chemometrics

OPEN ACCESS

Edited by:
Yufei Ma,
Harbin Institute of Technology, China

Reviewed by:
Ye Tian,
Ocean University of China, China
Lianbo Guo,
Huazhong University of Science and Technology, China

****Correspondence:***
Qianqian Wang
qqwang@bit.edu.cn

Specialty section:
This article was submitted to Optics and Photonics, a section of the journal Frontiers in Physics

Received: *23 November 2021*
Accepted: *05 January 2022*
Published: *01 February 2022*

Citation:
Khan MN, Wang Q, Idrees BS, Xiangli W, Teng G, Cui X, Zhao Z, Wei K and Abrar M (2022) A Review on Laser-Induced Breakdown Spectroscopy in Different Cancers Diagnosis and Classification. Front. Phys. 10:821057. doi: 10.3389/fphy.2022.821057

INTRODUCTION

Cancer is a kind of disease caused by the uncontrolled growth of abnormal cells in body organs. These abnormal cells are also called cancer cells, tumor cells, or malignant cells. These cells may invade other normal tissue of the body. The second major cause of death worldwide is cancer; therefore, cancer is a critical issue that impacts all human communities [1]. In a broader sense, there are more than 277 different types of cancer diseases [2]. Scientists have found multiple stages of cancer. Many scientific and therapeutic efforts are underway to identify and combat cancer effectively. For this purpose, some X-ray-based imaging techniques like particle-induced X-ray emission (PIXE), energy-dispersive X-ray spectroscopy (EDX), and X-ray fluorescence microscopy (XRF) were used [3–5]. Still, these techniques have low sensitivity and accuracy [6]. Recently several other analytical approaches are generally used as a reference point in clinical research, such as polymerase chain reaction and histopathological analysis [7]. Such techniques involve a skilled person with experience, and the research process is time-consuming and complicated. Molecular spectroscopy like near-infrared (NIR) and Raman Spectroscopy (RS) [8] were also used, which is very simple and non-destructive. Still, they give only the molecular structure of the tissue sample and have relatively weak signals and complex spectral background.

Laser-induced breakdown spectroscopy is a type of laser-based atomic emission spectroscopy. LIBS has already become a known and popular analytical spectroscopic technique for studying the elementary form of any kind of sample, along with solid, liquid, or gas [9, 10]. A high-energy laser pulse targets a material substrate (sample) to be analyzed through LIBS, resulting in plasma production due to the interaction between laser and material substrate. The spectrometer detects the radiation emitted as plasma cools and sends it to a computer, where the signals are collected and processed for further analysis. LIBS offers the most well-known benefits [11], 1) *in-situ* and stand-off detection capabilities; 2) no or little sample preparation; 3) micro-analysis capability when microscopically connected; 4) availability of multi-element analysis; 5) ability to analyze solids, liquids, and gases; and 6) simplicity. LIBS analyses are available for all types of biomaterials and can detect almost all elements; furthermore, when coupled with chemometrics and machine learning algorithms, the technique provides an excellent ability to quantitatively and qualitatively analyze unknown substances in real-time. Moreover, the LIBS instrument isn't complicated and usually composed of a laser source, spectrometer, optical system, detector, etc. And access to samples in LIBS mainly includes focusing optics [12]. To achieve cancer diagnosis, LIBS was usually used for pathological detection. The current gold standard in cancer diagnosis is the histopathological examination in patient tissue biopsies or surgical excisions [8, 13]. LIBS biomedical application is mainly divided into two categories [14]. The first category analyzes and studies the microorganism (e.g., molds, yeast, bacteria), which causes different human diseases [15]. In the second category, a clinical specimen of human or animal-like (tissue samples, blood or other fluid samples, teeth and bones, etc.) is analyzed and studied [16]. In biomedical applications, significantly different kinds of cancer detection and classification are among the fastest-growing fields of study at LIBS. In the related application especially in cancer diseases diagnosis, LIBS was used by Kumar et al. [17] firstly to distinguish between normal and malignant cells of dog hemangiosarcoma and showed the variation or difference in constituent elements of the tissues sample. Similarly, Melikechi et al. [18] used mice blood plasma as a sample to detect the epithelial ovarian cancer (EOC) and concluded that LIBS can be used as a novel approach to detect EOC. Gondal et al. [19] studied the determination of heavy metals in colon cancer using normal and malignant tissue samples of humans. They concluded that LIBS is a compatible technique for the assessment and identification of heavy metals such as Pb, Hg, and Cr in cancerous colon tissues. Rizk et al. [20] reported variations of different trace elements levels like Mn, Cu, Fe, Na, Mg, K, and Ca of liver cancer by LIBS. In the same fashion, Teran-Hinojosa et al. [21] employed LIBS to find the correlation in elemental concentration between fibrotic and healthy samples of mice liver tissues. For lymphoma, and multiple myeloma (MM), Chen et al. [22, 23] used whole blood and serum sample to differentiate between normal and cancer blood samples. They preferred the entire blood sample instead of serum because the entire blood sample consists of large nutrients and can get good LIBS spectra for analysis. Similarly, Chu et al. [24] reported the classification of nasopharyngeal carcinoma using LIBS combined with chemometrics. LIBS was also used to diagnose colorectal cancer [25], cervical cancer [26], breast cancer [27], and melanoma [28]. LIBS cancer tests are fast, accurate, and less invasive. Because of their tremendous potential for early identification of different cancer diseases, LIBS and machine learning techniques give patients with more therapy alternatives and higher survival rates.

The main objective of this paper is to review and survey the relevant development in the biomedical field of LIBS, particularly in different cancer detection and analysis over the last decade. Specifically, the latest results of diagnosis, classification, and determination of different kinds of cancers (breast cancer, liver cancer, melanoma, blood cancer, stomach cancer, etc.) by using LIBS were discussed. This paper presents the measurement and detection by LIBS of various substrate samples (such as tissues, tissue in pelletized form, tissue homogenization, blood sample, blood serum, etc.) and early cancer detection. Finally, emerging developments and perceptions of the LIBS were proposed in the study of different kinds of cancers, and new possible approaches to current LIBS problems.

LIBS FUNDAMENTALS

It is essential to understand the plasma physics behind LIBS to provide an optimal environment for LIBS measurements. A considerable number of different environmental conditions impact the features and lifetime of plasma, which caused changes in spectral emissions and the efficiency of this method for chemical atomic level research. Laser ablation and matter interaction worked on the principle of quantum mechanics laws describing photons emission and absorption by atoms. Two pioneer researchers of LIBS, Miziolek, and Cremers, have published technical details of this field [29]. The LIBS cycle contains the following sequence of events, where 1) focus a high-power laser pulsed beam on the specific material substrate 2) laser-matter interaction takes place, and hot plasma plume is produced, 3) the hot plasma plume collected through optical fibre, that equipped with high-resolution gratings and collecting optical lens 4) the corresponding LIBS signal is then evaluated to determine and measure the relative existence of the target material substrate chemical constituents. In **Table 1**, some literature about LIBS in different cancer diseases is discussed and briefly summarizes the experimental techniques, sample preparation, spectra measurements, and different chemometric methods. In the medical field, sample collection is a huge issue and especially in cancer types of diseases. So it is essential to select the best and suitable sample type for laser ablation to collect the best spectra.

For excitation and de-excitation purposes, a high-energy pulsed laser (Nd: YAG laser with typical wavelength 1,064 nm) is applied to the sample (usually within nanosecond range) in LIBS [29], because of its durability, ease of use, and high energy peak pulse. Similarly, Nd: YAG laser second and third harmonic wavelengths 532 and 355 nm are also often used as excitation sources [37, 38]. The femtosecond (fs) laser is also used in various

TABLE 1 | Preparation and presentation of samples as well as mehtods used (in cancer diseases) for LIBS data analysis.

References	Sample materials	Cancer type	Methods	Laser/spectrometer/and no. of shots	Elemental emission lines (nm)
[17]	Paraffin-embedded tissues/(dog liver sample)	Liver cancer	Elemental analysis	Nd: YAG (532 nm, 10 Hz, 5 ns, 10 mJ)/(UV–visible Echelle optical spectrograph, range 200–700 nm)	Al 394.4 and 396.15, Ca 393.37, 396.85, 610.27, and 612.22
[20]	Paraffin blocks	Liver cancer (Human tissues)	ANN (Artificial Neural Network)	Nd: YAG (532 nm, 5 ns, 125 mJ)/200–1,000 nm	Cu 570.02, Fe 252.47,263.22,370.78 517.15, Na 589.59,589.99, Mg 383.23, 383.82, Ca422.67,428.93,430.25, and K 766.49, 850.34
[23]	Serum sample/(Human serum sample)	lymphoma and Multiple myeloma cancer patients	PCA, LDA, QDA, kNN	Nd: YAG (1,064 nm, 5 Hz, 8 ns, 73 mJ)/Four-channel spectrometer range 200–850 nm,/100 LIBS spectra were collected, for each sample	Ca I422.67, 526.56, Ca II 393.36, 396.85, Na I 588.99, 589.59, 819.48, K I 766.49, 769.90, H 656.27, O 777.19, 844.64 and N 742.36, 744.23, 746.83
[22]	Whole blood sample/ (Human blood sample)	Lymphoma	PCA (Principal Component Analysis), LDA (Linear Discriminant Analysis), kNN (k nearest neighbor)	Nd: YAG (1,064 nm, 5 Hz, 8 ns, 73 mJ)/Four-channel spectrometer range 200–850 nm,/100 LIBS spectra were collected, for each sample	Ca I 422.67, 526.56, Ca II 393.36, 396.85, Fe I 371.99, 373.49, 374.56, 374.95, 438.35, K I 766.49, 769.90, Mg I 516.73, 517.27, Na I 568.82, 588.99, 589.59
[30]	Pellets and excised tissue sample/(mice sample)	Melanoma	PCA,LDA	Nd: YAG (532 nm, 5 Hz, 5 ns, 7–9 mJ)/ 187–1,045 nm at a resolution of about 0.1 nm/ 15 shots	Ca II 393.366, 369.847, Mg II 279.553, 280.170, K I 766.49, 769.90
[28]	biological fluids (blood and tissue homogenates)/(mice sample)	skin cancer melanoma	LDA. FDA (Fisher Discriminant Analysis), SVM (Support Vector Machine), Gradient Boosting	150-fs Ti-Sapphire laser (775 nm, 50 ns, 1.44 mJ)/ spectrsometer range 190–975 nm, resolution 0.013–0.056 nm/	Na I 589.59, Ca I 422.67, Mg I 285.21
[31]	Four fresh tissue glioma samples/(Human tissue sample)	Glioma brain tumour	SVM	Nd: YAG (1,064 nm, 1 Hz, 5 ns, 40 mJ)/Spectrometer range 190–1,100 nm resolution 0.2–0.3 nm/For each sample, 200 spectra were collected	Mg 279.1, 279.8, Ca 393.4, 396.8, 422.7, Na 589.0, 589.6, H 656.3, N 818.5, K 766.5, 769.9 and O 777.4
[24]	In total, 160 serum samples were donated by 100 healthy controls and 60 NPC patients/(Human serum sample)	nasopharyngeal carcinoma	ELM(Extreme Learning Machine), RF(Random Forest)	Nd:YAG (532 nm, 10 Hz, 8 ns, 30 mJ)/echelle spectrometer spectral range: 200–950 nm/The number of laser shots was 40	Na 588.99, 589.59, K 766.49, 769.90, Zn 330.26, Mg 279.55, Al394.40, 396.15 and C–N 385.09, 385.47, 387.14, 388.34
[25]	Tissue sample/(Human tissues)/Samples from 41 patients with breast cancer and 32 patients with colorectal cancer	breast cancer and colorectal cancer	Elemental analysis	Nd:YAG (532 nm,5 ns, 100 mJ)/echelle spectrometer/50 spectra collected from each sample	Ca 373.6, 422.6, and Mg 280.2, 285.2
[26]	Tissue samples (in paraffin blocks)/(Human tissues)	cervical cancer	PCA, SVM	Nd:YAG (532 nm, 10 Hz, 8 ns, 30 mJ)/echelle spectrometer 200–900 nm/ 140 spectra collected	Na 588.95, 589.59, Mg 279.55, 280.27, K 766.49, 769.90, Ca 393.37, 396.85, 422.68

(Continued on following page)

TABLE 1 | (*Continued*) Preparation and presentation of samples as well as mehtods used (in cancer diseases) for LIBS data analysis.

References	Sample materials	Cancer type	Methods	Laser/spectrometer/and no. of shots	Elemental emission lines (nm)
[32]	Tissue slices of roughly 5 mm × 5 mm×2 mm are cut before the laser/Human tissues	Breast cancer (IDC-Invasive ductal carcinoma)	Elemental analysis	Nd:YAG (1,064 nm, 10 ns, 1 Hz, 150 mJ)/(Avantes Ava Spec 2048, NA = 0.22) range of 200–1,100)/200 LIBS spectra are collected from each sample	Mg I 285.213, Mg II 279.553 and 280.27, Ca I 422.67, 435.5, and 616.217, Ca II 317.933, 393.366, and 396.847, Na I 588.99 and 589.59, Na II 339.92, K I 766.48, 769.89, N I 742.364, 744.229, 746.831,818.802
[33]	Tissue slices of roughly 5 mm × 5 mm×2 mm/ (Human Tissues)	breast, colon, larynx, and Tongue	Elemental analysis	Nd:YAG (1,064 nm, 10 ns, 1Hz, 150 mJ)/(Avantes, Ava Spec 2048, having NA = 0.22) range of 200–1,100 nm/200 plasma emission spectra are taken from each sample	Mg I 285.21, Mg II 279.55,280.27, Na II 339.92, Ca I 422.67 and 435.5, 616.21, Ca II 317.93, 315.88, 318.13, 393.36, 396.84, Na I 588.99 and 589.59, H 656.3 and Hb 486.13, O I 777.2, 777.4, 777.5 and 844.6, N I 742.36, 744.22, 746.83, 818.8, 821.63, 824.23, 868.02, 868.34, 868.61
[34]	Paraffin tissue blocks/ (Human tissue)	Gastric cancer	Elemental analysis	Nd:YAG (1,064 nm, 1 Hz, 6 ns?30 mJ)/Echelle spectrometer/	Ca 315.92, 317.96, 393.32, 396.8, Mg 279.56 and 280.3
[35]	Blood plasma/ovarian cancer/176 sample including normal patients		PCA, SKB(SelectKBest algorithm)	Nd:YAG (1,064 nm, 7 ns , and 30 mJ)/echelle spectrometer range from 230 to 900 nm	K 766.48, 769.89, Na 588.96 and 589.58, Mg 279.55,280.27, Fe 623.96 and 634.8
[36]	Lung tumor/90 samples are used	Lung cancer	SVM, PCA, Gradient Tree, RF	Nd:YAG (1,064 nm, 10 ns, 10 Hz, 65 mJ)/Mechelle spectrometer/They collected 140 LIBS spectrum	C 247.8, Mg 279.8, C-N 358.4,388.3, 417.6, Ca 393.3, 396.8, 422.7, Na 588.99, 589.59, K 766.5, 769.9

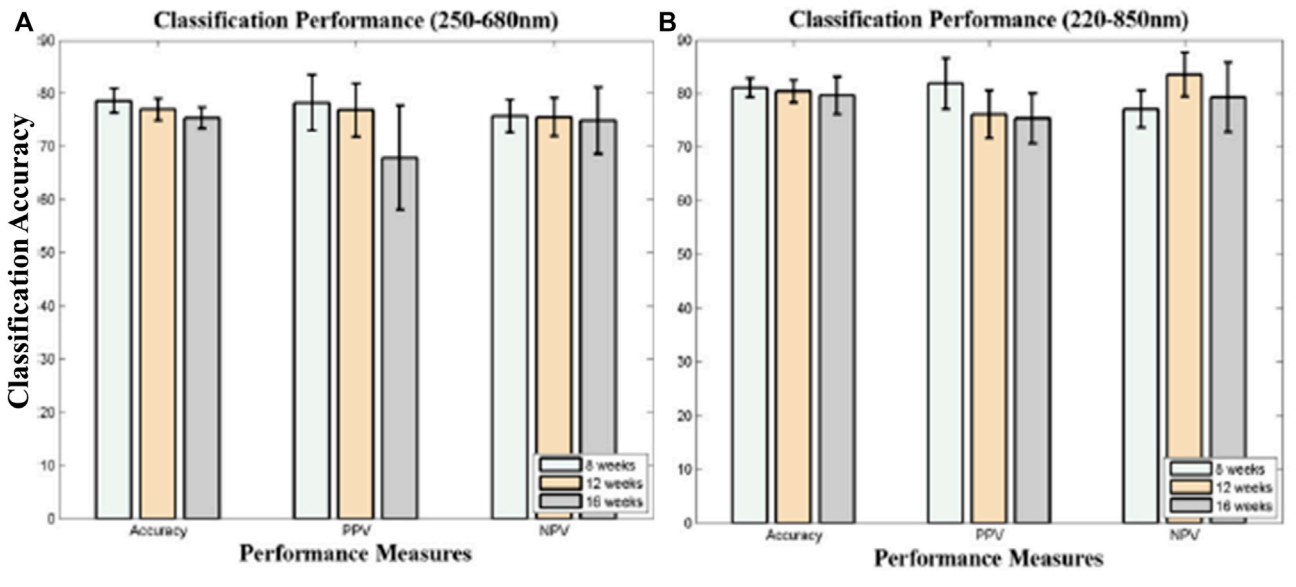

FIGURE 1 | The achieved classification accuracy result of RF technique **(A)** in the wavelength range of 250–680 nm **(B)** and 220–850 nm [18].

applications of LIBS [29]. In LIBS analysis, the pulsed laser energy and laser spot size are very significant to infuse on the sample's surface [39].

LIBS ANALYSIS FOR DIFFERENT CANCERS

Ovarian Cancer

Ovarian cancer, often known as ovaries cancer, is one of the most frequent cancers in women. Ovarian cancer is the fifth leading cause of death for women. In 2018, new cases of ovarian cancer diagnosis patients reached around 21,750 in the United States (US); an additional 13,940 deaths were also reported [40]. Ovarian cancer is one of the leading causes of death among gynecological cancers (cancer that occurs inside the reproductive organs. Cervical, ovarian, uterine, vaginal, and vulvar are five primary forms of cancer that involve a woman's reproductive organs). Usually, there are no unique signs and symptoms; consequently, 70% of cases are found as the disease is grown at an early stage [41, 42]. For the identification of ovarian cancer, Melikechi et al. [18] conducted a preliminary investigation on the blood sample of the transgenic mice to identify and classify ovarian tumors in the wild type (normal) and transgenic mice (cancerous). For further LIBS analysis, they collected blood samples from mice at different ages of 8, 12, and 16 weeks. A total of 56 blood plasma samples were used in the experiment, 28 of each class (normal and cancerous).

This finding backs up the theory that as the tumour load in the animals grows, plasma specimens will deviate more from control specimens. When all six data are combined, however, the accuracy of classification for each age group drops. We believe this drop is because the LIBS chamber has to be re-opened after collecting LIBS spectra from one set of blood plasma samples to load the new blood plasma samples. The results of RF are shown in **Figure 1**. They concluded that more research is needed to classify ovarian cancer and identify atomic and ionic lines in the ablated samples. Another interesting perspective is to continue with the physical understanding of the selected set of wavelengths for good classification results.

Yue et al. [35] used LIBS combined with machine learning techniques to diagnose and classify ovarian cancer. They also used the blood plasma of 176 patients, including ovarian cyst and normal samples. For cancer diagnosis, they achieved sensitivity and specificity 71.4 and 86.5%, respectively. In the experiment, they detected emission lines from certain minor elements in blood plasma, Fe, Si, P, and Cu, but the contribution in classification was minimal. Consequently they considered the major metal elements, K, Na, Mg, and Ca are because these elements are essential electrolytes in blood and play a critical role in preserving homeostasis in the body. As a result, an imbalance in their proportions in a patient shows a state of abnormality.

Furthermore, direct analysis of blood-related liquids is preferred for a clinical approach among various operation modes with different types of biological samples because LIBS corresponds to an easy, cost-effective, and widely used implementation of biomedical test that is suitable for a wide coverage screening and can be incorporated in a routine physical examination.

Lymphoma and Multiple Myeloma (MM)

Most blood cancers, also known as hematologic malignancies, begin in the bone marrow, which produces blood. When dysfunctional blood cells begin to develop out of control, they disrupt the function of healthy/normal blood cells, which fight infection and create new blood cells. A blood cancer diagnosis is also a big problem in clinical medicine today [43–45]. Multiple myeloma (MM), Leukaemia, and malignant lymphoma are the three most common types of blood cancer [46]. There are two key obstacles in diagnosing blood cancer: distinguishing cancer from normal blood cells and identifying the different forms of blood cancer. Lymphoma and multiple myeloma (MM) are cancers of the blood cells that affect the body's hematopoietic and lymphatic systems. In 2015 about 29,300 died from lymphoma, and 9,200 died from MM, respectively, in China [47]. Three papers have been published to diagnose blood cancer through LIBS in 2017, 2018, and 2020 respectively.

X. Chen et al. presents a rapid and robust diagnosis and discrimination of lymphoma and MM using LIBS performed on serum samples in combination with different chemometric techniques [23]. They used k nearest neighbors (kNN), principal component analysis (PCA), linear discriminant analysis (LDA) and quadratic discriminant analysis (QDA) to build the malignancy diagnosis and discrimination models for further analysis. PCA scores are used for best features selection. In terms of precision of discrimination, the area under the curve (AUC), sensitivity, and accuracy, the kNN model displays the best results. The ROC curves for all classification models are shown in **Figure 2A**. The average specificity of classification was achieved at 96.0%. In the second paper, for discrimination of lymphoma using LIBS, the whole blood is taken as a sample [22]. Instead of serum samples, whole blood samples are used because they contain more components and have more spectral signatures for the study of discrimination. All blood samples from lymphoma patients and healthy controls were analysed and compared using the LIBS spectrum. Chemometric approaches have been used to study discrimination, including PCA, LDA classification, and kNN classification. Both kNN and LDA models have demonstrated extremely excellent discriminating efficiency, as shown in **Figure 2B**, with an accuracy of over 99.7%, a sensitivity of over 99.6%, and a specificity of over 99.7%. It is assumed, however, that the incidence of cancer is not connected to either one or two unique elements but rather to several forms of elements. The confusing impact of other mild disorders can be minimized to a restricted degree by using discrimination models based on multivariate analysis instead of univariate analysis. Yet, it can help boost the robustness of the discrimination models by incorporating benign disease controls in the model.

Similarly, in the third paper, a technique uses random subspace method (RSM) based ensemble learning such as RSM-LDA in conjunction with LIBS [48]. They studied the Leukemia subtypes of blood cancer like acute myeloid leukemia (AML), chronic myelogenous leukemia (CML), and MM and lymphoma. The variable importance (VI) of the selected

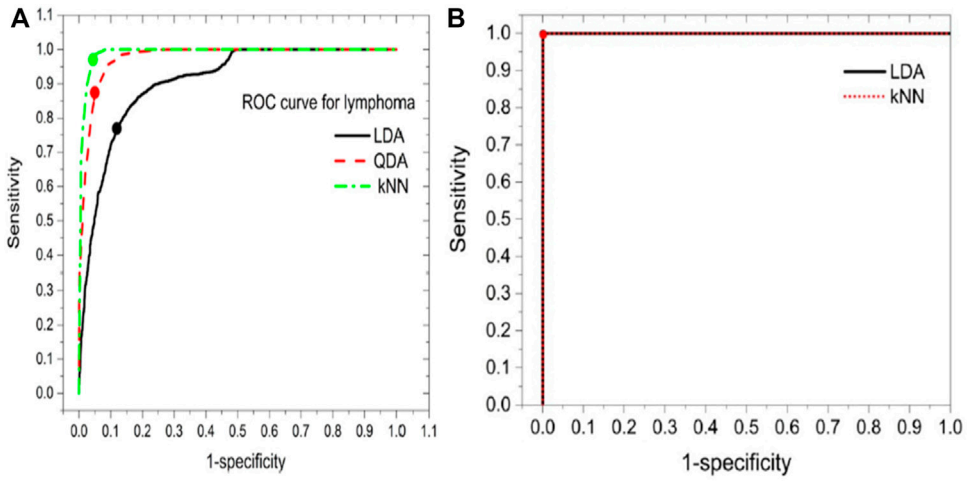

FIGURE 2 | (A) The ROC curve for the lymphoma class of different classification models [23]. **(B)** Receiver operating curve (ROC) for the lymphoma class of LDA and kNN models [22].

lines was determined to evaluate the significance of the function. The RSM-LDA model has the highest overall precision rate and AUC, compared to LDA and kNN, which means that the RSM-LDA model has the highest accuracy, as shown in **Figure 3**. Furthermore, **Figure 4** manifests the best performing classification ROC curve for four different blood cancers. With the RSM-LDA model, the overall accuracy ratings for AML vs healthy control (HC), CML vs HC, MM vs HC, and lymphoma vs HC ranged from 94.33, 94.49, 94.61, and 94.38%–98.77, 96.54, 98.78, and 96.62%, respectively. In the above two papers of blood cancer, the serum sample and whole blood sample are used on filter paper, while in the third paper about blood cancer the whole blood sample used in the form of pellets.

Skin Cancer (Melanoma)

Skin cancer is one of the leading causes of death worldwide. Squamous Cell Carcinoma (SCC), Basal Cell Carcinoma (BCC), and Merkel cell cancer are known as non-melanoma skin cancer (NMSC). These NMSC and melanoma are categorized as skin cancer. In 2018, NMSC (excluding basal cell carcinomas, BCCs) was the world's fifth most prevalent form of cancer, causing more than 1 million new cases and 65,000 deaths, while melanoma was the 21st in cancers lethality rank. Malignant melanoma is the most severe form of skin cancer. It leads to higher patient mortality due to late pathology diagnosis of almost 300,000 new incidents and 60,000 fatalities [49] and its increased risk of developing systemic metastases [50]. In this regard, Han et al. [30] concentrated on the feasibility of LIBS to differentiate between lesions in the surrounding dermis from melanoma. Using homogenized pellet extracts from melanoma-implanted mice, and performed a qualitative and quantitative elemental analysis of melanomas and the underlying dermis. Based on these results, they also analyzed distinguishable elements from real skin tissues of melanoma-implanted mice, reflecting the clinical

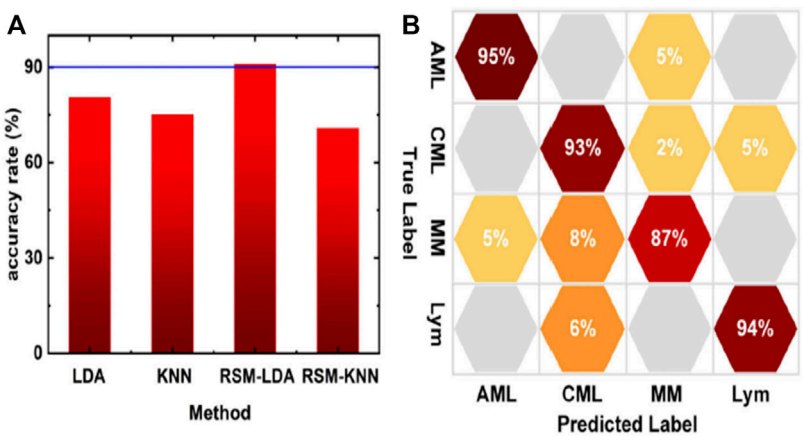

FIGURE 3 | (A) The accuracy rate of different models **(B)** confusion matrix of RSM-LDA [48].

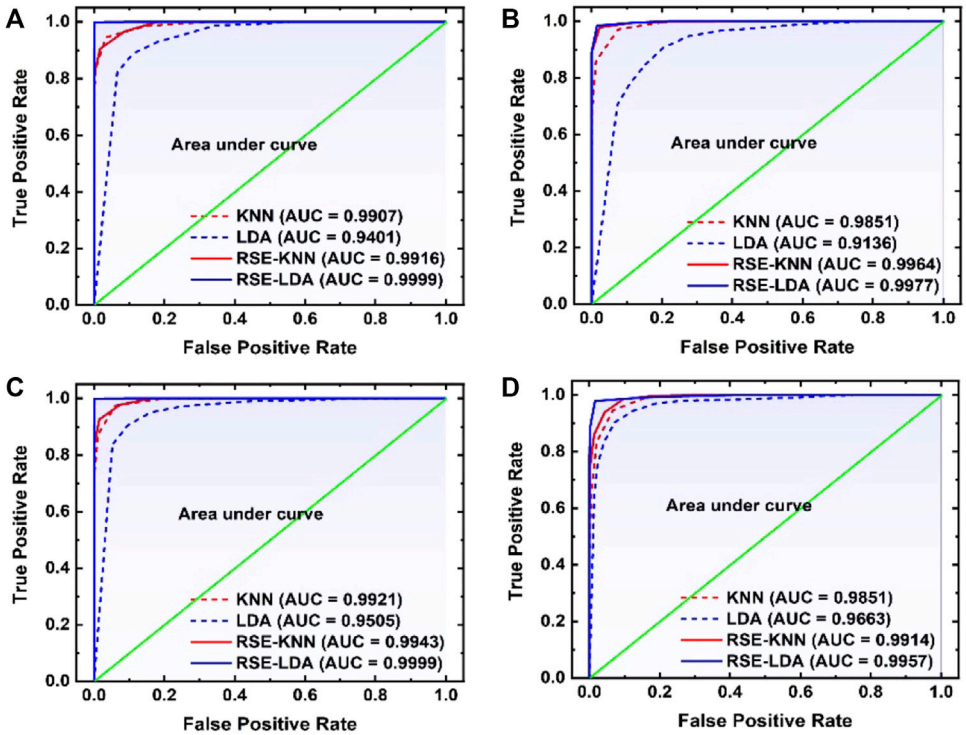

FIGURE 4 | The ROC curve was used to compare four different models for **(A)** AML versus healthy control (HC), **(B)** CML vs HC, **(C)** MM vs HC, and **(D)** lymphoma vs HC [48].

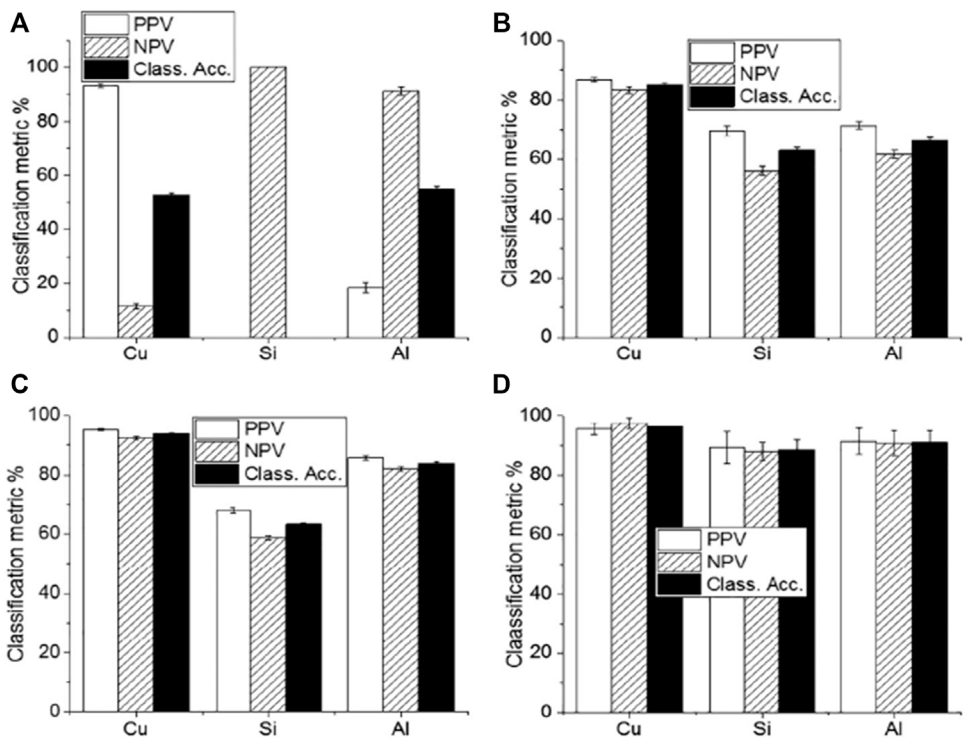

FIGURE 5 | The classification accuracy result of **(A)** LDA **(B)** FDA **(C)** SVM and **(D)** Gradient boosting with different substrates of Cu, Si and Aluminum [54].

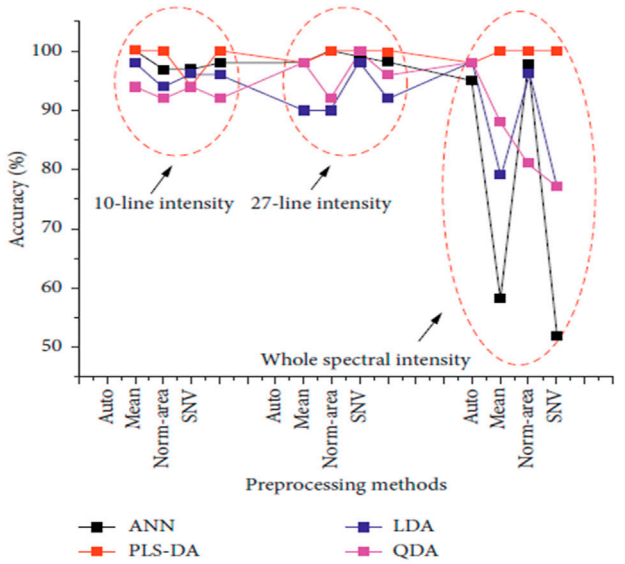

FIGURE 6 | The classification accuracy of ANN, PLS-DA, LDA, and QDA models by using multiple preprocessing methods with different input data types [53].

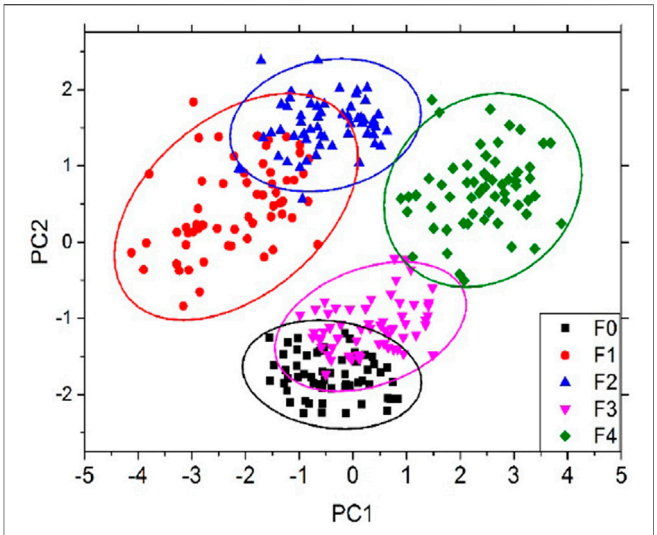

FIGURE 7 | PCA score of different MTAVIR scores from F0 to F4 [57].

situation. The sensitivity and specificity of LDA classifier for pellet samples were shown to be 99.4 and 100%, respectively, while those for tissue samples were shown to be 96.7 and 99.7%, respectively. Rosalba et al. [28] collect and compare the blood serum and tissue homogenate LIBS spectra harvested from a pre-clinical model of melanoma. The use of four distinct classification algorithms (LDA, FDA, SVM, and Gradient Boosting) is effective. The results of these four algorithms were compared, and Gradient Boosting was found to provide the best precision for classification as shown in **Figure 5**. The classification accuracy could be significantly impaired by various substrates, with Cu substrate the best outcomes in the experimental circumstances used. Similarly, the findings of the fs-LIBS research and analysis were reported by Moon et al. [51] elemental mapping of a study of cryosectioned melanoma as an Imaging procedure for differentiating the areas of the tumour and dermis. They concluded that dermis and skin cancer fields are distinguished and compatible in the LIBS elemental mapping picture with the histologically calculated ones, showing the viability of LIBS as a beneficial tool for quicker decision Regions of Skin Cancer. To improve the classification accuracy of normal and melanoma samples, Ekta et al. [52] used the Joint Mutual Information Estimation (MIE) and Weighted Average (WA) methods. To test and pick representative spectral lines, the MIE procedure was used, while column-wise Gaussian weighted lines based on the chosen feature lines and surrounding spectral lines, averaging was used to process two-dimensional spectral images. Khan et al. [53] recently used LIBS combined with chemometric methods to examine and discriminate against human melanoma FFPE tissue samples instead of animal samples, and achieved good classification results as shown in **Figure 6**.

Liver Cancer

In humans, the liver is the sixth most common primary cancer site, and it is frequently linked with cirrhosis and inflammation [55]. Kumar et al. [17]used LIBS for the first time to classify a dog's liver tissue to identify liver cancer. The findings demonstrate that the ratios of calcium (Ca), copper (Cu) and sodium (Na) to potassium (K) line concentrations are higher in a malignant sample than those in a normal one. They also used inductively coupled plasma emission spectroscopy (ICPES) to compare the results with LIBS and achieved good approximation results of both methods.

For the diagnosis and classification of liver cancer, Sherbini et al. [20] used a scaled conjugate gradient back-propagation ANN to construct a diagnostic model to differentiate between 26 malignant samples and four regulars (zero cancer level) samples randomly selected from patients with liver cancer aged 6–56 years. All the malignant samples were accurately identified.

Hepatic fibrosis is chronic liver damage that can progress to cirrhosis, hepatic failure, and finally hepatocellular carcinoma (HCC) or liver cancer [56]. Hinojosa et al. [57] used LBS to demonstrate the differentiation of chronic liver injury known from normal for hepatic fibrosis liver diseases. For this purpose, they used a fibrotic and normal liver sample of mice. PCA is used for further classification analysis of different fibrotic levels of METAVIR score system (histopathological system for liver tissues identification) from F0 to F4, F0 is considered the normal one as shown in **Figure 7**. They also concluded that an increase in calcium (Ca) concentration found in cirrhosis (a late stage of scaring also known as fibrosis) could be linked to intracellular or extracellular calcium buildup. Although the findings are preliminary, LIBS might be used as a stand-alone, quick way to identify hepatic fibrosis at an early stage.

Brain Tumor

Glioma is a prominent brain tumor, which arises in the brain and spinal cord. According to World Health Organization (WHO),

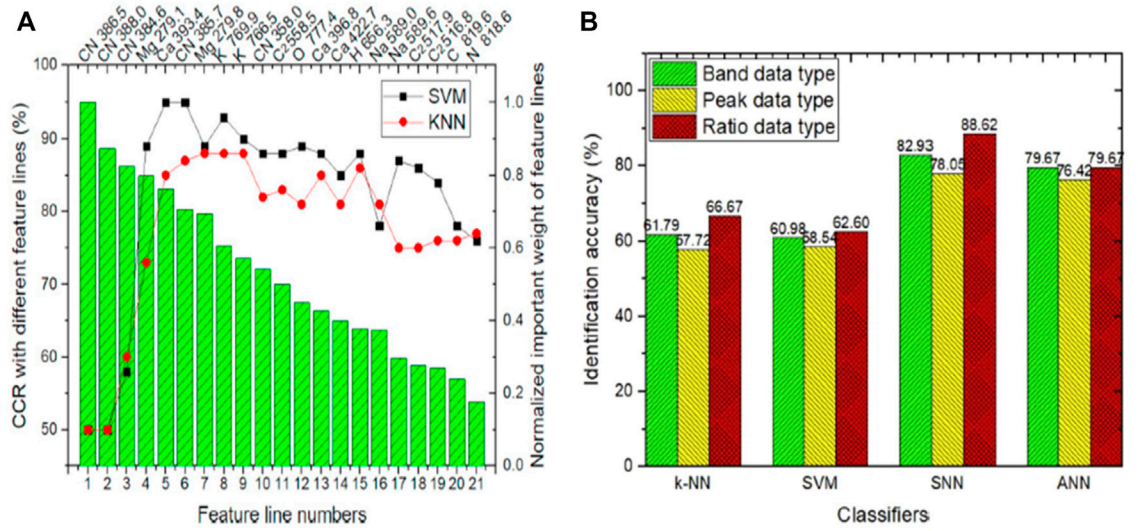

FIGURE 8 | (A) Classification result of SVM and kNN of infiltrative glioma [31]. **(B)** The identification accuracy of an infiltrative and non-infiltrative brain tumour [61].

glioma is graded in four different categories: Grade I, which is typically curable by surgery; grade II, known as lower-grade glioma (LLG), grade III, known as anaplastic astrocytoma, and grade IV, known as Glioblastoma Multiform (GBM) which is the most severe kind with the lowest survival rate [58–60]. For the first time, Teng et al. [31] proposed LIBS to discriminate the infiltrative glioma boundary based on elemental components. In this work, they used fresh glioma and infiltrating boundary tissue samples for laser ablation. They concluded that to discriminate the glioma boundary, Mg and Ca are linked to the development of tumors and play a more critical factor in tumour formation.

Similarly, the CN band also contains relevant details for recognition of Tumors boundaries. They used two different chemometric models, SVM and kNN, for glioma and infiltrative boundary classification. For discrimination of glioma and infiltrating boundary SVM achieved 95% correct classification rate (CCR), which is better than kNN as shown in **Figure 8A**.

Similarly, for four different types of brain tumour (glioma, meningioma, hemangiopericytoma, and craniopharyngioma) classification Teng et al. [61] performed LIBS combined with machine learning techniques. They proposed to use the molecular fragment spectra (MFS) for further brain tumors diagnosis. Molecular fragments play a key role in the diagnosis of brain tumor, in literature, few researchers have worked on this. The MFS in LIBS is very new and commonly not practiced in biological samples. The most often used signals in LIBS research are the atomic spectra (AS). In this article, they used 12 patients' tissue samples of four types of brain tumor. The four types above of brain tumors were diagnosed and classified as infiltrative and non-infiltrative tumors. Instead of the conventional machine learning technique, they established and implemented the spiking neural network (SNN) in MFS data analysis. They investigated the development processes of MFS in brain tissue in-depth, looking at three different types of formation mechanisms: combination, rearrangement, and break. The recognition precision reached 88.62% in 1–2 s, together with the proposed SNN brain-like computing system. This study presented three different MFS data types, with the ratio data type best suited for diagnosing various brain tumors. Due to substantial overfitting, the traditional machine learning methods kNN, ANN, and SVM did not perform well. SNN, as a third-generation neural network, has the potential to tackle this problem effectively, as shown in **Figure 8B**.

Nasopharyngeal Carcinoma

Nasopharyngeal carcinoma (NPC) is a rare subtype of head and neck cancer with a highly unbalanced endemic spread [62]. There is about one new occurrence for every 100,000 people every year in most parts of the world. The incident rate of NPC is 20–50 per 100,000 in southern China and Southeast Asia [63, 64]. For NPC discrimination, Chu et al. [65] used LIBS combined with chemometric methods. In this research, a total of 160 serum samples was used, including 100 healthy controls and 60 NPC patients.

Similarly, different chemometric methods like kNN, extreme learning machine (ELM) and feature extraction RF were used for classification and identification of NPC. The serum sample was dropped on a boric acid substrate for laser ablation. The major elements (Na, Mg, K, and Zn) from LIBS spectra were selected for diagnosis and further classification purposes. They concluded that, the variable importance of three lines (K I 766.49, K I 769.90, and Na I 589.59 nm) with RF extraction are much greater than the average variable importance. The accuracy rate, sensitivity, and specificity of NPC serum and healthy controls were 98.330, 99.022, and 97.751%, respectively, using the RF coupled with the ELM classifier. Furthermore, the RF-ELM model's AUC was 0.987, which means that it has huge diagnostic efficiency.

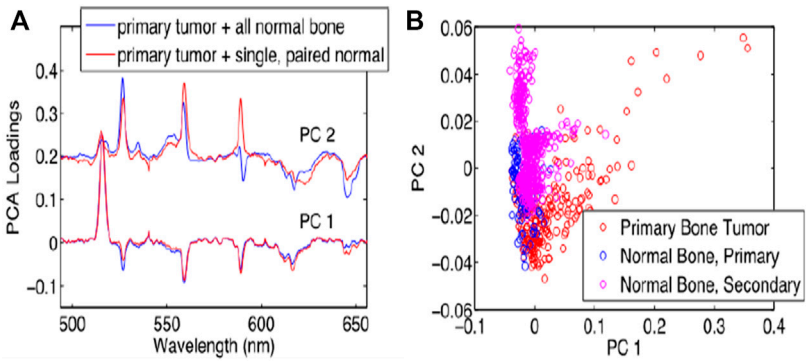

FIGURE 9 | PCA result of different bone by fsLIBS [74].

Cervical Cancer

In 2018, there were nearly 570,000 cases of cervical cancer and 311,000 deaths reported. Cervical cancer is the fourth most widespread cancer among women. It is ranked after breast cancer (2.1 million cases), colorectal cancer (0.8 million), and lung cancer (0.7 million) in 2018 [66]. For the identification of cervical cancer Wang et al. [26] used paraffin-embedded tissue samples of normal and cervical cancer patients. They coupled LIBS with chemometric methods PCA and SVM for classification purposes. It was hard to distinguish between normal and cervical cancer tissue using the raw spectra. PCA was performed, but the result of PCA was overlapped, hard to differentiate the cervical and normal sample. Then for normal tissues and cervical cancer tissues identification, SVM and PCA-SVM were used. The findings found that the PCA-SVM identification accuracy is much better than SVM and increased from 93.06 to 94.44%. They also concluded that LIBS technology has a lot of potential for cancer diagnosis in real-time. To achieve the best calcification and discrimination results the sample numbers should be raised in the future.

Stomach Cancer

Stomach cancer is also known as gastric cancer. In worldwide cancer ranking, it is on fifth number. According to Cancer Global Observatory, in 2018, over one million new cases were reported [67]. For gastric cancer identification, Seifalinezhad et al. used spark discharge assisted laser-induced breakdown spectroscopy (SD-LIBS) in investigating the possibility of distinguishing neoplastic (cancerous) from non-neoplastic (normal) stomach tissues [68]. In this study, they also found the difference between neoplastic and non-neoplastic gastric tissues emission spectra. The study concentrated on an *in vitro* comparison of elemental concentrations in distinct tissues. Depending on these observations, the intensities of Ca and Mg in cancerous spectra are higher than the normal sample spectra obtained from the same person. Likewise, they also concluded that the number of samples used in this study was insufficient to draw a firm conclusion, and more research is needed to generalize this concept. Furthermore, the SD-LIBS technique should become easier to use in future *in vivo* studies.

Breast Cancer and Cervical Cancer

Breast cancer is the most top cancer among women throughout the world. In all-female cancer-related diseases, breast cancer is responsible for up to 16%. It is estimated that 2,088,849 new cases were reported, and 626,679 people died of breast cancer in 2018, and the most (69%) of deaths occur in developing countries, while this cancer is considered an acquired world disease [49]. Ghasemi et al. [69] used LIBS and acoustic response (AR) techniques to classify malignant human breast tissues from normal tissue. Here, using an acoustic analyzer, for sensing audio signals during microplasma generation. The signals distinguish the tissues according to the audio level and the spectral changes during the laser-induced development of micro-plasma. In malignant tissues, LIBS indicates a noticeable increase in trace elements such as calcium (Ca), sodium (Na), and magnesium (Mg) as determined by the characteristic emissions inside the laser induced micro-plasma.

Similarly, Hussain et al. [25] used spectroscopic techniques such as LIBS to recognize two human forms of cancer, including breast and colorectal cancer, as well as condition grade and incidence assessment. They found distinct variations in the density of calcium (Ca) and magnesium (Mg) spectral lines in the LIBS spectrum of non-neoplastic and malignant breast and colorectal tissue samples. To differentiate between cancerous *in vitro* human tissues of interest (breast, colon, larynx, and tongue) and normal ones, Ghasemi et al. [33] used the LIBS method. Using the laser mediated plasma spectrum, the trace elements are investigated. They concluded that the concentration of trace elements (such as calcium, sodium, and magnesium) in cancerous tumors is considerably higher in terms of the signature emissions of calcium (Ca), sodium (Na), and magnesium (Mg) within the laser-induced plasma. They also figure out that the plasma temperature is measurably higher for cancerous tissues than normal ones. Likewise, Wei et al. [70] Implemented multi-elemental LIBS mapping, based on conventional histopathological tumor therapeutic impact analysis and associated anti-tumour pathways, would offer a new approach to estimating the anti-tumor therapeutic effect and the molecular process, in line with the possible growth of precision medicine. Collectively, four distinctive elements from tumour tissues, calcium (Ca), copper (Cu), magnesium (Mg), and sodium

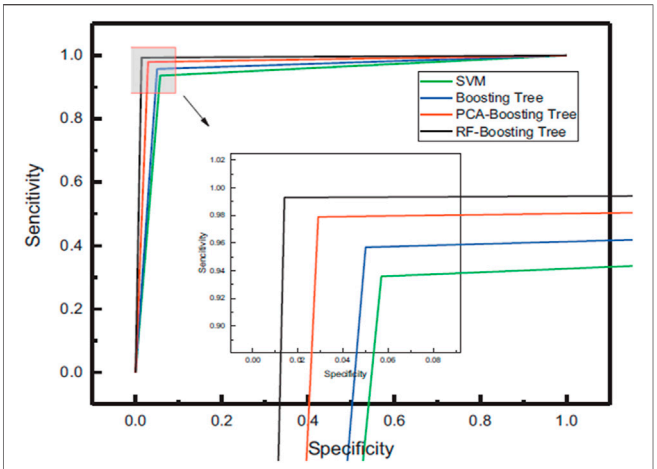

FIGURE 10 | Four different classification models ROC curves [36].

(Na), were studied to project tumor therapeutic effects and investigate the potential of biological elements in the study of anti-tumor mechanisms. In addition, the complementarity and compatibility of elemental imaging focused on LIBS with conventional histopathology will offer a new avenue for the study of anti-tumor therapy.

Bone Cancer

Bone cancer occurs when abnormal cells in bone grow out of control [71]. It damaged normal bone tissue. The most prevalent bone cancer is osteosarcoma. This is responsible for almost two-thirds of all bone cancers cases. About 1,200 patients are diagnosed annually in the United States with osteosarcoma [72–75]. For the classification of bone tumors, Gill et al. [74] proposed research to understand the variations in femtosecond LIBS (fsLIBS) spectra. For laser ablation, they used samples of a primary bone tumour, a secondary bone tumour, and normal bone in this study. Essential differences in the fsLIBS signal between the primary tumor of the bone and normal bone samples were observed. They compared the separation of tumour and normal tissue with many other "normal" bone samples using a PCA decomposition of this combined data set. The PCA results revealed that the PCs of the two data sets substantially overlap, which shows that even when fresh new normal bone tissue is added to the data, the chemical distinctions between normal and cancerous tissue remain consistent. In tumor tissue, the magnesium (Mg) peak level (516 nm) increases compared to the calcium (Ca) peak intensity (526 nm) as well as PCA results are shown in **Figure 9**. The explanation why they did not notice a difference in the spectrum between metastatic bone tumor and normal bone may be because primary cancer cells migrate across the body, and other forms of cells may not cause a metabolic change (such as bone).

Colon Cancer

Colon cancer is one of the world's leading cancers and, along with lung, prostate and breast cancer, is considered among the major killers [75]. Gondala et al. [19] proposed a study to examine the samples of malignant and nonmalignant colon tissue using the LIBS technique and to ascertain a link between the accumulations of such heavy metals responsible for the formation of colon tissue malignancy. They found that LIBS is a reliable tool for detecting heavy metals in cancerous colon tissues, such as Hg, Cr, and Pb. These heavy metals were found in the malignant tissues, although these elements were not identified in control (healthy) colon tissue samples.

The ICP-OES methodology has been used to determine the authenticity and to validate the consistency of LIBS results. In addition, by concentrating on specific elements such as Hg and Cr in control tissues, electron temperature and electron density were calculated for the plasma derived from the malignant and control tissues to show that the plasma was in the LTE condition [19].

Lung Cancer

Lung cancer has long been seen as a significant public health issue. Every year, around 1.35 million people are diagnosed with the disease, with 1.18 million dying. This statistic is considerably higher than other cancers like breast and colon cancer, and the death rate in China and other countries is still rising [76]. The line between the lung tumour and the border tissue is blurry, during surgery. Recurrence can shorten a patient's life if tumour excision is incomplete [77]. Lin et al. [36] used LIBS combined with machine learning techniques to differentiate lung boundaries from lung tissues. For this purpose, they used 90 tissue samples of lung tumor and lung boundary from 45 patients, of which 20 men and 25 were female, respectively. They used SVM and Boosting Tree classification models that employ PCA and RF to enhance accuracy, sensitivity, specificity, ROC curves, and AUC through 10-fold cross-validation. The RF-Boosting tree outperformed the competition in classification and recognition, with an accuracy of 98.9%, sensitivity and specificity of 99.3 and 98.6%, respectively, and an AUC of 0.988., as shown in **Figure 10**. The use of RF features increases data retention, reduces training time, and avoids duplicate data and interference. The combination of LIBS with an RF-Boosting Tree model to detect lung tumour boundaries is a rapid and accurate method.

SUMMARY AND FUTURE PROSPECTUS

In this review we discussed developments in LIBS technologies and critical discoveries on the identification and discrimination of various cancers. LIBS's extraordinary discrimination findings based on different samples (tissues, blood) samples are extremely promising. **Table 1** lists the LIBS technique studies on various cancers published in the literature, organized with varying sample categories. This table also recorded information on the laser, spectrometer, and analytical instruments used in the experiments. LIBS is a valuable and credible method for distinguishing between malignant and benign tissues and classifying normal tissues. A significant research project is to find ways to reduce the gap between LIBS laboratory research and clinical translation.

Any kind of sample can be analyzed using LIBS in a typical laboratory environment. It is vital to prevent any surface

contamination when processing the sample to perform repeatable LIBS analysis. Furthermore, instrumental parameters (such as laser energy and sample surface orientation about the laser focus) must be monitored and maintained during the whole experiment. LIBS can also be used in combination with other spectroscopic techniques, including Raman spectroscopy [78], and laser-induced fluorescence [79, 80]. These multi-modal methods hold massive potential because they can gather detailed information about the samples' composition.

Furthermore, in-depth evaluation and analysis with high precision are needed for various aspects such as the economy, health, and lifestyle. To this end, new methods for medical samples analysis are being tested regularly to keep up with scientific advancements. Preliminary tests on a variety of different tissues or fluids samples have shown extremely impressive findings for LIBS. The number of applications requiring different chemometric data processing has grown significantly in recent years to enhance the system's capability. Chemometrics is also used to solve a variety of practical problems, such as the exploitation of biologically active species, the effective use of biomarkers, the advancement of clinical diagnosis, the monitoring and prediction of a patient's condition, drug design, and the classification of toxic chemical substances [81].

Regarding future developments and practical uses of LIBS in cancer detection and classification, the following suggestions were made: 1) Suitable chemometric methods and preprocessing methods should be used to enhance LIBS calibration and classification accuracy. Chemometrics models' performance, accuracy, and pattern recognition in cancer detection and classification differ depending on the sample type and model type utilized. Further performance improvements of LIBS technology in various application fields, especially in the medical area, will undoubtedly be part of the future advancement of chemometrics analysis of LIBS data. Preprocessing methods combination with chemometrics, we believe, play a critical role in LIBS. 2) For a deeper understanding and practical use, the mechanism of laser-matter interaction for medical samples should be investigated further. While signal enhancement and data processing methods have enhanced efficiency, the mechanisms beyond these methods are still unknown. 3) For successful LIBS analysis, the input data must be of the highest quality, optimizing the experimental parameters and controlling them during LIBS measurements. 4) To achieve the best calssification and discrimination results the sample numbers should be raised in the future.

Finally, this review aims to assist those who wish to use the LIBS technique in a medical setting in gaining a basic understanding of the prerequisites and shortcomings to do a thorough study of this field. The reader is also faced with various chemometrics tools that can be used in LIBS measurements to obtain valid qualitative and quantitative data, especially in different cancers detection and classification.

AUTHOR CONTRIBUTIONS

MK, BI and WX, contributed to conception and design of the study. GT and XC organized the database. KW wrote the first draft of the manuscript. QW wrote sections of the manuscript and reviewed carefully. MA also reviewed the paper. ZZ contribution is the review of the revise version, she also contributed in the literature of LIBS in different cancers, especially designed the **Table 1** in the review manuscript. All authors contributed to manuscript revision, read, and approved the submitted version.

FUNDING

This work was supported by the National Natural Science Foundation of China (62075011) and Graduate Technological Innovation Project of Beijing Institute of Technology (2019CX20026).

REFERENCES

1. Hassanpour SH, Dehghani M. Review of Cancer from Perspective of Molecular. *J Cancer Res Pract* (2017) 4(04):127–9. doi:10.1016/j.jcrpr.2017.07.001
2. Das P, Srivastav AK, Muthukannan MR. A Study on Molecular Targeted Approaches to Cancer Therapy and the Role of Chalcones in Chemoprevention. *Eur J Mol Clin Med* (2021) 8(03):3254–3267. Available from: https://ejmcm.com/article_11701.html.
3. Singh Kainth H, Khandelwal D, Singh R, Singh G, Puri S. Role of Trace Elements in Breast Cancer and Their Characterization Using X-Ray Fluorescence Techniques. In: *Trace Elements and its Effects on Human Health and Disease*. London, UK: IntechOpen (2020). doi:10.5772/intechopen.95491
4. Ladeira LCM, Dos Santos EC, Valente GE, da Silva J, Santos TA, dos Santos Costa Maldonado IR. Could Biological Tissue Preservation Methods Change Chemical Elements Proportion Measured by Energy Dispersive X-ray Spectroscopy? *Biol Trace Elem Res* (2020) 196(1):168–72. doi:10.1007/s12011-019-01909-x
5. Puja P, Vinita NM, Devan U, Velangani AJ, Srinivasan P, Yuvakkumar R, et al. Fluorescence Microscopy-based Analysis of Apoptosis Induced by Platinum Nanoparticles against Breast Cancer Cells. *Appl Organomet Chem* (2020) 34(9):e5740. doi:10.1002/aoc.5740
6. Busser B, Moncayo S, Coll J-L, Sancey L, Motto-Ros V. Elemental Imaging Using Laser-Induced Breakdown Spectroscopy: A New and Promising Approach for Biological and Medical Applications. *Coord Chem Rev* (2018) 358:70–9. doi:10.1016/j.ccr.2017.12.006
7. Meenu S, Sairam ST, Panicker AS, Oommen S, Sankaran R. Comparison of Polymerase Chain Reaction (PCR), Microbiological and Histopathological Observations in the Diagnosis of Endometrial Tuberculosis. *J Obstet Gynecol India* (2020) 70(6):510–5. doi:10.1007/s13224-020-01367-9
8. Santos IP, Barroso EM, Bakker Schut TC, Caspers PJ, van Lanschot CGF, Choi D-H, et al. Raman Spectroscopy for Cancer Detection and Cancer Surgery Guidance: Translation to the Clinics. *Analyst* (2017) 142:3025–47. doi:10.1039/c7an00957g
9. Chen T, Zhang T, Li H. Applications of Laser-Induced Breakdown Spectroscopy (LIBS) Combined with Machine Learning in Geochemical and Environmental Resources Exploration. *Trac Trends Anal Chem* (2020) 133:116113. doi:10.1016/j.trac.2020.116113
10. Harmon RS, Senesi GS. Laser-Induced Breakdown Spectroscopy - A Geochemical Tool for the 21st century. *Appl Geochem* (2021) 128:104929. doi:10.1016/j.apgeochem.2021.104929
11. Arantes de Carvalho GG, Bueno Guerra MB, Adame A, Nomura CS, Oliveira PV, Pereira de Carvalho HW, Jr, et al. Recent Advances in LIBS and XRF for the Analysis of Plants. *J Anal Spectrom* (2018) 33(6):919–44. doi:10.1039/c7ja00293a
12. Thakur SN, Singh JP. Fundamentals of LIBS and Recent Developments. In: *Laser-Induced Breakdown Spectroscopy*. Amsterdam, Netherlands: Elsevier (2020). p. 3–22. doi:10.1016/b978-0-12-818829-3.00001-0

13. de Carvalho LFDCES, Saito Nogueira M. New Insights of Raman Spectroscopy for Oral Clinical Applications. *Analyst* (2018) 143:6037–48. doi:10.1039/c8an01363b
14. Jolivet L, Leprince M, Moncayo S, Sorbier L, Lienemann C-P, Motto-Ros V. Review of the Recent Advances and Applications of LIBS-Based Imaging. *Spectrochimica Acta B: At Spectrosc* (2019) 151:41–53. doi:10.1016/j.sab.2018.11.008
15. Morel S, Leone N, Adam P, Amouroux J. Detection of Bacteria by Time-Resolved Laser-Induced Breakdown Spectroscopy. *Appl Opt* (2003) 42:6184. doi:10.1364/ao.42.006184
16. Rehse SJ, Salimnia H, Miziolek AW. Laser-induced Breakdown Spectroscopy (LIBS): an Overview of Recent Progress and Future Potential for Biomedical Applications. *J Med Eng Technol* (2012) 36(2):77–89. doi:10.3109/03091902.2011.645946
17. Kumar A, Yueh F-Y, Singh JP, Burgess S. Characterization of Malignant Tissue Cells by Laser-Induced Breakdown Spectroscopy. *Appl Opt* (2004) 43(28):5399. doi:10.1364/ao.43.005399
18. Melikechi N, Markushin Y, Connolly DC, Lasue J, Ewusi-Annan E, Makrogiannis S. Age-specific Discrimination of Blood Plasma Samples of Healthy and Ovarian Cancer Prone Mice Using Laser-Induced Breakdown Spectroscopy. *Spectrochimica Acta Part B: At Spectrosc* (2016) 123:33–41. doi:10.1016/j.sab.2016.07.008
19. Gondal MA, Aldakheel RK, Almessiere MA, Nasr MM, Almusairii JA, Gondal B. Determination of Heavy Metals in Cancerous and Healthy colon Tissues Using Laser Induced Breakdown Spectroscopy and its Cross-Validation with ICP-AES Method. *J Pharm Biomed Anal* (2020) 183:113153. doi:10.1016/j.jpba.2020.113153
20. El Sherbini AM, Hagras MM, Farag HH, Mohamed RM. Diagnosis and Classification of Liver Cancer Using LIBS Technique and Artificial Neural Network. *Int J Sci Res* (2015) 4:1153. doi:10.7717/peerj-cs.270/fig-1
21. Teran-Hinojosa E, Sobral H, Sánchez-Pérez C, Pérez-García A, Alemán-García N, Hernández-Ruiz J. Differentiation of Fibrotic Liver Tissue Using Laser-Induced Breakdown Spectroscopy. *Biomed Opt Express* (2017) 8(8):3816–27. doi:10.1364/boe.8.003816
22. Chen X, Li X, Yang S, Yu X, Liu A. Discrimination of Lymphoma Using Laser-Induced Breakdown Spectroscopy Conducted on Whole Blood Samples. *Biomed Opt Express* (2018) 9(3):1057. doi:10.1364/boe.9.001057
23. Chen X, Li X, Yu X, Chen D, Liu A. Diagnosis of Human Malignancies Using Laser-Induced Breakdown Spectroscopy in Combination with Chemometric Methods. *Spectrochimica Acta Part B: At Spectrosc* (2018) 139:63–9. doi:10.1016/j.sab.2017.11.016
24. Chu Y, Chen T, Chen F, Tang Y, Tang S, Jin H, et al. Discrimination of Nasopharyngeal Carcinoma Serum Using Laser-Induced Breakdown Spectroscopy Combined with an Extreme Learning Machine and Random forest Method. *J Anal Spectrom* (2018) 33(12):2083–8. doi:10.1039/c8ja00263k
25. El-Hussein A, Kassem AK, Ismail H, Harith MA. Exploiting LIBS as a Spectrochemical Analytical Technique in Diagnosis of Some Types of Human Malignancies. *Talanta* (2010) 82(2):495–501. doi:10.1016/j.talanta.2010.04.064
26. Wang J, Yang LP, Zhu YY, Hao MZ, Li X. Identification of Cervical Cancer Using Laser-Induced Breakdown Spectroscopy Coupled with Principal Component Analysis and Support Vector Machine. *Lasers Med Sci* (2018) 33:1381–6. doi:10.1007/s10103-018-2500-2
27. Li X, Yang S, Chen X, Yao G, Liu A, Yu X. Multi-elemental Imaging of Breast Cancer Tissues Using Laser-Induced Breakdown Spectroscopy. In: 2019 Conference on Lasers and Electro-Optics Europe & European Quantum Electronics Conference (CLEO/Europe-EQEC). Munich, Germany: IEEE (2019). p. 1. doi:10.1109/cleoe-eqec.2019.8871560
28. Gaudiuso R, Ewusi-Annan E, Melikechi N, Sun X, Liu B, Campesato LF, et al. Using LIBS to Diagnose Melanoma in Biomedical Fluids Deposited on Solid Substrates: Limits of Direct Spectral Analysis and Capability of Machine Learning. *Spectrochimica Acta Part B: At Spectrosc* (2018) 146:106–14. doi:10.1016/j.sab.2018.05.010
29. Cremers DA, Radziemski LJ. *Handbook of Laser-Induced Breakdown Spectroscopy*. Hoboken, NJ, USA: John Wiley & Sons (2013). doi:10.1007/978-3-642-20668-9
30. Han JH, Moon Y, Lee JJ, Choi S, Kim Y-C, Jeong S. Differentiation of Cutaneous Melanoma from Surrounding Skin Using Laser-Induced Breakdown Spectroscopy. *Biomed Opt Express* (2016) 7(1):57. doi:10.1364/boe.7.000057
31. Teng G, Wang Q, Zhang H, Xiangli W, Yang H, Qi X, et al. Discrimination of Infiltrative Glioma Boundary Based on Laser-Induced Breakdown Spectroscopy. *Spectrochimica Acta Part B: At Spectrosc* (2020) 165:105787. doi:10.1016/j.sab.2020.105787
32. Ghasemi F, Parvin P, Hosseini Motlagh NS, Amjadi A, Abachi S. Laser Induced Breakdown Spectroscopy and Acoustic Response Techniques to Discriminate Healthy and Cancerous Breast Tissues. *Appl Opt* (2016) 55(29):8227–35. doi:10.1364/ao.55.008227
33. Ghasemi F, Parvin P, Reif J, Abachi S, Mohebbifar MR, Razzaghi MR. Laser Induced Breakdown Spectroscopy for the Diagnosis of Several Malignant Tissue Samples. *J Laser Appl* (2017) 29(4):042005. doi:10.2351/1.4989376
34. Seifalinezhad A, Bahreini M, Hassani Matin MM, Tavassoli SH. Feasibility Study on Discrimination of Neo-Plastic and Non-neoplastic Gastric Tissues Using Spark Discharge Assisted Laser Induced Breakdown Spectroscopy. *J Lasers Med Sci* (2018) 10(1):64–9. doi:10.15171/jlms.2019.10
35. Yue Z, Sun C, Chen F, Zhang Y, Xu W, Shabbir S, et al. Machine Learning-Based LIBS Spectrum Analysis of Human Blood Plasma Allows Ovarian Cancer Diagnosis. *Biomed Opt Express* (2021) 12(5):2559–74. doi:10.1364/boe.421961
36. Lin X, Sun H, Gao X, Xu Y, Wang Z, Wang Y. Discrimination of Lung Tumor and Boundary Tissues Based on Laser-Induced Breakdown Spectroscopy and Machine Learning. *Spectrochimica Acta Part B: At Spectrosc* (2021) 180:106200. doi:10.1016/j.sab.2021.106200
37. Fahad M, Abrar M. Laser-induced Breakdown Spectroscopic Studies of Calcite (CaCO3) marble Using the Fundamental (1064 Nm) and Second (532 Nm) Harmonic of a Nd:YAG Laser. *Laser Phys* (2018) 28(8):085701. doi:10.1088/1555-6611/aac5cd
38. Martínez-Hernández A, Oujja M, Sanz M, Carrasco E, Detalle V, Castillejo M. Analysis of Heritage Stones and Model wall Paintings by Pulsed Laser Excitation of Raman, Laser-Induced Fluorescence and Laser-Induced Breakdown Spectroscopy Signals with a Hybrid System. *J Cult Heritage* (2018) 32:1–8. doi:10.1016/j.culher.2018.02.004
39. Verma A. *Speculating the Impact of Physics in Medical World* (2020). doi:10.1016/j.ejmp.2018.06.183
40. Indini A, Nigro O, Lengyel CG, Ghidini M, Petrillo A, Lopez S, et al. Immune-Checkpoint Inhibitors in Platinum-Resistant Ovarian Cancer. *Cancers* (2021) 13(7):1663. doi:10.3390/cancers13071663
41. Is W, Cancer O. *What Is Ovarian Cancer?* (2021). 1–14. Available from: https://www.cdc.gov/cancer/ovarian/basic_info/.
42. Prat J, D'Angelo E, Espinosa I. Ovarian Carcinomas: at Least Five Different Diseases with Distinct Histological Features and Molecular Genetics. *Hum Pathol* (2018) 80:11–27. doi:10.1016/j.humpath.2018.06.018
43. Ohmachi K, Ogura M, Suehiro Y, Ando K, Uchida T, Choi I, et al. A Multicenter Phase I Study of Inebilizumab, a Humanized Anti-CD19 Monoclonal Antibody, in Japanese Patients with Relapsed or Refractory B-Cell Lymphoma and Multiple Myeloma. *Int J Hematol* (2019) 109(6):657–64. doi:10.1007/s12185-019-02635-9
44. Stecco A, Buemi F, Iannessi A, Carriero A, Gallamini A. Current Concepts in Tumor Imaging with Whole-Body MRI with Diffusion Imaging (WB-MRI-DWI) in Multiple Myeloma and Lymphoma. *Leuk Lymphoma* (2018) 59(11):2546–56. doi:10.1080/10428194.2018.1434881
45. Graklanov V, Popov V. Vitamin D Levels in Patients with Non-hodgkin Lymphoma/diffuse Large B-Cell Lymphoma, Chronic Lymphocytic Leukemia and Multiple Myeloma. *J Int Med Res* (2020) 48(7):030006052094342. doi:10.1177/0300060520943421
46. Ravi P, KumarCerhan SK, Maurer JRMJ, Ansell DSM, Rajkumar SV. Defining Cure in Multiple Myeloma: a Comparative Study of Outcomes of Young Individuals with Myeloma and Curable Hematologic Malignancies. *Blood Cancer J* (2018) 8(3):1–7. doi:10.1038/s41408-018-0065-8
47. Bongaarts J. World Health Organization Health in 2015: From MDGs, Millennium Development Goals, to SDGs, Sustainable Development Goals Geneva: WHO Press, 2016. 212 P. $60.00 (pbk.). *Popul Develop Rev* (2016) 42:575. doi:10.1111/padr.12006
48. Chu Y, Chen F, Sheng Z, Zhang D, Zhang S, Wang W, et al. Blood Cancer Diagnosis Using Ensemble Learning Based on a Random Subspace Method in Laser-Induced Breakdown Spectroscopy. *Biomed Opt Express* (2020) 11(8):4191–202. doi:10.1364/boe.395332

49. Bray F, Ferlay J, Soerjomataram I, Siegel RL, Torre LA, Jemal A. Erratum: Global Cancer Statistics 2018: GLOBOCAN Estimates of Incidence and Mortality Worldwide for 36 Cancers in 185 Countries. *CA A Cancer J Clin* (2020) 70:313. doi:10.3322/caac.21609
50. Turner N, Ware O, Bosenberg M. Genetics of Metastasis: Melanoma and Other Cancers. *Clin Exp Metastasis* (2018) 35(5):379–91. doi:10.1007/s10585-018-9893-y
51. Moon Y, Han JH, Choi J-h., Shin S, Kim Y-C, Jeong S. Mapping of Cutaneous Melanoma by Femtosecond Laser-Induced Breakdown Spectroscopy. *J Biomed Opt* (2018) 24(03):1. doi:10.1117/1.jbo.24.3.031011
52. Srivastava E, Jang H, Shin S, Choi J, Jeong S, Hwang E. Weighted-averaging-based Classification of Laser-Induced Breakdown Spectroscopy Measurements Using Most Informative Spectral Lines. *Plasma Sci Technol* (2019) 22(1): 015501. doi:10.1088/2058-6272/ab481e
53. Khan MN, Wang Q, Idrees BS, Teng G, Cui X, Wei K. Discrimination of Melanoma Using Laser-Induced Breakdown Spectroscopy Conducted on Human Tissue Samples. *J Spectrosc* (2020) 2020:1–11. doi:10.1155/2020/8826243
54. Gaudiuso R, Ewusi-Annan E, Melikechi N, Sun X, Liu B, Campesato LF, et al. Using LIBS to Diagnose Melanoma in Biomedical Fluids Deposited on Solid Substrates: Limits of Direct Spectral Analysis and Capability of Machine Learning. *Spectrochimica Acta Part B: At Spectrosc* (2018) 146(April): 106–14. doi:10.1016/j.sab.2018.05.010
55. Li X, Ramadori P, Pfister D, Seehawer M, Zender L, Heikenwalder M, The Immunological and Metabolic Landscape in Primary and Metastatic Liver Cancer, *Nat Rev Cancer* (2021) 21:541–57. doi:10.1038/s41568-021-00383-9
56. Sun M, Tan, L, Hu M. The Role of Autophagy in Hepatic Fibrosis. *Am J Transl Res* (2021) 13(6):5747–57. doi:10.1007/s10067-020-05111-6
57. Teran-Hinojosa E, Sobral H, Sánchez-Pérez C, Pérez-García A, Alemán-García N, Hernández-Ruiz J. Differentiation of Fibrotic Liver Tissue Using Laser-Induced Breakdown Spectroscopy. *Biomed Opt Express* (2017) 8(8):3816. doi:10.1364/boe.8.003816
58. Myronenko A. 3D MRI Brain Tumor Segmentation Using Autoencoder Regularization. *Int MICCAI Brainlesion Workshop* (2019) 11384:311–20. doi:10.1007/978-3-030-11726-9_28
59. Ari A, Hanbay D. Deep Learning Based Brain Tumor Classification and Detection System. *Turk J Elec Eng Comp Sci* (2018) 26(5):2275–86. doi:10.3906/elk-1801-8
60. Abiwinanda N, Hanif M, Hesaputra ST, Handayani A, Mengko TR. Brain Tumor Classification Using Convolutional Neural Network. *World congress Med Phys Biomed Eng* (2019) 68(1):183–9. doi:10.1007/978-981-10-9035-6_33
61. Teng G, Wang Q, Yang H, Qi X, Zhang H, Cui X, et al. Pathological Identification of Brain Tumors Based on the Characteristics of Molecular Fragments Generated by Laser Ablation Combined with a Spiking Neural Network. *Biomed Opt Express* (2020) 11(8):4276–89. doi:10.1364/boe.397268
62. Chen Y-P, Chan ATC, Le Q-T, Blanchard P, Sun Y, Ma J. Nasopharyngeal Carcinoma. *Lancet (London, England)* (2019) 394(10192):64–80. doi:10.1016/b978-0-12-814936-2.00001-8
63. Cui Q, Feng F-T, Xu M, Liu W-S, Yao Y-Y, Xie S-H, et al. Nasopharyngeal Carcinoma Risk Prediction via Salivary Detection of Host and Epstein-Barr Virus Genetic Variants. *Oncotarget* (2017) 8(56):95066–74. doi:10.18632/oncotarget.11144
64. Chu YW, Chen F, Tang Y, Chen T, Yu YX, Jin HL, et al. Diagnosis of Nasopharyngeal Carcinoma from Serum Samples Using Hyperspectral Imaging Combined with a Chemometric Method. *Opt Express* (2018) 26(22):28661–71. doi:10.1364/oe.26.028661
65. Chu Y, Chen T, Chen F, Tang Y, Tang S, Jin H, et al. Discrimination of Nasopharyngeal Carcinoma Serum Using Laser-Induced Breakdown Spectroscopy Combined with an Extreme Learning Machine and Random forest Method. *J Anal Spectrom* (2018) 33(12):2083–8. doi:10.1039/c8ja00263k
66. Marc A, Weiderpass E, Bruni L, de Sanjosé S, Saraiya M, Ferlay J, et al. Articles Estimates of Incidence and Mortality of Cervical Cancer in 2018 : a Worldwide Analysis. *Lancet Glob Health* (2019) 19:1–13. doi:10.1016/S2214-109X(19)30482-6
67. Bray F, Ferlay J, Soerjomataram I, Siegel RL, Torre LA, Jemal A. Global Cancer Statistics 2018: GLOBOCAN Estimates of Incidence and Mortality Worldwide for 36 Cancers in 185 Countries. *CA: A Cancer J Clinicians* (2018) 68(6): 394–424. doi:10.3322/caac.2160910.3322/caac.21492
68. Seifalinezhad A, Bahreini M, Hassani Matin MM, Tavassoli SH. Feasibility Study on Discrimination of Neo-Plastic and Non-neoplastic Gastric Tissues Using Spark Discharge Assisted Laser Induced Breakdown Spectroscopy. *J Lasers Med Sci* (2019) 10(1):64–9. doi:10.15171/jlms.2019.10
69. Ghasemi F, Parvin P, Hosseini Motlagh NS, Amjadi A, Abachi S. Laser Induced Breakdown Spectroscopy and Acoustic Response Techniques to Discriminate Healthy and Cancerous Breast Tissues. *Appl Opt* (2016) 55(29):8227. doi:10.1364/ao.55.008227
70. Wei H, Zhao Z, Lin Q, Duan Y. Study on the Molecular Mechanisms against Human Breast Cancer from Insight of Elemental Distribution in Tissue Based on Laser-Induced Breakdown Spectroscopy (LIBS). *Biol Trace Elem Res* (2020) 199:1686–92. doi:10.1007/s12011-020-02292-8
71. Tarver T, Albano J, Samuels A, Ward ME, Thum JM. Cancer Facts & Figures 2012. American Cancer Society (ACS). *J Consumer Health Internet* (2012) 16: 366–7. doi:10.1080/15398285.2012.701177
72. Ferguson JL, Turner SP. Bone Cancer: Diagnosis and Treatment Principles. *Am Fam Physician* (2012) 98(4):205–13. Available from: https://pubmed.ncbi.nlm.nih.gov/30215968/.
73. PDQ Pediatric Treatment Editorial Board. Ewing Sarcoma Treatment (PDQ®). In: *PDQ Cancer Information Summaries [Internet]*. Bethesda, Maryland: National Cancer Institute United States (2018). Available from: https://pubmed.ncbi.nlm.nih.gov/26389350/.
74. Gill RK, Smith ZJ, Panchal RR, Bishop JW, Gandour-Edwards R, Wachsmann-Hogiu S. Preliminary fsLIBS Study on Bone Tumors. *Biomed Opt Express* (2015) 6(12):4850–8. doi:10.1364/boe.6.004850
75. Grothey A, Sobrero AF, Shields AF, Yoshino T, Paul J, Taieb J, et al. Duration of Adjuvant Chemotherapy for Stage III Colon Cancer. *N Engl J Med* (2018) 378(13):1177–88. doi:10.1056/nejmoa1713709
76. Visser MPJ, van Grimbergen I, Hölters J, Barendregt WB, Vermeer LC, Vreuls W, et al. Performance Insights of Endobronchial Ultrasonography (EBUS) and Mediastinoscopy for Mediastinal Lymph Node Staging in Lung Cancer. *Lung Cancer* (2021) 156:122–8. doi:10.1016/j.lungcan.2021.04.003
77. Osarogiagbon RU, Smeltzer MP, Faris NR, Ray MA, Fehnel C, Ojeabulu P, et al. Outcomes after Use of a Lymph Node Collection Kit for Lung Cancer Surgery: A Pragmatic, Population-Based, Multi-Institutional, Staggered Implementation Study. *J Thorac Oncol* (2021) 16(4):630–42. doi:10.1016/j.jtho.2020.12.025
78. Dhanada VS, George SD, Kartha VB, Chidangil S, Unnikrishnan VK. Hybrid LIBS-Raman-LIF Systems for Multi-Modal Spectroscopic Applications: a Topical Review. *Appl Spectrosc Rev* (2021) 56(6):1–29. doi:10.1080/05704928.2020.1800486
79. Shen XK, Wang H, Xie ZQ, Gao Y, Ling H, Lu YF. Detection of Trace Phosphorus in Steel Using Laser-Induced Breakdown Spectroscopy Combined with Laser-Induced Fluorescence. *Appl Opt* (2009) 48(13):2551–8. doi:10.1364/ao.48.002551
80. Li J, Hao Z, Zhao N, Zhou R, Yi R, Tang S, et al. Spatially Selective Excitation in Laser-Induced Breakdown Spectroscopy Combined with Laser-Induced Fluorescence. *Opt Express* (2017) 25(5):4945–51. doi:10.1364/oe.25.004945
81. Peris-Díaz MD, Krężel A. A Guide to Good Practice in Chemometric Methods for Vibrational Spectroscopy, Electrochemistry, and Hyphenated Mass Spectrometry. *Trac Trends Anal Chem* (2021) 135:116157. doi:10.1016/j.trac.2020.116157

Conflict of Interest: The authors declare that the research was conducted in the absence of any commercial or financial relationships that could be construed as a potential conflict of interest.

frontiers in Physics

ORIGINAL RESEARCH
published: 04 February 2022
doi: 10.3389/fphy.2022.835189

Measurements of Atmospheric Water Vapor by a 1.316 µm Optical Fiber Laser Heterodyne Radiometer

Jun Huang[1,2,3], *Yinbo Huang*[1,3], *Xingji Lu*[1,3]*, *Dandan Liu*[4], *Zihao Yuan*[1,2,3], *Gang Qi*[1,2,3] *and Zhensong Cao*[1,3]

[1]Key Laboratory of Atmospheric Optics, Anhui Institute of Optics and Fine Mechanics, HFIPS, Chinese Academy of Sciences, Hefei, China, [2]Science Island Branch of Graduate School, University of Science and Technology of China, Hefei, China, [3]Advanced Laser Technology Laboratory of Anhui Province, Hefei, China, [4]College of Electrical and Optoelectronic Engineering, West Anhui University, Luan, China

A passive optical fiber laser heterodyne radiometer prototype with a semiconductor laser near 1.316 µm as the local oscillator was built, parameters of the prototype have been optimized. Using the prototype, the water vapor concentration in the atmospheric column was measured with a spectral resolution of 0.009 cm^{-1} in late October and early November of 2020, the collection time was approximately 3 min, and the signal-to-noise ratio was better than 120. The water vapor column concentration and profiles were inversed based on the optimal estimation method. Compared with the measurement of the Fourier transform spectrometer (EM27/SUN) which was performed simultaneously, the inversion results deviated by less than 14%, and the variation trend of the water vapor concentration showed good consistency. It is demonstrated that the 1.316 µm optical fiber laser heterodyne radiometer possesses good stability and accuracy in the field measurement of atmospheric water vapor concentration.

Keywords: laser heterodyne, optical fiber, water vapor concentration, optimal estimation method, field experiment

OPEN ACCESS

Edited by:
Yufei Ma,
Harbin Institute of Technology, China

Reviewed by:
Chuanliang Li,
Taiyuan University of Science and Technology, China
Ying He,
Harbin Institute of Technology, China

***Correspondence:**
Xingji Lu
xjlu@aiofm.ac.cn

Specialty section:
This article was submitted to Optics and Photonics, a section of the journal Frontiers in Physics

Received: *14 December 2021*
Accepted: *14 January 2022*
Published: *04 February 2022*

Citation:
Huang J, Huang Y, Lu X, Liu D, Yuan Z, Qi G and Cao Z (2022) Measurements of Atmospheric Water Vapor by a 1.316 µm Optical Fiber Laser Heterodyne Radiometer. Front. Phys. 10:835189. doi: 10.3389/fphy.2022.835189

INTRODUCTION

Water vapor is an important greenhouse gas (GHG) that absorbs the most radiation in the atmosphere and contributes approximately 60% of the total radiative forcing [1]. In the context of global warming, the water vapor concentration and temperature will rise due to the increase in each other, forming a positive feedback relationship. It will lead to changes in the water vapor concentration in the upper troposphere (5–10 km) [2]. Therefore, the measurement and long-term monitoring of water vapor concentration in the upper atmosphere are of great significance for the study of the above problems. In addition to global warming, in the field of optoelectronic engineering, besides the effect of scattering and refraction of atmospheric particles, the absorption of atmospheric molecules is also the key to the continuous decay of laser energy during the propagation process. The absorption of laser energy by water vapor will induce thermal blooming and laser nonlinear distortion, which can seriously affect the effect of laser propagation [3].

After decades of effort, several approaches have been proposed and played unique roles in the long-term monitoring of water vapor concentrations, such as satellite remote sensing, LIDAR, and sounding balloons [4–6], these approaches are suitable for different scenarios. The satellite detection range is wide, while the temporal and spatial resolution is low. Although LIDAR detection accuracy is high, the detection range is limited. The sounding balloon can simultaneously detect a variety of atmospheric parameters and detection heights up to 30 km, but the cost is high, and the path is not controllable [7]. A

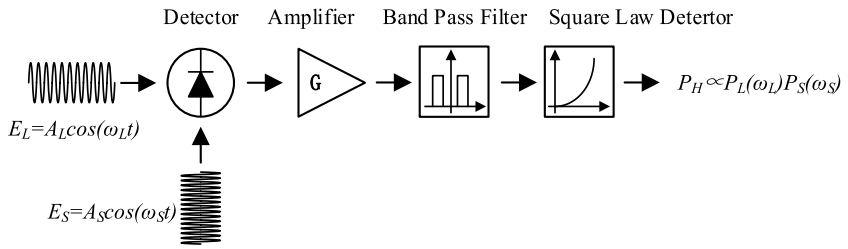

FIGURE 1 | Schematic diagram of the principle of laser heterodyne.

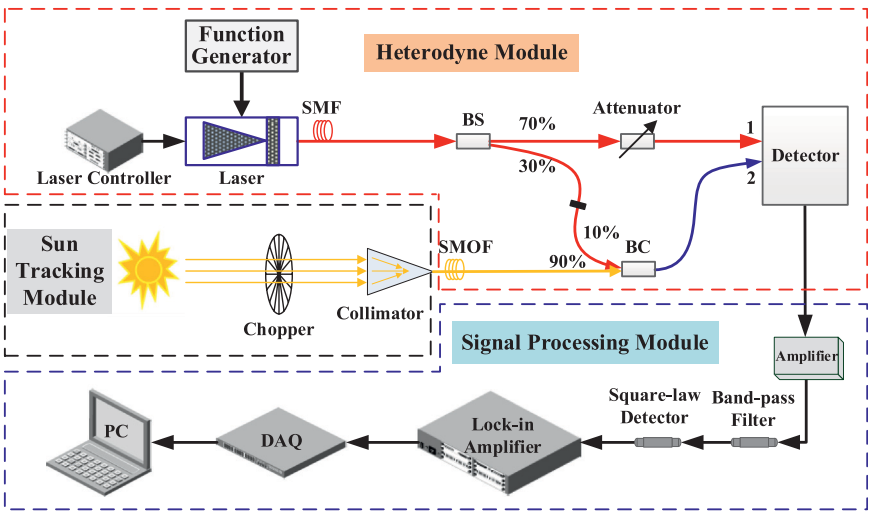

FIGURE 2 | Schematic diagram of the LHR.

ground-based Fourier transform spectrometer with high resolution is capable of trace gas measurement in atmospheric columns, but the device is usually large and expensive.

Laser spectroscopy has been widely used in trace gas detection. The detection sensitivity is up to ppt level [8, 9] and the volume is getting smaller [10, 11]. In the measurement of atmospheric trace gases, laser heterodyne radiometers (LHRs) have been used extensively, because of their inherent high spectral resolution ($\upsilon/\Delta\upsilon$ up to approximately 10^8), easy system integration, and other characteristics [12]. In the atmosphere, the spectral width of molecular spectroscopy is affected by temperature, pressure, etc. The spectral resolution of LHR is generally better than 0.01 cm^{-1}. Therefore, the absorption information of atmospheric molecules in a low-pressure environment can be measured. On the other hand, the measurement results and assumptions about the high-altitude water vapor concentration can be verified.

With the development of optical fiber communication technology, the production process of near-infrared fiber is very mature, and its price is relatively low. This facilitates the development of compact optical fiber LHR. The optical fiber structure is convenient to build and adjust and has a strong vibration and deformation resistance, and the system will be more stable. In recent years, research on optical fiber LHR has made some progress. In 2014, Wilson EL et al. developed a 1,573.6 nm optical fiber LHR to achieve high sensitivity measurement of CO_2 absorption spectra [13], and in 2019, they developed a portable and autonomous 1.64 μm LHR [14]. In 2014, Rodin A et al. used a 1.65 μm optical fiber LHR to achieve absorption measurements of CH_4 and CO_2 with a signal-to-noise ratio (SNR) of 120 with an exposure time of 10 min [15]. The groups of Gao X and Kan R also reported the study of optical fiber LHR [16, 17]. However, the above studies generally focus on the measurement of carbon-containing GHGs, and there are few studies on the content and characteristics of water vapor concentration. As a GHG whose concentration changes rapidly in the atmosphere, the measurement of water vapor concentration requires a high measurement rate while ensuring the SNR of the instrument.

We have accumulated some experience in the measurement of absorption spectra of various atmospheric molecules in several wavelengths [18–20]. In this paper, the semiconductor laser emitting at 1.316 μm was used as the local oscillator, according to our knowledge, the wavelength of the local oscillator is the shortest of

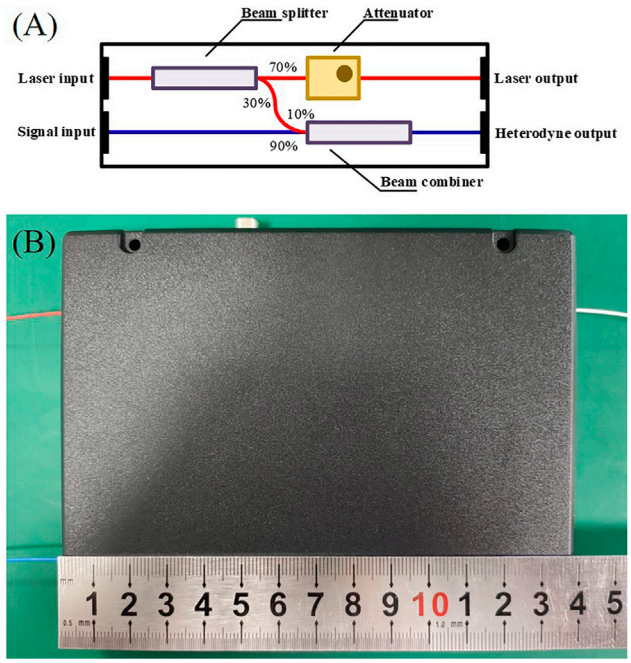

FIGURE 3 | Structure diagram **(A)** and physical diagram **(B)** of the heterodyne module.

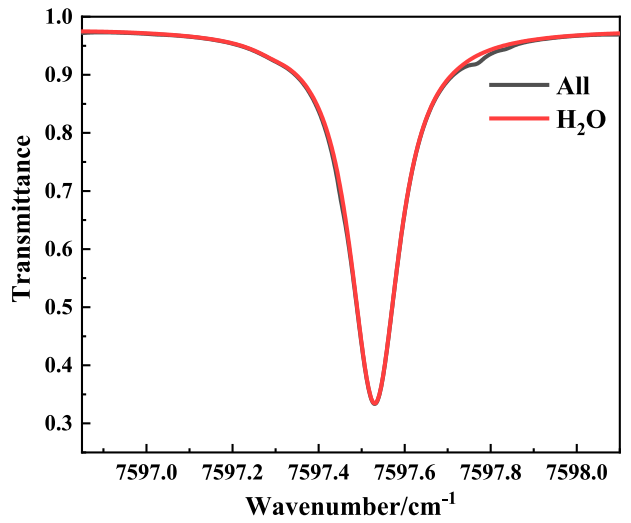

FIGURE 4 | Simulation results of atmospheric molecular absorption in the measurement range.

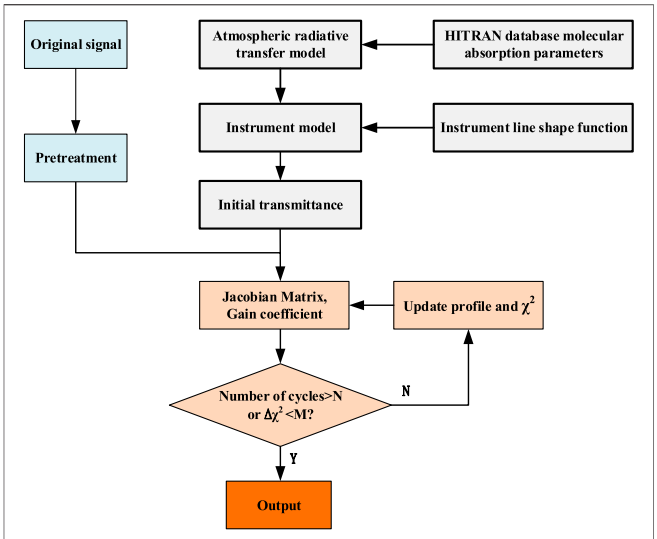

FIGURE 5 | Inversion process of atmospheric molecular concentration based on the OEM.

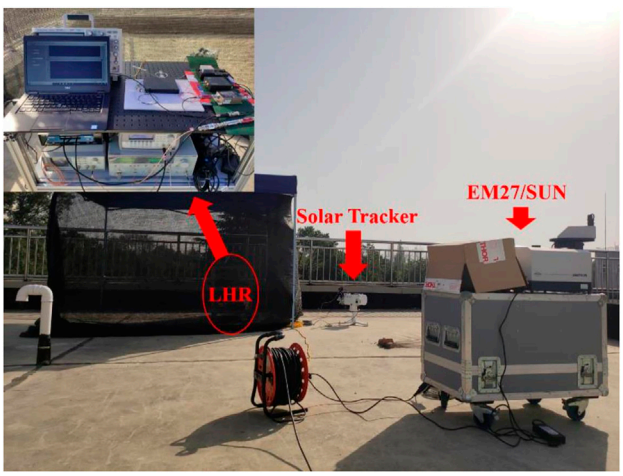

FIGURE 6 | Field measurements for water vapor by the LHR and EM27/SUN.

all publications. The 1.316 μm region is rich in water vapor transitions with suitable line intensities, which provides a favorable condition for the measurement of water vapor concentration in the atmosphere column. The required optoelectronic devices are commercially available, which provides many options for the design and development of LHRs. To evaluate the accuracy of the LHR on water vapor concentration measurement, a Fourier transform infrared spectrometer (Brucker, EM27/SUN) with a resolution of 0.5 cm^{-1} [21] was used to perform simultaneous measurements.

INSTRUMENT DESIGN AND DATA PROCESSING

The principle of laser heterodyne is similar to that of radio. A laser beam is used as the local oscillator to beat with the signal containing information, and the heterodyne signal is generated on the mixer. It can realize the amplification of the signal by the local oscillator [12, 22, 23]. The basic principle is shown in **Figure 1**.

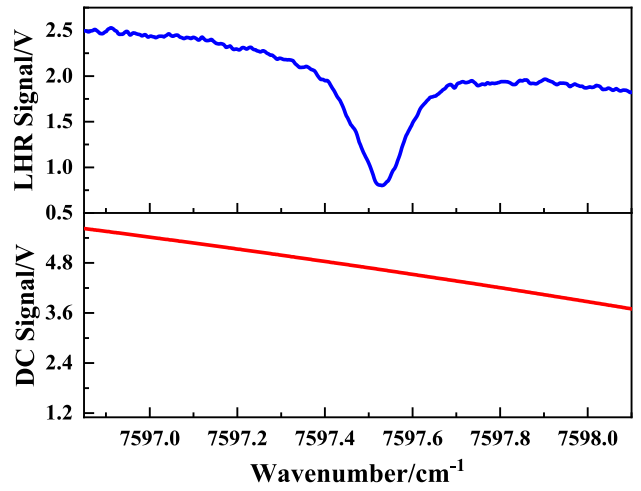

FIGURE 7 | Spectral signal of the LHR and DC signal of the local oscillator.

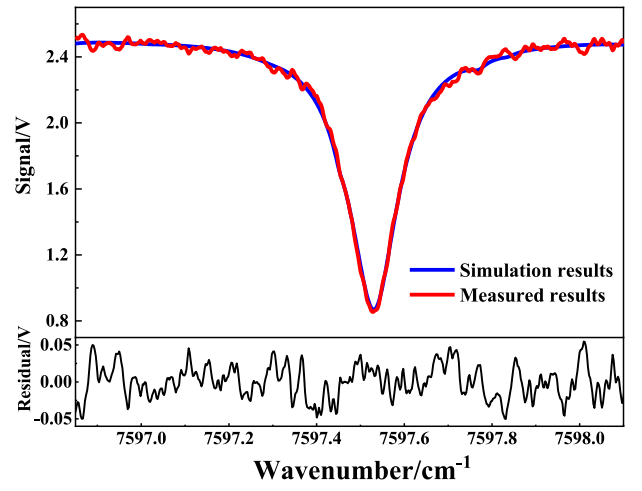

FIGURE 9 | Measured and simulated water vapor absorption spectra and residuals.

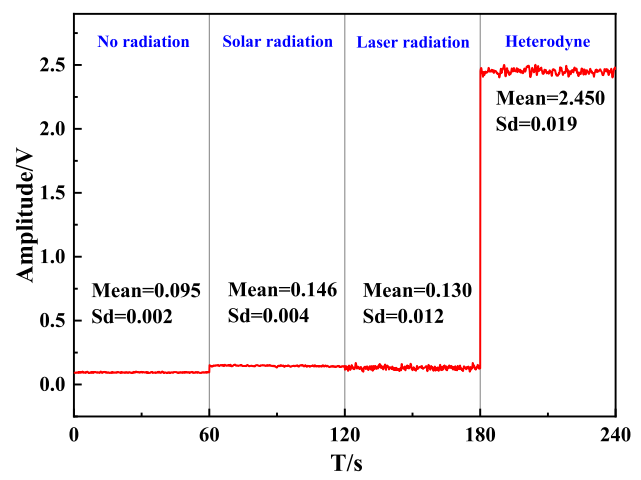

FIGURE 8 | The noise of LHR and the standard deviation of noise in four cases.

According to the principle of laser heterodyne, the power of the heterodyne signal is proportional to the power of the local oscillator and signal [22, 23].

$$P_H \propto P_L(\omega_L)P_S(\omega_S) \tag{1}$$

In heterodyne detection, the signal is generally weak, while the intensity of the local oscillator is several orders of magnitude higher than that of the signal. Therefore, the local oscillator has a strong amplification effect on the signal, which can achieve highly sensitive spectral detection.

The system structure of the prototype is schematically shown in **Figure 2**. The solar tracker and the attached light collection devices realize the stable tracking and collection of sunlight, which contains the absorption information of atmospheric molecules. The heterodyne module combines the collected sunlight with the local oscillator to generate the heterodyne signal. The signal processing technology is used to amplify, bandpass filter, and square-law detect the heterodyne signal and finally realize the output and acquisition of the heterodyne spectral signal.

In the solar tracking module, the tracking accuracy of the solar tracker (EKO, STR21G) is higher than 0.01°. Its built-in GPS sensor provides precise position state parameters for the initial alignment to track the Sun, and a four-quadrant sensor compensates for geometric positioning deviations. The sunlight is amplitude modulated by a chopper (SCITEC, 300CD) with a chopping frequency of approximately 1 kHz. The modulated sunlight is collected by a collimator (Thorlabs, F810APC-1310) and coupled directly into the single-mode fiber (SMF-28e), the attenuation of the fiber at 1,316 nm is less than 0.32 dB/km. The fiber interface type is FC/APC, which has an 8° polished end face to reduce the additional interference caused by light return reflections on the system.

The heterodyne module consists of a laser, beam combiner, beam splitter, attenuator, and photodetector devices. The central wavelength of the semiconductor laser (NTT, NLK1B5EAAA) is 1,315 nm with an output power of 25 mW (T = 25°C, I = 90 mA). The spectral linewidth of the laser is approximately 2 MHz, and the side mode suppression ratio is greater than 40 dB. The wavelength stability of the local oscillator was recorded by a wavelength meter (Bristol Instruments, 621A). The wavelength fluctuation during sampling is less than 0.0007 cm^{-1}. Through tests and considering the detector saturation threshold, the specific beam splitting ratio and beam combining ratio are shown in **Figure 2**. 70% of the local oscillator is attenuated by the attenuator and then enters input channel 1 of the balanced detector (Thorlabs, PDB470C-AC), and the remaining light passes through the 10% channel of the beam combiner and combines with sunlight from the 90% channel of the beam combiner, and the combined beam is fed into input channel 2 of the detector to yield the heterodyne signal. In LHR, the energy of the local oscillator is sufficient or even exceeds the demand, and the

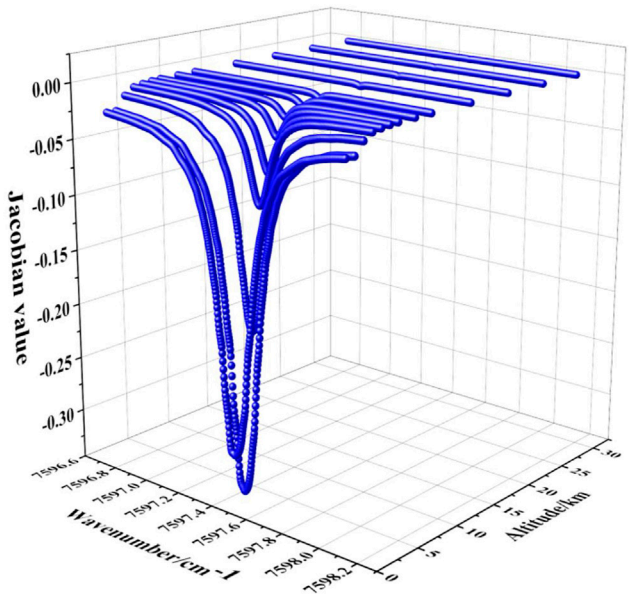

FIGURE 10 | The Jacobian matrix of water vapor in the wavelength scanning range.

fiber it passes through generally needs to increase the attenuation ratio or add an adjustable attenuator. The intensity of the signal light is weak and insufficient, so the transmittance of the channel of signal light input in the combiner is 90%, which is done to reduce the attenuation of the signal light as much as possible. The bandwidth (3 dB) of radio frequency (RF) output of the balanced detector is 100 Hz–400 MHz. It can effectively suppress the common-mode signal and amplify the differential-mode signal, which is suitable for the measurement of weak signals. According to the theory of heterodyne detection, the spot of the local oscillator and signal light should be equal in size and completely coincide, otherwise, the noncoincidence part will generate noise and contribute nothing to the useful signal, optical fiber structure is able to avoid the noise caused by spot mismatch. Compared to traditional free space versions, optical fibers can make the LHR more stable, compact, and coupling efficient. **Figure 3** shows the integrated design of the heterodyne module.

The signal processing module includes an RF amplifier, bandpass filter, square-law detector, lock-in amplifier, and acquisition card. The amplification gain of the RF amplifier (Spectrum, SPA.1411) is up to 100, and the bandwidth is 200 MHz. The electronic filter bandwidth is limited to 10–80 MHz by combining a high pass 10 MHz and a low pass 80 MHz filter. The spectral resolution of the system was approximately 0.009 cm^{-1} based on the instrument line function theory [18, 24]. The lock-in amplifier (Sine Scientific Instrument, OE1201) uses the chopping frequency of the chopper as the reference signal for signal demodulation, with an integration time of 30 ms and a sensitivity of 1 mV. The output signal of the lock-in amplifier is captured by the acquisition card and then recorded by a computer for real-time display and storage.

The inversion of gas concentration generally contains two processes: 1) constructing the atmospheric radiative transfer model (ARTM) and instrument model to simulate the convolution process of the solar spectrum with the atmospheric system and the spectral measurement system to obtain the simulated

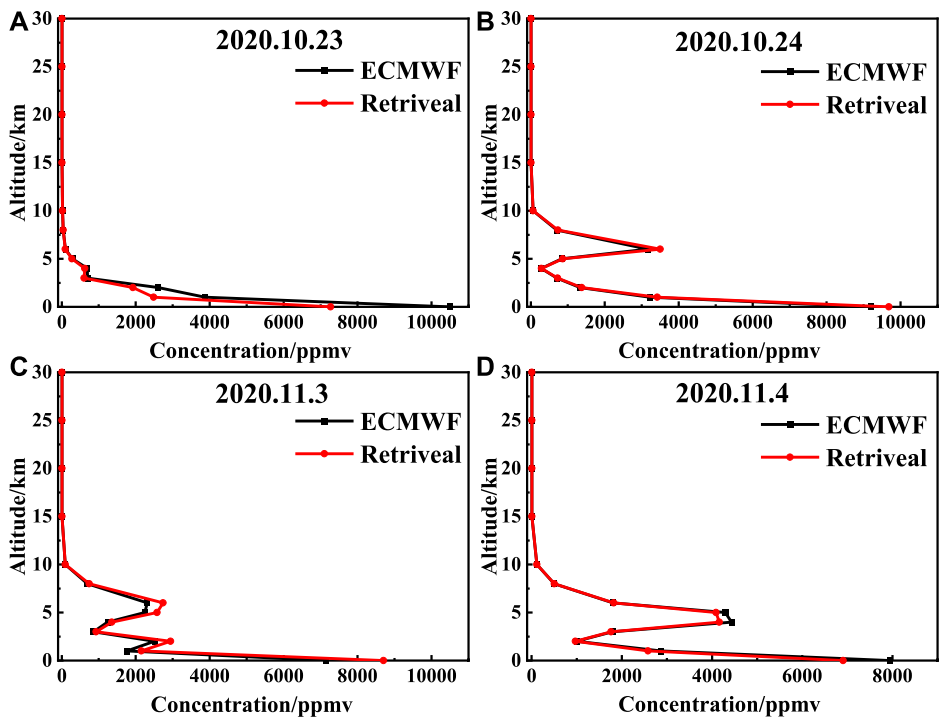

FIGURE 11 | Profiles of water vapor concentration in the atmosphere. **(A)**The variation of water vapor concentration with altitude is smooth. The higher the altitude, the lower the water vapor concentration. **(B–D)** Water vapor concentration has a maximum value in 5–8 km, which may be due to the strong water vapor transport process in the high altitude.

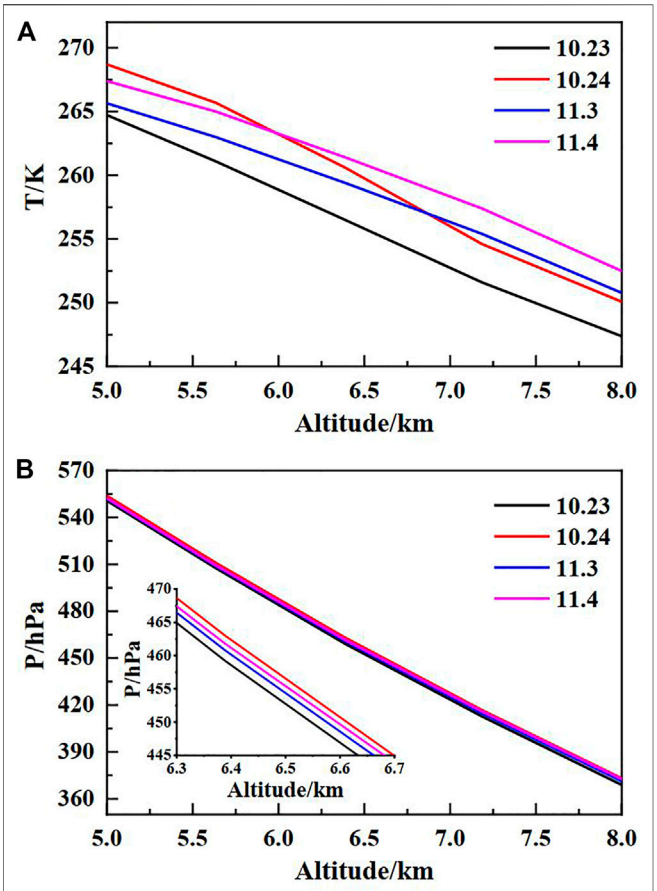

FIGURE 12 | Temperature **(A)** and pressure **(B)** curves for 5–8 km during the experimental period.

spectrum and 2) iterating the measured spectrum and the simulated spectrum in a loop according to the constraints to obtain the inversion results.

The ARTM can be obtained by processing molecular spectral line parameters from the HITRAN database with the line-by-line integrated radiative transfer model (LBLRTM), which is the prerequisite for spectral line selection and gas concentration inversion. The absorption of atmospheric molecules in the measurement range (7596.85–7598.10 cm^{-1}) was simulated with the United States Standard Atmospheric (1976) at the zenith angle of 45°. The simulation results are shown in **Figure 4**. There is a suitable absorption feature of water vapor with a transition of 7597.53 cm^{-1} [$S = 3.31 \times 10^{-24}$ $cm^{-1}/(molec \cdot cm^{-2})$] for measurement. Within the range, the absorption of other molecules only slightly affects the right wing range, and the impact is easily deducted during data processing.

The water vapor concentration inversion algorithm adopts the principle of the optimal estimation method (OEM), which was proposed by Rodgers CD based on the Bayesian statistical method [25]. The measured spectral data need to be preprocessed before inversion by the OEM, which contains a noise component, background offset, and DC modulation component of the local oscillator. Therefore, it is necessary to remove the influence of these factors for concentration inversion. The flow of the inversion is shown in **Figure 5**. According to the OEM for the inversion of the spectral data, the Jacobian matrix and gain coefficient need to be calculated. The Jacobian matrix characterizes the sensitivity of the transmittance or optical thickness to the gas concentration, which is calculated by the LBLRTM. The gain coefficient is obtained from the preprocessed spectral data and the initial transmittance. The Jacobian matrix is updated with each iteration because the sensitivity of different optical thicknesses to gas concentration changes due to the change in gas concentration. If the loop residual reaches the exit condition, the loop will be terminated, and the result will be shown. If the exit condition is not satisfied, the loop iterations continue until the exit condition is fulfilled. The output result is the water vapor vertical profile, and the column concentration of water vapor is obtained by integrating the concentration profile.

RESULTS AND COMPARISON

From 2020.10.23 to 2020.11.4, the water vapor absorption spectra were measured on Science Island in Hefei (N31.82°, E117.22°) by the 1.316 μm optical fiber LHR. Meanwhile, the EM27/SUN was used as a contrasting instrument to measure at the same place. **Figure 6** shows the actual situation of the field experiment, with the LHR on the left and the EM27/SUN on the right. For the LHR, the time of the wavelength scanning was 30 s, and the data were averaged 6 times, so the acquisition time was approximately 3 min.

The measurements were interrupted for a few days by cloudy and rainy weather, but it also gave more interesting weather-related features to the water vapor concentration profiles and column concentration variations. **Figure 7** shows the water vapor absorption spectral signal and the DC signal, and **Figure 8** shows the noise level and the corresponding standard deviation of the LHR for the four different cases. It can be seen from **Figure 7** that the change in the local oscillator power causes the skew of the spectral signal baseline, and this effect can be deducted in the data processing process. Overall, the SNR is better than 120. Of course, the SNR can be improved by increasing the average times of data appropriately, but in the case of the current SNR, the collection time of approximately 3 min is more conducive to the timely response to the concentration changes of water vapor. By comparing the noise in the four different cases, the main noise of the system is the shot noise caused by the local oscillator, which accounts for more than 60% of the total noise.

The DC modulation was subtracted from the spectral signal measured by the LHR and compared with the simulation results under the same conditions. The results are shown in **Figure 9**, where the red curve is the measured result, the blue curve is the simulated result, and the black curve is the residual between them. The measured results are in good agreement with the simulated results, and the maximum deviation is approximately 2%.

Since the gas concentration is negatively related to the transmittance, each element of the Jacobian matrix is nonpositive. The calculation results of the Jacobian matrix are shown in **Figure 10**. The atmosphere below 30 km is divided into 13 layers, each layer has different attenuation coefficients for water vapor. Since the water

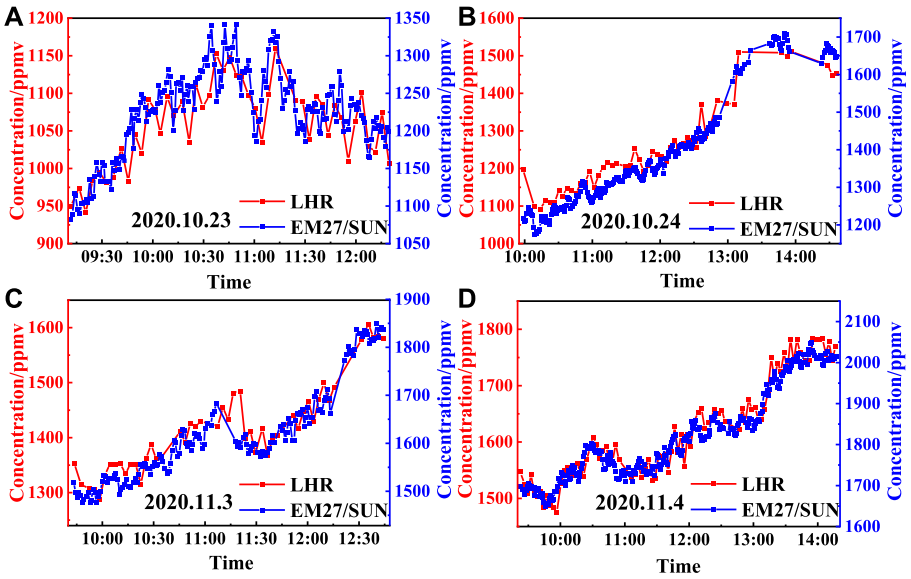

FIGURE 13 | Inversion results of water vapor concentration in the atmosphere. **(A)** The water vapor concentration measured by LHR and EM27/SUN changed rapidly and showed an unstable state. **(B–D)** Water vapor concentration showed a stable increasing trend during the measurement period.

TABLE 1 | Comparison of the LHR and EM27/SUN measurement results.

Date	Mean (ppmv)		Deviation	Correlation
	LHR	EM27/SUN		
10.23	1059.4	1225.4	13.5%	0.660
10.24	1253.9	1391.1	9.9%	0.944
11.3	1416.0	1617.0	12.4%	0.898
11.4	1620.1	1822.2	11.1%	0.928

vapor is mainly concentrated near the ground, the attenuation of the transmission by water vapor is also greater, so the layers are relatively fine. The intervals of each layer below 6 km are set at 1 km, and that between 6 and 10 km is set at 2 km. The water vapor concentration above 10 km is very weak, so the interval is set at 5 km.

The water vapor concentration was inverted by the OEM. **Figure 11** shows the variation of the water vapor concentration with altitude, i.e., the water vapor concentration profile. The black curve is the result obtained from the reanalysis data processing on the website of the European Centre for Medium-range Weather Forecasts (ECMWF), and the red curve is the inversion result. 10.24, 11.3, and 11.4 have obvious maximum water vapor concentrations at altitudes of 5–8 km. As mentioned earlier, rainy weather was interspersed during the measurement. Therefore, this may be due to the existence of a strong water vapor transport process at the corresponding altitude. As shown in **Figure 12**, the analysis of the temperature and pressure data (National Centers for Environmental Prediction, NCEP) reveals that anomalies are also reflected at the corresponding altitudes. The magnitude of the water vapor concentration maxima clearly corresponds to the temperature at altitudes of 5–8 km, with the highest average temperature at 11.4 and the lowest at 10.23. The maximum value of water vapor concentration and pressure value also have a similar trend, among which the pressure at 10.23 is the lowest. The increase in temperature and pressure may be due to the higher water vapor concentration that absorbed more radiation.

Hefei is in the mid-latitude zone of the Northern Hemisphere, which has a subtropical monsoon climate. October to November is the late autumn and early winter; hence, the water vapor content is relatively low, and the column concentration is generally below 2000 ppm. **Figure 13** shows the variation in water vapor concentration during the experiment. The red curve is the measurement result of the LHR, and the blue curve is the measurement result of the EM27/SUN. **Table 1** shows the comparison of the two measurement results. Compared with the EM27/SUN results, the overall inversion results of the LHR are lower, with deviations of 13.5%, 9.9%, 12.4%, and 11.1%, respectively. This may be related to the inversion algorithms of the two measurement methods and the parameter settings in the algorithms. However, the trends of water vapor concentration are consistent. The correlation coefficients of the two measurement results are 0.660, 0.944, 0.898, and 0.928. During the measurement, the temperature near the ground rose, the evaporation of water vapor increased, and the concentration of water vapor showed an upward trend. On October 23, the water vapor concentration changed rapidly, and the overall state was unstable. Both instruments measured an obvious V-shaped fluctuation from 10:45 to 11:10.

CONCLUSION

The 1.316 μm optical fiber LHR prototype was established, the heterodyne module was integrated and the system parameters were optimized, which made the prototype more compact and stable. The LHR was favorable in field measurements, and the

SNR and spectral resolution were approximately 120 and 0.009 cm^{-1}, respectively. The absorption spectrum of atmospheric water vapor in Hefei was measured, and the water vapor concentration was inverted by the OEM. The results were compared with the Fourier transform spectrometer which performed the measurements simultaneously, the variation trends of the two methods were consistent. This proves that the accuracy and practicality of the LHR are respectable in atmospheric molecular concentration measurements. Future work will focus on system integration and long-term monitoring of GHGs.

DATA AVAILABILITY STATEMENT

The raw data supporting the conclusion of this article will be made available by the authors, without undue reservation.

AUTHOR CONTRIBUTIONS

JH was responsible for the overall design and implementation of the experiment, data processing, and manuscript writing. YH and ZC provided inspiration for the theory and operation of the experiment and suggestions for the revision of manuscripts. XL guided the processing of laser heterodyne spectroscopy data, and DL was responsible for the processing of Fourier transform spectrometer data. ZY and GQ provided help for the construction of the experimental device and data collection.

FUNDING

This work was supported by the Strategic Priority Research Program of Chinese Academy of Sciences (Grant No. XDA17010104).

REFERENCES

1. Kiehl JT, Trenberth KE. Earth's Annual Global Mean Energy Budget. *Bull Amer Meteorol Soc.* (1997) 78(2):197–208. doi:10.1175/1520-0477(1997)078<0197:eagmeb>2.0.co;2
2. Soden BJ. Enlightening Water Vapour. *Nature* (2000) 406(6793):247–248. doi:10.1038/35018666
3. Smith DC. High-power Laser Propagation: Thermal Blooming. *Proc IEEE* (1977) 65(12):1679–1714. doi:10.1109/PROC.1977.10809
4. Chan KL, Valks P, Slijkhuis S, Köhler C, Loyola D. Total Column Water Vapor Retrieval for Global Ozone Monitoring Experience-2 (GOME-2) Visible Blue Observations. *Atmos Meas Tech* (2020) 13(8):4169–4193. doi:10.5194/amt-13-4169-2020
5. Lange D, Behrendt A, Wulfmeyer V. Compact Operational Tropospheric Water Vapor and Temperature Raman Lidar with Turbulence Resolution. *Geophys Res Lett* (2019) 46(24):14844–14853. doi:10.1029/2019GL085774
6. Brunamonti S, Jorge T, Oelsner P, Hanumanthu S, Singh BB, Kumar KR, et al. Balloon-borne Measurements of Temperature, Water Vapor, Ozone and Aerosol Backscatter at the Southern Slopes of the Himalayas during StratoClim 2016-2017. *Atmos Chem Phys* (2018) 18, 15937–15957. doi:10.5194/acp-18-15937-2018
7. Ren H-M, Li A, Li A, Hu Z-K, Huang Y-Y, Xu J, et al. Measurement of Atmospheric Water Vapor Vertical Column Concentration and Vertical Distribution in Qingdao Using Multi-axis Differential Optical Absorption Spectroscopy. *Acta Phys Sin* (2020) 69(20):204204. doi:10.7498/aps.69.20200588
8. Ma Y, Hong Y, Qiao S, Lang Z, xiaonan L. H-shaped Acoustic Micro-resonator Based Quartz-Enhanced Photoacoustic Spectroscopy. *Opt Lett* (2022). doi:10.1364/OL.449822
9. Liu X, Ma Y. Sensitive Carbon Monoxide Detection Based on Light-Induced Thermoelastic Spectroscopy with a Fiber-Coupled Multipass Cell[J]. *Chin Opt Lett* (2022) 20:031201. doi:10.3788/COL202220.031201
10. Ma Y, Hu Y, Qiao S, Lang Z, Liu X, He Y, et al. Quartz Tuning forks Resonance Frequency Matching for Laser Spectroscopy Sensing. *Photoacoustics* (2022) 25:100329. doi:10.1016/j.pacs.2022.100329
11. Liu X, Qiao S, Ma Y. Highly Sensitive Methane Detection Based on Light-Induced Thermoelastic Spectroscopy with a 2.33 μm Diode Laser and Adaptive Savitzky-Golay Filtering. *Opt Express* (2022) 30(2):1304–1313. doi:10.1364/OE.446294
12. Teich MC, Keyes RJ, Kingston RH. OPTIMUM HETERODYNE DETECTION AT 10.6 μm IN PHOTOCONDUCTIVE Ge:Cu. *Appl Phys Lett* (1966) 9(10):357–360. doi:10.1063/1.1754611
13. Wilson EL, Mclinden ML, Miller JH, Allan GR, Ott LE, Melroy HR, et al. Miniaturized Laser Heterodyne Radiometer for Measurements of CO2 in the Atmospheric Column. *Appl Phys B* (2014) 114(3):385–393. doi:10.1007/s00340-013-5531-1
14. Wilson EL, Digregorio AJ, Villanueva G, Grunberg CE, Souders Z, Miletti KM, et al. A Portable Miniaturized Laser Heterodyne Radiometer (Mini-LHR) for Remote Measurements of Column CH_4 and CO_2. *Appl Phys B* (2019) 125(211):1–9. doi:10.1007/s00340-019-7315-8
15. Rodin A, Klimchuk A, Nadezhdinskiy A, Churbanov D, Spiridonov M. High Resolution Heterodyne Spectroscopy of the Atmospheric Methane NIR Absorption. *Opt Express* (2014) 22(11):13825–34. doi:10.1364/OE.22.013825
16. Wang J, Sun C, Wang G, Zou M, Tan T, Liu K, et al. A Fibered Near-Infrared Laser Heterodyne Radiometer for Simultaneous Remote Sensing of Atmospheric CO_2 and CH_4. *Opt Lasers Eng* (2020) 129:106083. doi:10.1016/j.optlaseng.2020.106083
17. Deng H, Yang C, Xu Z, Li M, Huang A, Yao L, et al. Development of a Laser Heterodyne Spectroradiometer for High-Resolution Measurements of CO_2, CH_4, H_2O and O_2 in the Atmospheric Column. *Opt Express* (2021) 29(2):2003–2013. doi:10.1364/OE.413035
18. Lu X., Cao Z., Huang Y., Gao X., Rao R.. Laser Heterodyne Spectrometer for Solar Spectrum Measurement in the 3.53 μm Region. *Opt Precision Eng* (2018) 26(08):1846–1854. doi:10.3788/OPE.20182608.1846
19. Huang J, Huang Y, Lu X, Cao Z, Tan T, Liu D. Design of 3.66μm Laser Heterodyne Spectrometer and Retrieval of Water Vapor Column Concentration. *J Infrared Millim Waves* (2020) 39(05):610–618. doi:10.11972/j.issn.1001-9014.2020.05.012
20. Huang J., Huang Y., Lu X., Cao Z., Qi G., Yuan Z.. Measurement and Concentration Inversion of Ozone in Golmud by Laser Heterodyne Spectrometer. *ACTA PHOTONICA SINICA* (2021) 50(04):57–65. doi:10.3788/gzxb20215004.0401002
21. Gisi M. *Setup of Precise Camera Based Solar Tracker Systems and Greenhouse Gas Measurements Using a Modified Portable Spectrometer*. Eggenstein-Leopoldshafen, Germany: Institut für Meteorologie und Klimaforschung (2012). doi:10.5445/IR/1000031248
22. Melroy HR, Wilson EL, Clarke GB, Ott LE, Mao J, Ramanathan AK, et al. Autonomous Field Measurements of CO_2 in the Atmospheric Column with the Miniaturized Laser Heterodyne Radiometer (Mini-LHR). *Appl Phys B* (2015) 120(4):609–615. doi:10.1007/s00340-015-6172-3
23. Tan T, Cao Z, Wang G, Wang L, Liu K, Huang Y, et al. Study on the Technology of the 4.4 μm Mid-infrared Laser Heterodyne Spectrum. *Spectrosc Spectral Anal* (2015) 35 1516–1519. doi:10.3964/j.issn.1000-0593(2015)06-1516-04
24. Lu X, Cao Z, Tan T, Huang Y, Gao X, Rao R. Instrument Line Shape Function of Laser Heterodyne Spectrometer. *wlxb* (2019) 68(06):064208–142. doi:10.7498/aps.68.20181620

25. Rodgers CD. *Inverse Methods for Atmospheric Sounding: Theory and Practice*. Singapore: World Scientific (2000). doi:10.1142/9789812813718

Conflict of Interest: The authors declare that the research was conducted in the absence of any commercial or financial relationships that could be construed as a potential conflict of interest.

Publisher's Note: All claims expressed in this article are solely those of the authors and do not necessarily represent those of their affiliated organizations, or those of the publisher, the editors and the reviewers. Any product that may be evaluated in this article, or claim that may be made by its manufacturer, is not guaranteed or endorsed by the publisher.

frontiers in Physics

ORIGINAL RESEARCH
published: 09 February 2022
doi: 10.3389/fphy.2022.816734

Dynamic of Grating Thermal Deformation on Beam Quality for Spectral Beam Combining

Zhi-feng Deng, Sheng-bao Zhan, Ya Wang, Wen-ran Le and Shen-long Zha*

Institute of Electronic Engineering and Intelligent Manufacturing, Anqing Normal University, Anqing, China

For spectral beam combining, an experimental system of dynamic beam quality caused by the thermal deformation of a grating has been designed and established. According to the theoretical model established, the distribution of the temperature field, as well as the thermal deformation of the grating, has been analyzed. Further, the combined beam quality and the intensity distribution have been numerically calculated in detail. The results show that the maximum temperature and the grating thermal deformation increase with the extension of irradiation time, resulting in side lobes appearing in the intensity distribution. In the experiment, the measured combined beam quality factor M_x^2 was 1.29 without the thermal deformation. When the grating was heated by pump lasers at different times, M_x^2 can arrive at 1.34, 1.37, and 1.41, respectively. The results reveal that the combined beam quality increases with the increase in irradiation time and changes rapidly at the beginning of heating, consistent with the theoretical analysis. The discussion and analysis of the dynamic beam quality are potentially valuable for reducing the influence of thermal deformation on the beam quality.

Keywords: blazed grating, spectral beam combining, dynamic beam quality, grating thermal deformation, fiber laser

OPEN ACCESS

Edited by:
Yufei Ma,
Harbin Institute of Technology, China

Reviewed by:
Zhao Shanghong,
Air Force Engineering University, China
Hanlin Peng,
University of Electronic Science and Technology of China, China

****Correspondence:***
Sheng-bao Zhan
zhanshb@aliyun.com

Specialty section:
This article was submitted to Optics and Photonics, a section of the journal Frontiers in Physics

Received: *17 November 2021*
Accepted: *07 January 2022*
Published: *09 February 2022*

Citation:
Deng Z-f, Zhan S-b, Wang Y, Le W-r and Zha S-l (2022) Dynamic of Grating Thermal Deformation on Beam Quality for Spectral Beam Combining. Front. Phys. 10:816734. doi: 10.3389/fphy.2022.816734

1 INTRODUCTION

Spectral beam combining (SBC) technology is a well-established method for high-radiance lasers, which has a broad application prospect in optical sensing, laser medical treatment, and spectral analysis [1–8]. The beam quality factor is one of the key technical indexes to evaluate the beam quality in the SBC system. However, it can be influenced by many factors, such as the spectral line width, the disturbance of the laser array, and the dispersion characteristics of the grating [9–12]. As the powers of the laser array are increased, the grating thermal deformation, which induces degeneration of the combined beam quality, becomes more significant [13–15]. Zhou et al. reported the modulation of combined beam characteristics by volume Bragg gratings with thermal deformation. The transmitted and the diffracted beams experience wave-front aberrations with different degrees, thus leading to distinct beam deterioration [16]. Yang et al. presented the influence of multilayer dielectric grating thermal deformation on the SBC system and the beam quality of the combined beam degraded with increasing incident laser-beam power density [17]. Wang et al. investigated the grating deformation under different laser heating times [18]. However, to our best knowledge, the correspondence between irradiation time and the dynamic change of the beam quality has not been found, which is necessary to further understand the dynamic change of beam quality so as to provide a method to reduce thermal deformation and improve the quality of the combined beam.

Aiming at the above situation, the temperature distribution, as well as the thermal deformation of a blazed grating, was analyzed using the finite element method, and the combined beam M^2 after

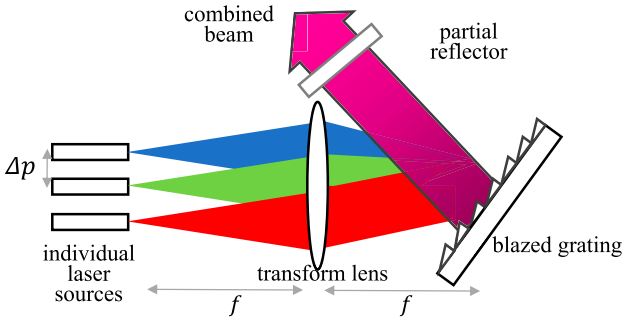

FIGURE 1 | Schematic of the spectral beam combining.

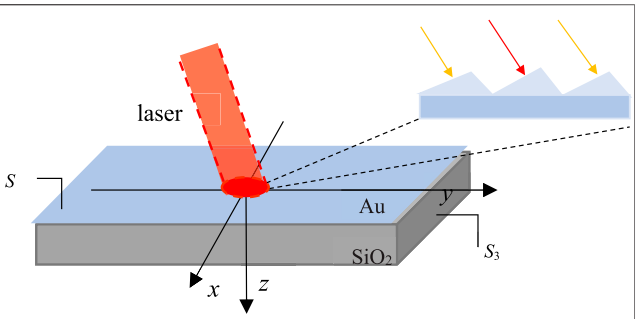

FIGURE 2 | Schematic diagram of the irradiated blazed grating.

grating deformation was calculated using the beam propagation model of the SBC system. Further, the SBC experimental system for measuring dynamic beam quality was designed and established. The results show that beam quality increases with the increase in irradiation time, which changes rapidly at the beginning of heating.

2 THEORETICAL MODELS

2.1 The Process of Grating Thermal Deformation

The schematic illustration of the SBC system is shown in **Figure 1**. The grating is a key element in the system, which can combine multiple laser beams of different wavelengths into one beam. When the high-power laser irradiates the grating, the grating temperature will increase, leading to grating thermal distortion.

For the blazed grating irradiated by laser array, the temperature distribution and the thermal deformation are mainly affected by the spot size and the intensity distribution of the laser field. Assuming that the incident laser is a Gaussian distribution, the different grooves will have different heat distributions, as shown in **Figure 2**. S_1 is the front surface covered with a film layer, S_2 is the backlit surface, and S_3 is the side surface. The heat flux $q\ (x, y, t)$ flowing into S_1 is the laser power density absorbed by the film layer, which can be expressed as $q\ (x, y, t) = AtI(x, y)$, where A represents the absorption coefficient of the film, t is the laser-irradiated time, $I\ (x, y)$ is power density distribution of incident laser on S_1, which can be written as $I\ (x, y) = I_0\ exp\ (-(x^2+y^2/r^2))$, where I_0 is the incident laser power density, and r is the spot radius of the incident laser on the grating. For the grating without the heat source, the temperature field distribution can be expressed by the differential equation of heat exchange [19]:

$$\frac{\partial}{\partial x}\left(k\frac{\partial T}{\partial x}\right)+\frac{\partial}{\partial y}\left(k\frac{\partial T}{\partial y}\right)+\frac{\partial}{\partial z}\left(k\frac{\partial T}{\partial z}\right)=\rho c\frac{\partial T}{\partial t}. \tag{1}$$

where T is the temperature in the location (x, y, z) at time t, k is the coefficient of heat conduction of grating, ρ is the density of grating material, c is the specific heat.

Besides the heat absorbed in the grating surface, there also exists convection to exchange heat. Therefore, the boundary condition can be written as

$$\begin{cases} -k\frac{\partial T}{\partial n}\Big|_{S_1} = q(x,y,t) - h(T_1 - T_0) \\ -k\frac{\partial T}{\partial n}\Big|_{S_2+S_3} = -h(T_1 - T_0) \end{cases}. \tag{2}$$

where h denotes convective heat transfer coefficient, T_0 is the ambient temperature, and T_1 is the surface temperature.

After the grating surface temperature rises, the grating begins thermal expansion, including the relief structure and substrate, as shown in **Figure 3**, where $\Delta\tau_1(x)$ represents the deformation of the relief structure in different positions and $\Delta\tau_2(x)$ represents the deformation of the substrate in different positions. As the laser power is absorbed by the grating, the groove angle, incident angle, and incident plane will change correspondingly, resulting in the change of the characteristics of the combined beam.

2.2 Propagation Model of SBC Systems With Thermal Deformation

The phase change caused by the grating deformation is represented by the optical path difference, including optical path differences within or between grooves, as shown in **Figure 4** and **Figure 5**, where α and β represent the incident angle and diffraction angle before thermal deformation, respectively, d denotes the grating period, a denotes the groove width, and φ is the angle of the groove before deformation. The x_1-axis on the observation plane is perpendicular to the z_1-axis. N_g and N_g' represent the normal of the grating plane before and after the thermal deformation, respectively. N_c and N_c' represent the normal of the groove plane before and after the thermal deformation, respectively.

The incident angle and diffraction angle of each individual element after thermal deformation can be written as

$$\alpha_q' = a + l - \Delta a = a + arctan\left(\frac{q\Delta p}{f}\right) - \Delta a. \tag{3}$$

$$\beta_q' = arcsin\left(sin\left(\alpha_q'\right) - \frac{m\lambda_q}{d}\right). \tag{4}$$

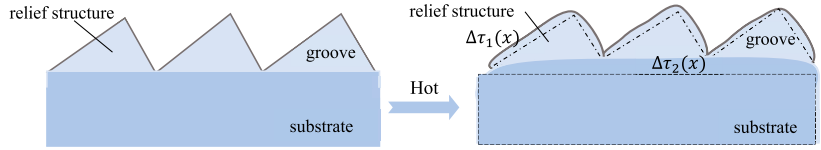

FIGURE 3 | Schematic illustration of the blazed grating before and after thermal deformation.

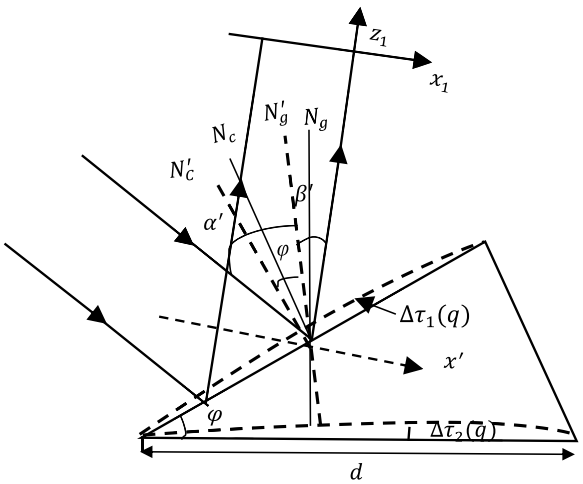

FIGURE 4 | Schematic diagram of optical path difference in the groove.

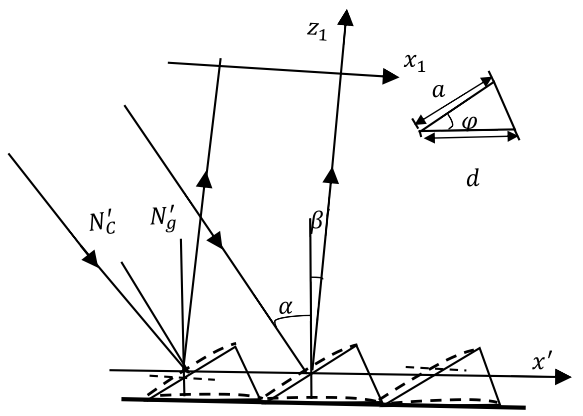

FIGURE 5 | Schematic diagram of optical path difference between grooves.

where q denotes the qth laser element and $q\Delta p$ is the distance between the zero point and the center point of the qth emitter (Δp denotes the distance of adjacent elements). l and λ_q represent the incident angle difference and wavelength of each individual element, respectively. Δa is the angle change of the normal of the grating plane. m is diffraction order.

Because $\Delta\tau_1(q)$ and $\Delta\tau_2(q)$ are far less than d, the groove angle after the deformation can be written as

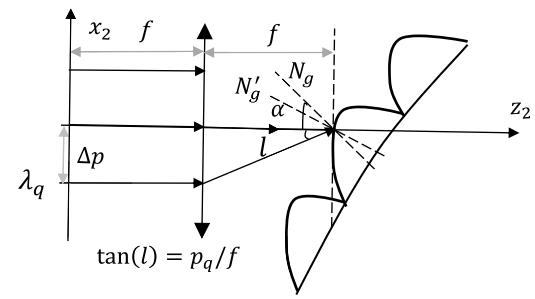

FIGURE 6 | The model of an individual beam passing through a transform lens.

$$\varphi'(q) = \varphi + \tan\left(\frac{\Delta\tau_2(q)}{a}\right) - \tan\left(\frac{\Delta\tau_1(q)}{a}\right). \tag{5}$$

To simplify the calculation, assume that each groove has a virtual groove parallel to the x-axis and the center coincides with the center of the actual groove. By the virtual groove, the optical path difference of the nth groove relative to the origin after thermal deformation can be expressed with Δ_1 (the optical path difference in grooves) and Δ_2 (the optical path difference between the grooves) [20]:

$$\begin{aligned}\Delta &= \Delta_1 + \Delta_2 \\ &= nd\sin(\alpha') + \frac{\sin(\alpha' - \varphi') - \sin(\beta' + \varphi')}{\cos(\beta' + \varphi')}(x' - nd\cos\beta').\end{aligned} \tag{6}$$

$$\left(nd\cos\beta' - \frac{a}{2}\cos(\beta' + \varphi')\right) \le x' \le \left(nd\cos\beta' + \frac{a}{2}\cos(\beta' + \varphi')\right).$$
$$n = -N, \ldots, -1, 0, 1, \ldots N. \tag{7}$$

The model of an individual beam propagating through the transform lens is given in **Figure 6**. The z_2-axis is the main optical axis of the lens, and the x_2-axis lies on the focal plane of the lens in object space. For each individual beam with a waist width of w_0, the field distribution on the incident plane of the grating can be expressed as a function of grating groove number n [21]:

$$E(n) = \sqrt{-\frac{ik_q}{2\pi f}}exp\left(ik_q\left(2f + \frac{nd\cos\alpha' p_q}{f}\right)\right) \times \int_{-\infty}^{+\infty} exp\left(-\frac{(x_0 - p_q)}{\omega_0^2}\right) \times exp\left(\frac{ik_q ndcos\alpha'}{2f}\left(-\frac{p_q x_0^2}{f^2} - 2x_0\right)\right)dx_0, \tag{8}$$

where $k_q = 2\pi/\lambda_q$ and f is the focal length of the transform lens. It is worth noting that the quartic-aberration produced by the transform lens is ignored.

Additionally, the field distribution on the observation plane can be regarded as the superposition of all the diffraction fields of the virtual groove. According to the diffraction integral method [22], the field distribution after the deformation of the jt h individual beam on the observation plane can be expressed as

$$E_j(x_1, z_1) = \sum_{n=-N}^{N} \sqrt{-\frac{ik_q}{2\pi z_1}} E(n) exp(ikz_1) \int_{nd\ cos\beta' - \frac{a}{2}\cos(\beta'+\varphi')}^{nd\ cos\beta + \frac{a}{2}\cos(\beta'+\varphi')} exp\{ik_q[\Delta_1 + \Delta_2]\} exp\left\{ik\frac{(x_1 - x')^2}{2z_1}\right\} dx' \tag{9}$$

where $\Delta_1+\Delta_2$ represents the phase factor induced by the deformed blazed grating.

For the incoherent superposition, the field distribution of the combined beam can be written as

$$I(x_1, z_1) = \sum_{J=-q}^{q} \left|E_J(x_1, z_1)\right|^2. \tag{10}$$

By utilizing the definition of the second-order intensity moments, after fitting the curve of the beamwidth D of the combined beam versus the propagation distance z_1, the beam quality M^2-factor on the x-axis can be calculated approximately by [23]

$$D_x^2(z) = Az_1^2 + Bz_1 + C \quad M_x^2 = \frac{\pi}{\lambda}\omega\theta \quad \omega = \sqrt{C - \frac{B^2}{4A}}, \quad \theta = \sqrt{A}. \tag{11}$$

where ω means the waist width and θ means the divergence angle.

3 SIMULATION RESULTS AND DISCUSSION

3.1 Parameters of Simulation

The parameters used in the simulation are divided into two parts, related to the thermal deformation of the grating and the quality of the combined beam. For the thermal deformation of the grating, the related parameters are as follows: the grating is with a side length of 5 cm, the coating thickness is 0.1 μm, the absorption coefficient of the film is 10 ppm [24], the convective heat transfer coefficient h is 5 W/(m^2·K), and the ambient temperature is 20°C. The spot radius r of the irradiated grating surface is 10 mm, and the power density is 200 W/cm^2. The grating with a substrate material is mainly composed of SiO_2, and the relief structure made of Al is selected for thermal deformation analysis. The material constants are shown in **Table 1** and **Table 2**, respectively [24].

For the quality of the combined beam, the related parameters are as follows: the line density is 1,200/mm, the groove angle $\varphi = 14.8°$, the interval between two adjacent emitters′ center $\Delta p = 300\ \mu m$, the beam waist width of an individual laser beam $\omega_0 = 100$ μm, the focal length of the transform lens $f = 10$ cm, the incidence angle of the center beam $\alpha = 38°$, the wavelengths (λ_q) of laser elements are arranged by $\lambda_q = \lambda_0 + 2q$, $q = \pm 1, \pm 2$, and the central wavelength (λ_0) of the combined array is 1,060 nm.

3.2 Dynamics of Grating Thermal Deformation

In order to solve **Eq. 1** and **Eq. 2**, the finite element method is adopted. For different irradiation times of 10, 30, and 60 s, the temperature distribution on the grating surface is shown in **Figures 7A,B,C**, where the color bar from blue to red represents the Kelvin temperature from 293 to 308 K, which corresponds to 20°C and 35°C. It can be seen from **Figure 7A** that the temperature in the region with higher power density is higher than that in the region with lower power density, and the temperature in the region with higher power density is up to 31.3°C. With the increase in irradiation time, the temperature away from the irradiation area also increases gradually, and the maximum temperature in the central area is 33.6°C, as shown in **Figure 7B**. The temperature distribution after being irradiated for 60 s is shown in **Figure 7C**, which corresponds to the maximum temperature of 35°C. It can be demonstrated that the range of temperature diffusion is further enlarged, resulting in a larger deformation area on the grating surface. The temperature gradually increases from the edge to the center of the surface because of the Gaussian distribution of the incident laser.

The thermal deformation of the substrate caused by a temperature change at the times of 10, 30, and 60 s is shown in **Figures 8A,B,C**, indicating that the maximum deformation value is 34.1, 48.6, and 62 nm. The results demonstrate that the thermal deformation increases with the irradiation time. In addition, the thermal deformation of the grating may increase with increasing temperature compared with **Figure 7**, and the deformation gradually decreases from the center to the edge of the surface.

The thermal deformation of the relief structure is similar to that of the substrate, as shown in **Figure 9**. It is worth noting that the deformation of the relief structure ignores the differences within the grooves to simplify calculations. The deformation of the substrate is greater than that of the relief structure at the same irradiation time due to the difference in the material constants. The largest thermal deformation of the substrate is 33.7, 46.5, and 59 nm at irradiation times of 10, 30, and 60 s.

Figure 10 gives the change of the highest temperature rise with the irradiation time at the power density of 2 kW/cm^2. The highest temperature rise increases nonlinearly with the increasing irradiation time because the heat dissipation increases with the increasing temperature of the grating surface and increases faster at the beginning of heating than after a period of time. The maximum thermal deformation of the grating surface under different laser irradiation times is shown in **Figure 11**, including the substrate structure and the relief structure. It can be suggested that the largest thermal deformation of the two structures increases nonlinearly with the increase in irradiation time. The deformation of the relief structure and the substrate is almost the same in the first 10 seconds. The deformation of the substrate is greater than that

TABLE 1 | Material constants of SiO_2.

Density ($kg{\cdot}m^{-3}$)	Specific heat [$J\ (kg{\cdot}K)^{-1}$]	Heat conductivity [$W{\cdot}(m{\cdot}K)^{-1}$]	Thermal expansion (K^{-1})	Young's modulus/(GPA)	Poisson's ratio
2,100	722	7.6	0.5×10^{-6}	73.1	0.17

TABLE 2 | Material constants of Al.

Density ($kg{\cdot}m^{-3}$)	Specific heat [$J\ (kg{\cdot}K)^{-1}$]	Heat conductivity [$W{\cdot}(m{\cdot}K)^{-1}$]	Thermal expansion (K^{-1})	Young's modulus/(GPA)	Poisson's ratio
2,689	896	273	23.2×10^{-6}	70	0.33

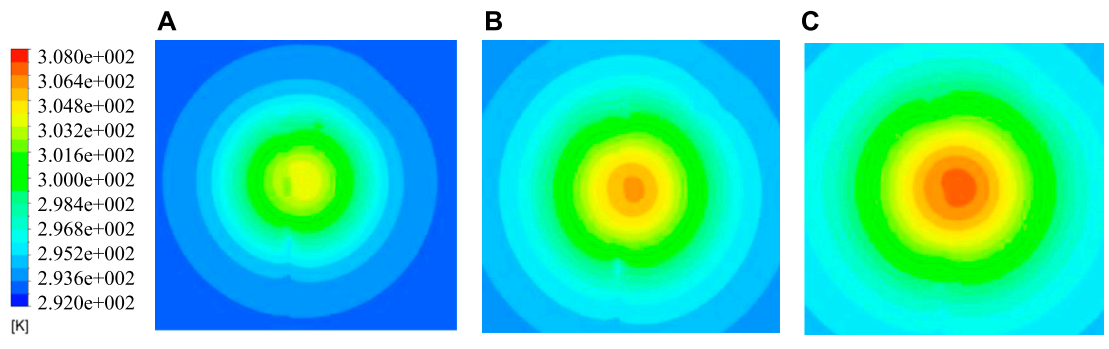

FIGURE 7 | The temperature distribution of grating surface at different irradiation times: **(A)** 10, **(B)** 30, and **(C)** 60 s.

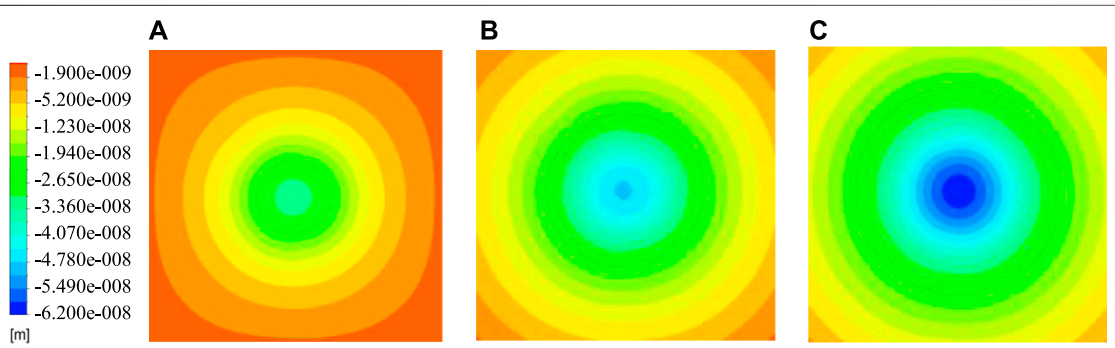

FIGURE 8 | Deformation diagram of the substrate at different irradiation times: **(A)** 10, **(B)** 30, and **(C)** 60 s.

of the relief structure with increasing time, related to the material constants and whether being directly irradiated by the laser.

3.3 Dynamics of Beam Quality

Assuming that three individual beams can be well combined into one and the beam quality factor without grating thermal deformation is 1.00, by means of the propagation model built up in **Section 2.2**, the combined beam intensity distribution and the curves of M^2 are shown in **Figure 12A**. Further, according to the grating surface deformation calculated in **Section 3.1**, the results for the irradiation time at 10, 30, and 60 s are depicted in **Figures 12B,C,D**, respectively. It can be suggested from **Figure 12B** that the combined beam generates the side lobes, and the calculated beam quality factor is 1.16. As the irradiation time increases, the main lobe of the combined beam becomes narrower, and the corresponding side lobes become increasingly obvious, as shown in **Figure 12C**. The side lobes become obvious because the diffractive angle of the beam is changed by the grating with thermal deformation and the beams passing through the grating inevitably deviate from the normal beam. **Figure 12D** gives the results at grating after being irradiated for 60 s, which calculated the beam quality as 1.56. The reason for the degradation of the beam quality is that the beam waist width and the divergence angle increase with the square of the beamwidth.

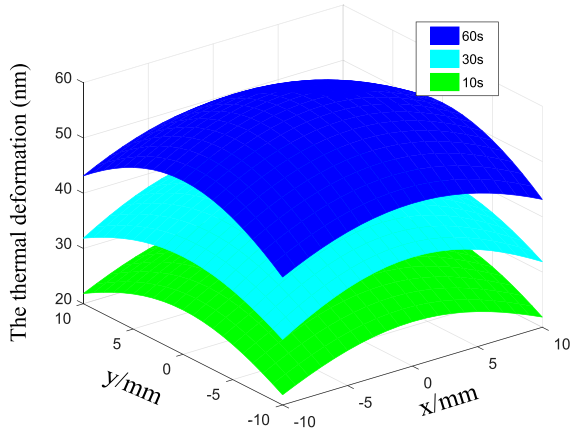

FIGURE 9 | Influence of different irradiation times on the thermal deformation of the relief structure.

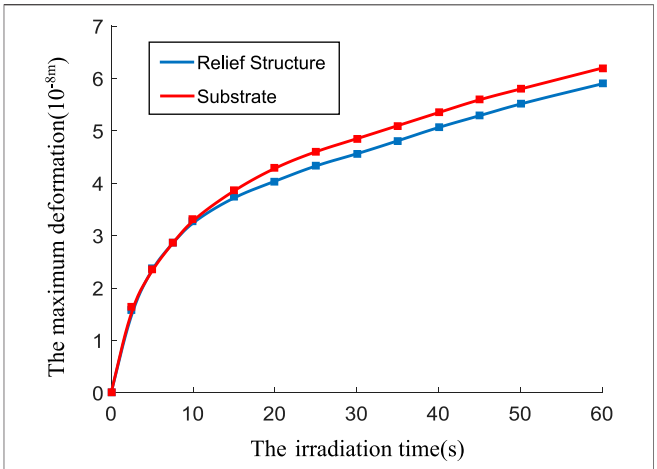

FIGURE 11 | Influence of different irradiation times on the thermal deformation.

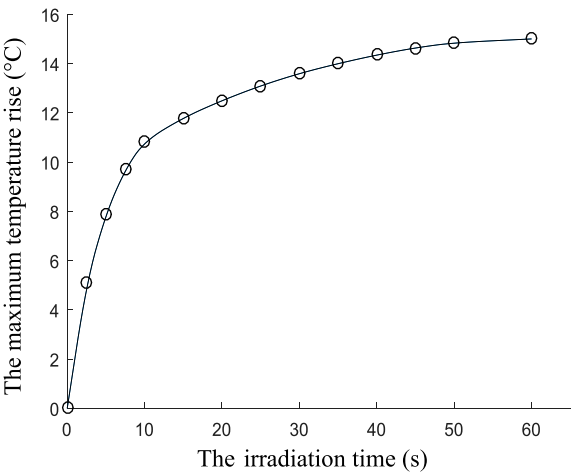

FIGURE 10 | Influence of different irradiation times on the maximum temperature rise.

Further, the variation of the beamwidth and divergence angle of the combined beam with the irradiation time are presented in **Figures 13A,B**. It can be seen that the beamwidths and the divergence angles of the combined beams remarkably rise with the increasing irradiation time. In addition, the divergence angle and the beamwidth increase rapidly in the first 10 seconds because the diffraction angle is affected by the thermal deformation.

4 EXPERIMENT SETUP AND RESULTS

4.1 Experimental Setup

To investigate the effect of the dynamic beam quality caused by the grating thermal deformation, an SBC experimental system was established, as shown in **Figure 14**. In the experiment, the pump is provided by a laser diode with a central wavelength of 976 nm through a coupled system consisting of an aspheric lens and a microscope objective. The fiber used is the Er/Yb codoped double-clad fibers named SM-EYDF-6/125-xp with lengths of 4.7 and 5.3 m. The oscillating resonator is constituted by an output coupling mirror with 10% reflectivity at 1,550 nm waveband and a dichroic mirror with 90% transmittivity for pump light and 95% reflectivity for signal light. The blazed grating with a groove frequency of 1,200 L/mm possesses no less than 60% diffraction efficiency. The Fourier transform lens is a bi-convex lens with a focal length of 50 mm. Due to the low output power of the combined beam, two pumped lasers with output power of 30 W were used to heat the grating, and the pumped lasers were adjusted to the same as the combined beam, including the beam size and irradiation area on the grating. According to the properties of thermoelastic deformation, each beam quality measurement is made after the grating is completely cooled and the measuring equipment has a delay of 15–30 s.

The spectrum of the output laser is examined by a spectrometer (model: MS9740A), the beam profile of the output laser is examined by means of a beam analyzer (model: BP209-IR), and the beam quality is analyzed via a measuring system with a software (model: M2MS, Thorlabs Beam 6.0).

4.2 Experimental Results and Discussion

4.2.1 Beam Characteristics Before the Grating Heated

After establishing the SBC experimental system, the spectrum and M_x^2 of a single laser element were measured, as shown in **Figure 15**. It can be seen that the M_x^2 after grating diffraction is 1.15 and 1.17, respectively. The measured maximum output power is 332 and 296 mW, respectively.

The combined beam quality and spectrum are shown in **Figure 16**. It can be seen that two lasers can be well combined into one beam, and the peaks wavelengths were located at 1,544.8 and 1,560.4 nm with spectra separation of 17.1 nm. The measured combining power was about 448 mW, with a combining efficiency of about 71.3%. Compared with the

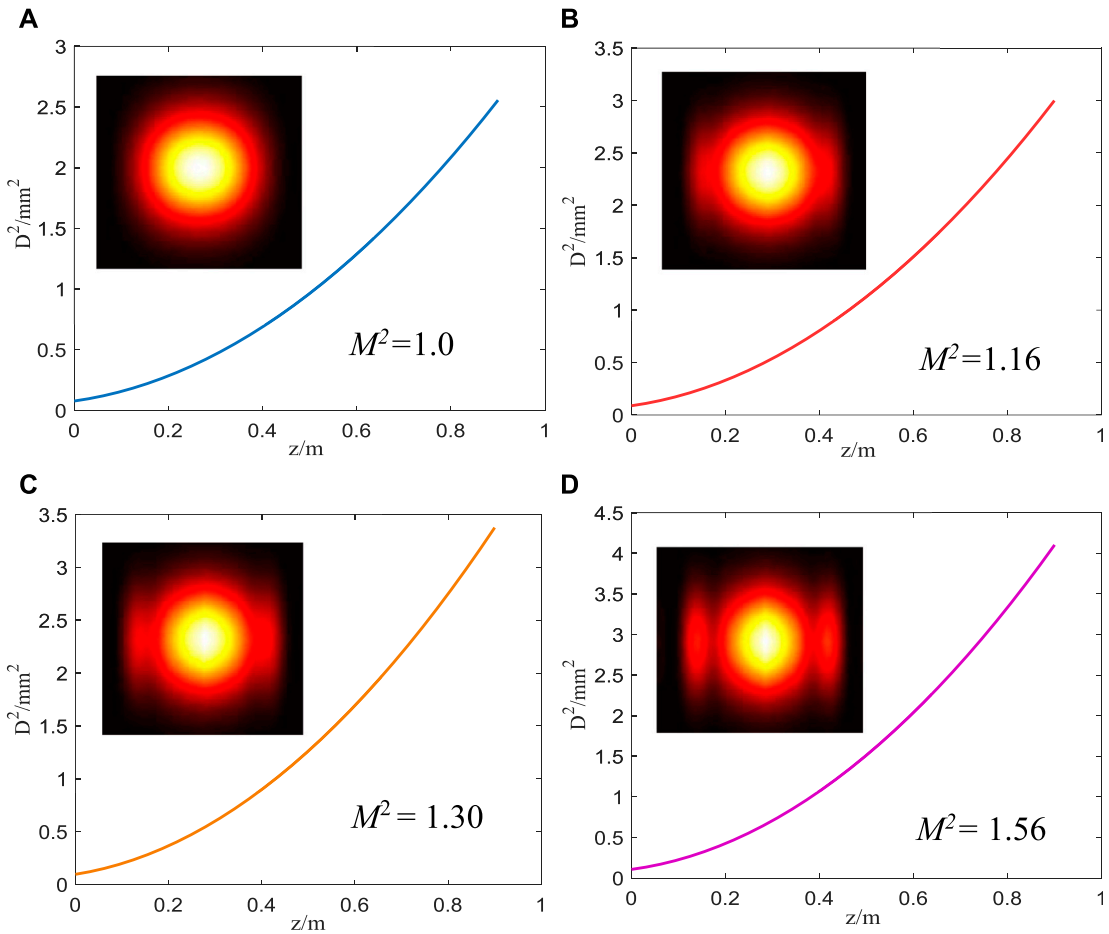

FIGURE 12 | The intensity distributions and the curves of M^2 of the combined beams **(A)** without deformation; **(B)** 10, **(C)** 30, and **(D)** 60 s.

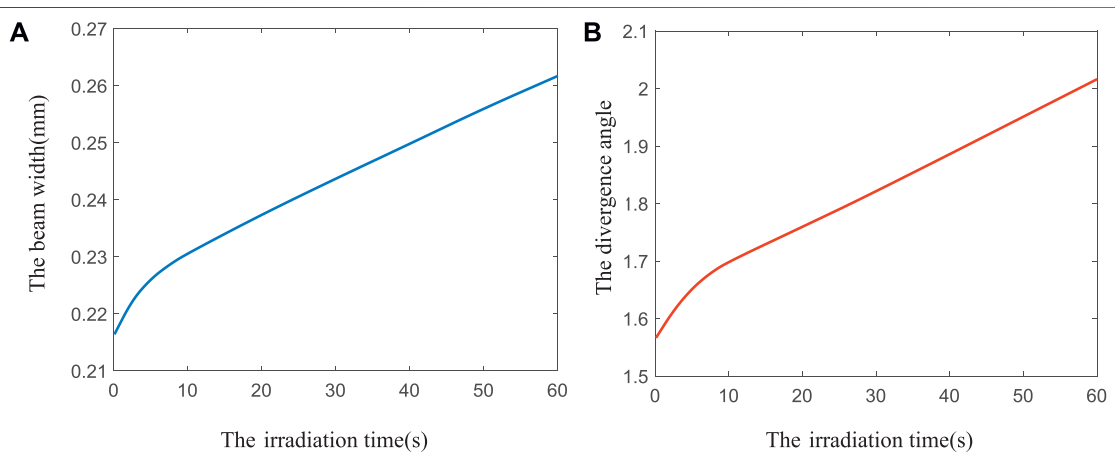

FIGURE 13 | The curve of beamwidth and divergence angle of the combined beam with the irradiation time: **(A)** beamwidth; **(B)** divergence angle.

single laser, the beam profile changes slightly, and M_x^2 degrades to 1.29. The reasons for the deterioration of beam quality after combination can be summarized as 1) the grating scattering and etching errors will modulate the near field phase and 2) the lens aberration changes the intensity distribution and diffraction direction of each individual beam.

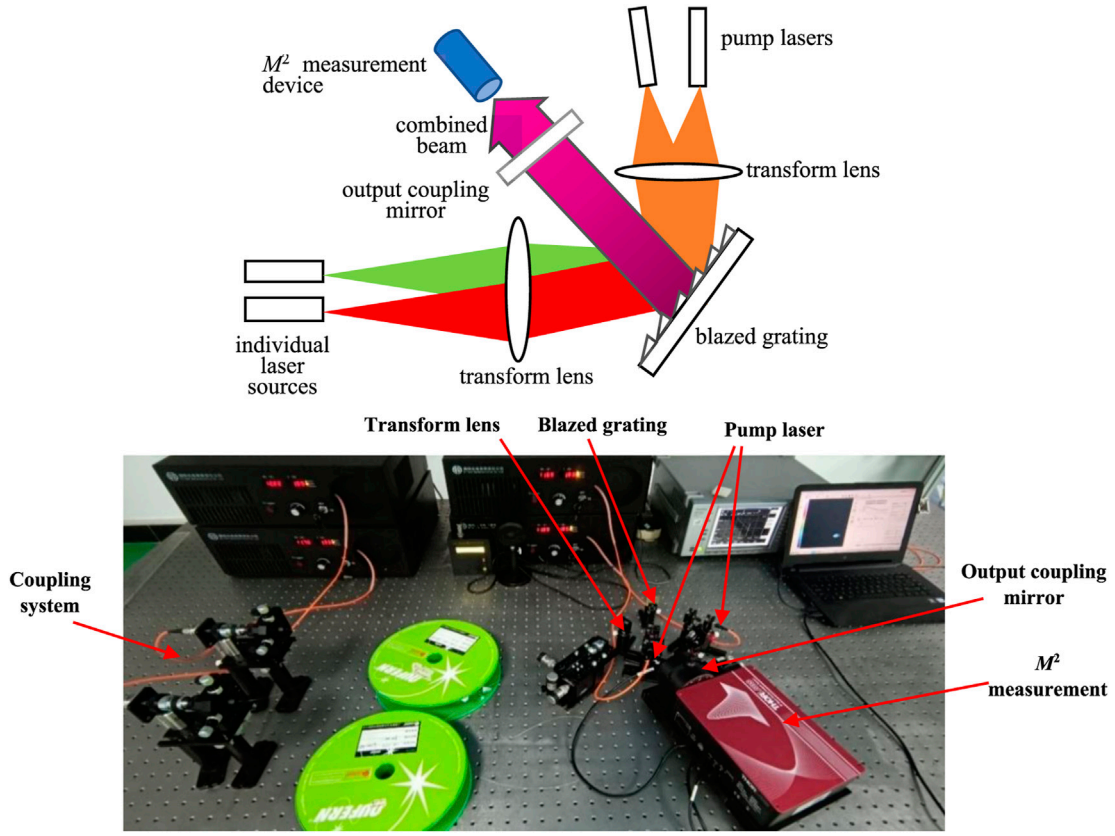

FIGURE 14 | The schematic diagram of the experiments and experimental setup for grating thermal deformation.

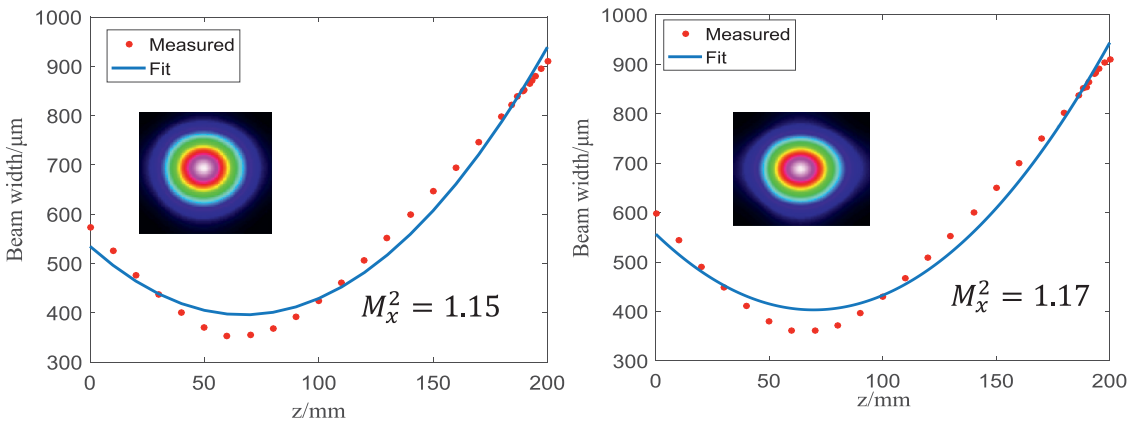

FIGURE 15 | The beam characteristics of the single laser element.

4.2.2 Beam Characteristics After the Grating Heated

After the combined beam was measured, the grating was heated by two pumped lasers at different times. The measured beam profile and beam quality are shown in **Figure 17**. From **Figure 17A**, it can be seen that after grating was heated for 30 s, the measured M_x^2 degraded to 1.34 and the beam profile hardly changed. The degradation of beam quality is because the grating is suddenly heated by the pumped lasers, resulting in the grating temperature gradient alters, which will cause the thermal deformation of the grating surface. Further, the diffractive angle of the beams was changed by the grating with thermal deformation.

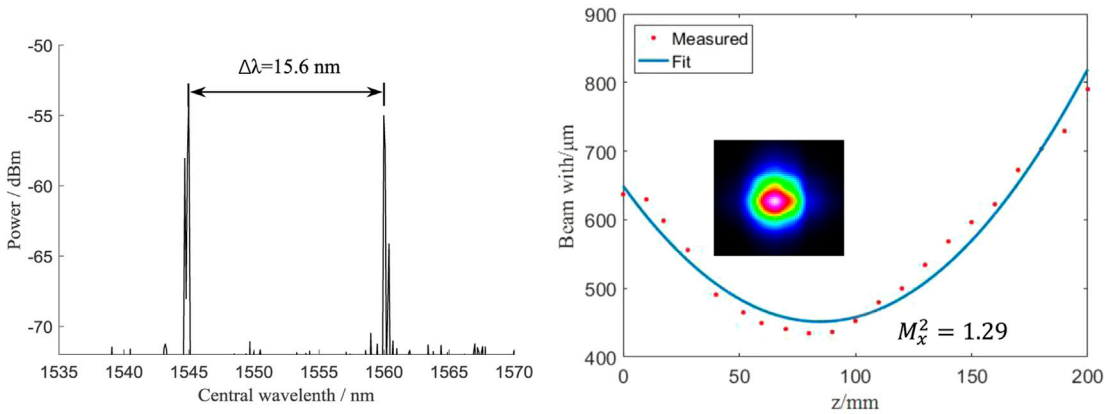

FIGURE 16 | The combined beam spectral and beam quality.

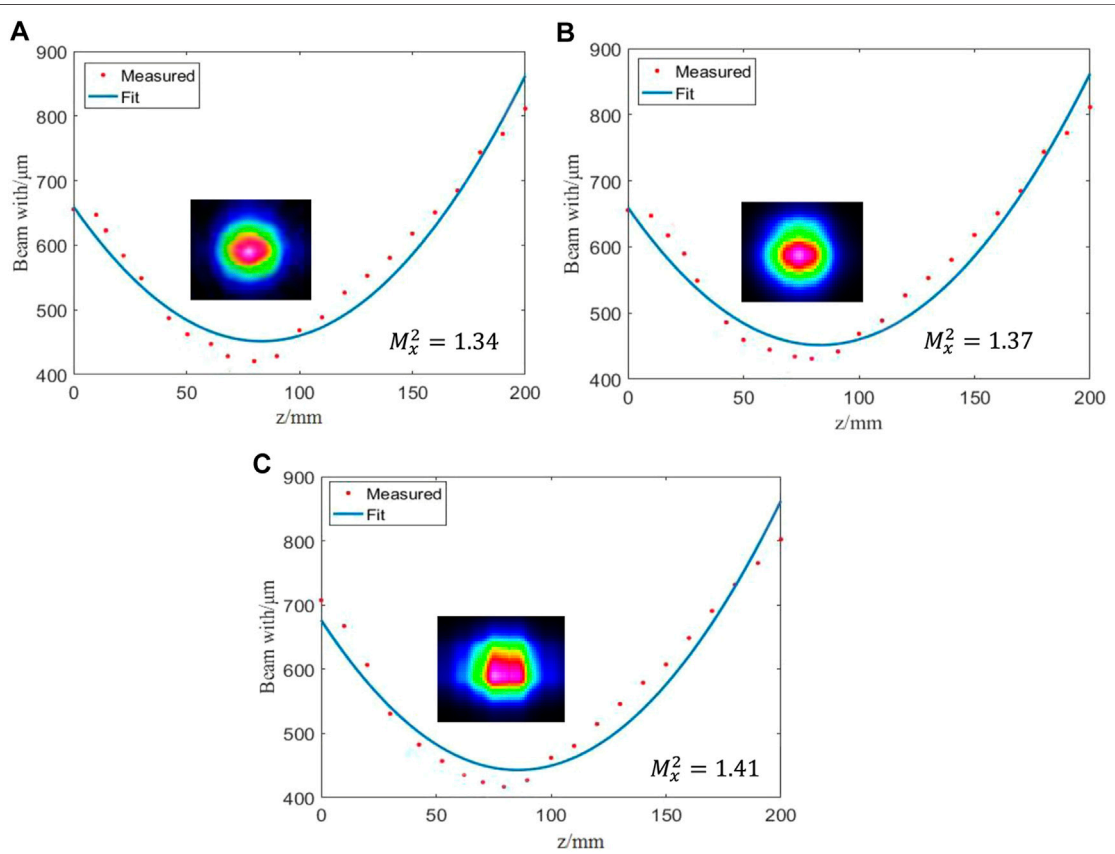

FIGURE 17 | Measured beam profile and quality factor: **(A)** 30, **(B)** 60, and **(C)** 120 s.

Figure 17B gives the results at grating after irradiation for 60 s. Apparently, the measured M_x^2 is 1.37, and the beam profile flattened in the center and widened slightly in the *x*-axis. The beam quality degradation is because the grating thermal deformation gradually increases with the increase in irradiation time, and both the beamwidths and the divergence angles of the combined beams rise with the thermal deformation.

Figure 17C gives the results at grating after irradiation for 120 s, indicating that the measured M_x^2 is 1.41, and irregular distortion occurs in the beam profile. The reason is that the thermal deformation is further increased with the increase in

irradiation time. The crosstalk intensified between adjacent elements by the beams deviating from the normal beam. Moreover, by summarizing **Figures 17A–C**, it can be found that the beam quality degrades continuously with the increasing irradiation time, corresponding to thermal deformation that varies with irradiation time, which is consistent with the theoretical analysis.

5 CONCLUSION

In this paper, the model including the thermal deformation of the grating, as well as the beam propagation of the SBC system, has been developed. By means of the model, the intensity distribution and M^2 of the combined beam were analyzed in detail. The analysis indicates that the deformation of the substrate is greater than that of the relief structure in the same irradiation time as well, which is related to the material constants. This study further shows that the main lobe of the combined beam narrowed and the side lobes widened, which is the main reason for the beam quality of the combined beam degeneration. Further, the influences of the grating with thermal deformation on beam quality were investigated experimentally. The measured beam quality factor M_x^2 is 1.29 without the thermal deformation. When the grating is heated at different times, M_x^2 can arrive at 1.34, 1.37, and 1.41 at 30, 60, and 120 s, respectively. The experimental results indicate that the beam quality changes rapidly at the beginning of heating. Next efforts will focus on how to lower the influence of the thermal effect in the SBC system.

DATA AVAILABILITY STATEMENT

The original contributions presented in the study are included in the article/Supplementary Material. Further inquiries can be directed to the corresponding author.

AUTHOR CONTRIBUTIONS

Z-fD wrote the manuscript. S-bZ directed analysis and experiment. S-lZ and W-rL designed experiments. YW carried out experiments.

FUNDING

This work was supported by the National Natural Science Foundation of China (no. 41805014) and the Natural Science Foundation of Anhui Province, China (nos. 1808085MF189, KJ2019A0565, and KJ2019A0576). Natural Science Foundation of Anhui Province, China (gxbjZD2021063).

REFERENCES

1. Ma Y, He Y, Tong Y, Yu X, Tittel FK Quartz-tuning-fork Enhanced Photothermal Spectroscopy for Ultra-high Sensitive Trace Gas Detection. *Opt Express* (2018) 26:32103–10. doi:10.1364/OE.26.032103
2. Liu X, Qiao S, Ma Y Highly Sensitive Methane Detection Based on Light-Induced Thermoelastic Spectroscopy with a 2.33 Mm Diode Laser and Adaptive Savitzky-Golay Filtering. *Opt Express* (2022) 30:1304–13. doi:10.1364/OE.446294
3. Stoev ID, Seelbinder B, Erben E, Maghelli N, Kreysing M Highly Sensitive Force Measurements in an Optically Generated, Harmonic Hydrodynamic Trap. *eLight* (2021) 1:7. doi:10.1186/s43593-021-00007-7
4. Qiao S, Ma Y, He Y, Patimisco P, Sampaolo A, Spagnolo V Ppt Level Carbon Monoxide Detection Based on Light-Induced Thermoelastic Spectroscopy Exploring Custom Quartz Tuning forks and a Mid-infrared QCL. *Opt Express* (2021) 29:25100–8. doi:10.1364/OE.434128
5. Ma Y, Hong Y, Qiao S, Lang Z, xiaonan L H-shaped Acoustic Micro-resonator Based Quartz-Enhanced Photoacoustic Spectroscopy. *Opt Lett* (2022). doi:10.1364/OL.449822
6. Lang Z, Qiao S, He Y, Ma Y Quartz Tuning fork-based Demodulation of an Acoustic Signal Induced by Photo-Thermo-Elastic Energy Conversion. *Photoacoustics* (2021) 22:100272. doi:10.1016/j.pacs.2021.100272
7. Pavel N, Dascalu T, Salamu G, Dinca M, Boicea N, Birtas A Ignition of an Automobile Engine by High-Peak Power Nd:YAG/Cr4+:YAG Laser-Spark Devices. *Opt Express* (2015) 23:33028–37. doi:10.1364/OE.23.033028
8. Liu X, Ma Y. Sensitive Carbon Monoxide Detection Based on Light-Induced Thermoelastic Spectroscopy with a Fiber-Coupled Multipass Cell. *Chin Opt Lett* (2022) 20:031201. doi:10.3788/COL202220.031201
9. Zhou Taidou 周., Liang Xiaobao 梁., Zhao Lei 赵. 磊., Wang Lin 王. 琳., Li Chao 李. 超., Luo Yun 罗. 韵., et al. Effect of Volume Bragg Gratings Dispersion on Diffracted Beam Quality. *Chin J Lasers* (2017) 44(2):0201019–200. doi:10.3788/CJL201744.0201019
10. ChenZhang F, Zhang J, Ma J, Wei C, Zhu R, Han B, et al. Beam Quality Analysis and Optimization for 10 kW-Level Spectral Beam Combination System. *Opt Commun* (2019) 444:45–55. doi:10.1016/j.optcom.2019.03.030
11. Bourgeade A, Donval T, Gallais L, Lamaignère L, Rullier J-L Modeling Surface Defects in Fused Silica Optics for Laser Wave Propagation. *J Opt Soc Am B* (2015) 32:655–63. doi:10.1364/JOSAB.32.000655
12. Bai G, Shen H, Yang Y, Zhao X, Zhang J, Zhang H, et al. Theoretical Analysis of Beam Quality Degradation in Spectral Beam Combining of Fiber Laser Array with Beam Deviation. *Opt Laser Techn* (2018) 105:281–7. doi:10.1016/j.optlastec.2018.03.010
13. Yin S, Zhang B, Dan Y Effects of the Deformation of Reflection Volume Bragg Gratings on the M2-Factor of Super-gaussian Laser Beams. *Opt Commun* (2010) 283:1418–23. doi:10.1016/j.optcom.2009.12.005
14. Marchenko A, Lishman B, Wrangborg D, Thiel T Thermal Expansion Measurements in Fresh and saline Ice Using Fiber Optic Strain Gauges and Multipoint Temperature Sensors Based on Bragg Gratings. *J Sensors* (2016) 2016:1–13. doi:10.1155/2016/5678193
15. Peng Y, Peng F, Han J Influence of thermal Deformations of Resonators on Propagation Properties of Laser Annular Beams through Turbulent Atmosphere. *Opt Laser Techn* (2013) 45:272–7. doi:10.1016/j.optlastec.2012.05.039
16. Zhou TD, Liang XB, Li C, Zhao L, Wang JJ, Jing F Spectral Beam Combining of Fiber Lasers by Using Reflecting Volume Bragg Gratings. *Chin Phys Lett* (2016) 33:124–205. doi:10.1088/0256-307x/33/12/124205
17. Yang L, Wu Z, Zhang B Influence of thermal Deformation of a Multilayer Dielectric Grating on a Spectrally Combined Beam. *Appl Opt* (2016) 55(32):9091–1. doi:10.1364/AO.55.009091
18. Wang H, Song Y, Yang Y, Xian Y, You Y, Liu M, et al. Simulation and Experimental Study of Laser-Induced thermal Deformation of Spectral Beam Combination Grating. *Opt Express* (2020) 28(22):33334. doi:10.1364/OE.408832

19. Peng R. *Influence of thermal Distortion on the Propagation of Beams in High Energy Laser Channel*. Changsha, China: National University of Defense Technology (2009). p. 30–4. (in Chinese).
20. Zhang Y, Zhang B Analysis of Beam Quality for the Laser Beams after Spectral Beam Combining. *Optik* (2010) 121(13):1236–42. doi:10.1016/j.ijleo.2009.01.002
21. Wu Z, Yang L, Zhong Z, Zhang B. Influence of Laser Array Performance on Spectrally Combined Beam. *J Mod Opt* (2016) 63(19):1972–80. doi:10.1080/09500340.2016.1183056
22. Lu BD. *Propagation and Control of High-Power Lasers*. Beijing: National Defence Industry Press (1999). p. 23–4. ISBN: 9787118019551.
23. Chang-ming Z Investigation on the Experimental Measurement of Laser Beam Quality. *Laser Technol* (2000) 24(6):341–4.
24. Macleod HA *Thin-Film Optical Filters*. Arizona: CRC Press (2001).

Conflict of Interest: The authors declare that the research was conducted in the absence of any commercial or financial relationships that could be construed as a potential conflict of interest.

frontiers in Physics

ORIGINAL RESEARCH
published: 15 February 2022
doi: 10.3389/fphy.2022.832225

Efficient Solution of Emissivity for the Area Blackbody Based on the Multiple Reflection Method

*Jian Xing, Dingyu Liu and Shuanglong Cui**

College of Information and Computer Engineering, Northeast Forestry University, Harbin, China

At present, the Monte Carlo method is the only method to evaluate the area blackbody emissivity, so it needs to be compared and verified with other calculation methods. In particular, the efficiency of Monte Carlo is low when the micro-cavity structure of the area blackbody is more complex for higher emissivity. An efficient algorithm for calculating emissivity of the area blackbody based on the multiple reflection method was put forward in this article. A multiple reflected light path that radiated into the inner micro-cavity structure of the area blackbody was simulated. The ratio of the outgoing light intensity to the incident light intensity was obtained by setting a threshold of the outgoing light intensity, and then the area blackbody emissivity was calculated. The simulation results showed that, compared with the Monte Carlo method, the results of the emissivity calculation were similar, and calculation efficiency was increased more than 100 times under the same micro-cavity structure. A practical area blackbody was made based on the simulation results from the proposed multiple reflection method, and the emissivity measurement experiments were carried out and compared to the cavity blackbody at the same temperature. The results showed that the emissivity was near one and stable for the NIR (Near Infrared) spectrum range when the temperature was higher than 280°C. Thus, the feasibility of the multiple reflection method for calculating the area blackbody emissivity was verified. The multiple reflection method proposed in this article provided one more design path for developing area blackbodies with more complex micro-cavity structures.

Keywords: area blackbody, emissivity solution, multiple reflection method, Monte Carlo method, micro-cavity structure

OPEN ACCESS

Edited by:
Yufei Ma,
Harbin Institute of Technology, China

Reviewed by:
Tsing-Hua Her,
University of North Carolina at Charlotte, United States
Arindam Dasgupta,
Missouri University of Science and Technology, United States

****Correspondence:***
Shuanglong Cui
cuishuanglong@nefu.edu.cn

Specialty section:
This article was submitted to Optics and Photonics, a section of the journal Frontiers in Physics

Received: *09 December 2021*
Accepted: *18 January 2022*
Published: *15 February 2022*

Citation:
Xing J, Liu D and Cui S (2022) Efficient Solution of Emissivity for the Area Blackbody Based on the Multiple Reflection Method. Front. Phys. 10:832225. doi: 10.3389/fphy.2022.832225

1 INTRODUCTION

In recent years, with the rapid development of infrared radiation metrology, spectral detection technology, and thermal imaging technology, it is significant to develop the blackbody radiation source for calibration [1–4]. Cavity blackbody has been maturely developed and applied to calibrate a small infrared instrument, but it cannot meet the calibration requirements for a large aperture area source infrared detection instrument; so, the demand for the area blackbody is becoming stronger. But, the emissivity calculation method of the cavity blackbody does not apply to area blackbodies; therefore, the solution of emissivity for the area blackbody is very important [5].

In the development of the blackbody, it is important to evaluate and measure its radiation capability. Buckley proposed the integral equation method in the 1930s and then gradually improved it by Sparrow and Bedford et al [6]. The integral equation method assumes that the reflection occurring on the inner wall of the blackbody cavity is ideal diffuse reflection and then establishes the

emissivity integral model of each to solve in parallel. In the case that the reflection of the cavity surface is regarded as an ideal diffuse reflection, the integral equation method can be used in the theory to solve the emissivity of the blackbody cavity with any shape. However, it is difficult to meet the ideal diffuse reflection conditions in reality, especially in the area blackbody evaluation, this method has a large error with the actual situation, and the calculation process is complex [7].

The Monte Carlo method is commonly used to calculate the emissivity of the blackbody cavity. Prokhorov A V used the Monte Carlo method to analyze the radiation on the surface of the concentric circular trapezoidal groove and the emission and reflection characteristics of normal and directional angles [8]. C Monte proposed the evaluation standard of cavity emissivity of vacuum terahertz blackbody based on the Monte Carlo method [9]. The heat transfer simulation of a blackbody at low temperature was proposed by Prokhorov A V, but it was also limited to the cavity [10]. Pahl R J proposed a new fast convergence Monte Carlo method but was also used for the blackbody cavity structure [11]. Yikun Zhao calculated and compared the emissivity of two blackbody cavities by the Monte Carlo method and pointed out that the emissivity of the V-shaped cavity was higher [12]. Futao Sun used the Monte Carlo method to calculate the effective emissivity of a cylindrical isothermal cavity, analyzed some factors affecting the effective emissivity of the cavity, and discussed the influence of the spectral emissivity of the cavity wall material on the effective emissivity of the cavity, providing a theoretical basis for the design and calculation of blackbody cavities [13]. JiuLi Shen used the Monte Carlo method to calculate the effective emissivity of the conical blackbody cavity. When the distance from the detector to the cavity orifice is 15 times the cavity radius, the effective emissivity of the conical blackbody cavity is larger [14]. Tingting Xing established a cylindrical blackbody cavity model based on the Monte Carlo method and calculated the effective emissivity of the blackbody cavity model. The results show that when the length–diameter ratio is large, the aperture ratio is small, and the emissivity of the cavity material is large, the effective emissivity of the blackbody cavity is large [15]. Shimizu Y designed a high-precision 100 mm × 80 mm polydimethylsiloxane area blackbody in the room temperature range, and the emissivity is not less than 0.998 [16]. Olschewski F designed a stratospheric balloon-borne, in which the blackbody emissivity of the micro-cone low temperature (−40 to 20°C) surface with a size of 5 mm × 5 mm and a height of 9 mm reaches 0.99 [17]. Bae JiYong designed a small area blackbody emissivity of 0.99 for infrared remote sensing calibration [18]. Chang Anbang's master thesis used the Monte Carlo method to evaluate the emissivity of the V-groove area blackbody, but it also needs other theories to verify it [19]. Yuan S, Naveh D, Watanabe K, Taniguchi T, and Xia F reconstructed unknown spectra from their corresponding photo response vectors by the wavelength and bias-dependent responsivity matrix from the spectra of a tunable blackbody source [20].

In this article, the multiple reflection method integrates the secondary reflection method of Gouffe and the micro-surface element method of DeVos. The basic theory of multiple reflections is deduced and simulated for comparison to the Monte Carlo method. An area blackbody is made according to theoretical calculation of the multiple reflection method, and emissivity is measured by a cavity blackbody under the same temperature to verify its applicability.

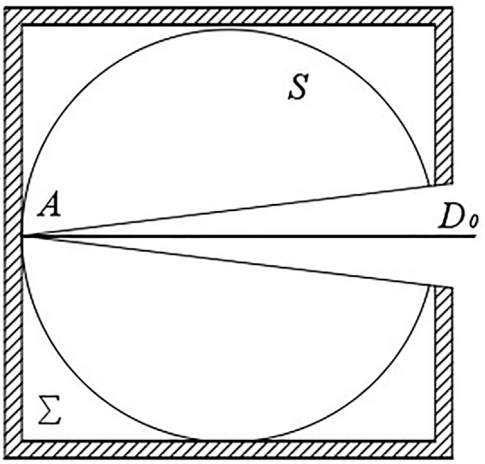

FIGURE 1 | Circular blackbody cavity diagram.

2 MULTIPLE REFLECTION THEORY

The multiple reflection method divides the inner wall of the cavity into infinite micro-faces. The directional radiation intensity of each micro-face is composed of the directional radiation intensity of the micro-face itself and the directional radiation intensity reflected by other micro-faces to the micro-face.

As shown in **Figure 1**, it is assumed that a beam of light vertically enters D_0 at the opening of the blackbody cavity, and the residual light absorbed by the bottom micro-plane element A will reflect the inner surface of the cavity, and a part of it will escape from D_0 at the opening. Therefore, it can be considered that the ratio of the product of the inner surface S of the spherical cavity and the D_0 area at the opening to the reflectivity ρ is equal to the ratio of the total beam energy to the energy of the escaped beam.

When only one reflection is considered, the absorption rate of the blackbody cavity α_1 is calculated as:

$$\alpha_1 = 1 - \rho\frac{D_0}{\pi l^2}, \tag{1}$$

where ρ represents the reflectivity of the inner wall of the cavity in the formula, D_0 represents the area at the opening and l represents the bottom micro-plane element A radius.

However, since there will not be only one reflection in practice, there will still be residual energy continuing to reflect in the inner wall of the cavity. The energy e_1 is left in the cavity after the first reflection for the next reflection, and the same can be said for the

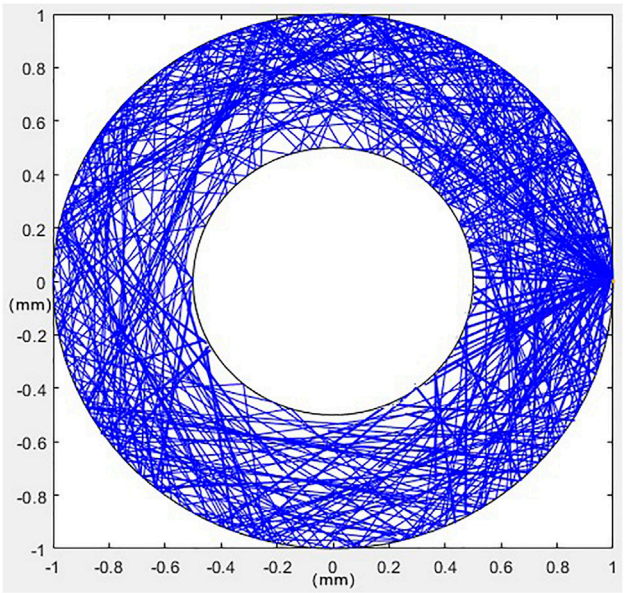

FIGURE 2 | Planar concentric cavity simulation with 1,000 rays.

energy e_2 that escapes from the opening after a secondary reflection:

$$e_1 = \rho\left(1 - \frac{D_0}{\pi l^2}\right); \tag{2}$$

$$e_2 = \rho^2\left(1 - \frac{D_0}{\pi l^2}\right)\frac{D_0}{\Sigma}, \tag{3}$$

where $\sum$ represents the cavity inner wall surface area.

The energy of the beam that finally escapes from the opening e consists of two parts: the energy carried by the beam that escapes directly from a single reflection and the energy that escapes from the opening after multiple reflections:

$$\begin{aligned} e &= \rho\frac{D_0}{\pi l^2} + \rho^2\left(1 - \frac{D_0}{\pi l^2}\right)\frac{D_0}{\Sigma}\left[1 + \rho\left(1 - \frac{D_0}{\Sigma}\right) + \rho^2\left(1 - \frac{D_0}{\Sigma}\right)^2 \right. \\ &\quad \left. + \ldots\right]. \\ &= \rho\frac{D_0}{\pi l^2} + \frac{\rho^2\left(1 - \frac{D_0}{\pi l^2}\right)\frac{D_0}{\Sigma}}{1 - \rho\left(1 - \frac{D_0}{\Sigma}\right)}. \end{aligned} \tag{4}$$

When the total incident energy is set to 1, the reflectivity ρ_0 is the total energy escaping from the opening e. Thus, the emissivity of the black cavity ε can be obtained by subtracting the reflectivity ρ_0 by the total incident energy:

$$\varepsilon = 1 - \rho_0 = 1 - e = 1 - \frac{\rho^2\left(1 - \frac{D_0}{\pi l^2}\right)\frac{D_0}{\Sigma}}{1 - \rho\left(1 - \frac{D_0}{\Sigma}\right)} - \rho\frac{D_0}{\pi l^2}. \tag{5}$$

The multiple reflection method can simulate a more realistic optical path motion trajectory, and then a better calculation of radiant energy can be obtained. It is more concise and clear than the calculation process of the integral equation and avoids the error caused by randomness. The multiple reflection method can be used to verify the calculation results of the Monte Carlo method.

A planar concentric cavity is used for simulating the multiple reflection method. The emissivity of the surface is specified as 0.9, and the radii of the two concentric circles are 1 and 0.5 mm, respectively. When the light intensity is less than 10^{-10} (i.e., 10 reflections on the surface), it is considered to be completely absorbed. The incident position is located on the inner wall on the right side of the big circle. The simulation results are shown in **Figure 2**.

3 SIMULATION

In the design of the area blackbody, surfaces with concentric V-shaped slots are often used because they have a higher effective emissivity than other slotted (e.g., rectangular-slotted) surfaces [21]. Emissivity tends to be uniform regardless of whether the material itself is diffuse or specular reflecting. This type of a radiating surface was usually used and evaluated by the Monte Carlo method.

3.1 V-Groove Model Construction

To compare with calculation results of the Monte Carlo method, the same circular V-groove area blackbody model with a diameter of 50 mm is constructed in this article according to Ref. [19], as shown in **Figure 3**.

The parameters of the V-groove model are shown in **Table 1**:

For the multiple reflection simulation, the amount of light is input, and the light enters the V-groove. The intensity of the light gradually decays through multiple reflections (as shown in **Figure 4**). The emissivity of the surface coating is 0.93. When the intensity of the light is less than 10^{-5} (i.e., after five reflections at the inner wall) [22], it is considered to be completely absorbed, and the light with less than five times reflections is emitted. Finally, the emissivity is calculated according to **Eq. 5**.

3.2 The Amount of Incident Rays

The number of incident rays is an important factor in the emissivity of an area blackbody. It is important to select several incident rays that tend to stabilize the emissivity for the simulation to avoid the chance of sample size problems affecting the emissivity calculation. Repeatedly increasing the number of incident rays in simulation, the 13th (middle) V-groove was selected for simulation. The emissivity was calculated according to **Eq. 5**, and the results are shown in **Figure 5**.

As can be seen from **Figure 5**, when the number of incident rays is less, the calculated emissivity fluctuates widely and cannot avoid the influence of chance on the emissivity calculation due to the small number of incident rays. However, when the number of incident rays exceeds 20,000, the emissivity calculation results tend to be smooth. So, the number of incident rays in the emissivity simulation experiment is chosen to be 20,000.

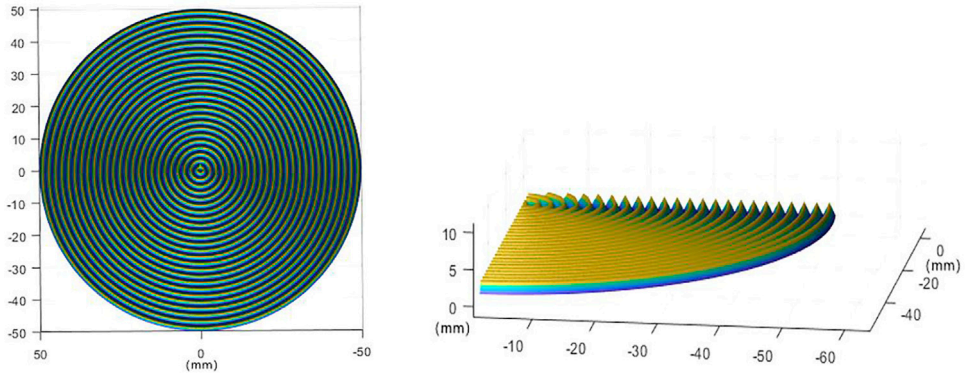

FIGURE 3 | V-slot model drawing.

TABLE 1 | V-groove model parameters.

Parameter name	Parameter value
V-groove spacing	2 mm
V-groove height	1.73 mm
V-groove angle and number	60°, 25
Emissivity of the reflective surface-coating material	0.93
Diameter of the area blackbody	100 mm

3.3 Emissivity Simulation

This simulation uses the established V-groove area blackbody model to simulate the local emissivity in the radius direction of the bottom surface of this blackbody at an incident of 20,000 rays. The model has an overall radius of 50 mm; each V-groove is 2-mm wide and is divided into areas of 10 mm length along the radius (i.e., five adjacent V-grooves are divided into one area, making a total of five areas), and the local emissivity in each area is simulated by varying the angle of incidence of the incident light. A total of five simulations were carried out for each of these areas, and the results of the simulated localized emissivity were matched to the five V-grooves in the area. **Figure 6A** shows the simulation process for the 20–30 mm area:

As shown in **Figure 6A**, the red light is the incident light, and the green light is the reflected light passing through the area blackbody. After the light has been reflected by the V-groove area blackbody, the vast majority of the light has been absorbed (i.e., the light intensity is less than 0.1% of the initial intensity) and only some of the light can be returned by reflection. But, the reflected intensity of the high emissivity coating is also substantially attenuated, and thus the emissivity of the area blackbody is improved.

According to the aforementioned steps, the five regions were simulated five times according to the order of the radius length from small to large, so that the local emissivity value of each V-shaped groove can be obtained.

The emissivity calculated by the multiple reflection method has been obtained through several simulations. Then, it is

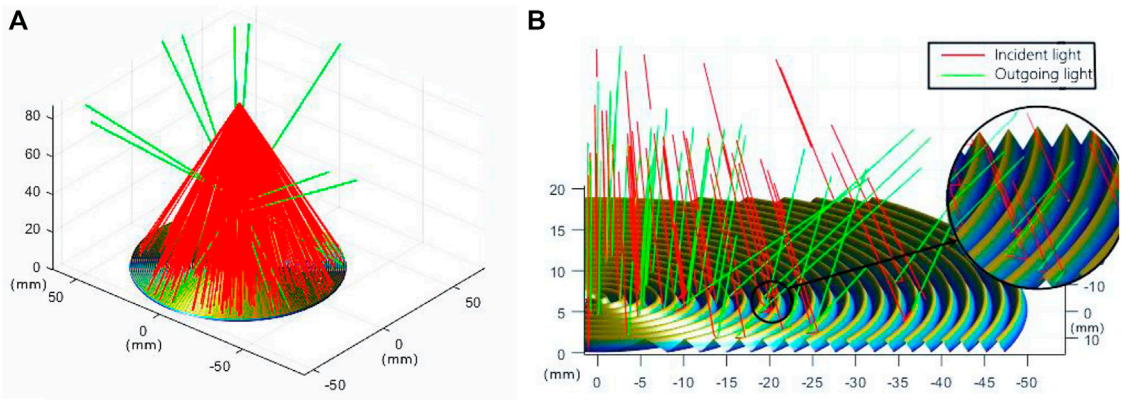

FIGURE 4 | Light reflection path inside the V-groove simulated by the multiple reflection method (point light resource height is 20 cm). **(A)** Overall incident effect schematic and **(B)** local effect schematic.

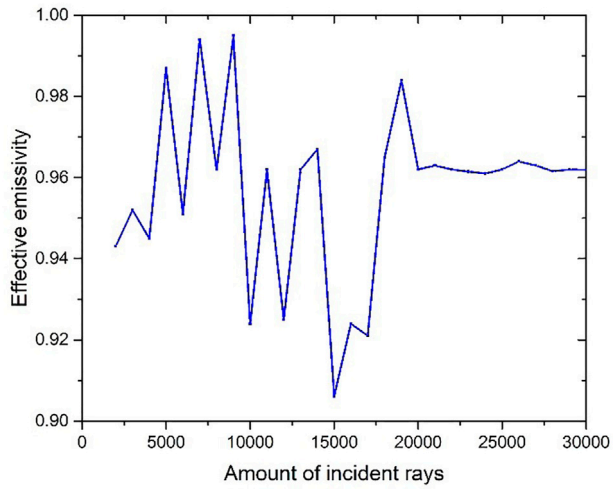

FIGURE 5 | Emissivity stability varies with the amount of incident rays.

compared with the emissivity calculated using the Monte Carlo method (2,000,000 incident lines). The reliability of the method is verified.

The maximum and minimum local effective emissivity values calculated using the Monte Carlo method are 0.9946 and 0.9928, respectively. The minimum local effective emissivity is higher than 0.99. The simulation results shown in **Figure 6B** are obtained by using the two methods[19].

As can be seen from **Figure 6B**, the local emissivity calculated by using the multiple reflection method fluctuates in the range from 0.9928–0.9946 in the 15–35 mm area. The local emissivity of the edge area fluctuates outside the range, but there is no large gap. The overall trend shows a positive correlation. Therefore, the calculation results obtained by the two methods are close.

TABLE 2 | Experimental conditions.

Environment index	Specification
Ambient temperature/°C	20 ± 5
Relative humidity/RH	<80%
Electromagnetism	Avoid strong electromagnetic interference
Vibration	Avoid mechanical vibration
Incline	Place horizontally

4 AREA BLACKBODY PERFORMANCE EXPERIMENT

4.1 Experimental Environment

In this article, an experiment was carried out to verify the feasibility of the multiple reflection method. The experimental conditions are shown in **Table 2**:

The local emissivity of the area blackbody is first measured using a spectrometer and other equipment. Then, a blackbody model is created based on the dimensions of the experimental area blackbody, and the theoretical emissivity is calculated using the multiple reflection method.

4.2 Emissivity Measurement and Calculation

Due to the complexity of the area blackbody and the limitations of infrared radiation measurement accuracy, no equipment can be used for the direct measurement of the area blackbody emissivity. So, a comparative experimental method is used to measure the

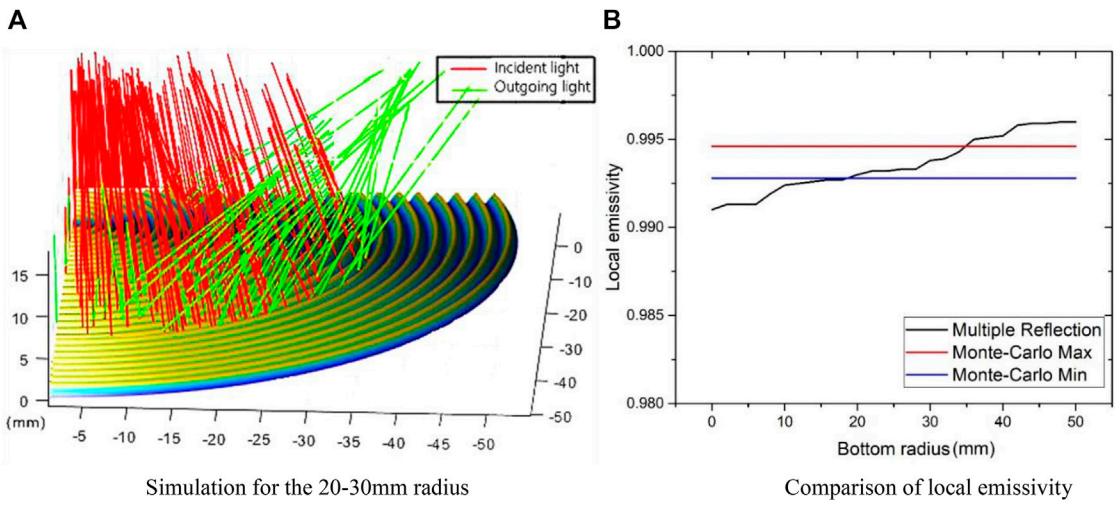

FIGURE 6 | Simulation results obtained by the multiple reflection method with the bottom radius. **(A)** Simulation for 20–30 mm radius and **(B)** comparison of local emissivity.

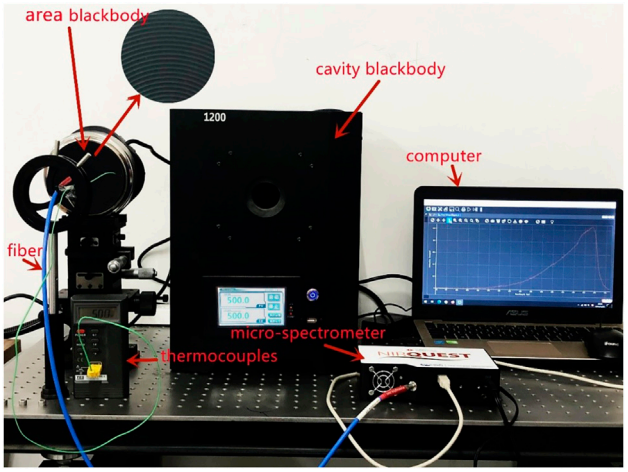

FIGURE 7 | Experimental scenario (measured cavity blackbody and area blackbody radiation intensity with wavelength at the same temperature).

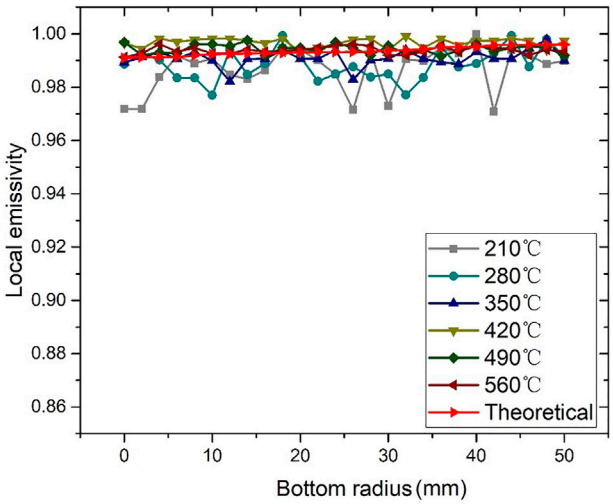

FIGURE 9 | Comparison of theoretical and measured emissivity.

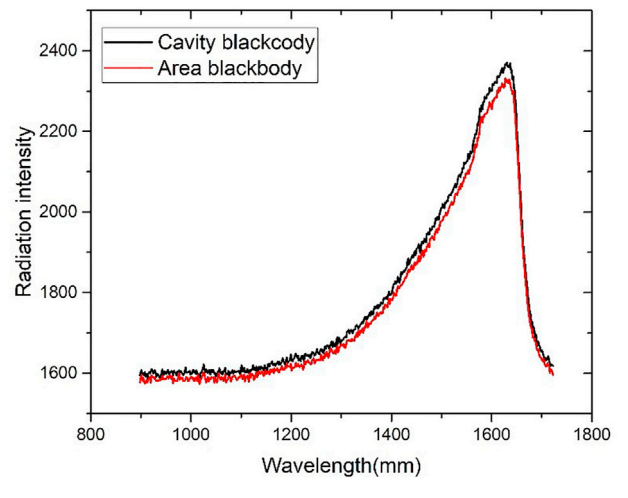

FIGURE 8 | Experiment results at 420°C (cavity blackbody and area blackbody radiation intensity with wavelength).

area blackbody emissivity. The cavity blackbody is used as the standard because the effective cavity blackbody emissivity has been relatively well. The area blackbody emissivity is obtained by the ratio of radiation intensity measured using the spectrometer at the same temperature.

The Ocean Optics NIRQuest512 micro-spectrometer and thermocouples are used for this experiment, and the experimental scenario is shown in **Figure 7**.

First, the standard cavity blackbody and the area blackbody to be measured were fixed in parallel and adjusted to the same temperature. The thermocouple is fixed on the surface of the area blackbody to monitor the temperature. The radiation intensities of the cavity blackbody and the area blackbody are measured using the spectrometer at the same distance. At 420°C, the cavity blackbody and the area blackbody at the radius of 30 mm are tested. The data are collated as shown in **Figure 8**:

Since the emissivity of the cavity blackbody is close to 1, the measured radiation intensity is divided by the radiation intensity of the cavity blackbody, and the average value is the local emissivity of the area blackbody at that position. Keep the temperature constant, and change the position of the fiber by adjusting the three-dimensional optical platform. Repeat the aforementioned steps to measure the emissivity of different positions of the area blackbody.

Afterward, the temperature was changed, and the aforementioned steps were repeated to measure the emissivity at different temperatures and different radius positions. A total of six different temperatures were chosen for this experiment, namely 210, 280, 350, 420, 490, and 560°C. The emissivity at each temperature and position was collated to give the following **Figure 9**.

The dimensions of the area blackbody used for this emissivity measurement experiment are as follows:

The area blackbody model was constructed from **Table 3**. The multiple reflection method used in **Section 3.3** is applied to the simulation model of the area blackbody. The model is divided into different areas in order of radius from small to large. Then, the local emissivity of different positions on the area blackbody

TABLE 3 | Dimensions of the area blackbody.

Specification name	Specification parameter
External shape	Rotundity
Micro-cavity shape	V-groove
External dimension/mm	100
Micro-cavity size/mm	2
Number of micro-cavities	25

model is obtained by the simulation calculation for each area. The results of the simulation are shown in **Figure 9**.

4.3 Discussion of Experimental Results

The measured emissivity was obtained by comparison with the cavity blackbody at different temperatures, and the theoretical emissivity was then calculated based on the multiple reflection method. The theoretical emissivity is around 0.993, with maximum fluctuations not exceeding 0.003. The average of the theoretical and measured emissivity is collated as shown in **Figure 9**:

As can be seen from **Figure 9**, the radiation intensity on the surface of the blackbody is relatively uniform, with fewer fluctuations, and is closer to the theoretical emissivity. This leads to the conclusion that the theoretical values obtained using the emissivity calculation method based on the multiple reflection method coincide with the measured values, which proves the feasibility of the method.

5 CONCLUSION

The multiple reflection method is proposed to calculate the area blackbody emissivity in this article. This method integrates the secondary reflection method of Gouffe and the micro-surface element method of DeVos. The emissivity calculated by the multiple reflection method is similar to that calculated by the Monte Carlo method, and the two algorithms are verified against each other. However, the efficiency of the multiple reflection method is greatly improved. The measured emissivity results in the experiment are equivalent to the theoretical results, which proves the feasibility of the multiple reflection method. This efficient method of calculating the area blackbody emissivity provides a theoretical basis for the area blackbody design of higher emissivity.

DATA AVAILABILITY STATEMENT

The original contributions presented in the study are included in the article/Supplementary Material; further inquiries can be directed to the corresponding author.

AUTHOR CONTRIBUTIONS

JX: conceptualization, resources, validation, supervision, and funding acquisition; DL: writing—original draft, software, formal analysis, data curation, and experiment; SC: methodology, investigation, writing—reviewing and editing, and project administration.

FUNDING

This work was supported by the National Natural Science Foundation of China (No. 61975028).

REFERENCES

1. Liu X, Qiao S, Ma Y. Highly Sensitive Methane Detection Based on Light-Induced Thermoelastic Spectroscopy with a 2.33 Mm Diode Laser and Adaptive Savitzky-Golay Filtering. *Opt Express* (2022) 30(2):1304–13. doi:10.1364/OE.446294
2. Ma Y, Hu Y, Qiao S, Lang Z, Liu X, He Y, et al. Quartz Tuning forks Resonance Frequency Matching for Laser Spectroscopy Sensing. *Photoacoustics* (2022) 25: 100329. doi:10.1016/j.pacs.2022.100329
3. Liu XN, Ma YF. Sensitive Carbon Monoxide Detection Based on Light-Induced Thermoelastic Spectroscopy with a Fiber-Coupled Multipass Cell. *Chin Opt Lett* (2022) 20:031201. doi:10.3788/COL202220.031201
4. Ma Y, Hong Y, Qiao S, Lang Z, xiaonan L. H-shaped Acoustic Micro-resonator Based Quartz-Enhanced Photoacoustic Spectroscopy. *Opt Lett* (2022). doi:10.1364/OL.449822
5. Wijethunge D, Zhang L, Tang C, Du A. Tuning Band Alignment and Optical Properties of 2D van der Waals Heterostructure via Ferroelectric Polarization Switching. *Front Phys* (2020) 15(6):7. doi:10.1007/s11467-020-0987-z
6. Sparrow EM, Jonsson VK. Radiant Emission Characteristics of Diffuse Conical Cavities. *J Opt Soc Am* (1963) 53(7):816–8. doi:10.1364/JOSA.53.000816
7. Cai LL, Tian HX, Wu F, Dong J. Calculate on Effective Emissivity of High-Temperature Blackbody Cavity. *Acta Metrologica Sinica* (2016). doi:10.3969/j.issn.1000-1158.2016.06.11
8. Prokhorov AV, Hanssen LM, Mekhontsev SN, et al. Radiation Properties of IR Calibrators with V-Grooved Surfaces. *Proc SPIE - Int Soc Opt Eng* (2006) 6205: 620505. doi:10.1117/12.667557
9. Monte C, Gutschwager B, Adibekyan A, Hollandt J. A Terahertz Blackbody Radiation Standard Based on Emissivity Measurements and a Monte-Carlo Simulation. *J Infrared Milli Terahz Waves* (2014) 35(8):649–58. doi:10.1007/s10762-014-0056-1
10. Prokhorov AV, Martin JE. Monte Carlo Simulation of the Radiative Heat Transfer from a Blackbody to a Cryogenic Radiometer. *Proc SPIE - Int Soc Opt Eng* (1996) 160–8. doi:10.1117/12.257153
11. Pahl RJ, Shannon MA. Analysis of Monte Carlo Methods Applied to Blackbody and Lower Emissivity Cavities. *Appl Opt* (2002) 41(4):691–9. doi:10.1364/AO.41.000691
12. Zhao Y, Wang J, Feng G, Cao B. Comparative Study on Radiation Properties of Blackbody Cavity Model Based on Monte Carlo Method. *Int J Thermophys* (2020) 41(6). doi:10.1007/s10765-020-02648-1
13. Sun FT. Calculation of the Effective Emissivities of Blackbody Cavity by the Monte-Carlo Method. *J Astronautic Metrology Meas* (2010) 30(2). doi:10.3969/j.issn.1000-7202.2010.02.007
14. Shen JL, Xing TT, Fei WU. Research on the Effective Emissivity of Conical Blackbody Cavity Based on Monte-Carlo Method. *Acta Metrologica Sinica* (2018) 39(3). doi:10.3969/j.issn.1000-1158.2018.03.14
15. Xing TT, Shen JL, Cai LL. Research on Effective Emissivity of Blackbody Cavity High Temperature Sensor Based on Monte-Carlo Method. *Transducer Microsystem Tech* (2017) 36(6), 7–9. doi:10.13873/j.1000-9787(2017)06-0007-03
16. Shimizu Y, Koshikawa H, Imbe M, Yamaki T, Amemiya K. Large-area Perfect Blackbody Sheets Having Aperiodic Array of Surface Micro-cavities for High-Precision thermal Imager Calibration. *Opt Express* (2020) 28(15):22606. doi:10.1364/OE.397136
17. Olschewski F, Monte C, Adibekyan A, Reiniger M, Gutschwager B, Hollandt J, et al. A Large-Area Blackbody for In-Flight Calibration of an Infrared Interferometer Deployed on Board a Long-Duration Balloon for Stratospheric Research. *Atmos Meas Tech* (2018) 11(8):4757–62. doi:10.5194/amt-2017-41710.5194/amt-11-4757-2018

18. Bae JY, Choi W, Hong S-J, Kim S, Kim E, Lee C-H, et al. Design, Fabrication, and Performance Evaluation of Portable and Large-Area Blackbody System. *Sensors* (2020) 20(20):5836. doi:10.3390/s20205836
19. Chang'anbang. *Design, Development, and Testing of Surface Blackbody Radiation Source*. Harbin: Harbin University of Technology (2019). doi:10.27061/d.cnki.ghgdu.2019.002260
20. Yuan S, Naveh D, Watanabe K, Taniguchi T, Xia F. A Wavelength-Scale Black Phosphorus Spectrometer. *Nat Photon* (2021) 15:601–7. doi:10.1038/s41566-021-00787-x
21. Mekhontsev SN, Sapritsky VI, Prokhorov AV, Khromchenko VB, Samoilov ML. *Modeling, Design, and Characterization of Medium-Background Blackbodies for Full-Aperture Calibration of Spaceborne Infrared Systems and Imagers*. Beijing: International Society for Optics and Photonics (1998). doi:10.1117/12.318101
22. Fang Qian-qian 方., Fang Wei 方., Wang Kai 王. Calculation of Effective Emissivity of Blackbody Cavities by Monte-Carlo Method. 中国光学 (2012) 5(2):167–73. doi:10.3788/co.20120502.0167

Conflict of Interest: The authors declare that the research was conducted in the absence of any commercial or financial relationships that could be construed as a potential conflict of interest.

frontiers in Physics

ORIGINAL RESEARCH
published: 16 February 2022
doi: 10.3389/fphy.2022.857371

Optical Feedback Linear Cavity Ringdown Spectroscopy

Xingping Wang[1,2], *Gang Zhao*[3,4*†], *Kang Jiao*[3,4], *Bing Chen*[2], *Ruifeng Kan*[2], *Zhenhua Cong*[5], *Jianguo Liu*[2*†] and *Weiguang Ma*[3,4]

[1]Department of Precise Machinery and Precise Instrument, University of Science and Technology of China, Hefei, China, [2]Key Laboratory of Environmental Optics and Technology, Anhui Institute of Optics and Fine Mechanics, Chinese Academy of Sciences, Hefei, China, [3]State Key Laboratory of Quantum Optics and Quantum Optics Devices, Institute of Laser Spectroscopy, Shanxi University, Taiyuan, China, [4]Collaborative Innovation Center of Extreme Optics, Shanxi University, Taiyuan, China, [5]School of Information Science and Engineering, Shandong University, Jinan, China

Optical feedback cavity ringdown spectroscopy is presented with a linear Fabry–Pérot cavity and a cost-effective DFB laser. To circumvent the low coupling efficiency caused by the broad laser linewidth, an optical feedback technique is used, and an enhanced coupling efficiency of 31%, mainly limited by impedance mismatch and mode mismatch, is obtained. The trigger of the ringdown event is realized by the shutoff of the laser driving current, and a novel method with the aid of one electronic switch is applied to avoid the ringdown events excited by the unexpected cavity modes during the process of laser current recovery. As a result, the ringdown signal with a signal-to-noise ratio of 2500 is achieved. Through continuous monitoring, the fractional uncertainty of the empty cavity ringdown times is assessed to be 0.04%. An Allan variance analysis indicates a detection sensitivity of 4.3×10^{-10} cm^{-1} is resulted at an integration time of 120 s, even with a moderate finesse cavity. To further improve the long-term stability, we regularly rectify the empty cavity ringdown time, and an improvement factor of 2.5 is demonstrated.

Keywords: CRDS, laser absorption spectroscopy, high sensitivity, optical feedback, Fabry–Pérot cavity

OPEN ACCESS

Edited by:
Yufei Ma,
Harbin Institute of Technology, China

Reviewed by:
Ke Chen,
Dalian University of Technology, China
Qi Wang,
Northeastern University, China

***Correspondence:**
Gang Zhao
gangzhao@sxu.edu.cn
Jianguo Liu
jgliu@aiofm.ac.cn

†These authors have contributed equally to this work

Specialty section:
This article was submitted to Optics and Photonics, a section of the journal Frontiers in Physics

Received: *18 January 2022*
Accepted: *25 January 2022*
Published: *16 February 2022*

Citation:
Wang X, Zhao G, Jiao K, Chen B, Kan R, Cong Z, Liu J and Ma W (2022) Optical Feedback Linear Cavity Ringdown Spectroscopy. Front. Phys. 10:857371. doi: 10.3389/fphy.2022.857371

INTRODUCTION

Laser absorption spectroscopy is an effective way for trace gas detection due to its advantages of high sensitivity and high stability. To improve the detection sensitivity, a variety of methods, such as cavity ringdown spectroscopy [1, 2], cavity-enhanced absorption spectroscopy [3, 4], thermoelastic spectroscopy [5, 6], and photoacoustic spectroscopy [7, 8], have been proposed. Cavity ringdown spectroscopy (CRDS) is a well-established spectroscopic technique with the merit of high sensitivity [1, 2]. It leverages an optical cavity to prolong the interaction length between the laser and the intracavity gas, and thus, an amplified absorption signal can be obtained. With superior coating technologies, the amplification factor larger than 10^5 and the detection sensitivity for trace gas detection down to 10^{-13} cm^{-1} could be achieved [9, 10]. On the other hand, CRDS deduces the intracavity absorption information from the variation of the ringdown times, rather than the amplitudes of the cavity transmission modes. Thus, it is immune to laser intensity noise and frequency-to-amplitude noise, which is the main limitation of cavity-enhanced absorption spectroscopy (CEAS). In addition, CRDS is a calibration-free technique that can result in absolute gas concentration. Therefore, in recent decades, CRDS has been widely applied in a variety of application fields [11–13].

To provide regular cavity ringdown events, the laser frequency or cavity length, as well as cavity longitudinal mode frequency, is modulated [14]. However, due to the much broader laser linewidth

compared to the cavity mode width, only a small proportion of the light could be coupled into the cavity at a time, leading to a rather low coupling efficiency. Simulation shows that the coupling efficiency could be improved by nearly 100 times with the narrowing of laser linewidth in CRDS [15]. However, diode lasers, the most prevalent light source in the CRDS application field, have a linewidth of several MHz, which is much larger than the cavity linewidth. As a result, a feeble light will be observed in the cavity transmission and the performance of CRDS will be limited by detector noise and electronic noise.

To circumvent this problem, frequency-locked CRDS has been proposed [16]. By locking the laser to the cavity, or vice versa, *via* the Pound–Drever–Hall method, the laser linewidth is narrowed, and accordingly, high coupling efficiency is attained. However, for a diode laser, because of its large and broadband frequency noise, it is difficult to lock it to a high finesse cavity.

Optical feedback is an alternative method, which is exclusively suitable for a diode laser. The leakage of the intracavity light from the cavity front mirror, acting as an external superb light source with narrow linewidth, returns to the laser, and an injection frequency locking of the laser to the cavity is realized. Optical feedback CRDS (OF-CRDS) was first proposed by Morville based on a V-shape cavity [17, 18]. The improvement of the coupling efficiency by a factor of more than 20 times and neat cavity modes have been observed. Following the first implementation, most existing OF-CRDS setups are based on a V-shape cavity [19–22]. This is because this cavity geometry could separate the intracavity leak-out light from the unwanted direct reflection at the cavity front mirror, which are suspected to generate optical feedback competition with each other. Recently, our group has introduced a linear Fabry–Pérot cavity-based optical feedback CEAS (OF-CEAS) without special care of unwanted direct reflection [23]. By this, optical feedback linear cavity-enhanced absorption spectroscopy (OF-LCEAS) has been developed [3]. The intracavity absorption is derived directly from the amplitude attenuation of the cavity transmission modes. Compared to the V-shape cavity, the Fabry–Pérot cavity is more universal and less sensitive to mechanical vibration and could possess higher finesse. Therefore, it improves the applicability of OF-CEAS.

In this study, optical feedback linear cavity ringdown spectroscopy (OF-LCRDS) based on a linear Fabry–Pérot cavity and a cost-effective DFB laser is presented. Due to the advantages of CRDS over CEAS, a better performance is expected. The ringdown event is excited by changing the laser current below the threshold of emitting quickly. A novel strategy to avoid the trigger of unexpected ringdown events during the laser current recovery is provided. To improve the long-term stability, the optical feedback phase is actively controlled and the empty cavity ringdown time is rectified with the ringdown time at the laser frequency far away from the absorption. The experimental details are presented at first. A ringdown signal with high fidelity is shown. Also, the detection sensitivity is evaluated by the Allan variance plot [24]. Finally, a spectrometer is used to detect CH_4 concentration and its long-term stability is examined.

EXPERIMENTAL SETUP

The schematic diagram of the experimental setup for OF-LCRDS is shown in **Figure 1**. A distributed feedback laser diode (Eblana, EP1653-7-DM-TO56-A04) with a TO footprint, emitted at a wavelength of 1.65 μm, is utilized, which addresses three overlapping strong CH_4 transitions around 6046.9 cm^{-1} with a line strength of around 1×10^{-21} cm^{-1}/(molecule × cm^{-2}). The output light passes through, in sequence, a mode-matching lens, a half-wave plate (λ/2), two reflectors, a polarization beam splitter (PBS), and a quarter wave plate (λ/4). By rotating the λ/4, the feedback ratio could be adjusted.

The light is then injected into a Fabry–Pérot (FP) cavity. The cavity consists of two identical mirrors with a reflectivity of 99.96%, corresponding to a finesse of around 7850. The two mirrors are separated with a length of 39.4 cm, implying a free spectral range of 380 MHz. The maximum coupling efficiency between the laser and the cavity is measured to be around 31%, mainly limited by impedance mismatch and mode mismatch, by monitoring the cavity reflection when the laser frequency is locked to the cavity mode [25]. To control the feedback phase to be an integer multiple of 2π for an effective optical feedback [23], two strategies are utilized. A translation stage mounting the laser and a PZT adhered to one of the reflectors are responsible for coarse and fine phase adjustments, respectively. A correction voltage is sent to the PZT to realize active and real-time compensation, which is generated from the judgment of the asymmetry of the cavity transmission mode. To avoid the usage of an extra optical switch which will deteriorate the stability of optical feedback by introducing optical phase shift and fluctuation, the ringdown event is excited by directly and abruptly cutting off the laser current using a homemade electronic switch, i.e., ES_1. The cavity transmission and ringdown signals are captured using a PD (Thorlabs, PDA 10CS-EC) and then sent to another homemade electronic switch, i.e., ES_2, which is used to filter out the unexpected cavity modes (detailed information will be given in *Ringdown Signal*). The output of ES_2 is divided into two parts. One is sent to a data acquisition (DAQ) card, and the other is sent to a pulse generator, where the latter generates two pulse signals with different starting times and duty ratios to control the ES_1 and ES_2, respectively.

To get the error signal for the control of the optical feedback phase, the symmetry of the arch-shape cavity mode should be acquired before performing the trigger action. Here, the method similar to that in [18] is adopted to show that the ringdown event is excited on the falling edge of the cavity mode. By changing the laser current below the threshold of the laser emitting quickly, the ringdown event can be observed in the cavity transmission. An exponential function is used to fit the ringdown signal by the least square method.

RESULTS AND DISCUSSION

Ringdown Signal

Special measures to avoid the trigger of unwanted ringdown events during the laser current recovery have been taken, and their effect is illustrated in **Figure 2** by the time sequence of process signals. The black curve in **Figure 2A** is the cavity

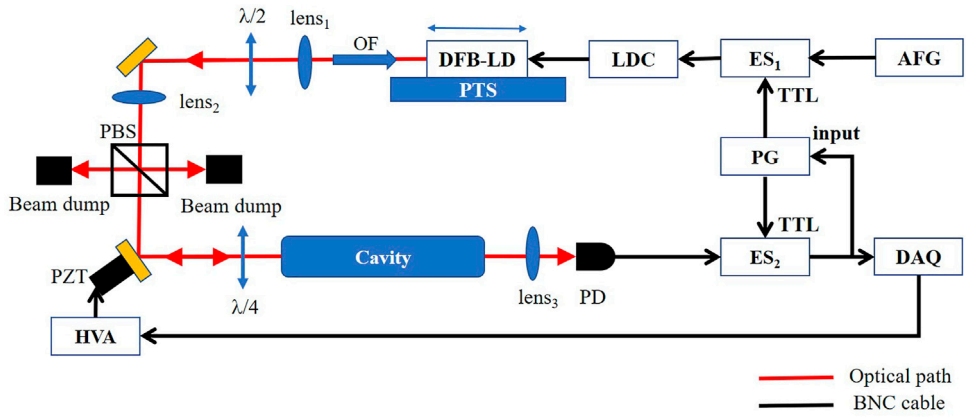

FIGURE 1 | Experimental setup for OF-LCRDS. PG: pulse generator; $ES_{1,2}$: homemade electronic switch; AFG: arbitrary function generator; LDC: laser diode controller; DFB-LD: distributed feedback diode laser; PTS: precision translation stage; $\lambda/2$: half-wave plate; PBS: polarization beam splitter; PZT: piezoelectric transducer; HVA: high voltage amplifier; PD: photodetector; and DAQ: data acquisition card.

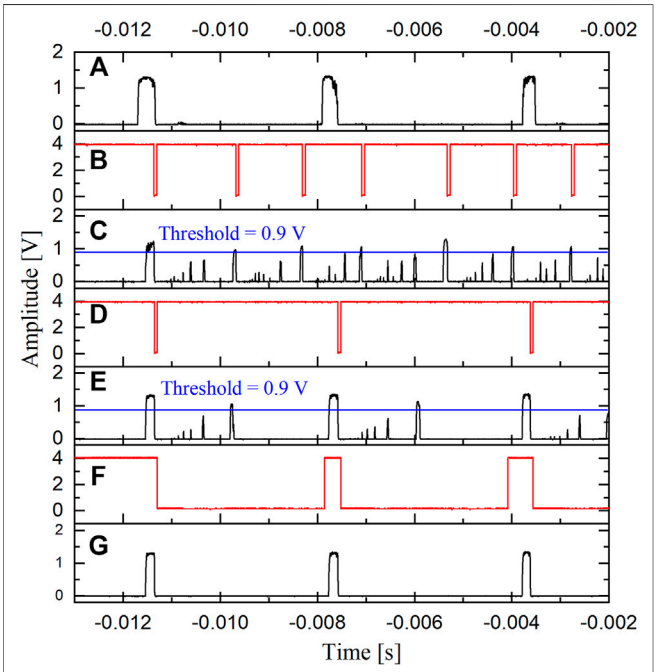

FIGURE 2 | The time sequence of the process signals. **(A)** The cavity transmission modes without the trigger of ringdown event; **(B)** the pulse signal to the ES_1; **(C)** the cavity transmission modes of OF-LCRDS, and a series of messy cavity modes are observed under this situation; **(D)** the pulse signal to the ES_1 with the ES_2; **(E)** the cavity transmission modes of OF-LCRDS with the ES_2; **(F)** the pulse signal to the ES_2 to filter out the unexpected modes; and **(G)** the signal to the DAQ card with the ES_2.

transmission signals for CEAS when the laser current is scanned. There are three successive cavity longitudinal modes, all of which have a typical arch profile. At these points, the laser frequency is briefly locked to the corresponding cavity mode with the time scale of 0.5 ms, even though the nominal linewidth of the laser offered by the manufacturer is 5 MHz and the linewidth of the cavity mode is 54 kHz. This verifies the effect of the optical feedback that could suppress most of the laser frequency noises.

When a falling edge is detected and its amplitude drops below the trigger threshold, a pulse signal with 60 μs duration is generated by the PG and then sent to the ES_1 to cut off the laser current. As a result, one ringdown event is observed. The output signal of the PG is shown in **Figure 2B** with a trigger threshold voltage of 0.9 V for the cavity transmission signal. The curves in **Figure 2C** are the corresponding cavity transmission modes. After 60 μs, the output of the PG would return to its initial state. However, the recovery of the laser wavelength is relatively slow and several unexpected cavity modes might be stimulated during its recovery process, exemplified by the cavity transmission modes with relatively lower amplitude, as in **Figure 2C**. It would also excite the ringdown event if it satisfies the requirement of the trigger. Consequently, a series of messy cavity ringdown events stimulated at uncertain laser frequencies are resulted, just as illustrated in **Figures 2B,C**. This problem could be solved if a higher threshold voltage for the ringdown trigger is set, whereas this strategy is not suitable for the case of large variation of the laser power. For example, a large scanning range of the laser frequency for the detection of a complete absorption spectrum will result in intrinsic variation of the laser power along with the scanning of the laser current.

Here, to address the problem, another electronic switch, i.e., the ES $_2$, is added after the PD, which is controlled by the PG and can filter out these unexpected modes. **Figure 2F** depicts the control signal to the ES_2. Initially, the ES_2 is turned on and the PG can receive the output of the PD. A pulse with a duration of 3.4 ms which lags behind the pulse to the ES_1 is generated by the PG and sent to the ES_2. After the ringdown signal has been recorded using the DAQ card, it will turn off the ES_2 and, thus, cut the link between the PG and the PD. After the laser wavelength gets stable, the ES_2 is turned on again and another ringdown event could be triggered. **Figures 2D,E,G** show the output of the PG to the ES_1, the output of the PD, and the input of the DAQ card by using this new strategy, respectively. It is clear to see, even though

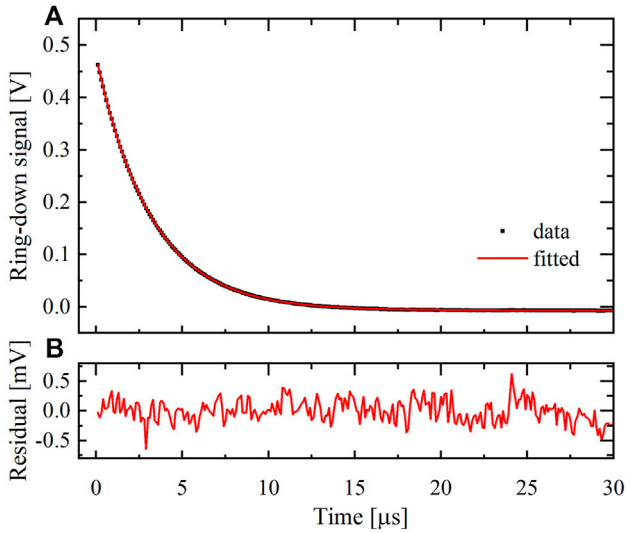

FIGURE 3 | (A) Measured single ringdown event (black dot) and its fitting result by an exponential function (red line). **(B)** The fitting residual.

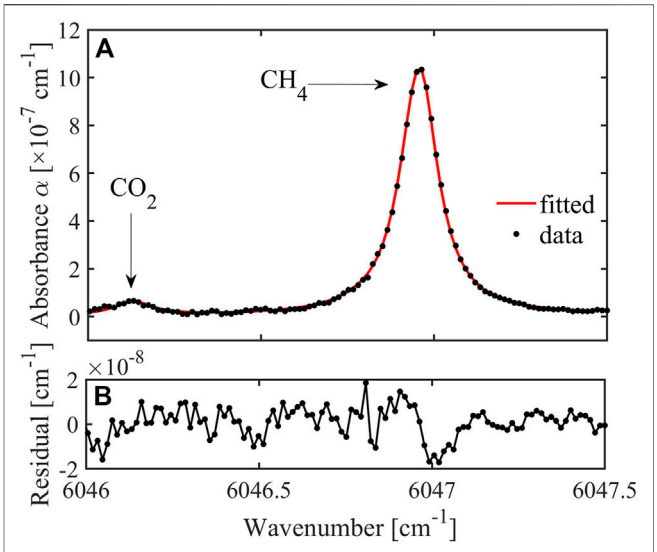

FIGURE 5 | (A) Measured CH_4 absorption spectrum and its fitting result with Lorentz function; **(B)** fitting residual.

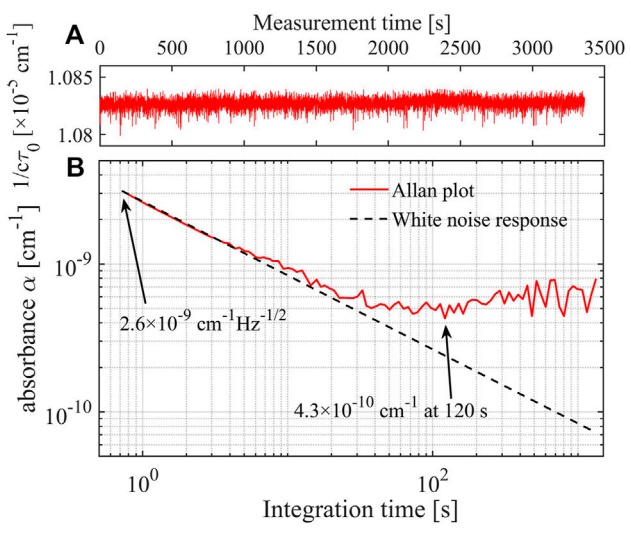

FIGURE 4 | Long-term ringdown time measurement of a single cavity longitudinal mode. **(A)** Empty cavity decay rate; **(B)** Allan variance plot.

the numerous cavity transmission modes are still observed during the recovery of the laser frequency, they do not affect the regular trigger of the desired ringdown event. As a result, three ringdown events corresponding to the three consecutive cavity modes are observed, as shown in **Figure 2G**. With the improvement of the coupling efficiency, large amplitude of the cavity transmission mode as well as the cavity ringdown signal with high repeatability and high signal-to-noise ratio is obtained, illustrated by the black dot in **Figure 3A**. The red curve is the fitting result based on an exponential decay function; and the lower panel is the fitting residual. An excellent signal-to-noise ratio (SNR) of 2500, defined as the ratio of the peak value and the standard deviation of the residual, is obtained. Also, no strong structure has been found in the fitting residual.

Evaluation of the Detection Limit

To estimate the detection sensitivity of OF-LCRDS, a series of ringdown events for a single longitudinal mode of the empty cavity was consecutively measured for around 1 h. This is realized by tuning the laser frequency with a triangle wave signal at a rate of 2 Hz. The red curve in **Figure 4A** depicts the measured empty cavity decay rate, $1/(c{\cdot}\tau_0)$, over time (c is the speed of light, and τ_0 is the empty cavity ringdown time). It demonstrates a 0.04% fractional uncertainty of the ringdown times, i.e., $\sigma(\tau_0)/E(\tau_0)$ [$\sigma(\tau_0)$ is the standard deviation of τ_0, and $E(\tau_0)$ is the mean value of τ_0], which is among the state-of-the-art of CRDS results. Slow fluctuations can be seen in **Figure 4A**, and it is suspected to be caused by the environmental temperature change which leads to the variation of the cavity length and mechanical vibration which leads to the light hitting the different spots of the cavity mirrors. There is also sparse impulse noise which is attributed to the electric noise and etalon effect. The Allan variance plot [24] is shown as a red curve in **Figure 4B**. A white noise response of 2.6×10^{-9} cm^{-1} $Hz^{-1/2}$ was obtained, which is illustrated by the dash line in black. Also, the system reached its detection limit of 4.3×10^{-10} cm^{-1} at an integration time of 120 s, corresponding to a minimal detection of CH_4 concentration of 1.2 ppb by a CH_4 transition at 6046.9 cm^{-1}.

Measurement of the CH_4 Absorption Spectrum

Then, the absorption spectrum of CH_4 is measured. We filled the cavity with the ambient air of our lab located at Taiyuan,

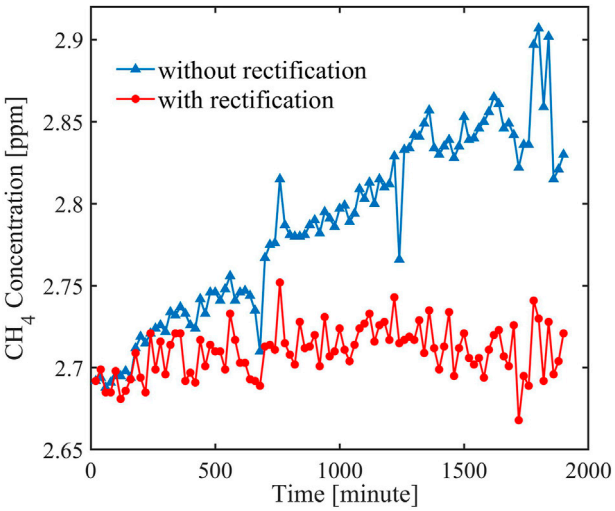

FIGURE 6 | Long-term measurement of CH_4 with constant concentration.

China, which is filtered by using a desiccant first. The intracavity pressure was set to 0.92 atm, i.e., the local atmospheric pressure. In the experiment, each cavity mode was scanned 50 times for average ringdown time. The laser current is scanned by a triangular wave with a frequency scanning range of around 0.5 FSR at a rate of 50 Hz. The shift of the adjacent cavity mode is realized by stepping the central value of the laser current, and it took 7 min to get a whole spectrum. The empty cavity ringdown time is measured at the wavelength of 6047.5 cm^{-1}, which is 18 GHz away from the center of the nearest strong absorption transition. The obtained absorption spectrum is shown as the black dots in **Figure 5A**. With a total laser frequency scanning range of 45 GHz, 118 successive cavity modes are stimulated and a CO_2 absorption line is observed besides the CH_4 absorption line, shown as a small bump in **Figure 5**. The spectral parameters from the HITRAN database [26] and Lorentzian line-shape function are used to fit the measurement spectrum. The fitted curve is displayed as a red line in **Figure 5A**, and the fitting residual is presented in **Figure 5B**. The theoretical model shows a good consistency with the measured spectrum, and the signal-to-residual ratio of 156 is obtained. The retrieved CH_4 concentration is 2.73 ppm.

Rectification of the Empty Cavity Ringdown Time

The variation of the empty cavity ringdown time, owing to temperature fluctuation and mechanical vibration, is the dominant limitation to the long-term stability of CRDS. To solve this problem, the empty cavity ringdown time is rectified regularly by the ringdown time at the laser frequency far away from the gas absorption transition. To verify the effectiveness of this method, a long-term concentration measurement with a time interval of 20 min and a duration of 34 h for CH_4 gas with a constant concentration has been performed. The dotted lines in blue and red in **Figure 6** are the measured concentrations without and with rectification, respectively. Without rectification, the drift range of retrieved concentration is 0.2 ppm within this measurement time. After the rectification, the drift range is suppressed to 0.08 ppm, which shows an improvement with a factor of 2.5.

CONCLUSION

In summary, we have developed optical feedback linear cavity ringdown spectroscopy. The ringdown event is excited by changing the laser current below the threshold of emitting quickly. An effective method to avoid the ringdown events excited by the unexpected cavity modes during the process of current recovery is introduced with one electronic switch. The coupling efficiency of the laser to the FP cavity is improved to 31%, mainly limited by the mode mismatch and impedance mismatch, by optical feedback, and consequently, ringdown signals with high fidelity are achieved. The fractional uncertainty of empty cavity ringdown time is 0.04%, yielding a minimal detection of CH_4 concentration of 1.2 ppb at the integration time of 120 s. The long-term retrieved concentration drift is improved by 2.5 times within 34 h through rectifying the empty cavity ringdown time during the measurement of each spectrum. This novel technique paves the way for the construction of a robust and sensitive CRDS instrument for trace gas detection.

DATA AVAILABILITY STATEMENT

The raw data supporting the conclusion of this article will be made available by the authors, without undue reservation.

AUTHOR CONTRIBUTIONS

XW: data curation, formal analysis, methodology, and writing—original draft. GZ: conceptualization, supervision, validation, visualization, writing—review and editing. KJ: formal analysis. BC: software and validation. RK: resources and writing—review and editing. ZC: resources and validation. JL: supervision, funding acquisition, project administration, and writing—review and editing. WM: writing—review and editing.

FUNDING

This work was supported by the equipment development project of the Chinese Academy of Sciences (Grant No. ZDKYYQ20200006), National Natural Science Foundation of China (Grant Nos. 61875107, 61905136, 61905134, 62175139, and 61805286), and Opening Foundation of Key Laboratory of Laser and Infrared System (Shandong University), Ministry of Education.

REFERENCES

1. Paldus BA, Kachanov AA. An Historical Overview of Cavity-Enhanced Methods. *Can J Phys* (2005) 83:975–99. doi:10.1139/p05-054
2. Romanini D, Ventrillard I, Méjean G, Morville J, Kerstel E. Introduction to Cavity Enhanced Absorption Spectroscopy. In: G Gagliardi L Hans-Peter, editors. *Cavity-enhanced Spectroscopy and Sensing*. New York, NY: Springer (2014). p. 1–60. doi:10.1007/978-3-642-40003-2_1
3. Tian J, Zhao G, Fleisher AJ, Ma W, Jia S. Optical Feedback Linear Cavity Enhanced Absorption Spectroscopy. *Opt Express* (2021) 29:26831–40. doi:10.1364/OE.431934
4. Głuszek A, Senna Vieira F, Hudzikowski A, Wąż A, Sotor J, Foltynowicz A, et al. Compact Mode-Locked Er-Doped Fiber Laser for Broadband Cavity-Enhanced Spectroscopy. *Appl Phys B* (2020) 126:1–6. doi:10.1007/s00340-020-07489-2
5. Liu X, Qiao S, Ma Y. Highly Sensitive Methane Detection Based on Light-Induced Thermoelastic Spectroscopy with a 2.33 Mm Diode Laser and Adaptive Savitzky-Golay Filtering. *Opt Express* (2022) 30:1304–13. doi:10.1364/OE.446294
6. Liu X, Ma Y. Sensitive Carbon Monoxide Detection Based on Light-Induced Thermoelastic Spectroscopy with a Fiber-Coupled Multipass Cell [Invited]. *Chin Opt Lett* (2022) 20:031201. doi:10.3788/COL202220.031201
7. Ma Y, Hu Y, Qiao S, Lang Z, Liu X, He Y, et al. Quartz Tuning forks Resonance Frequency Matching for Laser Spectroscopy Sensing. *Photoacoustics* (2022) 25:100329. doi:10.1016/j.pacs.2022.100329
8. Ma Y, Hong Y, Qiao S, Lang Z, Liu X. H-shaped Acoustic Micro-resonator-based Quartz-Enhanced Photoacoustic Spectroscopy. *Opt Lett* (2022) 47:601–4. doi:10.1364/OL.449822
9. Winkler G, Perner LW, Truong G-W, Zhao G, Bachmann D, Mayer AS, et al. Mid-infrared Interference Coatings with Excess Optical Loss below 10 Ppm. *Optica* (2021) 8:686–96. doi:10.1364/OPTICA.405938
10. Cole GD, Zhang W, Martin MJ, Ye J, Aspelmeyer M. Tenfold Reduction of Brownian Noise in High-Reflectivity Optical Coatings. *Nat Photon* (2013) 7:644–50. doi:10.1038/nphoton.2013.174
11. Fleisher AJ, Long DA, Liu Q, Gameson L, Hodges JT. Optical Measurement of Radiocarbon below Unity Fraction Modern by Linear Absorption Spectroscopy. *J Phys Chem Lett* (2017) 8:4550–6. doi:10.1021/acs.jpclett.7b02105
12. Hu M, Chen B, Yao L, Yang C, Chen X, Kan R. A Fiber-Integrated CRDS Sensor for In-Situ Measurement of Dissolved Carbon Dioxide in Seawater. *Sensors* (2021) 21:6436. doi:10.3390/s21196436
13. Tao L-G, Liu A-W, Pachucki K, Komasa J, Sun YR, Wang J, et al. Toward a Determination of the Proton-Electron Mass Ratio from the Lamb-Dip Measurement of HD. *Phys Rev Lett* (2018) 120:153001. doi:10.1103/PhysRevLett.120.153001
14. Hodges JT, Layer HP, Miller WW, Scace GE. Frequency-stabilized Single-Mode Cavity Ring-Down Apparatus for High-Resolution Absorption Spectroscopy. *Rev Scientific Instr* (2004) 75:849–63. doi:10.1063/1.1666984
15. Hahn JW, Yoo YS, Lee JY, Kim JW, Lee H-W. Cavity Ringdown Spectroscopy with a Continuous-Wave Laser: Calculation of Coupling Efficiency and a New Spectrometer Design. *Appl Opt* (1999) 38:1859–66. doi:10.1364/ao.38.001859
16. Paldus BA, Harb CC, Spence TG, Wilke B, Xie J, Harris JS, et al. Cavity-locked Ring-Down Spectroscopy. *J Appl Phys* (1998) 83:3991–7. doi:10.1063/1.367155
17. Morville J, Kassi S, Chenevier M, Romanini D. Fast, Low-Noise, Mode-By-Mode, Cavity-Enhanced Absorption Spectroscopy by Diode-Laser Self-Locking. *Appl Phys B* (2005) 80:1027–38. doi:10.1007/s00340-005-1828-z
18. Morville J, Romanini D, Kachanov AA, Chenevier M. Two Schemes for Trace Detection Using Cavity Ringdown Spectroscopy. *Appl Phys B* (2004) 78:465–76. doi:10.1007/s00340-003-1363-8
19. Baran SG, Hancock G, Peverall R, Ritchie GAD, van Leeuwen NJ. Optical Feedback Cavity Enhanced Absorption Spectroscopy with Diode Lasers. *Analyst* (2009) 134:243–9. doi:10.1039/B811793D
20. Wan F, Zhou F, Hu J, Wang P, Wang J, Chen W, et al. Highly Sensitive and Precise Analysis of SF6 Decomposition Component CO by Multi-Comb Optical-Feedback Cavity Enhanced Absorption Spectroscopy with a 2.3 μm Diode Laser. *Sci Rep* (2019) 9:9690. doi:10.1038/s41598-019-46190-z
21. Tan Z, Long X. A Developed Optical-Feedback Cavity Ring-Down Spectrometer and its Application. *Appl Spectrosc* (2012) 66:492–5. doi:10.1366/11-06291
22. Hippler M, Mohr C, Keen KA, McNaghten ED. Cavity-enhanced Resonant Photoacoustic Spectroscopy with Optical Feedback Cw Diode Lasers: A Novel Technique for Ultratrace Gas Analysis and High-Resolution Spectroscopy. *J Chem Phys* (2010) 133:044308. doi:10.1063/1.3461061
23. Zhao G, Tian J, Hodges JT, Fleisher AJ. Frequency Stabilization of a Quantum cascade Laser by Weak Resonant Feedback from a Fabry-Perot Cavity. *Opt Lett* (2021) 46:3057–60. doi:10.1364/OL.427083
24. Werle P, Mücke R, Slemr F. The Limits of Signal Averaging in Atmospheric Trace-Gas Monitoring by Tunable Diode-Laser Absorption Spectroscopy (TDLAS). *Appl Phys B* (1993) 57:131–9. doi:10.1007/BF00425997
25. Zhao G, Hausmaninger T, Ma W, Axner O. Differential Noise-Immune Cavity-Enhanced Optical Heterodyne Molecular Spectroscopy for Improvement of the Detection Sensitivity by Reduction of Drifts from Background Signals. *Opt Express* (2017) 25:29454–71. doi:10.1364/OE.25.029454
26. Gordon IE, Rothman LS, Hill C, Kochanov RV, Tan Y, Bernath PF, et al. The HITRAN2016 Molecular Spectroscopic Database. *J Quant Spectros Radiat Transfer* (2017) 203:3–69. doi:10.1016/j.jqsrt.2017.06.038

Conflict of Interest: The authors declare that the research was conducted in the absence of any commercial or financial relationships that could be construed as a potential conflict of interest.

frontiers in Physics

REVIEW
published: 01 March 2022
doi: 10.3389/fphy.2022.853966

Improvement of the Detection Sensitivity for Tunable Diode Laser Absorption Spectroscopy: A Review

Shan Lin[1,2], *Jun Chang*[1]*, *Jiachen Sun*[1] *and Peng Xu*[3]

[1]School of Information Science and Engineering and Shandong Provincial Key Laboratory of Laser Technology and Application, Shandong University, Qingdao, China, [2]Key Laboratory of Laser and Infrared System of Ministry of Education, Shandong University, Qingdao, China, [3]Jinan Jingheng Electronics Co., Ltd., Jinan, China

Tunable Diode Laser Absorption Spectroscopy (TDLAS), a trace gas sensing technology based on infrared absorption spectroscopy, has been developed rapidly in the past few decades. The advantages of low cost and easy miniaturization could be applied in real-time monitoring. As an important factor, the detection sensitivity of TDLAS has been improved by a variety of methods. In this review paper, the important advances in TDLAS detection sensitivity are discussed, including the selection of absorption lines, the improvement of diode lasers, the design of effective optical paths, data demodulation, and the suppression of background interference. For gases with high application values, such as CH_4, CO_2, and NO, we summarize the detection sensitivity that the existing TDLAS system has been achieved, combined with the above-improved process. However, considering the principle of infrared absorption, the increase in detection sensitivity could reach an ultra-limit. Therefore, the hypothesis of the sensitivity limit of TDLAS is proposed at the end of the paper, through the quantization analysis.

Keywords: TDLAS, trace gas sensing, infrared absorption spectroscopy, tunable diode lasers, detection sensitivity, quantization

OPEN ACCESS

Edited by:
Yufei Ma,
Harbin Institute of Technology, China

Reviewed by:
Qiang Wang,
Changchun Institute of Optics, Fine Mechanics and Physics (CAS), China
Cunguang Zhu,
Liaocheng University, China
Wei Wei,
Los Alamos National Laboratory (DOE), United States

***Correspondence:**
Jun Chang
changjun@sdu.edu.cn

Specialty section:
This article was submitted to Optics and Photonics, a section of the journal Frontiers in Physics

Received: *13 January 2022*
Accepted: *08 February 2022*
Published: *01 March 2022*

Citation:
Lin S, Chang J, Sun J and Xu P (2022) Improvement of the Detection Sensitivity for Tunable Diode Laser Absorption Spectroscopy: A Review. Front. Phys. 10:853966. doi: 10.3389/fphy.2022.853966

INTRODUCTION

Real-time monitoring of trace gas concentrations has become more significant in the domains of business, agriculture, social life, and environmental protection in recent years. Trace gas sensing detection of spectroscopy approach is widely employed in different industries, such as environmental monitoring, combustion diagnosis, and aerospace, due to its benefits of high sensitivity, low cost, real-time monitoring, and non-invasiveness [1–3]. In the early 1970s, tunable diode lasers were applied to trace gases detection, greatly improving the portability of optical gas sensing technology and reducing detection costs [4]. With the improvement of the output power and wavelength stability of semiconductor lasers, many spectroscopy-based techniques such as tunable diode laser absorption spectroscopy (TDLAS), photoacoustic spectroscopy (PAS) [5, 6], photothermal spectroscopy (PTS) [7], cavity ring-down spectroscopy (CRDS) [8], and other detection methods have been widely used [9, 10].

In PAS, quartz-enhanced photoacoustic spectroscopy (QEPAS) is the most commonly used technique. While the quartz tuning fork improves the anti-interference and selectivity of QEPAS, it also has a long process of accumulating acoustic energy and is easily disturbed by strong electromagnetic environment. As another indirect absorption spectroscopy technique, PTS has high sensitivity and is not affected by scattering and background signals. However, the cost of the

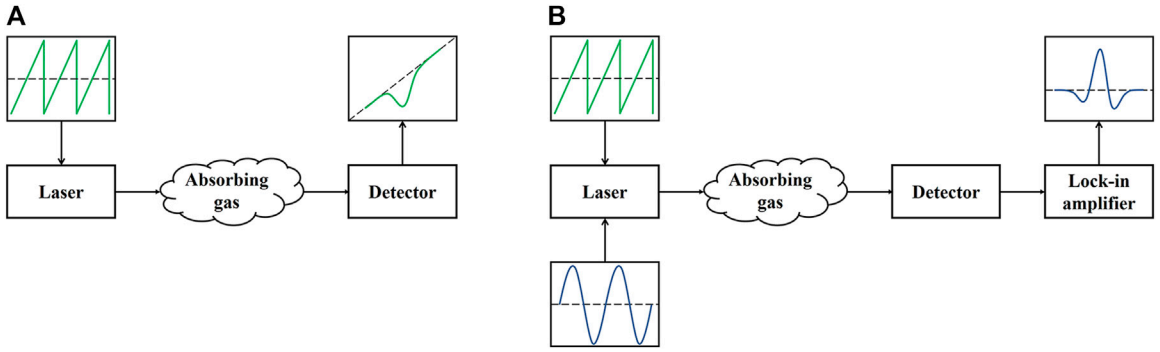

FIGURE 1 | (A) Scanned-wavelength direct absorption spectroscopy. **(B)** Scanned-wavelength modulation spectroscopy.

PTS system is high, and it is not suitable for large-scale industrial applications at this stage. As for CRDS, the absorption optical path could be extended to thousands of meters by the optical mirror, so the detection accuracy is extremely high. However, this method has relatively high requirements on the experimental system and is difficult to be used for on-site online measurement. TDLAS has strong adaptability to complex environments, high selectivity, low cost, and the measurement results meet most actual needs. Its application value has always been the focus of researchers.

With the development of related technologies, researchers are paying more and more attention and hoping to improve the detection sensitivity of the TDLAS system through a variety of methods. These approaches mainly include the selection of absorption lines and diode lasers, the improvement of the effective optical path, the demodulation of data, and the suppression of background interference, which together achieved a quite ideal detection effect. However, based on the principle of infrared absorption, there should be a limitation of the detection sensitivity, which is related to the type of gas and the laser energy involved in the absorption.

Therefore, this review covers the evolution of TDLAS detection sensitivity in recent years, discusses the improvement of key components in the existing system, and compares the detection sensitivity with different improved techniques. However, the improvement of TDLAS sensitivity is not endless. Through the quantization analysis of gas infrared absorption, the assumption about the ultra-limit of TDLAS detection sensitivity is proposed at the end of this paper.

PRINCIPLE

According to Beer Lambert's law, the attenuation of light intensity is related to the concentration of the absorbing medium, the length of the optical path, and the lineshape. Based on this theory, the output wavelength of the tunable diode lasers could be tuned by current, temperature, and other ways to cover the gas absorption lines. The photon energy is absorbed by the gas molecules through the optical path, and the transmitted light intensity is attenuated. Then the absorption information of the gas can be obtained by detecting the variation of light intensity. Scanned-wavelength direct absorption spectroscopy (DAS) and scanned-wavelength modulation spectroscopy (WMS) are two commonly used detection techniques.

As shown in **Figure 1**, a low-frequency triangular wave, sawtooth wave, or trapezoidal wave is used to drive the diode laser in scanned-wavelength direct absorption spectroscopy so that its output wavelength changes in the same way. After scanning the characteristic absorption peak of the corresponding gas, the concentration information of the gas can be obtained through the photodetector and the related data processing modules. The high-frequency sinusoidal signal is superimposed on the low-frequency scanning signal in wavelength-modulation spectroscopy, which can effectively suppress the interference of the system noise. The harmonic signal is generated after being absorbed by the gas, and its amplitude is proportional to the concentration of the gas to be measured [11].

METHODS TO IMPROVE TDLAS DETECTION SENSITIVITY

Researchers have done a lot of work to improve the sensitivity of TDLAS, mainly including the selection of absorption lines, the improvement of diode lasers, the design of effective optical path, signal demodulation, and the suppression of background interference.

The Selection of Absorption Lines

The fundamental, overtone, and difference bands are mostly concentrated in the infrared area, which features a lot of absorption lines. **Figure 2** shows the linestrength of various infrared absorption transitions for a few common species in the range of 400–10,000 cm^{-1} at 296 K. Therefore, it is important to select an appropriate absorption line for trace gas detection. Firstly, the absorption lines should be sufficiently independent to avoid interference from other gases that are abundant in the atmosphere, such as H_2O and CO_2 [12]. Furthermore, the line strength should be appropriate to improve the detection sensitivity of the TDLAS system [13, 14]. The line strength of the gas absorption spectroscopy

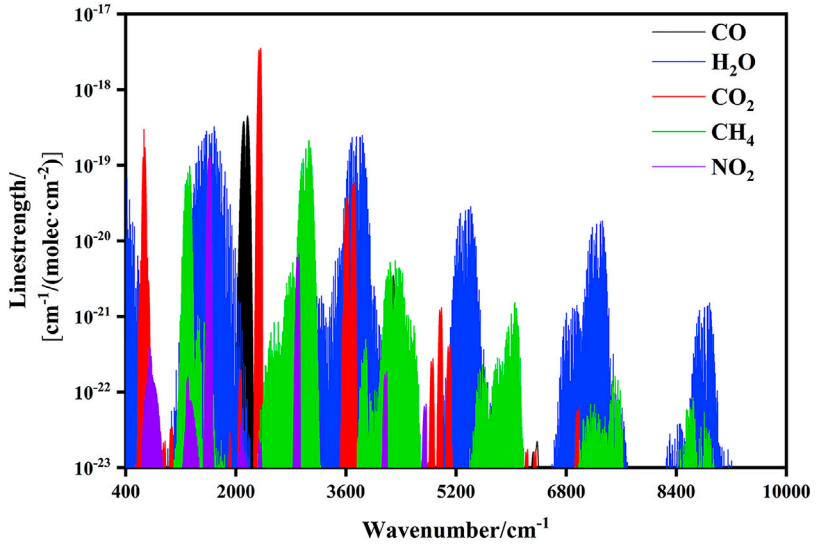

FIGURE 2 | Absorption lines of typical atmospheric species in the infrared. Data are taken from the spectroscopic database HITRAN.

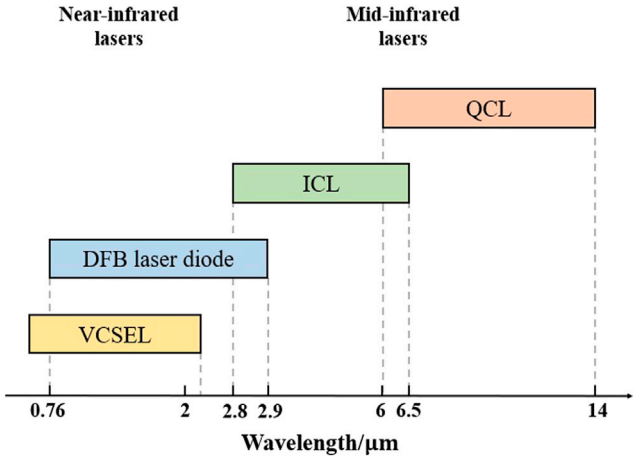

FIGURE 3 | The characters of VCSEL, DFB laser diode, ICL, and QCL, according to the data from Nanoplus.

represents the absorption capacity of a specific wavelength, which is related to the distribution of low-energy particles and the transition probability of the gas molecules. Therefore, the absorption line strength is most affected by temperature. Moreover, the lineshape function is highly significant when simulating the profile of the gas absorption spectroscopy, and different lineshape functions might reflect different broadening mechanisms. The Doppler effect of molecular motion dominates spectroscopy broadening in high-temperature and low-pressure conditions, and it is commonly characterized by the Doppler line profile. As for low-temperature and high-pressure conditions, the collision of molecular motion plays a dominant role and the Lorentzian line profile is generally used to describe the line broadening [15]. In most cases, the effects of Lorentz broadening and Gaussian broadening must be evaluated at the same time, and the Voigt profile is the convolution of the Gaussian and Lorentzian profiles [16].

Databases such as GEISA, HITEMP, and HITRAN provide detailed spectral parameters [17–19], covering more than 709,000 transitions for most atmospheric species. The individual spectral line data including line strength, wavenumber, and lower state energy, are suitable for analysis and selection of absorption lines. Furthermore, the relevant data are corrected and supplemented by related researchers, which helped to further improve the accuracy of gas detection [20].

The Improvement of Diode Lasers

As the light source, the linewidth of the laser should be narrow. It should also have the characteristics of stable performance, compact structure, and high output power. Therefore, the main applications for trace gas monitoring in the laboratory and industrial settings are distributed feedback laser diode (DFB-LD), vertical cavity surface emitting lasers (VCSEL), and the mid-infrared lasers including interband cascade lasers (ICL) and quantum cascade lasers (QCL), the characters are shown in **Figure 3**.

DFB-LD is a type of useful tunable diode laser that is operated on the principle of grating mode selection to get a specific wavelength depending on the Bragg gratings contained in the laser structure. The effective refractive index of the grating will be changed by temperature, leading to the change of output wavelength. Therefore, the tuning range of the DFB-LD is closely related to the effective refractive index of the grating material. In 1973, Nakamura et al. developed the first DFB laser, which achieved a narrow linewidth output near 830 nm [21]. However, the early GaAs DFB lasers have extremely high threshold conditions and need to operate at extremely low temperatures, making it difficult for large-scale applications [22]. In addition to GaAs, other III-VI group semiconductor

materials, such as InP, can achieve longer output wavelength and are successfully achieved operation under low-temperature conditions (<0°C) [23]. Sakai et al. exploited the separate-confinement heterostructure to obtain a 1.5-μm continuous wavelength output that can operate continuously between −20°C and 58°C, with a threshold current as low as 50 mA at room temperature [24, 25]. Since then, the DFB laser's application potential as a light source used for the optical sensors has been discovered. Morris et al. used graded-index separate-confinement heterostructure to achieve a 760 nm continuous single-mode tunable laser with a critical current of 25 mA, temperature tuning rate of 0.06 nm/°C, current tuning rate of 0.0075 nm/mA, and the tunable wavelength range is 4.2 nm, and successfully used for O_2 detection [26]. Doussiere et al. designed a novel structure that integrates a relatively short distributed-Bragg grating near the output facet and a high reflectivity facet coating on the rear facet [27]. And they achieved the single-mode power over 200 mW at case temperature up to 60°C is consistently obtained for current below 300 mA.

DFB-LD is usually modulated by the current and temperature to control the range of output wavelength. Its tuning efficiency is closely related to the frequency of the driving current and the material of the laser diode, and it will have a great impact on the signal-to-noise ratio (SNR) and residual amplitude modulation. Sun J et al. found that tuning efficiency is affected by the different materials inside the DFB-LD, which is a robust parameter guiding us to choose favorable DFB-LD [28]. Since the injection current has a great influence on the internal temperature of the DFB-LD, which leads to the fluctuation of output wavelength range, suppressing the change of the internal temperature of the DFB-LD is beneficial to improve the sensitivity of the gas detection system [29]. Compared with traditional LD sources, the biggest advantage of DFB-LD is that it can be used in complex industrial environments and on-site detection. Wei Y et al. employed the 1.62 μm fiber-coupled DFB diode laser as the light source to achieve a ppm-level high sensitivity detecting system for the multi-point ethylene concentration detection, meeting the needs of fire warning in coal mine goafs [30]. Wang Z et al. chose the absorption line of water vapor at 1,368.5597 nm for detection and achieved the lowest detection limit of 790 ppb [31]. Using a single DFB diode laser emitting at 2.33 μm, Shao L et al. presented a spectrometer for constantly measuring atmospheric CO and CH_4 [32]. According to the Allan variance, the respective minimum detection limits for CO and CH_4 are 0.73 and 36 ppb at 122 s and 137 s.

Although the DFB-LD may provide extremely narrow laser output, the tuning range is limited; nevertheless, VCSEL compensates for this shortage. The VCSELs have good wavelength tunability and can achieve a tuning range of 10 cm^{-1} at a modulation frequency around 1 MHz. Soda H et al. proposed the concept of vertical cavity surface emission for the first time and obtained dynamic single longitudinal mode semiconductor lasers by shortening the cavity length [33]. And they successfully prepared the first VCSEL operated at 77 K, but its threshold current is as high as 0.9 A. Later, they further realized a pulsed VCSEL made of GaAs/GaAlAs. The threshold current under 77 K conditions was reduced to 350 μA, but the threshold current under room temperature conditions was 1.2 A [34]. K. Iga et al. developed a VCSEL that can operate continuously at room temperature in 1989. Since then, the advancement of VCSEL has ushered in a major turning point, with the technology progressing towards long wavelengths. The advent of the devices continuously operated at the wavelength of 1,310 nm and 1,550 nm under room temperature has greatly enriched the wavelength detection range of VCSELs [35, 36].

With the maturity of VCSELs, the excellent characteristics have become the focus of researchers in the field of gas sensing. Wang J et al. used the VCSEL with a wide current-tuning frequency range as the light source to detect oxygen in a high-pressure environment [37]. The wider tuning range enables VCSELs to obtain more spectral information and then realize the simultaneous detection of multiple gases with a single light source and the correction of gas concentration. Chen J et al. employed VCSEL to achieve simultaneous detection of CO and CH_4 at 2.3 μm at an effective absorption path length of 20 cm, with detection accuracy reaching the ppm-level [38]. Wang Y et al. used a VCSEL with output wavelengths over the range from 1,682.7 nm to 1,685.7 nm achieving a detectable concentration of 300 ppm with relative errors below 5% is sufficient for successful early warning of propane leaks in the petrochemical and oil-gas storage and transportation industries [39]. At the same time, VCSELs have well-developed uses in the near-infrared region for detecting the concentrations of CO, CO_2, CH_4, and other typical gas. Chen J et al. achieved the first 2.3 μm VCSEL-based CO sensor. They employed an absorption cell with a 10 cm optical path length that can detect CO in 1 s with a ppm resolution [40]. And with the development of miniaturization, the VCSELs with a micro-electro-mechanical system(MEMS) capable of spans of 2–110 nm and repetition rates of 10–1,000 kHz, which successfully applied to the absorption spectroscopy detection of H_2O and HF in the range of 1,321–1,354 nm [41].

Compared with the near-infrared band, the fundamental band of most gas molecules is mainly concentrated in the mid-infrared band. Therefore, many researchers are considering the use of tunable diode lasers in the mid-infrared band for trace gas detection to increase the SNR and sensitivity of the system. Theoretically, Lead salt diode lasers made from IV-VI semiconductor materials can operate in the 3–30 μm spectral region [42]. However, due to the structural of IV–VI materials, Lead salt diode lasers must work in cryogenic temperatures, and problems such as beam divergence, multi-mode competition, and low output power are not suitable for gas absorption spectroscopy detection [43]. The temperature properties and output light intensity of the telluride-based semiconductor laser are better than those of the lead salt laser, however, it is difficult to achieve a wavelength range of more than 5 μm [44, 45]. The appearance of Interband Cascade lasers (ICL) and Quantum Cascade lasers (QCL) ameliorates these problems. Different from the inter-band transition process of traditional semiconductor lasers, the laser generation process of QCLs only involves the conduction band and the electrons in it to achieve the inversion of the number of particles between different quantum well energy levels and radiate laser light. Based on this idea, Faist J et al. designed the first

quantum cascade laser in 1994, with an output wavelength of about 4.2 μm, an output power of only 8.5 mW under 10 K conditions, and a threshold current density as high as 14 kA/cm^2 [46]. In the following 20 years, the rapid development of QCLs has been achieved in terms of operating temperature, output performance, and wavelength coverage. In 1997, a DFB-QCL capable of working at room temperature was successfully developed. The output wavelengths were 5.4 and 8 μm respectively, and the former can achieve a peak power of 60 mW at 300 K [47]. In 2001, Faist J et al. further realized the QCL with an output wavelength of 9.1 μm, which operated continuously at room temperature, with an output power of 17 mW at 292 K and a maximum continuous operating temperature of 321 K [48].

With continuous improvement, QCLs have gradually become the most competitive light source in the mid-to-far infrared band and have shown extremely high application value in trace gas detection. Although long-wavelength devices still require low-temperature cooling, the continuous output within 16 μm could be achieved at room temperature, through the design of quantum wells [49], which are suitable for monitoring the greenhouse gases like CH_4, NO, N_2O. Kasyutich et al. used a continuous wave DFB-QCL and a single-pass absorption cell with an optical path length of only 21 cm to detect CO, N_2O, and NO, with detection limits of 2.8, 0.6, and 2.7 ppm, respectively [50]. Using a novel compact MGC, Ren W et al. demonstrated the construction of a single-QCL based absorption sensor for the simultaneous detection of atmospheric CH_4 and N_2O at 7.8 μm. The detection limit of 5.9 ppb for CH_4 and 2.6 ppb for N_2O was achieved respectively, at the 1-s averaging time [51]. Maity et al. selected the absorption line of C_2H_2 at 1,311.76 cm^{-1} and achieved the lowest detection limit of the ppb level within the integration time of 110 s [52].

The electrons of ICLs could transition between the conduction and valence band, enabling semiconductor materials with a narrow bandgap to be used. Therefore, the wavelength range of ICLs is narrower, which makes up for the lack between traditional semiconductor diode lasers and QCLs. Yang et al. produced DFB-ICL with a single-mode lasing wavelength of 3.3 μm by introducing distributed feedback Bragg gratings, and its working temperature reached 175 K [53]. In 2006, under the temperature of 78 K, the continuous output power of ICL was increased to 1.1 W [54]. In the same year, under the adjustment of the temperature controller, the 3.3 μm ICL achieved continuous operation at a temperature of 264 K [55]. In 2013, Nanoplus provided 3–6 μm commercial ICLs. This wavelength region includes fundamental C-H, O-H, and N-H stretch vibrations [56–58] and it covers an important gap in wavelength coverage between diode lasers and QCLs. Song F et al. proposed the sensor system with a 3,291 nm ICL and a multi-pass gas cell with a 16 m optical path length. A limit of detection of ~13.07 ppb with an averaging time of 2 s was achieved using the DSP-based digital lock-in amplifier (DLIA) and a limit of detection of ~5.84 ppb was obtained using the LabVIEW-based DLIA with the same averaging time [59].

In general, among the above tunable lasers, it can be found that DFB-LD is suited for large-scale production applications. DFB-LD could operate at room temperature without the use of a complicated cooling device, and the line width could exceed 1 MHz. However, the tuning range of DFB-LD is small, and the absorption line strength in the near-infrared region is lower than mid-infrared, so it is difficult to achieve extremely sensitive detection results. VCSELs are cheap to produce, have a wide tuning range and low thresholds. As mid-infrared laser sources, QCL and ICL could achieve higher detection sensitivity. But these types of lasers are expensive and need to operate at low temperatures. They are therefore suitable for extremely high demands on detection results or for experimental exploration.

The Design of Effective Absorption Path

In absorption spectroscopy gas sensor detection, in addition to the selection of an appropriate light source, the design of an effective absorption path is also very important to improve the detection sensitivity and SNR of the system. According to the Beer-Lambert law, the effective interaction length of the laser energy and the gas sample has a significant effect on the absorption signal. In the traditional absorption spectroscopy gas sensing technology, a multipath absorption cell is often used to increase the effective absorption optical path. In 1942, White proposed a long optical path absorption cell composed of three concave mirrors with the same radius of curvature and named by his name [60]. Although the White cell achieves a long absorption path through multiple reflections between the mirrors, the design of this three-sided mirror makes the entire device bulky and the mirrors need to be strictly aligned. Herriott simplified the structure of the white cell and designed a new type of multi-optical path absorption cell [61]. The Herriott cell only retains two concave mirrors. The incident light enters the absorption cell through a hole of one mirror, and after multiple reflections in it, it exits from the same hole. Compared with White cell, the structure of the Herriott cell has been greatly simplified, and by adjusting the structure of the two mirrors, an effective absorption path of tens of meters to hundreds of meters can be achieved [62]. Although Herriott cell improves the problem to a certain extent, the structure of this kind of absorption cell is often complex to achieve a long absorption path. Moreover, once the optical path is fixed, the number of reflections cannot be changed and the effective absorption path cannot be flexibly adjusted. This is not conducive to practical engineering applications, so researchers have been exploring the miniaturization of multi-path absorption cells. Through the precise design of the absorption cell, the light spot covers the entire mirror surface as much as possible, although the path of a single absorption is not long, it can finally achieve long optical path absorption through hundreds of reflections [63]. To further improve the detection limit, this kind of multi-reflection long optical path absorption cell is gradually applied to the mid-infrared gas detection system and realizes the detection of C_2H_6, N_2O, and CH_4 at the ppb or even ppt level [62, 64, 65].

Based on the idea of multiple reflections, another cavity enhancement technique that combines the resonant characteristics of the optical resonator with the laser gain characteristics is designed to obtain a long absorption optical path. In 1998, O'Keefe and Engeln almost simultaneously

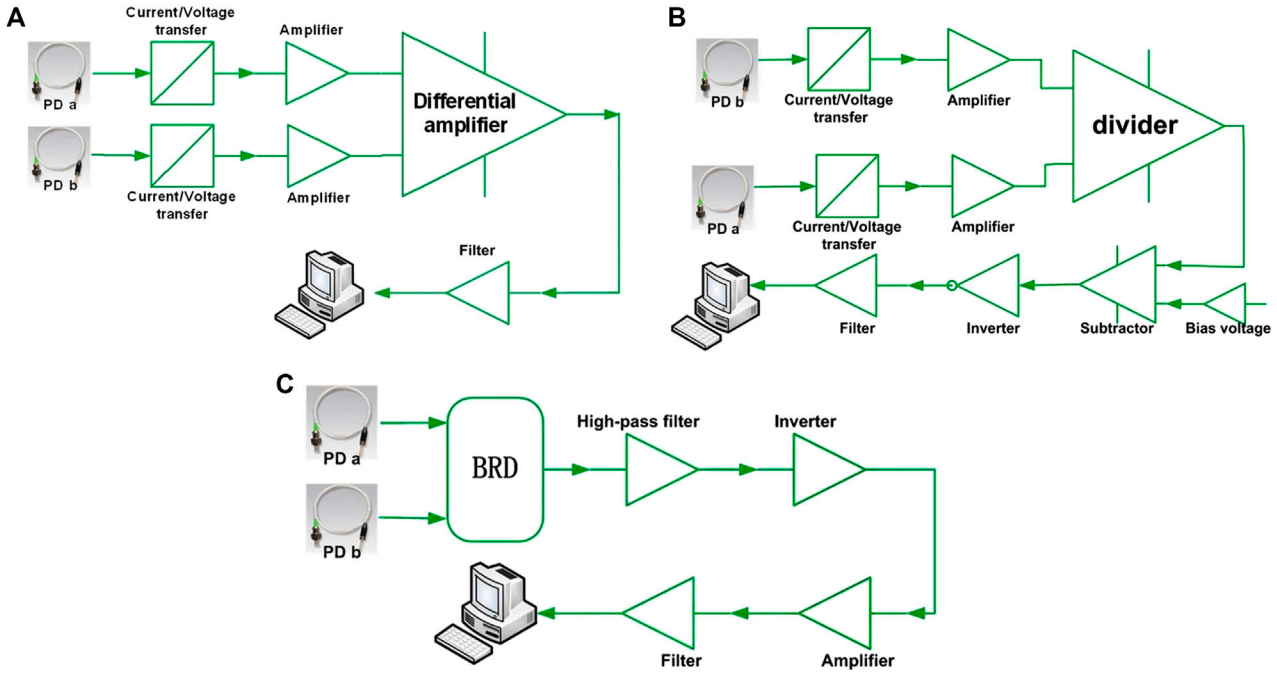

FIGURE 4 | Schematic diagram of the **(A)** subtraction demodulation circuit **(B)** division demodulation circuit **(C)** BRD demodulation circuit.

proposed the technique to detect the integration of the light intensity passing through the resonant cavity [66, 67]. The method uses a semiconductor laser as a coherent light source, and uses a cavity mirror with high reflectivity to form a resonant cavity to achieve an extremely long effective absorption optical path, and detects the target gas by detecting the time-integrated light intensity passing through the cavity. Paul et al. proposed an off-axis incident cavity enhancement method considering the sensitivity in different environments [68]. This method effectively suppresses cavity mode noise by exciting more high-order transverse modes in the resonant cavity and has a simple optical structure and stronger adaptability to different conditions, so it is widely used in the field of gas detection. Barry et al. applied the integrated cavity to the study of methane near 1.73 μm using a tunable diode laser and achieved a detection sensitivity of 1.8×10^{-7} cm^{-1} for mirror reflectivities of 99.84% [69]. With the maturity of mid-infrared semiconductor lasers, more and more researchers have begun to combine them with cavity enhancement technique. Rao et al. used a quantum cascade laser with a tuning range of 1,601–1,670 cm^{-1} to detect the concentration of NO_2, and the lowest detection limit improved to 28 ppt [70]. In a recent study, Mhanna et al. used a 3.3 μm DFB-ICL as the light source and obtained an effective absorption path length of 1.39 km through the off-axis incidence. They finally realized the detection of the ppt level of benzene vapor [71].

Signal Demodulation and Background Interference Suppression

The method for signal demodulation, as well as the suppression of background interference, plays a key role in enhancing the detection accuracy and sensitivity, in addition to selecting appropriate components for a gas detection system.

Signal Demodulation

A low-frequency scanning signal must be used to tune the tunable laser in scanned-wavelength direct absorption spectroscopy so that the modulated wavelength can sweep the characteristic absorption peak of the gas to be measured. However, in the detection of trace gases, weak signal changes are usually drowned out by background signals. Therefore, the output of the laser is usually divided into two paths, one as the signal and the other as the reference, and the signal generated by the gas absorption is extracted by the method of differential demodulation. The commonly used processing methods include subtraction, division, Balanced Ratiometric Detector (BRD), and the schematic diagrams of the three demodulation methods are shown in **Figure 4**.

In the subtractive demodulation algorithm, the light is divided into two paths through the coupler, one path does not pass through the gas cell and serves as the reference; the other is absorbed by the gas to be measured, and serves as the signal. The two signal lights are converted into current signals by the photodetector, and after gain amplification, enter the subtractor, and demodulate the absorption peak of the gas. Here we assumed the intensity of reference light $I_{ref}(\nu)$ and signal light $I_{sig}(\nu)$ are respectively expressed as:

$$I_{ref}(\nu) = I_0(\nu) \tag{1}$$

$$I_{sig}(\nu) = I_0(\nu)\exp(-\alpha CL) \tag{2}$$

Then the output signal $I_{out}(\nu)$ through subtractor is:

$$I_{out}(\nu) = I_0(\nu) - I_0(\nu)\exp(-\alpha CL) \tag{3}$$

In trace gas detection, $\alpha CL \ll 1$, $\exp(-\alpha CL)$ can be approximately expressed as $1 - \alpha CL$, then the above formula can expressed as:

$$I_{out}(\nu) = I_0(\nu)\alpha CL \tag{4}$$

It can be seen that subtractive demodulation is greatly affected by the input light intensity. The principle of subtractive demodulation is simple and easy to operate. To determine the concentration of water vapor, Wang Q et al. devised a novel method based on the differential value of two adjacent absorption peaks [72]. Two absorption lines at 1,367.862 nm and 1,368.597 nm are selected to integrate the adjacent absorption peaks, the accuracy and resolution can reach to 20 and 10 ppm, respectively.

However, in actual detection or facing some harsh environments, the stability of the input optical power cannot be guaranteed, and the subtractive demodulation has certain problems. On this basis, dual-optical division demodulation has been developed. The structure of division demodulation is similar to that of subtraction. The biggest difference is that it used the division circuit to demodulate the absorbed signal. The reference signal and the detection signal can still be expressed as **Eqs 1**, **2**. After the division operation, the output signal can be expressed as:

$$I_{out}(\nu) = \exp(-\alpha CL) \approx 1 - \alpha CL \tag{5}$$

The initial intensity in the two signals are canceled out after the division operation, and the output signal is related with the concentration of the gas, theoretically eliminating the influence of input optical power fluctuations. Although the divider has a good suppression effect on the fluctuation of optical power, it is more suitable for eliminating the noise in the low-frequency range.

Although BRD is still a differential demodulation method, it can directly normalize the current signal output by the photodetector, avoiding the process of voltage transfer [73]. The voltage V at the output of the BRD system could be given by:

$$\mathrm{V} = -\ln\left(\frac{I_{ref}}{I_{sig}} - 1\right) \tag{6}$$

As mentioned above, I_{ref} and I_{sig} refer to the current from the reference beam and the signal beam, respectively. According to **Eqs 1**, **2**, the relationship between the measured voltage and the concentration of the gas can be expressed as:

$$\mathrm{V} = -\ln\left(\exp(-\alpha CL) - 1\right) \tag{7}$$

When weak absorption is applied to **Eq. 7**, the measured voltage is nearly proportional to absorbance and consequently V is proportional to concentration C. The working bandwidth of this method is affected by the photodetector, which can usually reach GHz. Sonnenfroh, Upschulte and the others [74, 75] explored and proved that the BRD can be applied to the gas absorption spectroscopy of tunable diode lasers. By adding matching resistors, Wang Q et al. improved the influence of conductivity mismatch on the measured absorption spectra. With the application of averaging and filtering, absorption sensitivity of 1.093×10^{-6} for water vapor at 1,368.597 nm has been demonstrated, and the corresponding concentration is 71.8 ppb in just a 10 cm path length [76]. Zhu C et al. comprehensively compared the three demodulation methods of subtraction, division, and BRD [77]. The division approach has a variance of only 0.29% when the ambient temperature varies by 1°C, which exceeds the subtraction method (2.90%) and the BRD method (0.55%).

As another important technique of TDLAS, wavelength-modulation spectroscopy has a very important impact on improving detection sensitivity. Wavelength modulated spectroscopy superposes high frequency modulated signal based on low-frequency scanning wave, which provides the possibility for the application of harmonic detection technique [78, 79]. In general, the system noise below 1 kHz is mainly 1/f noise. In the harmonic detection technique, each harmonic component carries the concentration information generated by gas absorption. After periodic modulation of a certain frequency by the laser, the signal could be moved to the relatively high-frequency area by the harmonic component, so that the 1/f noise can be effectively suppressed. However, not all harmonic components can effectively reflect gas concentration. With the number of harmonics increasing, the amplitude gradually decreases, and the amplitude of odd harmonics is zero at the center of the absorption line. Therefore, harmonic detection usually needs to be combined with the phase-locked amplification technique to achieve trace gas detection.

Phase-locked amplification is a commonly used weak signal detection technique. Through the two key steps of phase-sensitive detection and low-pass filtering [80], according to the frequency and phase of the signal to be measured, the DC component that carries the amplitude of the useful signal is extracted. Wei W et al. used wavelength modulation spectroscopy combined with signal–reference beam method for trace gas detection, which not only achieved common-mode noise suppression but also improved the SNR. The measurement accuracy of the system can reach 1 ppm for an optical path length of 10 cm verified by trace water vapor detection experiments [81]. Wang F et al. have expanded the functionality of the phase-locked amplification technique, which can accurately measure the phase information from the extremely weak signal. As shown in **Figure 5A**, hanging amplitudes and phases of the sinusoidal signals, a phase detection linearity of 0.99999 R-square is achieved by the phase demodulator. The output of low-pass filter S_{R1} and S_{R2} are shown in **Figure 5B** and the noises of the signals are shown in **Figure 5C**. **Figure 5D** is the noise levels comparison of phase detection. They achieved a resolution of better than ±0.005% in 0.99% O_2 [82].

To further eliminate the influence of common-mode interference, researchers have proposed a method of normalizing the second harmonic signal using the first harmonic [83]. The influence such as light intensity fluctuations and random scattering in the optical path could be eliminated in this way. To eliminate the influence of light

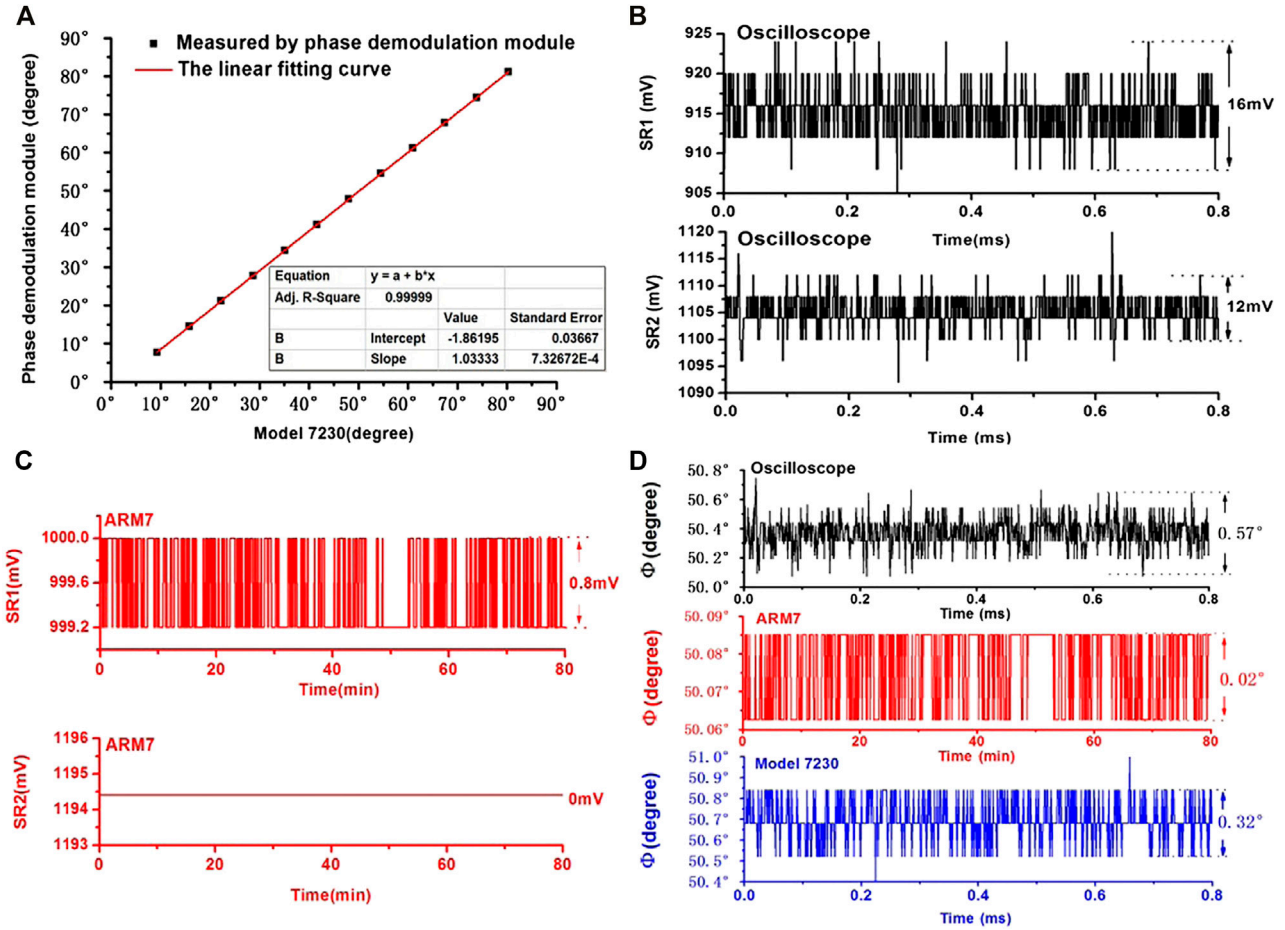

FIGURE 5 | Functional verification of the phase demodulator. **(A)** Phase detection linearity. **(B)** Signals SR1, SR2. **(C)** Signals S_{R1}, S_{R2} after 160,000 times of average algorithm. **(D)** Noise levels comparison of phase detection.

intensity fluctuations in wavelength modulation, Yang C et al. obtained gas concentration by measuring the first harmonic phase angle that is independent of light intensity [84]. This method has great potential in the applications of the WMS technique especially under high modulation frequencies or modulation-amplitude limited conditions. Roy et al. suggested a method in which the 1f WMS and 2f WMS signals are normalized by the linear and non-linear intensity modulation components, respectively [85]. With a single-pass detection limit of 3 ppb for CO (using 1f WMS and 4.05 m route length) and 45 ppb for CO_2 (using 2f WMS and 20 cm path length), the system has an optimum integration time of 17 s and 69 s, respectively.

Background Interference Suppression

The main interference includes non-absorptive background caused by light dispersion, optical path loss, etc., and additional absorption background caused by device packaging or poor coupling.

Non-absorptive background fluctuations for gas detection systems, especially in low-concentration detection, will affect the output light intensity and seriously interfere with the final detection results. In order to eliminate this part of the impact, Wang F et al. proposed a demodulation algorithm based on the head-tail technique for single-beam water vapor detection under rough environmental conditions. The experiment indicates that, when the light power attenuates 4%, the deviation in a single-beam system is 1.29%, which is superior to a dual-beam subtraction system whose deviation is 8.45% [86]. Wei W et al. presented an artificial absorption peak technology, which created an artificial absorption peak of known concentration next to the real absorption peak without being overlapped. The artificial absorption peak technology can suppress the effect of non-absorption transmission losses and noise on the selection of potential reference points in the sensor system. The signal of the artificial absorption peak is added to the driving signal of the laser, and as shown in **Figure 6**, the reference points become easier to distinguish. When the non-absorption transmission losses change between 0 and 70%, measurement error reaches as low as 0.425% (0.17 ppm) with the DA method and 0.225% (0.09 ppm) with the WMS method [87].

A large part of the extra absorptive background interference comes from the background absorption in the free space inside the

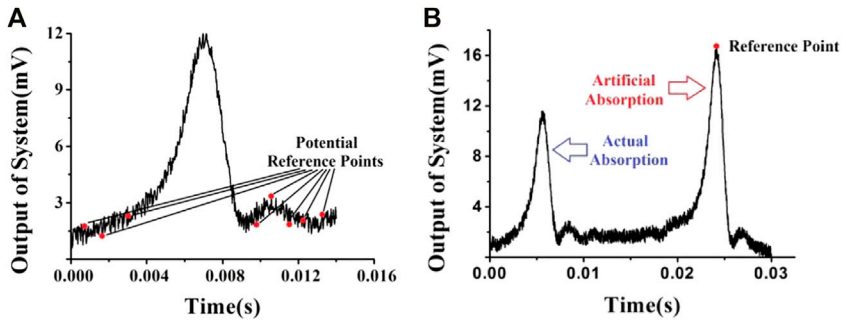

FIGURE 6 | (A) Detected signal of a single absorption line with the DA method, revealing that noise increases the difficulty and uncertainty of the selection of the reference point. **(B)** Differential detection of the signals of two absorption peaks, one of which is artificial. By creating an artificial absorption peak next to the real absorption zone, the reference point becomes easier to distinguish.

TABLE 1 | Summary of TDLAS trace gas sensors or instruments.

Molecule	Laser type	Wavelength/cm^{-1}	Technique	EAP	Acquisition time	MDL	References
CH_4	DFB-QCL	1,275.04	WMS	57.6 m	1-s	5.9 ppb	[51]
	DFB-ICL	2968.4–2968.85	WMS	580 m	290 s	560 ppt	[64]
	DFB-LD	4297.56	WMS	72 m	137 s	36 ppb	[91]
N_2O	DFB-QCL	1,274.61	WMS	57.6 m	1-s	2.6 ppb	[51]
	DFB-QCL	2190.2	DAS	76 m	1 s	0.49 ppb	[92]
CO	DFB-QCL	2,190.2	DAS	76 m	1 s	0.35 ppb	[92]
	DFB-ICL	2,131	WMS	3.99 m	10 s	0.6 ppb	[93]
CO_2	DFB-QCL	2,282.9	DAS	76 m	1 s	170 ppb	[92]
	DFB-LD	6,335	WMS	55.1 m	30 s	7.5 ppm	[94]
NO	DFB-QCL	1,900.08	WMS	1 m	3 s	42 ppb	[95]
	DFB-ICL	1,929.03	DAS	82 mm	10 ms	30 ppm	[96]

MDL: minimum detection limit.
EAP: effective absorption path.

optoelectronic device. When detecting gases with high components in the atmosphere, such as oxygen, water vapor, and carbon dioxide, these gases would inevitably remain inside the device and become the background interference of the detection system. The signal received by the detector not only contains the absorption information of the gas to be measured but also carried the intrinsic absorption signal inside the device, which will have a great impact on the detection of trace gases. Wang Q et al. chose a strong absorption line near 1,368.6 nm for water vapor and designed a simple test to verify the existence of background absorption inside the optoelectronic device [88]. Zhu CG et al. also found the distortion of the absorption spectroscopy caused by the water vapor in the gap between the end faces of the optical elements [89]. Wang Q et al. proposed a method of reasonable recombination of the collimator and the PD to suppress the influence of background absorption in the system [76]. However, this method is cumbersome to operate due to the effect of the pairing of optoelectronic devices. Lv GP et al. combined the dual-beam differential method to achieve time-domain differential correction through optical switches, thereby suppressing the influence of water vapor inside the device [90]. Wang Y et al. directly used waterless optical components, combined with Herriot cell, to reduce the impact of background absorption from 726 to 25 ppm [39].

Combining with the above-improved methods, we summarize the detection sensitivity that the existing TDLAS system can achieve for gases with great application value, as shown in **Table 1**.

THE HYPOTHESIS OF THE SENSITIVITY LIMIT

The sensitivity of the TDLAS system has always been an issue of concern to researchers, and a lot of work has been done to achieve the lowest limit. The most common one is to increase the length of the effective optical path. Through a variety of methods, the absorption optical path of tens or even hundreds of meters can be obtained to achieve ppb, ppt, or even lower detection limit. However, considering that there is always a

limit to the number of low-state gas molecules. When a certain "threshold" is captured, the significance of continuing to improve the detection limit for practical research becomes quite limited.

According to the assumptions of quantum mechanics, atoms or molecules could only exist in specific quantum states, and each quantum state has discrete energy and angular momentum. For TDLAS, the energy of the molecule to be measured is also quantized. At room temperature, molecules are at the lowest state. Infrared absorption spectroscopy gas sensing involves the absorption of gas molecules caused by the transition from the ground state to the first or second excited state. Therefore, when discussing the detection sensitivity limit of a gas sensor system based on infrared absorption spectroscopy, the number of low-state gas molecules participating in the absorption should be considered. According to the Boltzmann distribution, we determine the number of molecules of the absorbed species on effective optical path for absorption, N:

$$N = \mathrm{n}_i \frac{Q(T)}{g'' \exp\left(-\frac{hcE_i}{kT}\right)} \tag{8}$$

Where g'' is degeneracy for the lower-state i energy E_i of absorption transition, $Q(T)$ is Partition function of absorbed species at temperature T, E_i is the lower-state i energy of absorption transition, and k is Boltzmann's constant.

If there is only one low-state gas molecule in the effective optical path, $\mathrm{n}_i = 1$, N can be expressed according to **Eq. 8**:

$$N = \frac{Q(T)}{g'' \exp\left(-\frac{hcE_i}{kT}\right)} \tag{9}$$

The lowest detection limit that the system can achieve under this condition is obtained when its absorption transition occurs, which is the "threshold" we mentioned. It can be seen that N will vary depending on absorbed species, specific absorption transition, and temperature T. To correlate N and the detection limit of TDLAS, we used integrated absorbance (IA). The IA under the condition of N is represented as:

$$\mathrm{IA} = \int \ln\left(\frac{I_0}{I_t}\right) d\nu = n_d S_{ij}^* L = \frac{N}{W} \cdot S_{ij}^* \tag{10}$$

Where S_{ij}^* is spectral line intensity and n_d is number density of molecules, which is related to the effective area of the beam W and the effective absorption path L. n_d can be expressed as:

$$n_d = \frac{N}{W \cdot L} \tag{11}$$

Sun J et al. analyzed the distribution of the number of gas molecules at low energy states, and combined with the integrated absorbance, proposed the concept of inherent limit (IL). They chose the R(76) line near 2,390.522470 cm^{-1} of CO_2 and P(7) line near 2,115.628975 cm^{-1} of CO to explore IL at different temperatures and corresponding absorption. And they proposed a constructive method to change the IL [97].

CONCLUSION AND OUTLOOK

This paper reviews the important developments of TDLAS technology in recent years and the improvement of system detection sensitivity. With the improvement of the system structure and key processing devices; the innovation of data acquisition and signal processing technology, TDLAS has played a very important role in the online and real-time monitoring of gas concentration. The development of the semiconductor diode laser industry has enabled the laser wavelength to cover most of the spectral range, making TDLAS detection light sources more choices. Moreover, its capability of narrow linewidth and high-power output provides a basic guarantee for the improvement of the sensitivity and detection limit of the TDLAS system. With the improvement of the effective optical path, the TDLAS system is continuously developing towards miniaturization and portability while improving detection accuracy. Simultaneously, the optimization of data processing provides many new possibilities for TDLAS detection.

However, as an important indicator of the development of the TDLAS system, the increase in sensitivity will ultimately reach an ultra-limit, which is determined by the principle of gas infrared absorption. If the number of molecules in the low-state cannot meet the transition conditions, the infrared absorption will not occur, and the TDLAS system will not be able to detect the corresponding concentration information. Therefore, through the quantization analysis of the absorption process, this paper put forward and analyzed the hypothesis of the sensitivity limit of TDLAS technology, which has reference significance for future development.

AUTHOR CONTRIBUTIONS

SL is responsible for the writing and conception of the overall content of this review paper. JS is responsible for investigation. JC and PX are responsible for correcting the details of the paper.

REFERENCES

1. Sun H, Ma Y, He Y, Qiao S, Yang X, Tittel FK. Highly Sensitive Acetylene Detection Based on a Compact Multi-Pass Gas Cell and Optimized Wavelength Modulation Technique. *Infrared Phys Techn* (2019) 102:103012. doi:10.1016/j.infrared.2019.103012
2. Laj P, Klausen J, Bilde M, Plaß-Duelmer C, Pappalardo G, Clerbaux C, et al. Measuring Atmospheric Composition Change. *Atmos Environ* (2009) 43:5351–414. doi:10.1016/j.atmosenv.2009.08.020
3. Hanson RK. Applications of Quantitative Laser Sensors to Kinetics, Propulsion and Practical Energy Systems. *Proc Combustion Inst* (2011) 33: 1–40. doi:10.1016/j.proci.2010.09.007

4. Hinkley ED. High-resolution Infrared Spectroscopy with a Tunable Diode Laser. *Appl Phys Lett* (1970) 16:351–4. doi:10.1063/1.1653222
5. Ma Y, Hong Y, Qiao S, Lang Z, Liu X. H-shaped Acoustic Micro-resonator-based Quartz-Enhanced Photoacoustic Spectroscopy. *Opt Lett* (2022) 47(3): 601–4. doi:10.1364/OL.449822
6. Ma Y, Hu Y, Qiao S, Lang Z, Liu X, He Y, et al. Quartz Tuning forks Resonance Frequency Matching for Laser Spectroscopy Sensing. *Photoacoustics* (2022) 25:100329. doi:10.1016/j.pacs.2022.100329
7. Wang Q, Wang Z, Zhang H, Jiang S, Wang Y, Jin W, et al. *Dual-comb Photothermal Spectroscopy*. Research Square (2021). [Preprint]. doi:10.21203/rs.3.rs-1106913/v103
8. Hu M, Hu M, Wang W, Wang Q. Wavelength-scanned All-Fiber Cavity Ring-Down Gas Sensing Using an L-Band Active Fiber Loop. *Appl Phys B* (2022) 128(2): 1–7. doi:10.1007/s00340-022-07757-3
9. Liu X, Qiao S, Ma Y. Highly Sensitive Methane Detection Based on Light-Induced Thermoelastic Spectroscopy with a 2.33 μm Diode Laser and Adaptive Savitzky-Golay Filtering. *Opt Express* (2022) 30(2):1304–13. doi:10.1364/OE.446294
10. Liu X, Ma Y. Sensitive Carbon Monoxide Detection Based on Light-Induced Thermoelastic Spectroscopy with a Fiber-Coupled Multipass Cell [Invited]. *Chin Opt Lett* (2022) 20(3):031201. doi:10.3788/COL202220.031201
11. Magalhaes F, Carvalho JP, Ferreira LA, Araujo FM, Santos JL. Methane Detection System Based on Wavelength Modulation Spectroscopy and Hollow-Core Fibres. In: SENSORS, 2008 IEEE, Lecce, Italy, October 26–29, 2008 (2008). p. 1277–80. doi:10.1109/ICSENS.2008.4716677
12. Lu H, Zheng C, Zhang L, Liu Z, Song F, Li X, et al. A Remote Sensor System Based on TDLAS Technique for Ammonia Leakage Monitoring. *Sensors* (2021) 21(7):2448. doi:10.3390/s21072448
13. Pogány A, Ott O, Werhahn O, Ebert V. Towards Traceability in CO_2 Line Strength Measurements by TDLAS at 2.7μm. *J Quantitative Spectrosc Radiative Transfer* (2013) 130:147–57. doi:10.1016/j.jqsrt.2013.07.011
14. Pogány A, Klein A, Ebert V. Measurement of Water Vapor Line Strengths in the 1.4-2.7 μm Range by Tunable Diode Laser Absorption Spectroscopy. *J Quant Spectrosc Radiat Transf* (2015) 165:108–22. doi:10.1016/j.jqsrt.2015.06.023
15. Meng Y, Liu T, Liu K, Jiang J, Wang T, Wang R, et al. Temperature and Pressure Measurement Based on Tunable Diode Laser Absorption Spectroscopy with Gas Absorption Line Width Detection. *Proc SPIE* (2014) 9274:927423. doi:10.1117/12.2073852
16. Ngo NH, Lisak D, Tran H, Hartmann JM. An Isolated Line-Shape Model to Go beyond the Voigt Profile in Spectroscopic Databases and Radiative Transfer Codes. *J Quant Spectrosc Radiat Transf* (2013) 129:89–100. doi:10.1016/j.jqsrt.2013.05.034
17. Jacquinet-Husson N, Scott NA, Chédin A, Crépeau L, Armante R, Capelle V, et al. The GEISA Spectroscopic Database: Current and Future Archive for Earth and Planetary Atmosphere Studies. *J Quant Spectrosc Radiat Transf* (2008) 109:1043–59. doi:10.1016/j.jqsrt.2007.12.015
18. Rothman LS, Gordon IE, Barber RJ, Dothe H, Gamache RR, Goldman A, et al. HITEMP, the High-Temperature Molecular Spectroscopic Database. *J Quant Spectrosc Radiat Transf* (2010) 111:2139–50. doi:10.1016/j.jqsrt.2010.05.001
19. Rothman LS, Gordon IE, Babikov Y, Barbe A, Chris Benner D, Bernath PF, et al. The HITRAN2012 Molecular Spectroscopic Database. *J Quant Spectrosc Radiat Transf* (2013) 130:4–50. doi:10.1016/j.jqsrt.2013.07.002
20. Mondelain D, Chelin P, Valentin A, Hurtmans D, Camy-Peyret C. Line Profile Study by Diode Laser Spectroscopy in the $12CH_4$ $\nu_2+\nu_4$ Band. *J Mol Spectrosc* (2005) 233:23–31. doi:10.1016/j.jms.2005.05.012
21. Nakamura M, Yariv A, Yen HW, Somekh S, Garvin HL. Optically Pumped GaAs Surface Laser with Corrugation Feedback. *Appl Phys Lett* (1973) 22: 515–6. doi:10.1063/1.1654490
22. Streifer W, Burnham R, Scifres D. Effect of External Reflectors on Longitudinal Modes of Distributed Feedback Lasers. *IEEE J Quan Electron.* (1975) 11: 154–61. doi:10.1109/JQE.1975.1068581
23. Mikami O. 1.55 μm GaInAsP/InP Distributed Feedback Lasers. *Jpn J Appl Phys* (1981) 20(7):L488–L490. doi:10.1143/JJAP.20.L488
24. Sakai K, Utaka K, Akiba S, Matsushima Y. 1.5 μm Range InGaAsP/InP Distributed Feedback Lasers. *IEEE J Quan Electron.* (1982) 18(8):1272–8. doi:10.1109/JQE.1982.1071682
25. Lee T-P. Recent Advances in Long-Wavelength Semiconductor Lasers for Optical Fiber Communication. *Proc IEEE* (1991) 79(3):253–76. doi:10.1109/5.75084
26. Morris NA, Connolly JC, Martinelli RU, Abeles JH, Cook AL. Single-mode Distributed-Feedback 761-nm GaAs-AlGaAs Quantum-Well Laser. *IEEE Photon Technol Lett* (1995) 7(5):455–7. doi:10.1109/68.384508
27. Doussiere P, Tashima M, Djie H, Lee KW, Wong V, Venables D, et al. 830nm High Power Single Mode DFB Laser for High Volume Applications. In: SPIE OPTO, San Francisco, CA (2012). p. 82770A. doi:10.1117/12.910238
28. Sun J, Chang J, Wang F, Zhang Q, Wang Z, Xie Y, et al. Tuning Efficiency of Distributed Feedback Laser Diode for Wavelength Modulation Spectroscopy. *IEEE Sensors J* (2019) 19:9722–7. doi:10.1109/JSEN.2019.2927043
29. Xie Y, Chang J, Chen X, Sun J, Zhang Q, Wang F, et al. A DFB-LD Internal Temperature Fluctuation Analysis in a TDLAS System for Gas Detection. *IEEE Photon J.* (2019) 11:1–8. doi:10.1109/JPHOT.2019.2916800
30. Wei Y, Chang J, Lian J, Liu T. A Coal Mine Multi-point Fiber Ethylene Gas Concentration Sensor. *Photonic Sens* (2015) 5:67–71. doi:10.1007/s13320-014-0206-z
31. Wang Z, Chang J, Liu Q, Tian C, Zhang Q. Gas Absorption center-based Wavelength Calibration Technique in QEPAS System for SNR Improvement. *Photonic Sens* (2018) 8:358–66. doi:10.1007/s13320-018-0502-0
32. Shao L, Fang B, Zheng F, Qiu X, He Q, Wei J, et al. Simultaneous Detection of Atmospheric CO and CH_4 Based on TDLAS Using a Single 2.3 μm DFB Laser. *Spectrochim Acta A: Mol Biomol Spectrosc* (2019) 222:117118. doi:10.1016/j.saa.2019.05.023
33. Soda H, Iga K-i., Kitahara C, Suematsu Y. GaInAsP/InP Surface Emitting Injection Lasers. *Jpn J Appl Phys* (1979) 18(12):2329–30. doi:10.1143/JJAP.18.2329
34. Iga K, Ishikawa S, Ohkouchi S, Nishimura T. Room-temperature Pulsed Oscillation of GaAlAs/GaAs Surface Emitting Injection Laser. *Appl Phys Lett* (1984) 45(4):348–50. doi:10.1063/1.95265
35. Baba T, Yogo Y, Suzuki K, Koyama F, Iga K. Near Room Temperature Continuous Wave Lasing Characteristics of GaInAsP/InP Surface Emitting Laser. *Electron Lett* (1993) 29(10):913–4. doi:10.1049/el:19930609
36. Uomi K, Yoo SJB, Scherer A, Bhat R, Andreadakis NC, Zah CE, et al. Low Threshold, Room Temperature Pulsed Operation of 1.5 μm Vertical-Cavity Surface-Emitting Lasers with an Optimized Multi-Quantum Well Active Layer. *IEEE Photon Technol Lett* (1994) 6(3):317–9. doi:10.1109/68.275476
37. Wang J, Sanders ST, Jeffries JB, Hanson RK. Oxygen Measurements at High Pressures with Vertical Cavity Surface-Emitting Lasers. *Appl Phys B* (2001) 72: 865–72. doi:10.1007/s003400100539
38. Chen J, Hangauer A, Bachmann A, Lim T, Kashani K, Strzoda R, et al. CO and CH_4 Sensing with Single Mode 2.3 μm GaSb-Based VCSEL. In: Conference on Lasers and Electro-Optics, Baltimore, MD, May 31–June 5, 2009 (2009). p. CThI2. doi:10.1364/CLEO.2009.CThI2
39. Wang Y, Wei Y, Chang J, Zhang T, Liu T, Sun T, et al. Tunable Diode Laser Absorption Spectroscopy- Based Detection of Propane for Explosion Early Warning by Using a Vertical Cavity Surface Enhanced Laser Source and Principle Component Analysis Approach. *IEEE Sensors J* (2017) 17(15): 4975–82. doi:10.1109/JSEN.2017.2713769
40. Chen J, Hangauer A, Strzoda R, Amann M-C. VCSEL-based Calibration-free Carbon Monoxide Sensor at 2.3 μm with In-Line Reference Cell. *Appl Phys B* (2011) 102:381–9. doi:10.1007/s00340-010-4011-0
41. Stein BA, Jayaraman V, Jiang JY, Cable A, Sanders ST. Doppler-limited H_2O and HF Absorption Spectroscopy by Sweeping the 1,321-1,354 Nm Range at 55 kHz Repetition Rate Using a Single-Mode MEMS-Tunable VCSEL. *Appl Phys B* (2012) 108:721–5. doi:10.1007/s00340-012-5135-1
42. Tacke M. New Developments and Applications of Tunable IR lead Salt Lasers. *Infrared Phys Techn* (1995) 36:447–63. doi:10.1016/1350-4495(94)00101-p
43. Werle P, Slemr F, Gehrtz M, Bräuchle C. Quantum-limited FM-spectroscopy with a lead-salt Diode Laser. *Appl Phys B* (1989) 49(2):99–108. doi:10.1007/BF00332268
44. Nicolas J-C, Baranov AN, Cuminal Y, Rouillard Y, Alibert C. Tunable Diode Laser Absorption Spectroscopy of Carbon Monoxide Around 235 μm. *Appl Opt* (1998) 37(33):7906–11. doi:10.1364/AO.37.007906
45. Hasenberg TC, Miles RH, Kost AR, West L. Recent Advances in Sb-Based Midwave-Infrared Lasers. *IEEE J Quan Electron.* (1997) 33:1403–6. doi:10.1109/3.605563

46. Faist J, Capasso F, Sivco DL, Sirtori C, Hutchinson AL, Cho AY. Quantum cascade Laser. *Science* (1994) 264(5158):553–6. doi:10.1126/science.264.5158.553
47. Faist J, Gmachl C, Capasso F, Sirtori C, Sivco DL, Baillargeon JN, et al. Distributed Feedback Quantum cascade Lasers. *Appl Phys Lett* (1997) 70:2670–2. doi:10.1063/1.119208
48. Faist J, Beck M, Aellen T, Gini E Quantum-cascade Lasers Based on a Bound-To-Continuum Transition. *Appl Phys Lett* (2001) 78:147–9. doi:10.1063/1.1339843
49. Capasso F. High-performance Midinfrared Quantum cascade Lasers. *Opt Eng* (2010) 49:111102. doi:10.1117/1.3505844
50. Kasyutich VL, Holdsworth RJ, Martin PA. Mid-infrared Laser Absorption Spectrometers Based upon All-Diode Laser Difference Frequency Generation and a Room Temperature Quantum cascade Laser for the Detection of CO, N_2O and NO. *Appl Phys B* (2008) 92:271–9. doi:10.1007/s00340-008-3097-0
51. Ren W, Jiang W, Tittel FK. Single-QCL-based Absorption Sensor for Simultaneous Trace-Gas Detection of CH_4 and N_2O. *Appl Phys B* (2014) 117:245–51. doi:10.1007/s00340-014-5828-8
52. Maity A, Pal M, Maithani S, Banik GD, Pradhan M. Wavelength Modulation Spectroscopy Coupled with an External-Cavity Quantum cascade Laser Operating between 7.5 and 8 μm. *Laser Phys Lett* (2018) 15(4):045701. doi:10.1088/1612-202X/aaa61a
53. Yang RQ, Hill CJ, Yang BH, Wong CM, Muller RE, Echternach PM. Continuous-wave Operation of Distributed Feedback Interband cascade Lasers. *Appl Phys Lett* (2004) 84:3699–701. doi:10.1063/1.1738184
54. Canedy CL, Bewley WW, Lindle JR, Kim CS, Kim M, Vurgaftman I, et al. High-power and High-Efficiency Midwave-Infrared Interband cascade Lasers. *Appl Phys Lett* (2006) 88:161103. doi:10.1063/1.2195778
55. Mansour K, Qiu Y, Hill CJ, Soibel A, Yang RQ. Mid-infrared Interband cascade Lasers at Thermoelectric Cooler Temperatures. *Electron Lett* (2006) 42(18):1034–5. doi:10.1049/el:20062442
56. Ren W, Luo L, Tittel FK. Sensitive Detection of Formaldehyde Using an Interband cascade Laser Near 3.6 μm. *Sensors Actuators B: Chem* (2015) 221:1062–8. doi:10.1016/j.snb.2015.07.078
57. Ye W, Li C, Zheng C, Sanchez NP, Gluszek AK, Hudzikowski AJ, et al. Mid-infrared Dual-Gas Sensor for Simultaneous Detection of Methane and Ethane Using a Single Continuous-Wave Interband cascade Laser. *Opt Express* (2016) 24:16973. doi:10.1364/OE.24.016973
58. Li C, Dong L, Zheng C, Lin J, Wang Y, Tittel F. Ppbv-level Ethane Detection Using Quartz-Enhanced Photoacoustic Spectroscopy with a Continuous-Wave, Room Temperature Interband cascade Laser. *Sensors* (2018) 18:723. doi:10.3390/s18030723
59. Song F, Zheng C, Yu D, Zhou Y, Yan W, Ye W, et al. Interband cascade Laser-Based Ppbv-Level Mid-infrared Methane Detection Using Two Digital Lock-In Amplifier Schemes. *Appl Phys B* (2018) 124:124. doi:10.1007/s00340-018-6916-y
60. White JU. Long Optical Paths of Large Aperture. *J Opt Soc Am* (1942) 32:285. doi:10.1364/JOSA.32.000285
61. Herriott DR, Schulte HJ. Folded Optical Delay Lines. *Appl Opt* (1965) 4(8):883–9. doi:10.1364/AO.4.000883
62. Li C, Dong L, Zheng C, Tittel FK. Compact TDLAS Based Optical Sensor for Ppb-Level Ethane Detection by Use of a 3.34 μm Room-Temperature CW Interband cascade Laser. *Sensors Actuators B: Chem* (2016) 232:188–94. doi:10.1016/j.snb.2016.03.141
63. Liu K, Wang L, Tan T, Wang G, Zhang W, Chen W, et al. Highly Sensitive Detection of Methane by Near-Infrared Laser Absorption Spectroscopy Using a Compact Dense-Pattern Multipass Cell. *Sensors Actuators B: Chem* (2015) 220:1000–5. doi:10.1016/j.snb.2015.05.136
64. Xia J, Feng C, Zhu F, Ye S, Zhang S, Kolomenskii A, et al. A Sensitive Methane Sensor of a Ppt Detection Level Using a Mid-infrared Interband cascade Laser and a Long-Path Multipass Cell. *Sensors Actuators B: Chem* (2021) 334:129641. doi:10.1016/j.snb.2021.129641
65. Shen F, Akil J, Wang G, Poupin C, Cousin R, Siffert S, et al. Real-time Monitoring of N_2O Production in a Catalytic Reaction Process Using Mid-infrared Quantum cascade Laser. *J Quant Spectrosc Radiat Transf* (2018) 221:1–7. doi:10.1016/j.jqsrt.2018.09.022
66. Engeln R, Berden G, Peeters R, Meijer G. Cavity Enhanced Absorption and Cavity Enhanced Magnetic Rotation Spectroscopy. *Rev Scientific Instr* (1998) 69:3763–9. doi:10.1063/1.1149176
67. O'Keefe A. Integrated Cavity Output Analysis of Ultra-weak Absorption. *Chem Phys Lett* (1998) 293:331–6. doi:10.1016/S0009-2614(98)00785-4
68. Paul JB, Lapson L, Anderson JG. Ultrasensitive Absorption Spectroscopy with a High-Finesse Optical Cavity and off-axis Alignment. *Appl Opt* (2001) 40:4904–10. doi:10.1364/ao.40.004904
69. Barry HR, Corner L, Hancock G, Peverall R, Ritchie GAD. Cavity-enhanced Absorption Spectroscopy of Methane at 1.73 μm. *Chem Phys Lett* (2001) 333(3-4):285–9. doi:10.1016/S0009-2614(00)01388-9
70. Rao GN, Karpf A. Extremely Sensitive Detection of NO_2 Employing off-axis Integrated Cavity Output Spectroscopy Coupled with Multiple-Line Integrated Absorption Spectroscopy. *Appl Opt* (2011) 50:1915–24. doi:10.1364/AO.50.001915
71. Mhanna M, Zhang G, Kunnummal N, Farooq A. Cavity-enhanced Measurements of Benzene for Environmental Monitoring. *IEEE Sensors J* (2021) 21:3849–59. doi:10.1109/JSEN.2020.3026981
72. Wang Q, Chang J, Zhu C-G, Li C, Song F-J, Liu Y-N, et al. Detection of Water Vapor Concentration Based on Differential Value of Two Adjacent Absorption Peaks. *Laser Phys Lett* (2012) 9:421–5. doi:10.7452/lapl.201210015
73. Hobbs PCD. Shot Noise Limited Optical Measurements at Baseband with Noisy Lasers (Proceedings Only). In: Advances in Intelligent Robotics System, Boston, MA, 1990 (1991). p. 1376. doi:10.1117/12.25014
74. Sonnenfroh DM, Allen MG. Ultrasensitive, Visible Tunable Diode Laser Detection of NO_2. *Appl Opt* (1996) 35(21):4053–8. doi:10.1364/AO.35.004053
75. Upschulte B, Allen M, Upschulte B, Allen M. Diode Laser Measurements of Line Strengths and Self-Broadening Parameters of Water Vapor between 300 and 1100 K Near 1.31 Micron. In: 35th Aerospace Sciences Meeting and Exhibit, Reno, NV, January 6–9, 1997 (1997). p. 319. doi:10.2514/6.1997-319
76. Wang Q, Chang J, Zhu C, Liu Y, Lv G, Wang F, et al. High-sensitive Measurement of Water Vapor: Shot-Noise Level Performance via a Noise Canceller. *Appl Opt* (2013) 52:1094. doi:10.1364/AO.52.001094
77. Zhu C, Chang J, Wang P, Wang W, Wang Q, Liu Y, et al. Reliability Analysis and Comparison of Demodulation Methods for Dual-Beam Wavelength-Modulation Spectroscopy Water Vapor Detection. *Appl Opt* (2013) 52:4171. doi:10.1364/AO.52.004171
78. Che L, Ding Y-J, Peng Z-M, Li X-H. Calibration-free Wavelength Modulation Spectroscopy for Gas Concentration Measurements under Low-Absorbance Conditions. *Chin Phys. B* (2012) 21:127803–70. doi:10.1088/1674-1056/21/12/127803
79. Yin S, Liu Y, Dong T. Trace Gas Detect Based on Spectral Analysis and Harmonic Ratio. *Opt Rev* (2020) 27:304–11. doi:10.1007/s10043-020-00597-6
80. Aguirre J, Medrano N, Calvo B, Celma S. Lock-in Amplifier for Portable Sensing Systems. *Electron Lett* (2011) 47(21):1172–3. doi:10.1049/el.2011.2472
81. Wei W, Chang J, Huang Q, Zhu C, Wang Q, Wang Z, et al. Wavelength Modulation Spectroscopy with Signal-Reference Beam Method for Highly Sensitive Gas Detection. *Appl Phys B* (2015) 118:75–83. doi:10.1007/s00340-014-5956-1
82. Wang F, Chang J, Chen X, Wang Z, Wang Q, Wei Y, et al. Optical Fiber Oxygen Sensor Utilizing a Robust Phase Demodulator. *Measurement* (2017) 95:1–7. doi:10.1016/j.measurement.2016.09.022
83. Rieker GB, Jeffries JB, Hanson RK. Calibration-free Wavelength-Modulation Spectroscopy for Measurements of Gas Temperature and Concentration in Harsh Environments. *Appl Opt* (2009) 48:5546–60. doi:10.1364/AO.48.005546
84. Yang C, Mei L, Deng H, Xu Z, Chen B, Kan R. Wavelength Modulation Spectroscopy by Employing the First Harmonic Phase Angle Method. *Opt Express* (2019) 27:12137. doi:10.1364/OE.27.012137
85. Roy A, Chakraborty AL. Intensity Modulation-Normalized Calibration-free 1f and 2f Wavelength Modulation Spectroscopy. *IEEE Sensors J* (2020) 20:12691–701. doi:10.1109/JSEN.2020.3000470
86. Wang F, Chang J, Zhu C, Wang Z, Liu Y, Wei W, et al. Demodulation Algorithm Used in Single-Beam System Immune to Light Power Drift. *Appl Opt* (2015) 54:2032–8. doi:10.1364/AO.54.002032
87. Wei W, Chang J, Cao L, Liu Y, Chen X, Zhu C, et al. Artificial Absorption Creation for More Accurate Tunable Diode Laser Absorption Spectroscopy Measurement. *Opt Commun* (2017) 399:112–9. doi:10.1016/j.optcom.2017.04.052

88. Wang Q, Chang J, Song F, Wang F, Zhu C, Liu Z, et al. Measurement and Analysis of Water Vapor inside Optical Components for Optical Fiber H_2O Sensing System. *Appl Opt* (2013) 52(26):6445–51. doi:10.1364/AO.52.006445
89. Zhu CG, Chang J, Wang PP, Sun BN, Wang Q, Wei W, et al. Improvement of Measurement Accuracy of Infrared Moisture Meter by Considering the Impact of Moisture inside Optical Components. *IEEE Sensors J* (2014) 14:920–5. doi:10.1109/JSEN.2013.2291033
90. Lv GP, Chang J, Huang QJ, Wang QP, Wang Q, Wang ZL. Suppressing the Impact of Water Vapor inside Optical Components for Optical Fiber H_2O Sensing System. *Opt Quant Electron* (2015) 47:663–72. doi:10.1007/s11082-014-9942-y
91. Shao L, Fang B, Zheng F, Qiu X, He Q, Wei J, et al. Simultaneous Detection of Atmospheric CO and CH_4 Based on TDLAS Using a Single 2.3 μm DFB Laser. *Spectrochim Acta A Mol Biomol Spectrosc* (2019) 222:117118. doi:10.1016/j.saa.2019.05.023
92. Hundt PM, Tuzson B, Aseev O, Liu C, Scheidegger P, Looser H, et al. Multi-species Trace Gas Sensing with Dual-Wavelength QCLs. *Appl Phys B* (2018) 124:124. doi:10.1007/s00340-018-6977-y
93. Ghorbani R, Schmidt FM. ICL-based TDLAS Sensor for Real-Time Breath Gas Analysis of Carbon Monoxide Isotopes. *Opt Express* (2017) 25:12743. doi:10.1364/OE.25.012743
94. Li C, Shao L, Jiang L, Qiu X, Wei J, Ma W. Simultaneous Measurements of CO and CO_2 Employing Wavelength Modulation Spectroscopy Using a Signal Averaging Technique at 1.578 μm. *Appl Spectrosc* (2018) 72:1380–7. doi:10.1177/0003702818766904
95. Cui H, Wang F, Huang Q, Yan J, Cen K. Sensitive Detection of NO Using a Compact Portable CW DFB-QCL-Based WMS Sensor. *Appl Opt* (2020) 59:9491–8. doi:10.1364/AO.402484
96. Diemel O, Pareja J, Dreizler A, Wagner S. An Interband cascade Laser-Based *In Situ* Absorption Sensor for Nitric Oxide in Combustion Exhaust Gases. *Appl Phys B* (2017) 123:123. doi:10.1007/s00340-017-6741-8
97. Sun J, Chang J, Zhang Q, Xu P, Zhang Z. Absorption Quantization in the Diagnosis of Absorption Spectroscopy. In: AOPC 2021: Optical Sensing and Imaging Technology, Beijing, China (2021). p. 15–20. doi:10.1117/12.2599852

Conflict of Interest: Author PX was employed by Jinan Jingheng Electronics Co., Ltd.

The remaining authors declare that the research was conducted in the absence of any commercial or financial relationships that could be construed as a potential conflict of interest.

Publisher's Note: All claims expressed in this article are solely those of the authors and do not necessarily represent those of their affiliated organizations, or those of the publisher, the editors and the reviewers. Any product that may be evaluated in this article, or claim that may be made by its manufacturer, is not guaranteed or endorsed by the publisher.

frontiers in Physics

ORIGINAL RESEARCH
published: 04 March 2022
doi: 10.3389/fphy.2022.843171

Near-Infrared Dual-Gas Sensor System for Methane and Ethane Detection Using a Compact Multipass Cell

Zhenhai Xi[1†], Kaiyuan Zheng[1†], Chuantao Zheng[1], Haipeng Zhang[1], Fang Song[1], Chunguang Li[2]*, Weilin Ye[3], Yu Zhang[1], Yiding Wang[1] and Frank K. Tittel[4]*

[1]State Key Laboratory of Integrated Optoelectronics, College of Electronic Science and Engineering, Jilin University, Changchun, China, [2]College of Biological and Agricultural Engineering, Jilin University, Changchun, China, [3]Key Laboratory of Intelligent Manufacturing Technology of Ministry of Education, College of Engineering, Shantou University, Shantou, China, [4]Department of Electrical and Computer Engineering, Rice University, Houston, TX, United States

In this invited paper, a compact dense-pattern multipass cell-based near-infrared sensor system was demonstrated for detection of parts-per-billion in volume (ppbv)-level methane (CH_4) and ethane (C_2H_6). The dimension size of the fabricated gas cell is 18.5 × 8 × 9 cm^3 with an absorption path length of 9.39 m. CH_4 measurement was realized within a spectral range of 6,046–6,048 cm^{-1} and an absorption line of 6,046.95 cm^{-1}. The spectral range for C_2H_6 detection is 5,951–5,953 cm^{-1} with an absorption line of 5,951.73 cm^{-1}. Allan deviation analysis was used for evaluating the dual-gas sensing performance, and a detection limit of 78 ppbv for CH_4 and 190 ppbv for C_2H_6 were achieved, respectively, with an averaging time of 0.8 s. Furthermore, CH_4 measurement in the indoor and outdoor atmosphere was both performed to verify the field sensing capability of the sensor system. Compared with two separate sensor systems for CH_4/C_2H_6 sensing, the proposed dual-gas sensor system using two near-infrared lasers and one multipass cell has the advantages of low-cost, compact-size without decreasing the selectivity and sensitivity.

Keywords: infrared absorption, dual-gas detection, laser absorption spectroscopy, multi-pass cell, atmospheric gas monitoring

OPEN ACCESS

Edited by:
Yufei Ma,
Harbin Institute of Technology, China

Reviewed by:
Kun Liu,
Chinese Academy of Sciences (CAS), China
Huadan Zheng,
Jinan University, China

***Correspondence:**
Chuantao Zheng
zhengchuantao@jlu.edu.cn
Chunguang Li
lichunguang@jlu.edu.cn

†These two authors contributed equally to this research work

Specialty section:
This article was submitted to Optics and Photonics, a section of the journal Frontiers in Physics

Received: *25 December 2021*
Accepted: *28 January 2022*
Published: *04 March 2022*

Citation:
Xi Z, Zheng K, Zheng C, Zhang H, Song F, Li C, Ye W, Zhang Y, Wang Y and Tittel FK (2022) Near-Infrared Dual-Gas Sensor System for Methane and Ethane Detection Using a Compact Multipass Cell. Front. Phys. 10:843171. doi: 10.3389/fphy.2022.843171

INTRODUCTION

Methane (CH_4) and ethane (C_2H_6) are the two most abundant alkanes in the atmosphere [1–3]. CH_4 is widely distributed in nature and is one of the main greenhouse gases. Atmospheric CH_4 concentration detection is of great significance for climate research and atmospheric monitoring. CH_4 is also the main component of natural gas and biogas. CH_4 leakage has become the major safety hazard in the industrial field including coal mines, natural gas transportation and other industries [4–7]. Therefore, it is necessary to monitor the CH_4 concentration in real time, so that people can respond and evacuate when leakage occurs.

C_2H_6 is the second-largest component of natural gas after CH_4, which can be treated as a target gas for natural gas leakage monitoring. Also, highly-sensitive C_2H_6 detection has found applications in human breath analysis as a non-invasive method to identify different diseases [8–10]. CH_4 and C_2H_6 molecules all have absorption peaks in the near-infrared range. Therefore, compact near-infrared laser source can be used for the two gas species detection. Compared with mass spectrometry and gas chromatography, infrared absorption spectroscopy, including photothermal and

photoacoustic spectroscopy [11–16], provides a less-costly approach for CH_4 and C_2H_6 concentration detection, and enables real-time measurement without the need for pretreatment or accumulation of target gas samples.

Tunable diode laser absorption spectroscopy (TDLAS) is an effective non-contact method for trace gas detection, which uses a single, narrow-band near-/mid-infrared laser to scan gas absorption peaks with to increase sensitivity and selectivity [17–20]. In TDLAS, an optical absorption cell design is generally based on White [21], Herriott [22, 23] or other multipass cell (MPC) [24, 25]. Compared with White cell, Herriott-based MPC has the advantages of simpler structure and more compact size. In recent years, Herriott MPC has been widely used in various applications [26] and the main development is the change of spot distribution, *i.e.* from initial single-ring Herriott to dense spot distribution. Herriott-based MPC is widely used in TDLAS sensor systems due to its improvement in effective path length and therefore in gas absorption ability. A dense-pattern (DP)-MPC with a light absorption path length of 26.4 m was designed by Gao *et al.*, and the CH_4 measurement accuracy reached 79 parts-per-billion in volume (ppbv) [27]. A mini-MPC with an absorption optical path length of 4.2 m was designed by Dong *et al.* The optical system is highly integrated, and the CH_4 measurement accuracy reached 117 ppbv [28]. The gas absorption coefficient can also be improved by optimizing the Herriott cell configuration. A double-spot ring Heriot cell (DSR-HC) with an optical path length of 20 and 6 m was designed by Zheng *et al.*, respectively. Two different optical paths provide different detection ranges for C_2H_2 detection. The practicability of the sensor is improved by increasing the detection range of C_2H_2. The detection limits under the two absorption path lengths were 7.9 parts-per-million in volume (ppmv) and four ppmv, respectively [29].

Most reported MPC-based TDLAS sensor systems were designed for single-gas detection. If they are used to detect multi-gas species, two sets of systems are required, which increases the whole size of the sensor system. Especially in the harsh geographical environment, it is difficult to transport safely and operate normally, which virtually limits the function of the sensor. In order to overcome the above-mentioned issue, a near-infrared dual-gas TDLAS sensor was developed using two distributed feedback (DFB) lasers, i.e. 1654 nm for CH_4 and 1,680 nm for C_2H_6 detection, respectively. Compared to a sensor system based on mid-infrared lasers [30], near-infrared lasers are lower in cost and a sensor system based on such sensors is smaller in size, which is conducive to the integration and commercial use of the sensor system. In addition, in order to further reduce the size of the sensor system, a DP-MPC was developed, with an absorption path length of 9.39 m. Furthermore, a LabVIEW based data-processing system, which consists of a scan signal generator and a signal acquisition module was developed. Such a system can perform the normal operation of driving two DFB lasers as well as extracting the ppbv-level CH_4 and C_2H_6 concentration employing a laptop and a data acquisition (DAQ) card. The practicability of the sensor system was verified by continuous monitoring of the indoor and atmospheric CH_4 concentration levels.

EXPERIMENTAL SET-UP

Simulation and Modelling of the Compact MPC

A model of the compact MPC was designed based on MATLAB, and the reflection of light in the cell was simulated using a similar method with Ref. [31]. The radius of curvature of the used spherical mirror is 150 mm with a diameter of 50.8 mm and a mirror reflectivity of >95%. The obtained spot distribution on the two mirrors is shown in **Figures 1A,B**, where the first 20 reflection points are labeled. On mirror A, the injection hole (IH) shown as a blue circle is labeled as 0, the second reflection point is labeled 2, the third is labeled 4, the fourth is labeled 6, and so on. The connection of the first ten reflection points (numbered as 0, 2, . . . , 18) will form the first ellipse. The next ten reflection points (numbered as 20, 22, . . . 38) will be offset clockwise, and also the connection between them forms the second ellipse. It can be seen that the second ellipse can be treated as the clockwise rotation of the first ellipse. A similar distribution can be found on mirror B. All the reflection points and the formed rings on mirror A and mirror B are found to rotate clockwise to form the spot distribution. When the light is reflected for the 809th on mirror B, it escapes through the injection hole on mirror A. There are 810 reflections between the mirrors, 40 and a half ellipses and five rings are formed on each mirror. **Eq. 1** is used to calculate the total optical path length

$$L = \sum_{i=1}^{N} \sqrt{\left[(x_i - x_{i-1})^2 + (y_i - y_{i-1})^2 + (z_i - z_{i-1})^2 \right]} \quad (1)$$

where (x_i, y_i, z_i) is the coordinates of the ith reflection point, and $N = 810$ is the total reflection number. Due to the limitation in laser power and the mirror reflection loss, the signal derived by output from the detector cannot be large with too many reflections. Therefore, the laser beam was designed to exit in advance with 76 reflections. As shown in the model in **Figures 1C,D**, when the light is reflected for the 76th time, it escapes through the designed ejection hole (EH) on mirror B, reaches the detector for optoelectrical conversion, and the derived electrical signal enters a data acquisition (DAQ) card for data processing. The total optical path length with 76 reflections was calculated to be 9.36 m through simulation.

According to the designed model and optimized parameters, a compact MPC with 76 reflections was fabricated, whose photo is shown in **Figure 2A**. The spot distribution of the mirror shown in the inset was obtained using a He-Ne laser as a trace laser, which basically coincides with the simulated spot distribution in **Figure 1D**. The external dimension size of the fabricated gas cell is $18.5 \times 8 \times 9$ cm^3 with an internal volume of 683.9 mL. Two optical windows (i.e. CaF_2 lens) were placed at both sides with the same aperture as the reflection mirror, and the groove where the window is placed was designed to tilt 15° to prevent the infrared light from directly reflecting into the laser collimator resulting in laser damage. An air inlet and outlet were equipped on the gas cell, separately for gas injection and ejection, and the whole gas chamber was sealed for a good gas tightness. Glass glue was used to fix the optical window at both ends of the MPC, and the upper opening was sealed with a sealing ring to ensure air tightness.

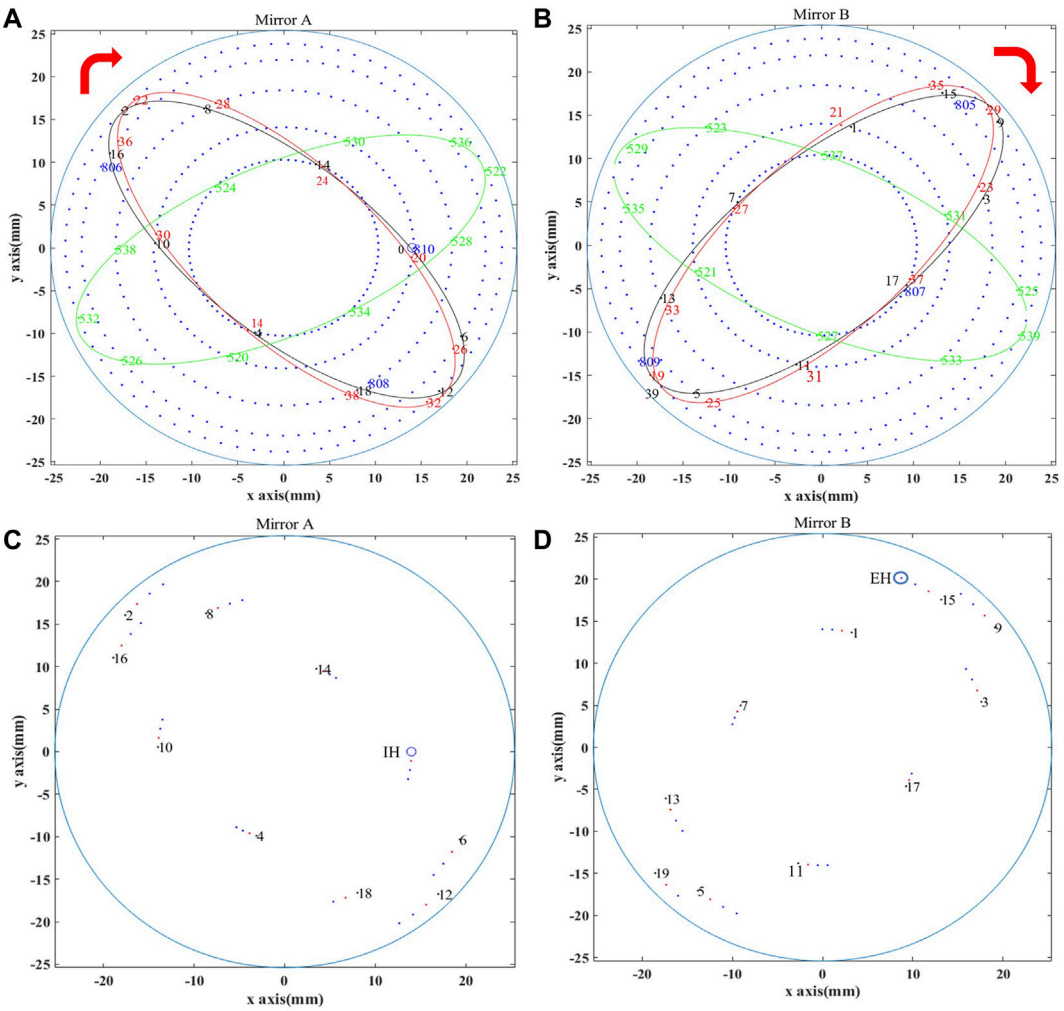

FIGURE 1 | Complete spot distribution of **(A)** Mirror A and **(B)** Mirror B in simulation. Spot distribution of **(C)** Mirror A and **(D)** Mirror B in simulation with mirror refraction.

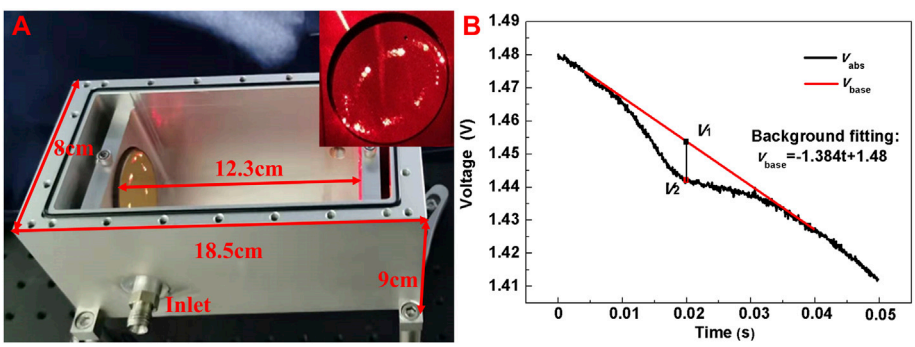

FIGURE 2 | (A) Photograph of the fabricated multi-pass cell design with an external size of 18.5 × 8 × 9 cm^3 and a physical spot distribution of Mirror B in the inset **(B)** Measured CH_4 absorption signal (black curve) with the compact MPC at a concentration level of 20 ppmv. The red curve shows the background fitting signal.

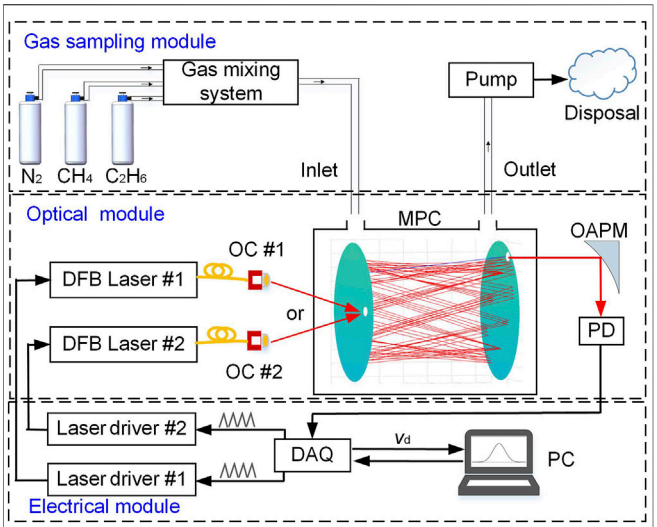

FIGURE 3 | Structural diagram of the CH_4/C_2H_6 dual-gas sensor system, consisting of an electrical part, an optical part and a gas sampling part. PC: Personal computer PD: Photodetector, MPC: Multipass cell, OAPM: Off-axis parabolic mirror, DAQ: Data acquisition, DFB: Distributed feedback laser, and laser driver includes temperature controller and current driver.

With a sealing detection, the air leakage rate was measured to be 2.4×10^{-3} TorrL/s.

To determine the actual effective optical path length, a saw-tooth scan signal with a frequency of 50 Hz was used to change the current of the DFB laser and a CH_4 sample with a concentration level of 20 ppmv was injected into the compact MPC. The output signal from the detector with CH_4 absorption, defined as $v_{abs}(t)$, is shown in **Figure 2B**. The red line is the background fitting signal, expressed as $v_{base}(t)$. A differential signal can be obtained by subtracting v_{abs} from v_{base}, which represents gas absorption. The maximum absorption (i.e. $v_{base}-v_{abs}$) occurred at t = 0.1986 s and the corresponding voltage ($V_2 = v_{abs}$ (t = 0.1986 s)) is 1.443 V. The non-absorption voltage ($V_1 = v_{base}$ (t = 0.1986 s)) is 1.453 V. Then the absorbance (α) can be calculated from **Eq. 2**, as

$$\alpha = -\ln(V_2/V_1) \quad (2)$$

According to **Eq. 2**, the absorbance is 0.0069, and the actual total optical path is determined to be 9.39 m by referring to the high-transmission (HITRAN) molecular absorption database, which are highly consistent with the simulation result of 9.36 m.

Sensor Structure Design

An overall sensor system structure is shown in **Figure 3**, which is divided into three parts, including an optical part, an electrical part and a gas sampling part. In the optical part, two near-infrared DFB lasers were used as the excitation source for the detection of CH_4 and C_2H_6. In order to facilitate the optical path establishment, the two lasers followed the same light propagation path. For CH_4 detection, the laser operating temperature was set to 20°C, and the center current was set to 84 mA for targeting the absorption line at 6046.95 cm^{-1}. For C_2H_6 detection, the laser was operated at 26°C with a center current of 90 mA for targeting the absorption line at 5951.73 cm^{-1}. The emitted infrared laser beams were combined and the collimated laser beam enters the MPC through an optical fiber collimator. A fiber adapter as well as an optical switch can be used to automatically exchange the 1,654 nm and 1,680 nm laser for different gas detection. Because of the loss resulting from light reflection, the light power will be reduced after multiple reflections. An off-axis parabolic lens was therefore added at the exit to focus the light intensity, and then the signal amplitude output from a Ge transimpedance photodetector was increased. The electrical part included a laptop (HP model BH872PHB), a DAQ card (Model USB-6211, National Instrument, United States), two current and temperature integrated drive modules (LDTC0520, Wavelength, United States). Laser direct absorption spectroscopy (LDAS) technique was used for CH_4 and C_2H_6 dual-gas detection, which is easy to realize and suitable for portable applications, compared to wavelength modulation spectroscopy (WMS). A scan signal was generated by the DAQ card controlled by the LabVIEW platform to drive the DFB laser. The output signal from the detector was sampled by the DAQ card, and synchronous sampling was realized triggered by the signal generation module. With respect to the gas sampling module, the MPC was equipped with an inlet and an outlet, allowing gas flow during measurements. CH_4/C_2H_6:N_2 mixtures were diluted from a standard 50 ppmv CH_4 sample and a 100 ppmv C_2H_6 sample in N_2 using a commercial gas mixing system (Series 4,000, Environics).

DUAL-GAS SENSOR PERFORMANCE

Absorption Lines Selection for CH_4 and C_2H_6

The selected absorption line of CH_4 is shown in **Figure 4A**. According to the simulation results of HITRAN, under the conditions of temperature of 300 K, pressure of 760 Torr and optical path length of 1 m, the absorbance of CH_4 at a concentration level of two ppmv and H_2O at a concentration level of 2% were obtained. It can be seen that when the H_2O concentration is high, it will have a certain influence on the detection of CH_4. Therefore, a dehumidification treatment was performed in the gas inlet to reduce the interference of H_2O. CH_4 has a strong absorption line located at 6046.95 cm^{-1}. Accordingly, we chose the laser emission wavelength range of 6046–6048 cm^{-1} for CH_4 detection. **Figure 4C** shows the current variation within the selected wavenumber range when the temperature of the DFB laser is 19°C, 20 and 21°C. In **Figure 4E**, the emission spectrum under a laser driving current of 10–120 mA was measured at 20°C. In order to cover the CH_4 absorption line, the laser temperature was set at 20°C and the central current at 84 mA.

The selected C_2H_6 absorption line is shown in **Figure 4B**. According to the simulation results of HITRAN, under the condition of temperature of 300 K, pressure of 760 Torr and optical path length of 1m, the C_2H_6 absorption line with one ppmv concentration was obtained. C_2H_6 has a strong absorption

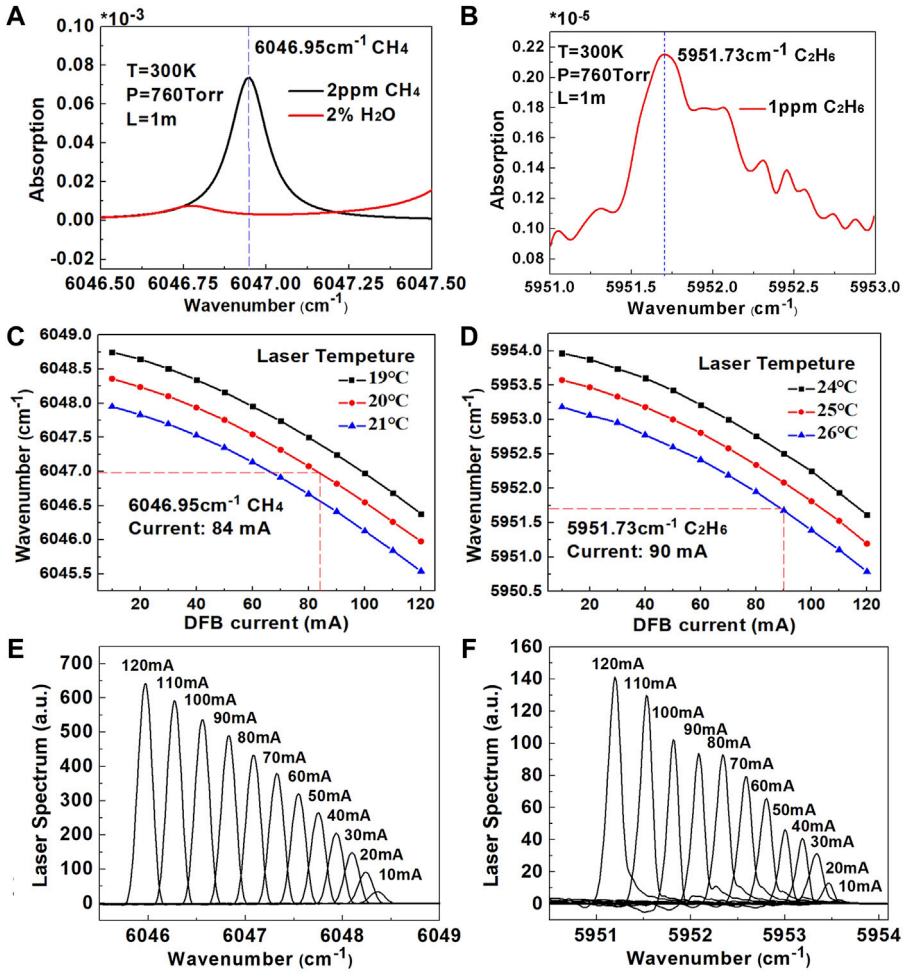

FIGURE 4 | (A) The simulated absorbance of 2% H_2O, two ppmv CH_4 from 6046.5 cm^{-1} to 6047.5 cm^{-1} at a temperature of 300 K, a pressure of 760 Torr, and an optical path length of 1 m **(B)** The simulated absorbance of one ppmv CH4 from 5,951 cm to 1 to 5,953 cm-1 at a temperature of 300 K, a pressure of 760 Torr, and an optical path length of 1 m **(C)** Plot of the DFB emission wavenumber as a function of the current at laser temperatures of 19°C, 20°C and 21°C, respectively **(D)** Plot of the DFB emission wavenumber as a function of the current at laser temperatures of 24°C, 25 and 26°C, respectively **(E)** Emission spectrum at 20°C of the DFB laser for CH_4 detection **(F)** Emission spectrum at 26°C of the laser for C_2H_6 detection.

line at 5,951.73 cm^{-1}, and the selected wavenumber range is 5,951–5,953 cm^{-1} for C_2H_6 detection. **Figure 4D** shows the current variation in the selected wavenumber range at a laser temperature of 24°C, 25 and 26°C. The laser drive temperature was set at 26°C, and the central current was 90 mA for C_2H_6 detection. In **Figure 4F**, the emission spectrum of the laser under a current of 10–120 mA was measured at a temperature of 26°C.

CH_4 Sensor Performance

The measured amplitude of the differential signal of CH_4 (i.e. $\nu_d = \nu_{base} - \nu_{abs}$) at different concentration levels of 0, 5, 10, 15 and 20 ppmv is shown in **Figure 5A**. In order to speeding the response of the sensor, a high sampling frequency was adopted, and one data point was acquired per 0.8 s. The amplitude (defined as Amp(ν_d), in V) at each concentration was recorded for 40 s, leading to 50 points. The average value of these 50 data was used to obtain the linear relationship between CH_4 concentration and the amplitude, as shown in **Figure 5B**. The linear relationship is expressed by **Eq. 3** with a good linear fitting degree of 99.97%, as

$$C_{CH_4} = 2037.42458 \times \mathrm{Amp}(\nu_d) - 0.05898 \quad (3)$$

where C_{CH4} (in ppmv) is the concentration of CH_4. Then, the CH_4 sample with a concentration of 0 ppmv was injected into the MPC to observe the stability of the whole system, and the overall observation time was ~16 min. The sampled signal amplitude was substituted in **Eq. 3** to calculate the corresponding CH_4 concentration levels. Curve of CH_4 concentration level changing with measurement time is shown in **Figure 5C**, which is relatively stable overall and verifies the reliability of the whole sensor system. The measured concentration was then used for Allan variance analysis to obtain the detection limit of the CH_4 sensor, as shown in **Figure 5D**. The first data point is the minimum concentration that can be detectable, which indicates that the 1σ detection limit of CH_4 is 71 ppbv at an averaging time

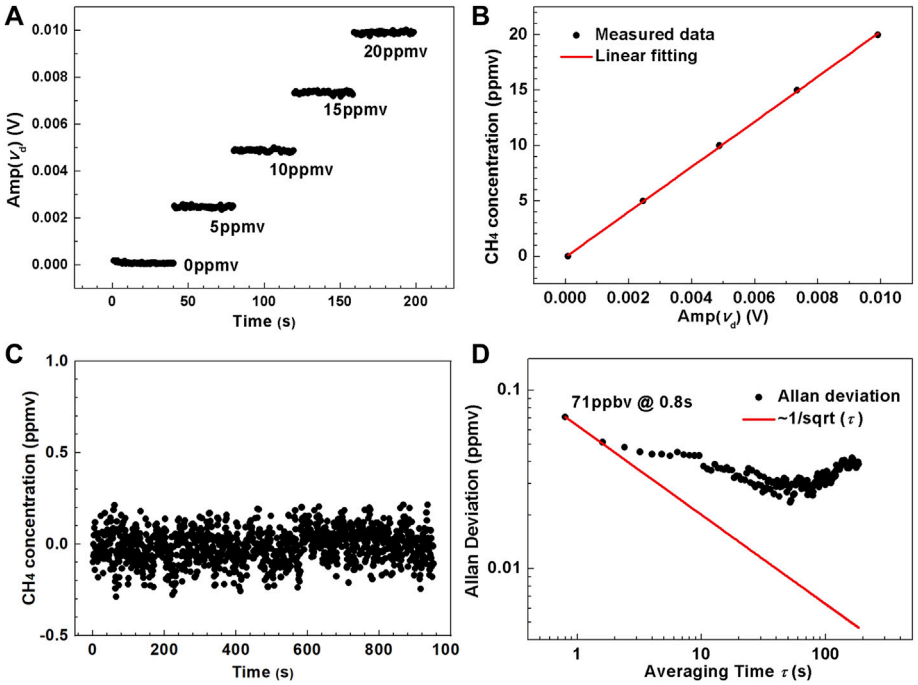

FIGURE 5 | (A) Measured amplitude of the differential absorption signal versus calibration time *t* under different CH_4 concentration levels ranging from 0 to 20 ppmv **(B)** Experimental data and fitting curve of CH_4 concentration versus the averaged amplitude of the differential absorption signal. **(C)** Measured CH_4 concentration by passing pure N_2 into the compact MPC. **(D)** Allan-Werle deviation plot as a function of averaging time, τ, based on the data shown in **Figure 6C**.

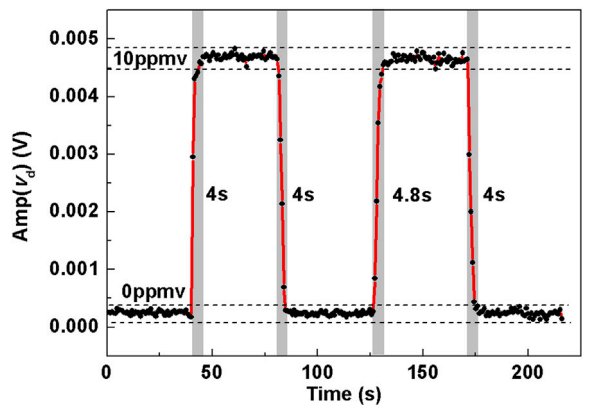

FIGURE 6 | Pure N_2 and 10 ppmv CH_4 were injected into the compact MPC in turn to obtain the rise time and fall time of the sensor for CH_4 detection.

of 0.8 s. As integration time increases, system noise occurs leading to the decrease of sensor stability. This type of noise is the sensor system drift, mainly originating from the drift of the near-infrared detector, the laser power and wavelength as well as the electrical circuits for signal processing.

The response time of the sensor system for CH_4 detection was determined by the measured time that was needed for the CH_4 concentration exchange between 0 ppmv and 10 ppmv. The sampling time for each data point was 0.8 s, as shown in **Figure 6**. Several repeated experiments were done to change the concentration level either from 0 ppmv to 10 ppmv or from 10 ppmv to 0 ppmv for multiple times. At each time the concentration became stable, 40 points were recorded. The response time was measured to be 4 s.

C_2H_6 Sensor Performance

As shown in **Figure 7A**, the measured amplitude (Amp(ν_d)) of C_2H_6 at six different concentration levels of 0, 2, 4, 6, 8, and 10 ppmv were obtained. A data point was derived per 0.8 s, and the total time for recording the amplitude at each concentration was 40 s. The linear relationship between C_2H_6 concentration C_{C2H6} (in ppmv) and Amp(ν_d) (in V) was obtained as shown in **Figure 7B**, expressed as

$$C_{C_2H_6} = 10929.09126 \times \mathrm{Amp}(\nu_d) + 0.29314 \quad (4)$$

Then the C_2H_6 concentration was set to 0 ppmv to observe the stability of the whole system, and the overall observation time was 18 min. The real-time C_2H_6 amplitude was substituted into **Eq. 4** to calculate the corresponding concentration. The variation of C_2H_6 concentration with time is shown in **Figure 7C**, which proved the overall stability and verified the reliability of the whole sensor system. The obtained concentration was used for Allan variance analysis, and the C_2H_6 detection limit of the sensor system was achieved, as shown in **Figure 7D**. The first point is the minimum concentration detected, and the subsequent data is the deviation value, which indicates that the limit of detection of C_2H_6 is 189 ppbv at an averaging time of 0.8 s.

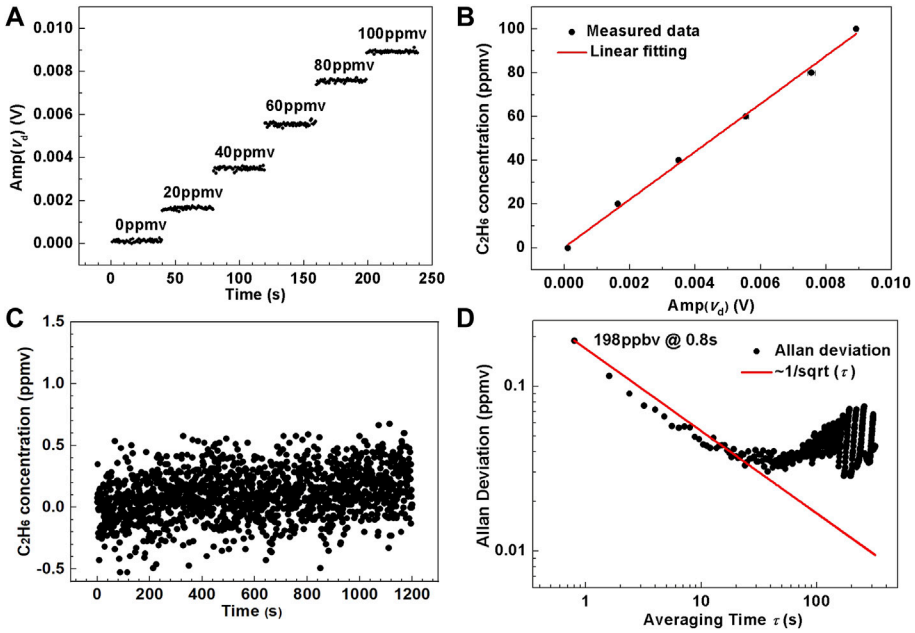

FIGURE 7 | (A) Measured amplitude of the differential absorption signal versus calibration time *t* under different C_2H_6 concentration levels ranging from 0 to 100 ppmv. **(B)** Experimental data and fitting curve of C_2H_6 concentration versus the averaged amplitude of the differential absorption signal. **(C)** Measured C_2H_6 concentration by passing pure N_2 into the compact MPC. **(D)** Allan-Werle deviation plot as a function of averaging time, τ, based on the data shown in **Figure 7C**.

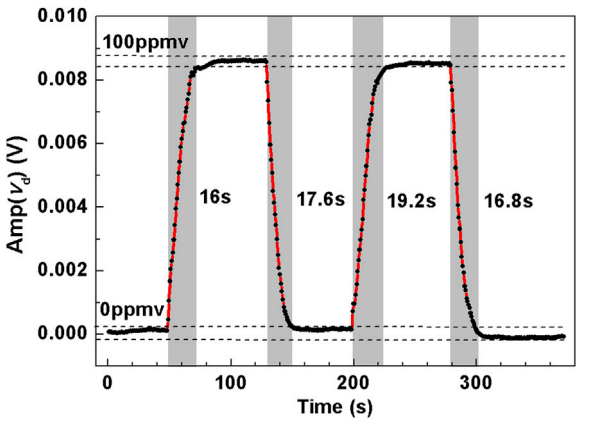

FIGURE 8 | Dynamic measurement by injecting pure N_2 and 100 ppmv C_2H_6 into the compact MPC in turn to obtain the rise time and fall time of the sensor for C_2H_6 detection.

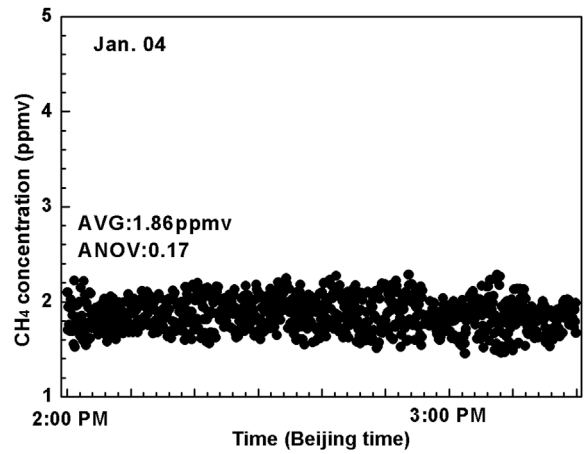

FIGURE 9 | Measured concentrations of CH_4 in ambient air during ~1.2 h period on 4 Jan 2021 inside the laboratory (located in Tang Aoqing building, Jilin University).

Then, the response characteristics of the dual-gas sensor system for C_2H_6 detection was determined by measuring the response time by switching the C_2H_6 concentration level between 0 ppmv and 100 ppmv. The sampling time for each data point was 0.8 s. The response time from 0 ppm to 100 ppmv for the first concentration exchange was about 16 s. Then several repeated experiments were done, that is, either from 0 ppmv to 100 ppmv or from 100 ppmv to 0 ppmv. 40 data points were recorded each time when the measured concentration was stabilized. As shown in **Figure 8**, The measured response time was maintained at 16–20 s.

FIELD SENSING APPLICATION

In order to verify the performance and practicability of the sensor, the demonstrated dual-gas sensor system was used to monitor the

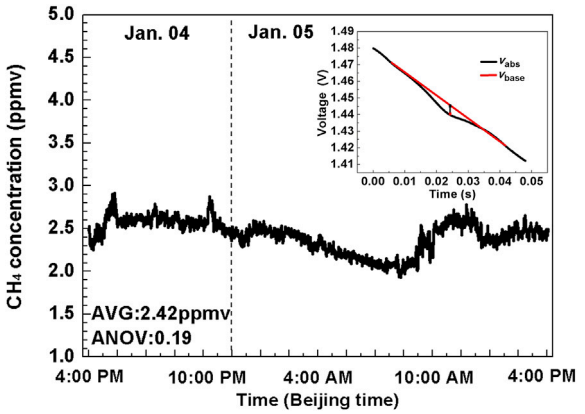

FIGURE 10 | Measurement results of CH_4 monitoring in the atmosphere for ~24 h time duration on the Jilin University campus. The inset shows the waveform of a recorded absorption signal.

CH_4 concentration levels in the laboratory and the CH_4 concentration levels in the outdoor atmosphere.

Indoor CH_4 Monitoring

The sensor system was evaluated by measuring the indoor CH_4 concentration levels in a laboratory environment on 4 January 2021 between 2:00 p.m. and 3:20 p.m. The laboratory is located at Tang Aoqing building (GPS position, 125.291,448° E, 43.831,747° N) of Jilin University, Changchun, Jilin Province, China. The total measurement duration was 1.2 h with a sampling interval of 0.8 s (i.e. no averaging on the sampling data). As shown in **Figure 9**, fluctuations in CH_4 concentration levels were observed during the measurement from 1.5 ppmv to 2.2 ppmv, and the concentration of CH_4 showed an average of ~1.86 ± 0.17 ppmv (1σ). Since the air circulation in the laboratory was relatively slow, the change of CH_4 concentration was not obvious. It thus can be observed that the CH_4 concentration level in the laboratory was relatively stable during this period.

Outdoor Atmospheric CH_4 Monitoring

The sensor system was re-evaluated by measuring the outdoor CH_4 concentration levels in the atmosphere. The outside air was pumped into the gas cell via a Poly Tetra Fluoroethylene (PTFE) for outdoor atmospheric CH_4 testing. Pre-treatment was carried out before the atmosphere enters the gas cell to remove ambient impurities, aerosols and water vapor. The outside air was pumped into the gas cell via a PTFE filtered tube to detect the outdoor CH_4 concentration levels for 1 day. The measurement was conducted in zone D, Tang Aoqing building, Jilin University, Changchun, and the measurement time was from 4:40 p.m. on 4 January 2021 to 4:40 p.m. on 5 January 2021. The sampling data was averaged per 40 s (i.e. 50 data points were averaged as one data point). As shown in **Figure 10**, it can be concluded from the variation trend that the CH_4 concentration decreased at night and was eventually down to 2.2 ppmv–2.3 ppmv. The CH_4 concentration level suddenly increased at 10:00 a.m. with a peak up to 2.7 ppmv and was eventually around 2.6 ppmv at 4:00 p.m. in the next day. Over the 1 day, the measured CH_4 concentration ranged between 2.2 and 2.8 ppmv, with an average value of 2.42 ± 0.19 ppmv.

CONCLUSION

A dense-pattern MPC-based near-infrared sensor system was demonstrated for CH_4/C_2H_6 dual-gas detection. Two laser beams were injected into the MPC with an effective path length of 9.39 m. Both indoor and outdoor CH_4 concentration levels were measured to verify the performance of the sensor system. Compared with the traditional single-ring Herriott cell, the volume of the DP-based gas cell is obviously reduced and the optical path becomes longer by increasing the reflection number, and the reduced size leads to an enhanced stability and high sensitivity. Compared with a single-gas sensor, the size of the developed dual-gas sensor system becomes smaller and more convenient for field detection. The dual-gas sensor system extends the application of MPC in the field of infrared absorption spectroscopic gas sensing. Further optimization of optical path will be carried out to improve the sensitivity of C_2H_6 detection, so as to monitor the ppb-level C_2H_6 in the atmosphere.

DATA AVAILABILITY STATEMENT

The original contributions presented in the study are included in the article/supplementary material further inquiries can be directed to the corresponding authors.

AUTHOR CONTRIBUTIONS

ZX and KZ performed the experiments and wrote the manuscript. CZ and YW supported the experiments and revised the manuscript. HZ. analyzed and verified the experimental results. FS, CL, WY, YZ, YW, and FT provided technical guidance and helped to revise the paper. The manuscript was written through contributions of all authors. All authors have given approval to the final version of the manuscript.

FUNDING

National Natural Science Foundation of China (Nos. 61960206004, 61805099, and 62175087), Science and Technology Development Program of Jilin Province, China (Nos. 20200401059GX and 20200201228JC), Science and Technology Research Program of Department of Education, Jilin Province, China (No. JJKH20211088KJ), Key R and D Program of Changchun (No. 21ZGN24), Program for JLU Science and Technology Innovative Research Team (JLUSTIRT, 2021TD-39).

REFERENCES

1. Jin W, Bao H, Zhao P, Zhao Y, Qi Y, Wang C, et al. Recent Advances in Spectroscopic Gas Sensing with Micro/Nano-Structured Optical Fibers. *Photonic Sens* (2021) 11(2):141–57. doi:10.1007/s13320-021-0627-4
2. Zhu X, Xu F, He Q, Xing Z, Zhang S, Zhang X. Detection of Intermediates for Diatomic [TaO]+ Catalyzed Gas-Phase Reaction of Methane Coupling to Ethane and Ethylene by ICP-MS/MS. *Microchemical J* (2021) 161:105762. doi:10.1016/j.microc.2020.105762
3. Liu X, Qiao S, Ma Y. Highly Sensitive Methane Detection Based on Light-Induced Thermoelastic Spectroscopy with a 2.33 μm Diode Laser and Adaptive Savitzky-Golay Filtering. *Opt Express* (2022) 30(2):1304–13. doi:10.1364/OE.446294
4. Bamberger I, Stieger J, Buchmann N, Eugster W. Spatial Variability of Methane: Attributing Atmospheric Concentrations to Emissions. *Environ Pollut* (2014) 190:65–74. doi:10.1016/j.envpol.2014.03.028
5. Zheng H, Liu Y, Lin H, Kan R, Patimisco P, Sampaolo A, et al. Sub-ppb-level CH4 Detection by Exploiting a Low-Noise Differential Photoacoustic Resonator with a Room-Temperature Interband cascade Laser. *Opt Express* (2020) 28(13):19446–56. doi:10.1364/OE.391322
6. Hevia MAG, Ordóñez S, Díez FV. Effect of the Catalyst Properties on the Performance of a Reverse Flow Reactor for Methane Combustion in Lean Mixtures. *Chem Eng J* (2007) 129(1–3):1–10. doi:10.1016/j.cej.2006.10.028
7. Kamieniak J, Randviir EP, Banks CE. The Latest Developments in the Analytical Sensing of Methane. *Trac Trends Anal Chem* (2015) 73:146–57. doi:10.1016/j.trac.2015.04.030
8. Li C, Dong L, Zheng C, Lin J, Wang Y, Tittel F. Ppbv-Level Ethane Detection Using Quartz-Enhanced Photoacoustic Spectroscopy with a Continuous-Wave, Room Temperature Interband cascade Laser. *Sensors* (2018) 18(3):723. doi:10.3390/s18030723
9. Etiope G, Ciccioli P. Earth's Degassing: A Missing Ethane and Propane Source. *Science* (2009) 323(5913):478. doi:10.1126/science.1165904
10. Chen F, Jiang S, Jin W, Bao H, Ho HL, Wang C, et al. Ethane Detection with Mid-infrared Hollow-Core Fiber Photothermal Spectroscopy. *Opt Express* (2020) 28(25):38115–26. doi:10.1364/OE.410927
11. Ma Y, Hu Y, Qiao S, Lang Z, Liu X, He Y, et al. Quartz Tuning Forks Resonance Frequency Matching for Laser Spectroscopy Sensing. *Photoacoustics* (2022) 25:100329. doi:10.1016/j.pacs.2022.100329
12. Lin H, Zheng H, Montano BAZ, Wu H, Giglio M, Sampaolo A, et al. Ppb-Level Gas Detection Using On-Beam Quartz-Enhanced Photoacoustic Spectroscopy Based on a 28 kHz Tuning fork. *Photoacoustics* (2022) 25:100321. doi:10.1016/j.pacs.2021.100321
13. Ma Y, Hong Y, Qiao S, Lang Z, Liu X. H-Shaped Acoustic Micro-Resonator-Based Quartz-Enhanced Photoacoustic Spectroscopy. *Opt Lett* (2022) 47(3):601–4. doi:10.1364/OL.449822
14. Lv H, Zheng H, Liu Y, Yang Z, Wu Q, Lin H, et al. Radial-Cavity Quartz-Enhanced Photoacoustic Spectroscopy. *Opt Lett* (2021) 46(16):3917–20. doi:10.1364/OL.432308
15. Ma Y. Recent Advances in QEPAS and QEPTS Based Trace Gas Sensing: A Review. *Front Phys* (2020) 8:268. doi:10.3389/fphy.2020.00268
16. Liu X, Ma Y. Sensitive Carbon Monoxide Detection Based on Light-Induced Thermoelastic Spectroscopy with a Fiber-Coupled Multipass Cell [Invited]. *Chin Opt Lett* (2022) 20(3):031201. doi:10.3788/COL202220.031201
17. Wang F, Jia S, Wang Y, Tang Z. Recent Developments in Modulation Spectroscopy for Methane Detection Based on Tunable Diode Laser. *Appl Sci* (2019) 9(14):2816. doi:10.3390/app9142816
18. Upadhyay A, Wilson D, Lengden M, Chakraborty AL, Stewart G, Johnstone W. Calibration-Free WMS Using a Cw-DFB-QCL, a VCSEL, and an Edge-Emitting DFB Laser with *In-Situ* Real-Time Laser Parameter Characterization. *IEEE Photon J.* (2017) 9(2):6801217. doi:10.1109/JPHOT.2017.2655141
19. Lan L, Ghasemifard H, Yuan Y, Hachinger S, Zhao X, Bhattacharjee S, et al. Assessment of Urban CO2 Measurement and Source Attribution in Munich Based on TDLAS-WMS and Trajectory Analysis. *Atmosphere* (2020) 11(1):58. doi:10.3390/atmos11010058
20. Sur R, Sun K, Jeffries JB, Hanson RK, Pummill RJ, Waind T, et al. TDLAS-Based Sensors for *In Situ* Measurement of Syngas Composition in a Pressurized, Oxygen-Blown, Entrained Flow Coal Gasifier. *Appl Phys B* (2014) 116(1):33–42. doi:10.1007/s00340-013-5644-6
21. White JU. Long Optical Paths of Large Aperture. *J Opt Soc Am* (1942) 32(5):285–8. doi:10.1364/JOSA.32.000285
22. Herriott DR, Schulte HJ. Folded Optical Delay Lines. *Appl Opt* (1965) 4(8):883–9. doi:10.1364/AO.4.000883
23. Herriott D, Kogelnik H, Kompfner R. Off-Axis Paths in Spherical Mirror Interferometers. *Appl Opt* (1964) 3(4):523–6. doi:10.1364/AO.3.000523
24. McManus JB, Kebabian PL, Zahniser MS. Astigmatic Mirror Multipass Absorption Cells for Long-Path-Length Spectroscopy. *Appl Opt* (1995) 34(18):3336–48. doi:10.1364/AO.34.003336
25. Cui R, Dong L, Wu H, Li S, Yin X, Zhang L, et al. Calculation Model of Dense Spot Pattern Multi-Pass Cells Based on a Spherical Mirror Aberration. *Opt Lett* (2019) 44(5):1108–11. doi:10.1364/OL.44.001108
26. Tarsitano CG, Webster CR. Multilaser Herriott Cell for Planetary Tunable Laser Spectrometers. *Appl Opt* (2007) 46(28):6923–35. doi:10.1364/AO.46.006923
27. Liu K, Wang L, Tan T, Wang G, Zhang W, Chen W, et al. Highly Sensitive Detection of Methane by Near-Infrared Laser Absorption Spectroscopy Using a Compact Dense-Pattern Multipass Cell. *Sensors Actuators B: Chem* (2015) 220:1000–5. doi:10.1016/j.snb.2015.05.136
28. Cui R, Dong L, Wu H, Ma W, Xiao L, Jia S, et al. Three-Dimensional Printed Miniature Fiber-Coupled Multipass Cells with Dense Spot Patterns for Ppb-Level Methane Detection Using a Near-IR Diode Laser. *Anal Chem* (2020) 92(19):13034–41. doi:10.1021/acs.analchem.0c01931
29. Dong M, Zheng C, Yao D, Zhong G, Miao S, Ye W, et al. Double-Range Near-Infrared Acetylene Detection Using a Dual Spot-Ring Herriott Cell (DSR-HC). *Opt Express* (2018) 26(9):12081–91. doi:10.1364/OE.26.012081
30. Ye W, Li C, Zheng C, Sanchez NP, Gluszek AK, Hudzikowski AJ, et al. Mid-Infrared Dual-Gas Sensor for Simultaneous Detection of Methane and Ethane Using a Single Continuous-Wave Interband cascade Laser. *Opt Express* (2016) 24(15):16973–85. doi:10.1364/OE.24.016973
31. Zhong G, Ma Z, Wang J, Zheng C, Zhang Y, Wang Y, et al. Near-Infrared Tunable Laser Absorption Spectroscopic Acetylene Sensor System Using a Novel Three Mirror-Based, Dense Pattern Gas Cell. *Sensors* (2020) 20(5):1266. doi:10.3390/s20051266

Conflict of Interest: The authors declare that the research was conducted in the absence of any commercial or financial relationships that could be construed as a potential conflict of interest.

frontiers in Physics

REVIEW
published: 07 March 2022
doi: 10.3389/fphy.2022.865029

Recent Progress in Nonlinear Frequency Conversion of Optical Vortex Lasers

Jie Liu[1†], *Yanmin Duan*[1†], *Zhihong Li*[1], *Ge Zhang*[2] *and Haiyong Zhu*[1*]

[1]*Wenzhou Key Laboratory of Micro-Nano Optoelectronic Devices, Wenzhou University, Wenzhou, China,* [2]*Key Laboratory of Optoelectronic Materials Chemistry and Physics, Fujian Institute of Research on the Structure of Matter, Chinese Academy of Sciences, Fuzhou, China*

Optical vortices are optical fields that possess a helical phase and orbital angular momentum, which have found the application in micromanipulation, optical communication, orbital angular momentum entanglement, super-resolution imaging, metrology, etc. The urgent need for the wide spreading applications of vortex lasers is to increase the wavelength versatility. In this study, the nonlinear frequency conversion of vortex lasers with a focus on sum frequency generation stimulated Raman scattering, and optical parametric oscillators were meticulously reviewed. The characteristics of the topological charge transfer and output beam profiles of different frequency conversion were discussed. As the precise tuning of optical fields in both temporal and spatial domains shall be the trend of future studies, it is our hope that this review shall serve as a reference for future research. Combining these techniques with the streaming methods to produce optical vortices, i.e., annular pump, off-axis pump, reflection mirror with defect spots, spherical aberration, and birefringence, it is advisable to expand the wavelength and fill the wavelength gap in the ultraviolet, visible, and infrared bands.

Keywords: optical vortex, solid-state laser, frequency conversion, orbital angular momentum, Laguerre–Gaussian

OPEN ACCESS

Edited by:
Yufei Ma,
Harbin Institute of Technology, China

Reviewed by:
Luming Zhao,
Jiangsu Normal University, China
Zhenqiang Chen,
Jinan University, China

***Correspondence:**
Haiyong Zhu
hyzhu.opt@gmail.com

†These authors have contributed equally to this work and share first authorship

Specialty section:
This article was submitted to Optics and Photonics, a section of the journal Frontiers in Physics

Received: *29 January 2022*
Accepted: *14 February 2022*
Published: *07 March 2022*

Citation:
Liu J, Duan Y, Li Z, Zhang G and Zhu H (2022) Recent Progress in Nonlinear Frequency Conversion of Optical Vortex Lasers. Front. Phys. 10:865029. doi: 10.3389/fphy.2022.865029

INTRODUCTION

Optical vortex is a beam with doughnut shape intensity profile—characterizing a dark region in the center and a helical phase [1]. Its concept was first introduced by Coullet et al. [2] in 1989. It has an azimuthal phase term $e^{i\theta l}$, where l is the azimuthal index, known as the topological charge, and θ is the azimuthal angle. Intensive studies were initiated since Allen's work in 1992 [3], for it proved that optical vortices carry orbital angular momentum (OAM). He et al. [4] also reported the direct observation of the OAM transfer from the beam to the absorptive particles in 1995 by trapping single CuO particles in a Laguerre–Gaussian (LG) beam.

Optical vortices were later found to be extremely useful. Early works have demonstrated its availability to facilitate particle-trapping [5, 6]. Compared with conventional optical tweezers, the LG beam can create stronger adherence and produce no dissipative force. Another application of optical vortices is quantum communication since Zeilinger et al. [7] realized high-order OAM entanglement in 2001. In 2008, Barreiro et al. [8] successfully beat the capacity limit in quantum communication by taking advantage of an OAM-carrying beam. Furthermore, over 10,000 $\hbar$ OAM were generated in a quantum-entangled state by parametric down conversion in 2016 [9]. It is robust owing to its resistance to disturbance when passing through atmospheric turbulence. The development of the mode-division multiplexing technique [10, 11] has also significantly promoted its actualization.

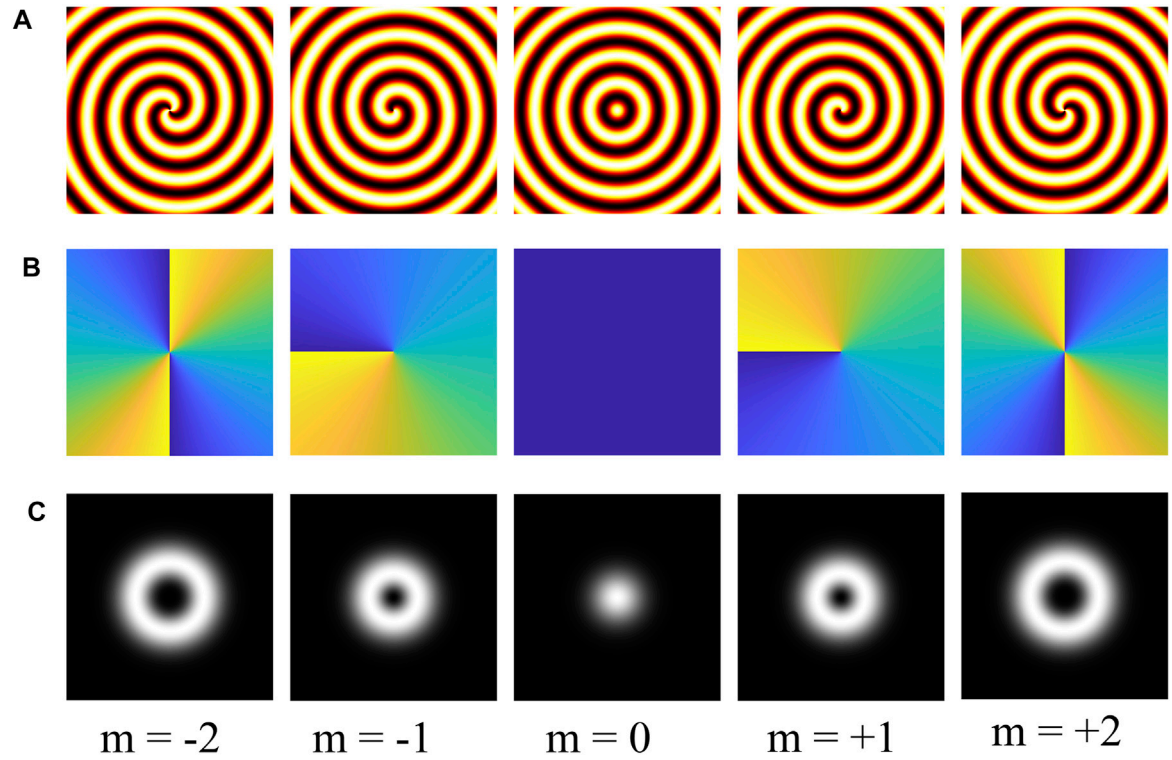

FIGURE 1 | (A) Illustration of corkscrew wavefronts of a vortex beam (m = 2, 1, 0, −1, and −2, respectively); **(B)** the corresponding phase information of the vortex beam with the topological order m = 2, 1, 0, −1, and −2, respectively; **(C)** the corresponding intensity distribution profile of the vortex beam with topological order m = 2, 1, 0, −1, and −2.

The study of optical vortices could benefit astronomical observations as well. In 2003, Harwit [12] made a theoretical work to associate optical vortex generation with the astronomical process. Further analysis of this information told additional properties of the stellar object. In 2011, Fabrizio et al. [13] made an observation of twisted light in rotating blackhole. Due to the rotational Doppler effect [14–16], it is advantageous in remote sensing, image restoration, super-resolution imaging, metrology, and so on [17–23]. Researchers found that due to the low diffraction limit, the vortex beam could replace the trivial Gaussian beam to improve the resolution of imaging, e.g., stimulated emission depletion, which can be of great use to biological and clinical medicine research [24]. Other recent applications in 2021 point to high-dimension OAM-entanglement, and phase-gradient protection was also reported [25–28]. Many other exciting applications with regard to optical vortices are yet to be found. Methods to characterize optical vortices have been developed including using interference fringes such as the Mach–Zehnder interferometer, or using diffraction methods such as by using a triangular aperture [29, 30].

Nevertheless, much like the lasers in its early stage of development, the widespread use of this twisted photon source requires it to cover a wide spectrum. Thankfully, nonlinear frequency conversion techniques have provided numerous possibilities to achieve this objective. This study summarizes some of the most prestigious vortex laser designs and their results. Frequency conversion techniques such as second harmonic generation (SHG), sum frequency generation (SFG), high-order harmonic generation (HHG), stimulated Raman scattering (SRS), and optical parametric oscillation (OPO) are investigated and presented as detailed as possible. Furthermore, some proposals will be put forward with respect to the problems that still need to be addressed.

VORTEX BEAM GENERATION

Optical vortex could refer to any beam with singularities and intrinsic OAM. For beams with OAM, wavefront dislocations are presented. In general term, the OAM beam could be written in the following expression:

$$u(r, \theta, z) = u_0(r, \theta, z) \exp(-il\theta) \exp(-ikz).$$

The phase term is expressed as follows: $\phi(r, \theta, z) = l\theta + kz$. θ is the azimuthal angle. l is the azimuthal index related to the spiral phase. Owing to its wavefront dislocation, a vortex beam propagates in a corkscrew way, such as depicted in **Figure 1**. They are the results of superposition of eigenmodes.

Following the scalar Helmholtz equation under the paraxial condition gave a set of eigenmodes, such as Hermite–Gaussian, Laguerre–Gaussian, and Bessel. Conventional lasers are Gaussian

beams $TEM_{0,0}$. For high-order modes $TEM_{m,n}$, m and n being the indices of *x* and *y* axes, the diffraction loss is severe. So to keep the lasing condition favorable for high-order modes, a certain mechanism to inhabit the fundamental transverse patterns is required.

Nowadays, several ways are already developed to obtain optical vortices. They can be categorized into two types—extra-cavity and intracavity. For extra-cavity, the most common way is forked pattern grating with a spatial light modulator [31, 32], digital macrodevices [33], etc. The spiral phase plate, q-plate, and metasurface materials can be used to produce vortex beam as well. For all the apparent benefits of these methods, they do have one fatal flaw—the lack of flexibility. Once manufactured, the operable range of these components was fairly limited. Even though tremendous efforts have been put to it, metasurface materials still have a long way to go. For the intracavity approach, which can directly produce optical vortices without additional components, the lay-out is usually configured very compact and robust when compared to the extra-cavity approach, reducing the cost for space, and hence reducing the spatial loss since there is no need of additional optical elements. Therefore, it is easier to obtain a beam with high beam quality. In light of these advantages, the intracavity method may be the apt choice for the production of vortex laser.

In general, the basic principle to directly produce such tailored optical fields is by breaking the lasing symmetry to enable the oscillator of high-order modes. The methods to produce intracavity OAM-carrying beams mainly include the following: annular pump, off-axis pump, reflection mirror with defect spots, and inserting lens with high spherical aberrations.

The annular pump approach is based on a central-null pumping configuration, which was usually obtained through axicons [34–37], capillary fiber [38–41], or center-punched mirror [42–46]. In 2017, Zhang et al [47] achieved a direct $LG_{0,1}$ vortex output in a Yb:$MgWO_4$ laser, which manifested handedness control without additional elements. In 2021, they realized a tunable topological charge as high as 18th with an axicon [48]. Off-axis pumping [49–55] is to achieve the asymmetric pumping condition, which can efficiently hinder the oscillation of low-order modes. It is realized mainly by tilting the crystal or shifting the position of the pump spot on the crystal. It tends to produce high-order Hermite–Gaussian (HG) modes and is in need of an additional astigmatism converter [56–58] to be transformed to the vortex mode. The defect spot approach [59–62] is to choose a defect mirror as the output coupler or as rear mirror. If the defect spot radius to mode radius is kept within a reasonable range, then the corresponding mode will be produced. Intracavity lens with short focus can introduce large spherical aberrations, which were said to be an effective mechanism for mode separation. Intracavity lens were yet another method [63–70]. Early in 2009, Senatsky et al. [63] realized circular $LG_{0,m}$ modes by inserting the intracavity lens. Recently in 2021, Wang et al. [69] developed this method by using a plano-concave cavity and a long-focus lens followed by a short focus lens. $LG_{0,l}$ doughnut beams were produced with *l* ranging from ±10 to ±33. Apart from a real lens, the thermal lensing effect could also be utilized for the same purpose, which were already explicitly demonstrated by Okida et al. in 2009 [65, 66] and 2011 [67].

These methods are constantly developing over the years. In **Figure 2**, we presented a summary concerning intracavity generation of vortex beams. Other unconventional approaches such as using volume Bragg grating and other diffractive elements have also been developed over these years [71–86]. Many reports have already performed a thorough review of the development of optical vortex lasers concerning its generation, tunability, and control of vortex handedness. In 2011, Sensky et al. [87] reviewed LG mode selection in diode-pumped solid-state lasers. In 2018, Wang et al. [88] gave a review on the progresses of optical vortex generation with a focus on the development of optical devices. In 2019, at the 30th anniversary since the start of the topic, Shen et al. [89] reviewed the advances of optical vortices and its many applications. In 2021, Fu et al. [90] reviewed the measurement of the OAM-spectrum and its application in various fields. These reviews have given the generation, tunability, and improvement of power performance of optical vortices, as well as the potential application, a thorough investigation. Nevertheless, another technique for filling in the wavelength gap is by nonlinear frequency conversion. In 2017, Omatsu et al. [91] and Lee at al [92] have respectively made reviews in this regard, with special attention to their work in this area. However, in the last 5 years, there have been many new achievements in nonlinear frequency conversion of OAM-carrying optical vortices. Therefore, in the following section, we will summarize latent results and introduce some of the most interesting phenomena during the nonlinear process. An extended discussion for their potential applications will also be given.

FREQUENCY CONVERSION OF VORTEX BEAMS

The urgent need for the wide spreading applications of vortex lasers is to increase the wavelength versatility. For instance, in communication systems, 1.5 μm light can achieve low crosstalk. By detecting the OAM spectrum of a visible beam, contrast enhancement of imaging is possible. $\chi^{(2)}$ and $\chi^{(3)}$ nonlinear optical effects such as SFG, SRS, and OPO are the ideal choice to further expand the wavelength coverage of optical vortices. In this section, a general review on the frequency-conversion experiments on vortex lasers will be presented, along with some elaborations on the dynamic process of the topological charge transfer.

SHG/SFG/HHG

In this section, details would cover the SHG, SFG, and HHG. SHG is a $\chi^{(2)}$ nonlinear effect. Under the phase-matching condition, a photon at frequency ω will become a photon of frequency 2ω. For conventional beams, the phase-matching condition is achieved through birefringence phase-matching and quasi-phase matching. For birefringence phase-matching, there were mainly two techniques—angle-tuned critical phase matching and temperature-tuned non-critical phase matching (NCPM) [93–95]. The well-studied nonlinear crystals include KTP,

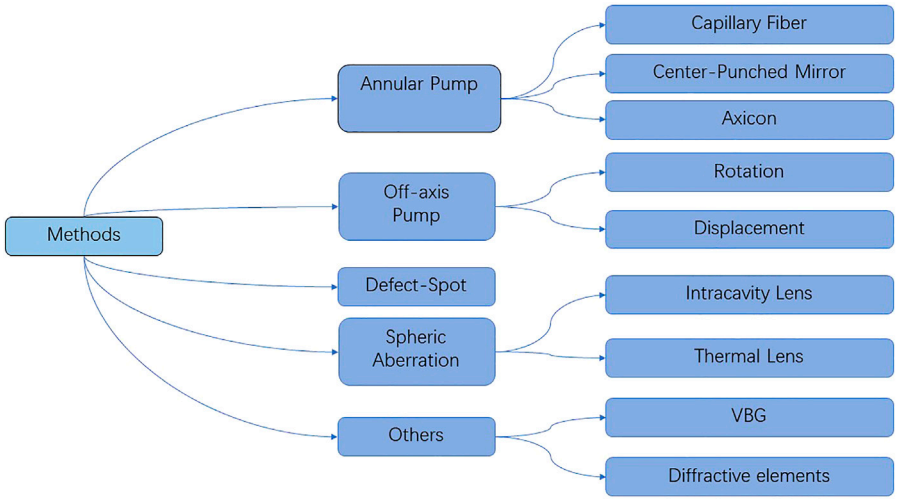

FIGURE 2 | Generalization of various methods that gives rise to a direct vortex mode without extra-cavity components.

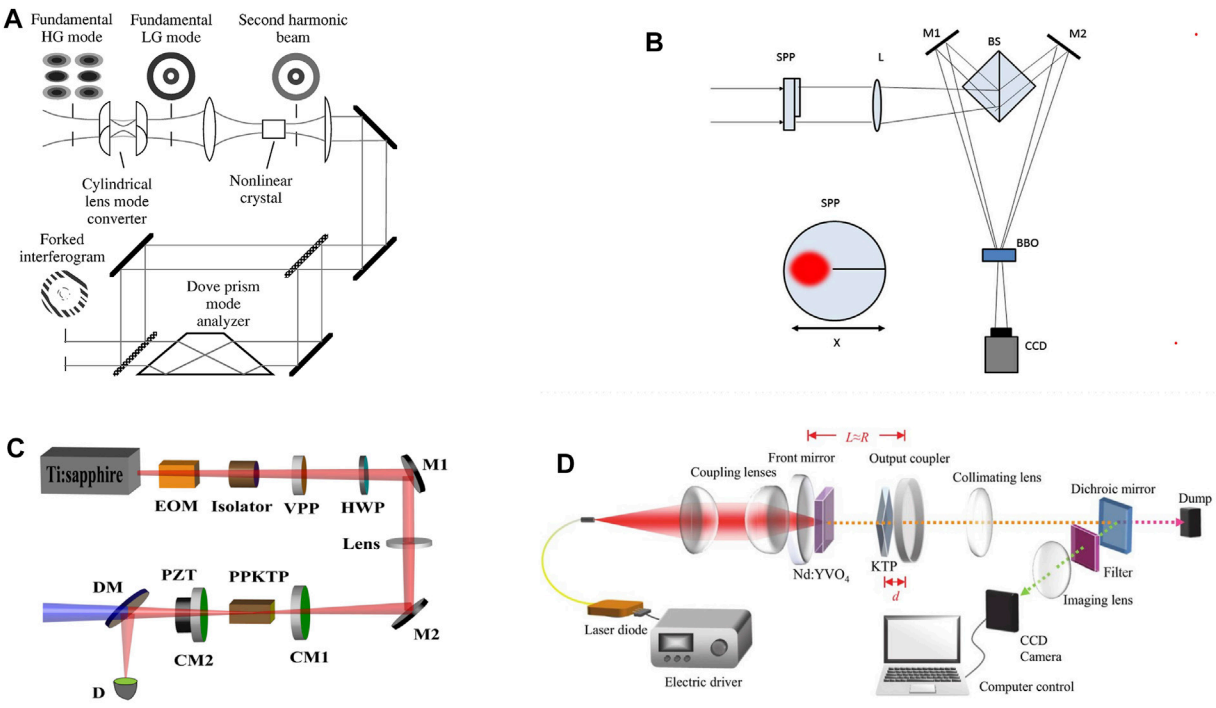

FIGURE 3 | (A) SHG of the LG beam converted from a HG mode by a mode converter; [99] **(B)** Off-axis SHG where the topological charge was introduced by a half-integer spiral phase plate; [101] **(C)** quasi-phase-matched SHG of the vortex beam with a periodic-poled KTP [104]; **(D)** intra-cavity SHG of the bottle beam by an intra-cavity KTP [109].

BBO, LBO, and so on. For quasi-phase matching, periodical crystals such as PPKTP and PPLN were studied in a number of reports [96, 97]. Phase-matching in conventional cases is governed mainly by two rules—the conservation of linear momentum $(n_1\omega_1 + n_2\omega_2 = n_3\omega_3)$ and the conservation of energy $(\omega_1 + \omega_2 = \omega_3)$. For the $\chi^{(2)}$ process of a vortex beam, conservation of the angular momentum should also be considered in the phase match condition $(l_1 + l_2 = l_2)$.

As early as 1996, Padgett et al. [98], who were among the earliest pioneers who studied optical vortices, reported SHG of an LG mode vortex beam by deploying a pair of cylindrical lenses as the mode converter. The fundamental HG mode was

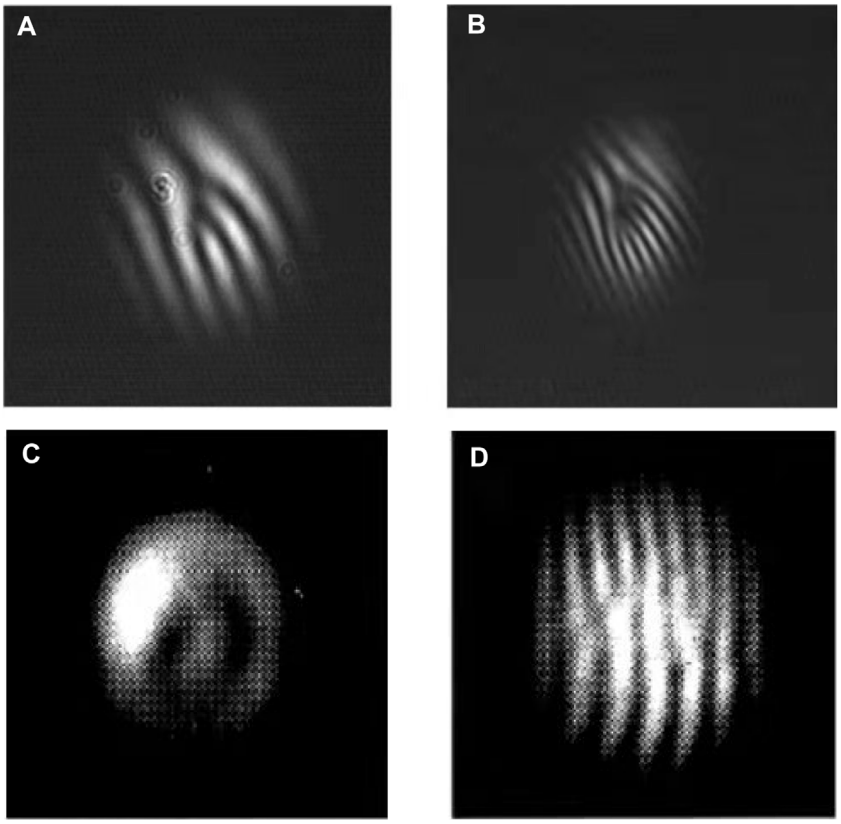

FIGURE 4 | Forked interference fringes [99] of **(A)** fundamental wave **(B)** SHG wave; and **(C)** Spatial distribution and interference patterns **(D)** of the SHG wave with the influence of walk-off [100].

converted into the LG mode which contains the OAM, at the work of the π/2-mode-converter. Padgett's theoretical simulations, as well as extra-cavity experiments (by making use of gadgets such as the q-plate, spiral phase plate, and so on) have confirmed that during an SHG process. The topological charge of the corresponding LG mode will also be doubled, signifying the law of conservation of angular momentum. In 1997, Courtial et al. [99] reported the SHG of an LG beam again, where their experimental configuration is depicted in **Figure 3A**. The topological charge was doubled for the SHG process, as shown in **Figures 4A,B**. In 1998, Berzanskis et al. [100] investigated the influence of walk-off on sum-frequency mixing of optical vortex lasers in type-I critical phase-matching cut KDP crystals. Two zeroes in the vortex field distribution were observed, as shown in **Figures 4C,D**, and the separation between the cores of two vortices was larger in the longer crystal. In 2011, Fabio et al. [101] employed a BBO crystal for the SHG experiment. The experimental configuration is shown in **Figure 3B**. Two femtosecond beams with opposite sign fractional topological charges served as the fundamental, which were achieved through the spiral phase plate. Each fundamental carried an OAM equivalent of 1/2 $\hbar$, while the SHG fields remain zero. This also proved that the conservation law remains true for vortex beams obtained through half-integer SPP.

Photonic crystals were suggested to produce twisted light by Bloch in 2012 [102]. In 2014, Zhou et al. [103] conducted an SHG experiment using periodically poled KTP (PPKTP) and successfully produced an ultraviolet beam with the OAM higher to 100 $\hbar$. Later the same year, Zhou et al. [104] proposed to improve the power performance by proper alignment of the quasi-phase-matching crystal and pumping it with the vortex beam. PPKTP with the dimension of 1 mm × 2 mm×10 mm was used. A conversion efficiency as high as 10.3% and SHG-power of 22.5 mW were achieved. The experimental configuration is shown in **Figure 3C**. The benefit of quasi-phase matching is the devoid of the walk-off effect and having a large acceptance angle. In 2018, Xu et al. [105] achieved the third harmonic generation (THG) with tunable topological orders by the acute use of quasi-phase matching. They demonstrated the control of OAM by using two orthogonally polarized beams at the same frequency by carrying different topological charges to pass through the periodically poled $LiTaO_3$ optical superlattice. After a cascaded nonlinear process in the crystal, the obtained beam carried a topological charge identical to that of the input OAM-carrying LG beam. Wang et al. [106] designed nonlinear fork gratings with supercell structures in lithium niobate crystals. The development of lithium niobate photonic crystals and their application in wavefront modulation have suggested a possible route to generate the second harmonic wave. They combined the

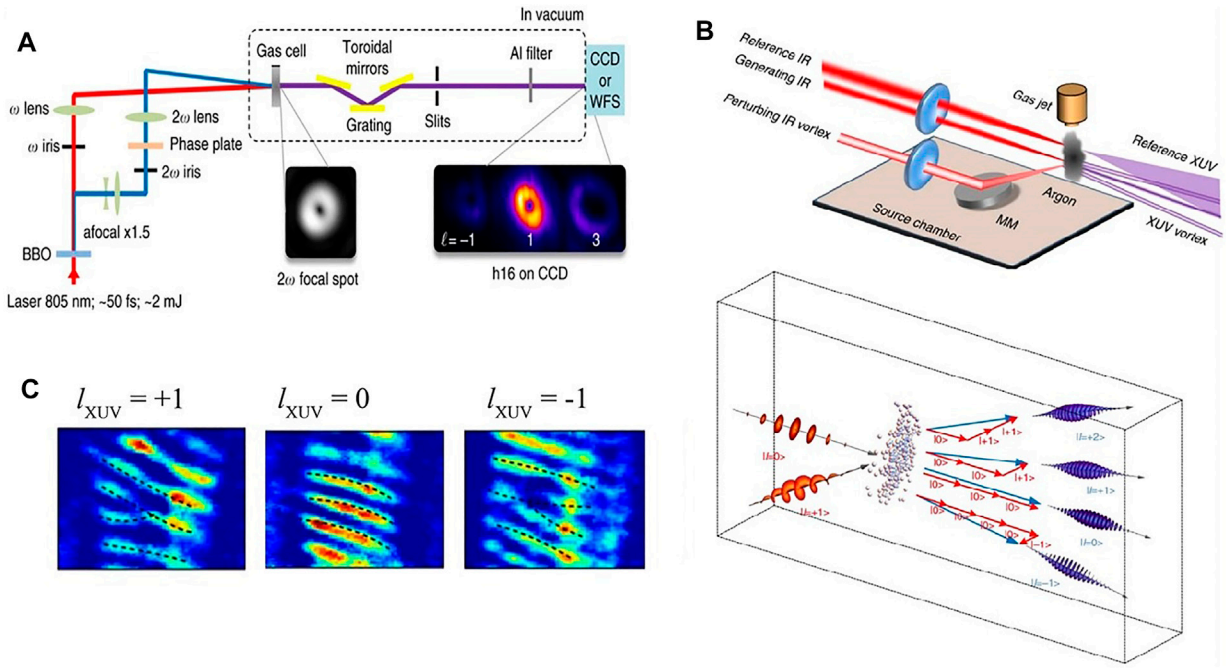

FIGURE 5 | (A) HHG for XUV with tunable OAM [113] **(B)** HHG for extreme based on the Argon gas jet [114] **(C)** interferogram of **(B)** with a plane-wave as reference beam, recorded in the CCD camera.

fork pattern and constructed them in the $LiNbO_3$ crystal and produced a vortex beam with the OAM range from l = -3 to l =3.

In 2012, Ding et al. [107] experimentally displayed an infrared light with the OAM being up converted into visible light through four-wave-mixing *via* a ladder-type configuration in ^{85}Rb atoms in a vapor cell. Two pump beams were imprinted with the OAM by a computer-generated hologram. Regardless of the different topological charges the two pump beam carries, all results remain identical apart from the conversion efficiency and the temperature of the vapor cell. In 2017, Zhao et al. [108] observed the frequency doubling effect of the topological charge with a composite vortex beam. A 2-f system was built while a laser at the wavelength 1,064 nm after alignment and magnification were separated by a beam split, then to form a composite vortex beam after passing through a vortex phase plate. Two beams were then converged to the KTP crystal for frequency doubling. A filter ($T_{532nm} > 85\%$, $T_{1064nm} < 1\%$) was used to filter out the fundamental light. They observed that for an input composite vortex, the frequency-doubled beam was also composite (coherent superposition of the pure LG mode). Tung et al. [109] also reported a frequency-doubled vortex beam in 2018, which they designated as the bottle beam. The experimental configuration is in **Figure 3D**. The KTP crystal was placed inside the fundamental cavity, with some small distance d from the output coupler. As d varied from 1.8 to 3 mm, the recorded transverse pattern changes drastically. The green bottle beam was generated with a narrow 3-D dark core. This suggested that shortening the distance between the SHG-crystal and the output coupler can be a possible route toward mode tunability. It was interesting to observe that while the wave remained perfectly a central-dark spatial profile in the near field, for the far field, it propagated; however, it resembles a circular beam with a shining spot in the middle. Such a beam was said to have a unique advantage when both the doughnut shaped beam and the ordinary Gaussian beam are required because they can be tailored, respectively.

In 2021, Gui et al. [110] demonstrated the SHG of a beam with spatiotemporal orbital angular momentum (ST-OAM). ST-OAM is a form of structured electromagnetic field recently identified. It features a space-time spiral phase structure and a transverse OAM which were perpendicular to the energy-density flow. They observed the modification of the OAM pulse by complex spatiotemporal astigmatism, in conjunction with multiple phase singularities. A 400-nm second-harmonic and an ST-OAM pulse with undetermined charge l were obtained. A temporal OAM beam can have a short pulse width and high peak power. This is useful in super-resolution imaging. The Airy beam could contain vortex characteristics. Li et al. [111] observed the Airy vortex beam when the fundamental wave modulated by SLM interacted with nonlinear media. SHG of the vortex Airy beam was observed. In 2021, Liu et al. [112] manages to control vortex characteristics in the Airy beam. Loading of OAM is controlled electrically, which showed great potential in information processing.

In 2017, Gauther et al. [113] studied HHG for producing the XUV beam with tunable OAM. Their configuration is shown in **Figure 5A**, where a femtosecond pump beam at the wavelength of 805 nm is frequency-doubled by a BBO crystal; then, they were separated, and the 2ω-beam was introduced a topological charge by a spiral phase plate. Both the fundamental ω-beam and the

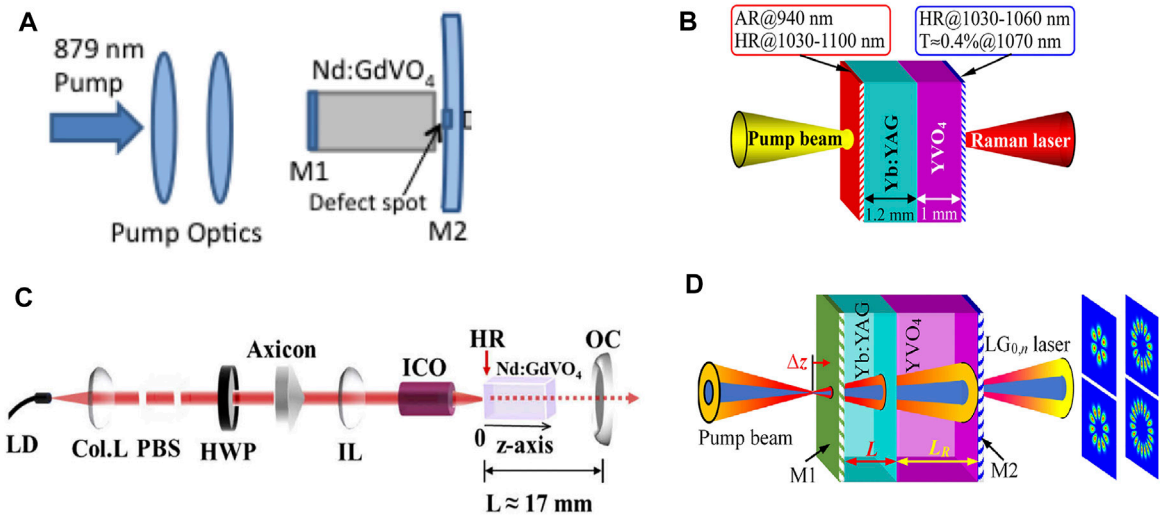

FIGURE 6 | (A) Nd:$GdVO_4$ self-Raman vortex laser with defect spot mirror for first Stokes output [60] **(B)** Yb:YAG/YVO_4 microchip Raman vortex laser with off-axis pumping for the frequency-comb output [122] **(C)** Nd:$GdVO_4$ self-Raman vortex laser with annular pumping design by an axicon for multi-Stokes output [123] **(D)** microchip Raman vortex laser based on annular pumping for $LG_{0,n}$ petal-mode generation [124].

2ω-beam were converged in the same gas cell for HHG. They have demonstrated that for HHG of order q, it follows $q = n_1 + 2n_2$, while n_1, n_2 are the number of photons absorbed from the ω and 2ω beams. The topological charge of the HHG-output follows $l = n_1 l_\omega + n_2 l_{2\omega}$. In 2017, Kong et al. [114] also reported the HHG experiment based on the gas jet. Two arms of beam at wavelength 800 nm with different topological charges $(l_1 = 0, l_2 = 1)$ were reported. Extreme ultraviolet with order $l = \pm 1, 0$ was produced. Details are illustrated in **Figure 5B** and **Figure 5C**. In 2020, Fan et al. [115] reported the generation of the polarized vortex beam in the waveband of extreme ultraviolet based on HHG of a gas-jet. HHG is an effective and efficient approach for achieving the generation of EUV, and it is also a promising scheme to achieve a tunable high OAM beam since the resultant topological charge of the HHG wave was $l_{nth} = n \cdot l_f$, where l_f is the topological charge of the fundamental wave, and n is the order.

Overall, we have summarized the important results concerning SHG, SFG, and HHG. First, extensive works have explicitly confirmed that during such process, the change of the topological charge abided by the laws of conservation. Second, the walk-off on frequency conversion with critical phase-matching leads to the collapse of vortex field distribution; therefore, the noncritical phase matching and quasi-phase matching crystals are excellent candidates for SHG/SFG of the vortex beam. Finally, SHG, THG, and HHG are efficient to obtain visible and ultraviolet beam with the OAM. For n-order high harmonic generation, if the OAM of the fundamental beam is 1, the HHG beam should naturally have $n \cdot l\hbar$ OAM.

Stimulated Raman Scattering

Stimulated Raman Scattering, or SRS in short, is a third-order nonlinear effect. Many materials with Raman configuration were used for Stokes output, such as vanadates, tungstates, molybdates, and KTP family crystals [116–121]. Self-Raman experiments are most popular because it can ensure the compactness and attribute to versatile wavelength operation.

Vanadate laser crystals have a unique structure that enables the relatively low threshold output. In 2014, Lee et al. [60] used Nd:$GdVO_4$ self-Raman to achieve the first Stokes line at 1,173 nm with the experimental configuration shown in **Figure 6A**, corresponding to the Raman shift of 882 cm^{-1}. At the incident pump power of 6.8 W, the fundamental and the Stokes output were both produced with the output power at 400 and 380 mW, respectively. The $LG_{0,1}$ mode was observed, and the transfer of its topological charge to the Stokes field was also recorded. The vortex output was attributed to the annular gain profile and the Fresnel diffraction loss by the defect spot mirror. To improve the compactness, a microchip laser might be the choice. In 2015, Lee et al. reported a YVO_4/Nd:YVO_4 self-Raman laser with off-axis pumping for the high-order Hermite–Gaussian beam generation. The HG mode order of the first Stokes wave can be up to $TEM_{28,0}$. The output power was higher than 1.0 W from $TEM_{0,0}$ to $TEM_{3,0}$ at a pump power of 18.6 W [121]. In 2018, Dong et al. [122] designed a Raman microchip laser with the combination of the Yb:YAG and YVO_4 crystals; the overall length was 2.2 mm. The corresponding design is shown in **Figure 6B**. The optical vortices realized by tilting the laser crystal with off-axis pumping geometry. Different frequency combs were obtained as the pump power increased, and it remained perfectly a doughnut-shaped intensity profile. The vortex characteristics were identified by using an interferogram. In 2020, Ma et al. [123] came up with the annular pumping scheme by an axicon. **Figure 6C** is a portrait of their experimental design. Nd: $GdVO_4$ was used to serve both as the laser medium and the Raman medium. The annular beam output carried zero OAM for both the first Stokes of 1,108 nm and 1,173 nm were achieved. **Figure 7** shows the spatial intensity profiles of the fundamental and Stokes waves, as well as the interferogram of the Stokes waves. Compared between the spatial

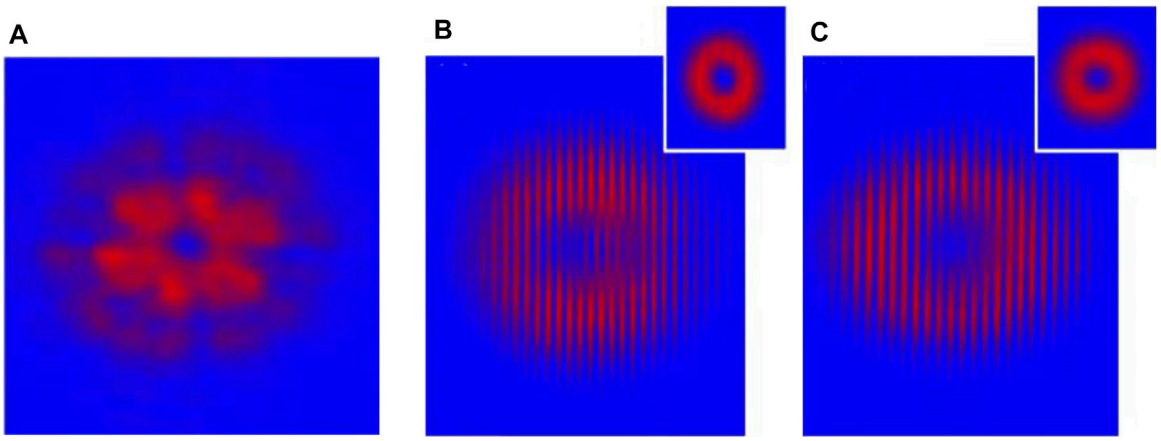

FIGURE 7 | (A) Spatial profile of the fundamental beam; **(B)** spatial profile (top right) and the interference fringes of the 1,108 nm Stokes output; **(C)** spatial profile (top right) and the interference fringes of the 1,173 nm Stokes output [123].

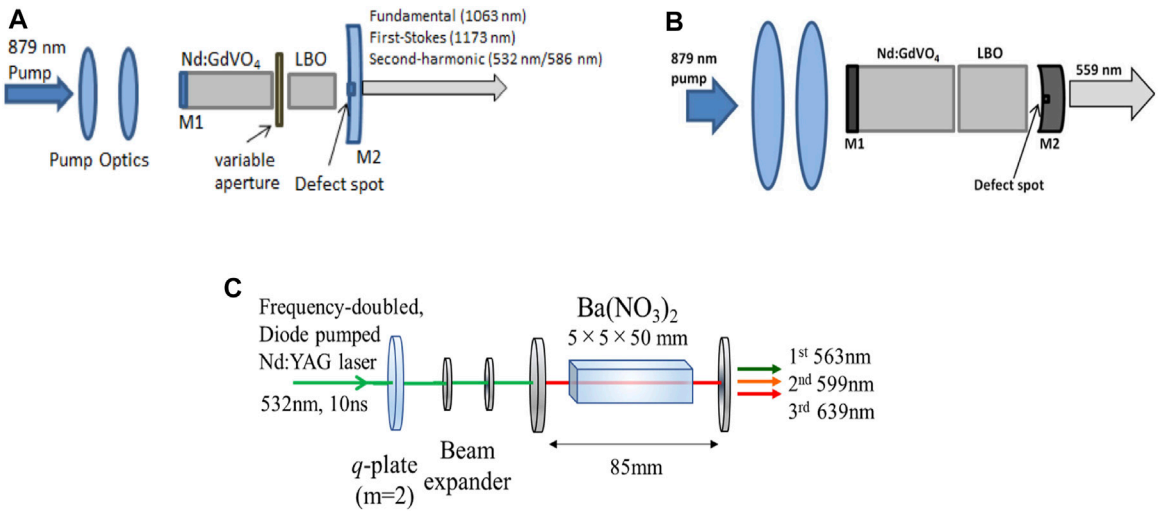

FIGURE 8 | (A) SHG of Nd:$GdVO_4$ self-Raman for 532/586 nm vortex output [125] **(B)** SFG of Nd:$GdVO_4$ self-Raman for 559 nm vortex output [126] **(C)** cascaded $Ba(NO_3)_2$ Raman for 563/599/639 nm vortex output with extra-cavity configuration [129].

intensity profiles of the fundamental and Stokes waves, obvious beam-cleaning phenomena could be observed. More recent, Miao et al. reported the petal-like Raman laser in a Yb:YAG/YVO_4 microchip laser with annular pumped with the setup shown in **Figure 6D**. The $LG_{0,n}$ mode petal-like lasers with order of n tuning from 3 to 11 had been obtained. [124].

The aforementioned self-Raman lasers had expanded the optical vortices in the near-infrared waveband. If the Raman combined with SHG and SFG, the optical vortices in the visible waveband also could be expanded. In 2014, Lee et al. [125] also combined this vortex Raman laser design with the LBO crystal for the SHG of both the fundamental and the first Stokes waves to produce the 532/586 nm laser. The experimental configuration is depicted in **Figure 8A**. **Figure 9** shows the fork interferogram of the first Stokes wave and its SHG with yellow light. The OAM has been transferred to Stokes field in the Raman process and then doubled in the SHG process. In 2016, the SFG of the fundamental and the first Stokes wave for 559 nm vortex laser generation was also reported by his team [126] with the experimental configuration shown in **Figure 8B**. The jointing of self-Raman effects and an LBO crystal, along with the defect spot mirror cavity design, has enabled the multi-wavelength operation. If the wavelength selection mechanism based on vanadate crystals be introduced [127, 128], it will put forward the application of a selective multi-wavelength vortex laser. It is natural to include our future work in the areas of vortex Raman operation, particularly to introduce vortex characteristics into the visible band laser.

During the Raman process, it is evident to see that the transfer of a topological process occurs as a result of the superposition of fundamental modes, $HG_{1,0}$, $HG_{0,1}$. It is modeled by Lee et al. [60]

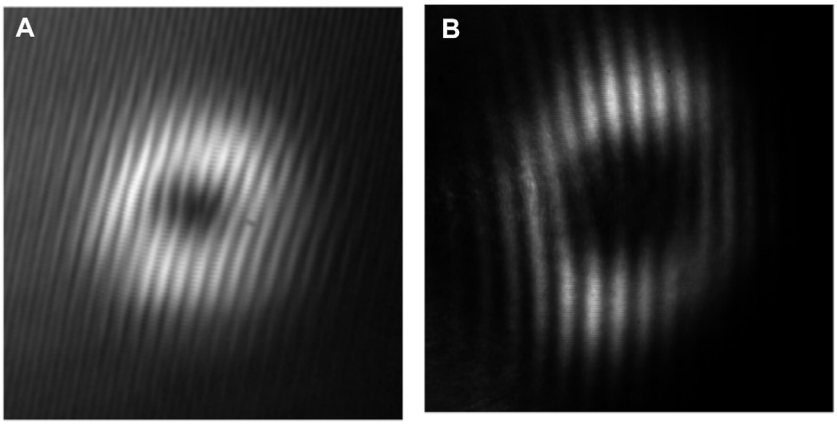

FIGURE 9 | Forked interference fringes of **(A)** 1,173 nm Stokes fields and **(B)** SHG of the first Stokes (1,173 nm) for 586-nm yellow beam [125].

TABLE 1 | Performance of the selected experiment for Raman vortex generation.

Vortex generation method	Pump wavelength (nm)	Laser/Raman media (SHG/SFG crystal)	Output beam profile	Wavelength Output power (pump power)	Year [Ref]
Reflection mirror with defect spots	879	Nd:$GdVO_4$	$LG_{0,1}$	1,173 nm 380 mW (6.8 W)	2013 [60]
Off-axis pumping	808	Nd:YVO_4/YVO_4	HG, $TEM_{0,0}$-$TEM_{28,0}$	1,176 nm >1 W (18.6 W) for $TEM_{0,0}$-$TEM_{3,0}$	2015 [121]
Off-axis pumping	940	Yb:YAG/YVO_4	Single $LG_{1,0}$ two-vortex array four-vortex array	1,072.49–1,080.13 nm 1.16 W (6.28 W)	2018 [122]
Annular pumping design by fiber coupling	940	Yb:YAG/YVO_4	$LG_{0,3}$-$LG_{0,11}$ petal like modes	1,075.4–1,088.7 nm 126 mW (8.3 W)	2022 [124]
Annular pumping design by an axicon	879	Nd:$GdVO_4$	Annular profile carried zero OAM	1,108 nm 49.8 mW (5.6 W) 1,173 nm 133.4 mW (5.6 W)	2020 [123]
$LG_{0,2}$ green laser pumping	532	$Ba(NO_3)_2$	$LG_{0,2}$	1st:563 nm 49 mW (360 mW) 2nd: 599 nm 16 mW (360 mW) 3rd: 639 nm 15 mW (360 mW)	2021 [129]
Reflection mirror with defect spots	879	Nd:$GdVO_4$ (NCPM-LBO)	$LG_{0,1}$	586 nm 727 mW (17.7 W)	2014 [125]
Reflection mirror with defect spots	879	Nd:$GdVO_4$ (NCPM-LBO)	Annular profile carried zero or two OAM	559 nm >800 mW (>20 W)	2016 [126]

They also observed an interesting phenomenal for the SFG field: it possesses a +2 or 0 topological charge while an annular profile is retained in the near field but only to degrade into a bright spot in the far field. The SFG field was different in the near and far fields. They explained this because the SFG field was not resonated by the laser cavity and not an eigenmode of the resonator.

In addition to expanding visible optical vortices through SHG of the Raman laser, the cascade Raman excited by the 532 nm laser also had been reported to fill the gap in the visible waveband of optical vortices. In 2021, Omatsu et al. [129] realized the cascaded Raman output with a 5 mm × 5 mm×50 mm $Ba(NO_3)_2$ (Raman shift 1,046 cm-1). A 10 ns green pulse at wavelength 532 nm served as the pump beam. A topological charge of 2 was introduced to the pump *via* a q-plate. The design is shown in **Figure 8C**. Wavelengths of first, second, and third Stokes at 563 nm, 599 nm, and 639 nm, respectively, had been achieved.

Table 1 lists performance data of aforementioned experiments for Raman vortex generation. According to the research progress of the Raman vortex laser, intracavity Raman is popular and has been widely reported. Compact configuration can be easily achieved as the fundamental laser and the Raman output shared the same cavity. It is also concluded as follows: first, the topological charge used to transfer to the Stokes waves in the Raman process according to the published work. Second, the

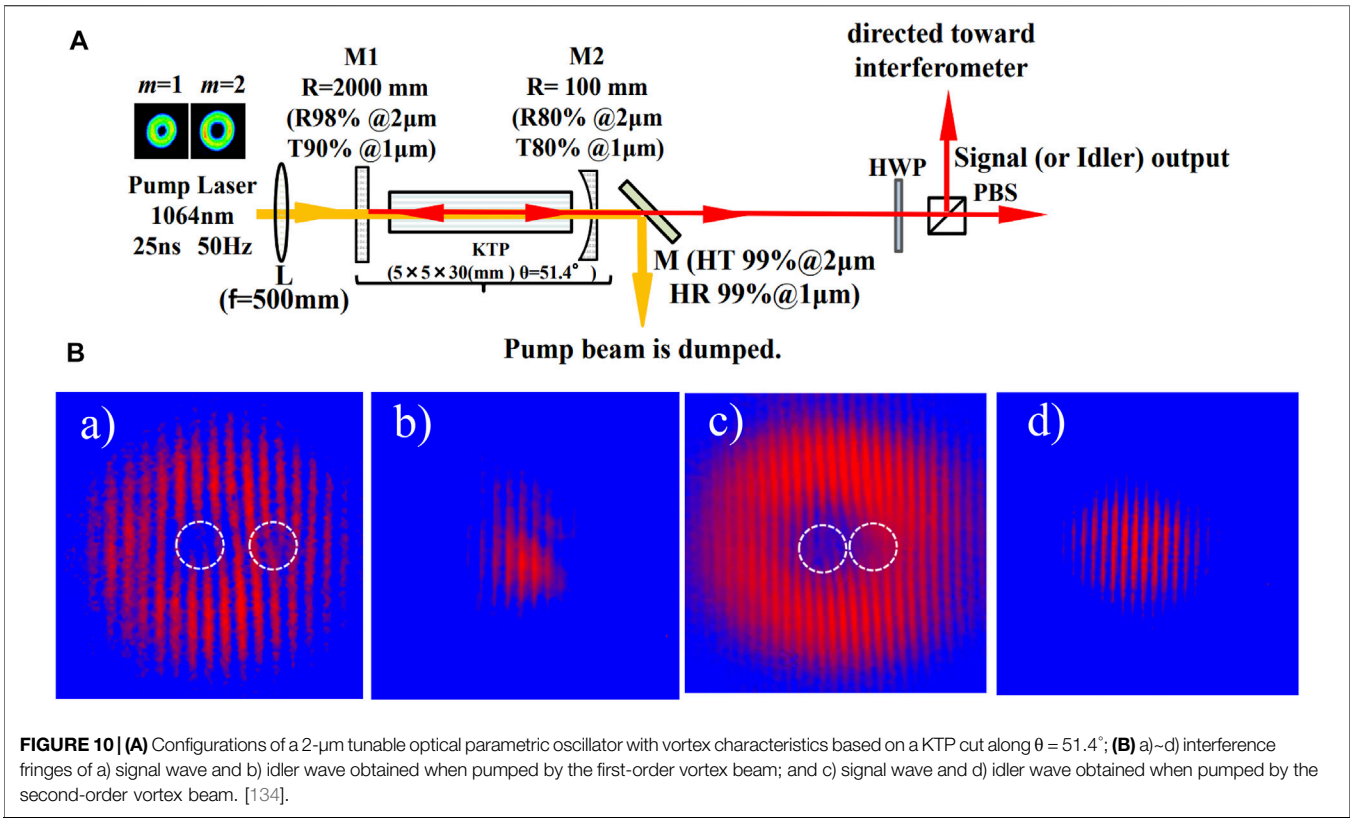

FIGURE 10 | (A) Configurations of a 2-μm tunable optical parametric oscillator with vortex characteristics based on a KTP cut along θ = 51.4°; **(B)** a)~d) interference fringes of a) signal wave and b) idler wave obtained when pumped by the first-order vortex beam; and c) signal wave and d) idler wave obtained when pumped by the second-order vortex beam. [134].

Raman vortex laser was ideal to maintain a better beam quality than the fundamental laser, due to the Raman beam cleanup effect. Third, stimulated Raman scattering and its combination with second-order nonlinear optical frequency conversion can expand the wavelength of vortex light in infrared and visible bands.

Optical Parametric Oscillator

Optical parametric oscillators, or OPO in short, are a useful nonlinear technique known for the application of tunable and mid-infrared laser generation [130–132]. For a given pump frequency ω_p, a signal frequency ω_s and an idler frequency ω_i were produced. It should satisfy the phase-matching condition—the conservation of linear momentum ($n_p\omega_p = n_s\omega_s + n_i\omega_i$) and the conservation of energy ($\omega_p = \omega_s + \omega_i$). If the pump is a vortex beam, conservation of angular momentum ($l_p = l_s + l_i$) also should be satisfied. Many reports have discussed the extension of the wavelength-tunable range in the OPO laser; however, little is known for tuning OAM-related properties. The transfer of the topological charge is also a problem worth looking into.

One interesting property to be investigated during an OPO process of a vortex beam is the possible mechanism for the topological charges to be transferred from the pump beam to the signal beam. In 1999, Maleev et al. [133] reported the violation of the conservation law for topological charge transfer in parametric down conversion. No further reports have followed that conclusion. Usually speaking, a LG_{0l} mode excited OPO will produce a signal wave and an idler wave, both with the topological order split in half to be $l/2$. However, this fact was first proved unsolid by Yusufu et al. [134] in their study published in 2012 where a 30 mm KTP crystal with $\theta = 51.4^{\circ}$ was employed as the nonlinear crystal for the OPO. **Figure 10A** is their experimental configuration. According to the self-interference fringes of both signal and idler waves in **Figure 10B**, the topological order of the pump beam was transferred to the signal wave solely without sharing its value with the resultant idler wave, and the idler wave was a Gaussian profile without any phase singularity. A tunable vortex parametric laser source with a wavelength-tunable range from 1.953 to 2.158 μm has been achieved. They also give the walk-off effect a thorough account as to their influence for vortex optical parametric source. In fact, they showed that it is indeed the plano-concave cavity and the walk-off effect that prevented the lasing of the idler wave even in the Gaussian mode; therefore anisotropic transfer of the topological charge was possible. To avoid the walk-off effect of critical phase matching, an efficient OPO vortex source could be obtained by compensating the walk-off effect with two cascaded KTP with experimental configuration, as shown in **Figure 11A** [135]. Without the cascaded crystal, the signal and the idler were respectively limited to 1923–1955 nm and 2,376–2,335 nm. After difference-frequency generation by a ZGP crystal, tunable vortex output at wavelength 6.3–12 μm was achieved.

Apart from compensating the walk-off effect with two cascaded crystals, the quasi-phase matching and non-critical phase matching without walk-off were widely used. For the

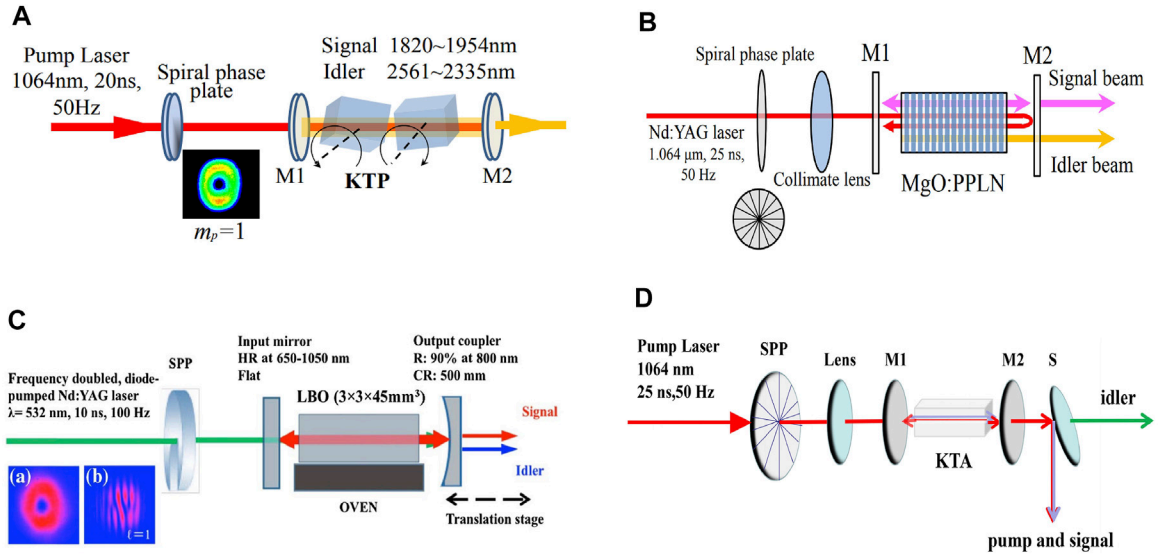

FIGURE 11 | (A) setups of mid-infrared (6.3–12 *μm*) vortex parametric generation with walk-off compensating design based on two KTP [135]; **(B)** configurations of the tunable 3 *μm* optical parametric vortex laser based on MgO: PPLN [136] **(C)** configurations of the tunable vortex beam output with NCPM-LBO [140] **(D)** configurations of the optical parametric oscillator for the vortex output based on KTA with the plane–plane cavity for selective topological transfer [142].

quasi-phase matching, Yusufu et al. [136] reported a tunable vortex laser based on the parametric source with a periodically poled crystal MgO: PPLN. A 1064 nm Nd: YAG laser was chosen as the seed light, and a spiral phase plate was adopted for tailing the pump light into a vortex beam. They obtained the milli-joule-level 3 μm output (2.14 mJ maximum output with a conversion efficiency of 10.2%). They observed the transfer of the topological charge from the pump to the idler. The experimental configuration is shown in **Figure 11B**. In 2019, Sharma et al. [137] reported the vortex mode at order $l = 1$ with doubly resonating the optical parametric oscillator based on MgO-doped periodic poled lithium tantalate. At the green pump beam, the same order and sign were achieved at the frequency tunable across 970–1,174 nm. The vortex dipole is generated by controlling the beam overlap. In 2020, Tong et al. [138] reported the femtosecond vortex beam generated from an OPO based on a MgO:PPLN crystal with a polarization period of 31 μm. The pulse duration was variable from ~400 fs to ~1.1 ps. 1~ sixth-order femtosecond vortex beam were realized after mode converting by cylindrical lens. More recent, in 2022, they also demonstrated the tunable high-order optical vortices with topological charge transfer to the non-resonant idler beam using a picosecond optical parametric oscillator [139]. The mid-infrared vortex beams of orders $l = 1 - 5$ with tunability across the 2,493–4,035 nm spectral range was achieved.

For the non-critical phase matching, Mamuti et al. [140] reported the superposition of laser modes that carried orbital angular momentum by a parametric process with the use of NCPM-LBO, which is illustrated in **Figure 11C** The tunability of the topological charge was realized mainly by two mechanisms: 1) the shortening of the laser cavity provided a change in mode spatial overlapping, which caused the lasing conditions favorable for certain modes. 2) the non-critical phase matching not only avoided large the walk-off effect, but it also provided the favorable mode-overlapping condition; therefore, the tunable topological charges were realized at different frequencies. Depicted in **Figure 12A** is the spatial profile and the interference fringes of the signal and the idler wave from a compact cavity. The selective OAM transferred to either the signal or the idler was also realized simply by shortening the extended cavity. Since the mode radius at the plano-concave cavity changes while the cavity length extended, the spatial overlapping thus changes as well. This combined with the NCPM-LBO for tunable frequencies create a condition for separating the signal wave from the idler wave. When the cavity length was suited for the lasing condition of the signal or the idler wave, the topological charge will be transferred to it simultaneously. From Figure 11A a~f) is the spatial profile, and the corresponding interference fringes of the signal wave at the lasing signal frequency of 930 nm; g)~l) are the spatial profile and the corresponding interference fringes of the idler wave at frequency 1,243 nm. The tunable OAM ranging from $l = -2$ to $l = 3$ was reported. In 2019, they reported wheel-mode generation (seen **Figure 12B**) using the same configuration as in **Figure 11C**. They suggested the pump source with a short coherence time for producing larger OAM-carrying beam [141]. $l_s = 2 \sim 4$ was realized. The wheel-shaped modes are actually the coherent superposition of multiple OAM states. In 2021, Ababaike et al. [142] reported the milli-joule level vortex optical parametric source, with an NCPM-KTA crystal and a singly resonant linear plane-parallel cavity. The experimental configuration is shown in **Figure 11D**. In this report, selective topological transfer to the signal or to the idler output was achieved by changing the output coupler. In the low-Q cavity with partial reflective coated for the signal wave, the OAM was transferred to the signal (1.535 μm), while in the high-Q cavity with high reflective coated for the signal wave, it was manifested as the 3.468 *μm*

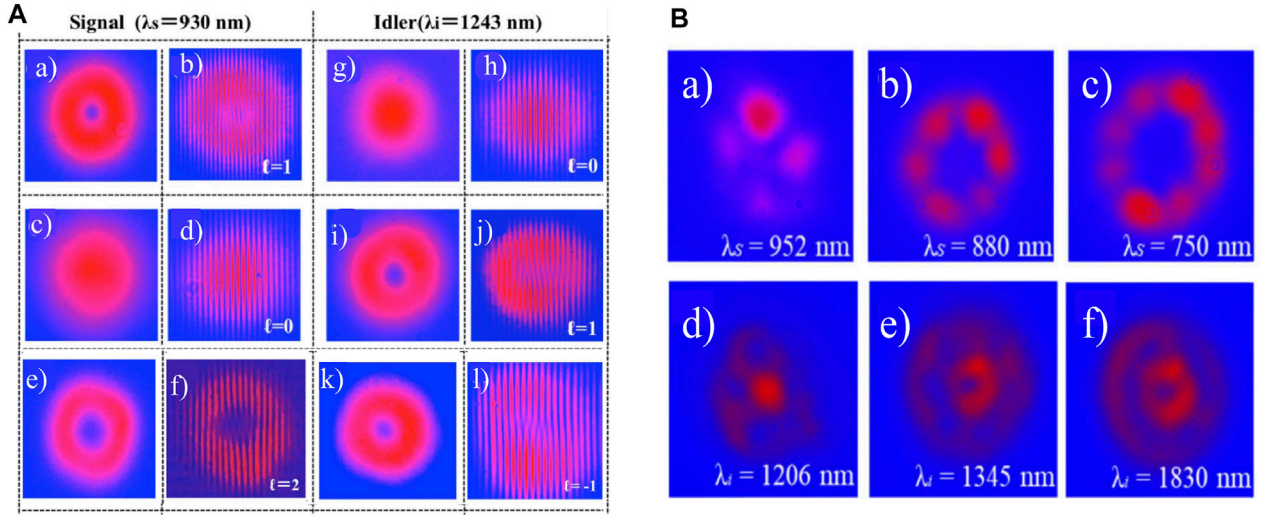

FIGURE 12 | (A) a), c), and e) (the first row) are the spatial profiles of the signal wave with the topological charge to be *l* = 1, 0, 2, respectively; b). d). and f). are the corresponding forked interference fringes; g). i). and k). are the spatial profiles of the idler wave, corresponding to topological charge of l = 0, 1, and −1; h), j), and l) is the corresponding interference fringes [140]; **(B)** a)~b) are the flower modes of the signal wave in the range 745–955 nm, and d)~f) is the wheel-shaped idle wave with the topological charge *l* = 0 & 4, −1 &5, −2&6 [141].

idler output. This OAM switching effect between the idler and the signal wave could be explained with intracavity photon lifetime. Moreover, noncritical phase-matching KTA is also a potential candidate for special wavelength vortex laser generation; based on cascaded frequency conversion [143–145], the cascaded OPO could fill the wavelength gap in the mid-infrared band.

According to the above results, all the reported OPO vortex lasers were extra-cavity pumped. Compensating the walk-off effect with two cascaded crystals, quasi-phase matching crystals and non-critical phase-matching crystals were used to avoid the walk-off effect. More importantly is the selective transfer of the topological charge and the tunability of OAM and wavelength, which have been reported. OPO has been used for mid-infrared widely tunable laser generation. The high-order vortex beam and anisotropic transfer of the topological charge to signal and idler waves were possible in OPO with a reasonable design.

SUMMARY AND OUTLOOK

To summarize, we presented introduction to the research on frequency conversion techniques for the optical vortices, such as sum frequency generation, scatted Raman scattering, and optical parametric oscillation for the expanding of wavelength versatility from the XUV region to the middle-infrared region. Some of those methods were found to be privy to real applications, such as the applications in free space communication, optical machining, and super-resolution imaging. Some important issues have reviewed including the topological transfer during nonlinear frequency conversion. During the SHG process, OAM is doubled. As for the high-order harmonics, if n is the order, l is the topological charge of the fundamental wave; then, the HHG wave should have a topological charge of $n \cdot l$. For sum-frequency generation, it obeys: $l_{\omega_1} + l_{\omega_2} = l_{\omega_3}$. For the Raman process, transfer of the topological charge from the fundamental wave to the Stokes fields have been reported by many references, and due to the Raman bean cleanup effect, [146] it remains excellently a good beam quality. For a singly parametric oscillator, more importantly is the selectively topological charge transfer and the tunability of the OAM and wavelength, which have been reported. Due to problems such as walk-off effects, some quasi-phasing matching materials and non-critical phase matching were also developed, i.e., photonic crystals, periodic niobate lithium, optical superlattices, etc. These materials have enabled the SHG, THG, HHG, and OPO of vortex beams, which greatly increase the wavelength versatility.

Furthermore, the development of the optical vortex, with particular respect to the tunability of its handedness and selective transfer of its topological charges, has made many applications possible. Although there have been sufficient studies on both the generation of optical vortices and the expanding of the tunable wavelength *via* techniques of nonlinear optics, most of them were driving by an extra-cavity vortex source. Intra-cavity direct generation approaching has not yet been able to produce an optical beam with sufficient power to surpass the yield. Further research should focus on pulse-sharpening *via* Q-switching or mode-locking [147]. An ultra-short optical vortex will prove more useful, in combination with nonlinear frequency conversion. The compactness needs to be improved as well. Future attention might be given to the combination of both intracavity optical vortex generation and the nonlinear frequency expansion for the efficient generation of tunable

optical vortices in the wavelength, OAM value, and the helicities. The diffractive method for the efficient means of tailoring the optical field should also be considered and developed with an improved accuracy.

The purpose of this yet comprehensive review is to provide some clarity concerning the development of optical vortices and the corresponding frequency conversion techniques and the involved OAM transfer dynamics. We have summarized some of those key components and important results. Further research both computational and experimental should be conducted to achieve selective frequency-mixing, selective topological charge transfer, or the tunability of OAM-related properties.

AUTHOR CONTRIBUTIONS

JL, YD, and HZ prepared the draft. All authors contributed to the discussion and revision of the manuscript. HZ was responsible for the manuscript.

FUNDING

This study was supported by the National Natural Science Foundation of China (62075167 and 61875199) and the Wenzhou Basic Scientific Research Project (G2020013).

REFERENCES

1. Andrews DL, Babiker M. The Angular Momentum of Light. [M]. *Cambridge* (2005) 95:053903.
2. Coullet P, Gil L, Lega J. Defect-mediated Turbulence. *Phys Rev Lett* (1989) 62: 1619–22. doi:10.1103/physrevlett.62.1619
3. Allen L, Beijersbergen MW, Spreeuw RJC, Woerdman JP. Orbital Angular Momentum of Light and the Transformation of Laguerre-Gaussian Laser Modes. *Phys Rev A* (1992) 45:8185–9. doi:10.1103/physreva.45.8185
4. He H, Friese MEJ, Heckenberg NR, Rubinsztein-Dunlop H. Direct Observation of Transfer of Angular Momentum to Absorptive Particles from a Laser Beam with a Phase Singularity. *Phys Rev Lett* (1995) 75(5): 826–9. doi:10.1103/physrevlett.75.826
5. Sinclair G, Leach J, Jordan P, Gibson G, Yao E, Laczik ZJ, et al. Interactive Application in Holographic Optical Tweezers of a Multi-Plane Gerchberg-Saxton Algorithm for Three-Dimensional Light Shaping. *Opt Express* (2004) 12:1665–70. doi:10.1364/OPEX.12.001665
6. Zhao Y, Shapiro D, Mcgloin D, Chiu DT, Marchesini S. Direct Observation of the Transfer of Orbital Angular Momentum to Metal Particles from a Focused Circularly Polarized Gaussian Beam. *Opt Express* (2009) 17: 23316–22. doi:10.1364/OE.17.023316
7. Mair A, Vaziri A, Weihs G, Zeilinger A. Entanglement of the Orbital Angular Momentum States of Photons. *Nature* (2001) 412(6844):313–6. doi:10.1038/35085529
8. Barreiro JT, Wei T-C, Kwiat PG. Beating the Channel Capacity Limit for Linear Photonic Superdense Coding. *Nat Phys* (2008) 4:282–6. doi:10.1038/nphys919
9. Fickler R, Campbell G, Buchler B, Lam PK, Zeilinger A. Quantum Entanglement of Angular Momentum States with Quantum Numbers up to 10,010. *Proc Natl Acad Sci USA* (2016) 113(48):13642–7. doi:10.1073/pnas.1616889113
10. Willner AE, Huang H, Yan Y, Ren Y, Ahmed N, Xie G, et al. Optical Communications Using Orbital Angular Momentum Beams. *Adv Opt Photon* (2015) 7:66–106. doi:10.1364/AOP.7.000066
11. Yao AM, Padgett MJ. Orbital Angular Momentum: Origins, Behavior and Applications. *Adv Opt Photon* (2011) 3:161. doi:10.1364/aop.3.000161
12. Harwit M. Photon Orbital Angular Momentum in Astrophysics. *ApJ* (2003) 597(2):1266–70. doi:10.1086/378623
13. Tamburini F, Thidé B, Molina-Terriza G, Anzolin G. Twisting of Light Around Rotating Black Holes. *Nat Phys* (2011) 7:195–7. doi:10.1038/nphys1907
14. Zhang W, Gao J, Zhang D, He Y, Xu T, Fickler R, et al. Free-space Remote Sensing of Rotation at the Photon-Counting Level. *Phys Rev Appl* (2018) 10: 044014. doi:10.1103/physrevapplied.10.044014
15. Qiu S, Liu T, Ren Y, Li Z, Wang C, Shao Q. Detection of Spinning Objects at Oblique Light Incidence Using the Optical Rotational Doppler Effect. *Opt Express* (2019) 27:24781–92. doi:10.1364/OE.27.024781
16. Emile O, Emile J, Brousseau C. Rotational Doppler Shift upon Reflection from a Right Angle Prism. *Appl Phys Lett* (2020) 116(22):221102. doi:10.1063/5.0009396
17. Qin H, Zhao W, Zhao W, Zhang C, Liu Y, Wang G, et al. Evaluation of Saturation Intensity Based on the FWHM of CW Stimulated Emission Depletion Microscopy. *Optik* (2018) 166:219–26. doi:10.1016/j.ijleo.2018.04.036
18. Liu X, Qiao S, Ma Y. Highly Sensitive Methane Detection Based on Light-Induced Thermoelastic Spectroscopy with a 2.33 μm Diode Laser and Adaptive Savitzky-Golay Filtering. *Opt Express* (2022) 30(2):1304–13. doi:10.1364/OE.446294
19. Ma Y, Hong Y, Qiao S, Lang Z, Liu X. H-shaped Acoustic Micro-resonator-based Quartz-Enhanced Photoacoustic Spectroscopy. *Opt Lett* (2022) 47(3): 601–4. doi:10.1364/OL.449822
20. Zhuang YY, Zhang YJ, Zhu HY. Enhancing Near-Field Photolithography by Surface Plasmon Polaritons Excited from Negative-Refractive-index Nanofilms. *J Russ Laser Res* (2011) 32:120–4. doi:10.1007/s10946-011-9196-0
21. Fang C, Zhang Y, Zhu H. Optimizing the Optical Field Distribution of Near-Field SIL Optical Storage System Using Five-Zone Binary Phase Filters. *Opt Commun* (2012) 285:3042–5. doi:10.1016/j.optcom.2012.02.070
22. Ma Y, Hu Y, Qiao S, Lang Z, Liu X, He Y, et al. Quartz Tuning forks Resonance Frequency Matching for Laser Spectroscopy Sensing. *Photoacoustics* (2022) 25:100329. doi:10.1016/j.pacs.2022.100329
23. Liu X, Ma Y. Sensitive Carbon Monoxide Detection Based on Light-Induced Thermoelastic Spectroscopy with a Fiber-Coupled Multipass Cell [Invited]. *Chin Opt Lett* (2022) 20:031201. doi:10.3788/COL202220.031201
24. Moneron G, Medda R, Hein B, Giske A, Westphal V, Hell SW. Fast STED Microscopy with Continuous Wave Fiber Lasers. *Opt Express* (2010) 18: 1302–9. doi:10.1364/OE.18.001302
25. Chen YF, Hsieh MX, Ke HT, Yu YT, Liang HC, Huang KF. Quantum Entanglement by a Beam Splitter Analogous to Laser Mode Transformation by a Cylindrical Lens. *Opt Lett* (2021) 46:5129–32. doi:10.1364/OL.439322
26. Chen Y, Wang J, Wang C, Zhang S, Cao M, Franke-Arnold S, et al. Phase Gradient protection of Stored Spatially Multimode Perfect Optical Vortex Beams in a Diffused Rubidium Vapor. *Opt Express* (2021) 29:31582–93. doi:10.1364/OE.439716
27. Asadpour SH, Kirova T, Qian J, Hamedi HR, Juzeliūnas G, Paspalakis E. Azimuthal Modulation of Electromagnetically Induced Grating Using Structured Light. *Sci Rep* (2021) 11:20721. doi:10.1038/s41598-021-00141-9
28. Sun Z, Xu B, Wu B, Wang X, Ying H. High Efficiency Focusing and Vortex Generator Based on Polarization-Insensitive Gallium Nitride Metasurface. *Nanomaterials* (2021) 11:2638. doi:10.3390/nano11102638
29. Hickmann JM, Fonseca EJS, Soares WC, Chávez-Cerda S. Unveiling a Truncated Optical Lattice Associated with a Triangular Aperture Using Light's Orbital Angular Momentum. *Phys Rev Lett* (2011) 105:053904. doi:10.1103/PhysRevLett.105.053904
30. de Araujo LEE, Anderson ME. Measuring Vortex Charge with a Triangular Aperture. *Opt Lett* (2011) 36:787–9. doi:10.1364/OL.36.000787
31. Ostrovsky AS, Rickenstorff-Parrao C, Arrizón V. Generation of the "perfect" Optical Vortex Using a Liquid-crystal Spatial Light Modulator. *Opt Lett* (2013) 38:534–6. doi:10.1364/OL.38.000534
32. Heckenberg NR, Mcduff R, Smith CP, White AG. Generation of Optical Phase Singularities by Computer-Generated Holograms. *Opt Lett* (1992) 17:221. doi:10.1364/OL.17.000221

33. Gong L, Ren Y, Liu W, Wang M, Zhong M, Wang Z, et al. Generation of Cylindrically Polarized Vector Vortex Beams with Digital Micromirror Device. *J Appl Phys* (2014) 116:183105. doi:10.1063/1.4901574
34. Arlt J, Dholakia K. Generation of High-Order Bessel Beams by Use of an Axicon. *Opt Commun* (2000) 177:297–301. doi:10.1016/s0030-4018(00)00572-1
35. Endo M. Generation of Doughnut-like Beams by Means of a W-Axicon Resonator with a Movable Axicon Element. *Quan Electron Laser Sci Conf* (2005) 2005:1591–3. doi:10.1109/QELS.2005.1549217
36. Bisson JF, Li J, Ueda K, Senatsky Y. Radially Polarized Ring and Arc Beams of a Neodymium Laser with an Intra-cavity Axicon. *Opt Express* (2006) 14:3304–11. doi:10.1364/OE.14.003304
37. Ma Y, Lee AJ, Pask HM, Miyamoto K, Omatsu T. Direct Generation of 1108 nm and 1173 nm Laguerre-Gaussian Modes from a Self-Raman Nd:GdVO4 Laser. *Opt Express* (2020) 28(16):24095–103. doi:10.1364/OE.400007
38. Kim JW, Mackenzie JI, Hayes JR, Clarkson WA. High Power Er:YAG Laser with Radially-Polarized Laguerre-Gaussian (LG01) Mode Output. *Opt Express* (2011) 19:14526–31. doi:10.1364/OE.19.014526
39. Kim DJ, Kim JW, Clarkson WA. High-power Master-Oscillator Power-Amplifier with Optical Vortex Output. *Appl Phys B* (2014) 117:459–64. doi:10.1007/s00340-014-5855-5
40. Kim DJ, Kim JW. Direct Generation of an Optical Vortex Beam in a Single-Frequency Nd:YVO4 Laser. *Opt Lett* (2015) 40:399–402. doi:10.1364/OL.40.000399
41. Lin D, Daniel JMO, Clarkson WA. Controlling the Handedness of Directly Excited Laguerre-Gaussian Modes in a Solid-State Laser. *Opt Lett* (2014) 39:3903–6. doi:10.1364/OL.39.003903
42. Zhao Y, Liu Q, Zhou W, Shen D. ~1 mJ Pulsed Vortex Laser at 1645 nm with Well-Defined Helicity. *Opt Express* (2016) 24:15596. doi:10.1364/OE.24.015596
43. Liu Q, Zhang B, Qi S, Li Y, Fan X, Zhao Y, et al. Integration of Helicity-Control and Pulse-Modulation for Vortex Laser Based on a Black Phosphorus Plate. *Opt Express* (2016) 24:30031. doi:10.1364/OE.24.030031
44. Liu Q, Zhao Y, Zhou W, Shen D. Vortex Operation in Er:LuYAG crystal Laser at ~1.6 μm. *Opt Mater* (2017) 71:31–4. doi:10.1016/j.optmat.2016.06.034
45. Ding M, Chen Y, Wang J, Yin D, Wang Y, Liu P, et al. 2.7 μm Optical Vortex Beam Directly Generated from an Er:Y2O3 Ceramic Laser. *Opt Lett* (2019) 44(20):4973–6. doi:10.1364/OL.44.004973
46. Chen Y, Ding M, Wang J, Wang L, Liu Q, Zhao Y, et al. High-energy 2 μm Pulsed Vortex Beam Excitation from a Q-Switched Tm:LuYAG Laser. *Opt Lett* (2020) 45(3):722–5. doi:10.1364/ol.384201
47. Lu J, Lin H, Zhang G, Li B, Zhang L, Lin Z, et al. Direct Generation of an Optical Vortex Beam from a Diode-Pumped Yb:MgWO4laser. *Laser Phys Lett* (2017) 14:085807. doi:10.1088/1612-202X/aa7878
48. Li K, Tang K, Lin D, Wang J, Li B, Liao W, et al. Direct Generation of Optical Vortex Beams with Tunable Topological Charges up to 18th Using an Axicon. *Opt Laser Technol* (2021) 143:107339. doi:10.1016/j.optlastec.2021.107339
49. Dong JS, Ma J, Ren YY, Xu G, Kaminskii A. Generation of Ince–Gaussian Beams in Highly Efficient, Nanosecond Cr, Nd: YAG Microchip Lasers. *Laser Phys Lett* (2013) 10(8):085803. doi:10.1088/1612-2011/10/8/085803
50. Lee CY, Chang CC, Cho CY, Tuan PH, Chen YF. Generation of Higher Order Vortex Beams from a YVO4/Nd:YVO4 Self-Raman Laser via off-Axis Pumping with Mode Converter. *IEEE J Select Top Quan Electron.* (2015) 21(1):318–22. doi:10.1109/jstqe.2014.2324754
51. Dong J, Bai S-C, Liu S-H, Ueda K-I, Kaminskii AA. A High Repetition Rate Passively Q-Switched Microchip Laser for Controllable Transverse Laser Modes. *J Opt* (2016) 18:055205. doi:10.1088/2040-8978/18/5/055205
52. Shen Y, Meng Y, Fu X, Gong M. Wavelength-tunable Hermite-Gaussian Modes and an Orbital-Angular-Momentum-Tunable Vortex Beam in a Dual-Off-axis Pumped Yb:CALGO Laser. *Opt Lett* (2018) 43(2):291–4. doi:10.1364/OL.43.000291
53. Huang X, Xu B, Cui S, Xu H, Cai Z, Chen L. Direct Generation of Vortex Laser by Rotating Induced off-Axis Pumping. *IEEE J Select Top Quan Electron.* (2018) 24(5):1601606. doi:10.1109/jstqe.2018.2814789
54. He H-S, Chen Z, Li H-B, Dong J. Low-threshold, Nanosecond, High-Repetition-Rate Vortex Pulses with Controllable Helicity Generated in Cr,Nd:YAG Self-Q-Switched Microchip Laser. *Laser Phys* (2018) 28:055802. doi:10.1088/1555-6611/aaad4c
55. Yuan Y, Tong L, Cai F, Zhang W, Cai Y, Zhao L. Direct Generation of Optical Vortex Arrays by Rotating in an All-Solid-State Yb:CALGO Laser. *Opt Mater Express* (2021) 11(6):1594–602. doi:10.1364/OME.425827
56. Beijersbergen MW, Allen L, van der Veen HELO, Woerdman JP. Astigmatic laser mode converters and transfer of orbital angular momentum. *Opt Commun* (1993) 96(1):123–32. doi:10.1016/0030-4018(93)90535-D
57. Tung JC, Liang HC, Lu TH, Huang KF, Chen YF. Exploring Vortex Structures in Orbital-Angular-Momentum Beams Generated from Planar Geometric Modes with a Mode Converter. *Opt Express* (2016) 24(20):22796–805. doi:10.1364/OE.24.022796
58. Tung JC, Omatsu T, Liang HC, Huang KF, Chen YF. Exploring the Self-Mode Locking and Vortex Structures of Nonplanar Elliptical Modes in Selectively End-Pumped Nd:YVO_4 Lasers: Manifestation of Large Fractional Orbital Angular Momentum. *Opt Express* (2017) 25(9):22769–79. doi:10.1364/OE.25.022769
59. Ito A, Kozawa Y, Sato S. Generation of Hollow Scalar and Vector Beams Using a Spot-Defect Mirror. *J Opt Soc Am A* (2010) 27(9):2072–7. doi:10.1364/JOSAA.27.002072
60. Lee AJ, Omatsu T, Pask HM. Direct Generation of a First-Stokes Vortex Laser Beam from a Self-Raman Laser. *Opt Express* (2013) 21(10):12401–9. doi:10.1364/OE.21.012401
61. Qiao Z, Xie G, Wu Y, Yuan P, Ma J, Qian L, et al. Generating High-Charge Optical Vortices Directly from Laser up to 288th Order. *Laser Photon Rev* (2018) 12(8):1800019. doi:10.1002/lpor.201800019
62. Wang S, Zhao Z, Ito I, Kobayashi Y. Direct Generation of Femtosecond Vortex Beam from a Yb:KYW Oscillator Featuring a Defect-Spot Mirror. *OSA Continuum* (2019) 2(3):523–30. doi:10.1364/OSAC.2.000523
63. Senatsky Y, Bisson J-F, Shelobolin A, Shirakawa A, Ueda K. Circular Modes Selection in Yb:YAG Laser Using an Intracavity Lens with Spherical Aberration. *Laser Phys* (2009) 19(5):911–8. doi:10.1134/S1054660X09050028
64. Thirugnanasambandam MP, Senatsky Y, Ueda K-i. Generation of Radially and Azimuthally Polarized Beams in Yb:YAG Laser with Intra-cavity Lens and Birefringent crystal. *Opt Express* (2011) 19(3):1905. doi:10.1364/OE.19.001905
65. Okida M, Hayashi Y, Omatsu T, Hamazaki J, Morita R. Characterization of 1.06 μm Optical Vortex Laser Based on a Side-Pumped Nd:GdVO4 Bounce Oscillator. *Appl Phys B* (2009) 95(1):69–73. doi:10.1007/s00340-009-3438-7
66. Chard SP, Shardlow PC, Damzen MJ. High-power Non-astigmatic TEM00 and Vortex Mode Generation in a Compact Bounce Laser Design. *Appl Phys B* (2009) 97(2):275–80. doi:10.1007/s00340-009-3642-5
67. Okida M, Huang JY, Chen YF, Omatsu T. Controllable Direction Switching of Vortex Output in a Nd: YVO4 Bounce Laser. In: Conference on Lasers and Electro-Optics Europe and 12th European Quantum Electronics Conference (CLEO EUROPE/EQEC) (2011). p. 1. doi:10.1109/CLEOE.2011.5942477
68. Thirugnanasambandam MP, Senatsky Y, Ueda K-i. Generation of Radially and Azimuthally Polarized Beams in Yb:YAG Laser with Intra-cavity Lens and Birefringent crystal. *Opt Express* (2011) 19(3):1905–14. doi:10.1364/OE.19.001905
69. Wang M, Ma Y, Sheng Q, He X, Liu J, Shi W, et al. Laguerre-Gaussian Beam Generation via Enhanced Intracavity Spherical Aberration. *Opt Express* (2021) 29(17):27783–90. doi:10.1364/oe.436110
70. Omatsu T, Okida M, Lee A, Pask HM. Thermal Lensing in a Diode-End-Pumped Continuous-Wave Self-Raman Nd-Doped GdVO4 Laser. *Appl Phys B* (2012) 108(1):73–9. doi:10.1007/s00340-012-4919-7
71. Bisson J-F, Senatsky Y, Ueda K-I. Generation of Laguerre-Gaussian Modes in Nd:YAG Laser Using Diffractive Optical Pumping. *Laser Phys Lett* (2005) 2(7):327–33. doi:10.1002/lapl.200510008
72. Liu Q, Zhao Y, Ding M, Yao W, Fan X, Shen D. Wavelength- and OAM-Tunable Vortex Laser with a Reflective Volume Bragg Grating. *Opt Express* (2017) 25(19):23312–9. doi:10.1364/OE.25.023312
73. Geberbauer JWT, Kerridge-Johns WR, Damzen MJ. >30 W Vortex LG01 or HG10 Laser Using a Mode Transforming Output Coupler. *Opt Express* (2021) 29(18):29082–94. doi:10.1364/OE.432674
74. Otsuka K, Chu S-C. Generation of Vortex Array Beams from a Thin-Slice Solid-State Laser with Shaped Wide-Aperture Laser-Diode Pumping. *Opt Lett* (2009) 34(1):10–2. doi:10.1364/ol.34.000010

75. Tung JC, Hsieh YH, Omatsu T, Huang KF, Chen YF. Generating Laser Transverse Modes Analogous to Quantum Green's Functions of Two-Dimensional Harmonic Oscillators. *Photon Res* (2017) 5(6):733–9. doi:10.1364/PRJ.5.000733
76. Li N, Xu B, Cui S, Qiu X, Luo Z, Xu H, et al. High-Order Vortex Generation from CW and Passively Q-Switched Pr:YLF Visible Lasers. *IEEE Photon Technol Lett* (2019) 31(17):1457–60. doi:10.1109/lpt.2019.2931907
77. Chen YF, Lan YP, Wang SC. Generation of Laguerre-Gaussian Modes in Fiber-Coupled Laser Diode End-Pumped Lasers. *Appl Phys B* (2001) 72: 167–70. doi:10.1007/s003400000433
78. Naidoo D, Aït-Ameur K, Brunel M, Forbes A. Intra-cavity Generation of Superpositions of Laguerre-Gaussian Beams. *Appl Phys B* (2012) 106:683–90. doi:10.1007/s00340-011-4775-x
79. Zhang W, Wei K, Huang L, Mao D, Jiang B, Gao F, et al. Optical Vortex Generation with Wavelength Tunability Based on an Acoustically-Induced Fiber Grating. *Opt Express* (2016) 24:19278–85. doi:10.1364/oe.24.019278
80. Shen Y, Ren G, Yang Y, Yao S, Xiao S, Jiang Y, et al. Generation of the Tunable Second-Order Optical Vortex Beams in Narrow Linewidth Fiber Laser. *IEEE Photon Technol Lett* (2017) 29(19):1659–62. doi:10.1109/lpt.2017.2742519
81. Liu Q, Zhao Y, Ding M, Yao W, Fan X, Shen D. Wavelength- and OAM-Tunable Vortex Laser with a Reflective Volume Bragg Grating. *Opt Express* (2017) 25:23312–9. doi:10.1364/OE.25.023312
82. Zhao Y, Wang T, Mou C, Yan Z, Liu Y, Wang T. All-Fiber Vortex Laser Generated with Few-Mode Long-Period Gratings. *IEEE Photon Technol Lett* (2018) 30(8):752–5. doi:10.1109/lpt.2018.2815041
83. Yan R, Li M, Li X, Zhao C, Zhou Y, Jiang Y. Vortex Laser Generation and Chirality Control in a LD End Pumped Nd:YVO4 Laser. *Optik* (2021) 236: 166669. doi:10.1016/j.ijleo.2021.166669
84. Tian B, Yu J, Zhang B. A Method for Generating LG0l Vortex Beams with Tunable Topological Charges Based on Tube Lasers. *Opt Commun* (2021) 491:126939. doi:10.1016/j.optcom.2021.126939
85. Liu G, Fu S, Zhang X, Yin H, Li Z, Chen Z. Geometric Control of Vector Vortex Light Beams via a Linear Coupling System. *Opt Express* (2021) 29: 30694–705. doi:10.1364/OE.435152
86. Srinivasa Rao A, Miike T, Miamoto K, Omatsu T. Direct Generation of 523 nm Orbital Poincaré Mode from a Diode-Pumped Pr3+:LiYF4 Laser with an off-axis Optical Needle Pumping Geometry. *Opt Express* (2021) 29:30409–18. doi:10.1364/OE.439491
87. Senatsky Y, Bisson J-F, Li J, Shirakawa A, Thirugnanasambandam M, Ueda K-i. Laguerre-gaussian Modes Selection in Diode-Pumped Solid-State Lasers. *Opt Rev* (2012) 19(4):201–21. doi:10.1007/s10043-012-0032-8
88. Wang X, Nie Z, Liang Y, Wang J, Li T, Jia B. Recent Advances on Optical Vortex Generation. *Nanophotonics* (2018) 7(9):1533–56. doi:10.1515/nanoph-2018-0072
89. Shen Y, Wang X, Xie Z, Min C, Fu X, Liu Q, et al. Optical Vortices 30 Years on: OAM Manipulation from Topological Charge to Multiple Singularities. *Light Sci Appl* (2019) 8:90. doi:10.1038/s41377-019-0194-2
90. Fu SY, Huang L, Lv YL, Gao CQ Advances on the Measurement of Orbital Angular Momentum Spectra for Laser Beams. *Infrared Laser Eng* (2021) 50(9):20210145. doi:10.3788/IRLA20210145
91. Omatsu T, Miyamoto K, Lee AJ. Wavelength-versatile Optical Vortex Lasers. *J Opt* (2017) 19:123002. doi:10.1088/2040-8986/aa9445
92. Lee AJ, Omatsu T. Direct Generation of Vortex Laser Beams and Their Nonlinear Wavelength Conversion. *Vortex Dyn Opt Vortices* (2017) 2:57–82. doi:10.5772/66425
93. Duan Y-M, Zhou Y-M, Sun Y-L, Li Z-H, Zhang Y-J, Wang H-Y, et al. Frequency Doubling of Acousto-Optic Q-Switched Nd:YVO4 Cascaded Raman Laser for Narrow Pulse-Width 657 nm Laser. *Acta Phys Sin* (2021) 70:224209. doi:10.7498/aps.70.20210695
94. Chen S, Cheng M, Zhu H, Mao T, Zhang X, Zhou Q, et al. Orange, Yellow and green Emissions Generated in Q-Switched Nd:YALO3/YVO4 Raman Laser. *J Lumin* (2019) 214:116555. doi:10.1016/j.jlumin.2019.116555
95. Mao T, Duan Y, Chen S, Chen M, Zhang X, Zhou Q, et al. Yellow and Orange Light Selectable Output Generated by Nd:YAP/YVO4/LBO Raman Laser. *IEEE Photon Technol Lett* (2019) 31(13):1112–5. doi:10.1109/lpt.2019.2920145
96. Fang X, Kuang Z, Chen P, Yang H, Li Q, Hu W, et al. Examining Second-Harmonic Generation of High-Order Laguerre-Gaussian Modes through a Single Cylindrical Lens. *Opt Lett* (2017) 42:4387–90. doi:10.1364/OL.42.004387
97. Zhang Y, Duan Y, Wang Z, Zhang D, Zhang J, Zhang Y, et al. Continuous-Wave Widely Tunable MgO:PPLN Optical Parametric Oscillator with Compact Linear Cavity. *IEEE Photon Technol Lett* (2018) 30(20):1756–9. doi:10.1109/lpt.2018.2868736
98. Dholakia K, Simpson NB, Padgett MJ, Allen L. Second-harmonic Generation and the Orbital Angular Momentum of Light. *Phys Rev A* (1996) 54: R3742–R3745. doi:10.1103/physreva.54.r3742
99. Courtial J, Dholakia K, Allen L, Padgett MJ. Second-harmonic Generation and the Conservation of Orbital Angular Momentum with High-Order Laguerre-Gaussian Modes. *Phys Rev A* (1997) 56(5):4193–6. doi:10.1103/PhysRevA.56.4193
100. Berzanskis A, Matijosius A, Piskarskas A, Smilgevicius V, Stabinis A. Sum-frequency Mixing of Optical Vortices in Nonlinear Crystals. *Opt Commun* (1998) 150:372–80. doi:10.1016/S0030-4018(97)00591-9
101. Bovino FA, Braccini M, Giardina M, Sibilia C. Orbital Angular Momentum in Noncollinear Second-Harmonic Generation by off-axis Vortex Beams. *J Opt Soc Am B* (2011) 28:2806–11. doi:10.1364/JOSAB.28.002806
102. Bloch NV, Shemer K, Shapira A, Shiloh R, Juwiler I, Arie A. Twisting Light by Nonlinear Photonic Crystals. *Phys Rev Lett* (2012) 108(23):233902. doi:10.1103/PhysRevLett.108.233902
103. Zhou Z-Y, Ding D-S, Jiang Y-K, Li Y, Shi S, Wang X-S, et al. Orbital Angular Momentum Light Frequency Conversion and Interference with Quasi-phase Matching Crystals. *Opt Express* (2014) 22:20298–310. doi:10.1364/oe.22.020298
104. Zhou Z-Y, Li Y, Ding D-S, Zhang W, Shi S, Shi B-S, et al. Highly Efficient Second Harmonic Generation of a Light Carrying Orbital Angular Momentum in an External Cavity. *Opt Express* (2014) 22:23673–8. doi:10.1364/OE.22.023673
105. Xu Z, Lin Z, Ye Z, Chen Y, Hu X, Wu Y, et al. Control the Orbital Angular Momentum in Third-Harmonic Generation Using Quasi-Phase-Matching. *Opt Express* (2018) 26:17563–70. doi:10.1364/OE.26.017563
106. Wang H, Wei D, Xu X, Wang M, Cui G, Lu Y, et al. Controllable Generation of Second-Harmonic Vortex Beams through Nonlinear Supercell Grating. *Appl Phys Lett* (2018) 113:221101. doi:10.1063/1.5050423
107. Ding D-S, Zhou Z-Y, Shi B-S, Zou X-B, Guo G-C. Linear Up-Conversion of Orbital Angular Momentum. *Opt Lett* (2012) 37:3270–2. doi:10.1364/OL.37.003270
108. Zhao YL, Li FS, Qiu XD, Zhang WH, Lu QH, Chen LX Frequency Doubling Effect of Topological Charge of Composite Vortex in Frequency Doubling Process. *Laser Optoelectron Prog* (2017) 54:051901. doi:10.3788/LOP54.051901
109. Tung JC, Ma YY, Miyamoto K, Chen YF, Omatsu T. Bottle Beam Generation from a Frequency-Doubled Nd:YVO4 Laser. *Sci Rep* (2018) 8:16576. doi:10.1038/s41598-018-34783-z
110. Gui G, Brooks NJ, Kapteyn HC, Murnane MM, Liao C-T. Second-harmonic Generation and the Conservation of Spatiotemporal Orbital Angular Momentum of Light. *Nat Photon* (2021) 15:608–13. doi:10.1038/s41566-021-00841-8
111. Li H, Liu H, Chen X. Nonlinear Generation of Airy Vortex Beam. *Opt Express* (2018) 26:21204–9. doi:10.1364/OE.26.021204
112. Liu Y, Chen W, Tang J, Xu X, Chen P, Ma CQ, et al. Switchable Second-Harmonic Generation of Airy Beam and Airy Vortex Beam. *Adv Opt Mater.* (2021) 9(4):2001776. doi:10.1002/adom.202001776
113. Gauthier D, Ribič PR, Adhikary G, Camper A, Chappuis C, Cucini R, et al. Tunable Orbital Angular Momentum in High-Harmonic Generation. *Nat Commun* (2017) 8:14971. doi:10.1038/ncomms14971
114. Kong F, Zhang C, Bouchard F, Li Z, Brown GG, Ko DH, et al. Controlling the Orbital Angular Momentum of High Harmonic Vortices. *Nat Commun* (2017) 8:14970. doi:10.1038/ncomms14970
115. Fan X, Liang H-J, Shan L-Y, Yan B, Gao Q-H, Ma R, et al. Extreme Ultraviolet Polarization Vortex Beam Based on High Harmonic Generation. *Acta Phys Sin* (2020) 69:044203. doi:10.7498/aps.69.20190834
116. Ma Y, Yu X, Li X. Performance Improvement in a Directly 879 nm Dual-End-π-Polarized-Pumped CW and Pulsed GdVO4/Nd:GdVO4 Laser. *Appl Opt* (2012) 51(5):600–3. doi:10.1364/AO.51.000600

117. Zhang L, Duan Y, Mao X, Li Z, Chen Y, Zhang Y, et al. Passively Q-Switched YVO4 Raman Operation with 816 and 890 cm−1 Shifts by Respective Raman Configurations. *Opt Mater Express* (2021) 11:1815–23. doi:10.1364/OME.427483
118. Duan Y, Zhang J, Zhu H, Zhang Y, Xu C, Wang H, et al. Compact Passively Q-Switched RbTiOPO4cascaded Raman Operation. *Opt Lett* (2018) 43:4550–3. doi:10.1364/OL.43.004550
119. Duan Y, Zhu H, Wang H, Zhang Y, Chen Z. Comparison of 115 Mm Nd:YAG\KTA Raman Lasers with 234 and 671 cm−1 Shifts. *Opt Express* (2016) 24:5565–71. doi:10.1364/OE.24.005565
120. Pask HM. The Design and Operation of Solid-State Raman Lasers. *Prog Quan Electron* (2003) 27(1):3–56. doi:10.1016/S0079-6727(02)00017-4
121. Lee CY, Chang CC, Cho CY, Tuan PH, Chen YF. Generation of Higher Order Vortex Beams from a YVO4/Nd:YVO4 Self-Raman Laser via off-Axis Pumping with Mode Converter. *IEEE J Sel Top Quan Electron* (2015) 21(1):318–22. doi:10.1109/JSTQE.2014.2324754
122. Dong J, Wang X, Zhang M, Wang X, He H. Structured Optical Vortices with Broadband Comb-like Optical Spectra in Yb:Y3Al5O12/YVO4 Raman Microchip Laser. *Appl Phys Lett* (2018) 112:161108. doi:10.1063/1.5024051
123. Ma Y, Lee AJ, Pask HM, Miyamoto K, Omatsu T. Direct Generation of 1108 nm and 1173 nm Laguerre-Gaussian Modes from a Self-Raman Nd:GdVO4 Laser. *Opt Express* (2020) 28(16):24095–103. doi:10.1364/OE.400007
124. Miao Y, Zhang L, Dong J. Broadband Petal-Like Raman Laser. *Annalen der Physik* (2022) 2022:2100476. doi:10.1002/andp.202100476
125. Lee AJ, Zhang C, Omatsu T, Pask HM. An Intracavity, Frequency-Doubled Self-Raman Vortex Laser. *Opt Express* (2014) 22:5400–9. doi:10.1364/OE.22.005400
126. Lee AJ, Pask HM, Omatsu T. A Continuous-Wave Vortex Raman Laser with Sum Frequency Generation. *Appl Phys B* (2016) 122:64. doi:10.1007/s00340-016-6334-y
127. Duan Y, Zhou Y, Zhu H, Li Z, Jin X, Tang D. Selective Frequency Mixing in a Cascaded Self-Raman Laser with a Critical Phase-Matched LBO crystal. *J Lumin* (2022) 244:118698. doi:10.1016/j.jlumin.2021.118698
128. Duan Y, Sun Y, Zhu H, Mao T, Zhang L, Chen X. YVO4 Cascaded Raman Laser for Five-Visible-Wavelength Switchable Emission. *Opt Lett* (2020) 45:2564–7. doi:10.1364/OL.392566
129. Nishigata Y, Sasaki S, Miyamoto K, Omatsu T. Cascaded Vector Vortex Mode Generation from a Solid-State Raman Laser. *Appl Opt* (2021) 60:10638–42. doi:10.1364/AO.443596
130. Duan Y, Zhang J, Guo J, Zhu H, Zhang Y, Xu C, et al. Potassium Titanyl Arsenate Based Cascaded Optical Parametric Oscillator Emit at 2.5μm Derived by Neodymium-Doped Yttrium Lithium Fluoride Laser. *JPN J Appl Phys* (2018) 57:040304. doi:10.7567/JJAP.57.100311
131. Zhu H, Duan Y, Wang H, Shao Z, Zhang Y, Zhang G, et al. Compact Nd:YAlO3/RbTiOPO4 Based Intra-Cavity Optical Parametric Oscillator Emit at 1.65 and 3.13 μm. *IEEE J Sel Top Quan Electron* (2015) 21(1):1600105. doi:10.1109/jstqe.2014.2302352
132. Duan Y, Zhu H, Ye Y, Zhang D, Zhang G, Tang D. Efficient RTP-Based OPO Intracavity Pumped by an Acousto-Optic Q-Switched Nd:YVO_4 Laser. *Opt Lett* (2014) 39(5):1314–7. doi:10.1364/OL.39.001314
133. Maleev ID, Deykoon AM, Swartzlander GA, Soskin MS, Sergienko AV. Violation of Conservation of Topological Charge in Optical Down Conversion. Technical Digest. In: Summaries of Papers Presented at the Quantum Electronics and Laser Science Conference (1999). p. 99. doi:10.1109/QELS.1999.807359
134. Yusufu T, Tokizane Y, Yamada M, Miyamoto K, Omatsu T. Tunable 2-μm Optical Vortex Parametric Oscillator. *Opt Express* (2012) 20:23666–75. doi:10.1364/OE.20.023666
135. Furuki K, Horikawa M-T, Ogawa A, Miyamoto K, Omatsu T. Tunable Mid-infrared (6.3-12 μm)optical Vortex Pulse Generation. *Opt Express* (2014) 22:26351–7. doi:10.1364/OE.22.026351
136. Yusufu T, Niu S, Tuersun P, Tulake Y, Miyamoto K, Omatsu T. Tunable 3 Mm Optical Vortex Parametric Oscillator. *Jpn J Appl Phys* (2018) 57:122701. doi:10.7567/JJAP.57.122701
137. Sharma V, Aadhi A, Samanta GK. Controlled Generation of Vortex and Vortex Dipole from a Gaussian Pumped Optical Parametric Oscillator. *Opt Express* (2019) 27:18123–30. doi:10.1364/OE.27.018123
138. Tong H, Xie G, Qiao Z, Qin Z, Yuan P, Ma J, et al. Generation of a Mid-infrared Femtosecond Vortex Beam from an Optical Parametric Oscillator. *Opt Lett* (2020) 45:989–92. doi:10.1364/ol.388096
139. Sharma V, Chaitanya Kumar S, Samanta GK, Ebrahim-Zadeh M. Tunable, High-Power, High-Order Optical Vortex Beam Generation in the Mid-infrared. *Opt Express* (2022) 30:1195–204. doi:10.1364/OE.443345
140. Mamuti R, Araki S, Nishida S, Miyamoto K, Omatsu T. Tunable Near-Infrared Optical Vortex Parametric Laser with Versatile Orbital Angular Momentum States. *Appl Opt* (2018) 57:10004–8. doi:10.1364/AO.57.010004
141. Mamuti R, Goto S, Miyamoto K, Omatsu T. Generation of Coupled Orbital Angular Momentum Modes from an Optical Vortex Parametric Laser Source. *Opt Express* (2019) 27:37025–33. doi:10.1364/OE.27.037025
142. Ababaike M, Wang S, Aierken P, Omatsu T, Yusufu T. Near and Mid-infrared Optical Vortex Parametric Oscillator Based on KTA. *Sci Rep* (2021) 11:8013. doi:10.1038/s41598-021-86945-1
143. Zhu H, Duan Y, Feng Z, Zhang G, Xu C, Zhang Y, et al. Generation of 2-μm Light Based on a Noncritical Phase Matching OPO Technique. *IEEE Photon Technol Lett* (2013) 25(7):690–3. doi:10.1109/lpt.2013.2247395
144. Duan Y, Zhu H, Xu C, Ruan X, Cui G, Zhang Y, et al. Compact Self-Cascaded KTA-OPO for 2.6 μm Laser Generation. *Opt Express* (2016) 24:26529–35. doi:10.1364/OE.24.026529
145. Zhu H, Guo J, Duan Y, Zhang J, Zhang Y, Xu C, et al. Efficient 1.7 μm Light Source Based on KTA-OPO Derived by Nd:YVO_4 Self-Raman Laser. *Opt Lett* (2018) 43:345–8. doi:10.1364/OL.43.000345
146. Murray JT, Austin WL, C. Powell R. Intracavity Raman Conversion and Raman Beam Cleanup. *Opt Mater* (1999) 11(4):353–71. doi:10.1016/S0925-3467(98)00033-0
147. Ma YF, Zhang JW, Li H, Yu X. High Stable Electro-Optical Cavity-Dumped Nd:YAG Laser. *Laser Phys Lett* (2012) 9(8):561–3. doi:10.7452/lapl.201210041

Conflict of Interest: The authors declare that the research was conducted in the absence of any commercial or financial relationships that could be construed as a potential conflict of interest.

Publisher's Note: All claims expressed in this article are solely those of the authors and do not necessarily represent those of their affiliated organizations, or those of the publisher, the editors, and the reviewers. Any product that may be evaluated in this article, or claim that may be made by its manufacturer, is not guaranteed or endorsed by the publisher.

frontiers in Physics

BRIEF RESEARCH REPORT
published: 10 March 2022
doi: 10.3389/fphy.2022.820177

Compound Cavity Passively Q-Switched Single-Longitudinal-Mode Diode-Pumped Laser

Bin Chen[1,2], Zhenxu Bai[1,2], Guijuan Zhao[1,2], Yu Zhang[1,2], Bingzheng Yan[1,2], Yaoyao Qi[1,2], Jie Ding[1,2], Kun Wang[3], Yulei Wang[1,2] and Zhiwei Lu[1,2]**

[1]Center for Advanced Laser Technology, Hebei University of Technology, Tianjin, China, [2]Hebei Key Laboratory of Advanced Laser Technology and Equipment, Tianjin, China, [3]School of Energy and Environmental Engineering, Hebei University of Technology, Tianjin, China

A compact solid-state single-longitudinal-mode (SLM) Q-switched laser based on a compound cavity is demonstrated. SLM operation is achieved through the enhancement of mode competition (*via* manipulation of the effective reflectivity of the resonator mirrors and intracavity field accumulation time) and does not require the use of a feedback loop. In this work, SLM emission with a linewidth of 254.3 MHz is demonstrated, and a high SLM ratio of up to 99.6% is achieved. The laser operates at a repetition rate of 10 Hz, producing 10 ns pulses with a pulse energy of 14.81 mJ.

Keywords: single-longitudinal-mode, self-seed injection, passively Q-switched, laser technique, compound cavity

OPEN ACCESS

Edited by:
Yufei Ma,
Harbin Institute of Technology, China

Reviewed by:
Zhenqiang Chen,
Jinan University, China
Quan Sheng,
Tianjin University, China

****Correspondence:***
Zhenxu Bai
baizhenxu@hotmail.com
Zhiwei Lu
zhiweilv@hebut.edu.cn

Specialty section:
This article was submitted to Optics and Photonics, a section of the journal Frontiers in Physics

Received: *22 November 2021*
Accepted: *19 January 2022*
Published: *10 March 2022*

Citation:
Chen B, Bai Z, Zhao G, Zhang Y, Yan B, Qi Y, Ding J, Wang K, Wang Y and Lu Z (2022) Compound Cavity Passively Q-Switched Single-Longitudinal-Mode Diode-Pumped Laser. Front. Phys. 10:820177. doi: 10.3389/fphy.2022.820177

INTRODUCTION

In recent years, lasers with different spectral and time-domain characteristics have been widely used in spectral detection, space exploration, manufacturing, etc. [1–4]. Across the domains of coherent optical communications, sodium guide star technology, gravitational wave detection, and non-linear optics, solid-state single-longitudinal-mode (SLM) laser sources with a narrow spectral bandwidth are attracting significant interest [5–10]. These lasers, which often also carry additional characteristics such as broad wavelength tuning capability, high pulse energy, and good beam quality, are enabling a host of new techniques and methodologies. SLM laser sources that operate in the near-infrared spectral region are also gaining traction as the ideal laser sources for molecular spectroscopy [11].

From a practical standpoint, lasers which operate with a SLM must have an effective means of eliminating the spikes created by the beat frequency of adjoining longitudinal modes; this is because these spikes are the most common source of damage to laser system components [12–14]. A number of methods have been used to produce SLM output from solid-state lasers include twisted-mode cavities (TMC) [15], ring cavities [16], the application of etalons or gratings [17–19], microchip lasers [15, 16], and seed injection lasers [20, 21]. However, it should be noted that many of these approaches yield laser outputs with quite low SLM ratio (herein defined as the ratio of the number of single longitudinal mode pulses to the total number of pulses in a certain time). This is due to the wide gain bandwidth and narrow longitudinal mode spacing which is a common characteristic of solid-state lasers. Recent demonstrations (circa 2016–2020) of SLM output from a number of different solid-state laser designs are summarized in **Table 1**. Here the summary focusses on advancements in cavity design and mode-selecting/isolating capability.

The prior literature shows that the primary approaches to generating SLM output are based on threshold regulation and mode competition enhancement [18–24]. In comparison to ring cavities, it

TABLE 1 | Summary of recently reported SLM lasers.

Author(s)	Resonant cavity layout	SLM selection mechanism	Output characteristics
Zhenxu Bai et al. [22], (2016)	Standing wave cavity	Three-plane resonant reflector and saturable absorber	M^2: 1.45 Pulse width: 10.7 ns Pulse energy: 10 mJ (10 Hz) Linewidth: <2.9 GHz
Wencai Li et al. [23], (2017)	Fiber ring cavity	Seed injection	Repetition rate: 1–100 kHz Pulse width: 50–400 ns Pulse energy: 3 μJ (1 kHz) Linewidth: 1.5 MHz
Feng Xue et al. [16], (2018)	Ring cavity	F-P etalon and saturable absorber	M^2: 1.35 Pulse width: 43 ns Pulse energy: 431 μJ Linewidth: <132.5 MHz
ShuTao Dai et al. [24], (2018)	Self-filtering unstable cavity	Seed injection	Pulse width: 16 ns Pulse energy: 50 mJ Energy fluctuation: 1.05% Linewidth: <132.5 MHz
Long Jin et al. [19], (2020)	Standing wave cavity	F-P etalon and Q-switched pre-lasing	Repetition rate: 10 kHz Pulse width: 81.1 ns Pulse energy: 3.94 μJ Linewidth: 33 MHz
I. G. Marienko et al. [25], (2020)	Standing wave cavity	Seed injection and dispersive prism	Slope efficiency: 43% Pulse width: 8 ns Pulse energy: 6 mJ Linewidth: 100 MHz
Duo Jin et al. [15], (2020)	Standing wave cavity	Three-plane resonant reflector, saturable absorber and TMC	SLM ratio: 96.2% Pulse width: 9.8 ns Symmetric pulses: 0.64

is commonly shown that standing wave cavities can generate higher energy pulses with narrower pulse width and with minor beam distortion. A standing-wave cavity is also more desirable from a practical standpoint as it is often more robust and easier to handle in comparison to a ring cavity design. Additionally, standing wave cavities may quite easily integrate with mode selection devices/approaches such as injection-seeding and Fabry-Perrot (F-P) etalons to produce SLM output [19, 25]. It should be noted that the emission from SLM lasers which make use of passive mode selection techniques (TMC and three-plane resonant reflector) typically exhibit inferior SLM ratio unless multiple intracavity components are used [15]. In this case, the insertion of multiple components (such as F-P etalons) increases the loss within the cavity and limits energy output [19, 26]. Injection-seeding can be used to achieve a high SLM ratio; however, it is a bulky, costly, and complicated approach which also typically requires high maintenance. Cavity-stabilization loops are also a source of significant technical complications for injection-seeded lasers [25, 27]. There is, hence, a need for new and novel approaches which may improve the simplicity, robustness, and affordability of high SLM ratio lasers.

One such approach which may address this need is to utilize a mode selection strategy based on a compound cavity combined with a TMC. Here, a compound cavity comprising two distinct cavities is used for longitudinal mode selection, replacing conventional devices such as etalons or gratings. The application of a compound cavity increases mode competition within the laser and also acts as a frequency-selector, suppressing

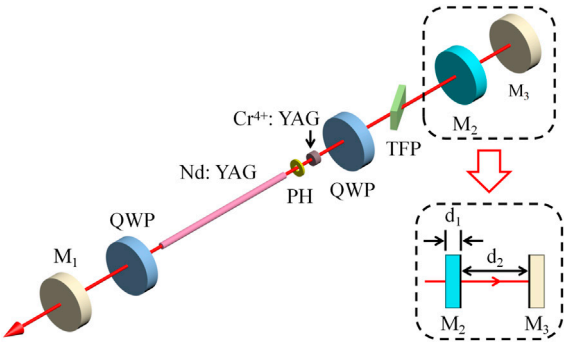

FIGURE 1 | Schematic diagram of the compound cavity passively Q-switched single-longitudinal-mode diode-pumped laser. QWP, quarter-wave plate; PH, pinhole; TFP, thin-film polarizer. (Illustration: resonant mirror frequency selector.)

numerous longitudinal and transverse modes. The above feature is the main difference between the compound cavity and the three-plane resonant reflector. In the three-plane resonant reflector, the inserted mirror is coupled with the output mirror for use as the output mirror. In this work, a compound cavity was integrated into a passively Q-switched, standing wave cavity which provided significant round-trip gain. The long transit time of the laser field within the passively Q-switched cavity was beneficial in limiting the generation of multiple-longitudinal-modes. The considerable laser gain combined with small initial transmittance of the passive Q-switch was conducive to obtaining

laser pulses with a short pulse duration and high peak power. The TMC (formed using quarter wave plates) was integrated into the laser as a means of limiting the effect of spatial hole burning; this further improved the laser's single-mode operation. The laser was capable of operating with output pulse frequencies from 1 to 10 Hz with high energy stability (the root mean square energy fluctuation was <1%).

EXPERIMENTAL SETUP AND NUMERICAL ANALYSIS

The setup of the compound cavity, passively Q-switched SLM diode-pumped laser device is shown in **Figure 1**. The physical length of the cavity was 420 mm. The back cavity mirror M_3 and the resonant mirror M_2 constituted a resonant sub-cavity. Quarter-wave plates (QWPs) were used to form a TMC which limited the spatial hole burning in the laser gain medium. The front cavity mirror M_1 had a reflectivity of 60% at 1,064 nm. The resonant mirror M_2 had a reflectivity of 10% at 1,064 nm on the side facing mirror M_3, and was anti-reflection coated (for 1,064 nm) on the side facing mirror M_1. The back cavity mirror M_3 had a reflectivity of more than 99.5% at 1,064 nm. The laser gain medium was an Nd:YAG (Φ 3 × 78 mm) crystal with a 1% Nd^{3+} doping concentration; both faces of the crystal were coated anti-reflecting at 1,064 nm. A diode pump laser with a repetition rate of 10 Hz and a pulse duration of 250 μs was used in a side-pumping configuration (this was done so as to minimize thermal loading within the laser crystal). The laser was passively Q-switched by a saturable absorber Cr^{4+}:YAG crystal (Φ 6 × 3.25 mm), which had an initial transmittance of 12.23%. The laser produced Q-switched output when the pump energy was ~0.5 J. The laser was p-polarized via the inclusion of a thin-film polarizer (TFP); a 2 mm pinhole (PH) was used to control the intracavity transverse modes.

In **Figure 1**, the resonant mirror (M_2) is used to induce frequency selection within the laser. The means by which this is achieved can be modeled theoretically using thin-film analysis methods in combination with laser signal build-up times. Such an analysis is presented below. We start by calculating the transmission matrix. As outlined in **Figure 1**, for a plate of thickness d_1, and plate separation of d_2, the transmission matrix is given by [28]:

$$M_j = \begin{bmatrix} \cos\delta_j & -\frac{i}{n_j}\sin\delta_j \\ -in_j\sin\delta_j & \cos\delta_j \end{bmatrix} \tag{1}$$

where δ_j is the phase delay of light passing through the medium. The expression of δ_j is given by:

$$\delta_j = \frac{2\pi}{\lambda} n_j d_j \cos\theta_j \tag{2}$$

where n and d are the refractive index and thickness of the jth media, respectively. λ and θ are the incident wavelength and angle of incidence, respectively. The total transmission matrix is expressed as:

$$M = \prod_i M_i = \begin{bmatrix} m_{11} & im_{12} \\ im_{21} & m_{22} \end{bmatrix} \tag{3}$$

The combined reflectivity of the compound frequency selector system as a function of wavelength is then given by:

$$R(\lambda) = \frac{(m_{11}P_0 - m_{22}P_1)^2 + (m_{12}P_1 \cdot P_0 - m_{21})^2}{(m_{11}P_0 + m_{22}P_1)^2 + (m_{12}P_1P_0 + m_{21})^2} \tag{4}$$

where P_0 and P_1 are the parameters which depend on the medium in which both ends of the resonant reflector system are placed. If placed in air, then $P_0 = P_1 = \cos\theta_0$.

In this work, the thickness of the resonant mirror M_2 is d_1 = 6.35 mm, and the refractive index is 1.51. The distance between M_2 and M_3 is d_2 = 5 cm. From this, one can calculate the combined reflectivity of the system, as a function of wavelength. This was done for the wavelength range 1,063.8–1,064.4 nm in 0.01 pm steps, and this is shown as the blue plot in **Figure 2A**. The envelope period of the reflectivity depends on d_1, and the period of the fine structure depends on d_2. When the separation distance is greater than the thickness, such a structure has a peak reflection of 40%. When this occurs, the reflectivity of M_2 is less than M_1, and M_2 becomes the output mirror of the sub-resonant cavity.

When the laser is operating in a low gain state, the round-trip gain is [15]:

$$G = R\left(T_0T_pT_d\right)^2 \exp\left[2g_0l\frac{(\Delta\lambda/2)^2}{(\lambda-\lambda_0)^2 + (\Delta\lambda/2)^2}\right] \tag{5}$$

where T_0, T_p and T_d are the initial transmittance of the Cr^{4+}: YAG, the transmittance of the TFP, and the transmittance of the PH, respectively. Δλ is the fluorescence linewidth of the gain medium, and g_0 is the small-signal gain coefficient at the laser center wavelength. l is the length of the gain medium, and R is the reflectivity of the resonant mirror frequency selector (as detailed above).

In a standing wave cavity, the number of longitudinal modes of oscillation in the resonant cavity is determined by the gain linewidth Δv of the gain medium and the longitudinal mode interval Δv_q of the resonant cavity. The gain linewidth of Nd:YAG is Δv_0 = 200 GHz, and the longitudinal mode interval of the resonant cavity is $\Delta v_q = c/2L$, where c is the speed of light and L is the optical length of the resonant cavity. Note also that in a compound cavity laser design, longitudinal modes of the resonant cavity must also be supported within the compound cavity if they are to oscillate.

The net gain difference between two adjacent longitudinal modes is proportional to the transit time. Therefore, as the transit time increases, the desired signal gradually accumulates from noise, while at the same time suppressing other longitudinal modes [29]. For passively Q-switched lasers, the laser field build-up process typically requires hundreds to thousands of transits, and this is conducive to the accumulation of laser gain and energy

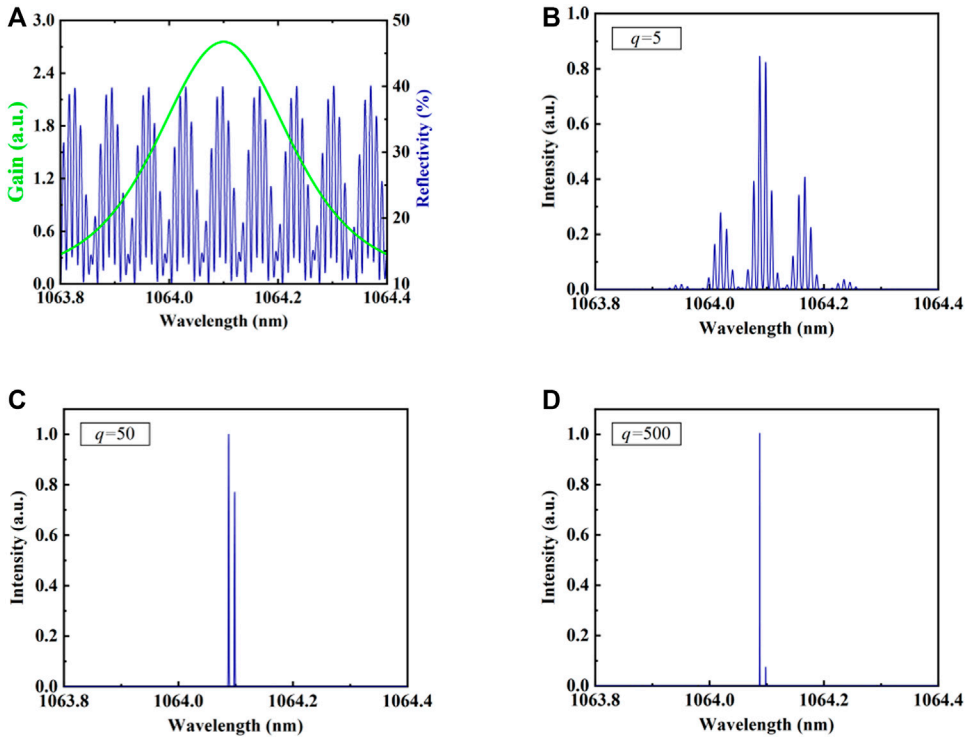

FIGURE 2 | (A) Gain spectrum (green trace) and the reflectivity of the resonant mirror (blue trace) as a function of laser wavelength; **(B)** modeled laser spectrum as a function of wavelength for q = 5 transits; **(C)** modeled laser spectrum as a function of wavelength for q = 50 transits; and **(D)** modeled laser spectrum as a function of wavelength for q = 500 transits.

within a SLM, with a high SLM ratio [30]. The number of loop transits (or round trips) that a laser field undertakes during its build-up from noise to typical output power levels is given by q [28, 31]. It has been calculated that passively Q-switched systems typically require $q > 500$ before the field is output.

In a practical laser, the difference in gain between two adjacent longitudinal modes can be a mere 0.5%. Nevertheless, this minor difference in gain is significant in the context of laser systems wherein laser modes build from noise to megawatt power levels; here the laser modes with the lowest losses emerge as the dominant modes. This effect can be demonstrated through modeling of the laser spectrum. The theoretical spectrum of the laser in this work was modeled for increasing numbers of transits (q) and the resultant spectra are shown in **Figures 2B–D**. It can be seen from the figures that as the number of transits increase, there is a progressive decrease in the number of gain regions that are present in the spectrum. In the case of q = 500 transits, the difference in intensity between the primary gain region and its adjacent neighbor is more than an order of magnitude.

EXPERIMENTAL RESULTS AND DISCUSSION

As this system does not require the use of additional external components (such as piezoelectric transducers and external circuits) to actively adjust cavity mirrors, and does not need injection seeding, the laser system is inherently simple, low cost, and easy to maintain.

The experimental results showed that the insertion angle of the resonant mirror (M_2) had a significant effect on the output characteristics of the laser. When the insertion angle was large (>1°), the insertion of a resonant mirror would lead to significant loss and poor energy stability, resulting in an increase in the laser threshold and linear jitter of the output beam. The spatial characteristics of the output beam were recorded with a laser beam profiler (DataRay WinCamd-LCM). Images of the near-field spatial profiles of the laser output for a range of mirror M_2 insertion angles (<0.1°) are shown in **Figure 3A**. The plots show that a near-perfect Gaussian-like output spot is generated when mirror M_2 is aligned perfectly parallel with the primary laser cavity (formed by mirrors M_1 and M_3). Angular deviation of M_2 led to the formation of two distinct cavities within the laser system. This resulted in undesired oscillation of transverse modes and mode competition. The end result was a reduction in output energy and stability, and deterioration of the mode profile. The system also exhibited some sensitivity to fluctuations in the ambient temperature and the temperature of the water used to cool the laser gain crystal. These fluctuations in the range of ±1°C had the effect of changing the length of the laser cavity and drove mode jumps and occasionally multi-longitudinal mode operation [25]. It is anticipated that this sensitivity can be overcome through simple engineering to improve the temperature-stability of the system.

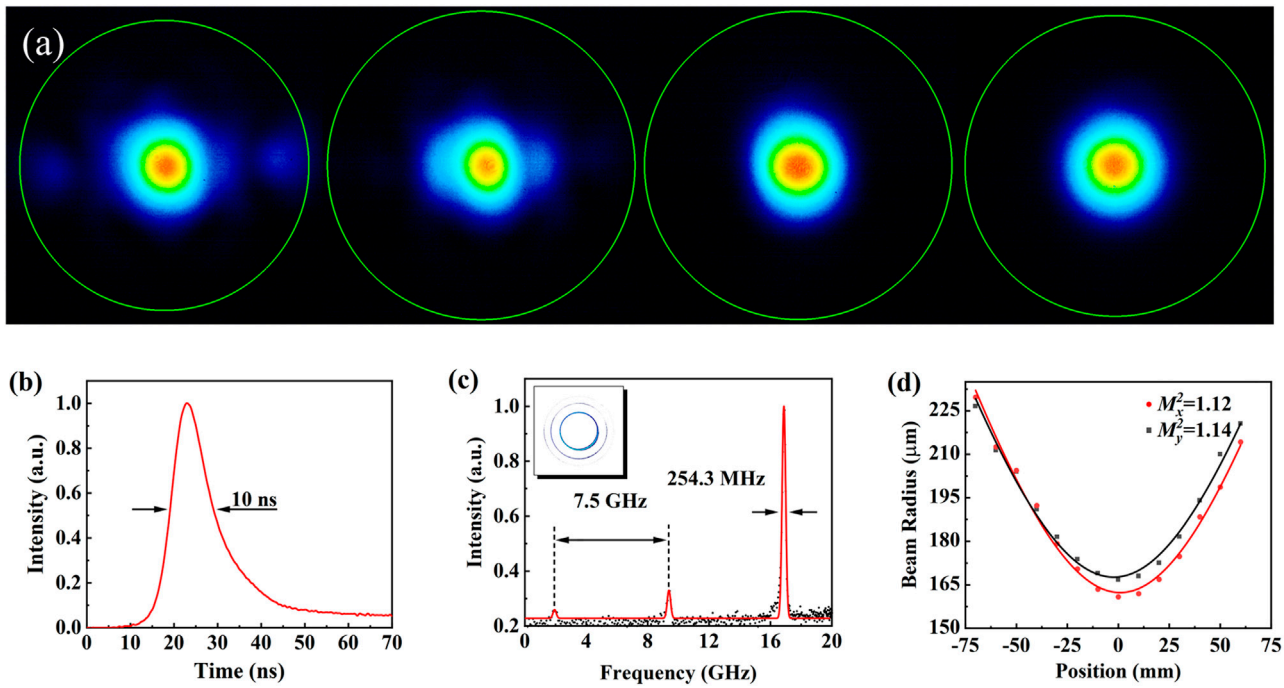

FIGURE 3 | (A) Near-field intensity distribution of the laser output for different M_2 insertion angles from 0.1 to 0° (left-to-right); **(B)** plot of a typical laser output pulse at maximum pulse energy; **(C)** plot of the laser output linewidth as determined using a Fabry-Perot interferometer (inset: typical interferogram from the Fabry-Perot interferometer); and **(D)** plot of the laser beam propagation characteristics and fits used for determination of the beam quality factor.

The output energy was measured using a laser energy meter (OPHIR PE50BB-DIF-C and OPHIR NOVA II). The average pulse energy was 14.81 mJ (at a pump energy of about 0.5 J), and the pulse energy fluctuation was 0.82% over 10,000 shots (taken over a period of ~1 h). The temporal waveform of the output was detected using a fast photodetector (THORLABS DET08C) and was recorded on an oscilloscope (Tektronix MSO64). The pulse shape of the output is shown in **Figure 3B**. The average pulse width was 10.18 ns. Due to the long time required for passive Q-switching to turn off completely when operating at high pump energy, there is a slight tail in the output pulse. It was observed that the TMC had the effect of removing secondary emission peaks in the output when operating at high pump energies.

A home-made Fabry-Perot interferometer with a 7.5 GHz free spectral range and 144 MHz bandwidth was used to examine the spectral properties of the laser output. The emission spectrum of the laser output is shown in **Figure 3C**; also shown inset is an interferogram of the output. The single ring in each interference order indicates that the laser operates with a SLM. The spectrum shows that the laser output linewidth is 254.3 MHz. We believe that this relatively broad linewidth is the result of the length of the laser cavity and the time required for the passive Q-switched to establish oscillation. The SLM ratio of the laser was determined in real-time by examining the output waveform and looking for the presence of any beat frequency components (using the oscilloscope). The measured SLM ratio was ~99.6% over 3,000 shots. Under the same experimental conditions, when TMC is used without a compound cavity, the output waveform is unstable, and it is difficult to achieve SLM ratios greater than 95%.

The beam quality factor of the output was measured, as shown in **Figure 3D**. Standard Gaussian beam propagation fits were used to determine beam quality factors in the *x* and *y* directions of 1.12 and 1.14, respectively. We believe that the significantly better beam quality in this work in comparison to the work summarized in **Table 1** results from the PH and the resonant mirror controlling the transverse modes within the cavity. Future work is focused on reducing the overall cavity length, improving the cavity engineering to achieve stable SLM output without mode hopping, and to investigate methods of further increasing energy output.

CONCLUSION

In conclusion, a pulsed laser utilizing a compound cavity, which operates in SLM with no active cavity stabilization, has been demonstrated. The output has a SLM ratio of 99.6% and a linewidth of 253.4 MHz at a repetition rate of 10 Hz. The pulse width was 10.18 ns, and the average beam quality factor was 1.13. The average pulse energy was 14.81 mJ, with 0.82% pulse energy fluctuations as measured over a 1-h stability test. The compound cavity proposed in this paper has the advantages of a high SLM ratio, high single pulse energy, high energy stability, low cost, compact structure, and is comparatively low maintenance.

DATA AVAILABILITY STATEMENT

The raw data supporting the conclusion of this article will be made available by the authors, without undue reservation.

AUTHOR CONTRIBUTIONS

BC: design of the study, investigation, data curation, writing—original draft. ZB: methodology, writing—review and editing, and supervision. GZ: methodology, data curation, and investigation. YZ: methodology, data curation, and investigation. BY: investigation, writing—original draft, and writing—review and editing. YQ: investigation, and writing—review and editing. JD: investigation, and writing—review and editing. KW: methodology, and supervision. YW: conceptualization, methodology, and supervision. ZL: conceptualization, methodology, supervision, and funding acquisition. All authors contributed to the article and approved the submitted version.

FUNDING

This work was supported by the National Natural Science Foundation of China (No. 61927815).

REFERENCES

1. Williams RJ, Kitzler O, Bai Z, Sarang S, Jasbeer H, McKay A, et al. High Power Diamond Raman Lasers. *IEEE J Select Top Quan Electron.* (2018) 24(5):1–14. doi:10.1109/jstqe.2018.2827658
2. Liu X, Qiao S, Ma Y. Highly Sensitive Methane Detection Based on Light-Induced Thermoelastic Spectroscopy with a 2.33 μm Diode Laser and Adaptive Savitzky-Golay Filtering. *Opt Express* (2022) 30(2):1304–13. doi:10.1364/oe.446294
3. Liu X, Ma Y. Sensitive Carbon Monoxide Detection Based on Light-Induced Thermoelastic Spectroscopy with a Fiber-Coupled Multipass Cell. *Chin Opt Lett* (2022) 20:031201. doi:10.3788/COL202220.031201
4. Bai Z, Yuan H, Liu Z, Xu P, Gao Q, Williams RJ, et al. Stimulated Brillouin Scattering Materials, Experimental Design and Applications: A Review. *Opt Mater* (2018) 75:626–45. doi:10.1016/j.optmat.2017.10.035
5. Qiao S, Ma Y, He Y, Patimisco P, Sampaolo A, Spagnolo V. Ppt Level Carbon Monoxide Detection Based on Light-Induced Thermoelastic Spectroscopy Exploring Custom Quartz Tuning Forks and a Mid-infrared QCL. *Opt Express* (2021) 29(16):25100–8. doi:10.1364/OE.434128
6. Bode N, Meylahn F, Willke B. Sequential High Power Laser Amplifiers for Gravitational Wave Detection. *Opt Express* (2020) 28(20):29469–78. doi:10.1364/oe.401826
7. Bai Z, Zhao Z, Tian M, Jin D, Pang Y, Li S, et al. A Comprehensive Review on the Development and Applications of Narrow-Linewidth Lasers. In: *Microwave and Optical Technology Letters* (2021). Hoboken: Wiley Online Library. p. 1–12. doi:10.1002/mop.33046
8. Huo X, Qi Y, Zhang Y, Chen B, Bai Z, Ding J, et al. Research Development of 589 nm Laser for Sodium Laser Guide Stars. *Opt Lasers Eng* (2020) 134:106207. doi:10.1016/j.optlaseng.2020.106207
9. Guan H, Novack A, Galfsky T, Ma Y, Fathololoumi S, Horth A, et al. Widely-tunable, Narrow-Linewidth III-V/silicon Hybrid External-Cavity Laser for Coherent Communication. *Opt Express* (2018) 26(7):7920–33. doi:10.1364/oe.26.007920
10. Bai Z, Williams RJ, Kitzler O, Sarang S, Spence DJ, Wang Y, et al. Diamond Brillouin Laser in the Visible. *APL Photon* (2020) 5(3):031301. doi:10.1063/1.5134907
11. Kerdoncuff H, Christensen JB, Lassen M. Quantum Frequency Conversion of Vacuum Squeezed Light to Bright Tunable Blue Squeezed Light and Higher-Order Spatial Modes. *Opt Express* (2021) 29(19):29828–40. doi:10.1364/oe.436325
12. Yang X, Kitzler O, Spence DJ, Williams RJ, Bai Z, Sarang S, et al. Single-frequency 620 nm Diamond Laser at High Power, Stabilized via Harmonic Self-Suppression and Spatial-hole-burning-free Gain. *Opt Lett* (2019) 44(4):839–42. doi:10.1364/ol.44.000839
13. Schuhmann K, Kirch K, Nez F, Pohl R, Wichmann G, Antognini A. Spatial Hole Burning in Thin-Disk Lasers and Twisted-Mode Operation. *Appl Opt* (2018) 57(11):2900–8. doi:10.1364/ao.57.002900
14. Ma Y, He Y, Tong Y, Yu X, Tittel FK. Quartz-tuning-fork Enhanced Photothermal Spectroscopy for Ultra-high Sensitive Trace Gas Detection. *Opt Express* (2018) 26(24):32103–10. doi:10.1364/oe.26.032103
15. Jin D, Bai Z, Wang Q, Chen Y, Liu Z, Fan R, et al. Doubly Q-Switched Single Longitudinal Mode Nd:YAG Laser with Electro-Optical Modulator and Cr^{4+}:YAG. *Opt Commun* (2020) 463:125500. doi:10.1016/j.optcom.2020.125500
16. Xue F, Zhang S, Cong Z, Huang Q, Guan C, Wu Q, et al. Diode-end-pumped Single-Longitudinal-Mode Passively Q-Switched Nd:GGG Laser. *Laser Phys Lett* (2018) 15(3):035001. doi:10.1088/1612-202x/aa9b21
17. Rao CS, Kundu S, Ray AK. SLM Operation of a High Repetition Rate BBO Optical Parametric Oscillator Pumped by DPSSL at 355 nm. *Opt Laser Techn* (2021) 138:106878. doi:10.1016/j.optlastec.2020.106878
18. Wang L, Shen Z, Feng X, Li F, Cao Y, Wang X, et al. Tunable Single-Longitudinal-Mode Fiber Laser Based on a Chirped Fiber Bragg Grating. *Opt Laser Techn* (2020) 121:105775. doi:10.1016/j.optlastec.2019.105775
19. Jin L, Dai W, Yu Y, Dong Y, Jin G. Single Longitudinal Mode Q-Switched Operation of Pr:YLF Laser with Pre-lase and Fabry-Perot Etalon Technology. *Opt Laser Techn* (2020) 129:106294. doi:10.1016/j.optlastec.2020.106294
20. Nägele M, Stoppel K, Dekorsy T. Passively Q-Switched 914 nm Microchip Laser for Lidar Systems. *Opt Express* (2021) 29(15):23799–809. doi:10.1364/oe.432340
21. Marianovich A, Spiekermann S, Brendel M, Wessels P, Neumann J, Weyers M, et al. Wedged Nd:YVO_4 Crystal for Wavelength Tuning of Monolithic Passively Q-Switched Picosecond Microchip Lasers. *Opt Express* (2021) 29(13):19790–5. doi:10.1364/oe.430870
22. Bai Z, Wang Y, Lu Z, Chen Y, Li S, Yuan H, et al. A Single -Longitudinal-Mode Nd:Ce:YAG Q-Switched Laser Based on a Three-Plan Resonant Reflector. *J Russ Laser Res* (2016) 37(4):382–8. doi:10.1007/s10946-016-9585-5
23. Li W, Liu H, Zhang J, Yao B, Feng S, Wei L, et al. Mode-hopping-free Single-Longitudinal-Mode Actively Q-Switched Ring Cavity Fiber Laser with an Injection Seeding Technique. *IEEE Photon J.* (2017) 9(1):1–7. doi:10.1109/jphot.2017.2654999
24. Dai S-T, Wu H-C, Shi F, Deng J, Ge Y, Weng W, et al. Development of an Injection-Seeded Single-Frequency Laser by Using the Phase Modulated Technique. *Chin Phys. B* (2018) 27(5):054212. doi:10.1088/1674-1056/27/5/054212
25. Marienko IG, Zhi M, Khizhnyak AI, Sokolov AV. Injection-seeded Single-Longitudinal-Mode Ti:Sapphire Laser with No Active Stabilization. *Opt Express* (2020) 28(17):25444–59. doi:10.1364/oe.401030
26. Lei Y, Mao A, Li Y, Zhang Y, Liu H, Zhang Y. Research on Single Longitudinal Mode Laser Based on F-P Etalon and Q-Switched Delay. *Optik* (2018) 167:1–6. doi:10.1016/j.ijleo.2018.02.018
27. Wang W, Qi H, Song Z, Guo J, Ni J, Wang C, et al. Seed-injected, Actively Q-Switched Fiber Ring Laser Using an AOM of Zero-Order Transmission. *Opt Commun* (2020) 467:125747. doi:10.1016/j.optcom.2020.125747
28. Chebotayev V, Beterov I, Lisitsyn V. Selection and Self-Locking of Modes in He-Ne Lasers with Non-linear Absorption. *IEEE J Quan Electron.* (1968) 4(5):339. doi:10.1109/jqe.1968.1075149

29. Sooy WR. The Natural Selection of Modes in a Passive Q-Switched Laser. *Appl Phys Lett* (1965) 7(2):36–7. doi:10.1063/1.1754286
30. Cole B, Goldberg L, Trussell CW, Hays A, Schilling BW, McIntosh C. Reduction of Timing Jitter in a Q-Switched Nd:YAG Laser by Direct Bleaching of a Cr^{4+}:YAG Saturable Absorber. *Opt Express* (2009) 17(3):1766–71. doi:10.1364/oe.17.001766
31. Thevar TM, Watson J. Longitudinal Mode Selection in a Dye Q-Switched Ruby Laser: a Comparison between Theoretical and Experimental Results. In: *High-Power Lasers: Solid State, Gas, Excimer, and Other Advanced Lasers*, 2889 (1996). Washington: SPIE (International Society for Optical Engineering). p. 60–9.

Conflict of Interest: The authors declare that the research was conducted in the absence of any commercial or financial relationships that could be construed as a potential conflict of interest.

frontiers in Physics

ORIGINAL RESEARCH
published: 11 March 2022
doi: 10.3389/fphy.2022.862578

Analysis of Metal Elements Contained in Graphite Target Coated With Chinese Medicinal Material Nanoparticles Using LIBS

Weiwei Han[1], *Yongqiang Wang*[1], *Yaopeng Yin*[2], *Xuerui Li*[1], *Duixiong Sun*[1]* *and Maogen Su*[1]*

[1]Key Laboratory of Atomic and Molecular Physics and Functional Material of Gansu Province, College of Physics and Electronic Engineering, Northwest Normal University, Lanzhou, China, [2]National Ancient Wall Painting and Earthen Archaeological Site Engineering Research Centre, Dunhuang, China

A nanoparticle-coated graphite target (NCGT) is presented to improve the analysis accuracy and stability of laser-induced breakdown spectroscopy (LIBS). A stable, relatively homogeneous, and close to optically thin laser-induced breakdown plasma was obtained by dispersing sample nanoparticles on a high-purity graphite substrate. Spectral structures dominated by the characteristic lines of carbon and the samples can greatly simplify spectral identification and avoid line interference. To maximize the analysis accuracy and stability, a series of experimental conditions were optimized step by step according to the spectral intensity and signal-to-noise ratio of the lines. Based on the final optimized conditions, the relative standard deviation values of Mg, Fe, and Sr elemental content in Chinese medicinal material (CMM) samples were reduced from 17.7, 16.6, 12.1% of the pressed target to 4.8, 9.5, and 4.5% of the NCGT, respectively. Comparisons with the inductively coupled plasma mass spectrometry (ICP-MS) results demonstrated that the present method has great potential for detection of LIBS.

Keywords: laser-induced breakdown spectroscopy, nanoparticle-coated graphite target, Chinese medicinal material, metal elements, plasma parameters

OPEN ACCESS

Edited by:
Yufei Ma,
Harbin Institute of Technology, China

Reviewed by:
Ronger Zheng,
Ocean University of China, China
Runhua Li,
South China University of Technology, China

***Correspondence:**
Duixiong Sun
sundx@nwnu.edu.cn
Maogen Su
sumg@nwnu.edu.cn

Specialty section:
This article was submitted to Optics and Photonics, a section of the journal Frontiers in Physics

Received: *26 January 2022*
Accepted: *21 February 2022*
Published: *11 March 2022*

Citation:
Han W, Wang Y, Yin Y, Li X, Sun D and Su M (2022) Analysis of Metal Elements Contained in Graphite Target Coated With Chinese Medicinal Material Nanoparticles Using LIBS. Front. Phys. 10:862578. doi: 10.3389/fphy.2022.862578

INTRODUCTION

In recent decades, there has been a burst of enthusiasm for the fundamental studies of laser-induced breakdown spectroscopy (LIBS) and its applications to many analytical fields because of its advantages of limited sample preparation, multi-elemental analysis, and its capability for remote and *in-situ* analysis of materials in any phase [1–3]. Benefit from the advantages of sensitive and rapid spectral technology [4–7], LIBS as a rapid analytical tool with great potential for determining the elemental composition of materials in the solid, liquid, and gaseous states, many investigations on the spectral stability [8, 9], data processing [10, 11, 12] have recently been developed and reported. Several techniques have been proposed for enhancing the sensitivity of LIBS like Double pulse LIBS [13], resonance LIBS [14], the use external electric or magnetic field [15, 16] and LIF-LIBS, but all these techniques require the use of an additional energy source or tunable lasers. On the contrary, Nanoparticle Enhanced LIBS just requires a minimum sample preparation that is the deposition of nanoparticle on the sample surface [17, 18]. Nevertheless, so far only few investigations have focused on the effect of this phenomenon due to the influence of various factors such as matrix effect.

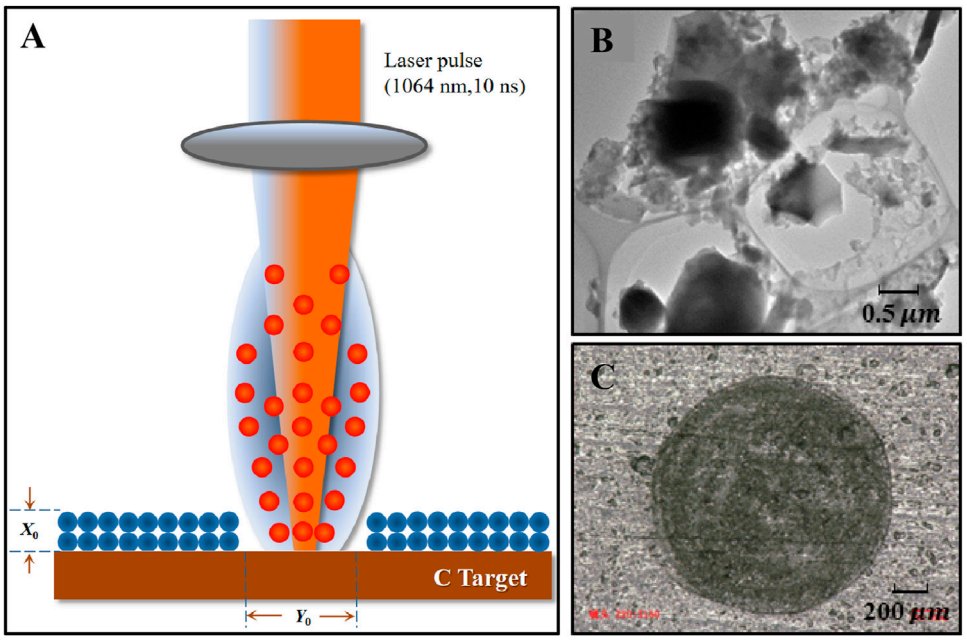

FIGURE 1 | Schematic of LIBS and sample target preparation. **(A)** Dispersed particles from LIBS, **(B)** TEM image of nanoparticle suspensions, **(C)** the image of ablated NCGT surface at the power density of 1.5×10^9 W/cm^2.

A key issue for accurate determination of trace elements in samples is to create a stable, close to optically thin, and relatively homogeneous plasma environment [19]. LIBS investigations have shown that most of the current mature laser and spectral detection instruments meet the requirements of LIBS detection with regards to stability and sensitivity [20], and high precision timing-control and detection-location [21] can easily assist in determining the optimized experimental conditions. However, for most LIBS spectroscopic measurements, two important factors affecting the instability of the spectral signal are the inhomogeneous distribution of the material on a target surface and the unevenness of the sample target surface [22, 23]. These two factors can result in the intensity and shape of the lines exhibiting unreasonable oscillations for some sensitive characteristic emission lines because of pulse-to-pulse fluctuations, for example, Mg II lines at 279.55 and 280.27 nm, and Ca II lines at 393.36 and 396.84 nm. Especially, self-absorption or self-reversed profiles may be observed in extreme cases.

Therefore, a suitable substrate for trace elements is necessary to improve the performance of LIBS detection. A high-purity graphite target could be considered as a kind of ideal substrate because of its simple spectral structure and hexagonal layered structure. As one of the most common elements, elemental carbon has the simplest spectral structure compared with other elements in the range 200–425 nm, exhibiting only an isolated resonance line at 247.86 nm and three CN molecular bands near 358 nm, 388.3 nm, and 421.6 nm. These features greatly simplify spectral identification. Meanwhile, the inherent compact nature of graphite can keep plasmas sufficiently stable during laser ablation so as to effectively enhance the spectral stability. Thus, a high purity graphite target is an excellent candidate for high precision LIBS investigations.

Another method to create an optically thin and relatively homogeneous plasma is by coating a small amount of sample onto the high purity graphite target surface as evenly as possible. Nanoparticles obtained by the ashing method could be an attractive choice since their small sizes enable a thin and even coating on the surface. And the main contents including metal elements were kept while a lot of C, H and O elements were burned in the ashing process, which further reduce the line identifications. One can expect that only sample nanoparticles with a thickness of less than 1 μm would be stripped upon low-energy laser pulse ablation. Therefore, such a plasma would be dominated by content originating from the graphite target while only a very small amount of content is from the sample.

In this work, a high purity graphite target was chosen to improve the stability of plasmas and to investigate the feasibility and capacity in Nanoparticle Enhanced LIBS detection. A traditional Chinese medicinal material (CMM) was specially selected as the analytical sample because of its therapeutic effects [24–26]. Laser-induced breakdown spectroscopy based on the nanoparticle-coated graphite target (LIBS-NCGT) was studied from the fundamental and application points of view. Our aim is to develop an analytical procedure to promote analysis efficiency of elements contained in the CMM samples based on the high-purity graphite targets.

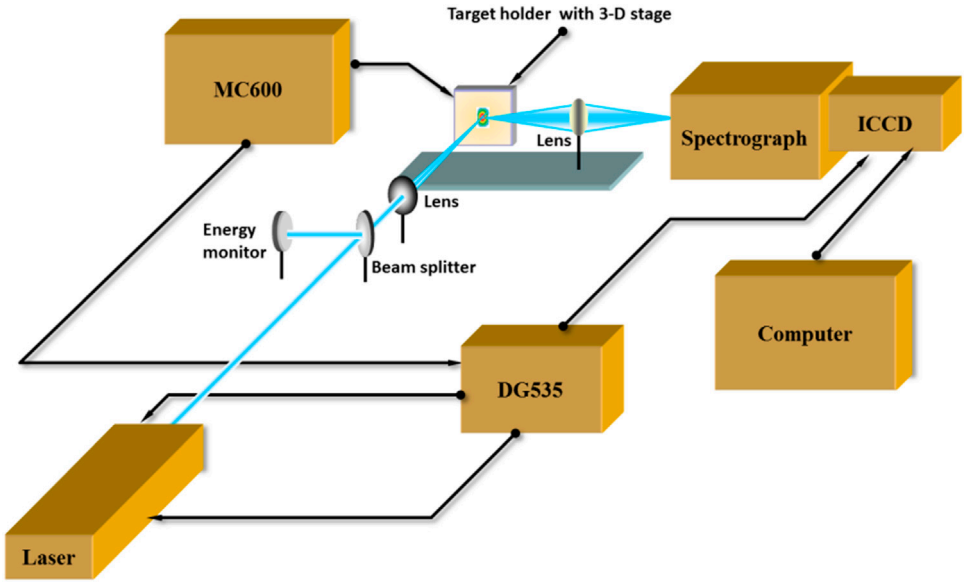

FIGURE 2 | Schematic of the experimental setup.

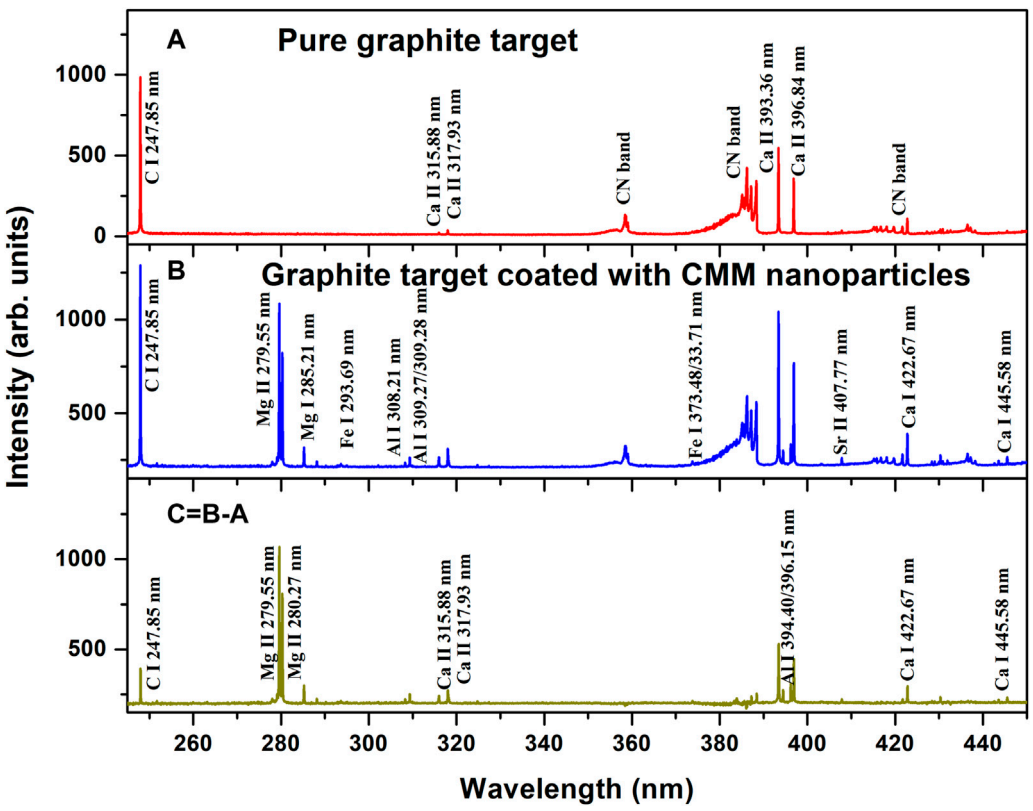

FIGURE 3 | LIBS spectra of the graphite target and the CMM NCGT. **(A)** Pure graphite target, **(B)** CMM NCGT sample, and **(C)** the result of **(B)**-**(A)**.

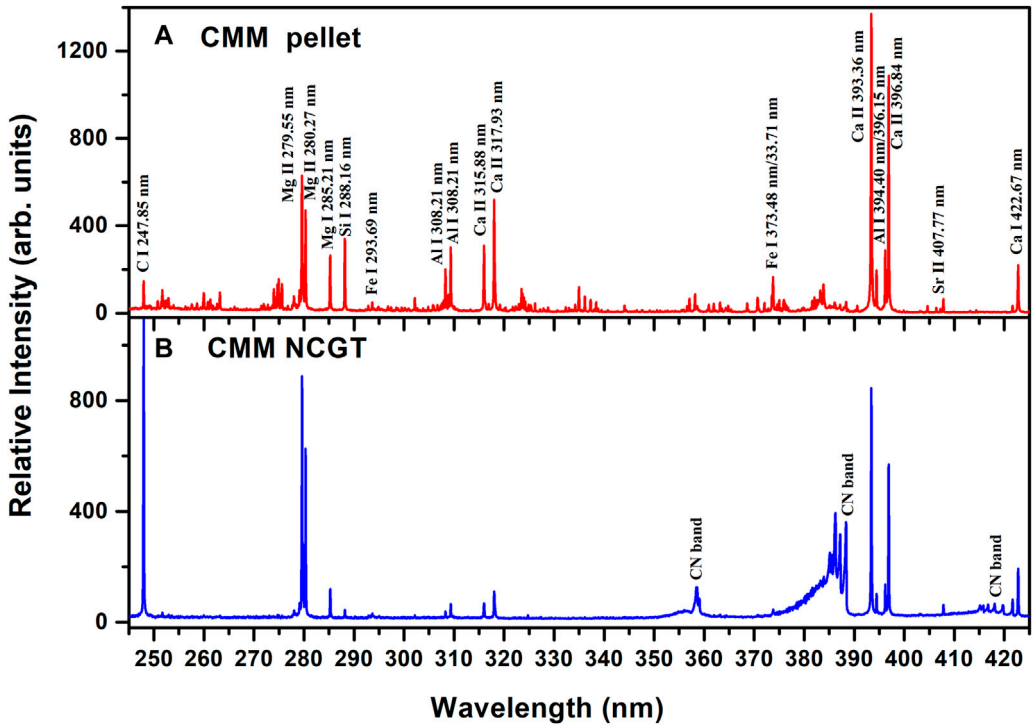

FIGURE 4 | LIBS spectra of the CMM pellet and the CMM NCGT sample. **(A)** CMM pellet and **(B)** CMM NCGT sample.

EXPERIMENTAL

Methods

A nanoparticle-coated graphite target (NCGT) was designed by coating sample nanoparticles onto a high purity graphite target surface, which was several microns in thickness and was sufficiently uniform in distribution. When a focused laser pulse ablates a target surface, a laser-induced breakdown plasma including massive graphite composition and trace sample composition will be produced. **Figure 1A** shows the diagram of dispersed particles from a laser-induced breakdown plasma. Here, the matrix effect of the graphite substrate is expected to be helpful to stabilize the plasma signal and reduce the interference of spectral lines. A uniformly distributed nanoparticle film coated on the graphite substrate can provide adequate sample species after ablation, and these species interact with carbon ions from graphite substrate in the plasma expansion so as to prominent the signals of sample composition.

Sample Target Preparation

A planar high-purity graphite (purity>99.999%) target was chosen as a substrate to carry the sample nanoparticles to be measured.

Codonopsis pilosula samples, produced in Ming County, Gansu, China, were prepared, which belongs to a perennial species of flowering plant in the bellflower family. Their root materials were chosen as sample and placed in an electric constant temperature drying box to dry for 40 min at 60°C, and were then transferred to an analytical grinding machine for grinding. These powders were filtered using a 300-mesh sieve. Powder samples (1.0 g) were weighed and then were pressed to pellet with a 20 mm diameter and a 2.5 mm thickness. Pellets of pure CMM were prepared for comparison.

Dry powder samples (5.0 g) were placed in a crucible and heated for 40 min, until the sample no longer released smoke, for regulated electric heating carbonization, and then placed into a muffle furnace to ash for 8 h at 600°C so that a white ash was produced after cooling in the muffle furnace.

The ash in the crucible was dissolved in analytical-grade ethanol, and then transferred to a 50 ml volumetric flask for ultrasonication for 60 min with an ultrasonic cleaning instrument (KQ-3200E) to produce a suspension.

Large numbers of nanoparticles having diameters of tens to several hundred nanometers were imaged with transmission electron microscopy (TEM), as shown in **Figure 1B**. The nanoparticle suspensions were uniformly coated on the graphite surface. After evaporation of the ethanol, the nanoparticles were evenly distributed on the graphite substrate. This was called the nanoparticle-coated graphite target (NCGT). **Figure 1C** shows the image of an ablated NCGT surface at the laser power density of 1.5×10^9 W/cm^2, the ablation had a diameter of 0.5 mm.

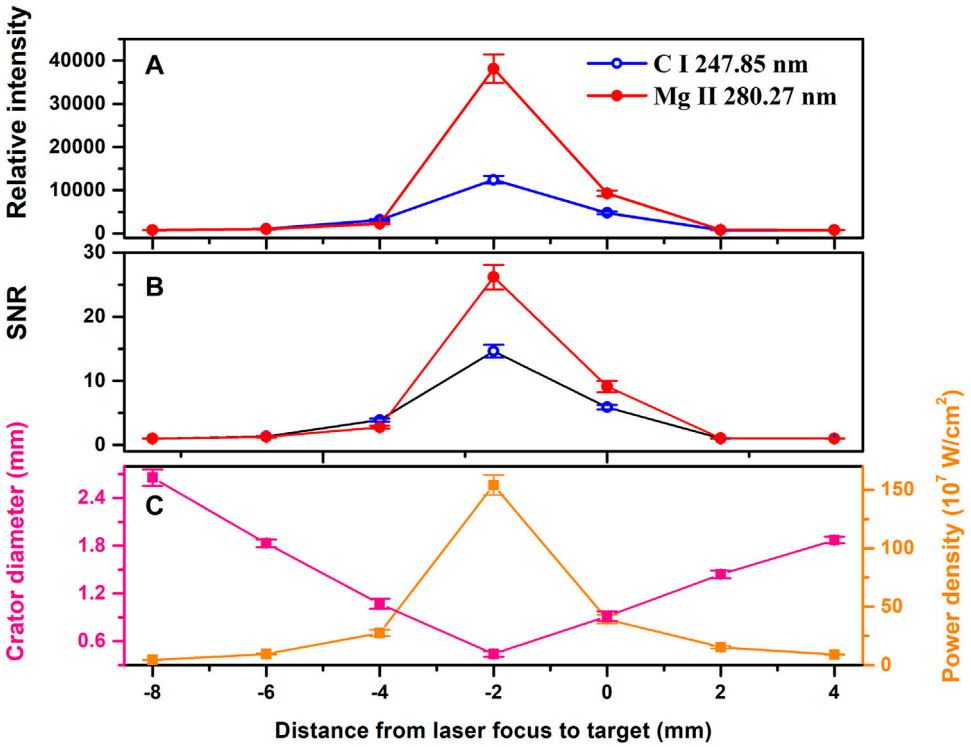

FIGURE 5 | Relative intensity, SNR, crater diameter, and power density as a function of the distance from the laser focus to the target. The time delay was 500 ns and the gate width was 200 ns **(A)** Relative intensity, **(B)** SNR, and **(C)** crater diameter and power density.

EXPERIMENTAL

A schematic of the experimental setup is shown in **Figure 2**. A 1064 nm Nd: YAG laser (PRO-350, Spectra-Physics) with a 10 ns pulse width, was used to produce plasmas when focused onto the planar NCGT surface. The target holder was positioned on a three-dimensional translation stage with a resolution of 0.1 mm to enable the presentation of a fresh area for each laser pulse. A lens positioned on a linear translation stage with the same resolution could be moved along the laser beam direction to adjust the focusing. The target and the lens can be moved simultaneously with the same step perpendicular to the normal of the target surface by controlling the translation stages. The space emission from the plasmas was collected with a quartz lens having a 50 mm focal-length onto the entrance slit of a spectrometer (Shamrock SR-500i, Andor technology) equipped with an intensified charge-coupled device (ICCD, iStar-DH734-18F-03, Andor technology). The spectral response of the intensity was calibrated using deuterium and tungsten halogen lamps (Aracight-D-CAL1205001). A digital delay generator (DG535, Stanford) was used to synchronize the laser pulse and the ICCD. Emissions from ten laser pulses were averaged for each measurement. The sample movement and spectral acquisition parameters were computer controlled and the experiments were performed in air at atmospheric pressure. To suppress background from the continuum plasma radiation and to enhance spectral stabilities, the experimental conditions were optimized step by step.

DISCUSSION

Comparison Between LIBS Spectra of Graphite Target and NCGT CMM Samples

Figures 3A,B plot LIBS spectra of the graphite target and CMM NCGT samples over the wavelength range of 245–450 nm, respectively, which were collected 1.5 mm from the target surface at a laser power density of 1.5×10^9 W/cm^2. The gate-width was 200 ns and the time delay were 500 ns It is clear that the spectral structure of the high purity graphite target in **Figure 3A** was very simple. In particular, there were no interference lines in the 250–357 nm range, except for two very weak Ca II lines at 315.88 and 317.93 nm. There were also three characteristic CN molecular bands around 358 nm, 388.36 nm, and 421 nm. Other peaks could easily be identified as Ca II lines at 393.36 and 396.84 nm, as well as Sr II lines at 407.77 nm. All of the lines were isolated and exhibited good resolution, with a maximum full width at half maximum (FWHM) of less than 0.11 nm. Finally, the rotational tail of the CN molecular band weakly interfered with these lines.

For CMM NCGT, new spectral lines in **Figure 3B** appeared at 279.55, 280.27, 285.21, 308.21, 309.27, 394.40, and

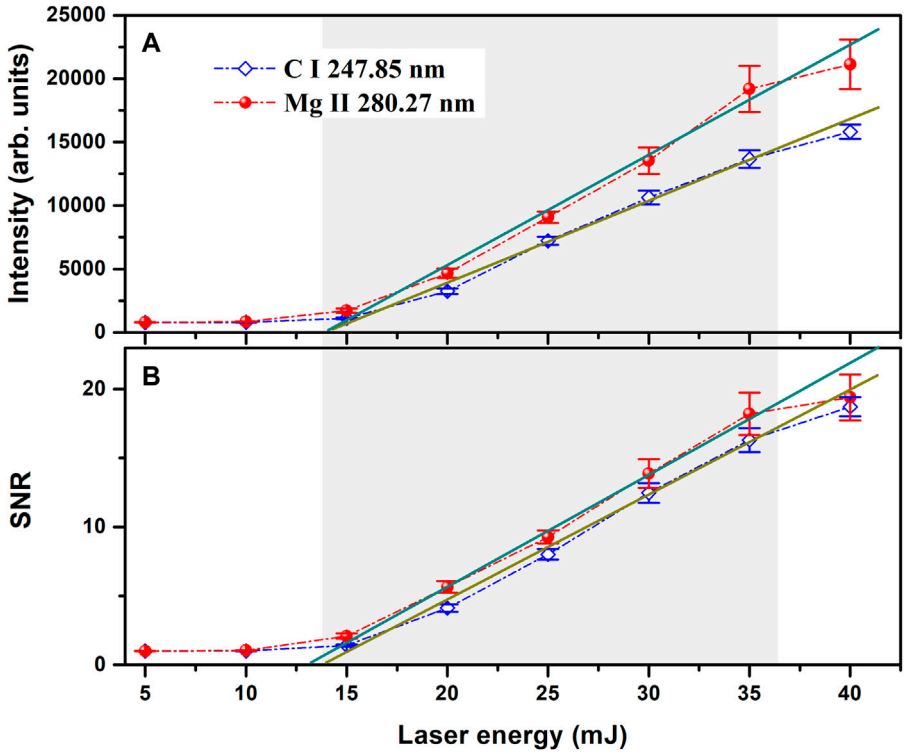

FIGURE 6 | Relative intensity and SNR as a function of laser energy. The time delay was 500 ns, and the gate width was 200 ns **(A)** Relative intensity, **(B)** SNR.

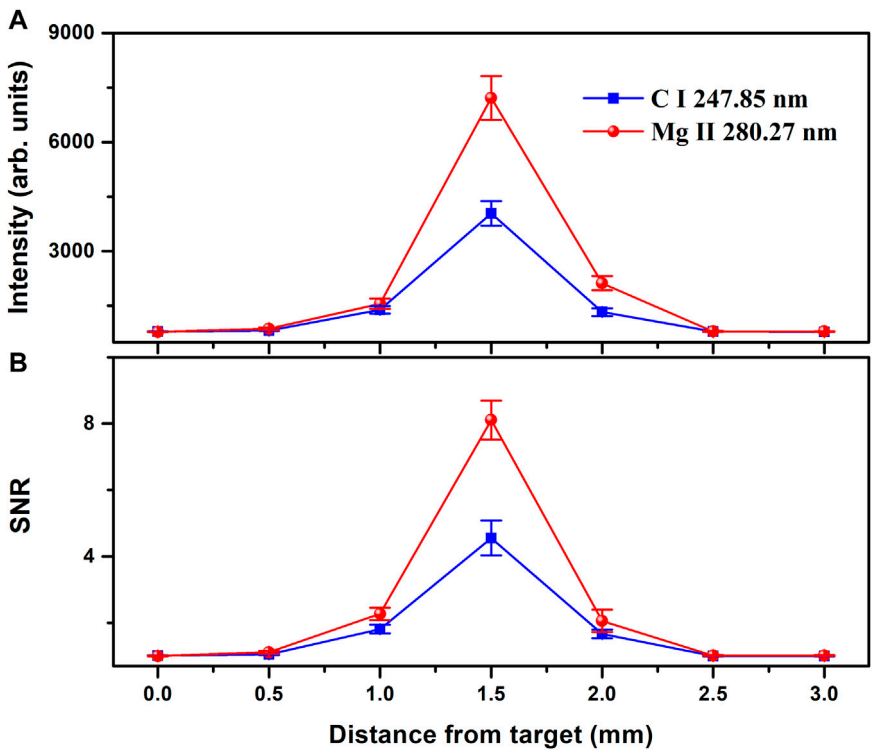

FIGURE 7 | Relative intensity and SNR as a function of detection distance from the target. **(A)** Relative intensity, **(B)** SNR.

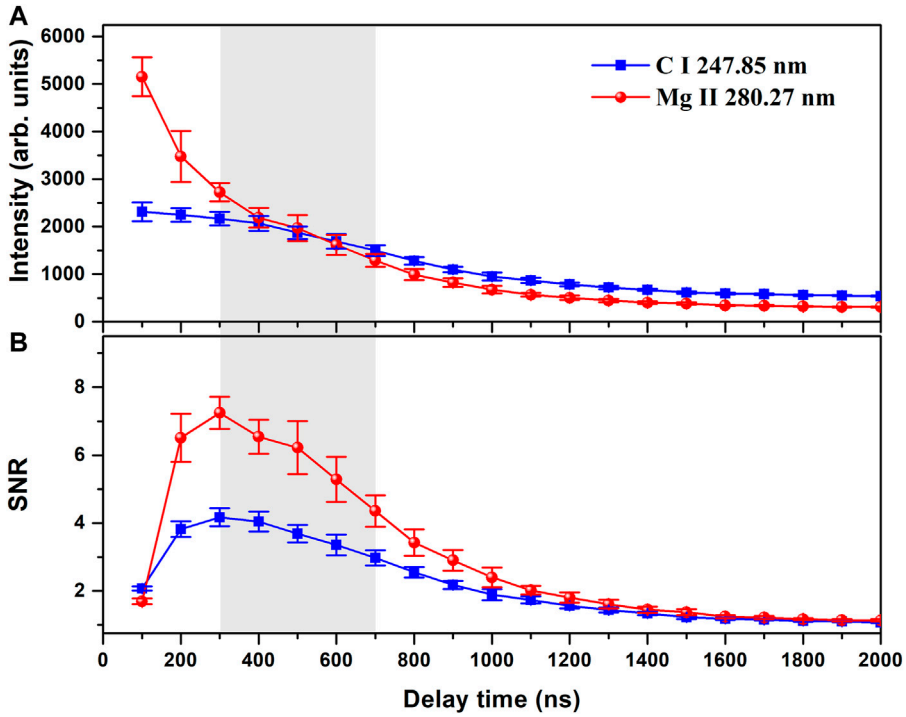

FIGURE 8 | (A) Relative intensity and **(B)**SNR as a function of delay time.

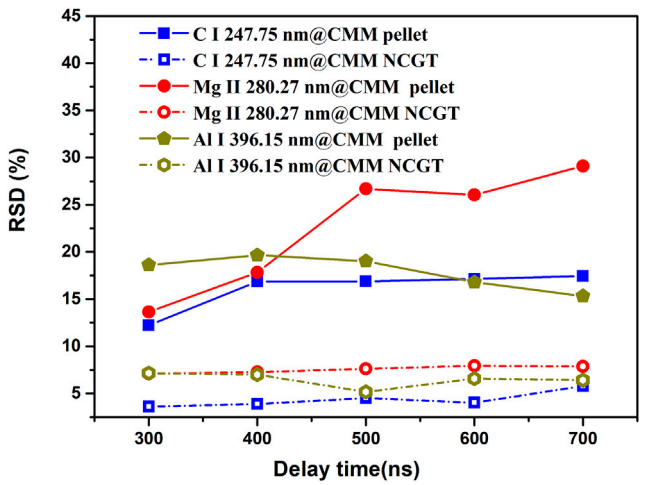

FIGURE 9 | Relative standard deviation as a function of delay time.

396.15 nm, Ca I 422.67 nm, Ca I 445.58 nm, which were respectively identified as Mg II, Al I, and Ca I. Some peaks were enhanced, such as the C I line at 247.85 nm, the Ca II lines at 315.88 and 317.93 nm, and the Ca II lines at 393.36 and 396.84 nm, as well as Sr I line at 407.77 nm. **Figure 3C** shows the result of subtracting spectrum (A) from spectrum (B). The result was contributions from the CMM sample; the graphite features in **Figure 3A** were weak, and the three CN molecular bands disappeared. This indicated that by this treatment, the spectra of Chinese herbal medicine nanoparticles can be obtained.

Figure 4A,B allow comparison between the LIBS spectra of pure CMM pellet and the graphite target coated with CMM nanoparticles, respectively. In **Figure 4A**, a total of 248 lines were identified as transitions of C I, Mg II, Si I, Fe I, Ca II, and Sr II ions, in addition to three weak CN bands. In **Figure 4B**, only 29 lines appeared, all of which were characteristic lines from ions mentioned above. Thus, they could be easily and rapidly identified.

Optimization of Conditions

Further optimization of the experimental conditions was very necessary for investigating the NCGT-LIBS detection capacity combined with the graphite substrate and nanoparticle homogeneity. Two analytical lines were selected. One was the C atomic line at 247.85 nm that represented the matrix nature of the graphite target, and the other was the sensitive Mg ionic line at 280.27 nm that represented the sample nanoparticles. Step-by-step optimization included the laser focusing, the laser energy, the detection position, and the time delay. The intensities and signal-to-noise ratios (SNRs) of the lines were used to evaluate the stabilities of the plasma signals and the degree of optimization.

Figure 5 shows the variation of the relative intensity, the SNR, diameter of the ablated crater, and the power density as a function of distance from laser focus to target. The movement range of the focus point was −8–4 mm from the target surface along the laser beam direction. The highest spectral intensity and SNR were at the −2 mm focus point. Here, the diameter of the ablated crater

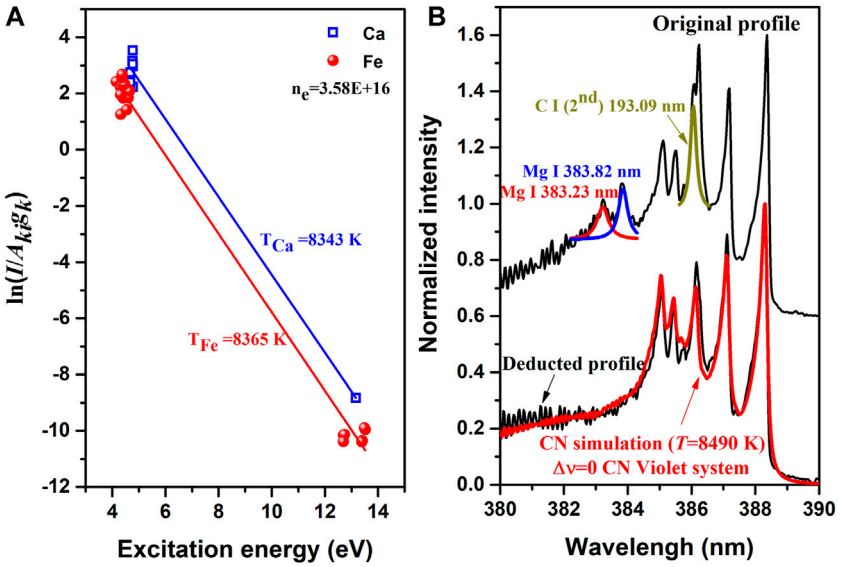

FIGURE 10 | Estimation of plasma parameters. **(A)** Saha-Boltzmann plots of Ca and Fe lines, and **(B)** Comparison between the electronic-transition spectra of CN violet bands in the 380–390 nm range and a simulated spectral profile at 8490 K using LIFBASE software.

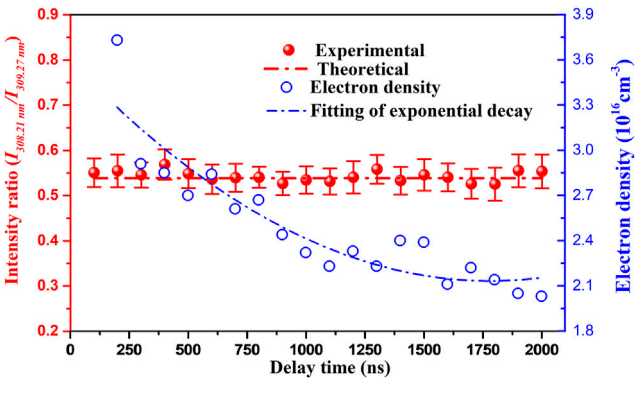

FIGURE 11 | Ratio of Al 308.21 nm to Al 309.27 nm intensities and the electron density as a function of delay time.

was approximately 0.3 mm, the laser power density was approximately 1.55 × 10^9 W/cm^2, and the corresponding laser energy was 25 mJ.

Under the optimized focusing conditions, line intensities as a function of laser energy were investigated. **Figures 6A,B** respectively plots the relative intensity and SNR values of the lines as a function of laser energy. Both increased with a near-linear trend over the range 15–35 mJ highlighted by the gray rectangular box in **Figure 6**. For clarity, the experimental data were linearly fitted, as displayed by the solid lines with correlation coefficients greater than 98%. When the laser energy was greater than 40 mJ, the intensity and SNR values became weaker because of instrument saturation. This indicated that the plasmas were optically thin, and with the increase of laser energy, the intensity of spectral lines increases linearly in the range 15–35 mJ. To ensure that weak signal was not lost and that strong signals were not saturated in the following optimizations, a laser energy of 25 mJ was used.

Figure 7 shows the relative intensity and the SNR at a laser energy of 25 mJ as a function of detection distance from the target. The space detection scale of the plasma was approximately 3 mm, and the best spectral signal and SNR values were obtained at 1.5 mm from the target surface. This value was thus fixed in the following optimization.

Figure 8 shows the (A) relative intensity and (B) SNR as a function of delay time. The spectral intensity rapidly decreased, while the SNR sharply increased initially with delay time, then gradually decreased down to 1 after 2 μs.

Figure 9 plots the relative standard deviation (RSD) of plasma signals for the CMM pellets and CMM NCGT samples for time delays in the range 300–700 ns RSD values of the C I and Mg II lines from the CMM NCGT samples were approximately three times lower than those from the CMM pellets, and were almost constant with increasing time delay. This indicated that the NCGT-LIBS method had good plasma stability for CMM LIBS investigations.

Diagnosis of Plasma Parameters

To investigate the physical property of the plasma based on graphite target coated CMM nanoparticles, the electron density and temperature were determined. The electron density was determined using the Stark broadening method [27]. Specifically, the Ca II line at 396.84 nm was used because of its sensitivity to Stark broadening. The line FWHM was determined by Lorentz fitting, and the electron density was estimated to be 3.58×10^{16} cm^{-3}. The plasma temperature was first deduced using the Saha-Boltzmann plot method [29]. Atomic and ionic lines of Ca and Fe were used to increase the precision of the temperature. **Figure 10A** shows Saha-Boltzmann plots of the two elements. The average plasma

temperature was approximately 8354 K. To check this value, **Figure 10B** shows the comparison between the acquired spectra of electronic-transitions in the CN violet band over the 380–390 nm range, along with a simulated spectrum at 8490 K using LIFBASE software [28]. The software can be used to generate simulated spectra across a broad temperature range at 100 K temperature increments using the Vogit profiles and a spectrometer resolution of 0.05 nm. The black solid line in the lower part of the figure is the result after deducting the contributions of emission lines of Mg I 383.82 nm, Mg I 383.23 nm and a second order emission C I line at 193.09 nm. The result indicated that the intensities across the simulated spectrum matched very well with the deducted experimental profile. Thus, reasonable temperature fits were obtained.

Optical Thickness

For intense atomic lines, such as some carbon and sodium lines from plant materials, self-absorption cannot be neglected. In this case, the approximation of an optically thin plasma is not applicable. Also, calibration-free LIBS (CF-LIBS) becomes invalid. CF-LIBS allows one to overcome the matrix effect by taking into account the plasma temperature and electron number density, as discussed by Ciucci *et al* [30]. However, when the sample nanoparticles are coated on a high-purity graphite substrate, the concentration of the analytes is much lower. Thus, self-absorption could be neglected, as confirmed in the following section.

Due to self-absorption, the intensity of an emission line is lower than that observed in an optically thin condition. Assuming an optically thin plasma and a local thermodynamic equilibrium (LTE) during signal acquisition, the measured integral line intensity [31]:

$$I_{\lambda}^{ki} = \frac{hc}{4\pi\lambda_{ki}} A_{ki} L N \frac{g_k}{U_s(T)} \exp\left(-\frac{E_k}{K_B T}\right) \tag{1}$$

where I_{λ}^{ki} is the intensity of a transition between two energy levels E_k and E_i, h is Planck's constant, c is the speed of light, λ is the transition wavelength, A_{ki} is the transition probability, L is the characteristic length of the plasma, N is the number density, g_k is the degeneracy, $U_s(T)$ is the partition function for the emitting species, k_B is Boltzmann's constant and T is the plasma temperature. For optically thin conditions, the theoretical doublet line intensity ratio of the same species can be expressed as:

$$\frac{I_1}{I_2} = \left(\frac{\lambda_{nm,Z}}{\lambda_{ki,Z}}\right)\left(\frac{A_{ki,Z}}{A_{nm,Z}}\right)\left(\frac{g_{k,Z}}{g_{n,Z}}\right) \exp\left(-\frac{E_{k,Z} - E_{n,Z}}{K_B T}\right) \tag{2}$$

For two emission lines having the same upper level (or as close as possible), the temperature effect of the Boltzmann factor on the reproducibility of the line intensity ratio is minimized. By neglecting the exponential factor under this condition, one can determine the theoretical value of the intensity ratio of the doublet lines by using the inherent atomic parameters of the transitions, which are independent of the experimental parameters. The doublet lines have similar energy level structures and close wavelengths, and their intensities are maximized. Here, the Al I lines at 308.21 and 309.27 nm were used to determine whether the plasmas from the CMM NCGT were optically thin. **Figure 11** shows the ratio of 308.21–309.27 nm line intensities as a function of the time delay. The line-dot-line represented the ratio of the theoretical transition probabilities, the red circles represent the experimental results, and the error bars represent the RSD of ten duplicate measurements. The experimental and theoretical results were in good agreement within the experimental error range over the entire plasma decay time. In addition, the electron number density at different delay times is also plotted in **Figure 11**. According to the McWhirter criteria [32], this density was sufficient to maintain the plasma in a LTE.

CONCLUSION

High-purity graphite targets are considered to be an ideal matrix for nanoparticle-enhanced LIBS due to their simple spectral structure. Chinese herbal medicine nanoparticles coated on high-purity graphite targets to study the feasibility and capacity. Under optimized experimental conditions, a stable, relatively homogeneous, and approximately optically thin laser-induced breakdown plasma is used to diagnosis the parameters of plasma. Line identifications were greatly simplified and a large improvement in spectral stability was obtained.

DATA AVAILABILITY STATEMENT

Publicly available datasets were analyzed in this study. This data can be found here: https://physics.nist.gov/PhysRefData/ASD/lines_form.html.

AUTHOR CONTRIBUTIONS

WH, DS and MS contributed to the proposition of ideas and experimental design of this study; WH and YW performed the Experimental operation and data processing; WH, DS and MS jointly wrote the article; XL and YY helped perform the general analysis with constructive discussions.

FUNDING

This work is supported by the National Natural Science Foundation of China (Grant Nos.61965015,11564037,61741513and11864036), the Special Fund Project for Guiding Scientific and Technological Innovation of Gansu Province (Grant No. 2019zx-10), Young Teachers Scientific Research Ability Promotion Plan of Northwest Normal University (Grant No. NWNU-LKQN2019-1), and Lanzhou Talent Innovation and Entrepreneurship Project (Grant No. 2020-RC-143).

REFERENCES

1. Yi R, Li J, Yang X, Zhou R, Yu H, Hao Z, et al. Spectral Interference Elimination in Soil Analysis Using Laser-Induced Breakdown Spectroscopy Assisted by Laser-Induced Fluorescence. *Anal Chem* (2017) 89:2334–7. doi:10.1021/acs.analchem.6b03969
2. Cahoon EM, Almirall JR. Quantitative Analysis of Liquids from Aerosols and Microdrops Using Laser Induced Breakdown Spectroscopy. *Anal Chem* (2012) 84:2239–44. doi:10.1021/ac202834j
3. Tsai S-JJ, Chen S-Y, Chung Y-S, Tseng P-C. Spatially Resolved, Laser-Induced Breakdown Spectroscopy, Development, and Application for the Analysis of Al and Si in Nickel-Based Alloys. *Anal Chem* (2006) 78:7432–9. doi:10.1021/ac060749d
4. Liu X, Qiao S, Ma Y. Highly Sensitive Methane Detection Based on Light-Induced Thermoelastic Spectroscopy with a 2.33 Mm Diode Laser and Adaptive Savitzky-Golay Filtering. *Opt Express* (2022) 30:1304–13. doi:10.1364/OE.446294
5. Ma Y, Hong Y, Qiao S, Lang Z, Liu X. H-shaped Acoustic Micro-resonator-based Quartz-Enhanced Photoacoustic Spectroscopy. *Opt Lett* (2022) 47:601–4. doi:10.1364/OL.449822
6. Liu X, Ma Y. Sensitive Carbon Monoxide Detection Based on Light-Induced Thermoelastic Spectroscopy with a Fiber-Coupled Multipass Cell [Invited]. *Chin Opt Lett.* (2022) 20:031201. doi:10.3788/COL202220.031201
7. Ma Y, Hu Y, Qiao S, Lang Z, Liu X, He Y, et al. Quartz Tuning forks Resonance Frequency Matching for Laser Spectroscopy Sensing. *Photoacoustics* (2022) 25:100329. doi:10.1016/j.pacs.2022.100329
8. Hohreiter V, Ball AJ, Hahn DW. Effects of Aerosols and Laser Cavity Seeding on Spectral and Temporal Stability of Laser-Induced Plasmas: Applications to LIBS. *J Anal Spectrom* (2004) 19:1289–94. doi:10.1039/b402190h
9. Sun D-X, Su M-G, Dong C-Z. Emission Signal Enhancement and Plasma Diagnostics Using Collinear Double Pulse for Laser-Induced Breakdown Spectroscopy of Aluminum Alloys. *Eur Phys J Appl Phys* (2013) 61:30802. doi:10.1051/epjap/2013120470
10. Li L, Wang Z, Yuan T, Hou Z, Li Z, Ni W. A Simplified Spectrum Standardization Method for Laser-Induced Breakdown Spectroscopy Measurements. *J Anal Spectrom* (2011) 26:2274–80. doi:10.1039/c1ja10194c
11. Hou ZY, Wang Z, Lui SL, et al. Improving data stability and prediction accuracy in laser-induced breakdown spectroscopy by utilizing a combined atomic and ionic line algorithm. *J Anal Spectrom* (2013) 28(1):107–13. doi:10.1039/C2JA30104K
12. Han W, Su M, Sun D, Yin Y, Wang Y, Gao C, et al. Analysis of Metallic Elements Dissolution in the Astragalus at Different Decocting Time by Using LIBS Technique. *Plasma Sci Technol* (2020) 22:085501. doi:10.1088/2058-6272/ab861b
13. Babushok VI, DeLucia FC, Jr, Gottfried JL, Munson CA, Miziolek AW. Double Pulse Laser Ablation and Plasma: Laser Induced Breakdown Spectroscopy Signal Enhancement. *Spectrochimica Acta B: At Spectrosc* (2006) 61:999–1014. doi:10.1016/j.sab.2006.09.003
14. Xiong G, Li S, Tse SD. Tuning Excitation Laser Wavelength for Secondary Resonance in Low-Intensity Phase-Selective Laser-Induced Breakdown Spectroscopy for *In-Situ* Analytical Measurement of Nanoaerosols. *Spectrochimica Acta Part B: At Spectrosc* (2018) 140:13–21. doi:10.1016/j.sab.2017.11.013
15. Harilal SS, Tillack MS, O'Shay B, Bindhu CV, Najmabadi F. Confinement and Dynamics of Laser-Produced Plasma Expanding across a Transverse Magnetic Field. *Phys Rev E* (2004) 69:0264132. doi:10.1103/PhysRevE.69.026413
16. Robledo-Martinez A, Sobral H, Garcia-Villarreal A. Effect of Applied Voltage and Inter-pulse Delay in Spark-Assisted LIBS. *Spectrochimica Acta Part B: At Spectrosc* (2018) 144:7–14. doi:10.1016/j.sab.2018.03.002
17. Dell'Aglio M, Alrifai R, De Giacomo A. Nanoparticle Enhanced Laser Induced Breakdown Spectroscopy (NELIBS), a First Review. *Spectrochimica Acta Part B: At Spectrosc* (2018) 148:105–12. doi:10.1016/j.sab.2018.06.008
18. Popov AM, Colao F, Fantoni R. Enhancement of LIBS Signal by Spatially Confining the Laser-Induced Plasma. *J Anal Spectrom* (2009) 24:602–4. doi:10.1039/b818849a
19. Hou J, Zhang L, Yin W, Zhao Y, Ma W, Dong L, et al. Investigation on Spatial Distribution of Optically Thin Condition in Laser-Induced Aluminum Plasma and its Relationship with Temporal Evolution of Plasma Characteristics. *J Anal Spectrom* (2017) 32:1519–26. doi:10.1039/c7ja00175d
20. Zhou B, Kane TJ, Dixon GJ, Byer RL. Efficient, Frequency-Stable Laser-Diode-Pumped Nd:YAG Laser. *Opt Lett* (1985) 10:62. doi:10.1364/OL.10.000062
21. Cao SQ, Su MG, Min Q, Sun DX, O'Sullivan G, Dong CZ. Spatio-temporally Resolved Spectral Measurements of Laser-Produced Plasma and Semiautomated Spectral Measurement-Control and Analysis Software. *Phys Plasmas* (2018) 25:023304. doi:10.1063/1.5016361
22. Yao S, Zhao J, Xu J, Lu Z, Lu J. Optimizing the Binder Percentage to Reduce Matrix Effects for the LIBS Analysis of Carbon in Coal. *J Anal Spectrom* (2017) 32:766–72. doi:10.1039/C6JA00458J
23. Winefordner JD, Gornushkin IB, Correll T, Gibb E, Smith BW, Omenetto N. Comparing Several Atomic Spectrometric Methods to the Super Stars: Special Emphasis on Laser Induced Breakdown Spectrometry, LIBS, a Future Super star. *J Anal Spectrom* (2004) 19:1061–83. doi:10.1039/b400355c
24. Wang Y, Su M, Sun D, Wu C, Zhang X, Lu Q, et al. Comparative Study of Magnesium and Calcium in Codonopsis Pilosula Samples Detected by CF-LIBS and LCGD-AES. *Microchemical J* (2018) 137:318–23. doi:10.1016/j.microc.2017.11.011
25. Shi J, Cao B, Wang X-W, Aa J-Y, Duan J-A, Zhu X-X, et al. Metabolomics and its Application to the Evaluation of the Efficacy and Toxicity of Traditional Chinese Herb Medicines. *J Chromatogr B* (2016) 1026:204–16. doi:10.1016/j.jchromb.2015.10.014
26. Chan K. Chinese Medicinal Materials and Their Interface with Western Medical Concepts. *J ethnopharmacology* (2005) 96:1–18. doi:10.1016/j.jep.2004.09.019
27. Qian M, Ren C, Wang D, Zhang J, Wei G. Stark Broadening Measurement of the Electron Density in an Atmospheric Pressure Argon Plasma Jet with Double-Power Electrodes. *J Appl Phys* (2010) 107:063303. doi:10.1063/1.3330717
28. Aguilera JA, Aragón C. Multi-element Saha-Boltzmann and Boltzmann Plots in Laser-Induced Plasmas. *Spectrochimica Acta Part B: At Spectrosc* (2007) 62:378–85. doi:10.1016/j.sab.2007.03.024
29. Luque J. LIFBASE: Database and Spectral Simulation Progrm (Versional. 6). SRI Report MP 99-.009 1999.(2021) Available at: http://www.kinetics.nsc.ru/chichinin/databases/Lifbase.pdf.
30. Ciucci A, Corsi M, Palleschi V, Rastelli S, Salvetti A, Tognoni E. New Procedure for Quantitative Elemental Analysis by Laser-Induced Plasma Spectroscopy. *Appl Spectrosc* (1999) 53:960–4. doi:10.1366/0003702991947612
31. Cowan RD, Kim YK. The Theory of Atomic Structure and Spectra. *Phys Today* (1982) 35:57. doi:10.1063/1.2915135
32. Huddlestone RH, Leonard SL, Furth HP. Plasma Diagnostic Techniques. *Phys Today* (1966) 19:94–5. doi:10.1063/1.3048484

Conflict of Interest: The authors declare that the research was conducted in the absence of any commercial or financial relationships that could be construed as a potential conflict of interest.

frontiers in Physics

ORIGINAL RESEARCH
published: 11 March 2022
doi: 10.3389/fphy.2022.847036

In Situ Study of Cave 98 Murals on Dunhuang Grottoes Using Portable Laser-Induced Breakdown Spectroscopy

Yaopeng Yin[1†], Zongren Yu[1†], Duixiong Sun[2†], Zhongwei Shan[1], Qiang Cui[1], Yiming Zhang[2], Yaqi Feng[1], Biwen Shui[1], Zhuo Wang[1], Zhiyuan Yin[1], Bolong Chai[1], Wenyuan Zhang[1], Chenzhong Dong[2] and Bomin Su[1*]*

[1]National Research Center for Conservation of Ancient Wall Paintings and Earthen Sites, Dunhuang, China, [2]Key Laboratory of Atomic and Molecular Physics and Functional Materials of Gansu Province, College of Physics and Electronic Engineering, Northwest Normal University, Lanzhou, China

The investigation of painted layers on murals at Cave 98 from Dunhuang Grottoes was carried out *in situ* using portable laser-induced breakdown spectroscopy (LIBS) for the first time. The ablation effect of laser pulses on a mural surface was evaluated under fixed experimental parameters, and the results showed that the influence of laser ablation on ancient murals was acceptable. Then the pigments used in the red, green, and blue layers were indicated with the LIBS spectral data of the corresponding color coupled with a classifiable model of pigments based on the principal component analysis (PCA) method. Finally, the depth profiling of the multilayer structure composed with overlapped painted layers was determined based on the pigment size information of the superficial green layer and the relationship of laser shots and ablation depth, and the thickness of the superficial green layer was analyzed quantitatively, which fits well with the result of the cross-sectional analysis. Therefore, this work can shed light on the great potential for ancient mural applications in LIBS.

Keywords: Mogao Grottoes, Dunhuang murals, portable LIBS, *in situ* analysis, painted layers

OPEN ACCESS

Edited by:
Yufei Ma,
Harbin Institute of Technology, China

Reviewed by:
Mingyin Yao,
Jiangxi Agricultural University, China
Hongbin Ding,
Dalian University of Technology, China

***Correspondence:**
Zongren Yu
13588975@qq.com
Bomin Su
suboming@hotmail.com

†These authors have contributed equally to this work

Specialty section:
This article was submitted to Optics and Photonics, a section of the journal Frontiers in Physics

Received: *01 January 2022*
Accepted: *25 January 2022*
Published: *11 March 2022*

Citation:
Yin Y, Yu Z, Sun D, Shan Z, Cui Q, Zhang Y, Feng Y, Shui B, Wang Z, Yin Z, Chai B, Zhang W, Dong C and Su B (2022) In Situ Study of Cave 98 Murals on Dunhuang Grottoes Using Portable Laser-Induced Breakdown Spectroscopy. Front. Phys. 10:847036. doi: 10.3389/fphy.2022.847036

INTRODUCTION

As an important artistic crystallization of various cultural integrations on the ancient Silk Road, the Mogao Grottoes is the largest, oldest, and the best-preserved Buddhist grottoes with the richest contents in the world today, so it is also named "Library on the Wall" because it carries vast historical, cultural, and scientific information. The UNESCO World Heritage Site (inscribed the List in 1987) contains 735 caves excavated into the 1.6 km of cliff face, encompassing approximately 45,000 m^2 of chromatic murals and more than 2,000 painted sculptures [1].

The Mogao Grottoes is famous for its massive chromatic murals as shown in **Figure 1**, which were drawn using all kinds of colorful mineral pigments on dry ground according to the secco technique [2]. However, these precious murals are suffering from damage due to the influence of air, light, humidity in grottoes, and human factors over a long time period [3]. The composition information of mineral pigments used on painted layers is the basis for revealing reasons for these different types of damage, such as flaking, detachment, net cracking, and paint loss; therefore, it can provide guidance for selecting the most appropriate materials and conservation methods, along with determination of

FIGURE 1 | Photograph of Mogao Grottoes and typical ancient murals in these caves.

suitable processes for possible restoration of the paintings. On the other hand, the information can give a rich source of exchanges involved and cultural trade development from the perspective of scientific investigations of ancient murals made from different pigments. Therefore, pigment research on Dunhuang ancient murals has become a focus of great concern.

With the development of laser technology, the laser measurement techniques have attracted a considerable amount of research in the area due to its technical features, such as high sensitivity, noninvasive, and *in situ* [4–7]. Laser-induced breakdown spectroscopy (LIBS) technology has great application potential in the field of cultural heritage analysis with the advantages of rapid, multi-element analysis, no sampling, minimal damage, and *in situ* analysis [8–10], which meet the strict requirements for cultural objects. Based on the contribution significantly from ongoing advances in laser, spectrometer, and detector technologies, the development of several mobile LIBS instruments provides a lot of opportunities for analytical campaigns on site, such as at museums, conservation laboratories and even outdoors at excavation sites [11, 12]. In a different investigation, several Minoan bronze-age artifacts such as beads, vessels, and decorative plaques and figurines made of faience were analyzed by mobile LIBS [13]. The main objective of different types of stones, which are the main construction materials in this class of historical buildings, was qualitatively discriminated among sandstone, limestone, and cement mortar [14–19]. An interesting analysis has enabled the identification of the main minerals present in several building stones using a compact system based on a stand-off LIBS sensor [20]. The objectives of jewelry [21], glass artifacts [22], ceramics, and pottery [23, 24] were investigated using LIBS technique. In some different studies with a similar objective, painting [25, 26], pigments on illuminated manuscripts [27] simulated murals [28], and wall painting fragments [29, 30] were carried out a quick survey utilizing the compact portable LIBS system. In fact, ancient murals are types of art painted on the wall around caves, which resulted in these immovable murals being not permitted to be taken to the laboratory for analysis, so the portable LIBS system was regarded as a useful tool to carry out painted layer research of murals *in situ* and real time in Mogao Caves.

Therefore, in this work, a portable LIBS was used to analyze the information of mural painted layers on-site in a cave for the first time. For this study, the murals on the south wall of Cave 98 were chosen to be analyzed; the analytical area is approximately 1.8 m^2 (about 2.0 m × 0.9 m). The laser ablation on the mural was illustrated using optical microscope. Based on our previous experimental results, the different types of pigments were indicated and classified by combing the LIBS spectrum with a classifiable model. Furthermore, the depth profile of overlap painted layers was revealed, and the thickness of these layers was also analyzed in Cave 98.

EXPERIMENTAL APPROACH AND MURAL SAMPLES

Portable Laser-Induced Breakdown Spectroscopy Apparatus

The schematic and imaging of the portable LIBS setup are presented in **Figure 2**. In our studies, all spectrum data were obtained using the portable *LIBSCAN 100 ULTRA*, which offers a highly versatile, adaptable, and upgradeable product suitable for use either in a laboratory environment or in the field. The main components of the *LIBSCAN 100 ULTRA* are the LIBSCAN 100 console and LIBSCAN head [31].

The LIBSCAN 100 console contains the optical spectrometers with eight channels and electrical circuits for the laser safety interlock. The detection spectra were collected within the wavelength range from 200 to 800 nm, with a maximum

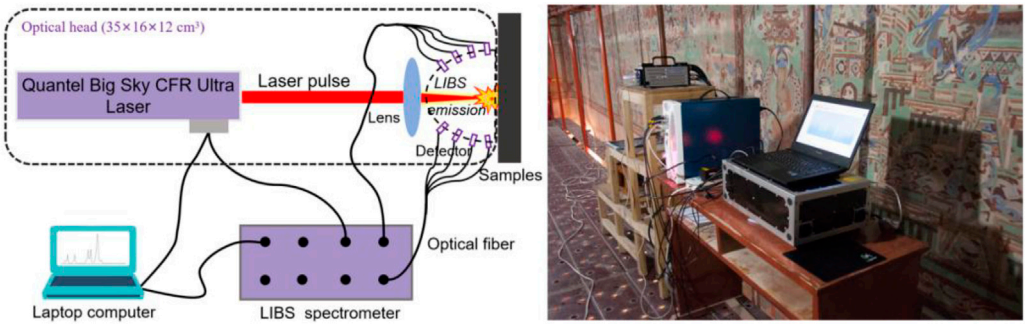

FIGURE 2 | Schematic and imaging of the portable laser-induced breakdown spectroscopy (LIBS) setup.

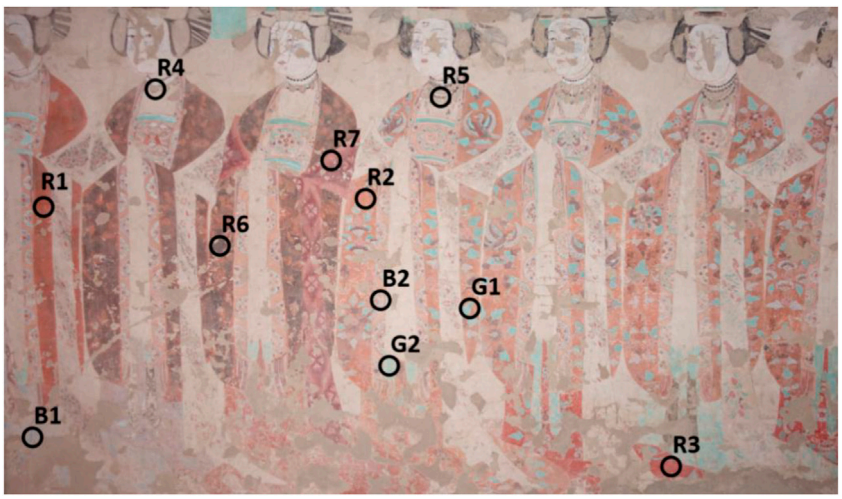

FIGURE 3 | Areas of ancient murals in the south wall of Cave 98 about 2.0 m × 0.9 m.

resolution of 0.07 nm in the range of 410 and 500 nm. The LIBS spectra were recorded with a delay time of 1,800 ns and a gate width of 3,000 ns with respect to the laser pulse.

The LIBSCAN head contains the laser and associated optics required to focus the laser beam onto a sample, and the plasma light was collected for transmission to the spectrometers located within the LIBSCAN 100 console. The head is designed to accommodate a miniature CCD camera, and associated components are used with the optional imaging kit. A Quantel Big Sky CFR Ultra GRM and ICE 450 cooling group was used to produce laser light at 1,064 nm, generating 7-ns pulses, laser pulse energy up to 100 mJ, repetition rate of 1–10 Hz, and in a 6.5 mm diameter beam.

Mural Samples

Mogao Cave 98 is located on the first floor of the southern section of the South District. The cave was built in about 925 AD by a governor of the Return-to-Allegiance Army named Cao Yijin. There are about 693.1 m^2 murals on wall around the cave. The outstanding feature of murals in the cave is that a large number of donor images were presented in the areas under the chamber wall, as shown in **Figure 3**.

There are 223 visible donor images included according to statistical survey, and the species of pigments used in these areas are particularly abundant, the red with different tones, and green, white, and blue are all existing in these areas. So, the female donor images in the south wall of Cave 98 were chosen to be analyzed. In our current studies, the red, blue, and green mineral pigments were selected to be investigated using LIBS. The test locations are illustrated in **Figure 3** indicated by black circles.

RESULTS AND DISCUSSIONS

Laser Ablation Effect

Considering that a small amount of material is removed involving the laser ablated on the sample surface in an LIBS measurement (mass removal about a few nanograms), so the LIBS is termed as a microdestructive technique. Therefore, it is necessary to analyze the influence of laser ablation on the surface ancient murals *in*

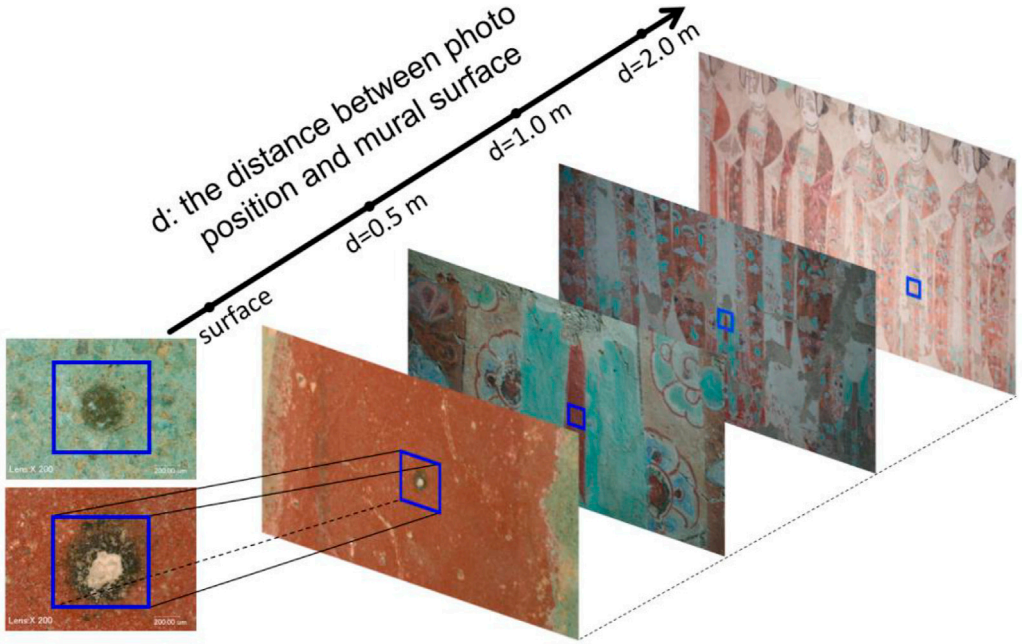

FIGURE 4 | Photographs of laser-ablated area after five laser pulses on the same spot at different distances from the surface.

situ before carrying out measurements. It is notable that the energy of the laser pulse was fixed at 10 mJ according to the study of laser ablation, which prevents excessive damage to the murals [26].

Under the optimized experimental parameters, the laser-ablated areas in red- and green-painted layers were visualized by digital photographs and images of optical microscopy. **Figure 4** presents photographs of the laser ablated area after five laser pulses ablated on the same spot, and these pictures were taken at different distances from the mural surface. As shown in **Figure 4**, the values of d indicate the distances from camera to mural surface, for example, $d = 0.5$ m meant that the picture was recorded at the location of 0.5 m from the surface. The picture at the position of $d = 0.5$ m is a key reference to evaluate the effect of laser ablation because most visitors and researchers are prohibited from going into this range [32]. From the picture, the trace left on the object surface is hardly visible with the naked eye, so the laser-ablated crater cannot be observed outside of this distance range at all. So, the minor damage was regarded as acceptable and agreed on from the perspective of appreciation of ancient murals.

From the images of optical microscopy, which were taken at 200× magnification, there are obvious differences in laser-ablated areas between red and green layers. As can be seen from **Figure 4**, the ablation effect in the green and red layer is different due to the various physicochemical properties of the two kinds of mineral pigments, that is, the red-painted layer was not penetrated after laser ablation under the fixed parameters; only the discoloration was observed on the red layer, so, the ablation area is defined as the range of black area. However, the green layer was penetrated with the same laser ablation; in fact, the ablation area was divided into two different parts, the penetrated area located inside the area caused the Gaussian profile laser and the discoloration area caused by the thermal effect with laser ablation. It is clear that the diameter values of ablated areas are 246 ± 11 and 272 ± 25 μm on the green and red layers, respectively. It is notable that the range of ablation area on the green layer is indicated as the penetrated area. Actually, the color in the region of the laser ablation has become black in the green-painted layer, the laser ablation area in the red layer penetrated in the center, and the edge range of the ablation crater started to turn in color from red to black in the diameter range of 655 ± 50 μm. Furthermore, the edge morphology of the ablated crater was analyzed, and the microscopy pictures showed that the interaction of laser pulse and painted layers did not cause significant changes in the depth profile structure of the painted layer. This meant that the effect of laser ablation on the stability of ancient murals was negligible.

Based on the above statement, the portable LIBS technique was, therefore, feasible in the field of mural pigment analysis from the views of mural appreciation and stability of painted layers.

Pigments Indication and Classification

Most of the pigments used in Dunhuang murals were manufactured from colored mineral materials, such as red pigments of cinnabar, red lead, and hematite, green pigments of malachite and atacamite, and blue pigments of lapis lazuli and azurite. In order to obtain stable spectral data and improve the accuracy of the measurement on mural-painted layers with different colors, the average method of cumulative pulse ablation was employed to weaken the impact of sample surface irregularities on spectral fluctuation. The cumulative number means that one single shot ablated on a fresh location

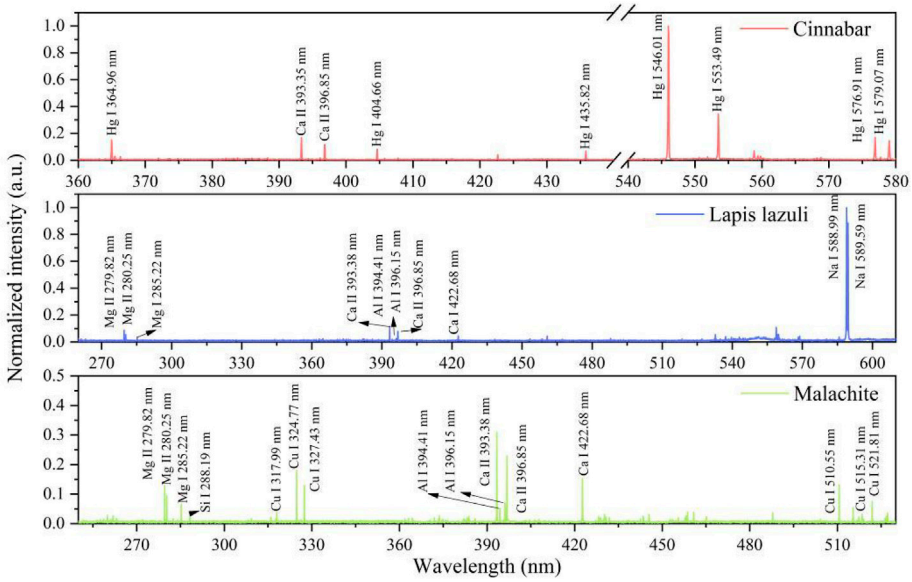

FIGURE 5 | Stable LIBS spectra of cinnabar, lapis lazuli, and malachite pigments.

and different locations were used to acquire the average spectra; the value of the cumulative number was fixed as 10 to obtain the stable spectra in this part work. The stable LIBS spectra of the three typical types of pigments are presented in **Figure 5**. In order to compensate for spectral signal changes due to matrix effects and influence in experimental conditions, the intensities of these two selected lines subtracted the values of background signals and then were normalized by using the min–max normalization method. As can be seen from the figure, the LIBS spectra of various color pigments were different and were shown to be dominated by several characterized elements, including Hg and Ca in red cinnabar, Mg, Al, Ca, and Na in blue lapis lazuli, Fe, Cu, Mg, and Ca in green malachite pigment, with the use of spectroscopic data from the National Institute of Standards and Technology (NIST) Atomic Spectra Database (ASD) [33]. From the figure, it is also found that the quality of the LIBS spectra is excellent and the signal-to-noise, especially for the characteristic lines, is high. It means that the LIBS spectral data could illustrate the elemental information of these mineral pigments.

As shown in **Figure 3**, the red, green, and blue pigments are commonly utilized in different areas according to the contents of the mural surface. For the purpose of indication of the pigments on the murals, a classifiable model of pigments was established coupled with principal component analysis (PCA). Before forming a PCA model, the optimum number of principal components (PCs) must be determined so as not to under- or over-represent datasets. The appropriate way to determine the rank is to analyze the number of features captured by each principal component against the principal component number. The two PC models (more than 80% variance) was optimum for capturing all the important information buried in the dataset. The other high-order PCs were not included because they did not show any evidence of clusters or other relevant information. Then 100 spectral data points from the simulated samples of different colorful paintings were used to build a classifiable model of the murals coupling with the PCA method. In caves, considering the sensitivity and fragility of the murals, only 40 spectral data were collected in each area and were used to classify the pigments.

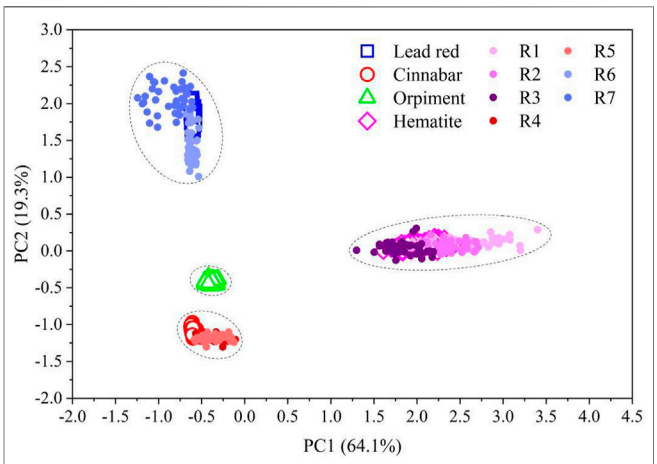

FIGURE 6 | Score plots of PC1 and PC2 for the variance between 250 and 600 nm of R1–R7 areas on the mural.

It is a very interesting phenomenon that different shades of the red hues (dark red, light red, or pink red) were presented on necklace, skirts, and shawl as indicated with the label of R1 to R7. **Figure 6** presents the plots of the scores for PC1 and PC2 for the spectral data variance obtained from the simulated painted layers (hollow symbols) and *in situ* murals (solid circle points) of the red pigments over the range of 250–600 nm. As can be seen from the

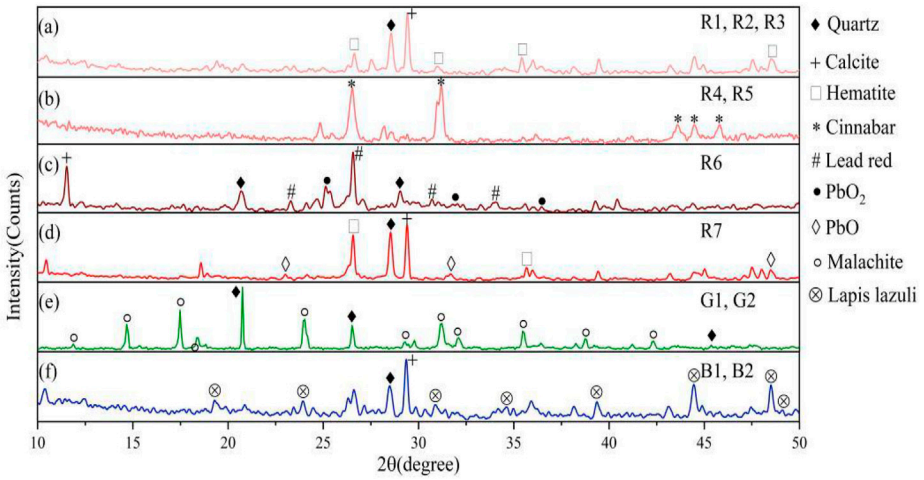

FIGURE 7 | X-ray diffraction (XRD) patterns of pigments in red **(A–D)**, green **(E)**, and blue **(F)** areas on murals in caves.

figure, the 400 spectral data from different pigments of red lead, cinnabar, orpiment, and hematite were classified into four distinct groups as calibration sets according to the scores in PC1 and PC2. As presented in the figure, PC1 and PC2 explain 64.1% and 19.3%, respectively, 83.4% of the total variance in the data matrix. As shown in **Figure 6**, the scores of PC1 varied from 1.2 to 3.6 for the hematite group, and −1.3 to 0 for the red lead, cinnabar, and orpiment groups; the scores of PC1 meant that the hematite data can be distinguished clearly from other three pigment data according to the first principal component. The scores of PC2 varied from −1.3 to −0.8, −0.5 to −0.5, and 0.8 to 2.5 for cinnabar, orpiment, and red lead, respectively, and it demonstrated that these spectral data of the three pigments could be clustered into three separate groups. In short, the classifiable model of these four kinds of pigments was established according to the two-dimensional principal component analysis.

Actually, considering the composition of these painted layer, coupled with the loading vectors at some characteristic lines in the spectra, it could be concluded that the feature elements of each mineral pigment provided the dominant contributions to the first and second principal components. Then the classifiable model was applied to identify and classify the unknown pigments on the murals; the spectral data of the red pigments from seven sites on the murals, which are labeled R1 to R7 in the picture presented in **Figure 3**, were analyzed under the classifiable model.

As shown in **Figure 6**, it is obvious that the 40 spectral data for each area were located in different clusters; the points of R1, R2, and R3 tended to be located in the hematite cluster, the points of R4 and R5 tended to distribute in the cinnabar group, and the spectral data of R6 and R7 tend to locate near the same area of red lead.

The score results of painted layers indicated that the pigments of R1, R2, and R3 were hematite, the cinnabar pigment was used in the R4 and R5 areas, and red lead was used in the areas of R6 and R7. It is notable that the points were closely distributed in the cluster of the hematite and cinnabar groups except for the points of R6 and R7. As can be seen from the figure, the data points of R6 and R7 were not closely overlapping each other among them, and the unexpected phenomena were revealed using the further x-ray diffraction (XRD) analysis by obtaining some pigment powders presented on these areas.

Figure 7 presents the XRD patterns of red, blue, and green pigments in different areas on murals in caves. The patterns in **Figure 7A** illustrates that the components of pigments were the same as hematite in the R1, R2, and R3 areas, and as cinnabar in the R4 and R5 areas in **Figure 7B**, and it can be seen that these XRD analytical results were in good agreement with the results from the classifiable model based on the combination of LIBS and PCA method for the R1 to R5 case. However, the XRD result of the dark red pigment in the R6 areas in **Figure7C** shows that the components of the painted layer were a mixture of red lead and lead dioxide (PbO_2); the lead dioxide was mainly from the products of lead red discoloration, and this resulted in the spectral data including the mixture information, which caused the fluctuation of data points in the R6 area among the lead red group.

Similar results were also observed in the R7 area in **Figure 7D**; the materials of the painted layer was a mixture of orange lead (PbO) and hematite, but the lead-based pigment was not lead red because the orange lead pigment is not commonly used in the murals existing in caves, and actually the orange was usually mistaken for lead red according to the elemental analysis of lead by the x-ray fluorescence (XRF) analysis in our previous investigation. So, it is the first time to find orange lead in the view of scientific testing. The indication of different lead-containing pigments using the LIBS technique will be further studied in our later work.

The same method was used to achieve pigment classification for the green- and blue-painted layers. As shown in **Figure 3**, the green color was presented on decoration in clothing, and the spectral data from these area (G1, G2) tended to locate the cluster of malachite pigment sets in **Figure 8A**, which has been reported in our

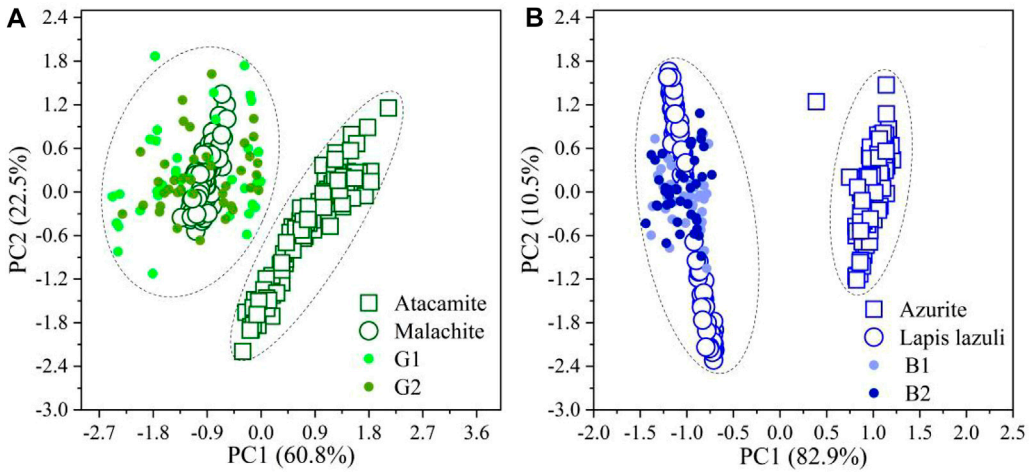

FIGURE 8 | Score plots of PC1 and PC2 for the variance from 250 to 530 nm of green **(A)** and blue **(B)** areas mural.

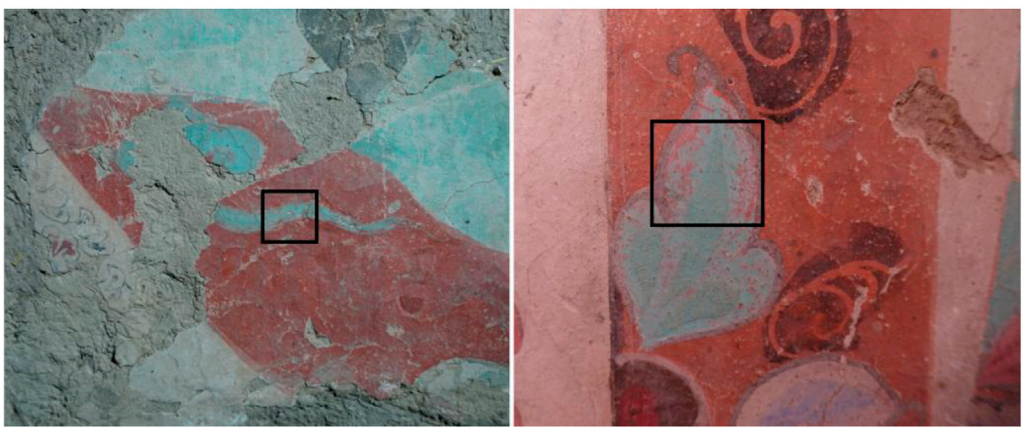

FIGURE 9 | Photo of overlapped painted layer in mural.

previous work about indication of green pigments [26]; the distribution of points in this figure demonstrated that the malachite pigment was used to present the green color in the murals. **Figure 8B** gives the classifiable results for blue pigments; the results show that the blue pigment was lapis lazuli mineral powder. Furthermore, the XRD analysis on the green- and blue-painted layers was carried out, and the results are included in **Figures 7E,F**, respectively. The validation results of XRD were very well fitted with the results from the classifiable model based on LIBS coupled with the PCA method.

Depth Profiling Analysis of Murals

Dunhuang murals are the typical secco according to the painting technique. The painted layers of these murals are often composed of several layers, so the painted layers are actually a multilayer structure. The profiling information of these layers is the basis of establishing appropriate conservation procedures for restoration and protection of the ancient murals. Therefore, in this part work, the LIBS technique was used to achieve the depth profiling analysis of murals with multilayers.

Figure 9 presents an example of multilayer murals, as shown in the areas indicated with the black box in the figure. As can be seen in the figure, the red layer was applied with a green layer in the labeled area. Because the components of the red and green layers have been indicated as hematite and malachite pigments in previous research, respectively, the lines of iron (Fe I 385.99 nm) and copper (Cu I 324.75 nm) element were considered to be indicators of red- and green-painted layers, respectively. The background of these characteristic lines was subtracted from the corresponding signal, and the min–max method was used to complete the intensity normalization for the aim of canceling the spectral signal fluctuation result of matrix effects and surface roughness of murals.

In fact, the superficial green layer was irradiated with the laser shots in the initial ablation, and then the intensities of copper lines presented a significant decreasing trend when the green layer was

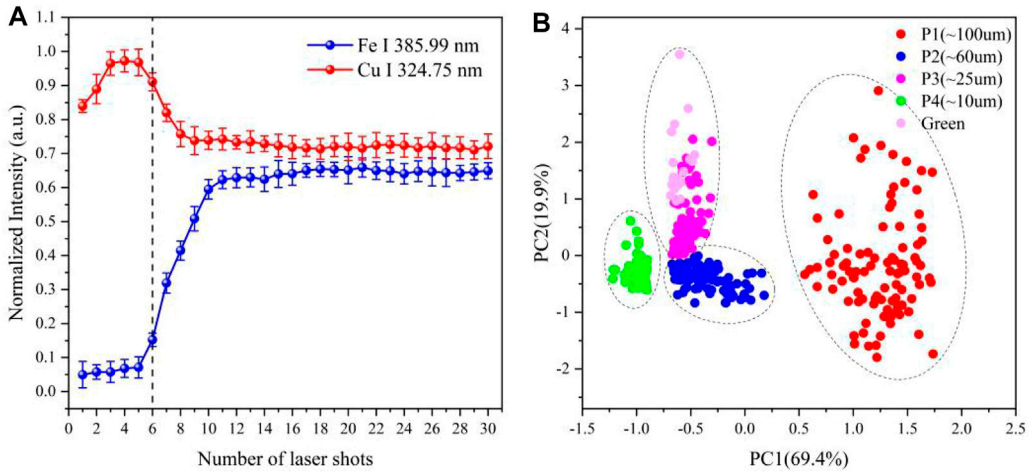

FIGURE 10 | (A) Normalized intensities of Cu and Fe lines versus number of laser shots used to irradiate a single spot in overlapped painted areas and **(B)** cluster classification of green pigments in four types of particle size fractions.

penetrated by the successive laser pulse with an increasing number of ablation shots in the same spot; in contrast, the signal of iron lines seemed to intensify at the same time. Therefore, the depth profiling structure of murals was determined using varied trends of indicator element lines for the corresponding painted layer.

Figure 10 presents the varied trends of characteristic line intensities for copper and iron with different numbers of laser pulse shots at the same point, which can give stratigraphic information in this area. From **Figure 10**, the normalized intensity trends of characteristic lines clearly indicated that the green-painted layers could be penetrated using six laser pulses. That is, the penetration numbers of laser shots on the overlapped painted area were determined as six by means of this method.

It is necessary to get the average ablation rate (AAR) of laser pulse ablated on the green layers in order to obtain the thickness of the painted layer. From our previous research about the AAR of laser pulse on the green layer, the results showed that the AAR of laser pulse was influenced significantly by the pigment size of the green-painted layer, the AAR value gradually became larger with the decreasing pigment sizes on green layers [28]. Therefore, the pigment size in the green area labeled in **Figure 9** was estimated first by using a classifiable model of green pigment sizes from our reported results [30]. In the current work, the pigment size in this green area was estimated with 20 spectral data by employing the classifiable model of green pigment, and the result is included in **Figure 10B**. The 20 spectral points tended to be located in the P3 group, where the mean diameter was about 25 μm.

On the whole, the thickness of the green layer was determined quantitatively based on the information of green pigment size and the relationships of laser pulses and ablation depth for corresponding pigment size fractions. The expression of fitting relationship was concluded as $Y = 18.5X + 4.8$ on the painted layers for the group (~22.6 μm), where Y indicates the laser ablation depth, and X indicates the penetration numbers of laser pulses. The thickness

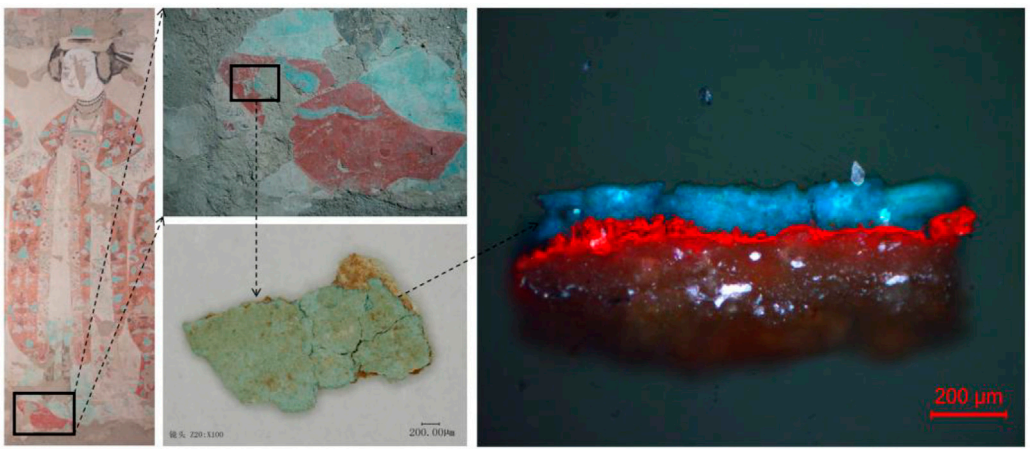

FIGURE 11 | Microscopy images of cross-sections for the mural pieces.

was calculated at approximately 115.8 μm. To confirm our result, a cross-sectional analysis of this area was prepared in our laboratory, as shown in **Figure 11**. The microscope image shows that the thickness of the layer was 108.8 ± 5.1 μm, which was consistent with the estimated results from our evaluated results employing the LIBS technique.

CONCLUSION

In this paper, a portable LIBS system was used to analyze the mural-painted layers in the cave for the first time. First, the laser ablation effect on the mural surface using microscopy images, the size of the ablation crater, and the stable ablation edge suggested that the microdestructive effect was acceptable from the view of mural conservation. Second, the mural pigments in Cave 98 were indicated by using the pigment classifiable model, and the pigments commonly used in red, green, and blue areas were determined. Finally, the multilayer overlapped painted areas were analyzed *in situ* by the portable LIBS, and the thickness of the superficial green layer was calculated quantitatively according to the reported studies.

The above research shows that the portable LIBS technique is a potential way to achieve *in situ* accurately illustrated information about ancient murals. On the one hand, the information is significant for possible restoration and conservation of murals. On the other hand, the accurate spectral data of mural-making materials can provide an opportunity for in-depth illustration of the historical information.

DATA AVAILABILITY STATEMENT

The raw data supporting the conclusion of this article will be made available by the authors, without undue reservation.

AUTHOR CONTRIBUTIONS

YY, ZY, and DS contributed to the design of the study and wrote the first draft of the manuscript. YY, ZY, and DS contributed equally as first authors in this paper. ZS, QC, YZ, and WZ completed the profiling analysis with optical microscopy. YF and BSh performed the XRD analysis of the mural-painted layers. BC provided all mural pictures in the caves. YZ and WZ organized the spectral data. CD and BSu contributed to the idea and conception of the research. All authors contributed to the manuscript revision, and read and approved the submitted version.

FUNDING

This work was supported by the National Key Research and Development Program of China (Grant No. 2019YFC1520701), the National Natural Science Foundation of China (Grant No. 61965015), the Industrial Support Program for Colleges of Gansu Province (Grant No. 2020C-17), and the Science and Technology Project of Gansu Province (Grant Nos. 21JR7RA759 and 21JR7RA131).

REFERENCES

1. Fan J. The Conservation and Management of the Mogao Grottoes. *Dunhuang Res* (2000) 63:1–4. doi:10.13584/j.cnki.issn1000-4106.2000.01.001
2. Duan X. Study on the Making Materials of the wall Paintings at the Mogao Grottoes. *Dunhuang Res* (1988) 3:41–59.
3. Sun M, Zhang D, Wang Z, Ren J, Chai B, Sun J. What's Wrong with the Murals at the Mogao Grottoes: A Near-Infrared Hyperspectral Imaging Method. *Sci Rep* (2015) 5:14371. doi:10.1038/srep14371
4. Liu X, Qiao S, Ma Y. Highly Sensitive Methane Detection Based on Light-Induced Thermoelastic Spectroscopy with a 2.33 Mm Diode Laser and Adaptive Savitzky-Golay Filtering. *Opt Express* (2022) 30:1304–13. doi:10.1364/oe.446294
5. Ma Y, Hong Y, Qiao S, Lang Z, Liu X. H-shaped Acoustic Micro-resonator-based Quartz-Enhanced Photoacoustic Spectroscopy. *Opt Lett* (2022) 47: 601–4. doi:10.1364/ol.449822
6. Liu X, Ma Y. Sensitive Carbon Monoxide Detection Based on Light-Induced Thermoelastic Spectroscopy with a Fiber-Coupled Multipass Cell [Invited]. *Chin Opt Lett* (2022) 20:031201. doi:10.3788/col202220.031201
7. Ma Y, Hu Y, Qiao S, Lang Z, Liu X, He Y, et al. Quartz Tuning forks Resonance Frequency Matching for Laser Spectroscopy Sensing. *Photoacoustics* (2022) 25: 100329. doi:10.1016/j.pacs.2022.100329
8. Cremers A, Radziemski L. *Handbook of Laser-Induced Breakdown Spectroscop*. Wiley (2006).
9. Hahn DW, Omenetto N. Laser-induced Breakdown Spectroscopy (LIBS), Part I: Review of Basic Diagnostics and Plasma-Particle Interactions: Still-Challenging Issues within the Analytical Plasma Community. *Appl Spectrosc* (2010) 64(12):335–66. doi:10.1366/000370210793561691
10. Hahn DW, Omenetto N. Laser-Induced Breakdown Spectroscopy (LIBS), Part II: Review of Instrumental and Methodological Approaches to Material Analysis and Applications to Different Fields. *Appl Spectrosc* (2012) 66(4): 347–419. doi:10.1366/11-06574
11. Siano S, Salimbeni R. Advances in Laser Cleaning of Artwork and Objects of Historical Interest: The Optimized Pulse Duration Approach. *Acc Chem Res* (2010) 43(6):739–50. doi:10.1021/ar900190f
12. Paraskevi P, Alexandros S, Savas G, Costas F. Recent Studies of Laser Science in Paintings Conservation and Research. *Acc Chem Res* (2010) 43(6):771–81. doi:10.1021/ar900224n
13. Brysbaert A, Siozos P, Vetters M, Philippidis A, Anglos D. Materials Analyses of Pyrotechnological Objects from LBA Tiryns, Greece, by Means of Laser-Induced Breakdown Spectroscopy (LIBS): Results and a Critical Assessment of the Method. *J Archaeological Sci* (2017) 83:49–61. doi:10.1016/j.jas.2017.06.007
14. Giurato L, Candura A, Grasso G, Spoto G. *In Situ* identification of Organic Components of Ink Used in Books from the 1900s by Atmospheric Pressure Matrix Assisted Laser Desorption Ionization Mass Spectrometry. *Appl Phys A* (2009) 97(2):263–9. doi:10.1007/s00339-009-5390-0
15. Kautek K, Qujja M, Castillejo M, Ferrence S, Betancourt P, Anglos D. Analysis of Archaeological Objects with LMntI, a New Transportable LIBS Instrument. In *Lasers in the Conservation of Artworks*. Berlin, Heidelberg: Springer (2005) 100:443–9. doi:10.1007/3-540-27176-7_56
16. Bertolini A, Carelli G, Francesconi F, Francesconi M, Marchesini L, Marsili P, et al. Modì: a New mobile Instrument for *In Situ* Double-Pulse LIBS Analysis. *Anal Bioanal Chem* (2006) 385(2):240–7. doi:10.1007/s00216-006-0413-6
17. Cuñat J, Palanco S, Carrasco F, Simón MD, Laserna JJ. Portable Instrument and Analytical Method Using Laser-Induced Breakdown Spectrometry for *In Situ* Characterization of Speleothems in Karstic Caves. *J Anal Spectrom* (2005) 20(4):295–300. doi:10.1039/b417161f
18. Martin M, Castillejo M, Torres R, Guerra F, Silva D. LIBS Spectra of Polychromes with a Low Cost CCD Camera Based Detector. *J Cult Heritage* (2000) 1:293. doi:10.1016/s1296-2074(00)00172-2

19. Castillejo M, Martín M, Oujja M, Silva D, Torres R, Domingo C, et al. Spectroscopic Analysis of Pigments and Binding Media of Polychromes by the Combination of Optical Laser-Based and Vibrational Techniques. *Appl Spectrosc* (2001) 55(8):992–8. doi:10.1366/0003702011953135
20. De Giacomo A, Dell'Aglio M, Casavola A, Colonna G, De Pascale O, Capitelli M. Elemental Chemical Analysis of Submerged Targets by Double-Pulse Laser-Induced Breakdown Spectroscopy. *Anal Bioanal Chem* (2006) 385: 303–11. doi:10.1007/s00216-006-0323-7
21. Chen YQ, Mo JY, Zhou Q, Lou Y, Li RH. Quantitative Analysis of Copper Impurity in Silver Jewellery by Laser-Ablation Laser-Induced Breakdown Spectroscopy. *Guang Pu Xue Yu Guang Pu Fen Xi* (2015) 35(3):782–6. doi:10.3964/j.issn.1000-0593(2015)03-0782-05
22. Carmona N, Oujja M, Rebollar E, Römich H, Castillejo M. Analysis of Corroded Glasses by Laser Induced Breakdown Spectroscopy. *Spectrochimica Acta B* (2005) 60(7-8):1155–62. doi:10.1016/j.sab.2005.05.016
23. Colao F, Fantoni R, Lazic V, Spizzichino V. Laser-induced Breakdown Spectroscopy for Semi-quantitative and Quantitative Analyses of Artworks-Application on Multi-Layered Ceramics and Copper Based Alloys. *Spectrochimica Acta B: At Spectrosc* (2002) 57(7):1219–34. doi:10.1016/s0584-8547(02)00054-x
24. Resano M, García-Ruiz E, Vanhaecke F. Laser Ablation-Inductively Coupled Plasma Mass Spectrometry in Archaeometric Research. *Mass Spectrom Rev* (2010) 29(1):55–78. doi:10.1002/mas.20220
25. Kaszewska EA, Sylwestrzak M, Marczak J, Skrzeczanowski W, Iwanicka M, Szmit-Naud E, et al. Depth-Resolved Multilayer Pigment Identification in Paintings: Combined Use of Laser-Induced Breakdown Spectroscopy (LIBS) and Optical Coherence Tomography (OCT). *Appl Spectrosc* (2013) 67:960–72. doi:10.1366/12-06703
26. Yin Y, Sun D, Su M, Yu Z, Su B, Shui B, et al. Investigation of Ancient wall Paintings in Mogao Grottoes at Dunhuang Using Laser-Induced Breakdown Spectroscopy. *Opt Laser Technol* (2019) 120:105689. doi:10.1016/j.optlastec.2019.105689
27. Duchene S, Bruder R, Sirven JB, au J. Chemometrics and Laser Induced Breakdown Spectroscopy (LIBS) Analyses for Identification of Wall Paintings Pigments. *Cac* (2010) 6(1):60–5. doi:10.2174/157341110790069600
28. Yin Y, Sun D, Yu Z, Su M, Shan Z, Su B, et al. Influence of Particle Size Distribution of Pigments on Depth Profiling of Murals Using Laser-Induced Breakdown Spectroscopy. *J Cult Heritage* (2021) 47:109–16. doi:10.1016/j.culher.2020.10.006
29. Giussani B, Monticelli D, Rampazzi L. Role of Laser Ablation-Inductively Coupled Plasma-Mass Spectrometry in Cultural Heritage Research: a Review. *Analytica Chim Acta* (2009) 635(1):6–21. doi:10.1016/j.aca.2008.12.040
30. Yin Y, Yu Z, Sun D, Su M, Wang Z, Shan Z, et al. A Potential Method to Determine Pigment Particle Size on Ancient Murals Using Laser Induced Breakdown Spectroscopy and Chemometric Analysis. *Anal Methods* (2021) 13(11):1381–91. doi:10.1039/d0ay01546f
31. Sorauf K, Bauer A, Miziolek A, Frank C. Spectral Data Analysis Approaches for Improved Provenance Classification. *Next-generation Spectroscopic Tech VIII, SPIE Proc.* (2015) 9482(12):01–10. doi:10.1117/12.2177913
32. Shigeo A, Yoko T, Stephen R, Michiyo M, Takayasu K, Su B, et al. *Conservation and Painting Techniques of Wall Paintings on the Ancient Silk Road*. Singapore: Springer Nature (2021).
33. *NIST Atomic Spectra Database*: Available from: http://www.nist.gov/pml/data/asd.cfm (Accessed February 15, 2021).

Conflict of Interest: The authors declare that the research was conducted in the absence of any commercial or financial relationships that could be construed as a potential conflict of interest.

frontiers in Physics

ORIGINAL RESEARCH
published: 16 March 2022
doi: 10.3389/fphy.2022.848943

Phase Diversity-Based Fourier Ptychography for Varying Aberration Correction

Meng Xiang[1,2], *An Pan*[3], *Jinpeng Liu*[1,2,4], *Teli Xi*[1,2,4], *Xin Guo*[1], *Fei Liu*[1,2,4]* *and Xiaopeng Shao*[1,2,4]

[1]Academy of Advanced Interdisciplinary Research, Xidian University, Xi'an, China, [2]Xi'an Key Laboratory of Computational Imaging, Xi'an, China, [3]Xi'an Institute of Optics and Precision Mechanics, Chinese Academy of Sciences, Xi'an, China, [4]School of Physics and Optoelectronic Engineering, Xidian University, Xi'an, China

Fourier ptychography (FP) is geared toward high-resolution imaging with a large field of view efficiently. In the original illumination-based FP scheme, the aberrations in optical systems can be well reconstructed, which plays a prominent role in simple and compact optical arrangements. Unfortunately, the reconstruction strategy for recovering an optical system's pupil function fails to carefully consider the nature of the field-dependent pupil function in the aperture-scanning FP scheme, which affects the quality of the reconstructed image to a certain extent. Based on this observation, we report a phase diversity-based FP (PDFP) scheme for varying aberration correction. We image USAF resolution target with the proposed PDFP scheme and demonstrate our ability to correct varying aberration and improve image quality. The reported approach allows aperture-scanning FP technology to use simpler optical systems for imaging and may facilitate the further development of FP in practical applications such as industrial inspection and long-distance imaging.

Keywords: Fourier ptychography, varying aberration, phase diversity, aperture scanning, high-resolution imaging

OPEN ACCESS

Edited by:
Yufei Ma,
Harbin Institute of Technology, China

Reviewed by:
He Xiaoliang,
Jiangnan University, China
Jianming Wen,
Kennesaw State University, United States

****Correspondence:***
Fei Liu
feiliu@xidian.edu.cn

Specialty section:
This article was submitted to Optics and Photonics, a section of the journal Frontiers in Physics

Received: *05 January 2022*
Accepted: *07 February 2022*
Published: *16 March 2022*

Citation:
Xiang M, Pan A, Liu J, Xi T, Guo X, Liu F and Shao X (2022) Phase Diversity-Based Fourier Ptychography for Varying Aberration Correction. Front. Phys. 10:848943. doi: 10.3389/fphy.2022.848943

INTRODUCTION

In recent years, the photoelectric imaging system has been widely used in many fields, such as land, sea, and air [1–4]. It has long been known that imaging a distant target has demonstrated typically results in low spatial resolution as a result of the diffraction limit effect. It is very important to find a long-range imaging technology that can effectively break through the diffraction limit without relying on a large aperture. Fourier ptychographic microscopy (FPM) [5] is a very promising technology, which breaks the trade-off between resolution and field of view (FOV) [6] with phase recovery [7] and aberration correction [8]. The current FP platform has been successfully applied in high-throughput imaging (digital pathology) [9], quantitative phase imaging [10, 11], 3-dimensional imaging [12, 13], and biomedicine field [14].

The sample's Fourier spectrum in the original FP demonstration is scanned by angularly varying illumination using a LED array [5], generating an extended synthesized numerical aperture (NA) of the optical system. Then we can reconstruct a high-resolution image breaking through the diffraction limit of the low NA objective lens. However, the limitation of the illumination-based FP is that the samples must be thin [8]. When the sample's thickness does not satisfy the thin-sample requirement, this one-to-one mapping relationship between the illumination angle and the shift of the Fourier spectrum is invalid, leading to the ineffectiveness of the phase retrieval algorithm. Unlike the

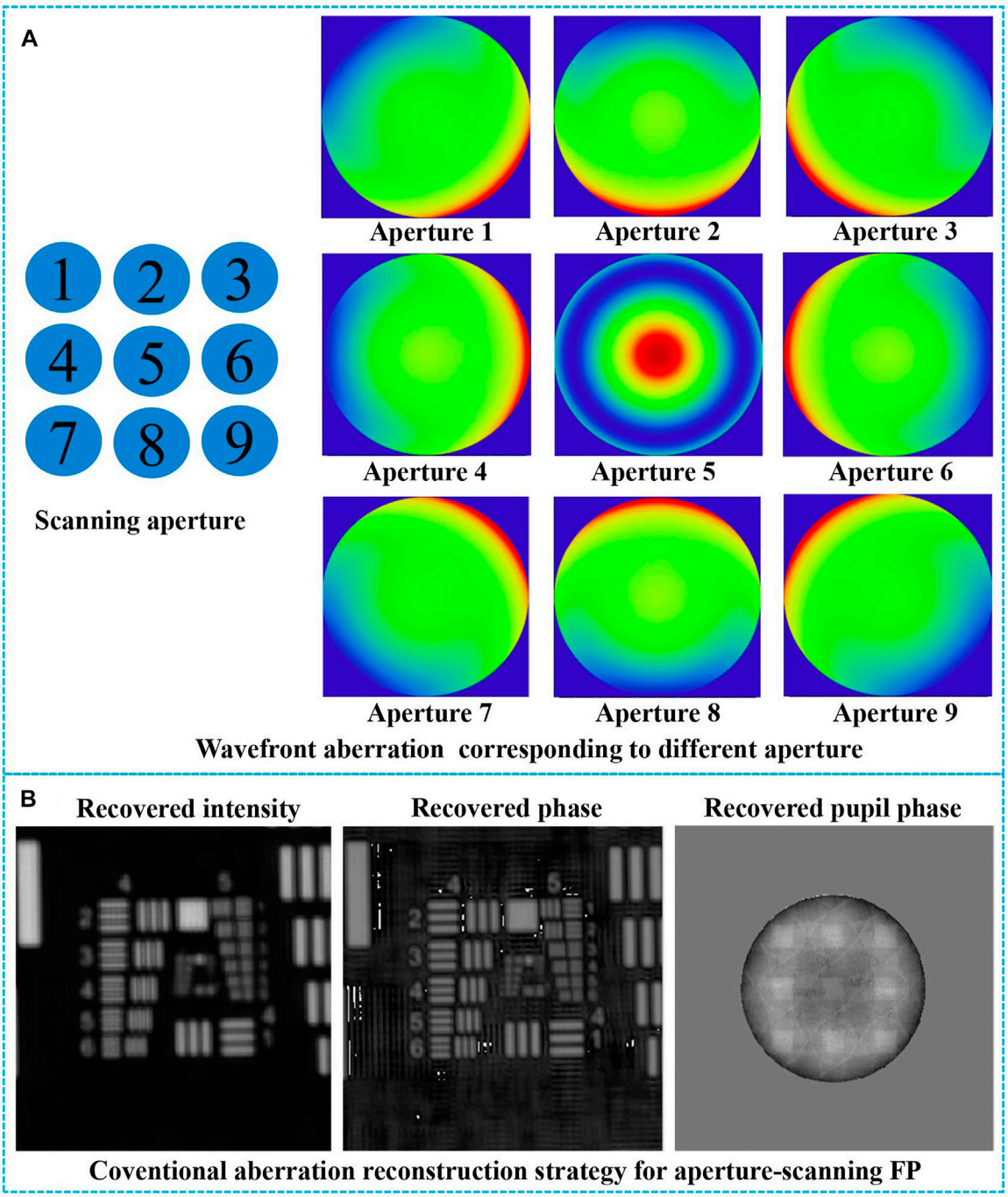

FIGURE 1 | (A) The pupil functions corresponding to different apertures in the process of aperture scanning. **(B)** The recovered amplitude, phase, and pupil phase by the conventional aberration correction Fourier ptychography (FP) algorithm.

angularly varying illumination FP configuration, the optical field exiting the sample (not enters it) is modulated by the scannable aperture with aperture-scanning FP, in which a removable mask is placed at the pupil plane of the optical system. Then the sample's thickness becomes irrelevant during reconstruction, and the thin specimen requirement can be circumvented [15, 16]. After reconstruction, the optical field can be propagated back along the optical axis to any plane for digital refocusing. Compared to the traditional illumination-based FP model, the FP framework is extended for macroscopic imaging settings by the aperture-scanning FP scheme, and the previous work [17, 18] has shown that aperture-scanning FP has good potential as a long-distance imaging method.

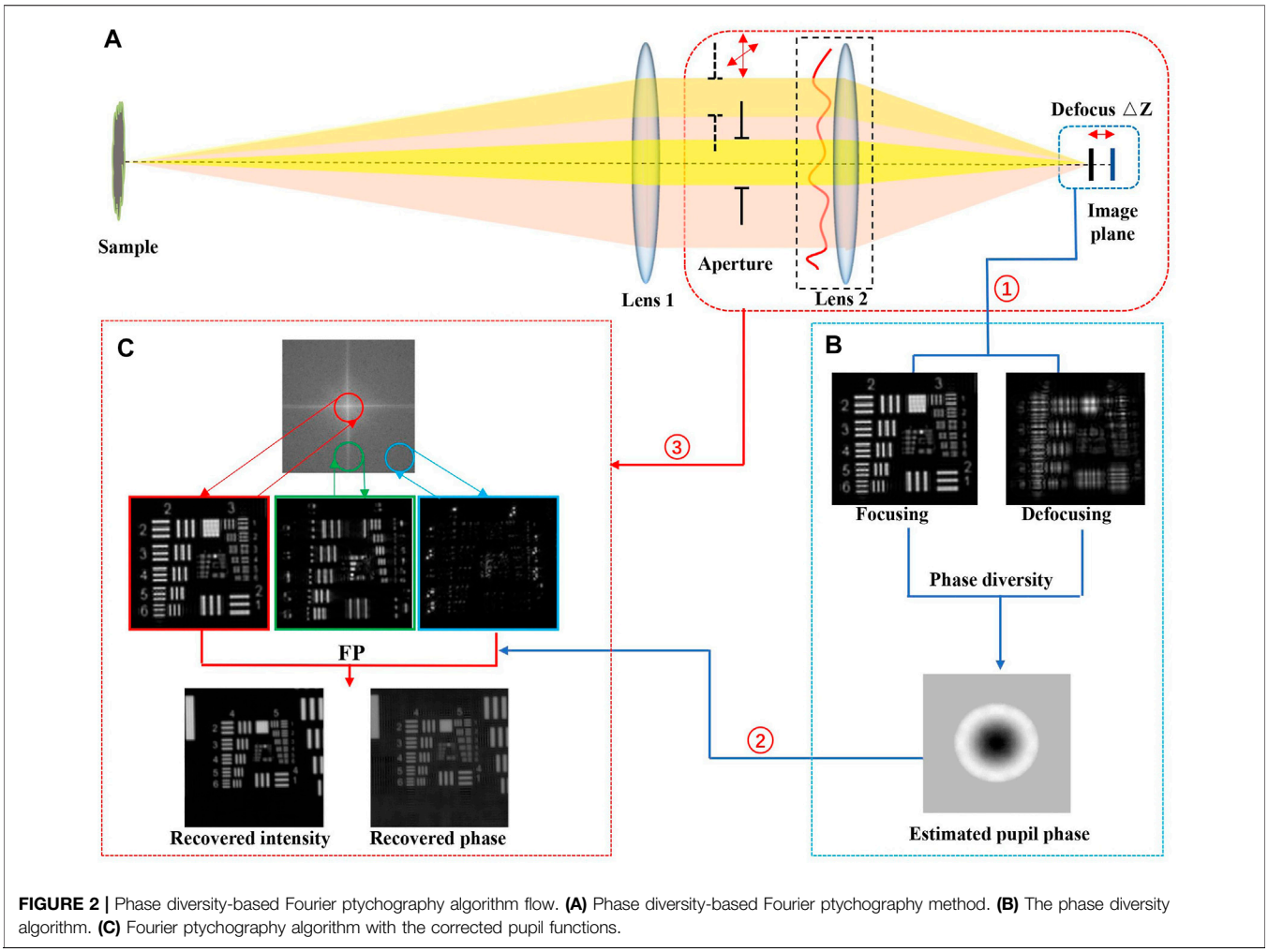

FIGURE 2 | Phase diversity-based Fourier ptychography algorithm flow. **(A)** Phase diversity-based Fourier ptychography method. **(B)** The phase diversity algorithm. **(C)** Fourier ptychography algorithm with the corrected pupil functions.

The original intention of Fourier ptychography (FP)-based long-distance imaging is to use simpler optical devices to achieve higher imaging quality. In reality, there is no perfect aberration-free optical lens, especially for simpler optical systems, where fewer optical surfaces also lead to more prominent aberration problems, which come from imperfect design, manufacturing, and alignment of optical elements. The measurement and elimination of optical aberrations play a prominent role in the computational imaging platform with a simpler and compact optical arrangement. In the current illumination-based FP implementation, the pupil aberration in each small FOV can be regarded as spatially invariant and can be partially recovered in the optimization process [19, 20]. The problem of aberration correction is redefined as a computational problem that can be solved by the acquired images, avoiding the challenges with aberration correction, which is essential for a simpler configuration optical imaging platform. However, the original FP aberration recovery strategy assumes that the pupil function of the system is fixed during the image acquisition process [20] and does not consider the difference between the pupil aberration and the scannable position in the aperture-scanning FP system, which affects the quality of the reconstructed image to a certain extent. As an example, we simulate the wave aberrations corresponding to the same aperture at different positions during the aperture-scanning process, as shown in **Figure 1A**. **Figure 1B** shows the result of pupil phase reconstruction using the conventional aberration correction FP algorithm. The results showed that the pupil phase cannot be reconstructed correctly, which will affect the quality of the reconstructed image.

METHODS

Based on this observation, we report a phase diversity (PD)-based FP (PDFP) scheme for varying aberration correction, as shown in **Figure 2A**. For the purpose of testing the reported method for macroscopic imaging, the light field exiting the sample is collected by the collimator where the light from objects is closer to real-world scenes, passing through the scannable aperture (or a spatial light modulator) and reimaged on the camera. A circular aperture is placed at the pupil plane of the optical system, and the different passbands of the optical field are transmitted to the image plane by scanning the sub-aperture. A sequence of low-resolution intensity images corresponding to different sub-apertures with

different spatial frequency information of the light field is captured. To ensure acquiring redundant information to recover information merely from intensity images by the phase retrieval algorithm, the adjacent apertures should have a certain degree of overlap. With the use of the proposed method, the recovery of the full pupil function can be performed based on the PD algorithm by simply acquiring an in-focus image and an out-of-focus image with a big aperture that does not need to be moved to multiple positions. The sub-aperture pupil functions corresponding to different scannable positions are selected from the full pupil function and embedded in the FP reconstruction algorithm to correct the varying aberrations.

PD algorithm is an unconventional imaging technique introduced by Gonsalves and Chidlaw [21], which uses a set of focused images and defocused images for the characterization of wavefront aberrations. The focused image is only degraded by systematic aberrations, while the defocused image is also affected by additional known defocus aberration. It should be noted that the PD technique relies on finding the aberrations that produce multiple images of the same sample with known diversities at the pupil. In addition to the traditional defocus diversities, the pupil differences can also come from wavelength diversities, spiral phase-mask diversities, and so on [22]. The PD algorithm can be applied to both point target and extended target for aberration recovery, enabling near-diffraction-limited imaging. Further details for the PD algorithm are available in [23].

The recovery process of the PDFP scheme is briefly outlined as follows. The algorithm sketch is shown in **Figure 2**.

1) Initialize the high-resolution image estimate: we assume the high-resolution sample is $o(x, y)$, and the field at the Fourier plane is $O(k_x, k_y) = \mathcal{F}\{o(x, y)\}$. The initial guess could be random or the up-sampling of a low-resolution image.
2) Reconstruct the full pupil function: reconstruct the full pupil function $P(x, y)$ using the PD algorithm by acquiring an in-focus image and an out-of-focus image with a big aperture, as shown in **Figure 2B**.
3) Generate a low-resolution sample image: an x–y motion stage is used to scan the small aperture at the Fourier plane, as shown in **Figure 2A**, and we capture an intensity image $I^c_{m,n}(x, y)$ for each position of the sub-aperture. We select small sub-regions (corresponding to different aperture positions) of the initial guess's Fourier spectrum and apply the inverse Fourier transformation to generate a low-resolution image $\varphi_{m,n}(x, y)$ of the sample.

$$\boldsymbol{\varphi}^{e}_{m,n}(\boldsymbol{x}, \boldsymbol{y}) = \mathcal{F}^{-1}\{\boldsymbol{O}(\boldsymbol{k}_x - \boldsymbol{k}_{x,m,n}, \boldsymbol{k}_y - \boldsymbol{k}_{y,m,n})\boldsymbol{P}_{m,n}(\boldsymbol{k}_x, \boldsymbol{k}_y)\}$$

where $\mathcal{F}^{-1}$ is the inverse Fourier transform operator, and $(k_{x,m,n}, k_{y,m,n})$ is the coordinates corresponding to the scannable sub-aperture.

4) Replace by the intensity measurement: the sample's amplitude component $|\varphi^e_{m,n}(x, y)|$ is sequentially updated with the square root of the low-resolution intensity measurements $I^c_{m,n}(x, y)$ acquired by different sub-apertures.

$$\boldsymbol{\varphi}^{u}_{m,n}(\boldsymbol{x}, \boldsymbol{y}) = \sqrt{\boldsymbol{I}^{c}_{m,n}(\boldsymbol{x}, \boldsymbol{y})}\frac{\boldsymbol{\varphi}^{e}_{m,n}(\boldsymbol{x}, \boldsymbol{y})}{|\boldsymbol{\varphi}^{e}_{m,n}(\boldsymbol{x}, \boldsymbol{y})|}$$

5) Update the Fourier spectrum: we apply Fourier transformation to this updated sample image $\varphi^u_{m,n}(x, y)$ and replace its corresponding region of the sample's estimate Fourier spectrum $O(k_x, k_y)$. And the sub-aperture pupil functions $P_{m,n}(k_x, k_y)$ of the corresponding scannable apertures could be intercepted from the full pupil function $P(x, y)$.

$$\boldsymbol{O}(\boldsymbol{k}_x, \boldsymbol{k}_y) = \mathcal{F}\{\boldsymbol{\varphi}^{u}_{m,n}(\boldsymbol{x}, \boldsymbol{y})\}\boldsymbol{P}_{m,n}(\boldsymbol{k}_x, \boldsymbol{k}_y) + \boldsymbol{\varphi}^{e}_{m,n}(\boldsymbol{x}, \boldsymbol{y})[\boldsymbol{1} - \boldsymbol{P}_{m,n}(\boldsymbol{k}_x, \boldsymbol{k}_y)]$$

6) Repeat for other apertures: repeat steps 2–5 for different apertures and continue until the entire Fourier space has been modified with all the captured low-resolution images.
7) High-resolution image: repeat steps 2–6 until a convergent solution is achieved. At the end of the recovery process, the converged Fourier spectrum solution is transformed back to the spatial domain to obtain a high-resolution sample image.

A set of simulation experiments was carried out to evaluate the reconstructed results by the conventional FP, aberration correction FP, and our PDFP method, as shown in **Figure 3**. The conventional FP algorithm does not perform aberration correction, and the aberration correction FP algorithm is based on the traditional EPRY algorithm [7]. The focused image and defocused image are shown in **Figures 3B,C**. **Figure 3A** shows the real pupil phase, and **Figure 3D** shows the recovered pupil phase by the PD algorithm. In comparison, the PD method could recover the pupil phase from the measurements successfully. The low-resolution raw data are shown in **Figure 3E1**. The recovered results by the conventional FP, aberration correction FP, and our PDFP method are shown in **Figures 3F1–H1**. **Figures 3E2–H2** are the close-ups of **Figures 3E1–H1**. Group 2 element 6 in **Figures 3H1,H2** can be well resolved, which is impossible to discern in the other results. It is clear that the resolution of the recovered image resolution by our PDFP scheme is better than that of the conventional FP and aberration correction FP method.

RESULTS

The experimental setup of the transmissive mode PDFP is shown in **Figure 4**. For the illumination, light from a laser (λ = 650 nm, bandwidth = 10 nm) was collimated into parallel light to illuminate the sample. A collimator (f = 500 mm) and illumination imaging lens (f = 75 mm) served as the forward and inverse Fourier transforming equipment. We used a CCD camera (6.5-μm pixel size, 16-bit dynamic range) to capture the sample's low-resolution intensity images. Moreover, an x–y motion stage (repeat positioning accuracy is 3 μm) was used to scan the variable circular aperture. For testing the resolution of

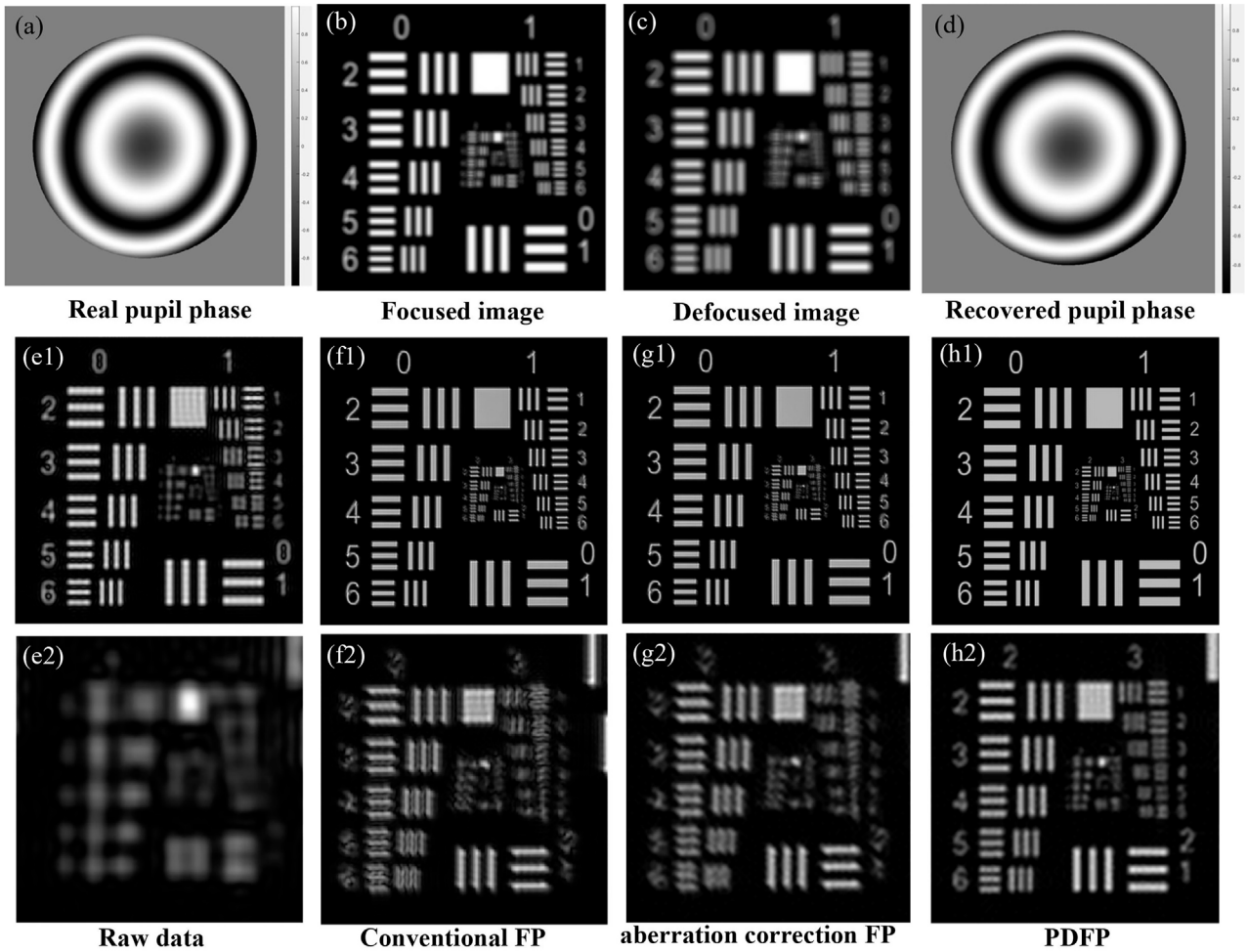

FIGURE 3 | The comparison of simulation experimental results by the conventional Fourier ptychography (FP), aberration correction FP, and the proposed phase diversity-based FP (PDFP) method. **(A)** The real pupil phase. **(B)** The focused image. **(C)** The defocused image. **(D)** The recovered pupil phase by the phase diversity algorithm. **(E1)** The low-resolution raw data. **(F1)** The recovered results with conventional FP. **(G1)** The correction results by aberration correction FP. **(H1)** The correction results of our PDFP method. **(E2–H2)** Close-ups of panels **(E1–H1)**.

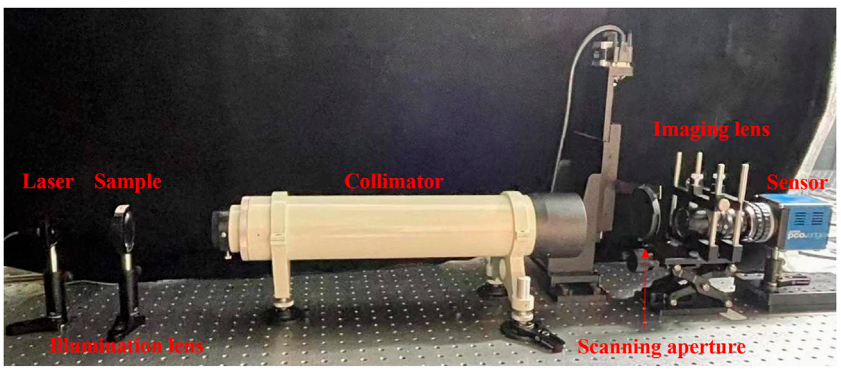

FIGURE 4 | The phase diversity-based Fourier ptychography (PDFP) experimental setup.

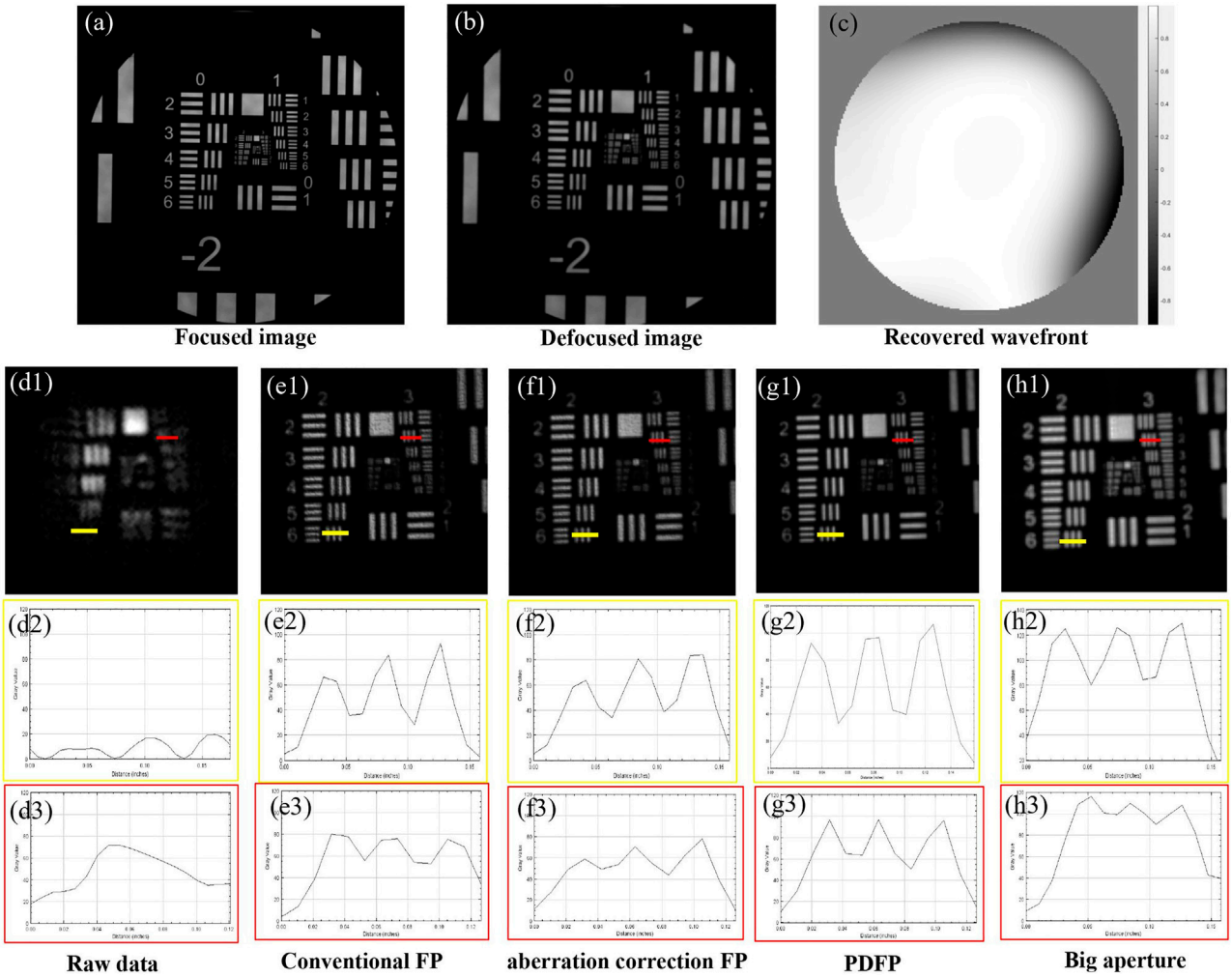

FIGURE 5 | The experimental results by the conventional Fourier ptychography (FP), aberration correction FP, and the proposed phase diversity-based FP (PDFP) method. **(A)** The focused image. **(B)** The defocused image. **(C)** The recovered pupil phase. **(D1)** Low-resolution raw data. **(E1)** The recovered results with conventional FP. **(F1)** The result by aberration correction FP. **(F1)** The correction results of our PDFP method. **(D2–H2)** Line profiles of group 2 element 6 panels **(D1–H1)**. **(D3–H3)** Line profiles of group 3 element 2.

the system, a negative USAF1951 resolution target is used as the sample. The big aperture was set to 9 mm, and one focused image and one defocused image with a defocus distance of 0.35 mm were captured, which are used to restore the full pupil function. We chose a small aperture size of 2.5 mm (0.002 NA), where the region of overlapping ratio (in one dimension) with its adjacent aperture is 74%. We used 11×11 scanning steps to synthesize a 9-mm aperture (equaling an NA of NAsyn = 0.009, corresponding to 10.6-μm imaging resolution) and 121 low-resolution intensity images were captured. The method of scanning the aperture mechanically in our prototype is just a demonstration, and devices such as digital micromirror devices or spatial light modulators can be used instead [24; 25].

We compared the conventional FP, aberration correction FP, and the proposed PDFP method by imaging a USAF resolution target, as shown in **Figure 5**. The focused image and defocused image are shown in **Figures 5A,B**. The recovered wavefront by the PD algorithm is shown in **Figure 5C**. The raw image captured by the experimental setup is shown in **Figure 5D1**. And the resolution of this raw image (260-μm periodicity, corresponding to 39-μm imaging resolution) is limited by the small circular aperture. The reconstructed high-resolution images by the conventional FP, aberration correction FP, and our PDFP method are shown in **Figures 5E1–G1**. According to the Nyquist sampling theorem, a 5.3-μm pixel size is needed to fully characterize the image when the aperture is fully open (9 mm, corresponding to 10.6-μm resolution). However, the pixel size of our camera is 6.5 μm (typical specifications for commercial CCD sensors). Due to pixel aliasing limitations, the imaging resolution is 13 μm, which is twice of pixel size, as shown in **Figure 5H1**. **Figures 5D2–H2** show line profiles of group 2 element 6 in **Figures 5D1–H1**. **Figures 5D3–H3** show line profiles of group 3 element 2 in **Figures 5D1–H1**. And group 2 element 6 (71-μm periodicity, corresponding to 10.65-μm

imaging resolution) can be resolved by our PDFP method, which matches well with the theoretical resolution defined by the synthesized NA, as shown in **Figure 5G2**. As we can see, due to the influence of aberration, group 2 element 6 in reconstruction results of the conventional FP and the aberration correction FP cannot be resolved well, as shown in **Figures 5E2,F2**. Moreover, the line profiles of group 3 element 2 by our PDFP method are significantly better than the other results. From the comparison, it can be seen that the reconstruction result of our PDFP method is better than the traditional FP algorithm, and the pixel aliasing problem can be avoided, resulting in image quality improved.

DISCUSSION

In summary, we implemented a PDFP imaging system that reconstructs the high-resolution image with aberration correction from a sequence of low-resolution intensity images. This PDFP configuration has a few advantages: 1) the thin-sample requirement of angularly varying illumination FP is circumvented, extending the FP scheme to macroscopic imaging settings. 2) System aberrations can be better corrected by shifting optical design complexity to computational algorithms, allowing the use of simpler optical systems with fewer optical surfaces for imaging. 3) The "pixel aliasing problem" can be solved by imposing a smaller aperture at the Fourier plane of the optical system. And the sensor (CCD or CMOS) with a larger pixel size can be used to provide better noise performance or bring down the cost of the imaging system. This method still has certain limiting factors in correcting aberrations, its time efficiency is low, and it is not applicable to some time-varying aberrations. This PDFP scheme reported in this work expands the scope of application for aperture-scanning FP, and its reflective mode can be used for semiconductor devices, metallic structures, ceramic surfaces, synthetic aperture imaging, and remote sensing.

DATA AVAILABILITY STATEMENT

The original contributions presented in the study are included in the article/Supplementary Material, further inquiries can be directed to the corresponding author.

AUTHOR CONTRIBUTIONS

All authors listed have made a substantial, direct, and intellectual contribution to the work and approved it for publication.

FUNDING

This work was supported by the National Natural Science Foundation of China (62075175, 61975254, 12104500) and Fundamental Research Funds for the Central Universities (Nos. XJS210506, JC2113).

REFERENCES

1. Liu X, Qiao S, Ma Y. Highly Sensitive Methane Detection Based on Light-Induced Thermoelastic Spectroscopy with a 2.33 Mm Diode Laser and Adaptive Savitzky-Golay Filtering. *Opt Express* (2022) 30:1304–13. doi:10.1364/oe.446294
2. Ma Y, Hong Y, Qiao S, Lang Z, Liu X. H-shaped Acoustic Micro-resonator-based Quartz-Enhanced Photoacoustic Spectroscopy. *Opt Lett* (2022) 47:601–4. doi:10.1364/ol.449822
3. Liu X, Ma Y. Sensitive Carbon Monoxide Detection Based on Light-Induced Thermoelastic Spectroscopy with a Fiber-Coupled Multipass Cell. *Chin Opt Lett* (2022) 20:031201. doi:10.3788/col202220.031201
4. Liu F, Han P, Wei Y, Yang K, Huang S, Li X, et al. Deeply Seeing through Highly Turbid Water by Active Polarization Imaging. *Opt Lett* (2018) 43:4903–6. doi:10.1364/ol.43.004903
5. Zheng G, Horstmeyer R, Yang C. Wide-field, High-Resolution Fourier Ptychographic Microscopy. *Nat Photon* (2013) 7:739–45. doi:10.1038/nphoton.2013.187
6. Ou X, Horstmeyer R, Yang C, Zheng G. Quantitative Phase Imaging via Fourier Ptychographic Microscopy. *Opt Lett* (2013) 38:4845–8. doi:10.1364/ol.38.004845
7. Ou X, Zheng G, Yang C. Embedded Pupil Function Recovery for Fourier Ptychographic Microscopy. *Opt Express* (2014) 22:4960–72. doi:10.1364/oe.22.004960
8. Xiang D, Xu S, Horstmeyer R. *Towards a Vectorial Treatment of Fourier Ptychographic microscopy. Computational Optical Sensing and Imaging*. Washington, DC: Optical Society of America (2020)22-26 June 2020.
9. Pan A, Zhang Y, Zhao T, Wang Z, Dan D, Lei M, et al. System Calibration Method for Fourier Ptychographic Microscopy. *J Biomed Opt* (2017) 22:1. doi:10.1117/1.JBO.22.9.096005
10. Pan A, Zhang Y, Wen K, Zhou M, Min J, Lei M, et al. Subwavelength Resolution Fourier Ptychography with Hemispherical Digital Condensers. *Opt Express* (2018) 26:23119–31. doi:10.1364/oe.26.023119
11. Sun J, Chen Q, Zhang J, Fan Y, Zuo C. Single-shot Quantitative Phase Microscopy Based on Color-Multiplexed Fourier Ptychography. *Opt Lett* (2018) 43:3365–8. doi:10.1364/ol.43.003365
12. Horstmeyer R, Chung J, Ou X, Zheng G, Yang C. Diffraction Tomography with Fourier Ptychography. *Optica* (2016) 3:827–35. doi:10.1364/optica.3.000827
13. Chowdhury S, Chen M, Eckert R, Ren D, Wu F, Repina N, et al. High-resolution 3D Refractive index Microscopy of Multiple-Scattering Samples from Intensity Images. *Optica* (2019) 6:1211–9. doi:10.1364/optica.6.001211
14. Guo K, Zhang Z, Jiang S, Liao J, Zhong J, Eldar YC, et al. 13-fold Resolution Gain through Turbid Layer via Translated Unknown Speckle Illumination. *Biomed Opt Express* (2018) 9:260–75. doi:10.1364/boe.9.000260
15. Dong S, Horstmeyer R, Shiradkar R, Guo K, Ou X, Bian Z, et al. Aperture-scanning Fourier Ptychography for 3D Refocusing and Super-resolution Macroscopic Imaging. *Opt Express* (2014) 22:13586–99. doi:10.1364/oe.22.013586
16. Ou X, Chung J, Horstmeyer R, Yang C. Aperture Scanning Fourier Ptychographic Microscopy. *Biomed Opt Express* (2016) 7:3140–50. doi:10.1364/boe.7.003140
17. Holloway J, Wu Y, Sharma MK, Cossairt O, Veeraraghavan A. SAVI: Synthetic Apertures for Long-Range, Subdiffraction-Limited Visible Imaging Using Fourier Ptychography. *Sci Adv* (2017) 3:e1602564. doi:10.1126/sciadv.1602564
18. Song P, Jiang S, Zhang H, Huang X, Zhang Y, Zheng G. Full-field Fourier Ptychography (FFP): Spatially Varying Pupil Modeling and its Application for Rapid Field-dependent Aberration Metrology. *APL Photon* (2019) 4:050802. doi:10.1063/1.5090552

19. Chung J, Martinez GW, Lencioni KC, Sadda SR, Yang. C. Computational Aberration Compensation by Coded-Aperture-Based Correction of Aberration Obtained from Optical Fourier Coding and Blur Estimation. *Optica* (2019) 6:647–61. doi:10.1364/optica.6.000647
20. Chung J, Kim J, Ou X, Horstmeyer R, Yang C. Wide Field-Of-View Fluorescence Image Deconvolution with Aberration-Estimation from Fourier Ptychography. *Biomed Opt Express* (2016) 7:352–68. doi:10.1364/boe.7.000352
21. Robert A. Gonsalves. "Phase Retrieval and Diversity in Adaptive Optics. *Opt Eng* (1982) 21:215829.
22. Echeverri-Chacón S, Restrepo R, Cuartas-Vélez C, Uribe-Patarroyo N. Vortex-enhanced Coherent-Illumination Phase Diversity for Phase Retrieval in Coherent Imaging Systems. *Opt Lett* (2016) 41:1817–20.
23. Zhang P, Yang C, Xu Z, Cao Z, Mu Q, Xuan L. High-accuracy Wavefront Sensing by Phase Diversity Technique with Bisymmetric Defocuses Diversity Phase. *Sci Rep* (2017) 7:15361–10. doi:10.1038/s41598-017-15597-x
24. Lofdahl MG, Kendrick RL, Harwit A, Mitchell KE, Duncan AL, Seldin JH, et al. Phase Diversity experiment to Measure Piston Misalignment on the Segmented Primary Mirror of the Keck II Telescope. *Space Telescopes Instr V* (1998) 3356:1190–1201. doi:10.1117/12.324519
25. Liang C-K, Lin T-H, Wong B-Y, Liu C, Chen HH. Programmable Aperture Photography: Multiplexed Light Field Acquisition. *ACM SIGGRAPH* (2008) 27:1–10. doi:10.1145/1399504.1360654

Conflict of Interest: The authors declare that the research was conducted in the absence of any commercial or financial relationships that could be construed as a potential conflict of interest.

frontiers in Physics

ORIGINAL RESEARCH
published: 25 March 2022
doi: 10.3389/fphy.2022.853266

Diffuse Imaging Approach for Universal Noninvasive Blood Glucose Measurements

Ming Liu[1,2,3†], *Ge Xu*[1,2†], *Yuejin Zhao*[1,2,3*], *Lingqin Kong*[1,2,3*], *Liquan Dong*[1,2,3], *Fen Li*[1,2,4*] *and Mei Hui*[1,2]

[1]School of Optics and Photonics, Beijing Institute of Technology, Beijing, China, [2]Beijing Key Laboratory for Precision Optoelectronic Measurement Instrument and Technology, Beijing, China, [3]Yangtze Delta Region Academy of Beijing Institute of Technology, Jiaxing, China, [4]National Astronomical Observatories, Chinese Academy of Science, Beijing, China

We proposed a diffuse imaging approach for universal noninvasive blood glucose measurements based on visible light, which can predict the blood glucose concentration without personal calibration. The proposed approach used a CCD to obtain diffuse images from human index finger pulp. The denoising autoencoder algorithm adopted effectively extracted the scattering information highly related to blood glucose concentration from the diffuse images, and the gradient boosting regression algorithm enabled an accurate calculation of blood glucose concentration without prior personalized calibration. *In vivo* experimental results showed that the proposed approach had a mean absolute error of 19.44 mg/dl, with all the predicted results observed within the clinically acceptable region (Region A: 78.9%) in the Clarke error grid analysis. Compared to other blood glucose concentration measurement methods of scattering coefficient, this new method does not require individual calibration, therefore it is easier to implement and popularize, which is critical for the noninvasive monitoring of blood glucose concentration.

Keywords: noninvasive blood glucose concentration monitoring, diffuse image, scattering coefficient, gradient boosting regression, deep feature

OPEN ACCESS

Edited by:
Karol Krzempek, Wrocław University of Science and Technology, Poland

Reviewed by:
Xiaojun Yu, Northwestern Polytechnical University, China
Santosh Kumar, Liaocheng University, China

***Correspondence:**
Yuejin Zhao
yjzhao@bit.edu.cn
Lingqin Kong
konglingqin3025@bit.edu.cn
Fen Li
feny2004@sina.com

†*These authors have contributed equally to this work*

Specialty section:
This article was submitted to Optics and Photonics, a section of the journal Frontiers in Physics

Received: *12 January 2022*
Accepted: *28 February 2022*
Published: *25 March 2022*

Citation:
Liu M, Xu G, Zhao Y, Kong L, Dong L, Li F and Hui M (2022) Diffuse Imaging Approach for Universal Noninvasive Blood Glucose Measurements. Front. Phys. 10:853266. doi: 10.3389/fphy.2022.853266

1 INTRODUCTION

Diabetes mellitus (DM) is a metabolic endocrine disease characterized by hyperglycaemia, which may cause many complications, such as heart disease, disability, and even death. DM has become the third serious threat to human health after cardio cerebrovascular disease and cancer in the world [1, 2]. According to the International Diabetes Federation, there were approximately 463 million adults with DM worldwide in 2019, with this number expected to increase to 700 million by 2045 [3]. The blood glucose concentration measurement method used clinically is to draw blood from a patient's vein or fingertips, and then a chemical test paper is used to determine the blood glucose concentration from the blood. This method not only makes the patient susceptible to infection, but also increases the economic burden and causes mental pain. In recent years, lots of efforts have been put into research and development in noninvasive measurement methods of blood glucose based on optical methods to solve these issues [4–7]. These optical methods specifically include near-infrared spectroscopy, Raman spectroscopy, bioimpedance spectroscopy [5, 6], thermal emission spectroscopy, and blood glucose measurement sensors based on cutting-edge tapered [9] optical fiber sensors [8–10].

The strong scattering property of skin tissue makes the scattered light more sensitive to the change of blood glucose concentration. Researchers have found that blood glucose levels may be predicted using the variation of scattering coefficient [11, 12]. Bruulsema et al [13] found a strong correlation between blood glucose concentration and scattering coefficient in DM patients. They provided a new idea that the scattering coefficient was estimated noninvasively based on measurements of the diffuse reflectance on the skin. This study was performed to evaluate the sensitivity of the tissue scattering coefficient in response to step changes in the blood glucose levels, and further verified the study in 41 DM patients. Heinemann et al. [14] demonstrated that in the visible and near-infrared light region, the effect of scattering was much higher than that of absorption in tissue. An increase in blood glucose concentration led to a decrease in the scattering coefficient of turbid suspension in both phantom studies and type I diabetic patients. Tianjin University's research [15] further demonstrated that the effect of the scattering coefficient on the diffuse reflectance was greater than that of the absorption coefficient. In their study, they separated the absorption coefficient and scattering coefficient of human tissue [16, 17]. However, although the relationship between blood glucose concentration and scattering coefficient has been studied to a certain extent, the accurate measurement model of blood glucose concentration by using scattering coefficient has not been further promoted [19, 20].

Deep learning algorithm shows strong computing power in the medical field, the optical method combing the deep learning algorithms is considered as one of the most promising measurement methods to set up a blood glucose model and has received extensive attention and research [18–21]. Bob Zhang [22] addressed a noninvasive method to detect DM patients based on facial block color features by using an image sensor with a collaborative representation classifier. In the collaborative representation classifier, the healthy facial color feature and the diabetic facial color feature were used to establish the relationship to determine whether the patient had DM. However, this classifier just classified the healthy people and the DM patients, which belonged to quantitative analysis, and did not measure the blood glucose concentration. Segman [23] employed a personal calibration procedure to associate blood glucose concentration and multiple optical signals which were derived from a fingertip response to light emission in the range of visible to infrared light. However, this model obtained the blood glucose concentration value in an invasive way to establish the personal calibration procedure. The model was only suitable for the individual of blood glucose measurement and did not have a universal application. Therefore, establishing a universal model for the measurement of blood glucose concentrations remains challenging. As for how to establish a universal model for the prediction of blood glucose concentration by using scattering information from human tissue has not been well understood.

In this paper, we presented a noninvasive blood glucose concentration measurement approach based on diffuse imaging. We used the denoising autoencoder (DAE) [24] to extract the weak blood glucose signal from the diffuse images of human fingertips, and a universal blood glucose calibration model was established between the diffuse images and scattering coefficient by gradient boosting regression (GBR) [25]. The experimental results showed consistency with the existing invasive device measurements.

2 METHODS

Compared with the absorption coefficient, the scattering coefficient is not susceptible to interference from other components in the tissue fluid, so it is more likely to establish a general model by using the relationship between the scattering coefficient and blood glucose concentration. Theoretical and *in vitro* studies [13, 26] also showed that visible light absorbed very little blood glucose. Heinemann [27] investigated changes of blood glucose concentration induced by an oral glucose experiment that can be monitored by registration of scattering coefficient changes. The scattering coefficient of biological tissue is mainly caused by the mismatch between the refractive index of the scattering particle n_s in the tissue fluid and the refractive index of the tissue fluid n_m. Under the assumption that the scattering condition is approximately consistent with the Rayleigh-Gans theory [26], the scattering coefficient can be expressed as

$$\boldsymbol{\mu}_s = \boldsymbol{k}\left(\frac{n_s - n_m}{n_m}\right)^2 \tag{1}$$

where k is a proportionality factor related to particle size, wavelength, particle density, and scattering angle. The change value of the scattering coefficient caused by the change of blood glucose concentration is written as

$$\Delta\boldsymbol{\mu}_s = \boldsymbol{k}\left(\frac{n_s - n_{mc}}{n_{mc}}\right)^2 - \boldsymbol{k}\left(\frac{n_s - n_{m0}}{n_{m0}}\right)^2 \tag{2}$$

where n_{mc} is the refractive index of the tissue fluid when blood glucose concentration is c_g, n_{m0} is the refractive index of the tissue fluid when blood glucose concentration is 0. The change of tissue fluid refractive index caused by the change of blood glucose concentration is small, we can consider as $n_{mc}^2 = n_{m0}^2$ in the high order term:

$$\Delta\boldsymbol{\mu}_s = \boldsymbol{2kn_s}\left(\frac{\boldsymbol{n_{m0} - n_{mc}}}{\boldsymbol{n_{m0}^2}}\right) \tag{3}$$

Assuming that the scattering coefficient is μ_{s0} when the concentration of blood glucose is 0, we can deduce that $n_{mc} - n_{m0} = \Delta n \times c_g$. Δn means that the refractive index of the scattering tissue fluid changes as a fixed constant when the blood glucose concentration changes by 1 mg/dl. When the concentration of glucose is c_g, the scattering coefficient can be expressed as

$$\boldsymbol{\mu}_s = \Delta\boldsymbol{\mu}_s + \boldsymbol{\mu}_{s0} = -\frac{\boldsymbol{2kn_s}\Delta\boldsymbol{n}}{\boldsymbol{n_{m0}^2}}\boldsymbol{c_g} + \boldsymbol{k}\left(\frac{n_s - n_{m0}}{n_{m0}}\right)^2 \tag{4}$$

According to the [28], the refractive index of the scatter particle n_s is 1.46 and when the concentration of blood glucose is 0, the refractive index of the tissue fluid n_{m0} is 1.35,

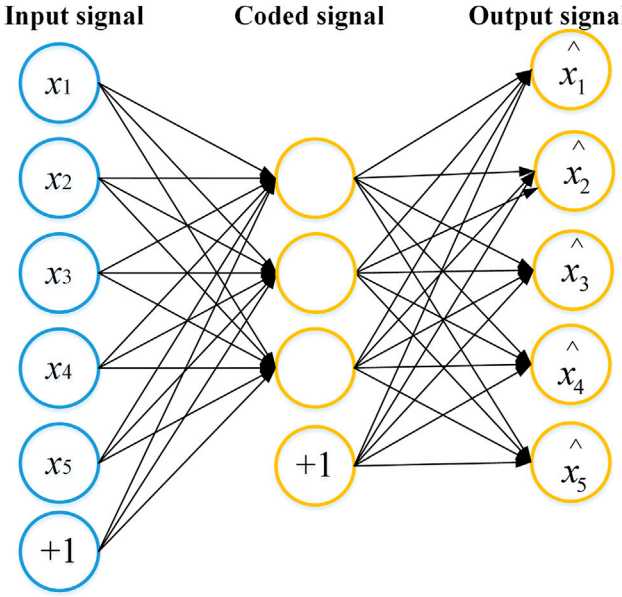

FIGURE 1 | The network structure of the autoencoder. The autoencoder consists of an encoder and a decoder. The encoder converts an input signal into a coded signal, and the decoder converts the coded signal into an output signal. The output signal reproduces the raw input signal as much as possible.

respectively. The refractive index of the scattering tissue fluid changes $\Delta n = 1.515 \times 10^{-6}$ mg/dl. Based on the **Eq. 4**, the scattering coefficient caused by the change of blood glucose concentration is as follows:

$$\mu_s = 2.43 \times 10^{-6} c_g - 6.64 \times 10^{-3} \quad (5)$$

Equation 5 indicates that the change of scattering coefficient caused by the change of blood glucose concentration is still slight. Therefore, the accuracy of the instrument is not enough to obtain the changing relationship of blood glucose concentration from the scattering coefficient by the diffuse reflectance spectroscopy method. Compared with the one-dimensional diffuse reflectance spectroscopy information, the two-dimensional diffuse images contain more features related to the scattering information from the change of blood glucose concentration.

Extracting useful information from the diffuse images and eliminating the interference factors independent of the blood glucose concentration, which are critical to build an accurate model. In this paper, we adopted the DAE network to extract the weak scattering information caused by the change of blood glucose concentration in two-dimensional diffuse images, and estimated the blood glucose concentration by combining with the GBR algorithm. The network structure of the autoencoder is shown in **Figure 1**. The autoencoder consists of an encoder and a decoder. The encoder converts an input signal into a coded signal, and the decoder converts the coded signal into an output signal. The output signal reproduces the input signal as much as possible.

The DAE randomly adds noise to the input signal of the autoencoder, so that features extracted from the whole DAE network structure occupies the robustness. The core idea of DAE is to select the best feature, which is extracted from the raw data by using the autoencoder. The best feature refers to the feature that can be used to recover the raw data when the raw data is corrupted. The network structure of the DAE is shown in **Figure 2A**, where input x (the ROIs of the raw diffuse images) is corrupted according to the stochastic mapping distribution to get $\bar{x}$. Subsequently, $\bar{x}$ was used as the input to the network. By training $\bar{x}$, the output z (reconstruct images) would finally be nearly equal to the original input x. The loss function is the cross-entropy, which can be expressed by the below equation:

$$L_H(x, z) = -\sum_j \left[x_j \log z_j + (1 - x_j) \log (1 - z_j) \right] \quad (6)$$

After training N epochs, the loss function on the training set converged to less than the threshold we set. Then, we extracted the vector s from the DAE middle layer as the deep features of the diffuse images. Specifically, the dimension of the deep feature is the scattering information of the raw diffuse images extracted in the middle layer of the DAE network. Finally, we used the deep features as the input x of the regression model to establish a universal GBR model connecting the deep features and blood glucose concentration. The GBR algorithm uses regression trees as weak learners with its structure shown in **Figure 2B**.

The basic function of the GBR algorithm is a binary regression tree. First initialize a regression tree, and then learn the next regression tree according to the residual of the previous regression tree. The regression tree was learned to obtain the final model by fitting the residual of the current model. Let us denote $Q = (s_1, y_1), (s_2, y_2), \ldots, (s_n, y_n)$, where s_i is the input composed of the deep features extracted from diffuse images by DAE, and y_i is the reference values of the blood glucose concentration from the invasive method. We suppose T_1, T_2, ... T_M as the M regression trees, C_{1j}, C_{2j}, ..., C_{mj} is the corresponding output of mth ($m = 1, 2 \ldots M$) regression trees, where j is the number of leaf nodes ($j = 1,2 \ldots J$) and R_{jm} is leaf node area. The final fitting regression tree is as follows:

$$f_M(s) = \sum_{m=1}^{M} \sum_{j=1}^{J} C_{mj} \quad (7)$$

The negative gradient of the loss function is used as an approximation of the residual in the GBR algorithm. The negative gradient the loss function of the ith subject in mth regression tress can be expressed as:

$$r_{im} = -\left[\frac{\partial L(y_i, f(s_i))}{\partial f(s_i)} \right] f(s) = f_{m-1}(s) \quad (8)$$

where $L(y, f(s))$ represents the loss function, $f(s)$ is the prediction values of the blood glucose concentration, respectively.

The fit residual error of jth leaf node ($j = 1, 2, \ldots, J$) is as follow:

$$r_{jm} = \arg\min_c \sum_{s_i \in R_{jm}} L(y_i, f_{m-1}(s_i) + \gamma) \quad (9)$$

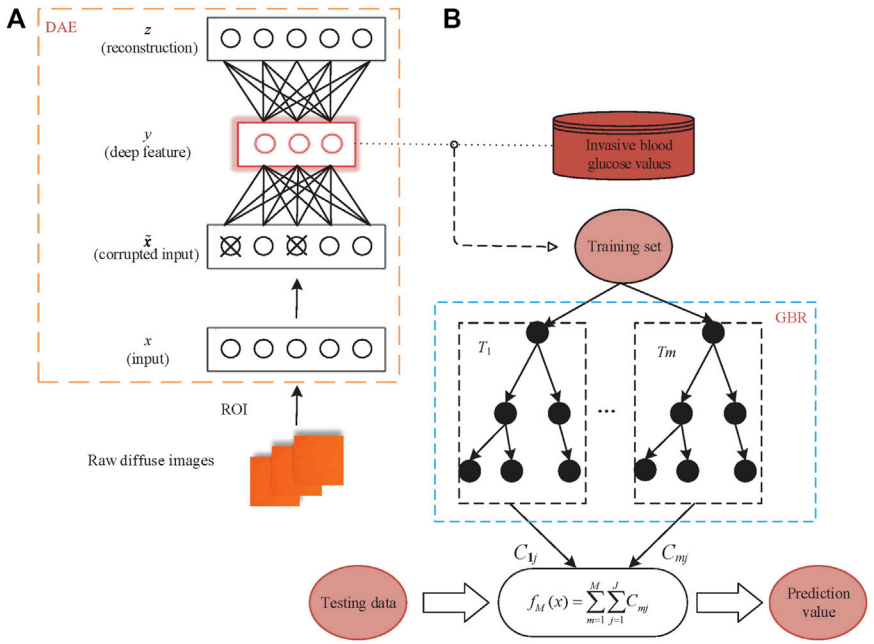

FIGURE 2 | Detailed network structure of the proposed algorithm **(A)** the DAE model; **(B)** the GBR model.

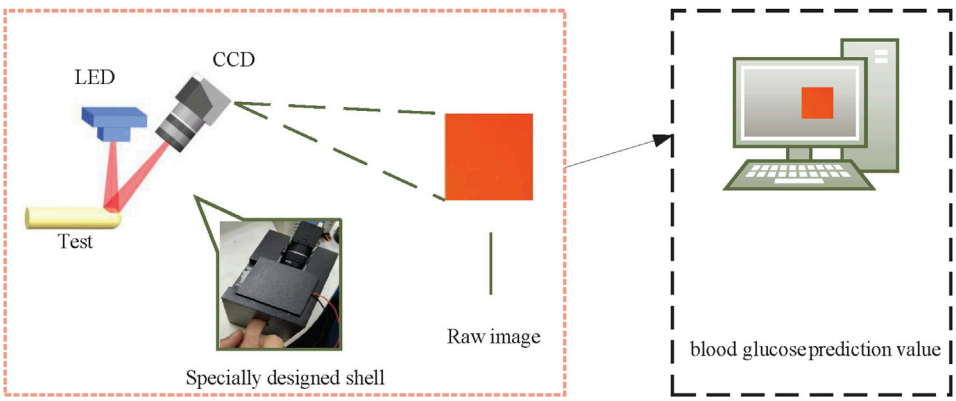

FIGURE 3 | Diagram of the system. A specially designed shell is used to fix the LED, CCD and a position for the test.

By updating $f_{m-1}(x)$, we can eventually calculate the blood glucose prediction $f(s)$.

3 EXPERIMENTAL SYSTEM

Figure 3 shows the experimental system for obtaining the diffuse images of fingers. The experimental system is composed of an imaging system, a light-emitting diode (LED) red light source, a specially designed shell and a computer. The imaging system includes a 1/1.2″ CCD sensor (FLIR co. BFLY-U3-23S6C-C), and a lens (ZLKC. VM0812MP) with an 8 mm focal length, and a 1.4 F-number. The frame rate captured by the CCD sensor is set to 25 frames/s and pixel resolution is 640 × 480 pixels. The size of the LED light source is 20 mm × 20 mm, which is integrated by four monochromatic lights with a wavelength of 625 nm. The angle between the light path of the illumination and imaging is 45°. The rated current is 700 mA and the voltage is 9–10 V. The imaging accuracy is 50 db and the speed of exposure is 30 ms. This specially designed shell reduces the interference from the external ambient light, measurement location, and image capture angle, and fixes the CCD and light source while retaining the collection hole of the test site. To avoid variation caused by the inconsistent measurement positions of different individuals, we collect diffuse images from the index finger pulp with a relatively stable surface and abundant blood vessels. The light, emitted from

TABLE 1 | The detailed information of the subjects from the healthy and the DM patients.

Gender (male/female)	The healthy		DM patients (early-state)		DM patients (long-term)	
	Male	Female	Male	Female	Male	Female
Number (people)	23	26	30	24	47	38
Average age (years)	25.5	24.5	35.2	40.1	46.8	47.3
Duration (years)	—	—	2.3	1.9	4.6	5.2

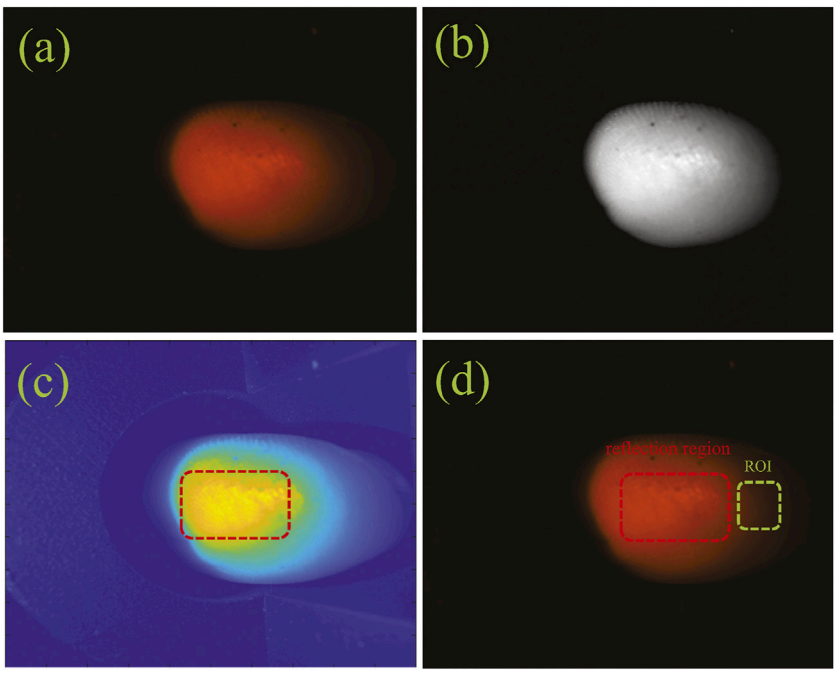

FIGURE 4 | The ROI of a diffuse image: **(A)** the original diffuse image; **(B)** the gray image; **(C)** the reflection image; **(D)** the ROI image.

the LED red light source, which is irradiated to the index finger. Then, the light is diffused by the index finger. Finally, the diffuse images of the index fingers are obtained by the CCD target surface and transmitted to the computer to process.

4 DATA PROCESSING AND ANALYSIS

The research protocol was approved by the Medical Ethics Committee of Medical and Laboratory Animal of Beijing Institute of Technology with approval code 2021-004. We obtained 188 image data from different subjects including 49 healthy people and 139 DM patients. The healthy people were from the Beijing Key Laboratory for Precision Optoelectronic Measurement Instrument and Technology with an average age of 25.0, and the DM patients were from the Xian Tao First People's Hospital Diabetes Center and Taiyuan Central Hospital Diabetes Center with an average age of 43.3. The healthy were verified *via* hospital examinations. The 139 DM patients included 54 early-stage patients with an average duration of 2.1 years and 85 long-term patients with an average duration of 4.9 years. The detailed information of the subjects was shown in **Table 1**. During *in vivo* experiment, every subject was required to place the left-hand index finger in the collection hole of the specially designed shell to capture a diffuse image, while the right index finger was used to collect reference blood glucose concentration value by invasive blood glucose measurement instrument. The reference blood glucose concentration value for *in vivo* subjects was obtained by using a commercial device (Rightest glucometer GM300).

The most intuitive and basic information representation method of diffuse images is the gray value and gradient. High gray value (high energy) and high gradients (high energy changes) in the diffuse images can remove most of the redundant information. The following factors are crucial considerations for the selection of ROI size for diffuse images. First, the specular reflection in the captured diffuse images occupied a larger proportion and was an important factor affecting the accuracy of this proposed method. The specular reflection area almost did not carry tissue optical information, which interfered with our choice of ROI area. Thus, we chose the ROI with a special size from the rest region of the diffuse images instead of the specular reflection region. In addition, every subject

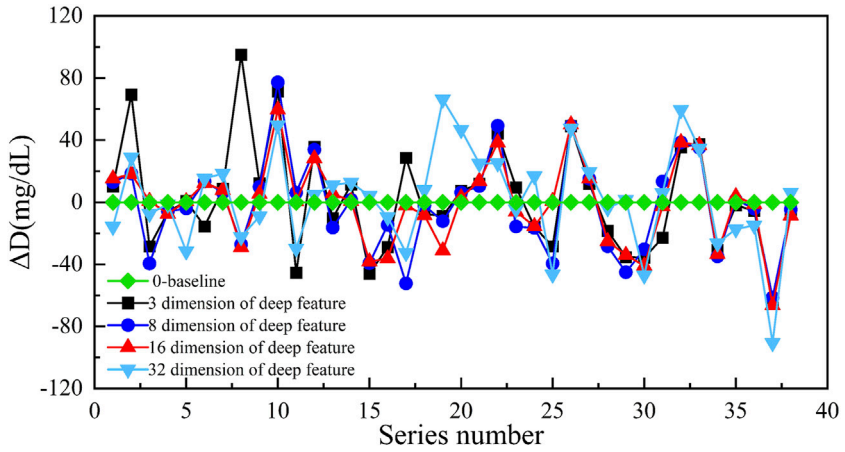

FIGURE 5 | The prediction result of different dimensional deep features (the ordinate is the difference between the predicted value and reference value, and the abscissa is the number of samples).

TABLE 2 | The prediction results of different dimension of deep features.

Dimension of deep features	MSE (mg/dl)	RMSE (mg/dl)	MAE (mg/dl)
1 × 3	65.34	34.38	26.64
1 × 8	50.04	30.06	23.58
1 × 16	38.70	26.46	19.44
1 × 32	55.08	31.50	24.12

TABLE 3 | Performances of the different algorithms.

Model method	MSE (mg/dL)	RMSE (mg/dL)	MAE (mg/dL)	R
PLSR	78.84	37.62	32.04	0.25
SVR	67.50	34.92	27.54	0.46
Our method	38.70	26.46	19.44	0.73

also had different finger sizes, so we need to keep the same selection size in all diffuse images from subjects' fingers. Finally, we considered that the ROI had a certain brightness but did not involve specular reflection, and also took into account the size of the subject's finger. So we selected a region with a size of 28 × 28 pixels centered on the maximum gray value of the diffuse image as the ROI region after removing the specular reflection information. The diffuse image obtained by a subject's finger and the ROI were shown in **Figure 4**. We got the ROIs with 28 × 28 pixels of diffuse images from 188 subjects.

We approximately adopted the 4:1 ratio when dividing into the training set and testing set from those ROIs. To train the DAE, we selected an ROI with the size of 28 × 28 pixels as the input, then extracted different dimensions from the DAE middle layer as the deep features of diffuse images. We extracted the deep features of 150 training subjects in different dimensions and adopted the GBR algorithm to establish the models of different dimension deep features, the results from the 38 testing subjects were as shown in **Figure 5**. The results showed that when the 1 × 16 dimensional vectors were selected as the deep features, the difference between the predicted value and the reference value was the smallest. Simultaneously, the prediction accuracy of the prediction model corresponding to the deep features of different dimensions were shown in **Table 2**. The results were evaluated in terms of the mean absolute error (MAE), root mean squared error (RMSE), and mean squared error (MSE).

The results of **Table 2** indicated that when we chose the 1 × 16 dimensional deep features, the MAE was the smallest (19.44 mg/dl). Hence, we selected the 1 × 16 dimensional deep features as the input to establish the GBR model to predict the blood glucose concentration in this paper. We believed that the reason was the uneven distribution of subjects' blood glucose concentration. The most range of the blood glucose concentration from the subjects was concentrated in 90 mg/dl–234 mg/dl with a proportion of 87.5%. In addition, the number of subjects also limited the dimensionality of the deep features extracted. Indeed, the dimension of deep features depends on the number of blood glucose samples used for training and the range of concentration values of blood glucose samples. Due to the limitation of sample size and concentration range, when the dimension of the deep features is too small, the scattering information of the diffuse images cannot be fully carried. When the dimension of deep features is too abundant, the DAE network will appear overfitting. These will lead to an increase in the prediction error of blood glucose concentration.

We compared the performance of the proposed method with several different multivariate calibration methods in different testing subjects. The results were still evaluated in terms of MAE, RMSE, and MSE. In addition, we added the Pearson correlation coefficient (R) as an evaluation indicator. Previous studies [29] had shown that the prediction results of the support vector regression (SVR) model were more accurate than the partial least squares regression (PLSR) method. Our experimental results also confirmed this conclusion.

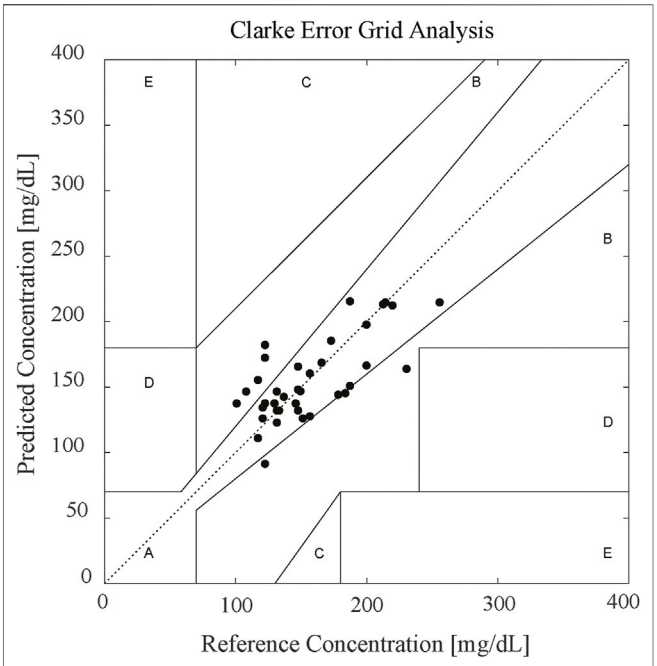

FIGURE 6 | CEG result of 38 *in vivo* subjects. 78.9% of the estimated blood glucose values fell in zone A and 100% in the clinically acceptable zones A and B.

The comparative results of 38 testing subjects were shown in **Table 3**. The values of MAE, RMSE, and MSE indicated that the proposed method achieved highly improved results as compared with the other commonly used multivariate correction methods. Furthermore, the results from the proposed model were consistent with the invasive results with an R of 0.73. The 38 testing subjects were from different individuals (including healthy and DM patients), which also demonstrated the universal applicability of the proposed model.

To further verify the accuracy, we used Clarke error grid (CEG) analysis to compare the results from the predicted blood glucose concentration values of 38 subjects with the invasive reference blood glucose concentration. **Figure 6** presents the CEG analysis, where the scatter plot can be divided into five regions. These regions quantify the accuracy of the blood glucose concentration reference values as compared to the predicted blood glucose concentration values in terms of the different types of errors. The CEG analysis results showed 78.9% of the estimated blood glucose concentration values fell in zone A and 100% in the clinically acceptable zones A and B, demonstrating the efficacy of the proposed noninvasive blood glucose concentration measurement method. Our method adopted significantly improved the prediction accuracy as compared with the other commonly used multivariate correction methods.

In fact, the number and the distribution of blood glucose concentration values from subjects affected the accuracy of the prediction model. The blood glucose concentrations obtained from different subjects were densely distributed in the 90 mg/dl–234 mg/dl range, sparsely distributed near the upper and lower limits of the range. Therefore, the prediction concentrations of the blood glucose had a larger error near the upper and lower limits of 90 mg/dl–234 mg/dl range, which increased the average error of the GBR model. By increasing the number of subjects near the upper and lower limits of blood glucose concentration values, the accuracy of the prediction model can be further improved. Moreover, the number of subject samples affected the selection of the optimal dimension of the deep features extracted by the DAE network, which determined the prediction accuracy of the blood glucose concentration. Expanding the number of the subject samples can obtain a more reliable dimension selection of the deep features.

5 CONCLUSION

In this paper, a universal calibration model for the noninvasive measurement of blood glucose concentration based on diffuse images was presented. This model connecting the scattering information and blood glucose concentration was established by extracting the deep features of the acquired diffuse images. First, a diffuse image of the left-hand index finger pulp from each subject was collected *via* a special shell and recorded by the CCD. After that, the deep features DAE network extracted from the diffuse images were used in the GBR model to establish the relationship between blood glucose concentration and scattering information. Finally, *in vivo* experimental results indicated the feasibility of the proposed method for the noninvasive prediction value of blood glucose concentration with an MAE of 19.44 mg/dl and an R of 0.73 in 1×16 dimensional deep features.

In this case, ambient temperature-controlled at 26řC and relative humidity is 33%. The room temperature and humidity during the measurement are in a controlled manner. Indeed, there still has a limitation of our study that the recruited subjects were all Asian. For future works, we should be combined with other physiological parameters (such as skin color, hydration, temperature, and humidity, etc.) to improve accuracy and correlation with blood glucose levels. We will also aim to collect more diffuse images of subjects' fingers, enrich the distribution of blood glucose concentration values from DM patients and healthy individuals to further improve the prediction accuracy of the model. In addition, we will select the more reliable dimension of deep features due to the increased number of subject samples.

DATA AVAILABILITY STATEMENT

The raw data supporting the conclusion of this article will be made available by the authors, without undue reservation.

ETHICS STATEMENT

The studies involving human participants were reviewed and approved by the Medical Ethics Committee of Medical and

Laboratory Animal of Beijing Institute of Technology with approval code 2021-004. The patients/participants provided their written informed consent to participate in this study. Written informed consent was obtained from the individual(s) for the publication of any potentially identifiable images or data included in this article.

AUTHOR CONTRIBUTIONS

All authors listed have made a substantial, direct, and intellectual contribution to the work and approved it for publication.

FUNDING

This work was supported by the National Natural Science Foundation of China (No. 61705010, No. 11774031, No. 61935001).

ACKNOWLEDGMENTS

The authors thank Xian Tao First People's Hospital Diabetes Center and Taiyuan Central Hospital Diabetes Center for providing the Statistical dataset support.

REFERENCES

1. American Diabetes Association. Diagnosis and Classification of Diabetes Mellitus. *Diabetes Care* (2014) 37(1):81–90. doi:10.2337/dc10-S062
2. Ogurtsova K, da Rocha Fernandes JD, Huang Y, Linnenkamp U, Guariguata L, Cho NH, et al. IDF Diabetes Atlas: Global Estimates for the Prevalence of Diabetes for 2015 and 2040. *Diabetes Res Clin Pract* (2017) 128:40–50. doi:10.1016/j.diabres.2017.03.024
3. IDF, Diabetes Atlas. *International Diabetes Federation* (2019). AvaliableAt: https://www.idf.org/aboutdiabetes/what-is-diabetes/facts-fifigures.html.
4. Hull EL, Matter NI, Olson BP, Ediger MN, Magee AJ, Way JF, et al. Noninvasive Skin Fluorescence Spectroscopy for Detection of Abnormal Glucose Tolerance. *J Clin Translational Endocrinol* (2014) 1(3):92–9. doi:10.1016/j.jcte.2014.06.003
5. Delbeck S, Vahlsing T, Leonhardt S, Steiner G, Heise HM. Non-invasive Monitoring of Blood Glucose Using Optical Methods for Skin Spectroscopy-Opportunities and Recent Advances. *Anal Bioanal Chem* (2019) 411(1):63–77. doi:10.1007/s00216-018-1395-x
6. He R, Wei H, Gu H, Zhu Z, Zhang Y, Guo X, et al. Effects of Optical Clearing Agents on Noninvasive Blood Glucose Monitoring with Optical Coherence Tomography: a Pilot Study. *J Biomed Opt* (2012) 17(10):101513. doi:10.1117/1.JBO.17.10.101513
7. So CF, Chung JWY, Siu MSM, Wong KS. Improved Stability of Blood Glucose Measurement in Humans Using Near Infrared Spectroscopy. *Spectroscopy* (2011) 25(3-4):137–45. doi:10.3233/SPE-2011-050710.1155/2011/542790
8. Yang Q, Zhu G, Singh L, Wang Y, Singh R, Zhang B, et al. Highly Sensitive and Selective Sensor Probe Using Glucose Oxidase/gold Nanoparticles/graphene Oxide Functionalized Tapered Optical Fiber Structure for Detection of Glucose. *Optik* (2020) 208:164536. doi:10.1016/j.ijleo.2020.164536
9. Gong P, Li X, Zhou X, Zhang Y, Chen N, Wang S, et al. Optical Fiber Sensors for Glucose Concentration Measurement: A Review. *Opt Laser Tech* (2021) 139:106981. doi:10.1016/j.optlastec.2021.106981
10. Cano Perez JL, Gutiérrez-Gutiérrez J, Perezcampos Mayoral C, Pérez-Campos EL, Pina Canseco Md. S, Tepech Carrillo L, et al. Fiber Optic Sensors: A Review for Glucose Measurement. *Biosensors* (2021) 11(3):61. doi:10.3390/bios11030061
11. Kohl M, Essenpreis M, Böcker D, Cope M. Influence of Glucose Concentration on Light Scattering in Tissue-Simulating Phantoms. *Opt Lett* (1994) 19(24):2170–2. doi:10.1364/OL.19.002170
12. Yu L-P, Wu J-S, Chang S-Y, Chou C. Glucose Detection in a Highly Scattering Medium with Diffuse Photon-Pair Density Wave. *J Innov Opt Health Sci* (2017) 10(01):1650032. doi:10.1142/S1793545816500322
13. Bruulsema JT, Hayward JE, Farrell TJ, Patterson MS, Heinemann L, Berger M, et al. Correlation between Blood Glucose Concentration in Diabetics and Noninvasively Measured Tissue Optical Scattering Coefficient. *Opt Lett* (1997) 22(3):190–2. doi:10.1364/OL.22.000190
14. Heinemann L, Schmelzeisen-Redeker G. Non-invasive Continuous Glucose Monitoring in Type I Diabetic Patients with Optical Glucose Sensors. *Diabetologia* (1998) 41(7):848–54. doi:10.1007/s001250050998
15. Chen W, Liu R, Luo Y, Han Y, Xu K. Preliminary Study of Mechanism of Non-invasive Blood Glucose Measurement Based on Near-Infrared Diffuse Reflectance Spectroscopy. In: Proc. SPIE 5696, Complex Dynamics and Fluctuations in Biomedical Photonics II. 29 March 2005; San Jose, CA, 5696. (SPIE: United States) (2005). p. 91–100. doi:10.1117/12.589597
16. Liu J, Han T, Han G, Cai Z, Zhang Z, Liu B, et al. Optimum Source-Detector Separators for Diffuse Light in Noninvasive Tissue Constituent Sensing. *JM3A* (2016) 11. doi:10.1364/CANCER.2016.JM3A.11
17. Liu J, Han T, Jiang J, Xu K. Specialized Source-Detector Separations in Near-Infrared Reflectance Spectroscopy Platform Enable Effective Separation of Diffusion and Absorption for Glucose Sensing. *Biomed Opt Express* (2019) 10(9):4839–58. doi:10.1364/BOE.10.004839
18. Geng Z, Tang F, Ding Y, Li S, Wang X. Noninvasive Continuous Glucose Monitoring Using a Multisensor-Based Glucometer and Time Series Analysis. *Sci Rep* (2017) 7(1):1–10. doi:10.1038/s41598-017-13018-7
19. Sen Gupta S, Kwon T-H, Hossain S, Kim K-D. Towards Non-invasive Blood Glucose Measurement Using Machine Learning: An All-Purpose PPG System Design. *Biomed Signal Process Control* (2021) 68:102706. doi:10.1016/j.bspc.2021.102706
20. Zhang G, Mei Z, Zhang Y, Ma X, Lo B, Chen D, et al. A Noninvasive Blood Glucose Monitoring System Based on Smartphone PPG Signal Processing and Machine Learning. *IEEE Trans Ind Inf* (2020) 16(11):7209–18. doi:10.1109/TII.2020.2975222
21. Gusev M, Poposka L, Spasevski G, Kostoska M, Koteska B, Simjanoska M, et al. Noninvasive Glucose Measurement Using Machine Learning and Neural Network Methods and Correlation with Heart Rate Variability. *J Sensors* (2020) 2020:1–13. doi:10.1155/2020/9628281
22. Zhang B, Kumar BVKV, Zhang D. Noninvasive Diabetes Mellitus Detection Using Facial Block Color with a Sparse Representation Classifier. *IEEE Trans Biomed Eng* (2014) 61(4):1027–33. doi:10.1109/TBME.2013.2292936
23. Segman Y. Device and Method for Noninvasive Glucose Assessment. *J Diabetes Sci Technol* (2018) 12(6):1159–68. doi:10.1177/1932296818763457
24. Vincent P, Larochelle H, Bengio Y, Manzagol P-A. Extracting and Composing Robust Features with Denoising Autoencoders. In: Proceedings of the 25th International Conference on Machine Learning (ICML '08) New York, NY: Association for Computing Machinery. (2008). p. 1096–1103. doi:10.1145/1390156.1390294
25. Friedman J, Hastie T, Tibshirani R. Additive Logistic Regression: a Statistical View of Boosting (With Discussion and a Rejoinder by the Authors). *Ann Stat* (2000) 28(2):337–407. doi:10.1214/aos/101612046310.1214/aos/1016218223
26. Maier JS, Walker SA, Fantini S, Franceschini MA, Gratton E. Possible Correlation between Blood Glucose Concentration and the Reduced Scattering Coefficient of Tissues in the Near Infrared. *Opt Lett* (1994) 19(24):2062–4. doi:10.1364/OL.19.002062

27. Heinemann L, Krämer U, Klötzer H-M, Hein M, Volz D, Hermann M, et al. Noninvasive Glucose Measurement by Monitoring of Scattering Coefficient during Oral Glucose Tolerance Tests. *Diabetes Tech Ther* (2000) 2(2):211–20. doi:10.1089/15209150050025168
28. Jacques SL. Origins of Tissue Optical Properties in the UVA, Visible, and NIR Regions. *OSA TOPS Advances Optical Imaging Photon Migration* (1996) 2:364–9.
29. Rachim VP, Chung W-Y. Wearable-band Type Visible-Near Infrared Optical Biosensor for Non-invasive Blood Glucose Monitoring. *Sensors Actuators B: Chem* (2019) 286:173–80. doi:10.1016/j.snb.2019.01.121

Conflict of Interest: The authors declare that the research was conducted in the absence of any commercial or financial relationships that could be construed as a potential conflict of interest.

Publisher's Note: All claims expressed in this article are solely those of the authors and do not necessarily represent those of their affiliated organizations, or those of the publisher, the editors and the reviewers. Any product that may be evaluated in this article, or claim that may be made by its manufacturer, is not guaranteed or endorsed by the publisher.

frontiers | Frontiers in Physics

ORIGINAL RESEARCH
published: 04 April 2022
doi: 10.3389/fphy.2022.865240

A New Estimation Method for Rotor Size of UAV Based on Peak Time-Shift Effect in Micro-Doppler Lidar

Yong Zhang[1,2], *Dongmei Li*[1,2], *Yi Han*[3], *Zhen Yang*[1,2]*, *Xin Dai*[1,2], *Xinmin Guo*[1,2] and *Jianlong Zhang*[1,2]

[1]National Key Laboratory of Science and Technology on Tunable Laser, Harbin Institute of Technology, Harbin, China, [2]Department of Optoelectronic Information Science and Technology, School of Astronautics, Harbin Institute of Technology, Harbin, China, [3]School of Instrument Science and Engineering, Institute of Functional Materials and Acoustooptic Instruments, Harbin Institute of Technology, Harbin, China

The aim of this study was to solve the problem that the existing identification parameters of rotor unmanned aerial vehicles (UAVs) are few and limited by the detection mode, and an identification method for estimating the rotor blade width based on the peak time-shift effect is proposed for the first time. Taking the width of the rotor blade as the parameter to identify the rotor of UAVs, the time-shift effect and its relationship with rotor blade width are verified by theoretical analysis and simulation. The proposed time-shift method has the characteristics of high-precision extraction of rotor width, and its effectiveness is verified by simulation and experiments. The aspect ratio of the rotor is accurately extracted based on the proposed time-shift method under the condition of an unknown pitch angle. Simulation results show that the estimation accuracy of the width and aspect ratio is up to 98 and 98.4%, respectively. The experimental results show that the relative errors of the width and aspect ratio are less than 7 and 4%, respectively. This study provides the theoretical basis and technical support for the high-accuracy identification of rotorcraft UAVs.

Keywords: UAV, laser radar, micro-Doppler, peak time-shift method, size estimation

OPEN ACCESS

Edited by:
Qun Hao,
Beijing Institute of Technology, China

Reviewed by:
Hong Gu,
Tianjin Polytechnic University, China
Xu Yang,
Zhejiang Sci-Tech University, China

***Correspondence:**
Zhen Yang
sailoryz@hit.edu.cn

Specialty section:
This article was submitted to Optics and Photonics, a section of the journal Frontiers in Physics

Received: *29 January 2022*
Accepted: *07 March 2022*
Published: *04 April 2022*

Citation:
Zhang Y, Li D, Han Y, Yang Z, Dai X, Guo X and Zhang J (2022) A New Estimation Method for Rotor Size of UAV Based on Peak Time-Shift Effect in Micro-Doppler Lidar. Front. Phys. 10:865240. doi: 10.3389/fphy.2022.865240

INTRODUCTION

The rotor blade is the main power component of the rotorcraft, and its rotating motion modulates the Doppler echo generated by the UAV fuselage motion to form micro-Doppler signals [1–3]; therefore, the echo signal contains the size information of the rotor [4–6]. Different types of rotorcraft UAVs have different blade parameter information [7], mainly including blade width and aspect ratio of a rotor blade, which are crucial reference indexes for identifying rotorcraft UAVs [8–10].

At present, there are only three parameters available for rotor UAV identification: rotor blade length [11–13], number of blades [14–16], and number of rotors [17]. The different models of rotor blades reflect different information and can extract different parameters. In a certain establishing model, the whole rotor blade is equivalent to a point target and used to simulate the rotation of the rotor [18–20]. This model can vividly reflect the motion trajectory of rotor blades. Unfortunately, this model is too rough and has a big difference from the actual echo signal. Chen et al. [21] equated rotor blades to linear scatterers. Based on this modeling, the length of the rotor blade, number of blades, and number of the rotor can be extracted. On the contrary, this kind of modeling lacks lot of detailed information [22, 23]. Chen et al. [24] discretized the rotor blade

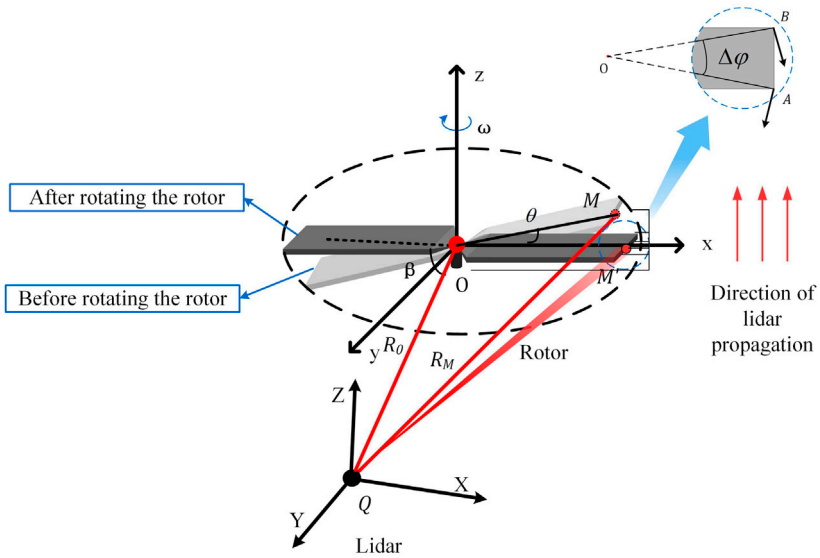

FIGURE 1 | Relative position of the rotor and laser line of sight.

into scattering panel elements with uniform scattering coefficients and equally spaced distribution. The echo of a rotor blade is superimposed by the echo, which is formed by countless scattering surface elements. Jiang et al. [25] verified through this model that the envelope shape in the time–frequency diagram formed by different blade width and blade tip sweep angle is different. Wang et al. [26] confirmed that the greater the rotor blade width, the greater the sub-frequency band. However, the peak phenomenon in the time–frequency diagram was not introduced in detail, ignoring the contribution of rotor blade width to peak time-shift. In addition, the contribution of rotor blade thickness to echo could not be verified, either. Based on the aforementioned research results, it is necessary to establish a new model to verify the influence of various parameters of rotor blades on laser micro-Doppler echo. Based on this model, a new identification parameter of the rotor UAV is extracted. The width and aspect ratio of the rotor blade are urgently required to establish a high-precision identification method that can accurately identify the width and aspect ratio parameters of the UAV blade.

As the parameters of rotorcraft UAV identification based on the laser micro-Doppler effect are few and cannot be accurately identified [27, 28], this study proposed the UAV parameter high-precision identification avenue based on the time-shift method for the first time. By using the high spatial resolution lidar [29–31] and establishing a cuboid geometric model with multiple scattering points, it ensures that the echo signal contains a lot of details of the rotor [32–34]. Based on the proposed time-shift method, the influence of blade width on the micro-Doppler echo signal is studied with the proven correctness by simulation and experiment. The results show that the proposed method can achieve a high recognition rate extraction of rotor width and aspect ratio. The UAV width recognition rate is 98% and its aspect ratio is 98.4% in simulation, while they are 93 and 96% in theoretical verification, which provides the technical support for further recognition of UAVs.

THEORETICAL MODELING AND ANALYSIS OF THE SINGLE-BLADE ROTOR

Multipoint Scattering Rotor Echo Modeling

As shown in the small diagram in **Figure 1**, the light emitted by the lidar shines on the rotating rotor blade target of rotorcraft UAVs and scatters, and the rotating motion of the rotor blade modulates the echo signal and forms the micro-Doppler echo signal. The micro-Doppler echo signal contains geometric structure information such as the length, width, and length–width ratio of the rotor blade target. The rotor blade targets are identified by extracting the information from the micro-Doppler. Assuming that the rotation center of the rotor blade is located at the coordinate origin O, α is azimuth which is zero here, along with β which is the pitching angle. The distance between the lidar and rotor center is R_0, where z_0 is the height of the rotor blade, the distance between the scattering point on the blade and the rotor center is l_M ($l_M << R_0$), and the scattering point rotates around the z-axis at constant angular velocity ω. Supposing that the initial phase of point M on the rotor blade is ϕ_0, the rotor blade passes through time t from point M to point M'. Based on single-point modeling, the baseband signal returned by the scattering point at distance R is [2, 3].

$$s_R(t) = \exp\left\{\begin{array}{l} -j2\pi f_0 t - j\dfrac{4\pi}{\lambda}R_0 - j\dfrac{4\pi}{\lambda}z_0\sin\beta \\ -j\dfrac{2\pi}{\lambda}l_M\cos\beta\left(\cos\phi_0\cos\omega t - \sin\phi_0\sin\omega t\right) \end{array}\right\}. \tag{1}$$

The rotor blade is equivalent to a cuboid with a certain thickness, and it has meshed. The points on the meshing are

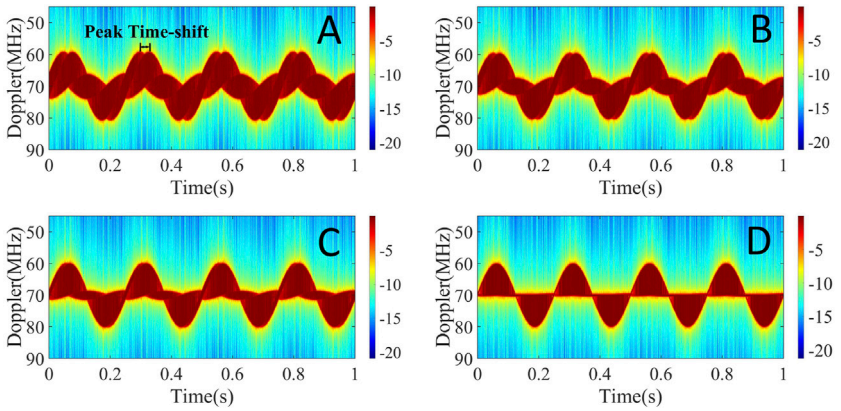

FIGURE 2 | Time–frequency diagram of the different rotor widths. Length: width: height **(A)** 40:30:1. **(B)** 40:20:1. **(C)** 40:10:1. **(D)** 40:1:1.

named scattering points to replace the central points of the scattering surface element of the rotor blade. Let the coordinates of scattering points be (x_i, y_j, and z_k), where i, j, and k are integers; the distance between the rotor center O and each scattering point is $l_M(x, y, z) = (x^2 + y^2 + z^2)^{1/2}$. Then, the scattering echo signal is modified as follows:

$$s_R(t) = \sigma \sum_{i=-\frac{x}{2}}^{\frac{x}{2}} \sum_{j=0}^{y} \sum_{k=-\frac{z}{2}}^{\frac{z}{2}} \exp\left\{ \begin{array}{l} -j2\pi f_0 t - j\frac{4\pi}{\lambda}\left(R_0^{'} + z_0 \sin\beta\right) \\ -j\frac{2\pi}{\lambda} l_M(x_i, y_j, z_k)\left[\cos\beta(\cos\phi_0 \cos\omega t - \sin\phi_0 \sin\omega t)\right] \end{array} \right\}, \tag{2}$$

where $R_0^{'} = R_0^{'} + l_M(x, y, z)$ σ is the scattering coefficient

Contribution of Rotor Width to Echo

The relative position of the rotor and lidar is shown in **Figure 1**. The distance between the lidar and target rotor is much larger than the length of the rotor L, and the visible laser is a parallel ray (parallel line with an arrow on the right of the **Figure 1**). To simplify the calculation, the lidar is equivalent to point Q, and the line QO is parallel to the lidar line of sight. The distance between lidar Q and the rotation center O of the rotor blade is R_0, and the distance between Q and point M on the top of the rotor blade is R_M. θ is the rotation angle of the line between point M and the rotation center O of the rotor blade around the x-axis, and its magnitude is complementary to the included angle between the linear velocity direction and radial velocity direction of point M. From the references of [13, 30], it can be known that

$$f_M = \frac{2}{\lambda}\omega L \sin\theta \cos\beta. \tag{3}$$

According to **Eq. 3**, the micro-Doppler frequency-shift generated by scattering points on rotor blades is related to ω and θ. When $\theta = \pm n\pi$, the micro-Doppler shift reaches the minimum value zero. So, the time–frequency diagram is periodic.

As shown in the upper right corner of **Figure 1**, points A and B are the two vertices of the blade, and the width of the rotor blade is AB. The rotor rotates at the same angular velocity. When $\theta = \pm(2n+1)\frac{\pi}{2}$, the maximum micro-Doppler frequency-shift is generated due to the influence of the length of the rotor blade, and its magnitude is

$$f_{L-\max} = \frac{2\omega L}{\lambda}\cos\beta. \tag{4}$$

However, when the connection between rotor apex A and rotor blade rotating center O is perpendicular to the radar line of sight (OA is perpendicular to the radar line of sight), the micro-Doppler frequency-shift generated by vertex B does not reach the maximum value. When OA rotates $\Delta\phi$ angle, the linear velocity direction of vertex B is parallel to the radar line of sight direction and the micro-Doppler frequency-shift reaches the maximum value. According to **Eq. 4**, the maximum frequency-shift of the micro-Doppler is related to L. The distance between vertex A and B and rotor blade center O is the greatest. Therefore, in this process, the micro-Doppler frequency-shift gradually decreases from the maximum frequency-shift at point A to the minimum value at the center point AB and then increases gradually to the maximum value at point B, that is, two peak values appear, and the time taken to generate the two peak values is the time taken for the angle change $\Delta\phi$, which is called the peak time-shift Δt in this study, and

$$\Delta t = \frac{\Delta\varphi}{\omega}. \tag{5}$$

TABLE 1 | Echo signal simulation parameters of the rotor single blade.

Simulation parameters of the rotor single-blade echo signal			
Laser wavelength	1.064 nm	Rotational frequency	4 Hz
Laser frequency	70 MHz	Blade length	0.24 m
Angle of pitch	30°	Leaf length–height ratio	40:1

SIMULATION ANALYSIS OF THE ECHO SIGNAL FOR THE ROTOR BLADE

As shown in the small diagram in **Figure 1**, the larger the width of the rotor blade is the bigger the phase $\Delta\phi$ of the corresponding

rotation center o is. Combining with **Eq. 5**, it can be found that under the condition of the same rotation frequency of the rotor, the larger the $\Delta\phi$ is the longer the rotor rotates around the whole width. To verify that the simultaneous peak effect of the rotor blade width contributes to the micro-Doppler echo is more intuitive, the rotor blade width was simulated with equal columns of the 0.06-m interval based on the fixed rotor blade length. The numerical values are 0.18 m, 0.12 m, 0.06 m, and 0.01 m. The peak can be clearly seen in **Figure 2A**. There is a large distance between the two peaks. The peak of **Figure 2B** decreases relative to the peak in **Figure 2A**. Similarly, the peaks of **Figures 2C,D** gradually decrease relative to the previous simulation time–frequency map. The width relative to the length of the rotor blade can be considered a line when the width ratio of the rotor blade is 40:1:1. The same results, as in [18–20] linear modeling, correct the results of this study. **Table 1** shows the parameters used in the simulation, in which the results are shown in **Figure 2**.

The laser micro-Doppler echo signal formed by the rotor blade rotation is a time-varying nonstationary signal. Then, the original time–frequency diagram can be obtained. However, the data span ambassador in the original time–frequency map has a large dynamic range using the log compression dynamic range. Meanwhile, the points in the time–frequency map are discrete, and Gaussian smoothing is taken and filtered.

Figure 2 shows that the simulation time–frequency diagram changes periodically and the time spectrum is a visually twisted rope, completing four cycles within a second, which expressed the rotation of the rotor as 4 HZ. As can be seen from **Figure 2A**, there are two peaks at the peak location in one cycle. In **Figure 2A**, the physical quantity of abscissa is time, the physical quantity of ordinate is micro-Doppler frequency, and the maximum micro-Doppler frequency shift generated at the peak is 11 MHz. The interval between the two peak values is the time-shift. When the aspect ratio decreases in equal proportion, the time-shift decreases with the decrease of rotor width. As shown in the simulation time–frequency diagram, according to the proportional relation of the aspect ratio, the width of the rotor blade in **Figure 2A** is the largest, and the corresponding time-shift is larger. When the rotation frequency is the same, the longer it takes for the vertex at one end of the width to reach the peak formed by the other vertex the larger the interval between the two peaks and the bigger the time-shift. The aforementioned simulation verification and analysis show that the time-shift effect does exist and the time-shift method can be used to estimate the width of the rotor blade.

ROTOR SIZE ESTIMATION BASED ON THE PEAK TIME-SHIFT METHOD

It can be seen from the aforementioned section that the echo signal time–frequency diagram will show a peak time-shift due to the influence of rotor width. In this section, the time-shift method will be used for parameter estimation and error analysis of the rotor width and aspect ratio.

Rotor Width Estimation

Assuming that the pitch angle of the rotor is 30°, the rotation frequency $f_0 = 4$ Hz, and the maximum micro-Doppler frequency-shift corresponding to the length of the rotor is $f_{L-\max}$, the length of the rotor can be obtained from **Eq. 4** as follows:

$$L = \frac{f_{L-\max}\lambda}{2\omega\cos\beta}. \tag{6}$$

The ratio of length to width of the selected rotors in this study is not less than 3:1, in which the width can be approximated as $W = 2L\sin(\frac{\Delta\varphi}{2})$. Combining **Eqs 5**, **6**, the width can be obtained as follows:

$$W = 2L\sin\left(\frac{\Delta\varphi}{2}\right) = \sin\left(\frac{\omega\cdot\Delta t}{2}\right)\frac{\lambda f_{L-\max}}{\omega\cos\beta}. \tag{7}$$

The simulation results show that the thickness of the rotor blade has no contribution to the maximum micro-Doppler frequency-shift, rotation frequency, and waveform envelope in the time–frequency diagram after processing. Therefore, this article does not study the correlation effect of rotor blade thickness. In the simulation calculation of the contribution of the rotor blade size to echo signal, the width is changed by adjusting the aspect ratio, and the thickness of the rotor is set as 1/40 of the length. According to **Eq. 7**, the width of the rotor blade determines the peak (Δt) in the time–frequency diagram. According to the characteristics of the time–frequency diagram, the rotor blade rotation frequency ω and the maximum micro-Doppler frequency-shift $f_{L-\max}$ can be extracted as shown in **Figure 3A**.

The laser micro-Doppler echo signal formed by the rotating rotor blade is transformed into the original time–frequency diagram by a short-time Fourier transform. The original time–frequency map has some disadvantages, such as less low-frequency details reserved, low contrast between time–frequency features and background, unsmooth edge leading to time–frequency spectrum repetition period, and the unclear edge of the outer envelope. Logarithmic transformation and Gaussian filtering are used to smooth the edge noise of the original time–frequency graph in order to compress the dynamic range of the data while increasing the low-frequency details, and the time-spectrum envelope is clearer.

The outer envelope function of the time–frequency diagram is extracted, and its derivative is used to calculate the maximum value of the function. The outer envelope function takes time as a variable, and the maximum value of the function is the maximum frequency-shift of micro-Doppler. According to the maximum value of the envelope function, the corresponding occurrence time is calculated. The two nearest adjacent maximum values and the corresponding time interval are the peak value of the micro-Doppler frequency-shift and its corresponding time-shift, respectively.

Substituting the laser wavelength $\lambda = 1064$ nm, $\omega = 8\pi$ rad/s, sampling rate 10,000, and pitch angle $\beta = 30°$into **Eq. 7**, the results are shown in **Table 2**. The length of the simulation setting is 0.24 m. According to the equivalent length–width

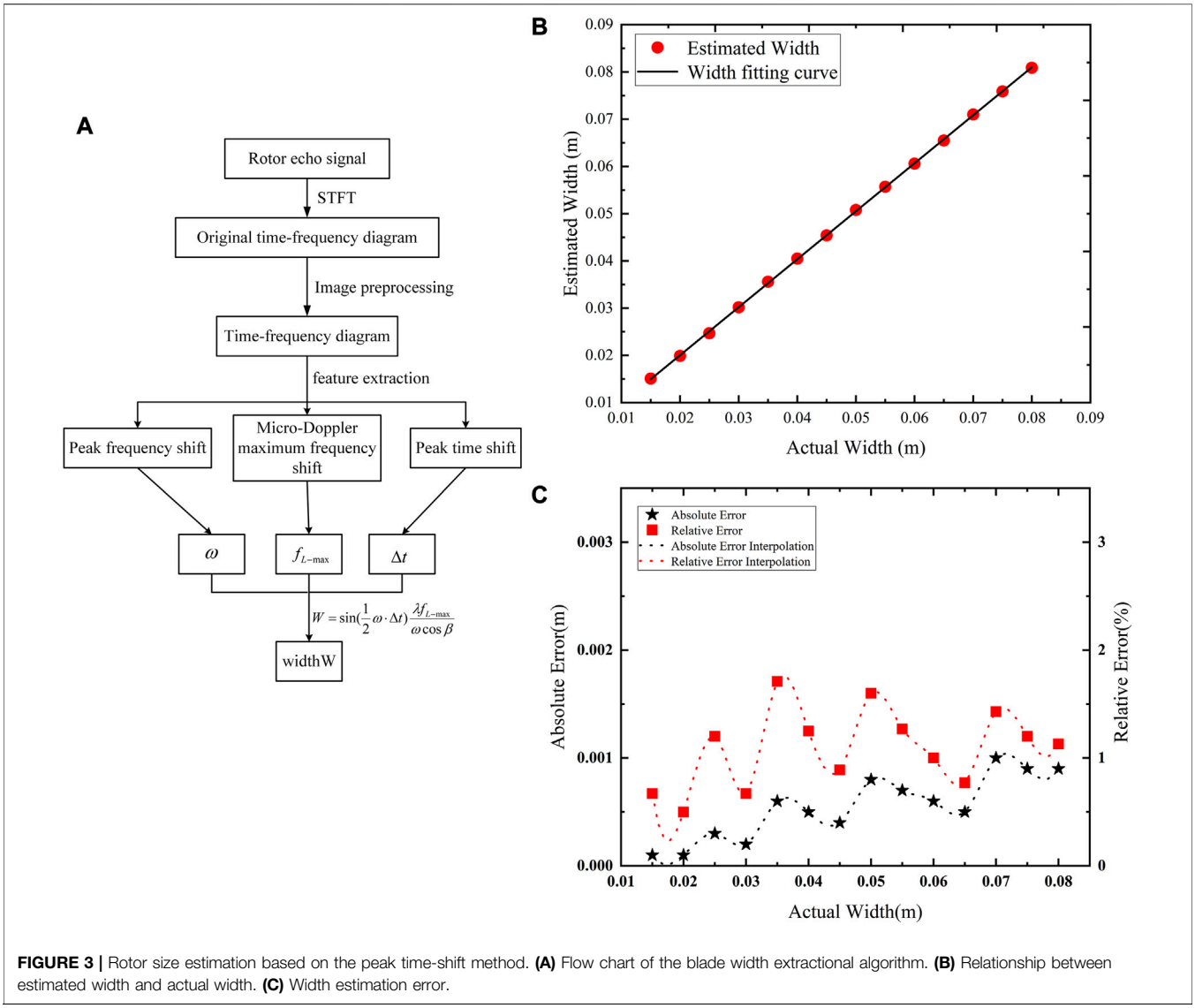

FIGURE 3 | Rotor size estimation based on the peak time-shift method. **(A)** Flow chart of the blade width extractional algorithm. **(B)** Relationship between estimated width and actual width. **(C)** Width estimation error.

TABLE 2 | Width estimation results.

Actual width (m)	$f_{L\text{-max}}$ (MHz)	Δt (s)	Estimated width (m)	Relative error (%)
0.080	9.95	0.0133	0.0809	1.13
0.075	9.93	0.0125	0.0759	1.20
0.070	9.92	0.0117	0.0710	1.43
0.065	9.90	0.0108	0.0655	0.77
0.060	9.89	0.0100	0.0606	1.00
0.055	9.88	0.0092	0.0557	1.27
0.050	9.87	0.0084	0.0508	1.6
0.045	9.86	0.0075	0.0454	0.89
0.040	9.85	0.0067	0.0405	1.25
0.035	9.84	0.0059	0.0356	1.71
0.030	9.83	0.0050	0.0302	0.67
0.025	9.83	0.0041	0.0247	1.2
0.020	9.82	0.0033	0.0199	0.5
0.015	9.82	0.0025	0.0151	0.67

TABLE 3 | Estimation results of the aspect ratio.

Actual aspect ratio	Δt (s)	Estimated aspect ratio	Absolute error	Relative error (%)
3.00:1	0.0133	3.01	0.01	0.33
3.20:1	0.0125	3.20	0.00	0
3.43:1	0.0117	3.41	0.02	0.58
3.69:1	0.0108	3.70	0.01	0.27
4.00:1	0.0100	3.99	0.01	0.25
4.36:1	0.0092	4.33	0.03	0.69
4.80:1	0.0084	4.75	0.05	1.04
5.33:1	0.0075	5.31	0.02	0.38
6.00:1	0.0067	5.95	0.05	0.83
6.86:1	0.0059	6.75	0.11	1.60
8.00:1	0.0050	7.96	0.04	0.50
9.60:1	0.0041	9.71	0.11	1.15
12.00:1	0.0033	12.06	0.06	0.50

ratio of the real rotor blade between 4:1 and 16:1, the width value of the rotor blade is set to be between 0.08 and 0.015 m. Based on this, this study extracted the width of the rotor blade in turn based on the peak method and the equal difference decreasing law of the width of the rotor blade. The average value of the peak value ($f_{L-\max}$) and time-shift (Δt) in each cycle of the time–frequency diagram of each group of experiments was calculated and recorded. The extraction results are shown in **Table 2**.

The relationship between the estimated width and the actual rotor width can be obtained according to **Table 2**, as shown in **Figure 3B**. The line is the linear fitting result of the estimated width. The slope of the line is 1.016 and the sum of squares of residuals is 5.37×10^{-7}, which is extremely linear, indicating that the estimated result is consistent with the real width value.

The width estimation error obtained from **Table 2** is shown in **Figure 3C**. The red dotted line and black dotted line are cubic spline interpolation curves of the width estimation error of the rotor blade. When the length is constant, the vibration amplitude increases with the increase of the width from 0.015 to 0.045 m and decreases with the increase of the width from 0.045 to 0.080 m. Similarly, the extraction result of the width of the rotor blade is related to the length–width ratio of the rotor blade. The higher the length–width ratio of the rotor blade, the smaller the time-shift of the time–frequency diagram formed. Due to the influence of time resolution, the larger the extracted time-shift (Δt) error is the larger the estimated error of the rotor blade is. The amplitude of the error vibration decreases slowly. In other words, when the actual width is large, the absolute error is enormous too, but not more than 1 mm. The relative error fluctuates around 1.09%, and the maximum relative error is less than 2%. In conclusion, the time-shift method proposed in this study can estimate the rotor width accurately, and the estimation results have high credibility.

The main error sources of width estimation in this study are as follows:

1) Discrete error: In the process of modeling, the model is gridded; in a word, the model is dispersed. The degree of model dispersion will have a certain influence on estimation accuracy. The more the grid dividing the higher the estimation accuracy is recognized and the smaller the error will be. The discrete error is inevitable, so this study minimizes the error as far as possible within a reasonable range.
2) Maximum frequency-shift extraction error: Because there is no absolute edge in the time–frequency graph and the frequency resolution in this study is 0.01 MHz, there is an error in the extraction of the maximum frequency-shift of the micro-Doppler, which leads to the error of width estimation.
3) Time-shift extraction error: Because the peak time-shift generated by the smaller rotor width is relatively small, the time resolution in this study is 0.1 ms, and it is difficult to accurately extract the time difference between the two peak values, so the error is generated.

Estimation of the Rotor Aspect Ratio

According to **Eq. 7**, the estimated width is related to the pitch angle. However, the real situation is the generally unknown pitching angle, so it is hard to estimate the width directly. Combined with **Eqs 6**, **7**, we can get

$$\frac{L}{\mathrm{W}} = \frac{1}{2\sin\left(\frac{1}{2}\omega \cdot \Delta t\right)}. \tag{8}$$

As shown in **Eq. 8**, the expression of the aspect ratio of the rotor only includes the rotation speed ω and the time-shift Δt, which has nothing to do with the pitch angle parameter. In other words, the aspect ratio of the rotor can also be solved by the unknown pitch angle. The simulation calculation is carried out according to the following process, and the estimated results of the time-shift rotor aspect ratio are shown in **Table 3**.

The flow chart of the rotor aspect ratio estimation algorithm based on the time-shift method is shown in **Figure 4A** The relationship between the estimated aspect ratio and actual aspect ratio is drawn according to **Table 3**, as shown in **Figure 4B**. The red dot is the estimated aspect ratio of simulation, and the black line is the linear fitting result of the real ratio and estimated ratio. The straight slope is 1.007, and the sum of squares of residual errors is 0.029. The results show that the simulated aspect ratio is close to the set aspect ratio. The absolute and relative errors of the estimated aspect ratio are shown in **Figure 4C**. The red curve and green curve are the cubic spline interpolation results of the absolute and relative errors, respectively. It shows that the

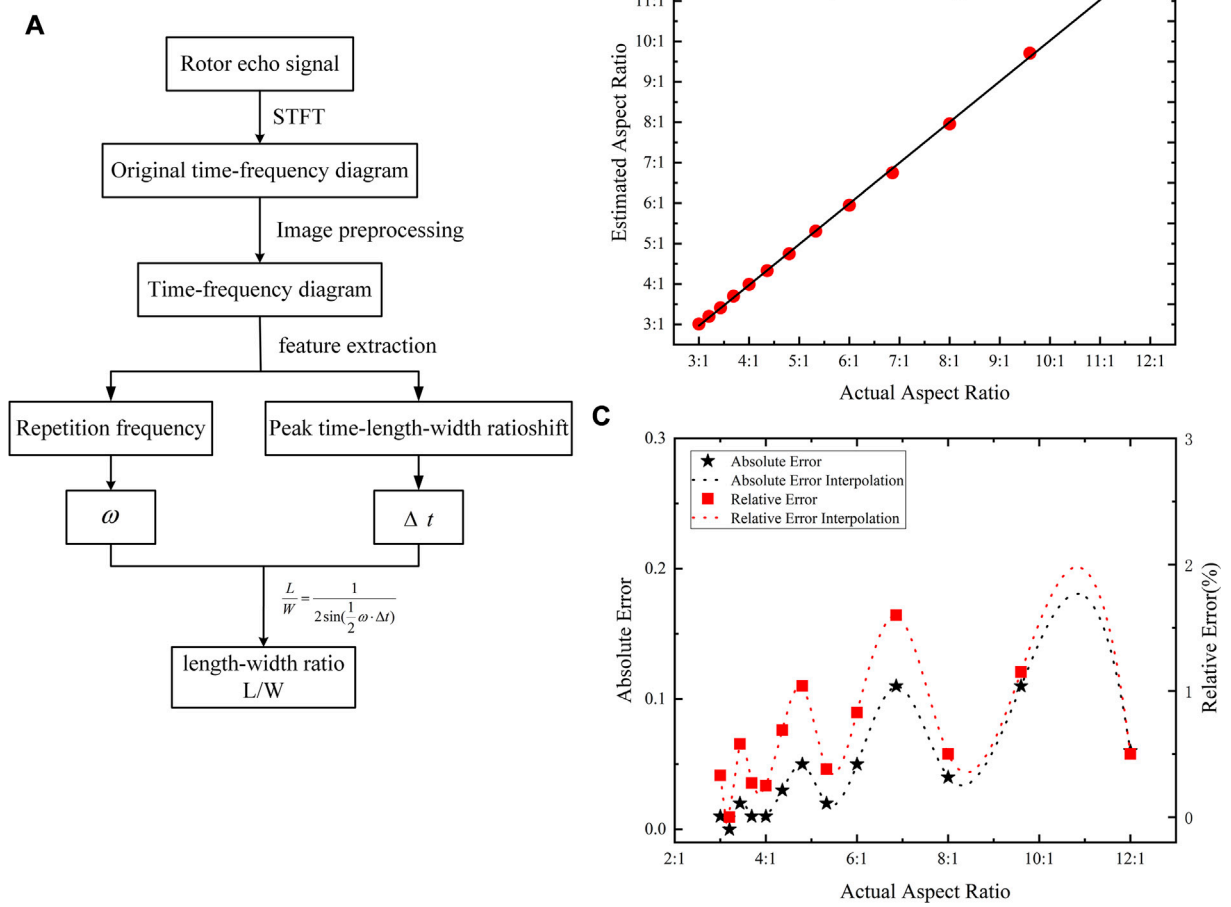

FIGURE 4 | (A) Flow chart of the rotor aspect ratio estimation algorithm based on the time-shift method. **(B)** Relationship between the estimated aspect ratio and actual aspect ratio. **(C)** Estimation error of the aspect ratio.

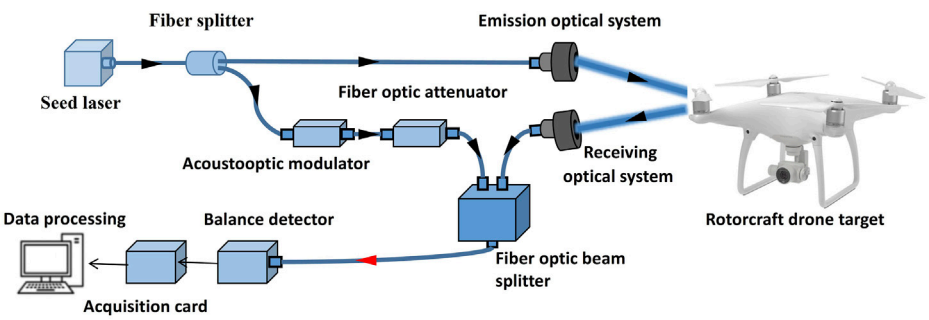

FIGURE 5 | Schematic diagram of the rotor blade echo experiment.

absolute error of the estimated aspect ratio fluctuates between 0 and 0.2, while the absolute error shows a rising trend with the increase of the aspect ratio. Similarly, the relative error increases with the increase of the aspect ratio, and the actual maximum relative error is only 1.6%. Similar to the width estimation, the estimation error of the aspect ratio mainly comes from the discrete error introduced by model meshing and the extraction error of time-shift, while the extraction result of frequency-shift

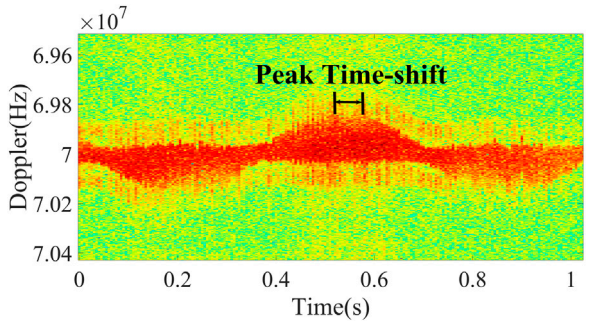

FIGURE 6 | Experimental result of the time–frequency diagram.

Eigen light incident acousto-optic modulator with a frequency-shift of 70 MHz. The outgoing light passes through the fiber attenuator and enters the fiber buncher. The two beams are mixed in the fiber combination and transmitted to the balance detector to form heterodyne interference and retain the difference frequency part. The optical signal is converted into an electrical signal collected by the acquisition card. Finally, the time–frequency diagram is obtained by computer processing.

In this experiment, the pulsed lidar at 70 GHz was used. The distance between the laser and target is 80 m, and the spot diameter of the laser beam is about 3 cm. The number of revolutions of the motor is 500 r/min, and the target rotating the power supply voltage is 6 V. **Figure 6** shows the time–frequency diagram obtained using experimental measurements when the equivalent length–width ratio of rotor blades is 3:1. The length and width of a single blade of the rotor are 9 and 3 mm, respectively, and its rotation frequency is 1.59 Hz. The time–frequency diagram after data processing mainly comprises two parts: the main part with the envelope of the micro-Doppler echo signal formed by the rotation of the rotor blade and the irregular burr edge part formed by noise. In the time–frequency diagram, the two vertical lines are the peaks formed by the two tip points of the rotor width, and the optimal envelope function in the time–frequency diagram is extracted, and the maximum frequency-shift of the rotor and the corresponding t are calculated through several iterations. The five groups of data were averaged for each group, and the time when the peak occurred and the corresponding maximum frequency-shift were recorded. The experimental and simulation results are as follows:

TABLE 4 | Comparison between experimental results and simulation results.

	True value	Simulation estimated value	Experimental estimated value	Simulation relative error (%)	Experimental relative error (%)
Width	3 mm	3.03 mm	2.9 mm	1.13	3.33
	3 mm	3.03 mm	3.1 mm	1.00	3.33
Length–width ratio	3:1	3.01	3.047	0.33	1.57
	4:1	3.99	4.1807	0.25	4.52

does not affect the estimation of the aspect ratio. Therefore, the relative error of the estimation result of the aspect ratio is smaller than that of the width estimation result. It can be seen from the aforementioned analysis that the time-shift method proposed in this study has a good effect and high credibility in the estimation of the rotor aspect ratio parameters.

EXPERIMENTAL VERIFICATION OF UAV PARAMETER ESTIMATION

Different types of rotor UAVs have different rotor blade size information, but the same type of rotor UAVs has the same size information. The micro-Doppler echo signal formed by rotor blade rotation of the same UAVs carries the same information. Based on this, a single rotor blade contains the micro-Doppler echo information formed by all the rotor blades. The rotor UAVs can be recognized by extracting the information of a single rotor blade. The equivalent width and aspect ratio of rotor blades are important parameters to identify UAVs with different signals. In this study, the equivalent width and length–width ratio of the rotor are extracted by the following experimental devices, and the correctness of the simulation experiment is verified.

Figure 5 is a schematic diagram of a UAV rotor blade parameter estimation experimental device. The laser beam from the 100-mW seed laser is divided into signal light and intrinsic light using a fiber beam splitter. The signal light with 90% of the total power is reflected after irradiating to the target of the rotor blade through the transmitting optical system. The reflected micro-Doppler echo signal is transmitted to the optical fiber buncher through the receiving optical system, that is, the

As the accuracy of the simulation is higher than that of the experiment, it can be concluded from **Table 4** that the maximum relative error of rotor width recognition is 3.33%, and the maximum relative error of the aspect ratio is 4.52%. The aforementioned comparison results prove the feasibility of the UAV parameter estimation method proposed in this study, which can accurately extract the rotor width and aspect ratio.

CONCLUSION

Aiming at the problems of low spatial resolution and few parameters of the rotor UAVs identified by the microwave radar, this study proposes a method for identifying the rotor

UAV blade parameters based on the peak time-shift method and high spatial resolution lidar. To solve the problem of the lack of rotor geometric structure information in single-point scattering modeling of rotorcraft UAV identified by the microwave radar, a rectangular multipoint scattering geometric model is established in this study. This method can identify two crucial parameters of rotorcraft UAV, rotor width, and aspect ratio with high accuracy.

Based on the established multipoint scattering rotor echo model, the contribution of rotor width to the micro-Doppler echo signal is studied theoretically, and the existence of the time-shift effect is verified using theoretical analysis and simulation. Based on the relationship between the contribution of rotor width to the echo and the time-shift effect, the UAV parameter estimation method based on the time-shift effect is proposed. The estimation accuracy of the rotor width is 98 and 93%. The aspect ratio of the UAV rotor is extracted using the time-shift method. The results show that the relative errors of the aspect ratio of the UAV rotor identified by the simulation and experiment are less than 1.6 and 4%, respectively. This study proposes a new parameter estimation method for laser micro-Doppler identification of rotorcraft UAVs and provides a theoretical and technical basis for further identification of details and structural parameters of rotorcraft UAVs.

DATA AVAILABILITY STATEMENT

The original contributions presented in the study are included in the article/Supplementary Material, further inquiries can be directed to the corresponding authors.

AUTHOR CONTRIBUTIONS

DL: provided innovation and wrote the manuscript; XD and YH: helped with the experiment; YZ: theoretical and experimental guidance; ZY, XG, and JZ: guidance in the writing of the manuscript.

REFERENCES

1. He J, Zhang Q, Luo Y, Yang X, Wen X. Micro-Doppler Effect Analysis Based on Inverse Synthetic Aperture Imaging LADAR. *IEEE* (2010) 5(10):2071–4. doi:10.1109/ICOSP.2010.5656117
2. Martin J, Mulgrew B. Analysis of the Effects of Blade Pitch on the Radar Return Signal from Rotating Aircraft Blades. *Radar Conf* (1992) 365(92): 446–9.
3. de Wit JJM, Harmanny RIA, Molchanov P. Radar Micro-doppler Feature Extraction Using the Singular Value Decomposition. *Radar Conf* (2014) 1–6. doi:10.1109/RADAR.2014.7060268
4. Zhao C, Luo G, Wang Y. UAV Recognition Based on Micro-doppler Dynamic Attribute-Guided Augmentation Algorithm. *Remote Sens* (2021) 13(6):1–17. doi:10.3390/rs13061205
5. Zhao Y, Su Y. Cyclostationary Phase Analysis on Micro-doppler Parameters for Radar-Based Small UAVs Detection. *IEEE Trans Instrum Meas* (2018) 67(9):2048–57. doi:10.1109/TIM.2018.2811256
6. Peng B, Liu Z, Wei X, Li X. Sinusoidal Frequency Modulation Sparse Recovery for Precession Rate Estimation Using Low-Frequency Long-Range Radar. *IEEE Sensors J* (2015) 15(12):7329–40. doi:10.1109/JSEN.2015.2469133
7. Ritchie M, Fioranelli F, Griffiths H, Torvik B. Micro-drone RCS Analysis. *Radar Conf* (2015) 452–6. doi:10.1109/RadarConf.2015.7411926
8. Kim BK, Kang H-S, Park S-O. Experimental Analysis of Small Drone Polarimetry Based on Micro-doppler Signature. *IEEE Geosci Remote Sensing Lett* (2017) 14(10):1670–4. doi:10.1109/LGRS.2017.2727824
9. Singh AK, Kim YH. Accurate Measurement of Drone's Blade Length and Rotation Rate Using Pattern Analysis with W-band Radar. *Electron Lett* (2018) 54(8):523–5. doi:10.1049/el.2017.4494
10. Ciattaglia G, Santis AD, Disha D, Spinsante S, Castellini P, Gambi E, et al. Performance Evaluation of Vibrational Measurements through mmWave Automotive Radars. *Remote Sens* (2020) 13(1):1–20. doi:10.3390/rs13010098
11. Yang WY, Hoon PJ, Woo BJ. Automatic Feature Extraction from Jet Engine Modulation Signals Based on an Image Processing Method. *IET Rada Son Nav* (2015) 9(7):783–9. doi:10.1049/iet-rsn.2014.0281
12. Yong YW, Hoon PJ, Young SW, Hoon MN. Robust and Fast Algorithm for Estimating Fundamental Periodicity of Jet Engine Modulation Signals. *IET Radar, Sonar & Navigation* (2016) 10(7):1286–94. doi:10.1049/iet-rsn.2015.0526
13. Wit JJM, Harmanny RIA, Prémel-Cabic G. Micro-Doppler Analysis of Small UAVs. *Cochrane Database Syst Rev* (2012) 150(4):210–3.
14. Chen YB, Li SD, Yang J. Rotor Blade echo Modeling and Flicker Mechanism Analysis. *J Phys* (2016) 65(13):287–97. doi:10.7498/aps.65.138401
15. Baczyk MK, Samczynski P, Kulpa K. Micro-Doppler Signatures of Helicopters in Multistatic Passive Radars. *Iet Radar Sonar Nav* (2015) 9(9):1276–83. doi:10.1049/iet-rsn.2015.0125
16. Izzo A, Ausiello L, Clemente C, Soraghan JJ. Loudspeaker Analysis: A Radar Based Approach. *IEEE Sensors J* (2020) 20(3):1223–37. doi:10.1109/JSEN.2019.2946987
17. Passafiume M, Rojhani N, Collodi G, Cidronali A. Modeling Small UAV Micro-doppler Signature Using Millimeter-Wave FMCW Radar. *Electronics* (2021) 10(6):747. doi:10.3390/electronics10060747
18. Wang Y, Yang S, Yin H, Huo C, Man L. Sparse Time-frequency Analysis for Aircraft Target Classification with Low Sampling Rate and Short Observation Time. *Int J Numer Model* (2021) 35(1):1–20. doi:10.1002/jnm.2928
19. Thayaparan T, Abrol S, Riseborough E, Stankovic L, Lamothe D, Duff G. Analysis of Radar Micro-doppler Signatures from Experimental Helicopter and Human Data. *IET Radar Sonar Navig.* (2007) 1(4):289–99. doi:10.1049/iet-rsn:20060103
20. Zhang P, Li G, Huo C, Yin H. Exploitation of Multipath micro-Doppler Signatures for Drone Classification. *IET Radar, Sonar & Navigation* (2020) 14(9):586–92. doi:10.1049/iet-rsn.2019.0105
21. Chen VC, Fayin Li F, Shen-Shyang Ho SS, Wechsler H. Micro-Doppler Effect in Radar: Phenomenon, Model, and Simulation Study. *IEEE Trans Aerosp Electron Syst* (2006) 42(1):2–21. doi:10.1109/taes.2006.1603402
22. Chen VC. Micro-Doppler Effect of Micromotion Dynamics: A Review. Independent Component Analyses, Wavelets, and Neural Networks. *Proc SPIE Int Soc Opt Eng* (2003) 5(102):240–9. doi:10.1117/12.488855
23. Rahman S, Robertson DA. Radar Micro-doppler Signatures of Drones and Birds at K-Band and W-Band. *Sci Rep* (2018) 8(8):1–11. doi:10.1038/s41598-018-35880-9
24. Chen YB, Li SD, Yang J. Rotor Blades echo Modeling and Mechanism Analysis of Flashes Phenomena. *Acta Physica Sinica* (2016) 65(13):281–91. doi:10.7498/aps.65.138401
25. Jiang XW, Zhao QJ, Meng C. Effect of Helicopter Roter Blade Shape on its Radar Signal Characteristics. *Acta Aeronautica et Astronautica Sinica* (2014) 35(11):3123–36. doi:10.7527/S1000-6893.2014.0060
26. Wang YP, Hu YH, Guo LR, Xu SL. Research on Laser Detection Method of Rotor Chord Based on Micro-dopper Effect. *Acta Photonic sinica* (2017) 46(7): 0712003. doi:10.3788/gzxb20174607.0712003
27. Dierking MP, Duncan BD. Periodic, Pseudonoise Waveforms for Multifunction Coherent Ladar. *Appl Opt* (2010) 49(10):1908–22. doi:10.1364/AO.49.001908
28. Tahmoush D. Review of micro-Doppler Signatures. *IET Radar, Sonar & Navigation* (2015) 9(9):1140–6. doi:10.1049/iet-rsn.2015.0118

29. Ma Y, Hong Y, Qiao S, Lang Z, Liu X. H-shaped Acoustic Micro-resonator-based Quartz-Enhanced Photoacoustic Spectroscopy. *Opt Lett* (2022) 47(3): 601–4. doi:10.1364/OL.449822
30. Liu X, Ma Y. Sensitive Carbon Monoxide Detection Based on Light-Induced Thermoelastic Spectroscopy with a Fiber-Coupled Multipass Cell [Invited]. *Chin. Opt. Lett.* (2022) 20(3):031201. doi:10.3788/COL202220.031201
31. Ma Y, Hu Y, Qiao S, Lang Z, Liu X, He Y, et al. Quartz Tuning forks Resonance Frequency Matching for Laser Spectroscopy Sensing. *Photoacoustics* (2022) 25: 100329. doi:10.1016/j.pacs.2022.100329
32. Jian M, Lu Z, Chen VC. Experimental Study on Radar Micro-doppler Signatures of Unmanned Aerial Vehicles. *Radar Conf* (2017) 0854–7. doi:10.1109/RADAR.2017.7944322
33. Wang XR, Wang PC, Cao XB, Victor CC. Interferometric Angular Velocity Measurement of Rotating Blades: Theoretical Analysis, Modeling and Simulation Study. *IET Radar Sonar Nav* (2019) 3(13): 438–44. doi:10.1049/iet-rsn.2018.5205
34. Musa SA, Raja Syamsul Azmir RA, Sali A, Ismail A, Abd Rashid NE. Micro-Doppler Signature for Drone Detection Using FSR: a Theoretical and Experimental Validation. *J Eng* (2019) 2019(21):7918–23. doi:10.1049/joe.2019.0795

Conflict of Interest: The authors declare that the research was conducted in the absence of any commercial or financial relationships that could be construed as a potential conflict of interest.

Publisher's Note: All claims expressed in this article are solely those of the authors and do not necessarily represent those of their affiliated organizations, or those of the publisher, the editors, and the reviewers. Any product that may be evaluated in this article, or claim that may be made by its manufacturer, is not guaranteed or endorsed by the publisher.

frontiers | Frontiers in Physics

ORIGINAL RESEARCH
published: 13 April 2022
doi: 10.3389/fphy.2022.874956

The Research of Long-Optical-Path Visible Laser Polarization Characteristics in Smoke Environment

Zhan Juntong[1,2]*, *Bao Shicheng*[1,2], *Zhang Su*[1,2]*, *Fu Qiang*[1,2], *Li Yingchao*[1,2], *Duan Jin*[1] and *Zhang Wei*[1,2]

[1]Jilin Provincial Key Laboratory of Space Optoelectronics Technology, Changchun University of Science and Technology, Changchun, China, [2]Institute of Optoelectronic Engineering, Changchun University of Science and Technology, Changchun, China

The concentration of smoke in an environment can cause obvious interference to visible light intensity imaging, and it is a non-negligible factor in the polarized imaging of ground-based targets. Smoke particles cause severe scattering of photon intensity, resulting in polarization. In this case, low-visibility targets can be effectively identified by detecting the polarization dimension of targets. However, the polarization transmission of smoke in an environment is unclear, and the theoretical simulation lacks experimental reliability verification. To study this problem, this study constructs a polarization transmission model in a smoke environment and simulates and analyzes the scattering of visible polarized light at 450, 532, and 671 nm under different smoke densities. The optical thickness is determined to establish a reliable connection between the simulation and the external field long optical path test and verify the transmission of polarized light. Results show that the method has a 60% confidence in the polarization transmission model. With the increase in optical thickness, the degree of polarization (DOP) of the three wavelengths in the visible light band decreases, and the DOP of each polarized light decreases. No obvious difference is found between the DOPs of circularly polarized light at 450 nm and linearly polarized light. The DOP of circularly polarized light at 532 nm is 1–5% higher than that of linearly polarized light, 1–10% higher than that of the outdoor test, 1–5% higher than that of circularly polarized light at 671 nm, and 2–15% higher than that of the outdoor test. Therefore, the shorter the wavelength in the visible band, the higher the DOP. With the increase in wavelength, the polarization characteristics of circularly polarized light are gradually better than those of linearly polarized light.

Keywords: smoke environment, long optical path, optical thickness, polarization, visible laser

OPEN ACCESS

Edited by:
Yufei Ma,
Harbin Institute of Technology, China

Reviewed by:
Fei Liu,
Xidian University, China
Haipeng Chen,
Northeast Electric Power University, China

****Correspondence:***
Zhan Juntong
zhanjuntong@cust.edu.cn
Zhang Su
susiezhang21@126.com

Specialty section:
This article was submitted to Optics and Photonics, a section of the journal Frontiers in Physics

Received: *13 February 2022*
Accepted: *16 March 2022*
Published: *13 April 2022*

Citation:
Juntong Z, Shicheng B, Su Z, Qiang F, Yingchao L, Jin D and Wei Z (2022) The Research of Long-Optical-Path Visible Laser Polarization Characteristics in Smoke Environment. Front. Phys. 10:874956. doi: 10.3389/fphy.2022.874956

INTRODUCTION

With the development of intelligent transportation and navigation, the demand for optical sensors that can penetrate a strong scattering environment has increased. At present, the low-visibility conditions caused by haze lead to frequent traffic accidents, abnormal airplane landings, and navigation ship accidents. Such scenarios have a significant economic impact, cause a huge waste of human, material, and time resources, and limit the development of transportation, aviation,

navigation, and other fields [1, 2]. Haze poses a major safety challenge to the spatial perceptive ability in these fields and thus must be effectively detected in low-visibility environments, such as a car driving on a foggy road, a plane trying to land in the fog, or a ship in the sea fog [3–6].

The emission of a large number of fine particles can cause haze easily. Using the persistence and memory of visible polarized laser can effectively improve the action distance of the scattering environment, which has aroused the interest of researchers. Recently, polarimetric imaging has been widely exploited in target detection [7, 8], remote sensing [9, 10], and biomedical imaging [11, 12].

This study aims to characterize the propagation of polarized laser in different bands in a real haze long optical path environment. Our previous work simulated the polarization change of a short optical path linearly polarized laser in an oil mist particle environment and showed that linearly polarized laser in different bands is sensitive to concentration change. In the present work, we determine the characteristics of laser polarization with haze concentration change combined with numerical simulation and real long optical path haze environment test. In addition, we summarize the polarization transmission law of multiple band and polarization states.

Considering the lack of polarization characteristic tests in a real haze environment, few studies have shown the transmission law of polarized laser in haze environments with different concentrations. In addition, the influence of visibility on polarization characteristics in real haze weather remains unclear to date.

Most previous studies performed the numerical simulation of the polarization characteristics of fog particles or the indoor simulation of a fog environment with a short optical path and a single wavelength.

Wu analyzed the influence of a 550-nm laser on the polarization of dust particle and dig particle's Muller matrix. The depolarization coefficient of dust particles was 0.6, and that of dig particles was 0.8. Dust particles have stronger depolarization than dig particles, which means that when illuminated by polarized light, dust particles produce scattered light with less polarization than dig particles. However, an analysis of the influence of the concentrations of dust and dig particles on polarization remains lacking [13]. John D. van der Laan simulated the evolution of circular and linear polarization in a polystyrene microsphere environment model with particle diameters of 0.1, 2.0, and 3.0 μm and an illuminating wavelength of 543.5 nm [14]. Xiangwei Zeng expressed the transmission distance by the relative distance of particles at the band of 0.5–4.2 μm. The circular linear polarization difference at a 0–1.5 relative distance of a single particle was numerically simulated [15]. Using the fog particle distribution model, D. Vander and J.B. Wright studied changes in the polarization degree (DOP) of 0.4- to 1.2-μm circularly polarized light with a wavelength under optical thicknesses of 5, 10, and 15 [16]. Ryan investigated the depolarization of a linearly polarized 514-nm wavelength beam through 1 m of laboratory-generated fog [17]. Their work was limited to a single fog concentration. Jinkui Chu et al. experimentally explored polarization state persistence through the polystyrene microsphere turbid liquid environments of 530-nm particles at varying concentrations. The scattering solution was held in a glass cubic cuvette at a length of 2.6 cm. At different concentrations, circularly polarized light had superior polarization state persistence to linearly polarized light [18]. Vanitha Sankaran analyzed the polarization discrimination of 632-nm coherently propagating light in polystyrene samples placed in a 1-cm path-length glass cuvette to simulate turbid media. The results indicated that polarization was maintained even after unpolarized irradiance through each sample had been extinguished by several orders of magnitude [19].

These studies produced a useful conclusion on polarized light propagation. However, polarization transmission characteristics in a real haze environment remain difficult to determine because they are carried out in well-established and well-controlled environments. In fact, the combined effects of changes in the density and size of particle scatterers in haze environments and changes in atmospheric conditions are difficult to model in the laboratory.

In the present study, we use the optical thickness to characterize and unify the haze concentration of the real ground haze environment and the simulated haze environment, obtain the variation law of laser polarization characteristics in different polarization states, find the detection laser wavelength and polarization state suitable for different concentration haze environments, establish the polarization transmission model around the optical thickness, and verify the model by performing a real field long path polarization test. These works are helpful to study the effects of different optical thicknesses on the transmission characteristics of different polarized lasers. The circular polarization and multiple linear polarizations of different wave bands are sensitive to the change in real haze concentration.

This article is organized as follows. *Monte Carlo Method of Particle Swarm Optimization* covers the background of polarization and the polarization-tracking Monte Carlo simulations. *Numerical Results for Polarization Characteristics* describes the smog environments of interest, including their particle distributions. *Experiments* presents general comments about the transmission results and details the results for each polarization at wavelengths ranging from 450 to 671 nm and over increasing optical thickness/range. *Conclusion* concludes that circularly polarized light maintains its signal better than linearly polarized light through the 450-, 532-, and 671-nm bands.

MONTE CARLO METHOD OF PARTICLE SWARM OPTIMIZATION

Concentration Characterization of Polarized Scattering of Smoke Particles

When visible light is transmitted in smoke particles, the Stokes parameter of reaction polarization characteristics is calculated as follows [20]:

$$\begin{pmatrix} I_0 \\ Q_0 \\ U_0 \\ V_0 \end{pmatrix} = \begin{pmatrix} M_1 & M_2 & 0 & 0 \\ M_2 & M_1 & 0 & 0 \\ 0 & 0 & S_{21} & -D_{21} \\ 0 & 0 & D_{21} & S_{21} \end{pmatrix} \begin{pmatrix} I_1 \\ Q_1 \\ U_1 \\ V_1 \end{pmatrix}, \quad (1)$$

$$M = \begin{pmatrix} M_1 & M_2 & 0 & 0 \\ M_2 & M_1 & 0 & 0 \\ 0 & 0 & S_{21} & -D_{21} \\ 0 & 0 & D_{21} & S_{21} \end{pmatrix} = \frac{1}{k^2 r^2} \begin{bmatrix} F_{11} & F_{12} & 0 & 0 \\ F_{12} & F_{22} & 0 & 0 \\ 0 & 0 & F_{33} & F_{34} \\ 0 & 0 & -F_{34} & F_{33} \end{bmatrix}. \quad (2)$$

The matrix element of the scattering phase function matrix of soot particles and its expression can be written as follows:

$$\langle F_{ij} \rangle = \frac{\int_{r_{\min}}^{r_{\max}} Q_{sca}(r) n(r) \pi r^2 P_{ij}(r) dr}{\int_{r_{\min}}^{r_{\max}} Q_{sca}(r) n(r) \pi r^2 dr}, \quad (3)$$

where $n(r)$ is the logarithmic particle spectrum distribution of transmission medium particles, and it can be expressed as follows:

$$n(r) = \frac{N_0}{\sqrt{2\pi} \lg\sigma} \exp\left[-\frac{(\lg r - \lg r_m)^2}{2(\lg\sigma)^2} \right], \quad (4)$$

where $n(r)$ is the logarithmic particle spectrum distribution; N_0 is the number of aerosol particles per unit volume of air (number/cm^{-3}), which represents the concentration of particles; r_m is the geometric mean radius; and σ is the geometric standard deviation. The relationship between particle concentration and Stokes parameter can be obtained; in other words, the relationship between particle concentration and polarization characteristics can be obtained. However, it is hard to obtain the number of aerosol particles in the actual environment. Thus, we hierarchically describe the transmission medium by optical thickness. The relationship among particle spectrum distribution, scattering coefficient, and absorption coefficient is shown as follows:

$$\mu_s = \pi \int_{r_1}^{r_2} r^2 Q_{sc} n(r) dr, \ \mu_a = \pi \int_{r_1}^{r_2} r^2 Q_{ab} n(r) dr, \quad (5)$$

where μ_s is the scattering coefficient, μ_a is the absorption coefficient, and μ_t is the extinction coefficient. The relationship between extinction coefficient and particle spectrum distribution is shown as follows:

$$\mu_t = \mu_t + \mu_t = \pi \int_{r_1}^{r_2} r^2 Q n(r) dr. \quad (6)$$

According to Beer's law, the relationship between optical thickness τ, transmission distance S, and extinction coefficient μ_t is shown as follows:

$$\tau = \mu_t S = S\pi \int_{r_1}^{r_2} r^2 Q n(r) dr, \quad (7)$$

where Q is the extinction factor. The aforementioned formula shows that different concentrations of smoke can be represented by the optical thickness τ, and Q is directly proportional to the optical thickness. The aforementioned formula can be achieved by changing the optical thickness in the Monte Carlo transmission model. The optical thickness can also be controlled in the experiment, and the extinction factor can be calculated by the Monte Carlo polarization transmission model of smoke particles. Therefore, using the optical thickness to characterize the concentration of smoke particles can connect the experiment with the simulation.

Relational Model Between Smoke Particle Concentration and Polarization Transmission Characteristics

The reference plane is defined as shown in **Figure 1**. The yellow line and the direction of photons at the scattering point determine the propagation direction of photons. The included angle between them is the scattering angle. The *X*-axis, *Z*-axis, and scattering plane constitute the reference plane before and after scattering. For every scattering that occurs, the Stokes component must be adjusted to make the reference plane a new reference plane.

After defining the reference plane, we set the scattering coefficient μ_s, absorption coefficient μ_a, extinction coefficient of atmosphere $\mu_t = \mu_s + \mu_a$, incident wavelength of laser v, particle diameter r, particle complex refractive index m, and initial values of Stokes parameters of light with different polarization states. Photons are incident in the positive direction of the z-axis. The initial position μ_0 is (0, 0, 0), and the initial direction cosine D_0 is (0, 0, 1). The polarization reference plane is composed of an x-axis and a z-axis. We define the initial Stokes parameters of photons and set each Stokes parameter after scattering to 0.

The step length of particle transmission is the photon free path, and the relationship between optical thickness and photon free path is given as follows:

$$S_1 = \ln(\xi) \frac{\tau}{S}. \quad (8)$$

Once the photon free path is determined, the photons move. The current location (x, y, z) and transmission direction (μ_x, μ_y, μ_z) determine that the coordinate (x', y', z') of the next scattering point reached by the photon is given as follows:

$$\begin{cases} x' = x + \mu_x S_1 \\ y' = y + \mu_y S_1 \\ z' = z + \mu_z S_1 \end{cases}. \quad (9)$$

Whether the photon emits the boundary determined by the reference plane is determined according to the coordinate position. If it emits the boundary determined by the reference plane, the Stokes parameter of the photon is calculated. By contrast, the Stokes component must be adjusted to make the reference plane a new meridional plane, and then the particle radius must be selected again.

After photons collide with particles, the sampling of the scattering angle α and azimuth angle β is obtained from the joint probability density function (PDF), and the relationship

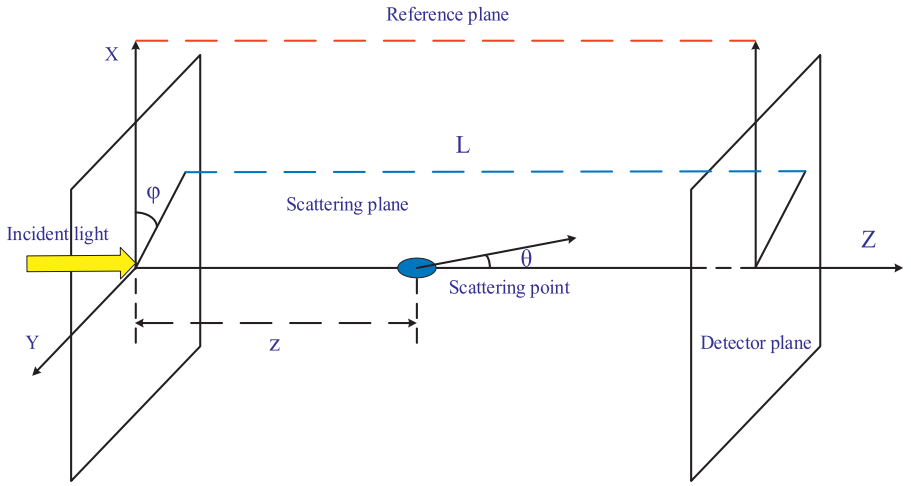

FIGURE 1 | Definition of reference plane.

between the function PDF and incident light's Stokes component $[I_0, Q_0, U_0, V_0]^T$ is follows:

$$\rho(\alpha,\beta) = m_{11}(\alpha) + m_{12}(\alpha)\left[Q_0\cos(2\beta) + U_0\sin(2\beta)\right]/I_0, \quad (10)$$

where $m_{11}(\alpha)$ and $m_{12}(\alpha)$ are the corresponding elements in Mueller matrix $M(\alpha)$ of spherical particles:

$$M(\alpha) = \begin{bmatrix} m_{11}(\alpha) & m_{12}(\alpha) & 0 & 0 \\ m_{12}(\alpha) & m_{11}(\alpha) & 0 & 0 \\ 0 & 0 & m_{33}(\alpha) & m_{34}(\alpha) \\ 0 & 0 & -m_{34}(\alpha) & m_{33}(\alpha) \end{bmatrix}. \quad (11)$$

$m_{11}(\alpha)$, $m_{12}(\alpha)$, $m_{33}(\alpha)$, and $m_{34}(\alpha)$ have the following relationship with scattering amplitude values S_1 and S_2:

$$\begin{aligned} m_{11}(\alpha) &= \frac{1}{2}\left(|S_1|^2 + |S_2|^2\right), m_{12}(\alpha) = \frac{1}{2}\left(|S_1|^2 - |S_2|^2\right), \\ m_{33}(\alpha) &= \frac{1}{2}\left(S_1S_2^* - S_1^*S_2\right), m_{44}(\alpha) = \frac{i}{2}\left(S_1S_2^* - S_2^*S_1\right). \end{aligned} \quad (12)$$

The energy weight of photos after n times of scattering becomes:

$$W_n = W_{n-1} \times \mu_s/(\mu_s + \mu_a). \quad (13)$$

When the photon energy weight is lower than a certain threshold (i.e., 10^{-4}) or fly away from the boundary, the photon transmission is terminated. When a photon is emitted from the boundary of the polydisperse system, its Stokes vector must undergo the last rotation to ensure that the reference plane is the same as the plane where the detector is located, and the rotation angle is follows:

$$\omega = \pm\tan^{-1}\left(\mu_y/\mu_x\right). \quad (14)$$

The reflection mode takes a positive sign, and the transmission takes a negative sign. Due to different scattering paths, the time of photons arriving at the detector is different. For a beam whose polarization component is shaped like $[I(t), Q(t), U(t), V(t)]^T$, the time-domain polarization degree is defined as follows:

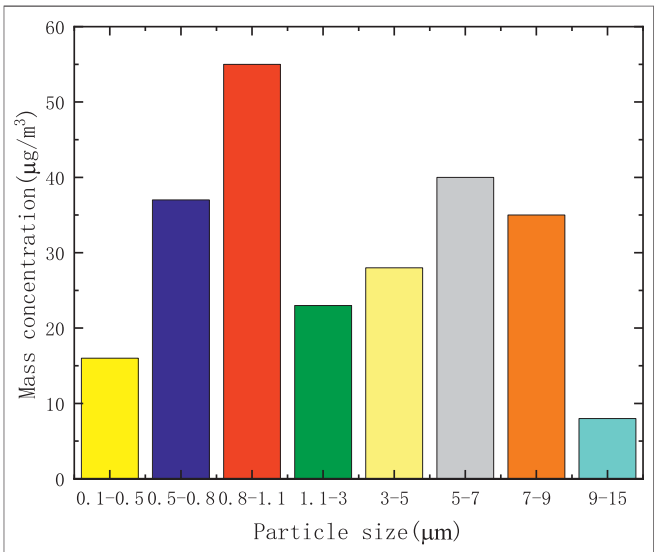

FIGURE 2 | Distribution of PM10 particle size content in winter.

$$DOP(t) = \frac{\sqrt{Q^2(t) + U^2(t) + V^2(t)}}{I(t)}. \quad (15)$$

The total polarization degree of the scattered beam is defined as **Eq. 15**, where I, Q, U, and V represent the cumulative values of photon polarization components arriving at the detector at different times.

According to **Eqs 7**, **8**, **13**, and **15**, after substituting the changes in the optical thickness τ and extinction factor Q into the Monte Carlo polarization simulation of smoke particles, the original free path, scattering angle and azimuth sampling, and photon energy weight also change. Finally, an improved relationship model between smoke particle concentration and polarization transmission characteristics can be obtained.

TABLE 1 | Comparison between outdoor visibility and optical thickness.

Wavelength = 450 nm		Wavelength = 532 nm		Wavelength = 671 nm	
Outdoor visibility (km)	Optical thickness	Outdoor visibility (km)	Optical thickness	Outdoor visibility (km)	Optical thickness
10	0.3	10	0.4	10	0.5
6	0.5	6	0.6	6	0.8
5	0.6	5	0.8	5	1
4	0.8	4	0.9	4	1.2
3	1.1	3	1.3	3	1.6
2	1.6	2	1.9	2	2.4
0.6	5.3	0.6	6.3	0.6	8

NUMERICAL RESULTS FOR POLARIZATION CHARACTERISTICS

Environments

When winter comes in December, northern China starts heating, and the haze weather is the most serious. At this time, the climate is dry with minimal precipitation, which can almost eliminate the impact of humidity on aerosol particles. Soot particles are the main factor affecting visibility. The PM10 index is the highest in the whole year, and the particle content of 0.8–1.1 μm is the highest [21]. The relationship between particle size and concentration is displayed in **Figure 2**.

In this study, the physical parameter of optical thickness is used to unify the visibility of a real haze environment and the concentration of simulated haze. Thus, the two results can verify each other. The visibility of the real haze environment is tested as follows.

The relationship between visibility V and transmittance T is shown in **Eq. 16**:

$$V = \frac{3.91 \times \left(\frac{\lambda}{0.55}\right)}{-\ln T}. \tag{16}$$

The relationship between transmittance T and optical thickness τ can be obtained according to the Beer–Lambert Law:

$$T = \exp(-\tau). \tag{17}$$

Eqs 16, **17** are combined to obtain the conversion formula of visibility and optical thickness:

$$V = \frac{3.91 \times \left(\frac{\lambda}{0.55}\right)}{\tau}. \tag{18}$$

Thus, the relationship between outdoor visibility and optical thickness under different central wavelengths is shown in **Table 1**.

Simulation Results and Analysis

We simulate the polarization characteristics of six types of polarized light passing through the real smoke environment. PM 1 μm particle size with the largest distribution percentage in smoke particles is up to more than 50%, so we select the simulated smoke particle radius 1 μm, and the refractive index is 1.53 + 0.008i, and the number of particles set during simulation is 10^6. The smoke particles adopt the logarithmic particle spectrum distribution, and the optical thickness is measured according to the real smoke environment. The polarization states of simulated polarized light are 0°, 45°, 90°, 135°, left-handed circular polarization, and right-handed circular polarization. The simulation results are shown in **Figures 3**, **4**.

As shown in **Figures 3A–C**, the DOP changes of left-handed and right-handed circularly polarized light are consistent, and the DOP changes of the three linearly polarized light are also consistent. It can be seen that because the DOP difference between left-handed circularly polarized light and right-handed circularly polarized light is less than 1%, the DOP curves of the two overlap; the DOP difference of 0°, 45°, and 90° linearly polarized light is less than 1%, resulting in the three DOP curves overlapping. The DOP difference between circularly polarized light and linearly polarized light in a thick smoke environment (the optical thickness after stabilization is greater than 1.0) is more obvious than that in a thin smoke environment (the optical thickness after stabilization is 0.3–1) because circularly polarized light has better polarization-maintaining ability. When the polarized light passed through the smoke, it would cause multiple scattering, and multiple scattering would cause depolarization. As the concentration increased, multiple scattering increased, then there would be more polarized light depolarized. With the increase in wavelength, the polarization characteristic of circularly polarized light is better than that of linearly polarized light. At 450 nm, the difference between circularly polarized light and linearly polarized light is not obvious; at 532 nm, the DOP of circularly polarized light is approximately 10% higher than that of linearly polarized light; at 671 nm, the DOP of circularly polarized light is approximately 20% higher than that of linearly polarized light. In the case of a long wavelength, the polarization-maintaining characteristic of circularly polarized light is better than that of linearly polarized light. However, with the increase in optical thickness, the DOP of the outgoing polarized light of the three wavelengths decreases gradually. When the concentration increases, the number of collisions of photons in the transmission medium increases, resulting in depolarization.

Figures 4A–E represent the variation curve of polarization with visibility when the incident polarized light is divided into 0° linear polarized light, 90° linear polarized light, 45° linear polarized light, left-handed circular polarized light, and right-handed circular polarized light. The DOP at 450-nm wavelength is higher than those at 532- and 671-nm wavelength. This result

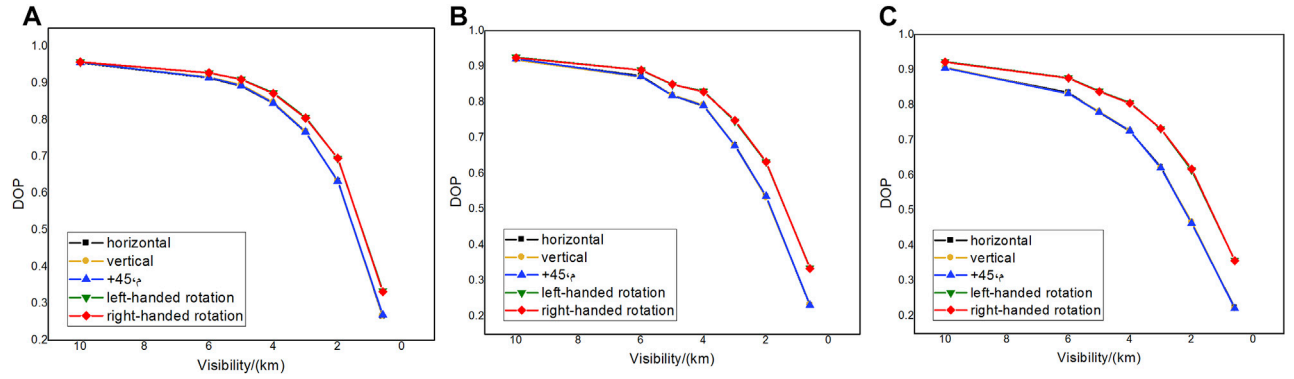

FIGURE 3 | Simulation curves of polarization transmission characteristics at different wavelengths:**(A)** 450 nm, **(B)** 532 nm, and **(C)** 671 nm.

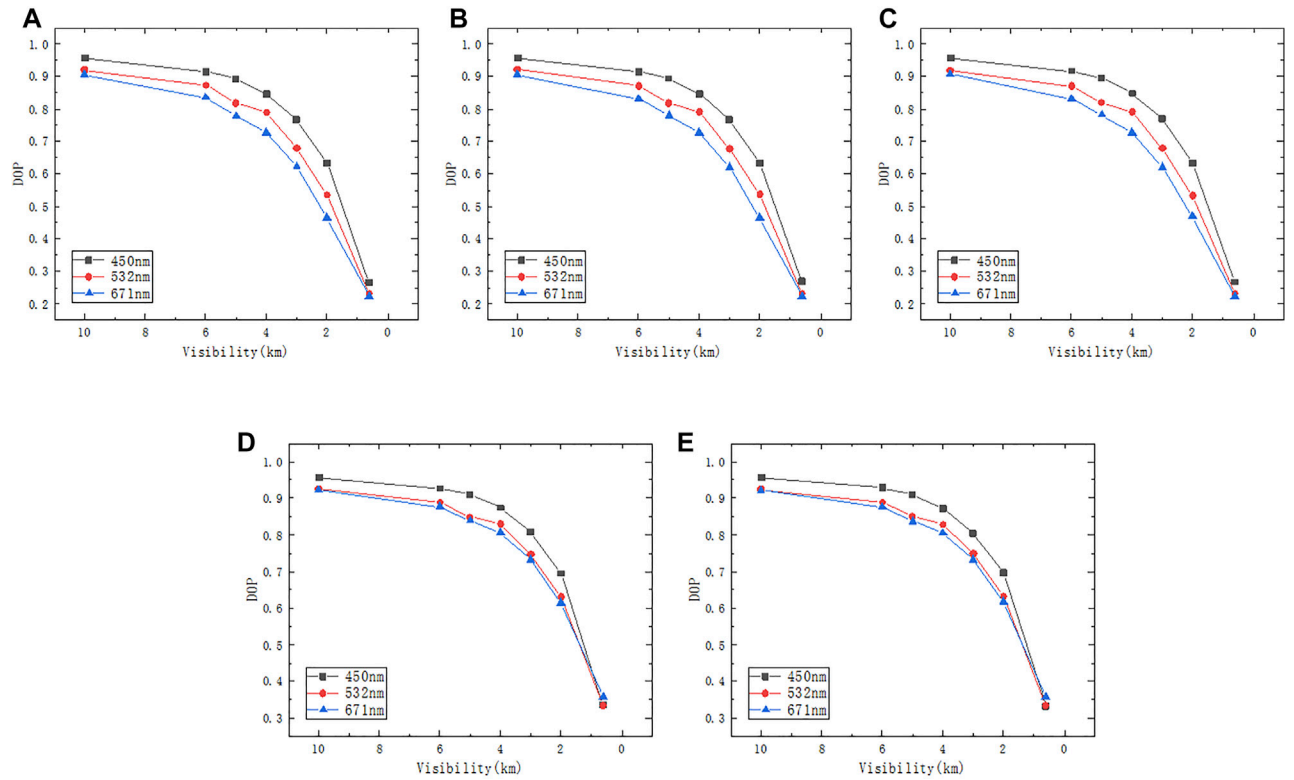

FIGURE 4 | Simulation curves of polarization transmission characteristics of different polarization states:**(A)** 0°, **(B)** 45°, **(C)** 90°, **(D)** left-hand rotation, and **(E)** right-hand rotation.

can be ascribed to the fact that the reflectivity of smoke increases with the increase in wavelength in the visible band [22], and the relationship between spectral reflectivity and spectral DOP is inversely proportional. Therefore, the DOP at 450-nm wavelength is higher than that at 671-nm wavelength. The aforementioned simulation results show that in the visible band, the shorter the wavelength, the higher the DOP, and the polarization-maintaining characteristic of circularly polarized light is more obvious when the wavelength is longer.

EXPERIMENTS

Experimental Setup

We designed a series of experiments to compare the polarization state change of parallel linearly and circularly polarized light interacting with scattering media. The experimental scheme is shown in **Figure 5**.

The test in the real haze environment and experimental scenario is shown in **Figure 6**. Polarized light modulation is

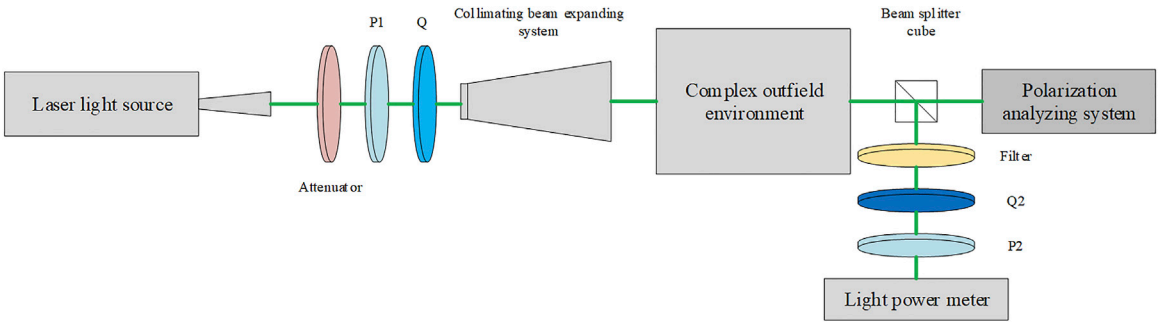

FIGURE 5 | Experimental scheme.

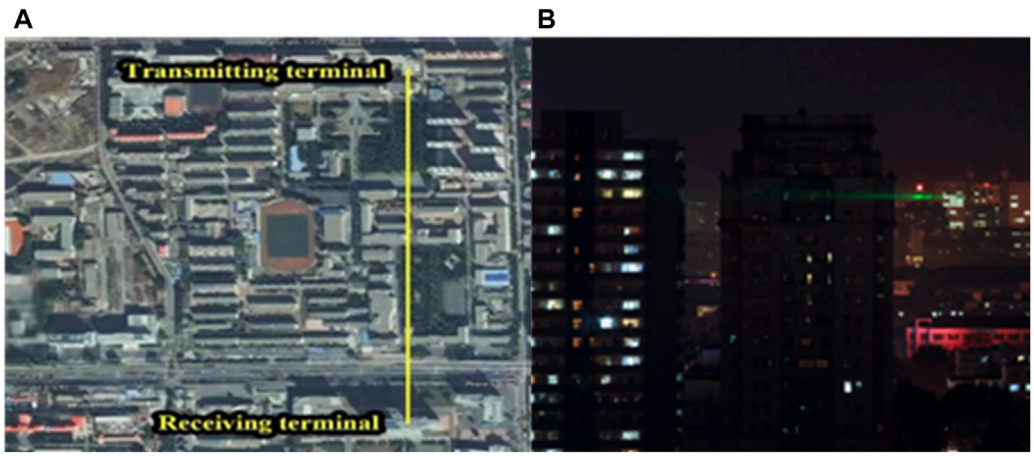

FIGURE 6 | (A) Distance between field test sites is 1 km; **(B)** experimental scene light path diagram.

performed, and the distance between the transmitting and receiving ends is 1 km. A multiband laser beam (450, 532, 671 nm) is launched and polarized as the input to pass through scattering media and be collected by a detector. An attenuator and a quarter wave plate are sequentially placed in front of the laser source to produce uniformly circularly polarized light. A pass-through polarizer (labeled P1) and a quarter wave plate (labeled Q1) are placed in front of the laser source successively to obtain five types of stable polarized light, namely, 0° linear polarized light, 45° linear polarized light, 90° linear polarized light, left-handed circularly polarized light, and right-handed circularly polarized light. Linearly polarized (without using Q1) or right/left circularly polarized light is obtained by rotating them to different positions. The aforementioned six polarized lights pass through the smoke and dust atmospheric environment with a different visibility of 1 km. The prism at the receiving end divides the collected polarized scattered light into two channels. One channel records the changes in the polarization state and DOP through the polarization state-measuring instrument, and one channel reaches the optical power meter through a quarter wave plate, polarizer, and filter, which are used to calibrate and verify the accuracy of output light.

The transmission band of the polarizer is 400–700 nm, the transmittance of each wavelength can reach more than 80%, the extinction ratio is 1,000:1, and the actual output power of the laser is 49.99 mw (the output wavelengths are 450, 532, and 671 nm).

Measuring Method

The polarized light with different polarization states generated by the transmitting end is scattered by the real smoke environment and divided into two beams by the light splitting prism. One beam enters the polarization state-measuring instrument, and the other enters the optical power meter. The polarization information of a monochromatic plane wave can be characterized by four Stokes parameters: I, Q, U, and V. Full polarization information can be obtained using the rotation of polarizer and wave plate at different angles. β is the included angle between the fast axis and the horizontal direction, and δ is the magnitude of the phase delay. The two are multiplied to obtain the actual Muller matrix of the polarizer, and then the final outgoing light intensity is multiplied by the incident Stokes vector as follows:

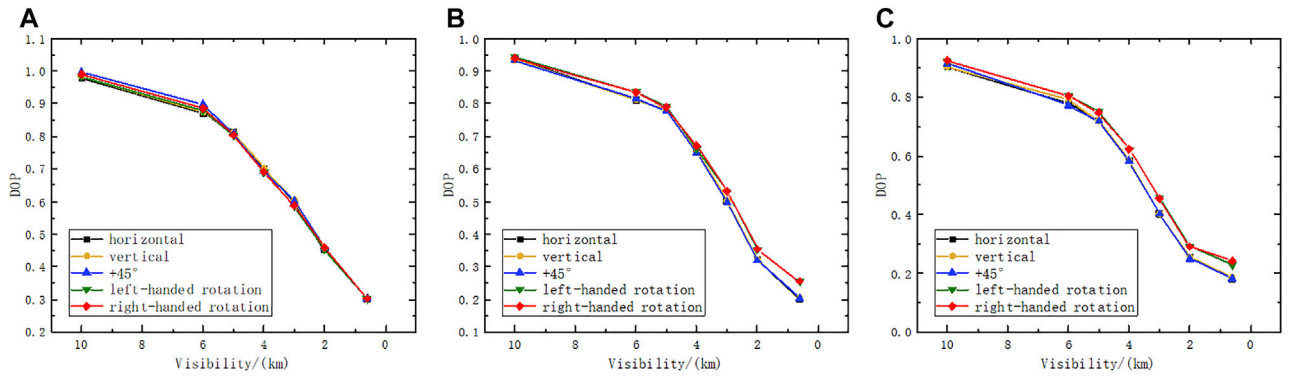

FIGURE 7 | Field test curves of polarization transmission characteristics at different wavelengths:**(A)** 450 nm, **(B)** 532 nm, and **(C)** 671 nm.

$$I' = \frac{1}{2}\begin{pmatrix} I + (\cos 2\theta(\cos^2 2\beta + \sin^2 2\beta \cos\delta) + \sin 2\theta \cos 2\beta \sin 2\beta(1 - \cos\delta)Q \\ +(\cos 2\theta \cos 2\beta \sin 2\beta(1 - \cos\delta) + \sin 2\theta(\sin^2 2\beta + \cos^2 2\beta \cos\delta)U \\ +(-\cos 2\theta \sin 2\beta \sin\delta + \sin 2\theta \cos 2\beta \sin\delta)V \end{pmatrix}. \tag{19}$$

The aforementioned formula indicates that the four Stokes vectors I, Q, U, and V can be calculated by measuring the light intensity in any four directions. The angles selected in this study are 0°, 60°, and 120°. After calculation, the incident Stokes vector can be obtained as follows:

$$\begin{cases} I = \frac{1}{2}(I'(60, 45, \frac{p}{2}) + I'(120, 45, \frac{p}{2}) - 3I'(0, 45, \frac{p}{2})), \\ Q = 2I'(0, 0, 0) - \frac{1}{2}I'(60, 45, 0) - \frac{1}{2}I'(120, 45, \frac{p}{2}) + \frac{3}{2}I'(0, 45, \frac{p}{2}), \\ U = \frac{2\sqrt{3}}{3}(I'(60, 45, \frac{p}{2}) - I'(120, 45, \frac{p}{2})), \\ V = \frac{1}{2}(I'(60, 45, \frac{p}{2}) + I'(120, 45, \frac{p}{2}) - I'(0, 45, \frac{p}{2})). \end{cases} \tag{20}$$

The circular polarization component is added to the measurement method to realize the full polarization characteristic measurement of the target and compensate for the error caused by the previous polarization characteristic measurement only for the linear polarization component.

Experimental Results and Discussion

The transmission experiment of polarized light with three wavelengths and six polarization states is carried out under seven visibility environments. According to the relationship between optical thickness and outdoor visibility in **Table 1**, the researchers tested and recorded the polarization characteristics data under different visibility conditions. **Figures 7**, **8** data are the statistical results of the 1-month test on polarization characteristics in different visibilities. The experimental results are plotted, as shown in **Figures 7**, **8**.

As shown in **Figures 7A–C**, the DOP changes of left-handed and right-handed circularly polarized light are consistent, and the DOP changes of the three linearly polarized light are also consistent. It can be seen that because the DOP difference between left-handed circularly polarized light and right-handed circularly polarized light is less than 3%, and the DOP curves of the two overlap; the DOP difference of 0°, 45°, and 90° linearly polarized light is less than 3%, resulting in the three DOP curves overlapping. With the increase in wavelength, the polarization characteristic of circularly polarized light is better than that of linearly polarized light. At 450 nm, the difference between circularly polarized light and linearly polarized light is not obvious. At 532 nm, the DOP of circularly polarized light is 1–10% higher than that of linearly polarized light. At 671 nm, the DOP of circularly polarized light is 2–15% higher than that of linearly polarized light.

The three groups of wavelength field test data in **Figures 7A–C**) show that for any polarized light of any wavelength, the DOP decreases gradually with the increase in transmission environment concentration. This result can be ascribed to the fact that the polarized light belongs to multiple scattering when passing through the smoke. In addition, the higher the smoke concentration, the higher the scattering times, the more the backscattering will increase, and the more the depolarization of polarized light occurs. When the concentration is low, the forward scattering of polarized light increases. Thus, the DOP will be greater than that when the concentration is high. In the visible light band at 450 nm, the DOP of circularly polarized light is close to that of linearly polarized light. The DOP of 532-nm circularly polarized light is slightly higher than that of linearly polarized light by 1–10%. Moreover, the higher the concentration, the more obvious the difference between the DOPs of circularly polarized light and linearly polarized light. The DOP of circularly polarized light is gradually higher than that of linearly polarized light. When the wavelength of polarized light increases to 671, the outgoing polarization degree of circularly polarized light is higher than that of linearly polarized light by 2–15% at all concentrations. This finding is consistent with the simulation results of concentration and polarized light transmission characteristics. With the increase in wavelength, the DOP of circularly polarized light is slightly higher than that of linear polarization. Therefore, if the polarization-maintaining characteristics of circularly polarized light are used, a long wavelength band must be used as much as possible because the polarization-maintaining characteristics of circularly

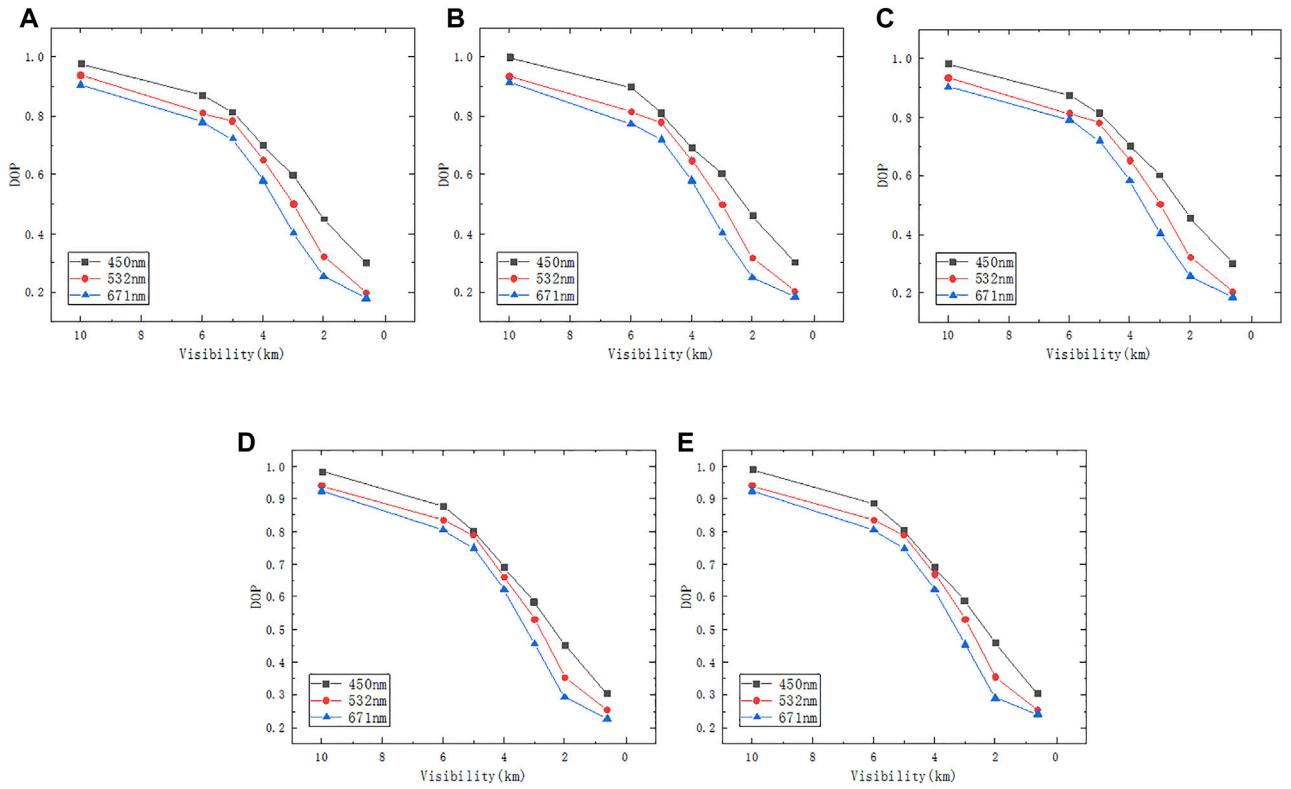

FIGURE 8 | Field test curves of polarization transmission characteristics of different polarization states:**(A)** 0°, **(B)** 45°, **(C)** 90°, **(D)** left-hand rotation, and **(E)** right-hand rotation.

TABLE 2 | Calculation results of confidence of 450 nm polarized light simulation and test verification.

Polarization state	Horizontal (%)	+45°	Vertical	Left-hand rotation	Right-hand rotation
Confidence	83.06	83.58%	83.34%	78.46	79.07%

TABLE 3 | Calculation results of confidence of 532 nm polarized light simulation and test verification.

Polarization state	Horizontal	+45°	Vertical	Left-hand rotation	Right-hand rotation
Confidence	78.13%	77.96%	78.54%	72.44%	72.83%

polarized light of the same wavelength are better than those of linearly polarized light in this case.

Figures 8A–E show that in the smoke environment, the DOP at 450 nm of the five polarization states is higher than that at 532 and 671 nm. The simulation results of the change in DOP with dust concentration under different wavelength conditions are consistent.

The confidence between the test and simulation data is calculated as follows:

$$M = 1 - \left(\sum_{1}^{n} \frac{|R - R_m|}{R_m} \right) / n \times 100\%, \tag{21}$$

where R and R_m are the DOP values obtained by simulation and measurement under the same conditions. The simulation and measurement experiments are carried out for seven optical thicknesses, $n = 7$. Thus, the DOP confidence of five polarization states is calculated. The calculation results are as follows:

The confidence calculation results in **Tables 2–4** show that in the visible band, the visibility is 0.6–10 km, the particle size is 0.7 μm, the particle refractive index is 1.53 + 0.008i, and the optical thickness is in the range of 0.3–8. The lowest confidence of the simulation model is 60.08%, and the highest is 83.58%. All confidence calculation results are greater than 60%, indicating that the results of the simulation model are reliable.

TABLE 4 | Calculation results of confidence of 671 nm polarized light simulation and test verification.

Polarization state	Horizontal	+45°	Vertical	Left-hand rotation	Right-hand rotation
Confidence	71.22%	70.91%	72.06%	60.08%	61.12%

When testing the polarization characteristics in the field smoke environment, outdoor environmental factors such as wind force, temperature, and humidity will always affect the accuracy of the experimental measurement, resulting in inevitable errors in the data obtained from the field test. Therefore, in the subsequent experimental research, we should consider the outdoor environmental factors as variables to obtain the influence law of environmental factors on the experimental test to reduce errors. In addition, the simulation only focuses on the multiple polarization scattering characteristics of smoke particles with the same particle size. In the future, the external field and experimental research on the polarization characteristics of multiple particle sizes should be carried out.

CONCLUSION

In a smoke particle environment, the changes in polarization characteristics of visible polarized light transmitted through the medium are studied. By analyzing the size distribution of particles in a smoke environment, the polarization characteristic model of multiple scattering of polarized light in the visible band is established based on the Monte Carlo method, and the transmission characteristics of polarized light are studied by combining indoor and outdoor experiments. With the increase in optical thickness, the DOP at three wavelengths in the visible light band decreases, and the DOP of each polarized light decreases. No obvious difference exists between the DOP of circularly polarized light at 450 nm and linearly polarized light. The DOP of circularly polarized light at 532 nm is 1–5% higher than that of linearly polarized light, 1–10% higher than that of outdoor test, 1–5% higher than that of circularly polarized light at 671 nm, and 2–15% higher than that of outdoor test. Moreover, the DOP of the three wavelengths is always 450 nm > 532 nm > 671 nm. Therefore, the shorter the wavelength in the visible band, the higher the DOP. With the increase in wavelength, the polarization characteristics of circularly polarized light are slightly better than those of linearly polarized light. In the case of a long wavelength band, the polarization-maintaining characteristics of circularly polarized light at the same wavelength are better than those of linearly polarized light. In the follow-up work, we will carry out experimental research on the influence of particle size on polarization characteristics, expand the research scope to the near-infrared band, master the influence law of outdoor real environment on polarization characteristics, and provide a theoretical basis for the development of polarization imaging.

DATA AVAILABILITY STATEMENT

The raw data supporting the conclusion of this article will be made available by the authors, without undue reservation.

AUTHOR CONTRIBUTIONS

ZJ conceived the project, conducted the experiment, and wrote the manuscript. All authors contributed to discussions during its preparation. ZJ supervised the project.

FUNDING

This research was funded by the National Natural Science Foundation of China (Nos. 61890963 and 61905025), Key project of Education Department of Jilin Province (JJKH20220738KJ and JJKH20220737KJ), and Project of Science and Technology Department of Jilin Province (Nos. 20210201093GX and 20200201261JC).

REFERENCES

1. Evans KF, Stephens GL. A New Polarized Atmospheric Radiative Transfer Model. *J Quantitative Spectrosc Radiative Transfer* (1991) 46(5):413–23. doi:10.1016/0022-4073(91)90043-p
2. Fade J, Panigrahi S, Carré A, Frein L, Hamel C, Bretenaker F, et al. Long-range Polarimetric Imaging through Fog. *Appl Opt* (2014) 53(18):3854–65. doi:10.1364/ao.53.003854
3. Liu X, Qiao S, Ma Y. Highly Sensitive Methane Detection Based on Light-Induced Thermoelastic Spectroscopy with a 2.33 Mm Diode Laser and Adaptive Savitzky-Golay Filtering. *Opt Express* (2022) 30(2):1304–13. doi:10.1364/oe.446294
4. Ma Y, Hong Y, Qiao S, Lang Z, Liu X. H-shaped Acoustic Micro-resonator-based Quartz-Enhanced Photoacoustic Spectroscopy. *Opt Lett* (2022) 47(3):601–4. doi:10.1364/ol.449822
5. Liu X, Ma Y. Sensitive Carbon Monoxide Detection Based on Light-Induced Thermoelastic Spectroscopy with a Fiber-Coupled Multipass Cell. *Chin Opt Lett* (2022) 20(3):031201. doi:10.3788/col202220.031201
6. Ma Y, Hu Y, Qiao S, Lang Z, Liu X, He Y, et al. Quartz Tuning forks Resonance Frequency Matching for Laser Spectroscopy Sensing. *Photoacoustics* (2022) 25:100329. doi:10.1016/j.pacs.2022.100329
7. Chun CSL, Sadjadi FA. Polarimetric Laser Radar Target Classification. *Opt Lett* (2005) 30(14):1806–8. doi:10.1364/ol.30.001806
8. Anna G, Goudail F, Dolfi D. Optimal Discrimination of Multiple Regions with an Active Polarimetric Imager. *Opt Express* (2011) 19(25):25367–78. doi:10.1364/oe.19.025367
9. Tyo JS, Goldstein DL, Chenault DB, Shaw JA. Review of Passive Imaging Polarimetry for Remote Sensing Applications. *Appl Opt* (2006) 45(22):5453–69. doi:10.1364/ao.45.005453

10. Tan S, Narayanan RM. Design and Performance of a Multiwavelength Airborne Polarimetric Lidar for Vegetation Remote Sensing. *Appl Opt* (2004) 43(11):2360–8. doi:10.1364/ao.43.002360
11. Anastasiadou M, Martino AD, Clement D, Liège F, Laude-Boulesteix B, Quang N, et al. Polarimetric Imaging for the Diagnosis of Cervical Cancer. *Phys Stat Sol*(c). (2008) 5(5), 1423–6. doi:10.1002/pssc.200777805
12. Baldwin AM, Chung JR, Baba JS, Spiegelman CH, Amoss MS, Cote GL. Mueller Matrix Imaging for Cancer Detection. *Proc IEEE* (2003) 1022: 1027–30. doi:10.1109/iembs.2003.1279419
13. Wu F, Yang Y, Jiang J, Zhang P, Li Y, Xiao X, et al. Classification between Digs and Dust Particles on Optical Surfaces with Acquisition and Analysis of Polarization Characteristics. *Appl Opt* (2019) 58(4):1073–83. doi:10.1364/ao.58.001073
14. Van der Laan JD, Wright JB, Scrymgeour DA, Kemme SA, Dereniak EL. Evolution of Circular and Linear Polarization in Scattering Environments. *Opt Express* (2015) 23(25):31874–88. doi:10.1364/oe.23.031874
15. Zeng X, Chu J, Cao W, Kang W, Zhang R. Visible-IR Transmission Enhancement through Fog Using Circularly Polarized Light. *Appl Opt* (2018) 57(23):6817. doi:10.1364/ao.57.006817
16. Van der Laan JD, Wright JB, Kemme SA, Scrymgeour DA. Superior Signal Persistence of Circularly Polarized Light in Polydisperse, Real-World Fog Environments. *Appl Opt* (2018) 57(19):5464–73. doi:10.1364/ao.57.005464
17. Ryan JS, Carswell AI. Laser Beam Broadening and Depolarization in Dense Fogs. *J Opt Soc Am* (1978) 68(7):900–8. doi:10.1364/josa.68.000900
18. Chu J, Wu Q, Zeng X, Li Y. Forward Transmission Characteristics in Polystyrene Solution with Different Concentrations by Use of Circularly and Linearly Polarized Light. *Appl Opt* (2019) 58(25):6750–4. doi:10.1364/ao.58.006750
19. Sankaran V, Schönenberger K, Walsh JT, Maitland DJ. Polarization Discrimination of Coherently Propagating Light in Turbid media. *Appl Opt* (1999) 38(19):4252–61. doi:10.1364/ao.38.004252
20. Liao YB. *Polarization Optics*. China (2003).
21. He SY. *Particle Size Distribution Characteristics of Chemical Components of Atmospheric Particulate Matter in Nanjing*. Nanjing: Nanjing University (2020).
22. Hao L, Yang W, Wu TW, Zhao JQ, Shi GY. Optical Properties and Radiative Forcing Effects of Dust Aerosol. *J Desert Res* (2010) 30(06):1477–82.

Conflict of Interest: The authors declare that the research was conducted in the absence of any commercial or financial relationships that could be construed as a potential conflict of interest.

frontiers | Frontiers in Physics

ORIGINAL RESEARCH
published: 13 April 2022
doi: 10.3389/fphy.2022.853813

Early Noninvasive Monitoring of Hypoxic State of Diabetic Foot Based on Diffuse Reflectance Spectroscopy

Ge Xu[1,2], *Liquan Dong*[1,2,3]*, *Jing Yuan*[1,2], *Yuejin Zhao*[1,2,3], *Ming Liu*[1,2,3], *Mei Hui*[1,2] and *Lingqin Kong*[1,2,3]*

[1]School of Optics and Photonics, Beijing Institute of Technology, Beijing, China, [2]Beijing Key Laboratory for Precision Optoelectronic Measurement Instrument and Technology, Beijing, China, [3]Yangtze Delta Region Academy of Beijing Institute of Technology, Jiaxing, China

Early accurate diagnosis and assessment severity of the hypoxic state of diabetic foot is of paramount importance. In this paper, a noninvasive monitoring method of the hypoxic state of the diabetic foot based on diffuse reflectance spectroscopy is proposed. Monte Carlo simulation method is used to imitate the effect on diffuse reflectance of the foot from different blood volume fractions and blood oxygen saturations. Moreover, the *in vivo* experiments of the hypoxic state of the foot based on the binding method is carried out using an integrating sphere system. Monte Carlo simulation results show that the diffuse reflectance of the foot under normal state and hypoxic state is significantly different. *In vivo* experimental results are highly consistent with the Monte Carlo simulation results. *In vivo* experiments further indicate that six characteristic wavelengths (440, 469, 514, 540, 560, and 576 nm) of the diffuse reflectance are more able to distinguish the normal oxygen state and hypoxic states of the foot. The proposed method promotes the development and application of the diffuse reflectance spectroscopy method in the noninvasive detection of biological tissue.

Keywords: diffuse reflectance spectroscopy, monte carlo simulation, diabetic foot, hypoxic state, blood oxygen saturation, blood volume fraction

OPEN ACCESS

Edited by:
Yufei Ma,
Harbin Institute of Technology, China

Reviewed by:
Xiaojun Yu,
Northwestern Polytechnical University, China
Nina Reistad,
Lund University, Sweden

***Correspondence:**
Liquan Dong
kylind@bit.edu.cn
Lingqin Kong
konglingqin3025@bit.edu.cn

Specialty section:
This article was submitted to Optics and Photonics, a section of the journal Frontiers in Physics

Received: *13 January 2022*
Accepted: *16 March 2022*
Published: *13 April 2022*

Citation:
Xu G, Dong L, Yuan J, Zhao Y, Liu M, Hui M and Kong L (2022) Early Noninvasive Monitoring of Hypoxic State of Diabetic Foot Based on Diffuse Reflectance Spectroscopy. Front. Phys. 10:853813. doi: 10.3389/fphy.2022.853813

1 INTRODUCTION

Diabetes mellitus (DM) is a metabolic disorder disease characterized by hyperglycemia. According to the statistics of the World Health Organization, the complications caused by DM are more than 100, involving diabetic retinopathy, diabetic nephropathy, and even death [1, 2]. Among these complications, the incidence rate of diabetic foot is as high as 25% [3]. The etiology of diabetic foot is extremely complicated. Peripheral arterial disease (PAD) plays a major role in the pathogenesis of diabetic foot, which has been generally recognized. PAD is a common finding in DM patients with diabetic foot complications and is associated with poor outcomes, such as amputation. PAD leads to vasoconstriction, which will block the vascular microcirculation, reduce the blood supply of the lower limbs, and finally generate foot infection and gangrene. Pay special attention to the oxygen assessment and blood perfusion of the vascular microcirculation of the foot, especially the changes of blood volume fraction and blood oxygen saturation, which is very important to monitor the deterioration degree of foot lesions. Timely diagnosis and treatment of the foot may even reverse the occurrence of foot complications in the preclinical stage. Doppler test [4], percutaneous oxygen tension [5], and angiography may be the most prevalent used approaches

for clinically monitoring the blood oxygen status of the lower extremity vascular microcirculation in patients with DM. However, these methods not only rely on expensive instruments and professional knowledge to evaluate the vascular microcirculation state and blood perfusion in the diabetic foot, but also are difficult to judge these changes in real-time and quickly.

The diffuse reflectance spectroscopy (DRS) method uses optical analysis methods to obtain real-time optical information such as physiology, morphology, and composition of human tissue, which has become one of the main noninvasive research methods of human tissue. DRS method has been widely used to characterize normal and malignant states of different types of human tissues including colon [6], cervix [7], ovary [8], breast [9], liver [10], lung [11], and skin tumors [12]. Recently, the DRS method has been gradually applied to the study of diabetic foot. Kumar et al. [13] quantitatively measured localized blood volume fraction from various sites of the human foot sole by using the DRS. The investigation also illustrated that the blood volume fractions were different from four sites of the human foot sole. Anand et al. [14] implemented a DRS approach to monitor blood oxygenation of diabetic foot. This study mainly indicated the relationships among diffuse reflectance intensity measurements, tissue oxygenation, and wound healing process. However, these related studies only achieved the measurement of diffuse reflectance spectra of the diabetic foot in DM patients and studied a simple analysis of these spectra. Pathological analysis of diabetic foot is insufficient. In addition, for DM patients without diabetic foot complications, monitoring the diffuse reflectance spectra of the foot is also very important for preventing the occurrence and deterioration of diabetic foot. Lower extremities of DM patients with an early diabetic foot complication often suffer from numbness, weakness, and other symptoms [15, 16]. Unfortunately, these symptoms are often ignored due to no obvious wound on the surface of the DM patients' foot. Due to lack of foot care, foot hygiene and minor wounds are underestimated, which further leads to the deterioration of foot ulcers. To our best of knowledge, the DRS method has not been demonstrated to be devoted to exploring the pathology of the hypoxic state of diabetic foot.

The purpose of our current research is to qualitatively determine the pathological mechanism of the hypoxic state of the diabetic foot by simulation and *in vivo* experiments. In this paper, Monte Carlo (MC) [17] simulation is implemented to imitate the hypoxic state of the foot. In the MC simulation experiments, a nine-layer skin model in terms of optical characteristics of the foot skin tissue is established. Combined with the skin tissue model, the hypoxic state of the foot is created by adjusting blood oxygen saturation and blood volume fraction. Based on the MC simulation experiments, the pathological mechanism of the hypoxic state of the foot is analyzed. The MC simulation results are further verified by *in vivo* experiments, i.e., binding the subjects' toes with the elastic bands to imitate the hypoxic state of the foot. To elucidate the effect of changes in the hypoxia degree on the diffuse reflectance, experiments on the hypoxia degree in the toes are also performed. The pathological mechanism of foot hypoxia and the significance of foot hypoxia monitoring are indicated based on MC simulation and *in vivo* experiments.

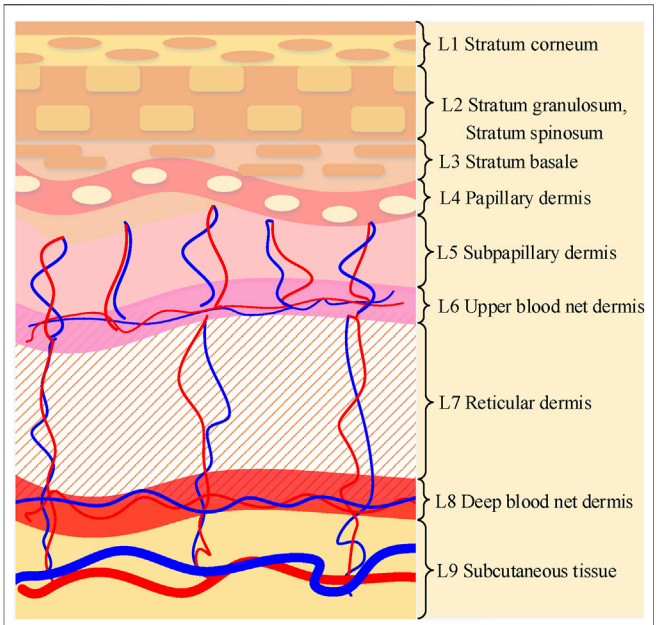

FIGURE 1 | Illustration of nine-layer structure of skin tissue: stratum corneum (L1), stratum granulosum and stratum spinosum (L2), stratum basale (L3), papillary dermis (L4), subpapillary dermis (L5), upper blood net dermis (L6), reticular dermis (L7), deep blood net dermis (L8) and subcutaneous tissue (L9), respectively.

2 MATERIALS AND METHODS

2.1 Monte Carlo Simulation

To accurately simulate the changes of the diffuse reflectance resulting from blood oxygen saturation and blood volume fraction of DM patients' foot, an appropriate skin tissue model is required to establish. Due to the multi-layer structure and physiological characteristics of skin tissue, the establishment of the skin tissue model is extremely complex. The traditional three-layer tissue model is composed of *epidermis*, dermis, and subcutaneous tissue, which is simple and convenient to calculate. However, the traditional skin tissue model assumes that chromophores are uniformly distributed on the *epidermis* or dermis. Therefore, the traditional skin tissue model makes the simulation value deviate greatly from the truth value in terms of diffuse reflectance.

In this paper, we adopt the nine-layer skin tissue model designed by Maeda [18]. The *epidermis* and dermis of the nine-layer skin tissue model are finely divided on the basis of the three-layer traditional tissue model. **Figure 1** shows the nine-layer structure of the skin tissue model. The stratum corneum (L1) is located above the *epidermis*. The epidermal layer is mainly composed of stratum granulosum and stratum spinosum (L2), and the stratum basale (L3). The dermis is under the *epidermis* and classified into five layers consisting of the papillary dermis

(L4), subpapillary dermis (L5), upper blood net dermis (L6), reticular dermis (L7), and deep blood net dermis (L8), respectively. The subcutaneous tissue (L9) is under the dermis.

Each layer of skin tissue contains particular chromophores, which determines each layer of skin tissue with specific optical absorption properties. The baseline absorption of both *epidermis* and dermis is expressed by the following $\mu_{a.baseline}$ [19], approximated as a function of wavelength λ:

$$\mu_{a.baseline}(\lambda) = 7.84 \times 10^{7} \times \lambda^{-3.255} \tag{1}$$

The absorption coefficient of the dermis depends on a minor baseline skin absorption (water, fat, and other absorption components) and a dominant hemoglobin absorption due to the cutaneous blood perfusion.

$$\mu_{a.dermis}(\lambda) = B_f\left[S\mu_{a.oxy}(\lambda) + (1-S)\mu_{a.deoxy}(\lambda)\right] + (1-B_f)\mu_{a.baseline}(\lambda) \tag{2}$$

where B_f denotes blood volume fraction, S denotes the blood oxygen saturation. $\mu_{a.oxy}$ and $\mu_{a.deoxy}$ are the absorption coefficient of oxyhemoglobin and deoxyhemoglobin respectively, for the hematocrit Ht = 45% [20].

The chromophore of the *epidermis* is mainly melanin. The absorption coefficient of the *epidermis* is followed as:

$$\mu_{a.epidermis}(\lambda) = M_f\mu_{a.mel}(\lambda) + (1-M_f)\mu_{a.baseline}(\lambda) \tag{3}$$

where M_f denotes the melanin volume fraction and $\mu_{a.mel}$ denotes the melanin absorption coefficient. The values of M_f and $\mu_{a.mel}$ are from Ref. [21].

The fibrous components in the dermis such as collagen and elastin, are related to the scattering properties of the skin tissue. Scattering properties are the contributions due to Rayleigh scattering by the small-scale structure associated with the collagen fibers and other cellular structures and the Mie scattering by the large cylindrical dermal collagen fibers.

The reduce scattering coefficients of the Rayleigh scattering and Mie scattering can be written as $\mu'_{s.Rayleigh}$ and $\mu'_{s.Mie}$, respectively.

$$\mu'_{s.Rayleigh} = (2 \times 10^{12})\lambda^{-4} \tag{4}$$

$$\mu'_{s.Mie} = (2 \times 10^{15})\lambda^{-1.5} \tag{5}$$

The scattering theory of **Eq. 4** and **Eq. 5** comprehensively analyzes the relationship between wavelength and various components in skin tissue. The scattering coefficient of the *epidermis* and dermis can be approximated as a standard value by using the relation equation given by Gemert [22].

$$\mu_s(\lambda) = \frac{\mu'_{s.Rayleigh} + \mu'_{s.Mie}}{1-g} \tag{6}$$

where the anisotropy parameter (g) of the *epidermis* and dermis is approximately written as:

$$g(\lambda) = 0.62 + 0.29 \times 10^{-3} \times \lambda \tag{7}$$

The refractive index is given by Meglinski [23], and the tissue thickness is from the Das [24]. We adjust the above parameters of optical properties in each layer of skin tissue based on data from these empirical literature, and finally establish the skin tissue model of the foot. MC simulation is employed to simulate the diffuse reflectance spectra of the foot according to these parameters of optical properties.

2.2 Experiment Setup

A single integrating sphere system designed by our team to measure the diffuse reflectance spectra of the foot *in vivo* is shown in **Figure 2**. The single integrating sphere system mainly consists of a deuterium tungsten halogen light source (HYBEC, HBL-273) with the wavelength in the range of 190–800 nm, an integrating sphere (Aimealth Technology Co., Ltd., Beijing), a photomultiplier tube (Hamamatsu, R928) and a computer. The power of the single integrating sphere system is 20W. The light emitted from the halogen light is split through a monochromator in the beam-splitting system to emit light of a specific wavelength, and then reaches the sample port of the integrating sphere through a series of mirrors. Subsequently, the light reflected by the sample tissue, carrying the optical information of the tissue, undergoes a series of reflections and refractions in the integrating sphere, and is finally received by the photomultiplier tube. The photomultiplier tube transmits the received diffuse light to the computer. The computer processed the diffuse reflectance spectra of the foot under the control of the self-made spectroscopy software.

For each measurement, the diffuse reflectance spectra of the white reflectance standard (SRS-99-010, Labsphere, Inc., North Sutton, NH) and background noise are measured first. The diffuse reflectance of the sample tissue ($M_R(\lambda)$) is calculated according to the diffuse reflectance spectra of the sample tissue, the white reflectance standard, and the background noise. **Eq. 8** is written as follows:

$$M_R(\lambda) = \frac{R(r) - R_{dark}}{R_{std} - R_{dark}} \tag{8}$$

where the diffuse reflectance spectrum of the sample tissue is expressed as $R(r)$, the diffuse reflectance spectrum of the white reflectance standard is expressed as R_{std}, and the diffuse reflectance spectrum of the background noise is expressed as R_{dark}.

The subjects' great toes are selected as our measurement site since great toes are easy to bind and measure. The diffuse reflectance spectrum of each subject's great toe is measured in the same environment and kept clean. To avoid interference from external pressure, we choose the same type of elastic bands, the same number loops of an elastic band, and the same binding time to control the pressure [25] for every subject *in vivo* experiments. During the measurement process, the same site of the subjects' foot is chosen each time. First, the diffuse reflectance spectrum of the subjects' great toes under a normal state is measured by the integrating sphere system. Subsequently, the diffuse reflectance spectrum from the same site of a great toe is measured again when the subjects' great toe is bound over time t.

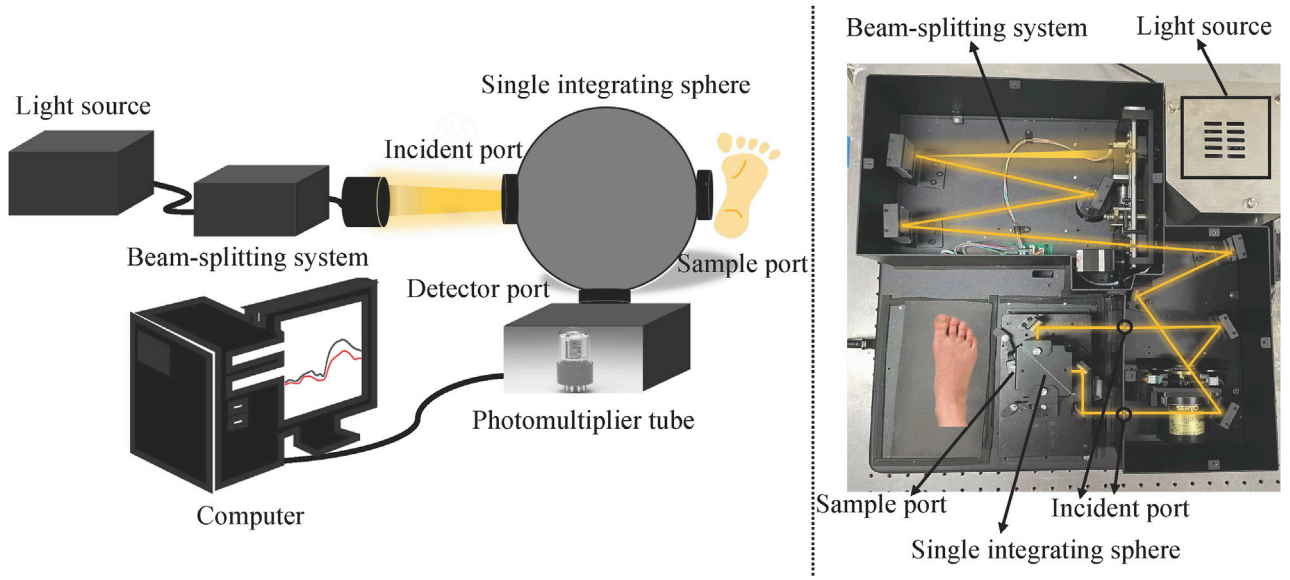

FIGURE 2 | Scheme of the integrated single integrating sphere system (Left); Physical diagram of the single integrating sphere system (Right). The light emitted from the halogen light is split through a monochromator in the beam-splitting system to emit light of a specific wavelength, focuses on the incident port and reaches the sample port. Subsequently, the light reflected by the sample tissue through a series of reflections and refractions in the integrating sphere, which is finally received by the photomultiplier tube at the detection port.

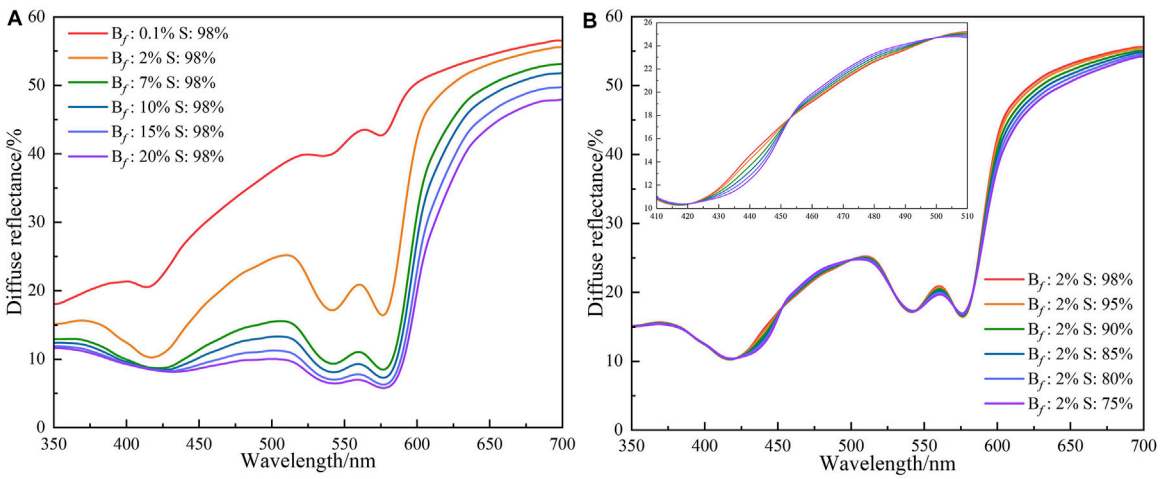

FIGURE 3 | The diffuse reflectances of different blood volume fraction and blood oxygen saturation: **(A)** The blood oxygen saturation is 98%, and the blood volume fraction is 0.1%, 2%, 7%, 10%, 15%, and 20%; **(B)** The blood volume fraction is 2%, and the blood oxygen saturation is 75%, 80%, 85%, 90%, 95%, and 98%.

3 RESULTS AND DISCUSSION

3.1 Results and Analysis of MC Simulation Experiments

The changes in blood volume fraction and blood oxygen saturation mainly affect the optical parameters of the dermis and subcutaneous tissue, specifically the L4-L9 layer of the skin tissue model (Shown in **Figure 1**). Adjusting blood volume fraction and blood oxygen saturation of the L4-L9 layer, the diffuse reflectance of the great toes under normal state and hypoxic state are simulated.

For healthy people, the blood volume fraction is between 2% and 7% and the blood oxygen saturation is above 95%. To simulate the diffuse reflectance under different oxygen states, different concentration ranges of blood volume fraction and blood oxygen saturation are set based on parameters of healthy people. First, the blood volume fraction varies over a wide range, while the oxygen saturation maintains a healthy parameter to simulate diffuse reflectance. Subsequently, the blood volume fraction maintains unchanged, and the blood oxygen saturation is changed in a large range, thereby

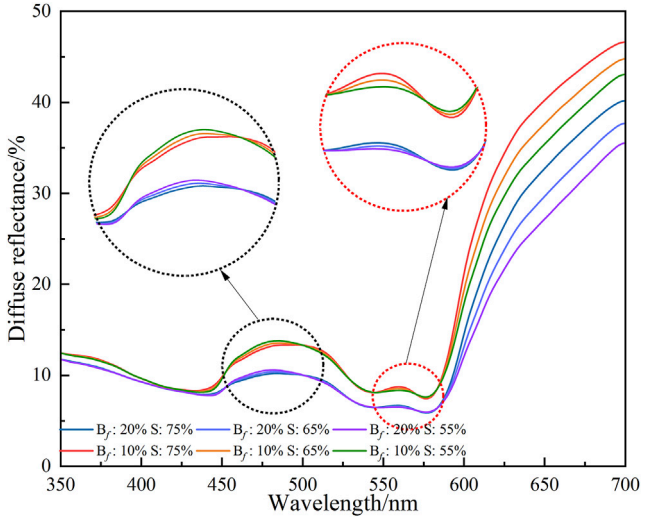

FIGURE 4 | The diffuse reflectances of more blood volume fraction and lower blood oxygen saturation. The blood oxygen saturation is 55%, 65%, and 75%, respectively. The blood volume fraction is 10% and 20%, respectively.

realizing the simulation of diffuse reflectance. The simulation results are shown in **Figure 3**. B_f denotes blood volume fraction and S denotes the blood oxygen saturation. **Figure 3A** indicates the diffuse reflectance in the blood volume fraction with the range of 0.1%–20% and the blood oxygen saturation with 98%. When the blood oxygen saturation remains constant at 98%, the diffuse reflectance decreases as the blood volume fraction increases. When the blood volume fraction is less than the normal level (<2%), the gap from peak and valley of diffuse reflectance in the wavelength range of 540–580 nm gradually gets smaller. When the blood volume fraction is higher than the normal level (>7%), the variation amplitude of the diffuse reflectance in the wavelength range of 440–520 nm is lower than the normal blood volume fraction. **Figure 3B** shows the changes of the diffuse reflectance of the skin tissue when the blood volume fraction is at a healthy level and the blood saturation changes from healthy states (95%, 98%) to abnormal states (75%, 80%, 85%, and 90%). When the blood volume fraction is 2%, although the blood oxygen saturation decreases from the normal level (more than 95%) to the abnormal level, the diffuse reflectance basically maintains the same trend. However, the shape of the diffuse reflectance produces a flip in the wavelength range of 400–440 nm. This flip is mainly due to changes in the absorption coefficients of oxyhemoglobin and deoxyhemoglobin. The diffuse reflectance exhibits pathological features when the blood volume fraction is above healthy levels and blood oxygen saturation is below healthy levels.

To verify the above analysis, further simulations are carried out with increased blood volume fraction and decreased blood oxygen saturation. The blood volume fraction we adopted is above the healthy level (2%–7%), which is 10% and 20%, respectively. The blood oxygen saturation is lower than the healthy level (95%–100%) and is set to 55%, 65%, and 75%, respectively. The simulation results of diffuse reflectance based on the MC algorithm are shown in **Figure 4**. The simulated diffuse reflectance of the great toe first bulge and then descend with the wavelength range of 450–530 nm compared with the diffuse reflectance under normal state. The diffuse reflectance of oxyhemoglobin and deoxyhemoglobin (543–585 nm) are attenuated under hypoxia compared with normal conditions. Combining the optical characteristic parameters of oxyhemoglobin and deoxyhemoglobin, when the blood volume fraction increases and the blood oxygen saturation decreases, the absorption coefficient of the tissue will increase (the effect of oxygen saturation on the absorption coefficient predominates when fluctuations in the fractional blood volume are small). The other optical properties caused by blood volume fraction and blood oxygen saturation are ignored. Therefore, the absorption coefficient of the skin tissue increases, while the scattering coefficient remains relatively unchanged, which will lead to an increase in light absorption and a corresponding decrease in diffuse reflectance. **Figure 4** shows that when the blood volume fraction is from 10% to 20% (oxygen saturation remains the same), the diffuse reflectance in the wavelength range of 400–500 nm significantly decrease. **Figure 4** indicates the pathology of the diabetic foot, i.e., hypoxia results in increased blood volume fraction and decreased blood oxygen saturation in localized areas of the foot.

The above MC simulation results show that hyperglycemia damages the nerve fiber and reduces blood supply, causing tissue hypoxia and metabolism alteration in the lower limbs. The vasoconstriction of the lower limbs of DM patients leads to insufficient blood supply and tissue hypoxia. In terms of optical characteristic parameters, these problems lead to increased blood volume fraction and decreased oxygen saturation in the local area.

3.2 Results and Analysis of *In vivo* Experiments

To further verify the simulation results of MC under hypoxia state, *in vivo* experiments are implemented. The occurrence of the diabetic foot means that the patient already has DM. A variety of complications DM accompanied that have a certain impact on blood circulation. Therefore, to analyze the pathological mechanism of the hypoxic state of the diabetic foot, healthy people are selected as our subjects. We imitate the hypoxic state of the diabetic foot by binding elastic bands to the great toes of healthy people and measure the diffuse reflectance spectra of great toes by a single integrating sphere system (See **Section 3**). A total of 34 healthy subjects (19 men and 15 women), aged 20–35 years, are studied. The research protocol is approved by

TABLE 1 | The detailed information of the subjects.

	The Healthy Subjects	
Gender (male/female)	male	female
Number (people)	19	15
Average age (years)	32.2	28.5

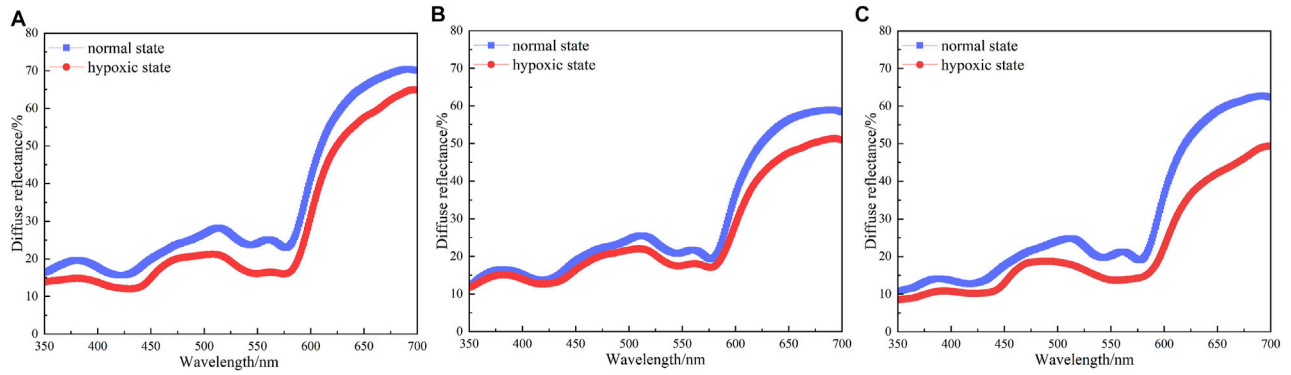

FIGURE 5 | The diffuse reflectances of three subjects under normal state and hypoxic state. **(A)** The diffuse reflectance of the subject A; **(B)** The diffuse reflectance of the subject B; **(C)** The diffuse reflectance of the subject C.

TABLE 2 | The absorption maxima of chromophores and characteristic wavelengths.

Chromophores	Absorption Maxima/nm	Characteristic Wavelengths/nm
Melanin	—	440
β-carotene	476	469
Bilirubin	450	514
Oxyhemoglobin	540	540
Deoxyhemoglobin	555	560
Oxyhemoglobin	576	576

the Medical Ethics Committee of Medical and Laboratory Animal of Beijing Institute of Technology with approval code 2021–004. Detailed information on healthy subjects is from the Beijing Institute of Technology shown in **Table 1**.

Figure 5 shows the diffuse reflectance of the great toes of three subjects (A, B, and C) under normal state and hypoxic state (binding time *t* for 1 min). The blue solid lines represent the diffuse reflectances under normal state, and the red solid lines represent the diffuse reflectances under hypoxic state. The trends of diffuse reflectances of three subjects' great toes under normal state and hypoxic state in the wavelength range of 350–700 nm are roughly consistent and are corresponding with the MC simulation results (Shown in **Figure 3** and **Figure 4**). When the toe is bound by an elastic band, the transport of oxygen is blocked and the local tissue swells. Compared with the diffuse reflectances under normal state, the amplitudes and shapes of diffuse reflectances of three subjects' great toes are moving down in wavelength range 350–700 nm under the hypoxic state. The peaks and valleys of the diffuse reflectances almost completely disappear, specifically in the wavelength range of blood oxygen saturation and hemoglobin sensitive area, i.e., wavelength in the range with 540–580 nm. The diffuse reflectances have inflection points at some special wavelengths compared with the normal oxygen state. The wavelengths of these inflection points are 440, 469, 514, 540, 560, and 576 nm, respectively. In all subjects, these diffuse reflectances under normal state are consistent with the related literature [26], which can confirm the correctness of the diffuse reflectance from MC simulated and the integrating sphere system collected. Combined with the absorption maxima of some chromophores of the skin tissue and inflection points of the subject's diffuse reflectances, six average wavelengths are selected as the characteristic wavelengths. The six characteristic wavelengths are shown in **Table 2**.

In fact, hypoxia problems can also cause the skin on the foot to darken, appearing red or purple. Prolonged hypoxia can cause foot skin ulcers and even cause more serious lesions. However, the color change of skin tissue caused by hypoxia is not obvious at first. Due to the thicker skin of the foot, it is still difficult to distinguish the hypoxia degree from the color of the foot despite chronic hypoxia. In addition, due to the lack of sensitivity of the foot skin, we also lack special attention to these changes. To further prove the effect of blood volume fraction and blood oxygen saturation to the toes involving the surface skin color and diffuse reflectance, we achieve the hypoxia degree experiment. In the hypoxia degree experiment, we adopt the same binding method for the great toes as the above experiment, only change the binding time for the hypoxia degree experiment. The time when the great toe is not tied with the elastic band is taken as the initial time, and the corresponding diffuse reflectance is marked as the normal state. As the time for the great toes to bind the elastic band increased, the diffuse reflectance of the great toes are measured in 1st, 10th, 20th and 30th min, respectively. Finally, five diffuse reflectances within 30 min from each subject are obtained. We capture the image area where the toes are bound with the elastic within 30 min. The device for collecting images is an ordinary camera (FLIR co. BFLY-U3-23S6C-C) with a

FIGURE 6 | The change of skin color and degree of edema of great toe from subject A. The red numbers in the figures indicate the time when the toe is bound by the elastic band.

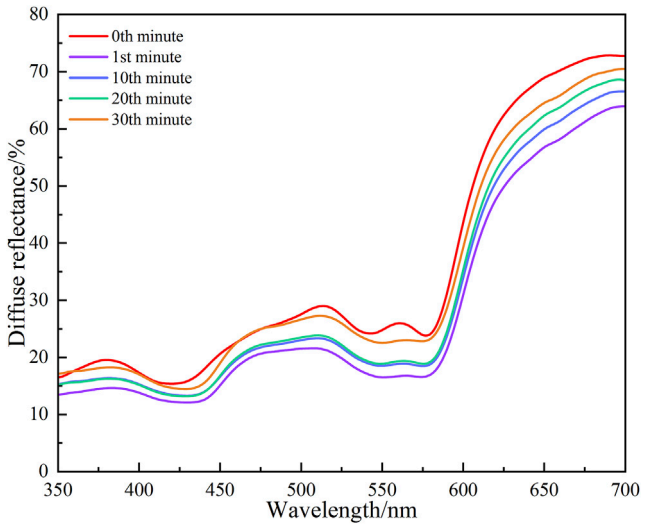

FIGURE 7 | Diffuse reflectances of subject A in hypoxia degree experiment with time followed by 0th, 1st, 10th, 20th, and 30th min, respectively.

resolution of 1920 × 1,200 pixels. The skin color change and degree of edema of the great toe in the subject A are shown in **Figure 6**. With the increase of great toe binding time, the skin color presents a changing dark red. The elastic band prevents the blood flow of the great toe, causes insufficient oxygen supply, so the great toe is swollen. However, when the great toe binding time is too long, the effect of the degree of hypoxia on changes in skin color was difficult to distinguish.

The diffuse reflectances obtained by the hypoxia degree experiment from subject A are shown in **Figure 7**. **Figure 7** shows that the characteristics of the diffuse reflectances under different binding times are consistent with the results of our simulation and *in vivo* experiments. More specifically, the diffuse reflectances obviously increase with binding time t in the 1st, 10th, 20th, and 30th min, respectively. A similar trend is also found from the diffuse reflectances of other subjects' great toes. When the great toe is just bound, the blood oxygen saturation decreases rapidly and the blood volume fraction increases, so the absorption coefficient of the skin tissue increases. The absorption coefficient of the skin tissue increases, while the change of the scattering coefficient is ignored, resulting in an increase in the absorption of light by the tissue and a decrease in the diffuse reflectance obtained by the integrating sphere. When the binding time t reaches a certain level, the local hyperemia of the great toe begins to increase relatively slowly, i.e., the blood volume fraction maintains a relatively stable change state. Although the blood volume fraction changes slowly with the increase of the binding time t, the blood oxygen saturation is still decreasing, resulting in a decrease in the absorption coefficient of the tissue based on the initial state, which makes the tissue diffuse reflectance obtained by the integrating sphere increase steadily. This explains the increase of the amplitudes of the diffuse reflectances under a hypoxic state over binding time t. To further analyze the diffuse reflectances at characteristic wavelengths, the diffuse reflectance value at the 0th minute is set to R_0 and the diffuse reflectance value at other times is set to the R_{minute}. The value changes of diffuse reflectance can be written as **Eq. 9**.

$$\Delta reflectance = \left| \frac{R_{minure} - R_0}{R_0} \right| \tag{9}$$

The values of $\Delta reflectance$ at six characteristic wavelengths with binding time t are shown in **Table 3**. **Table 3** indicates that at any characteristic wavelength, the value of $\Delta reflectance$ decreases with the increase of binding time t. The minimum value of $\Delta reflectance$ is 0.01 at 469 nm wavelength. At characteristic wavelengths of the oxyhemoglobin (540 and 576 nm), the values of $\Delta reflectance$ are basically the same at different binding times t. Especially at the 20th and 30th min, the values of $\Delta reflectance$ at these two wavelengths are 0.20 and 0.04, respectively. **Figure 8** shows that when the time changes from the 10th minute to the 20th min, the values of $\Delta reflectance$ at the characteristic wavelengths are relatively smooth. From the 1st min to the 10th min (the hypoxia state just starts) and the 20th min to the 30th min (longer duration of the hypoxia), the changes of $\Delta reflectance$ fluctuate greatly. However, the effect on skin color is not obvious. These results illustrate that the diffuse reflectances at these characteristic wavelengths are more meaningful for the evaluation of the hypoxia degree. *In vivo* experiments illustrate that when lower extremity vascular microcirculation is hindered and the oxygen supply is insufficient, the diffuse reflectances of the tissue are obviously different from those of the normal state, especially at these characteristic wavelengths. Therefore,

TABLE 3 | The change values of diffuse reflectances at characteristic wavelengths with binding time *t*.

Average Characteristic Wavelengths/nm	*Δreflectance*			
	1st min	10th min	20th min	30th min
440	0.30	0.22	0.22	0.14
469	0.17	0.12	0.11	0.01
514	0.26	0.20	0.18	0.06
540	0.29	0.21	0.20	0.04
560	0.36	0.28	0.26	0.12
576	0.30	0.22	0.20	0.04

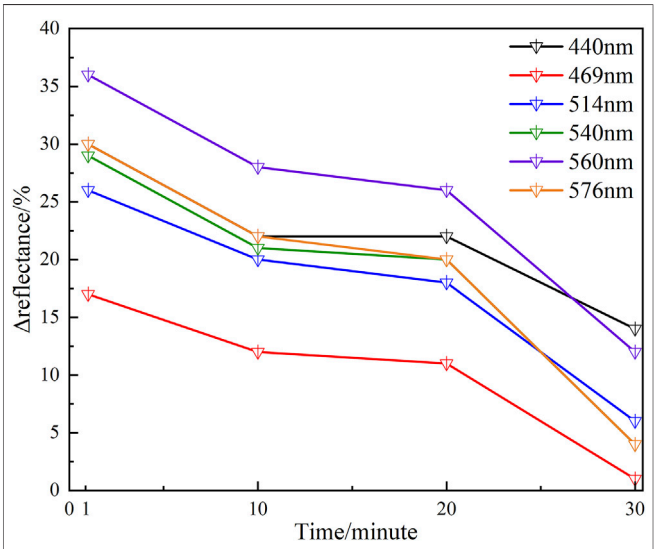

FIGURE 8 | The values of the *Δreflectance* over binding time *t*.

monitoring diffuse reflectance at characteristic wavelengths timely to evaluate the blood oxygen supply level has great potential to prevent tissue lesions caused by insufficient oxygen supply. The hypoxic state simulation of the great toes is caused by pressure generated by the binding elastic bands in this method. In fact, the pressure also affects the absorption coefficient and scattering coefficient of the skin, resulting in changes in the diffuse reflectance of the skin tissue [27]. Moreover, the diffuse reflectances at characteristic wavelengths have some differences due to the influence of individual and hypoxic degrees. Therefore, comprehensively analyzing the changes of diffuse reflectances at multiple characteristic wavelengths to determine the hypoxia degree of the great toes is necessary. Indeed, the diffuse reflectances of patients with the diabetic foot are more complex due to pathology. Patients with such hypoxic symptoms may also be accompanied by other diseases. Thus, when the diffuse reflectances from the patient's foot are matching the phenomenon of the hypoxic condition, further combining the patient's usual symptoms and clinical diagnosis to determine the patient suffering from the degree of the diabetic foot. Monitoring the diffuse reflectance of the patient's foot to determine whether the patient has symptoms of hypoxia, and early treatment is adopted to prevent the symptoms from further worsening, which is of great significance for the prevention of diabetic foot.

4 CONCLUSION

We propose and demonstrate a noninvasive DRS method for the assessment and monitoring of the hypoxic state in the diabetic foot. Based on MC simulation, a nine-layer skin tissue model is established. This model is used to simulate the diffuse reflectance of the pathological mechanism of hypoxia in the diabetic foot. MC simulation experiments show that the diffuse reflectances under the hypoxic condition are quite different from under a normal state. Subsequently, we verify the MC simulation results are consistent with the *in vivo* experiments by the toes binding method. *In vivo* experiments further indicate that the diffuse reflectances at characteristic wavelengths are extremely effective to distinguish the healthy state and hypoxic state.

For DM patients with symptoms such as lower extremity hypoxia, monitoring the diffuse reflectance rather than the change in foot skin color can prevent further deterioration of the hypoxic state. Our preliminary results illustrate that the DRS approach has the potential to quantitatively determine the hypoxic state of the foot in a noninvasive manner. This method provides a novel idea for the detection of the most susceptible part of diabetic foot ulcers and is expected to prevent the occurrence of the diabetic foot.

DATA AVAILABILITY STATEMENT

The raw data supporting the conclusion of this article will be made available by the authors, without undue reservation.

ETHICS STATEMENT

The studies involving human participants were reviewed and approved by the Medical Ethics Committee of Medical and Laboratory Animal of Beijing Institute of Technology with approval code 2021-004. The patients/participants provided their written informed consent to participate in this study. Written informed consent was obtained from the individual(s) for the publication of any potentially identifiable images or data included in this article.

AUTHOR CONTRIBUTIONS

All authors listed have made a substantial, direct, and intellectual contribution to the work and approved it for publication.

FUNDING

This work was supported by the National Natural Science Foundation of China (Nos. 61705010, 11774031, and 61935001).

REFERENCES

1. Sen S, Chakraborty R. EDITORIAL (Thematic Issue: Treatment and Diagnosis of Diabetes Mellitus and its Complication: Advanced Approaches). *Mrmc* (2015) 15(14):1132–3. doi:10.2174/1389557515141510061546 16
2. Schmidt AM. Highlighting Diabetes Mellitus. *Atvb* (2018) 38(1):e1–e8. doi:10.1161/atvbaha.117.310221
3. Boulton AJM, Armstrong DG, Albert SF, Frykberg RG, Hellman R, Kirkman MS, et al. Comprehensive Foot Examination and Risk Assessment. *Diabetes care* (2008) 31(8):1679–85. doi:10.2337/dc08-9021
4. Beckert S, Witte MB, Konigsrainer A, Coerper S. The Impact of the Micro-lightguide O2C for the Quantification of Tissue Ischemia in Diabetic Foot Ulcers. *Diabetes care* (2004) 27(12):2863–7. doi:10.2337/diacare.27.12.2863
5. Cina C, Katsamouris A, Megerman J, Brewster DC, Strayhorn EC, Robison JG, et al. Utility of Transcutaneous Oxygen Tension Measurements in Peripheral Arterial Occlusive Disease. *J Vasc Surg* (1984) 01(2):362–71. doi:10.1016/0741-5214(84)90069-7
6. Zonios G, Perelman LT, Backman V, Manoharan R, Fitzmaurice M, Van Dam J, et al. Diffuse Reflectance Spectroscopy of Human Adenomatous colon Polyps *In Vivo*. *Appl Opt* (1999) 38(31):6628–37. doi:10.1364/ao.38.006628
7. Mirabal YN, Chang SK, Atkinson EN, Malpica A, Follen M, Richards-Kortum R. Reflectance Spectroscopy for *In Vivo* Detection of Cervical Precancer. *J Biomed Opt* (2002) 7(4):587–94. doi:10.1117/1.1502675
8. Utzinger U, Brewer M, Silva E, Gershenson D, Blast RC, Follen M, et al. Reflectance Spectroscopy for *In Vivo* Characterization of Ovarian Tissue. *Lasers Surg Med* (2001) 28(1):56–66. doi:10.1002/1096-9101(2001)28:1<56::aid-lsm1017>3.0.co;2-l
9. Volynskaya Z, Haka AS, Bechtel KL, Fitzmaurice M, Shenk R, Wang N, et al. Diagnosing Breast Cancer Using Diffuse Reflectance Spectroscopy and Intrinsic Fluorescence Spectroscopy. *J Biomed Opt* (2008) 13(2):024012. doi:10.1117/1.2909672
10. Keller A, Bialecki P, Wilhelm TJ, Vetter MK. Diffuse Reflectance Spectroscopy of Human Liver Tumor Specimens - towards a Tissue Differentiating Optical Biopsy Needle Using Light Emitting Diodes. *Biomed Opt Express* (2018) 9(3):1069–81. doi:10.1364/boe.9.001069
11. Evers DJ, Nachabé R, Klomp HM, van Sandick JW, Wouters MW, Lucassen GW, et al. Diffuse Reflectance Spectroscopy: a New Guidance Tool for Improvement of Biopsy Procedures in Lung Malignancies. *Clin Lung Cancer* (2012) 13(6):424–31. doi:10.1016/j.cllc.2012.02.001
12. Borisova E, Troyanova P, Pavlova P, Avramov L. Diagnostics of Pigmented Skin Tumors Based on Laser-Induced Autofluorescence and Diffuse Reflectance Spectroscopy. *Quan Electron.* (2008) 38(6):597–605. doi:10.1070/qe2008v038n06abeh013891
13. Kumar A, Chellappan K, Nasution A, Kanawade RV. Diffuse Reflectance Spectroscopy Based Blood Oxygenation Monitoring: a Prospective Study for Early Diagnosis of Diabetic Foot. *Proc SPIE* (2021) 11651:116510T. doi:10.1117/12.2583022
14. Anand S, Sujatha N, Narayanamurthy VB, Seshadri V, Poddar R. Diffuse Reflectance Spectroscopy for Monitoring Diabetic Foot Ulcer - A Pilot Study. *Opt Lasers Eng* (2014) 53:1–5. doi:10.1016/j.optlaseng.2013.07.020
15. Hile C, Veves A. Diabetic Neuropathy and Microcirculation. *Curr Diab Rep* (2003) 3(6):446–51. doi:10.1007/s11892-003-0006-0
16. Greenman RL, Panasyuk S, Wang X, Lyons TE, Dinh T, Longoria L, et al. Early Changes in the Skin Microcirculation and Muscle Metabolism of the Diabetic Foot. *The Lancet* (2005) 366(9498):1711–7. doi:10.1016/s0140-6736(05)67696-9
17. Doronin A, Meglinski I. Online Object Oriented Monte Carlo Computational Tool for the Needs of Biomedical Optics. *Biomed Opt Express* (2011) 2(9):2461–9. doi:10.1364/BOE.2.002461
18. Maeda T, Arakawa N, Takahashi M, Aizu Y. Monte Carlo Simulation of Spectral Reflectance Using a Multilayered Skin Tissue Model. *Opt Rev* (2010) 17(3):223–9. doi:10.1007/s10043-010-0040-5
19. Jacques SL. *Skin Optics Summary*. Portland: Oregon Medical Laser Center News (1998).
20. Prahl S. *Optical Absorption of Hemoglobin*. Portland: Oregon Medical Laser Center News (2021). Available at: http://omlc.ogi.edu/spectra/hemoglobin/ (Accessed on: January, 2021).
21. Jacques SL, McAuliffe DJ. The Melanosome: Threshold Temperature for Explosive Vaporization and Internal Absorption Coefficient during Pulsed Laser Irradiation. *Photochem Photobiol* (1991) 53(6):769–75. doi:10.1111/j.1751-1097.1991.tb09891.x
22. Van Gemert MJC, Jacques SL, Sterenborg HJCM, Star WM. Skin Optics. *IEEE Trans Biomed Eng* (1989) 36(12):1146–54. doi:10.1109/10.42108
23. Meglinski IV, Matcher SJ. Computer Simulation of the Skin Reflectance Spectra. *Comp Methods Programs Biomed* (2003) 70(2):179–86. doi:10.1016/s0169-2607(02)00099-8
24. Das K, Yuasa T, Maeda T, Nishidate I, Funamizu H, Aizu Y. Simple Detection of Absorption Change in Skin Tissue Using Simulated Spectral Reflectance Database. *Measurement* (2021) 182:109684. doi:10.1016/j.measurement.2021.109684
25. Reif R, Amorosino MS, Calabro KW, A'Amar O, Singh SK, Bigio IJ. Analysis of Changes in Reflectance Measurements on Biological Tissues Subjected to Different Probe Pressures. *J Biomed Opt* (2008) 13(1):010502. doi:10.1117/1.2870115
26. Cooksey CC, Allen DW. Reflectance Measurements of Human Skin from the Ultraviolet to the Shortwave Infrared (250 Nm to 2500 Nm). *SPIE ProceedingsActive and Passive Signatures IV* (2013) 8734:152–60. doi:10.1117/12.2015821
27. Chan EK, Sorg B, Protsenko D, O'Neil M, Motamedi M, Welch AJ. Effects of Compression on Soft Tissue Optical Properties. *IEEE J Select Top Quan Electron.* (1996) 2(4):943–50. doi:10.1109/2944.577320

Conflict of Interest: The authors declare that the research was conducted in the absence of any commercial or financial relationships that could be construed as a potential conflict of interest.

Publisher's Note: All claims expressed in this article are solely those of the authors and do not necessarily represent those of their affiliated organizations, or those of the publisher, the editors and the reviewers. Any product that may be evaluated in this article, or claim that may be made by its manufacturer, is not guaranteed or endorsed by the publisher.

frontiers | Frontiers in Physics

BRIEF RESEARCH REPORT
published: 27 April 2022
doi: 10.3389/fphy.2022.876222

High Stability Industrial-Grade Nd: YVO_4 Picosecond Laser Amplifier With High Average Output Power

Zhenao Bai[1,2]*, *Yakai Zhang*[2], *Weiran Lin*[1], *Xiaochao Yan*[1] and *Zhongwei Fan*[1]*

[1]Aerospace Information Research Institute, Chinese Academy of Sciences, Beijing, China, [2]Center for Advanced Laser Technology, Hebei University of Technology, Tianjin, China

We demonstrate a high-power Nd: YVO_4 picosecond laser amplifier that is capable of generating 51.5 W of average output power at a wavelength of 1,064 nm, with a repetition rate of 70 MHz and a pulse duration of 8.5 ps. This system encompasses three stages of laser diode end-pumped Nd: YVO_4 amplification including two double-pass amplifiers and a single-pass amplifier. Laser output with near-diffraction-limited beam quality (M^2 < 1.1) was maintained throughout the entire power scaling range of the laser. The system exhibited very high output power stability with a root-mean-square amplitude fluctuation of less than 0.2% over a period of 15 h of continuous operation.

Keywords: high-power, high repetition rate, picosecond, laser amplifier, Nd:YVO_4

OPEN ACCESS

Edited by:
Yufei Ma,
Harbin Institute of Technology, China

Reviewed by:
Haiyong Zhu,
Wenzhou University, China
Chaitanya Kumar Suddapalli,
The Institute of Photonic Sciences (ICFO), Spain

***Correspondence:**
Zhenao Bai
baizhenao@hotmail.com
Zhongwei Fan
fanzhongwei@aoe.ac.cn

Specialty section:
This article was submitted to Optics and Photonics, a section of the journal Frontiers in Physics

Received: *15 February 2022*
Accepted: *01 April 2022*
Published: *27 April 2022*

Citation:
Bai Z, Zhang Y, Lin W, Yan X and Fan Z (2022) High Stability Industrial-Grade Nd: YVO_4 Picosecond Laser Amplifier With High Average Output Power. Front. Phys. 10:876222. doi: 10.3389/fphy.2022.876222

INTRODUCTION

Lasers characterized by different duration of emission have shown different advantages in respective fields [1–5]. Short pulse lasers with high output power and high repetition rates have found significant application in fields such as nonlinear optical frequency conversion [6–8], precision materials processing [9–11], satellite ranging [12, 13], gas detection [14], and optoelectronic countermeasures [15]. The ultrashort pulse duration [typically in the range of picoseconds (ps)] of these lasers is shorter than the electron-lattice relaxation time of many materials [16, 17], allowing a significant reduction in heat transfer between the laser pulse and the material, during the interaction between the laser photons and the material molecules. As such, laser pulses in the ps-range are often used in applications such as precision laser machining, biomedicine, and laser cleaning (particularly of precious and historical artifacts). While femtosecond lasers offer even shorter pulse durations, it is typically easier to design and construct lasers which output ps-pulses with high pulse energy and high power output. As such, picosecond lasers are a powerful tool in the study of the interaction between light and matter [18].

One of the most commonly used methods to generate ps-pulse duration laser outputs is mode-locking. Mode-locking is capable of producing laser pulses down to ~10 ps, however, this is typically accompanied by extremely low pulse energy (~nJ) and low average power (~mW). This therefore limits the range of applications of these laser sources. To address this shortcoming, laser amplifiers are often applied to increase the power scaling capabilities of these systems. These amplifiers are mainly divided into two categories: regenerative amplifiers and traveling-wave amplifiers. Regenerative amplifiers have the advantages of high gain, high stability, and low seed laser power requirements, and the amplification of a pulsed laser can be regulated by the pressurization time of the electro-optical crystal. However, due to its resonant cavity design, the amplification of spontaneous radiation can occur which reduces the pulse contrast. Furthermore, the electro-optical crystal needs to be driven using a high-frequency and high voltage signal which

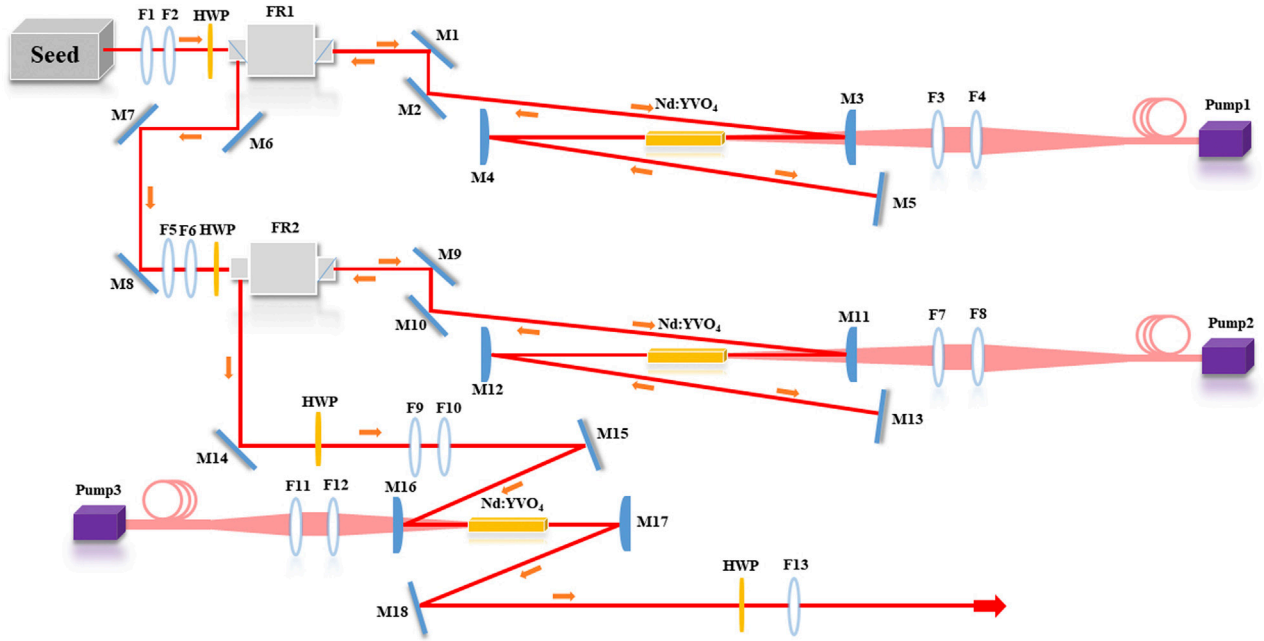

FIGURE 1 | Schematic showing the layout of the high-power, high-repetition rate picosecond laser amplifier system. HWP, half-wave plate; FR, Faraday rotator; M, mirrors; F, focus lens.

matches the seed laser frequency. Also, for high repetition rates (in the MHz-range), a frequency selection module also needs to be added [19] and this greatly increases the complexity of the overall system. Other deleterious effects which may occur during amplification include multiplicative period bifurcation effects and gain narrowing [20, 21]. In comparison, traveling wave amplifiers are more compact, comprising fewer optical components which also introduce fewer optical losses. Although the regenerative amplifier can achieve an amplification factor of over 10^6 times, high-power picosecond lasers based on the traveling-wave amplification process offers the advantages of higher stability and robustness, and is therefore more suitable for industrial applications. At present, Nd:YAG, Nd:YLF and Nd:YVO_4 are commonly used gain media for 1 μm picos amplifiers. Among them, Nd:YVO_4 has a large emission cross-section, which facilitates the gain of the system and thus achieves high optical conversion efficiency during the amplification.

In recent years, there have been numerous reports on picosecond amplifiers using traveling-wave configurations. In 2018, Cheng et. al. [22] demonstrated ps-pulsed output with an average power of 11.34 W using single-pass amplification of a self-developed picosecond seed source with a repetition rate of 3.2 GHz and an average power of 1.38 W. In 2019, Liu et. al. [23] demonstrated laser output with a maximum power of 16.19 W and an optical-optical conversion efficiency of 51.07% by double-pass amplifying a single pulse from a ps-pulsed seed laser. The seed laser had a repetition rate of 500 kHz and pulse energy of 7.68 μJ. Compared with regenerative amplification techniques, which are limited by the need for high-frequency voltage drivers, traveling-wave amplification techniques can directly amplify lasers with repetition rates from the kHz to GHz range. In 2020, Dong et. al. [24] demonstrated a two-stage amplification system to amplify the output from a seed laser with a pulse width of 10.2 ps and a repetition rate of 18.9 MHz. One of the most appealing advantages of the traveling wave amplification technique is that it can be used in a multi-pass and/or cascaded manner in order to make up for its shortcomings of low single-pass and double-pass amplification.

In this brief report, we demonstrate a stable picosecond laser amplifier that utilizes three fiber-coupled LD directly pumped Nd:YVO_4 amplifier stages. Key to the efficient operation of this multi-stage amplification setup is the precise matching of the spatial modes of the pump laser and seed laser spatial profiles, and this is achieved by using a lens set for pump and seed light shaping, resulting in high pumping efficiency and high beam quality output. We observe that thermally-induced effects have little impact on the output laser beam quality, and thus high beam quality is maintained with efficient amplification. We use this design to amplify a seed laser which has an average power of 320 mW, a pulse duration of 8.2 ps and a repetition rate of 70 MHz to an output with an average power of 51.5 W, and a pulse duration of 8.5 ps.

EXPERIMENT AND RESULTS

The setup of the experimental laser system is shown in **Figure 1**. It consists of a laser oscillator, two double-pass amplifiers and a single-pass amplifier. The seed laser (FPS200-MO-70MHZ; EKSPLA, Lithuania) had an output wavelength of 1,064 nm, a

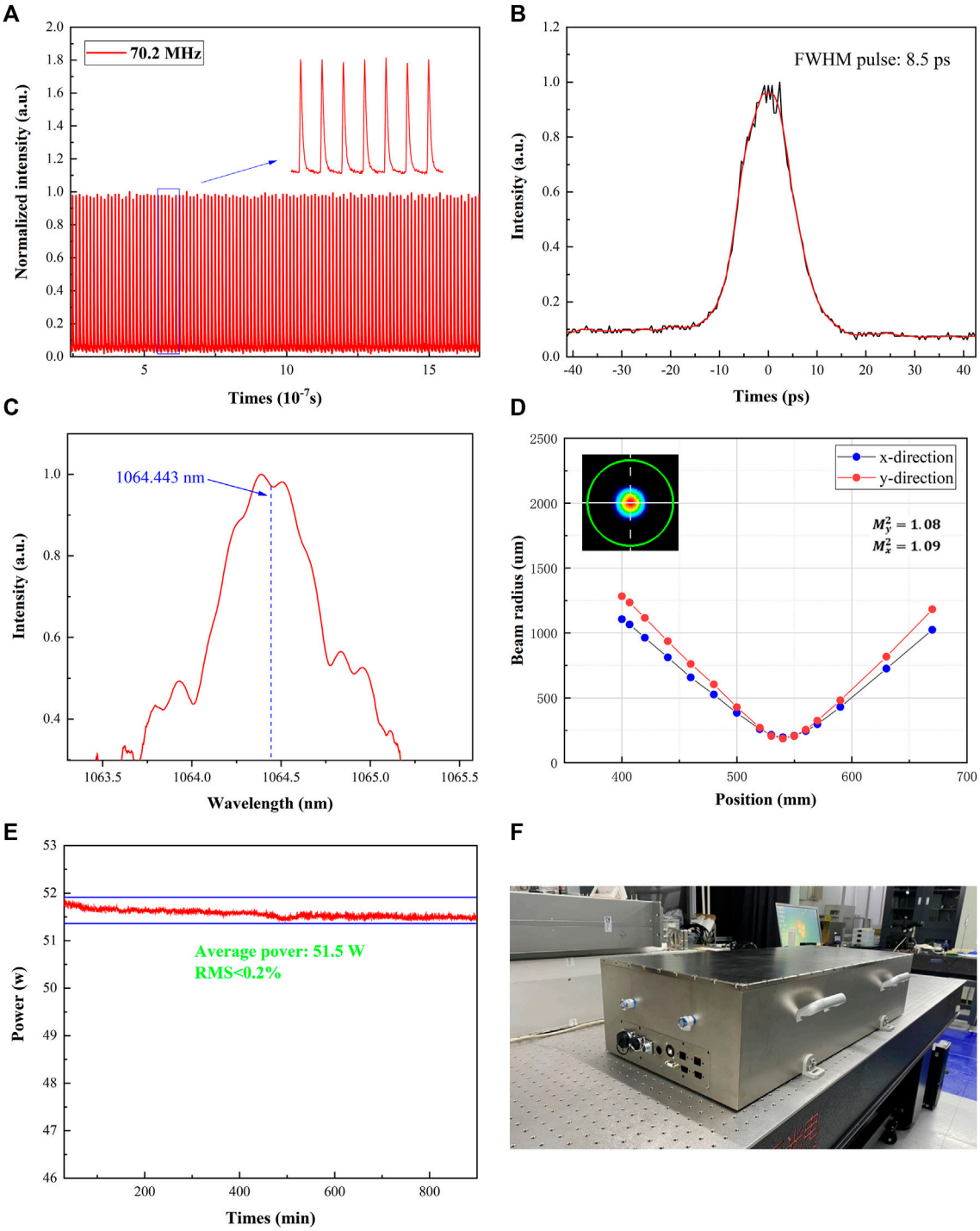

FIGURE 2 | Compilation of output characteristics of the amplified ps-pulse duration laser beam. **(A)** Normalized pulse characteristics of the output with a close-up shown inset; **(B)** temporal characteristic of a single output pulse with an autocorrelation trace; **(C)** normalized wavelength spectrum of the amplified laser output; **(D)** plot of the focusing characteristics of the output laser beam along with the near-field spatial profile (inset); **(E)** plot tracking the stability of the output power over a period of 15 h; and **(F)** photograph of the packaged picosecond laser amplifier.

repetition rate of 70 MHz, a pulse width of 8.2 ps and an average power of 320 mW. The seed was collimated and focused using lens sets F1 [radius of curvature (ROC) of 15.5 mm] and F2 (ROC = 93 mm), then passes a half-wave plate (HWP) to adjust its polarization angle. It then entered the first double-pass pre-amplification stage through an optical isolator consisting of a

polarizing beam splitter and a Faraday rotator (HPDFSI-06-100-5-H-H-P; EMGO-TECH, ZhuHai, China), which serves to protect the optical components from being damaged by the amplified laser pulse. The first stage amplifier used a 0.7 at. % doped Nd:YVO_4 crystal as the gain medium (with dimensions 4 mm × 4 mm × 30 mm). The crystal is wrapped by indium foil and then dissipated through a copper heat sink with cooling water temperature of 25°C. The crystal was end-pumped with a fiber-coupled LD pump source (NLIGHT; United States) with a central wavelength of 808 nm and a spectral width of 1.5 nm. The pump laser was collimated and focused by passing through a plano-convex lens set to achieve mode matching of the pump laser to that of the laser beam under amplification, thus maximizing the amplification efficiency. M3 and M4 are two 1,064 nm high-reflection (HR) convex mirrors with R = 1,500 mm. M3 also has anti-reflective (AR) coating at 808 nm wavelength. The seed laser was reflected from the polarizing beam splitter of the optical isolator after passing through the gain medium twice, at which point the laser was S-polarized. The S-polarized laser was then re-shaped and passed through the HWP, changing the polarization state of the laser to P-polarized. The P-polarized laser beam then passed through the optical isolator of the second stage amplifier and entered the second double-pass amplification stage. The structure of the second amplifier stage was the same as that of the first stage. The pre-amplified laser was amplified twice again in the second stage before being reflected by the polarizing beam splitter of the second optical isolator into the final (third-stage) single-pass amplifier. This single-pass amplification stage also used a 4 mm × 4 mm × 30 mm Nd:YVO_4 crystal as the gain medium and was also end-pumped with a fiber-coupled LD pump source with a central wavelength of 808 nm. After the third single-pass amplification stage, the laser was collimated by a convex lens and then output.

In our experiments, the injection pump and amplified beam in each stage were shaped through the lens to achieve optimum mode matching. The spot diameter of the output seed is 1.2 mm. After shaping by the lens set at each stage, the spot diameter at the center of the crystal is set to be 1.3 mm, then is adjusted to be 1.4 mm at one-third of the crystal. In each amplification stage of the system, the Nd:YVO_4 crystal was pumped with an incident diode pump power of 110 W. We also observed that the gain crystal absorbs ~83% of the pump laser field. In the first amplifier stage, the power of the seed laser was amplified to ~2.1 W in a single pass and then to ~10 W in a double pass through the gain medium. We attribute the relatively low photo-optical conversion efficiency to the low power of the seed laser. Following amplification in the second stage double-pass amplifier, the optical power increased to ~35 W. After amplification in the third stage, single-pass amplifier, the average output power rose to 51.5 W. The photo-optical conversion efficiency was ~30.9%.

Shown in **Figures 2A,B**, the pulse characteristics of the amplified output. A photodiode (PulseCheck SM1600; Ape, Germany) was used to measure the pulse train. It can be seen that the frequency of the laser output after final amplification was 70.2 MHz, and the pulse width (as measured using a autocorrelator and normalized) was slightly broadened to 8.5 ps. We attribute the slight broadening of the output to the effects of dispersion and gain narrowing which occurs during the amplification process. The wavelength spectrum of the amplified output (as measured using a spectrometer and normalized) is shown in **Figure 2C**; the central wavelength was 1,064.4 nm, and the measured linewidth was 0.22 nm. **Figure 2D** shows the focusing characteristics of the output beam and the inset shows the near-field spatial profile of the output. The output beam had a radius of 1.2 mm and a beam pointing stability of 2.8 μrad. The beam quality factor (M^2) of the output was measured to be 1.08 and 1.09 along the x and y axis directions, respectively. The experimental results indicate that thermally-induced effects do not appear to manifest in these amplifiers, both in the case of single-pass and double-pass amplification. **Figure 2E** shows a plot of the power stability of the laser output as measured over a period of 15 h (with the system at room temperature). This plot shows that the system had excellent output stability with a root-mean-square (RMS) power fluctuation of less than 0.2%. The polarization ratio of the output beam was measured to be 220:1. These results serve to demonstrate that through the application of a three-stage amplification setup, high average power, high repetition rate picosecond-pulse laser output with very high stability can be achieved.

CONCLUSION

In this study, a cascaded, picosecond laser amplifier utilizing both double-pass and single-pass configurations was constructed and characterized. This amplifier design was used to amplify a beam produced by a mode-locked laser which had an average power of 320 mW, a pulse duration of 8.2 ps and a repetition rate of 70 MHz. The resultant amplified output had an average power of 51.5 W, a pulse duration of 8.5 ps, a spectral width of 0.22 nm, and a repetition rate of 70.2 MHz. Notably the amplifier design ensured that the beam quality of the output was maintained (with a measured M^2 value of 1.08 being recorded) and the output power was very stable, exhibiting the RMS fluctuation of less than 0.2%.

We believe that the results demonstrated in this work are of great significance for the future realization of practical and industrially-applied, high power, high repetition rate, high beam quality and stable picosecond pulsed laser sources. Furthermore, the moderate single pulse energy (~μJ) of this system also makes it an ideal source for applications in nonlinear optics, such as second-order nonlinear frequency conversion [25, 26], and high-power crystalline-based wavelength convertors using the stimulated Raman/Brillouin scattering process [27–31].

DATA AVAILABILITY STATEMENT

The raw data supporting the conclusions of this article will be made available by the authors, without undue reservation.

AUTHOR CONTRIBUTIONS

All authors listed have made a substantial, direct, and intellectual contribution to the work and approved it for publication.

FUNDING

This work was supported by the Guangdong Key Research & Development Program (2018B090904003).

REFERENCES

1. Zervas MN, Codemard CA. High Power Fiber Lasers: a Review. *IEEE J Select Top Quan Electron.* (2014) 20(5):219–41. doi:10.1109/jstqe.2014.2321279
2. Li S, Wang Q, Song R, Hou F, Gao M, Gao C. Laser Diode Pumped High-Energy Single-Frequency Er:YAG Laser with Hundreds of Nanoseconds Pulse Duration. *Chin Opt Lett* (2020) 18(3):031401. doi:10.3788/col202018.031401
3. Song J, Wang Z, Wang X, Lü R, Teng H, Zhu J, et al. Generation of 601 fs Pulse from an 8 kHz Nd:YVO_4 Picosecond Laser by Multi-Pass-Cell Spectral Broadening. *Chin Opt Lett* (2021) 19(9):093201. doi:10.3788/col202119.093201
4. Ma Y, Hu Y, Qiao S, Lang Z, Liu X, He Y, et al. Quartz Tuning forks Resonance Frequency Matching for Laser Spectroscopy Sensing. *Photoacoustics* (2022) 25:100329. doi:10.1016/j.pacs.2022.100329
5. Lang Z, Qiao S, Ma Y. Acoustic Microresonator Based In-Plane Quartz-Enhanced Photoacoustic Spectroscopy Sensor with a Line Interaction Mode. *Opt Lett* (2022) 47(6):1295–8. doi:10.1364/ol.452085
6. Li K, Zhang L, Xu D, Zhang G, Yu H, Wang Y, et al. High-power Picosecond 355 nm Laser Based on $La_2CaB_{10}O_{19}$ Crystal. *Opt Lett* (2014) 39(11):3305–7. doi:10.1364/ol.39.003305
7. Bai Z, Yuan H, Liu Z, Xu P, Gao Q, Williams RJ, et al. Stimulated Brillouin Scattering Materials, Experimental Design and Applications: A Review. *Opt Mater* (2018) 75:626–45. doi:10.1016/j.optmat.2017.10.035
8. Chen L, Bai Z, Pan Y, Chen M, Li G. Two-millijoule, 1-kHz, 355-nm Picosecond Laser Pulse Generation in LiB_3O_5 crystal. *Opt Eng* (2013) 52(8):086107. doi:10.1117/1.oe.52.8.086107
9. Shen D, Qian J, Wang C, Wang G, Wang X, Zhao Q. Facile Preparation of Silver Nanoparticles in Bulk Silicate Glass by High-Repetition-Rate Picosecond Laser Pulses. *Chin Opt Lett* (2021) 19(1):011901. doi:10.3788/col202119.011901
10. Du K, Brüning S, Gillner A. High-power Picosecond Laser with 400W Average Power for Large Scale Applications. In: Laser-Based Micro-and Nanopackaging and Assembly VI, Proceedings SPIE 8244, San Francisco, California, United States, 21-26 January 2012. (2012). p. 82440. doi:10.1117/12.915676
11. Weber R, Graf T, Freitag C, Feuer A, Kononenko T, Konov VI. Processing Constraints Resulting from Heat Accumulation during Pulsed and Repetitive Laser Materials Processing. *Opt Express* (2017) 25:3966–79. doi:10.1364/oe.25.003966
12. Zhang H, Long M, Deng H, Cheng S, Wu Z, Zhang Z, et al. Developments of Space Debris Laser Ranging Technology Including the Applications of Picosecond Lasers. *Appl Sci* (2021) 11(21):10080. doi:10.3390/app112110080
13. Bai Z, Chen H, Gao X, Li S, Qi Y, Bai Z. Highly Compact Nanosecond Laser for Space Debris Tracking. *Opt Mater* (2019) 98:109470. doi:10.1016/j.optmat.2019.109470
14. Leffler T, Brackmann C, Ehn A, Kaldvee B, Aldén M, Berg M, et al. Range-resolved Detection of Potassium Chloride Using Picosecond Differential Absorption Light Detection and Ranging. *Appl Opt* (2015) 54:1058–64. doi:10.1364/ao.54.001058
15. Kalisky O, Kalisky O. The Status of High-Power Lasers and Their Applications in the Battlefield. *Opt Eng* (2010) 49(9):091003. doi:10.1117/1.3484954
16. Bai Z, Bai Z, Sun X, Liang Y, Wang K, Jin D, et al. A 33.2 W High Beam Quality Chirped-Pulse Amplification-Based Femtosecond Laser for Industrial Processing. *Materials* (2020) 13(12):2841. doi:10.3390/ma13122841
17. Je G, Malka D, Kim H, Hong S, Shin B. A Study on Micro Hydroforming Using Shock Wave of 355 nm UV-Pulsed Laser. *Appl Surf Sci* (2017) 417:244–9. doi:10.1016/j.apsusc.2017.02.146
18. Sugioka K, Cheng Y. Ultrafast Lasers-Reliable Tools for Advanced Materials Processing. *Light Sci Appl* (2014) 3(4):e149. doi:10.1038/lsa.2014.30
19. Bai Z, Bai Z, Kang Z, Lian F, Lin W, Fan Z. Non-Pulse-Leakage 100-kHz Level, High Beam Quality Industrial Grade Nd:YVO_4 Picosecond Amplifier. *Appl Sci* (2017) 7(6):615. doi:10.3390/app7060615
20. Wu Y, Yani G, Yilin H, Qingnan X, Quan Z, Weixin M, et al. Progress in High Energy All-Solid-State Regenerative Amplifier. *High Power Laser Part Beams* (2020) 32(11):76–86. doi:10.11884/HPLPB202032.200089
21. Bai C, Tian W, Wang G, Zhen L, Xu R, Zhang D, et al. Progress on Yb-Doped All-Solid-State Femtosecond Laser Amplifier with High Repetition Rate. *Chin J Lasers* (2021) 05:82–97. doi:10.3788/cjl202148.0501005
22. Cheng M, Wang Z, Cao Y, Meng X, Zhu J, Wang J, et al. High Power Diode-Pumped Passively Mode-Locked Nd:YVO_4 Laser at Repetition Rate of 3.2 GHz. *Chin Phys. B* (2019) 28(5):054205. doi:10.1088/1674-1056/28/5/054205
23. Liu X, He H, Song Y, Wang C, Wang Z. 500-kHz Level High Energy Double-Pass Nd:YVO_4 Picosecond Amplifier with Optic–Optic Efficiency of 51%. *Appl Sci* (2019) 9(2):219. doi:10.3390/app9020219
24. Dong X, Li P, Li S, Wang D. High Gain Fiber-Solid Hybrid Double-Passing End-Pumped Nd: YVO_4 Picosecond Amplifier with High Beam Quality. *Chin Phys B* (2020) 29:054207. doi:10.1088/1674-1056/ab8218
25. Chen H, Bai Z, Wang J, Zhang B, Bai Z Hundred-watt green Picosecond Laser Based on LBO Frequency-Doubled Photonic crystal Fiber Amplifier. *Infrared Laser Eng* (2021) 50(11):20200522. doi:10.3788/IRLA20200522
26. Chu Y, Zhang X, Chen B, Wang J, Yang J, Jiang R, et al. Picosecond High-Power 213-nm Deep-Ultraviolet Laser Generation Using β-BaB_2O_4 crystal. *Opt Laser Techn* (2021) 134:106657. doi:10.1016/j.optlastec.2020.106657
27. Duan Y, Sun Y, Zhu H, Mao T, Zhang L, Chen X. YVO_4 Cascaded Raman Laser for Five-Visible-Wavelength Switchable Emission. *Opt Lett* (2020) 45(9):2564–7. doi:10.1364/ol.392566
28. Duan Y, Zhou Y, Zhu H, Li Z, Jin X, Tang D. Selective Frequency Mixing in a Cascaded Self-Raman Laser with a Critical Phase-Matched LBO crystal. *J Lumin* (2022) 244:118698. doi:10.1016/j.jlumin.2021.118698
29. Warrier AM, Lin J, Pask HM, Mildren RP, Coutts DW, Spence DJ. Highly Efficient Picosecond diamond Raman Laser at 1240 and 1485 nm. *Opt Express* (2014) 22(3):3325–33. doi:10.1364/oe.22.003325
30. Bai Z, Zhang Z, Wang K, Gao J, Zhang Z, Yang X, et al. Comprehensive thermal Analysis of diamond in a High-Power Raman Cavity Based on FVM-FEM Coupled Method. *Nanomaterials* (2021) 11(6):1572. doi:10.3390/nano11061572
31. Bai Z, Williams RJ, Kitzler O, Sarang S, Spence DJ, Wang Y, et al. Diamond Brillouin Laser in the Visible. *APL Photon* (2020) 5(3):031301. doi:10.1063/1.5134907

Conflict of Interest: The authors declare that the research was conducted in the absence of any commercial or financial relationships that could be construed as a potential conflict of interest.

Publisher's Note: All claims expressed in this article are solely those of the authors and do not necessarily represent those of their affiliated organizations, or those of the publisher, the editors and the reviewers. Any product that may be evaluated in this article, or claim that may be made by its manufacturer, is not guaranteed or endorsed by the publisher.

frontiers | Frontiers in Physics

ORIGINAL RESEARCH
published: 02 May 2022
doi: 10.3389/fphy.2022.894925

Electric Field Enhancement Effect of Aluminum Grating With Nanosecond Pulsed Laser Irradiation

Jiamin Wang[1,2], Kuo Zhang[1], Jinghua Yu[1,2], Yin Zhang[1,2], Yanhui Ji[1,2], Jirigalantu[3], Wei Zhang[3], Wenhao Li[3], Changbin Zheng[1] and Fei Chen[1]**

[1]State Key Laboratory of Laser Interaction with Matter, Changchun Institute of Optics, Fine Mechanics and Physics, Chinese Academy of Sciences, Changchun, China, [2]University of Chinese Academy of Sciences, Beijing, China, [3]National Engineering Research Center for Diffraction Gratings Manufacturing and Application, Changchun, China

Aluminum grating has wide applications in laser systems and photoelectric equipment. Research on the laser damage characteristics of aluminum grating has guiding significance and application value for improving the laser damage resistance. The aim of this study is to investigate the characteristics of damage induced by nanosecond pulsed lasers on the aluminum grating. To better understand the laser damage characteristics of aluminum grating, herein, Maxwell's equations were numerically solved according to the finite difference time-domain method, and the electric field model of 1,064 nm Gaussian laser damage aluminum grating was established. The simulation results showed that the light field is modulated by the grating; furthermore, the maximum value of the electric field occurred at the ridge of the grating when the laser is irradiated vertically. Analysis suggested that the electric field distribution is in accordance with the laser energy distribution, and the distribution region of the maximum electric field is a vulnerable location. To further verify the local electric field enhancement effect, based on the 1-on-1 laser damage measurement method, an experimental study of the nanosecond laser (@1,064 nm, 6.5 ns) damage to the aluminum grating was carried out. Moreover, the damage morphology was analyzed using a scanning electron microscope (SEM), and the simulation results showed good agreement with the experimental results.

Keywords: nanosecond pulsed laser, aluminum grating, electric field enhancement effect, damage characteristics, damage morphology

OPEN ACCESS

Edited by:
Yufei Ma,
Harbin Institute of Technology, China

Reviewed by:
Cheng Wang,
ShanghaiTech University, China
Gopala Krishna Podagatlapalli,
Gandhi Institute of Technology and Management (GITAM), India
Chaoyang Wei,
Shanghai Institute of Optics and Fine Mechanics (CAS), China

****Correspondence:***
Changbin Zheng
zhengchangbin@ciomp.ac.cn
Fei Chen
feichenny@126.com

Specialty section:
This article was submitted to Optics and Photonics, a section of the journal Frontiers in Physics

Received: *12 March 2022*
Accepted: *04 April 2022*
Published: *02 May 2022*

Citation:
Wang J, Zhang K, Yu J, Zhang Y, Ji Y, Jirigalantu, Zhang W, Li W, Zheng C and Chen F (2022) Electric Field Enhancement Effect of Aluminum Grating With Nanosecond Pulsed Laser Irradiation. Front. Phys. 10:894925. doi: 10.3389/fphy.2022.894925

1 INTRODUCTION

In recent years, with the development of high-peak intensity laser technology [1–4], the interaction between laser and film materials has become an important topic for scholars [5–10]. On the one hand, the diffraction gratings are an important pulse compression element in the high-peak power laser system [11–13], and its laser-induced damage threshold (LIDT) limits the laser energy output and affects the operational cost of refurbishment or replacement of the optics. On the other hand, the gratings whose general structure is to deposit films on a glass substrate with regular grooves on the surface of the film play a critical role in spectroscopy equipment. In laser systems and photoelectric imaging equipment, to achieve an optimal design of gratings and the practical value for high-power laser systems, it is highly important to study the laser damage characteristic and mechanism of gratings.

For thin film structure materials, the electric field enhancement effect could easily induce frequent damage at some locations, such as the nodule defects [14], impurities, contaminations [15], and the interface between the substrate and the thin film, which will generally expand the damaged area. The influence of these factors will significantly decrease the LIDT of the thin film. Compared to the thin film, the grating is a surface relief structure formed on the surface of the thin film. Ignoring the contamination and defects introduced in the processing, the periodic structure of the grating itself has a modulation effect on the light field; meanwhile, the redistribution of the light field also determines the position where damage is more likely to occur during laser irradiation. Many studies have focused on the multilayer dielectric gratings in the fs [14, 16, 17] or ps regimes [18, 19]. For ultrashort pulsed lasers, initially, the back edges of the grating pillar, which is in correspondence with the electric field intensity maximum, incurred damage [20]. However, there are few reports on the damage characteristics of nanosecond pulsed laser on the aluminum grating. In addition, the incident angle between the laser and the material has an important influence on LIDT, which is closely related to the maximum value of the electric field [21]. Previous studies have shown that when the laser is incident obliquely, the electric field of the grating is stronger at the gate ridge opposite to the incident direction [20, 22], forming a burr structure [23]. In the practical application process, the situation of the normal incidence of the laser must also be considered. It is crucial to explore the influence of the redistribution of the optical field of the grating and the damage characteristics by the electric field induced by the gratings under the condition of the normal incidence of the laser. Furthermore, the characteristics of laser damage induced by electric field enhancement of aluminum film grating need to be further clarified.

In this work, to study the damage characteristics of the aluminum grating irradiated by laser, we used the finite difference time-domain (FDTD) method to solve Maxwell's equation and numerically simulated the electric field distribution of the aluminum grating. To verify the simulation result, the single pulse damage induced by the nanosecond laser (@1,064 nm, 6.5 ns) on the aluminum grating was experimentally studied; the experimental damage morphology was found to be in good agreement with the simulated electric field distribution.

2 SIMULATION METHOD

Nanosecond pulsed laser damage of aluminum grating involves complex damage mechanisms. It is difficult to reveal damage mechanism and characteristics of aluminum grating only through experimental research. A laser is a type of electromagnetic wave; the distribution of the electric field, which determines the energy distribution of the laser to some extent, is modulated by the periodic structure of the grating when the grating is irradiated. Therefore, to deepen the understanding of damage characteristics of an aluminum film by laser @1,064 nm, in this section, we simulated the electric field distribution of 1,064 nm Gaussian laser irradiating the aluminum grating from a microscopic point of view and explored the influence of laser field on the grating damage characteristics.

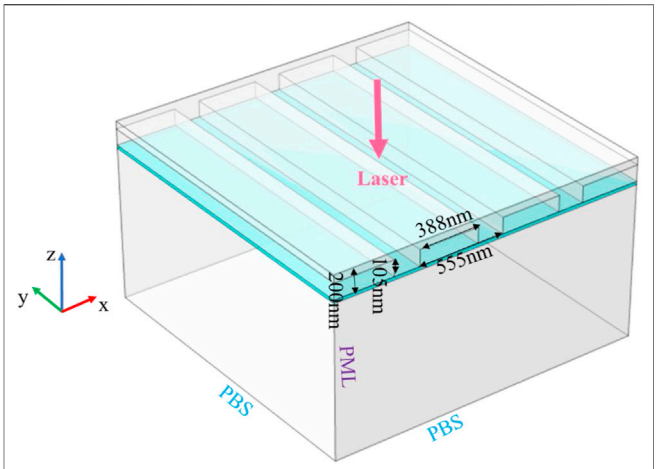

FIGURE 1 | Electric field model of the grating.

2.1 Electric Field Model

Based on the FDTD method, we simulate the electric field of 1,064 nm Gaussian laser-irradiated aluminum film grating. Before we started modeling, we made the following assumptions: 1) the grating is ideal without considering defects, impurities, pollution, etc.; 2) the grating ridge is rectangular; and 3) the Gaussian beam waist radius is set to 300 um, and the grating line density is 1800 gr/mm. Owing to the size difference between the spot diameter and the grating period of the order of 10^3, it is computationally intensive to completely simulate the entire region of laser action. Thus, from a microscopic point of view, we only simulate the electric field distribution of four grating ridges in the laser action center to reveal the influence of grating electric field distribution on laser damage morphology.

The three-dimensional model of the aluminum grating irradiated by 1,064 nm Gaussian laser is established, as shown in **Figure 1**, which only calculated the 3D model of four grids to save computer resources. Based on our actual grating samples (introduced in the third section), the grating period is 555 nm, the duty cycle is 0.7, the remaining layer thickness is 20 nm, and the ridge height is 105 nm. Because the real substrate thickness of gratings is 6 mm, the sum of the heights of the residual layers and ridges is 125 nm. Owing to the difference in thickness, on the one hand, the original scale modeling is inconvenient to show the results. On the other hand, as we focus on damage to the grating structure, the gratings could be considered as functionally damaged, and the use of the original proportional modeling results in wastage of computing resources. Therefore, we only calculate and simulate the electric field distribution of the substrate film interface and grating structure. The (n, k) parameters of air and the aluminum film are (1,0) and (1.3763, 10.245) @1064 nm [24], respectively. The parameters of the K9 glass are taken from the material library of CDGM

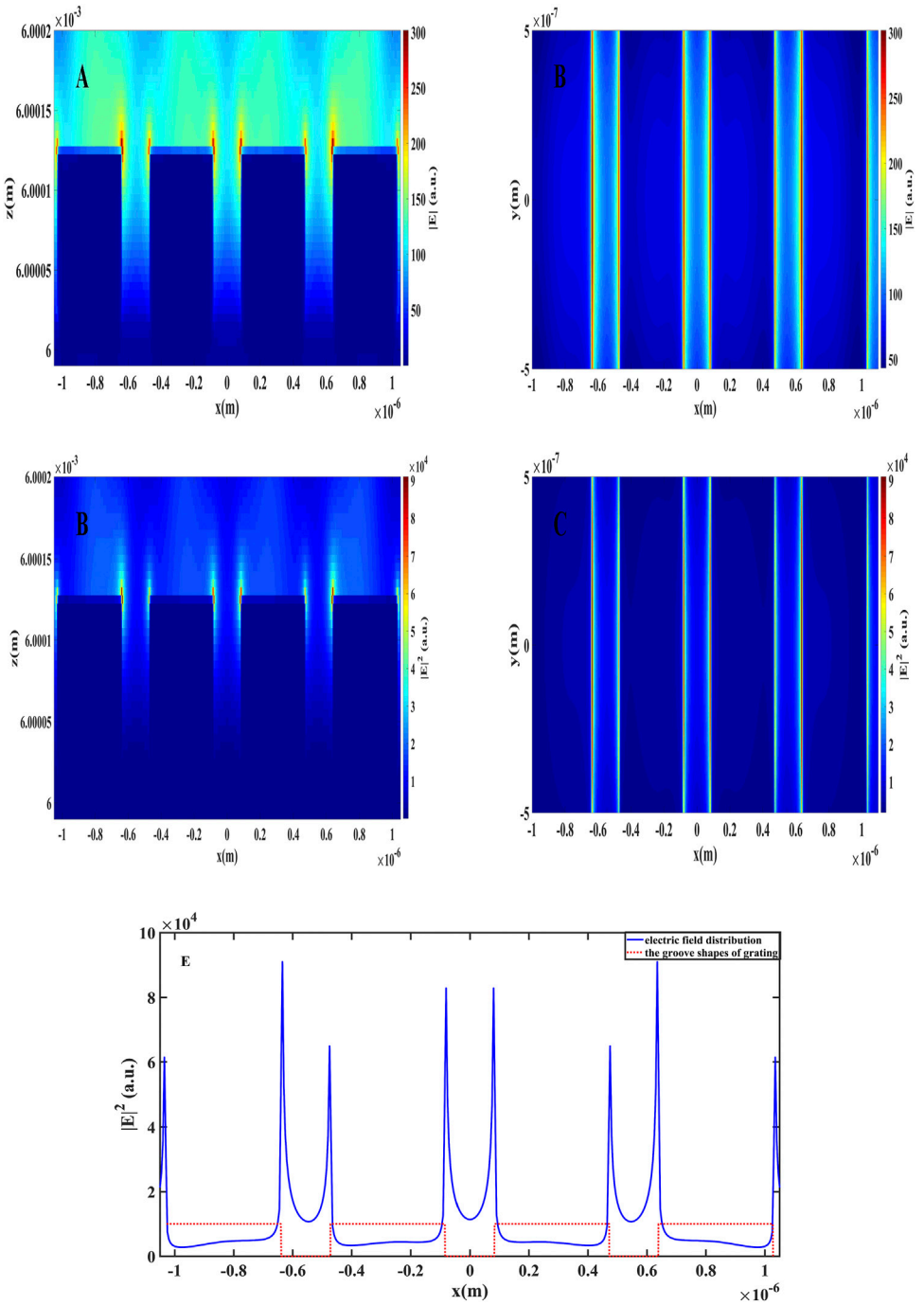

FIGURE 2 | Electric field distribution of aluminum grating: **(A)** electric field of the x-z plane (y = 0); **(B)** electric field of the x-y plane (z = 6000125 nm); **(C)** $|E|^2$ distribution of the x-z plane; **(D)** $|E|^2$ distribution of the x-y plane (z = 6000125 nm); and **(E)** $|E|^2$ distribution in the x direction (y = 0 nm, z = 6000125 nm).

H-K9L. Next, boundary conditions are set as shown in **Figure 1**. The periodic boundary conditions (PBS) are set in the *x* and *y* directions to simulate the periodic structure. The perfect matching layer (PML) is set in the z-direction; the boundary of the perfect matching layer is at least half a wavelength away from the object. At the top of the grating, the laser is incident vertically, and the beam waist radius of the Gaussian beam is 300 μm; the laser action position is (0, 0, 6000125 nm), and the grid element and precision are 2 nm and 8, respectively.

Furthermore, Maxwell's equations are solved numerically based on FDTD, as shown in **Eq. 1**, and vector ***E*** represents the electrical field; μ_r and ε_r are the relative permittivity and the relative permeability, respectively; and k_0 is the wavenumber of free space, and its expression is shown in **Eq. 2**, where ω, ε_0, and

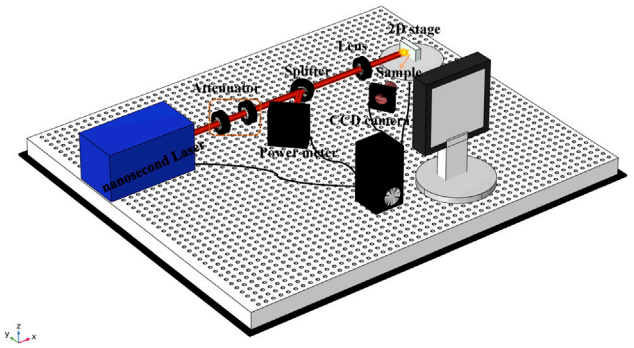

FIGURE 3 | Diagram of the experimental setup of nanosecond laser damage to the gratings.

μ_0 are the angular frequency, permittivity of free space, and permeability of free space, respectively. c_0 is the speed of the wave in free space.

$$\frac{\nabla \boldsymbol{E}}{\mu_r} - k_0^2 \varepsilon_r \boldsymbol{E} = 0, \tag{1}$$

$$k_0 = \frac{\omega}{c_0} = \omega\sqrt{\varepsilon_0 \mu_0}. \tag{2}$$

2.2 Simulation Results

The calculation results are shown in **Figure 2**. **Figures 2A,C** are the x-z sections of |E| and $|E|^2$ along the y = 0 direction, respectively. **Figures 2B,D** are the x-y sections of |E| and $|E|^2$ on the grating surface, respectively. It can be seen from **Figure 2** that the maximum value of the |E| or $|E|^2$ appeared at the ridge angle of the grid ridge. The simulation results of the electric field distribution show that the grating modulates and distributes the light field when the laser is irradiated vertically on the surface of the grating, which results in local electric field enhancement at the ridge corner of the aluminum grating. The position of the maximum electric field represents the position of the maximum light intensity, which implies that damage is most likely to occur at the ridge corner of the grating.

Figure 2E shows the electric field distribution of the four ridges in the center of the top layer of the grating along the x-axis. The solid blue line shown in **Figure 2E** represents the change in the electric field of the ridge along the x-direction, and the red dashed line represents the raster ridge outline. It shows that the curve of $|E|^2$ is axisymmetrically distributed at the center of laser action x = 0, representing the same electric field at the same position from the laser center. With the periodic structure of the grating, the electric field is distributed periodically, and the square of the electric field mode at the edge of the grating ridge is significantly larger than that in the middle region of the grid. This indicates a significant electric field enhancement at the ridge corner that is consistent with the results given in **Figures 2A–D**.

As a Gaussian electromagnetic wave, the electric field distribution in the optical structure of the laser reflects the energy distribution of the laser. The relation between the laser intensity and the electric field amplitude of the incident laser can be expressed as **Eq. 3** [25].

$$I(t) = \frac{1}{2} c n_0 \varepsilon_0 |\boldsymbol{E}(t)|^2, \tag{3}$$

where n_0 is the refractive index of the dielectric at the central frequency of the incident laser and ε_0 is the permittivity of free space.

3 EXPERIMENT

3.1 Experimental Setup

To verify the electric field model and explore the damage characteristics of the aluminum grating with nanosecond pulsed laser irradiation, we carried out an experimental study. The experimental device is shown in **Figure 3**.

The nanosecond pulsed laser system (@1,064 nm, 6.5 ns, 10 Hz, maximum single pulse energy 900 mJ) produced by Beamtech Optronics Co., Ltd. in China was used; this system has an energy stability (RMS) of ≤1%. The emitted laser energy is adjusted by an attenuator consisting of a half-wave plate and a polarizer. The reflected beam split by the beam splitter reaches the energy meter (Ophir, PE50-DIF-C), which is used for the real-time monitoring of energy to the target vertically. The transmitted beam is focused at the center of the target surface through the plane convex lens (f = 100 mm). Using the knife-edge method test, the waist radius of the nanosecond Gaussian beam is found to be 300 μm. The gratings are placed on a three-dimensional displacement platform (1 μm accuracy), and the position of laser action can be precisely controlled by a computer. Damage is monitored by online plasma flash detection and a charge-coupled device (CCD). The dust from the surface of the sample is cleaned before the experiment begins. The experiment was carried out in the air under 10000-level laboratory conditions. Based on the 1-on-1 damage threshold test method, the damage morphology was tested at 10 points under the same energy density. The laser fluence was gradually increased, and the damage morphology was observed using a Nomarski microscope (EB-4, produced by Taiwan Yiye International Co., LTD., with a total magnification of 200X) and SEM (S-4800, produced by HITACHI, Japan, maximum magnification is 20000X). The definition of LIDT is according to LIDT ISO 21254 standards [26]. Damage is defined to be a visible change in the surface morphology under the offline microscope. Here, owing to the uncertainties in laser energy measurement and facula effective area measurement, the relative error of the damage threshold by measurement is assessed closer to 3%.

3.2 Aluminum Grating

The aluminum gratings were designed to have a groove density of 1800 gr/mm and were produced by the National Engineering Research Center for Diffraction Gratings Manufacturing and Application in China. A resin glue of 30 μm thickness was spun onto 40 × 40 × 6 mm^3 K9 glass substrates. A 125-nm-thick aluminum film of 99.9999% purity was used to fabricate the surface relief grating structure using E-beam evaporation. The

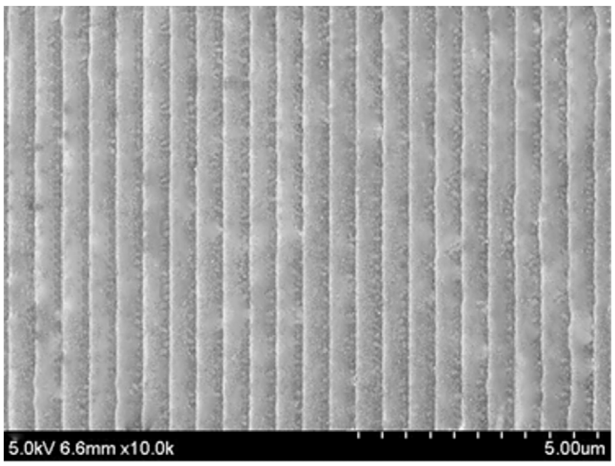

FIGURE 4 | SEM image of aluminum film grating.

photo-resistant material was spun onto the aluminum film, a photo-resistant grating structure was manufactured using a holographic method, and the structures of the photo-resistant gratings were transferred to the aluminum film layer by reactive ion beam etching. Finally, gratings with a diffraction efficiency of 70% were made. It can be seen that the grid lines in **Figure 4** are clear and continuous.

3.3 Experimental Results

To analyze the damage morphology under different laser energy densities, we carried out a parametric scan of the laser energy density based on the experimental research in **Section 3**. With the change in the energy density of the single pulse of the applied laser, the grid incurred different degrees of damage. The damage probability is 100% at 0.67 J/cm^2 and 0% at 0.63 J/cm^2. The continued reduction of the laser resulted in no damage to the energy density.

In this section, to verify the effectiveness of the model and reveal the influence of the electric field enhancement effect on laser damage, the damage morphologies were compared and analyzed based on the experimental research in **Section 3**. To study the grid damage, we focused on the damage morphology of 0.67 J/cm^2, as shown in **Figure 5**.

Figure 5 shows the micro-damage morphology of grating ridges, which was measured experimentally. **Figure 5A** is the overall damage morphology measured at a laser energy density of 0.67/cm^2. **Figures 5B and C** are the SEM images that are magnified 5000X from the central and the edge of the damaged region in **Figure 5A**. **Figure 5D** is magnified 20000X of the marginal damaged area. Comparing **Figures 5B and C**, it can be found that owing to the energy distribution of the Gaussian laser, the degree of damage to the grid in the damaged area is reduced from the center to the edge. **Figure 5D** from right to left indicates the direction away from the laser action position, and it can be found that damage can easily occur at the corner of the ridge. Furthermore, the damage morphology at the gate ridge was observed, and it was found that the main damage mechanism of nanosecond laser damage to the aluminum grating was thermal-induced film peeling and ablation. The electric field distribution determines the energy distribution of the laser in the grating, and it leads to preferential ablation at the corner of the grid ridge.

4 DISCUSSION

In this section, we will compare the experimental and simulation results to verify the local electric field enhancement effect of the

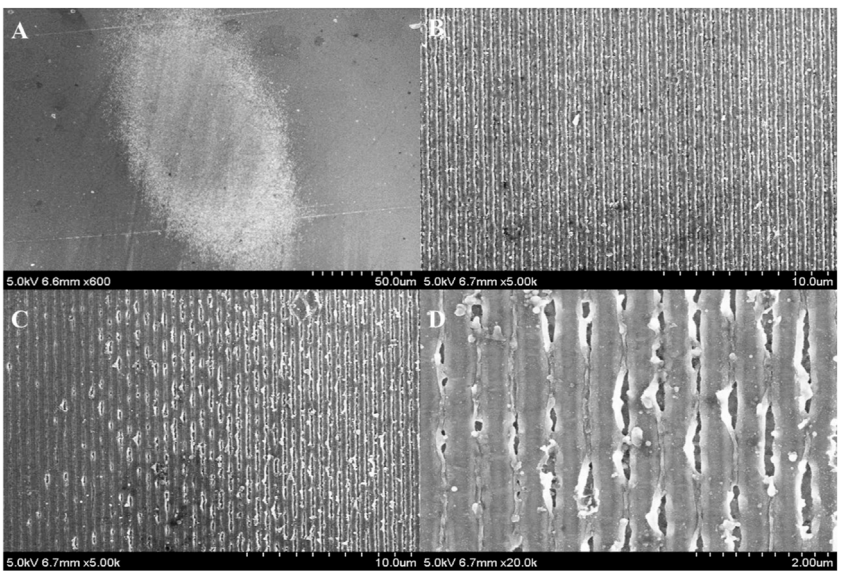

FIGURE 5 | Damage morphology of aluminum grating under a laser energy density of 0.67 J/cm^2.

grating ridge. **Figure 4** shows the grating without laser damage, and it shows that the grating has clear and regular grid lines. Compared with the damaged morphology vertically irradiated by the laser, as shown in **Figure 5D**, it can be found that the grating grid was damaged. The grid damage was more serious in areas closer to the center of the laser spot; the damage location was at the edge of the grid ridge. This morphology is consistent with the conclusion given in **Figure 2** of the electric field simulation results. The main reason for damage is that when the laser irradiates the grating surface vertically, the Gaussian distribution of the laser light field is modulated by the grating structure. Consequently, the electric field is locally enhanced at the ridge angle of the grating, and the distribution of the electric field represents the distribution of laser energy. Therefore, the density of laser energy is high at the ridge angle of the grating. Under the same irradiation conditions, the ridge corner area of the grid ridge preferentially reaches the melting point of the material, which results in the occurrence of ablation and spalling.

To achieve high diffraction efficiency, there is an optimal incidence angle of grating in the process of grating design and research. For the research of grating laser damage, more emphasis has been placed on the oblique incidence of laser; however, the vertical incidence of laser is also important in the process of practical application. Laurent Gallais et al. conducted an electrical simulation on the grating waveguide structure irradiated by laser and found that when the laser is in oblique incidence, it is easy to form a burr structure at the rear edge of the excitation incidence direction owing to the electric field enhancement effect [23]. Lingyun Xie studied the laser oblique incidence rectangular multilayer dielectric grating and clearly verifies that damage initiates at the edge of the grating pillars where the maximum EFI exists [20]. These studies show that the grating ridge area could be easily damaged by the laser, and the maximum value of the electric field corresponds to the position of LIDT, which is similar to the conclusion given in this study. The result of this study is that when the laser is vertically incident, there is the maximum value of the electric field at the ridge angle of the grating ridge, which makes it highly prone to laser damage. Therefore, compared to existing research, the present research work is credible and meets the requirements for practical applications.

5 CONCLUSION

The aim of this study was to explore the characteristics of damage induced by nanosecond pulsed laser on the aluminum grating. First, FDTD was used to numerically solve the electric field distribution of nanosecond laser-irradiated aluminum grating, wherein it was found that the local electric field enhancement effect occurred in corner of the ridges of the grating. Second, to verify the local enhancement effect at the corner of the grating ridge, an experimental study of nanosecond laser (@1,064 nm, 6.5 ns) damage to the aluminum grating was carried out based on the 1-on-1 laser damage measurement method. The results suggest that damage could easily occur at the grating ridges. The reason for analysis is that the modulation of the electric field by the grating makes the laser energy redistribute on the surface of the grating, which makes the film layer highly prone to ablation and peeling at the ridge angle of the gate ridge. It has good consistency with the electric field simulation of the aluminum grating. Our research results have guided significance for the design of grating and military application. This method will be further developed by considering more influencing factors, such as impurity, defects, and contamination.

DATA AVAILABILITY STATEMENT

The original contributions presented in the study are included in the article/Supplementary Material; further inquiries can be directed to the corresponding authors.

AUTHOR CONTRIBUTIONS

JW was the main author and was responsible for the first draft of the manuscript. All authors provided reviews and comments on the subsequent versions of the manuscript. JW was responsible for a theoretical simulation, acquisition of theoretical data, and analysis of results. CZ analyzed and guided the experiment. FC contributed to the writing and structure of the thesis. KZ, JY, YZ, and YJ explained the results and provided suggestions to improve the manuscript. GJ, WZ, and WL provide guidance on grating and grating theory knowledge. All of the authors read and approved the final manuscript.

FUNDING

The study was supported by the Major Innovation Project of CIOMP, CAS (E10302Y3M0), Fund project of the State Key Laboratory of Laser-Matter Interaction (SKLLIM1904), National Natural Science Foundation (61904178), Member of the Youth Innovation Promotion Association of the Chinese Academy of Sciences (2020227), and Funding of "Xuguang Talents" from CIOMP, National Natural Science Foundation of China (General Program 62075216).

ACKNOWLEDGMENTS

The authors also gratefully acknowledge the National Engineering Research Center for Diffraction Gratings Manufacturing and Application to support the samples.

REFERENCES

1. Salamin YI, Carbajo S. A Simple Model for the fields of a Chirped Laser Pulse with Application to Electron Laser Acceleration. *Front Phys* (2019) 7:2. doi:10.3389/fphy.2019.00002
2. Qi P, Luo Y, Shi B, Li W, Liu D, Zheng L, et al. Phonon Scattering and Exciton Localization: Molding Exciton Flux in Two Dimensional Disorder Energy Landscape. *eLight* (2021) 1:2. doi:10.1186/s43593-021-00006-8
3. Liu X, Ma Y. Sensitive Carbon Monoxide Detection Based on Light-Induced Thermoelastic Spectroscopy with a Fiber-Coupled Multipass Cell [Invited]. *Chin Opt Lett* (2022) 20(3):031201. doi:10.3788/COL202220.031201
4. Strickland D. Nobel Lecture: Generating High-Intensity Ultrashort Optical Pulses. *Rev Mod Phys* (2019) 91(3). doi:10.1103/RevModPhys.91.030502
5. Lozhkarev VV, Freidman GI, Ginzburg VN, Katin EV, Khazanov EA, Kirsanov AV, et al. 200 TW 45 Fs Laser Based on Optical Parametric Chirped Pulse Amplification. *Opt Express* (2006) 14(1):446–54. doi:10.1364/OPEX.14.000446
6. Hitaishi VP, Mazurenko I, Vengasseril Murali A, de Poulpiquet A, Coustillier G, Delaporte P, et al. Nanosecond Laser-Fabricated Monolayer of Gold Nanoparticles on ITO for Bioelectrocatalysis. *Front Chem* (2020) 8:431. doi:10.3389/fchem.2020.00431
7. Xie C, Meyer R, Froehly L, Giust R, Courvoisier F. *In-situ* Diagnostic of Femtosecond Laser Probe Pulses for High Resolution Ultrafast Imaging. *Light Sci Appl* (2021) 10(1):1–13. doi:10.1038/s41377-021-00562-1
8. Jiang L, Wang A-D, Li B, Cui T-H, Lu Y-F. Electrons Dynamics Control by Shaping Femtosecond Laser Pulses in Micro/nanofabrication: Modeling, Method, Measurement and Application. *Light Sci Appl* (2018) 7(2):17134. doi:10.1038/lsa.2017.134
9. Nakamura A, Mizuta T, Shimotsuma Y, Sakakura M, Otobe T, Shimizu M, et al. Picosecond Burst Pulse Machining with Temporal Energy Modulation [Invited]. *Chin Opt Lett* (2020) 18(12):123801. doi:10.3788/COL202018.123801
10. Zhang W, Fu S, Kong W, Wang G, Xing F, Zhang F, et al. Review of Pulse Compression Gratings for Chirped Pulse Amplification System. *Opt Eng* (2021) 60(2):020902. doi:10.1117/1.Oe.60.2.020902
11. Zhou C. Chirped Pulse Amplification: Review and Prospective from Diffractive Optics [Invited]. *Chin Opt Lett* (2020) 18(11):110502. doi:10.3788/COL202018.110502
12. Lang Z, Qiao S, Ma Y. Acoustic Microresonator Based In-Plane Quartz-Enhanced Photoacoustic Spectroscopy Sensor with a Line Interaction Mode. *Opt Lett* (2022) 47(6):1295–8. doi:10.1364/OL.452085
13. Ma Y, Hu Y, Qiao S, Lang Z, Liu X, He Y, et al. Quartz Tuning forks Resonance Frequency Matching for Laser Spectroscopy Sensing. *Photoacoustics* (2022) 25:100329. doi:10.1016/j.pacs.2022.100329
14. Zou X, Kong F, Jin Y, Chen P, Chen J, Xu J, et al. Influence of Nodular Defect Size on Metal Dielectric Mixed Gratings for Ultra-short Ultra-high Intensity Laser System. *Opt Mater* (2019) 91:177–82. doi:10.1016/j.optmat.2019.02.027
15. Liu F, Jiao H, Ma B, Paschel S, Balasa I, Ristau D, et al. Influence of the Surface and Subsurface Contaminants on Laser-Induced Damage Threshold of Anti-reflection Sub-wavelength Structures Working at 1064 Nm. *Opt Laser Technology* (2020) 127:106144. doi:10.1016/j.optlastec.2020.106144
16. Xu J, Zou X, Chen J, Zhang Y, Wang Y, Jin Y, et al. Metal Dielectric Gratings with High Femtosecond Laser Damage Threshold of Twice as Much as that of Traditional Gold Gratings. *Opt Lett* (2019) 44(11):2871–4. doi:10.1364/OL.44.002871
17. Kong F, Chen S, Liu X, He K, Jin Y, Liu S, et al. Femtosecond Laser Damage of All-Dielectric Pulse Compression Gratings. *Laser Phys* (2014) 24(10):106101. doi:10.1088/1054-660x/24/10/106101
18. Hoffman BN, Kozlov AA, Liu N, Huang H, Oliver JB, Rigatti AL, et al. Mechanisms of Picosecond Laser-Induced Damage in Common Multilayer Dielectric Gratings. *Opt Express* (2020) 28(17):24928–36. doi:10.1364/oe.395197
19. Garasz K, Kocik M. Experimental Investigations on Laser Ablation of Aluminum in Sub-picosecond Regimes. *Appl Sci* (2020) 10(24):8883. doi:10.3390/app10248883
20. Xie L, Zhang J, Zhang Z, Ma B, Li T, Wang Z, et al. Rectangular Multilayer Dielectric Gratings with Broadband High Diffraction Efficiency and Enhanced Laser Damage Resistance. *Opt Express* (2021) 29(2):2669–78. doi:10.1364/OE.415847
21. Neauport J, Lavastre E, Razé G, Dupuy G, Bonod N, Balas M, et al. Effect of Electric Field on Laser Induced Damage Threshold of Multilayer Dielectric Gratings. *Opt Express* (2007) 15(19):12508–22. doi:10.1364/OE.15.012508
22. Chen J, Huang H, Zhang Y, Wang Y, Kong F, Wang Y, et al. Reducing Electric-Field-Enhancement in Metal-Dielectric Grating by Designing Grating with Asymmetric ridge. *Sci Rep* (2018) 8(1):1–6. doi:10.1038/s41598-018-22479-3
23. Gallais L, Rumpel M, Moeller M, Dietrich T, Graf T, Abdou Ahmed M. Investigation of Laser Damage of Grating Waveguide Structures Submitted to Sub-picosecond Pulses. *Appl Phys B* (2020) 126(4):1–8. doi:10.1007/s00340-020-07419-2
24. Rakić AD. Algorithm for the Determination of Intrinsic Optical Constants of Metal Films: Application to Aluminum. *Appl Opt* (1995) 34(22):4755–67. doi:10.1364/AO.34.004755
25. Chen S, Zhu M, Li D, He H, Zhao Y, Shao J, et al. Effects of Electric Field Distribution and Pulse Duration on the Ultra-short Pulse Laser Damage Resistance of Laser Coatings. *Int Soc Opt Photon* (2010) 7842:78420D. Effects of electric field distribution and pulse duration on the ultra-short pulse laser damage resistance of laser coatings[C]//Laser-Induced Damage in Optical Materials: 2010. doi:10.1117/12.867225
26. ISO. *Lasers and Laser-Related Equipment—Test Methods for Laser-Induced Damage Threshold—Part 2*. International Organization for Standardization (ISO): Geneva, Switzerland (2011). I.J.I.O.f.S. 21254-2: 2011.

Conflict of Interest: The authors declare that the research was conducted in the absence of any commercial or financial relationships that could be construed as a potential conflict of interest.

frontiers | Frontiers in Physics

ORIGINAL RESEARCH
published: 17 May 2022
doi: 10.3389/fphy.2022.865455

Automatic and Label-Free Analysis of the Microstructure Feature Differences Between Normal Brain Tissue, Low-Grade, and High-Grade Gliomas Using the Combination of Multiphoton Microscopy and Image Analysis

Zanyi Wu[1†], Xingfu Wang[2†], Na Fang[3†], Yuanxiang Lin[1], Liqin Zheng[4], Yihui Xue[1], Shanshan Cai[5], Jianxin Chen[4], Ni Lin[3] and Dezhi Kang[1]**

[1]Department of Neurosurgery, The First Affiliated Hospital of Fujian Medical University, Fujian Key Lab of Individualized Cancer Immunotherapy, Fuzhou, China, [2]Department of Pathology, the First Affiliated Hospital of Fujian Medical University, Fuzhou, China, [3]The School of Medical Technology and Engineering, Fujian Medical University, Fuzhou, China, [4]Key Laboratory of OptoElectronic Science and Technology for Medicine of Ministry of Education, Fujian Provincial Key Laboratory of Photonics Technology, Fujian Normal University, Fuzhou, China, [5]Department of Pathology, The Second Affiliated Hospital, Fujian Medical University, Quanzhou, China

Accurate intraoperative identification of gliomas is of utmost importance. This task often remains a challenge for the pathologist and neurosurgeon because of the absence of full intraoperative microstructure feature details of the tumor. Here, multiphoton microscopy (MPM), based on second harmonic generation (SHG) and two-photon excited fluorescence (TPEF), is applied for label-free detecting the microstructure feature differences between normal brain tissue, low-grade, and high-grade gliomas. MPM can not only capture the difference of their qualitative microstructure features such as increased cellularity, nuclear atypia, microvascular proliferation, and necrosis that are significant for diagnosing and grading of glioma, but also visualize some additional features such as collagen deposition that cannot be seen by conventional methods. In addition, automated image analysis algorithms are developed to automatically and accurately calculate the quantitative diagnostic features: collagen content, the number and area of nuclei to further quantitatively analyze the microstructure features difference of collagen deposition, cellularity, and nuclear atypia between normal brain tissue, low-grade, and high-grade gliomas. With the development of two-photon fiberscope, combined MPM and image processing techniques may become an imaging tool for assisting intraoperatively diagnosing and grading gliomas.

Keywords: multiphoton microscopy, harmonic generation, two-photon excited fluorescence, high-grade gliomas, low-grade gliomas, image analysis

OPEN ACCESS

Edited by:
Yufei Ma,
Harbin Institute of Technology, China

Reviewed by:
Chandra Sekhar Yelleswarapu, University of Massachusetts Boston, United States
Xiaojun Yu, Northwestern Polytechnical University, China

****Correspondence:***
Ni Lin
ssytnx@126.com
Dezhi Kang
kdz99988@vip.sina.com

[†]These authors have contributed equally to this work

Specialty section:
This article was submitted to Optics and Photonics, a section of the journal Frontiers in Physics

Received: *10 February 2022*
Accepted: *22 March 2022*
Published: *17 May 2022*

Citation:
Wu Z, Wang X, Fang N, Lin Y, Zheng L, Xue Y, Cai S, Chen J, Lin N and Kang D (2022) Automatic and Label-Free Analysis of the Microstructure Feature Differences Between Normal Brain Tissue, Low-Grade, and High-Grade Gliomas Using the Combination of Multiphoton Microscopy and Image Analysis. Front. Phys. 10:865455. doi: 10.3389/fphy.2022.865455

INTRODUCTION

The goal of glioma surgery is "maximum safe resection" and the procedure is an invasive one. It is therefore important to determine before and during surgery whether the lesion is a glioma and whether the glioma is a high-grade or low-grade. Current techniques of intraoperative histopathological diagnosis including frozen sectioning and cytological preparations performed neuropathologist and skilled technicians. However, these techniques have limitations. First, in order to minimize damage to normal brain tissue, the size of tissue samples available for intraoperative neuropathological analysis is often small, which may affect diagnostic accuracy, especially when considering the heterogeneous nature of brain tumors [1]. Second, some brain tumors have histopathological features that are rarely seen and may be misclassified [2]. Third, the typical processing of intraoperative tissue samples, such as fixation and embedding, not only time-consume, but also leads to the appearance of artefacts and the loss of some biological components, which may affect the subjectivity of interpretation during subsequent diagnosis and delay surgery [3]. Four, in traditional intraoperative pathology, the pathologist often uses a light microscope to view the lesions on the pathology slides, which is relatively inefficient [4]. With the current shortage of pathologists and the increasing demand for screening biopsies for various diseases, the traditional method of reading further increases the burden and responsibility of pathologists [5]. Furthermore, and most importantly, this labelled pathological findings lack direct guidance for preoperative or intraoperative assessment, and do not simultaneously reflect the broader signal in biological tissue. Therefore, there is an urgent need for a new intraoperative imaging technique which can label-free provide pathological-images of the tissue microstructure feature.

Multiphoton microscopy (MPM), based on two photon excitation fluorescence (TPEF) and second-harmonic generation (SHG), represents a promising new adjunctive technology in the *in vivo* and real-time diagnosis of tissue [6, 7]. In comparison to conventional histopathology methods, MPM technique allows for the real-time simultaneous excitation of multiple endogenous signals in different components of biological tissue without the need for additional staining. Besides, combined with custom-developed image processing algorithms, it more reliably and rapidly shows the morphological characteristics and offer quantitative information of unstained tissues. Many previous reports have demonstrated that MPM enables tissue adjunctive diagnosis at the cellular level, for instance, skin aging [8], liver fibrosis [9], basal cell carcinoma [10], ovarian cancer [11], gastric cancer [12], breast cancer [13], colonic adenoma [14].

Previous studies also support the hypothesis that brain tumors and normal brain tissue can be well discerned based on label-free MPM imaging [15–22]. Gliomas were shown to have a specific morphochemistry in the TPEF images, with cell proliferation bearing enlarged nuclei. In unlabelled multiphoton images, several diagnostic features of some brain tumors in unstained multiphoton images have been determined and may be used as tumor markers [17]. Cytological and architectural features required for pathological tumor typing and grading in 55 lesions of the central nervous system can be retrieved by label-free multiphoton microscopy [21]. Moreover, a study of 382 tumor patients indicated that the combined analysis of texture parameters of the CARS and TPEF signal proved to be most suited for the discrimination of nontumor brain versus brain tumors leading to a correct rate of 96% [22].

In the present study, we aim to provide the basis for clinical translation of label-free multiphoton imaging as an intraoperative tool for gliomas delineation. Therefore, we imaged fresh unstained human normal brain tissue, low-grade, and high-grade gliomas using the combination of TPEF and SHG. Several qualitative microstructure features differences between normal brain tissue, low-grade, and high-grade gliomas, such as collagen deposition [23, 24], increased cellularity, nuclear atypia, microvascular proliferation, and necrosis were visualized. To describe the degree of collagen deposition, increased cellularity and nuclear atypia, some automated image analysis algorithms based on image segmentation technology were developed to automatically calculate the quantitative diagnostic features: the collagen content, the number, and area of nuclei.

MATERIALS AND METHODS

Sample Preparation

From 2014 to 2018, 20 glioma patients (10 high-grade gliomas, 10 low-grade gliomas) and 5 traumatic brain injury patients from the Department of Neurosurgery at the First Affiliated Hospital of Fujian Medical University were invited to join in the research. The research was approved by Fujian Medical University Clinical Research Screening Committee for Studies Involving Human Subjects. All of the subjects signed a written consent prior to the research. During neurosurgical procedures, the structurally normal tissue and glioma specimens were taken from the same patient to carry out the conventional diagnostic procedure. After resection, the specimens were delivered to the pathology department within 30 min. To verify the feasibility of MPM in tissue detail imaging, each specimen was divided into two parts. One portion of the fresh tissue was processed as five serial frozen slices by cryostat microtome. The middle slice with thickness of nearly 5 μm was stained with H&E staining for histological comparison with MPM outcomes. The remaining 4 slices with thickness of nearly 20 μm were sandwiched between microscope slide and a cover slip for MPM imaging (**Figure 1**). The other part of the fresh tissue is left in the pathology department to be processed into paraffin blocks for subsequent histopathological examinations (including standard hematoxylin and eosin staining, specific staining, and immunohistochemistry et) and molecular pathology examinations for the final diagnosis of glioma. Gliomas were classified and graded according to the criteria outlined by the 2016 World Health Organization. The pathological diagnoses were reaffirmed independently by two experienced neuropathologists.

Multiphoton Microscopic Imaging System

The MPM imaging system used in this study was previously mentioned in detail [25]. Briefly, this system is composed of a Zeiss LSM 510 system (Zeiss, Jena, Germany) and a Ti:sapphire

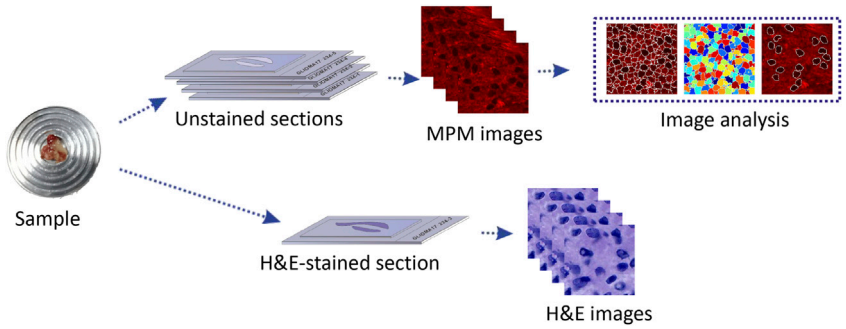

FIGURE 1 | Demonstration of preparation and analysis of the frozen sections in this study.

femtosecond laser (Mira 900-F, Coherent Inc., Santa Clara, CA, United States), which can be tuned in the range of 700–980 nm. In this study, the laser power was set as 5 mw and excitation wavelength at 810 nm. 63×Plan-Apochromat oil immersion objective allows to focus the excitation beam and collect the backward signals. META detector is made up of an optimized 32-channel photomultiplier tube (PMT) array and high-quality reflective grating to detect the emission signals in the backward direction. In this system, 8 independent channels are included, of which individual channel(s) can be selected to capture emission signals, covering wavelength from 377 to 716 nm. And then images can be obtained. In this research, 2 independent channels were chosen to detect TPEF and SHG signals from the specimens. One channel detected TPEF signals, covering wavelength from 430 to 716 nm; the other channel detected SHG signals, covering wavelength from 387 to 419 nm. In order to strengthen the contrast of TPEF/SHG images, TPEF images were shown in red and SHG images were shown in green. All images were obtained at 2.56 μs per pixel and had a 12-bit pixel depth. The image acquisition time was 1.97 s/frame with a resolution of 512 pixels × 512 pixels.

Image Analysis Methods

Analysis of Collagen Density

MPM images were segmented and analyzed through custom-developed software in MATLAB Image Processing Toolbox (The MathWorks, Inc.). The patients enrolled in this study were split into training/test datasets at a ratio of 2:1. We collected 300 MPM images from the fresh *ex vivo* brain tissues without staining, obtaining 120, 120, and 60 images of diagnosed low-grade glioma, high-grade glioma and normal brain tissues, respectively. In our experiment, collagen content, number, and area of nuclei were automatically calculated by our self-written program. Collagen density was calculated as the ratio of SHG pixels to all pixels in every image. In order to calculate collagen content, MPM images were analyzed through the following algorithm: First, the SHG image was converted to grayscale image and then a Gaussian filter (size = 5, sigma = 1) was used to reduce noise and enhance the collagen details of image; Next, the enhanced results were carried out by Otsu threshold segmentation and mathematical morphological processing; Finally, the segmentation template was obtained, and collagen ratio was calculated according to the occupied area of the collagen. The flowchart of the algorithm is shown in **Figure 2A**.

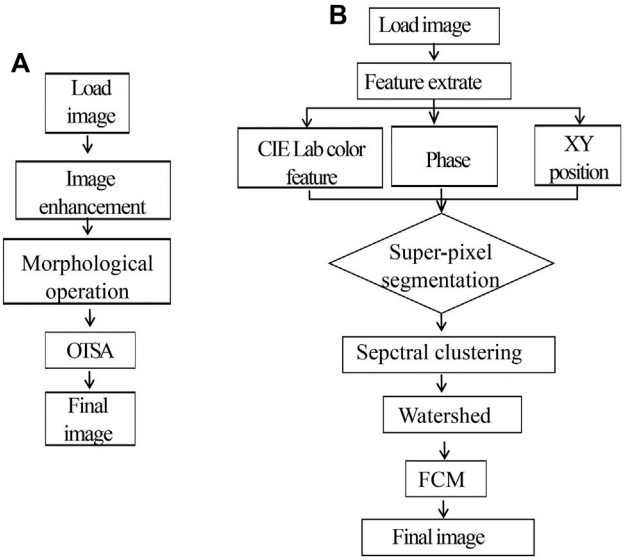

FIGURE 2 | (A) Flowchart of the proposed collagen density segmentation. **(B)** Flowchart of the proposed nuclear density and size segmentation.

Analysis of Nucleus Density and Size

The segmentation approach based on watershed was used to depict cell boundaries and automatically calculate the number and area of nuclei. The flowchart of this algorithm is shown in **Figure 2B**. Detailed analysis steps were as following: first, the original MPM image in RGB color space was changed to CIE Lab space; then six-dimensional characteristic quantity was extracted, including image color space LAB color feature, phase, and XY position. Next, distance measurement was performed for the extracted six-dimensional eigenvectors, image pixels were clustered by similarity matrix spectrum, and segmentation was carried out with the marked watershed algorithm method. In the CIE Lab color space, the darkest one is selected with Fuzzy C-Means algorithm (FCM) as the final segmentation result; meanwhile, number and area of nuclei can be automatically calculated based on the segmentation results.

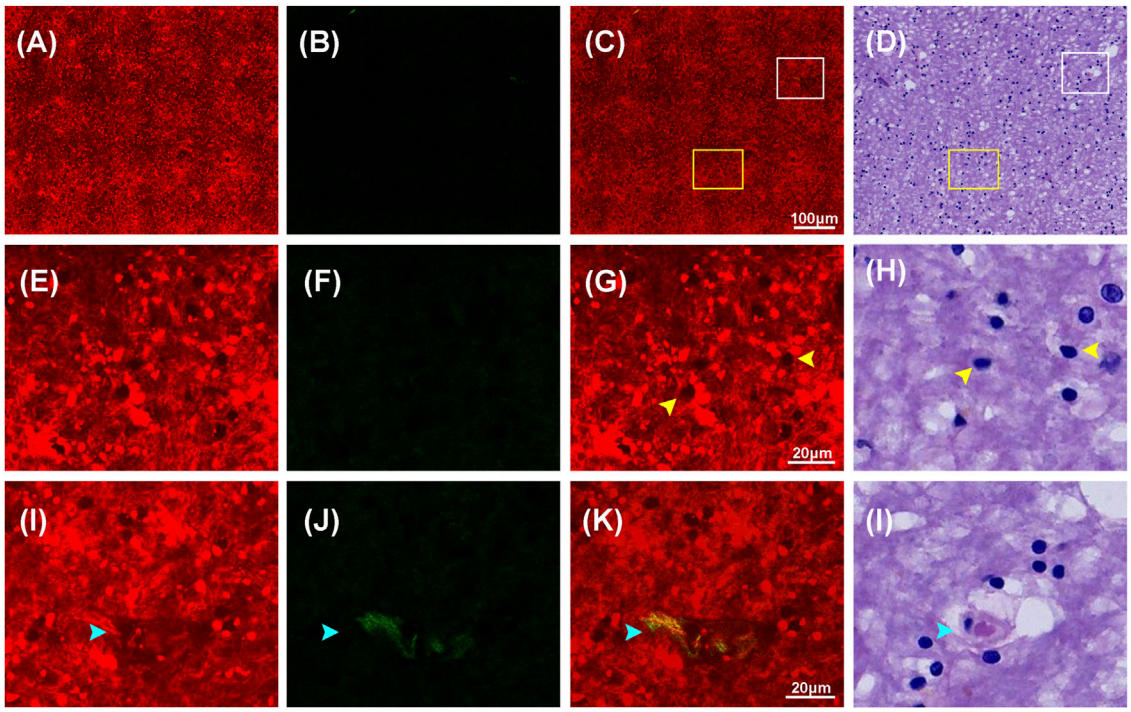

FIGURE 3 | Representative MPM images and the corresponding images of H&E stained normal brain (white matter) tissue. **(A–D)** TPEF, SHG, TPEF/SHG overlaid images, and corresponding image of H&E stained normal brain tissue. **(E–H)** The magnified TPEF, SHG, TPEF/SHG overlaid images, and corresponding H&E image of the selected area (yellow square box) in **Figure 3C**. **(I–L)** The magnified TPEF, SHG, TPEF/SHG overlaid, and corresponding H&E image of the selected area (white square box) in **Figure 3C**. Yellow arrowheads: cells in normal brain tissue; cyan arrowhead: blood vessel in normal brain tissue.

RESULTS

Multiphoton Microscopic Imaging of Normal Human Brain Tissue

Figure 3 showed representative TPEF/SHG images and the corresponding H&E images of the normal brain tissue. **Figures 3A–D** showed the large-scale MPM images and the corresponding H&E stained images of the normal brain tissue (white matter), demonstrating the capability of MPM to displayed large-area histoarchitectural features. In the large-scale images, major components of the brain, such as extracellular matrix, cells, and blood vessels emitted strong multiphoton signals, which could be explicitly identified in multiphoton images. **Figures 3E–L** showed the selected regions at higher magnifications (yellow and white box in **Figure 3C**). In the magnified images, more details of cells and blood vessels were revealed. MPM showed that nonfluorescent cell nuclei were marked as dark spot while the tightly condensed matrix emitted strong TPEF signals was color-coded in red, highlighting the distinguishable individual cells. Those cells (yellow arrowheads) of round shape and uniform size were found to be evenly distributed in the normal brain tissue. A blood vessel (cyan arrowhead) could be identified owing to its tubular structure defined by elastin and collagen. The identified blood vessel was marked in yellow because collagen in the wall emitted strong SHG signals while elastin produced comparable TPEF signals. Except for blood vessel wall, SHG signals were not detected, indicating that the stroma in the normal brain tissue had limited collagen content. These results were consistent with what have been previously reported [23]. These characteristics can also be seen in the corresponding H&E-image. However, collagen could not be displayed in H&E images as clearly as this in MPM images.

Multiphoton Microscopic Imaging of Low-Grade Glioma

The structural differences of low-grade gliomas were featured as variably increased cellularity and slight nuclear atypia, which also helped to distinguish between normal and abnormal tissue. **Figure 4** displays MPM images and the corresponding H&E images of low-grade gliomas. Compared with the normal brain tissue, low-grade gliomas showed moderate architectural and cytological abnormalities in MPM images. As it could be seen in the large-scale images in **Figures 4A–D**, cell density in low-grade gliomas was greatly increased compared to normal brain tissue. **Figures 4E–L** showed higher magnification images of selected areas from **Figure 4C**. In **Figures 4E–H**, MPM images could clearly reveal morphological details of tumor cells (yellow arrowheads) in low-grade gliomas. The tumor cells were of medium size with slightly enlarged nuclear, distinct cell borders, and round, oval or short fusiform nuclei. However, nuclear atypia was not obvious as it was only seen in a fraction of cells. In addition, the morphology of extracellular

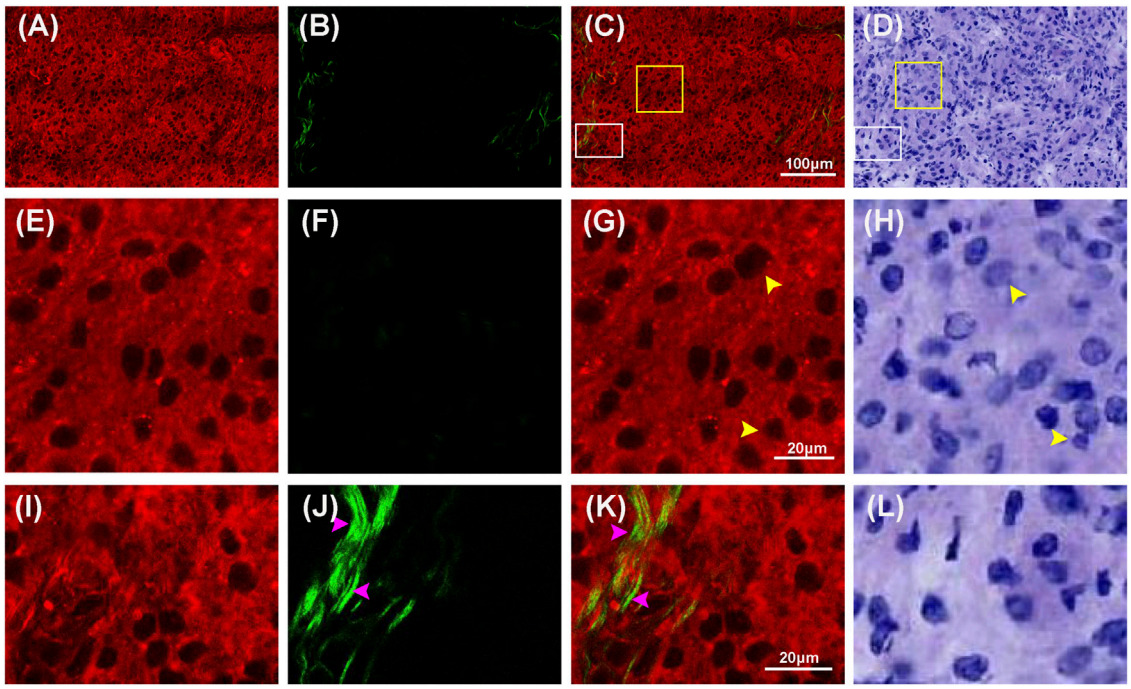

FIGURE 4 | Representative MPM images and the corresponding images of H&E stained low-grade glioma. **(A–D)** TPEF, SHG, TPEF/SHG overlaid images, and corresponding image of H&E stained low-grade glioma. **(E–H)** The magnified TPEF, SHG, TPEF/SHG overlaid images, and corresponding H&E image of the selected area (yellow square box) in **Figure 4C**. **(I–L)** The magnified TPEF, SHG, TPEF/SHG overlaid images, and corresponding H&E image of the selected area (white square box) in **Figure 4C**. Yellow arrowheads: cells in low-grade glioma; pink arrowhead: collagen in low-grade glioma.

matrix was moderately changed. A few of collagen fibers were found to be irregularly scattered in the red extracellular matrix background. More collagen details were presented in **Figures 4I–L**. Through SHG signals, collagen fibres (pink arrowheads) with reticular morphology were shown in green. A few of collagen fibres were shown in yellow, meaning they concurrently generated comparable SHG and TPEF signals, indicating that they might have a distinct photochemical composition. These details were readily correlated with those in the corresponding H&E images. However, for these collagen differences between normal brain tissue and low-grade gliomas could also not be displayed clearly in H&E images as those in MPM images. The research findings showed that the microstructure features of low-grade gliomas could be well characterized by MPM technology.

Multiphoton Microscopic Imaging of High-Grade Glioma

Compared to normal tissue and low-grade gliomas, high-grade gliomas have features such as variably increased cellularity, obvious nuclear atypia, microvascular proliferation, intense vascular proliferation, and necrosis. **Figures 5**, **6** showed representative TPEF/SHG images and the corresponding H&E images of the central tumor region and necrotic area of high-grade glioma (glioblastoma), respectively. Unlike normal brain tissue and low-grade gliomas, high-grade gliomas showed more severe architectural and cytological abnormalities in MPM images. **Figures 5A–D** clearly revealed the increased cellularity, obvious nuclear atypia, and intense vascular proliferation in the high-grade glioma tissue (tumor central region). In the magnified images (**Figures 5E–L**), the entire area of high-grade gliomas was almost filled with tumor cells that had indistinct cell borders and were unevenly distributed. The nuclei had larger areas and more severe nuclear pleomorphism. Intense vascular proliferation, seen as important histopathological hallmark of high-grade glioma, was easily detected via SHG signals that were emitted by collagen in the vessel walls. Blood vessels (cyan arrowheads) of different sizes and shapes were found to be scattered in the extracellular matrix. Compared with low-grade gliomas, more SHG signals were detected as denser collagen deposition (pink arrowheads) was notably presented in high-grade gliomas. Microvascular proliferation and necrosis, seen as two fundamental features of glioblastoma and two major predictors of the aggressive diffuse astrocytomas [26–28], were well characterized in **Figure 6**. Compared with its surrounding tumor cells, the tumor necrotic had been identified owing to their "pseudopalisading" pattern (**Figures 6A,E**) and higher TPEF signal intensity (yellow arrowheads). Near the necrotic core, the reactive hyperplasia of vascular endothelial cells in the blood vessel wall was visualized in the glomerulus-like arrangement (**Figure 6K**); emitted TPEF signals in the endothelial cells (cyan arrowheads) were weaker than those of the surrounding tumor cells. Thus, microvascular proliferation could be readily recognized in MPM images. These morphological characteristics of high-grade gliomas were also seen in the corresponding H&E images. Again, same as low-grade gliomas, collagen deposition was excluded since it could not well display in

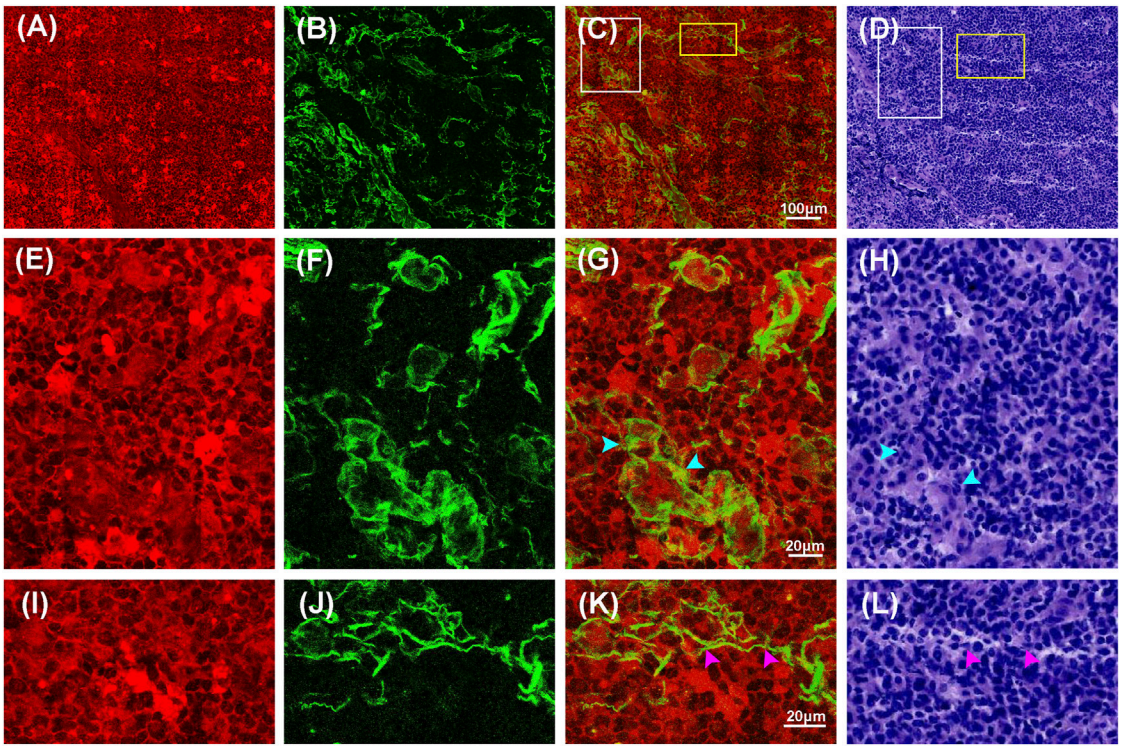

FIGURE 5 | Representative MPM images and the corresponding H&E stained images of high-grade glioma (tumor central region). **(A–D)** TPEF, SHG, TPEF/SHG overlaid and corresponding H&E image of high-grade glioma. **(E–H)** The magnified TPEF, SHG, TPEF/SHG overlaid images, and corresponding H&E image of the selected area (white square box) in **Figure 5C**. **(I–L)** The magnified TPEF, SHG, TPEF/SHG overlaid images, and corresponding H&E image of the selected area (yellow square box) in **Figure 5C**. Cyan arrowheads: blood vessels in high-grade glioma; pink arrowhead: collagen in high-grade glioma.

H&E images. These results indicated that characteristics of high-grade gliomas could be well captured by MPM. To some extent, MPM had a better effect than H&E-stained technology.

Automatic Identification of Glioma

In order to further characterize the morphological differences between low-grade and high-grade gliomas, quantitative analysis was conducted. The collagen content, number and area of nuclei were automatically calculated through the proposed image analysis method. **Figures 7A–D** showed the representative collagen segmentation images. The collagen enhancement segmentation image (**Figure 7B**), perivascular collagen position segmentation image (**Figure 7C**), and final segmentation image (**Figure 7D**) can all be well correlated with original SHG images (**Figure 7A**) at the subcellular level. More segmentation details could be seen in the magnified images from **Figures 7E–H**. Results of comparing collagen density between normal brain tissue, low-grade gliomas, and high-grade gliomas using this collagen analysis method were shown in **Figure 7I**; **Table 1**, respectively. Quantitative analysis results showed that the collagen density of high-grade gliomas (0.157 ± 0.023) was significantly higher than that of low-grade gliomas (0.013 ± 0.005) and normal brain tissue (0.005 ± 0.001). The more severe the malignant tumor was, the higher the contents of collagen could be. These results were consistent with the other research findings [23].

Figure 8 showed the processing results of nuclear segmentation. The number of nuclei, and the mean and standard deviation of the nuclear area could be automatically calculated. **Figures 8A–E** illustrated the representative nuclear segmentation results. As it was shown in **Figure 8A**, the original MPM image indicated low SNR as the cell boundaries were not clear and difficult to be precisely positioned by human eyes. The segmentation result after spectral clustering was shown in **Figure 8B**. In **Figure 8C**, image noises were reduced while cell boundaries were enhanced after watershed segmentation. Then the average gray-scale based on the above segmentation results was applied to correctly depict cells from the complicated background. The final segmentation image was shown in **Figure 8D**. In this image, cells can be automatically positioned and cell boundaries can be correctly depicted from the complicated background. In this way, cell number and nuclear area could be automatically quantified. MPM images (**Figure 8A**) well matched with segmentation results (**Figure 8D**) at the subcellular level. The comparison results of cell density, mean and standard deviation of nuclear parameters between normal brain tissue, low-grade gliomas, and high-grade gliomas using this analysis method were shown in **Figures 8E,F** and **Table 1**, respectively. Quantitative analysis results revealed that compared to low-grade glioma, nuclear number was sharply increased and presented a larger standard deviation in high-grade gliomas. In summary, MPM and image analysis method

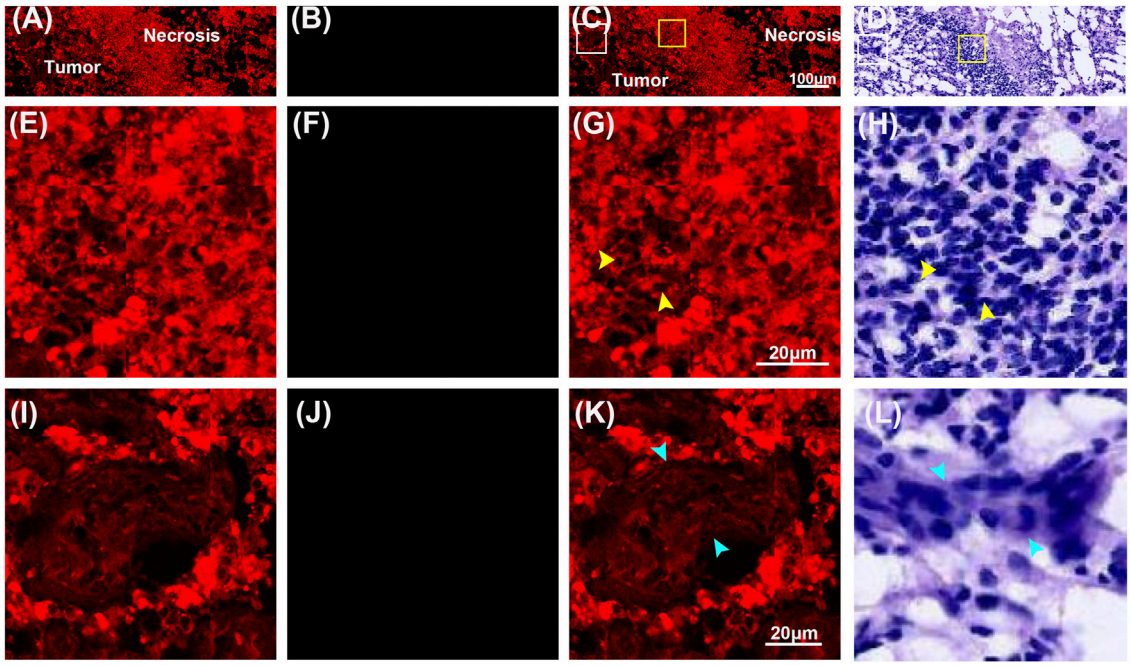

FIGURE 6 | Representative MPM images and the corresponding images of H&E stained high-grade glioma (necrotic area). **(A–D)** TPEF, SHG, TPEF/SHG overlaid images, and the corresponding H&E image of high-grade glioma. **(E–H)** The magnified TPEF, SHG, TPEF/SHG overlaid images, and corresponding H&E image of the selected area (white square box) in **Figure 6C**. **(I–L)** The magnified TPEF, SHG, TPEF/SHG overlaid images, and corresponding H&E image of the selected area (yellow square box) in **Figure 6C**. Yellow arrowhead: tumor cells; cyan arrowheads: endothelial cells.

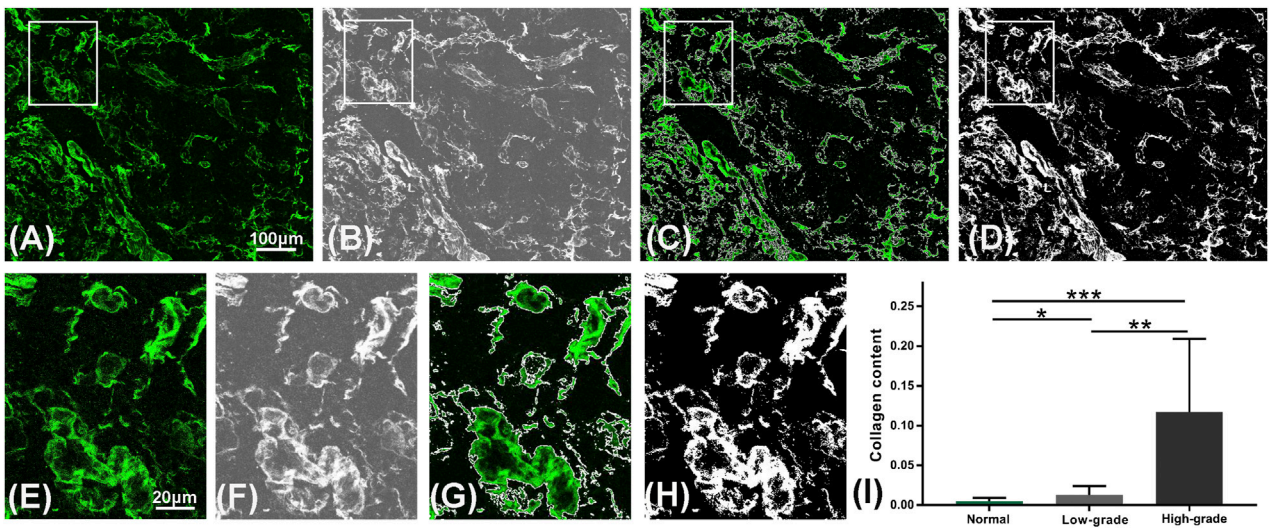

FIGURE 7 | Quantitative analysis of collagen. **(A–D)** Representative segmentation results of the automatic analysis algorithm: an original SHG image in a high-grade glioma **(A)**, the result after image enhancement **(B)**, the segmentation result of collagen position **(C)** and the final segmentation result of collagen content **(D)** are displayed from left to right. **(E–H)** Magnified region marked in **(A–D)**. **(I)** Collagen content variations in the normal brain tissue, low-grade and high-grade gliomas using the algorithm.

provided quantitative assessment of morphological changes of low-grade and high-grade glioma tissues. Above results showed that collagen density, cell density, and mean and standard deviation of nuclear area are representative features to different normal brain tissue, low-grade, and high-grade gliomas. Comprehensive analysis of them could rapidly offer additional assessment metrics to pathologists and surgeons. Thus, MPM combined with image analysis

TABLE 1 | Quantitative parameters of low-grade and high-grade gliomas.

Tissue type	Collagen content		Nuclear number (per 10,000 μm^2)		Nuclear area (μm^2)	
	Mean	SD	Mean	SD	Mean	SD
Normal brain tissue	0.005	0.004	16.0	5.1	22.6	5.3
Low-grade glioma	0.013	0.011	37.3	19.7	31.83	13.49
High-grade glioma	0.117	0.092	112.7	67.3	50.38	23.62

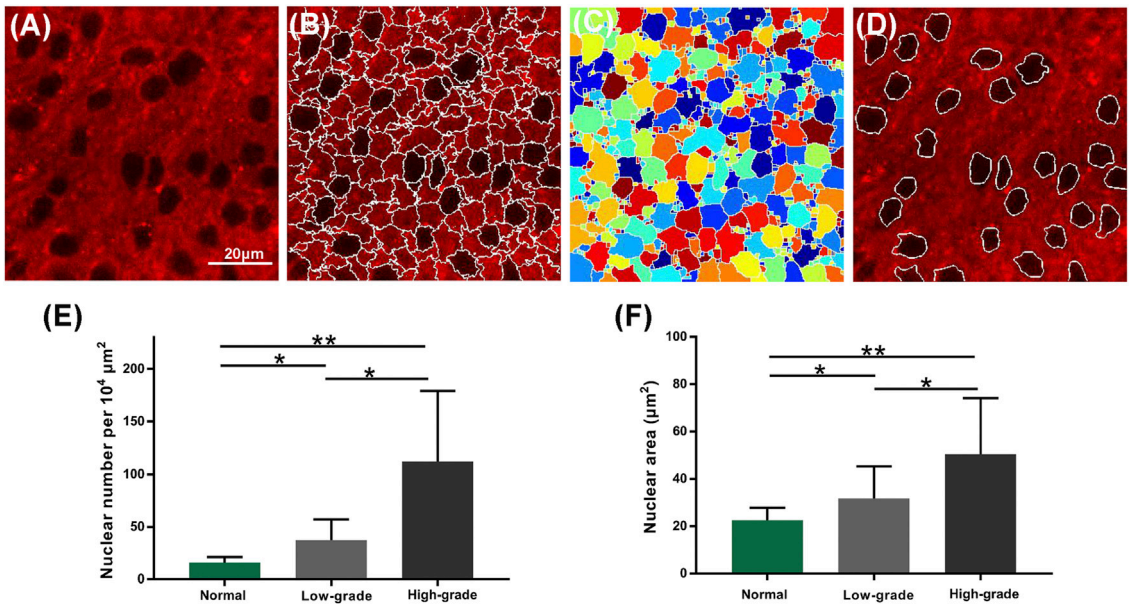

FIGURE 8 | Quantitative analysis of number and area of nuclei. **(A–E)** Representative nuclear segmentation results of the automated analysis algorithm: an original MPM image in a low-grade glioma **(A)**, the result after super-pixel segmentation and spectral clustering **(B)**, the result after watershed segmentation **(C)**, and the final segmentation results **(D)** are displayed from left to right. **(E)** Number of nuclei of normal brain tissue, low-grade, and high-grade gliomas quantified using this algorithm. **(F)** Area of nuclei of normal brain, low-grade, and high-grade gliomas quantified using this algorithm.

method has the potential to establish an objective standard about grading of gliomas.

DISCUSSION

MPM, based on intrinsic TPEF and SHG signals, shows label-free images by allowing the nonlinear excitation of different intrinsic biomacromolecules, and obtaining the subcellular resolution from unstained and fresh tissue [29–31]. In this study, we used label-free MPM to obtain the microstructures of human normal, low-grade and high-grade brain tissues. Our results show that the morphology, content and morphology of the main components including cells, blood vessels and collagen in these three tissues have apparently different properties. Based on these differences, several diagnostic features including increased cellularity, nuclear atypia, intense vascular proliferation, microvascular proliferation, and necrosis can be extracted to distinguish between normal, low-grade and high-grade brain tissues, Meanwhile, collagen deposition, an additional feature that cannot be seen by the conventional methods, is clearly observed in MPM images. Compared to classic traditional intraoperative diagnosis techniques, MPM can affords real-time imaging of brain tissues without destructive procedures and staining. In addition, all images were acquired at a rate of 2.56 μs per pixel. Therefore, multichannel detection, combined with increased accuracy and speed, makes MPM highly suitable for characterizing morphologic features of cell, blood vessel and collagen at subcellular resolution.

Automated image analysis has become a powerful tool for solving biomedical problems in macroscopic image [32]. In this study, several image analysis algorithms were developed to calculate the determination of collagen location, collagen content, nuclei area, nuclei number and nuclei area variance in this study. Relay on this, the extent of collagen deposition, nuclei size, cellularity and nuclear atypia can be rapidly and quantitatively analysed. Thus, our research may be taken as an alternative and adjunctive approach to the diagnosis and grading of brain tumors. While compared with pathologist's examination and traditional MPM technique, our proposed method can quickly display image characteristics and

reduce amount of manual observation. Recent research studies indicate that MPM combined with image analysis method has major advantages in the feasibility of clinical translation [33].

Regarding the applicability of the proposed method in clinical settings, some limitations remain to be addressed. The number of patients enrolled in this study was relatively small. More data of patients should be evaluated. Besides, current label-free MPM images cannot get the depth in micrometer, the high-resolution images are often acquired by *ex vivo* histopathologic section or *in vivo* intraoperative biopsy. Fortunately, the advances of two-photon microendoscope and fiberscope have provided insights and feasibility in clinical practice [34–39]. The miniaturized two-photon fiberscope has enabled high-resolution optical recording of neural activity at the cellular level from freely moving animals in their natural behaviors [39]. Then small-diameter (350 um) gradient refractive index (GRIN) lens with side-view design could be inserted to solid tissues [37–39]. Under the fixation condition, the high-quality MPM images in many centimeters could be obtained from the object plane. From a recent clinical resection case of glioblastoma, multiphoton tomography showed its ability to rapidly identify the native glioma tissues without tissue staining or processing [40]. Thus, the proposed method in this study combined with MPM endomicroscopy could be taken as a powerful diagnosis tool for the auxiliary diagnosis and grading of gliomas in the operating room to offer real-time histology-like images and perform automated image analysis for higher diagnostic accuracy of neuropathology.

In the future, our research will focus on enrolling more patients, the intraoperative *in vivo* imaging through MPM microendoscopes and the optimization of algorithms for quantitative diagnosis. As probes and optical fiber are miniaturized and optimized, it is anticipated that our combined method may be used for auxiliary diagnosis and grading of gliomas in the operating room to offer real-time histology-like images and perform automated image analysis for higher diagnostic accuracy of neuropathology.

CONCLUSION

In summary, we demonstrated the capability of label-free MPM to identify differences of microstructure features between normal brain, low-grade and high-grade gliomas, revealing key microstructure features including collagen deposition, increased cellularity, nuclear atypia, microvascular proliferation, and necrosis were visualized. Furthermore, the combination of label-free MPM and image processing provided a supplementary methodology for quantitatively analysis microstructure features differences. Therefore, our presented method provides insights about both morphological and quantitative information of the gliomas tissues, which has the great potential for becoming a valid intraoperative imaging tool for assisting in diagnosing and grading of gliomas.

DATA AVAILABILITY STATEMENT

The original contributions presented in the study are included in the article/supplementary material, further inquiries can be directed to the corresponding authors.

ETHICS STATEMENT

The studies involving human participants were reviewed and approved by the Fujian Medical University Clinical Research Screening Committee for Studies Involving Human Subjects. Written informed consent to participate in this study was provided by the participants' legal guardian/next of kin.

AUTHOR CONTRIBUTIONS

ZW, YL, and YX contributed to sample acquisition and subject recruitment; XW, SC contributed to sample processing and evaluation; JC, DK contributed to experiment design, plan and data analysis. ZW, NL, and NF wrote the initial version of the manuscript and all authors contributed to the revisions.

FUNDING

This research was funded by the National Natural Science Foundation of China (Grant No. 62105063); The Natural science foundation of Fujian province (2018J01851, 2021J01811); and Special Funds of the Central Government Guiding Local Science and Technology Development (2017L3009); Fujian Provincial Health Technology Project (2020GGA054).

ACKNOWLEDGMENTS

The authors thank Hua Lin in the First Affiliated Hospital of Fujian Medical University for preparation of samples used in the study.

REFERENCES

1. Lauko A, Lo A, Ahluwalia MS, Lathia JD. Cancer Cell Heterogeneity & Plasticity in Glioblastoma and Brain Tumors. *Semin Cancer Biol* (2021): 1–14. doi:10.1016/j.semcancer.2021.02.014
2. Louis DN, Perry A, Reifenberger G, von Deimling A, Figarella-Branger D, Cavenee WK, et al. The 2016 World Health Organization Classification of Tumors of the Central Nervous System: a Summary. *Acta Neuropathol* (2016) 131:803–20. doi:10.1007/s00401-016-1545-1
3. Uematsu Y, Owai Y, Okita R, Tanaka Y, Itakura T. The Usefulness and Problem of Intraoperative Rapid Diagnosis in Surgical Neuropathology. *Brain Tumor Pathol* (2007) 24:47–52. doi:10.1007/s10014-007-0219-z
4. Somerset HL, Kleinschmidt-DeMasters BK. Approach to the Intraoperative Consultation for Neurosurgical Specimens. *Adv Anat Pathol* (2011) 18:446–9. doi:10.1097/pap.0b013e3182169934

5. Malatesta M. Histological and Histochemical Methods - Theory and Practice. *Eur J Histochem* (2016) 60:60. doi:10.4081/ejh.2016.2639
6. Squirrell JM, Wokosin DL, White JG, Bavister BD. Long-term Two-Photon Fluorescence Imaging of Mammalian Embryos without Compromising Viability. *Nat Biotechnol* (1999) 17:763–7. doi:10.1038/11698
7. Centonze VE, White JG. Multiphoton Excitation Provides Optical Sections from Deeper within Scattering Specimens Than Confocal Imaging. *Biophys J* (1998) 75:2015–24. doi:10.1016/S0006-3495(98)77643-X
8. Cicchi R, Kapsokalyvas D, De Giorgi V, Maio V, Van Wiechen A, Massi D, et al. Scoring of Collagen Organization in Healthy and Diseased Human Dermis by Multiphoton Microscopy. *J Biophoton* (2010) 3:34–43. doi:10.1002/jbio.200910062
9. Tai DCS, Tan N, Xu S, Kang CH, Chia SM, Cheng CL, et al. Fibro-C-Index: Comprehensive, Morphology-Based Quantification of Liver Fibrosis Using Second Harmonic Generation and Two-Photon Microscopy. *J Biomed Opt* (2009) 14:044013. doi:10.1117/1.3183811
10. Balu M, Zachary CB, Harris RM, Krasieva TB, König K, Tromberg BJ, et al. *In Vivo* multiphoton Microscopy of Basal Cell Carcinoma. *JAMA Dermatol* (2015) 151:1068–74. doi:10.1001/jamadermatol.2015.0453
11. Kirkpatrick ND, Brewer MA, Utzinger U. Endogenous Optical Biomarkers of Ovarian Cancer Evaluated with Multiphoton Microscopy. *Cancer Epidemiol Biomarkers Prev* (2007) 16:2048–57. doi:10.1158/1055-9965.EPI-07-0009
12. Chen J, Zhuo S, Chen G, Yan J, Yang H, Liu N, et al. Establishing Diagnostic Features for Identifying the Mucosa and Submucosa of normal and Cancerous Gastric Tissues by Multiphoton Microscopy. *Gastrointest Endosc* (2011) 73: 802–7. doi:10.1016/j.gie.2010.12.016
13. Wu X, Chen G, Lu J, Zhu W, Qiu J, Chen J, et al. Label-free Detection of Breast Masses Using Multiphoton Microscopy. *PLoS One* (2013) 8:e65933. doi:10.1371/journal.pone.0065933
14. Zhuo S, Yan J, Chen G, Chen J, Liu Y, Lu J, et al. Label-free Monitoring of Colonic Cancer Progression Using Multiphoton Microscopy. *Biomed Opt Express* (2011) 2:615–9. doi:10.1364/BOE.2.000615
15. Kantelhardt SR, Leppert J, Kantelhardt JW, Reusche E, Hüttmann G, Giese A. Multi-photon Excitation Fluorescence Microscopy of Brain-Tumour Tissue and Analysis of Cell Density. *Acta Neurochir (Wien)* (2009) 151:253–62. doi:10.1007/s00701-009-0188-6
16. Kantelhardt SR, Leppert J, Krajewski J, Petkus N, Reusche E, Tronnier VM, et al. Imaging of Brain and Brain Tumor Specimens by Time-Resolved Multiphoton Excitation Microscopy *Ex Vivo*1. *Neuro Oncol* (2007) 9: 103–12. doi:10.1215/15228517-2006-034
17. Leppert J, Krajewski J, Kantelhardt SR, Schlaffer S, Petkus N, Reusche E, et al. Multiphoton Excitation of Autofluorescence for Microscopy of Glioma Tissue. *Neurosurgery* (2006) 58:759–67. doi:10.1227/01.NEU.0000204885.45644.22
18. Galli R, Uckermann O, Tamosaityte S, Geiger K, Schackert G, Steiner G, et al. CARS and Non-linear Microscopy Imaging of Brain Tumors. In: European Conference on Biomedical Optics, May 12, 2013 (2013). 89970E. doi:10.1117/12.2031729
19. Uckermann O, Galli R, Mackenroth L, Geiger K, Steiner G, Koch E, et al. Optical Biochemical Imaging: Potential New Applications in Neuro-Oncology. *Eur Assoc Neuro Oncol Mag* (2014) 4:20–6.
20. Jiang L, Wang X, Wu Z, Du H, Wang S, Li L, et al. Label-free Imaging of Brain and Brain Tumor Specimens with Combined Two-Photon Excited Fluorescence and Second Harmonic Generation Microscopy. *Laser Phys Lett* (2017) 14:105401. doi:10.1088/1612-202x/aa7c9a
21. Romeike BFM, Meyer T, Reichart R, Kalff R, Petersen I, Dietzek B, et al. Coherent Anti-stokes Raman Scattering and Two Photon Excited Fluorescence for Neurosurgery. *Clin Neurol Neurosurg* (2015) 131:42–6. doi:10.1016/j.clineuro.2015.01.022
22. Uckermann O, Galli R, Mark G, Meinhardt M, Koch E, Schackert G, et al. Label-free Multiphoton Imaging Allows Brain Tumor Recognition Based on Texture Analysis-A Study of 382 Tumor Patients. *Neuro-Oncology Adv* (2020) 2:2. doi:10.1093/noajnl/vdaa035
23. Payne LS, Huang PH. The Pathobiology of Collagens in Glioma. *Mol Cancer Res* (2013) 11:1129–40. doi:10.1158/1541-7786.MCR-13-0236
24. Huijbers IJ, Iravani M, Popov S, Robertson D, Al-Sarraj S, Jones C, et al. A Role for Fibrillar Collagen Deposition and the Collagen Internalization Receptor Endo180 in Glioma Invasion. *PLoS ONE* (2010) 5:e9808. doi:10.1371/journal.pone.0009808
25. Zhuo S, Chen J, Luo T, Zou D, Zhao J. Multimode Nonlinear Optical Imaging of the Dermis in *Ex Vivo* Human Skin Based on the Combination of Multichannel Mode and Lambda Mode. *Opt Express* (2006) 14:7810–20. doi:10.1364/oe.14.007810
26. Raza SM, Lang FF, Aggarwal BB, Fuller GN, Wildrick DM, Sawaya R. Necrosis and Glioblastoma: a Friend or a Foe? A Review and a Hypothesis. *Neurosurgery* (2002) 51:2–13. doi:10.1097/00006123-200207000-00002
27. Burger PC, Green SB. Patient Age, Histologic Features, and Length of Survival in Patients with Glioblastoma Multiforme. *Cancer* (1987) 59:1617–25. doi:10.1002/1097-0142(19870501)59:9<1617::aid-cncr2820590916>3.0.co;2-x
28. Homma T, Fukushima T, Vaccarella S, Yonekawa Y, Di Patre PL, Franceschi S, et al. Correlation Among Pathology, Genotype, and Patient Outcomes in Glioblastoma. *J Neuropathol Exp Neurol* (2006) 65:846–54. doi:10.1097/01.jnen.0000235118.75182.94
29. Denk W, Strickler JH, Webb WW. Two-Photon Laser Scanning Fluorescence Microscopy. *Science* (1990) 248:73–6. doi:10.1126/science.2321027
30. Zipfel WR, Williams RM, Webb WW. Nonlinear Magic: Multiphoton Microscopy in the Biosciences. *Nat Biotechnol* (2003) 21:1369–77. doi:10.1038/nbt899
31. Zipfel WR, Williams RM, Christie R, Nikitin AY, Hyman BT, Webb WW. Live Tissue Intrinsic Emission Microscopy Using Multiphoton-Excited Native Fluorescence and Second Harmonic Generation. *Proc Natl Acad Sci U.S.A* (2003) 100:7075–80. doi:10.1073/pnas.0832308100
32. Ljosa V, Carpenter AE. Introduction to the Quantitative Analysis of Two-Dimensional Fluorescence Microscopy Images for Cell-Based Screening. *Plos Comput Biol* (2009) 5:e1000603. doi:10.1371/journal.pcbi.1000603
33. Streets AM, Li A, Chen T, Huang Y. Imaging without Fluorescence: Nonlinear Optical Microscopy for Quantitative Cellular Imaging. *Anal Chem* (2014) 86: 8506–13. doi:10.1021/ac5013706
34. Helmchen F, Denk W, Kerr JND. Miniaturization of Two-Photon Microscopy for Imaging in Freely Moving Animals. *Cold Spring Harb Protoc* (2013) 2013: 904–13. doi:10.1101/pdb.top078147
35. Piyawattanametha W, Cocker ED, Burns LD, Barretto RPJ, Jung JC, Ra H, et al. *In Vivo* brain Imaging Using a Portable 29 G Two-Photon Microscope Based on a Microelectromechanical Systems Scanning Mirror. *Opt Lett* (2009) 34: 2309–11. doi:10.1364/ol.34.002309
36. Engelbrecht CJ, Johnston RS, Seibel EJ, Helmchen F. Ultra-compact Fiber-Optic Two-Photon Microscope for Functional Fluorescence Imaging *In Vivo*. *Opt Express* (2008) 16:5556–64. doi:10.1364/oe.16.005556
37. Jung JC, Mehta AD, Aksay E, Stepnoski R, Schnitzer MJ. *In Vivo* Mammalian Brain Imaging Using One- and Two-Photon Fluorescence Microendoscopy. *J Neurophysiol* (2004) 92:3121–33. doi:10.1152/jn.00234.2004
38. Levene MJ, Dombeck DA, Kasischke KA, Molloy RP, Webb WW. *In Vivo* multiphoton Microscopy of Deep Brain Tissue. *J Neurophysiol* (2004) 91: 1908–12. doi:10.1152/jn.01007.2003
39. Murray TA, Levene MJ. Singlet Gradient index Lens for Deep *In Vivo* Multiphoton Microscopy. *J Biomed Opt* (2012) 17:021106. doi:10.1117/1.JBO.17.2.021106
40. Kantelhardt SR, Kalasauskas D, König K, Kim E, Weinigel M, Uchugonova A, et al. *In Vivo* multiphoton Tomography and Fluorescence Lifetime Imaging of Human Brain Tumor Tissue. *J Neurooncol* (2016) 127:473–82. doi:10.1007/s11060-016-2062-8

Conflict of Interest: The authors declare that the research was conducted in the absence of any commercial or financial relationships that could be construed as a potential conflict of interest.

Publisher's Note: All claims expressed in this article are solely those of the authors and do not necessarily represent those of their affiliated organizations, or those of the publisher, the editors and the reviewers. Any product that may be evaluated in this article, or claim that may be made by its manufacturer, is not guaranteed or endorsed by the publisher.

frontiers | Frontiers in Physics

BRIEF RESEARCH REPORT
published: 23 May 2022
doi: 10.3389/fphy.2022.913774

A Theoretical Study of Tunable Brillouin Lasers Based on a Diamond Suspended Waveguide

Wuyue Wang[1,2], Yu Yu[1,2,3], Zhenxu Bai[1,2], Yunfei Li[1,2], Gong Wang[1,2], Kai Li[1,2], Changyu Song[1,2], Zhiyong Wang[1,2], Sensen Li[3], Yuhai Li[3], Tongyu Liu[3], Xiusheng Yan[3], Yulei Wang[1,2] and Zhiwei Lu[1,2]*

[1]Center for Advanced Laser Technology, Hebei University of Technology, Tianjin, China, [2]Hebei Key Laboratory of Advanced Laser Technology and Equipment, Tianjin, China, [3]Science and Technology on Electro-Optical Information Security Control Laboratory, Tianjin, China

In this work we detail the design of a novel, hybrid waveguide structure which enables independent control of phonon modes and optomechanical driving forces, thereby yielding customizable Brillouin coupling over a very broad bandwidth. The Brillouin gain reaches 4400 $W^{-1}m^{-1}$, with tunable phonon frequencies from 1–95 GHz. This hybrid waveguide relies on tuning of its width and enables photon-phonon conversion based on the Brillouin nonlinear effect, and importantly, it can guide and manipulate the phonons emitted by the Brillouin effect on a chip-level device. There is hence excellent potential for this technique to be applied in microwave sources using the on-chip Brillouin photoacoustic coupling mechanism.

Keywords: diamond, tunable, suspended waveguide, optic, Brillouin

OPEN ACCESS

Edited by:
Yufei Ma,
Harbin Institute of Technology, China

Reviewed by:
Mingxuan Cao,
Wuyi University, China
Rui Min,
Beijing Normal University, China

***Correspondence:**
Yu Yu
yuyu1990@hebut.edu.cn

Specialty section:
This article was submitted to Optics and Photonics, a section of the journal Frontiers in Physics

Received: *06 April 2022*
Accepted: *04 May 2022*
Published: *23 May 2022*

Citation:
Wang W, Yu Y, Bai Z, Li Y, Wang G, Li K, Song C, Wang Z, Li S, Li Y, Liu T, Yan X, Wang Y and Lu Z (2022) A Theoretical Study of Tunable Brillouin Lasers Based on a Diamond Suspended Waveguide. Front. Phys. 10:913774. doi: 10.3389/fphy.2022.913774

INTRODUCTION

Stimulated Brillouin scattering (SBS) is a third-order nonlinear optical process that uses the interaction of two photons in a medium to generate new photons and phonons [1–3]. Therefore, the SBS effect can be used to force interaction between acoustic and optical waves, thereby generating higher frequency photons and phonons. Customizable slow light can be generated through techniques such as waveguide SBS photon-phonon coupling [4, 5], radio frequency (RF)-photon signal processing [6, 7], narrow linewidth laser sources [8–10], RF-waveform synthesis [11, 12] and optical frequency comb generators [11, 13, 14]. Silicon is the ideal platform for nanophotonic devices because it is compatible with complementary metal-oxide semi-conductors (CMOS). It enables nanoscale traveling-wave photon-phonon coupling through Brillouin interactions to achieve high-performance signals [1, 15–18]. In the case of nano-scale silicon-based optical waveguides, tight optical confinement results in significantly enhanced Raman and Kerr nonlinearities [19–21]. In 2013, Rakich's group proposed a novel type of photon-phonon hybrid waveguide, which proved for the first time the process of forward SBS (FSBS) nonlinearity and gain in a silicon waveguide [22]. In their work, the structure comprised a suspended waveguide with Si_3N_4 on both sides and Si in the middle. Due to the significant difference in refractive index between silicon ($n = 3.5$) and silicon nitride ($n = 2.0$), the structure tightly confines the optical field mode to the central region of the silicon waveguide. The silicon nitride films on both sides guide the phonons to perform photon-phonon coupling within the silicon waveguide core. The SBS gain reached 2570 $W^{-1}m^{-1}$, and a tunable phonon range of 1–18 GHz was realized.

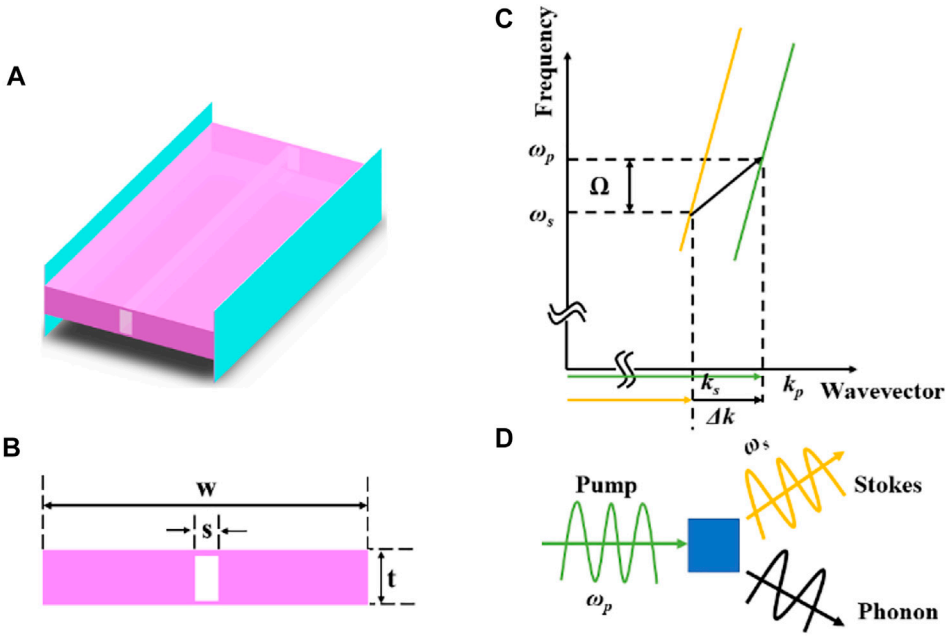

FIGURE 1 | (A) Schematic diagram of the suspended waveguide structure. **(B)** Front view of the suspended waveguide highlighting the internal air slot; $t = 215$ nm, $w = 800$ nm, air slot length $s = 2$ nm. **(C)** Frequency-wavevector plot showing the interaction of the pump, Stokes and phonon waves in the FSBS process; the optical curves represent the optical resonances generated for different spatial modes. **(D)** Schematic diagram of the generation of Stokes and phonon waves produced by the annihilation of a pump wave.

As diamond and silicon both belong to the fourth group of elements, they have many similar optical properties. Compared to silicon, diamond has lower loss and higher nonlinear coefficient across a wide range of operating wavelengths and can be used for highly accurate phase-matching [23]. In addition, diamond has excellent physical and chemical stability, especially with regard to its extremely high thermal stability, enabling it to overcome the inevitable thermal effect which can plague traditional laser gain media at high powers [24, 25]. Meanwhile, its wide spectral transmission range enables the operating wavelength of diamond lasers to cover the ultraviolet, visible to mid-infrared [24, 26]. Moreover, diamond has been proved to be a promising Brillouin material for its high Brillouin gain coefficient and large Brillouin frequency shift [27]. Currently, tens of watts of single-frequency and cascaded Brillouin lasing have been realized in diamond based on free-space structures [27, 28]. However, there are very few studies on the characteristics of diamond Brillouin lasers which employ a waveguide structure. Therefore, it is important to investigate schemes which will yield higher Brillouin gain, especially in the form of highly integrated and tunable on-chip Brillouin lasers.

In this brief report, we detail the design of a novel type of photon-phonon waveguide structure utilizing forward SBS (multi-mode SBS). Here, the optical field is coupled in different spatial modes to achieve the customizable FSBS of a traveling wave. The Brillouin gain reaches 4400 $W^{-1}m^{-1}$, and the generation of phonons with frequencies across the range 1–95 GHz is realized. The simulation results show that the nonlinear (Brillouin) enhancement caused by the radiation pressure due to the design of the structure far exceeds the nonlinear enhancement caused by the material. We believe that this enhanced broadband coherent phonon emission paves the way for hybrid on-chip CMOS signal processing technologies.

THEORETICAL MODEL

The FSBS process involves the interaction between pump, Stokes (or anti-Stokes) and acoustic waves [29, 30]. Specifically, in the FSBS process, the optical waves (pump and Stokes) propagate in the same direction while the acoustic (phonon) wave propagates perpendicular to the optical waves [31, 32]. Phase matching of the FSBS process requires the conservation of energy and momentum yielding the following conditions:

$$\overrightarrow{k_A} = \overrightarrow{k_p} - \overrightarrow{k_s} \tag{1}$$

$$\Omega = \omega_p - \omega_s \tag{2}$$

Where, $\vec{k}_A, \vec{k}_p$ and $\vec{k}_s$ represent pump, Stokes, and acoustic waves, respectively. Considering the propagation direction of optical waves, SBS can be categorized as FSBS and backward SBS (BSBS). In this paper, we only focus on the coupling between modes in FSBS.

For the FSBS process, let us assume that the propagation directions of the pump wave and Stokes wave are both along the z-axis, so the optical wave field of the pump wave and Stokes wave can be described as:

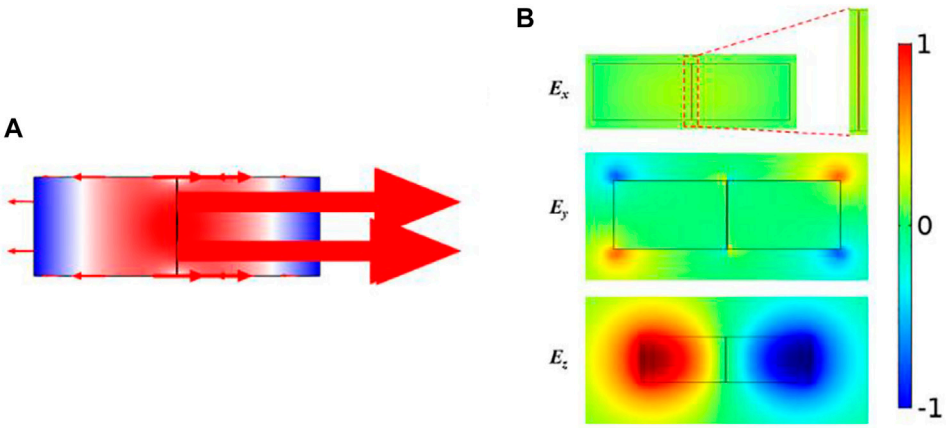

FIGURE 2 | Data obtained showing the radiation pressure distribution of the designed waveguide in the case of an acoustic mode $m = 0$. **(A)** Schematic diagram showing the radiation pressure distribution of the slot waveguide. **(B)** The guiding lateral profile of the fundamental optical mode highlighting the E_x, E_y and E_z field components.

$$E_P(z,t) = \tilde{E}_p(x,y)e^{i(k_p z - \omega_p t)} \tag{3}$$

$$E_s(z,t) = \tilde{E}_s(x,y)e^{i(k_s z - \omega_s t)} \tag{4}$$

Where E_p *(z, t)* is the pump optical wave, and E_s *(z, t)* is the Stokes optical wave. Using small signals as an approximate replacement, when the power of the pump wave in the waveguide is greater than the power of the Stokes wave, the coupling between the two optical waves should meet the following conditions [33]:

$$\frac{dP_p}{dz} = -\left(\alpha + \beta P_p + \gamma P_p^2\right)P_p \tag{5}$$

$$\frac{dP_s}{dz} = \left(\alpha - gP_p + 2\beta P_p + \gamma P_p^2\right)P_s \tag{6}$$

Where P_p and P_s are the power of the pump wave and the power of the Stokes wave respectively, α is the linear loss coefficient of optical wave caused by the structure, size, and other parameters of the material. β and γ are nonlinear loss coefficients (including two-photon absorption and free-carrier absorption). In **Eqn. 6**, g represents the Brillouin gain coefficient, which has a Lorentzian shape and can be expressed as [34]:

$$g(\Omega) = \sum_m G_m \frac{(\Gamma_m/2)^2}{(\Omega - \Omega_m) + (\Gamma_m/2)^2} \tag{7}$$

Ω_m is the characteristic frequency that is satisfied by the total characteristic equation of the acoustic mode when the acoustic loss is ignored. Γ_m is the loss coefficient of acoustic mode when acoustic loss is taken into account [35], depending on the mechanical quality factor Q_m with the relation given as: $Q_m = \frac{\Omega_m}{\Gamma_m}$ [36]; subscript m is the mth acoustic mode ($m = 1,2,3 \ldots\ldots$).

Considering the acoustic loss, the peak value of the SBS gain spectrum can be simplified as follows:

$$G_m = \frac{2\omega Q_m}{\Omega_m^2 V_{gp} V_{gs}} \frac{\left|\langle f, u_m\rangle\right|^2}{\langle E_p, \varepsilon E_p\rangle \langle E_s, \varepsilon E_s\rangle \langle u_m, \rho u_m\rangle} \tag{8}$$

Where V_g, ε, and ρ are the optical group velocity, conductivity and density, respectively. f is the total of the optical forces of the pump and Stokes waves. It is assumed that $\omega_m \approx \omega_s = \omega$ and $\langle X, Y\rangle = \int X^* \cdot Y ds$ integrally cover the entire waveguide cross sectional. It is the overlap integral between the total optical force [37] and a single mth optical eigen-mode, and it represents the optical-mechanical coupling strength of the suspended waveguide [38].

The acoustic displacement field is included in the total optical force, satisfying the phase-matching conditions of **Equations 1**, **2** [35]. To facilitate the calculation u_m, the elastic loss in the isotropic medium can be ignored, and the ideal acoustic equation should satisfy:

$$-\rho\partial_t^2 u_i + \sum_{jkl} \partial_j c_{ijkl} \partial_k u_l = -f_i \tag{9}$$

Where C_{ijkl} denotes the photo-elastic tensor, and f_i is the ith component of the total optical force of the acoustic field ∂_j is the derivative along the *jth* space direction of j, in which $j \in \{x, y, z\}$. When the driving force f_i is absent in **Eqn. 9**, the displacement component u_{mi} of the acoustic field in different modes can be obtained. Hybrid acoustic waves (HAW) include transverse waves and vertical displacement components which are excited in the waveguide structures.

To more clearly describe **Eqn. 8** and **8** can be transformed into:

$$G_m = C_{OT_m}\left|Q_{C_m}\right|^2 \tag{10}$$

Where $Q_{Cm} = \langle f, u_m\rangle$ denotes the influence of optomechanical coupling on G_m, while $C_{OT_m} = C_{FV_m} C_{EF_m}$ is the influence of other factors (including optical group velocity, material quality factor, optical energy flow, and phonon energy flow) on G_m, where, $C_{FV_m} = \frac{2\omega Q_m}{\Omega_m^2 v_{gp} v_{gs}}$, $C_{EF_m} = \frac{1}{\langle E_p, \varepsilon E_p\rangle \langle E_s, \varepsilon E_s\rangle \langle u_m, \rho u_m\rangle}$. From the two parameters in the above expression, we can see that in the waveguide structure, the angular frequency, the group velocity of the optical waves, the energy flow of the optical and acoustic waves, and the characteristics of the waveguide material are all related to C_{OTm}.

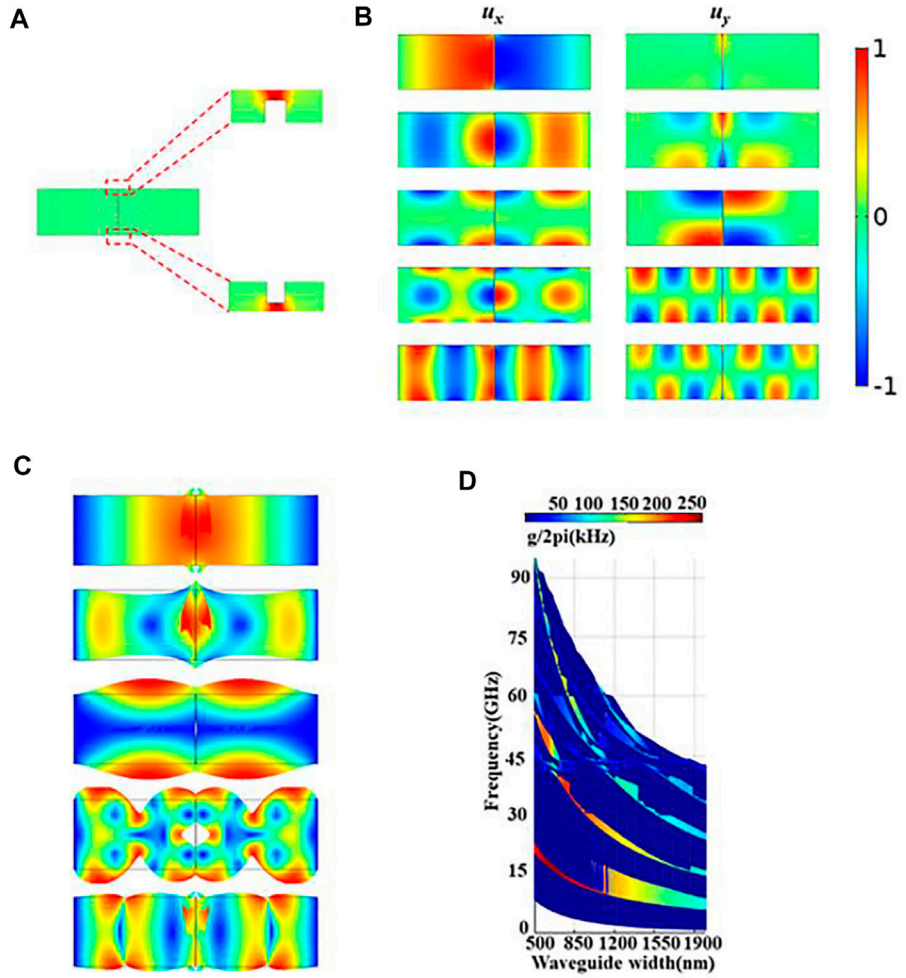

FIGURE 3 | (A) Distribution diagram of the total optical force within the waveguide. **(B)** Displacement diagrams of phonons in the *x* and *y* directions for each mode. **(C)** Representations of the mode distribution diagram of each acoustic mode determined in b which satisfies phase matching when the waveguide width is 800 nm. **(D)** Finite element simulation of the photoacoustic coupling rate varying with the width of the waveguide in the slot waveguide structure. The depth of the color represents the coupling efficiency.

In the suspended waveguide structure, the linear sum of all overlap integrals between a single optical force and the *m*th acoustic eigenmode during the optical-mechanical coupling process can be expressed as:

$$Q_{C_m} = \sum_n \langle f^n, u_m \rangle \tag{11}$$

It is worth noting that the contribution of a single overlap integral depends on the optical force, and its relative phase is affected by interference effects. In a nano-level waveguide, the Brillouin gain coefficient in **Eqn. 8** needs to consider two influencing factors: the electrostriction force and the radiation pressure, namely $f^{Total} = f^{PE} + f^{MB}$. Electrostriction is the secondary response of mechanical strain excited by an external electric field. The *i*th component of the electrostriction force is defined as [39]:

$$f_i^{PE} = -\sum_{ij} \frac{\partial}{\partial j} \sigma_{ij} \tag{12}$$

Where σ_{ij} is the electrostriction tensor that is given by:

$$\sigma_{ij} = -\frac{1}{4}\varepsilon_0 \varepsilon_r^2 p_{ijkl}\left(E_{pk}E_{sl}^* + E_{pl}E_{sk}^*\right) \tag{13}$$

Where p_{ijkl} denotes the photo-elastic tensor, and ε_r and ε_0 are the relative permittivity and vacuum permittivity of the material respectively. Since common materials used in integrated photonics have either a cubic crystalline lattice (e.g., silicon) or are isotropic (e.g., silica glass), and most waveguide structures are fabricated to be aligned with the principal axes of the material, we consider the crystal material of the waveguide to have spatial symmetry. p_{ijkl} is zero if it contains odd number of a certain component, and **Eqn. 13** can be written as:

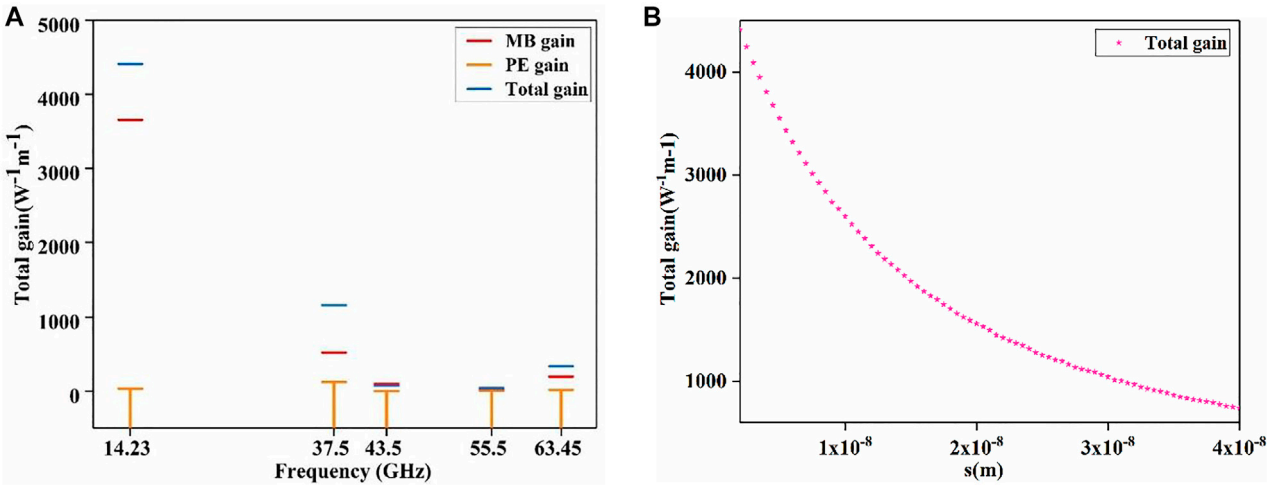

FIGURE 4 | (A) Plot showing the Brillouin gain as a function of frequency with the waveguide width set to w = 800 nm; the red line represents the MB effect, the orange line the PE effect, and the blue line the total gain. **(B)** Calculated FSBS gain coefficients as the width of the air slot s is varied.

$$\begin{bmatrix}\sigma_{xx}\\ \sigma_{yy}\\ \sigma_{zz}\\ \sigma_{yz}\\ \sigma_{xz}\\ \sigma_{xy}\end{bmatrix} = -\frac{1}{2}\varepsilon_0 n^4 \begin{bmatrix} p_{11} & p_{12} & p_{13} & & & \\ p_{12} & p_{22} & p_{23} & & & \\ p_{13} & p_{23} & p_{33} & & & \\ & & & p_{44} & & \\ & & & & p_{55} & \\ & & & & & p_{66}\end{bmatrix} \times \begin{bmatrix} E_{px}E_{sx}^* \\ E_{py}E_{sy}^* \\ E_{pz}E_{sz}^* \\ E_{py}E_{sz}^* + E_{pz}E_{sy}^* \\ E_{px}E_{sz}^* + E_{pz}E_{sx}^* \\ E_{px}E_{sy}^* + E_{py}E_{sx}^* \end{bmatrix} \tag{14}$$

When the acoustic wave with frequency Ω excited by the electrostriction body force propagates, the dielectric constant inside the bulk medium changes by $\Delta\varepsilon$. In this process, the photon-phonon interaction mainly occurs inside the medium. The electrostriction force is generated by the dynamic mechanical response of the medium to the optical waves, and the relative permittivity inside the medium changes so that a complex spatial force distribution occurs inside the medium. Its magnitude and direction are determined by the photo-elasticity tensor of the material, and the electrostriction body force becomes $f^{PE}e^{i(qx-\Omega t)}$ according to **Eqn. 14**, with vector components:

$$\begin{aligned} f_x^{PE} &= -iq\sigma_{xx} - \partial_y\sigma_{xy} - \partial_z\sigma_{xz} \\ f_y^{PE} &= -iq\sigma_{xy} - \partial_y\sigma_{yy} - \partial_z\sigma_{yz} \\ f_z^{PE} &= -iq\sigma_{xz} - \partial_y\sigma_{zy} - \partial_z\sigma_{zz} \end{aligned} \tag{15}$$

Radiation pressure acts only on boundaries where the gradient of ε_r is not equal to zero [40]. It can be derived from the Maxwell tensors between material 1 and 2, which can be written as:

$$f_i^{\mathrm{MB}} = \left(T_{2ij} - T_{1ij}\right)n_j \tag{16}$$

$$T_{ij} = \varepsilon_0\varepsilon_r\left(E_iE_j - \frac{1}{2}\sigma_{ij}E^2\right) \tag{17}$$

Where n is the normal vector points from material one to material 2. For the waveguide with constant horizontal direction, only the transverse component of the force can contribute to the SBS gain coefficient.

RESULTS

The factors affecting SBS gain mainly include electrostriction force and radiation pressure. Since waveguide size needs to reach the order of micrometers to nanometers, the SBS nonlinearity caused by the material will be weakened, resulting in lower SBS gain of the entire waveguide. So we need to design some specific structures to increase the SBS gain. At the micro-nanometer scale, the SBS nonlinearity caused by radiation pressure also plays a key role. Our waveguide model adds an air slot in the center of the waveguide, this results in an increase in the radiation pressure, and the contribution to the SBS nonlinearity caused by the radiation pressure is much higher than that from the material itself. In addition, the use of suspended waveguides better promote photon-phonon coupling because the suspended waveguide better confines the optical field and the acoustic field in the waveguide in comparison to a waveguide within the substrate [41].

As shown in **Figure 1A**, the Brillouin laser system is made from a diamond wafer. The diamond parameters are as follows: Young's modulus E = 1,220 GPa, Poisson's ratio ν = 0.07, density ρ = 3515 kg/m^3, photo-elastic tensor p_{11} = −0.249, p_{12} = 0.043, p_{44} = −0.172, relative Permittivity ε = 5.86. The outline of the air slot is shown in **Figure 1B**. The thickness of the diamond wafer was t = 215 nm, wafer width w = 800 nm, and width of the air slot s = 2 nm. The waveguide width was variable with width w = 500–2,000 nm, and the displacement field associated with the waveguide mode satisfying the phase matching relationship is shown in **Figure 1C**. In the FSBS, the m = 0 order acoustic mode phase-matching conditions are shown in **Eqs. 1**, **2**. This multi-

mode, suspended waveguide provides low-loss guidance for different types of acoustic modes, resulting in higher mechanical quality factor (Q_m) cavity modes with altered free-spectral-range (FSR). As shown in **Figure 1D**, when the pump wave with frequency ω_p was injected into the slot waveguide, a beat frequency signal with frequency Ω was generated. Under the action of the beat frequency signal, an optical force was be generated in the waveguide, and the exciting optical force caused the waveguide material compress or expand, creating an acoustic signal:

Finite Element Simulation using COMSOL software was applied to examine the in the inter-mode FSBS; here the pump and the Stokes waves were injected into the optical waveguide as different modes. At the time, the incident pump frequency, Stokes frequency, and the generated phonon frequency satisfy **Eqs. 1**, **2** (s = 2 nm, w = 800 nm). To simplify the calculation, we assumed that the optical quality factor Q = 1,000 and the transformation of the eigenfrequency of the optical mode did not affect the optical quality factor Q. By examining the results shown in **Figure 2A**, it was found that the radiation pressure at the central air slot was significantly higher than that compared to other sections. **Figure 2B** shows the distribution diagram of the electric field components when m = 0 (basic optical mode). It can be observed that both optical and acoustic waves were guided in the thin film waveguide of **Figure 1A**. The optical wave was confined in the air slot by total internal reflection, guiding the TE-like optical mode. This produced strong Brillouin coupling, which significantly improved the photon-phonon coupling efficiency.

We calculated the total optical force as shown in **Figure 3A**. The result was consistent with the previous conjecture. Due to the existence of an air slot, most of the optical force was concentrated in the air slot. The acoustic displacement presented a symmetric and anti-symmetric spatial pattern in different directions for different acoustic modes. These are plotted in **Figure 3B**, and the pump wave is 1,550 nm. Efficient selection of waveguide and acoustic modes enables autonomous regulation of the photon-phonon coupling. As shown in **Figure 3C**, when the waveguide width was 800 nm, the slot waveguide exhibited five acoustic modes (m = 5) under the action of the PE and the MB effect. Especially between the first-order acoustic breathing mode and the TE optical mode, the strain component of the acoustic and the optical mode had a significant overlap integral, which significantly improved the photon-phonon coupling efficiency. **Figure 3A** and **Figure 3B** show that the higher the degree of agreement between the optical force and acoustic mode distribution, the higher the photon-phonon coupling efficiency. In the case of the first-order acoustic mode, the optical force and the acoustic displacement distribution in this mode had a very high degree of overlap. At the same time, with the increase of the mode order, the overlap integral of the optical force and the acoustic displacement became smaller, so the degree of Brillouin coupling gradually decreased. Since optical fields are symmetrically distributed in space, only the acoustic field modes with symmetry or anti-symmetry can produce effective Brillouin coupling with the optical field, as shown in **Figure 3C**. When the Brillouin spectrum changes with the size of the waveguide, a Brillouin resonance of 1–95 GHz is produced, achieving unprecedented nonlinear tunability. For example, in the case of the first-order acoustic mode, when the waveguide, initially 2000 nm wide, becomes 500 nm wide, the frequency of the acoustic wave shifts from 6.14 to 22.8 GHz, and a strong Brillouin resonance occurs at this frequency. In **Figure 3D**, it can be observed that in the case of the first-order acoustic mode, the photon-phonon coupling efficiency reaches the maximum, which is due to the optical force distribution mentioned above and the modal distribution of the acoustic wave being very consistent.

In the case where the optical quality factor was set to Q = 1,000 and the waveguide width was set to w = 800 nm, the resultant Brillouin gain is as shown in **Figure 4A**. In the case of a first-order mode, the Brillouin gain reaches a maximum of 4400 $W^{-1}m^{-1}$. It can be seen that the gain is mainly produced by the MB effect, while the Brillouin gain produced by the PE effect is minimal. With the increase in the mode order, the Brillouin gain gradually decreases. This is due to the mismatch of the optical force distribution due to the complicated profile of the model in space so that the rapid spatial oscillation of the elastic mode largely offsets the overlap integral. At the same time, it can be observed that in the case of the third-order acoustic mode, the partial gain (SBS nonlinearity caused by the radiation pressure) exceeds the total gain. This is due to the coupling between the third-order breathing mode and the surrounding TE modes, the competition between the photo-elastic effect, and the moving boundary effect [42]. The boundary and volume integrand have opposite phases for this geometry, causing a self-canceling effect.

Next, the effect of the air slot width s on the FSBS gain coefficient was studied. We fixed the geometric size letting w = 800 nm and t = 215 nm. Then we varied s from 2 to 40 nm and calculated the FSBS gain coefficients. The corresponding FSBS gain coefficients are plotted in **Figure 4B**. The results show that as the air slot width S decreased, the total Brillouin gain decreased. This strong photon-phonon coupling phenomenon is produced by the combined action of electrostriction force and nanoscale radiation pressure, and the narrow air slot in the middle has considerable radiation pressure. The emergence of large radiation pressure-induced coupling represents a new form of boundary-induced Brillouin nonlinearity and a new form of boundary-mediated Brillouin coupling in subwavelength structures. This novel waveguide geometry enables independent control of acoustic modes and optomechanical driving forces, creating customizable Brillouin coupling over a 1–95 GHz bandwidth. The finite element simulations show that the FSBS effect is produced in the suspended slot waveguide and the obtained SBS gain reaches 4400 $W^{-1}m^{-1}$.

CONCLUSION

In this work, we designed a novel hybrid waveguide system. We demonstrated a Brillouin laser with a slot waveguide structure, which leveraged the favorable refractive index and the photo-elastic characteristics of diamond to

generate a broad Brillouin frequency shift. The design uses the FSBS effect and by adjusting the cross-sectional width of the slot waveguide, achieves tuning of the frequency of the SBS acoustic wave. Multiphysics simulations reveal that the strength of photon-phonon coupling is dependent on the combined action of electrostriction force and nanoscale radiation pressure, with the narrow air slot in the middle of the waveguide generating considerable radiation pressure. The photon-phonon coupling induced by significant radiation pressure is a new form of Brillouin coupling which is induced by boundary-induced Brillouin nonlinearity and subwavelength structures. This suspended waveguide structure enables independent control of the acoustic wave and enables customizable Brillouin coupling over an ultra-wide bandwidth of 1–95 GHz. According to the PE and MB effect, the SBS laser of this slot waveguide shows an SBS gain of 4400 $W^{-1}m^{-1}$. At the same time, multiple transverse acoustic modes were coupled to produce relatively flat Brillouin gain across the 1–95 GHz frequency range. Therefore, this slot waveguide width tuning scheme can yield photon-phonon conversion based on the Brillouin nonlinear effect and guide and manipulate the phonons emitted by the Brillouin process on a chip. Therefore, we believe that this technique provides a means by which microwave sources can be produced via an on-chip Brillouin photoacoustic coupling mechanism.

DATA AVAILABILITY STATEMENT

The raw data supporting the conclusions of this article will be made available by the authors, without undue reservation.

AUTHOR CONTRIBUTIONS

WW: Investigation, Methodology, Writing—original draft, Writing—review and editing. YY: Conceptualization, Methodology, Writing—review and editing, Supervision, Funding acquisition. ZB: Investigation, Methodology, Writing—review and editing. YL: Writing—review and editing, Supervision. GW: Writing—review and editing, Supervision. KL: Investigation. CS: Investigation. ZW: Investigation. SL: Investigation. YL: Investigation. TL: Investigation. XY: Investigation. YW: Supervision, Funding acquisition. ZL: Supervision, Funding acquisition.

FUNDING

This work was supported by the National Natural Science Foundation of China (Grant No. 62005074, No. 61927815, No. 62075056, and No. 62004059), Natural Science Foundation of Hebei Province (No. F2021202002) and National Defense Science and Technology Key Laboratory Foundation (No. 61421070302).

REFERENCES

1. Eggleton BJ, Poulton CG, Pant R. Inducing and Harnessing Stimulated Brillouin Scattering in Photonic Integrated Circuits. *Adv Opt Photon* (2013) 5(4):536–87. doi:10.1364/aop.5.000536
2. Bai Z, Yuan H, Liu Z, Xu P, Gao Q, Williams RJ, et al. Stimulated Brillouin Scattering Materials, Experimental Design and Applications: A Review. *Opt Mater* (2018) 75:626–45. doi:10.1016/j.optmat.2017.10.035
3. Cao C, Wang Y, Bai Z, Li Y, Yu Y, Lu Z. Developments of Picosecond Lasers Based on Stimulated Brillouin Scattering Pulse Compression. *Front Phys* (2021) 9:747272. doi:10.3389/fphy.2021.747272
4. Okawachi Y, Bigelow MS, Sharping JE, Zhu Z, Schweinsberg A, Gauthier DJ, et al. Tunable All-Optical Delays via Brillouin Slow Light in an Optical Fiber. *Phys Rev Lett* (2005) 94:153902. doi:10.1103/physrevlett.94.153902
5. Song KY, Herraez MG, Thevenaz L. Observation of Pulse Delaying and Advancement in Optical Fibers Using Stimulated Brillouin Scattering. *Opt Express* (2005) 13:82–8. doi:10.1364/opex.13.000082
6. Zhu Z, Gauthier DJ, Boyd RW. Stored Light in an Optical Fiber via Stimulated Brillouin Scattering. *Science* (2007) 318:1748–50. doi:10.1126/science.1149066
7. Liu B, Geng Y, Zhang Q, Han X, Xu J, Zhou H, et al. All-optical Carrier Recovery for Self-Homodyne Detection via Injection Locked Brillouin Laser in Whispering-Gallery-Mode Microcavity. *Chinese Optics Letters* (2021) 19(11): 111901. doi:10.3788/col202119.111901
8. Kobyakov A, Sauer M, Chowdhury D. Stimulated Brillouin Scattering in Optical Fibers. *Adv Opt Photon* (2009) 2:1–59. doi:10.1364/aop.2.000001
9. Lee H, Chen T, Li J, Yang KY, Jeon S, Painter O, et al. Chemically Etched Ultrahigh-Q Wedge-Resonator on a Silicon Chip. *Nat Photon* (2012) 6: 369–73. doi:10.1038/nphoton.2012.109
10. Grudinin IS, Matsko AB, Maleki L. Brillouin Lasing with a CaF2 Whispering Gallery Mode Resonator. *Phys Rev Lett* (2009) 102:043902. doi:10.1103/PhysRevLett.102.043902
11. Kang MS, Nazarkin A, Brenn A, Russell PSJ. Tightly Trapped Acoustic Phonons in Photonic crystal Fibres as Highly Nonlinear Artificial Raman Oscillators. *Nat Phys* (2009) 5:276–80. doi:10.1038/nphys1217
12. Schneider T, Junker M, Hannover D. Generation of Millimetre-Wave Signals by Stimulated Brillouin Scattering for Radio over Fibre Systems. *Electron Lett* (2004) 40:1500–2. doi:10.1049/el:20046461
13. Braje D, Hollberg L, Diddams S. Brillouin-Enhanced Hyperparametric Generation of an Optical Frequency Comb in a Monolithic Highly Nonlinear Fiber Cavity Pumped by a Cw Laser. *Phys Rev Lett* (2009) 102: 193902. doi:10.1103/physrevlett.102.193902
14. Damzen MJ, Lamb RA, Wong GKN. Ultrashort Pulse Generation by Phase Locking of Multiple Stimulated Brillouin Scattering. *Opt Commun* (1991) 82: 337–41. doi:10.1016/0030-4018(91)90470-x
15. Lang Z, Qiao S, Ma Y. Acoustic Microresonator Based In-Plane Quartz-Enhanced Photoacoustic Spectroscopy Sensor with a Line Interaction Mode. *Opt Lett* (2022) 47(6):1295–8. doi:10.1364/ol.452085
16. Ma Y, He Y, Tong Y, Yu X, Tittel FK. Quartz-tuning-fork Enhanced Photothermal Spectroscopy for Ultra-high Sensitive Trace Gas Detection. *Opt Express* (2018) 26(24):32103–10. doi:10.1364/oe.26.032103
17. Pant R, Poulton CG, Choi D-Y, Mcfarlane H, Hile S, Li E, et al. On-chip Stimulated Brillouin Scattering. *Opt Express* (2011) 19:8285–90. doi:10.1364/oe.19.008285
18. Kang MS, Butsch A, Russell PSJ. Reconfigurable Light-Driven Opto-Acoustic Isolators in Photonic crystal Fibre. *Nat Photon* (2011) 5:549–53. doi:10.1038/nphoton.2011.180
19. Jalali B, Raghunathan V, Shori R, Fathpour S, Dimitropoulos D, Stafsudd O. Prospects for Silicon Mid-IR Raman Lasers. *IEEE J Select Top Quan Electron.* (2006) 12:1618–27. doi:10.1109/jstqe.2006.885340
20. Foster MA, Turner AC, Sharping JE, Schmidt BS, Lipson M, Gaeta AL. Broad-band Optical Parametric Gain on a Silicon Photonic Chip. *Nature* (2006) 441: 960–3. doi:10.1038/nature04932
21. Rong H, Jones R, Liu A, Cohen O, Hak D, Fang A, et al. A Continuous-Wave Raman Silicon Laser. *Nature* (2005) 433:725–8. doi:10.1038/nature03346
22. Shin H, Qiu W, Jarecki R, Cox JA, Olsson RH, Starbuck A, et al. Tailorable Stimulated Brillouin Scattering in Nanoscale Silicon Waveguides. *Nat Commun* (2013) 4:1944. doi:10.1038/ncomms2943
23. Mildren R, Rabeau J, editors. *Optical Engineering of diamond*. John Wiley & Sons (2013). doi:10.1002/9783527648603

24. Williams RJ, Kitzler O, Bai Z, Sarang S, Jasbeer H, McKay A, et al. High Power diamond Raman Lasers. *IEEE J Selected Top Quan Electron* (2018) 24(5): 1602214. doi:10.1109/jstqe.2018.2827658
25. Bai Z, Zhang Z, Wang K, Gao J, Zhang Z, Yang X, et al. Comprehensive thermal Analysis of diamond in a High-Power Raman Cavity Based on FVM-FEM Coupled Method. *Nanomaterials* (2021) 11(6):1572. doi:10.3390/nano11061572
26. Li Y, Bai Z, Chen H, Jin D, Yang X, Qi Y, et al. Eye-safe diamond Raman Laser. *Results Phys* (2020) 16:102853. doi:10.1016/j.rinp.2019.102853
27. Bai Z, Williams RJ, Kitzler O, Sarang S, Spence DJ, Wang Y, et al. Diamond Brillouin Laser in the Visible. *APL Photon* (2020) 5(3):031301. doi:10.1063/1.5134907
28. Chen H, Bai Z, Yang X, Ding J, Qi Y, Yan B, et al. Enhanced Stimulated Brillouin Scattering Utilizing Raman Conversion in diamond. *Appl Phys Lett* (2022) 120(18):181103. doi:10.1063/5.0087092
29. Parameswaran KR, Route RK, Kurz JR, Roussev RV, Fejer MM, Fujimura M. Highly Efficient Second-Harmonic Generation in Buried Waveguides Formed by Annealed and Reverse Proton Exchange in Periodically Poled Lithium Niobate. *Opt Lett* (2002) 27(3):179–81. doi:10.1364/ol.27.000179
30. Miller GD, Batchko RG, Tulloch WM, Weise DR, Fejer MM, Byer RL. 42%-efficient Single-Pass Cw Second-Harmonic Generation in Periodically Poled Lithium Niobate. *Opt Lett* (1997) 22(24):1834–6. doi:10.1364/ol.22.001834
31. Eggleton BJ, Poulton CG, Rakich PT, Steel MJ, Bahl G. Brillouin Integrated Photonics. *Nat Photon* (2019) 13(15):1–14. doi:10.1038/s41566-019-0498-z
32. Damzen MJ, Vlad V, Mocofanescu A. *Stimulated Brillouin Scattering: Fundamentals and Applications*. CRC Press (2010). doi:10.1201/9781420033465
33. Mirnaziry SR, Wolff C, Steel MJ, Eggleton BJ, Poulton CG. Stimulated Brillouin Scattering in Silicon/chalcogenide Slot Waveguides. *Opt Express* (2016) 24(5):4786–800. doi:10.1364/oe.24.004786
34. Agrawal GP. *Nonlinear Fiber Optics*, IV. Academic Press (2006).
35. Zhou L, Lu Y, Fu Y, Ma H, Du C. Design of a Hybrid On-Chip Waveguide with Giant Backward Stimulated Brillouin Scattering. *Opt Express* (2019) 27(18): 24953. doi:10.1364/oe.27.024953
36. Qiu W, Rakich PT, Shin H, Dong H, Soljačić M, Wang Z. Stimulated Brillouin Scattering in Nanoscale Silicon Step-index Waveguides: A General Framework of Selection Rules and Calculating SBS Gain. *Opt Express* (2013) 21(25): 31402–19. doi:10.1364/oe.21.031402
37. Aryanfar I, Wolff C, Steel MJ, Eggleton BJ, Poulton CG. Mode Conversion Using Stimulated Brillouin Scattering in Nanophotonic Silicon Waveguides. *Opt Express* (2014) 22:29270–82. doi:10.1364/oe.22.029270
38. Yu Z, Sun X. Giant Enhancement of Stimulated Brillouin Scattering with Engineered Phoxonic crystal Waveguides. *Opt Express* (2018) 26(2): 1255–67. doi:10.1364/oe.26.001255
39. Rakich PT, Davids P, Wang Z. Tailoring Optical Forces in Waveguides through Radiation Pressure and Electrostrictive Forces. *Opt Express* (2010) 18(14):14439–53. doi:10.1364/oe.18.014439
40. Gordon JP. Radiation Forces and Momenta in Dielectric media. *Phys Rev A* (1973) 8(1):14–21. doi:10.1103/physreva.8.14
41. Wang W, Yu Y, Li Y, Bai Z, Wang G, Li K, et al. Tailorable Brillouin Light Scattering in a Lithium Niobate Waveguide. *Appl Sci* (2021) 11(18):8390. doi:10.3390/app11188390
42. Gao W, Chen L, Jiang W, Zhang Z, Zhang X, Gao P, et al. Stimulated Brillouin Scattering by the Interaction between Different-Order Optical and Acoustical Modes in an As2Se3 Photonic crystal Fiber. *Chin Opt Lett* (2020) 18(1):010602. doi:10.3788/col202018.010602

Conflict of Interest: The authors declare that the research was conducted in the absence of any commercial or financial relationships that could be construed as a potential conflict of interest.

frontiers | Frontiers in Physics

ORIGINAL RESEARCH
published: 25 May 2022
doi: 10.3389/fphy.2022.914970

100 kHz Narrow-Linewidth Burst-Mode MOPA Laser System With Uniform Envelope

Xin Yu [1,2], Shanchun Zhang [1,2], Jiangbo Peng [1,2], Zhen Cao [1,2], Long Gao [1,2] and Wenbei Liu [1,2]*

[1]National Key Laboratory of Science and Technology on Tunable Laser, Harbin Institute of Technology, Harbin, China, [2]Institute of Opt-Electronics, Harbin Institute of Technology, Harbin, China

In this study, a 100-kHz narrow-linewidth burst-mode laser system combined with a master oscillator power amplifier (MOPA) structure was reported with a stable pulse burst profile over 2 ms duration. A theoretical model was established to characterize and compensate the variation characteristics of coefficient of variation (COV) within a burst envelope for the double-pass three-stage amplification system, in terms of different parameter factors. Simulated results yielded similar tendency with the measured ones. For a stable burst envelope with a COV of 2.72% and 2.93%, output pulse energy at a 100 kHz repetition rate was scaled up to 1.08 and 4.38 mJ in the case of an input average pulse energy of 8.6 and 116.51 nJ, respectively. Corresponding M_x^2 and M_y^2 values with 2.2 and 2.4 were endowed with 1.08 mJ output single-pulse energy and 2.7 and 2.1 for 4.38 mJ pulse energy. The spectral linewidth of amplified pulses was measured to be less than 83.1 and 67.9 MHz, with respect to output pulse duration of 10.3 and 96.1 ns, respectively.

Keywords: burst-mode, narrow-linewidth, double-pass amplification, MOPA, COV

OPEN ACCESS

Edited by:
Qun Hao,
Beijing Institute of Technology, China

Reviewed by:
Xinzhong LI,
Henan University of Science and Technology, China
Lifa Hu,
Jiangnan University, China
Fei Chen,
Changchun Institute of Optics, Fine Mechanics and Physics (CAS), China

****Correspondence:***
Jiangbo Peng
pengjiangbo@hit.edu.cn

Specialty section:
This article was submitted to Optics and Photonics, a section of the journal Frontiers in Physics

Received: *07 April 2022*
Accepted: *22 April 2022*
Published: *25 May 2022*

Citation:
Yu X, Zhang S, Peng J, Cao Z, Gao L and Liu W (2022) 100 kHz Narrow-Linewidth Burst-Mode MOPA Laser System With Uniform Envelope. Front. Phys. 10:914970. doi: 10.3389/fphy.2022.914970

1 INTRODUCTION

The parameter measurements (e.g., temperature, velocities, and mixture fraction) for high-speed flows have greatly boosted the advancements of aerospace and scramjet by use of optical imaging techniques [1–6]. Especially, the solid-state laser system, with a high rate and high energy [7–11], has great potential for optical diagnostic applications, such as planar laser-induced fluorescence (PLIF) [12–14], particle imaging velocimetry (PIV) [15, 16], and filtered Rayleigh scattering (FRS) [17, 18]. Among those measuring techniques, FRS serves as a promising approach in imaging high-speed reacting flames and non-reacting jets for its strong suppression in background noise, with the same wavelength as an input laser, from the Mie scattering and windows and highlights weaker broadened Rayleigh–Brillouin scattering (RBS) signal intensity. Typically, the turbulent reacting and non-reacting flow fields are commonly featured with frequencies up to hundreds of kilohertz [19], and the adopted laser sources are required with high-rate operation to enable high temporal resolution for sufficient analysis of time-varying flow information *via* the FRS imaging technique. In addition, the collected FRS imaging intensity is dependent on pulsed laser energy, which allows for the laser system with high-energy pulses to enhance the signal-to-noise ratio (SNR) in supersonic–hypersonic flow fields. As a result of advancement in the diode-pumped solid-state (DPSS) laser, it is capable of producing a pulsed laser with frequencies up to tens to hundreds of kilohertz [20, 21]. However, severe thermal loading at the high repetition rate comes into formation in the gain module to further constrain high-energy pulse laser generation.

The burst-mode technique, coupled with DPSS sources, can provide an effective method for both high-rate and high-energy pulsed laser, which is filled with multiple benefits featured with high efficiencies and significant beam characteristics compared with a traditional repetitively Q-switched continuously pulsed laser. Hence, such an effective pulse burst laser has attracted much more interests for achieving high repetition rate with significant pulse energy at low average power, by integrating a series of pulses into a burst envelope and reducing the duty cycle for thermal dissipation. In 2014, Slipchenko et al reported a 100-kHz dual-wavelength diode-pumped Nd:YAG burst-mode laser centered at 1,064 nm, with average pulse energy as high as 40 mJ per pulse over 100 ms burst duration [22]. In 2017, Wu et al illustrated a 100-kHz cavity-dumped burst-mode laser system with 2 ms burst duration, realizing the maximum pulse energy of 9.47 mJ per pulse and the energy extraction efficiency of 30% [23]. In 2019, Smyser et al investigated a burst-mode laser system for generating a high-peak power pulse laser, from which peak power reached 1.24 GW at the 100-kHz repetition rate over 1 ms burst duration with a transform-limited pulse width of 234 fs [24].

In supersonic–hypersonic flow field diagnosis, the FRS scheme necessitates to put forward some additional requirements for performances of laser sources further (e.g., narrow spectral linewidth, stable burst envelope, and so on). Specifically, such narrow-linewidth sources can enhance the transmission purity of stimulated RBS with a temperature-based thermal broadening spectral profile, when a molecular iodine vapor cell serves as a filtering narrow-linewidth background with a similar spectrum to that of the input laser and stable pulse-to-pulse intensity distribution benefits a series of time-relevant uniform FRS imaging intensity within recorded length. In the burst-mode laser system, a short-cavity oscillator based on Q-switching could provide with high-energy pulses, as illustrated in [25, 26], while seeding of those Q-switching lasers is restrictive of their applications in which narrow-linewidth is requisite. During burst-mode amplification, it is interestingly found that the first several pulses are endowed with higher- or lower-intensity distribution, resulting in inhomogeneous intensity variation within the burst envelope, which could further yield significant fluctuation of collected imaging intensity for flow field diagnosis. Hence, a theoretical model is built to give possible investigation and compensation for pulse intensity variation in terms of multiple factors, resulting in dynamic equilibrium in both pumping and amplification for a stable burst envelope. The burst-mode laser could play a significant component in optical diagnosis based on the FRS imaging technique, especially for these measuring relevant to multiple parameters in high-speed flow fields. In 2018, Feng et al illustrated the FRS intensity sensitivity to temperature and pressure in hot jets by utilizing a burst-mode source with total burst energy of 20 mJ per burst and 30 pulses within a burst at 63 MHz spectral linewidth [27].

In this work, a 100-kHz burst-mode master oscillator power amplifier (MOPA) laser was illustrated with narrow spectral linewidth for a stable burst envelope. Pulse intensity variation was investigated within the burst envelope theoretically and experimentally for multiple parameter factors. A stable burst envelope was characterized with the coefficient of variation (COV) of 2.72% and 2.93%, with respect to the burst energy of 217.08 and 880.38 mJ per burst at 2 ms duration, respectively. Relevant spectral linewidth was measured to be less than 83.1 and 67.9 MHz.

2 THEORETICAL ANALYSIS

In terms of burst envelope intensity variation, it is investigated starting from pulse amplification. The process of amplification is first based on the energy stored in the gain medium before the arrival of the input beam, and then the pulse is amplified with depletion of some particles when passing through an amplifier. For stored energy, the basic expression illustrated in the study mentioned in reference [28] has been deduced by Mance et al by means of solving the differential equation. If we take into account the necessary energy transfer factors, the stored energy E_{store} could be further developed and presented in **Eq. 1**, where E_i is initial energy storage in gain medium, τ_f is upper-level fluorescence lifetime of the Nd:YAG crystal, P is pump peak power, η_a is absorption efficiency of the input pump beam in active medium, η_s is Stokes transfer efficiency, and η_q is expressed as quantum transfer efficiency.

$$E_{store}(t) = E_i \exp\left(-\frac{t}{\tau_f}\right) + P\tau_f\eta_a\eta_s\eta_q\left(1 - \exp\left(-\frac{t}{\tau_f}\right)\right). \quad (1)$$

Output energy after amplification could be illustrated by the Frantz–Nodvik formula [29, 30] in the case of known input energy E_{in}, saturation energy fluence E_{sat}, pump area S_p, and small signal gain factor G_0, the expression of which is given by

$$E_{out} = E_{sat}S_p \ln\left\{1 + \left[\exp\left(\frac{E_{in}}{E_{sat}S_p}\right) - 1\right]G_0\right\}, \quad (2)$$

where the small signal gain factor G_0 is determined by stored energy E_{store}, saturation energy fluence E_{sat}, and pump area S_p. The nonlinear relationship among these parameters is denoted as follows:

$$G_0 = \exp\left(\frac{E_{store}}{E_{sat}S_p}\right). \quad (3)$$

The pump and amplification cycle for the pulse burst laser is exhibited in **Figure 1A**. To simplify the cycle process, some assumptions are carried out for neglecting the amplified spontaneous emission (ASE) effect and ignoring pump time during pulse laser duration. Initially, there is no energy stored in gain medium, resulting in $E_i = 0$, before pump injecting into the active medium and then stored energy comes into formation during pump time τ (delay time between pumping and the first pulse amplification) by using $E_i = 0$ in **Eq. 1**; after that the first pulse within the burst envelope is amplified through **Eq. 2** on basis of accumulated energy storage. Meanwhile, the remaining energy is endowed as E_i to prepare stored energy for the next pulse during pump time τ_p, and the second pulse reaches its amplification with energy being extracted. Such an iteration process is repeated continuously within the burst envelope until output pulses obey convergence distribution featured

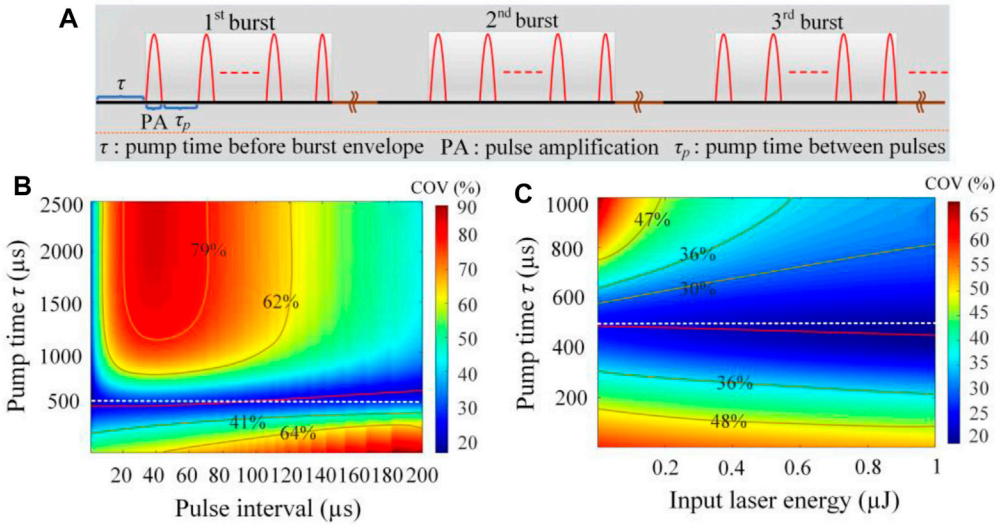

FIGURE 1 | (A) Schematic of the pump and amplification cycle for the pulse burst laser; **(B)** COV versus pump time τ and pulse interval; **(C)** COV versus pump time τ and input seed energy.

TABLE 1 | Basic parameter values used in the simulation.

E_{in} (nJ)	E_{sat} (J/cm^2)	τ_f (μs)	η_q (%)	η_a (%)	η_s (%)
116	0.667	230	90	85	76

with stable tendency. As for double-pass or multistage amplification, an additional process is supplemented here such that the output from the first pass is the input of the second pass and output of the previous stage becomes the input for next stage. Therefore, a model suitable for pulsed pumped amplification could be established to investigate the intensity variation within the burst envelope in diverse burst-mode amplification configurations.

Figure 1B illustrates the dependence of COV (defined as the ratio of standard deviation within the burst envelope into the mean) on pump time τ and pulse interval in the double-pass, three-stage amplification system over 2 ms burst duration based on the aforementioned model. In this simulation, the adopted basic parameter values are given in **Table 1**, and amplifiers are provided with pump areas of 0.071, 0.071, and 0.283. With increasing pump time τ from 1 μs and decreasing from 2,500 μs, the variation of the COV exerts a gradual upward and downward trend, respectively and then finally possesses relatively stable distribution at approximately 500 μs (dashed white line) in the range of the pulse interval from 1 to 200 μs(5 kHz–1 MHz) toward the amplification system with pump peak power of 900 W, 900 W, and 2800 W for constant energy transfer factors. At higher pump time τ, the first few pulses could obtain more stored energy due to high gain in active medium, resulting in less energy for subsequent amplification. Moreover, the opposite could occur in burst-mode amplification with lower pump time τ. The obvious COV variation for different pump time τ, at a specific repetition rate, is mainly due to the lack of dynamic equilibrium in pumping and amplification. Typically, it is conducive to reach high-energy pulse amplification for a low repetition rate. In that case, relatively high pump time τ is required to compensate for the excessive energy extraction to sustain dynamic equilibrium between pumping and amplification within the burst envelope at the low repetition rate compared with high frequency. Hence, there is an increasing trend of pump time τ at stable COV distribution (red line) based on simulated results, with respect to a pump interval range of 1–200 μs (5 kHz–1 MHz).

The COV versus pump time τ and input seed energy is presented in **Figure 1C** at a 100-kHz repetition rate. The COV variation also shows a trend of decreasing first and then increasing in the case of increasing pump time τ from 1 to 1,000 μs for different input laser energy (1 nJ–1 μJ), induced by non-equilibrium for pumping and amplification. At stable COV distribution, pump time τ versus input seed energy is indicated with a red line. With increasing of input laser energy from 1 nJ–1 μJ, the pump time τ for achieving a stable envelope shows a decreasing trend, moving away from the white dashed line gradually (τ = 500 μs). Due to increase of input laser energy, the saturation effect tends to come into formation in pulse amplification, resulting in the burst envelope close to steady-state distribution. Consequently, lower pump time τ is required to compensate for weaker variation within the burst envelope at higher input laser energy. In addition, the variation of the COV is endowed with approximately decreasing tendency at specific pump time τ for increasing the input laser energy in the range of 1 nJ–1 μJ, which might also be attributed to saturation effect.

3 EXPERIMENTAL SETUP

The schematic of the fiber-bulk MOPA burst-mode laser system is presented in **Figure 2**. The fiber laser seed is provided with 24-

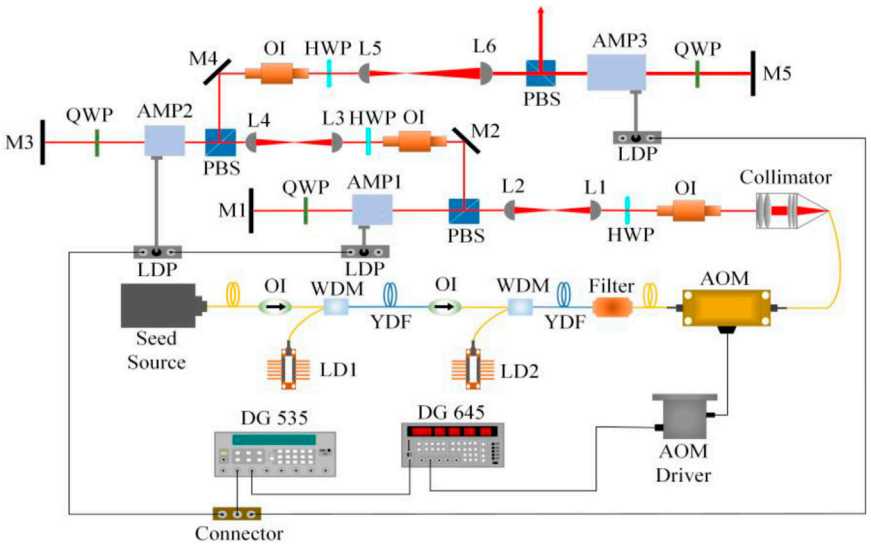

FIGURE 2 | Optical layout of the burst-mode laser system. OI: optical isolator, LD: laser diode, WDM: wavelength division multiplex, YDF: Ytterbium-doped fiber, AOM: acousto-optic modulator, HWP: half-wave plate, PBS: polarizing beam splitter, QWP: quarter-wave plate, AMP: amplifier module, DG: delay generator, and LDP: laser diode power supply.

mW continuous wave (CW) laser centered at 1,064.201 nm with spectral linewidth of less than 10 kHz. The spectral wavelength is tunable over a spanning of 30 GHz by adjusting the voltage imposed on a piezoelectric transducer (PZT) to match the seed laser wavelength. Both the 975-nm laser diodes (LDs) are coupled into two Yb-doped fiber amplification stages to scale CW seed power up to the watt level. A fiber-coupled acousto-optic modulator (AOM) is introduced into the optical path for the slicing-amplified CW laser into a pulse train with arbitrary duration, which is directly controlled by an AOM driver that is dependent on an external SRS DG645 delay generator. The AOM is preferred in enhancing the contrast ratio of laser intensity to the background due to its faster falling edge than the electro-optic modulator (EOM) can do. For an all-fiber system, the used gain fiber and transmission fiber are featured with single longitudinal mode and polarization maintenance, which is with respect to the fiber size of 5/130 μm and a numerical aperture (NA) of 0.12 for gain fiber and 6/125 μm and 0.1 in transmission fiber.

The pulse amplification system consists of three LD side-pumped Nd:YAG modules, with Nd^{3+} doping concentration and rod dimensions of 1 at% and $\Phi 3 \times 67$ mm^2 (AMP1 and AMP2), 1 at% and $\Phi 6 \times 85$ mm^2 (AMP3), respectively. First, two amplifier modules are involved with three diode arrays distributed at an angle of 120° for each other, and the third contains seven diode arrays arranged symmetrically in different directions. All the amplification stages are designed in double-pass configurations for realizing the high-gain pulsed laser. Two pairs of plano-convex lenses (f_{L1} = +50 mm and f_{L2} = +50 mm; f_{L3} = +50 mm and f_{L4} = +50 mm) are responsible for delivering excellent beam characteristics for pulses amplification, while another one (f_{L5} = +100 mm, f_{L6} = +200 mm) is used for matching the pulsed laser with AMP3. The optical isolator (OI) is placed in front of each amplifier so as to prevent feedback of backward beam propagation. Amplified pulses are returned through a 0° reflector with high reflectivity (HR) coated at 1,064 nm and then passed through a quarter-wave plate (QWP) the second time and are eventually reflected by a polarizing beam splitter (PBS), close to AMP3, with the maximum polarization extinction ratio (PER) of more than 30 dB. The operation temperature was set to 25°C for the burst-mode laser amplification system.

For time-sequence controlling of the burst-mode laser system, an SRS DG535 is utilized to offer two channels with a delay time, one is first connected with laser diode power supplies (LDP) for synchronous triggering of pumping, and another one is applied to DG645 for AOM modulation after a delay time. The time controlling on the whole is accomplished using the SRS DG535 delay generator combined with an SRS DG645 delay generator.

4 RESULTS AND DISCUSSION

4.1 Seed Characterization

Output single-pulse energy was measured and plotted in **Figure 3** for different repetition rates over 2 ms burst duration. From the measured results, the obtained pulse energy was provided with an approximately linear increase with the increasing of absorbed pump power and possessed similar distribution at different repetition rates. In **Figure 3A**, the maximum output pulse energy was expressed as 8.61, 8.47, 8.67, and 8.64 nJ for absorbed pump power of 2.53 W at the injected modulation signal with single-pulse duration of 10 ns, with respect to the repetition rate of 10 kHz, 20 kHz, 50 kHz, and 100 kHz, respectively. In the case of injected electric signal varying into 100 ns, the corresponding maximum output pulse energy reached

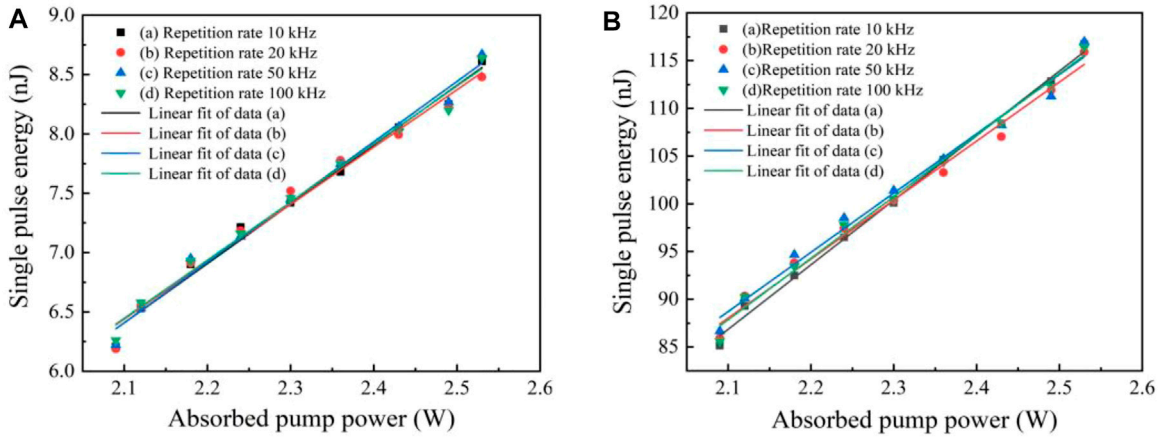

FIGURE 3 | Output single-pulse energy versus absorbed pump power. **(A)** For electric signal input with single-pulse duration of 10 ns. **(B)** At modulation signal input with a single pulse width of 100 ns.

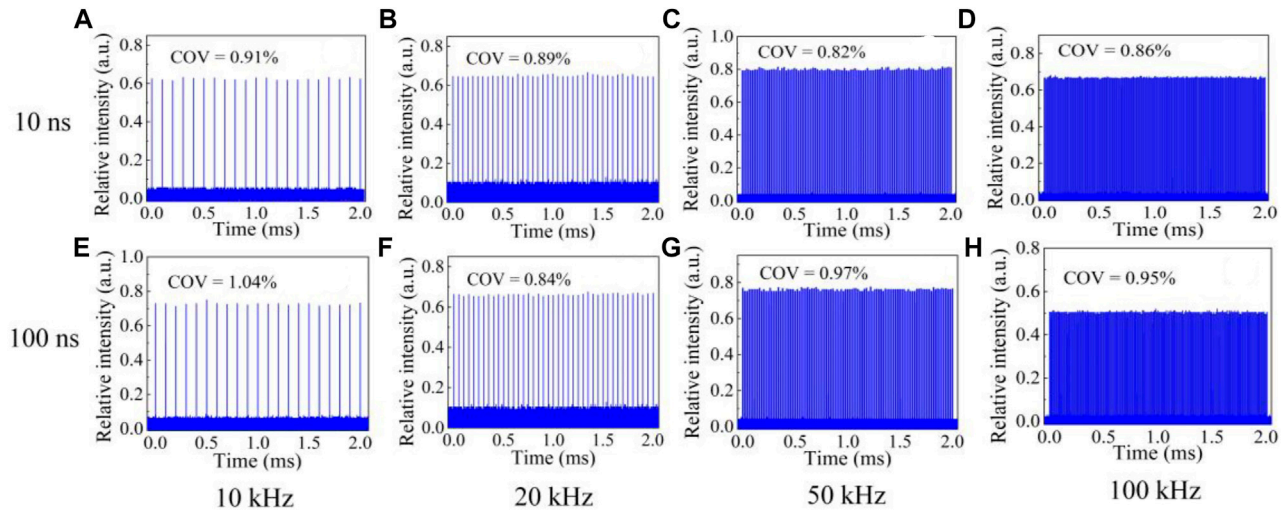

FIGURE 4 | Recorded output pulse-burst profile at different repetition rates in terms of electric signal input with duration of 10 and 100 ns, respectively. **(A)** At 10 kHz repletion rate for 10 ns electric signal input. **(B)** At 20 kHz repletion rate for 10 ns electric signal input. **(C)** At 50 kHz repletion rate for 10 ns electric signal input. **(D)** At 100 kHz repletion rate for 10 ns electric signal input. **(E)** At 10 kHz repletion rate for 100 ns electric signal input. **(F)** At 20 kHz repletion rate for 100 ns electric signal input. **(G)** At 50 kHz repletion rate for 100 ns electric signal input. **(H)** At 100 kHz repletion rate for 100 ns electric signal input.

116.75, 115.92, 116.94, and 116.41 nJ as exhibited in **Figure 3B**, from which the enlarged resulted from the higher-duty cycle in the injected modulation signal.

Figure 4 presented the recorded output burst envelope with 2 ms duration in the range of repetition rates from 10 to 100 kHz, consisting of pulses counts with 21–201. It could be seen that there was no obvious emergence of pulses loss in burst train distribution. As shown in **Figures 4A–D**, the output burst envelope was uniformly distributed with a COV of 0.91%, 0.89%, 0.82%, and 0.86% for the electric signal input of 10 ns, corresponding to 10 kHz, 20 kHz, 50 kHz, and 100 kHz repetition rates, respectively. In terms of the input modulation signal changing into 100 ns, the relevant burst train with a COV of 1.04%, 0.84%, 0.97%, and 0.95% was further formed and exhibited in **Figures 4E–H**, respectively. The recorded output burst envelope was possessed with uniform and flat distribution at the repetition rate of 10–100 kHz, indicating the stable modulation characteristics for the external electric signal input with arbitrary duration.

At the 100-kHz repetition rate, the output individual pulse waveform approximately exerted Gaussian-like distribution as shown in **Figure 5C** due to the faster rising/falling time of 10 ns for the AOM in the case of the external square wave signal input with 10 ns in **Figure 5A**. Moreover, the nearly flat-top pulse

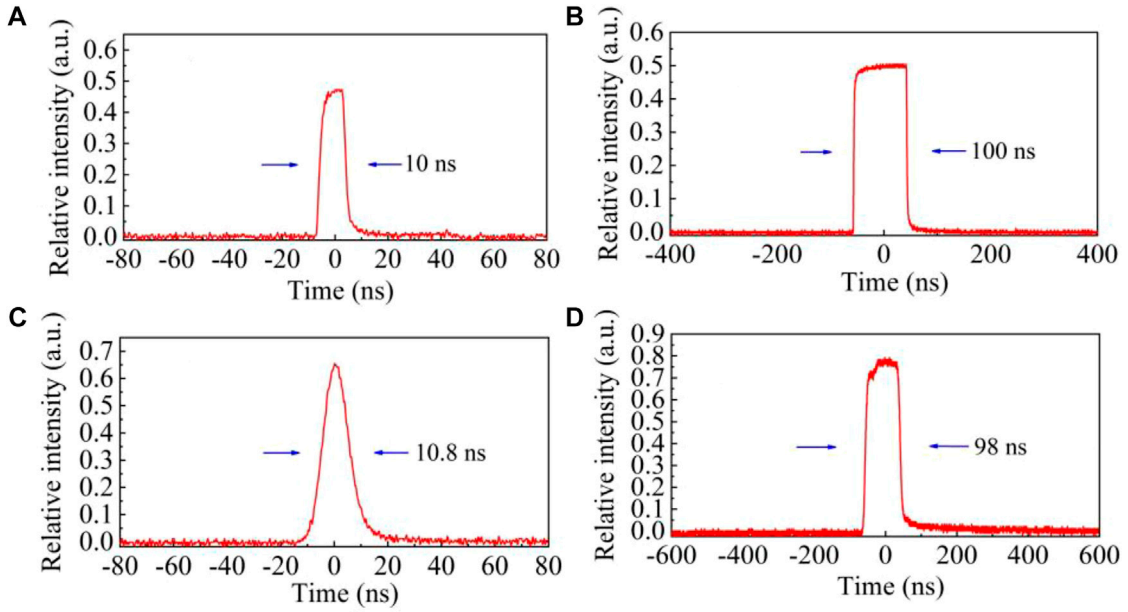

FIGURE 5 | Recorded input electric signal waveform and the output single-pulse laser profile at the 100 kHz repetition rate. **(A)** Input electric signal waveform with duration of 10 ns. **(B)** Input electric signal profile with duration of 100 ns. **(C)** Output single pulse laser with pulse duration of 10.8 ns. **(D)** Output single pulse laser with a pulse width of 98 ns.

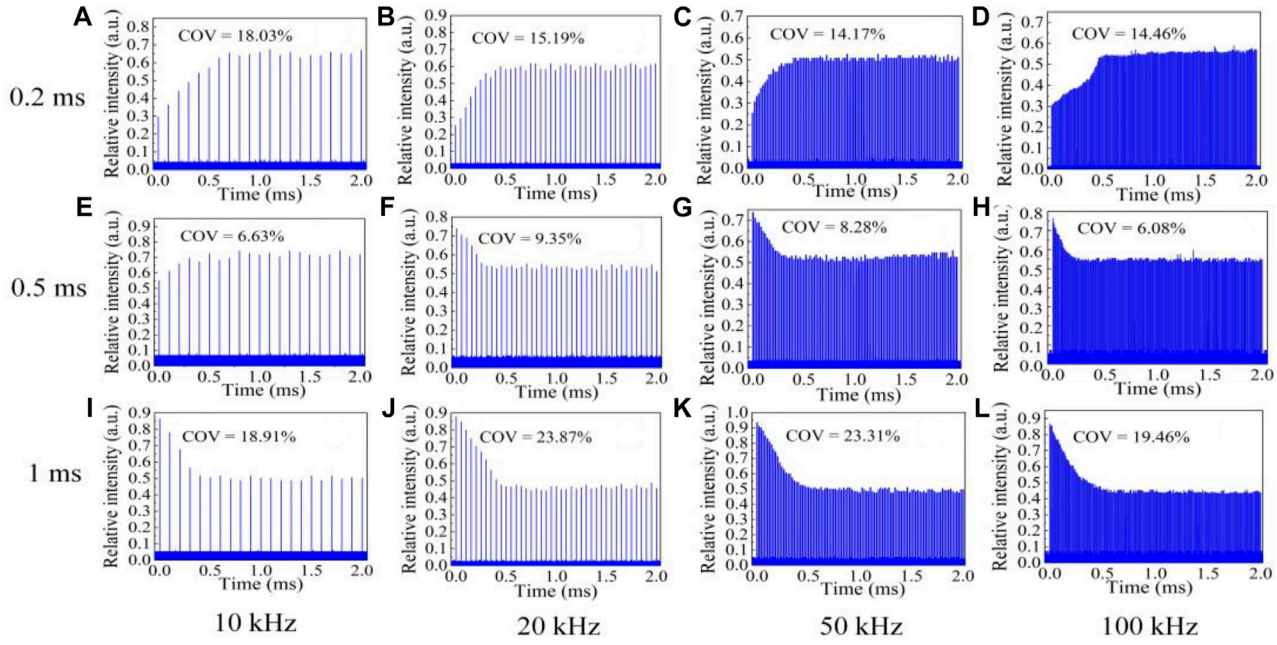

FIGURE 6 | Recorded pulse-burst distribution at different pump time τ for different repetition rates. **(A)** At 10 kHz repetition rate for pump time τ with 0.2 ms. **(B)** At 20 kHz repetition rate for pump time τ with 0.2 ms. **(C)** At 50 kHz repetition rate for pump time τ with 0.2 ms. **(D)** At 100 kHz repetition rate for pump time τ with 0.2 ms. **(E)** At 10 kHz repetition rate for pump time τ with 0.5 ms. **(F)** At 20 kHz repetition rate for pump time τ with 0.5 ms. **(G)** At 50 kHz repetition rate for pump time τ with 0.5 ms. **(H)** At 100 kHz repetition rate for pump time τ with 0.5 ms. **(I)** At 10 kHz repetition rate for pump time τ with 1 ms. **(J)** At 20 kHz repetition rate for pump time τ with 1 ms. **(K)** At 50 kHz repetition rate for pump time τ with 1 ms. **(L)** At 100 kHz repetition rate for pump time τ with 1 ms.

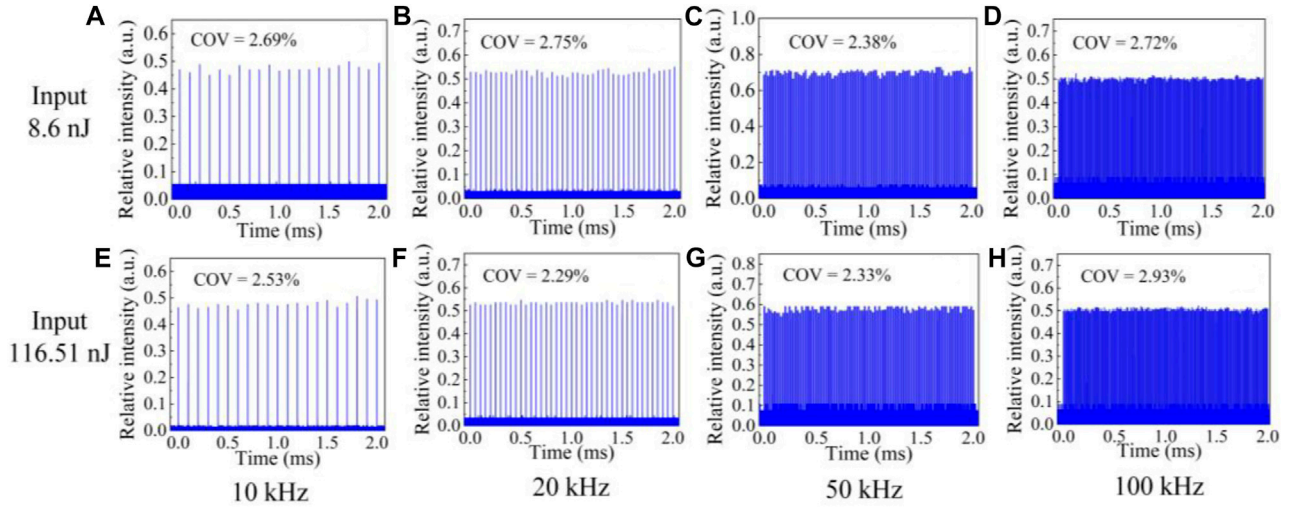

FIGURE 7 | Recorded stable burst envelope output at different repetition rates for different input energy. **(A)** At 10 kHz repetition rate for 8.6 nJ input. **(B)** At 20 kHz repetition rate for 8.6 nJ input. **(C)** At 50 kHz repetition rate for 8.6 nJ input. **(D)** At 100 kHz repetition rate for 8.6 nJ input. **(E)** At 10 kHz repetition rate for 116.51 nJ input. **(F)** At 20 kHz repetition rate for 116.51 nJ input. **(G)** At 50 kHz repetition rate for 116.51 nJ input. **(H)** At 100 kHz repetition rate for 116.51 nJ input.

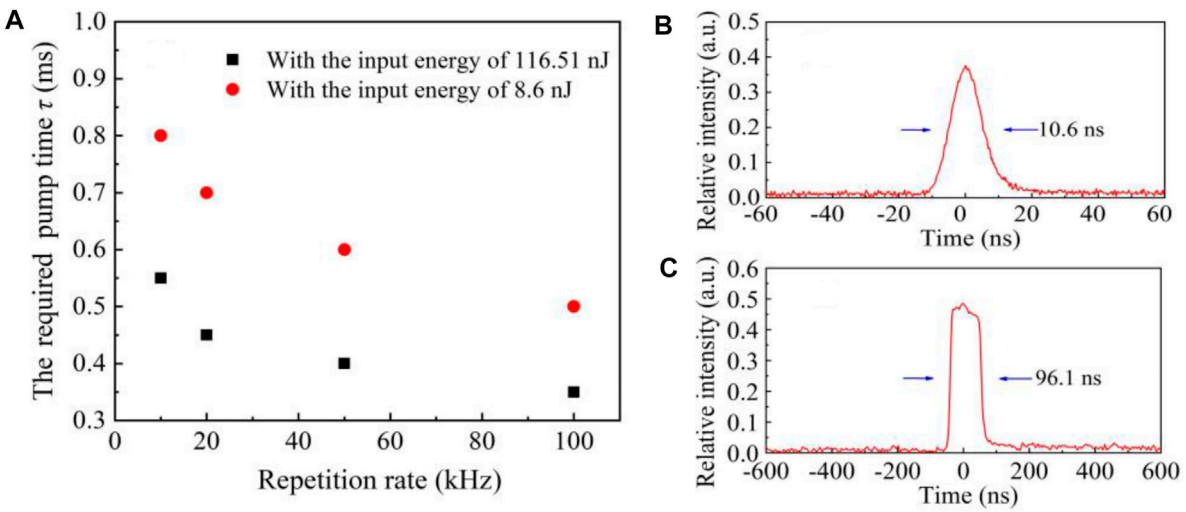

FIGURE 8 | (A) Pump time τ versus repetition rate at stable burst profile distribution for different input energy. **(B)** Recorded output single-pulse profile at the 100 kHz repetition rate with a pulse width of 10.6 ns. **(C)** Recorded output single-pulse waveform at the 100-kHz repetition rate for pulse duration with 96.1 ns.

profile distribution is presented in **Figure 5D** for an external electric signal input of 100 ns shown in **Figure 5B**. The output pulse laser duration was measured as 10.8 and 98 ns, with respect to the output pulse energy of 8.64 and 116.41 nJ, respectively.

4.2 Free-Space Operation

The output burst envelope during 2 ms duration, through a double-pass, three-stage amplification construction, was recorded and presented in **Figure 6** at different pump time τ (pump time before burst envelope), with the average input pulse energy of 116.51 nJ for the repetition rate of 10 kHz, 20 kHz, 50 kHz, and 100 kHz. In the first few pulse distribution, it was exerted with gradually increasing intensity distribution at pump time τ of 0.2 ms as shown in **Figures 6A–D**, which was induced by weaker amplification of the initial pulse to accumulate more stored energy for subsequent pulses. However, the relatively higher intensity dispersion occurred in the first several pulses due to excessive compensation brought by higher pump time τ of

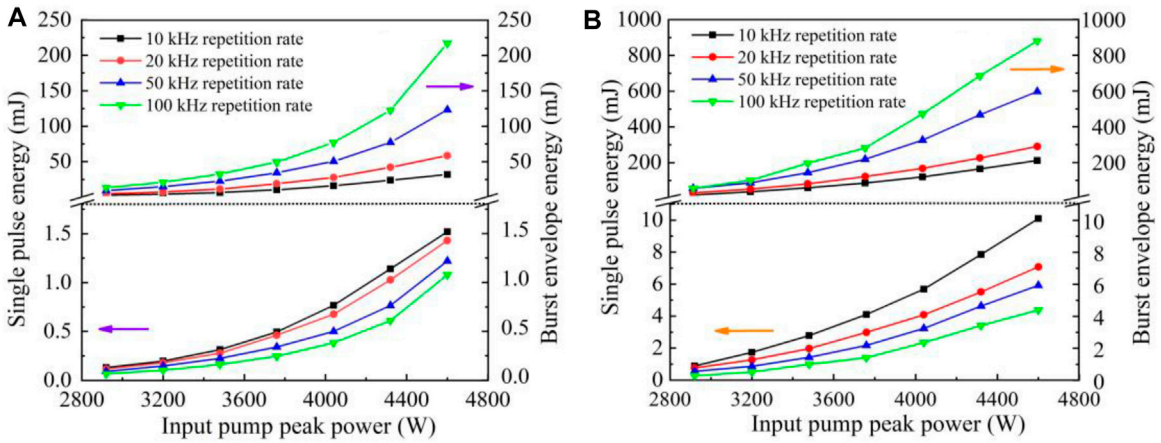

FIGURE 9 | Output burst energy and single-pulse energy versus input pump peak power at different repetition rates during double-pass amplification. **(A)** At the input single-pulse energy of 8.6 nJ. **(B)** For the input single-pulse energy of 116.51 nJ.

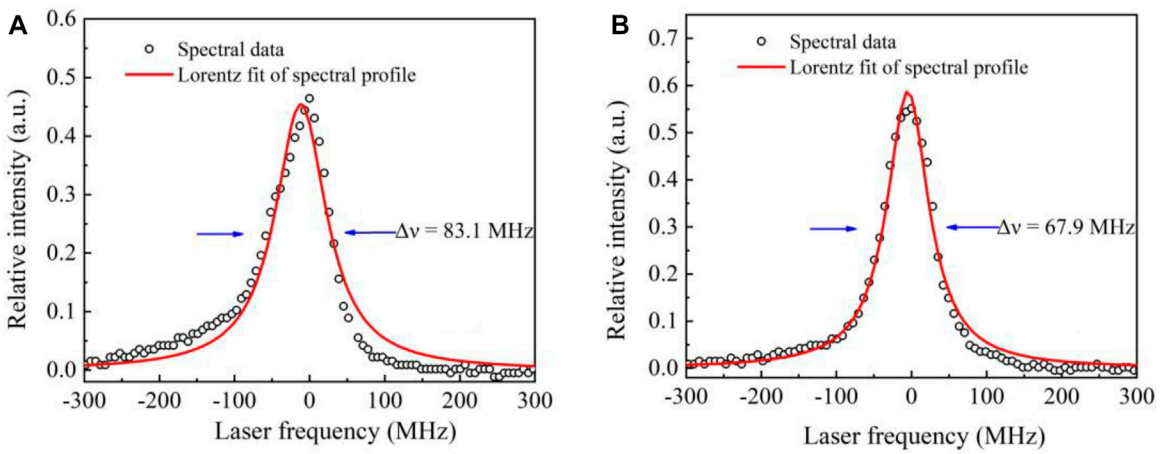

FIGURE 10 | Spectral profile of MOPA output at the 100-kHz repetition rate. **(A)** For 1.08 mJ single-pulse energy output with a pulse width of 10.3 ns. **(B)** At 4.38 mJ single-pulse energy output with pulse duration of 96.1 ns.

1 ms, resulting in a convex burst envelope with the triangle-like distribution. For a horizontal comparison at pump time τ of 0.5 ms, the pulse burst distribution in **Figure 6E** was different and induced by inadequate compensation, while the excessive compensation occurred in **Figures 6F–H**. Compared with pump time τ of 0.2 and 1 ms, it yielded decreasing variation of the COV within the burst envelope for different repetition rates at a pump time τ of 0.5 ms. Such a variation trend of COV was consistent with the simulated results. Also, it was found in later experiments that the dispersion of the recorded burst envelope was provided with similar variation tendency for input pulse energy varying into 8.6 nJ.

For stable pulse burst profile output, it is exhibited in **Figure 7** at repetition rates of 10 kHz, 20 kHz, 50 kHz, and 100 kHz in terms of the input pulse energy of 8.6 and 116.51 nJ. The COV of recorded burst train, from **Figures 7A–D**, was measured to be 2.69%, 2.75%, 2.38%, and 2.72% at 8.6 nJ pulse energy input, corresponding to a COV with 2.53%, 2.29%, 2.33%, and 2.93% presented in **Figures 7E–H** for 116.51 nJ pulse energy input. At stable burst envelope distribution, the required pump time τ versus the repetition rate was investigated and given in **Figure 8A**, with respect to different pulse energy input. There was a decreasing trend for pump time τ with increasing of the repetition rate from 10 to 100 kHz, also shown was endowed with decreasing tendency of pump time τ for higher pulse-energy input, indicating the consistent trend with the simulated ones in the abovementioned section. At the 100 kHz repetition rate, the output single-pulse profile with a duration of 10.6 and 96.1 ns is recorded in **Figures 8B, C**, respectively. Here, it could be seen that relatively steep distribution emerged for leading edge compared with the trailing edge at the output pulse temporal waveform with 96.1 ns duration, resulting from consumption of more inversion particles in leading edge during approximately flat-top pulse amplification.

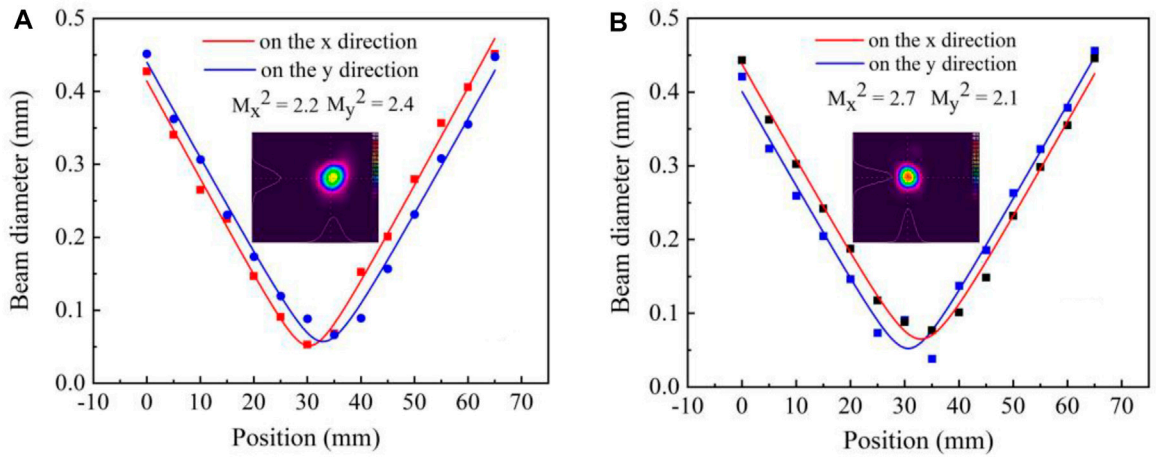

FIGURE 11 | Output beam diameter versus beam position on different directions for the 100-kHz repetition rate. **(A)** At output 1.08 mJ single-pulse energy with a pulse width of 10.3 ns. **(B)** At output 4.38 mJ single- pulse energy with a pulse width of 96.1 ns.

The double-pass output laser energy was measured and plotted in **Figures 9A, B** at different repetition rates for the stable burst envelope distribution, in terms of the input single-pulse energy of 8.6 and 116.51 nJ respectively. The amplified single-pulse energy at a lower repetition rate was provided with obvious advantages over a higher repetition rate with the increasing of input pump peak power, while the contrary tendency occurred in variation of burst envelope energy. In the case of the input single-pulse energy of 8.6 nJ, the maximum output single-pulse energy, at total input pump peak power with 4600 W, was measured to be 1.52 and 1.43 mJ for repetition rates of 10 and 20 kHz, 1.22 and 1.08 mJ at a repetition rate of 50 and 100 kHz, which corresponded to the burst envelope energy of 31.92, 58.63, 123.22, and 217.08 mJ, respectively. Moreover, it was scaled up to as high as 10.1, 7.08, 5.92, and 4.38 mJ due to the higher input single-pulse energy of 116.51 nJ, respectively, resulting in burst envelope energy with 212.1, 290.28, 597.92, and 880.38 mJ. At the 100 kHz repetition rate, the resulting amplification factor (the ratio of output pulse energy into input pulse energy) was endowed with 1.26×10^5 (51 dB) at the input single-pulse energy of 8.6 nJ and 3.76×10^4 (45.75 dB) was provided for 116.51 nJ single-pulse energy input.

The spectral profile of the MOPA output, at the 100 kHz repetition rate, was measured by means of the scanning Fabry–Perot interferometer with a free spectral range (FSR) of 10 GHz and resolution of 67 MHz. From **Figure 10A**, the measured spectral linewidth, FWHM of Lorentz fit, was expressed as 83.1 MHz for 1.08 mJ pulse energy output, operating with 10.3 ns pulse width. At the output pulse energy of 4.38 mJ, the measured spectral linewidth with 67.9 MHz, approximately the spectral resolution, is shown in **Figure 10B**, with respect to pulse duration of 96.1 ns In fact, the obtained spectral profile could be regarded as the convolution between the Fabry–Perot resonator mode and Fourier transform of relevant pulse duration from the actual MOPA output, resulting in the broadened spectral profile. Hence, the actual spectral linewidth was less than the measured ones for the 100-kHz repetition rate at maximum MOPA output.

Utilizing the 90/10 knife-edge method [31–33], the obtained M^2 curves of the output beam on the different directions are presented in **Figure 11A** and **Figure 11B** at the 100 kHz repetition rate for different output laser energy, respectively. As shown in **Figure 11A**, the measured M^2 values, on the x and y directions, were expressed as 2.2 and 2.4 at a maximum output 1.08 mJ single-pulse energy with a pulse duration of 10.3 ns Moreover, the M^2 values were measured to be 2.7 and 2.1 with the maximum output single pulse energy of 4.38 mJ for a pulse width of 96.1 ns in **Figure 11B**, respectively. The inter-burst interval was set as 100 ms to allow for the release of thermal loading. There was no emergence of serious beam distortion for recorded two-dimensional (2D) beam profiles with approximately smooth mode distribution.

5 CONCLUSION

In summary, a burst-mode MOPA laser system was characterized with excellent output characteristics in this study. Relevant characteristics for burst envelope distribution were simulated and discussed in detail under the action of multiple parameters (input pulse energy, repetition rate, and pump time τ), indicating the steady-state distribution approximately approaching 0.5 ms pump time τ. A double-pass, three-stage amplified burst envelope over 2 ms duration, at different pump time τ, was investigated in the experiment for the repetition rate from 10 to 100 kHz, corresponding to the input pulse energy of 8.6 and 116.51 nJ, respectively. Here, it could be illustrated that the COV variation tendency was consistent with that of the simulated ones. Maximum output pulse energy reached 10.1, 7.08, 5.92, and 4.38 mJ at the repetition rate of 10 kHz, 20 kHz, 50 kHz, and 100 kHz, respectively. In terms of the 100-kHz repetition rate, the output beam was endowed with uniform

mode distribution with M_x^2 and M_y^2 of 2.2 and 2.4 at 1.08 mJ pulse energy and 2.7 and 2.1 for 4.38 mJ pulse energy output. The relevant spectral linewidth was less than 83.1 and 67.9 MHz, with respect to output pulse duration of 10.3 and 96.1 ns respectively. It was believed that such a burst-mode laser system could possess great potential for its application in high-speed field diagnosis based on the FRS technique.

DATA AVAILABILITY STATEMENT

The original contributions presented in the study are included in the article/Supplementary Material; further inquiries can be directed to the corresponding author.

AUTHOR CONTRIBUTIONS

XY: experimental guidance and writing. SZ: theoretical analysis, experimental investigation, and writing. JP: theoretical guidance and experimental guidance. ZC: experimental operation, writing, and data analysis. LG: experimental operation, data process, and writing. WL: experimental operation and data recording. All authors involved could make significant contributions to this manuscript.

FUNDING

This research was funded by the National Natural Science Foundation of China (Grant No. 62175053).

REFERENCES

1. Krishna Y, Mahuthannan AM, Luo X, Lacoste DA, Magnotti G. High-speed Filtered Rayleigh Scattering Thermometry in Premixed Flames through Narrow Channels. *Combustion and Flame* (2021) 225:329–39. doi:10.1016/j.combustflame.2020.10.053
2. Fugger CA, Hsu PS, Jiang N, Yi T, Slipchenko MN, Felver JJ, et al. 10-kHz Simultaneous Dual-Plane Stereo-PIV and OH-PLIF Imaging. *Appl Phys B* (2020) 126:1–9. doi:10.1007/s00340-020-07522-4
3. Papageorge MJ, Arndt C, Fuest F, Meier W, Sutton JA. High-speed Mixture Fraction and Temperature Imaging of Pulsed, Turbulent Fuel Jets Auto-Igniting in High-Temperature, Vitiated Co-flows. *Exp Fluids* (2014) 55:1–20. doi:10.1007/s00348-014-1763-z
4. Ma Y, He Y, Tong Y, Yu X, Tittel FK. Quartz-tuning-fork Enhanced Photothermal Spectroscopy for Ultra-high Sensitive Trace Gas Detection. *Opt Express* (2018) 26:32103–10. doi:10.1364/OE.26.032103
5. Lang Z, Qiao S, Ma Y. Acoustic Microresonator Based In-Plane Quartz-Enhanced Photoacoustic Spectroscopy Sensor with a Line Interaction Mode. *Opt Lett* (2022) 47:1295–8. doi:10.1364/OL.452085
6. Liu X, Ma Y. Sensitive Carbon Monoxide Detection Based on Light-Induced Thermoelastic Spectroscopy with a Fiber-Coupled Multipass Cell [Invited]. *Opt Lett* (2022) 20:031201. doi:10.3788/col202220.031201
7. Ma Y, Yu X, Li X, Fan R, Yu J. Comparison on Performance of Passively Q-Switched Laser Properties of Continuous-Grown Composite GdVO_4/Nd:GdVO_4 and YVO_4/Nd:YVO_4crystals under Direct Pumping. *Appl Opt* (2011) 50:3854–9. doi:10.1364/AO.50.003854
8. Ma YF, Zhang JW, Li H, Yu X. High Stable Electro-Optical Cavity-Dumped Nd:YAG Laser. *Laser Phys Lett* (2012) 9:561–3. doi:10.7452/lapl.201210041
9. Ma Y, Yu X, Li X. Performance Improvement in a Directly 879 Nm Dual-End-π-Polarized-Pumped CW and Pulsed GdVO4/Nd:GdVO4 Laser. *Appl Opt* (2012) 51:600–3. doi:10.1364/AO.51.000600
10. Zha S, Chen Y, Li B, Lin Y, Liao W, Zou Y, et al. High-repetition-rate 1.5 Mm Passively Q-Switched Er:Yb:YAl3(BO3)4 Microchip Laser. *China Opt Express* (2021) 19:071402. doi:10.3788/COL202119.071402
11. Liu X, Tan C, Cheng Y, Wei J, Zhu M, Chen X, et al. 7 kHz Sub-nanosecond Microchip Laser Amplified by a Grazing Incidence Double Pass Slab Amplifier. *China Opt Express* (2021) 19:021403. doi:10.3788/COL202119.021403
12. Peng J, Cao Z, Yu X, Yang S, Yu Y, Ren H, et al. Analysis of Combustion Instability of Hydrogen Fueled Scramjet Combustor on High-Speed OH-PLIF Measurements and Dynamic Mode Decomposition. *Int J Hydrogen Energ* (2020) 45:13108–18. doi:10.1016/j.ijhydene.2020.02.216
13. Peng J, Cao Z, Yu X, Qi H, Sun R, Yu Y, et al. Oscillation Characterization of Volatile Combustion of Single Coal Particles with Multi-Species Optical Diagnostic Techniques. *Fuel* (2020) 282:118845. doi:10.1016/j.fuel.2020.118845
14. Peng J, Gao L, Yu X, Qin F, Liu B, Cao Z, et al. Combustion Oscillation Characteristics of a Supersonic Ethylene Jet Flame Using High-Speed Planar Laser-Induced Fluorescence and Dynamic Mode Decomposition. *Energy* (2022) 239:122330. doi:10.1016/j.energy.2021.122330
15. Miller JD, Jiang N, Slipchenko MN, Mance JG, Meyer TR, Roy S, et al. Spatiotemporal Analysis of Turbulent Jets Enabled by 100-kHz, 100-ms Burst-Mode Particle Image Velocimetry. *Exp Fluids* (2016) 57:1–17. doi:10.1007/s00348-016-2279-5
16. Smyser ME, Rahman KA, Slipchenko MN, Roy S, Meyer TR. Compact Burst-Mode Nd:YAG Laser for kHz-MHz Bandwidth Velocity and Species Measurements. *Opt Lett* (2018) 43:735–8. doi:10.1364/OL.43.000735
17. Wu PP, Miles RB. High-energy Pulse-Burst Laser System for Megahertz-Rate Flow Visualization. *Opt Lett* (2000) 25:1639–41. doi:10.1364/OL.25.001639
18. Krishna Y, Mahuthannan AM, Lacoste DA, Magnotti G. 50-kHz-rate Rayleigh and Filtered Rayleigh Scattering Thermometry Using a Pulse-Burst Laser. *AIAA Scitech 2021 Forum* (2021). doi:10.2514/6.2021-0724
19. Thurow B, Jiang N, Samimy M, Lempert W. Narrow-linewidth Megahertz-Rate Pulse-Burst Laser for High-Speed Flow Diagnostics. *Appl Opt* (2004) 43:5064–73. doi:10.1364/AO.43.005064
20. Zhao M, Zhang Z, Feng X, Zong M, Liu J, Xu X, et al. High Repetition Rate Passively Q-Switched Laser on Nd:SRA at 1049 Nm with MXene Ti3C2Tx. *China Opt Express* (2020) 18:041401. doi:10.3788/col202018.041401
21. Tang T, Zhang F, Wang M, Wang Z, Xu X. Two-dimensional Tellurene Nanosheets as Saturable Absorber of Passively Q-Switched Nd:YAG Solid-State Laser. *China Opt Express* (2020) 18:041403. doi:10.3788/col202018.041403
22. Slipchenko MN, Miller JD, Roy S, Meyer TR, Mance JG, Gord JR. 100 kHz, 100 Ms, 400 J Burst-Mode Laser with Dual-Wavelength Diode-Pumped Amplifiers. *Opt Lett* (2014) 39:4735–8. doi:10.1364/OL.39.004735
23. Wu W, Li X, Yan R, Zhou Y, Ma Y, Fan R, et al. 100 kHz, 31 Ns, 189 J Cavity-Dumped Burst-Mode Nd:YAG MOPA Laser. *Opt Express* (2017) 25:26875–84. doi:10.1364/OE.25.026875
24. Smyser ME, Slipchenko MN, Meyer TR, Caswell AW, Roy S. Burst-mode Laser Architecture for the Generation of High-Peak-Power MHz-Rate Femtosecond Pulses. *OSA Continuum* (2019) 2:3490–8. doi:10.1364/OSAC.2.003490
25. Yan R, Li X, Zhou Y, Wu W, Liu Z, Wen X, et al. 2.5 MW, 2.0 Ns MOPA Burst Mode Laser at 86 kHz. *Optik* (2019) 185:418–22. doi:10.1016/j.ijleo.2018.12.119
26. Yan R, Li X, Zhang Y, Liu Z, Wen X, Chen D, et al. High-repetition-rate, High-Peak-Power Burst Mode Laser with YAG/Nd:YAG/Cr4+:YAG Composite crystal. *Optik* (2018) 175:263–7. doi:10.1016/j.ijleo.2018.09.016
27. Feng D, Goldberg BM, Naphade M, Shneider MN, Miles RB. A Model Study of Filtered Rayleigh Scattering Sensitivity to Pressure and Temperature. *AIAA Scitech* (2018). doi:10.2514/6.2018-2042
28. Mance JG, Slipchenko MN, Roy S. Regenerative Amplification and Bifurcations in a Burst-Mode Nd:YAG Laser. *Opt Lett* (2015) 40:5093–6. doi:10.1364/OL.40.005093

29. Wu P, Lempert WR, Miles RB. Megahertz Pulse-Burst Laser and Visualization of Shock-Wave/boundary-Layer Interaction. *AIAA J* (2000) 38:672–9. doi:10.2514/3.14459
30. Frantz LM, Nodvik JS. Theory of Pulse Propagation in a Laser Amplifier. *J Appl Phys* (1963) 34:2346–9. doi:10.1063/1.1702744
31. Zhang S, Ma Y, Liu X, Ding S, Yu X, Zhang Q. Continuous Wave and Rhenium Disulfide Passively Q-Switched Nd:GdLaNbO4 Laser under Direct Pumping. *Opt Commun* (2020) 473:125977. doi:10.1016/j.optcom.2020.125977
32. Ma Y, Zhang S, Peng Z, Ding S, Sun H, Peng F, et al. Investigation on 1065 Nm Laser Performance with Nd:GdLaNbO4 Mixed crystal and Molybdenum Disulfide. *Opt Laser Technol* (2019) 120:105715. doi:10.1016/j.optlastec.2019.105715
33. Ma Y, Zhang S, Zhang Z, Liu X, Ding S, Liu W, et al. Continuous Wave and SnSe2/PdSe2 Passively Q-Switched Nd:GdNbO4 Laser under Direct Pumping. *Opt Laser Technol* (2021) 133:106558. doi:10.1016/j.optlastec.2020.106558

Conflict of Interest: The authors declare that the research was conducted in the absence of any commercial or financial relationships that could be construed as a potential conflict of interest.

frontiers | Frontiers in Physics

REVIEW
published: 01 June 2022
doi: 10.3389/fphy.2022.887171

A Brief Review of Calibration-Free Laser-Induced Breakdown Spectroscopy

Ning Zhang[1], Tianxue Ou[1], Meng Wang[2], Zhanjian Lin[1], Chao Lv[1], Yuzhi Qin[1], Jiaming Li[1], Huan Yang[2]*, Nan Zhao[1] and Qingmao Zhang[1]*

[1]Guangdong Provincial Key Laboratory of Nanophotonic Functional Materials and Devices, School of Information and Optoelectronic Science and Engineering, South China Normal University, Guangzhou, China, [2]Sino-German College of Intelligent Manufacturing, Shenzhen Technology University, Shenzhen, China

The calibration-free laser-induced breakdown spectroscopy (CF-LIBS) technique requires no reference samples of the same matrix to establish the calibration curve, not affected by the matrix effect. In recent years, the CF-LIBS technology has greatly progressed, and the accuracy of quantitative analysis has gradually improved. The purpose of this review was to introduce the CF-LIBS fundamental and modified algorithms. The Boltzmann plot method, Saha–Boltzmann plot method, and column density Saha–Boltzmann plot (CD-SB) method were discussed. Moreover, as a critical factor in CF-LIBS, the self-absorption effect and its influence on CF-LIBS were also introduced. CF-LIBS has been applied in a variety of fields, such as environmental protection, explorations of space, cultural heritage preservation, and geological survey, which were also described in this review.

Keywords: CF-LIBS, quantitative analysis, elemental analysis, self-absorption effect, applications

OPEN ACCESS

Edited by:
Qun Hao,
Beijing Institute of Technology, China

Reviewed by:
Jayr Amorim,
Instituto de Tecnologia da Aeronáutica (ITA), Brazil
Yingbin Xing,
Huazhong University of Science and Technology, China

****Correspondence:***
Jiaming Li
jmli@m.scnu.edu.cn
Huan Yang
yanghuan@sztu.edu.cn

Specialty section:
This article was submitted to Optics and Photonics, a section of the journal Frontiers in Physics

Received: *02 March 2022*
Accepted: *27 April 2022*
Published: *01 June 2022*

Citation:
Zhang N, Ou T, Wang M, Lin Z, Lv C, Qin Y, Li J, Yang H, Zhao N and Zhang Q (2022) A Brief Review of Calibration-Free Laser-Induced Breakdown Spectroscopy. Front. Phys. 10:887171. doi: 10.3389/fphy.2022.887171

1 INTRODUCTION

The types and compositions of elements in materials have an impact on their properties, either directly or indirectly. It is crucial to make elemental analyses evaluate material performance. Conventional methods include atomic absorption spectrometry (AAS), inductively coupled plasma mass spectrometry (ICP-MS), inductively coupled plasma emission spectrometry (ICP-AES), X-ray fluorescence spectrometry (XRF), tunable diode laser absorption spectroscopy, quartz-enhanced photoacoustic spectroscopy, quartz-tuning-fork enhanced photothermal spectroscopy (QEPTS), and dual-comb absorption spectroscopy [1–3]. Due to their complicated operation and time-consuming process, these methods are usually used in laboratories. In recent years, scientists have been looking for and have developed new analytical assays with rapid response, easy operation, and high reliability.

Laser-induced breakdown spectroscopy (LIBS) is a new promising atomic spectrometry, more versatile than traditional methods [4]. LIBS is also often referred to as laser-induced plasma spectroscopy (LIPS) or laser spark spectroscopy. As the excitation source in LIBS, a pulsed laser beam is focused onto the sample surface by using a focusing lens. Through multiphoton ionization, atoms, ions, and molecules in the laser focus focal area absorb the laser energy and generate initial free electrons. With the inverse bremsstrahlung effect, the free electrons are accelerated by the electromagnetic field of the laser beam and then collide with particles in the ambient gas and sample materials to produce more free electrons. The newly created free electrons are also accelerated by the electric field, resulting in an electron avalanche ionization (EAI) process throughout the laser pulse duration [5]. During a breakdown phenomenon, plasma is generated on

the sample surface. The surface species can be quantitatively deduced by analyzing the plasma emission spectrum [6]. LIBS has become an attractive and popular technique in the field of chemical analysis due to its unique advantages, such as its application to liquids [7, 8], gases [9, 10], and solids [11, 12], no sample pretreatment, simultaneous detection of multiple elements, and noncontact remote detection in many fields, including laser cleaning [13, 14], environmental protection [15, 16], space exploration [17, 18], and cultural heritage preservation [19, 20].

Generally, a series of certified samples of similar matrices are required for the quantitative analysis to establish the calibration curves in LIBS, called the referenced calibration method (RCM). However, it is extremely difficult or even impossible to obtain similar referenced samples in many cases, such as soil, mining, and biological tissues, where the matrix effect is hardly avoided [21, 22]. Furthermore, the RCM requires consistency in the experimental conditions, such as laser power density, temperature, and humidity. The limitations to the reference sample have hindered the development of LIBS.

Ciucci was the first to propose a determination method without referenced samples: the calibration-free laser-induced breakdown spectroscopy (CF-LIBS) [23]. The elemental concentration information is determined by describing the physical states of the laser-induced plasmas through mathematical models. There is no need for referenced samples or calibration curves, and matrix effects can be effectively avoided. CF-LIBS has piqued researchers' interest since its introduction in 1999, although analytical accuracy is less satisfactory than the RCM.

In the past few decades, experimental modification and physical algorithmic improvements in CF-LIBS have been made by scholars all around the world. Analytical accuracy keeps increasing. To overview the development and the state-of-the-art CF-LIBS, this review included three parts: the essential assumptions and the basic mathematical model, a modified model combined with the Saha-Eggert equation, and the self-absorption and its effect on CF-LIBS. The purpose of this review was to give LIBS researchers some inspiration to promote the exploration.

2 FUNDAMENTAL ALGORITHM

The basic assumptions of CF-LIBS include (1) chemometric ablation, in which elemental composition and content in plasmas are the same as in samples [23, 24]; (2) local thermal equilibrium (LTE), ensuring the particles are in the excited energy level, following the Boltzmann distribution [25]; (3) optical thinness, meaning that the self-absorption in the selected spectral line can be ignored for calculation; and (4) elemental information wholeness, observed spectra including all the species of elements [26]. Based on the aforementioned assumptions, the spectral intensity at wavelength λ is as follows:

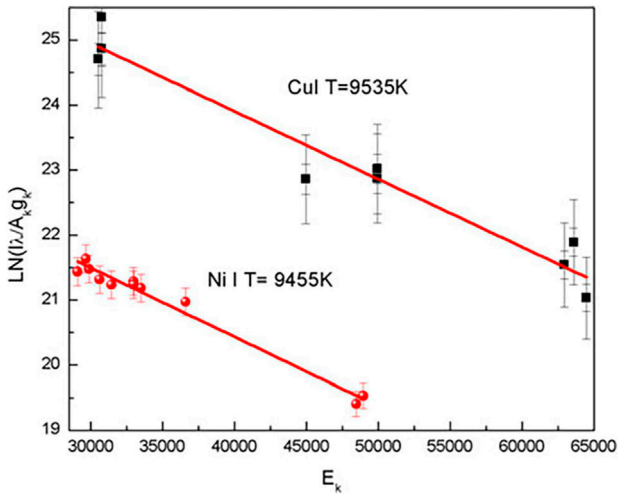

FIGURE 1 | Typical Boltzmann plots for estimating the plasma temperature. Emission lines from singly ionized Cu and Ni are used for obtaining the temperature. Reproduced with permission from [30], ©2016 Cambridge core.

$$I_\lambda^{ki} = FC_S A_{ki} \frac{g_k}{U_S(T)} e^{-\left(\frac{E_k}{k_B T}\right)}. \tag{1}$$

F is the experimental parameter involving the receiving system optical efficiency and plasma number density; C_S is the concentration of the emitting species s; A_{ki} is the spontaneous transition probability; g_k and E_k are the statistical weight and energy of the upper level k; k_B is the Boltzmann constant; $U_S(T)$ is the partition function at the temperature T. **Equation 1** should be transformed, and the logarithm of both sides should be considered:

$$ln\frac{I_\lambda^{ki}}{A_{ki}g_k} = -\frac{E_k}{k_B T} + ln\frac{FC_S}{U_S(T)}. \tag{2}$$

Equation 2 can be rewritten in a linear form:

$$y = mx + q_S, \tag{3}$$

$$y = ln\frac{I_\lambda^{ki}}{A_{ki}g_k}, \tag{4}$$

$$x = E_k, \tag{5}$$

$$m = -\frac{1}{k_B T}, \tag{6}$$

$$q_S = ln\frac{FC_S}{U_S(T)}. \tag{7}$$

A relationship of E_k and y can be linearly fitted, called the Boltzmann plot. The linear plot can be drawn by each type of atom and ion. The plasma temperature and concentration of species s can be deduced by the line slope m and intercept q_S, according to **Eqs 6**, **7**, respectively.

The partition function $U_S(T)$ is calculated as

$$U_S(T) = \sum g_k e^{-E_k/K_B T}. \quad (8)$$

The value of F can be determined through normalization, which states that the sum of all species in the sample equals 1:

$$\sum C_S = \frac{1}{F} \sum U_S(T) e^{q_S} = 1. \quad (9)$$

Then, the concentration of each element in the sample can be determined as

$$C_S = \frac{1}{F} U_S(T) e^{q_S}. \quad (10)$$

Ideally, an accurate elemental determination requires two conditions [27–29]: (1) the fitting linear curve of the same species has high linearity (R^2 close to 1) and (2) the fitting lines of various species are nearly parallel (shown in **Figure 1** [30]). However, the analytical accuracy is generally influenced by five factors: (I) the measured spectral intensities are inaccurate; (II) the Boltzmann plot established for atomic lines generally yields a lower plasma temperature than for ionic lines; (III) the transition species are close to but not in LTE conditions (due to ionization/recombination reactions through electronic impacts); (IV) plasma in LIBS is optically thick and thermally inhomogeneous, and the temperature in the plasma center is much higher than that at the plasma periphery; and (V) **Equation 1** is ideal and cannot accurately describe the plasma [19, 31].

The laser-induced plasma is transient and inhomogeneous. It only approximately meets the conditions for LTE within the appropriate temporal and spatial window [19]. Deviation from LTE conditions will badly influence the analytical accuracy. The McWhirter criterion is the most commonly used criterion for verifying LTE, especially because in plasma with the presence of high-density particles, the collisional transitions dominate the radiative transitions between all states. It is a necessary but not sufficient condition for LTE because it only applies to homogeneous and static plasmas [32]. The McWhirter criterion can be used as

$$N_e > 1.6 \times 10^{12} T^{\frac{1}{2}} (\Delta E)^3, \quad (11)$$

where ΔE represents the maximum adjacent energy level gap.

The obtained spectral intensity is proportional to the relative efficiency: the light emitted by the plasma is coupled to the spectrometer, where the detector converts the optical signal into an electrical signal. Because the transmission and conversion efficiency of the optical system and the spectrometer are wavelength-dependent, the spectral intensity obtained directly must be corrected:

$$I(\lambda) = I_0(\lambda) \cdot E(\lambda), \quad (12)$$

where $E(\lambda)$ is the relative efficiency; $I(\lambda)$ is the signal intensity output from the spectral detector; and $I_0(\lambda)$ is the spectral intensity emitted from the plasma. The spectral response can vary significantly in different spectral regions, so spectral correction must be performed across a wide range of wavelengths [31, 33]. A deuterium-halogen tungsten lamp, a combination of deuterium/halogen broadband source, a mercury lamp, and diffusely scattered pulsed laser light sources are general calibration light sources [34].

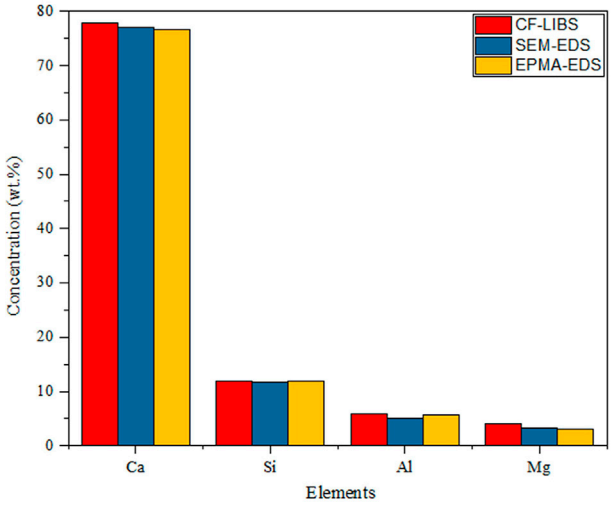

FIGURE 2 | Relative elemental abundance of the limestone sample at the fundamental harmonic (1064 nm) of the Nd:YAG laser. Reproduced with permission from [35], ©2018 Institute Of Physics.

The Boltzmann plot was applied by researchers in various fields. Fahad et al. quantified the composition of the limestone, as shown in **Figure 2**; the results of the CF-LIBS technique compared to scanning electron microscopy combined with energy-dispersive X-ray spectroscopy and electron probe microanalysis are in good agreement [35]. Pandhiji et al. used the CF-LIBS method to quantify the elements in the coral skeleton, except for Sn(Certified data: 10 ppm and CF-LIBS data: 6 ppm); all of the values were in general agreement with the verified values. The results were somewhat different compared to ICP-MS, and the reason for this disagreement may be that the CF-LIBS data were related to the surface of the coral, while the ICP-MS data were related to its overall mass [36]. In the following year, they determined toxic heavy metals (Cd, Co, Pb, Zn, Cr, etc.) in soil samples from four industrial areas by the calibration curves, CF-LIBS, and ICP-OES methods. The results showed that the limits of detection (LOD) for Cd and Zn in soil were 0.2 and 1.0 ppm, respectively, and the ICP-OES method was in good agreement with the CF-LIBS method [37]. Similarly, Kumar et al. created a Boltzmann plot for different elements (Ca, Fe, and Pb) in the sludge to determine the concentrations of toxic elements Cr and Pb [38]. Agrawal et al. used CF-LIBS as a quality control tool to monitor the composition of various mineral elements in food additives. The quantitative analysis results were consistent with those on the additive label. The presence of new (not on the label) elements and non-detected elements may be related to errors in the food additive and was not reported by the manufacturer due to low concentrations [39]. Yang et al. used CF-LIBS to quantify the H/D concentration ratio in titanium alloys, and the relative error of the H/D concentration ratio was only 1.33% when a Boltzmann plot was used to calculate the plasma temperature (choosing the spectral line of titanium) due to the scarcity of H and D elemental spectral lines, as well as their susceptibility to interference from titanium spectral lines [40].The quantitative analysis of the composition of elements in different

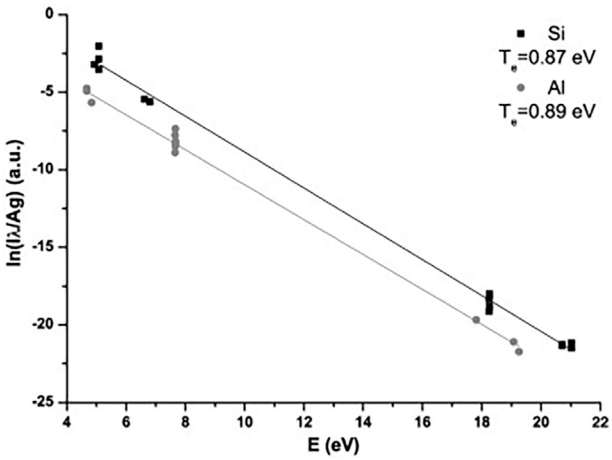

FIGURE 3 | Saha–Boltzmann plot for silicon and aluminum. Reprinted from [44], Copyright (2013), with permission from Elsevier.

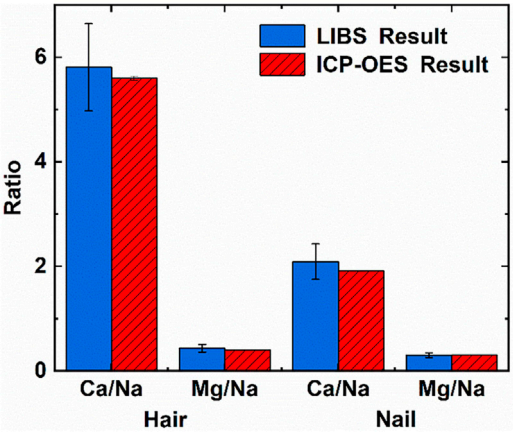

FIGURE 4 | Comparison of ICP-OES and LIBS results in hair and nails. Reprinted from [45], Copyright (2021), with permission from Elsevier.

karats of gold by Ahmed et al. showed that the Au content increases from 75.9% to 92.7%, with increasing gold purity (18–22 K), and the corresponding Cu content decreases from 17% to 5.7% [41]. Hamad et al. analyzed the composition of pressed cement samples, and the calculated elemental concentrations agreed with the XRF results with a maximum relative percentage error of 5% [42].

Under optimized experimental conditions, CF-LIBS allows more accurate elemental content analysis, with results comparable to those of XRF, ICP-MS, ICP-OES, AAS, and RCM in LIBS. Moreover, a series of standard samples are not required, making it more cost-effective and less time-consuming. When referenced samples are unavailable for establishing calibration curves, CF-LIBS is the only choice for the quantitative analysis using LIBS.

3 MODIFIED ALGORITHM

3.1 Saha–Boltzmann Plot

Species in the same ionized state generally do not have enough spectral lines for representing the whole energy level and poor calculation accuracy of the plasma electron temperature. Yalcin et al. proposed a method of introducing the Saha–Eggert equation with the Boltzmann plot (Saha–Boltzmann plot method) in 1999 [43] and studied the effects of environmental conditions and laser energy on the plasma temperature. This method indeed improved the accuracy and reliability of temperature measurements.

The Saha–Boltzmann plot method must satisfy the condition of LTE, as well as the Boltzmann plot method. The Saha–Eggert equation describes the totality of neutral and singly ionic states of the same elements under the LTE condition:

$$\frac{N^{II}}{N^{I}} = \frac{1}{N_e}\frac{2U^{II}(T)}{U^{I}(T)}\exp\left(-\frac{E_{ion}}{k_BT}\right)\frac{(2\pi m_e k_B T)^{\frac{3}{2}}}{h^3}, \tag{13}$$

where N^I and N^{II} represent the number density of species in the atomic and single ionic states of the same element, respectively; m_e is the electron mass; E_{ion} is the first ionization energy.

N is proportional to C_S, $C_S = bN$. **Equation 1** can be modified as

$$I_\lambda^{ki} = FC_S A_{ki}\frac{g_k}{U_S(T)}e^{-\frac{E_k}{k_BT}} = F_N N A_{ki}\frac{g_k}{U_S(T)}e^{-\frac{E_k}{k_BT}}. \tag{14}$$

Combining **Equations 13**, **14**, the intensity of the ionic line can be rewritten as

$$I_{jh}^{II} = F_N N^I A_{jh}^{II} g_j^{II}\frac{\exp\left(-\frac{E_j^{II}}{k_BT}\right)}{U^I(T)}\left(\frac{2(2\pi m_e k_B T)^{\frac{3}{2}}}{N_e h^3}\right)\exp\left(-\frac{E_{ion}}{k_BT}\right). \tag{15}$$

Rearranging the aforementioned equation and taking the logarithm of both sides, we obtained the following equation:

$$y^* = m\cdot x^* + q, \tag{16}$$

where $y^* = \ln\left(\frac{I_{jh}}{A_{jh}g_j}\right) - \ln\left(\frac{2(2\pi m_e k_B T)^{\frac{3}{2}}}{N_e h^3}\right)$, $x^* = E_{ion} + E_j$, and $m = -\frac{1}{k_BT}$, $q = \ln\left(\frac{F_N N^I}{U_S(T)}\right)$. To improve the accuracy and precision of plasma temperature, several emission lines that cover a wide range of upper energies were used (as shown in **Figure 3**, Ref. [44]). To some extent, this method mitigates the effect of line strength decline due to self-absorption [45]. This method is becoming increasingly popular among researchers in a variety of studies. Zhang et al. assessed the Ca/Na and Mg/Na ratios in human biological tissues and compared them to the ICP-OES method, revealing that the relative errors in hair and nails were less than 10% (the specific comparison graph, as shown in **Figure 4**), demonstrating the analytical accuracy [45]. Veis et al. quantified the H/D ratio in Be/W mixture coatings [46]. Pribula et al. studied the composition of tungsten-based samples with protective carbon layers using the W III spectral line to obtain more accurate results (quantitative results significantly influenced by the self-absorption effect of single ionized atoms) [47]. Alicia

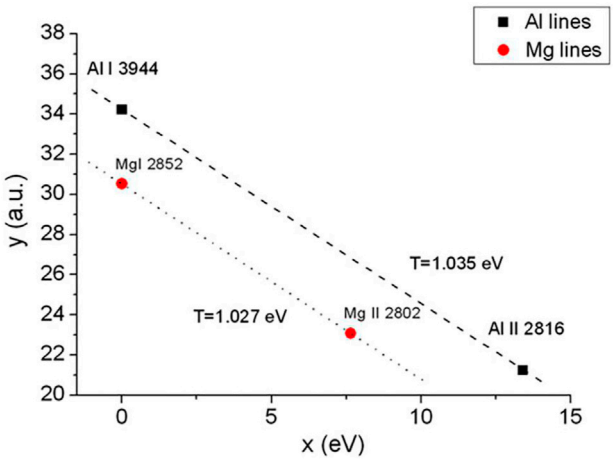

FIGURE 5 | Modified Saha–Boltzmann plot built by using the columnar density of self-absorbed lines from Al and Mg species. Reprinted from [51], Copyright (2013), with permission from Elsevier.

et al. explored the quantitative analysis of ps-CF and ns-CF LIBS for tungsten-based model materials (WCu) and found that the high linearity of the Saha–Boltzmann plot using the ps state resulted in a more accurate estimation of plasma temperature [48]. Horáková et al. measured the composition of acid pitchstone and found that the results agreed well with those of the electron microprobe analysis (EMPA) [49]. Wang et al. studied the emission spectra of *Codonopsis pilosula* to determine the elemental contents of Mg and Ca and compared them with liquid cathode glow discharge-atomic emission spectrometry (LCGD-AES) and inductively coupled plasma mass spectrometry (ICP-MS) [50].

3.2 Columnar Density Saha–Boltzmann Plot

The methods based on the Boltzmann plot and the Saha–Boltzmann plot both have significant limitations: (I) optical thinness is needed; (II) the plasma electron temperature cannot be accurately deduced by the slope of the Boltzmann or Saha–Boltzmann plot when only a small number of spectral lines for elements in the same ionization state can be observed.

The column density Saha–Boltzmann (CD-SB) method can effectively overcome the aforementioned limitations [51], where the column density of the ground state can be directly calculated. Furthermore, the presence of self-absorption in the resonance lines ensures long-term atomic evolution [52]. This method proposed by Cristoforetti and Tognoni opened up a new avenue for accurate plasma temperature calculation (the columnar density Saha–Boltzmann plot, shown in **Figure 5** [51]).

Similar to the conventional CF-LIBS method, the plasma is assumed to be spatially homogeneous over the measured time interval in the CD-SB plot method. **Equation 13** can be rewritten according to [51]:

$$\frac{n_i^{II}l}{g_i^{II}} = \frac{2\left(2\pi m_e k_B T\right)^{\frac{3}{2}}}{N_e h^3}\frac{n^I l}{U^I(T)}e^{-\frac{E_i^{II}+E_{ion}-\Delta E_{ion}}{k_B T}}. \tag{17}$$

This equation describes the equilibrium population of different ionization stages in terms of the number density of the lower level of an ionic transition ($n_i^{II}l$). E_i^{II} is the energy of the ionic transition at the lower energy level, and ΔE_{ion} is the reduced ionization energy due to the plasma environment, which is 1–2 orders of magnitude lower than the sum of ($E_i^{II}+E_{ion}$) and is generally negligible. The columnar density $n^I l$ can be determined as the following:

$$n^I l = 1770\frac{\Delta\lambda_0}{f\lambda_0^2}k(\lambda_0)l\times 10^{17}, \tag{18}$$

where λ_0 and $\Delta\lambda_0$ are in $\dot{A}$ units; the value of $k(\lambda_0)l$ can be evaluated by the self-absorption coefficient, and f is the line oscillator strength.

Similarly, the Boltzmann Equation can be rewritten as

$$\frac{n_i^I l}{g_i^I} = \frac{n^I l}{U^I(T)}e^{-\frac{E_i^I}{k_B T}}, \tag{19}$$

where E_i^I is the energy of the atomic transition at the lower energy level i.

Combining **Equations 17**, **19**, the column density Saha–Boltzmann equation can take the following format:

$$y^* = mx^* + q, \tag{20}$$

where $m = -\frac{1}{k_B T}$ and $q = ln\frac{n^I l}{U^I(T)}$; for atomic lines, $x^* = E_i^I$ and $y^* = ln\frac{n_i^I l}{g_i^I}$; for ionic lines, $x^* = E_i^{II} + E_{ion}$ and $y^* = ln\frac{n_i^{II} l}{g_i^{II}} - ln\frac{2\left(2\pi m_e k_B T\right)^{\frac{3}{2}}}{N_e h^3}$. The plasma temperature is deduced by the slope of the linear fitting curves in the CD-SB plot method. The y^* coordinate is calculated based on the column density of the atomic and ionic lines, rather than the intensity of spectral lines; the x^* coordinate indicates the lower (instead of higher in the Boltzmann plot method) energy level value.

Since its introduction in 2013, this method has piqued the interest of many researchers because there is no need to search for optically thin spectral lines, calibrate the detection system, or correct self-absorption (instead, using self-absorbed lines to establish the CD-SB plot directly). Safi et al. determined the electron temperature of plasmas in aluminum alloys, which shows that the CD-SB plot is more suitable for plasma temperature determination, especially in the later stages of plasma evolution [52]. Hu et al. utilized the CD-SB plot in conjunction with the standard reference line method to determine the elemental composition of aluminum-bronze and aluminum alloy samples, demonstrating that this method outperformed the traditional CF-LIBS method in terms of precision and accuracy [53]. As shown in **Figure 6**, the CD-SB method combined with the standard reference line improves the results of quantitative elemental analysis compared to the traditional CF-LIBS method. Overall, this method not only improves accuracy compared to the traditional CF-LIBS method but also eliminates the need for complex self-absorption correction procedures.

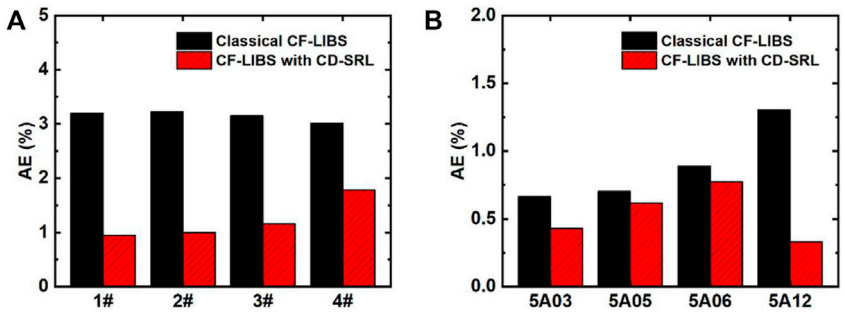

FIGURE 6 | AEs of aluminum-bronze alloy **(A)** and aluminum alloy **(B)** were calculated by classical CF-LIBS and CF-LIBS with CD-SRL. Reprinted from [53], Copyright (2021), with permission from Elsevier.

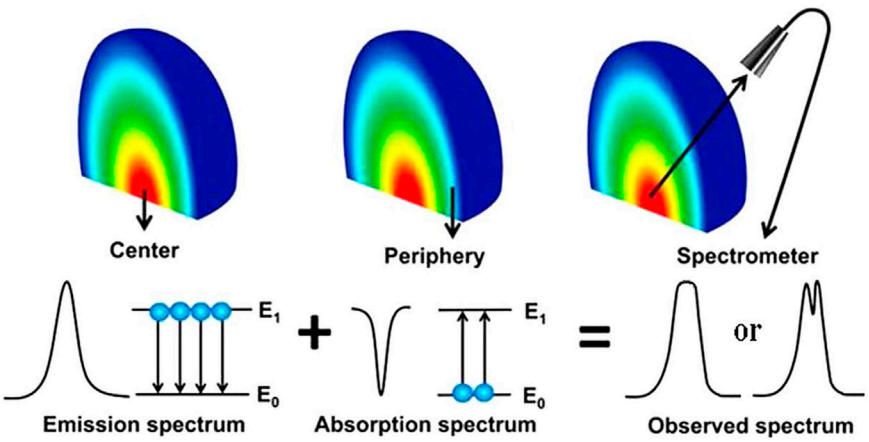

FIGURE 7 | Self-absorption process in the plasma (Refs. [54, 55]). Reproduced with permission from [54], ©2019 Institute Of Physics; Reproduced with permission from [55], ©2015 Optical Society of America.

4 SELF-ABSORPTION CORRECTION

4.1 Effect of Self-Absorption on CF-LIBS

The plasma is optically thin under ideal LIBS conditions, where the light emitted from the plasma is free from self-absorption. The intensities of spectral lines and elemental concentrations have a linear relationship. However, according to the classical radiation theory of spontaneous radiation and stimulated absorption, self-absorption is bound to exist, especially at higher elemental contents, corresponding to optically thick plasmas. The light emitted from the plasma center would be absorbed by atoms and ions at the plasma periphery. The self-absorption effect of the emission spectral lines increases the full width at half-maximum (FWHM), reduces the intensity, and even produces severe self-reversal phenomena. As a result, the optical information emitted from the plasma is distorted, far away from the original relationship with elemental contents. The complexity of laser-matter interactions, the inhomogeneity of the plasma, and the transient nature of plasma evolution make self-absorption a very complex phenomenon. The principle of the self-absorption process in plasma, including self-absorption and self-reversal, is shown in **Figure 7** [54, 55]), influenced by laser energy [56, 57], delay time [56–58], ambient gas [57, 59, 60], gas pressure [60], geometrical optical configuration [61, 62], and other methods [55, 63–65].

CF-LIBS was based on optically thin plasmas, without self-absorption. The electron temperature of the plasma was evaluated using the Boltzmann or Saha–Boltzmann plot, and the content of the elements in the sample was determined. Actually, inevitable self-absorption reduces the spectral intensity, resulting in an unrealistic higher value of the calculated plasma electron temperature, while the calculated intercept is lower.

4.2 Self-Absorbing Correction Improves the Accuracy of CF-LIBS

4.2.1 Curve of Growth

The curve of growth is a self-absorption correction model that can be applied to CF-LIBS to calculate plasma-related parameters in an iterative form based on the corrected experimental intensities. Gornushkin et al. first used the COG method for elemental analysis in stainless steel [66], establishing a Boltzmann

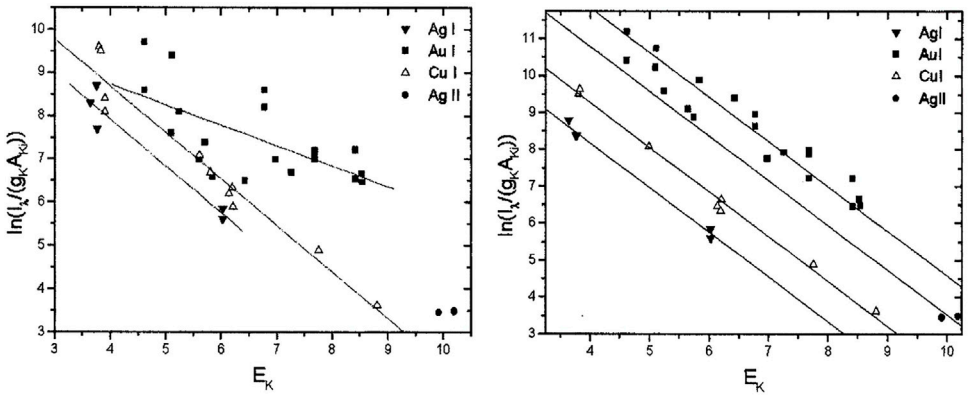

FIGURE 8 | Boltzmann plot for precious alloy Au917 (without self-absorption corrections) and the Boltzmann plot for precious alloy Au917 (with self-absorption corrections). Reprinted from [67], Copyright (2002), with permission from Elsevier.

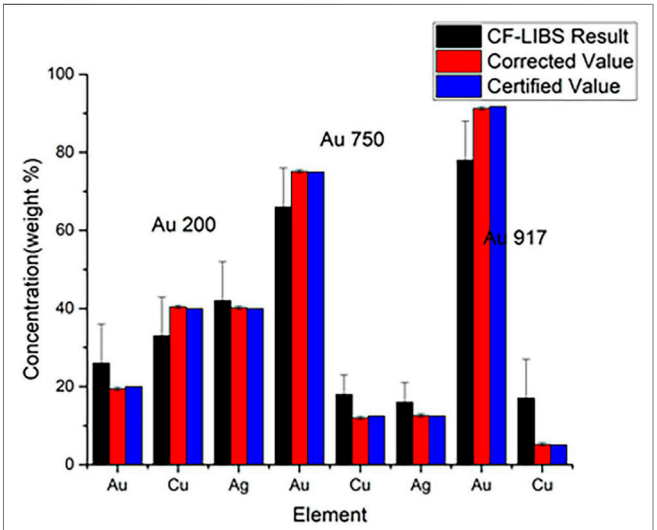

FIGURE 9 | Quantitative analysis for precious alloys. Reprinted from [67], Copyright (2002), with permission from Elsevier.

plot for the iron ion lines with different laser energies, and the results showed that the higher the temperature, the higher was the excitation of the higher energy states. Bulajic applied the COG model to CF-LIBS and used it to correct for self-absorption, elucidating the effect of self-absorption on the line profile [67]. The self-absorption was corrected by the plasma electron temperature, electron number density, Gaussian broadening, Lorentzian broadening, and optical path length using the COG method. Three different steel and ternary alloy samples were used to validate the COG model. The precious alloy Au917 was used to create a Boltzmann plot without self-absorption correction and with the COG method after self-absorption correction, as shown in **Figures 8**, **9**. It illustrates the findings of its quantitative analysis. The results demonstrated that the COG model could be applied with CF-LIBS, and the quantitative analysis results after self-absorption correction are very close to the certified values. Based on Bulajic's method, Praher et al. investigated the relationship between line broadening and self-absorption and proposed a simplified model [68]. Alfarraj et al. used the COG model, number density N, and absorption path length l to calculate the optical depth and self-absorption of strontium and aluminum lines under various conditions of different laser energies, gate delay time, and gate width time [69]. The COG method has been demonstrated to effectively correct self-absorption to improve the LIBS analysis performance. Nevertheless, this method and its variants have high algorithmic complexity, limiting practical applications.

4.2.2 Self-Absorption Coefficient

The so-called self-absorption coefficient method is to select an optically thin line (or H_α line) as an internal reference line (or theoretical FWHM) for self-absorption correction. Sun et al. proposed an internal reference for the self-absorption correction (IRSAC) method [27]. Several lines with ignorable self-absorption were selected as references to correct other lines with self-absorption based on the initial temperature and the intensity of the reference line. Finally, the optimal plasma temperature was determined by an iterative procedure until the convergence of the correlation coefficients on the Boltzmann plot. The Boltzmann plot of the aluminum alloy before and after correction is shown in **Figure 10** (see Ref. [27] for Fe-Cr alloy and Fe-Cr-Ni alloy). Similarly, Shakeel et al. applied the CF-LIBS method to Al-Si alloys, optimized the experimental conditions, removed background signals, and corrected for self-absorption with an internal reference line [70]. It is worth noting that the effectiveness of an optically thin plasma can be verified by comparing the intensity of two observed lines of the same element in the same state and transition energy level with the intensity calculated from the known atomic parameters [71, 72]. Based on this, Ahmed et al. constructed a Boltzmann plot with optically thin lines and compared it to the IRSAC method [73]. Dong et al. proposed an internal reference-external standard with the iteration correction (IRESIC) procedure based on the IRSAC approach, which requires a standard sample to estimate the plasma temperature using a genetic algorithm [74]. Furthermore, the internal reference line can be chosen

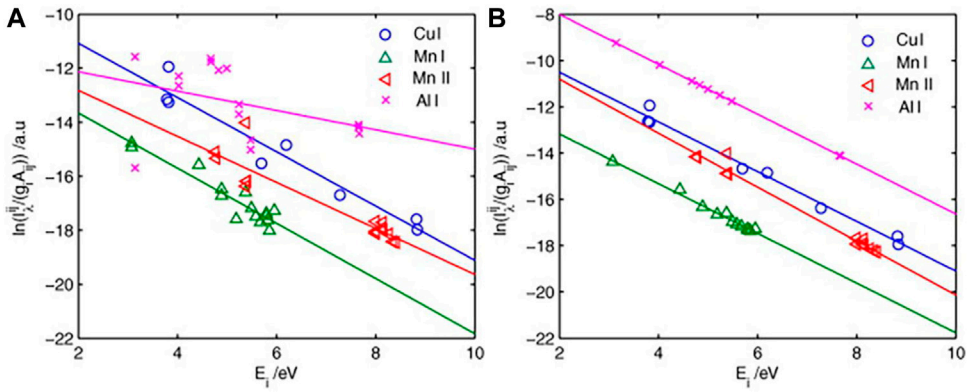

FIGURE 10 | (A) Initial Boltzmann plot derived from the raw line intensity of the aluminum alloy sample. **(B)** Boltzmann plot corrected by the IRSAC for the aluminum alloy sample. Reprinted from [27], Copyright (2019), with permission from Elsevier.

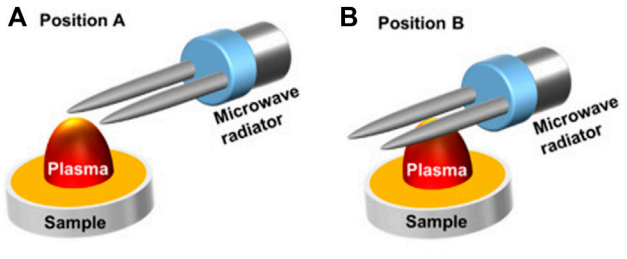

FIGURE 11 | Schematic presentation of two different microwave radiator locations related to the laser plasma and the sample in measurements: the two needles of a microwave radiator located about 2 mm above the sample surface and **(A)** 0.5 mm horizontally away from the ablation spot; **(B)** a 5-mm horizontal pass away from the ablation spot. Reprinted with permission from [84], ©The Optical Society.

manually or programmatically based on the emission coefficient [75], and temperature estimation can be optimized using a particle swarm algorithm [76]. However, the method of IRSAC still has some limitations: (I) the choice of the internal reference line has a significant impact on the final result, while it is not always possible to select the spectral line with the self-absorption coefficient $f^b_\lambda = 1$; (II) a spectral line with almost no self-absorption was chosen as the internal reference line for each element. After the last iteration, the Boltzmann plot may reveal that the fitted lines for various elements are not parallel. Eventually, setting the initial temperature of the element with the highest temperature estimated as the mean value of the temperatures determined by all elements may not be the best choice.

The self-absorption coefficient can be also expressed as [77]

$$SA = \left(\frac{\Delta\lambda}{\Delta\lambda_0}\right)^{1/\alpha}, \tag{21}$$

where $\alpha = -0.54$; $\Delta\lambda$ is the FWHM of the actual measured spectral line, and the Stark broadening can be separated t by the deconvolution method. The deconvolution method, however, is excessively time-consuming and can be approximated in the computation by assessing the actual measured width minus the Gauss instrumental broadening $\Delta\lambda \approx \Delta\lambda_{actual} - \Delta\lambda^2_{Gauss}/\Delta\lambda_{actual}$; $\Delta\lambda_0$ is the line FWHM, generally calculated by the H_α line. Using the H_α line for electron density measurement has the distinct advantage of providing a result that is not affected by self-absorption. Furthermore, there is also no need to scrounge around for electronic collision parameters [78, 79]. The specific formula for calculating the electron number density using the H_α is as follows:

$$N_e(H_\alpha) = 8.02 \times 10^{12}\left(\frac{\Delta\lambda_{1/2}}{\alpha_{1/2}}\right)^{3/2}, \tag{22}$$

where $\alpha_{1/2}$ is the half-width of the reduced Stark profiles and is a weak function of electron density and temperature, whose value can be found in [80]. Mansour obtained a more accurate electron temperature by analyzing the electron density ratio of the observation line to the optically thin H_α line, corrected for the self-absorption effect of the aluminum atomic line [81]. Similarly, Iqbal et al. compared the effect of self-absorption correction on the emission intensity of spectral lines using the internal reference line and density methods, respectively [82]. Based on Sun's method, Yang et al. proposed a modified method [83]: the spectral intensity was first corrected using the IRSAC method, and second the self-absorption effect was calculated, according to the electron number density and theoretical broadening.

4.2.3 Microwave-Assisted Excitation and Geometrical optical Configuration

The mechanism of microwave-assisted excitation is similar to the LIBS method of stimulated absorption, where the ground-state atoms in the plasma absorb microwave energy coupled to near-field radiation and transition to a higher energy level state. By adjusting the position of the sample relative to the microwave radiator, sharper peaks and better profiles were observed [84], and the schematic diagram of the device is shown in **Figure 11**.

Over a wide spectral range, the microwave-assisted approach can reduce multiple elemental self-absorption in LIBS. In addition, some exceptional geometries of optical systems can reduce the effects of self-absorption to a certain extent. In unusual parallel laser irradiation, the sample is ablated by a shockwave generated from the air breakdown plasma formed near the sample surface [61]; a dual pulse system with an orthogonal configuration of pre-ablation (the first pulse laser used to generate air breakdown plasma; the second laser is propagated perpendicular to the sample for sample ablation) and reheating models (the first laser is focused perpendicularly to the sample surface for sample plasma generation; the second laser propagated parallel to the sample for plasma heating) [85, 86]; the dual pulse system in collinear configuration [87, 88].

Although few people have studied the microwave-assisted and geometrical optical configuration in CF-LIBS, it gives us some inspiration to utilize the aforementioned methods in CF-LIBS.

5 CONCLUSION

Taking the matrix as part of the analysis interest, CF-LIBS can effectively avoid the matrix effect. It is based on basic assumptions of chemometric ablation, local thermal equilibrium, and optical thinness to describe the spectral intensity by mathematical models. The plasma electron temperature and elemental ratio are obtained by the slope and intercept of the Boltzmann plot. After normalization, the concentration of each element can be obtained. Generally speaking, the higher the linearity of the fitted lines for individual elements (same ionized state) and the more parallel the fitted lines for different elements, the higher will be the accuracy of the calculated results. The accuracy of the plasma electron temperature calculated by the Boltzmann plot method is low when only a small number of spectral lines of species in the same ionized state can be observed, or the corresponding energy level distribution range is small. The method of the Saha–Boltzmann plot was a modified method for solving this problem. CD-SB is another modified method, which can directly use atomic and ionic lines in the ground state. According to classical radiation theory, self-absorption exists. The self-absorption will inevitably affect the calculation of the plasma temperature and CF-LIBS accuracy. The methods for mitigating self-absorption are required, including the COG method, the self-absorption coefficient method, and the microwave-assisted and geometrical optical configuration methods. In recent years, CF-LIBS attracts increasing attention in a variety of fields, such as environmental protection, explorations of space, cultural heritage preservation, and geological survey.

AUTHOR CONTRIBUTIONS

NZ completed the manuscript, TO acquired the right to the pictures, and MW, ZL, CL, and YQ completed the collection of manuscripts. JL and HY revised the manuscript and provided funding support. NZ and QZ provided supervision and funding support. All the authors discussed the structure of the manuscript and commented on the manuscript.

FUNDING

This work was supported by the Key-Area Research and Development Program of Guangdong Province (2020B090922006), the National Natural Science Foundation of China (62005081 and 62105105), the Guangdong Basic and Applied Basic Research Foundation (2021A1515011932, 2020A1515110985, and 2019A1515111120), the Science and Technology Program of Guangzhou (202002030165), the Featured Innovation Project of Guangdong Education Department (2019KTSCX034), the Young Scholar Foundation of South China Normal University (19KJ13), and the Special Funds for the Cultivation of Guangdong College Students' Scientific and Technological Innovation ("Climbing Program" Special Funds) (pdjh2020b0153). Key R & D plan of Guangdong Province (2020B090924001), Natural Science Foundation of Top Talent of SZTU (2020103).

REFERENCES

1. Ma Y, He Y, Tong Y, Yu X, Tittel FK. Quartz-tuning-fork Enhanced Photothermal Spectroscopy for Ultra-high Sensitive Trace Gas Detection. *Opt Express* (2018) 26:32103–10. doi:10.1364/oe.26.032103
2. Lang Z, Qiao S, Ma Y. Acoustic Microresonator Based In-Plane Quartz-Enhanced Photoacoustic Spectroscopy Sensor with a Line Interaction Mode. *Opt Lett* (2022) 47:1295–8. doi:10.1364/ol.452085
3. Yang K, Li H, Gong H, Shen X, Hao Q, Yan M, et al. Temperature Measurement Based on Adaptive Dual-Comb Absorption Spectral Detection. *Chinese. Optic. Letter.* (2020) 18:051401. doi:10.3788/col202018.051401
4. AW Miziolek, V Palleschi, I Schechter, editors. *Laser Induced Breakdown Spectroscopy*. Cambridge University Press (2006).
5. Wu Y, Sawyer JC, Su L, Zhang Z. Quantitative Measurement of Electron Number in Nanosecond and Picosecond Laser-Induced Air Breakdown. *J Appl Phys* (2016) 119:173303. doi:10.1063/1.4948431
6. Yan C, Liang J, Zhao M, Zhang X, Zhang T, Li H. A Novel Hybrid Feature Selection Strategy in Quantitative Analysis of Laser-Induced Breakdown Spectroscopy. *Analytica Chim Acta* (2019) 1080:35–42. doi:10.1016/j.aca.2019.07.012
7. Samek O, Beddows D, Kaiser J, Kukhlevsky S, Liska M, Telle H, et al. Application of Laser-Induced Breakdown Spectroscopy to *In Situ* Analysis of Liquid Samples. *Opt Eng* (2000) 39.
8. Cahoon EM, Almirall JR. Quantitative Analysis of Liquids from Aerosols and Microdrops Using Laser Induced Breakdown Spectroscopy. *Anal Chem* (2012) 84:2239–44. doi:10.1021/ac202834j
9. Hanafi M, Omar MM, Gamal YEE-D. Study of Laser-Induced Breakdown Spectroscopy of Gases. *Radiat Phys Chem* (2000) 57:11–20. doi:10.1016/s0969-806x(99)00344-8
10. Sturm V, Noll R. Laser-induced Breakdown Spectroscopy of Gas Mixtures of Air, CO_2, N_2, and C_3H_8 for Simultaneous CHO, and N Measurement. *Appl Opt* (2003) 42:6221–5. doi:10.1364/ao.42.006221
11. Sabsabi M, Cielo P. Quantitative Analysis of Aluminum Alloys by Laser-Induced Breakdown Spectroscopy and Plasma Characterization. *Appl Spectrosc* (1995) 49:499–507. doi:10.1366/0003702953964408
12. Sattmann R, Sturm V, Noll R. Laser-induced Breakdown Spectroscopy of Steel Samples Using Multiple Q-Switch Nd:YAG Laser Pulses.

J Phys D: Appl Phys (1995) 28:2181–7. doi:10.1088/0022-3727/28/10/030
13. Maravelaki PV, Zafiropulos V, Kilikoglou V, Kalaitzaki M, Fotakis C. Laser-induced Breakdown Spectroscopy as a Diagnostic Technique for the Laser Cleaning of marble. *Spectrochimica Acta B: At Spectrosc* (1997) 52:41–53. doi:10.1016/s0584-8547(96)01573-x
14. Klein S, Stratoudaki T, Zafiropulos V, Hildenhagen J, Dickmann K, Lehmkuhl T. Laser-induced Breakdown Spectroscopy for On-Line Control of Laser Cleaning of sandstone and Stained Glass. *Appl Phys A: Mater Sci Process* (1999) 69:441–4. doi:10.1007/s003390051029
15. Zhang Y, Zhang T, Li H. Application of Laser-Induced Breakdown Spectroscopy (LIBS) in Environmental Monitoring. *Spectrochimica Acta Part B: At Spectrosc* (2021) 181:106218. doi:10.1016/j.sab.2021.106218
16. Zhao NJ, Meng DS, Jia Y, Ma MJ, Fang L, Liu JG, et al. On-line Quantitative Analysis of Heavy Metals in Water Based on Laser-Induced Breakdown Spectroscopy. *Opt Express* (2019) 27:A495–A506. doi:10.1364/oe.27.00a495
17. Dell'Aglio M, De Giacomo A, Gaudiuso R, Pascale OD, Senesi GS, Longo S. Laser Induced Breakdown Spectroscopy Applications to Meteorites: Chemical Analysis and Composition Profiles. *Geochimica et Cosmochimica Acta* (2010) 74:7329. doi:10.1016/j.gca.2010.09.018
18. David G, Meslin P-Y, Dehouck E, Gasnault O, Cousin A, Forni O, et al. Laser-Induced Breakdown Spectroscopy (LIBS) Characterization of Granular Soils: Implications for ChemCam Analyses at Gale Crater, Mars. *Icarus* (2021) 365:114481. doi:10.1016/j.icarus.2021.114481
19. Gaudiuso R, Dell'Aglio M, De Pascale O, Loperfido S, Mangone A, De Giacomo A. Laser-induced Breakdown Spectroscopy of Archaeological Findings with Calibration-free Inverse Method: Comparison with Classical Laser-Induced Breakdown Spectroscopy and Conventional Techniques. *Analytica Chim Acta* (2014) 813:15–24. doi:10.1016/j.aca.2014.01.020
20. Gaudiuso R, Dell'Aglio M, De Pascale O, Santagata A, De Giacomo A. Laser-induced Plasma Analysis of Copper Alloys Based on Local Thermodynamic Equilibrium: An Alternative Approach to Plasma Temperature Determination and Archeometric Applications. *Spectrochimica Acta Part B: At Spectrosc* (2012) 74-75:38–45. doi:10.1016/j.sab.2012.06.034
21. Mohamed WTY. Study of the Matrix Effect on the Plasma Characterization of Six Elements in Aluminum Alloys Using LIBS with a Portable Echelle Spectrometer. *Prog Phys* (2007) 2:42–48.
22. Xu W, Sun C, Tan Y, Gao L, Zhang Y, Yue Z, et al. Total Alkali Silica Classification of Rocks with LIBS: Influences of the Chemical and Physical Matrix Effects. *J Anal Spectrom* (2020) 35:1641–53. doi:10.1039/d0ja00157k
23. Ciucci A, Corsi M, Palleschi V, Rastelli S, Salvetti A, Tognoni E. New Procedure for Quantitative Elemental Analysis by Laser-Induced Plasma Spectroscopy. *Appl Spectrosc* (1999) 53:960–4. doi:10.1366/0003702991947612
24. Kaiser J, Novotný K, Martin MZ, Hrdlička A, Malina R, Hartl M, et al. Trace Elemental Analysis by Laser-Induced Breakdown Spectroscopy-Biological Applications. *Surf Sci Rep* (2012) 67:233–43. doi:10.1016/j.surfrep.2012.09.001
25. Loureiro J, Amorim J. *Kinetics and Spectroscopy of Low Temperature Plasmas*. Berlin: Springer (2016).
26. Tognoni E, Cristoforetti G, Legnaioli S, Palleschi V. Calibration-Free Laser-Induced Breakdown Spectroscopy: State of the Art. *Spectrochimica Acta Part B: At Spectrosc* (2010) 65:1–14. doi:10.1016/j.sab.2009.11.006
27. Sun L, Yu H. Correction of Self-Absorption Effect in Calibration-free Laser-Induced Breakdown Spectroscopy by an Internal Reference Method. *Talanta* (2009) 79:388–95. doi:10.1016/j.talanta.2009.03.066
28. Wang Y, Chen Y, Li R, Kang J, Gao J. Quantitative Elemental Analysis of Aluminum Alloys with One-point Calibration High Repetition Rate Laser-Ablation Spark-Induced Breakdown Spectroscopy. *J Anal Spectrom* (2021) 36:314–21. doi:10.1039/d0ja00398k
29. De Giacomo A, Gaudiuso R, Dell'Aglio M, Santagata A. The Role of Continuum Radiation in Laser Induced Plasma Spectroscopy. *Spectrochimica Acta Part B: At Spectrosc* (2010) 65:385–94. doi:10.1016/j.sab.2010.03.016
30. Ahmed N, Ahmed R, Rafiqe M, Baig MA. A Comparative Study of Cu-Ni Alloy Using LIBS, LA-TOF, EDX, and XRF. *Laser Part Beams* (2016) 35:1–9. doi:10.1017/s0263034616000732
31. Fu H, Ni Z, Wang H, Jia J, Dong F. Accuracy Improvement of Calibration-free Laser-Induced Breakdown Spectroscopy. *Plasma Sci Technol* (2018) 21:034001. doi:10.1088/2058-6272/aaead6
32. Huddlestone RH, Leonard SL. *Plasma Diagnostic Techniques*. Plasma Diagnostic Techniques (1965).
33. Khadr MH, Elgala H. Augmented Communications: Spectral Efficiency and Security Enhanced Visible Light Communications by Design. *Chinese. Optic.Letter.* (2020) 18:090601. doi:10.3788/col202018.090601
34. Taschuk MT, Godwal Y, Tsui YY, Fedosejevs R, Tripathi M, Kearton B. Absolute Characterization of Laser-Induced Breakdown Spectroscopy Detection Systems. *Spectrochimica Acta Part B: At Spectrosc* (2008) 63:525–35. doi:10.1016/j.sab.2008.01.004
35. Fahad M, Farooq Z, Abrar M, Shah KH, Iqbal T, Saeed S. Elemental Analysis of limestone by Laser-Induced Breakdown Spectroscopy, Scanning Electron Microscopy Coupled with Energy Dispersive X-ray Spectroscopy and Electron Probe Microanalysis. *Laser Phys* (2018) 28:125701. doi:10.1088/1555-6611/aae49d
36. Pandhija S, Rai AK. *In Situ* multielemental Monitoring in Coral Skeleton by CF-LIBS. *Appl Phys B* (2009) 94:545–52. doi:10.1007/s00340-008-3343-5
37. Pandhija S, Rai NK, Rai AK, Thakur SN. Contaminant Concentration in Environmental Samples Using LIBS and CF-LIBS. *Appl Phys B* (2010) 98:231–41. doi:10.1007/s00340-009-3763-x
38. Kumar R, Rai AK, Alamelu D, Aggarwal SK. Monitoring of Toxic Elements Present in Sludge of Industrial Waste Using CF-LIBS. *Environ Monit Assess* (2013) 185:171–80. doi:10.1007/s10661-012-2541-0
39. Agrawal R, Kumar R, Rai S, Pathak AK, Rai AK, Rai GK. LIBS: A Quality Control Tool for Food Supplements. *Food Biophys* (2011) 6:527–33. doi:10.1007/s11483-011-9235-y
40. Du Y, Wang Q, Yang R, Cui X. *Quantitative Determination of Hydrogen Isotope in Titanium Using LIBS*. SPIE (2019).
41. Ahmed N, Ahmed R, Baig MA. Analytical Analysis of Different Karats of Gold Using Laser Induced Breakdown Spectroscopy (LIBS) and Laser Ablation Time of Flight Mass Spectrometer (LA-TOF-MS). *Plasma Chem Plasma Process* (2018) 38:207–22. doi:10.1007/s11090-017-9862-2
42. Hamad TK, et al. Calibration Free Laser Induced Breakdown Spectroscopy (CF-LIBS) as a Tool for Quantitative Elemental Analysis of Iraqi Cement. *Anjs* (2018) 1:60–8. doi:10.22401/sic.i.08
43. Springer-VerlagYalcin S, Crosley D, Smith G, Faris G. Influence of Ambient Conditions on the Laser Air Spark. *Appl Phys B* (1999) 68:121. doi:10.1007/s003400050596
44. Horňáčková M, Horňáček M, Rakovský J, Hudec P, Veis P. Determination of Si/Al Molar Ratios in Microporous Zeolites Using Calibration-free Laser Induced Breakdown Spectroscopy. *Spectrochimica Acta Part B: At Spectrosc* (2013) 88:69. doi:10.1016/j.sab.2013.03.006
45. Zhang S, Hu Z, Zhao Z, Chen F, Tang Y, Sheng Z, et al. Quantitative Analysis of mineral Elements in Hair and Nails Using Calibration-free Laser-Induced Breakdown Spectroscopy. *Optik* (2021) 242:167067. doi:10.1016/j.ijleo.2021.167067
46. Veis P, Marín-Roldán A, Dwivedi V, Karhunen J, Paris P, Jõgi I, et al. Quantification of H/D Content in Be/W Mixtures Coatings by CF-LIBS. *Phys Scr* (2020) 2020:014073. doi:10.1088/1402-4896/ab7ebd
47. Pribula M, Krištof J, Suchoňová M, Horňáčková M, Plavčan J, Hakola A, et al. Use of the Near Vacuum UV Spectral Range for the Analysis of W-Based Materials for Fusion Applications Using LIBS. *Phys Scr* (2016) T167:014045. doi:10.1088/0031-8949/t167/1/014045
48. Marín Roldán A, Pisarčík M, Veis M, Držík M, Veis P. Calibration-free Analysis of a Tungsten-Based Target for Diagnostics of Relevant Fusion Materials Comparing Picosecond and Nanosecond LIBS. *Spectrochimica Acta Part B: At Spectrosc* (2021) 177:106055. doi:10.1016/j.sab.2020.106055
49. Horňáčková M, Veis P. Analysis of Acid Pitchstone (Iceland) Using Laser Induced Breakdown Spectroscopy. *LIBS* (2013) 18:1–8.
50. Wang Y, Su M, Sun D, Wu C, Zhang X, Lu Q, et al. Comparative Study of Magnesium and Calcium in Codonopsis Pilosula Samples Detected by CF-LIBS and LCGD-AES. *Microchemical J* (2018) 137:318–23. doi:10.1016/j.microc.2017.11.011
51. Cristoforetti G, Tognoni E. Calculation of Elemental Columnar Density from Self-Absorbed Lines in Laser-Induced Breakdown Spectroscopy: A Resource for Quantitative Analysis. *Spectrochimica Acta Part B: At Spectrosc* (2013) 79-80:63–71. doi:10.1016/j.sab.2012.11.010
52. Safi A, Tavassoli SH, Cristoforetti G, Legnaioli S, Palleschi V, Rezaei F, et al. Determination of Excitation Temperature in Laser-Induced Plasmas Using

Columnar Density Saha-Boltzmann Plot. *J Adv Res* (2019) 18:1–7. doi:10.1016/j.jare.2019.01.008
53. Hu Z, Chen F, Zhang D, Chu Y, Wang W, Tang Y, et al. A Method for Improving the Accuracy of Calibration-free Laser-Induced Breakdown Spectroscopy by Exploiting Self-Absorption. *Analytica Chim Acta* (2021) 1183:339008. doi:10.1016/j.aca.2021.339008
54. Hou J, Zhang L, Zhao Y, Wang Z, Zhang Y, Ma W, et al. Mechanisms and Efficient Elimination Approaches of Self-Absorption in LIBS. *Plasma Sci Technol* (2019) 21:034016. doi:10.1088/2058-6272/aaf875
55. Li J-M, Guo L-B, Li C-M, Zhao N, Yang X-Y, Hao Z-Q, et al. Self-absorption Reduction in Laser-Induced Breakdown Spectroscopy Using Laser-Stimulated Absorption. *Opt Lett* (2015) 40:5224–6. doi:10.1364/ol.40.005224
56. Yi R, Guo L, Li C, Yang X, Li J, Li X, et al. Investigation of the Self-Absorption Effect Using Spatially Resolved Laser-Induced Breakdown Spectroscopy. *J Anal Spectrom* (2016) 31:961–7. doi:10.1039/c5ja00500k
57. Rezaei F, Karimi P, Tavassoli SH. Estimation of Self-Absorption Effect on Aluminum Emission in the Presence of Different noble Gases: Comparison between Thin and Thick Plasma Emission. *Appl Opt* (2013) 52:5088–96. doi:10.1364/ao.52.005088
58. Hou J, Zhang L, Yin W, Yao S, Zhao Y, Ma W, et al. Development and Performance Evaluation of Self-absorption-free Laser-Induced Breakdown Spectroscopy for Directly Capturing Optically Thin Spectral Line and Realizing Accurate Chemical Composition Measurements. *Opt Express* (2017) 25:23024–34. doi:10.1364/oe.25.023024
59. Ibano K, Nishijima D, Ueda Y, Doerner RP. LIBS Measurement of Trace Tantalum and Rhenium in Tungsten for *In-Situ* Diagnostic of Nuclear Transmutation. *J Nucl Mater* (2019) 522:324–8. doi:10.1016/j.jnucmat.2019.05.030
60. Effenberger A, Jr., Scott J. Effect of Atmospheric Conditions on LIBS Spectra. *Sensors* (2010) 10:4907–25. doi:10.3390/s100504907
61. Pardede M, Karnadi I, Lie ZS, Jobiliong E, Tanra I, Hedwig R, et al. Unusual Parallel Laser Irradiation for Suppressing Self-Absorption in Single Pulse Laser-Induced Breakdown Spectroscopy. *Opt Express* (2021) 29:22593–602. doi:10.1364/oe.431784
62. Karnadi I, Pardede M, Tanra I, Hedwig R, Marpaung AM, Lie ZS, et al. Suppression of Self-Absorption in Laser-Induced Breakdown Spectroscopy Using a Double Pulse Orthogonal Configuration to Create Vacuum-like Conditions in Atmospheric Air Pressure. *Sci Rep* (2020) 10:13278. doi:10.1038/s41598-020-70151-6
63. Tang Y, Ma S, Yuan R, Ma Y, Sheng W, Zhan S, et al. Spectral Interference Elimination and Self-Absorption Reduction in Laser-Induced Breakdown Spectroscopy Assisted with Laser-Stimulated Absorption. *Opt Lasers Eng* (2020) 134:106254. doi:10.1016/j.optlaseng.2020.106254
64. Viljanen J, Sun Z, Alwahabi ZT. Microwave Assisted Laser-Induced Breakdown Spectroscopy at Ambient Conditions. *Spectrochimica Acta Part B: At Spectrosc* (2016) 118:29–36. doi:10.1016/j.sab.2016.02.002
65. Viljanen J, Zhao H, Zhang Z, Toivonen J, Alwahabi ZT. Real-time Release of Na, K and Ca during thermal Conversion of Biomass Using Quantitative Microwave-Assisted Laser-Induced Breakdown Spectroscopy. *Spectrochimica Acta Part B: At Spectrosc* (2018) 149:76–83. doi:10.1016/j.sab.2018.07.022
66. Gornushkin IB, Anzano JM, King LA, Smith BW, Omenetto N, Winefordner JD. Curve of Growth Methodology Applied to Laser-Induced Plasma Emission Spectroscopy. *Spectrochimica Acta Part B: At Spectrosc* (1999) 54:491–503. doi:10.1016/s0584-8547(99)00004-x
67. Bulajic D, Corsi M, Cristoforetti G, Legnaioli S, Palleschi V, Salvetti A, et al. A Procedure for Correcting Self-Absorption in Calibration Free-Laser Induced Breakdown Spectroscopy. *Spectrochimica Acta Part B: At Spectrosc* (2002) 57:339–53. doi:10.1016/s0584-8547(01)00398-6
68. Praher B, Palleschi V, Viskup R, Heitz J, Pedarnig JD. Calibration Free Laser-Induced Breakdown Spectroscopy of Oxide Materials. *Spectrochimica Acta Part B: At Spectrosc* (2010) 65:671–9. doi:10.1016/j.sab.2010.03.010
69. Alfarraj BA, Bhatt CR, Yueh FY, Singh JP. Evaluation of Optical Depths and Self-Absorption of Strontium and Aluminum Emission Lines in Laser-Induced Breakdown Spectroscopy (LIBS). *Appl Spectrosc* (2017) 71:640–50. doi:10.1177/0003702817693231
70. Shakeel H, Haq SU, Aisha G, Nadeem A. Quantitative Analysis of Al-Si alloy Using Calibration Free Laser Induced Breakdown Spectroscopy (CF-LIBS). *Phys Plasmas* (2017) 24:063516. doi:10.1063/1.4985327
71. Unnikrishnan VK, Mridul K, Nayak R, Alti K, Kartha VB, Santhosh C, et al. Calibration-free Laser-Induced Breakdown Spectroscopy for Quantitative Elemental Analysis of Materials. *Pramana - J Phys* (2012) 79:299–310. doi:10.1007/s12043-012-0298-1
72. Hou JJ, Zhang L, Zhao Y, Ma WG, Dong L, Yin WB, et al. Rapid Selection of Analytical Lines for SAF-LIBS Based on the Doublet Intensity Ratios at the Initial and Final Stages of Plasma. *Opt Express* (2019) 27:32184–92. doi:10.1364/oe.27.032184
73. Ahmed N, Abdullah M, Ahmed R, Piracha NK, Baig MA. Quantitative Analysis of a Brass alloy Using CF-LIBS and a Laser Ablation Time-Of-Flight Mass Spectrometer. *Laser Phys* (2017) 28:016002. doi:10.1088/1555-6611/aa962b
74. Dong J, Liang L, Wei J, Tang H, Zhang T, Yang X, et al. A Method for Improving the Accuracy of Calibration-free Laser-Induced Breakdown Spectroscopy (CF-LIBS) Using Determined Plasma Temperature by Genetic Algorithm (GA). *J Anal Spectrom* (2015) 30:1336–44. doi:10.1039/c4ja00470a
75. Aydin Ü, Roth P, Gehlen CD, Noll R. Spectral Line Selection for Time-Resolved Investigations of Laser-Induced Plasmas by an Iterative Boltzmann Plot Method. *Spectrochimica Acta Part B: At Spectrosc* (2008) 63:1060–5. doi:10.1016/j.sab.2008.08.003
76. Yang J, Li X, Xu J, Ma X. A Calibration-free Laser-Induced Breakdown Spectroscopy (CF-LIBS) Quantitative Analysis Method Based on the Auto-Selection of an Internal Reference Line and Optimized Estimation of Plasma Temperature. *Appl Spectrosc* (2018) 72:129–40. doi:10.1177/0003702817734293
77. El Sherbini AM, El Sherbini TM, Hegazy H, Cristoforetti G, Legnaioli S, Palleschi V, et al. Evaluation of Self-Absorption Coefficients of Aluminum Emission Lines in Laser-Induced Breakdown Spectroscopy Measurements. *Spectrochimica Acta Part B: At Spectrosc* (2005) 60:1573–9. doi:10.1016/j.sab.2005.10.011
78. Konjević N, Wiese WL. Experimental Stark Widths and Shifts for Spectral Lines of Neutral and Ionized Atoms. *J Phys Chem Reference Data* (1990) 19:1307
79. Stark-b. Available at: http://stark-b.obspm.fr/index.php/table. Accessed 1 March, 2022.
80. Griem HR. *Spectral Line Broadening by Plasmas* (1974).
81. Mansour SAM. Self-Absorption Effects on Electron Temperature-Measurements Utilizing Laser Induced Breakdown Spectroscopy (LIBS)-Techniques. *Opt Photon J* (2015) 03:12. doi:10.4236/opj.2015.53007
82. Iqbal SMZ, Uddin Z, Umar ZA, Ahmed N, Ahmed R, Baig MA. Analysis of Lakhra Coal by Calibration Free Laser-Induced Breakdown Spectroscopy (CF-LIBS) and Comparison of Self-Absorption Correction Procedures. *Anal Lett* (2021) 1–13. doi:10.1080/00032719.2021.1910831
83. Yang Y, Hao X, Ren L. Correction of Self-Absorption Effect in Calibration-free Laser-Induced Breakdown spectroscopy(CF-LIBS) by Considering Plasma Temperature and Electron Density. *Optik* (2020) 208:163702. doi:10.1016/j.ijleo.2019.163702
84. Tang Y, Li J, Hao Z, Tang S, Zhu Z, Guo L, et al. Multielemental Self-Absorption Reduction in Laser-Induced Breakdown Spectroscopy by Using Microwave-Assisted Excitation. *Opt Express* (2018) 26:12121–30. doi:10.1364/oe.26.012121
85. Ma Y, Zhang W, Xiong Z, Cui H, Li Q, Zhou R, et al. Accurate Sulfur Determination of Coal Using Double-Pulse Laser-Induced Breakdown Spectroscopy. *J Anal Spectrom* (2020) 35:1458–63. doi:10.1039/c9ja00448c
86. Gautier C, Fichet P, Menut D, Lacour J-L, L'Hermite D, Dubessy J. Quantification of the Intensity Enhancements for the Double-Pulse Laser-Induced Breakdown Spectroscopy in the Orthogonal Beam Geometry. *Spectrochimica Acta Part B: At Spectrosc* (2005) 60:265–76. doi:10.1016/j.sab.2005.01.006
87. Maher WE, Hall RB. Experimental Study of Effects from Two Laser Pulses. *J Appl Phys* (1976) 47:2486–93. doi:10.1063/1.322963

88. Abbas Q, Israr MA, Haq SU, Nadeem A. Exploiting Calibration Free Laser-Induced Breakdown Spectroscopy (CF-LIBS) for the Analysis of Food Colors. *Optik* (2021) 236:166531. doi:10.1016/j.ijleo.2021.166531

Conflict of Interest: The authors declare that the research was conducted in the absence of any commercial or financial relationships that could be construed as a potential conflict of interest.

Publisher's Note: All claims expressed in this article are solely those of the authors and do not necessarily represent those of their affiliated organizations, or those of the publisher, the editors, and the reviewers. Any product that may be evaluated in this article, or claim that may be made by its manufacturer, is not guaranteed or endorsed by the publisher.

frontiers | Frontiers in Physics

ORIGINAL RESEARCH
published: 09 June 2022
doi: 10.3389/fphy.2022.890197

Stray-Light Suppression of the Internally Occulted Reflecting Solar Corona Imager

*Guang Zhang[1,2], Yunqi Wang[1], Lingping He[1], Xiaodong Wang[1], Shuai Ren[1,2], Yubo Xuan[3], Fei Liu[4] and Bo Chen[1]**

[1]Changchun Institute of Optics, Fine Mechanics and Physics, Chinese Academy of Sciences (CAS), Changchun, China, [2]University of Chinese Academy of Sciences, Beijing, China, [3]College of Communication Engineering, Jilin University, Changchun, China, [4]School of Physics and Optoelectronic Engineering, Xidian University, Xi'an, China

In order to achieve a clear observation of the ultra-low brightness solar corona and provide a physical basis for forecasting space weather that seriously affects the human living environment, the stray-light suppression level becomes the key factor affecting the development of the coronagraph. In this study, a stray-light suppression method is adopted for Solar Corona Imager (SCI) which is a dual-waveband internally occulted reflecting coronagraph simultaneously and independently observing the inner corona in the HI Lyman-alpha (121.6 ± 10 nm) line and white-light (700.0 ± 40 nm) wavebands with a field-of-view (FOV) from 1.1 to 2.5 $R_\odot$ ($R_\odot$ stands for the mean solar radius). The scattered stray-light from the primary mirror, including the surface errors, cosmetic defects, and particulate contamination, is analyzed and suppressed, and the corresponding scattering models are established for simulation based on the laboratory testing. The stray-light measurement results for SCI in the laboratory show that the stray-light level can be suppressed to the order of 10^{-8} $B_\odot$ at 2.5 $R_\odot$ ($B_\odot$ is the mean brightness of the solar disk) in the white-light (WL) band, which is consistent with the stray-light level obtained by simulation and verifies the modeling and simulation.

Keywords: solar corona imager, internally occulted reflecting coronagraph, stray-light, surface quality, scattering

Edited by:
Yufei Ma,
Harbin Institute of Technology, China

Reviewed by:
Sanjay Gosain,
National Solar Observatory, United States
Debi Prasad Choudhary,
California State University, Northridge, United States
Ziyang Chen,
Huaqiao University, China

****Correspondence:***
Bo Chen
chenb@ciomp.ac.cn

Specialty section:
This article was submitted to Optics and Photonics, a section of the journal Frontiers in Physics

Received: *05 March 2022*
Accepted: *13 April 2022*
Published: *09 June 2022*

Citation:
Zhang G, Wang Y, He L, Wang X, Ren S, Xuan Y, Liu F and Chen B (2022) Stray-Light Suppression of the Internally Occulted Reflecting Solar Corona Imager. Front. Phys. 10:890197. doi: 10.3389/fphy.2022.890197

1 INTRODUCTION

The corona is the outermost layer of the Sun's atmosphere, extending from the edge of the solar chromosphere to several solar radii, which is composed of thin plasma. The ejection of the plasmas has a great impact on the space environment around the Earth. Research on coronal mass ejections (CMEs) is of great significance for exploring the response of different layers of the solar atmosphere to solar eruptions and for providing observation data for space weather forecasting and the safety of the space environment.

In the past decades, a number of solar coronagraphs have been developed, and a lot of high-quality imaging and spectroscopic data have been provided. The representative ones are OSO-7 in 1971, Skylab-HAO in 1973, SOHO LASCO-C1 in 1995, STEREO SECCHI-COR1 in 2006, Solar Orbiter-Metis in 2020, and ADITYA-L1 VELC planned for launch in 2022 [1–6]. Advanced Space-based Solar Observatory (ASO-S) is a mission proposed for the 25th solar maximum by the Chinese solar physics community, which is scheduled to be launched in 2022 for imaging the inner corona from 1.1 to 2.5 $R_\odot$ in the Lyman-alpha (121.6 ± 10nm) line and white-light (700.0 ± 40 nm) wavebands, which will not only advance our understanding of the underlying physics of solar eruptions but also help to improve forecast capability of space weather [7].

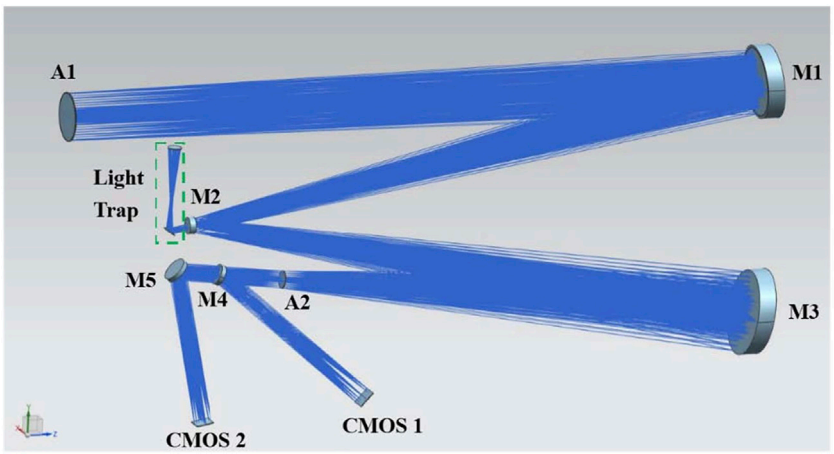

FIGURE 1 | Schematic optical layout of SCI.

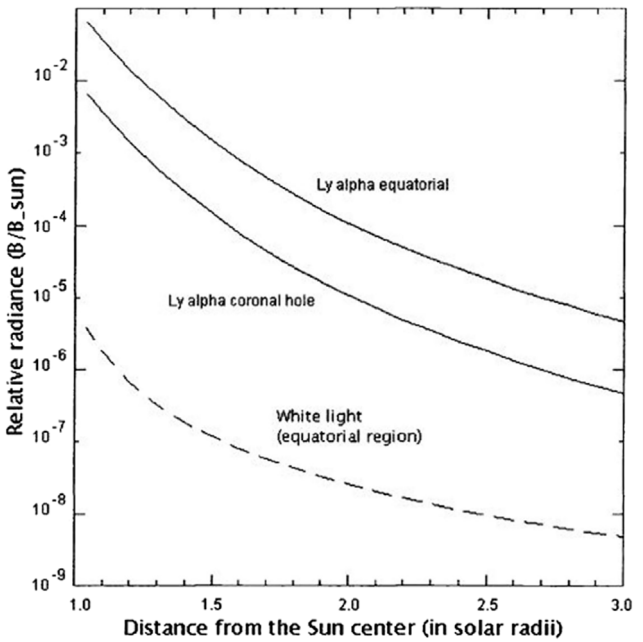

FIGURE 2 | Brightness of the corona compared to the solar disk in Lyman-alpha and white-light wavebands.

In this study, we describe the optical layout of the SCI instrument in **Section 2**, present the stray-light analysis and suppression in **Section 3**, present the stray-light measurement in **Section 4**, and summarize the study in **Section 5**.

2 DESCRIPTION OF SCI

The SCI employs an internally occulted design, which avoids the problems of low spatial resolution and large volume of the externally occulted coronagraph [8]. Due to the imaging observation of the inner corona in both Lyman-alpha and white-light wavebands, the two working wavebands are far away that the transmission optical system cannot achieve imaging of the two wavebands simultaneously. Therefore, an off-axis three-mirror reflective structure is applied that can effectively suppress the stray-light of the system. **Figure 1** shows the detailed optical layout of the SCI [9].

The sunlight illuminates the off-axis parabolic primary mirror (M1) through the entrance aperture (A1). M1 images the solar disk and the corona on a convex secondary mirror (M2), which has a cone-shaped hole to ensure the solar disk light passes through and enters the light trap behind M2. Then, the coronal light remains and is reflected from M2 to an off-axis third mirror (M3). A Lyot stop (A2) is placed in the conjugate plane of A1 imaged by M1, M2, and M3 to block the light diffracted from the edge of A1. A beam splitter (M4) composed of a multilayer film is used to separate the Lyman-alpha corona and the white-light corona to CMOS 1 and CMOS 2 [10].

3 STRAY-LIGHT SUPPRESSION OF SCI

The brightness of the corona is extremely weak compared to that of the solar disk, as shown in **Figure 2** [11]. In order to observe the corona from 1.1 to 2.5 $R_{\odot}$, the stray-light suppression level must be as low as 10^{-4} to 10^{-6} $B_{\odot}$ in Lyman-alpha wavebands and 10^{-6} to 10^{-8} $B_{\odot}$ in white-light wavebands. Therefore, stray-light suppression becomes the most important issue for SCI. Three main stray-light sources need to be suppressed, including the direct stray-light from the solar disk, the diffracted stray-light from the edge of A1 that is illuminated by the Sun, and the scattered stray-light from M1. For an internally occulted reflecting coronagraph, the scattered stray-light from the primary mirror determines the stray-light suppression level [12–15]. Owing to the extremely high requirements for stray-light suppression in the white-light wavebands, detailed analysis of the scattered stray-light in the white-light wavebands is required.

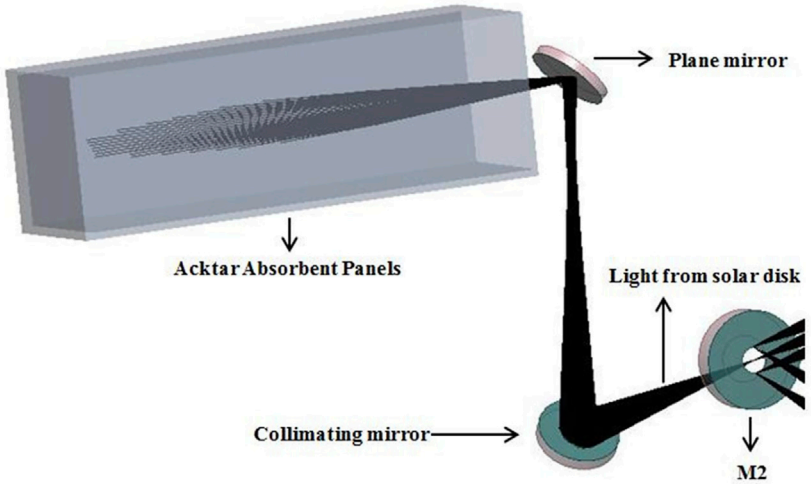

FIGURE 3 | Ray-tracing diagram of direct stray-light from the solar disk.

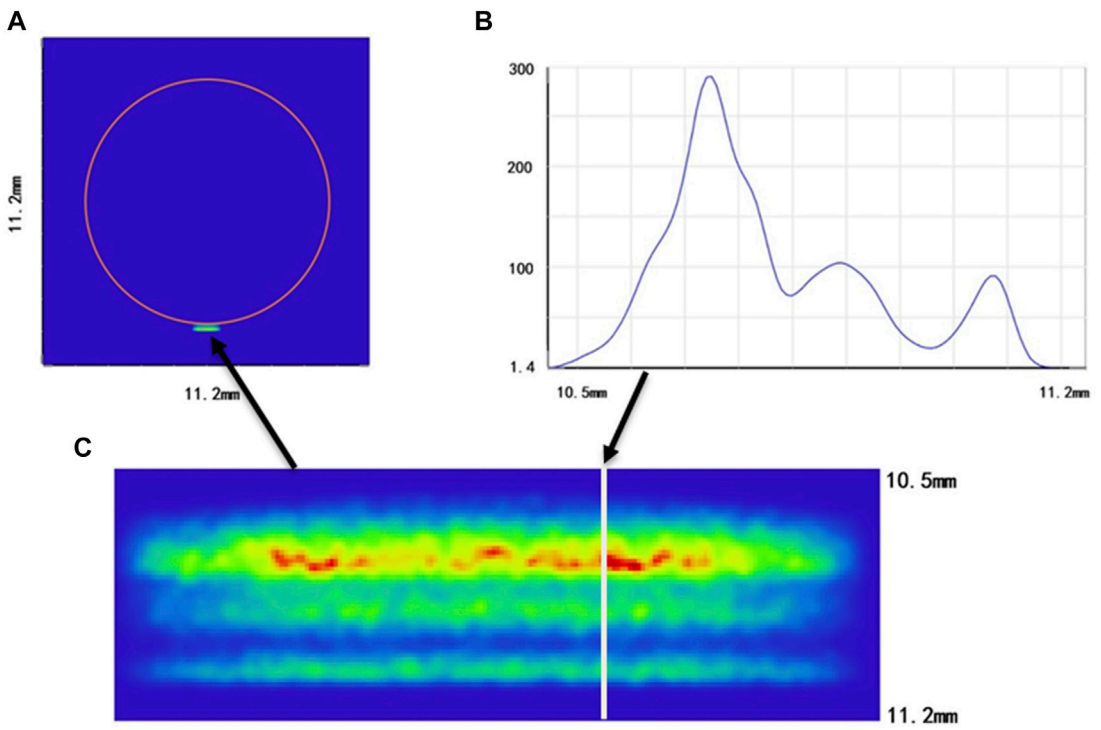

FIGURE 4 | Simulation results of diffracted stray-light at 700.0 nm. **(A)** Diffracted stray-light image at the Lyot stop A2 position. **(B)** Relative intensity distribution curve of diffracted stray-light from a radius of 10.5–11.2 mm. **(C)** Partial enlarged view of a diffracted stray-light image.

3.1 Direct Stray-Light From the Solar Disk

Because of no external occulter in front of M1 to block the solar disk light, the light will directly enter SCI and become the first source of stray-light. In order to eliminate the direct light from the solar disk, M2 is designed with a cone-shaped hole at the center as the internal occulter, which is located at the focal position of M1, to ensure that the solar disk light passes through and enters the light trap behind it. The taper of the cone-shaped hole is greater than the divergence angle of the light after M2 converges so that the direct light from the solar disk will not be scattered inside the cone-shaped hole. In order to reduce the concentration of solar energy in the light trap, a spherical collimating mirror is designed behind M2, and then the solar disk light is reflected to the plane mirror and finally absorbed by

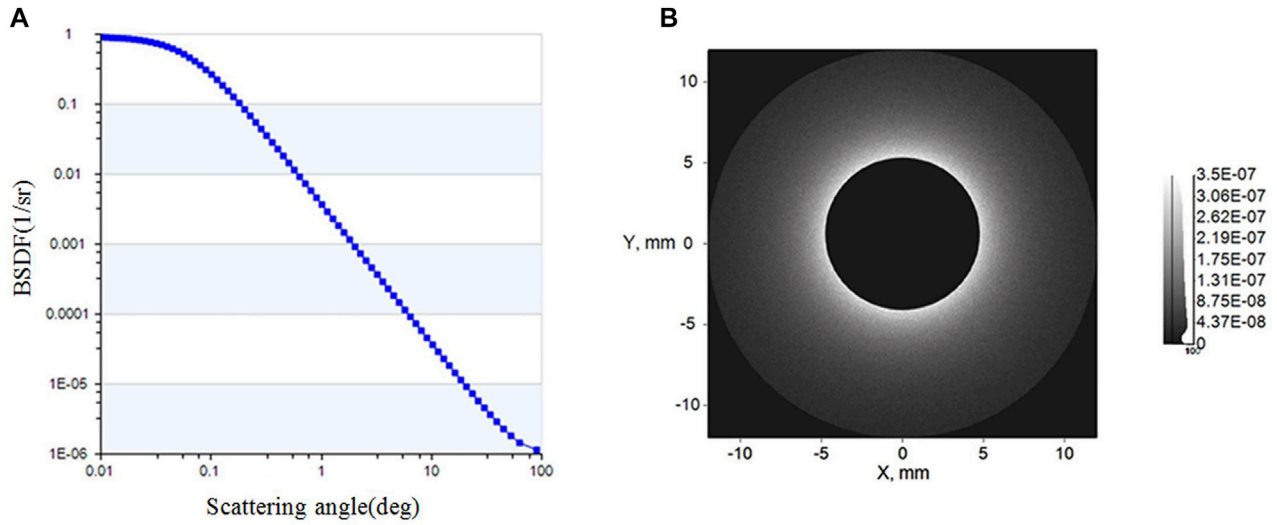

FIGURE 5 | Scattered stray-light simulation results from surface errors of M1 at 700 nm. **(A)** BSDF curve as a function of the scattering angle for M1 due to a surface roughness of 0.3 nm at 700 nm. **(B)** Stray-light distribution at the focal plane (CMOS2).

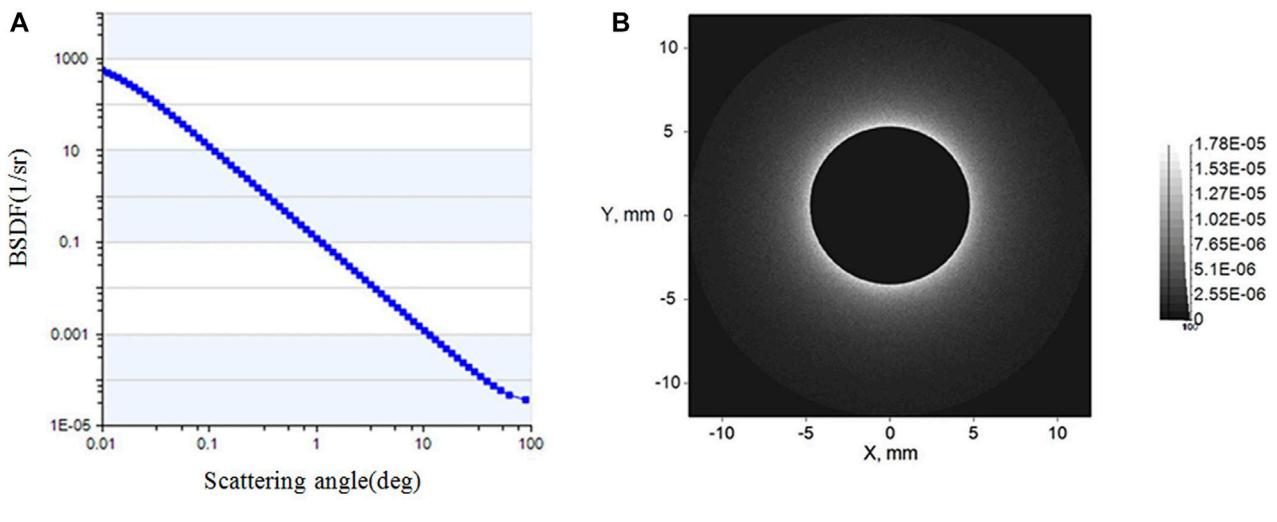

FIGURE 6 | Scattered stray-light simulation results from surface errors of M1 at 121.6 nm. **(A)** BSDF curve as a function of the scattering angle for M1 due to a surface roughness of 0.3 nm at 121.6 nm. **(B)** Stray-light distribution at the focal plane (CMOS1).

Acktar Absorbent Panels. The solar disk light will not return to the coronal imaging path to become stray-light. The ray-tracing process is shown in **Figure 3**. The design of the cone-shaped hole inside M2 and light trap ensures the elimination of direct stray-light from the solar disk.

3.2 Diffracted Stray-Light From the Edge of the Entrance Pupil A1

Since the entrance pupil A1 is directly exposed to strong sunlight, strong diffracted stray-light will be generated that need to be suppressed when the sunlight hits the edge of A1. The Lyot stop A2 is designed at the conjugate position of A1 imaged by M1, M2, and M3, to block the diffracted stray-light. The diffracted stray-light is displayed in **Figure 4**. By establishing a coherent light source with a wavelength of 700.0 nm at the position of A1, the distribution of the diffracted stray-light is simulated at its conjugate position, as shown in **Figure 4A**. The diffracted image of A1 is distributed in the range of its conjugate surface from 21.0 to 22.4 mm (shown in **Figures 4B,C**). The design of the Lyot stop A2 with the diameter of 21.0 mm can effectively prevent

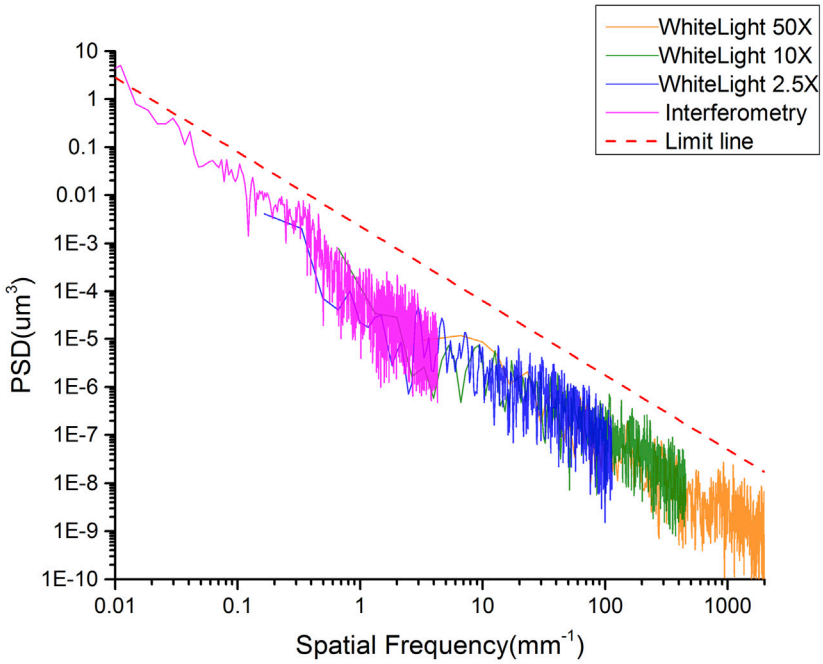

FIGURE 7 | Composite surface PSD function of M1 determined from different metrology instruments.

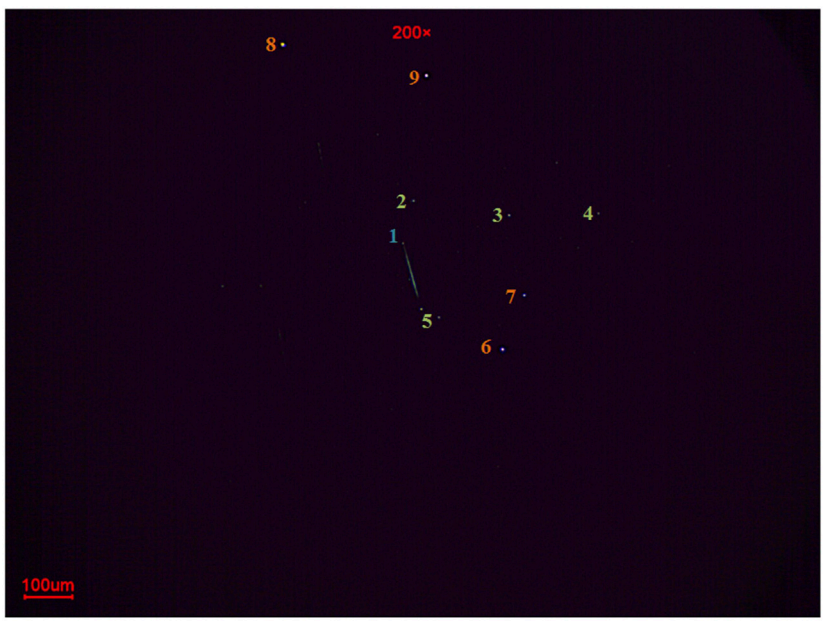

FIGURE 8 | Sub-field testing results from cosmetic defects using a dark-field microscope.

the diffracted stray-light from reaching the focal plane. The diffracted stray-light effect of 121.6 nm is similar to that of 700.0 nm, and the same size of A2 can block the diffracted stray-light of 121.6 nm, which is not repeated here.

3.3 Scattered Stray-Light From the Primary Mirror M1

For an internally occulted reflecting coronagraph such as SCI, the solar disk light will directly illuminate the surface of the

primary mirror M1, and strongly scattered stray-light is generated, which contributes the majority of the stray-light. It has been demonstrated that the stray-light level of the LASCO C1 coronagraph—an internally occulted coronagraph similar to SCI—is determined by the surface quality of the primary mirror [16]. Therefore, in order to achieve the high stray-light suppression level for SCI, excellent surface quality of the primary mirror is also required. The scattered stray-light resulting from the surface quality of the primary mirror needs to be analyzed and suppressed with emphasis, including the contribution of surface errors, cosmetic defects, and particulate contamination to the stray-light for SCI.

3.3.1 Scattered Stray-Light From Surface Errors of M1

In order to accurately evaluate the influence of the surface errors on the scattering, it is necessary to measure the surface errors in all relevant spatial frequencies. The power spectral density (PSD) of surface errors as a function of the spatial frequencies is accepted as an all-inclusive way to characterize optical surfaces, which can quantitatively describe the distribution of super-polished surface topography in spatial frequency ranges, and provides abundant data for the analysis of surface errors. The PSD [17] curve over the entire spatial frequency ranges can be obtained by Fourier transform of the surface profile errors as follows:

$$PSD(f) = \frac{1}{L}\left|\int_0^L z(x)\exp(-j2\pi fx)dx\right|^2. \quad (1)$$

Here, L is the sampling length that can represent its geometric characteristics. It is the diameter of the mirror if sampling using an interferometer, and it is the field-of-view corresponding to different objective magnifications if sampling using a white-light optical profiler. $z(x)$ is the surface profile error function, and "x" is the 1D coordinates of the sample along the surface. f is the spatial frequency. **Equation (1)** can be used to evaluate whether the surface errors of M1 meet the stray-light requirement for SCI. It is of great guidance to the surface polishing improvement.

According to the Harvey–Shack scattering theory, surface errors in different spatial frequency ranges have different effects on imaging quality [18–20]. Low-spatial frequency surface errors produce conventional aberrations, which affect the convergence of the Sun at the position of M2 and result in the stray-light of the inner FOV for SCI; mid-spatial frequency surface errors produce small-angle scattering, which affects the stray-light level of the inner FOV for SCI; and high-spatial frequency surface errors produce large-angle scattering, which affects the stray-light level of the outer FOV for SCI. Therefore, it is necessary to specify and measure the surface errors of M1 over the entire spatial frequency ranges to ensure that M1 meets the requirement, thereby suppressing the stray-light over the full FOV for SCI.

To specify the contribution of surface errors of M1 to the stray-light level, the Harvey–Shack ABg bidirectional scattering distribution function (BSDF) model is applied to characterize the surface errors of M1. This model is suitable for the scattering mainly caused by roughness, and the RMS roughness is much less than the wavelength. The BSDF function of an optical surface with an RMS roughness of "σ" [21, 22] is expressed in **Eq. (2)**:

$$BSDF = \frac{A}{B + (\sin\theta)^g}. \quad (2)$$

Here, $A = \pi 2 \cdot \Delta n^2\sigma^2/\lambda^2$, $B = (\lambda/2\pi l)^2$, and g is the logarithmic slope of the tail of BSDF. It is a dimensionless constant and is usually taken as 2, Δn is the change in the refractive index ($\Delta n = 2$ for mirrors), and λ is the wavelength. l is the auto-correlation length related to the scattering properties. When the RMS roughness of M1 is 0.3 nm and the wavelength is

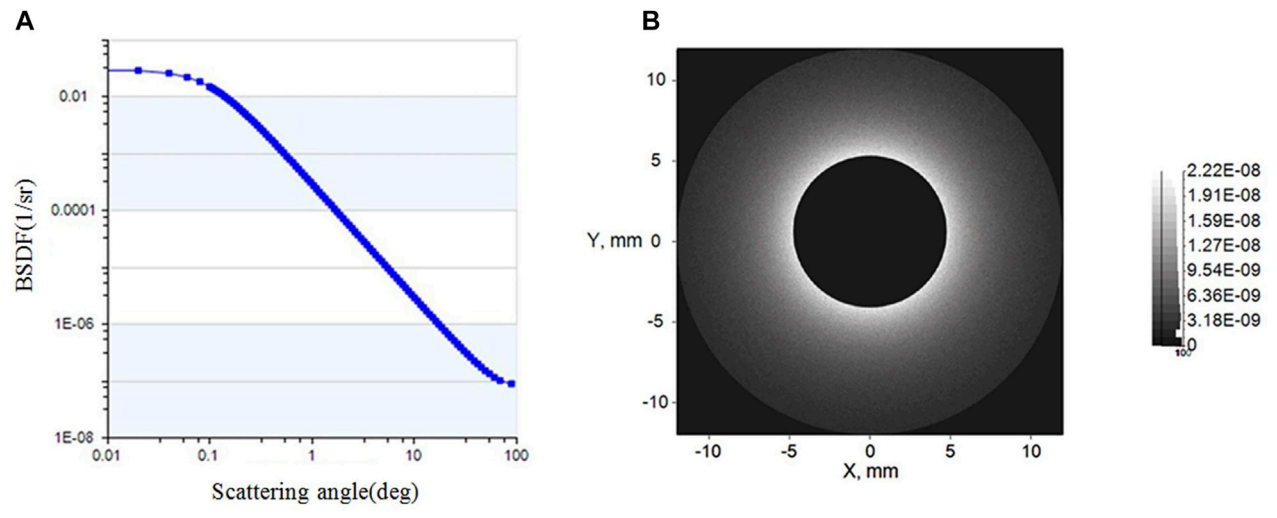

FIGURE 9 | Scattered stray-light simulation results from scratches of M1 at 700 nm. **(A)** BSDF curve as a function of the scattering angle. **(B)** Stray-light distribution at the focal plane.

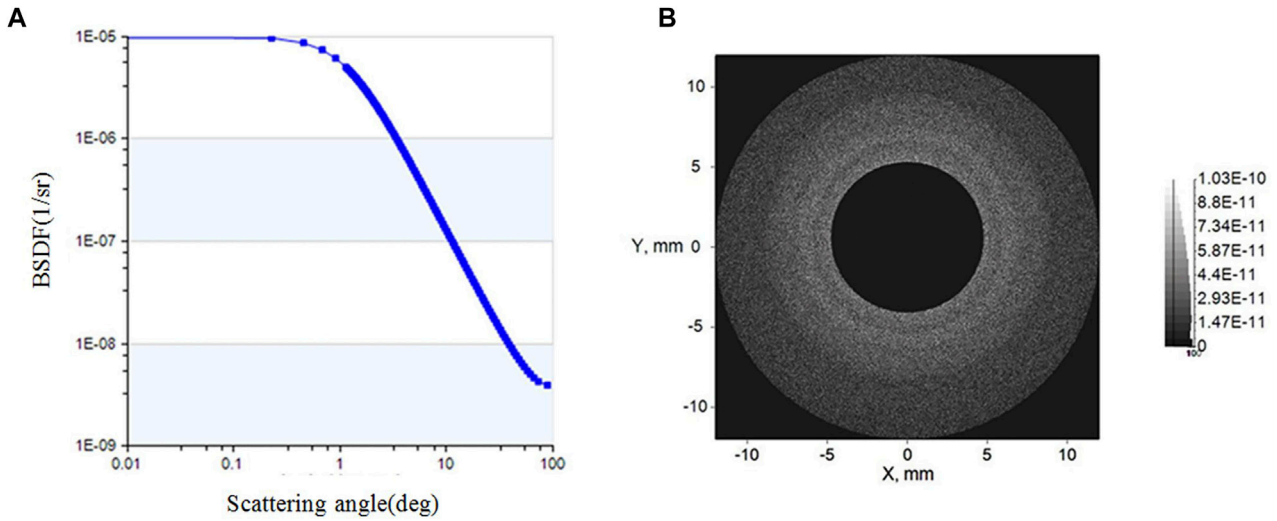

FIGURE 10 | Scattered stray-light simulation results from digs of M1 at 700.0 nm. **(A)** BSDF curve as a function of the scattering angle. **(B)** Stray-light distribution at the focal plane.

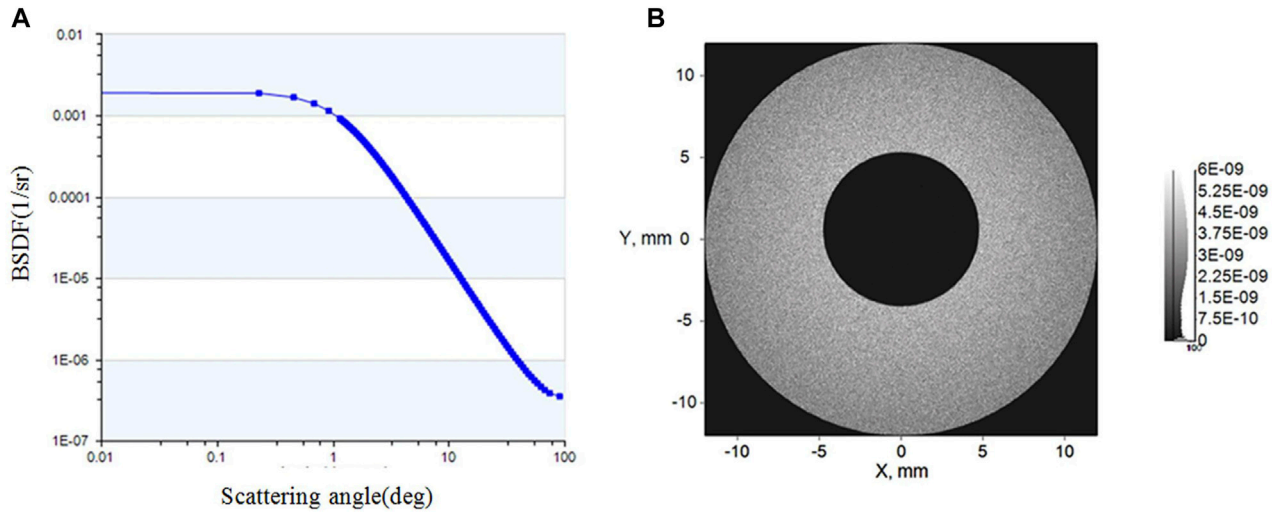

FIGURE 11 | Scattered stray-light simulation results from particulate contamination with CL100 at 700.0 nm. **(A)** BSDF curve as a function of the scattering angle. **(B)** Stray-light distribution at the focal plane.

700.0 nm, then A = 1.15×10^{-6} andB = 1.24×10^{-6}; the BSDF resulting from surface errors of M1 is shown in **Figure 5A**. A simulated solar disk source with a divergence angle of 32′ is established in non-sequential ray-tracing software to illuminate the SCI, and the stray-light distribution at the focal plane is simulated as shown in **Figure 5B**. Under this condition, the irradiance of the stray-light and the solar disk source at the focal plane can be obtained, and the ratio of the two represents the stray-light suppression level. Simulation results show that the stray-light suppression level can be as low as 10^{-7} $B_{\odot}$ at 1.1 $R_{\odot}$ and 10^{-8} $B_{\odot}$ at 2.5 $R_{\odot}$.

When the wavelength is 121.6 nm, then A = 3.82×10^{-5} andB = 3.75×10^{-8}; the BSDF resulting from the surface errors of M1 is shown in **Figure 6A**, and the stray-light distribution at the focal plane is shown in **Figure 6B**. The stray-light suppression level can be as low as 10^{-5} $B_{\odot}$ at 1.1 $R_{\odot}$ and 10^{-6} $B_{\odot}$ at 2.5 $R_{\odot}$.

After specifying surface errors of M1, different metrology instruments (laser interferometer for low-spatial frequency and white-light optical profiler for mid-spatial and high-spatial frequencies) are required to measure them. The spatial frequency range of different metrology instruments for measuring surface errors is determined by the sampling length

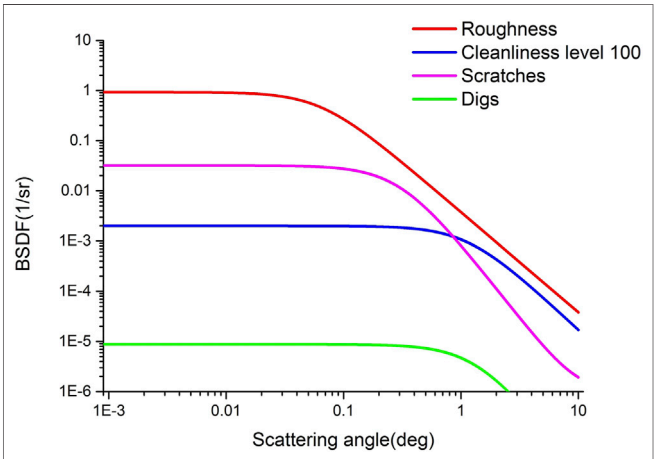

FIGURE 12 | BSDF curves as a function of the scattering angle for SCI M1 at 700.0 nm.

TABLE 1 | Summary of scattered stray-light level contributions at 700.0 nm.

Scattered stray-light source	1.1 $R_\odot$	2.5 $R_\odot$
Roughness	3.5×10^{-7}	4.4×10^{-8}
Scratches	2.2×10^{-8}	3.2×10^{-9}
Digs	1.0×10^{-10}	1.5×10^{-11}
Cleanliness level 100	6.0×10^{-9}	7.5×10^{-10}

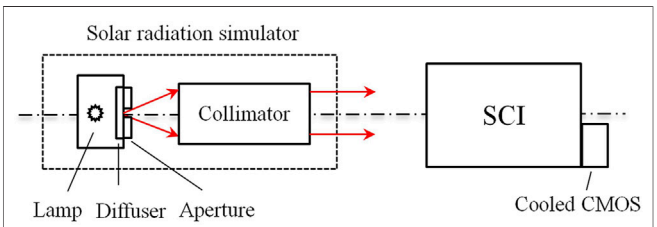

FIGURE 13 | Schematic diagram of the stray-light measurement device.

L and the resolution of CMOS [23]. The minimum spatial frequency that can be measured is $1/L$, where L is the FOV corresponding to different objective magnifications for the white-light optical profiler or the measurable aperture diameter for the laser interferometer. The maximum spatial frequency that can be measured is $1/(2d)$, which is the Nyquist cut-off frequency, where d is the sampling interval corresponding to the pixel size of CMOS [24, 25].

Since surface scatter phenomenon is a diffraction process, according to the grating equation (26), components with a spatial frequency greater than $1/\lambda$ will produce a small amount of optical scattering for SCI, which can be ignored. Therefore, the upper limit of the spatial frequency of the PSD curve is $1/\lambda$, and the lower limit of the frequency is $1/D$, where D is the aperture diameter of M1. According to the metrology data for different measuring instruments [27] in their specified spatial frequencies, the PSD [28] curve over the entire spatial frequencies is shown in **Figure 7**, which is obtained by **Eq. 1**. While measuring the surface errors, random errors such as mechanical vibration and electronic noise are removed by multiple phase averaging, and the system error is removed by subtracting the surface errors of the standard sample. The metrology data after removing random errors and system errors are under the PSD limit line of the polishing requirement; otherwise, another polishing and testing cycle is necessary.

3.3.2 Scattered Stray-Light From Cosmetic Defects of M1

Scratches and digs on the optical surface are cosmetic defects, which will generate unnecessary light scattering and contribute to stray-light for SCI. In order to quantify the stray-light level from cosmetic defects, a dark-field microscope is used to measure the number and size of scratches and digs on M1. The sub-field testing results are shown in **Figure 8**, in which mark 1 is a scratch, marks 2–5 are digs, and 6–9 are dust.

According to the Gary L. Peterson's cosmetic defects scattering theory, stray-light due to scratches or digs includes geometric refraction inside the scratches or digs and diffraction of light that passes around scratches or digs can be quantitatively analyzed by BSDF.

BSDF from scratches [29] is given by the expression:

$$BSDF_s = N_s \frac{wl}{\pi}\left[1 + \frac{\pi wl}{\lambda^2}\left(1 + \frac{\sin^2\theta}{l_s^2}\right)^{-3/2}\right]. \tag{3}$$

Here, $N_s = \frac{1}{\pi lD}$, $l_s = \left(\frac{1}{2\pi^2}\right)^{\frac{2}{3}} \frac{\lambda}{(w^2 l)^{\frac{1}{3}}}$, N_s is the density of the scratches (number of scratches per unit area), D is the diameter of the optical element, w and l are their typical width and length from microscopy, respectively, θ is the scattering angle with respect to the surface normal of the optical component, and l_s is the roll-off angle of the BSDF curve. We note that the factor l in the numerator of **Eq. (3)** will cancel with the factor of l in N_s, so the width has a dominant effect on the BSDF from scratches. According to the statistical testing results of scratches for M1 over the full FOV, the typical width w is less than 0.002 mm.

The Harvey–Shack scattering model based on the scalar diffraction theory can predict the scattering distribution of a super-polished optical surface, which is given by the expression:

$$BSDF = b_0\left(1 + \left(\frac{\sin\theta}{L}\right)^2\right)^{\frac{s}{2}}. \tag{4}$$

Here, b_0 is the intercept of the BSDF at the specular angle, θ is the scattering angle, and L is the shoulder of the BSDF curve and equals the sine of the shoulder angle. According to the calculation result of BSDF from scratches, a fitting Harvey–Shack scattering model is established with $b_0 = 3 \times 10^{-2}$, $L = 2 \times 10^{-3}$, and $s = -2$. The fitting BSDF curve is shown in **Figure 9A**, and the simulated stray-light distribution resulting from scratches is shown in **Figure 9B**.

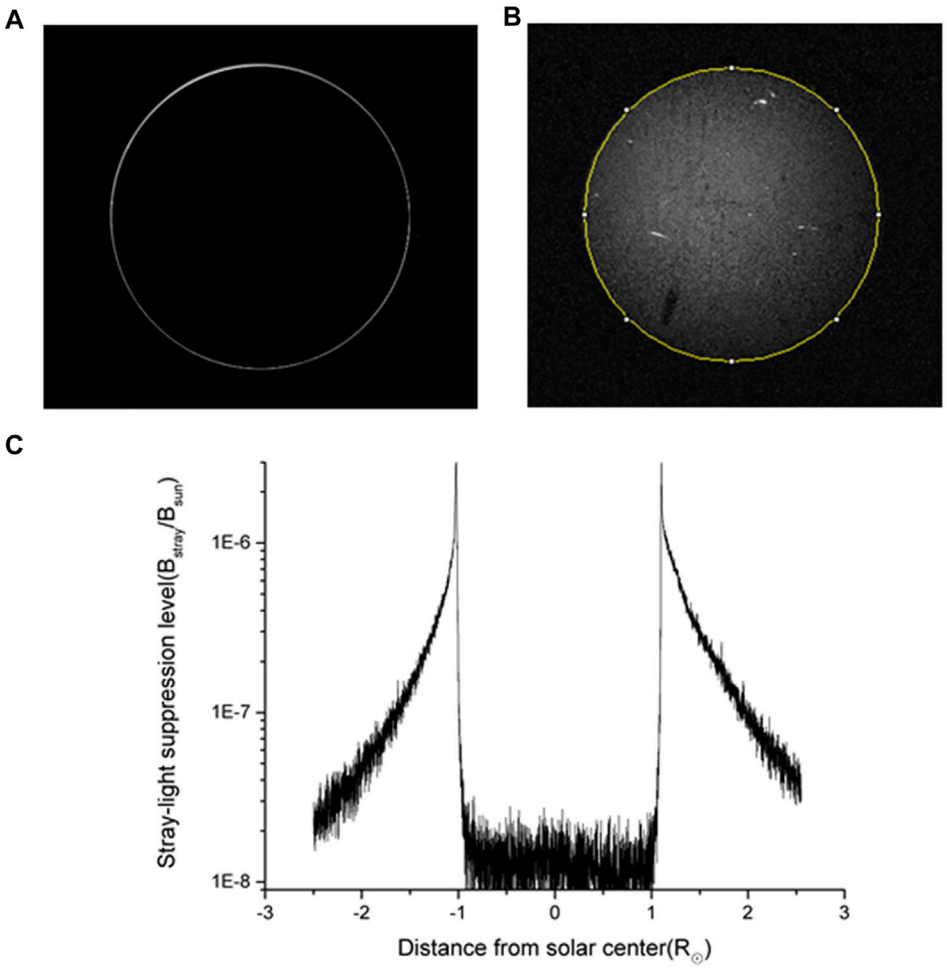

FIGURE 14 | (A) Stray-light image. **(B)** Solar disk image. **(C)** Stray-light suppression level as a function of the distance from the solar center.

BSDF from digs is given by the expression:

$$BSDF_d = \frac{1}{4}N_d d^2 \left[1 + \frac{\pi^2 d^2}{4\lambda^2}\left(1 + \frac{\sin^2\theta}{l_d^2}\right)^{-3/2}\right]. \quad (5)$$

Here, $N_d = {}^{1}/_{5\pi D^2}$, $l_d = \left(\frac{4}{\pi^4}\right)^{1/3}\frac{\lambda}{d}$, N_d is the density of the digs (number of digs per unit area), d is the diameter of the dig from microscopy, θ is the scattering angle, l_d is the roll-off angle, and D is the diameter of the optical element. Combined with the statistical testing result of digs for M1 over the full FOV, the diameter of the dig d is less than 0.01 mm. According to the calculation result of BSDF from digs, a fitting Harvey–Shack scattering model is established with $b_0 = 1 \times 10^{-5}$, $L = 2 \times 10^{-2}$, and $s = -2$. The fitting BSDF curve is shown in **Figure 10A**, and the simulated stray-light distribution resulting from digs at 700.0 nm is shown in **Figure 10B**.

3.3.3 Scattered Stray-Light From Particulate Contamination of M1

The surface BSDF scattering resulting from particulate contamination is a function of the particle density function $f(D)$ [30]. According to the Mie scattering theory, BSDF can be estimated when the MIL-STD-1264B Cleanliness Level (CL) is used to describe $f(D)$. Spyak and Wolfe's work shows that particulate contamination scattering is also shift invariant, and the Harvey–Shack model can be used to predict particle scattering in accordance with Spyak and Wolfe's BSDF curve. For particulate contamination scattering [31], the parameter b_0 in **Eq. (4)** can be taken by the total integrated scattering (TIS) [32] corresponding to the cleanliness level of M1 as follows:

$$b_0 = \frac{(TIS)L^s(s+2)}{2\pi\left[(1+L^2)^{\frac{(s+2)}{2}} - (L^2)^{\frac{(s+2)}{2}}\right]}. \quad (6)$$

According to the statistical testing results of dust for M1 over the full FOV, the cleanliness level for M1 is better than class 100, and the fitting parameters are inserted into the Harvey–Shack scattering model with $L = 2 \times 10^{-2}$, $TIS = 1.3 \times 10^{-5}$, $b_0 = 2 \times 10^{-3}$, and $s = -2.2$. The BSDF curve for cleanliness level 100 at 700.0 nm is shown in **Figure 11A**, and the simulated stray-light distribution resulting from particulate contamination is shown in **Figure 11B**.

According to the aforementioned BSDF **Eqs. 2–5**, combined with the testing results of the white-light optical profiler and the dark-field microscope for M1, the BSDF scattering curves resulting from roughness (red line), scratches (violet line), digs (green line), and particulate contamination with cleanliness level 100 (blue line) at 700.0 nm are shown in **Figure 12**. Their contributions to the stray-light level for SCI are shown in **Table 1**. After using the aforementioned testing results for stray-light simulation, the overall stray-light level for SCI can be suppressed to 10^{-8} $B_{\odot}$ at 700.0 nm.

4 STRAY-LIGHT MEASUREMENT FOR SCI

After analyzing the various factors that affect the stray-light suppression level of SCI, it is necessary to measure it in our laboratory. The stray-light measurement device includes a solar radiation simulator and a cooled CMOS camera as shown in **Figure 13**. A xenon lamp illuminates a diffuser and aperture mounted at the focal plane of the collimator to form a beam of simulated solar disk light [33]. The diameter of the aperture can be determined by $D = f \cdot \tan\Omega$, where f is the focal length of the collimator and Ω is the divergence angle of the simulated solar disk light and equals to $32'$.

While measuring stray-light, the optical axis of the solar radiation simulator is aligned with SCI, the solar disk light passes through M2 and enters the light trap of SCI, and the cooled CMOS camera only receives the stray-light image, as shown in **Figure 14A**. Then, the SCI is rotated and an attenuator is added so that the solar disk light illuminates the imaging area of M2, and the solar disk is imaged on the camera, as shown in **Figure 14B**. The full well of the camera is 51400 e, the readout noise is 1.5 e, the frame rate is set to 0.02, and 16-bit images are obtained. The stray-light suppression level of SCI is represented by the brightness ratio of the stray-light to the solar disk as B_{stray}/B_{sun}. The measurement should be carried out in an ultra-clean laboratory to reduce the impact of ambient stray-light caused by the scattering of particles in the air. In addition, the solar simulator should be installed inside a black shading box and far enough from SCI to ensure that stray-light from the solar simulator cannot enter SCI.

The measurement results show that the stray-light can be suppressed to the order of 10^{-8} $B_{\odot}$ at 700.0 nm, which is consistent with the simulation results combined with the testing surface roughness, cosmetic defects, and particulate contamination of the primary mirror.

5 DISCUSSION

In this study, the main sources of stray-light were analyzed and suppressed in detail, including the scattered stray-light from the primary mirror, the direct stray-light from the solar disk, and the diffracted stray-light from the edge of the entrance pupil. The surface errors, cosmetic defects, and particulate contamination of the primary mirror were tested in the laboratory. Based on the testing results, the corresponding scattering model was established for simulation, and the stray-light suppression level was verified via the laboratory stray-light measurement, and the influence of surface quality characteristics on the stray-light level for SCI was demonstrated. This modeling and simulation method based on the individual mirror laboratory testing is suitable for stray-light analysis and suppression of all coronagraphs.

DATA AVAILABILITY STATEMENT

The datasets presented in this article are not readily available because simulation and experimental data are obtained through repeated theoretical and practical research. Requests to access the datasets should be directed to GZ, zhangguang0920@163.com.

AUTHOR CONTRIBUTIONS

GZ contributed to the idea, modeling, and simulation of the stray-light suppression method. YW contributed to the design of the Solar Corona Imager and partial simulation. LH contributed to the measurement method. XW and SR contributed to the testing of the mirror. YX and FL performed the image data processing. BC modified the writing.

FUNDING

This work was partially supported by the Strategic Pioneer Program on Space Science of the Chinese Academy of Sciences (Grant No. XDA15320103), the National Natural Science Foundation of China (Grant No. 11427803), and the Joint Research Fund in Astronomy (Grant No. U2031122) under cooperative agreement between the National Natural Science Foundation of China and Chinese Academy of Sciences.

REFERENCES

1. Koomen MJ, Detwiler CR, Brueckner GE, Cooper HW, Tousey R. White Light Coronagraph in OSO-7. *Appl. Opt.* (1975) 14:743–51. doi:10.1364/AO.14.000743
2. Domingo V, Fleck B, Poland AI. The SOHO Mission: An Overview. *Sol Phys* (1995) 162:1–37. doi:10.1007/BF00733425
3. Frazin RA, Vásquez AM, Thompson WT, Hewett RJ, Lamy P, Llebaria A, et al. Intercomparison of the LASCO-C2, SECCHI-COR1, SECCHI-COR2, and Mk4 Coronagraphs. *Sol Phys* (2012) 280:273–93. doi:10.1007/s11207-012-0028-3
4. Kaiser ML, Kucera TA, Davila JM, St. Cyr OC, Guhathakurta M, Christian E. The STEREO Mission: An Introduction. *Space Sci Rev* (2008) 136:5–16. doi:10.1007/s11214-007-9277-0
5. Fineschi S, Antonucci E, Naletto G, Romoli M, Spadaro D, Nicolini G, et al. Metis: a Novel Coronagraph Design for the Solar Orbiter Mission. *Proc. SPIE* (2012) 8443:844384433H. doi:10.1117/12.927229
6. Venkata SN, Prasad BR, Nalla RK, Singh J. Scatter Studies for Visible Emission Line Coronagraph on Board ADITYA-L1 Mission. *J. Astron. Telesc. Instrum. Syst* (2017) 3:014002. doi:10.1117/1.JATIS.3.1.014002

7. Chen B, Li H, Song K-F, Guo Q-F, Zhang P-J, He L-P, et al. The Lyman-alpha Solar Telescope (LST) for the ASO-S Mission - II. Design of LST. *Res. Astron. Astrophys.* (2019) 19:159. doi:10.1088/1674-4527/19/11/159
8. Gong Q, Socker D. Theoretical Study of the Occulted Solar Coronagraph. *Proc. SPIE* (2004) 5526:208–19. doi:10.1117/12.549275
9. Wang YQ, Zhang G, He LP, Guo QF, Zhang HJ, Wang HF, et al. Solar Coronagraph Imager Based on Internal Occulting in Lyman-alpha and Visible Bands. *Opt Precis Eng* (2019) 28:303–14.
10. Wang X, Chen B, Huo T, Zhou H. Design of Second-Order 121.6-nm Narrowband Minus Filters Using Asymmetrically Apodized Thickness Modulation. *Appl. Phys. B* (2018) 124:1–6. doi:10.1007/s00340-018-7010-1
11. Vives S, Lamy PL, Vial J-C. Optical Design of the Lyman Alpha Coronagraph for the LYOT Microsatellite. *Proc. SPIE* (2004) 5171:298–306. doi:10.1117/12.506390
12. Fineschi S, Romoli M, Hoover RB, Baker PC, Zukic M, Kim J, et al. Stray Light Analysis of a Reflecting UV Coronagraph/Polarimeter with Multilayer Optics. *Proc. SPIE* (1994) 78–92. doi:10.1117/12.168591
13. Romoli M, Weiser H, Gardner LD, Kohl JL. Stray-Light Suppression in a Reflecting White-Light Coronagraph. *Appl. Opt.* (1993) 32:3559–69. doi:10.1364/AO.32.003559
14. Newkirk G, Bohlin D. Reduction of Scattered Light in the Coronagraph. *Appl. Opt.* (1963) 2:131–40. doi:10.1364/AO.2.000131
15. Landini F, Romoli M, Fineschi S, Antonucci E. Stray-light Analysis for the SCORE Coronagraphs of HERSCHEL. *Appl. Opt.* (2006) 45:6657–67. doi:10.1364/AO.45.006657
16. Brueckner GE, Howard RA, Koomen MJ, Korendyke CM, Michels DJ, Moses JD, et al. The Large Angle Spectroscopic Coronagraph (LASCO). *Sol Phys* (1995) 162:357–402. doi:10.1007/978-94-009-0191-9_1010.1007/bf00733434
17. Youngworth RN, Gallagher BB, Stamper BL. An Overview of Power Spectral Density (PSD) Calculations. *Proc.of SPIE* (2005) 586958690U. doi:10.1117/12.618478
18. Youngworth RN, Stone BD. Simple Estimates for the Effects of Mid-spatial-frequency Surface Errors on Image Quality. *Appl. Opt.* (2000) 39:2198–209. doi:10.1364/AO.39.002198
19. Stover JC, Harvey JE. Limitations of Rayleigh Rice Perturbation Theory for Describing Surface Scatter. *Proc. SPIE* (2007) 667266720B. doi:10.1117/12.739133
20. Harvey JE. Integrating Optical Fabrication and Metrology into the Optical Design Process. *Appl. Opt.* (2015) 54:2224–33. doi:10.1364/AO.54.002224
21. Harvey JE, Choi N, Schroeder S, Duparré A. Total Integrated Scatter from Surfaces with Arbitrary Roughness, Correlation Widths, and Incident Angles. *Opt. Eng* (2012) 51:013402. doi:10.1117/1.OE.51.1.013402
22. Choi N, Harvey JE. Numerical Validation of the Generalized Harvey-Shack Surface Scatter Theory. *Opt. Eng* (2013) 52:115103. doi:10.1117/1.OE.52.11.115103
23. Grochocki F, Fleming J. Stray Light Testing of the OLI Telescope. *Proc. SPIE* (2010) 7794:779477940W. doi:10.1117/12.862225
24. Lang Z, Qiao S, Ma Y. Acoustic Microresonator Based In-Plane Quartz-Enhanced Photoacoustic Spectroscopy Sensor with a Line Interaction Mode. *Opt. Lett.* (2022) 47:1295–8. doi:10.1364/OL.452085
25. Liu X, Ma Y. Sensitive Carbon Monoxide Detection Based on Light-Induced Thermoelastic Spectroscopy with a Fiber-Coupled Multipass Cell [Invited]. 中国光学快报 (2022) 20:031201. doi:10.3788/COL202220.031201
26. Harvey JE, Thompson AK. Scattering Effects from Residual Optical Fabrication Errors. *Proc. SPIE* (1995) 2576:155–74. doi:10.1117/12.215588
27. Church EL, Takacs PZ. Instrumental Effects in Surface Finish Measurement. *Proc. SPIE* (1989) 1009:46–55. doi:10.1117/12.949154
28. Dittman MG. K-correlation Power Spectral Density and Surface Scatter Model. *Proc.of SPIE* (2006) 6291:629162910R. doi:10.1117/12.678320
29. Peterson GL. A BRDF Model for Scratches and Digs. *Proc.of SPIE* (2012) 8495:849584950G. doi:10.1117/12.930860
30. Spyak PR, Wolfe WL. Scatter from particulate-contaminated mirrors. part 3: theory and experiment for dust and lambda=10.6 um. *Opt. Eng.* (1992) 31:1764–74. doi:10.1117/12.58710
31. Spyak PR, Wolfe WL. Scatter from Particulate-Contaminated Mirrors. Part 4: Properties of Scatter from Dust for Visible to Far-Infrared Wavelengths. *Opt. Eng.* (1992) 31:1775–84. doi:10.1117/12.58711
32. Dittman MG. Contamination Scatter Functions for Stray-Light Analysis. *Proc.of SPIE* (2002) 4774:99–110. doi:10.1117/12.481666
33. Ma Y, He Y, Tong Y, Yu X, Tittel FK. Quartz-tuning-fork Enhanced Photothermal Spectroscopy for Ultra-high Sensitive Trace Gas Detection. *Opt. Express* (2018) 26:32103–10. doi:10.1364/OE.26.032103

Conflict of Interest: The authors declare that the research was conducted in the absence of any commercial or financial relationships that could be construed as a potential conflict of interest.

frontiers | Frontiers in Physics

ORIGINAL RESEARCH
published: 13 June 2022
doi: 10.3389/fphy.2022.945995

MEMS Modulator-Based Mid-Infrared Laser Heterodyne Radiometer for Atmospheric Remote Sensing

Zhengyue Xue[1,2], Fengjiao Shen[3], Jun Li[1,2], Xiaohai Liu[2], Guishi Wang[2], Kun Liu[2], Xiaoming Gao[1,2], Weidong Chen[4] and Tu Tan[2]**

[1]School of Environmental Science and Optoelectronic Technology, University of Science and Technology of China, Hefei, China, [2]Anhui Institute of Optics and Fine Mechanics, Chinese Academy of Sciences, Hefei, China, [3]School of Advanced Manufacturing Engineering, Hefei University, Hefei, China, [4]Laboratoire de Physico-Chimie de l'Atmosphère, Université du Littoral Côte d'Opale, Dunkerque, France

The performance of a mid-infrared laser heterodyne radiometer (MIR-LHR) based on a micro-electro-mechanical system (MEMS) mirror is demonstrated in ground-based solar occultation mode. A MEMS mirror is employed as an alternative modulator to the traditional mechanical chopper. High-resolution (~0.0024 cm^{-1}) transmission spectrum near 3.93 μm was obtained for atmospheric observation of N_2O absorption. Operation of the MIR-LHR with laser-induced shot-noise limited performance was analyzed and experimentally achieved. The laser heterodyne spectrum obtained is consistent with Fourier-transform infrared (FT-IR) spectrometer and atmospheric transmission modeling. Compared to the traditional chopper, the MEMS mirror is smaller, lighter and lower power consumption which makes the system more stable and compact. The reported MIR-LHR in this article has great potential in aircraft instruments and satellite payloads.

Keywords: laser heterodyne radiometer, micro-electro-mechanical system, nitrous oxide, noise analysis, field measurement

OPEN ACCESS

Edited by:
Yufei Ma,
Harbin Institute of Technology, China

Reviewed by:
Shao Jie,
Zhejiang Normal University, China
Chuanliang Li,
Taiyuan University of Science and Technology, China

****Correspondence:***
Tu Tan
tantu@aiofm.ac.cn
Xiaoming Gao
xmgao@aiofm.ac.cn

Specialty section:
This article was submitted to Optics and Photonics, a section of the journal Frontiers in Physics

Received: *17 May 2022*
Accepted: *25 May 2022*
Published: *13 June 2022*

Citation:
Xue Z, Shen F, Li J, Liu X, Wang G, Liu K, Gao X, Chen W and Tan T (2022) MEMS Modulator-Based Mid-Infrared Laser Heterodyne Radiometer for Atmospheric Remote Sensing. Front. Phys. 10:945995. doi: 10.3389/fphy.2022.945995

INTRODUCTION

Long-term continuous observations of greenhouse gases (GHGs) in the atmospheric column are urgently needed to address global climate change and to improve scientific understanding of climate change [1]. At present, several approaches have been proposed and played unique roles in the monitoring of GHGs concentrations, such as satellite remote sensing, LIDAR, and sounding balloons, these approaches are suitable for different fields [2–5]. The detection range of satellite is wide, but the temporal and spatial resolution is low. The detection accuracy of LIDAR is high, however the detection range is limited. The sounding balloon can simultaneously detect a variety of atmospheric parameters and the detection height is up to 30 km, however the cost is high and the path is not uncertain. Laser spectroscopy has been widely used in trace gas detection [6–9]. Ground-based high-resolution Fourier-transform infrared (FT-IR) spectrometers are used to real-time obtain solar spectra and then retrieve vertical concentration profiles of the target GHGs, and the results can also be used for cross-validation of satellite observations [10, 11].

Laser heterodyne radiometer (LHR), which extracts absorption information from a broadband light source (such as the Sun or interstellar medium) by beating it with a narrow-band local oscillator (LO) in a high speed detector, has been widely applied for remote sensing of earth atmosphere and astronomy since the 1970s. Compared to the FT-IR measurement, LHR offers unique advantages

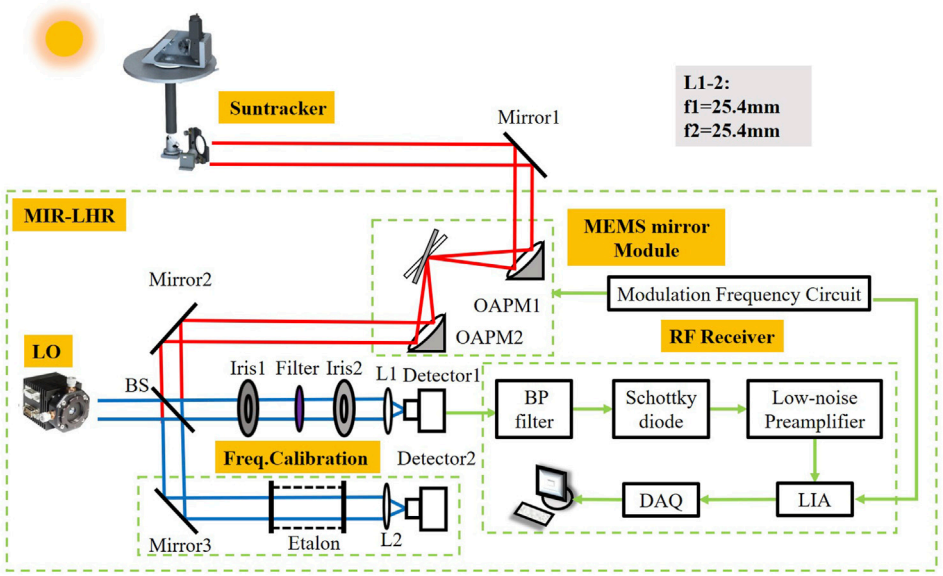

FIGURE 1 | Schematic of the developed MIR-LHR. BS: beam splitter; BP: band-pass; RF: radio frequency; DAQ: data acquisition card; LIA: lock-in amplifier; L: lens; OAPM: off-axis parabolic mirror.

including high spectral resolution, fast response time, small size and high sensitivity. Weidmann *et al.* and Shen *et al.* established mid-infrared (MIR) LHR systems to measure a variety of GHGs, such as CH_4, CO_2, H_2O, O_3 and N_2O in the atmospheric column [12, 13]. Wilson *et al.* and Wang *et al.* developed all-fiber coupled near-infrared (NIR) LHRs for the measurements of CH_4 and CO_2 absorption in the atmospheric column [14, 15]. Robinson et al. demonstrated a hollow waveguide-based miniaturized quantum cascade laser (QCL) heterodyne spectro-radiometer, meanwhile offers an efficient path to miniaturization of the MIR-LHR [16]. In general, sunlight modulation in a LHR system is performed to improve the measurement sensitivity. A mechanical chopper was usually used to realize such modulation. Wang *et al.* and Wilson *et al.* implemented a fiber optical switch to modulate the sunlight which made the LHR more compact and robust [17]. However, the fiber optical switch is only available for application in the near-infrared at the moment.

In this paper, we introduce a micro-electro-mechanical system (MEMS) mirror to modulate the sunlight in a MIR-LHR, which provides many options for the design and development of MIR-LHR. The developed system shows good performance in terms of its spectral resolution and stability. The developed MEMS modulator-based MIR-LHR was validated through measurement of N_2O absorption in the atmospheric column in ground-based solar occultation mode.

EXPERIMENTAL DETAILS

The MIR-LHR developed in the present work is schematically presented in **Figure 1**. A distributed feedback interband cascade laser (DFB-ICL) operating around 3.93 μm at room temperature is used as a LO. It is continuously tunable in frequency from

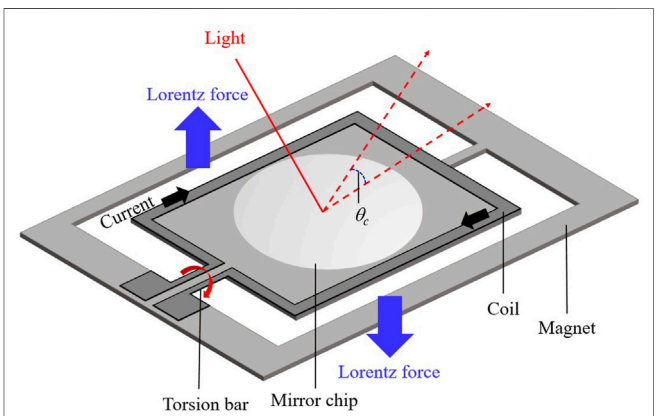

FIGURE 2 | Operation principle of the MEMS mirror.

2,535 cm^{-1} to 2,543 cm^{-1} with the optical output power of more than 15 mW. sunlight containing atmospheric absorption information is captured with a home-made high-precision solar tracker. Solar motion is tracked by photoelectric tracking and proportion-integral-derivative (PID) control with an accuracy of seven arc seconds.

A MEMS mirror (Hamamatsu, S12237–03P) is used to replace a conventional mechanical chopper to modulate the sunlight. As shown in **Figure 2**, the MEMS mirror is composed of a mirror chip and a magnet that generates a magnetic field. Electrical current passing through the coil produces a Lorentz force under the magnetic field based on Fleming's left-hand rule. This Lorentz force rotates the mirror and the angle of the rotation is proportional to the current injected in the coil. This Lorentz force causes the mirror to rotate at an angle proportional to the

TABLE 1 | Electrical and optical characteristics of the MEMS mirror.

Parameter	Symbol	Range	Unit
Drive current	I_s	±20	mA
Optical reflection angel	θ_s	±18	degrees
Drive frequency	f_s	0–100	Hz
Operating temperature	T_{case}	25 ± 10	C
Resonant frequency	f_{sR}	530 ± 30	Hz

current injected into the coil. The surface of the MEMS mirror is coated with aluminum to ensure high reflectance in the MIR spectral region. The modulation of sunlight is realized by the deflection of MEMS mirror. The MEMS mirror features a large optical reflection angle, high mirror reflectance and low power consumption.

The electrical and optical characteristics of the used MEMS mirror are shown in **Table 1**. In order to minimize the optical noise caused by reflection from other parts of the MEMS mirror, the solar beam size must be smaller than the mirror size (2.6 mm in diameter). According to the divergence angle of the sunlight (~9.2 mrad), a pair of OAPMs (OAPM1and OAPM2) is used to focus and collimate the sunlight to ensure sufficient signal power for the MIR-LHR. The distance between OAPM1 (f_1 = 152.4 mm) and OAPM2 (f_2 = 101.6 mm) is 27.5 cm, and the MEMS mirror is placed at the focal point of OAPM1. The solar power injected into the LHR system is increased by a factor of ~2.5 via collimation and focus of the OAPM pair.

As shown in **Figure 2**, the torsion bar serves as not only an axis of rotation but also a spring for restraining the mirror rotation. The mirror stops rotating and holds an angle when Lorentz force and elastic force of torsion bar spring are equal. The reflection angle and modulation frequency of the MEMS mirror can be adjusted by changing the amplitude and frequency of current in the coil, respectively. The theoretical optical reflection angle θ_c is expressed as follows [18, 19]:

$$\theta_c(t) = A_c * sin(2\pi f_s * t) \quad (1)$$

where A_c is the amplitude of the current flowing in the coil.

The actual optical reflection angle θ_s, affected by the temperature coefficient, can be expressed as:

$$\theta_s(I_s(t)) = \theta_c(t) + d\theta_s \quad (2)$$

where

$$I_s(t) = \sum_{n=0}^{m}\left[a(m,n) * \left\{A_c\left(1 - \left(\frac{f_s}{f_{sR}}\right)^2\right) * sin(2\pi f_s t + \phi)\right\}\right] \quad (3)$$

where *a(m, n)* is the correction factor, m is the order, ϕ is the phase, and the influence of the phase in the phase-locked demodulation is negligible [20].

Since resonance occurs when the mirror exhibits square wave motion, it is important to set the period of the square wave as close as possible to the integer multiple of the resonant frequency's reciprocal [21]. The characteristic resonant frequency of the used MEMS mirror is approximately 530 Hz in the operating temperature range of 25 ± 10°C.

The sunlight collected by the solar tracker is shaped and modulated by the MEMS modulator module, the modulation frequency and duty cycle of the MEMS mirror can be adjusted through its drive current (The duty cycle used in this study is fixed at 50%). The beam splitter is adopted as a mixing device to combine the modulated solar beam with the LO light beam from the ICL. The combined beams are filtered by an optical filter (with a FWHM (full width at half maximum) of 100 nm centered at 3.94 μm) and focused on the photomixer (Detector 1: PV-2TE-4, VIGO System S. A.). A small fraction of the ICL beam reflected through BS is used for frequency calibration, a germanium etalon (with a free spectral range of ~0.0246 cm^{-1}) followed by Detector two is applied for relative frequency metrology. The intermediate frequency (IF) signal at radio frequency (RF) from the AC output of the photomixer is filtered with a band-pass filter and converted into a DC signal by a Schottky diode (HEROTEK, DHM080BB). The IF signal is then amplified by a low-noise preamplifier (SR560, Stanford Research Systems) with a gain of 60 dB. The amplified IF signal is demodulated using a LIA (Standford, SRS850) at the modulation frequency of the MEMS mirror and is then acquired by a DAQ card (USB-6210, NI Inc.) at a sampling rate of 500 kHz via a LabVIEW-based program. The DC output of the photomixer for monitoring the ICL power is acquired by the DAQ card.

INSTRUMENT PERFORMANCE

In order to obtain the best signal-to-noise ratio (SNR), modulating frequency of the MEMS mirror was investigated. **Figure 3** shows the square wave responses of sunlight modulated by the MEMS mirror at different frequencies. The high-frequency oscillation is suppressed when the drive frequency f_s is 5.3 Hz **Figure 3A**, and the corresponding period (~0.188,679 s) is close to the integer multiple of the characteristic resonant frequency's reciprocal (~0.00188,679 s). When the drive frequency f_s is 8 Hz **Figure 3B**, the oscillation occurs, as shown in the inset of **Figure 3B**, and it takes time to stabilize the given optical reflection angle depending on the drive current I_s. Therefore, the modulation frequency of 5.3 Hz, which can reduce the influence of the oscillation of the MEMS mirror on the modulation, was selected for the further MIR-LHR measurements.

Due to the narrow linewidth of the ICL [~megahertz (MHz)], the spectral resolution of the LHR is usually determined by the electronic bandwidth of the band-pass filter. Subsequently, an appropriate band-pass filter was selected by analyzing the spectrum of heterodyne signal and background noise via a RF signal analyzer (Agilent Technologies, N9000A), as shown in **Figure 4**, As can be seen, several noise peaks appear in the regions from 10 to 40 MHz and 80–120 MHz, respectively (**Figure 4** in blue), which may significantly impact the LHR performance. Therefore, a filter with a pass-band of 45–81 MHz, which has low noise, was applied for LHR measurement. The selected pass-band results in a double-sideband spectral resolution of 72 MHz (0.0024 cm^{-1}).

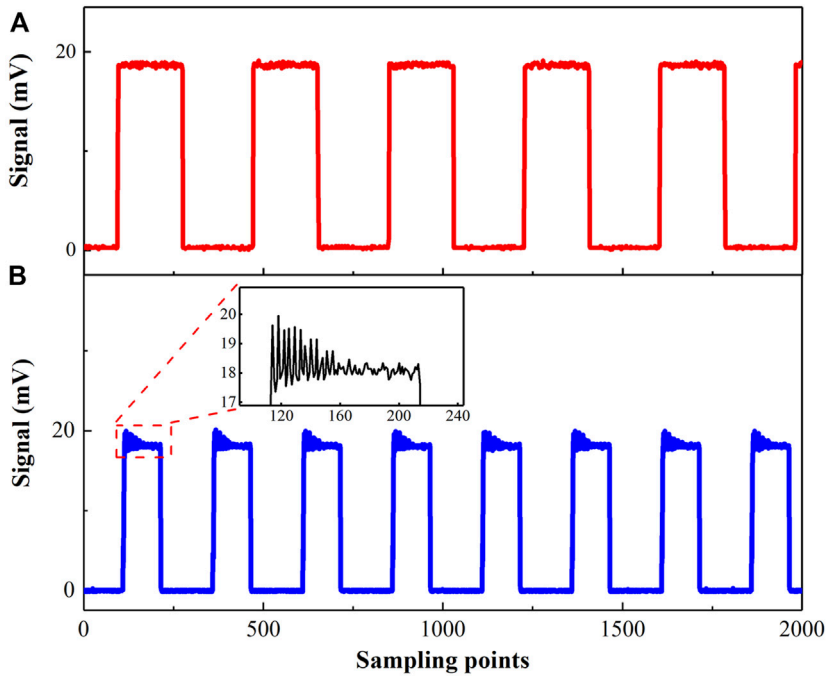

FIGURE 3 | Square wave responses at **(A)** 5.3 Hz; **(B)** 8 Hz, the inset: high-frequency oscillation features.

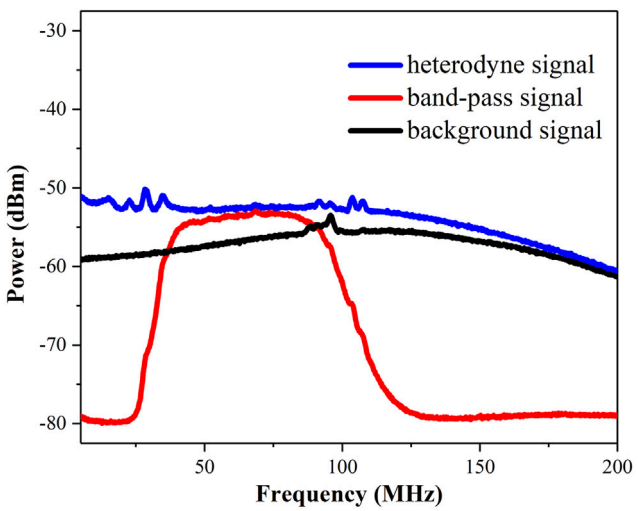

FIGURE 4 | Spectral analysis of heterodyne signal (*blue curve*); band-pass signal (*red curve*) and background signal (*black curve*).

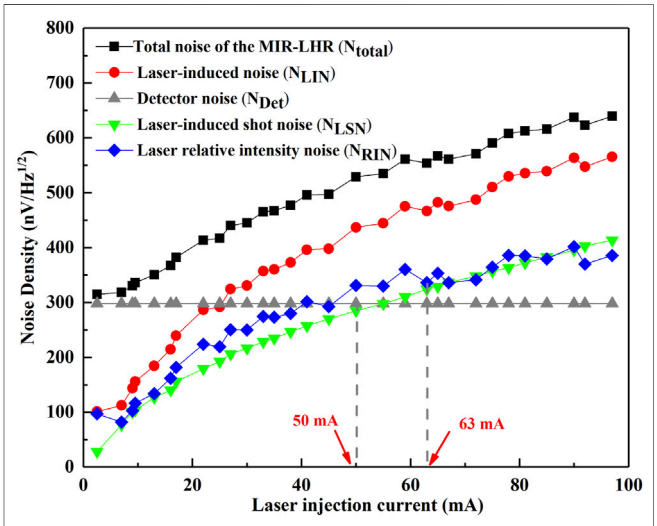

FIGURE 5 | Plots of measured system total noise density, laser-induced noise density, detection noise density, laser-induced shot noise density, and laser relative intensity noise density versus LO injection current, respectively.

As LO power is usually much larger than the incident sunlight power, the sunlight power induced noise can be rendered negligible in practical application, and the main dominant sources in a LHR receiver are detection noise, laser-induced noise, sunlight-induced noise [22]. The sunlight-induced noise can be rendered negligible because LO power is usually much larger than sunlight power. In order to obtain the optimal LO power range (as a linear function of the LO injection current) of the LHR system, it is necessary to analyze noise sources at different LO injection current. The total noise densities N_{total} from the RF output of the VIGO detector within a RF filter pass-band of 45–81 MHz were measured at different LO photocurrents using the signal analyzer, as plotted in **Figure 5** (*black square*). The total noise density N_{total} (nV/Hz$^{1/2}$) of a LHR system can be expressed by [22, 23]:

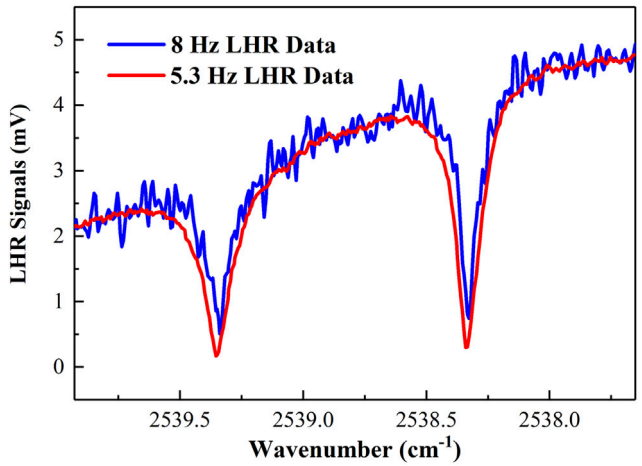

FIGURE 6 | Raw heterodyne signals at 5.3 Hz (*red curve*) and 8 Hz (*blue curve*) modulation frequencies, LO wavelength as a function of the injection current.

$$N_{\text{total}} = \sqrt{N_{Det}^2 + N_{LIN}^2} \tag{4}$$

and

$$N_{LIN}^2 = N_{LSN}^2 + N_{RIN}^2 \tag{5}$$

where N_{Det} was directly measured at the RF output of the VIGO detector without light incidence including the background noise, the Johnson noise, and the dark noise. N_{LIN} is the total laser-induced noise density, including laser-induced shot-noise N_{LSN} and laser relative intensity noise N_{RIN}.

Given the detection noise N_{Det} of 297 nV/Hz$^{1/2}$ (**Figure 5**, *gray triangle*) measured without LO light and the resolution bandwidth (RBW) is 1 MHz. The laser-induced noise density N_{LIN} (**Figure 5**, *red circle*) is obtained by subtracting the detection noise N_{Det} from the measured total noise density N_{total} based on **Eq 4**. The laser-induced shot-noise density N_{LSN} (**Figure 5**, *green triangle*) was calculated by [24]:

$$N_{LSN} = R_{ti} \cdot \sqrt{2 \cdot e \cdot I_{dc}} \tag{6}$$

with R_{ti} = 2200 V/A the transimpedance of the photomixer and I_{dc} is the LO injection current as a linear function of LO power. The laser relative intensity noise N_{RIN} is obtained by subtracting the laser-induced shot-noise density N_{LSN} from the laser-induced noise density N_{LIN} based on **Eq 5**. As shown in **Figure 5**, at LO injection current I_{dc} < 63 mA, the laser relative intensity noise N_{RIN} is larger than the laser-induced shot-noise density N_{LSN}. And at LO njection current >63 mA, the laser relative intensity noise N_{RIN} is approximately equal to the laser-induced shot-noise density N_{LSN}, and they are both larger than the detection noise N_{Det}. At LO injection current I_{dc} > 50 mA, N_{LSN} is larger than N_{Det}. Meanwhile, the maximum current tuning range of the LO (ICL) laser is 0–100 mA. Therefore, the optimal LO injection current I_{dc} of the LHR system should be in the range of 63–100 mA.

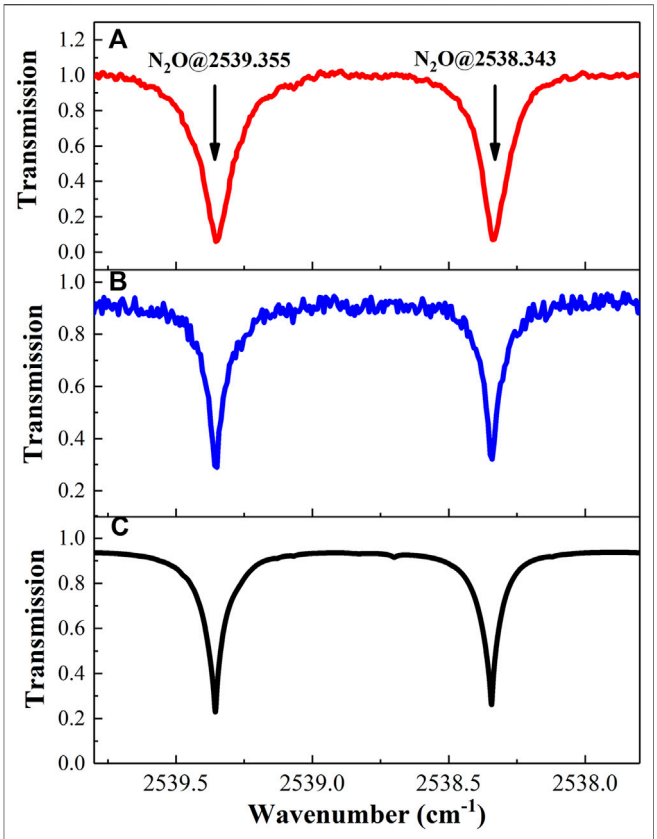

FIGURE 7 | (A) LHR spectrum, **(B)** FT-IR spectrum, and **(C)** atmospheric transmission modelling spectrum of N_2O in the atmospheric column.

FIELD RESULTS

LHR measurements have been performed in Hefei (31.9°N/117.166°E, 40 m above sea level) in China at 15:00 on 10 November 2021. The LO frequency was tuned from 2,537.552 cm^{-1} to 2,539.828 cm^{-1} via the current tuning in point-by-point mode with a current step of 0.1 mA, to detect two N_2O absorption lines at 2,538.343 cm^{-1} and 2,539.355 cm^{-1}, respectively. The LHR signals at MEMS modulation frequencies of 5.3 Hz (*red curve*) and 8 Hz (*blue curve*) are shown in **Figure 6**, where the LHR signal at 5.3 Hz modulation frequency exhibits higher SNR. **Figure 6** shows a calibration curve of the laser wavelength as a function of the laser current at temperature of 16°C.

The absorption spectrum of N_2O in the atmospheric column measured by the MIR-LHR system is shown in **Figure 7A**, accompanied a FT-IR spectrum **Figure 7B** measured with a Bruker IFS 125HR Fourier-transform spectrometer (FTS) (resolution: 0.02 cm^{-1}) recorded at the same location and same time. A calculated spectrum from the atmospheric transmission modeling is given as well in **Figure 7C**.

As expected, the LHR spectrum based on the MEMS mirror modulator is basically consistent with the two reference spectra. Since the laboratory is located in the middle of the round island,

affected by the interference of geographical position, water vapor absorption and absorption path (solar zenith angle), the line-shape and absorption depth of the LHR spectrum are slightly different from the two reference spectra [25]. Compared with FT-IR spectrum, LHR spectrum shows a higher SNR. Moreover, compared with traditional choppers, the MEMS modulator allows for a more compact, stable and versatile MIR-LHR because of its small size ($32.3 \times 32.3 \times 20\ mm^3$ vs $90 \times 120 \times 70\ mm^3$), light weight (0.1 vs 2 kg) and low power consumption (0.2 vs 20 W). It is worthwhile to note that the MEMS mirror can achieve simultaneous measurement of multi-channel and multi-band laser heterodyne spectra those cannot be achieved by traditional choppers, which expands the application of MIR-LHR in the field of atmospheric detection.

CONCLUSION

In conclusion, a MIR-LHR system using a MEMS mirror modulator was developed. The modulation frequencies of MEMS modulator-based MIR-LHR were experimentally investigated. The contributions of main noise sources in the LHR system were quantitatively analyzed. N_2O absorption in the atmospheric column was measured by the developed MIR-LHR system in the ground-based solar occultation mode. The measured LHR spectrum was consistent with the FT-IR spectrum and the atmospheric transmission modeling. Lighter, smaller and lower power consumption MEMS mirror has greatly improved the volume and stability of MIR-LHR, which makes MIR-LHR very suitable, not only for ground-based but also for aircraft- and satellite-based measurements.

DATA AVAILABILITY STATEMENT

The raw data supporting the conclusion of this article will be made available by the authors, without undue reservation.

AUTHOR CONTRIBUTIONS

ZX was responsible for the overall design and implementation of the experiment, data processing, and manuscript writing. TT and GW provided inspiration for the theory and operation of the experiment and suggestions for the revision of manuscripts. JL and XL provided help for the construction of the experimental device and data collection. WC and FS provided writing reviewing and editing. XG and KL: Supervision, Funding acquisition.

FUNDING

Key Project of the National Natural Science Foundation of China (41730103) and National Natural Science Foundation of China (41405022, 42075128).

REFERENCES

1. Deutscher NM, Griffith DWT, Bryant GW, Wennberg PO, Toon GC, Washenfelder RA, et al. Total Column CO₂ Measurements at Darwin, Australia - Site Description and Calibration against *In Situ* Aircraft Profiles. *Atmos Meas Tech* (2010) 3:947–58. doi:10.5194/amt-3-947-2010
2. Chan KL, Valks P, Slijkhuis S, Köhler C, Loyola D. Total Column Water Vapor Retrieval for Global Ozone Monitoring Experience-2 (GOME-2) Visible Blue Observations. *Atmos Meas Tech* (2020) 13:4169–93. doi:10.5194/amt-13-4169-2020
3. Lange D, Behrendt A, Wulfmeyer V. Compact Operational Tropospheric Water Vapor and Temperature Raman Lidar with Turbulence Resolution. *Geophys Res Lett* (2019) 46:14844–53. doi:10.1029/2019gl085774
4. Brunamonti S, Jorge T, Oelsner P, Hanumanthu S, Singh BB, Kumar KR, et al. Balloon-borne Measurements of Temperature, Water Vapor, Ozone and Aerosol Backscatter on the Southern Slopes of the Himalayas during StratoClim 2016-2017. *Atmos Chem Phys* (2018) 18:15937–57. doi:10.5194/acp-18-15937-2018
5. Ren H, Li A, Hu Z, Huang Y, Li X. Measurement of Atmospheric Water Vapor Vertical Column Concentration and Vertical Distribution in Qingdao Using Multi-axis Differential Optical Absorption Spectroscopy. *Acta Phys Sin* (2020) 69:204–6. doi:10.7498/aps.69.20200588
6. Ma Y, He Y, Tong Y, Yu X, Tittel FK. Quartz-tuning-fork Enhanced Photothermal Spectroscopy for Ultra-high Sensitive Trace Gas Detection. *Opt Express* (2018) 26:32103–10. doi:10.1364/oe.26.032103
7. Lang Z, Qiao S, Ma Y. Acoustic Microresonator Based In-Plane Quartz-Enhanced Photoacoustic Spectroscopy Sensor with a Line Interaction Mode. *Opt Lett* (2022) 47:1295–8. doi:10.1364/ol.452085
8. Li C, Shao L, Meng H, Wei J, Qiu X, He Q, et al. High-speed Multi-Pass Tunable Diode Laser Absorption Spectrometer Based on Frequency-Modulation Spectroscopy. *Opt Express* (2018) 26:29330–9. doi:10.1364/oe.26.029330
9. Ma Y, Feng W, Qiao S, Zhao Z, Gao S, Wang Y. Hollow-core Anti-resonant Fiber Based Light-Induced Thermoelastic Spectroscopy for Gas Sensing. *Opt Express* (2022) 30:18836–44. doi:10.1364/oe.460134
10. Pidwirny M. *Fundamentals of Physical Geography*. 2nd ed.. New Delhi: Cengage Learning (2006).
11. Tsai T. *External Cavity Quantum cascade Lasers for Spectroscopic Applications*. Princeton: Princeton University (2012). PhD Thesis
12. Tsai TR, Rose RA, Weidmann D, Wysocki G. Atmospheric Vertical Profiles of O3, N2O, CH4, CCl2F2, and H2O Retrieved from External-Cavity Quantum-cascade Laser Heterodyne Radiometer Measurements. *Appl Opt* (2012) 51:8779–92. doi:10.1364/ao.51.008779
13. Shen F, Wang G, Wang J, Tan T, Wang G, Jeseck P, et al. Transportable Mid-infrared Laser Heterodyne Radiometer Operating in the Shot-Noise Dominated Regime. *Opt Lett* (2021) 46:3171. doi:10.1364/ol.426432
14. Wilson EL, DiGregorio AJ, Villanueva G, Grunberg CE, Souders Z, Miletti KM, et al. A Portable Miniaturized Laser Heterodyne Radiometer (Mini-LHR) for Remote Measurements of Column CH_4 and CO_2. *Appl Phys B* (2019) 125:211. doi:10.1007/s00340-019-7315-8
15. Wang J, Sun C, Wang G, Zou M, Tan T, Liu K, et al. A Fibered Near-Infrared Laser Heterodyne Radiometer for Simultaneous Remote Sensing of Atmospheric CO_2 and CH_4. *Opt Lasers Eng* (2020) 129:106083. doi:10.1016/j.optlaseng.2020.106083
16. Robinson I, Butcher HL, Macleod NA, Weidmann D. Hollow Waveguide-Miniaturized Quantum cascade Laser Heterodyne Spectro-Radiometer. *Opt Express* (2021) 29:2299. doi:10.1364/oe.415371
17. Wang J, Wang G, Tan T, Zhu G, Sun C, Cao Z, et al. Mid-infrared Laser Heterodyne Radiometer (LHR) Based on a 3.53 μm Room-Temperature Interband cascade Laser. *Opt Express* (2019) 27:9610–9. doi:10.1364/OE.27.009610

18. Xue C, Zheng L, Zhang W, Zhang B, Jian A. A Dynamic Stress Analyzer for Microelectromechanical Systems (MEMS) Based on Raman Spectroscopy. *Raman Spectrosc* (2007) 4:38. doi:10.1002/jrs.1673
19. Ma X, Kuo GS. Optical Switching Technology Comparison: Optical MEMS vs. Other Technologies. *IEEE Commun Mag* (2003) 41:S23. doi:10.1109/mcom.2003.1244924
20. Pomeroy JW, Gkotsis P, Zhu M, Leighton G, Kirby P, Kuball M. Dynamic Operational Stress Measurement of MEMS Using Time-Resolved Raman Spectroscopy. *Microelectromech Syst* (2008) 17:1321. doi:10.1109/jmems.2008.2004849
21. Serrano JR, Kearney SP. Time-Resolved Micro-raman Thermometry for Microsystems in Motion. *Heat Transf* (2008) 130:122401. doi:10.1115/1.2976552
22. Wang Y, Nikodem M, Wysocki G. Cryogen-free Heterodyne-Enhanced Mid-infrared Faraday Rotation Spectrometer. *Opt Express* (2013) 21:740. doi:10.1364/oe.21.000740
23. Blaney TG. Signal-to-noise Ratio and Other Characteristics of Heterodyne Radiation Receivers. *Space Sci Rev* (1975) 17:691–702. doi:10.1007/bf00727583
24. Klimchuk AY, Nadezhdinskii AI, Ponurovskii YY, Shapovalov YP, Rodin AV. On the Possibility of Designing a High-Resolution Heterodyne Spectrometer for Near-IR Range on the Basis of a Tunable Diode Laser. *Quan Electron* (2012) 42:3. doi:10.1070/qe2012v042n03abeh014759
25. Kämpfer N. *Monitoring Atmospheric Water Vapor*. New York, NY: Springer (2013).

Conflict of Interest: The authors declare that the research was conducted in the absence of any commercial or financial relationships that could be construed as a potential conflict of interest.

Publisher's Note: All claims expressed in this article are solely those of the authors and do not necessarily represent those of their affiliated organizations, or those of the publisher, the editors and the reviewers. Any product that may be evaluated in this article, or claim that may be made by its manufacturer, is not guaranteed or endorsed by the publisher.

frontiers | Frontiers in Physics

ORIGINAL RESEARCH
published: 17 June 2022
doi: 10.3389/fphy.2022.907715

Design and Analysis of Novel Folded Optical Multi-Pass Cell

Gang Cheng[1], *Ya-Nan Cao*[1,2]*, *Xing Tian*[1], *Jia-Jin Chen*[3] *and Jing-Jing Wang*[4]

[1]State Key Laboratory of Mining Response and Disaster Prevention and Control in Deep Coal Mines, Anhui University of Science and Technology, Huainan, China, [2]Institute of Environment-Friendly Materials and Occupational Health of Anhui University of Science and Technology, Wuhu, China, [3]Anhui Institute of Optics and Fine Mechanics, Chinese Academy of Sciences, Hefei, China, [4]Institute of Atmospheric Science, Fudan University, Shanghai, China

A novel folded multi-pass cell consisting of three non-coaxial mirrors (spherical mirror or plane mirror) is proposed for laser spectroscopy. Three mirrors of the folded multi-pass cell can arrange in V-shape to form a stable non-coaxial multi-pass cell. Furthermore, in order to research the stability of the multi-pass cell under off-axis mirror's astigmatism circumstance, an equivalent coaxial multi-pass cell and modified ABCD matrix model for the spot pattern of the folded multi-pass cell is proposed, by which a series of the detailed numerical calculations were implemented to analyze the optical path length of the multi-pass cell. Many spot patterns obtained with a high fill factor improve the utilization efficiency of the surface of the mirror and produce a longer total optical path length. The several typical types of folded multi-pass cells consisting of the different mirrors and base lengths were selected to demonstrate the cell's self-consistent condition and power for a longer-optical path length. Three effective optical path lengths of 49.6, 97.6 and 173.6 m were obtained, respectively.

Keywords: folded multi-pass cell, non-coaxial mirror, modified ABCD matrix, dense spot pattern, long optical path length

OPEN ACCESS

Edited by:
Yufei Ma,
Harbin Institute of Technology, China

Reviewed by:
Yahui Liu,
Harbin Institute of Technology, China
Wu Zhenwei,
Hefei Institutes of Physical Science(CAS), China

***Correspondence:**
Ya-Nan Cao
cynpf@mail.ustc.edu.cn

Specialty section:
This article was submitted to Optics and Photonics, a section of the journal Frontiers in Physics

Received: *30 March 2022*
Accepted: *15 April 2022*
Published: *17 June 2022*

Citation:
Cheng G, Cao Y-N, Tian X, Chen J-J and Wang J-J (2022) Design and Analysis of Novel Folded Optical Multi-Pass Cell. Front. Phys. 10:907715. doi: 10.3389/fphy.2022.907715

INTRODUCTION

The multi-pass cell (MPC) is regarded as an important part of laser absorption spectroscopy for an effective long optical path length (OPL).In addition, due to its real-time online, high sensitivity, high selectivity non-contracted and non-intrusive advantages, the laser absorption spectroscopy is widely used in the fields of atmosphere, environmental pollution, and industrial process, industrial emissions for trace gas chemical composition analysis, and measurement (CH_4, CO_2, CO, HCHO, N_2O, NH_3, etc.) [1–10]. Early White cells, Herriot cells, and Chernin cells [11–13] are still used in a laser-based spectroscopic trace gas sensor due to the advantages of the MPC. The White cells, Herriot cells, and Chernin cells have some drawbacks, such as a relatively large volume, low effective utilization areas of mirrors and complex structure, which limits their application in miniaturization instruments. Considering the advantages of the MPC in laser spectroscopy, the design of miniaturized and weight light MPC will be one of the mainstream development trends in the future. For more compact size and longer OPL, recently, many various MPCs have been reported and developed, in which at least one spherical mirror was replaced with an aspherical mirror. In 2013, BélaTuzson et al. [14, 15] developed a toroidal MPC, which consisted of a single piece of reflective toroidal surface forming a near-concentric cavity in a circular configuration with a volume of merely 40 ml, for this new type of MPC, two effective OPLs of 2.2 and 4.1 m were chosen to demonstrate the cell's suitability. In 2015, Liu et al. [16] designed a novel compact dense-pattern multi-pass cell (DP-MPC) with a 280 ml sampling volume, whose minimum detectable

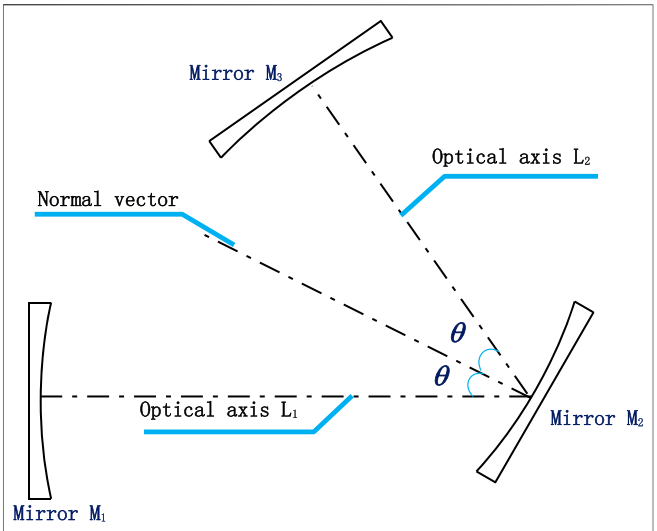

FIGURE 1 | Transmission of the rays in the folded MPC consisting of three mirrors M_1, M_2, and M_3; the reflection on the M_2, M_3 surface in the x–z plane of a Cartesian coordinate system; R radius of the curvature of the spherical mirror; L_1 L_2, mirror distance; θ inclination angle of the mirror M_2.

concentration of 100 ppb was obtained. In 2016, Dong et al. [17–19] developed the ultra-compact multi-pass gas cell, which offered a 54.6 m OPL in physical size of 17*6.5*5.5 cm^3 with a 220 ml sampling volume. In 2017, Ozharar et al. [20] designed an aspherical MPC, in which the focal length of aspherical mirrors varied inversely to the ray height from the optical axis, for aspherical MPC a very rich set of exotic spot patterns can be formed on the end mirrors by numerical simulations. In 2019, Kong et al. [21] reported a new design method for the multi-pass cell with a similar traditional configuration. For instance, the OPL is 20.4 m after the beam passes 183 times in the cell, and the sample volume is approximately 332.1 ml. In 2020, Cui et al. [22] reported three-dimensional printed miniature fiber-coupled multipass cells with an optical absorption path length of 4.2 m and dimensions of 4* 4*6 cm^3. A limitation of laser absorption spectroscopy originates from the requirement of the long OPL, especially when detecting the low concentrations of the trace gas on the order of ppm. In this article, a novel folded multi-pass cell consisting of three non-coaxial mirrors is presented. Three mirrors of the folded multi-pass cell can arrange in V-shape to form a stable non-coaxial multi-pass cell. Furthermore, in order to research the self-consistent condition of the multi-pass cell and the number of reflections, an equivalent coaxial multi-pass cell and modified ABCD matrix model for the spot pattern of the folded multi-pass cell is proposed, by which a series of the detailed numerical calculations were implemented to analyze the optical path length of the multi-pass cell. Due to the off-axis mirror's astigmatism, many dense spot patterns obtained with a high fill factor produce a longer total optical path length. The folded multi-pass cell with dense patterns shows superior characteristics, such as small volume, simple structure, long effective OPL, high detection sensitivity, and affordable cost, which make them very suitable for various field applications, particularly for trace gas sensing. The proposed MPCs can overcome the disadvantage of the number of reflection times possible for the Herriott cell and can achieve up to hundreds of reflections with a small overlap. Despite the optical interference fringes due to the small overlap tend to cause difficulties in multi-pass absorption spectroscopy and limit its sensitivity. The optical interference fringes can be effectively suppressed by wavelength-modulation spectroscopy (WMS) and frequency-modulation spectroscopy (FMS) [23].

OPTICAL SETUP OF THE FOLDED OPTICAL MULTI-PASS CELL

The optical setup for a novel folded optical multi-pass cell is shown in **Figure 1**. First, the incident ray transmits between two spherical mirrors (M_1 and M_2) and then reflects from the M_2 surface to the spherical mirror (M_3) surface; after that reflects from M_3 to M_2; at the last, the ray is transmitted to M_1 surface to complete a pass count in the structure of the folded MPC.

Compared with the coaxial MPC, the non-coaxial MPC is much more complicated. In order to simplify the analysis of complicated non-coaxial MPC, according to the theory of laser cavity, an equivalent coaxial multi-element MPC is proposed as displayed in **Figure 2**.

An equivalent cavity consists of two spherical mirrors and a lens that possesses different focal lengths in the meridian plane and sagittal plane due to the astigmatism of the off-axis spherical mirror M_2. In the meridian plane and sagittal plane, the focal length is defined as f_m = 0.5 R*cos (2θ), f_s = 0.5 R*sec (2θ), respectively. If the astigmatism of the off-axis spherical mirror is not considered, a set of beautiful spot patterns on the mirrors cannot be calculated by a numerical calculation model based on the ABCD matrix.

CALCULATION MODEL OF THE SPOT PATTERN OF THE FOLDED OPTICAL MULTI-PASS CELL

In this paper, in consideration of the astigmatism of the off axis spherical mirror (M_2), the modified 4*4 ABCD matrix describing one complete pass count is proposed, which consists of the standard transmission matrix and the standard reflection matrix of the ray:

$$M = \begin{bmatrix} A & B \\ C & D \end{bmatrix} = \begin{bmatrix} d^T & b^T \\ c^T & a^T \end{bmatrix} * \begin{bmatrix} 1 & 0 & 0 & 0 \\ \frac{-2}{R} & 0 & 1 & 0 \\ 0 & 1 & 0 & 0 \\ 0 & \frac{-2}{R} & 0 & 1 \end{bmatrix} * \begin{bmatrix} a & b \\ c & d \end{bmatrix} * \begin{bmatrix} 1 & 0 & 0 & 0 \\ \frac{-2}{R} & 0 & 1 & 0 \\ 0 & 1 & 0 & 0 \\ 0 & \frac{-2}{R} & 0 & 1 \end{bmatrix} \quad (1)$$

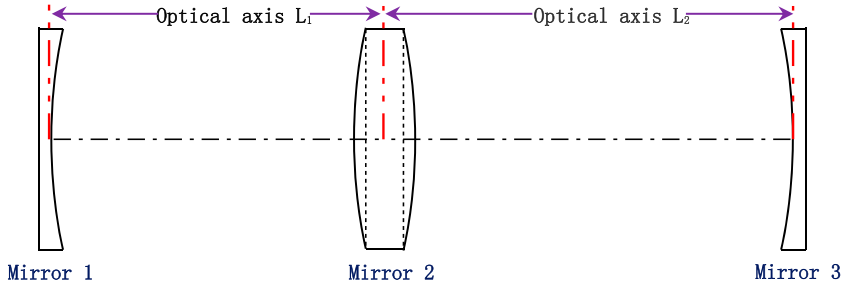

FIGURE 2 | As equivalent cavity, two spherical mirrors M_1, M_3, and an equivalent convex lens M_2; L_1 L_2, mirror distance.

$$m = \begin{bmatrix} a & b \\ c & d \end{bmatrix} = \begin{bmatrix} 1 & 0 & L_1 & 0 \\ 0 & 0 & 1 & 0 \\ 0 & 1 & 0 & L_1 \\ 0 & 0 & 0 & 1 \end{bmatrix} * \begin{bmatrix} 1 & 0 & 0 & 0 \\ \frac{-1}{f_m} & 0 & 1 & 0 \\ 0 & 1 & 0 & 0 \\ 0 & \frac{-1}{f_s} & 0 & 1 \end{bmatrix} * \begin{bmatrix} 1 & 0 & L_2 & 0 \\ 0 & 0 & 1 & 0 \\ 0 & 1 & 0 & L_2 \\ 0 & 0 & 0 & 1 \end{bmatrix} \tag{2}$$

where m = [a b; c d] is expressed as a one-way ABCD matrix in the cell.

If an incident ray enters the MPC from M_1 with the initial parameters $(x_0, x'_0)'$, $(y_0, y'_0)'$ on the M_1 surface. x_0, y_0, x'_0, y'_0 serve as incident location and inclination angle, respectively. After n pass counts, a ray is described by the coordinates $(x_{n-1}, x'_{n-1})'$, $(y_{n-1}, y'_{n-1})'$ of the point where it is located on the spherical mirror's surface.

$$\left(x\mathrm{n}-1, y\mathrm{n}-1, x'\mathrm{n}-1, y'\mathrm{n}-1\right) = \begin{bmatrix} \mathrm{A} & B \\ C & D \end{bmatrix}^n \left(x0, y0, x'0, y'0\right) \tag{3}$$

CONFINEMENT STABILITY OF THE FOLDED OPTICAL MPC

The theoretical study of the self-consistent condition of the MPC is the first step before designing any optical MPC (choice of the curvature radius, base length of the cell). Based on laser cavity theory, the optical cavity's eigenvalue method used to judge the stability of the cell is more concise. Taking one mirror as the reference plane, the corresponding eigenvalue lambda λ of the ABCD matrix of the equivalent MPC in the meridian plane or the sagittal plane is determined by **Eqs 4–6**. The criterion for a stable cell or cavity can be strictly exhibited as follow:

$$\left|\begin{bmatrix} A-\lambda E & B \\ C & D-\lambda E \end{bmatrix}\right| = 0 \tag{4}$$

$$\lambda^2 - (A+D)\lambda + 1 = 0 \tag{5}$$

$$\lambda_{1,2} = \frac{A+D}{2} \pm \sqrt{\left(\frac{A+D}{2}\right)^2 - 1} \tag{6}$$

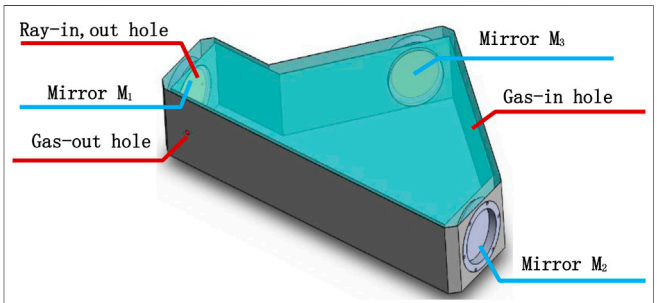

FIGURE 3 | Mechanical structure drawing of the V-shape MPC includes spherical mirrors M_1, M_2, and M_3; gas-in and gas-out hole, and ray-in and ray-out window.

When the $|A + D| > 2$, it is found that the lambda λ consists of a pair of real numbers, which means that in a cycle the ray $(x_0, x'_0)'$ or $(y_0, y'_0)'$ is at magnification (decrease) of λ times. So, under the self-consistent condition, the ray will diverge (converge) into a point-source of ray in the cavity, which is called an unstable cavity. When the $|A + D| < 2$, it is concluded that the lambda λ consists of a pair of conjugate complex numbers, whose real part and imaginary part stand for the curvature of the wavefront and the radius of the ray spot, respectively, according to the diagonalization of the complex wavefront. therefore, the optical cavity is stable.

OPTICAL ARRANGEMENT OF THE FOLDED OPTICAL MULTI-PASS CELL

The optical arrangement of the folded MPC involving three identical spherical mirrors is shown in **Figure 3**. As a requirement to get a long OPL, three high reflectivity dielectric-coating spherical mirrors (reflectivity of 99.993% at the wavelength of 1.573 μm) are employed to form a folded MPC. The three identical spherical mirrors have a diameter of (50.8 mm) and a radius of (1,000 mm), which are non-coaxial arrangements, and the arm's base lengths L_1 and L_2 are 150 mm, 200 mm, respectively. The spherical mirror M_1 and M_3 are 90° angles to the optical axis respectively, which is equivalent to θ with a value of 10° as shown in **Figure 1**. Around the MPC, there

TABLE 1 | Incident location (x_0, y_0, z_0), Incident vector (x', y', z'), Curvature radius (R) of three mirrors, M_2, M_3, Mirrors separated distance (L_1), (L_2), Volume (V) and Ratio (RLV) used to obtain the spot patterns depicted in **Figures 4**, **9**.

Pattern	(x_0, y_0, z_0) (mm)	(x', y', z')	L_1 (mm)	L_2 (mm)	R (mm)			OPL (m)	V (cm^3)	RLV (cm^{-2})
					M_1	M_2	M_3			
Figure 4	(0, 16, −199.5)	(−0.08, 0.008, 2.1)	2*102	2*102	103	∞	103	49.6	950	5
Figure 5	(16, 16, 209)	(0.007, 0.007, 2.1)	2*102	2*102	103	103	103	97.6	950	10
Figure 6	(15, 16, −155)	(0.008, 0.007, 1.5)	1.5*102	2*102	103	103	103	173.6	780	22

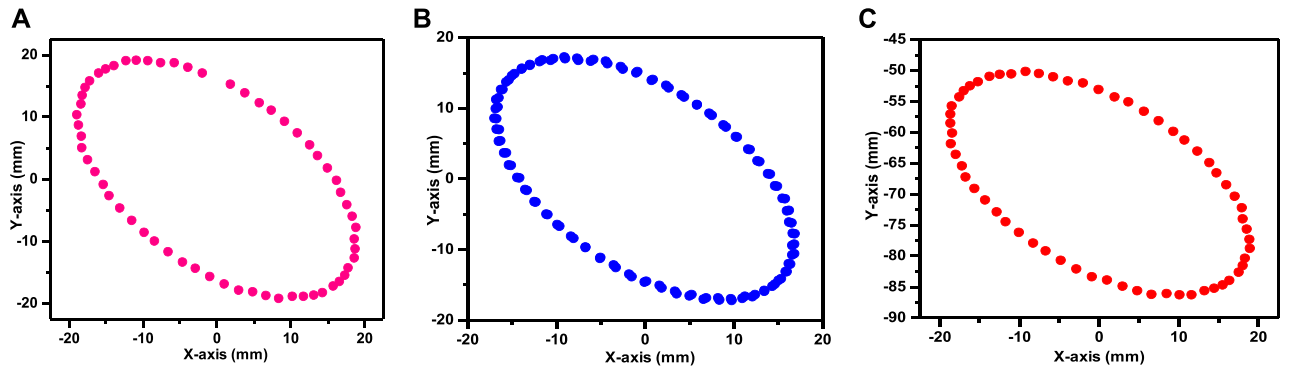

FIGURE 4 | Spot patterns simulated by optical software, **(A–C)** Spot patterns on spherical mirrors M_1, M_2, and M_3 of three different MPCs, respectively. The initial ray parameters for the spot pattern are listed in **Table 1**. Pass counts n = 61 times.

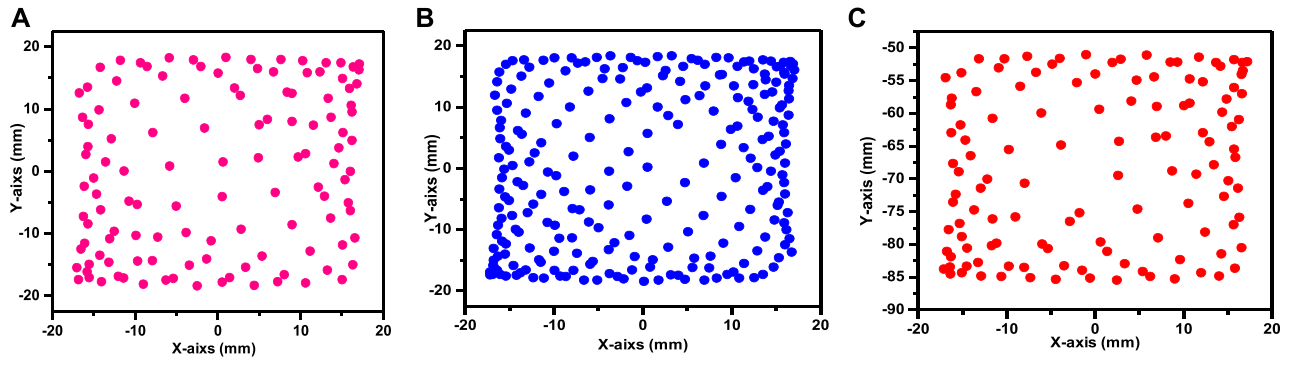

FIGURE 5 | Spot patterns simulated by optical software, **(A–C)** Spot patterns on spherical mirrors M_1, M_2, and M_3 of three different MPCs, respectively. The initial ray parameters for the spot pattern are listed in **Table 1**. Pass counts n = 122 times.

are gas-in and gas-out holes for gas change. The spherical mirror M_1 possess ray-in and ray-out windows as displayed in the mechanical structure drawing **Figure 3**.

RESULTS AND DISCUSSION

Three typical folded MPC are selected to show, whose eigenvalue λ is the conjugate complex numbers with value of (−0.28 ± 0.9600i, −0.28 ± 0.9600i), (−0.8487 ± 0.5289i, −0.8377 ± 0.5461i), (−0.7524 ± 0.6588i, −0.7393 ± 0.6734i), respectively, which means that those folded MPCs selected to show is stable. On the base of the stable cavity, by adjusting incident ray's parameters such as initial incident angle, initial entry location on M_1, mirrors separated distance (L_1) or distance (L_2) between mirrors, some satisfying number of the reflections on x-y plane of the mirrors can be obtained. Therefore, it is demonstrated that an original folded MPC is powerful to create a long OPL. In the calculation model, with a fixed inclination angle θ (10°) of the spherical mirror M_2, the longest OPL is the spot pattern of **Figure 6** with a value of 173.6 m. In fact, a ratio of the total OPL to the volume can better reflect the space utilization of the

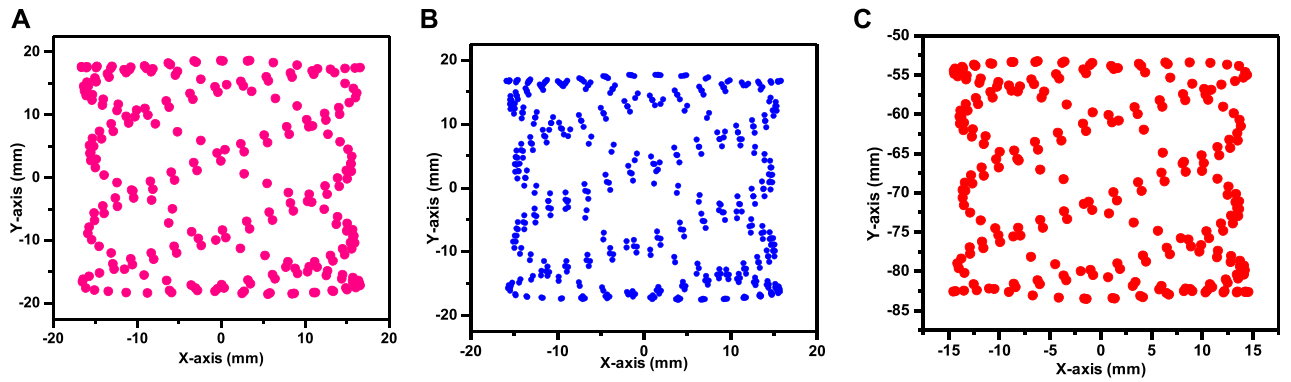

FIGURE 6 | Spot patterns simulated by optical software, **(A–C)** Spot patterns on spherical mirrors M_1, M_2, and M_3 of three different MPCs, respectively. The initial ray parameters for the spot pattern are listed in **Table 1**. Pass counts n = 248 times.

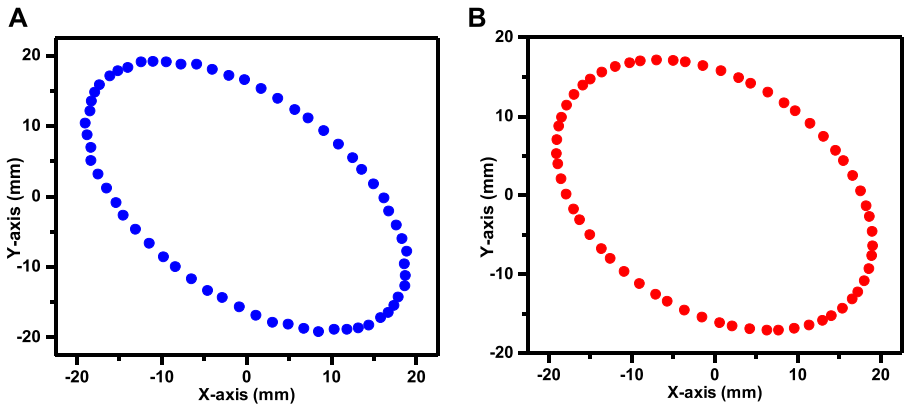

FIGURE 7 | (A,B) The spot patterns of three different MPCs (● blue dot, ● red dot) on spherical mirror M_1 stimulated by optical software and modified ABCD matrix model, respectively. The optical parameters of spot patterns are identical to that in **Figure 4**.

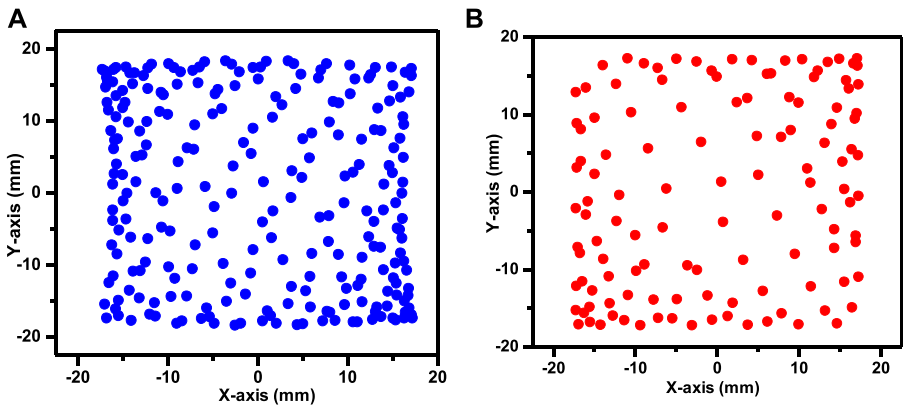

FIGURE 8 | (A,B) The spot patterns of three different MPCs (● blue dot, ● red dot) on spherical mirror M_1 stimulated by optical software and modified ABCD matrix model, respectively. The optical parameters of spot patterns are identical to that in **Figure 5**.

ray in the MPC. According to the ratio of OPL to V (RLV) in **Table 1**, the most efficient space utilization is the spot pattern with a value of 22 in **Figure 6**. Those extraordinary spot patterns result mainly from the astigmatism of the off-axis spherical mirror M_2, which plays an important role in the spot pattern evolution caused by the off-axis spherical mirror's astigmatism.

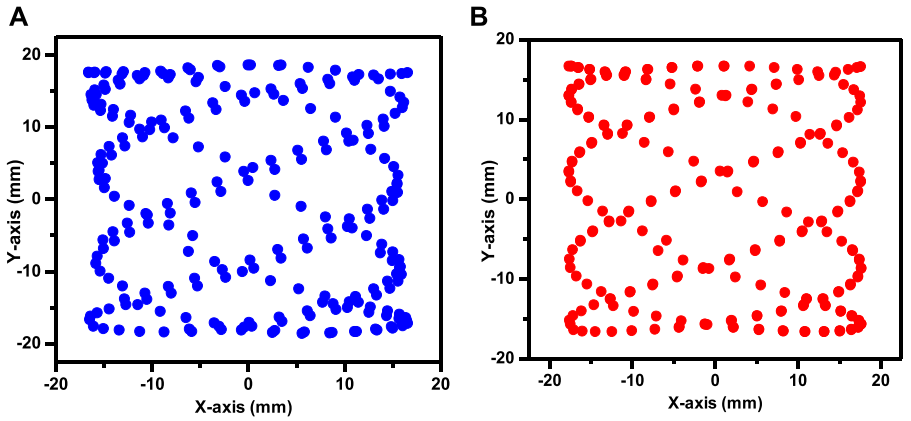

FIGURE 9 | (A,B) The spot patterns of three different MPCs (● blue dot, ● red dot) on spherical mirror M_1 stimulated by optical software and modified ABCD matrix model, respectively. The optical parameters of spot patterns are identical to that in **Figure 6**.

When the important ray's parameter such as the incident location (x_0, y_0, z_0), incident vector (x', y', z'), mirrors spacing (L_1), (L_2), and curvature radius (R) is depicted in **Table 1** of the spherical mirrors, each spot pattern in **Figures 4–6** can evolve more spot patterns to increase the spot density or down. In **Figures 4**, **6** the pass counts are 61 times, 122 times, and 248 times, respectively. It is found that the number of the reflection of the ray on the M_2 is twice as much as that on the M_1, M_3 mirror surface due to the folded MPC consisting of two subs-resonators. In **Figures 4–6** the OPL of the folded MPC is 49.6, 97.6 and 173.6 m under different ray parameters shown in **Table 1**.

In order to validate the calculation model based on the modified ABCD matrix, a comparison of the blue spot patterns in **Figures 7A–9A** simulated by optical software with the red spot patterns **Figures 7B–9B** from the modified ABCD matrix model shows that the consistency between the calculated and simulated spot patterns demonstrates the validity of the modified 4*4 ABCD matrix with the astigmatism of the off-axis mirror. It is found that the slight difference between **Figures 9A,B** mainly results from the ABCD matrix's paraxial approximation error which is amplified in hundreds of cycles. For non-paraxial rays, the paraxial approximation error will make the spot pattern seriously distorted in multiple cycles.

CONCLUSION

In conclusion, a new folded MPC and a modified ABCD matrix with astigmatism are proposed. The spot patterns from the calculation model and optical software show that the new folded MPC is powerful to the long OPL with rich spot patterns, which are very same as the cylindrical and astigmatic MPC. For the new MPC, the excellent ratio of the total OPL to the volume can realize a highly sensitive and compact gas sensor with a low cost due to the use of a common spherical mirror and plane mirror to form two subs-MPCs. Compact or portable MPCs such as the one displayed on paper have many uses in various fields such as climate change, atmospheric monitoring, and medical diagnostics. Further topics of interest include the manufacture and testing of the folded MPC, as well as the investigation of laser beam spot interference and thermal stability of the folded MPC of this type.

DATA AVAILABILITY STATEMENT

The original contributions presented in the study are included in the article/supplementary material, further inquiries can be directed to the corresponding author.

AUTHOR CONTRIBUTIONS

GC, Y-NC, XT, J-JC, and J-JW contributed to the writing of the manuscript and to the interpretation of results. GC: Conceptualization, Writing-Original draft preparation. Y-NC and XT: Software, Validation. J-JC and J-JW: Writing-Reviewing and Editing.

FUNDING

This research was funded by the Natural Science Foundation of Anhui Province (Grant Nos. 202004a07020046 and 1908085QD156); National Natural Science Foundation of China (NSFC) (Grant No. 62105005); Foundation of State Key Laboratory of Mining Response and Disaster Prevention and Control in Deep Coal Mines (Grant No SKLMRDPC19KF12); Research Foundation of the Institute of Environment-Friendly Materials and Occupational Health of Anhui University of Science and Technology (Wuhu) (Grant No. ALW2020YF04) for support.

REFERENCES

1. Ma Y, He Y, Tong Y, Yu X, Tittel FK. Quartz-tuning-fork Enhanced Photothermal Spectroscopy for Ultra-high Sensitive Trace Gas Detection. *Opt. Express* (2018) 26:32103–10. doi:10.1364/OE.26.032103
2. Wysocki G, Bakhirkin Y, So S, Tittel FK, Hill CJ, Yang RQ, et al. Dual Interband Cascade Laser Based Trace-Gas Sensor for Environmental Monitoring. *Appl. Opt.* (2007) 46:8202–10. doi:10.1364/ao.46.008202
3. Linnerud I, Kaspersen P, Jaeger T. Gas Monitoring in the Process Industry Using Diode Laser Spectroscopy. *Appl Phys B Lasers Opt* (1998) 67:297–305. doi:10.1007/s003400050509
4. Lang Z, Qiao S, Ma Y. Acoustic Microresonator Based In-Plane Quartz-Enhanced Photoacoustic Spectroscopy Sensor with a Line Interaction Mode. *Opt. Lett.* (2022) 47:1295–8. doi:10.1364/OL.452085
5. Zou J, Wang F. Simultaneous Measurement of SO2 and NO2 Concentration Using an Optical Fiber-Based LP-DOAS System. 中国光学快报 (2020) 18: 021201–33. doi:10.3788/COL202018.021201
6. Ma Y, Lewicki R, Razeghi M, Tittel FK. QEPAS Based Ppb-Level Detection of CO and N_2O Using a High Power CW DFB-QCL. *Opt. Express* (2013) 21: 1008–19. doi:10.1364/OE.21.001008
7. Tittel FK. Current Status of Midinfrared Quantum and Interband Cascade Lasers for Clinical Breath Analysis. *Opt. Eng* (2010) 49:111123. doi:10.1117/1.3498768
8. Werle P, Mucke R, Slemr F. The Limits of Signal Averaging in Atmospheric Trace-Gas Monitoring by Tunable Diode-Laser Absorption Spectroscopy (Tdlas). *Appl. Phys. B* (1993) 57:131–9. doi:10.1007/BF00425997
9. Liu X, Ma Y. Sensitive Carbon Monoxide Detection Based on Light-Induced Thermoelastic Spectroscopy with a Fiber-Coupled Multipass Cell [Invited]. 中国光学快报 (2022) 20:031201. doi:10.3788/COL202220.031201
10. Weibring P, Richter D, Fried A, Walega JG, Dyroff C. Ultra-high-precision Mid-IR Spectrometer II: System Description and Spectroscopic Performance. *Appl. Phys. B* (2006) 85:207–18. doi:10.1007/s00340-006-2300-4
11. White JU. Long Optical Paths of Large Aperture. *J. Opt. Soc. Am.* (1942) 32: 285–7. doi:10.1364/josa.32.000285
12. Chernin SM, Barskaya EG. Optical Multipass Matrix Systems. *Appl. Opt.* (1991) 30:51–8. doi:10.1364/AO.30.000051
13. Herriott D, Kogelnik H, Kompfner R. Off-Axis Paths in Spherical Mirror Interferometers. *Appl. Opt.* (1964) 3:523–6. doi:10.1364/AO.3.000523
14. Tuzson B, Mangold M, Looser H, Manninen A, Emmenegger L. Compact Multipass Optical Cell for Laser Spectroscopy. *Opt. Lett.* (2013) 38:257–9. doi:10.1364/OL.38.000257
15. Mangold M, Tuzson B, Hundt M, Jágerská J, Looser H, Emmenegger L. Circular Paraboloid Reflection Cell for Laser Spectroscopic Trace Gas Analysis. *J. Opt. Soc. Am. A* (2016) 33:913–9. doi:10.1364/JOSAA.33.000913
16. Liu K, Wang L, Tan T, Wang G, Zhang W, Chen W, et al. Highly Sensitive Detection of Methane by Near-Infrared Laser Absorption Spectroscopy Using a Compact Dense-Pattern Multipass Cell. *Sensors Actuators B Chem* (2015) 220:1000–5. doi:10.1016/j.snb.2015.05.136
17. Dong L, Li C, Sanchez NP, Gluszek AK, Griffin RJ, Tittel FK. Compact CH4 Sensor System Based on a Continuous-Wave, Low Power Consumption, Room Temperature Interband Cascade Laser. *Appl. Phys. Lett.* (2016) 108:011106. doi:10.1063/1.4939452
18. Dong L, Yu Y, Li C, So S, Tittel FK. Ppb-level Formaldehyde Detection Using a CW Room-Temperature Interband Cascade Laser and a Miniature Dense Pattern Multipass Gas Cell. *Opt. Express* (2015) 23:19821–30. doi:10.1364/OE.23.019821
19. Dong L, Tittel FK, Li C, Sanchez NP, Wu H, Zheng C, et al. Compact Tdlas Based Sensor Design Using Interband Cascade Lasers for Mid-IR Trace Gas Sensing. *Opt. Express* (2016) 24:A528–A535. doi:10.1364/OE.24.00A528
20. Ozharar S, Sennaroglu A. Mirrors with Designed Spherical Aberration for Multi-Pass Cavities. *Opt. Lett.* (2017) 42:1935–8. doi:10.1364/OL.42.001935
21. Kong R, Sun T, Liu P, Zhou X. Optical Design and Analysis of a Two-Spherical-Mirror-Based Multipass Cell. *Appl. Opt.* (2020) 59:1545–52. doi:10.1364/AO.381632
22. Cui R, Dong L, Wu H, Li S, Yin X, Zhang L, et al. Calculation Model of Dense Spot Pattern Multi-Pass Cells Based on a Spherical Mirror Aberration. *Opt. Lett.* (2019) 44:1108–11. doi:10.1364/OL.44.001108
23. Li S, Sun L. Natural Logarithm Wavelength Modulation Spectroscopy. *Chin Opt Lett* (2021) 19:031201. doi:10.3788/col202119.031201

Conflict of Interest: The authors declare that the research was conducted in the absence of any commercial or financial relationships that could be construed as a potential conflict of interest.

frontiers | Frontiers in Physics

ORIGINAL RESEARCH
published: 24 June 2022
doi: 10.3389/fphy.2022.942926

Calibration Methods of Atmospheric Aerosol Lidar and a Case Study of Haze Process

Chao Chen[1,2,3,4], Xiaoquan Song[1], Zhangjun Wang[2,3,1,4]*, Yubao Chen[5], Xiaopeng Wang[5], Zhichao Bu[5], Xi Zhang[6], Quanfeng Zhuang[2], Xin Pan[2], Hui Li[2], Feng Zhang[2], Xiufen Wang[2], Xianxin Li[2,3] and Ronger Zheng[1]*

[1]Faculty of Information Science and Engineering, Ocean University of China, Qingdao, China, [2]Institute of Oceanographic Instrumentation, Qilu University of Technology (Shandong Academy of Sciences), Qingdao, China, [3]R & D Center for Marine Sensors, Pilot National Laboratory for Marine Science and Technology (Qingdao), Qingdao, China, [4]Shandong SCICOM Shenguang Technology Co., Ltd, Qingdao, China, [5]CMA Meteorological Observation Centre, Beijing, China, [6]Haidian District Meteorological Service, Beijing, China

Lidar is a reliable tool for active remote sensing detection of atmospheric aerosols. A multi-wavelength aerosol lidar (MWAL) with 355 nm, 532 and 1064 nm as detection light sources has been developed and deployed for operational observations at Haidian District Meteorological Service of Beijing. The structure design, specifications, observation campaign, and detection principle of the MWAL are introduced. To ensure the accuracy and reliability of the lidar observation data, the calibration contents, and methods of lidar are proposed, including the correction, and gluing of the original data, the collimation of the transmitting and receiving optical axes, the testing of signal saturation, the correction of molecular Rayleigh fitting and the determination of the depolarization ratio correction factor. Finally, a haze process from 29 September to 2 October 2019 was observed and analyzed using the data of lidar, digital radiosonde, air quality and relative humidity observed by the Haidian District Meteorological Service. The detection results show the reliability of lidar which can effectively obtain the temporal and spatial variation characteristics of the haze. The profiles of aerosol extinction coefficient, potential temperature and relative humidity can be effectively used to analyze the haze thickness and the influence of relative humidity on aerosol particles. The data of air quality monitor shows that PM_{10} is the main pollutant and the ratio of $PM_{2.5}/PM_{10}$ is negatively correlated with relative humidity. Finally, the HYSPLIT trajectory tracking model of the National Oceanic and Atmospheric Administration (NOAA) is used to further study the source of pollutants in this haze process.

Keywords: atmospheric lidar, aerosol, calibration, depolarization ratio, haze

OPEN ACCESS

Edited by:
Yufei Ma,
Harbin Institute of Technology, China

Reviewed by:
Lingbing Bu,
Nanjing University of Information Science and Technology, China
Fei Gao,
Xi'an University of Technology, China

****Correspondence:***
Xiaoquan Song
songxq@ouc.edu.cn
Zhangjun Wang
zhangjunwang@qlu.edu.cn

Specialty section:
This article was submitted to Optics and Photonics, a section of the journal Frontiers in Physics

Received: *13 May 2022*
Accepted: *03 June 2022*
Published: *24 June 2022*

Citation:
Chen C, Song X, Wang Z, Chen Y, Wang X, Bu Z, Zhang X, Zhuang Q, Pan X, Li H, Zhang F, Wang X, Li X and Zheng R (2022) Calibration Methods of Atmospheric Aerosol Lidar and a Case Study of Haze Process. Front. Phys. 10:942926. doi: 10.3389/fphy.2022.942926

INTRODUCTION

In recent years, with the rapid development of urbanization and industrialization, pollution weather occurs frequently and lasts for a long time, which not only hurts transportation, but also seriously restricts the development of social and economic and threatens the health of people [1–3]. Atmospheric aerosols are the main factor of air pollution, playing an important role in the process of air pollution [4, 5]. Meanwhile, atmospheric aerosols are one of the important

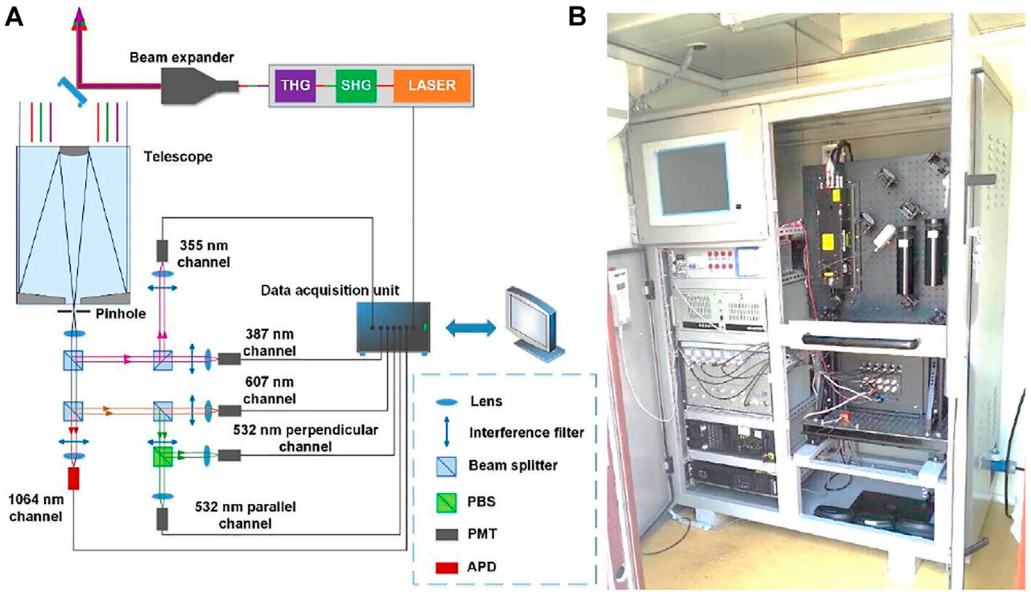

FIGURE 1 | (A) MWAL's structure. **(B)** MWAL's cabinet appearance.

TABLE 1 | The specifications of MWAL.

Parameters	Specifications
Transmitter	
Type	Lamp-pumped Nd:YAG
Laser wavelength	355 nm, 532 nm, 1064 nm
Pulse energy	40 mJ@ 355 nm, 30 mJ@532 nm, 60 mJ@1064 nm
Pulse duration	10 ns
Pulse repetition frequency	20 Hz
Beam divergence	200 μrad
Receiver	
Type	Schmidt-Cassegrain
Diameter	300 mm
Field of View	500 μrad
Range resolution	3.75 m
Receiving channels	355 nm, 387 nm, 532 nm-P, 532 nm-S, 607, and 1064 nm
Detector type	APD for 1064 nm PMT for 355 nm, 387 nm, 532 nm-P, 532 nm-S and 607 nm

research objects of atmospheric science and play an important role in many atmospheric photophysical and chemical processes [6, 7]. Weather and climate are affected by aerosol-radiation and aerosol-cloud interactions. The direct climatic effect of aerosols is to affect the balance of earth-atmosphere radiation by scattering and absorbing solar radiation, thereby affecting climate change. And the indirect climatic effect of aerosols is to act as the condensation nucleus of clouds, which changes the optical properties of clouds, cloud amount and cloud lifespan, and then affects the earth-atmosphere radiation balance [8, 9]. In conclusion, atmospheric aerosols have important impacts on weather, climate, living environment and human health.

Lidar is an active remote sensing technology, which uses the pulse laser as the detection light source and has significant advantages in the observation of atmospheric aerosols and clouds with high spatial and temporal resolution [10, 11]. Recently, with the rapid development of laser technology [12], signal detection technology and data processing technology, lidar technology has gradually matured. This has promoted its long-term operational observation in meteorological and environmental protection departments, contributing to the monitoring of the atmospheric environment and providing technical support for research on weather phenomena [13]. Micro-pulse lidar from Sigma Space Corporation, CIMEL ELECTRONIQUE's lidar CE370 and Raymetrics' ESS-D series lidars have become reliable routine observation equipments for aerosols and have been used all over the world [14, 15]. To ensure the reliability of long-term observations, atmospheric aerosol lidars need to be calibrated and tested regularly. Consequently, reliable and efficient calibrations and test methods are particularly important.

Institute of Oceanographic Instrumentation, Qilu University of Technology (Shandong Academy of Sciences) has developed a set of multi-wavelength aerosol lidar (MWAL), which has been deployed at Haidian District Meteorological Service (HDMS) of Beijing for operational observation. In the long-term observations, the methods of regular calibration and test of atmospheric aerosol lidar have been accumulated so that the process data of different weathers have been obtained. In this paper, the mechanical structure and technical parameters of the lidar system are introduced firstly, and then the observation campaigns and detection principles are outlined. The contents and methods of calibration of atmospheric aerosol lidar are discussed, and the calibration results are analyzed. Finally, a haze process in Beijing is studied by using the data of lidar,

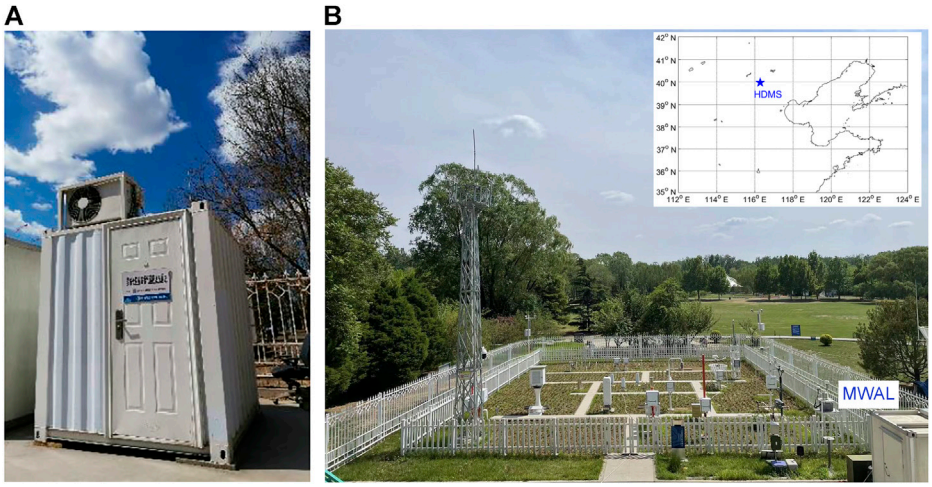

FIGURE 2 | (A) MWAL observed at HDMS. **(B)** Observation sites of HDMS.

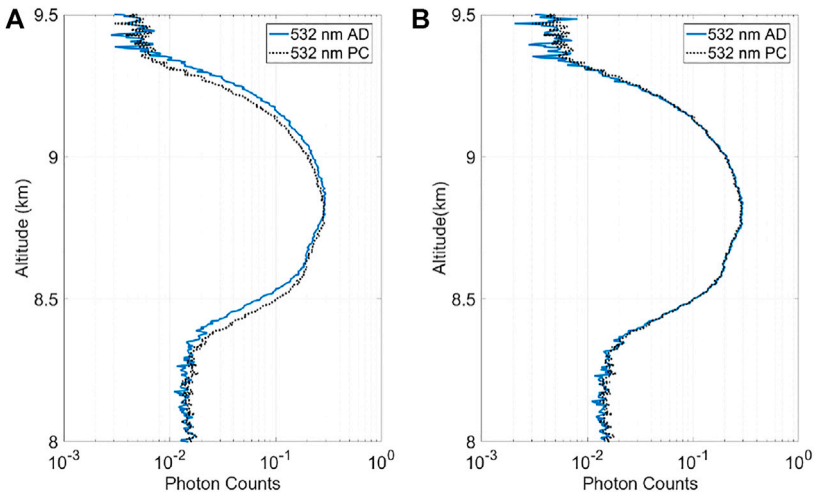

FIGURE 3 | (A) The data of AD mode and PC mode before data correction. **(B)** The data of AD mode and PC mode after data correction.

digital radiosonde and ground station atmospheric elements monitoring, and the source of the haze is analyzed by using the HYSPLIT trajectory model of the National Oceanic and Atmospheric Administration (NOAA).

THE AEROSOL LIDAR SETUP

The MWAL with three-wavelength lasers of 355, 532, and 1064 nm has been developed by the Institute of Oceanographic Instrumentation, Qilu University of Technology (Shandong Academy of Sciences) for automatic observations of tropospheric aerosols and clouds. The echo signals generated by the interaction between laser and atmospheric aerosols and molecules are received by a Schmidt-Cassegrain telescope with a diameter of 300 mm. After passing through the pinhole and the collimating lens, the echo signals are divided into multi-wavelength optical signals by the dichroic mirrors. Each respectively passes through the optical receiving channel composed of narrow-band interference filter, converging lens and photodetector to obtain elastic scattering signals at 355, 532, and 1064 nm, and N_2 Raman scattering signals at 387 and 607 nm. The 532 nm signal is divided into a parallel polarization component (532 nm-P) and a perpendicular polarization component (532 nm-S) by a polarizing beam splitter (PBS) with beam extinction ratio greater than 2000:1. The optical signals are converted into electrical signals after entering the photodetector and then collected by a six-channel Licel transient recorder. The MWAL can realize the real-time detection of atmospheric aerosol optical parameters within a

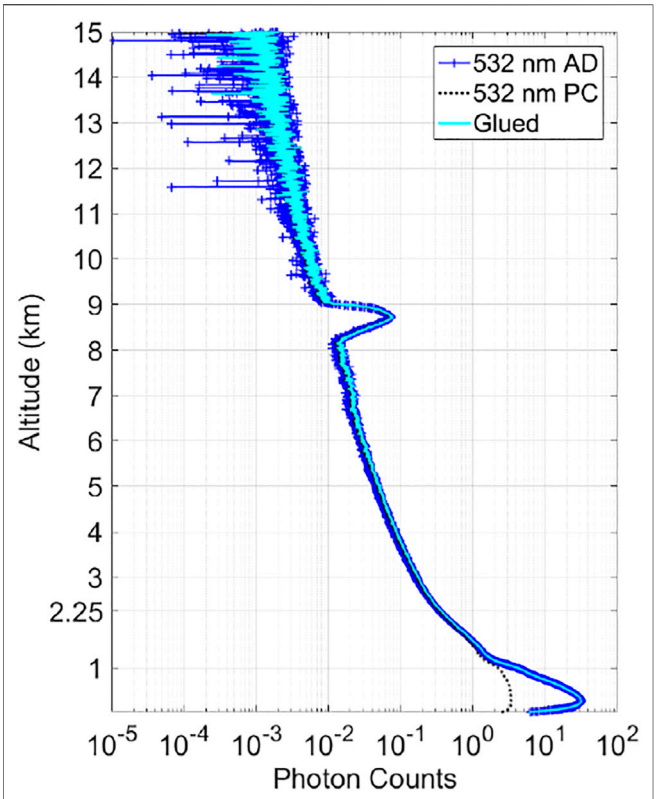

FIGURE 4 | The profiles of AD mode data, PC mode data and glued data.

range of 20 km and its optical structure is shown in **Figure 1A**. It is integrated and installed in a cabinet (**Figure 1B**), with the optical module installed on the right side, and the data collector, laser controller, industrial computer and circuit controller integrated on the left side. During the observation campaign, the cabinet is installed in a square cabin to ensure that the lidar works in a suitable temperature and humidity environment and can carry out continuous unattended observation all day.

The specifications of the MWAL are shown in **Table 1**.

OBSERVATION EXPERIMENTS

The MWAL is deployed at the Haidian Park Observation Site (39°59′N, 116°17′E) of the HDMS to conduct all-day operational observations, which can be used to observe and study the spatial and temporal distribution characteristics, optical characteristic parameters and depolarization ratio of atmospheric aerosols and clouds, providing technical support for urban atmospheric environment monitoring and atmospheric pollution research. **Figure 2A** shows the MWAL at the Haidian Park Observation Site of HDMS, the geographic location of which is shown in **Figure 2B**. A variety of meteorological elements and atmospheric environment monitoring instruments installed in the HDMS can effectively obtain the data of wind speed, wind direction, temperature, relative humidity, air quality data such as the concentrations of $PM_{2.5}$ and PM_{10}. The GTS1 digital radiosonde carried by hydrogen balloon is usually released at 7:15 and 19:15 local time every day to obtain the profiles of the meteorological elements such as temperature, humidity, wind, and pressure. Through the combination of various data, the weather process can be better studied.

THE PRINCIPLE OF LIDAR DETECTION

The lidar equation is the basis for describing the detection principle of lidar and provides the relationship between the lidar echo signal and the optical properties of the measured object. The atmospheric backscattered signal power $P(r)$ at distance r can be determined by the lidar equation [16]:

$$P(r) = \frac{kP_0A_r\beta(r)}{r^2} exp\left[-2\int_0^r \alpha(r')dr'\right] \quad (1)$$

where P_0 is the power of the transmitted laser, A_r is the effective receiving area of the telescope, and k is the lidar correction constant, which is related to the geometric overlap factor, the total transmittance, and the range resolution. $\alpha(r)$ and $\beta(r)$ respectively represent the extinction coefficient and backscattering coefficient of atmospheric molecules and aerosols, which reflect the optical characteristics of the atmosphere. Here, we mainly use the Fernald method [17] to retrieve the optical parameters of aerosols.

The MWAL emits a 532 nm linearly polarized pulsed laser into the atmosphere and the parallel polarization and perpendicular polarization components can be received by two detection channels. Generally, the signal power of the two polarization channels can be described as follows [18].

$$P_p(r) = \frac{k_pP_0A_r\beta_p(r)}{r^2} \exp\left[-2\int_0^r \alpha(r')dr'\right] \quad (2)$$

$$P_s(r) = \frac{k_sP_0A_r\beta_s(r)}{r^2} \exp\left[-2\int_0^r \alpha(r')dr'\right] \quad (3)$$

The depolarization ratio δ of atmospheric particles can be defined by the ratio of parallel polarization signal $P_p(r)$ and perpendicular polarization signal $P_s(r)$ as shown in **Eq. 4**, where K is the calibration factor.

$$\delta(r) = K\frac{P_s(r)}{P_p(r)} \quad (4)$$

δ is in the range of 0–1, which can be used to study the shape of aerosol particles in the air. The more irregular it is, the larger the depolarization ratio is (such as dust and ice crystals are typical non-spherical particles), while the depolarization ratio of spherical particles (such as water droplets) is relatively small [19, 20]. In a fine and cloudless weather, the depolarization is caused by the atmospheric molecules and δ is about 0.365% for 532 nm [21].

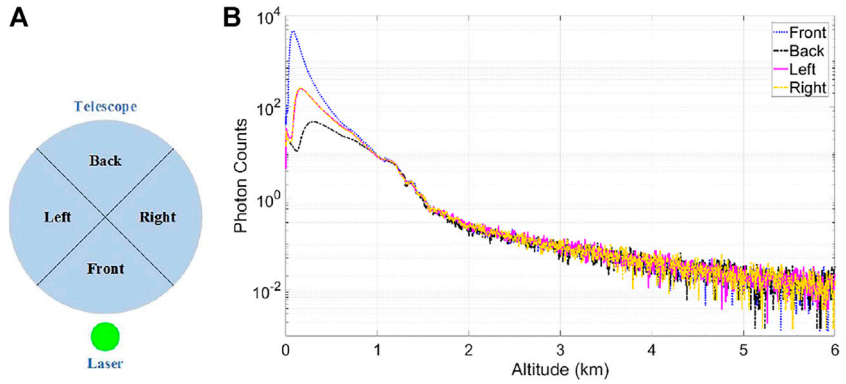

FIGURE 5 | (A) Four-quadrant division of the telescope. **(B)** Comparison of four-quadrant signals after collimation of the transmitting and receiving optical axes.

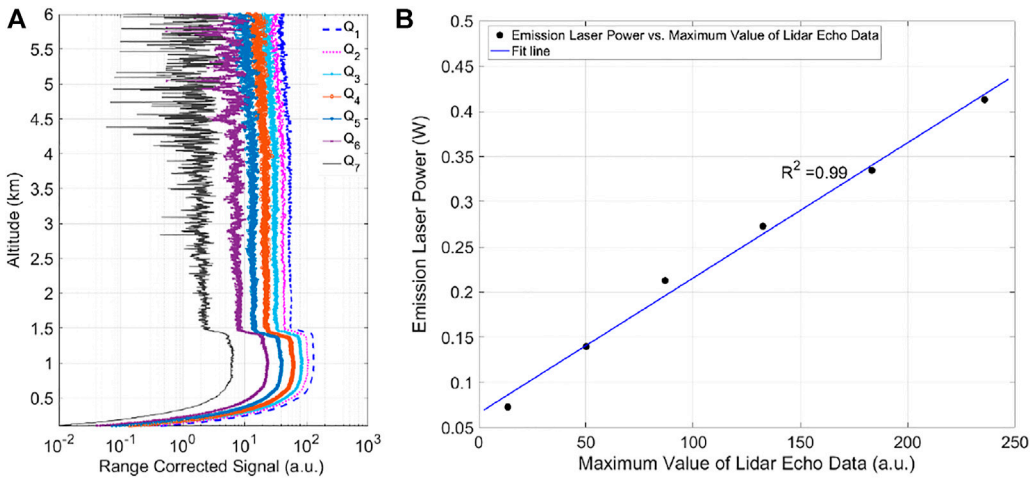

FIGURE 6 | (A) The echo signal profiles obtained with different emission laser powers. **(B)** The fitting line of the emission laser powers and the maximum value of the echo signal profiles.

SYSTEM CALIBRATION METHODS AND RESULTS

To ensure the accuracy and reliability of the lidar observation, it needs to be calibrated before and during the lidar observation. It mainly includes the correction and gluing of the original data, the collimation of the transmitting and receiving optical axes, the testing of signal saturation, the correction of molecular Rayleigh fitting and the determination of the depolarization ratio correction factor. The corresponding calibration methods are introduced, and the results are discussed.

Data Correction and Gluing

The MWAL uses a six-channel Licel transient recorder as the data collector, and each channel can simultaneously perform analog (AD) mode acquisition and photon counting (PC) mode acquisition with a range resolution of 3.75 m. AD mode has high responsivity to strong echo signals in near-range, while PC mode has higher sensitivity to weak light signals in long-distance. Therefore, gluing the data can effectively improve the signal-to-noise ratio, weak light signal detection capability and signal dynamic range.

Since the AD mode and PC mode in the Licel transient recorder are independent units, the data of the two modes may produce misalignment in the data recording. Therefore, it is necessary to correct the misalignment of data first. Taking the data at 0:00 on 9 September 2019 (local time, the same below) as an example, the signals of clouds from 8 to 9.5 km obtained by the two acquisition modes clearly show that the data collected by the AD mode is lagging the PC mode data (**Figure 3A**). After comparing the data of the two modes, the AD mode data can be alignment with the PC data by moving the AD data forward by nine points (**Figure 3B**).

Then it's necessary to glue the data collected in the AD mode and the PC mode after correcting the misalignment. Firstly, some proper range with a good linear relationship between AD mode data and PC mode data is selected as the gluing area, and then the

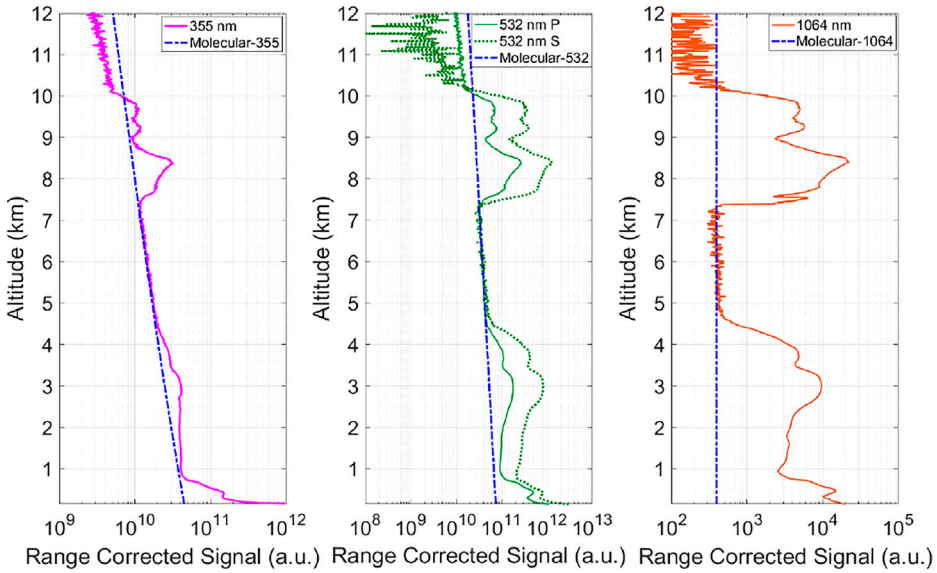

FIGURE 7 | Comparison of lidar range corrected signals and molecular Rayleigh signals of 355 nm, 532, and 1064 nm.

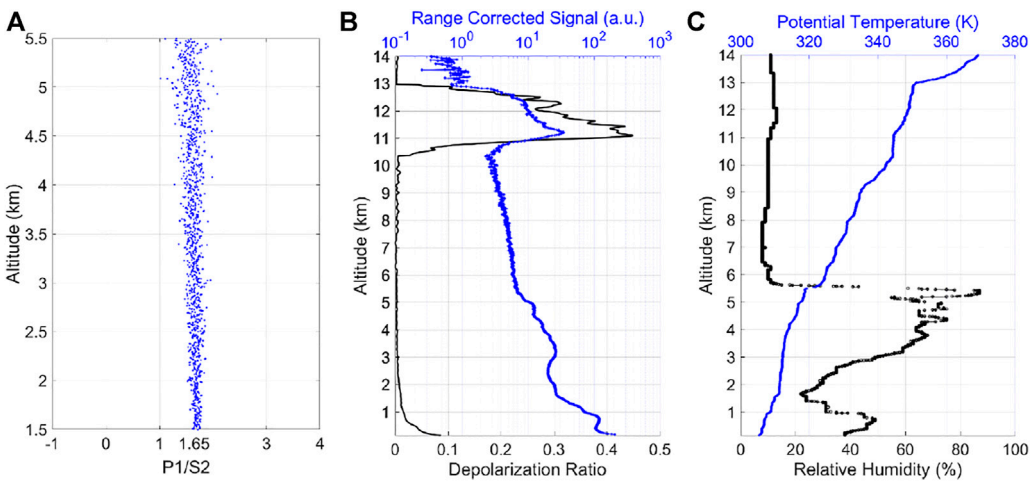

FIGURE 8 | (A) Correction factor *K*. **(B)** The profiles of range corrected signal and depolarization ratio at 19:15 on 20 June 2019. **(C)** The profiles of potential temperature and relative humidity at 19:15 on 20 June 2019.

coefficients a and b can be obtained by the least square method to convert the AD mode data into PC mode data [22, 23].

$$\sum_{i=1}^{n} \left(PC(i) - (a \cdot AD(i) + b)\right)^2 = N_{min} \tag{5}$$

where $PC(i)$ is the PC mode data and $AD(i)$ is the AD mode data. The glued data calculated by this method is shown in **Figure 4**, from which the glued altitude is 2.25 km. Below the glued altitude, the AD mode data has a better response to low-altitude strong signals. While, above the glued altitude, the change trend of the AD mode data and PC mode data is basically consistent. However, with the increase of altitude, PC mode data has a better signal-to-noise ratio than AD mode data. Accordingly, the dynamic range and detection distance of the signal are effectively improved through data gluing.

The Collimation of the Transmitting and Receiving Optical Axes

The collimation of the laser transmitting and receiving optical axes is the key to improve the signal receiving efficiency. The MWAL adopts the paraxial mode, that is, the transmitting optical axis is located on one side of the receiving telescope. Therefore, the collimation of the transmitting and receiving optical axes is to make them parallel. Here, we propose a method of signal

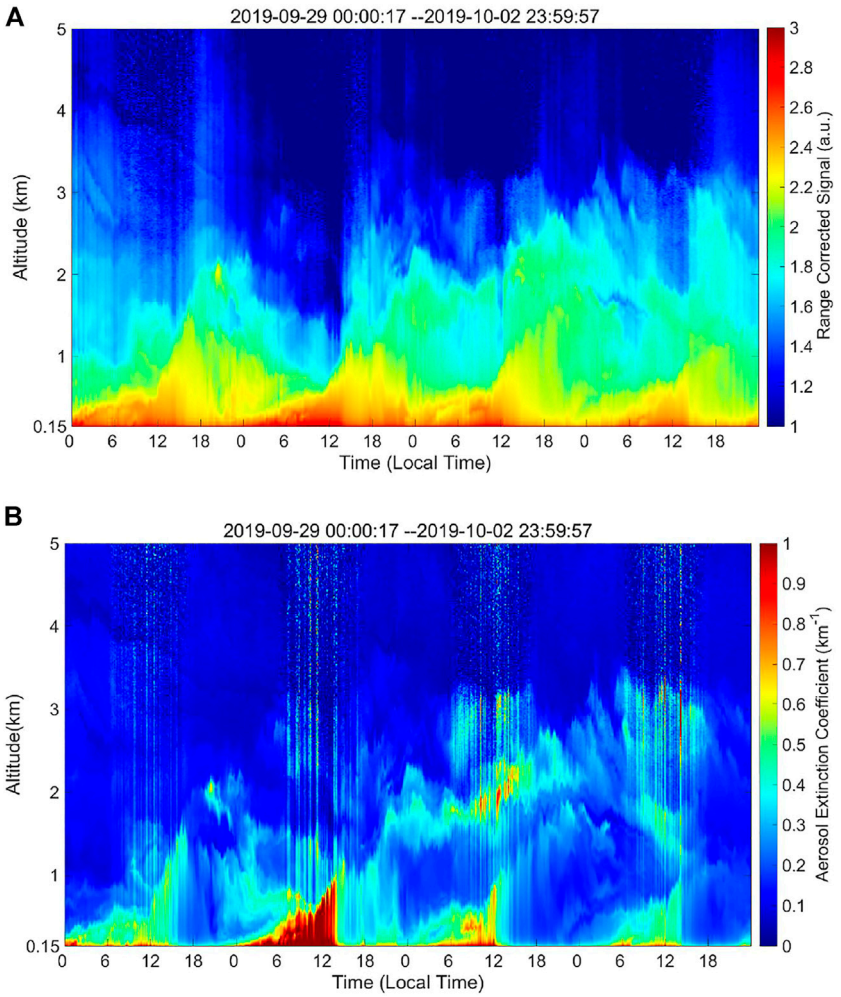

FIGURE 9 | (A) THI figure of range corrected signal at 532 nm from 29 September to 2 October 2019. **(B)** THI figure of extinction coefficient at 532 nm from 29 September to 2 October 2019.

comparison in the four-quadrant of the telescope to collimate the optical axes. Firstly, the telescope is divided into four quadrants (**Figure 5A**), and then the echo signals of the left and right quadrants are collected and compared. Adjust the direction of laser emission to make the signals of the left and right quadrants completely consistent. Next, the echo signals of the front quadrant and the back quadrant are collected respectively. Because the distance from the front quadrant to the emitting laser is different from the distance from the back quadrant to the emitting laser, the near-range signals of the two quadrants will be different. However, in the case of the collimation of the transmitting and receiving optical axes, the far-range signals of the two quadrants should be consistent. Consequently, the forward and backward directions of the emitting laser should be adjusted according to the far-range signals. When the optical axes of the transmitting and receiving are aligned using the above method, each quadrant collects data for 1 min. Taking the signal of 532 nm as an example, as shown in **Figure 5B**, the signals of the left and right quadrants are consistent, and the signals of the four quadrants coincide 1 km away. Below the altitude of 1 km, the signals of the four quadrants are different due to the different distances from the emitted laser to the different quadrants.

Signal Saturation Testing

During lidar observation, if the echo signal is saturated, it will lead to signal distortion and even cause damage to the detector. Therefore, it is necessary to test whether there is a problem with signal saturation. Cloudless weather with relatively stable atmospheric conditions is chosen for the test. Firstly, the output laser power is measured and its value is 0.495 W (Q_1) during the lidar observation, and then a group of data accumulated for 1 min is recorded. Secondly, the laser emission power is adjusted by setting different delay time of the Q-Switch of the laser. The average power of the outgoing laser measured by a power meter is 0.413 W (Q_2), 0.335 W (Q_3), 0.273 W (Q_4), 0.213 W (Q_5), 0.14 W (Q_6), and 0.073 W (Q_7) respectively, and the corresponding 6 groups of echo signals accumulated for 1 min are recorded. Taking the signal of 532 nm parallel channel as an example, the 7 groups range corrected signals of 532 nm parallel

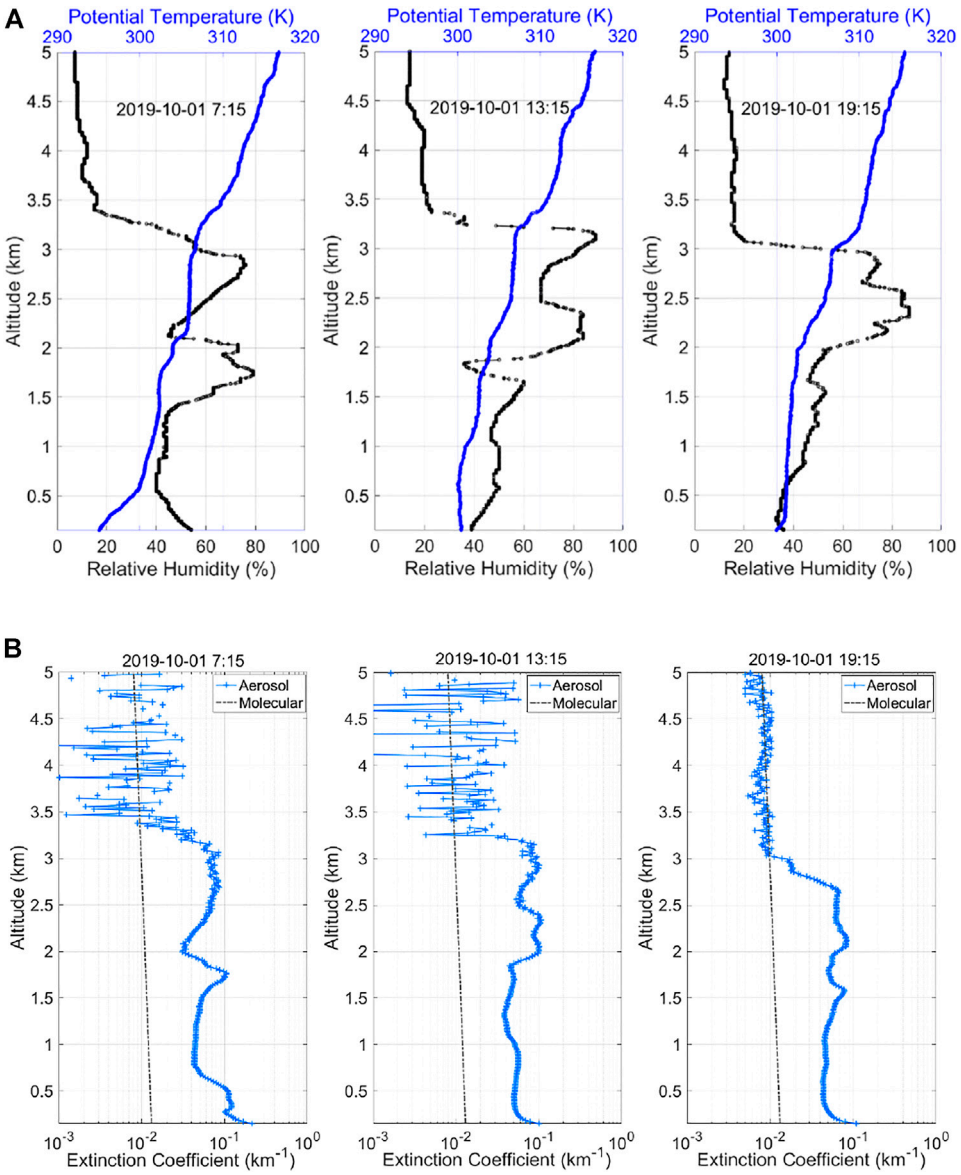

FIGURE 10 | (A) The profiles of potential temperature and relative humidity at 7:15, 13:15, and 19:15 on 1 October 2019. **(B)** The profiles of extinction coefficient at 7:15, 13:15, and 19:15 on 1 October 2019.

channels are drawn together in **Figure 6A**. With the attenuation of laser power, the signal profiles decrease in the same trend. It can be preliminarily judged that there is no saturation phenomenon when the lidar observes with the laser power of Q_1. A method of the linearity test is further used to verify the above inference. Taking the laser power Q_2 to Q_7 as ordinate and the maximum value of the corresponding 6 groups of echo signals as abscissa. A linear fitting line can be drawn, and then we can calculate the deviation between the actual measured value of Q_1 and the value calculated by the fitting line. If the deviation between the calculated value and the measured value of Q_1 is less than 5%, it indicates that the signal linearity is good and the signal is not saturated. If the deviation is greater than 5%, it is necessary to reduce the emission power of the laser for detection, and repeat the above test procedure until it reaches less than 5%.

As shown in **Figure 6B**, the coefficient of determination R^2 between the maximum value of the 6 groups of echo signal and emission laser power is 0.99. The calculated value of Q_1 is 0.518 W. Accordingly, the deviation between the calculated value and the measured value of Q_1 is 4.6%, indicating that there is no saturation phenomenon when the lidar observes with the laser power of Q_1.

Molecular Rayleigh Signal Fitting

At the altitudes with aerosols (such as low altitude) or clouds, the signal will be significantly enhanced because of Mie scattering. While at altitudes without aerosols, the lidar echo signal is mainly

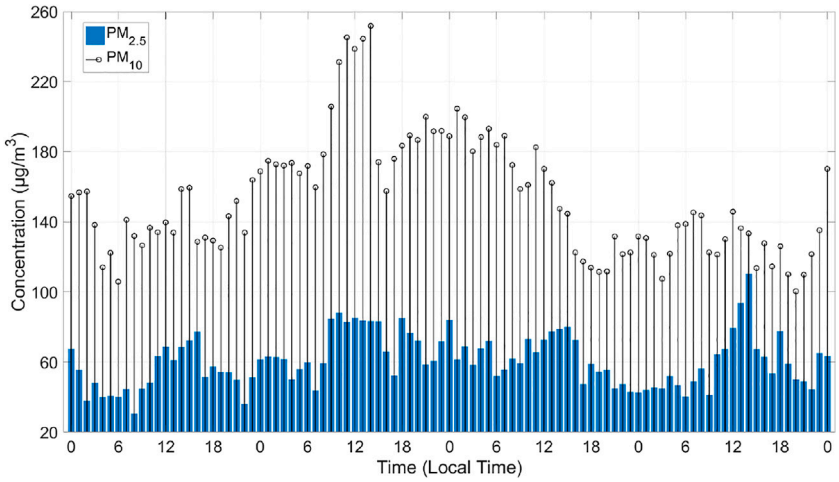

FIGURE 11 | Air quality monitoring data.

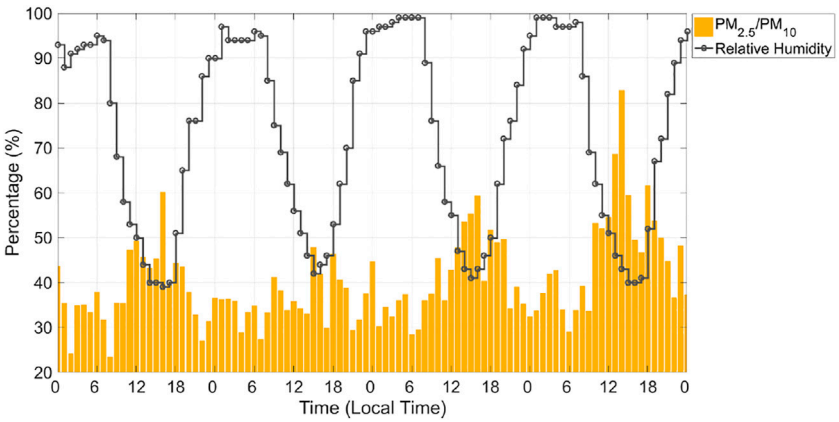

FIGURE 12 | Variation curves of ground relative humidity and $PM_{2.5}/PM_{10}$.

caused by molecular Rayleigh scattering. The molecular scattering signal obtained by the lidar can be compared with the standard atmospheric molecular Rayleigh signal to further check whether the lidar echo signal is normal [24]. In **Figure 7**, taking the observation data at 0:00 on 1 June 2021 as an example, the underlying aerosols are mainly distributed below 4.5 km, and clouds exist between 7.2 and 10 km from the range corrected signals of 355 nm, 532, and 1064 nm. The signals of aerosols and clouds are significantly larger than the molecular Rayleigh signals. However, the lidar echo signals of three wavelengths at the altitude between the underlying aerosols and clouds are in good agreement with the standard molecular Rayleigh signals.

Determination of Depolarization Ratio Correction Factor

The correction factor K for calculating the depolarization ratio δ is related not only to the depolarization effect of the lidar system, but also to the detection efficiency of the two detection channels [25]. Therefore, K is one of the important factors to calculate δ. In order to obtain K accurately, a 1/2 wave plate is installed between the laser and the beam expander. A clear day is selected for the determination of K. First, the direction of the optical axis of the 1/2 wave plate is parallel to the laser polarization direction, so that the polarization state of the laser emitted from the wave plate is the same as before. Here the data of the parallel polarization channel and perpendicular polarization channel are recorded as P1 and S1 respectively. Then the 1/2 wave plate is rotated so that the angle between the optical axis direction of the 1/2 wave plate and the laser polarization direction is 45°. The laser outgoing from the wave plate is still linearly polarized, and the angle between the polarization direction of the outgoing laser and the polarization direction of the original incident laser is 90°. In this case the data of the two polarization channels are recorded as P2 and S2 respectively. After subtracting the background from P1 and S2, a region where both signals are smooth is selected and the K is

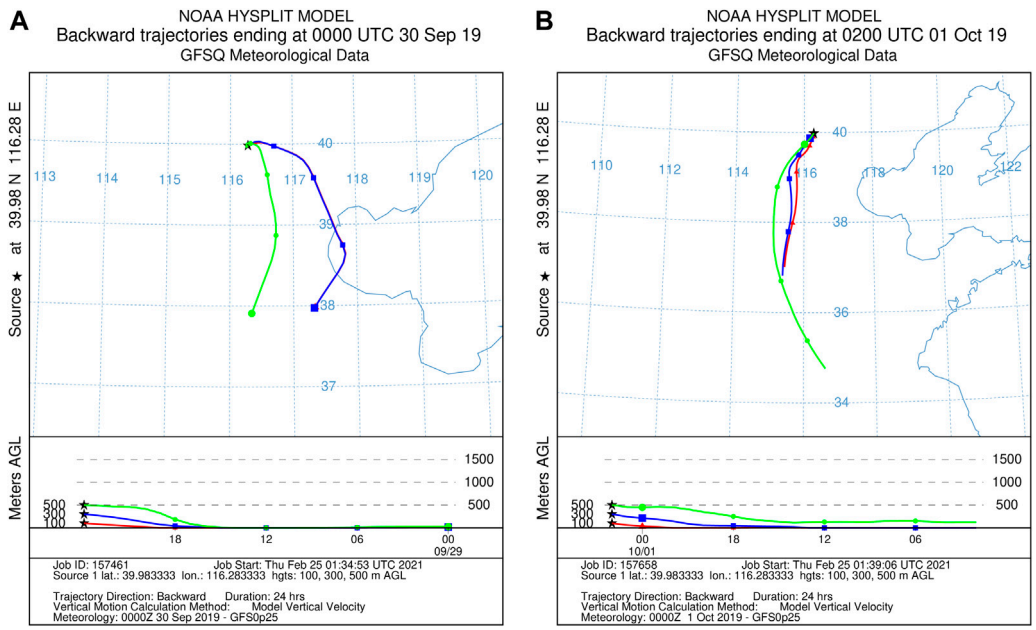

FIGURE 13 | (A) Backward trajectories of aerosols at the altitudes of 100, 300, and 500 m at 8:00 on 30 September 2019, Beijing time. **(B)** Backward trajectories of aerosols at the altitudes of 100, 300, and 500 m at 10:00 on 1 October 2019, Beijing time.

approximately 1.65 calculated by P1/S2 (as shown in **Figure 8A**). In addition, δ of atmospheric molecules (approximately 0.365%) and high-altitude cirrus clouds (30%–80%) can be used to further test and revise the K [26]. As shown in **Figure 8B**, the lidar observation data at 19:15 on 20 June 2019 is compared and analyzed with the potential temperature and relative humidity profiles of the digital radiosonde (**Figure 8C**). Through the lidar echo signal profile, the aerosols are mainly distributed below 5 km, which is consistent with the altitude of the maximum gradient absolute value of relative humidity and potential temperature. The lower δ below 5 km is probably due to the higher relative humidity. The main components of the atmosphere from 6 to 10.5 km are atmospheric molecules, and δ is relatively small. The cirrus clouds are distributed from 10.5 to 13 km with a δ higher than 0.4, where the potential temperature changes slowly and the relative humidity is lower than 15%, indicating that the cirrus clouds are mainly composed of ice crystals.

OBSERVATION EXAMPLE ANALYSIS OF A HAZE PROCESS

After the lidar is calibrated, it can better serve the monitoring of the atmospheric environment. Using the joint analysis of lidar and other meteorological data, the weather process can be better analyzed, and the performance of the lidar can be further tested. Taking a haze process in Beijing from 29 September to 2 October 2019 as an example, the weather process, temporal and spatial distribution, and possible sources of the haze are studied through the analysis of multiple observations data.

Comparative Analysis of Lidar and Digital Radiosonde Data

From 29 September to 2 October 2019, the MWAL observed a haze process in Beijing. From the time-height-indication (THI) figure of the range corrected signal of 532 nm in **Figure 9A**, the aerosols are mainly distributed below 3 km and the haze is heaviest on 30 September. From the THI figure of extinction coefficient (**Figure 9B**), we can see that the extinction coefficient near the ground is higher and haze occurs a similar diurnal change trend in these 4 days. The concentration of aerosols near-ground gradually increases after 0:00, and so does the haze thickness. The height and concentration of haze gradually decrease in the afternoon.

Taking the weather process on 1 October as an example, the lidar observation data and the digital radiosonde data at three moments are used for analysis. The potential temperature and relative humidity profiles at 7:15, 13:15, and 19:15 on 1 October (**Figure 10A**) show that the relative humidity is approaching or exceeding 80% and the potential temperature changes slowly at the altitude from 1.5 to 3.5 km. The changing trend of the extinction coefficient profiles in altitude at three times (**Figure 10B**) is consistent with that of the relative humidity. The altitude of the maximum absolute value of the aerosol extinction coefficient gradient is the same with the altitude of the maximum absolute value of the potential temperature and relative humidity gradient, indicating the thickness of the haze. At the altitude of 1.5–3.5 km, the increase of relative humidity may lead to an

increase of hygroscopic growth of aerosol particles and an increase of aerosols extinction coefficient.

Analysis of Ground Observation Data

In order to better analyze the air quality situation near the ground, we can clearly see the changes of the $PM_{2.5}$ and PM_{10} concentrations recorded by the air quality monitor from 29 September to 2 October 2019 (**Figure 11**). The concentrations of PM_{10} are all higher than 100 $\mu g/m^3$, with the higher PM_{10} concentration during the daytime on 30 September, and the highest value of 252 $\mu g/m^3$ at 14:00. The concentration of $PM_{2.5}$ reaches a maximum value of 110.6 $\mu g/m^3$ at 14:00 on 2 October. **Figure 12** shows the ratio of $PM_{2.5}/PM_{10}$ is more than 80% at this moment. The ratio of $PM_{2.5}/PM_{10}$ at other time is basically less than 50%, indicating that the haze is mainly caused by PM_{10} pollutants, which should be caused by the transportation of urban floating dust.

As shown in **Figure 12**, during the observation period from 29 September to 2 October 2019, the relative humidity changes regularly. Generally, the relative humidity is high at night, and decreases during the daytime due to the variation of temperature. The relative humidity is basically above 90% from 0:00 to 6:00, and close to 100% from 0:00 to 6:00 on 1 and 2 October. High relative humidity will cause the hygroscopic growth and the sedimentation of aerosol particles, so the aerosols extinction coefficient observed by lidar at night is relatively low. It can be seen from **Figure 12** that there is a negative correlation between relative humidity and $PM_{2.5}/PM_{10}$, that is, when the relative humidity is high, the proportion of $PM_{2.5}$ is relatively low.

HYSPLIT Trajectory Analysis

The ground meteorological data recorded by HDMS show that the south wind class 1 to 2 is dominant during this period, indicating thar the aerosols is mainly transported by the south wind and there is a lack of good diffusion conditions. The NOAA HYSPLIT trajectory model can support the source analysis of this haze. Taking the Haidian Park observation site of HDMS as the reference location, the backward trajectory of aerosols at different altitudes could be tracked. As shown in **Figure 13A**, the aerosols at the altitudes of 100, 300, and 500 m at 8:00 Beijing time on 30 September 2019, mainly come from near ground aerosols of Hebei and Shandong provinces to the south of Beijing. From **Figure 13B**, at 10:00 Beijing time on 1 October 2019, the aerosols at 100, 300, and 500 m also mainly originated from the near-ground of the south of Beijing.

CONCLUSION

A multi-wavelength aerosol lidar is carrying out an observation campaigns in HDMS of Beijing. The contents and methods of regular calibration of lidar are discussed, mainly including the correction and gluing of the original data, the collimation of the transmitting and receiving optical axes, the testing of signal saturation, the correction of molecular Rayleigh fitting and the determination of the depolarization ratio correction factor. All these can be used for the regular calibration of lidar operational observation to ensure the accuracy and reliability of the observed data. Finally, a haze process from 29 September to 2 October 2019 is analyzed by using the data of lidar, digital radiosonde, air quality and relative humidity of HDMS. The observation results show that the increase of extinction coefficient near the ground indicates the occurrence of haze phenomenon and the haze is most serious on 30 September. Comparing the profiles of potential temperature and relative humidity with the extinction coefficient profiles at three times on 1 October, it is found that the changing trend of the aerosol extinction coefficient in altitude is consistent with that of the relative humidity. High relative humidity will cause hygroscopic growth and the sedimentation of aerosol particles. Using the $PM_{2.5}$ and PM_{10} data recorded by the air quality monitor, it is analyzed that the haze is mainly caused by PM_{10} pollutants and the $PM_{2.5}/PM_{10}$ has a negative correlation relation with the relative humidity. It can be inferred that pollutants should be caused by the transportation of urban floating dust. The aerosols mainly originated from the near-ground of the south of Beijing by the analysis of NOAA's HYSPLIT trajectory model.

DATA AVAILABILITY STATEMENT

The raw data supporting the conclusions of this article will be made available by the authors, without undue reservation.

AUTHOR CONTRIBUTIONS

CC, XS, and ZW designed the research, YC, XUW (XOW), XZ and XP performed the experiments, ZB, QZ, HL, FZ, and XL analyzed the data, XOW (XUW) and RZ proposed the methods, CC and XS wrote the paper.

FUNDING

This work is jointly supported by the following project grants: National Key Research and Development Program of China (2021YFB3901304), Key Research and Development Plan of Shandong Province (2020CXGC010104), Development Fund Project of Institute of Oceanographic Instrumentation, Shandong Academy of Sciences (HYPY202106), Guangdong basic and Applied basic Research Fund (2020B1515120056), Qingdao Pilot National Laboratory for Marine Science and Technology (2021WHZZB0205and2021WHZZB1500) and International Cooperation Project of Shandong Academy of Sciences (2019GHZD02).

ACKNOWLEDGMENTS

Special thanks to CMA Meteorological Observation Centre and Haidian District Meteorological Service of Beijing for providing

observational support for multi-wavelength aerosol lidar and data support for digital radiosonde and ambient air quality monitoring, etc. The authors gratefully acknowledge the NOAA Air Resources Laboratory (ARL) for the provision of the HYSPLIT transport and dispersion model and/or READY website used in this publication.

REFERENCES

1. Zhang Y, Zhang Y, Yu C, Yi F. Evolution of Aerosols in the Atmospheric Boundary Layer and Elevated Layers during a Severe, Persistent Haze Episode in a Central China Megacity. *Atmosphere* (2021) 12(2):152. doi:10.3390/atmos12020152
2. Lang Z, Qiao S, Ma Y. Acoustic Microresonator Based In-Plane Quartz-Enhanced Photoacoustic Spectroscopy Sensor with a Line Interaction Mode. *Opt Lett* (2022) 47(6):1295–8. doi:10.1364/OL.452085
3. Cheng B, Ma Y, Feng F, Zhang Y, Shen J, Wang H, et al. Influence of Weather and Air Pollution on Concentration Change of PM2.5 Using a Generalized Additive Model and Gradient Boosting Machine. *Atmos Environ* (2021) 255: 118437. doi:10.1016/j.atmosenv.2021.118437
4. Wu J, Zhang Y, Wang T, Qian Y. Rapid Improvement in Air Quality Due to Aerosol-Pollution Control during 2012-2018: An Evidence Observed in Kunshan in the Yangtze River Delta, China. *Atmos Pollut Res* (2020) 11: 693–701. doi:10.1016/j.apr.2019.12.020
5. Chen C, Song X, Wang Z, Wang W, Wang X, Zhuang Q, et al. Observations of Atmospheric Aerosol and Cloud Using a Polarized Micropulse Lidar in Xi'an, China. *Atmosphere* (2021) 12:796. doi:10.3390/atmos12060796
6. Chang L, Li J, Chu Y, Dong Y, Tan W, Xu X, et al. Variability of Surface Aerosol Properties at an Urban Site in Beijing Based on Two Years of *In-Situ* Measurements. *Atmos Res* (2021) 256:105562. doi:10.1016/j.atmosres.2021.105562
7. Ma Y, He Y, Tong Y, Yu X, Tittel FK. Quartz-tuning-fork Enhanced Photothermal Spectroscopy for Ultra-high Sensitive Trace Gas Detection. *Opt Express* (2018) 26(24):32103–10. doi:10.1364/OE.26.032103
8. Kim D, Ramanathan V. Solar Radiation Budget and Radiative Forcing Due to Aerosols and Clouds. *J Geophys Res* (2008) 113:D02203. doi:10.1029/2007JD008434
9. Rader F, Traversi R, Severi M, Becagli S, Müller K-J, Nakoudi K, et al. Overview of Aerosol Properties in the European Arctic in Spring 2019 Based on *In Situ* Measurements and Lidar Data. *Atmosphere* (2021) 12:271. doi:10.3390/atmos12020271
10. Liu D, Yang Y, Cheng Z, Huang H, Zhang B, Ling T, et al. Retrieval and Analysis of a Polarized High-Spectral-Resolution Lidar for Profiling Aerosol Optical Properties. *Opt Express* (2013) 21:13084–93. doi:10.1364/OE.21.013084
11. Yorks JE, Selmer PA, Kupchock A, Nowottnick EP, Christian KE, Rusinek D, et al. Aerosol and Cloud Detection Using Machine Learning Algorithms and Space-Based Lidar Data. *Atmosphere* (2021) 12:606. doi:10.3390/atmos12050606
12. Ma Y, Feng W, Qiao S, Zhao Z, Gao S, Wang Y. Hollow-core Anti-resonant Fiber Based Light-Induced Thermoelastic Spectroscopy for Gas Sensing. *Opt Express* (2022) 30(11):18836–44. doi:10.1364/OE.460134
13. Yu S, Liu D, Xu J, Wang Z, Wu D, Shan Y, et al. Optical Properties and Seasonal Distribution of Aerosol Layers Observed by Lidar over Jinhua, Southeast China. *Atmos Environ* (2021) 257:118456. doi:10.1016/j.atmosenv.2021.118456
14. Pisani G, Boselli A, Coltelli M, Leto G, Pica G, Scollo S, et al. Lidar Depolarization Measurement of Fresh Volcanic Ash from Mt. Etna, Italy. *Atmos Environ* (2012) 62:34–40. doi:10.1016/j.atmosenv.2012.08.015
15. Cao X, Wang Z, Tian P, Wang J, Zhang L, Quan X. Statistics of Aerosol Extinction Coefficient Profiles and Optical Depth Using Lidar Measurement over Lanzhou, China since 2005-2008. *J Quantitative Spectrosc Radiative Transfer* (2013) 122:150–4. doi:10.1016/j.jqsrt.2012.09.016
16. Wang Z, Mao J, Li J, Zhao H, Zhou C, Sheng H. Six-channel Multi-Wavelength Polarization Raman Lidar for Aerosol and Water Vapor Profiling. *Appl Opt* (2017) 56:5620–9. doi:10.1364/AO.56.005620
17. Fernald FG. Analysis of Atmospheric Lidar Observations: Some Comments. *Appl Opt* (1984) 23:652–3. doi:10.1364/AO.23.000652
18. Xian J, Sun D, Xu W, Tian C, Tan Q, Han Y, et al. Calibration and Calculation of Polarization Lidar. *Earth Space Sci* (2019) 6:1161–70. doi:10.1029/2019EA000609
19. Liu L, Mishchenko MI. Spectrally Dependent Linear Depolarization and Lidar Ratios for Nonspherical Smoke Aerosols. *J Quantitative Spectrosc Radiative Transfer* (2020) 248:106953. doi:10.1016/j.jqsrt.2020.106953
20. Wu S, Song X, Liu B, Dai G, Liu J, Zhang K, et al. Mobile Multi-Wavelength Polarization Raman Lidar for Water Vapor, Cloud and Aerosol Measurement. *Opt Express* (2015) 23:33870–92. doi:10.1364/OE.23.033870
21. Alvarez JM, Vaughan MA, Hostetler CA, Hunt WH, Winker DM. Calibration Technique for Polarization-Sensitive Lidars. *J Atmos Ocean Tech* (2006) 23: 683–99. doi:10.1175/JTECH1872.1
22. Zhang Y, Yi F, Kong W, Yi Y. Slope Characterization in Combining Analog and Photon Count Data from Atmospheric Lidar Measurements. *Appl Opt* (2014) 53:7312–20. doi:10.1364/AO.53.007312
23. Gao F, Veberič D, Stanič S, Bergant K, Hua D-X. Performance Improvement of Long-Range Scanning Mie Lidar for the Retrieval of Atmospheric Extinction. *J Quantitative Spectrosc Radiative Transfer* (2013) 122:72–8. doi:10.1016/j.jqsrt.2012.11.027
24. Bucholtz A. Rayleigh-scattering Calculations for the Terrestrial Atmosphere. *Appl Opt* (1995) 34:2765–73. doi:10.1364/AO.34.002765
25. Wang L, Stanič S, Eichinger W, Song X, Zavrtanik M. Development of an Automatic Polarization Raman Lidar for Aerosol Monitoring over Complex Terrain. *Sensors* (2019) 19:3186. doi:10.3390/s19143186
26. Chen W-N, Chiang C-W, Nee J-B. Lidar Ratio and Depolarization Ratio for Cirrus Clouds. *Appl Opt* (2002) 41:6470–746. doi:10.1364/AO.41.006470

Conflict of Interest: Authors CC and ZW were employed by Shandong SCICOM Shenguang Technology Co., Ltd.

The remaining authors declare that the research was conducted in the absence of any commercial or financial relationships that could be construed as a potential conflict of interest.

frontiers | Frontiers in Physics

ORIGINAL RESEARCH
published: 24 June 2022
doi: 10.3389/fphy.2022.917688

Fiber-Enhanced Raman Spectroscopy for Trace-Gas Sensing in the High-Concentration Gas Background With an Anti-Resonant Hollow Core Fiber

Guochao Qian[1,2], *Fu Wan*[1,2]*, *Feng Zhou*[1], *Jianxin Wang*[1], *Weiping Kong*[1] and *Weigen Chen*[1,2]

[1]School of Electrical Engineering, Chongqing University, Chongqing, China, [2]State Key Laboratory of Power Transmission Equipment and System Security and New Technology, Chongqing University, Chongqing, China

In this article, with an anti-resonant hollow core fiber (ARHCF), fiber-enhanced Raman spectroscopy (FERS) for trace-gas sensing in a high-concentration gas background is demonstrated for the first time. The performance of the apparatus is verified by detecting trace-gas in the high concentration SF6 and gaseous impurities in the high concentration C_2H_6. With a 1.5 W laser source and 60 s exposure time, the limit of detection (LOD) of gases at tens of ppm levels is achieved, including carbonyl sulfide (COS), carbon tetrafluoride (CF_4), carbon dioxide (CO_2), carbon monoxide (CO), methane (CH_4), acetylene (C_2H_2), ethylene (C_2H_4), propyne (C_3H_4), propylene (C_3H_6), and propane (C_3H_8). Quantification of multi-gas with great accuracy exceeding 94% is also realized. It shows that the FERS can demonstrate the ability of multi-gas sensing with high selectivity, sensitivity, and accuracy.

Keywords: anti-resonant hollow core fiber, fiber-enhanced Raman spectroscopy, trace-gas sensing, SF6, high selectivity

OPEN ACCESS

Edited by:
Yufei Ma,
Harbin Institute of Technology, China

Reviewed by:
Jun Jiang,
Nanjing University of Aeronautics and Astronautics, China
Yingying Wang,
Jinan University, China
Haoxi Cong,
North China Electric Power University, China

***Correspondence:**
Fu Wan
fu.wan@hotmail.com

Specialty section:
This article was submitted to Optics and Photonics, a section of the journal Frontiers in Physics

Received: *11 April 2022*
Accepted: *29 April 2022*
Published: *24 June 2022*

Citation:
Qian G, Wan F, Zhou F, Wang J, Kong W and Chen W (2022) Fiber-Enhanced Raman Spectroscopy for Trace-Gas Sensing in the High-Concentration Gas Background With an Anti-Resonant Hollow Core Fiber. Front. Phys. 10:917688. doi: 10.3389/fphy.2022.917688

INTRODUCTION

Trace-gas sensing in a high-concentration gas background is important for environmental pollution [1], equipment fault diagnosis [2], chemical composition analysis [3], and gaseous energy detection [4]. For example, the natural gases extracted during the recovery and treatment of oilfield-associated gas contain acidic trace-gases such as hydrogen sulfide (H2S) and carbon dioxide (CO_2), which will react with water and cause corrosion of natural gas transportation pipelines [5]. Sulfur hexafluoride [6] (SF6), a preferred insulating and arc-quenching medium in gas insulation equipment, decomposes and produces trace characteristic gases during partial discharge or overheating. By obtaining the type and concentrations of the decomposition gases, the equipment failure can be accurately diagnosed [7]. The content of impurities in the high-purity gas represents the purification of the standard gas [8]. Therefore, accurate monitoring of the types and concentrations of trace gases in a high-concentration gas background is necessary.

In some applications, the concentration of characteristic gas is very low and the composition is complex, which requires a highly sensitive and selective gas analysis method. At present, the existing gas analysis methods are mainly divided into chemical sensor methods [9], gas chromatography (GC) methods [10], and optical methods. The chemical sensor method has high sensitivity, rapid

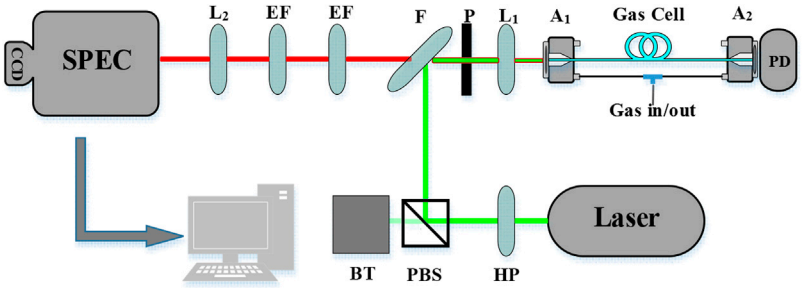

FIGURE 1 | Schematic diagram of the FERS setup. The FERS setup consists of the following components: half-wave plate (HP), polarization beam splitter (PBS), dichroic mirror (F), pinhole (P), achromatic lens (L1, L2), gas cell (A1, A2), photodetector (PD), edge filter (EF), beam trap (BT), spectrometer (SPEC), and personal computer (PC).

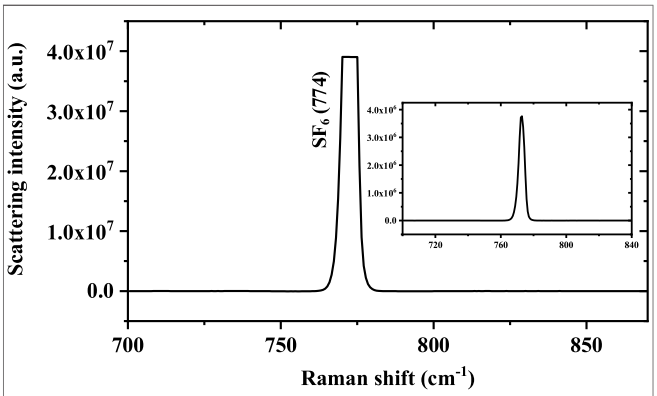

FIGURE 2 | Raman spectrum of 5 bar pure SF6.

response, and small volume, but there exist shortcomings of cross interference, poor long-term stability, and repeatability. Although GC has high sensitivity, it is time- and gas-consuming, and the aging of the chromatographic column is adverse to quantification. Optical methods are mainly based on absorption and scattering effects, such as infrared absorption spectroscopy [11], photoacoustic spectroscopy [12], photothermal spectroscopy [13], and Raman spectroscopy, both of which can provide exceptional sensitivity and selectivity. However, since homonuclear diatoms (O_2 and H_2, etc.) only have a weak electric four-dipole moment [14], the absorption effect is extremely weak, so it is difficult to realize the detection of trace homonuclear diatomic gases [15]. In addition, the absorption spectrum lines are relatively dense, and the absorption spectrum of a high-concentration background gas is likely to overlap with the trace-gas spectrum lines. Therefore, it is difficult to detect trace gases in a high-concentration gas background based on the absorption effect. Moreover, different gases can only produce absorption effects on specific laser wavelengths corresponding to the energy level of each gas, so multiple laser sources may be required when detecting multi-component gases.

Raman spectroscopy is another effective optical method for gas sensing based on scattering effects. When the incident light with frequency ν_0 passes through the gas, the incident laser light will excite gas molecules to generate spherical divergent Raman scattered light with frequency $\nu_0 \pm \nu_R$. Different gases have their own unique ν_R, namely Raman frequency shift, so Raman spectroscopy can detect the multicomponent gases (except for monatomic gases) simultaneously and highly selectively with a single-wavelength laser. It is worth noting that Raman spectroscopy can easily distinguish multi-component gases in a high-concentration gas background, owing to the relatively independent vibration Raman frequency shift with little overlapping. However, due to the extremely low gas Raman scattering cross section [16], the sensitivity is low, which limits its practical application in trace-gas detection [17], such as power transformer fault diagnosis [18].

The sensitivity of Raman spectroscopy can be improved when combined with an optical resonant cavity, namely, cavity-enhanced Raman spectroscopy (CERS) [19]. By locking the laser frequency to the resonant mode of a FP cavity, the laser will be confined and accumulated, resulting in quite a strong laser power buildup due to constructive interference. The sensitivity enhancement of CERS can reach three orders of magnitude. However, the resonant cavity has extremely high requirements for the collimation of the optical path, resulting in insufficient anti-interference ability and usually requiring tens of milliliters of gas volume, which is not suitable for many applications with only little gases.

Another method to enhance the sensitivity of Raman spectroscopy is combined with hollow core fiber or capillary, namely, fiber-enhanced Raman spectroscopy (FERS), which improves the collection efficiency of spherical divergent Raman scattered light to about 360°. It not only requires a small gas volume of microliters but also has a flexible layout. Compared to hollow-core capillary [20] with high-transmission loss [21], hollow-core fiber has lower transmission loss [22]. Therefore, FERS combined with hollow core fiber can achieve higher Raman signal enhancement. The hollow-core photonic crystal fiber (HCPCF) and anti-resonant hollow core fiber (ARHCF) are the most commonly used in FERS. Buric [23] uses FERS with HCPCF to analyze the fuel gases. The detection limit (LOD) of CH4 and C_3H_8 is less than 140 ppm bar with a laser of 100 mW at 514.5 nm and an exposure time of 1 s. Popp

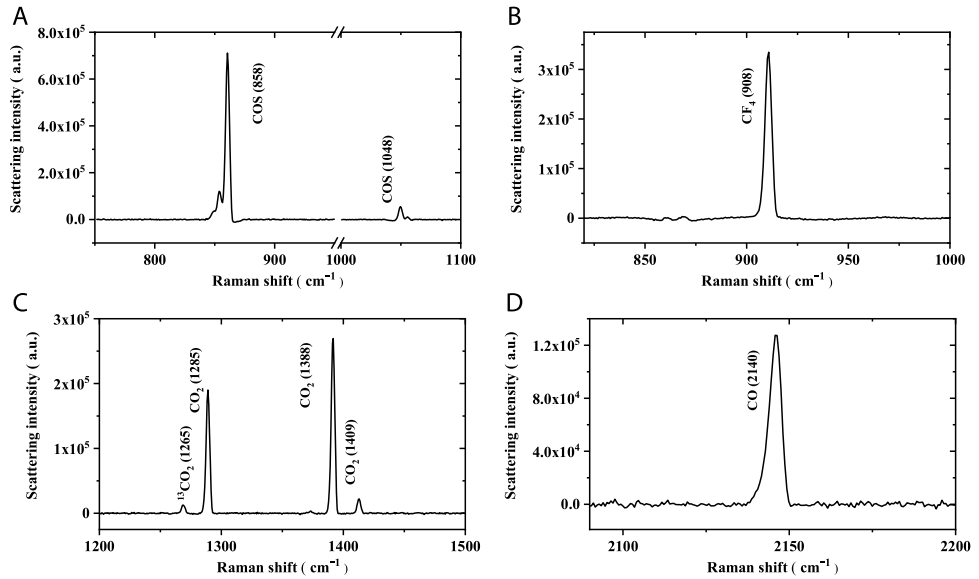

FIGURE 3 | Raman spectrum of 0.05 bar gases, **(A)** COS, **(B)** CF_4, **(C)** CO_2, and **(D)** CO.

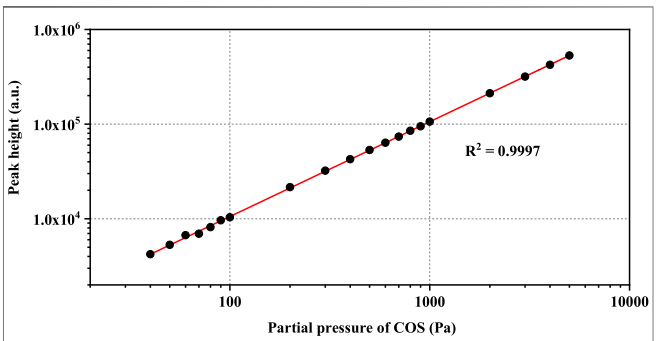

FIGURE 4 | Scattering intensity changes with partial pressure of COS. The R-square value is 0.9997.

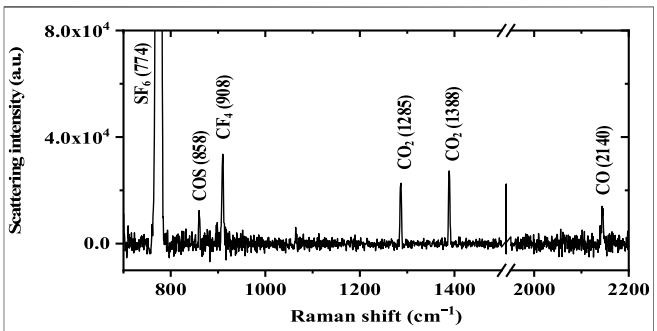

FIGURE 5 | Fiber-enhanced Raman spectrum of trace COS, CF_4, CO_2, and CO in the high-concentration SF_6 background.

[24–26] reported the highly selective and sensitive detection of complex gas mixtures (consisting of H_2, CH_4, N_2, O_2, and CO_2) by FERS with HCPCF. With a laser wavelength of 532 nm, laser power of 1.3 W, and 1 s exposure time, the LOD of N_2, O_2, CO_2, CH_4, and H_2 are 140, 160, 80, 4, and 90 ppm bar, respectively. Compared with the HCPCF, the ARHCF has a larger core diameter and is easier to achieve efficient coupling and has lower transmission loss of about 80 dB/km at 532 nm or 13.8 dB/km at 539 nm, which is more conducive to signal enhancement. In addition, Andreas Knebl [27] first applied the ARHCF in FERS. With a laser wavelength of 532 nm, 1.3 W power, and a 30 s exposure time, the LODs of O_2 and CO_2 are 125 and 25 ppm bar, respectively. Duluo Zuo [28] integrated ARHCF into the Raman system, by collecting scattering radiation in the forward direction and filtering of the background through selection of an appropriate integral region, the LODs of CH_4, C_2H_4, C_2H_2, C_2H_6, H_2, and CO were determined as 1.2, 1.7, 2.6, 2.9, 13.8, and 16.7 ppm bar, respectively, with the input excitation laser power of 200 mW and exposure time of 60 s.

To our best knowledge, fiber-enhanced Raman spectroscopy for trace-gas sensing in a high-concentration gas background has not been reported. Therefore, in this article, we build FERS with ARHCF to realize the detection of multi-component trace gases in a high-concentration gas background. The performance of the apparatus is verified by the detection of decomposition gas in the high-concentration sulfur hexafluoride [29] (SF6) and gaseous impurities in the high-concentration ethane.

EXPERIMENT SETUP

The experimental setup of the FERS with ARHCF in this work is shown in **Figure 1**. A solid Nd: YAG laser-emitting linearly polarized light with a wavelength of 532 nm and a power of 1.5 W is used as a light source. The half-wave plate (HP, Thorlabs

TABLE 1 | Measuring performance of FERS for SF6 depositions in the high-concentration SF6 background.

Component	LOD of calibration gas		Concentration		Relative error (%)
	In pascal	In ppm at 5 bar	Actual (ppm)	Measured (ppm)	
COS	11.6	23.2	100	105.6	5.6
CF_4	24.2	48.5	650	639.8	1.6
CO_2	19.7	39.4	450	437.3	2.8
CO	52.4	104.8	550	542.9	1.3

WPV10L-532) is used to adjust the polarization and power of the laser beam when cooperating with the polarization beam splitter (PBS, Thorlabs CCM1-PBS251). After reflecting by a dichroic mirror (F, Semrock LPD02-532RU-25), the laser beam passes through achromatic lens L1 (Thorlabs AC254-060-A), focuses into the ARHCF, and excites gas molecules in the core of ARHCF to generate spherical divergent Raman scattered light. The Raman scattering light is collected backward from the fiber enter end (A1) by the same lens (L1) and passes through the dichroic mirror (F) and the two long-pass edge filters EF (532 nm Semrock LP03-532RE-25), which are used to filter out laser radiation, Rayleigh scattering signals, and anti-Stokes Raman scattering light. Then, the remaining Stokes Raman scattering light is focused and coupled into the spectrometer (Andor SR500) through the achromatic lens L2 (Thorlabs AC254-075-A) and recorded using the CCD camera (Andor iDus 416). The grating line is 1,200/mm, and the blaze wavelength is 750 nm.

The core diameter of ARHCF is 26 um. The transmission band is 440–1,200 nm with a loss at 532 nm of 80 dB/km, and the fiber length used in this work is 0.5 m. The pinhole (P) is for preliminary spatial filtering, which can adjust the laser spot size and filter the silicon signal of fiber by making full use of the spatial distribution pattern. The two ends of the fiber are fixed on the tapered V-groove fiber holder (Thorlabs HFV002) for better laser beam coupling. The holder is fixed in our self-made gas cells (A1, A2), which contain a pressure sensor to facilitate real-time acquisition of total gas pressure. The power meter (PD, Thorlabs PDA100A-EC) is placed at the output end of the fiber to monitor the laser output power in time.

The specific coupling parameters are measured using the beam quality analyzer (Thorlabs BC207VIS/M). The mode field diameter of the laser at L1 is 2 mm. The calculated mode field diameter of the fiber is 19.5 um according to the Gaussian beam lens transformation principle as in **Eq. 1**: (75% of the core diameter [30])

$$F = \frac{\pi \omega_0 \omega_1}{\lambda}, \tag{1}$$

where F is the focal length of lens, λ is the laser wavelength, ω0 is the mode field diameter of the laser at a certain position, and ω1 is the mode field diameter of the fiber.

In order to achieve NA matching, the focal length of L1 needs to be 57.5 mm, which should be customized and expensive, so a 60-mm-focal length lens is used in this experiment. In order to precisely adjust the relative position of the achromatic lens L1 and the fiber to achieve efficient coupling, L1 is fixed on a manual three-axis micron-positioning stage. After measuring the incident and transmitted laser power through the ARHCF, which is 1.1 and 1.4 W, respectively, the coupling efficiency was calculated as about 85%.

Before loading the gas sample, the gas cells and ARHCF was first evacuated using a vacuum pump. Then, the measured gas was pumped into one of the gas cells (A2) to 5 bar. Finally, FERS of the measured gas can be detected after the internal pressure of the fiber reaches equilibrium.

RESULTS AND DISCUSSION

SF6 is widely applied as the preferred insulating and arc-quenching medium in gas-insulated switchgear (GIS) in power systems. The equipment will inevitably yield defects during preparation, installation, and operation. Over the long-term operation, some SF6 molecules decompose and produce several lower fluorides of sulfur SFX (X = 1, 2. . ..5) such as SF2, SF3, SF4, and SF5 through partial discharge, arc, spark, and overheating caused by insulation defects. In addition, if the solid insulation (organic materials such as epoxy resin) of GIS is damaged by partial discharge, trace carbon-containing gases such as COS, CF4, CO, and CO_2 will be generated. Accurate detection of these trace gases in the SF6 background can diagnose the type and severity of the insulation defects as well as GIS failures. So, in this experiment, we used this FERS apparatus to detect multi-component trace gases (COS, CF_4, CO_2, and CO) in a high-concentration SF6 background. In order to achieve the qualitative and quantitative analysis of the aforementioned multi-component gases, we need to detect reference spectra of a single gas first.

The experimental condition of SF6 is under 5 bar, which is the working pressure of a running GIS. **Figure 2** shows the Raman spectrum of pure SF6 under a low laser power of 100 mW. The peak position of the Raman spectrum is 774 cm^{-1}, which corresponds to the v1 transition vibration mode of the SF6 molecule and proves that the saturated Raman peak is an independent peak.

Figure 3 shows the Raman spectra of COS, CF_4, CO, and CO_2. **Figure 3A** shows the Raman spectrum of 0.05 bar COS (10,000 ppm of COS in Ar at 5 bar), and the exposure time is 60 s; the v1 transition at 858 cm^{-1} and 2v2 transition at 1,048 cm^{-1} are achieved, corresponding to the stretching vibration of C-S and bend vibration. According to three times the signal-to-noise ratio, the LOD is 11.6 Pa (858 cm^{-1}), corresponding to 23.2 ppm at 5 bar. **Figure 3B** shows the Raman spectrum of 0.05 bar CF_4 (10,000 ppm of CF_4 in Ar at

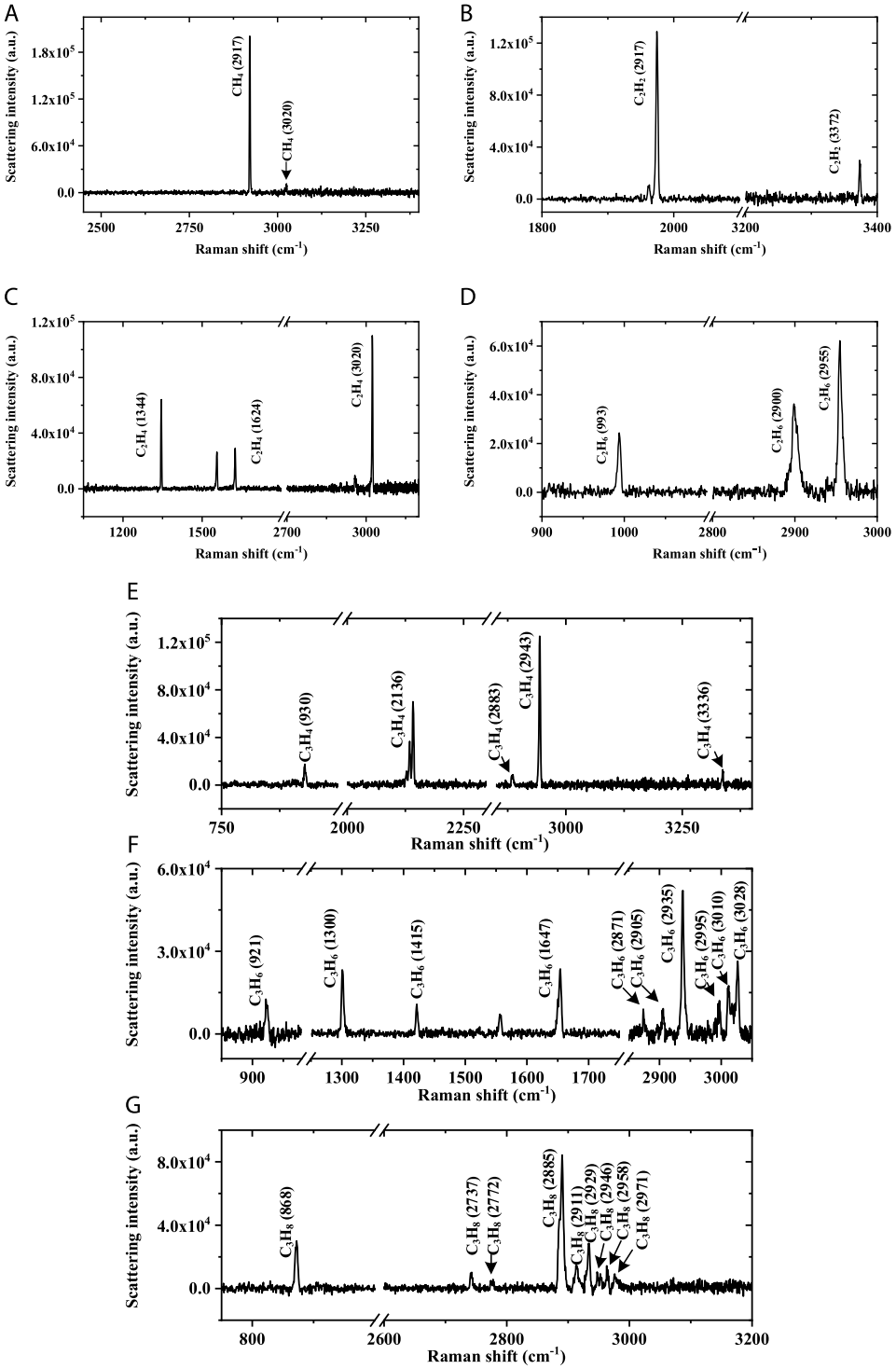

FIGURE 6 | Raman spectra of 250 Pa of **(A)** CH_4, **(B)** C_2H_2, **(C)** C_2H_4, **(D)** C_2H_6, **(E)** C_3H_4, **(F)** C_3H_6, and **(G)** C_3H_8.

5 bar), and the ν1 transition at 908 cm^{-1} is achieved, corresponding to the stretching vibration of C-F; the LOD is 24.2 Pa, equivalent to 48.5 ppm at 5 bar. **Figure 3C** shows the Raman spectrum of 0.05 bar CO_2 (10,000 ppm of CO_2 in Ar at 5 bar). A Fermi resonance pair (ν1/2ν2) is observed at 1,285 cm^{-1} (ν−) and 1,388 cm^{-1} (ν+), the hot band is observed at 1,409 cm^{-1}, and $13CO_2$ can be also observed at 1,265 cm^{-1}. A LOD of 0.54 Pa for CO_2 (1,388 cm^{-1}) is achieved, equivalent to 39.4 ppm at 5 bar **Figure 3D** shows the Raman spectrum of 0.05 bar CO (10,000 ppm of CO in Ar at 5 bar); the Q1 vibration of CO is

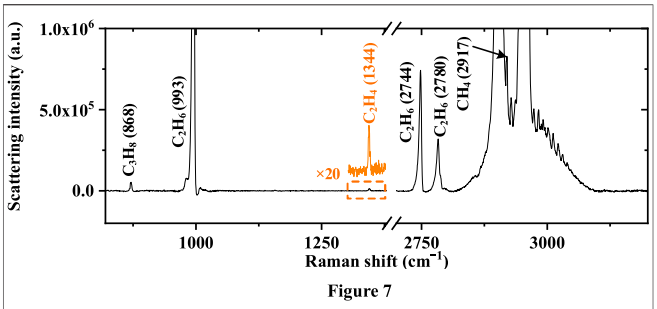

FIGURE 7 | Fiber-enhanced Raman spectrum of impurities in the high-concentration C_2H_6 background.

observed at 2,142 cm^{-1}, and the LOD is 52.4 Pa, corresponding to 104.8 ppm at 5 bar.

For online quantification of the concentrations of each gas in the high-concentration SF6 background, the Raman spectra of each gas should be taken at a known value of laser power, total pressure, exposure time, fiber length, and temperature. The test gas concentration (ratio of partial pressure to total pressure) will be acquired based on the peak intensity ratio of the calibration gas. We take COS, for example, as shown in **Figure 4**. This quantitative calibration is very robust owing to the linearity between partial pressure and Raman intensity, with an R-square value of 0.9997. The other gases have almost the same linear relationship.

Figure 5 shows the Raman spectra of trace multi-gas of COS, CF_4, CO_2, and CO in the high-concentration SF6 background (the concentration of each gas is COS: 100 ppm, CF_4: 650 ppm, CO_2: 450 ppm, and CO: 550 ppm, and the rest is SF6, the total pressure is 5 bar, and the exposure time is 60 s). Each peak can be identified for different gases, proving that Raman spectroscopy can be used to detect decomposition gas in the high concentration of SF6. Based on the built-up quantification curve of FERS, the calculated concentrations of COS, CF_4, CO_2, and CO are 105.6, 639.8, 437.3, and 542.9 ppm at 5 bar, respectively, which is basically consistent with the actual value. The measuring performance of FERS for SF6 depositions in the high-concentration SF6 background is summarized in **Table 1**.

Ethane of high-purity is an important raw material for the organic synthesis industry, but it often contains alkane impurities, such as methane, ethylene, acetylene, propane, propylene, and propyne. In this article, the FERS apparatus is also used to detect impurities in high-concentration ethane. Similarly, in order to be able to qualitatively and quantitatively analyze impurity gases, the detection of the aforementioned reference spectra of single gases, such as methane, ethylene, acetylene, propane, propylene, and propyne (from Chongqing Lihong company), is carried out first.

Figure 6 shows the Raman spectra of 250 Pa methane, ethane, ethylene, acetylene, propyne, propylene, and propane (500 ppm each gas in Ar at 5 bar). The Raman spectrum of CH4 is shown in **Figure 6** (a), which mainly contains ν_1 transition at 2,917 cm^{-1} and ν_3 transition at 3,020 cm^{-1}, and a LOD of 4.41 Pa for CH_4 (2,917 cm^{-1}) is achieved. The Raman spectrum of C_2H_2 is shown in **Figure 6B**, including ν1 transition at 3,372 cm^{-1} and the ν2 transition at 1972 cm^{-1}, and a LOD of 6.18 Pa for C_2H_2 (1972 cm^{-1}) is achieved. The Raman spectrum of C_2H_4 is shown in **Figure 6C**, which includes the δπs transition at 1,344 cm^{-1}, the ν2πs transition at 1,624 cm^{-1}, the 2δπa transition at 2,880 cm^{-1}, and the νπs transition at 3,020 cm^{-1}, and a LOD of 8.47 Pa for C_2H_4 (1,344 cm^{-1}) is achieved. The Raman spectrum of C_2H_6 is shown in **Figure 6D**, including the ν5 transition at 2,997 cm^{-1}, the ν3 transition at 2,900 cm^{-1}, and the 2ν10 transition at 2,955 cm^{-1}, and a LOD of 18.02 Pa for C_2H_6 (2955 cm^{-1}) is achieved. The Raman spectrum of C_3H_4 is shown in **Figure 6E**, including the ν1 transition at 3,336 cm^{-1}, the ν2 transition at 2,943 cm^{-1}, the 2ν7 transition at 2,883 cm^{-1}, the ν3 transition at 2,136 cm^{-1}, and the ν5 transition at 930 cm^{-1}, and a LOD of 7.79 Pa for C_3H_4 (2,943 cm^{-1}) is achieved. The Raman spectrum of C_3H_6 is shown in **Figure 6F**, including the 4ν14 transition at 3028 cm^{-1}, the 2ν2 transition at 3,010 cm^{-1}, the ν5 transition at 2,997 cm^{-1}, the ν1 transition at 2,937 cm^{-1}, the 2ν14 + ν6 transition at 2,905 cm^{-1}, the 2ν6 transition at 2,871 cm^{-1}, the ν6 transition at 1,415 cm^{-1}, the ν13 transition at 1,300 cm^{-1}, and the ν8 transition at 921 cm^{-1}, and a LOD of 36.1 Pa for C_3H_6 (2,935 cm^{-1}) is achieved. The Raman spectrum of C_3H_8 is shown in **Figure 6G**, including the ν1 transition at 2,976 cm^{-1}, the ν2 transition at 2,958 cm^{-1}, the 2ν4 transition at 2,946 cm^{-1}, the 2ν5 transition at 2,929 cm^{-1}, the 2ν11 transition at 2911 cm^{-1}, the ν3 transition at 2,885 cm^{-1}, the overtone 2ν6 transition at 2772 cm^{-1}, the ν5 + ν12 transition at 2,737 cm^{-1}, and the ν8 transition at 868 cm^{-1}, and a LOD of 16.64 Pa for C_3H_8 (2885 cm^{-1}) is achieved.

The simulation detection of methane, ethylene, acetylene, propane, propylene, and propyne was also achieved as shown in **Figure 7**, which proves that FERS apparatus can be used to detect impurities in high-concentration ethane. The concentration of gaseous impurities in C_2H_6 is summarized in **Table 2**.

TABLE 2 | Quantification of gaseous impurities in C_2H_6 based on FERS.

Component	Measured concentration (ppm)	LOD	
		In pascal	In ppm at 5 bar
CH_4	594.4	4.4	8.8
C_2H_2	<12.3	6.2	12.3
C_2H_4	104.2	8.4	16.9
C_3H_4	<15.6	7.8	15.6
C_3H_6	<72.2	36.1	72.2
C_3H_8	922.7	16.6	33.2

Figure 7 shows the Raman spectrum of alkane impurities in a high-concentration C_2H_6 background. The total pressure is 5 bar, and the exposure time is 60 s.

CONCLUSION

In this article, we demonstrate the utility of FERS with ARHCF as a unique analysis tool for trace-gas sensing in the high-concentration gas background of SF6 and C_2H_6. For NA matching, the 60-mm-focal length lens is employed in FERS. To obtain qualitative and quantitative analysis, the Raman spectra of COS, CF4, CO_2, CO, CH4, $C2H_2$, C_2H_4, C_2H_6, C_3H_4, C_3H_6, and C_3H_8 at standard concentration are acquired, respectively. With 60 s exposure time and 5 bar total pressure, the LOD for COS, CF4, CO_2, CO, CH4, $C2H_2$, C_2H_4, C_3H_4, C_3H_6, and C_3H_8 can be down to 23.2, 48.5, 39.4, 104.8, 8.8, 12.3, 16.9, 72.2, 15.6, and 33.3 ppm, respectively. It has been proved that the gas Raman scattering intensity has a good linear relationship with gas concentration. Quantification of multi-gas with great accuracy exceeding 94% is also realized. In order to further improve the performance of the system, in the future, we will improve the coupling efficiency of the ARHCF and reduce the signal noise to improve the signal-to-noise ratio of the system for practical multi-gas sensing.

DATA AVAILABILITY STATEMENT

The original contributions presented in the study are included in the article/Supplementary Material; further inquiries can be directed to the corresponding author.

AUTHOR CONTRIBUTIONS

GQ gets the first authorship. FW gets the senior authorship. FZ gets the last authorship. JW contributed equally and gets the last authorship. WK contributed equally and gets the last authorship. WC contributed equally and gets the last authorship.

FUNDING

This work was financially supported by the Project Fund for the National Natural Science Foundation of China (51977017), supported by the Chongqing Natural Science Foundation (cstc2021jcyj-msxmX0617), and supported by the National Engineering Laboratory for Ultra High Voltage Engineering Technology ((Kunming, Guangzhou), No. NEL202009).

REFERENCES

1. Davidson EA, Trumbore SE, Amundson R. Soil Warming and Organic Carbon Content. *Nature* (2000) 408(6814):789–90. doi:10.1038/35048672
2. Wang P, Chen W, Wang J, Tang J, Shi Y, Wan F. Multigas Analysis by Cavity-Enhanced Raman Spectroscopy for Power Transformer Diagnosis. *Anal Chem* (2019) 92(8):5969–77. doi:10.1021/acs.analchem.0c00179
3. Loubar K, Rahmouni C, Le Corre O, Tazerout M. A Combustionless Determination Method for Combustion Properties of Natural Gases. *Fuel* (2007) 86(16):2535–44. doi:10.1016/j.fuel.2007.02.024
4. Sieburg A, Knebl A, Jacob JM. Characterization of Fuel Gases with Fiber-Enhanced Raman Spectroscopy. *Anal Bioanal Chem* (2019) 411:7399–408. doi:10.1007/s00216-019-02145-x
5. Chen JB, Bo DC, Gao M. Problems in Desulfurization and Purification Process for Oilfield Associated Gas and Concerning Solutions. *Mod Chem Industry* (2018) 38(6):167–72. doi:10.16606/j.cnki.issn0253-4320.2018.06.038
6. Shen CC, Cai XL, Sang YB. Investigation of Multispectral SF6 Stimulated Raman Scattering Laser. *Chin Opt Lett* (2020) 18(5):051402. doi:10.1364/COL.18.05140210.3788/col202018.051402
7. Zhang X, Zhang Y, Tang J, Cui Z, Li Y, Zhou H, et al. Optical Technology for Detecting the Decomposition Products of SF6: a Review. *Opt Eng* (2018) 57(11):110901. doi:10.1117/1.OE.57.11.110901
8. Zhang W, Chen L, Xiong D. The Determination of the Impurities in High-Purity Methane by Plasma Chromatography. *Low Temperature and Specialty Gases* (2018) 36(04):31–6.
9. Zhang X, Gui Y, Dong X. Preparation and Application of TiO2 Nanotube Array Gas Sensor for SF6-Insulated Equipment Detection: a Review. *Nanoscale Res Lett* (2016) 11(1):1–13. doi:10.1186/s11671-016-1516-4
10. Olthoff JK, Van Brunt RJ, Herron JT. Detection of Trace Disulfur Decafluoride in Sulfur Hexafluoride by Gas Chromatography/mass Spectrometry. *Anal Chem* (1991) 63(7):726–32. doi:10.1021/ac00007a015
11. Cui RY, Dong L, Wu HP. Highly Sensitive and Selective CO Sensor Using a 2.33 μm Diode Laser and Wavelength Modulation Spectroscopy. *Opt Express* (2018) 26:24318–28. doi:10.1364/OE.26.024318
12. Lang ZT, Qiao SD, Ma YF. Acoustic Microresonator Based In-Plane Quartz-Enhanced Photoacoustic Spectroscopy with a Line Interaction Mode. *Opt Lett* (2022) 47(6):1295–8. doi:10.1364/OL.452085
13. Liu XN, Ma YF. Sensitive Carbon Monoxide Detection Based on Light-Induced Thermoelastic Spectroscopy with a Fiber-Coupled Multipass Cell. *Chin Opt Lett* (2022) 20(3):031201. doi:10.3788/COL202220.031201
14. Herzberg G. Quadrupole Rotation-Vibration Spectrum of the Hydrogen Molecule. *Nat* (1949) 163(4135):170. doi:10.1038/163170a0
15. Haken H, Wolf HC. *Molecular Physics and Elements of Quantum Chemistry: Introduction to Experiments and Theory*. 2nd ed. Berlin: Springer Science & Business Media (2004). p. 220.
16. Fenner WR, Hyatt HA, Kellam JM. Raman Cross Section of Some Simple Gases. *J Opt Soc A* (1973) 63(1):73–7. doi:10.1364/JOSA.63.000073
17. Bao HH, Jin W. Tuning of Group Delay with Stimulated Raman Scattering-Induced Dispersion in Gas-Filled Optical Fiber. *Chin Opt Lett* (2020) 18(6):060601. doi:10.3788/COL202018.060601
18. Singh S, Bandyopadhyay MN. Dissolved Gas Analysis Technique for Incipient Fault Diagnosis in Power Transformers: A Bibliographic Survey. *IEEE Electr Insul Mag* (2010) 26(6):41–6. doi:10.1109/MEI.2010.5599978
19. Wang PY, Chen WG, Wan F. Cavity-enhanced Raman Spectroscopy with Optical Feedback Frequency-Locking for Gas Sensing. *Opt Express* (2019) 27:33311–24. doi:10.1364/OE.27.033312
20. Rupp S, Off A, Seitz-Moskaliuk H. Improving the Detection Limit in a Capillary Raman System for *In Situ* Gas Analysis by Means of Fluorescence Reduction. *Sensors* (2015) 15:23110–25. doi:10.3390/s150923110
21. Knebl A, Yan D, Popp J. Fiber Enhanced Raman Gas Spectroscopy. *Trac-trend Anal Chem* (2018) 103:230–8. doi:10.1016/j.trac.2017.12.001
22. Gao S, Wang Y, Ding W. Conquering the Rayleigh Scattering Limit of Silica Glass Fiber at Visible Wavelengths with a Hollow-Core Fiber Approach. *Laser Photon Rev* (2020) 14:1900241. doi:10.1002/lpor.201900241
23. Buric MP, Chen KP, Falk J. Improved Sensitivity Gas Detection by Spontaneous Raman Scattering. *Appl Opt* (2009) 48(22):4424–9. doi:10.1364/AO.48.004424
24. Hanf S, Keiner R, Yan D. Fiber-Enhanced Raman Multigas Spectroscopy: A Versatile Tool for Environmental Gas Sensing and Breath Analysis. *Anal Chem* (2014) 86(11):5278–85. doi:10.1021/ac404162w
25. Hanf S, Bögözi T, Keiner R. Fast and Highly Sensitive Fiber-Enhanced Raman Spectroscopic Monitoring of Molecular H_2 and CH_4 for Point-of-Care

Diagnosis of Malabsorption Disorders in Exhaled Human Breath. *Anal Chem* (2014) 87(2):982–8. doi:10.1021/ac503450y
26. Yan D, Popp J, Frosch T. Analysis of Fiber-Enhanced Raman Gas Sensing Based on Raman Chemical Imaging. *Anal Chem* (2017) 89(22):12269–75. doi:10.1021/acs.analchem.7b03209
27. Knebl A, Domes R, Yan D. Fiber-Enhanced Raman Gas Spectroscopy for ^{18}O–^{13}c-Labeling Experiments. *Anal Chem* (2019) 91(12):7562–9. doi:10.1021/acs.analchem.8b05684
28. Bai Y, Xiong DS, Yao ZY. Analysis of CH_4, C_2H_6, C_2H_4, C_2H_2, H_2, CO, and H_2S by Forward Raman Scattering with a Hollow-Core Anti-resonant Fiber. *J Raman Spectrosc* (2022). doi:10.1002/jrs.6320
29. Tang J, Zeng F, Pan J. Correlation Analysis between Formation Process of SF6 Decomposed Components and Partial Discharge Qualities. *IEEE Trans Dielect Elect Insul* (2013) 20(3):864–75. doi:10.1109/TDEI.2013.6518956
30. Yao C, Gao SF, Wang YY. Silica Hollow-Core Negative Curvature Fibers Enable Ultrasensitive Mid-infrared Absorption Spectroscopy. *J Lightwave Technol* (2020) 38(7):2067–72. doi:10.1109/jlt.2019.2960804

Conflict of Interest: The authors declare that the research was conducted in the absence of any commercial or financial relationships that could be construed as a potential conflict of interest.

Publisher's Note: All claims expressed in this article are solely those of the authors and do not necessarily represent those of their affiliated organizations, or those of the publisher, the editors, and the reviewers. Any product that may be evaluated in this article, or claim that may be made by its manufacturer, is not guaranteed or endorsed by the publisher.

frontiers | Frontiers in Physics

ORIGINAL RESEARCH
published: 27 June 2022
doi: 10.3389/fphy.2022.943744

Te Film as a Saturable Absorber for the Mid-Infrared Er^{3+}-Doped ZBLAN Fiber Laser

Min Zhang, Liu Kang, Zhijian Ma, Peiguang Yan and Shaodong Hou*

Key Laboratory of Optoelectronic Devices and Systems of Ministry of Education and Guangdong Province, College of Physics and Optoelectronic Engineering, Shenzhen University, Shenzhen, China

We demonstrate a Q-switched Er^{3+}-doped ZBLAN fiber laser at 2.8 μm mid-infrared (mid-IR) region achieved by adopting Te as the saturable absorber mirror (SAM). The modulation depth and saturation intensity of the Te-SAM were measured to be ~7.2% and 10.81 MW/cm^2, respectively. Stable Q-switched laser pulses with the maximum pulse energy of 3.05 μJ and the minimum pulse width of 0.457 μs at the launched pump power of 4.51 W were obtained. Maximum average output power of 357 mW with repetition rate of 116.98 kHz were achieved. The signal-to-noise ratio (SNR) is 52 dB, which is higher than that of most 2.8 μm mid-infrared Q-switched fiber lasers reported so far. To the best of our knowledge, this is the first demonstration from a Q-switched fiber laser at 2.8 μm based on a Te-SAM.

Keywords: Q-switched, Er^{3+}-doped, ZBLAN fiber, mid-infrared, saturable absorber mirror

OPEN ACCESS

Edited by:
Yufei Ma,
Harbin Institute of Technology, China

Reviewed by:
Xiaohui Li,
Shaanxi Normal University, China
Quandong Huang,
Guangdong University of Technology, China

****Correspondence:***
Min Zhang
zhangmin@szu.edu.cn

Specialty section:
This article was submitted to Optics and Photonics, a section of the journal Frontiers in Physics

Received: *14 May 2022*
Accepted: *06 June 2022*
Published: *27 June 2022*

Citation:
Zhang M, Kang L, Ma Z, Yan P and Hou S (2022) Te Film as a Saturable Absorber for the Mid-Infrared Er^{3+}-Doped ZBLAN Fiber Laser. Front. Phys. 10:943744. doi: 10.3389/fphy.2022.943744

1 INTRODUCTION

In recent years, mid-infrared lasers have received enormous attentions owing to their substantial applications in gas detection, remote sensing, spectroscopy, and biomedical surgery [1–6]. In contrast to continuous-wave ones, mid-IR Q-switched fiber lasers feature the distinct advantages of high reliability, outstanding beam quality, excellent surface-to-volume ratio, and great efficiency, which promote their practical applications [7]. Up to present, semiconductor saturable absorption mirrors (SESAMs), Fe^{2+}:ZnSe crystals, black phosphorus (BP), graphene and topological insulators (Tls) have been widely applied as saturable absorbers (SAs) in mid-IR passively Q-switched fluoride fiber lasers at 2.8 μm [8–21]. SESAMs have controlled modulation depth but the limited bandwidths make them not suitable for broadband pulsed lasers. Fe^{2+}:ZnSe crystals exhibit a large saturable absorption cross section and high damage threshold (~2 J/cm^2). However, Fe^{2+}:ZnSe crystals usually have the characteristics of complex preparation process, relatively expensive cost and narrow absorption band. BP exhibits a large modulation depth but it is easy to oxidize in the ambient air. Despite graphene is characterized by zero bandgap, the modulation depth of single-layer graphene is only about 2.3% [22–28].

In this letter, we report, as far as we know, a 2.8 μm mid-IR Er^{3+}-doped ZBLAN Q-switched fiber laser using Te saturable absorber mirror (SAM) for the first time. The obtained maximum output power and pulse energy are 357 mW and 3.05 μJ, respectively. The results facilitate the application range of Te-SAM based Q-Switched fiber laser as well as affirm that Te is expected to be an effective SAM of mid infrared fiber laser.

2 PREPARATION AND CHARACTERIZATION OF TE SATURABLE ABSORBER MIRROR

In our experiment, Te-SAM were prepared by a common magnetron-sputtering deposition (MSD) method. First of all, Te target and gold mirror were simultaneously placed in a magnetron sputtering

chamber, the vacuum pressure of the chamber was pulled to about 10^{-3} Pascal. Then, the stimulated ionized Argon ions rapidly bombarded the Te target. Thus, the Te atoms was slowly deposited on the gold mirror. An uniformly arranged tellurium film could be obtained on the surface of the gold mirror after deposition, the coating time was set to 1 min. The Raman shift spectra were measured by a Raman spectrometer (LabRAM HR Evolution, HORIBA Scientific, 514 nm emission) with an excitation wavelength of 514 nm. **Figure 1A** presented the surface of Te film, measured by a scanning electron microscope with a dense and well-distributed shape. The cross-section image of Te SAM with cold field emission scanning electron microscope was displayed in **Figure 1B**, where the thickness of the Te film was approximately measured to be 40.7 nm. The thickness of the film was measured by the atomic force microscope (AFM) in **Figures 1A,C** highly uniform surface can be observed. As shown in **Figure 1D**, the Raman spectra of Te film showed two obvious peaks located at 122 cm^{-1} and 140 cm^{-1}, consistenting with the peaks reported in previous literature [29, 30], implying that the thin film used in the experiment has high purity. The nonlinear absorption of Te-coated fiber was studied by using a 2.8 μm ultrafast light source (pulse width: 350 fs, repetition rate: 68 MHz) built by our laboratory, and the experimental results were depcited in **Figure 2A**. The data conformed to the following equation:

$$T(I) = 1 - \Delta T \cdot \exp(-I/I_{sat}) - T_{ns}$$

Where $T(I)$ is the power-dependent transmission, I is the incident intensity, ΔT is the modulation depth, T_{ns} is the non-saturable loss, and I_{sat} is the saturation peak intensity. The modulation depth ΔT, saturation peak intensity I_{sat} and non-saturable loss T_{ns} were ~7.2%, ~10.81 MW/cm^2, ~76.1% respectively. The lower modulation depth can be improved by changing the thickness of Te film. To determine the composition of the magnetron deposition film, X-ray photoelectron spectroscopy (XPS) measurements (Thermo Fisher Scientific, K-Alpha+) were performed, and the data obtained were shown in **Figures 2B,C**, all calibrated with a C1s peak of 284.8 eV. The fully binding energy spectroscopic scan shows a low energy resolution, and all peaks were related to the expected elements except for the weak C1s peak caused by air pollution. **Figure 2B** shows the high resolution XPS spectra of the characteristic peaks of the Te sample for determining chemical states and elemental bonds. $Te3d_{3/2}$ and $Te3d_{5/2}$ peaks were found at 583.45 and 573.14 eV, which closely matched the chemical state of Te.

3 EXPERIMENTAL SETUP

Figure 3 depicts the schematic diagram of the passively Q-switched Er^{3+}-doped ZBLAN fiber laser. The pump was provided by a commercial 976 nm fiber coupled semiconductor laser (MChlight, Shenzhen) which can achieve higher pump efficiency with a maximum output power of 9 W, a core/cladding diameter of 105/125 μm and a numerical aperture of 0.22 NA. Two uncoated CaF_2 plano-convex lenses (L1 = 40 mm, T = 98.8% at 976 nm, T = 99.5% at 2.8 μm, L2 = 40 mm, T = 99.5% at 2.8 μm) were used to collimate and focus the pump beam into a 3 m long double-cladding 7 mol%-doped Er:ZBLAN fiber with a core diameter of 15 μm, 1st cladding diameter of 240*260 μm, 2nd cladding

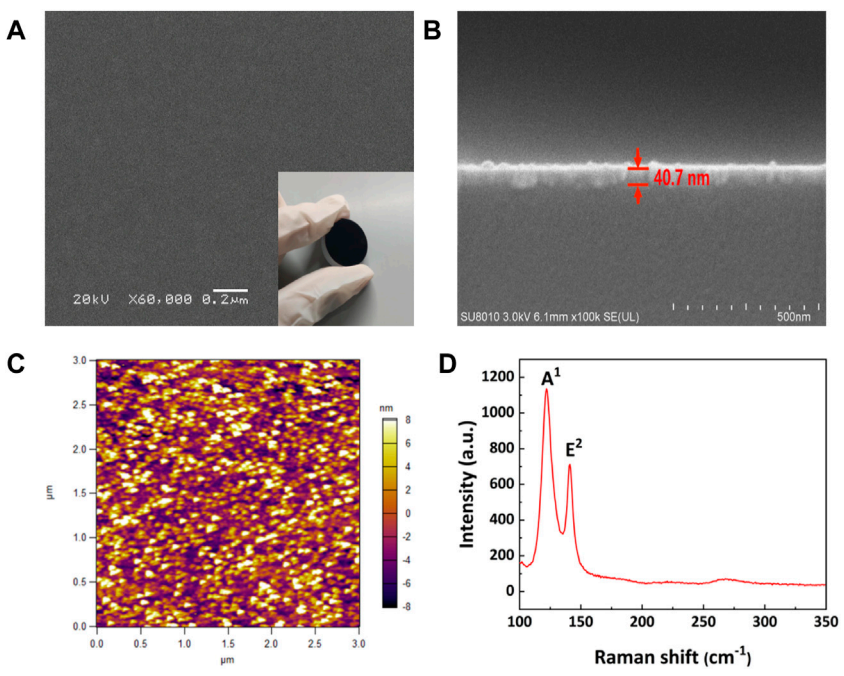

FIGURE 1 | (A) SEM image for surface topography and **(B)** the lateral surface of the Te-SAM. **(C)** AFM image. **(D)** Raman shift spectrum.

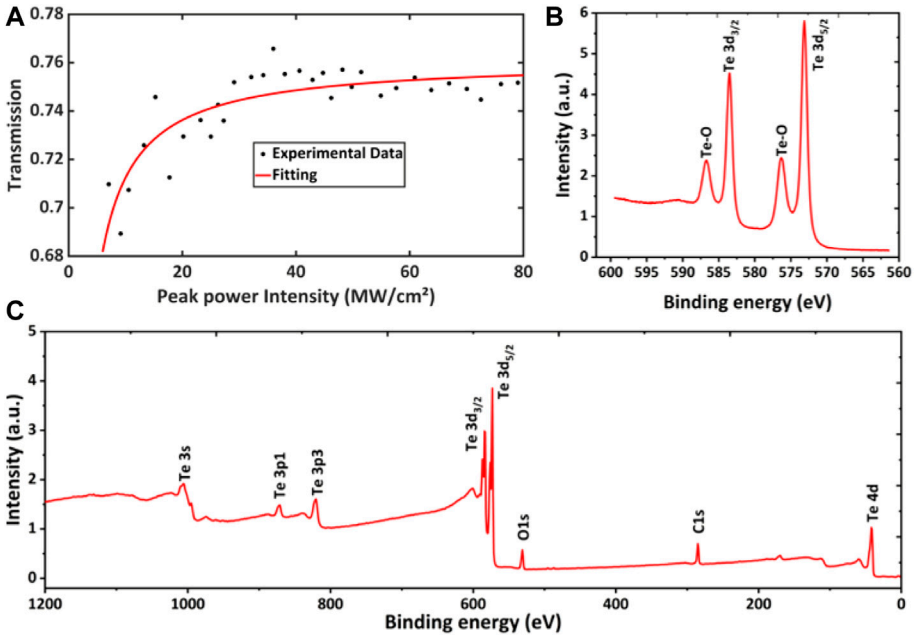

FIGURE 2 | (A) Nonlinear saturable absorption curve of the Te-SAM. **(B)** XPS core level spectrum of Te 3d. **(C)** Full XPS spectrum of fabricated Te film.

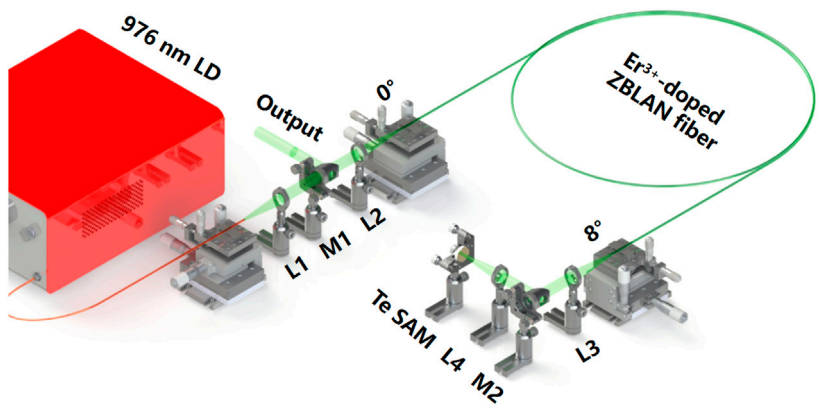

FIGURE 3 | The schematic of the Q-switched Er:ZBLAN fiber laser.

diameter of 290 μm, and a numerical aperture (NA) of 0.12. Between the two CaF_2 plano-convex lenses, a dichroic mirror M1 with high reflectance of 94% at around 2.8 μm and high transmittance of 97.6% at 976 nm was placed at a 45° angle of incidence surface to couple out the 2.8 μm laser. The front end of the fiber was angle-cleaved at 0° to provide ~4% Fresnel reflection, while the other fiber end was cleaved at angle of 8° to suppress parasitic oscillation. Two uncoated CaF_2 plano-convex lenses (L3 = 40 mm, T = 98.8% at 976 nm, T = 99.5% at 2.8 μm, L4 = 40 mm, T = 99.5% at 2.8 μm) were used to collimate and focus the 2.8 μm laser beam from the angle-cleaved fiber end onto the Te-SAM. Then another dichroic mirror M2 (T > 95% @ 976 nm & R > 99% @ 2.8 μm) was placed at 45° to couple out the surplus 976 nm pump light. The average output power of the cavity was acquired by a power meter (Laserpoint) together with an IR bandpass filter (Thorlabs, FB2750-500) placed before the detector which was used to remove the background light. An detector with a response time of ~2 ns was connected to a 4-GHz bandwidth digital oscilloscope (ROHDE & SCHWARZ, RTO2044) to measured the pulse temporal trains. The optical spectrum was monitored by a optical spectrum analyzer (YOKOGAWA, AQ6376) with a minimum scanning resolution of 0.1 nm. A RF spectrum analyzer (ROHDE & SCHWARZ, FSWP) with a scanning range of 1 MHz–8 GHz was utilized to analyze the radio frequency (RF) spectrum.

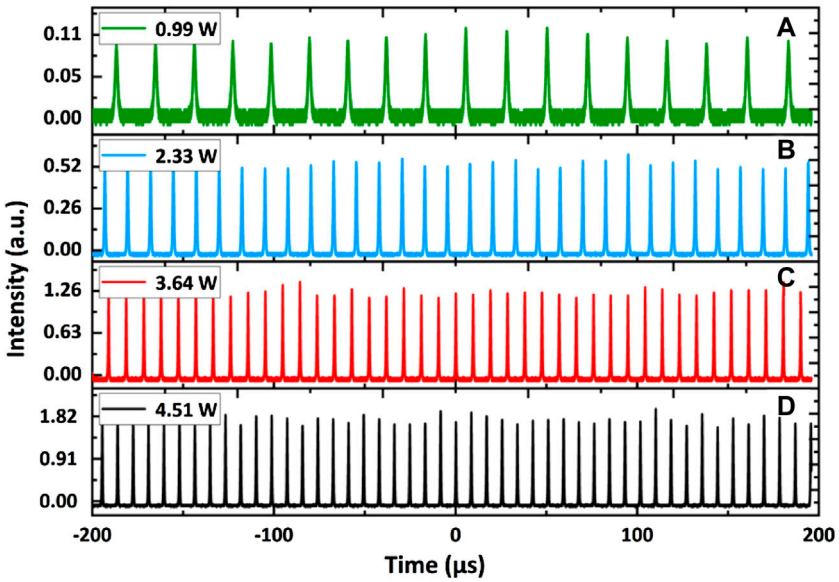

FIGURE 4 | Typical Q-switched pulse trains at the launched pump powers of **(A)** 0.99 W, **(B)** 2.33 W, **(C)** 3.64 W and **(D)** 4.51 W, respectively.

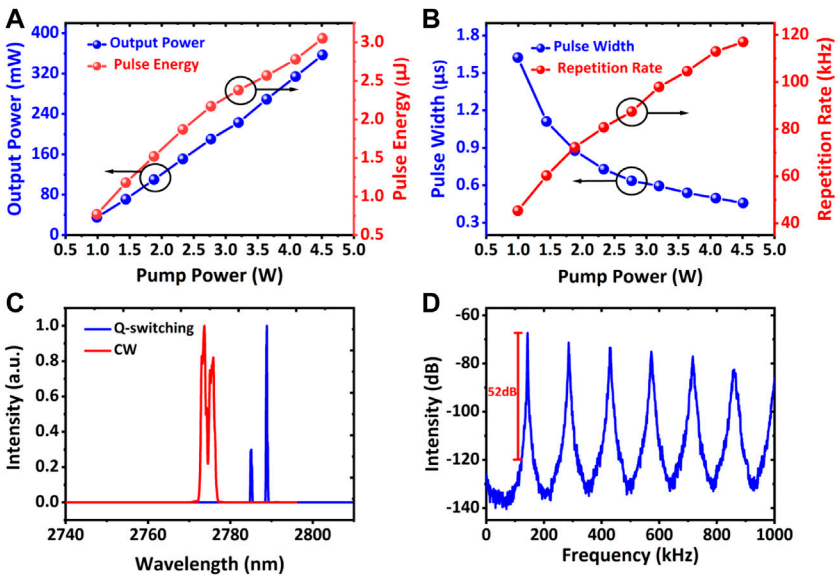

FIGURE 5 | (A) Average output power and pulse energy. **(B)** Repetition rate and pulse width of the Q-switched Er:ZBLAN fiber laser as a function of the pump power. **(C)** Spectrum of Q-switching and CW operation. **(D)** Fundamental repetition rate with RBW of 100 Hz.

4 EXPERIMENTAL RESULTS AND DISCUSSION

Figure 4 presents the Q-switched pulse sequences and pulses profiles under different pump powers. **Figure 5A** displays the measured output power and calculated pulse energy of Q-switched pulses as a function of the launched pump power. It can be achieved in the broad pump power range of 0.99–4.51 W with an output power of 35–357 mW at a slope efficiency of 9.2% and a pulse energy of 0.77–3.05 μJ. **Figure 5B** shows the pulse repetition rate and pulse width as a function of the launched pump power. As expected, with the increase of the launched pump power, the repetition rate increased and the pulse width decreased. When the pump power increased within the above range, the pulse repetition rate increasd from 45.34 to 116.98 kHz, and the pulse width decreased from 1.624 to 0.457 μs. In the system, CW began to oscillate when the launched pump power was about 0.87 W. A self-starting Q-switching train was observed

with a pulse width of 1.62 μs and a repetition rate of 45.34 kHz when the launched pump power exceeded the threshold of 0.99 W, as shown in **Figure 4A** and **Figure 5B**. As presented in **Figure 4B** and **Figure 5B**, stable Q-switching can be maintained by slightly increasing the launched pump power to 2.33 W and the pulse width was 0.73 μs at a repetition rate of 80.75 kHz. When the launched pump power continued to increase, the Q-switching operation can be maintained. Typical Q-switched pulse waveforms at launched pump power of 3.64 and 4.51 W are shown in **Figures 4C,D**. Their pulse width were 0.54 and 0.457 μs, respectively. At the same time, the corresponding repetition rates were 104.63 and 116.98 kHz, respectively. The optical and RF spectrum were measured at the maximum pump power of 4.51 W. **Figure 5C** depicts the pulse spectrum of the laser under continuous-wave (CW) centered at 2,775 nm and Q-switching operation centered at 2,782.35 nm, the recording range is 70 nm (from 2,740 to 2,810 nm). The signal-to-noise ratio (SNR) of the RF spectrum is measured to be 52 dB at a resolution bandwidth (RBW) of 100 Hz in a 1000-kHz scanning span, indicating a stable Q-switching regime, as shown in **Figure 5D**. When the launched pump power was higher than 4.51 W, the Q-switching pulse began to become unstable but Q-switching can still be realized by focusing.

5 CONCLUSION

In conclusion, we have presented a mid-infrared 2.8 μm Q-switched Er:ZBLAN fiber laser using Te as a Q-switcher for the first time to the best of our knowledge. The Te-SAM has a modulation depth of ~7.2% and saturation intensity of 10.81 MW/cm^2, respectively. Stable Q-switched pulse trains were obtained with a repetition rate of 116.98 kHz and a pulse width of 0.457 μs at the maximum launched pump power. The maximum pulse energy of 3.05 μJ, average output power of 357 mW were achieved, respectively. The signal-to-noise ratio (SNR) is 52 dB, which is higher than most known 2.8 μm mid infrared Q-switched fiber lasers. The research results not only indicate that Te is an excellent SA material for stable pulses generation in mid-IR Q-switched fiber lasers but also provides a cost-effective method for the preparation of mid-infrared SAM.

DATA AVAILABILITY STATEMENT

The original contributions presented in the study are included in the article/supplementary material, further inquiries can be directed to the corresponding author.

AUTHOR CONTRIBUTIONS

MZ guided the experiments, LK drafted the manuscript, ZM fabricated Te saturable absorber, PY and SH revised the text. All the authors contributed the conception and design of the experimental study.

FUNDING

This work was supported by the National Natural Science Foundation of China 61935014 and the Science and Technology Innovation Commission of Shenzhen under Grants 20200812163234001.

REFERENCES

1. Töpfer T, Petrov KP, Mine Y, Jundt D, Curl RF, Tittel FKRoom-temperature Mid-infrared Laser Sensor for Trace Gas Detection. *Appl Opt* (1997) 36(30): 8042–9. doi:10.1364/ao.36.008042
2. Walsh BM, Lee HR, Barnes NPMid Infrared Lasers for Remote Sensing Applications. *J Lumin* (2016) 169:400–5. doi:10.1016/j.jlumin.2015.03.004
3. Ma Y, Feng W, Qiao S, Zhao Z, Gao S, Wang YHollow-core Anti-resonant Fiber Based Light-Induced Thermoelastic Spectroscopy for Gas Sensing. *Opt Express* (2022) 30(11):18836–44. doi:10.1364/OE.460134
4. Lang Z, Qiao S, Ma YAcoustic Microresonator Based In-Plane Quartz-Enhanced Photoacoustic Spectroscopy Sensor with a Line Interaction Mode. *Opt Lett* (2022) 47(6):1295–8. doi:10.1364/ol.452085
5. Ma Y, He Y, Tong Y, Yu X, Tittel FKQuartz-tuning-fork Enhanced Photothermal Spectroscopy for Ultra-high Sensitive Trace Gas Detection. *Opt Express* (2018) 26(24):32103–10. doi:10.1364/oe.26.032103
6. Ma Y, Hu Y, Qiao S, Lang Z, Liu X, He Y, et al.Quartz Tuning forks Resonance Frequency Matching for Laser Spectroscopy Sensing. *Photoacoustics* (2022) 25: 100329. doi:10.1016/j.pacs.2022.100329
7. Fortin V, Bernier M, Bah ST, Vallée R30 W Fluoride Glass All-Fiber Laser at 294 μm. *Opt Lett* (2015) 40(12):2882–5. doi:10.1364/ol.40.002882
8. Li JF, Luo HY, He YL, Liu Y, Zhang L, Zhou KM, et al.Semiconductor Saturable Absorber Mirror Passively Q-Switched 2.97μm Fluoride Fiber Laser. *Laser Phys Lett* (2014) 11:065102. doi:10.1088/1612-2011/11/6/065102
9. Zhu G, Zhu X, Balakrishnan K, Norwood RA, Peyghambarian NFe2+:ZnSe and Graphene Q-Switched Singly Ho3+-Doped ZBLAN Fiber Lasers at 3 μm. *Opt Mater Express* (2013) 3(9):1365–77. doi:10.1364/ome.3.001365
10. Li J, Luo H, Zhai B, Lu R, Guo Z, Zhang H, et al.Black Phosphorus: a Two-Dimension Saturable Absorption Material for Mid-infrared Q-Switched and Mode-Locked Fiber Lasers. *Sci Rep* (2016) 6(1):30361. doi:10.1038/srep30361
11. Qin Z, Xie G, Zhang H, Zhao C, Yuan P, Wen S, et al.Black Phosphorus as Saturable Absorber for the Q-Switched Er:ZBLAN Fiber Laser at 28 μm. *Opt Express* (2015) 23(19):24713–8. doi:10.1364/oe.23.024713
12. Frerichs C, Unrau UBPassive Q-Switching and Mode-Locking of Erbium-Doped Fluoride Fiber Lasers at 2.7 Mm. *Opt Fiber Technol* (1996) 2(41): 358–66. doi:10.1006/ofte.1996.0041
13. Wang X, Xu J, Sun Y, Feng W, You Z, Sun D2 and 3 Mm Passively Q-Switched Bulk Pulse Laser Based on a MoS_2/graphene Heterojunction. *Laser Phys Lett* (2017) 15(1):15801. doi:10.1088/1612-202x/aa9158
14. Zhou L, Wei C, Wang D, Chi H, Le Zheng L, Jiang S, et al.Ti3C2Tx Nanosheets for High-Repetition-Rate Wideband-Tunable Q-Switched Fiber Laser Around 3 μm. *IEEE Photon Technol Lett* (2021) 33(10):515–8. doi:10.1109/lpt.2021.3072651
15. Li X, Yu X, Sun Z, Yan Z, Sun B, Cheng Y, et al.High-power Graphene Mode-Locked Tm/Ho Co-doped Fiber Laser with Evanescent Field Interaction. *Sci Rep* (2015) 5:16624. doi:10.1038/srep16624
16. Liu JS, Li XH, Guo YX, Qyyum A, Shi ZJ, Feng TC, et al.SnSe 2 Nanosheets for Subpicosecond Harmonic Mode-Locked Pulse Generation. *Small* (2019) 15(38):1902811. doi:10.1002/smll.201902811

17. Zhao Y, Guo P, Li X, Jin ZUltrafast Photonics Application of Graphdiyne in the Optical Communication Region. *Carbon* (2019) 149:336–41. doi:10.1016/j.carbon.2019.04.075
18. Feng J, Li X, Zhu G, Wang QJEmerging High-Performance SnS/CdS Nanoflower Heterojunction for Ultrafast Photonics. *ACS Appl Mater Inter* (2020) 12(38):43098–105. doi:10.1021/acsami.0c12907
19. Li X, Zhang C, Wang Y, Liu J, Liu JHydrazone Organic Compound with R2C═N-NR Substructure for Ultrafast Photonics. *J Phys Chem C* (2020) 124(41):22638–45. doi:10.1021/acs.jpcc.0c05434
20. Li XH, Guo YX, Ren Y, Peng JJ, Liu JS, Wang C, et al.Narrow-bandgap Materials for Optoelectronics Applications. *Front Phys* (2022) 17(1):13304. doi:10.1007/s11467-021-1055-z
21. Zhang C, Liu J, Gao Y, Li X, Lu H, Wang Y, et al.Porous Nickel Oxide Micron Polyhedral Particles for High-Performance Ultrafast Photonics. *Opt Laser Technol* (2022) 146:107546. doi:10.1016/j.optlastec.2021.107546
22. Ning S, Feng G, Dai S, Zhang H, Zhang W, Deng L, et al.Mid-infrared Fe2+:ZnSe Semiconductor Saturable Absorber Mirror for Passively Q-Switched Er3+-Doped ZBLAN Fiber Laser. *AIP Adv* (2018) 8(2):025121. doi:10.1063/1.5012847
23. Chen W, Lyu Y, Shi H, Kang Z, Zhang H, Qin G, et al.Mid-Infrared Q-Switched and Mode-Locked Fiber Lasers at 2.87 Mm Based on Carbon Nanotube. *IEEE J Selected Top Quan Electron* (2019) 25(4):1100206. doi:10.1109/JSTQE.2019.2899015
24. Guo C, Wei J, Yan P, Luo R, Ruan S, Wang J, et al.Mode-locked Fiber Laser at 2.8 μm Using a Chemical-Vapor-Deposited WSe2 Saturable Absorber Mirror. *Appl Phys Express* (2020) 13:012013. doi:10.7567/1882-0786/ab6031
25. Lee BC, Kim CM, Jang HK, Lee JW, Joo MK, Kim GTDegradation Pattern of Black Phosphorus Multilayer Field–effect Transistors in Ambient Conditions: Strategy for Contact Resistance Engineering in BP Transistors. *Appl Surf Sci* (2017) 419:637–41. doi:10.1016/j.apsusc.2017.04.126
26. Khirat M, Lazab M, Bettahar N, Rached DFirst-principles Calculations of the Band Ordering Conversion in theLaxSc2−xRuPbcompounds. *Solid State Commun* (2018) 276:14–8. doi:10.1016/j.ssc.2018.03.018
27. Tabert CJ, Carbotte JPMagnetization of the Metallic Surface States in Topological Insulators. *J Phys Condens Matter* (2014) 27(1):015008. doi:10.1088/0953-8984/27/1/015008
28. Xie HY, Chang R, Leung PTDipole Emission Characteristics Near a Topological Insulator Sphere Coated with a Metallic Nanoshell. *Results Phys* (2021) 23:104014. doi:10.1016/j.rinp.2021.104014
29. Sun J, Nie Q, Wang X, Dai S, Zhang X, Bureau B, et al.Structural Investigation of Te-Based Chalcogenide Glasses Using Raman Spectroscopy. *Infrared Phys Technol* (2012) 55:316–9. doi:10.1016/j.infrared.2012.03.003
30. Min J, Liang X, Chen J, Wang D, Li H, Zhang JInvestigation of Te Inclusions in CdZnTe Crystalline Material Using Raman Spectroscopy and IR Techniques. *Vacuum* (2012) 86:1003–6. doi:10.1016/j.vacuum.2011.11.009

Conflict of Interest: The authors declare that the research was conducted in the absence of any commercial or financial relationships that could be construed as a potential conflict of interest.

Publisher's Note: All claims expressed in this article are solely those of the authors and do not necessarily represent those of their affiliated organizations, or those of the publisher, the editors and the reviewers. Any product that may be evaluated in this article, or claim that may be made by its manufacturer, is not guaranteed or endorsed by the publisher.

frontiers | Frontiers in Physics

ORIGINAL RESEARCH
published: 01 July 2022
doi: 10.3389/fphy.2022.810933

Research on Unmanned Driving Interface Based on Lidar Imaging Technology

Yuli Wang[1]*, *Yanfei Zhu*[1] and *Hui Liu*[2]

[1]School of Mechanical Engineering, Southeast University, Nanjing, China, [2]State Key Laboratory of Mechanics and Control of Mechanical Structures, Nanjing University of Aeronautics and Astronautics, Nanjing, China

As an autonomous mobile robot, the unmanned intelligent vehicle is often installed with sensors to collect the road environment information, and then process the information and control the speed and steering. In this study, vehicle-mounted camera, laser scanning radar and other sensors were equipped to collect real-time environmental information to efficiently process and accurately detect the specific location and shape of the obstacle. This study then investigated the impact of two In-Vehicle Information Systems (IVISS) on both usability and driving safety. Besides, the laser perception sensing technology was applied to transmit the information of the surrounding around the real-time driving area to the vehicle system. Simulating vehicle checkerboard and hierarchical IVIS interface layouts, we also examined their usability based on task completion time, error rate, NASA-TLX, and System Usability Scale (SUS). It was suggested that the results offer a supporting evidence for further design of IVIS interface.

Keywords: smart car, laser radar, camera, obstacle detection, 3D target detection

OPEN ACCESS

Edited by:
Karol Krzempek,
Wrocław University of Science and Technology, Poland

Reviewed by:
Junhao Xiao,
National University of Defense Technology, China
Xiuhua Fu,
Changchun University of Science and Technology, China
Liqin Su,
China Jiliang University, China

***Correspondence:**
Yuli Wang
wyl8826@outlook.com

Specialty section:
This article was submitted to Optics and Photonics, a section of the journal Frontiers in Physics

Received: *08 November 2021*
Accepted: *16 February 2022*
Published: *01 July 2022*

Citation:
Wang Y, Zhu Y and Liu H (2022) Research on Unmanned Driving Interface Based on Lidar Imaging Technology. Front. Phys. 10:810933. doi: 10.3389/fphy.2022.810933

1 INTRODUCTION

With the ongoing economic and social development, vehicles on the road have soared dramatically in the recent decades, which created various problems such as traffic congestion, excessive energy consumption, environmental pollution, property damage and heavy casualty, and exposed the conflict between the existing transport infrastructure and the vehicles [1]. Many countries have thus initiated research projects to develop intelligent transportation systems [2] based on the latest technologies in the fields of information, automation, computer and management. Their common goal is to improve the efficiency of vehicles and transportation, enhance safety, minimize environmental pollution and expand the capacity of existing traffic [3]. The research of intelligent vehicle targets to address the abovementioned problems by reducing the human workload in driving tasks with the adoption of new technologies in lane warning monitoring, driver fatigue detection, automatic speed cruise control, etc. [4].

The key technology for driverless intelligent vehicles is the recognition and detection of obstacles [5], and the result of the detection determines the stability and safety of the intelligent vehicle driving [6]. Current obstacle detection methods include vision-based detection, radar-based detection and ultrasonic-based detection [7], which differentiate each other in their detection accuracy. Vision-based detection simply uses vehicle-mounted HD cameras to capture images of obstacles and environments. The exact location of an obstacle can then be calculated according to its position in the image, and its parameter values estimated by the camera. Vision-based detection is robust, allowing

TABLE 1 | Sensors used in unmanned intelligent vehicles.

Name	Country	Era	Sensor
HILARE	France	1979	Machine vision, LIDAR
NAVLAB-1	United States	1986	Grayscale cameras, sonar, LIDAR
NAVLAB-5	United States	1996	Colour cameras, LIDAR, GPS
ARGO	Italy	1998	Dual cameras, odometer
ANFM	Sweden	2001	Camera, ultrasound, radar
SANDSTORM	United States	2004	Colour cameras, LIDAR
STANLEY	United States	2005	Multi-lidar, monocular vision systems
BOSS	United States	2007	Multi-single-line LIDAR, 64-line LIDAR

real time analysis, but susceptible to light and other external factors [8]. Radar-based detection is just the opposite, having fairly strong resistance to external influences [9]. For example, three-dimensional LIDAR, though expensive, provides three-dimensional information about the obstacle during scanning and imaging, while 2D LIDAR, with a simple and stable system and fast response time, only scans a flat surface [10]. Ultrasound-based detection technology, with low resolution and accuracy, is seriously limited in providing comprehensive boundary data and obtaining environmental information, thus scarcely used in driverless intelligent vehicles [11].

However, there is no one-size-fits-all sensor perfect for obstacle detection by intelligent vehicles [12], although the commonly used sensors in intelligent vehicles contain inertial navigation, laser scanning radar, millimeter wave radar and on-board cameras [13]. Single sensors are unstable and incomprehensive when it comes to obtaining information about their surroundings. They need to complement each other [14], and now multi-sensor-based technology fusion has become a trend in intelligent vehicle research [15], which shows its advantages in obtaining target information, extracting the sensing area and finally completing the detection of obstacles [16]. Currently, convergence-based detection has developed to converge the data of multiple sensors. Reviewing the literature concerning the sensors used in unmanned intelligent vehicles that are developed in different countries as shown in **Table 1**, we found that the countries had made different trade-offs and improvements in technology selection based on their existing problems. Nevertheless, in China, the technology of this type of sensors still falls behind the developed countries.

In this study, we used a vehicle-mounted camera in conjunction with a laser scanning radar for obstacle recognition and detection [17], and developed a computational model for a theoretical framework to cognize visual and auditory information that allows high-speed real-time computation. This framework converged the information from multiple sensors, including the vision system, the Global Positioning System (GPS), the speed detection system and the laser scanning radar system, and endowed a driverless vehicle platform with natural environment perception and automatic decision-making capabilities in various road conditions. Aiming for the application in the driverless intelligent vehicle platform, this study also expects to achieve 1) autonomous driving along prescribed routes, 2) driving along lanes according to road signs and markings, as well as 3) autonomous obstacle avoidance, acceleration, and deceleration [18].

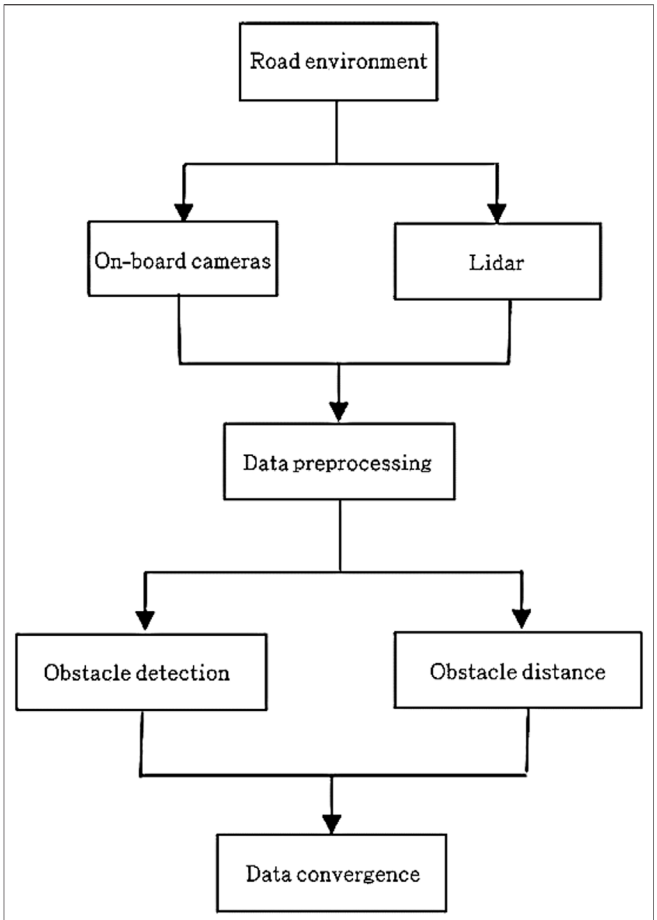

FIGURE 1 | Data convergence chart.

2 METHODS, EXPERIMENTS AND RESULT ANALYSIS

The collection of information about the external environment is the key to designing an unmanned intelligent vehicle, and the various data collection sensors installed on the vehicle are equivalent to the driver's eyes [19]. Only the timely and proper acquisition and processing of external environment data can ensure the safe and stable driving [20]. Considering that a single sensor cannot be complete or reliable for external environment information collection, this study thus used two sensors equipped with a laser scanning radar and on-board cameras to detect and recognize obstacles, and combined the data from both sensors, which is conducive to improving the accuracy and reliability of obstacle recognition [21].

2.1 Data Collection and Processing

In this study, the image processing was mainly implemented using the algorithmic functions of OpenCV, which is an open-

source computer vision library based on the Open Source Computer Vision Library developed by Intel Corporation. Composed of a series of C functions and some C classes, OpenCV supports the execution of different common algorithms in digital image processing and computer vision systems, which are highly portable and accessible to multiple operating systems without code modification and thus widely used in object recognition, image segmentation and machine vision. Besides, it runs in real time and can be compiled and linked to generate executable programs [22]. The modules of OpenCV adopted in this study are listed as follows:

- OpenCV_core: Core functional modules, including basic structures, algorithms, linear algebra, discrete Fourier transforms, etc. OpenCV_imgproc: Image processing module, including filtering, enhancement, morphological processing, etc.
- OpenCV_feature2d: 2D feature detection and description module, including image feature value detection, description matching, etc.
- OpenCV_video: Video module, including optical flow method, motion templates, target tracking, etc.
- OpenCV_objdetect: Target detection modules.
- OpenCV_calib3d: 3D module, including camera calibration, stereo matching, etc.

2.2 Multi-Sensor Data Convergence

Data convergence from multiple sensors in the research of unmanned intelligent vehicles is a technology for comprehensive analysis, processing and optimisation of the information acquired by multiple sensors [23]. Under certain guidelines, the collected data was integrated, utilized and synthesized in time and space to refine the target information and then improve the control system. Data convergence brings a linkage of each other in a certain way and then the optimization of all the collected data [24]. The process of data convergence is shown in **Figure 1**.

In this study, laser scanning radar and vehicle-mounted camera sensors were used for obstacle detection, and the information collected by the two sensors was converged and matched in time and space to maintain consistency in the collected data. Data convergence has a number of advantages in intelligent control as follows:

1) Providing the data collected by the whole system with a higher accuracy and reliability;
2) Enabling the system to obtain more information in the same amount of time;
3) Reducing the impact of natural external factors on the multi-sensor system;
4) Accelerating data processing and increasing information reuse.

2.2.1 Principle of Multi-Sensor Data Convergence

To fully utilize the information collected by multiple sensors, and then rationally process and analyze the collected data, this study formulated some principles to converge and match the redundant or complementary information of multiple sensors in space or time. The principles are as follows:

1) Multiple sensors of different types are used to collect data information of the detection target;
2) Feature values are extracted from the output data of the sensors;
3) The extracted feature values (e.g., clustering algorithms, adaptive neural networks or other statistical pattern recognition methods that can transform feature vectors into target attribute judgments, etc.) are processed by pattern recognition to complete the recognition of the target by each sensor;
4) The data from each sensor are converged using data convergence algorithms to maintain consistency in the interpretation and description of the detection target [25].

2.2.2 Multi-Sensor Data Convergence Algorithms

The selection of an effective data convergence method in a study is determined by the specific application context. The frequently-employed methods for multi-sensor data convergence include weighted averaging, Kalman filtering and multi-Bayesian estimation [26].

1) Weighted averaging

The weighted averaging method is the simplest and most intuitive of the algorithms for data convergence. It takes the redundant information provided by a group of sensors and weights the average, with the result being the data convergence value, which is a direct manipulation of the data source.

2) Kalman filtering

The Kalman filtering method is primarily used to converge redundant data from low-level real-time dynamic multi-sensors. The algorithm uses recursion of the statistical properties of the measurement model to determine the optimal convergence and data estimation in a statistical sense. In the model, the dynamical equations, i.e., the state equations [27], are used to describe the dynamics of the detection target. If the dynamical equations are known and the system and sensor errors fit the Gaussian white noise model, the Kalman filter will provide the optimal estimate of the converged data in a statistical sense. The recursive nature of the Kalman filter allows the system to process without the need for extensive data storage and computation.

3) Bayesian estimation

Bayesian estimation is one of the common methods for synthesizing high level information from multiple sensors in a static environment. It enables sensor information to combine according to probabilistic principles, with measurement uncertainties expressed as conditional probabilities. Bayesian estimation is adopted in the case that sensor

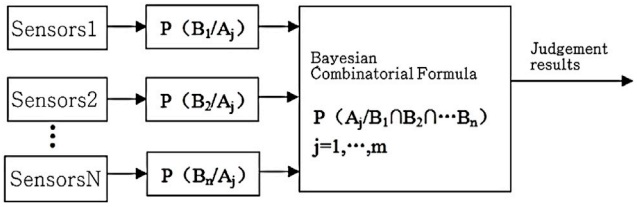

FIGURE 2 | Bayesian data convergence process.

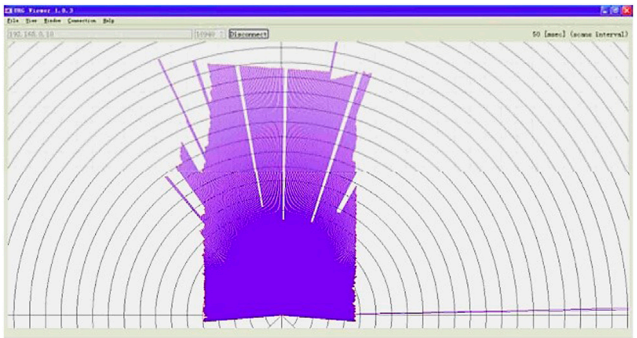

FIGURE 3 | Raw data collected by radar.

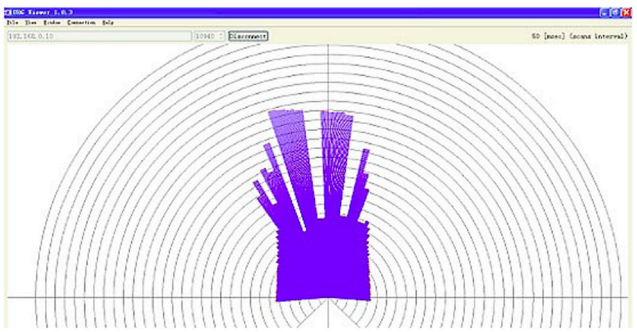

FIGURE 4 | Pre-processed data.

measurements have to be converged indirectly [28]. Treating each sensor as a Bayesian estimate, Multi Bayesian estimation synthesizes the associated probability distribution of each individual object into a joint posterior probability distribution function. It provides a final fused value of the multi-sensor information by using the likelihood function of the joint distribution function as the minimum and synthesizing the information with a prior model of the environment providing a characterisation of the whole environment.

In this study, Bayesian estimation was employed, based on the fact that n sensors of different types were involved to detect the same target. To ensure the target to identify m attributes, we proposed m hypotheses or propositions Ai, $i = 1...m$. The steps for the implementation of the Bayesian convergence algorithm are explicated as follows (**Figures 2–4**): Firstly, to n times observe *B1*, *B2...Bn* given by n sensors; secondly, to calculate the probability of each sensor's observation under each hypothesis being true; thirdly, to calculate the posterior probability of each hypothesis being true under multiple observations according to Bayesian formula; finally, to determine the result.

2.3 Radar and Camera Data Matching

2.3.1 Temporal Matching

Temporal matching of data is the process of synchronising the data collected by each sensor. The sampling frequency of different sensors is different, thus causing a variation among the collected data even although synchronously acquired. With the time variable as a parameter, the process of data synchronisation can be completed by granting different GPS times to different sensors, which is featured by a relatively high accuracy convergence of data and a strong impact on the real-time nature of data.

Considering that the sensors selected in this study differ greatly from each other in their sampling frequency, the firstly ensured was the synchronization of the information from LIDAR with that from camera during the data acquisition [29]. Then, two separate data collection threads were produced for the two sensors (the laser scanning radar and the camera) to collect the data from the two sensors at the same interval each time and then synchronise the two sets of data in time, i.e., matching the data.

2.3.2 Spatial Matching

Data matching in space is a multi-level and multi-side processing of the collected data, including the steps of automatic detection, correlation, estimation and combination of data and information from multiple sources. It aims to obtain more reliable and accurate information as well as most reliable information-based decision, i.e., to optimize the value of the target location based on the multi-source observations. Spatial matching of data is to unify the transformation relationship between the sensor coordinate system, image coordinate system and vehicle coordinate system in space. Once the constraint of equations for the camera parameters is removed, the interconversion relationships of the four coordinate systems can be determined, and then the data points scanned by the LIDAR can be projected onto the image coordinate system using the established camera model. Based on the previous theoretical model, the conversion relationship between the point in space $p(xs, ys, zs)$ and the corresponding point in the image coordinate system $p(xt, yt)$ is expressed as:

Where ρ is the distance from the LIDAR laser beam to the spatial point (xs, ys, zs), β is the angle swept by the LIDAR, α is the pitch angle of the LIDAR installation, h is the LIDAR installation height and p is a 3×4 matrix. This change allows the data collected by the LIDAR to accurately mirror in the image data space, thus enabling the spatial conversion between the two sets of data.

Spatial matching of data have some advantages. First, it is conducive for the control system to making the most accurate

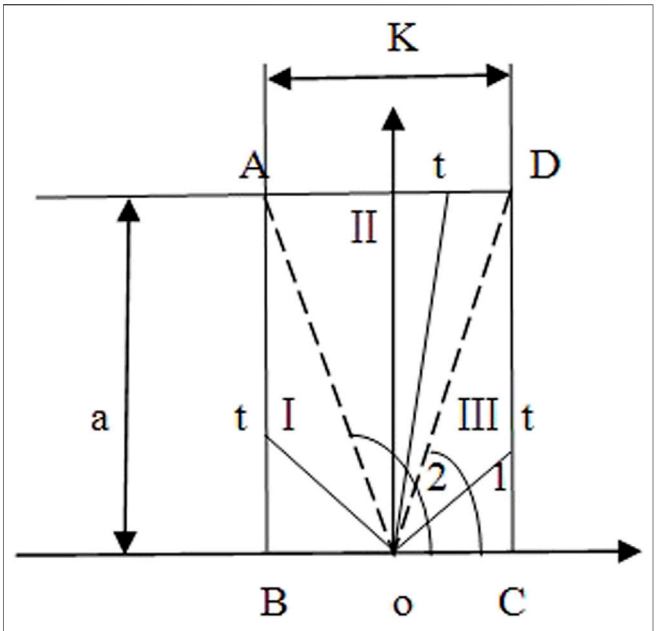

FIGURE 5 | Smart car front area in straight ahead.

judgment on the specific distance and location of the obstacle. Second, data matching in space facilitates the LIDAR scanned data to converge the image, then to form the target area on the image coordinate system in real time, and finally the recognition of the obstacle [30].

2.4 Radar-Based Obstacle Detection

2.4.1 Radar Data Pre-Processing

UXM-30LX-EW laser scanning radar was employed to pre-process the data in this study. It has the advantages of great detection range, large measuring range, high measurement accuracy and angular resolution. As the range of the laser scanning radar increases, the measurement accuracy will decrease. The scanning plane angle of the LIDAR was set at 190° horizontally, greater than the maximum angle captured by the camera. Unnecessary laser points have to be removed during the data convergence process to ensure the accuracy of the final results. Thus, in this study, we first removed the laser beam falling outside this angle according to the camera's shooting angle, which accelerates the operating, and then made judgment and analysis using the pre-processed radar data.

2.4.2 Obstacle Detection

The detection and identification of obstacles was performed in this study by the LIDAR installed in the front of the vehicle and the camera on the roof. To ensure the safety in roads, the control system of a vehicle must be able to control the braking or steering in an emergency when an obstacle such as a vehicle and pedestrian is found. However, when the vehicle is turning or travelling in a straight line, the scope for determining the presence of an obstacle in the area in front of the vehicle will change. For example, when a vehicle turns according to the traffic light, the obstacles in the area directly in front of the vehicle are not easy to

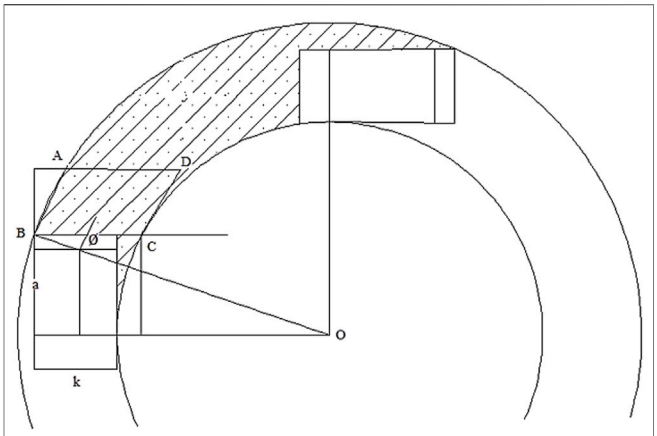

FIGURE 6 | Smart car right turn schematic.

FIGURE 7 | Collected raw images.

be detected and thus mistreated, leading to a sharp braking by the driverless intelligent vehicle and even a failure in fulfilling the required tasks such as turning [31]. Hereby, three actual road conditions were analysed and discussed.

1) When an unmanned vehicle is travelling straight ahead

In this situation, the area to be determined in this case is well defined. As shown in **Figure 5**, a rectangular area with length of *a* and width of *k* in front of the vehicle is the detection area, divided into three blocks marked as I, II and III.

2)When no one is turning right

Figure 6 shows the smart car right turn schematic. As is seen, the shaded part of the vehicle is the area through which the steering wheel of the unmanned vehicle turns to the right at a certain angle through an all-round corner, where the sensing area detected by the LiDAR is located. The quadrilateral ABCD was chosen as the sensing area in order to maximise the overlapping

FIGURE 8 | Pre-processed images.

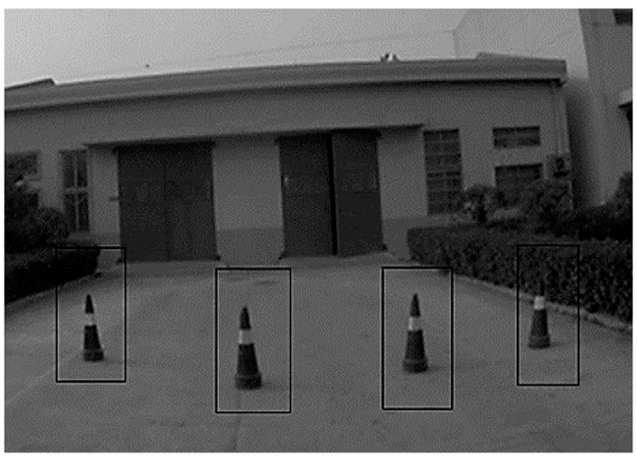

FIGURE 9 | Interested obstacle Areas.

area between the sensing area and the shaded area. The distance between AD and BC is marked as *s*, which on the one hand determines the size of the shaded area, and on the other hand is a function of the speed (marked as *v*) and determined by it, i.e., $s = f(v)$. Thus, it can be concluded that the shape of the quadrilateral ABCD obtained varies with the angle of rotation of the front wheels, and the area of this quadrilateral is the manifestation of the function of the speed and the angle of rotation of the front wheels.

2.5 Camera-Based Vision Detection of Obstacles

2.5.1 Image Data Preprocessing

During the capture and transmission of images, the data signal is very susceptible to the external environment, which brings image noise, variations in the quality of the captured images, and finally a direct influence on the recognition of obstacles and the convergence of other data. Therefore, the captured image in this study was pre-processed, such as image denoising, to provide a clear depiction of the real road

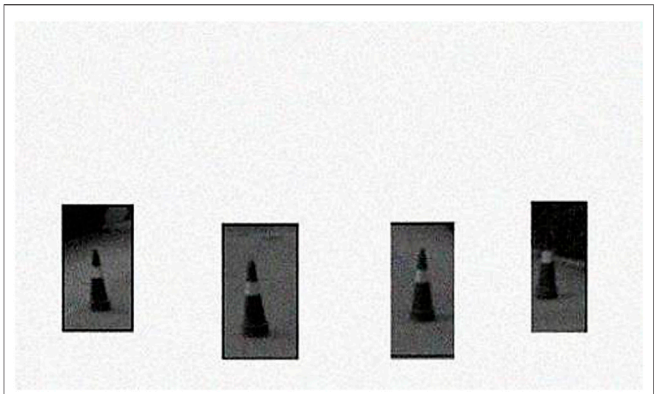

FIGURE 10 | Retaining images of the sensing area.

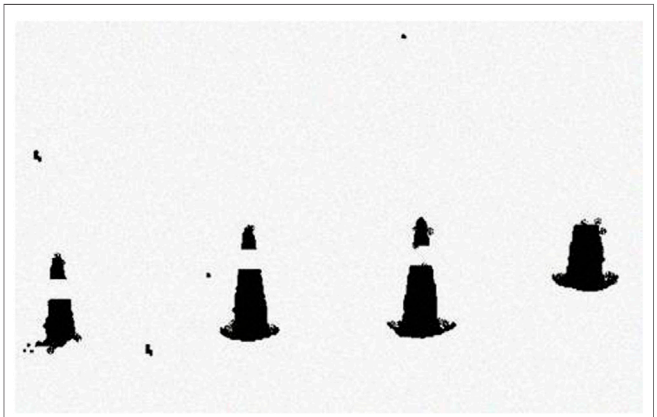

FIGURE 11 | Image segmentation process.

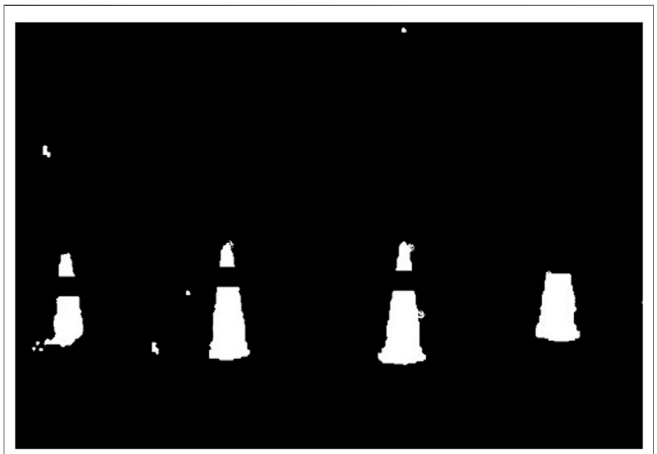

FIGURE 12 | Obstacle infographic.

conditions and then improve the accuracy of the obstacle detection recognition. The main methods for image pre-processing adopted in this process include image greyscaling, image denoising, image segmentation and the application of image morphology [32], for noise removal in image processing neighbourhood averaging, and median filtering, and for image segmentation threshold-based segmentation, region-based growth and merge segmentation, and eigenvalue space clustering-based segmentation.

2.5.2 Identification of Road Environment

Nowadays, the road system is very complicated especially after lane lines marked, thus becoming a great change for the vision system of driverless intelligent vehicles. Road recognition becomes a key to the obstacle detection system of these vehicles. It then necessitates the collection of lane recognition images and the identification of real obstacles in the lanes [33]. Considering this as well as the requirement for a high degree of accuracy in time and obstacle description, this study employed two main algorithms for lane recognition: 1) The overall road surface algorithm, mainly for the entire road surface gray detection and achieved using the area detection method; 2) the lane detection algorithm, achieved through the recognition of the edge or lane separation.

2.5.3 Extraction of Interested Obstacle Areas

For the images acquired by the camera, we only extracted the sensing area to avoid processing unnecessary parts of the image, then reduce the processing time of the system, and finally ensure the real-time performance of the system. Based on the data transmitted by the LIDAR, a fixed value was set to detect the location of the general area where the cone ahead was located, and the results are shown in **Figures 7–9**.

2.5.4 Obstacle Detection

The image segmentation technique is to segment the target from the image and contributed to providing convenience for the subsequent image processing. Spatial eigenvalues were adopted to extract the obstacle from the image during the obstacle detection of the captured by camera. **Figure 10** shows the image of the identified obstacle in the sensing area, where the grey scale value of the other parts of the image was placed at 0, and **Figure 11** the final results after image segmentation. As is seen in **Figure 11**, on the edge of the image exist some burrs and unsmooth points. Hereby, the image morphology of the open operation was introduced to remove the burrs and points, and then the region growth segmentation to segment the image, identify the information of the obstacle segmentation and finally recognize the basic information of the real obstacle, as shown in **Figure 12**. It is noted that when the specific information is detected, the system will transmit it to the planning and decision-making part of the intelligent vehicle, which then will plan a safe route to bypass the recognized obstacle and command the control system to follow the planned.

3 CONCLUSION

Multi-sensor technology is becoming more efficient, and has been increasingly employed in driverless intelligent vehicles in recent years. Multi-sensor data convergence includes the integration of vision systems with ultrasonic technology and laser scanning radar with vision systems. This technology in the study of unmanned intelligent vehicle obstacle detection effectively solved the problems of insufficient data collection by a single sensor and unstable unmanned intelligent vehicle [33]. OpenCV algorithm functions were proposed to achieve the detection of obstacles as well as the principle and algorithm of multi-sensor data convergence. This paper firstly introduced the method of obstacle identification and detection by laser scanning radar during the process of obstacle detection, including the pre-processing of laser data, and then elaborated the process of obstacle identification based on camera, the acquisition of the pre-processing of images, road recognition and finally detection of lane edges and obstacle detection [34].

The technical approaches to obstacle detection in this study can be summarised as follows: e current commonly used technology in driverless intelligent vehicles: LIDAR-based detection, vision system-based detection, ultrasonic-based detection and multi-sensor-based data convergence detection. The technical solution was proposed to determine according to the actual situation.

1) The multi-sensor data convergence involves the conversion of coordinates and data between sensors. In this study, the vehicle body coordinate system, sensor coordinate system and image coordinate system were designed as three separate coordinate systems, and the interconversion relationship among them was analysed, laying a foundation for the later processes.
2) In the radar obstacle detection, the collected data was firstly pre-processing to eliminate some camera shooting range outside the point, thereby improving the efficiency of the processing. Then, based on the driving condition of the vehicle in straight, left- and right-turn, three situations of the intelligent vehicle in front of the sensing area were discussed to determine the location of the obstacle in the sensing area, which is the preparation for the subsequent obstacle target extraction.
3) In view of the enormousness of the amount of the information contained in the camera-captured images of the road environment, it is a great challenge to reduce the processing time and enhance the efficiency of the system. Thus, in this study image pre-processing was first performed on the collected original pictures, the process of which includes image greyscaling, image denoising and other processing to retain the original information. Besides, the data from the laser scanning radar and the on-board camera were converged temporally and spatially, then the sensing area

extracted and the obstacle detection completed in the sensing area, which reduces the amount of and ensures the real-time performance of the algorithm and the robustness of the system.

Based on the above analysis, LIDAR or camera feature oriented data convergence is suggested to realize a more accurate identification and detection of obstacles. Moreover, a joint calibration of the radar and camera and error analysis will be helpful to improve the accuracy of the data acquisition [35, 36].

DATA AVAILABILITY STATEMENT

The raw data supporting the conclusion of this article will be made available by the authors, without undue reservation.

AUTHOR CONTRIBUTIONS

YW: Conceptualization (lead); writing—original draft (lead); formal analysis (lead); writing—review and editing (equal). YZ: Software (lead); writing—review and editing (equal). HL: Methodology (lead); writing—review and editing (equal).

REFERENCES

1. Mitsopoulos-Rubens E, Trotter MJ, Lenné MG. Effects on Driving Performance of Interacting with an In-Vehicle Music Player: a Comparison of Three Interface Layout Concepts for Information Presentation. *Appl Ergon* (2011) 42:583–91. doi:10.1016/j.apergo.2010.08.017
2. Kim H, Song H. Evaluation of the Safety and Usability of Touch Gestures in Operating In-Vehicle Information Systems with Visual Occlusion. *Appl Ergon* (2014) 45:789–98. doi:10.1016/j.apergo.2013.10.013
3. Cockburn A, Mckenzie B. 3D or Not 3D? Evaluating the Effect of the Third Dimension in a Document Management System. In Proceeding of the CHI 2001: Conference on Human Factors in Computing Systems, Seattle, WA, USA, March 2001, 2001; pp. 434–41.
4. Broy V, Althoff F, Klinker G. iFlip. A Metaphor for In-Vehicle Information Systems. *Working Conf Adv Vis Inter* (2006) 42:155–8. doi:10.1145/1133265.1133297
5. Lin C-T, Wu H-C, Chien T-Y. Effects of E-Map Format and Sub-windows on Driving Performance and Glance Behavior when Using an In-Vehicle Navigation System. *Int J Ind Ergon* (2010) 40:330–6. doi:10.1016/j.ergon.2010.01.010
6. Lavie T, Oron-Gilad T, Meyer J. Aesthetics and Usability of In-Vehicle Navigation Displays. *Int J Human-Computer Stud* (2011) 69:80–99. doi:10.1016/j.ijhcs.2010.10.002
7. Maciej J, Vollrath M. Comparison of Manual vs. Speech-Based Interaction with In-Vehicle Information Systems. *Accid Anal Prev* (2009) 41:924–30. doi:10.1016/j.aap.2009.05.007
8. Wickens CD. An Introduction to Human Factors Engineering. *Qual Saf Health Care* (2004) 11:393. doi:10.3969/j.issn.1004-3810.2008.z1.001
9. Horrey WJ, Wickens CD. Multiple Resource Modeling of Task Interference in Vehicle Control, hazard Awareness and In-Vehicle Task Performance. Proceeding of the Driving Assessment: the Second International Driving Symposium on Human Factors in Driver Assessment Training & Vehicle Design 2003. January 2003, 2003; pp. 7–12.
10. Tsimhoni O, Smith D, Green P. Address Entry while Driving: Speech Recognition versus a Touch-Screen Keyboard. *Hum Factors* (2004) 46:600–10. doi:10.1518/hfes.46.4.600.56813
11. Sodnik J, Dicke C, Tomažič S, Billinghurst M. A User Study of Auditory versus Visual Interfaces for Use while Driving. *Int J Human-Computer Stud* (2008) 66:318–32. doi:10.1016/j.ijhcs.2007.11.001
12. Salmon PM, Young KL, Regan MA. Distraction 'on the Buses': A Novel Framework of Ergonomics Methods for Identifying Sources and Effects of Bus Driver Distraction. *Appl Ergon* (2011) 42:602–10. doi:10.1016/j.apergo.2010.07.007
13. Ziefle M. Information Presentation in Small Screen Devices: the Trade-Off between Visual Density and Menu Foresight. *Appl Ergon* (2010) 41:719–30. doi:10.1016/j.apergo.2010.03.001
14. Chen M-S, Lin M-C, Wang C-C, Chang CA. Using HCA and TOPSIS Approaches in Personal Digital Assistant Menu-Icon Interface Design. *Int J Ind Ergon* (2009) 39:689–702. doi:10.1016/j.ergon.2009.01.010
15. Foley J. *SAE Recommended Practice Navigation and Route Guidance Function Accessibility while Driving (SAE 2364)*. Warrendale, PA, USA: Society of Automotive Engineers (2000). p. 11.
16. Green P. Visual and Task Demands of Driver Information Systems. *Driver Inf Syst* (1999) 41:517–31. doi:10.1109/LSENS.1999.2810093
17. Soukoreff RW, Mackenzie IS. Metrics for Text Entry Research: an Evaluation of MSD and KSPC, and a New Unified Error Metric. Proceeding of the Conference on Human Factors in Computing Systems, CHI 2003, Ft. Lauderdale, Florida, USA, April 2003, 2003; pp. 113–20.
18. Svenson O, Patten CJD. Mobile Phones and Driving: a Review of Contemporary Research. *Cogn Tech Work* (2005) 7:182–97. doi:10.1007/s10111-005-0185-3
19. Hart SG, Staveland LE. Development of NASA-TLX (Task Load Index): Results of Empirical and Theoretical Research. *Hum Ment Workload* (1988) 19:18–24. doi:10.1016/s0166-4115(08)62386-9
20. Brooke J. Sus-a Quick and Dirty Usability Scale. *Usability Eval Industry* (1996) 16:189–93. doi:10.4271/1996-01-1601
21. Dingus TA. Empirical Data Needs in Support of Model Building and Benefits Estimation. In: *Modeling ITS Collision Avoidance System Benefits: Expert Panel Proceedings*. Washington, DC: Intelligent Transportation Society of America (1997).
22. Tijerina L. Issues in the Evaluation of Driver Distraction Associated with In-Vehicle Information and Telecommunications Systems. *Transportation Res Inc* (2000) 32:42–4. doi:10.17845/156265.095643
23. Stanton NA. Advances in Human Aspects of Road and Rail Transportation. *Highw Saf* (2012) 12:32–9. doi:10.1260/916720.800753
24. Brookhuis KA, de Vries G, de Waard D. The Effects of mobile Telephoning on Driving Performance. *Accid Anal Prev* (1991) 23:309–16. doi:10.1016/0001-4575(91)90008-s
25. Causse M, Alonso R, Vachon F, Parise R, Orliaguet JP, Tremblay S, et al.Testing Usability and Trainability of Indirect Touch Interaction: Perspective for the Next Generation of Air Traffic Control Systems. *Ergonomics* (2014) 57:1616–27. doi:10.1080/00140139.2014.940400
26. Bhise VD, Bhardwaj S. *Comparison of Driver Behavior and Performance in Two Driving Simulators*. Detroit, United States: SAE World Congress and Exhibition (2008).
27. Lewis JR. Usability Testing. In: *Handbook of Human Factors and Ergonomics* (2006). p. 1275–316. doi:10.1002/0470048204.ch49
28. Zviran M, Glezer C, Avni I. User Satisfaction from Commercial Web Sites: The Effect of Design and Use. *Inf Manag* (2006) 43:157–78. doi:10.1016/j.im.2005.04.002
29. Recarte MA, Nunes LM. Mental Workload while Driving: Effects on Visual Search, Discrimination, and Decision Making. *J Exp Psychol Appl* (2003) 9:119–37. doi:10.1037/1076-898x.9.2.119
30. Reyes ML, Lee JD. Effects of Cognitive Load Presence and Duration on Driver Eye Movements and Event Detection Performance. *Transportation Res F: Traffic Psychol Behav* (2008) 11:391–402. doi:10.1016/j.trf.2008.03.004
31. Salmon PM, Lenné MG, Triggs T, Goode N, Cornelissen M, Demczuk V. The Effects of Motion on In-Vehicle Touch Screen System Operation: a Battle Management System Case Study. *Transportation Res Part F: Traffic Psychol Behav* (2011) 14:494–503. doi:10.1016/j.trf.2011.08.002
32. Metz B, Landau A, Just M. Frequency of Secondary Tasks in Driving - Results from Naturalistic Driving Data. *Saf Sci* (2014) 68:195–203. doi:10.1016/j.ssci.2014.04.002
33. Akyeampong J, Udoka S, Caruso G, Bordegoni M. Evaluation of Hydraulic Excavator Human-Machine Interface Concepts Using NASA TLX. *Int J Ind Ergon* (2014) 44:374–82. doi:10.1016/j.ergon.2013.12.002

34. Xian H, Jin L, Hou H, Niu Q, Lv H. Analyzing Effects of Pressing Radio Button on Driver's Visual Cognition. In: *Foundations and Practical Applications of Cognitive Systems and Information Processing* (2014). p. 69–78. doi:10.1007/978-3-642-37835-5_7
35. Chiang SH. *Liquid crystal Display Module and the Fabrication Method of the Same* (2004).
36. Reimer B, Mehler B, Coughlin JF, Roy N, Dusek JA. The Impact of a Naturalistic Hands-free Cellular Phone Task on Heart Rate and Simulated Driving Performance in Two Age Groups. *Transportation Res Part F: Traffic Psychol Behav* (2011) 14:13–25. doi:10.1016/j.trf.2010.09.002

Conflict of Interest: The authors declare that the research was conducted in the absence of any commercial or financial relationships that could be construed as a potential conflict of interest.

Publisher's Note: All claims expressed in this article are solely those of the authors and do not necessarily represent those of their affiliated organizations, or those of the publisher, the editors and the reviewers. Any product that may be evaluated in this article, or claim that may be made by its manufacturer, is not guaranteed or endorsed by the publisher.

frontiers | Frontiers in Physics

ORIGINAL RESEARCH
published: 05 July 2022
doi: 10.3389/fphy.2022.930007

Quartz Tube Enhanced Raman Scattering Spectroscopy

Ganshang Si[1,2], *Jiaxiang Liu*[1], *Zhengang Li*[1,2], *Zhiqiang Ning*[1,2] *and Yonghua Fang*[1,2]*

[1]*Key Laboratory of Environmental Optics and Technology, Anhui Institute of Optics and Fine Mechanics, Hefei Institutes of Physical Science, Chinese Academy of Sciences, Hefei, China,* [2]*University of Science and Technology of China, Hefei, China*

Raman spectroscopy is widely used in many fields with the advantages of simultaneous species detection and molecular fingerprint characteristics, but the low detection sensitivity limits its further development, especially for highly scattering or turbid mediums. In this consideration, a new method called quartz tube enhanced Raman scattering spectroscopy was proposed for the first time in this paper. A quartz tube was inserted into the powder sample to improve the coupling of light into the medium and increase the interaction volume of the laser with the sample ("volume-excitation"), multiple scattering of the light within the turbid medium resulted in an increased Raman signal. In this paper, the effect of different sizes of quartz tubes on the sensitivity enhancement was studied. The results show that the enhancement factor of the signal intensity was nearly 5.37 (the Raman signal of HCO_3^-) compared to traditional Raman spectroscopy technology. Furthermore, the method was successfully applied to improve the Raman signal intensity of the mixed sample (1:5, m (PO_4^{3-}):m (HCO_3^-)) and detect the baking soda powder buried under a 6 mm thick layer of potassium dihydrogen phosphate powder. The results show that the technology will open a new way for the quantitative analysis and detection of powder samples.

Keywords: Raman spectroscopy, quartz tube, powder samples, signal enhancement, new method

OPEN ACCESS

Edited by:
Yufei Ma,
Harbin Institute of Technology, China

Reviewed by:
Jing Yu,
Shandong Normal University, China
Ye Tian,
Ocean University of China, China

***Correspondence:**
Yonghua Fang
yhfang@aiofm.ac.cn

Specialty section:
This article was submitted to Optics and Photonics, a section of the journal Frontiers in Physics

Received: *27 April 2022*
Accepted: *16 May 2022*
Published: *05 July 2022*

Citation:
Si G, Liu J, Li Z, Ning Z and Fang Y (2022) Quartz Tube Enhanced Raman Scattering Spectroscopy. Front. Phys. 10:930007. doi: 10.3389/fphy.2022.930007

1 INTRODUCTION

In recent years, laser spectroscopy technology has made great progress, and its application fields have been continuously expanded [1–3]. With the most significant advantages such as simplicity, high chemical specificity, multicomponent and nondestructive detection, spectroscopy has been used in many fields [4], e.g., food adulteration [5], hazardous chemical detection [6], and drug analysis [7]. However, the Raman-scattering signal was very weak, which has an intensity lower than (10^{-6}) that of the excitation [8]. Therefore, approaches to enhance Raman scattering signals are always important to improve and realize related detection techniques. At present, the methods to improve the detection sensitivity mainly include UV resonance Raman spectroscopy (UV-RRS) [9], surface-enhanced Raman scattering (SERS) [10, 11], and tip-Enhanced Raman Spectroscopy (TERS) [12]. These methods were mainly developed for gas or liquid samples, and they are almost useless for powder samples. Thus, it is meaningful to explore new methods to enhance the Raman detection sensitivity for powder samples.

Many studies have been involved in approaches to improve the powder detection sensitivity of Raman spectroscopy. Mastousek et al. [13] suggested using a dielectric filter to selectively return reflected laser photons back to the samples. This technique provided a 6 times enhancement of the Raman signal, but the signal-to-noise ratio was only 2 times for powder samples. Anupam K et al. [14] suggested a simple procedure improving detection limits for micro-Raman by producing micro-

cavity in a reflecting metal substrate. Peter J. Larkin et al. [15] proposed increasing the path of action between the laser and the sample by drilling a conical/cylindrical hole in the tablet, thereby provided 3–5 times enhancement of Raman signal and 2 times increase of the accuracy. Lohumi S et al. [16] proposed a mirror was used to improve the detection sensitivity of Raman imaging spectroscopy, which increased the Raman signal intensity of powder samples by 2 times. Besides, it verified the feasibility of the technique used for food adulteration in the paper. Lednev V N et al. [17] suggested using a high-energy laser to act on the powder sample to produce a laser crater. Furthermore, using another low-energy laser to excite the Raman signal. The results showed that the detection sensitivity could be enhanced nearly 14 times. Besides, this research group optimized the experimental parameters, including laser wavelength, laser energy, particle size distribution, etc [18]. From the above analysis, the last technique was the better among those methods, but the high energy could damage the samples. In addition, it was difficult to detect deep target substances with the powder state for traditional Raman spectroscopy, because of the ability limitation of light penetration [19, 20]. At present, Transmission Raman spectroscopy (TRS) [21] and Spatially-offset Raman spectroscopy (SORS) [22] were representative and mature techniques, with commercial instruments in pharmaceuticals and other industries to chemically analyze powder samples. However, the TRS and SORS may have some disadvantages in some applications. Regarding SORS, the optimal spatial offset distance needs to be found for every detection. Furthermore, the packaging is easily damaged because of the high-power laser density. Regarding TRS, the sample needs to be completely taken out before the detection. In addition, the laser light source and detector have opposite positions. it is inconvenient that the portable device was realized.

As mentioned above, some methods have been used to improve the detection sensitivity for powder samples. To further explore a simple but effective method, quartz tube enhanced Raman spectroscopy was proposed in this paper. The feasibility of the technique was demonstrated by combining theoretical analysis and experimental research. The advantages of this method can be briefly summarized. First, the method has a simple structure and high signal collection efficiency. Second, the depth and position of detection can be flexibly changed according to requirements by this technology. Third, it can easily be extended to the fluorescence spectrum detection of powder samples.

2 MTHODS AND EXPERIMENTS

The power emitted by a Raman line of powder material is given by the product of the effective volume of light interacting with the sample, the number density of the emitting molecules, the Raman cross-section for that line, the laser intensity and the excited volume, etc. this is given by [23]:

$$I_i = k\Omega \frac{\partial \sigma}{\partial \Omega} n_i V I_0$$

Where k is the scattering coefficient, Ω is the solid angle of signal collection, V is the effective volume of light interacting with the sample, $\frac{\partial \sigma}{\partial \Omega}$ is the differential scattering cross-section, n_i is the number density of the emitting molecules, I_0 is excitation light power. As described above, the intensity of the Raman signal can be enhanced by increasing the power of the excitation light, effective volume V of the laser in the sample, and the collection solid angle Ω. About the proposed method, the effective volume V ("volume-excitation") was increased compared with the traditional method.

Kubelka-Munk theory in a one-dimensional approximation could be used to study the coupling of laser radiation into turbid samples [19, 24]. For thicker samples with an infinitely wide slab medium of thickness, only a small fraction of laser radiation will reach the target layer buried deeply in turbid media. Therefore, traditional Raman spectroscopy technology has lower detection sensitivity. In addition, it is difficult to detect the information of powder samples with deep layers and low concentrations for traditional method. About the proposed methods was shown in **Figure 1A**, a quartz tube was inserted into the powder sample to improve the coupling of light into the medium and prevent light energy loss, and multiple scattering of the light within the turbid medium. It is obvious from **Figure 1B** that more photons interacts with the sample and has a deeper penetration depth compared with the traditional method. Therefore, it can improve the detection sensitivity and detect deep-layer samples.

Quartz glass has a silicon dioxide content of up to 99.99% and better optical properties than other materials. It has high transmission in the wavelength range of 200–1,000 nm, which involves ultraviolet to near-infrared light. It has excellent physical properties, including high-temperature resistance and good chemical stability [25]. Therefore, the quartz tube was selected as a medium to guide the light in this study. **Figure 2** shows that the transmission of quartz is up to 93% in our target wavelength range of 785–1,000 nm.

A quartz tube enhanced Raman spectroscopy detection setup was built based on a 785 nm Raman probe (focal length of 7.5 mm). A diode-pumped 785 nm laser with an average power of 300 mW was used as the excitation source. A spectrometer (Ocean Optics-QEPro) was used to collect the Raman signal, and the main specifications were as follows: the spectral resolution is 0.91 nm, and the wavelength range is 650–1,000 nm. A cuvette was used to hold the sample; then, a quartz tube was inserted into the powder sample. The experimental setup and schematic diagram of the method are shown in **Figure 3**. Two groups of quartz tubes (a total of eight types) were used in the experiment; the lengths were 10 and 20 mm, and the inner diameter and outer diameter were 0.6 × 0.9, 1 × 1.3, 1.65 × 1.95, and 2 × 2.4 (mm) respectively. Baking soda powder ($NaHCO_3$, ≥99%) and potassium dihydrogen phosphate powder (KH_2PO_4, ≥99.5%) were used as samples in the experiment.

To prove the signal enhancement effect and practicability of quartz tube Raman spectroscopy technology for powder samples, three experiments were performed in this study. First, the Raman signal enhancement effect of the method for powder samples was studied using eight different sizes of quartz tubes. Second, quartz enhanced Raman spectroscopy technology was used to detect mixed powders. A mixed sample of baking soda and potassium dihydrogen phosphate powder (1:5, weight ratio) was detected by proposed method. Third,

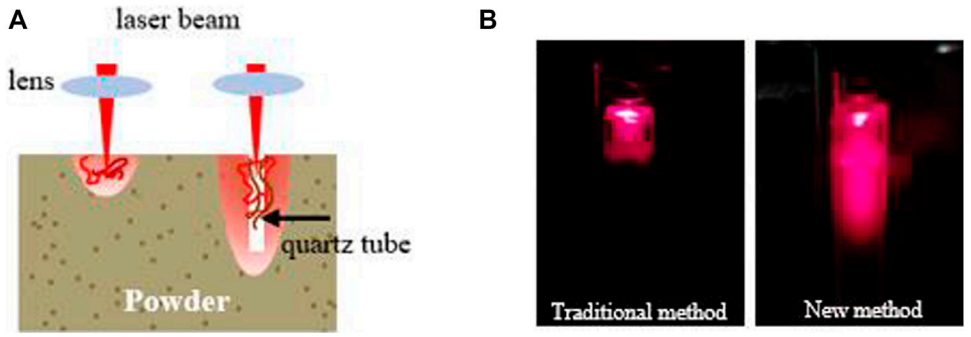

FIGURE 1 | (A) Diagram of two types of detection methods: traditional and Quartz tube enhanced Raman spectroscopy technology and **(B)** Image of scattering from a powder sample acquired using a cell phone camera: traditional and Quartz tube enhanced Raman spectroscopy technology.

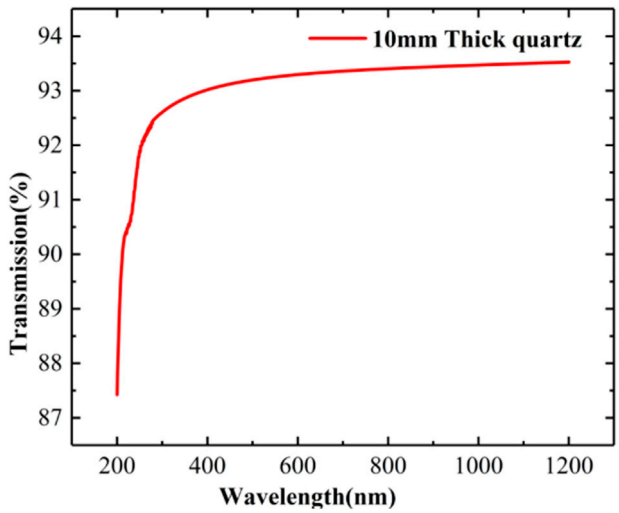

FIGURE 2 | Diagram of the transmittance curve of 10 mm thick quartz [26].

we verified the feasibility of this technology for detecting samples buried under powder. The baking soda powder was placed under a powder sample of potassium dihydrogen phosphate of approximately 6 mm thickness and was detected by Raman probe with a quartz tube (20 × 1.00 × 1.30 mm).

3 RESULTS AND DISCUSSION

3.1 The Method of Spectral Processing

The first step of the data collection was to obtain the background spectra; for the analysis, the dark spectra were subtracted from the raw spectra. The spectral collection parameters were set as follows: the exposure time was 3 s, and the accumulated cycle time was 1. The Raman original spectra of baking soda powder were obtained using traditional Raman spectroscopy technology as shown in **Figure 4A**. HCO_3^- has three Raman peaks, at 689 cm^{-1}, 1,043 cm^{-1} and 1,275 cm^{-1}. The strongest intensity was located at 1,043 cm^{-1} among the three Raman peaks. Therefore, the Raman peak was

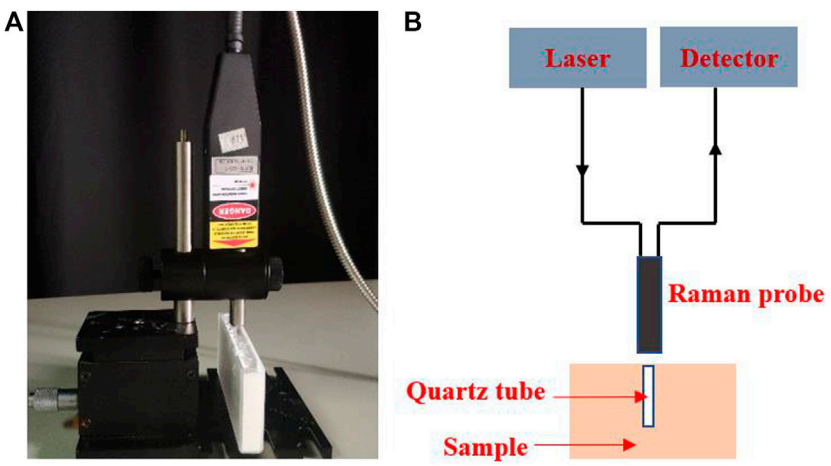

FIGURE 3 | Schematic of the quartz tube enhanced Raman spectroscopy system. **(A)** Experimental setup; **(B)** Schematic diagram.

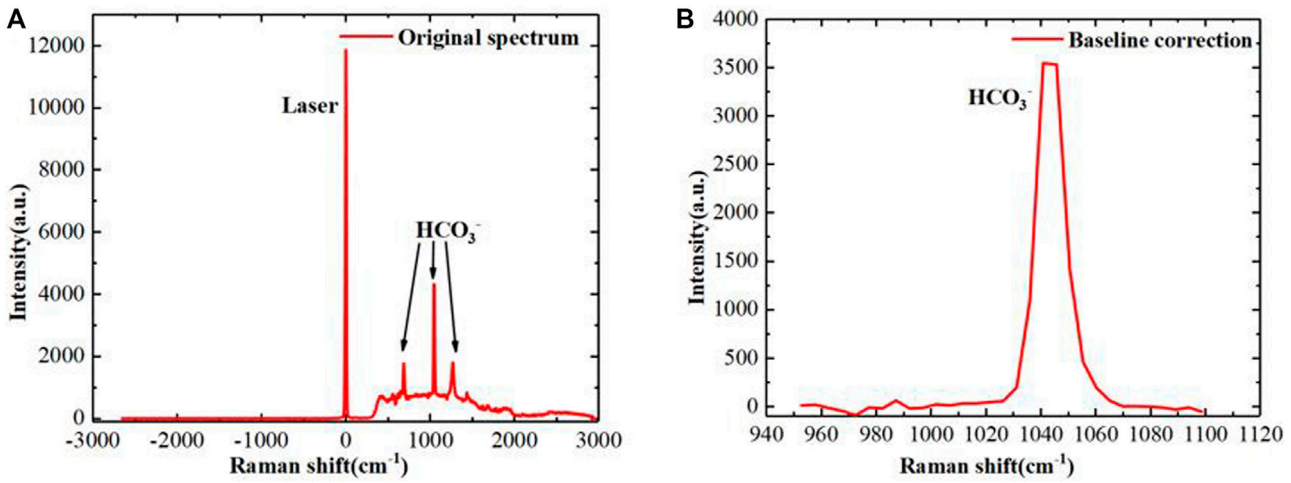

FIGURE 4 | Raman spectrum of baking soda. **(A)** original spectrum; **(B)** Raman spectrum of the baseline correction.

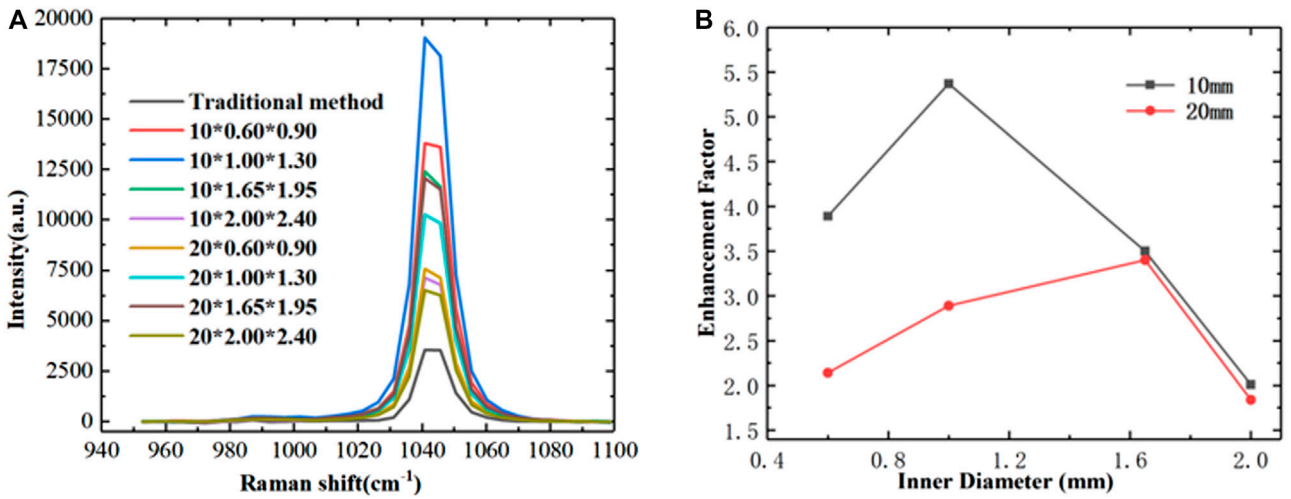

FIGURE 5 | Enhancement effect of different sizes of quartz tubes. **(A)** Raman spectrum of soda powder using different quartz tubes; **(B)** Enhancement factors of different quartz tubes.

used as a reference in the analysis. The Partial Least Squares, (PLS) data processing method was used to eliminate the influence of the baseline [27]. The spectrum range was 950–1,100 cm^{-1}, as shown in **Figure 4B**.

3.2 The Raman Signal With Different Quartz Tubes

The influence of different quartz tubes on the signal enhancement effect was studied by comparing it with the traditional method. The data processing method was identical to the aforementioned method. The enhancement factors of different sizes of quartz

TABLE 1 | Enhancement effect of Raman signals with different sizes of quartz tubes (mm).

Length	Inner diameter	Outter diameter	Enhancement factor
10	0.60	0.90	3.89
	1.00	1.30	5.37
	1.65	1.95	3.50
	2.00	2.40	2.01
20	0.60	0.90	2.14
	1.00	1.30	2.89
	1.65	1.95	3.40
	2.00	2.40	1.84

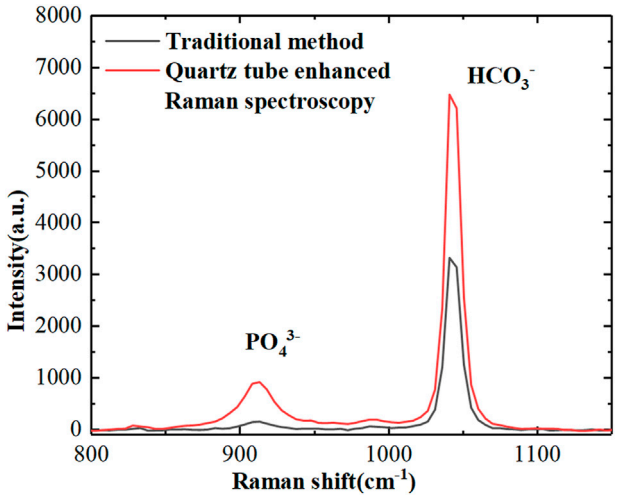

FIGURE 6 | Results comparison of quartz tube enhanced Raman spectroscopy and traditional Raman spectroscopy for mixed samples (1:5, m (PO_4^{3-}):m (HCO_3^-)).

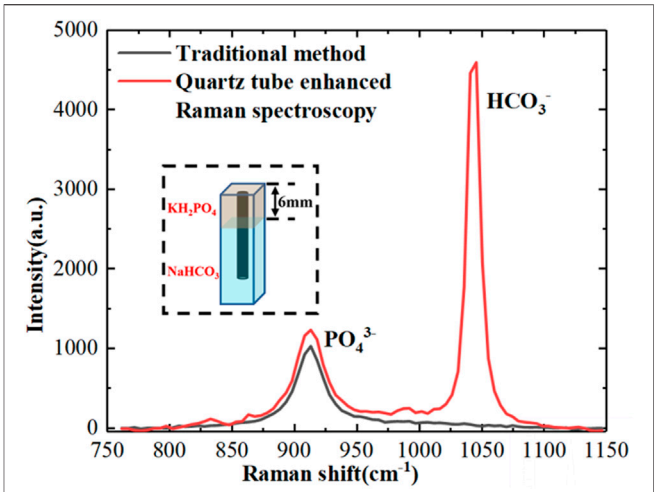

FIGURE 7 | Results comparison of quartz tube enhanced Raman spectroscopy and traditional Raman spectroscopy for powder samples with deep layers.

tubes are shown in **Figure 5**. The amplitude ratio of Raman bands (1,043 cm^{-1} at HCO_3^-) after background correction is defined as enhancement factor.

The quartz tubes of different sizes have obvious enhancements for powder samples as shown in **Figure 5**; **Table 1**. Compared to traditional Raman spectroscopy, the minimum enhancement factor was 1.84 (20*2.00*4.00 mm), and the maximum factor was up to 5.37 (10*1.00*1.30 mm). This result shows that quartz tube enhanced Raman spectroscopy technology has obvious advantages in the detection of powder samples and significantly improves the sensitivity of Raman spectra. For quartz tubes with the same length (10 or 20 mm), the signal enhancement factor does not linearly increase with increasing core diameter. In addition, the 20-mm-long quartz tube had a lower signal enhancement factor than the 10-mm-long tube.

An explanation of the above experimental phenomenon can be given as follows. The quartz tube enhanced Raman scattering spectroscopy method can be decomposed into two processes. First, the laser beam is coupled to the bottom of the quartz tube and interacts with the sample to generate the Raman signal. Most of the laser energy will be reflected during this process [24]. Second, the reflected laser interacts with the powder sample again to generate a Raman signal during the propagation process and collected by the device. This model of this method is similar to transmission Raman spectroscopy technology [19]. About the first process, it is obvious that the Raman signals generated by quartz tubes of different lengths are the same. However, the loss of the Raman signal of quartz tubes with a length of 20 mm more than 10 mm in the propagation process. Regarding the second process, the Raman signal intensity will first increase and then decrease with increasing quartz tube length. Based on the above analysis, it is easy to understand that the signal enhancement factor of quartz tubes of each size with a length of 20 mm was lower than that of tubes 10-mm-long.

3.3 The Ability of the Method to Detect the Mixed Sample

To demonstrate the ability of quartz tube enhanced Raman spectroscopy to detect the mixed samples, soda and potassium dihydrogen phosphate powder at a ratio of 5:1 (weight ratio) was prepared. A quartz tube (10 × 1 × 1.3 mm) was fully inserted into the mixed powder sample; then, the Raman probe was used to detect the Raman signals. Two methods were used to collect the spectrum of the same sample, and the spectra in the range of 800–1,150 cm^{-1} were processed to eliminate the baseline. The results are shown in **Figure 6**.

For the mixed sample, the Raman signal intensity using the proposed method has significantly increased compared to the traditional method from the above results. For traditional Raman spectroscopy technology, it was difficult to identify the spectral peaks because the signal intensity of PO_4^{3-} (913 cm^{-1}) was quite low. However, for quartz tube enhanced Raman spectroscopy, there was a significant enhancement of Raman signal intensity, and the Raman signals of PO_4^{3-} and HCO_3^- were clear. In addition, the two samples had different enhancement factors: the HCO_3^- enhancement factor was 2, but the Raman signal of PO_4^{3-} enhancement was nearly 4 times. The reason for this result was that the different particle sizes, Raman scattering cross-sections and compactness of the mixed sample cause different enhancement factors. This result shows that quartz tube enhanced Raman spectroscopy technology has obvious advantages in the detection of mixed powder samples.

3.4 The Ability of the Method to Detect the Buried Samples

To demonstrate the ability of the proposed method to detect buried samples, a related experiment was performed. A cuvette with dimensions of 10 × 10 × 50 mm was used to hold the sample

in the experiment. The depth of soda powder was approximately 44 mm at the bottom, and the depth of potassium dihydrogen phosphate powder was approximately 6 mm at the top. Two types of methods were used to detect the prepared sample, and the experimental results were further analyzed. A quartz tube (20 × 1 × 1.3 mm) was fully inserted into the prepared powder sample; then, the Raman probe was used to detect the Raman signals. The original spectra are processed to eliminate the baseline (range: 750–1,150 cm^{-1}), and the results are shown in **Figure 7**.

The results show that it was impossible to detect the Raman signal of HCO_3^- at the bottom using traditional Raman spectroscopy technology due to the limited laser penetration ability in the powder sample. However, the Raman signal of HCO_3^- was clear using quartz tube enhanced Raman spectroscopy, because the laser through the quartz tube contacted the buried sample in the deep layer. Therefore, the Raman signal of HCO_3^- (1,043 cm^{-1}) could be clearly observed, and the Raman signal of PO_4^{3-} was also enhanced. The experimental results show that quartz enhanced Raman spectroscopy technology has obvious effects on the detection target powder with the deep layer.

4 CONCLUSION

In summary, quartz tube enhancement Raman spectroscopy technology was reported for the first time in this paper. The influence of different parameters of quartz tubes on Raman signal enhancement was studied. The results show that compared with traditional Raman spectroscopy technology, the maximum enhancement factor of quartz enhancement technology could reach 5.37-fold. In addition, the feasibility of the technology to detect mixed powder and target samples buried in deep layers was validated using related experiments. As a whole, this technology will play an important role in food safety, hazardous chemical detection, drug analysis, etc., expanding the further development of Raman spectroscopy technology.

DATA AVAILABILITY STATEMENT

The original contributions presented in the study are included in the article/Supplementary Material; further inquiries can be directed to the corresponding author.

AUTHOR CONTRIBUTIONS

GS, JL, and YF planned and supervised the experiments, processed the raw data, and wrote and revised the manuscript. GS, ZL, and ZN advised on data processing. All authors contributed to the article and approved the submitted version.

FUNDING

This work was supported by the National Natural Science Foundation of China (61875207).

REFERENCES

1. Ma Y, He Y, Tong Y, Yu X, Tittel FK. Quartz-tuning-fork Enhanced Photothermal Spectroscopy for Ultra-high Sensitive Trace Gas Detection. *Opt Express* (2018) 26(24):32103. doi:10.1364/OE.26.032103
2. Huang F, Tian Y, Li Y, Ye W, Lu Y, Guo J, et al. Normalization of Underwater Laser-Induced Breakdown Spectroscopy Using Acoustic Signals Measured by a Hydrophone. *Appl Opt* (2021) 60(6):1595–602. doi:10.1364/AO.413853
3. Lang Z, Qiao S, Ma Y. Acoustic Microresonator Based In-Plane Quartz-Enhanced Photoacoustic Spectroscopy Sensor with a Line Interaction Mode. *Opt Lett* (2022) 47(6):1295. doi:10.1364/OL.452085
4. Das RS, Agrawal YK. Raman Spectroscopy: Recent Advancements, Techniques and Applications. *Vibrational Spectrosc* (2011) 57:163–76. doi:10.1016/j.vibspec.2011.08.003
5. Qin J, Kim MS, Chao K, Gonzalez M, Cho B-K. Quantitative Detection of Benzoyl Peroxide in Wheat Flour Using Line-Scan Macroscale Raman Chemical Imaging. *Appl Spectrosc* (2017) 71:2469–76. doi:10.1177/0003702817706690
6. Almaviva S, Chirico R, Nuvoli M, Palucci A, Schnürer F, Schweikert W. A New Eye-Safe UV Raman Spectrometer for the Remote Detection of Energetic Materials in Fingerprint Concentrations: Characterization by PCA and ROC Analyzes. *Talanta* (2015) 144:420–6. doi:10.1016/j.talanta.2015.06.075
7. Wang H, Williams L, Hoe S, Lechuga-Ballesteros D, Vehring R. Quantitative Macro-Raman Spectroscopy on Microparticle-Based Pharmaceutical Dosage Forms. *Appl Spectrosc* (2015) 69:823–33. doi:10.1366/14-07812
8. Liu M, Mu Y, Hu J, Li J, Zhang X. Optical Feedback for Sensitivity Enhancement in Direct Raman Detection of Liquids. *J Spectrosc* (2021) 2021:1–7. doi:10.1155/2021/5588417
9. Kumar V, Holtum T, Sebena D, Giese M, Voskuhl J, Schlücker S. Ultraviolet Resonance Raman Spectroscopy with a Continuously Tunable Picosecond Laser: Application to the Supramolecular Ligand Guanidiniocarbonyl Pyrrole (GCP). *Spectrochimica Acta A: Mol Biomol Spectrosc* (2021) 250:119359. doi:10.1016/j.saa.2020.119359
10. Choi JH, Choi M, Kang T, Ho TS, Choi SH, Byun KM. Combination of Porous Silk Fibroin Substrate and Gold Nanocracks as a Novel SERS Platform for a High-Sensitivity Biosensor. *Biosensors* (2021) 11:441. doi:10.3390/bios11110441
11. Li Z, Li C, Yu J, Li Z, Zhao X, Liu A, et al. Aluminum Nanoparticle Films with an Enhanced Hot-Spot Intensity for High-Efficiency SERS. *Opt Express* (2020) 28:9174. doi:10.1364/OE.389886
12. Tarun A, Hayazawa N, Yano T-A, Kawata S. Tip-heating-assisted Raman Spectroscopy at Elevated Temperatures. *J Raman Spectrosc* (2011) 42:992–7. doi:10.1002/jrs.2820
13. Matousek P. Raman Signal Enhancement in Deep Spectroscopy of Turbid Media. *Appl Spectrosc* (2007) 61:845–54. doi:10.1366/000370207781540178
14. Misra AK, Sharma SK, Kamemoto L, Zinin PV, Yu Q, Hu N, et al. Novel Micro-cavity Substrates for Improving the Raman Signal from Submicrometer Size Materials. *Appl Spectrosc* (2009) 63:373–7. doi:10.1366/000370209787598988
15. Larkin PJ, Santangelo M, Šašić S. Internal Multiple-Scattering Hole-Enhanced Raman Spectroscopy: Improved Backscattering Fourier Transform Raman Sampling in Pharmaceutical Tablets Utilizing Cylindrical-Conical Holes. *Appl Spectrosc* (2012) 66:892–902. doi:10.1366/12-06677
16. Lohumi S, Kim MS, Qin J, Cho B-K. Improving Sensitivity in Raman Imaging for Thin Layered and Powdered Food Analysis Utilizing a Reflection Mirror. *Sensors* (2019) 19:2698. doi:10.3390/s19122698

17. Lednev VN, Sdvizhenskii PA, Grishin MY, Filippov MN, Shchegolikhin AN, Pershin SM. Laser Crater Enhanced Raman Spectroscopy. *Opt Lett* (2017) 42: 607. doi:10.1364/OL.42.000607
18. Lednev VN, Sdvizhenskii PA, Grishin MY, Fedorov AN, Khokhlova OV, Oshurko VB, et al. Optimizing Laser Crater Enhanced Raman Scattering Spectroscopy. *Spectrochimica Acta Part A: Mol Biomol Spectrosc* (2018) 196: 31–9. doi:10.1016/j.saa.2018.01.070
19. Zhao J. Analytical Solution to the Depth-Of-Origin Profile of Transmission Raman Spectroscopy in Turbid Media Based on the Kubelka-Munk Model. *Appl Spectrosc* (2019) 73:1061–73. doi:10.1177/0003702819845914
20. Vargas WE, Niklasson GA. Applicability Conditions of the Kubelka-Munk Theory. *Appl Opt* (1997) 36:5580. doi:10.1364/AO.36.005580
21. Matousek P. Deep Non-invasive Raman Spectroscopy of Living Tissue and Powders. *Chem Soc Rev* (2007) 36(8):1292–304. doi:10.1039/b614777c
22. Olds WJ, Sundarajoo S, Selby M, Cletus B, Fredericks PM, Izake EL. Noninvasive, Quantitative Analysis of Drug Mixtures in Containers Using Spatially Offset Raman Spectroscopy (SORS) and Multivariate Statistical Analysis. *Appl Spectrosc* (2012) 66(5):530–7. doi:10.1366/11-06554
23. Yang DW. *Study of Cavity Enhanced Raman Spectroscopy (CERS) for the Detection of CO_2 and HCO_3^- Dissolved in Seawater [D]*. Qing Dao: China: Ocean University of China (2018).
24. Schrader B, Bergmann G. Die Intensität des Ramanspektrums polykristalliner Substanzen. *Z Anal Chem* (1967) 225:230–47. doi:10.1007/bf00983673
25. Englisch W. Quartz Glass for Space Optical Applications[C]. *Proc SPIE* (1989) 1118:42. doi:10.1117/12.960946
26. THORLABS. *UV Fused Silica High-Precision Windows* (2022). Available from: https://www.thorlabschina.cn/newgrouppage9.cfm?objectgroup_id=3983 (Accessed January 5, 2022).
27. Yi C, Lv Y, Xiao H, Ke K, Yu X. A Novel Baseline Correction Method Using Convex Optimization Framework in Laser-Induced Breakdown Spectroscopy Quantitative Analysis. *Spectrochimica Acta B: At Spectrosc* (2017) 138:72–80. doi:10.1016/j.sab.2017.10.014

Conflict of Interest: The authors declare that the research was conducted in the absence of any commercial or financial relationships that could be construed as a potential conflict of interest.

frontiers | Frontiers in Physics

TYPE Original Research
PUBLISHED 14 July 2022
DOI 10.3389/fphy.2022.964140

OPEN ACCESS

EDITED BY
Yufei Ma,
Harbin Institute of Technology, China

REVIEWED BY
James Barefield,
Los Alamos National Laboratory (DOE), United States
Lei Zhang,
Shanxi University, China

*CORRESPONDENCE
Dan Zhang,
danzhang19@mails.jlu.edu.cn
Anmin Chen,
amchen@jlu.edu.cn

SPECIALTY SECTION
This article was submitted to Optics and Photonics, a section of the journal Frontiers in Physics

RECEIVED 08 June 2022
ACCEPTED 28 June 2022
PUBLISHED 14 July 2022

CITATION
Wang Y, Gao H, Hong Y, Zhang D, Chen A and Jin M (2022), Influence of distance from lens to sample surface on spectral sensitivity of femtosecond laser-induced breakdown spectroscopy with NaCl water film.
Front. Phys. 10:964140.
doi: 10.3389/fphy.2022.964140

Influence of distance from lens to sample surface on spectral sensitivity of femtosecond laser-induced breakdown spectroscopy with NaCl water film

Ying Wang[1], Heyan Gao[1], Yanji Hong[1], Dan Zhang[2,3]*, Anmin Chen[2]* and Mingxing Jin[2]

[1]State Key Laboratory of Laser Propulsion and Application, Space Engineering University, Beijing, China, [2]Institute of Atomic and Molecular Physics, Jilin University, Changchun, China, [3]Key Laboratory for Microstructural Material Physics of Hebei Province, School of Science, Yanshan University, Qinhuangdao, China

Increasing the emission intensity of laser-induced breakdown spectroscopy (LIBS) is an effective way to improve the sensitivity of LIBS technology to elements analysis in liquid samples. In this work, the influence of the distance from lens to sample surface (DFLS) on the spectral emission of femtosecond laser-induced plasma of NaCl water film was studied by measuring Na atomic line. The results showed that the emission intensity of the spectral line presented the phenomenon of double peaks with an increase in the DFLS. The position for the highest spectral intensity was not geometric focal point of focusing lens, but was located in front of the geometric focal point. In addition, we carried out quantitative analysis on Na element with different concentrations, showing a calibration curve of Na element, and calculating limit of detection (LOD) and relative standard deviation (RSD) for different DFLSs. Subsequently, the changes in the LOD and RSD with the DFLS are discussed. With the increase of the DFLS, the LOD and RSD were greatly reduced. At the DFLS of 99.0 mm, the line intensity was highest, and the LOD and RSD were better. Therefore, it can be confirmed that femtosecond LIBS of water film can be optimized by changing the DFLS, the experiment shows great potential in real-time water quality monitoring.

KEYWORDS

laser-induced breakdown spectroscopy, femtosecond laser, distance from lens to sample surface, water film, NaCl

1 Introduction

Laser-induced breakdown spectroscopy (LIBS) is an analysis technique based on atomic emission spectroscopy of laser-induced plasma [1–5]. After decades of development, LIBS technology has become a very popular and effective element analysis method [6–8]. However, this technology is mainly for solid samples and gas samples, while the analysis of liquid samples is still rarely reported. In recent years, the LIBS technology is extensively used to the rapid chemical element analysis of liquids, which has many potential application prospects, including water quality monitoring [9, 10], environmental monitoring [11, 12], food industry quality monitoring [13–15], medical monitoring [16–18], etc. But, the use of LBS technology to detect liquid samples faces a series of problems, for example, dissolved gas, particulate material and bubbles generated by previous laser pulse can cause the laser beam to fail to be focused; the liquid evaporation causes the loss of laser energy, which reduces the availability of plasma excitation energy; high local density in the liquid leads to rapid quenching, which prohibits time-selective detection, etc. Due to the inherent problems mentioned above, LIBS technology has not fully developed its potential in the field of liquid sample analysis. In order to overcome these drawbacks, researchers are trying to find appropriate experimental methods and sample preparation methods to improve the stability and analytical sensitivity of liquid sample.

Enhanced laser-induced plasma emission intensity is the main way to make up for these disadvantages of LIBS technology. Based on solid samples, researchers believe that many methods, including double-pulse [19], spatial confinement [20–22], magnetic confinement [23], spark discharge enhancement [24–27], increasing sample temperature [28–31], changing the distance from lens to sample surface (DFLS) [32–34], can improve the stability and analytical sensitivity of liquid samples. Among them, the double-pulse method is frequently applied to the detection of liquid samples. Virendra et al reported that the characteristic spectral line intensity of double-pulse excitation was enhanced by at least 6 times compared with single pulse LIBS for liquid samples [35]. Kheireddine et al explored the basic characteristics of plasma generated by double-pulse lasers [10], and the enhancement mechanism of double-pulse LIBS was due to the prolongation of the plasma lifetime. They found that the application of the double-pulse method in the liquid samples had achieved significant results. In addition to the double-pulse method, spatial confinement, and magnetic confinement methods are great tools to improve the detection sensitivity of samples. However, in view of the instability of liquid samples, these methods are more difficult to implement. In view of this, the change in the DFLS is flexible and controllable method to improve the spectral intensity of laser-induced plasma, and is almost not limited by the instability of liquid samples. Changing the DFLS can result in a difference in the laser fluence, which has the great impacts on the properties and morphologies of the plasma, and further affecting the plasma emission [36]. In summary, the influence of the DFLS on the analysis of elements in the liquid samples is still a hot topic that worthy of further study and discussion.

For liquid samples, liquid splashes and ripples formed by laser ablation hinder the effective detection of plasma emission. Moreover, the optical components used in the experiment are contaminated by the splashes, which affect the reliability of the LIBS detection results. In order to overcome these problems, some researchers have proposed the following methods: laser ablation of laminar flow with sheath or carrier gas [16, 37], laser ablation droplets [38], laser ablation aerosol [39], laser ablation liquid jet [40–42], convert liquid phase to solid phase [43]. Among these sampling methods, the laminar flow technique of sheath or carrier gas has the higher measurement accuracy, but the operation is more difficult. In contrast, the liquid jet method shows some advantages, viz. simple operation and good measurement accuracy. Some research groups have proved that the use of jet technology could improve the sensitivity of LIBS technology to detect elements in liquids. For example, Yaroshchyk et al compared the laser-induced breakdown spectra of liquid jets and stationary liquid surfaces [44]. Under the same conditions, the limit of detection obtained by the jet method was 4 times lower than that obtained by a static liquid. Nevertheless, we considered that the volume of the interaction between the laser and the liquid substrate was a key factor affecting detection sensitivity. The use of a thinner liquid film can reduce the generation of droplets at the plasma emission site and further improve the detection sensitivity of LIBS.

In the above-discussed reports on liquid samples, nanosecond lasers are usually used as the main laser light source, but another way to improve sensitivity is to use femtosecond laser pulses to excite the plasma on the sample surface [45–47]. In contrast, the mechanical and thermodynamic parameters of femtosecond laser breakdown plasma are very different from those of nanosecond laser, which is why femtosecond LIBS has higher sensitivity [48, 49]. So far, the investigations on the femtosecond LIBS technology of liquid sample in film form are relatively lacking. In this paper, we investigated the influence of the DFLS on the spectral emission of NaCl plasma of femtosecond laser excitation in the atmosphere, and the variation of spectral line intensity with the DFLS for different NaCl concentrations was discussed. The trend in the limit of detection (LOD) and relative standard deviation (RSD) with the DFLS were obtained by measuring Na (I) spectral line. Based on these results, it is concludes that there is an appropriate DFLS that can help to improve the detection sensitivity of LIBS technology for quantitative analysis of specific elements in the liquid samples for femtosecond LIBS.

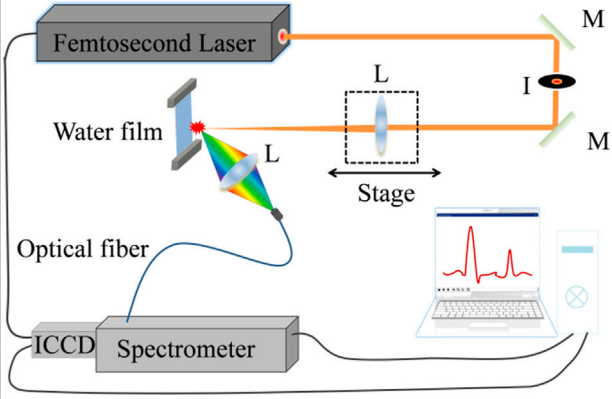

FIGURE 1
Experimental setup including mirror **(M)**, iris **(I)**, lens **(L)**, and intensified CCD (ICCD).

2 Experimental apparatus

2.1 Formation of NaCl water film

For the detection of liquid samples by LIBS technology, the sampling methods for obtaining spectral information mainly include static liquid, flowing droplets, and conversion of liquid to solid samples. The liquid jet method stands out from the above methods by reducing surface fluctuations and increasing the repetition rate, but the jet method still has the disadvantage, that is, the laser focus point cannot be determined on the liquid surface. Hence, we improved the liquid sampling method, and customized the water film forming device based on the liquid jet. Place two aluminum wires with a diameter of 0.2 mm and set an interval of 4.0 mm on both sides of the water nozzle, adjust the water flow rate to 40 ml/min, and let the NaCl solution form a stable flowing water film with thickness of about 0.2 mm under the action of gravity and surface tension. We adjust the distance between the laser focus point and the nozzle to be 2/3 of the length of the water film, which ensures the stability of the laser penetrating the water film. Adopting this sampling method can greatly reduce liquid splashing, avoid splashing droplets from polluting the optical lens, and ensure the high stability of the spectrum. However, it must be pointed out that the ablated plasma vaporizes the liquid and generates mist or droplets when the laser excited water film. Only after a small amount of splashing, the generated mist or droplets will cause more intense plasma emission [50].

2.2 Data acquisition device

The principle diagram of the experimental device is shown in Figure 1. The LIBS system was mainly composed of a laser and a spectrometer. In detail, an one-box ultrafast Ti:Sapphire amplifier (Coherent Libra) was used as laser light source to generate plasma. The output pulse wavelength of the femtosecond laser system was 800 nm, the pulse width was 50 fs, the laser energy was 2.9 mJ, and the maximum pulse repetition frequency was 1 kHz. The laser pulse was first transferred to the direction perpendicular to the sample through two mirrors, and then a quartz lens with a focal length of 100 mm was used to focus the beam onto the sample surface. In the experiment, the samples were NaCl solutions with different concentrations, and the concentrations were shown in Table 1. A plano-convex lens used to focus the beam was placed on a one-dimensional motorized translation stage (Zolix Instruments) to change the DFLS. The optical emission of the plasma generated by the laser focusing sample was collected by a lens (75 mm focal length and 50 mm diameter) that was 45° with the laser beam, and was focused into an optical fiber. The optical signal was transmitted to a spectrometer (Spectra Pro 500i, PI Acton) with three gratings (150, 1,200, and 2,400 line per mm) through the optical fiber, the grating used in the experiment was 1,200 line per mm, in which the spectral resolution was 0.04 nm. An intensified charge-coupled device (ICCD, PI-MAX4, Princeton Instruments) with 1,024 × 1,024 pixels was used to detect the dispersed light by the spectrometer. The ICCD chip was "KAI 1024 × 1,024" from Eastman Kodak Company. The ICCD worked in gate mode. Before the experiment, the ICCD chip was cooled to −20°C. The synchronization delay generator of the femtosecond laser triggered the ICCD to synchronize the delay between the laser pulse and the spectral signal. In order to reduce the interference of background emission, the delay time of ICCD was set to 0.5 μs and the gate width was fixed as 5 μs. The working mode of the femtosecond laser system was divided into single-shot and continuous-shot modes. In the current experiment, the single-shot working mode was adopted. The data output by ICCD was recorded by a computer. Each data was a result of 10 laser cumulative emission, 20 spectra were collected with each solution concentration. The whole experiment was carried out in a standard atmospheric pressure environment with an ambient temperature of 22°C and an air humidity of 40%.

3 Results and discussion

3.1 Effect of solution concentration on spectral intensity

In the beginning, adjusting the delay time and pulse width of the ICCD, it is expected to collect characteristic spectrum. When the NaCl film is at the focal point and the solution concentration is 4.00 μg/ml, the emission of Na atomic line generated by femtosecond laser will be detected and recorded. In order to increase the detection sensitivity and reduce the standard

TABLE 1 Concentration of Na element in NaCl solution.

Sample No	1#	2#	3#	4#	5#	6#	7#	8#
Concentration (μg/mL)	4.00	3.60	2.70	2.00	1.50	1.00	0.50	0.25

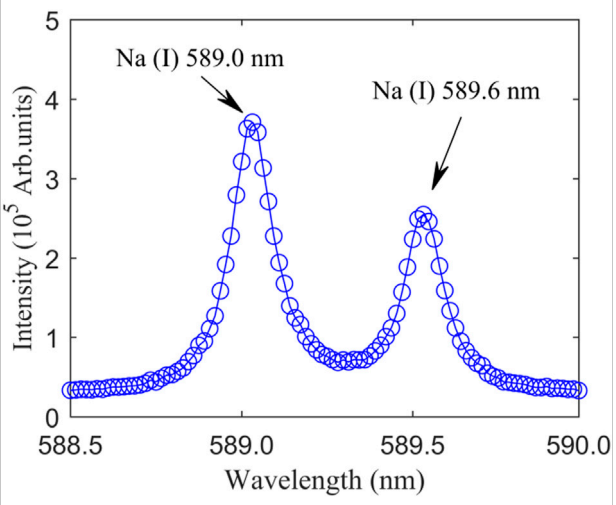

FIGURE 2
Typical emission spectrum of NaCl water solution plasma. The NaCl concentration is 4.00 μg/ml. The NaCl film is located at the focal point (DFLS = 100 mm).

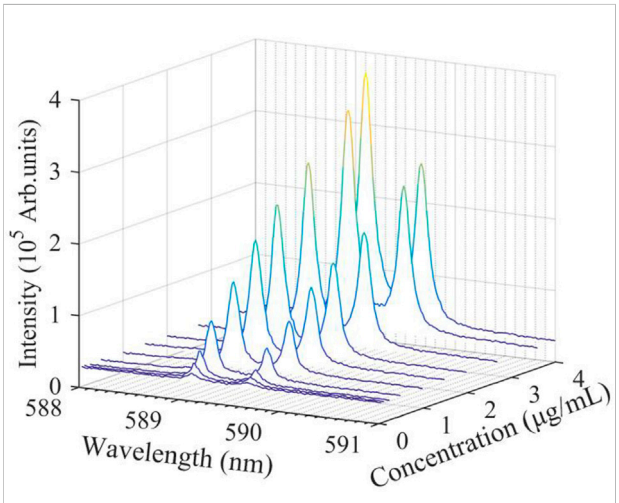

FIGURE 3
Evolution of Na atomic lines from laser-induced plasma with NaCl concentration of. The NaCl film is located at the focal point plane (DFLS = 100 mm).

deviation, we collected 10 spectrums of water film plasma and averaged them, as shown in Figure 2. It can be seen from Figure 2 that there are two obvious peaks in the wavelength range from 588.5 to 590.0 nm, namely Na (I) 589.0 nm and Na (I) 589.6 nm. According to the NIST atomic spectra database, the spectral lines of these two wavelengths are produced by $2p^6 3s$ (^{2}S)→$2^{p6}3p$ ($^2P^0$) transitions. The same element corresponds to different center wavelengths, and the difference is mainly due to the difference in the angular momentum of the upper and lower electron orbits and the difference in excited state energy levels during the transition.

We measured the emission line intensity of Na (I) in NaCl salt solution with different Na Cl concentrations (see Table 1), and obtained the dependence of spectral intensity on the concentration of NaCl solution, as shown in Figure 3. The DFLS was fixed at 100 mm (the sample film was at the focal point of the focusing lens). It can be observed from Figure 3 that the spectral line intensities of the Na (I) 589.0 nm and Na (I) 589.6 nm increase with increasing the concentration of NaCl. When the concentration is 0.25 μg/ml, the spectral line intensity of the element is weakest, and the signal-to-background ratio has a low value. The laser pulse power density must exceed the breakdown threshold of the sample before the laser interacts with the sample, while the plasma characteristics and laser energy breakdown threshold depend on the mass of the solute in the solution [51]. In the current experiment, when a high-power laser is focused on the surface of high-concentration NaCl water film, the sample is more likely to release a large number of atoms, ions and electrons. At this time, free electrons in the reverse bremsstrahlung emission greatly increase the energy of the absorbed photons themselves, resulting in an increase in the breakdown of the liquid sample, so the higher NaCl concentration will emit the stronger characteristic spectrum.

3.2 Effect of distance from lens to sample surface on spectral intensity

The laser is focused on the surface of the liquid sample, forming plasma plume. A small change in the DFLS will cause the absolute emission intensity of the plasma to change. In many published papers [52, 53], the DFLS was usually selected to be shorter than the focal length of focusing lens, which can effectively avoid air breakdown before the laser pulse reaches the sample surface. The concentration of NaCl solution was fixed at 4.00 μg/ml to ensure that the maximum content of Na in the plasma, which is convenient for exploring the influence of the DFLS on the spectral intensity of the liquid plasma. It can be clearly observed from Figure 4 that the intensity of the spectral

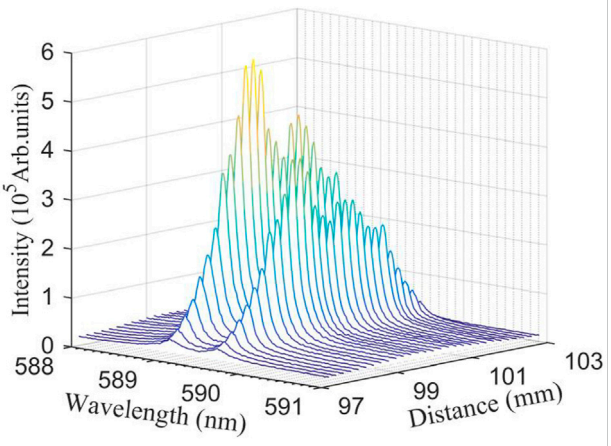

FIGURE 4
Evolution of spectral emission from laser-induced plasma with NaCl water film with DFLS. The NaCl concentration is 4.00 μg/ml.

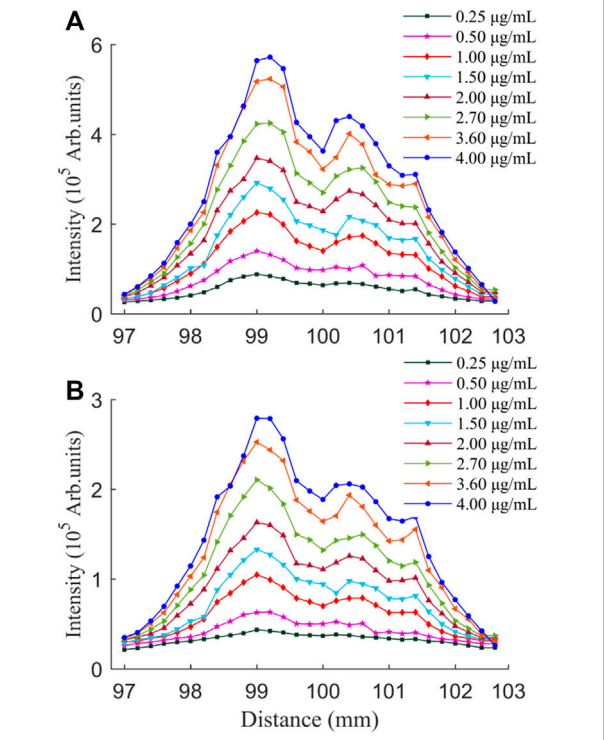

FIGURE 5
Evolution of emission peak intensities for Na (I) 589.0 nm **(A)** and 589.6 nm **(B)** with DFLS for different NaCl concentrations.

line increases with the increase of the DFLS, and along the direction of the femtosecond laser, the maximum value of emission intensity appears before the focus point, approximately at 99.0 mm. When the DFLS continues to increase to about 101.0 mm, another peak of emission intensity appears, but it is lower than the peak intensity before the focal point. In essence, the laser spot on the sample surface depends on the change in the DFLS. The size of the laser spot directly affects the laser fluence on the sample surface, and controls the coupling between laser and sample, resulting in a change in the emission intensity of laser-induced plasma [54]. In the experiment, as the DFLS increases from 97.0 to 99.0 mm, the laser spot gradually decreases and the laser fluence gradually increases, resulting in a significant increase in the spectral intensity of Na (I). The influence of the DFLS on the spectral intensity at different NaCl concentrations is discussed in detail below.

In order to study whether the influence of the DFLS on the plasma spectral intensity at low NaCl concentration is consistent with that at high NaCl concentration, we discussed the evolution of Na (I) 589.0 and 589.6 nm line intensities with the DFLS at different NaCl concentrations, as shown in Figure 5. For any NaCl concentration, the influence of the DFLS on the intensity of the characteristic spectral line is consistent. Moreover, it can be seen more intuitively from Figure 5 that, with the increase of the DFLS, the spectral intensity presents a double emission peaks. The two peaks of laser-induced plasma intensity can be obtained when the DFLS are 99.0 and 100.6 mm but the peak intensity value is not the same. This phenomenon is different from nanosecond LIBS. For nanosecond LIBS, the spectra before and after the focal point show a symmetrical distribution [55]. There is another phenomenon: when the sample surface is at the geometric focal point, the intensity of the spectral line is not maximum value. The main reason is the plasma shielding effect [54]. Different from nanosecond LIBS, the laser excitation source used in the experiment was femtosecond laser, and its nonlinear effect cannot be ignored. The nonlinear effect of ultra-short pulses will produce self-focusing, self-defocusing and re-focusing. The paper by Li et al stated that the focal length of the focusing lens may be shortened by the optical Kerr self-focusing effect [56]. Therefore, the first laser focusing position appeared in front of the focal point and generated stronger laser-induced plasma emission. As the DFLS increased, the plasma self-defocusing effect generated by tunneling or multi-photon ionization caused the plasma emission to decrease. Continue to increase the DFLS, the optical Kerr effect was still stronger than the defocusing effect of the plasma, so the re-focusing effect occurred, which is the reason for another peak intensity after the geometric focal point.

3.3 Effect of distance from lens to sample surface on quantitative analysis

Like most analytical methods, the quantitative analysis of LIBS is inseparable from the use of calibration curves. Before

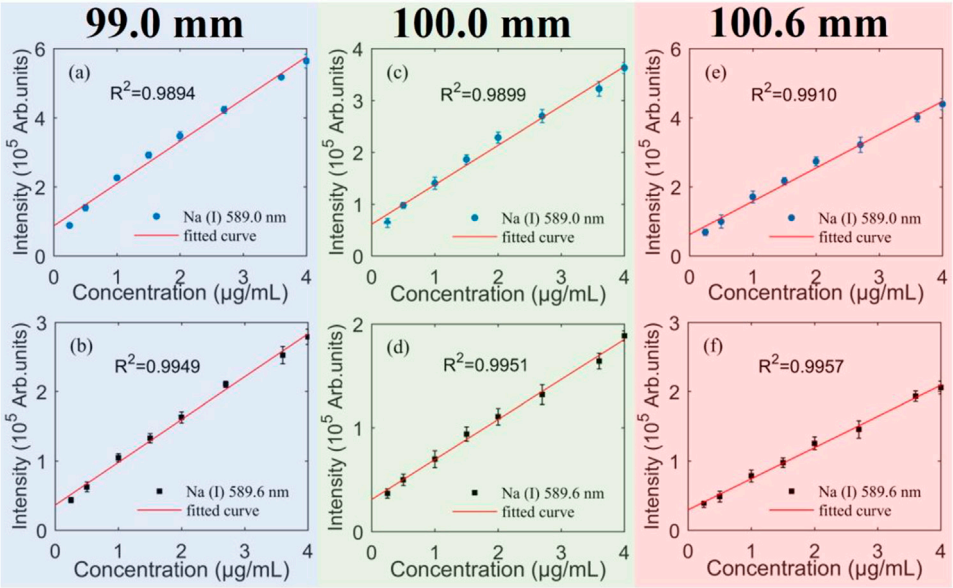

FIGURE 6
Calibration curves for Na (I) 589.0 nm (a, c, and e) and Na (I) 589.6 nm (b, d, and f) for three DFLSs. The DFLSs are 99.0 mm **(A,B)**, 100.0 mm **(C,D)**, and 100.6 mm **(E,F)**, respectively.

calibrating the element to be measured, it is assumed that the concentration of the element to be measured in the plasma is consistent with the element concentration in the corresponding sample. During the calibration and detection process, the calibration of Na element is achieved, when all parameters that affect the plasma characteristics are constant. For the purpose of increase the credibility of the calibration method, each data point collected was a result of 10 laser accumulations, and 25 spectra were collected at each NaCl concentration. Therefore, the calibration curve shown in Figure 6 is an average of multiple repeated tests. The figure shows the calibration curves of Na (I) at different DFLSs, three typical DFLSs are 99.0 mm (a and b), 100.0 mm (c and d), and 100.6 mm (e and f), respectively. And Figure 6 (a, c, and e) show the calibration curve of Na (I) 589.0 nm, and Figure 6 (b, d, and f) show the calibration curve of Na (I) 589.6 nm. In Figure 6, the linear correlation coefficient (R^2) of Na (I) 589.0 nm is greater than 0.98, and the R^2 of Na (I) 589.6 nm is greater than 0.99. Theoretically, if the measured spectral intensity is stable, the linear correlation coefficient between its intensity and concentration is close to 1. It indicates that the experimental method of femtosecond laser-excited NaCl thin film has a better stability in detecting the content of Na element for aqueous solution.

In the following content, we discussed the key indicators for the quantitative analysis of LIBS technology: LOD of element, which is usually calculated from the data extracted from the calibration curve. The LOD represents the lowest concentration of an element detected in the experiment. According to 3σ-IUPAC, the LOD of a certain element is the concentration for three times of the background standard

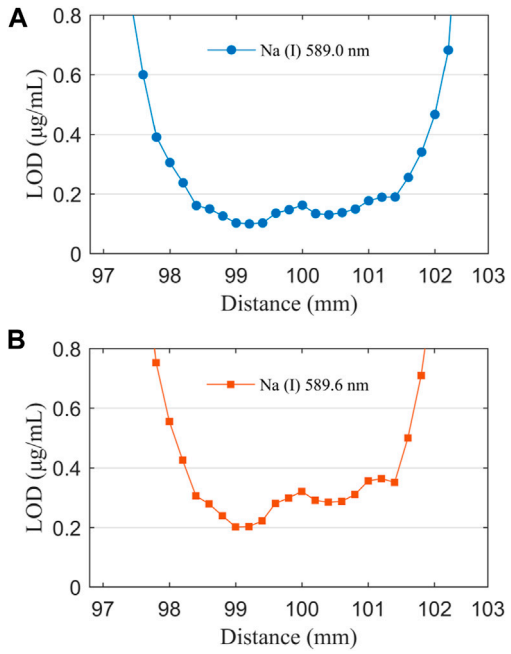

FIGURE 7
Evolution of LOD of Na (I) 589.0 nm **(A)** and Na (I) 589.6 nm **(B)** with DFLS.

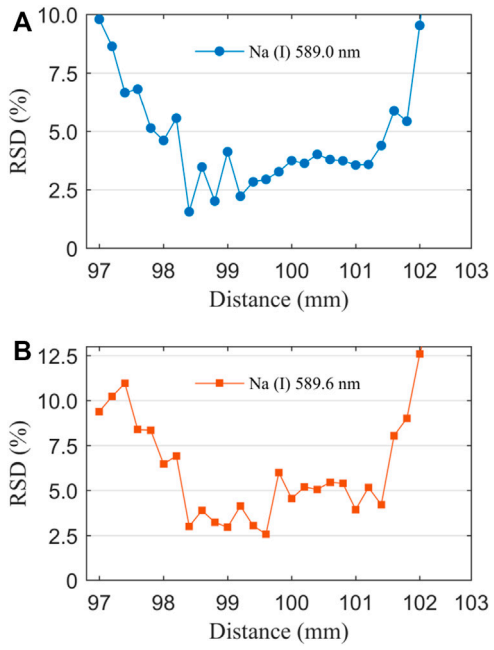

FIGURE 8
Evolution of RSD with DFLS for Na (I) 589.0 nm **(A)** and 589.6 nm **(B)**, the solute concentration is 4.00 μg/ml.

deviation of the line intensity σ: LOD = $3\sigma/S$, here S is the slope of the calibration curve of a characteristic atomic line. Figure 7 shows the evolution of the LOD of Na (I) with the DFLS. It is obvious from figure that the change in the DFLS has a positive effect on the reduction in the LOD. With the increase of the DFLS, the LOD decreased significantly. The LOD of Na (I) has a lower value in the range of the DFLS from 99.0 to 101.0 mm. At 99.0 mm, the LOD has the lowest value. Referring to the evolution of emission intensity with the DFLS in Figure 5, the maximum plasma emission intensity can be obtained at 99.0 mm, and the corresponding LOD has the minimum value. The reduction in the LOD further proves that selecting a optimized DFLS is an effective way to improve detection sensitivity.

3.4 Effect of distance from lens to sample surface on signal stability

Apart from this, the signal stability is an important parameter that affects the reliability of LIBS in detecting element concentrations in liquid samples. It is actually related to the RSD of a characteristic spectral line in repeated measurement spectra [57]. Laser-induced plasma is used as a pulse excitation source to atomize and ablate the sample. The instability between different excitation points as well as the instability of repeated laser pulses will limit the repeatability of detection [58]. Therefore, understanding the influence of the DFLS on signal stability is necessary to know the accuracy of the experiment. At a solute concentration of 4.00 μg/ml, the RSD as a function of the DFLS is presented in Figure 8. Similar to the change in the LOD, the RSD shows a trend that first decreases, stabilizes, and finally increases with the increase of the DFLS. In the range of the DFLS from 99.0 to 101.0 mm, the RSD is low, and fluctuating between 2.5 and 5.0%. In this study, the lower RSD further proves that the experimental method of femtosecond laser-induced NaCl thin film has better spectral stability at appropriate DFLS.

4 Conclusion

In this work, femtosecond LIBS had been used to detect specific element in aqueous solution. To date, the main difficulties affecting the application of LIBS technology in liquid samples are liquid splashing and low signal stability. In order to overcome this problem, we used femtosecond laser excitation source and changed the sampling method of the liquid sample. We customized the water film based on the liquid jet. The purpose is to make the sample form a stable flowing film, stabilizing the liquid; and femtosecond laser may minimize liquid splashing. Moreover, we studied the influence of the DFLS on the detection ability for NaCl aqueous solution. The focal length of the focusing lens was 100 mm. With the increase of the DFLS, the plasma emission presented double emission peak intensities. Before the geometric focal point of the focusing lens, the maximum line intensity of Na (I) lines was obtained. Essentially, the results were due to the nonlinear effect of femtosecond laser propagation in air. Subsequently, the different concentrations of Na element are quantitatively analyzed, plotting the calibration curve of Na element. In the three selected DFLSs, the R^2 of Na (I) 589.0 nm was greater than 0.98, and the R^2 of Na (I) 589.6 nm was greater than 0.99. According to the calibration curve, the LODs and RSDs at different DFLSs were obtained. As the DFLS increased, the LOD and RSD first decreased, and then increased. In the range of the DFLS from 99.0 to 101.0 mm, the two parameters had lower values. From the above discussion, it can be concluded that the combination of femtosecond laser and water film can significantly improve the analysis stability of liquid samples by optimized the DFLS.

Data availability statement

The raw data supporting the conclusions of this article will be made available by the authors, without undue reservation.

Author contributions

YW: writing—original draft and editing. HG: investigation. YH: investigation. DZ: investigation, methodology, and conceptualization. AC: investigation, methodology, and conceptualization. MJ: investigation.

Funding

We acknowledge the support by National Natural Science Foundation of China (Nos. 11674128, 11674124 and 11974138), and the Jilin Province Scientific and Technological Development Program, China (No. 20170101063JC).

Conflict of interest

The authors declare that the research was conducted in the absence of any commercial or financial relationships that could be construed as a potential conflict of interest.

Publisher's note

References

1. Singh JP, Almirall JR, Sabsabi M, Miziolek AW. Laser-induced breakdown spectroscopy (LIBS). *Anal Bioanal Chem* (2011) 400(10):3191–2. doi:10.1007/s00216-011-5073-5

2. Hou Z, Jeong S, Deguchi Y, Wang Z. Way-out for laser-induced breakdown spectroscopy. *Plasma Sci Technol* (2020) 22(7):070101. doi:10.1088/2058-6272/ab95f7

3. Wang Z, Dong F, Zhou W. A rising force for the world-wide development of laser-induced breakdown spectroscopy. *Plasma Sci Technol* (2015) 17(8):617–20. doi:10.1088/1009-0630/17/8/01

4. Chen A, Li S, Qi H, Jiang Y, Hu Z, Huang X, et al. Elongation of plasma channel generated by temporally shaped femtosecond laser pulse. *Opt Commun* (2017) 383:144–7. doi:10.1016/j.optcom.2016.08.079

5. Zhang N, Ou T, Wang M, Lin Z, Lv C, Qin Y, et al. A brief review of calibration-free laser-induced breakdown spectroscopy *Front Phys* (2022) 10:887171. doi:10.3389/fphy.2022.887171

6. Ma Y, Feng W, Qiao S, Zhao Z, Gao S, Wang Y, et al. Hollow-core anti-resonant fiber based light-induced thermoelastic spectroscopy for gas sensing *Opt Express* (2022) 30(11):18836. doi:10.1364/oe.460134

7. Ma Y, He Y, Tong Y, Yu X, Tittel FK. Quartz-tuning-fork enhanced photothermal spectroscopy for ultra-high sensitive trace gas detection. *Opt Express* (2018) 26(24):32103. doi:10.1364/oe.26.032103

8. Ma Y, Lewicki R, Razeghi M, Tittel FK. QEPAS based ppb-level detection of CO and N_2O using a high power CW DFB-QCL. *Opt Express* (2013) 21(1):1008. doi:10.1364/oe.21.001008

9. Yao M, Lin J, Liu M, Xu Y. Detection of chromium in wastewater from refuse incineration power plant near Poyang Lake by laser induced breakdown spectroscopy. *Appl Opt* (2012) 51(10):1552. doi:10.1364/ao.51.001552

10. Rifai K, Laville S, Vidal F, Sabsabi M, Chaker M. Quantitative analysis of metallic traces in water-based liquids by UV-IR double-pulse laser-induced breakdown spectroscopy. *J Anal Spectrom* (2012) 27(2):276–83. doi:10.1039/c1ja10178a

11. Wang Q, Ge T, Liu Y, Jiang L, Chen A, Han J, et al. Highly sensitive analysis of trace elements in aqueous solutions using surface-enhanced and discharge-assisted laser-induced breakdown spectroscopy. *J Anal Spectrom* (2022) 37(2):233–9. doi:10.1039/d1ja00415h

12. Zhang D, Chen A, Chen Y, Wang Q, Li S, Jiang Y, et al. Influence of substrate temperature on the detection sensitivity of surface-enhanced LIBS for analysis of heavy metal elements in water. *J Anal Spectrom* (2021) 36(6):1280–6. doi:10.1039/d1ja00003a

13. St-Onge L, Kwong E, Sabsabi M, Vadas EB. Rapid analysis of liquid formulations containing sodium chloride using laser-induced breakdown spectroscopy. *J Pharm Biomed Anal* (2005) 36(2):277–84. doi:10.1016/j.jpba.2004.06.004

14. Kongbonga YGM, Ghalila H, Onana MB, Lakhdar ZB. Classification of vegetable oils based on their concentration of saturated fatty acids using laser induced breakdown spectroscopy (LIBS). *Food Chem* (2014) 147:327–31. doi:10.1016/j.foodchem.2013.09.145

15. Abdel-Salam Z, Al Sharnoubi J, Harith MA. Qualitative evaluation of maternal milk and commercial infant formulas via LIBS. *Talanta* (2013) 115:422–6. doi:10.1016/j.talanta.2013.06.003

16. Cheung NH, Yeung ES. Distribution of sodium and potassium within individual human erythrocytes by pulsed-laser vaporization in a sheath flow. *Anal Chem* (1994) 66(7):929–36. doi:10.1021/ac00079a003

17. Khan MN, Wang Q, Idrees BS, Xiangli W, Teng G, Cui X, et al. A review on laser-induced breakdown spectroscopy in different cancers diagnosis and classification. *Front Phys* (2022) 10:821057. doi:10.3389/fphy.2022.821057

18. Xu F, Ma S, Zhao C, Dong D. Application of molecular emissions in laser-induced breakdown spectroscopy: A review. *Front Phys* (2022) 10:821528. doi:10.3389/fphy.2022.821528

19. Chen A, Li S, Li S, Jiang Y, Shao J, Wang T, et al. Optimally enhanced optical emission in laser-induced air plasma by femtosecond double-pulse. *Phys Plasmas* (2013) 20(10):103110. doi:10.1063/1.4825346

20. Shen X, Sun J, Ling H, Lu Y. Spectroscopic study of laser-induced Al plasmas with cylindrical confinement. *J Appl Phys* (2007) 102(9):093301. doi:10.1063/1.2801405

21. Li C, Guo L, He X, Hao Z, Li X, Shen M, et al. Element dependence of enhancement in optics emission from laser-induced plasma under spatial confinement. *J Anal Spectrom* (2014) 29(4):638. doi:10.1039/c3ja50368b

22. Wang X, Chen A, Wang Y, Zhang D, Sui L, Ke D, et al. Spatial confinement effect on femtosecond laser-induced Cu plasma spectroscopy. *Phys Plasmas* (2017) 24(10):103305. doi:10.1063/1.4986027

23. Lu Y, Zhou YS, Qiu W, Huang X, Liu L, Jiang L, et al. Magnetic field enhancement for femtosecond-laser-ablation mass spectrometry in ambient environments. *J Anal Spectrom* (2015) 30(11):2303–6. doi:10.1039/c5ja00225g

24. He X, Chen B, Chen Y, Li R, Wang F. Femtosecond laser-ablation spark-induced breakdown spectroscopy and its application to the elemental analysis of aluminum alloys. *J Anal Spectrom* (2018) 33(12):2203–9. doi:10.1039/c8ja00261d

25. Li K, Zhou W, Shen Q, Ren Z, Peng B. Laser ablation assisted spark induced breakdown spectroscopy on soil samples. *J Anal Spectrom* (2010) 25(9):1475. doi:10.1039/b922187e

26. Wang Q, Chen A, Xu W, Zhang D, Wang Y, Li S, et al. Time-resolved spectroscopy of femtosecond laser-induced Cu plasma with spark discharge. *Plasma Sci Technol* (2019) 21:065504. doi:10.1088/2058-6272/ab0fa6

27. Li Q, Chen A, Zhang D, Wang Q, Xu W, Qi Y, et al. Time-resolved electron temperature and density of spark discharge assisted femtosecond laser-induced breakdown spectroscopy. *Optik* (2021) 225:165812. doi:10.1016/j.ijleo.2020.165812

28. Wang Y, Chen A, Jiang Y, Sui L, Wang X, Zhang D, et al. Temperature effect on femtosecond laser-induced breakdown spectroscopy of glass sample. *Phys Plasmas* (2017) 24(1):013301. doi:10.1063/1.4973658

29. Wang Y, Chen A, Wang Q, Zhang D, Sui L, Li S, et al. Enhancement of optical emission generated from femtosecond double-pulse laser-induced glass plasma at different sample temperatures in air. *Plasma Sci Technol* (2019) 21(3):034013. doi:10.1088/2058-6272/aaefa1

30. Liu Y, Tong Y, Wang Y, Zhang D, Li S, Jiang Y, et al. Influence of sample temperature on the expansion dynamics of laser-induced germanium plasma. *Plasma Sci Technol* (2017) 19(12):125501. doi:10.1088/2058-6272/aa8acc

31. Yang X, Li S, Jiang Y, Chen A, Jin M Influence of distance between focusing lens and sample surface on laser-induced breakdown spectroscopy of brass at different sample temperatures. *Acta Phys Sin* (2019) 68(6):065201. doi:10.7498/aps.68.20182198

32. Wang Y, Chen A, Wang Q, Sui L, Ke D, Cao S, et al. Influence of distance between focusing lens and target surface on laser-induced Cu plasma temperature. *Phys Plasmas* (2018) 25(3):033302. doi:10.1063/1.5010076

33. Guo J, Shao J, Wang T, Zheng C, Chen A, Jin M. Optimization of distances between the target surface and focal point on spatially confined laser-induced breakdown spectroscopy with a cylindrical cavity. *J Anal Spectrom* (2017) 32(2):367–72. doi:10.1039/c6ja00396f

34. Zhang D, Chen A, Wang Q, Wang Y, Li S, Jiang Y, et al. Effect of lens focusing distance on laser-induced silicon plasmas at different sample temperatures. *Plasma Sci Technol* (2019) 21(3):034009. doi:10.1088/2058-6272/aaec9b

35. Rai VN, Yueh F-Y, Singh JP. Study of laser-induced breakdown emission from liquid under double-pulse excitation. *Appl Opt* (2003) 42(12):2094. doi:10.1364/ao.42.002094

36. Wang Q, Ge T, Liu Y, Chen A, Li S, Jin M, et al. Effect of the lens-to-target distance on the determination of Cr in water by the electro-deposition method and laser-induced breakdown spectroscopy. *J Anal Spectrom* (2021) 36(12):2675–83. doi:10.1039/d1ja00275a

37. Yoshiro I, Osamu U, Suaumu N. Determination of colloidal iron in water by laser-induced breakdown spectroscopy. *Analytica Chim Acta* (1995) 299:401–5. doi:10.1016/0003-2670(94)00313-b

38. Archontaki HA, Crouch SR. Evaluation of an isolated droplet sample introduction system for laser-induced breakdown spectroscopy. *Appl Spectrosc* (1988) 42(5):741–6. doi:10.1366/0003702884429049

39. Ng KC, Ayala NL, Srmeonsson JB, Winefordner JD. Laser-induced plasma atomic emission spectrometry in liquid aerosols. *Analytica Chim Acta* (1992) 269(1):123–8. doi:10.1016/0003-2670(92)85141-r

40. Samek O, Beddows DCS, Kaiser J, Kukhlevsky SV, Liska M, Telle HH, et al. Application of laser-induced breakdown spectroscopy to *in situ* analysis of liquid samples. *Opt Eng* (2000) 39(8):2248. doi:10.1117/1.1304855

41. Yaroshchyk P, Morrison RJS, Body D, Chadwick BL. Theoretical modeling of optimal focusing conditions using laser-induced breakdown spectroscopy in liquid jets. *Appl Spectrosc* (2004) 58(11):1353–9. doi:10.1366/0003702042475592

42. Kuwako A, Uchida Y, Maeda K. Supersensitive detection of sodium in water with use of dual-pulse laser-induced breakdown spectroscopy. *Appl Opt* (2003) 42(30):6052. doi:10.1364/ao.42.006052

43. Sarkar A, Alamelu D, Aggarwal SK. Determination of thorium and uranium in solution by laser-induced breakdown spectrometry. *Appl Opt* (2008) 47(31):G58. doi:10.1364/ao.47.000g58

44. Yaroshchyk P, Morrison RJS, Body D, Chadwick BL. Quantitative determination of wear metals in engine oils using laser-induced breakdown spectroscopy: A comparison between liquid jets and static liquids. *Spectrochimica Acta B: At Spectrosc* (2005) 60(7-8):986–92. doi:10.1016/j.sab.2005.03.011

45. Wang Y, Chen A, Wang Q, Zhang D, Li S, Jiang Y, et al. Study of signal enhancement in collinear femtosecond-nanosecond double-pulse laser-induced breakdown spectroscopy. *Opt Laser Tech* (2020) 122:105887. doi:10.1016/j.optlastec.2019.105887

46. Wang Q, Chen A, Xu W, Zhang D, Wang Y, Li S, et al. Effect of lens focusing distance on AlO molecular emission from femtosecond laser-induced aluminum plasma in air. *Opt Laser Tech* (2020) 122:105862. doi:10.1016/j.optlastec.2019.105862

47. Wang Q, Chen A, Qi H, Li S, Jiang Y, Jin M, et al. Femtosecond laser-induced breakdown spectroscopy of a preheated Cu target. *Opt Laser Tech* (2020) 121:105773. doi:10.1016/j.optlastec.2019.105773

48. Zhang D, Chen A, Wang X, Li S, Wang Y, Sui L, et al. Enhancement mechanism of femtosecond double-pulse laser-induced Cu plasma spectroscopy *Opt Laser Technol* (2017) 96:117–22. doi:10.1016/j.optlastec.2017.05.010

49. Yang F, Jiang L, Wang S, Cao Z, Liu L, Wang M, et al. Emission enhancement of femtosecond laser-induced breakdown spectroscopy by combining nanoparticle and dual-pulse on crystal SiO2. *Opt Laser Technol* (2017) 93:194–200. doi:10.1016/j.optlastec.2017.03.016

50. Knopp R, Scherbaum FJ, Kim JI. Laser induced breakdown spectroscopy (LIBS) as an analytical tool for the detection of metal ions in aqueous solutions. *Fresenius J Anal Chem* (1996) 355(1):16–20. doi:10.1007/s0021663550016

51. Sacchi CA. Laser-induced electric breakdown in water. *J Opt Soc Am B* (1991) 8(2):337. doi:10.1364/josab.8.000337

52. Shao J, Guo J, Wang Q, Chen A, Jin M. Influence of distance between focusing lens and sample surface on femtosecond laser-induced Cu plasma. *Optik* (2020) 220:165137. doi:10.1016/j.ijleo.2020.165137

53. Xu W, Chen A, Wang Q, Zhang D, Wang Y, Li S, et al. Generation of high-temperature and low-density plasma with strong spectral intensity by changing the distance between the focusing lens and target surface in femtosecond laser-induced breakdown spectroscopy. *J Anal Spectrom* (2019) 34(5):1018–25. doi:10.1039/c8ja00359a

54. Li X, Wei W, Wu J, Jia S, Qiu A. The Influence of spot size on the expansion dynamics of nanosecond-laser-produced copper plasmas in atmosphere. *J Appl Phys* (2013) 113(24):243304. doi:10.1063/1.4812580

55. Wang Y, Chen A, Li S, Ke D, Wang X, Zhang D, et al. Influence of distance between sample surface and focal point on spectral intensity of nanosecond laser-induced silicon plasma in air. *AIP Adv* (2017) 7(9):095204. doi:10.1063/1.4994983

56. Li SY, Guo FM, Song Y, Chen AM, Yang YJ, Jin MX, et al. Influence of group-velocity-dispersion effects on the propagation of femtosecond laser pulses in air at different pressures. *Phys Rev A (Coll Park)* (2014) 89(2):023809. doi:10.1103/physreva.89.023809

57. Popov AM, Drozdova AN, Zaytsev SM, Biryukova DI, Zorov NB, Labutin TA, et al. Rapid, direct determination of strontium in natural waters by laser-induced breakdown spectroscopy. *J Anal Spectrom* (2016) 31(5):1123–30. doi:10.1039/c5ja00468c

58. Lazic V, Ciaffi M. Laser-induced breakdown spectroscopy applied on liquid films: Effects of the sample thickness and the laser energy on the signal intensity and stability. *J Spectrosc* (2017) 2017:1–10. doi:10.1155/2017/7872504

frontiers | Frontiers in Physics

TYPE Original Research
PUBLISHED 26 July 2022
DOI 10.3389/fphy.2022.972054

OPEN ACCESS

EDITED BY
Yufei Ma,
Harbin Institute of Technology, China

REVIEWED BY
Ruijun Lan,
Yantai University, China
Cunguang Zhu,
Liaocheng University, China
Xiaohui Li,
Shaanxi Normal University, China

*CORRESPONDENCE
Wenjing Tang,
sps_tangwj@ujn.edu.cn
Wei Xia,
sps_xiaw@ujn.edu.cn

SPECIALTY SECTION
This article was submitted to Optics and Photonics,
a section of the journal
Frontiers in Physics

RECEIVED 17 June 2022
ACCEPTED 01 July 2022
PUBLISHED 26 July 2022

CITATION
Xu B, Tang W, Sun W, Wang J, Jiang K, Hu X and Xia W (2022), Watt-level high-stability all-solid-state passively Q-switched laser based on germanene nanosheets.
Front. Phys. 10:972054.
doi: 10.3389/fphy.2022.972054

Watt-level high-stability all-solid-state passively Q-switched laser based on germanene nanosheets

Baohao Xu, Wenjing Tang*, Wanggen Sun, Jing Wang, Kai Jiang, Xinyu Hu and Wei Xia*

School of Physics and Technology, University of Jinan, Jinan, China

Excellent Q-switching operations modulated by new two-dimensional (2D) saturable absorber (SA) materials with stable performance is a hot topic in all-solid-state pulsed laser research. In this work, the watt-level high-stability passive Q-switching operation in a solid-state Nd:YVO_4 laser utilizing the 2D germanene nanosheets as SA was first realized. The nonlinear optical properties of the germanene nanosheets (Ge-Ns) were characterized by experimental means. The stable Q-switched pulse sequence was acquired with a 60.6 ns narrowest pulse width and a 528.6 kHz maximal repetition rate. The average output power of 0.965 W and the corresponding pulse peak power of 30.12 W are obtained under the pump power of 7 W. The findings of the experiments demonstrate that germanene material has remarkable nonlinear optical properties and can be used as an excellent saturable absorber in the field of optical pulse modulation.

KEYWORDS

Germanene, passively Q-switched, solid-state laser, high peak power, high stablity

Introduction

Short pulse solid-state Q-switched lasers have a very wide range of applications in military, material processing, clinical applications, and nonlinear optics due to their high pulse energy and simple manufacturing [1–3]. At present, the Q-switching technique can be divided into passive Q-switched and active Q-switched according to the control mode. By contrast, the passive Q-switched technology has the advantages of simple structure and low cost [4, 5]. However, the saturable absorber (SA) is one of the key devices of passively Q-switched lasers. Extensive research has been carried out to better SAs since the first successful commercialization of semiconductor saturable absorber mirrors (SESAMs) in 1992 [6]. So far, in addition to SESAMs, many new two-dimensional (2D) nanomaterials have also been gradually proved to have excellent saturable absorption characteristics, such as graphene [7, 8], carbon nanotubes [9–11], topological insulators (TIs) [12, 13], transition metal dichalcogenides (TMDs) [14–17], MXenes [18, 19], Xenes [20–22], and black phosphorus (BP) [23–25]. Despite the fact that these 2D materials have been

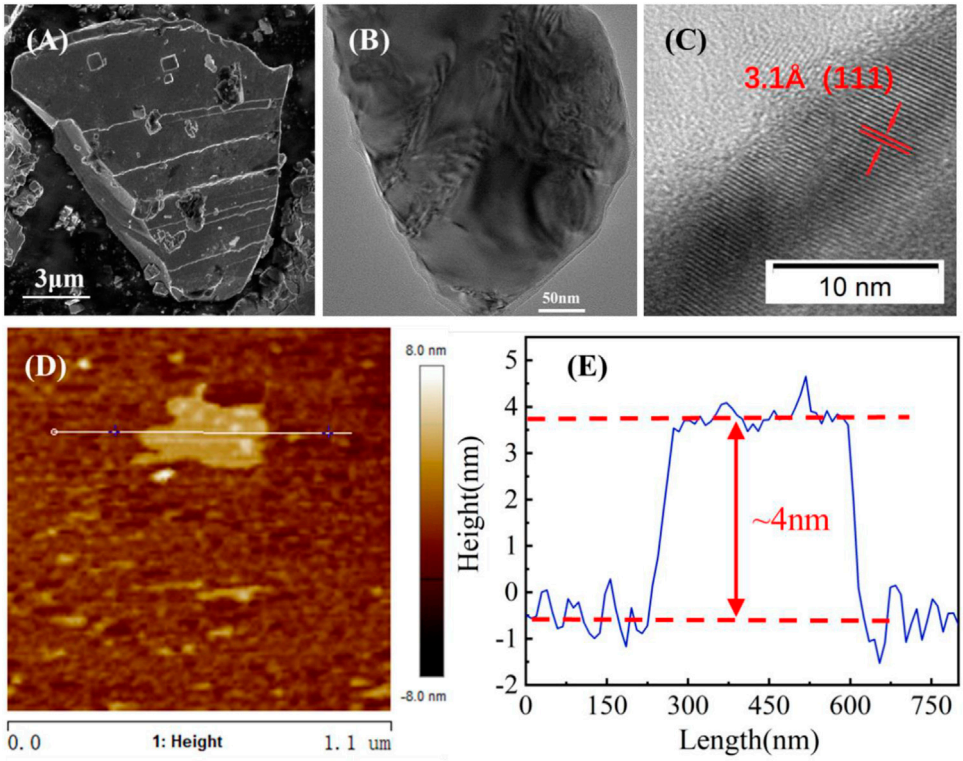

FIGURE 1
Characterizations of few-layer Ge-Ns. **(A)** SEM image of the germanene crystal powder sample; **(B,C)** HRTEM image with higher resolution; **(D)** AFM images; and **(E)** corresponding thickness profile of Ge-Ns.

employed effectively as broadband SAs, there are still some drawbacks that limit their applications in all-solid-state lasers. For example, the smaller the modulation depth (MD) (~2.3% for monolayer) of graphene, the larger the bandgap of TMDs, and the poorer the stability of BP [26–28]. Therefore, the exploration of new SA materials with better performance is necessary for Q-switched or mode-locking lasers.

As a germanium-based analog of graphene, germanene has been theoretically and experimentally proven to have the advantages of environmental friendliness, facile fabrication, and broadband absorption, indicating promising characteristics for optoelectronic fields [29]. In 2009, Cahangirov et al. first demonstrated that germanium has a stable honeycomb structure [30]. In 2014, Li et al. experimentally synthesized 2D germanene sheets on the Pt surface by electron beam evaporation technology [31]. In the same year, atom-thin, ordered 2D multiphase germanium film was prepared by Davila et al. using molecular beam epitaxy technology on the surface of gold [32]. In 2022, Sun et al. for the first time used germanene nanoplates as SA to realize the harmonic mode-locking operation with the order of fundamental frequency, second, fourth, fifth, and sixth based on the germanene–PVA film in an erbium-doped fiber laser [33]. Very recently, by the liquid-phase exfoliated method, the germanene nanosheets are prepared and used for the generation of ultrashort pulses in fiber lasers at 1,061.1, 1,559.3, and 1883.5 nm, respectively [34]. As a natural quantum well structure, the semiconductor layer of germanene acts as a reservoir, and the carriers in the layer have a substantially shorter relaxation period [29]. The optical bandgap of the germanium nanosheets has been calculated to be about 2.46 eV, corresponding to the wavelength of ~506 nm [34]. The broadband saturable absorption of the germanene nanosheets indicates the existence of sub-bandgap absorption, which may be caused by the high edge to surface area ratio of 2D germanene nanosheets [35]. Moreover, atomic vacancy defects can also reduce the bandgap and hence make contributions to the sub-bandgap absorption [36]. The nonlinear absorption coefficient of germanene nanosheets is much higher than that of graphene and has superior environmental durability to BP [37]. All the studies so far show that germanene is a kind of optical material with excellent properties. However, the research on the pulse modulation characteristics of germanene in solid-state lasers is still insufficient, and the relevant research on germanene in solid-state Q-switched lasers has not been found yet.

In this work, using self-made germanene nanosheets (Ge-Ns) as SA, a passively Q-switched Nd:YVO_4 laser with high stability

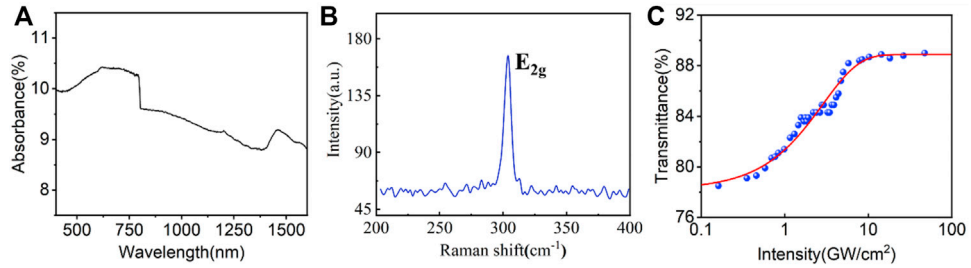

FIGURE 2
(A) Absorption spectrum; **(B)** Raman spectrum; and **(C)** nonlinear optical response of the Ge-N SA.

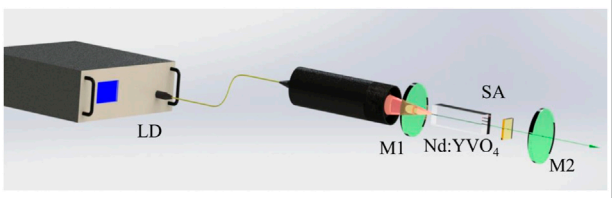

FIGURE 3
Schematic setup of the Nd:YVO_4 laser with germanene as the saturable absorber. LD: laser diode; SA: Ge-N saturable absorber.

was realized for the first time. The nonlinear optical parameters of the germanene nanosheets are characterized. Stable Q-switched pulses were obtained with the narrowest pulse width of 60.6 ns and the corresponding repetition rate of 528.6 kHz at the pump power of 7 W. The single pulse energy and peak power of 1.83 μJ and 30.12 W are calculated, respectively. As far as we know, this is the first time that the saturable absorption feature of germanene SA in a solid-state laser was demonstrated, indicating its capability of generating high stable Q-switched pulses in an all-solid-state laser.

Preparation and characterization of germanene saturable absorber

Using the liquid-phase exfoliated (LPE) method, the preparation process of 2D Ge-Ns is similar to our previous study [15]. The 2D germanene dispersion is ultrasonic for 10 h and centrifuged for 15 min at 5,000 rpm to remove the large size germanium crystals. Then, the desired 2D Ge-N solution was obtained. The rotary coating evaporation technology with a spin coating speed of 300 rpm was used to deposit Ge-Ns on the facet of an uncoated sapphire substrate.

The microscopic morphology and saturable absorption properties of the Ge-Ns are characterized. Figure 1A shows the configuration of the surface of the Ge crystal powder sample as seen through a field-emission scanning electron microscope (SEM, Sigma 500, Zeiss). The picture shows solid agglomerates of several microns with distinct layered structures which include the cleavage plane and cleavage step, indicating that the bonding force between layers is a weak van der Waals force. Figure 1B shows a picture of the prepared Ge-Ns measured using a high-resolution transmission electron microscope (HRTEM, JEM-2100). It can be seen that Ge-Ns are very thin and almost transparent. At a resolution of 50 nm, the layered structure of Ge-Ns can be easily observed, which is very different from Figure 1A. Changing the HRTEM resolution to 10 nm, the lattice spacing of 3.1 Å of the few-layer Ge-Ns can be observed from the HRTEM image, as shown in Figure 1C. The atomic force microscope (AFM, Bruker Multimode 8) was used to measure the thickness of the Ge-N sample. Figure 1D exhibits the obtained AFM image. The corresponding thickness profile of the sample is given in Figure 1E. It can be found that the average thickness of the sample is about ~ 4 nm, corresponding to 13 layers [38].

Figures 2A,B show the UV-Vis-NIR absorption spectrum and Raman spectrum of the Ge-N sample. The broadband absorption characteristic curve is measured from 400 to 1600 nm using a UV-Vis-NIR spectrophotometer. At 1064 nm, the light absorption rate of the Ge-N sample is 9.1%. The Raman spectrum was measured to analyze the chemical structure and vibration mode of the Ge-N sample. From the diagram, the prominent peak (E_{2g}) at 304.4 cm^{-1} can be observed, which is consistent with the previous reports [29, 34].

The nonlinear transmittance of Ge-N SA is measured by the double-optical-path method [15]. A solid-state Q-switched laser at 1.06 μm (120 ns pulse width, 15 kHz 95 repetition rate) was used as the laser source for testing. The experimental data of transmission *T(I)* shown in Figure 2C with symbols are fitted by the formula as follows:

$$T(I) = 1 - T_{ns} - \Delta T * exp\left(-\frac{I}{I_{sat}}\right).$$

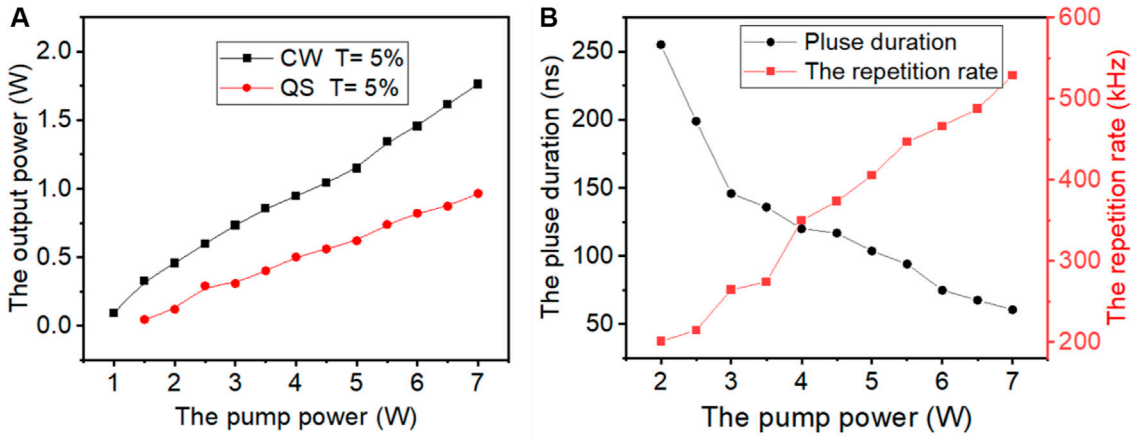

FIGURE 4
(A) Average output power. **(B)** Pulse duration and pulse repetition rate of the Ge-N SA-based Q-switched Nd:YVO_4 laser versus the pump power.

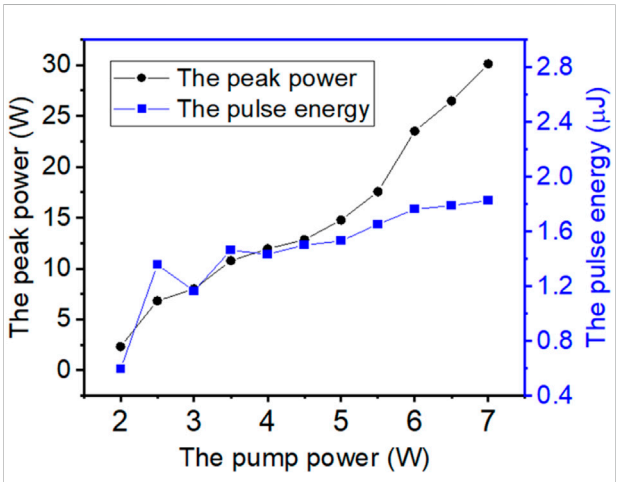

FIGURE 5
Peak powers and pulse energies of the Ge-N SA-based Q-switched Nd:YVO_4 laser versus the pump power.

Here, I and I_{sat} are the input intensity of the laser and saturation intensity of Ge-N SA, respectively, and ΔT is the modulation depth with a fitting value of 11.6%. The nonsaturable loss T_{ns} is about 12.2%.

Experimental setup and results

Experimental setup

Figure 3 shows the experimental setup for studying the lasing characteristics of Q-switched pulses using a passively Q-switched Nd:YVO_4 laser with Ge-N SA. To accomplish stable and effective Q-switching, a conventional 3-cm-long plane–plane cavity was used. A fiber-coupled laser diode (LD) emitting 808 nm was used as the pump source. Using an optical imaging system with a 1:1 imaging ratio, the pump beam with a spot radius of 200 μm was focused into a 3 mm^3 × 3 mm^3 × 8 mm^3 Nd:YVO_4 crystal. The Nd:YVO_4 crystal with the Nd-doping concentration of 0.5 at% was antireflection (AR) coated at 808 and 1,064 nm for a facet and AR coated at 1,064 nm for the other facet. As mature laser media for diode-pumped solid-state lasers, neodymium-doped crystals owe broad absorption bands and large emission cross sections as well as high environmental stability, which are beneficial to generate high peak power and narrow pulse width [39, 40]. M1 is a plane mirror with AR coated at 808 nm and high reflection (HR) coated at 1,064 nm. For the plane output coupler (OC) M2, the transmission (T) at 1,064 nm is 5%. The germanene SA was placed as close to the OC as possible to provide steady and effective Q-switching. A long-pass filter was also put behind the OC to reduce the residual pump power. The temporal pulse morphology was recorded using a digital oscilloscope (Tektronix DPO 4104B, United States) with a fast photo-detector (Thorlabs DET08 C/M, United States).

Experimental results and discussion

In the Nd:YVO_4 laser shown in Figure 3, the stable Q-switched laser oscillation based on Ge-N SA is realized when the pump power is increased above 1.8 W. As the pump power gradually increases, the output characteristics of the continuous wave (CW) and passively Q-switched pulses are measured.

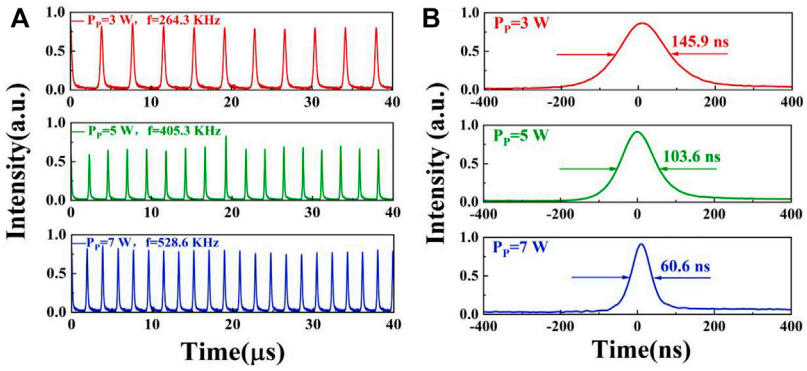

FIGURE 6
(A) Pulse sequence and **(B)** single pulse profiles of the passively Q-switched laser under the pump power of 3 W, 5 W, and 7 W.

TABLE 1 Passively Q-switching performances for the 1064 nm solid-state laser with different 2D SA materials.

SA type	Laser crystal	Pulse width (ns)	Repetition rate (kHz)	Pulse energy (μJ)	Peak power (W)	Ref
Graphene	Nd:YAG	400	850	0.68	1.69	[42]
BP	Nd:YAG	55	5,600	0.02	0.41	[43]
WS_2	Nd:YVO_4	98	392	0.441	4.5	[44]
WS_2	Nd:YAG	24	6,100	0.02	0.98	[43]
Antimonene	Nd:YAG	129	569.1	0.23	1.77	[45]
MoS_2/GaAs	Nd:YVO_4	51.3	769.7	0.417	8.14	[46]
Fe_3O_4	Nd:YVO_4	53	576.4	0.18	3.53	[47]
Carbon nanotube	Nd:YAG	1,200	95	4.5	3.75	[48]
Bi_2Te_3	Nd:YAG	576	28.57	5.24	9	[49]
Gold nanorods	Nd:YAG	3,100	50	19	6.13	[50]
Germanene	Nd:YVO_4	60.6	528.6	1.83	30.12	This work

The output power of CW and Q-switched pulses is shown in Figure 4A as a function of pump power. With the pump power of 7 W and the output coupler of 5%, the CW average output power is 1.762 W with the corresponding slope efficiency of 26%. Then, the Ge-N SA is put into the resonant cavity, and the average output powers of the passively Q-switched operation are recorded. At the pump power of 7 W, the maximum average output power of 0.965 W with the corresponding slope efficiency of 16.4% can be obtained. We have also been focusing on the state of Ge-N SA with increasing pump power. When the pump power reaches 7 W, the fluctuation of the average output power is measured at about 2.8%. By observation, there is no damage to Ge-N SA, and the distribution of Ge-Ns on the substrate seems to be uniform.

The pulse duration and repetition rate of the Ge-N-based Q-switched laser are measured and exhibited in Figure 4B. With the pump power ranging from 2 to 7 W, the pulse repetition rate gradually increases from 200.9 to 528.6 kHz, and the pulse width gradually narrows from 255 to 60.6 ns. This trend is consistent with the principle of passively Q-switched pulses [41].

The peak power and single pulse energy of passively Q-switched pulses are calculated by the measured pulse width, repetition rate, and average output power. Figure 5 shows the relationship between peak power and pulse energy and pump power. The maximum peak power of 30.12 W and single pulse energy of 1.83 μJ are obtained at the pump power of 7 W.

Figures 6A,B show the pulse train and single Q-switched pulse diagrams of the Ge-N SA-based Q-switched Nd:YVO_4 laser for a pump power of 2.5, 4.5, and 7 W, respectively. To further validate the stability of the Q-switching characteristics of germanene, the Q-switched laser based on Ge-Ns SA ran 6 h a day for 5 days under the pump power of 7 W. The Q-switched pulses keep high

repeatability, and the amplitude fluctuation is less than 7%. By employing the 90.0/10.0 scanning-knife-edge method, the beam quality factor M^2 of the Q-switched laser based on Ge-N SA was also measured to further demonstrate the robustness of the Q-switching system. In the horizontal and longitudinal planes, the calculated M_x^2 and M_y^2 are 1.96 and 1.51, respectively.

Table 1 lists some key parameters of all-solid-state Q-switched laser using different 2D nanomaterials as SA at 1,064 nm. It can be found that the single pulse energy and pulse peak power produced by germanene SA are larger than those of most other two-dimensional materials. The results show that germanene has good nonlinear optical properties and is suitable for generating stable Q-switched pulses with high peak power in a solid-state laser.

Conclusion

In summary, a 4-nm-thick germanene nanosheet was fabricated successfully by the LPE method and applied as SA to generate a Q-switched pulse in Nd:YVO_4 all-solid-state lasers for the first time. The nonlinear optical parameters of the germanene nanosheet at 1,064 nm are measured by experimental methods. The stable Q-switching operation with large single pulse energy and high peak power is realized. The shortest pulse width of 60.6 ns was obtained with a maximum repetition rate of 528.6 kHz, and the associated single pulse energy and peak power are 1.83 μJ and 30.12 W, respectively, when the pump power is 7 W. The results indicate that germanene has excellent optical nonlinear properties and has broad application prospects in the field of all-solid-state laser.

Data availability statement

The original contributions presented in the study are included in the article/Supplementary Material; further inquiries can be directed to the corresponding authors.

Author contributions

BX and WT conceived and designed the experiments, performed the experiments and analyzed the data, and drafted the manuscript; WS and JW contributed to performing the theoretical analysis; XH and KJ fabricated and characterized the saturable absorber; WX provided experimental equipment, and all authors contributed to writing and editing the manuscript. All authors read and agreed to the published version of the manuscript.

Funding

This research was funded by the National Natural Science Foundation of China, under grant number 62005094; Program of Jinan Introduced Innovation Team, under grant number 2018GXRC011; Natural Science Foundation of Shandong Province, under grant number ZR2021MF128; and Doctoral Fund Project from the University of Jinan, under grant number XBS1917.

Conflict of interest

The authors declare that the research was conducted in the absence of any commercial or financial relationships that could be construed as a potential conflict of interest.

Publisher's note

All claims expressed in this article are solely those of the authors and do not necessarily represent those of their affiliated organizations, or those of the publisher, the editors, and the reviewers. Any product that may be evaluated in this article, or claim that may be made by its manufacturer, is not guaranteed or endorsed by the publisher.

References

1. Byer RL. Diode laser-pumped solid-state lasers. *Science* (1988) 239(4841): 742–7. doi:10.1126/science.239.4841.742

2. Juhasz T, Lai ST, Pessot MA. Efficient short-pulse generation from a diode-pumped Nd:YLF laser with a piezoelectrically induced diffraction modulator. *Opt Lett* (1990) 15(24):1458–60. doi:10.1364/ol.15.001458

3. Ma YF, Zhang Y, Yu X, Li XD, Chen F, Yan RP, et al. Doubly Q-switched $GdVO_4$/Nd:$GdVO_4$ laser with AO modulator and Cr^{4+}:YAG saturable absorber under direct 879nm diode pumping to the emitting level. *Opt Commun* (2011) 284: 2569–72. doi:10.1016/j.optcom.2011.01.048

4. Zhang S, Huang H, Xu L, Wang M, Chen F, Xu J, et al. Continuous wave and passively Q-switched Nd:$Lu_xY_{1-x}VO_4$ laser at 1.34 μm with V^{3+} :YAG as the saturable absorber. *Opt Express* (2011) 19(3):1830–5. doi:10.1364/oe.19.001830

5. Ma YF, Zhang SC, Ding SJ, Liu XX, Yu X, Peng F, et al. Passively Q-switched Nd:$GdLaNbO_4$ laser based on 2D $PdSe_2$ nanosheet. *Opt Laser Technol* (2020) 124: 105959. doi:10.1016/j.optlastec.2019.105959

6. Keller U, Miller DAB, Boyd GD, Chiu TH, Ferguson JF, Asom MT, et al. Solid-state low-loss intracavity saturable absorber for Nd:YLF lasers: an antiresonant semiconductor fabry-perot saturable absorber. *Opt Lett* (1992) 17(7):505–7. doi:10.1364/ol.17.000505

7. Cho W, Kim J, Lee H, Bae S, Hong B, Choi S, et al. High-quality large-area monolayer graphene for efficient bulk laser mode-locking near 1.25 μm. *Opt Lett* (2011) 36:4089–91. doi:10.1364/ol.36.004089

8. Tang WJ, Zhao J, Yang KJ, Zhao SZ, Li GQ, Li DC, et al. 1.38 MW peak power dual-loss modulated sub-nanosecond green laser with EO and graphene. *Opt Mater (Amst)* (2016) 62:23–7. doi:10.1016/j.optmat.2016.09.036

9. Yim JH, Cho WB, Lee S, Ahn YH, Kim K, Lim H, et al. Fabrication and characterization of ultrafast carbon nanotube saturable absorbers for solid-state laser mode-locking near 1μm. *Appl Phys Lett* (2008) 93:161106. doi:10.1063/1.2999593

10. Yang Q, Wang Y, Liu D, Liu J, Zheng L, Su L, et al. Fabrication and characterization of double-wall carbon nanotube absorber for passive mode-locked Nd:$GdVO_4$ laser. *Laser Phys* (2011) 21:1689–93. doi:10.1134/s1054660x11170233

11. Lin XC, Zhang L, Tsang YH, Wang YG, Yu HJ, Yan SL, et al. Multi-walled carbon nanotube as a saturable absorber for a passively mode-locked Nd:YVO_4 laser. *Laser Phys Lett* (2013) 10:055805. doi:10.1088/1612-2011/10/5/055805

12. Liu H, Zheng XW, Liu M, Zhao N, Luo AP, Luo ZC, et al. Femtosecond pulse generation from a topological insulator mode-locked fiber laser. *Opt Express* (2014) 22(6):6868–73. doi:10.1364/oe.22.006868

13. Liu X, Yang K, Zhao S, Li T, Qiao W, Zhang H, et al. High-power passively Q-switched 2 μm all-solid-state laser based on a Bi_2Te_3 saturable absorber. *Photon Res* (2017) 5:461–6. doi:10.1364/prj.5.000461

14. Zhang H, Lu SB, Zheng J, Du J, Wen SC, Tang DY, et al. Molybdenum disulfide (MoS_2) as a broadband saturable absorber for ultra-fast photonics. *Opt Express* (2014) 22:7249–60. doi:10.1364/oe.22.007249

15. Tang W, Wang Y, Yang K, Zhao J, Zhao S, Li G, et al. 1.36 W passively Q-switched YVO_4/Nd:YVO_4 laser with a WS_2 saturable absorber. *IEEE Photon Technol Lett* (2017) 29(5):470–3. doi:10.1109/lpt.2017.2657325

16. Fan MQ, Li T, Zhao SZ, Li GQ, Ma HY, Gao XC, et al. Watt-level passively Q-switched Er:Lu_2O_3 laser at 2.84μm using MoS_2. *Opt Lett* (2016) 41(3):540–3. doi:10.1364/ol.41.000540

17. Fan M, Li T, Zhao J, Zhao S, Li G, Yang K, et al. Continuous wave and ReS_2 passively Q-switched Er:SrF_2 laser at ~3 μm. *Opt Lett* (2018) 43(8):1726–9. doi:10.1364/ol.43.001726

18. Cao LH, Chu HW, Pan H, Wang R, Li Y, Zhao SZ, et al. Nonlinear optical absorption features in few-layered hybrid $Ti_3C_2(OH)_2$/$Ti_3C_2F_2$ MXene for optical pulse generation in the NIR region. *Opt Express* (2020) 28(21):31499–509. doi:10.1364/oe.406035

19. Jhon YI, Koo J, Anasori B, Seo M, Lee JH, Gogotsi Y, et al. Metallic MXene saturable absorber for femtosecond mode-locked lasers. *Adv Mater* (2017) 29(40):1702496. doi:10.1002/adma.201702496

20. Xu N, Ma P, Fu S, Shang X, Jiang S, Wang S, et al. Tellurene-based saturable absorber to demonstrate large-energy dissipative soliton and noise-like pulse generations. *Nanophotonics* (2020) 9(9):2783–95. doi:10.1515/nanoph-2019-0545

21. Xing C, Xie Z, Liang Z, Liang W, Fan T, Ponraj JS, et al. Selenium nanosheets: 2D nonlayered selenium nanosheets: Facile synthesis, photoluminescence, and ultrafast photonics (advanced optical materials 24/2017). *Adv Opt Mater* (2017) 5(24):1770118. doi:10.1002/adom.201770118

22. Lu L, Liang Z, Wu L, Chen Y, Song Y, Dhanabalan SC, et al. Few-layer bismuthene: sonochemical exfoliation, nonlinear optics, and applications for ultrafast photonics with enhanced stability. *Laser Photon Rev* (2018) 12:1700221. doi:10.1002/lpor.201700221

23. Lu SB, Miao LL, Guo ZN, Qi X, Zhao CJ, Zhang H, et al. Broadband nonlinear optical response in multi-layer black phosphorus: an emerging infrared and mid-infrared optical material. *Opt Express* (2015) 23(9):11183–94. doi:10.1364/oe.23.011183

24. Zhang B, Lou F, Zhao R, He J, Li J, Su X, et al. Exfoliated layers of black phosphorus as saturable absorber for ultrafast solid-state laser. *Opt Lett* (2015) 40(16):3691–4. doi:10.1364/ol.40.003691

25. Tang W, Zhao J, Li T, Yang K, Zhao S, Li G, et al. High peak power mode-locking pulse generation in a dual-loss-modulated laser with BP-SA and EOM. *Opt Lett* (2017) 42(23):4820–3. doi:10.1364/ol.42.004820

26. Sun Z, Hasan T, Torrisi F, Popa D, Privitera G, Wang F, et al. Graphene mode-locked ultrafast laser. *ACS Nano* (2010) 4:803–10. doi:10.1021/nn901703e

27. Favron A, Gaufres E, Fossard F, Phaneuf-L'Heureux AL, Tang NYW, Levesque PL, et al. Photooxidation and quantum confinement effects in exfoliated black phosphorus. *Nat Mater* (2015) 14:826–32. doi:10.1038/nmat4299

28. Mao D, Zhang S, Wang Y, Gan X, Zhang W, Mei T, et al. WS_2 saturable absorber for dissipative soliton mode locking at 1.06 and 1.55 μm. *Opt Express* (2015) 23:27509–19. doi:10.1364/oe.23.027509

29. Li C, Kang J, Xie J, Wang Y, Zhou LI, Hu H, et al. Two-dimensional monoelemental germanene nanosheets: facile preparation and optoelectronic applications. *J Mater Chem C Mater* (2020) 8(46):16318–25. doi:10.1039/d0tc03892j

30. Cahangirov S, Topsakal M, Aktürk E, ahin HS, Ciraci S. Two- and one-dimensional honeycomb structures of silicon and germanium. *Phys Rev Lett* (2009) 102(23):236804. doi:10.1103/physrevlett.102.236804

31. Li L, Lu SZ, Pan J, Qin Z, Wang YQ, Wang Y, et al. Buckled germanene formation on Pt(111). *Adv Mater* (2014) 26(28):4820–4. doi:10.1002/adma.201400909

32. Dávila ME, Xian L, Cahangirov S, Rubio A, Le Lay G. Germanene: a novel two-dimensional germanium allotrope akin to graphene and silicene. *New J Phys* (2014) 16:095002. doi:10.1088/1367-2630/16/9/095002

33. Sun WG, Jiang K, Tang WJ, Su J, Chen K, Liu Q, et al. Germanene nanosheets for mode-locked pulse generation in fiber lasers. *Infrared Phys Technol* (2020) 123:104128. doi:10.1016/j.infrared.2022.104128

34. Wang Q, Kang J, Wang P, He J, Liu Y, Wang Z, et al. Broadband saturable absorption in germanene for mode-locked Yb, Er, and Tm fiber lasers. *Nanophotonics* (2022) 11:3127–37. doi:10.1515/nanoph-2022-0161

35. Trushin M, Kelleher EJR, Hasan T. Theory of edge-state optical absorption in two-dimensional transition metal dichalcogenide flakes. *Phys Rev B* (2016) 94:155301. doi:10.1103/physrevb.94.155301

36. Zhao G, Han S, Wang A, Wu Y, Zhao M, Wang Z, et al. 'Chemical weathering' exfoliation of atom-thick transition metal dichalcogenides and their ultrafast saturable absorption properties. *Adv Funct Mater* (2015) 25:5292–9. doi:10.1002/adfm.201501972

37. Mu H, Liu Y, Bongu SR, Bao X, Li L, Xiao S, et al. Germanium nanosheets with Dirac characteristics as a saturable absorber for ultrafast pulse generation. *Adv Mater* (2021) 33(32):2101042. doi:10.1002/adma.202101042

38. Galbiati M, Motta N, De CM, Camilli L. Group-IV 2D materials beyond graphene on nonmetal substrates: challenges, recent progress, and future perspectives. *Appl Phys Rev* (2019) 6(4):041310. doi:10.1063/1.5121276

39. Zhang HJ, Zhao SZ, Zhao J, Yang KJ, Li GQ, Li DC, et al. Generation of low repetition rate sub-nanosecond pulses in doubly QML Nd:$Lu_{0.5}Y_{0.5}VO_4$ and Nd:YVO_4 lasers with EO and transmission SSA. *Opt Laser Tech* (2015) 69:39–43. doi:10.1016/j.optlastec.2014.12.017

40. Ma YF, Yu X, Li XD, Fan RW, Yu JH. Comparison on performance of passively Q-switched laser properties of continuous-grown composite $GdVO_4$/Nd:$GdVO_4$ and YVO_4/Nd:YVO_4 crystals under direct pumping. *Appl Opt* (2011) 50(21):3854–9. doi:10.1364/ao.50.003854

41. Maker GT, Ferguson AI. Mode locking and Q switching of a diode laser pumped neodymium-doped yttrium lithium fluoride laser. *Appl Phys Lett* (1989) 54(5):403–5. doi:10.1063/1.100976

42. Wang Q, Wei ZY, Lin JJ, Zhang YD, Guo LW, Zhang ZG. Few-layer graphene as saturable absorber for Q-switched laser at sub-MHz repetition rate. In: *Advances in optical materials*. Washington: Optica Publishing Group (2011). paper AIThF3.

43. Tan Y, Guo Z, Ma L, Zhang H, Akhmadaliev S, Zhou S, et al. Q-switched waveguide laser based on two-dimensional semiconducting materials: tungsten disulfide and black phosphorous. *Opt Express* (2016) 24(3):2858–66. doi:10.1364/oe.24.002858

44. Zhang N, Zhang T, Wang Y, Song J. Compact stable passively Q-switched Nd:YVO_4 laser with tungsten disulfide saturable absorber. *Optik* (2016) 127(19):7689–93. doi:10.1016/j.ijleo.2016.05.109

45. Wang MX, Zhang F, Wang ZP, Wu ZX, Xu XG. Passively Q-switched Nd^{3+} solid-state lasers with antimonene as saturable absorber. *Opt Express* (2018) 26(4):4085–95. doi:10.1364/oe.26.004085

46. Zhang Hk, Zhang F, Li X, Chen LJ, Wang J, Wang LL, et al. Passively Q-switched Nd:YVO_4 laser with MoS_2/GaAs saturable absorber. *Opt Mater (Amst)* (2017) 70:153–7. doi:10.1016/j.optmat.2017.05.033

47. Wang X, Wang YG, Mao D, Li L, Chen ZD. Passively Q-switched Nd:YVO_4 laser based on Fe_3O_4 nanoparticles saturable absorber. *Opt Mater Express* (2017) 7(8):2913–21. doi:10.1364/ome.7.002913

48. Li CY, Bo Y, Zong N, Wang YG, Jiang BX, Pan YB, et al. LD-end-pumped passively Q-switched Nd:YAG ceramic laser with single wall carbon nanotube saturable absorber. *Opt Laser Tech* (2012) 44(7):2149–53. doi:10.1016/j.optlastec.2012.03.010

49. Lin YY, Lee P, Xu JL, Wu CL, Chou CM, Tu CY, et al. High-pulse-energy topological insulator Bi_2Te_3-based passive Q-switched solid-state laser. *IEEE Photon J* (2017) 8(4):1502710. doi:10.1109/jphot.2016.2581490

50. Huang HT, Li M, Wang L, Liu X, Shen DY, Tang DY, et al. Gold nanorods as single and combined saturable absorbers for a high-energy Q-switched Nd:YAG solid-state laser. *IEEE Photon J* (2015) 7(4):4501210. doi:10.1109/jphot.2015.2460552

frontiers | Frontiers in Physics

TYPE Original Research
PUBLISHED 29 August 2022
DOI 10.3389/fphy.2022.971919

OPEN ACCESS

EDITED BY
Yufei Ma,
Harbin Institute of Technology, China

REVIEWED BY
Siyuan Yu,
Harbin Institute of Technology, China
Hongzhan Liu,
South China Normal University, China
Tianshu Wang,
Changchun University of Science and Technology, China

*CORRESPONDENCE
Wei Wang,
wangwei2012@opt.ac.cn
Xiaoping Xie,
xxp@opt.ac.cn

†These authors have contributed equally to this work and share first authorship

SPECIALTY SECTION
This article was submitted to Optics and Photonics, a section of the journal Frontiers in Physics

RECEIVED 17 June 2022
ACCEPTED 18 July 2022
PUBLISHED 29 August 2022

CITATION
Gao D, Li T, Xie Z, Meng J, Jia S, Bai Z, Wang W and Xie X (2022), High-sensitivity multi-channel DPSK system with real-time phase lock controller for free-space optical communication. *Front. Phys.* 10:971919. doi: 10.3389/fphy.2022.971919

High-sensitivity multi-channel DPSK system with real-time phase lock controller for free-space optical communication

Duorui Gao[1,2†], Tianlun Li[3†], Zhuang Xie[1,2], Jiacheng Meng[1], Shuaiwei Jia[1,2], Zhaofeng Bai[1], Wei Wang[1*] and Xiaoping Xie[1,2*]

[1]State Key Laboratory of Transient Optics and Photonics, Xi'an Institute of Optics and Precision Mechanics, Chinese Academy of Sciences, Xi'an, China, [2]University of Chinese Academy of Sciences, Beijing, China, [3]Key Laboratory of Physical Electronics and Devices of Ministry of Education, School of Electronic Science and Engineering, Xi'an Jiaotong University, Xi'an, China

To overcome the power jitters in satellite-to-ground communications caused by atmospheric turbulence, a type of DPSK free-space communication system, assisted by a self-designed real-time phase lock controller, has been established. The system can effectively compensate for power swings in communication links and hence achieve high sensitivity. The wavelength division multiplexing technique is applied to a four-channel DPSK system to provide greater link capacity. With the data rate of a single channel as 2.5 Gbps and unencoded BER as 1×10^{-3}, reception sensitivity has been obtained at −53.58 dBm (13.69 photons/bit), −53.59 dBm (13.66 photons/bit), −53.61 dBm (13.59 photons/bit), and −53.63 dBm (13.53 photons/bit) for each independent channel, respectively. The gap between our sensitivity result and the theoretical limit has narrowed to about −3.5 dB. Simultaneously, the DPSK receiver, with our self-designed phase lock controller, has stabilized reception of optical power fluctuations that range from 0 to 40 dB. Additionally, the impact of a four-wave mixing effect on multi-channel system performance has been investigated in detail. Our experimental results present a novel solution for the superior performance of free-space communication links.

KEYWORDS

free-space optical communication, differential phase shift keying, delay line interferometer, phase lock controller, wavelength division multiplexing

Introduction

Because of its high-bandwidth, high-speed, and high-security features [1–5], free-space optical communication (FSOC) offers a feasible and valid solution for bottlenecks in microwave communication and for realizing massive real-time transmission of data. Concurrently, and because of the inherent benefits of its small size, lightweight, and low

power consumption—capable of keeping up with the communication demands of booming space activities—the FSOC terminal can be considered an ideal satellite payload [6, 7]. Thus far, the data rate of satellite laser communication links has been found to approach Gbps magnitude [8, 9]. However, through wavelength division multiplexing (WDM) technology, this rate is predicted to reach magnitudes of dozens, even hundreds, of Gbps [10, 11].

Under the diverse modulation method, the proven techniques of FSOC are mainly divided into two main categories: non-coherent and coherent communication systems. Intensity modulation and direct detection (IM-DD) are utilized in non-coherent systems, which have the advantages of simplicity of structure and high reliability (although with undesirable levels of reception sensitivity) [12]. By contrast, coherent communication systems, which combine phase modulation with coherent detection, deploy the coherent superposition of local-oscillator (LO) and signal optical fields, supporting high sensitivity, high modulation rates, and strong anti-interference capability [13, 14]. Coherent communication modes mainly consist of binary phase shift keying (BPSK) and differential phase shift keying (DPSK). Since the DPSK format has less strict requirements for laser source linewidth, many commercial or strategic demonstrations have a preference for such systems, including the Laser Communications Relay Demonstration (LCRD), Integrated LCRD Low-Earth Orbit User Modem and Amplifier Terminal (ILLUMA-T), and the Japanese Data Relay System (JDRS) [15–17]. Due to the turbulence of the atmosphere, satellite-to-ground laser communication links suffer from random optical power fluctuations of the order of milliseconds (ms), which lead to inferior demodulation of the DPSK signal and an increase in the system bit-error rate (BER). To weaken the negative impact of these random fluctuations, several methods have been explored to reduce the penalty associated with other photoelectric devices [18]. Clearly, the optimal solution is to fundamentally smooth out or level of this kind of power jitter.

To this end, a real-time phase lock controller, based on a large-scale power jitter compensation method, has been designed to effectively compensate for optical power swings ranging from 0 to 40 dB. Applying this controller and the WDM technique, the resulting four-channel DPSK communication system has competitive receiving sensitivity that approaches the theoretical limit. Meanwhile, the impact of the four-wave mixing effect of high transmitted optical power on multi-channel system performance is elaborated in detail. The phase-lock controller can be considered an alternative solution for the power fluctuation problem in FSO communication links. At the same time, the WDM technique can be effectively combined with our self-designed phase-lock controller, which means the controller has potential in the application of multiplexed high-speed laser communication systems. Our demonstration indicates that adding a phase lock controller to the DPSK system leads to an improvement in receiving sensitivity, which in turn lays a vital foundation for optimizing the performance of the receiving terminal while mitigating the effects of optical power jitter.

Principle and experiments

Principle large-scale power jitter compensation

In the high-speed DPSK transceiver system, a pseudo-random bit sequence (PRBS) from a pattern generator is differentially pre-encoded and then transferred to a Mach–Zehnder modulator (MZM) to generate the DPSK optical signal. The transmission function can be presented as follows: [19]

$$E_{out}(t) = E_{in}(t)\cos\left\{\frac{\pi}{2V_{\pi}}\left[V_{in}(t) - V_{bias}\right]\right\}\exp\left\{-j\frac{\pi V_{bias}}{2V_{\pi}}\right\}, \tag{1}$$

where $E_{out}(t)$ and $E_{in}(t) = e^{i\omega ct}$ represent output and input optical fields, respectively; $\omega_c = 2\pi f_0$ is the angular frequency of the optical carrier, with f_0 being the frequency; V_{π} is the half-wave voltage of MZM; and $V_{in}(t)$ and V_{bias} are the driving and bias voltage of MZM, respectively. When $V_{bias} = V_{\pi}$, $V_{in}(t) = V(t)\cdot a(t)$, with $a(t) = \pm 1$ [$a(t)$ represents the 1 or 0 bit in the pre-coded PRBS], the DPSK optical signal can be generated with the transmission function as follows: [20]

$$E_{out}(t) = -jE_{in}(t)\sin\left[\frac{\pi}{2}a(t)\right] = -ja(t)e^{i\omega_c t}, \tag{2}$$

After modulation, the optical signal was transferred to a high-power Er^{3+}-doped fiber amplifier (EDFA) before being routed to optical antenna for further transmission over the free-space channel. Subsequently, the DPSK signal can be captured by the receiving terminal and defined mathematically by the following transmission function:

$$E_{RX}(t) = A(t)E_{out}(t), \tag{3}$$

where $E_{RX}(t)$ represents the optical field of the received signal and $A(t)$ is the random fluctuation function of optical power.

After a certain free-space distance of transmission, the optical signal is detected by the collimator at the receiving terminal. As illustrated in Figure 1A, an optical coupler (OC1) is introduced before the normal demodulation process. One of the signal branches enters the delay line interferometer (DLI) (path 1, Figure 1A), and the other branch is transformed into the electrical signal via a photodetector (PD), before being imported into the phase-lock control system (path 2, Figure 1A). The path 1 optical signal is converted into a detectable electrical signal by a balanced photo-detector (BPD) and is processed by the integrated transimpedance amplifier

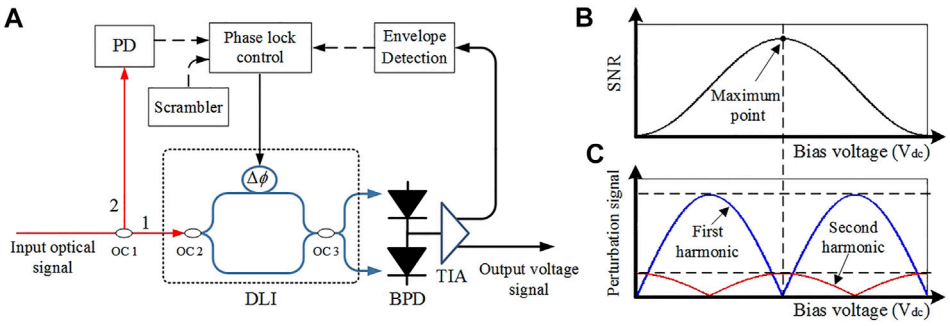

FIGURE 1
(A) The block diagram of the high-speed DPSK receiver system. **(B,C)** The relationship between SNR and the harmonic component of the perturbation signal with corresponding bias voltage.

(TIA). Next, one channel of the output electrical signal is inputted into the envelope detection unit for peak-to-peak detection and is then transferred into the phase lock controller. Subsequently, two independent electrical signals from path 1 and path 2 undergo time synchronization, power jitter removal, as well as correlation detection with a scrambler signal, in order to calculate and update the bias voltage of DLI in real time. The optimized bias voltage guarantees the working position of DLI, and thus ensures the superior DPSK receiving performance.

The output optical field after OC 2 can be resolved by the following matrix:

$$\begin{pmatrix} E_1 \\ E_2 \end{pmatrix} = \begin{pmatrix} E_{RX}(t) \\ E_{RX}(t-T) \end{pmatrix} = \begin{pmatrix} -jA(t)a(t)e^{j\omega_c t} \\ -jA(t-T)a(t-T)e^{j\omega_c(t-T)}e^{i\Delta\phi} \end{pmatrix}, \tag{4}$$

where T is the reciprocal of the system rate and $\Delta\phi$ is the absolute phase-delay. Since the variation frequency of spatial optical power swings is much less than the signal rate, the approximate condition $A(t)\approx A(t\text{-}T)$ can be adopted to simplify the calculation. Meanwhile, the transfer matrix M of the OC 3 can be expressed as

$$\mathrm{M} = \begin{pmatrix} \sqrt{\rho} & j\sqrt{\rho} \\ j\sqrt{\rho} & \sqrt{\rho} \end{pmatrix}, \tag{5}$$

where ρ is the splitting ratio of OC 3 (Figure 1A). Therefore, the matrix of the optical field at the output port of OC 3 can be conducted as

$$\begin{aligned} \begin{pmatrix} E_3 \\ E_4 \end{pmatrix} &= M\begin{pmatrix} E_1 \\ E_2 \end{pmatrix} \\ &= \begin{pmatrix} -jA(t)\sqrt{\rho}e^{j\omega_c t}\left[a(t-T)e^{-j\omega_c T} + je^{j\Delta\phi}a(t)\right] \\ -jA(t)\sqrt{\rho}e^{j\omega_c t}\left[ja(t-T)e^{-j\omega_c T} + e^{j\Delta\phi}a(t)\right] \end{pmatrix}. \end{aligned} \tag{6}$$

The optical signal expressed in Eq. 6 will be detected by a BPD and conditioned by a TIA. Assuming $\rho = 0.5$, the output current from BPD (I_1 and I_2) is supposed to be defined by the corresponding input optical field of BPD (E_3 and E_4) as follows:

$$\begin{cases} I_1 \propto P_1 = |E_3|^2 = A^2(t)\left[1 - a(t-T)a(t)\sin(\omega_c T + \Delta\phi)\right] \\ I_2 \propto P_2 = |E_4|^2 = A^2(t)\left[1 + a(t-T)a(t)\sin(\omega_c T + \Delta\phi)\right] \end{cases}. \tag{7}$$

It can be clearly seen that the value of the output current from BPD is proportional to the input optical power. By means of a differential operation, the output voltage V_{sig} of BPD can be calculated by [21]

$$V_{sig} = (I_1 - I_2)R \propto 2A^2(t)\left[a(t-T)a(t)\sin(\omega_c T + \Delta\phi)\right], \tag{8}$$

where R is the transimpedance. Simultaneously, the average output optical power of the other phase-lock branch ($\bar{P}_2$) can be expressed as

$$\bar{P}_2 = r(P_1 + P_2) = 2rA^2(t), \tag{9}$$

where r is the splitting ratio and P_1 and P_2 are the optical power for paths 1 and 2, respectively. Based on Eq. 9, $\bar{P}_2$ is proportional to the square of the jitter amplitude $A(t)$. Comparing $\bar{P}_2$ and $\bar{V}_{env}$ with the normalization method, the scaled factor k can be defined as

$$k = \frac{\bar{V}_{env}}{\bar{P}_2} \approx \frac{2A^2(t)\sin(\omega_c T + \Delta\phi)}{2rA^2(t)} = \frac{\sin(\omega_c T + \Delta\phi)}{2r}, \tag{10}$$

where $\bar{V}_{env}$ is the peak–peak valid value of V_{sig}. Since r and $\omega_c T$ are constant, k is independent of the power jitter, and is only related to the $\Delta\phi$ of DLI. Thus, k can be expediently adjusted to the maximum value to guarantee the best performance of the output signal-to-noise ratio by controlling the DLI phase difference.

According to the actual operation of correlation detection, determining the value and the direction of the compensation is a matter of great necessity. To solve this problem, it is considered preferable to introduce to the DLI a perturbation signal with quite a low frequency. Getting through the BPD and envelope

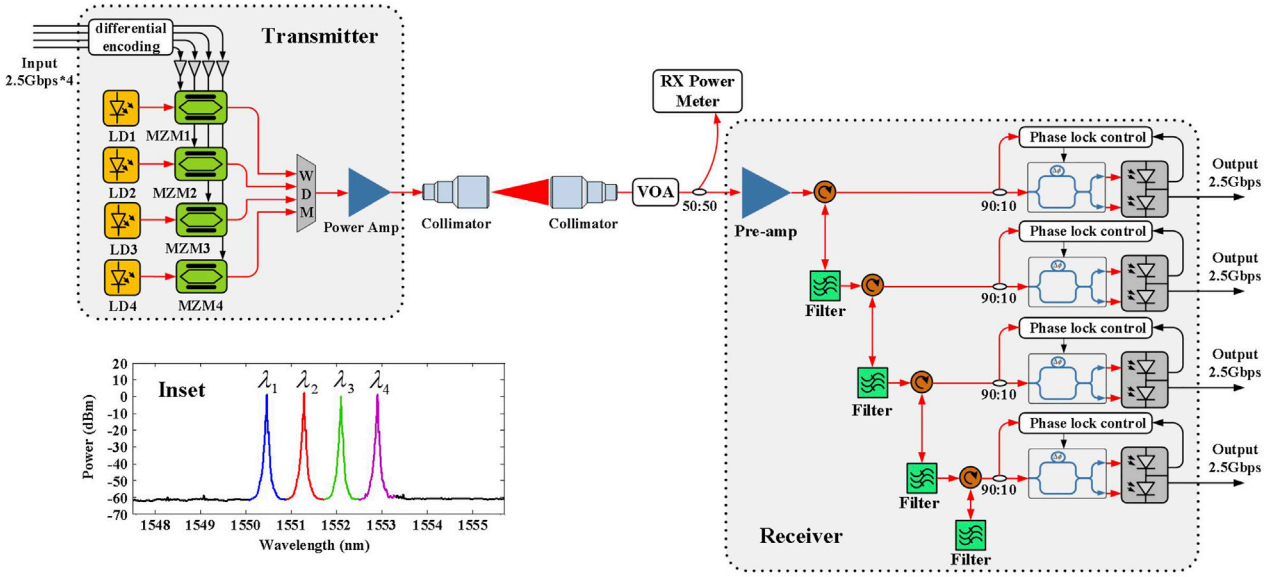

FIGURE 2
The architecture of the four-channel DPSK coherent communication system. Inset: the spectrum of the four-channel multiplexed signal.

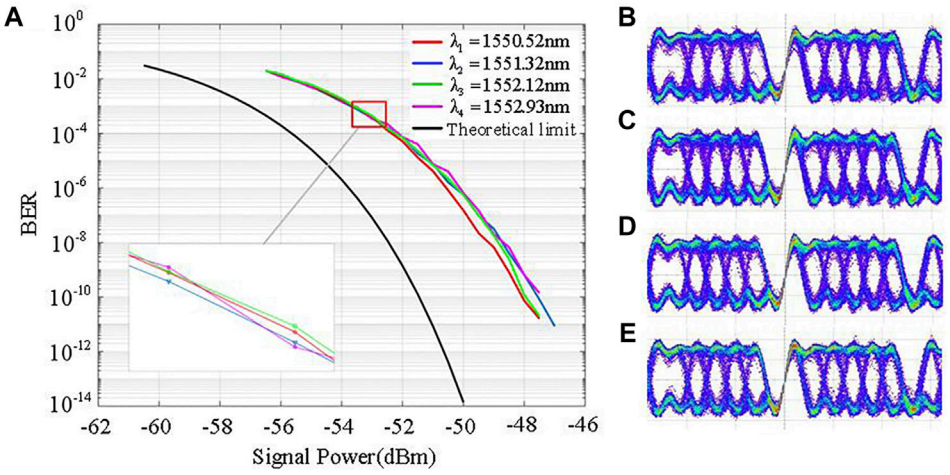

FIGURE 3
(A) BER for four channels of 2.5 Gbps DPSK signal. **(B–E)** Eye diagrams of four independent channels after demodulation.

detection, the extracted perturbation signal carries out the correlation detection with the initial perturbation signal at the phase lock controller (Figure 1A).

Generally, the phase difference of DLI $\Delta\phi$ can be expressed as [22]

$$\Delta\phi = \frac{\pi[V_{dc} + V_{dither}]}{V_{DLI}}, \tag{11}$$

where V_{dc} is the direct current (DC) bias voltage applied on the DLI; V_{DLI}, as the constant, is the required voltage for the DLI to realize phase changing by π. The frequency of perturbation signal $V_{dither} = v_0\cos(\omega_0 t)$ is 1 kHz and has no impact on the original signal. When $\varphi = \omega_c T + \pi V_{dc}/V_{\mathrm{DLI}}$ and $k' = 2rk$ are fixed, the updated scale factor k' of the feedback loop in the phase lock controller can be easily conducted as

TABLE 1 Reported BER results for different DPSK links.

Mode/Link type	Rate (Gbps)	Wavelength	Channel(s)	BER	Receive power (dBm)	Reference
RZ-DPSK Free space	10	~1,550 nm	1	10^{-3}	~ −43	[24]
DPSK Fiber	10	~1,550 nm	4	10^{-3}	~ −41	[25]
RZ-DPSK Fiber	10	~1,550 nm	1	10^{-4}	~ −17	[26]
NRZ-DPSK Fiber	10	~1,550 nm	1	10^{-3}	~ −23	[27]
NRZ-DPSK Free-space	10	~1,550 nm	4	10^{-3}	~ −53/per channel	This work

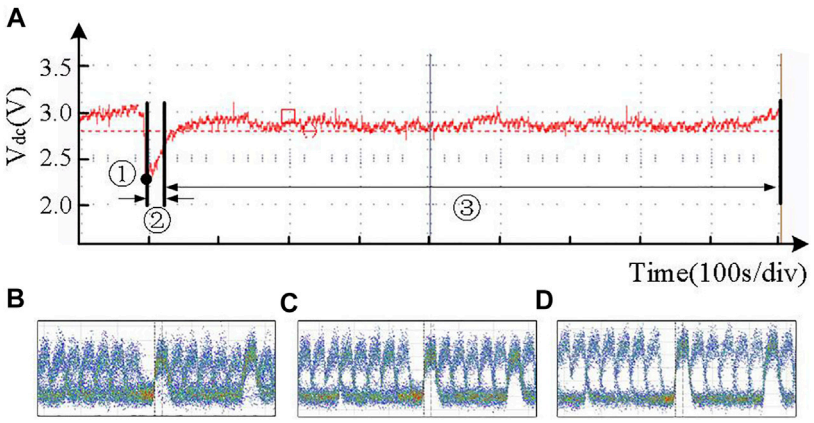

FIGURE 4
(A) Applied voltage on DLI for controlling the scale factor k'. **(B–D)** Eye diagrams for corresponding working point ①, part ②, and part ③.

$$k' = \sin\left(\varphi + \frac{\pi V_{dither}}{V_{\mathrm{DLI}}}\right) = \sin\varphi\cos\frac{\pi V_{dither}}{V_{\mathrm{DLI}}} + \cos\varphi\sin\frac{\pi V_{dither}}{V_{\mathrm{DLI}}}. \tag{12}$$

Expanding Eq. 12 by the Taylor series and keeping three terms, k' can be illustrated as

$$k' = \cos\varphi + v_0\cos(\omega_0 t)\sin\varphi - \frac{1}{2}v_0^2\cos^2(\omega_0 t)\cos\varphi - \frac{1}{6}v_0^3\cos^3(\omega_0 t)\sin\varphi, \tag{13}$$

And by further conducting, it can be expressed as follows:

$$k' = \left(1 - \frac{1}{4}v_0^2\right)\cos\varphi + \left(v_0 - \frac{1}{8}v_0^3\right)\cos(\omega_0 t)\sin\varphi - \frac{1}{4}v_0^2\cos(2\omega_0 t)\cos\varphi - \frac{1}{24}v_0^3\cos^3(\omega_0 t)\sin\varphi. \tag{14}$$

Based on Eq. 14, the maximum value of scale factor k' can be approached by monitoring the value of the harmonic component of the perturbation signal. For instance, the first harmonic component is $k_1' = (v_0 - v_0^3/8)\cos(\omega_0 t)\sin\varphi$, and the second harmonic component is $k_2' = -v_0^2\cos(2\omega_0 t)\cos\varphi/4$. Figures 1B,C illustrate the performance of the scale factor k' and the harmonic components of the perturbation signal under the same working bias voltage. When $\varphi = \omega_c T + \pi V_{dc}/V_{\mathrm{DLI}} = n\pi$, $n = \pm1, \pm2, \pm3, \ldots$, the first and second harmonic components correspond to the minimum and the maximum values, respectively. Thus, a superior signal-to-noise ratio (SNR) has been obtained. With our self-designed phase lock system, it is convenient to maintain the highest SNR of the output signal by continuously calculating and updating working voltages in real time, and apparently realizing the optimal coherent reception of the DPSK optical signal.

2.2 Experiment setup

In view of the correlation detection compensation method, the four-channel DPSK coherent communication system in this effort is presented in Figure 2. Four distributed-feedback

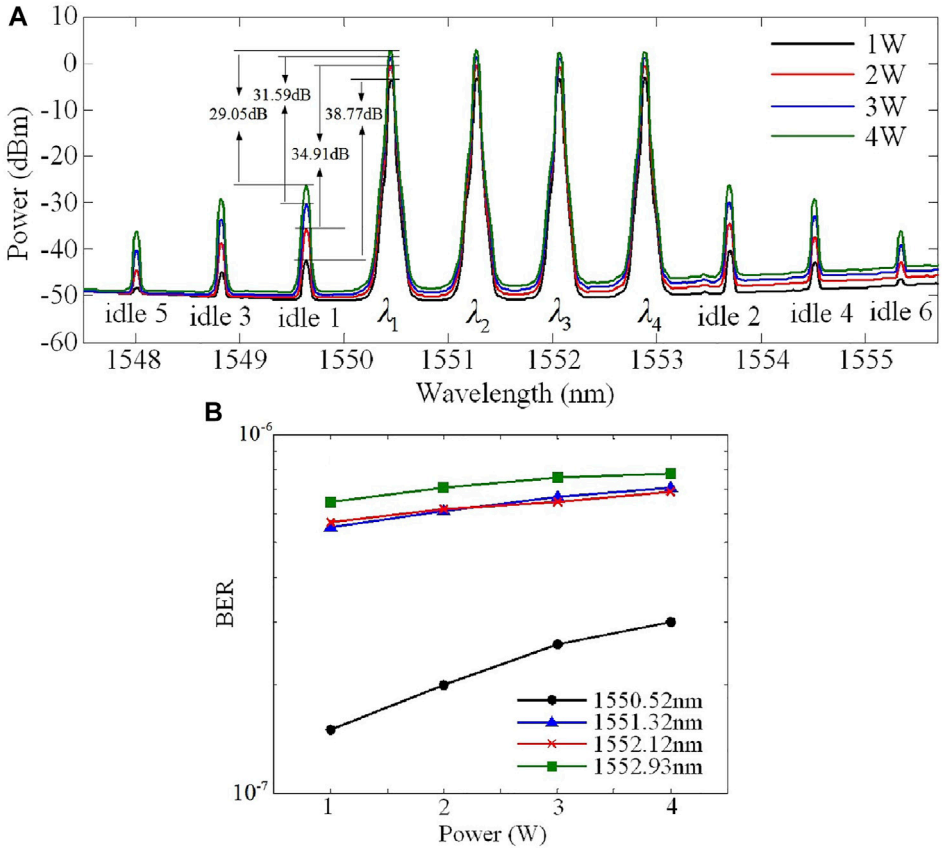

FIGURE 5
(A) The amplified spectrum of four channels. **(B)** The correlation between optical power and the system BER.

(DFB) continuous-wave (CW) lasers (RIO, RIO0075-3-ITU-1) generated four corresponding WDM pulse signals with 100 GHz channel spacing, 10 kHz linewidth, and the central wavelengths of λ_1 = 1,550.52 nm, λ_2 = 1,551.32 nm, λ_3 = 1,552.12 nm, and λ_4 = 1,552.93 nm, respectively. Each signal was independently modulated by a MZM (iXblue, MXAN-LN-10, V_π = 5.5 V), loaded with non-return-to-zero (NRZ) PRBS of length 2^7–1 from separate data sources. The inset of Figure 2 displays the spectrum of the four laser sources. The multiplexed signal is subsequently amplified by a high-power EDFA (KEOPSYS, CEFA-C-PB-HP) to prepare for coupling with the FSOC terminal, aimed at long-haul transmission over the free-space channel. In this effort, an electrical-control variable optical attenuator (VOA) is utilized to simulate the power jitter caused by atmospheric turbulence, and the spatial optical transmission distance is 1 m.

The faded optical signal—resulting from the power jitter caused by atmospheric turbulence—is supposed to be captured via the optical antenna of the receiving terminal and coupled to the follow-up fiber. The received optical signal is split into two separate branches via a 50:50 splitter. One of the optical paths is applied to monitor the light power in real time, while the other is pre-amplified and routed into four cascaded fiber-Bragg gratings (FBGs) to faultlessly denoise with the purpose of extracting four separate channels of the optical signal. Each filtered optical signal is imported into the corresponding DLI to proceed with the self-differential demodulation of our self-designed phase-lock controller, which compensates for the demodulation-efficiency drops from optical power swings. Ultimately, each individual signal is converted into a baseband electrical signal by its corresponding BPD (Discovery Semiconductors DSC-R422) for further measurement and analysis.

Results and discussion

Receiving sensitivity

Receiving sensitivity is an essential indicator when assessing the performance of the free-space optical receiver. Figure 3A

depicts the correlation between the communication BER and the received optical power for each single channel loaded with 2.5 Gbps PRBS. As the unencoded BER is 1×10^{-3}, which allows forward-error correction codes to further reduce the BER to the range of 10^{-9}, the receiving sensitivity of the four independent channels is measured as −53.58 dBm (13.69 photons/bit, 1,550.52 nm), −53.59 dBm (13.66 photons/bit, 1,551.32 nm), −53.61 dBm (13.59 photons/bit, 1,552.12 nm), and −53.63 dBm (13.53 photons/bit, 1,552.93 nm), respectively. It is impressive that there is only about −3.5 dBm loss compared with the theoretical limit, as −57.01 dBm (BER = $\exp(-\eta N_p/2)/2$, η is also set to 1, so that the sensitivity corresponds to an ideal photodetector; N_p is the number of photons) [23]. In our FSOC system, the penalty is mainly introduced by an optical pre-amplifier with a 4.5 dB noise coefficient, which is 1.5 dB larger than the theoretical limit of 3 dB. Additionally, about 1.5 dB loss caused by the out-of-band noise of the optical filter, and 0.5 dB loss from the phase lock controller are also taken into account. The eye diagrams for the four recovered channels of electrical signal are displayed in Figures 3B–E. Table 1 lists the reported BER performance of different DPSK communication systems. Compared with these results, the results of our experiment are objectively competitive.

Optical power jitter

An electrical-control VOA was applied to simulate the optical power jitter with a frequency of 100 Hz and its scale ranging from 0 to 40 dB. The applied voltage of the self-designed phase lock controller is illustrated in Figure 4A. Point ① denotes an initial voltage applied on DLI when the phase lock unit is switched on and implies a lower demodulated SNR (Figure 4B). After that, the phase lock controller commences calculating the scale factor k' of the initial voltage within part ②, keeping the scale factor at a maximum value by means of real-time voltage adjustment with progressive SNR (Figure 4C). Part ③ signifies that the scale factor k' is real-time locked at a maximum value (with the maximum SNR) by the phase lock system (Figure 4D).

On the strength of the above experiment and analysis, the optical power swings can be effectively compensated for using our self-designed phase lock system, which can productively optimize the coherent demodulation procedure.

Analysis of the FWM effect and transmitted optical power

Although high optical power is required for free-space long-haul transmission, the nonlinear optical (NLO) effects within the fiber receive a further boost from the increase in the optical power of the WDM system, especially the four-wave mixing (FWM) effect that occurs in the amplifying procedure within the transmitter. The optical amplification process has been utilized to investigate the probable influence brought about by FWM. Figure 5A exhibits the spectrum of four amplified laser sources, with the amplified power as 1, 2, 3, and 4 W, respectively. It is determined that the FWM effect occurs through optical amplification and generates multiple idle signals. With the increase in optical power, the FWM phenomenon is harder to ignore. The difference value between the signal light and idle 1 is 38.77, 34.91, 31.59, and 29.05 dB, corresponding to amplified power as 1, 2, 3, and 4 W. With the increase in the optical power, the BER is slightly increased (Figure 5B). The optical power of λ_1 = 1,550.52 nm is ~0.4 dB higher than that of the other wavelengths. After optical amplification and transmittance, the corresponding optical power at the receiving terminal is also ~0.4 dB higher than that of other wavelengths. Thus, the BER of 1,550.52 nm is better than the other three channels. Nonetheless, the BER remains at the same order of magnitude, which implies that the optical-power influence on the BER need not be over-considered.

Conclusion

In conclusion, a novel phase lock controller, based on the large-scale power jitter compensation method, has been designed to compensate for power fluctuations ranging from 0 to 40 dB. In applying the self-designed phase lock control unit, a high-sensitivity DPSK-based multi-channel communication system was established, which realized superior receiving performance. With the data rate of a single channel as 2.5 Gbps and unencoded BER as 1×10^{-3}, receiving sensitivity was obtained as −53.58 dBm (13.69 photons/bit), −53.59 dBm (13.66 photons/bit), −53.61 dBm (13.59 photons/bit), and −53.63 dBm (13.53 photons/bit) for each independent channel, respectively. The gap between the results of our experiment and the theoretical limit narrowed to about −3.5 dB. In addition, multi-channel communication system performance degradation caused by the FWM effect was confirmed to be negligible, which endows communication systems with the link capacity expansion potential of hundreds of Gbps in the future. As indicated by the experimentation, the self-designed phase lock controller has the stable performance and measurement precision to meet forthcoming requirements and hence has potential application for satellite-to-ground laser links.

Data availability statement

The original contributions presented in the study are included in the article/Supplementary Material, and further inquiries can be directed to the corresponding authors.

Author contributions

DG, WW, and XX conceived the idea for the study; DG and TL wrote the article; all authors discussed the results and revised the manuscript.

Funding

National Natural Science Foundation of China (61231012, 91638101); National Key Research and Development Program of China (2018YFC0307904-02); and Fundamental Research Funds for the Central Universities (xzy022021039).

Conflict of interest

The authors declare that the research was conducted in the absence of any commercial or financial relationships that could be construed as a potential conflict of interest.

Publisher's note

All claims expressed in this article are solely those of the authors and do not necessarily represent those of their affiliated organizations, or those of the publisher, the editors, and the reviewers. Any product that may be evaluated in this article, or claim that may be made by its manufacturer, is not guaranteed or endorsed by the publisher.

References

1. Willner AE, Liu C. Perspective on using multiple orbital-angular-momentum beams for enhanced capacity in free-space optical communication links. *Nanophotonics* (2021) 10:225–33. doi:10.1515/nanoph-2020-0435

2. Gao D, Xie Z, Ma R, Wang W, Bai Z, Jia S, et al. Development current status and trend analysis of satellite laser communication (invited). *Acta Phtonica Sin* (2021) 50:9–29.

3. Su Y, Wang W, Hu X, Hu H, Huang X, Wang Y, et al. 10 Gbps DPSK transmission over free-space link in the mid-infrared. *Opt Express* (2018) 26: 34515–28. doi:10.1364/oe.26.034515

4. Yu X, Zhang L, Zhang Y, Song Y, Tian M, Wang T, et al. 2.5 Gbps free-space optical transmission between two 5G airship floating base stations at a distance of 12 km. *Opt Lett* (2021) 46:2156–9. doi:10.1364/ol.419690

5. Aveta F, Refai HH, LoPresti PG. Multiple access technique in a high-speed free-space optical communication link: Independent component analysis. *Opt Eng* (2019) 58:036111. doi:10.1117/1.oe.58.3.036111

6. Ma Y, Lewicki R, Razeghi M, Tittel F. QEPAS based ppb-level detection of CO and N_2O using a high power CW DFB-QCL. *Opt Express* (2013) 21:1008–19. doi:10.1364/oe.21.001008

7. Mai VV, Kim H. Beaconless pat and adaptive beam control using variable focus lens for free-space optical communication systems. *APL Photon* (2021) 6:020801. doi:10.1063/5.0039108

8. Mirza J, Ghafoor S, Hussain A. All-optical generation and transmission of multiple ultrawideband signals over free space optical link. *Opt Eng* (2019) 58:1. doi:10.1117/1.oe.58.5.056103

9. Hamza AS, Deogun JS, Alexander DR. Classification framework for free space optical communication links and systems. *IEEE Commun Surv Tutorials* (2018) 21: 1346–82. doi:10.1109/comst.2018.2876805

10. Dong F, Chen G, Liu Z, Lin P, Zhang Y, Ma W, et al. Low SNR difference Nyquist-WDM channels with optical sinc-shaped pulses based on flat electro-optic frequency combs. *Appl Opt* (2020) 59:11389–95. doi:10.1364/ao.411962

11. Ma Y, Feng W, Qiao S, Zhao Z, Gao S, Wang Y. Hollow-core anti-resonant fiber based light-induced thermoelastic spectroscopy for gas sensing. *Opt Express* (2022) 30:18836–44. doi:10.1364/oe.460134

12. Han X, Li P, Chang C, Gao D, Zhang D, Liao P, et al. A comprehensive comparison and analysis of several intensity modulations based on the underwater photon-counting communication system. *Front Phys* (2022) 9:811. doi:10.3389/fphy.2021.815343

13. Wang L, Wang J, Tang X, Chen H, Chen X. Performance analysis of a spatial diversity coherent free-space optical communication system based on optimal branch block phase correction. *Opt Express* (2022) 30:7854–69. doi:10.1364/oe.448956

14. Geng C, Li F, Zuo J, Liu J, Yang X, Yu T, et al. Fiber laser transceiving and wavefront aberration mitigation with adaptive distributed aperture array for free-space optical communications. *Opt Lett* (2020) 45:1906–9. doi:10.1364/ol.383093

15. Shin WH, Lee JW, Ha IH, Han SK. Data rate enhancement of free space optical communication using pulse positioned differential phase shift keying. *Opt Express* (2021) 29:26039–47. doi:10.1364/oe.435060

16. Spellmeyer NW. Use of commercially available fiber optic components in emerging space laser communications applications: Optimizing performance, cost, and reliability. In: 2021 Optical Fiber Communications Conference and Exhibition (OFC); 6–11 June 2021; Washington, DC, United States (2021). p. 1–3.

17. Araki T. Current trends in space optical communication around the world and its R&D activities in JAXA. *IEICE Trans Fundamentals* (2018) E101-A:161–6. doi:10.1587/transfun.e101.a.161

18. Rose TS, Klimcak CM, Kozlowski DA, Sefler GA, Yura HT, Walston AA, et al. Wavelength tracking interferometer for DPSK lasercom links. In: 2011 International Conference on Space Optical Systems and Applications (ICSOS); 11-13 May 2011; Santa Monica, CA (2011). p. 306–11.

19. Caplan DO. Laser communication transmitter and receiver design. *J Optic Comm Rep* (2007) 4:225–362. doi:10.1007/s10297-006-0079-z

20. Seimetz M. *High-order modulation for optical fiber transmission*. Berlin/Heidelberg, Germany: Springer (2009).

21. Ghassemlooy Z, Popoola W, Rajbhandari S. *Optical wireless communications: System and channel modelling with matlab*. Florida, United States: CRC Press (2019).

22. Hemmati H. *Near-earth laser communications*. Boca Raton: CRC Press (2020).

23. Agrawal GP. *Fiber-optic communication systems*. New York: John Wiley & Sons (2012).

24. Elayoubi K, Rissons A, Lacan J, Antonin LS, Sotom M, Kernec AL. RZ-DPSK optical modulation for free space optical communication by satellites. In: 2017 Opto-Electronics and Communications Conference (OECC) and Photonics Global Conference (PGC); 31 July - 4 August 2017; Singapore (2017). p. 1–2.

25. Guan P., Roge K. M., Kjoller N. K., Mulvad H. C. H., Galili M., Morioka T., Oxenlowe L. K. (2015). All-optical WDM regeneration of DPSK signals using optical fourier transformation and phase sensitive amplification. 2015 European Conference on Optical Communication (ECOC), Valencia, Spain, 27 September – 1 October 2015 0228.

26. Mao Y, Liu B, Zhao D, Sun T, Zhao L, Ullah R, et al. All-optical 3R regeneration for DPSK signal based on a semiconductor optical amplifier scheme. *Appl Opt* (2020) 59:3526–9. doi:10.1364/ao.389952

27. El-Nahal FI. A WDM-PON with DPSK modulated downstream and OOK modulated upstream signals based on symmetric 10 Gbit/s wavelength reused bidirectional reflective SOA. *Optoelectronics Lett* (2017) 13:67–9. doi:10.1007/s11801-017-6227-2

frontiers | Frontiers in Physics

TYPE Original Research
PUBLISHED 06 September 2022
DOI 10.3389/fphy.2022.1003517

OPEN ACCESS

EDITED BY
Yufei Ma,
Harbin Institute of Technology, China

REVIEWED BY
Jiamiao Yang,
Shanghai Jiao Tong University, China
Xina Cheng,
Xidian University, China

*CORRESPONDENCE
Yong Song,
yongsong@bit.edu.cn

SPECIALTY SECTION
This article was submitted to Optics and Photonics,
a section of the journal
Frontiers in Physics

RECEIVED 26 July 2022
ACCEPTED 10 August 2022
PUBLISHED 06 September 2022

CITATION
Zhao Y, Song Y, Li G, Deng L, Bai Y and Wu X (2022), Multi-layer Rotation Memory Model-based correlation filter for visual tracking.
Front. Phys. 10:1003517.
doi: 10.3389/fphy.2022.1003517

Multi-layer Rotation Memory Model-based correlation filter for visual tracking

Yufei Zhao[1], Yong Song[2,3]*, Guoqi Li[1], Lei Deng[1], Yashuo Bai[2,3] and Xiyan Wu[2,3]

[1]Department of Precision Instrument, Center for Brain-Inspired Computing Research, Tsinghua University, Beijing, China, [2]School of Optics and Photonics, Beijing Institute of Technology, Beijing, China, [3]Beijing Key Laboratory for Precision Optoelectronic Measurement Instrument and Technology, Beijing, China

Object tracking technology is of great significance in laser image processing. However, occlusion or similar interference during visual object tracking may reduce the tracking precision or even cause tracking failure. Aiming at this issue, we propose a Multi-layer Rotation Memory Model-based Correlation Filter (MRMCF) for visual trackingin this paper. First, we establish a Multi-layer Rotation Memory (MRM) model, in which a set of three rotating concentric rings is used to simulate the three memory spacesand their updating processsimulate the memory spaces. Then we introduce the MRM model into the correlation filter tracking framework, which realizes realizing the dynamic updating of classifier parametersin the correlation filter. When the object is occluded or there is similar interference, the proposed tracker can use the Pre-occ classifier parameters stored in the memory spaces in the MRM model MRM memory spaces to retarget the object, thereby reducing the impact of these factors. The experimental results on the OTB50 dataset show that compared with trackers such as CNN-SVM, MEEM, Struck, etc., the proposed tracker achieves higher accuracy and success rate.

KEYWORDS

laser image processing, visual tracking, human visual system, memory model, correlation filter, object occlusion

1 Introduction

Object tracking technology has a wide range of application in laser spectroscopy including LiDAR (Light Detection And Ranging) image processing [1, 2], active laser detection [3, 4] and real-time laser tracker [5, 6], etc. Generally, object tracking is the task of estimating the state of an arbitrary object in each frame of a video sequence. In the most general setting, the object is only defined by its initial state in the sequence. Most current approaches address the tracking problem by constructing an object model, and these approaches are capable of differentiating between the object and background appearance [7, 8].

At present, there are mainly two types of object trackers: generative trackers and discriminative trackers. Among them, the basic idea of the generative trackers is to learn

an object appearance model and search for the most similar area in the image as the object area [9–12]. The discriminative trackers (also called detection-based trackers) regard the tracking problem as a detection problem. This kind of tracker trains a classifier using the object and the background area of the current frame as the position and negative sample, respectively. And the trained classifier is adopted to find the optimal object area in the next frame.

In the classifier training process of discriminative trackers, different training methods can be used, such as Correlation Filter (CF) [13–15], Deep Learning (DL) [16–18], and Support Vector Machine (SVM) [19, 20]. Among them, CF has been widely used due to its advantages of high speed and good robustness. Specifically, in the CF method, a classifier is firstly learned from a set of training samples. Then the classifier is trained by performing a cyclic shift operation on the training sample, which allows the training and detection process can be performed in the Fourier domain. The amount of calculation is greatly reduced, thereby obtaining higher efficiency. However, CF only considers the samples of the current frame during each training. Therefore, when facing common problems such as occlusion, deformation, or background clutter [8, 21], the CF does not consider the influence of previously appeared samples, and the trained classifier is not robust enough, which may lead to tracking failure.

On the other hand, the memory mechanism in the Human Visual System (HVS) can extract old information stored in the memory space when a new similar one appears. Therefore, the memory mechanism has the potential to solve the problem of occlusion during the tracking process. In terms of object tracking, Ma et al. [22] proposed a tracker based on an adaptive CF with long-term memory and short-term memory, which achieves long-term stable memory of the appearance of the object; Wan et al. [23] introduced Long Short-Term Memory (LSTM) into the tracking process, obtaining good tracking results; Mikami et al. [24] adopted the memory model for face posture tracking, and obtained higher robustness in the complex background.

However, the above methods are based on machine memory. Unlike human memory, machine memory does not consider some key characteristics of the memory mechanism in HVS, such as the uncertainty, fuzziness, and associativity of human brain memory. When the object disappears for a long time or is interfered with by similar objects during the tracking process, the tracking accuracy will be greatly reduced.

In this paper, we established an MRM model to update the classifier parameters in the CF tracker. The MRM model consists of multiple layers of concentric rings, which simulate different levels of memory space. When multiple similar information exists in the outer ring, these data will be merged and enter the inner ring. This process simulates the memory from shallow to deep. At the same time, each ring rotates at a certain speed, which simulates the dynamic update of the information stored in the memory space. Furthermore, we proposed an MRM model-based CF tracker, which can dynamically update the classifier parameters in the CF tracker and enable the CF tracker to remember object features. When the object is occluded or interfered with by similar objects, the proposed tracker can use the reliable classifier parameters stored in the MRM model to relocate the object, thereby improving the anti-interference ability. Comparison experiments show that compared with 18 comparison trackers such as CNN-SVM, MEEM, Struck, etc., the proposed tracker has advantages in tracking accuracy and tracking success rate, the results on the OTB50 are improved 4.9% and 3.7% compared with CNN and SVM, respectively.

2 Related works

One can find various surveys that review the most current developments in visual tracking research in [8, 25]. In this section, only the works that are most relevant to our own are covered, including correlation tracking methods and memory models for visual tracking.

2.1 Correlation tracking

Due to DCFs' exceptional accuracy and efficiency, the object tracking community has been studying them extensively in recent years. The Minimum Output Sum of Squared Error (MOSSE) high-speed tracker, proposed by Bolme et al. in [26], can be regarded as the ground-breaking work that first applied correlation filters to visual tracking. Henriques et al. [13] utilized the circulant structure of training samples and HOG features to develop Kernelized Correlation Filters (KCFs) in the Fourier domain. To maintain a manageable computational cost, Danelljan et al. [27] introduced Color Name (CN) descriptors and also advanced a proposal for an adaptive dimensionality reduction technique. To manage scale fluctuations of the target, Danelljan et al. [28] introduced a Discriminative Scale Space Tracker (DSST). To reduce model drift, Mueller et al. [29] included global context information in the typical construction of CFs. Ma et al. [30]proposed a Long-term Correlation Tracking (LCT) framework featuring a redetection module. When a tracking failure took place in this system, the redetector was engaged to retrace the target's location. By merging the HOG template model with the color histogram model, Bertinetto et al. [31] created the Staple algorithm, which improved the tracking robustness.

2.2 Memory model for visual tracking

Due to its ability to handle sequential input and acquire long-term dependencies, the recent and well-liked Long Short-Term

Memory (LSTM) network demonstrated significant promise in visual tracking. By fusing an LSTM and a residual framework, Kim et al. [32] created an RLSTM tracker for spatiotemporal attention learning. Through the use of an LSTM network, Yang et al. [33] learned a recurrent filter and modified it to account for target appearance fluctuations. To increase the precision of template-matching trackers, a dynamic memory network was developed in [34], where the LSTM was used to maintain target appearance variations with an accessible memory.

3 MRM model

3.1 Memory mechanism

To simulate memory, the process by which the human brain encodes, stores, and extracts from the received information, Atkinson and Shiffrin [35, 36] proposed the multi-store model. They believe that the received information will experience three stages of memory, i.e., sensory memory, short-term memory, and long-term memory. In each stage, the information will go through the process of encoding, storage, and extraction. Meanwhile, information that is rarely used or extracted will be forgotten.

Among the three memory spaces, sensory memory space stores basic sensory information, which is the first step of human brain memory. Short-term memory space stores and processes complex information, which is the main space for information processing. Long-term memory space stores a large amount of prior knowledge, which enables the human brain to recall various events and recognize various patterns. Only the information that is repeatedly appeared in the short-term memory space can be transferred to the long-term memory space for storage.

However, compared with human brain memory, existing memory models lack some key functions. For example: (1) The information extracted by human brain memory is often vague, especially when the extracted information occurred a long time ago; (2) Human brain memory always links multiple related information, the human brain searches the memory space for information related to the received information and merges them; (3) The quality of the information retrieved by the human brain memory is usually related to the time and effort spent in memorizing the information; (4) In some cases, the human brain cannot recall a message at a certain time, but it may succeed after a while.

In short, the memory mechanism in HVS has some key characteristics:

Uncertainty At a certain moment, only part of the information stored in the human brain can be retrieved, but not all the information is clearly presented in the brain;

Fuzziness Similar information in the memory space will be merged, resulting in that the stored information will gradually become blurred over time;

Associativity The human brain memory will associate the related old information in the memory space with the newly received information.

Existing memory models simply simulate the memory mechanism of the human brain, but not the characteristics of uncertainty, fuzziness, and associativity. This limits its application, such as difficulty in solving the problems of object occlusion and similar object interference during tracking.

3.2 Structure of MRM model

Based on the above analysis, we established an MRM model as shown in Figure 1.

The MRM model includes a three-layer concentric ring, a Filter unit, two Compare and Merge units, a Compare unit, and some Data Storage units (including Memorized Data units and Empty Data units). At the same time, there are three different types of windows in each of the three layers of concentric rings, namely the Input window, Output window, and Observation window.

The main functions of each component are as follows:

Three-layer concentric ring: Simulates the different memory spaces of the human brain and the dynamic update of information in the human brain memory space. Each layer of concentric rings simulates a memory space. From the outer to the inner layer, they are sensory, short-term, and long-term memory space. At the same time, each layer of concentric rings rotates at a certain speed, and the speed from the outer layer to the inner layer is v_1, v_2, and v_3.

Filter unit: Filters the information entering the memory space. The filter unit compares the input information with the information that exists in the outer concentric ring (i.e., the sensory memory space). When the distance between the input information and any information in the sensory memory space is within the tolerance distance, the input information can enter the memory space.

Compare and Merge unit: Screens the information in the shallow memory space and send the qualified information into the deep memory space. The specific process includes two operations: comparison and merging. Among them, the comparison operation simulates the associativity of the human brain, and the similarity is obtained by calculating the normalized Euclidean distance between the two pieces of information. The merging operation simulates the fuzziness of the human brain and realizes the fusion of information by calculating the average value of two or more pieces of information. There is one Compare and Merge unit between the outermost layer-the middle layer and the middle layer-the innermost layer, respectively.

Compare unit: Evaluates the similarity between the output information of each layer of memory space and the initial input information, ensuring that the most similar information to the initial input information is output. The specific process is the same as the comparison operation in the Compare and Merge unit.

Data Storage unit: Mainly used to store information. Each layer of concentric rings has multiple data storage units, including memorized data units and empty data units.

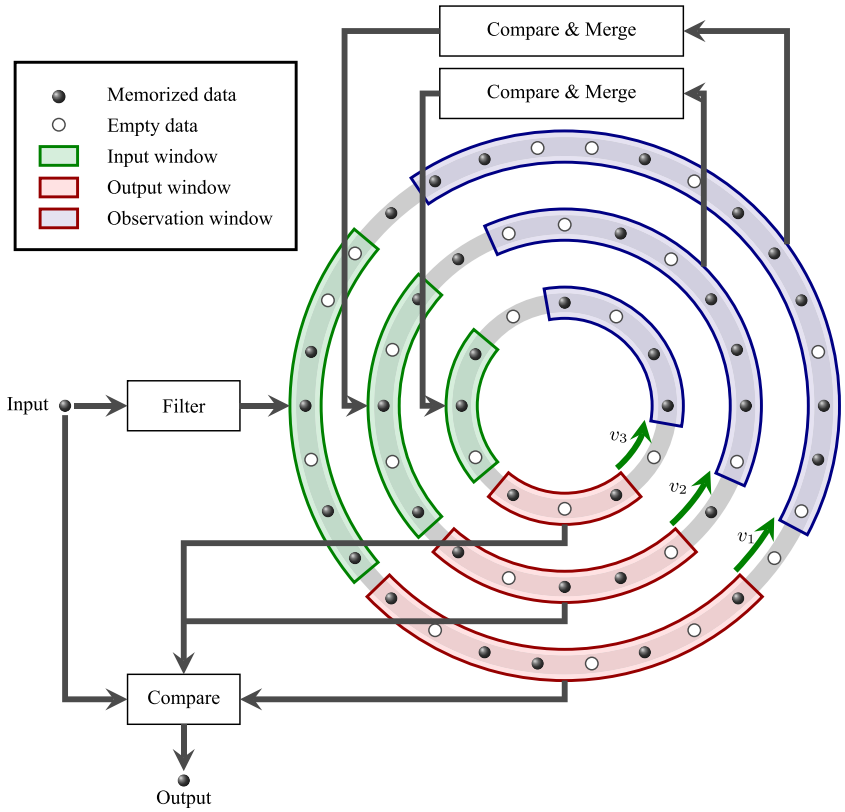

FIGURE 1
Schematic of MRM model, the input information enters three layers of concentric rings representing three different memory spaces through a filter unit, and the concentric rings rotate at different speeds, so that the input information can be transmitted to different locations in the memory space.

Window: Including input window, output window, and observation window. Three kinds of windows exist on each layer of the concentric ring. As the concentric ring rotates, any information will only appear in a specific window at any time. This simulates the uncertainty of human brain memory, that is, not all the stored information can be used at any time.

3.3 Workflow of MRM model

Figure 2 shows the workflow of the MRM model. The detailed process is as follows:

1) The filter unit evaluates whether the initial input information can enter the memory space. If it is permitted to enter, go to step (2). Otherwise, go to step (6);
2) The initial input information enters the sensory memory space and is named sensory input information. If there exists an empty data storage unit in the input window of the sensory memory space at the current moment, the sensory input information is directly stored in the corresponding unit. Otherwise, calculate the normalized Euclidean distance between the sensory input information and each piece of information in the input window, and merge it with the information with the smallest distance. At the same time, the normalized Euclidean distance between each information in the output window and the sensory input information is compared, and the information with the smallest distance will be let out as the sensory output information;
3) Use Compare and Merge unit to merge two or more pieces of information within the tolerance distance in the observation window of the sensory memory space. The merged information is fed into the short-term memory space, called short-term input information;
4) The process of inputting and outputting information in the short-term memory space is similar to step (2), and its output is called short-term output information;
5) Similar to step (3) and step (4), use Compare and Merge unit to merge two or more pieces of information within the tolerance distance in the observation window of the short-term memory space. Then input them into the long-term memory space, which is called long-term input information. At the same time, output long-term output information;

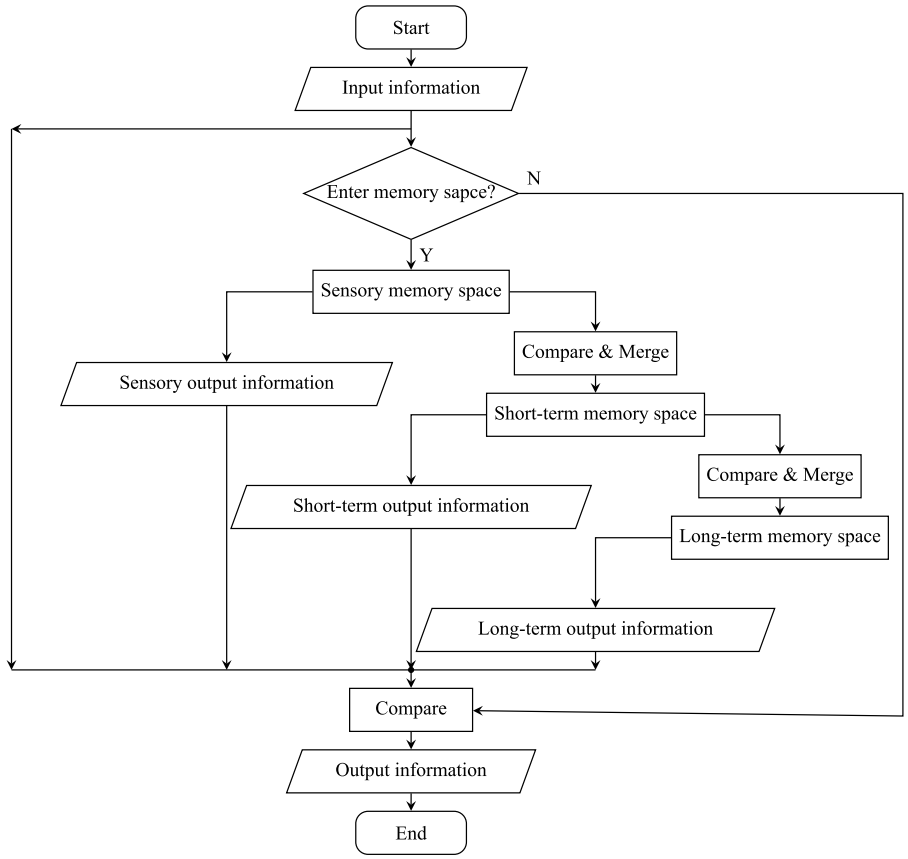

FIGURE 2
Workflow of the MRM model.

6) If there is no output in the three memory spaces, the initial input information is treated as the final output information. Otherwise, the distances between three output information and the initial input information are calculated separately, and the output information with the smallest distance from the initial input information is regarded as the final output information.

4 MRM-based CF tracker

After the establishment of the MRM model, we introduce it into the CF tracking framework and propose an MRM-based CF tracker.

4.1 CF tracking framework

A typical CF tracking framework mainly implements object tracking by repeating the detection-training-update process for each frame of the input image. When any frame of image is input, the search window of the current frame is first determined according to the predicted position in the previous frame, then the feature map of the search image is extracted. Next, the previously learned classifier is used to convolve the feature map to generate a response map. The position of the maximum value on the response map is regarded as the object position of the current frame. Finally, the classifier parameters are trained and updated according to the feature map at the current object position.

Let $(\hat{m}_{t-1}, \hat{n}_{t-1}, a, b)$ be the position and size information of the object in the $(t-1)$th frame of image, where $\hat{m}_{t-1}$ and $\hat{n}_{t-1}$ are the center coordinate of the tracking box, a and b are the width and height of the tracking box. Expand the tracking box to create a search window $(\hat{m}_{t-1}, \hat{n}_{t-1}, \rho a, \rho b)$ for the tth frame of image, where ρ is the expansion factor.

Extract the deep convolution feature map in the search window of the tth frame image, and use x_t to denote the cyclic shift of the feature map with size of $M \times N \times D \times L$ in the tth frame, where M, N, D, and L respectively represent the width, height, the number of channels and layer of the feature map. Then x_t $[d, l]$ represents the feature map of channel d in the lth layer of the tth frame of image, where $d \in \{1, \ldots, D\}$, $l \in \{1, \ldots, L\}$.

For the feature map of the lth layer, the corresponding classifier $w_{t-1}[d,l]$ of the $(t-1)$th frame image and the feature map $x_t[d,l]$ of the tth frame image are respectively subjected to Fourier transform, after the dot multiplication, sum along the channel, and the sub-response map $f_t[l]$ of this layer can be obtained through inverse Fourier transform, as shown in Eq. 1,

$$f_t[l] = \mathcal{F}^{-1}\left(\sum_{d=1}^{D} \mathcal{F}(w_{t-1}[d,l]) \odot \mathcal{F}(x_t[d,l])\right), \tag{1}$$

where $\mathcal{F}$ and $\mathcal{F}^{-1}$ represent DFT (Discrete Fourier Transform) and inverse DFT, respectively, and $\odot$ represents Hadamard product.

Then, take γ_l as the weight coefficient to add the sub-response maps $f_t[l]$ of all layers to get the total response map f_t, as shown in Eq. 2,

$$f_t = \sum_{l=1}^{L} \gamma_l \cdot f_t[l] = \sum_{l=1}^{L} \gamma_l \mathcal{F}^{-1}\left(\sum_{d=1}^{D} \mathcal{F}(w_{t-1}[d,l]) \odot \mathcal{F}(x_t[d,l])\right). \tag{2}$$

The position of the maximum value in the total response map f_t is the center position of the tracking box in the tth frame, as shown in Eq. 3,

$$(\hat{m}_t, \hat{n}_t) = \arg\max_{m,n} f_t(m,n), \tag{3}$$

where $(m, n) \in \{1, \ldots, M\} \times \{1, \ldots, N\}$.

Create a training sample set x_t' by cyclic shift at the object position $(\hat{m}_t, \hat{n}_t)$ of the tth frame image. Each sample has a 2-D Gaussian label, which can be expressed by Eq. 4,

$$y_{u,v} = \exp\left[-\frac{(u - M/2)^2 + (v - M/2)^2}{2\varepsilon^2}\right], \tag{4}$$

where $(u, v) \in \{1, \ldots, M\} \times \{1, \ldots, N\}$, and ε represents bandwidth.

Next, the new classifier $w_t'[l]$ of the lth layer in the tth frame image can be obtained by minimizing ℓ_2 loss function of the output $w_t[d,l]^* x_t'[d,l]$ and the corresponding Gaussian label $y_{u,v}$, that is,

$$w_t'[l] = \arg\min_{w_t[l]} \left\| \sum_{d=1}^{D} w_t[d,l]^* x_t'[d,l] - y \right\|^2 + \lambda \sum_{d=1}^{D} \|w_t[d,l]\|^2, \tag{5}$$

where λ is the regularization coefficient of ℓ_2, and * represents the correlation operation, that is, the operation shown in Eq. 1.

It can be solved by DFT

$$w_t'[d,l] = \mathcal{F}^{-1}\left(\frac{\mathcal{F}(y)^* \odot \mathcal{F}(x_t'[d,l])}{\sum_{i=1}^{D} (\mathcal{F}(x_t'[i,l]))^* \odot \mathcal{F}(x_t'[i,l]) + \lambda}\right), \tag{6}$$

where * represents conjugation, and $\odot$ represents Hadamard product.

By performing the above operations on each frame of the input image, the position of the object in each frame will be obtained, and the classifier can be updated at the same time.

4.2 Design of MRM-based CF tracker

Two MRM models are introduced in the CF framework to form an MRM-based CF tracker, which enhances the classifier's ability to resist the occlusion of objects and interference from similar objects.

Specifically, in the MRM-based CF tracker, when processing a new image, after the classifier training process in the conventional CF framework, the trained classifier is input into the MRM model and updated according to the MRM model update rules. Then a reliable classifier for the current frame will be output. This reliable classifier integrates the characteristics of similar classifiers stored in the MRM model, and can better deal with object occlusion and interference from similar objects in the tracking process. The overall framework of the proposed algorithm is shown in Figure 3.

On the other hand, considering that the classifier includes a large number of parameters, its update process in the MRM model includes many operations, which will lead to excessive calculations and affect the tracking speed. Therefore, we design a "Command-Follow" mechanism to update the classifier, as shown in Figure 3. In the command channel, send the histogram feature into an MRM model to get its update process. Then, in the follow channel, the classifier can be updated in another MRM model only according to the same update process, without participating in the calculation. Since the data amount of the histogram feature is usually much smaller than the classifier, the dynamic update of the classifier can be realized with less calculation.

The specific steps of the MRM-based CF tracker are as follows:

(1) Initialization: At the first frame, initialize the search window and the two MRM models in the command and follow channels. Then extract the histogram feature q_1 and deep features x_1 of the search window, and train a classifier W_1 at the same time;
(2) Classifier updating: When tracking the tth $(t > 1)$ frame image, first extract the histogram feature of the search window in the $(t-1)$th frame q_{t-1}. Then, update q_{t-1} with the MRM model in the command channel. According to the "Command-Follow" mechanism, the classifier W_{t-1} can be updated with the same update process with the MRM model in the follow channel. Finally, a reliable classifier $\hat{W}_{t-1}$ will be obtained;
(3) Object locating: Extract the deep feature of the search window in the $(t-1)$th frame image x_{t-1}, and calculate the response map by Eq. 2. Then the object locating location of the tth frame image can be obtained by Eq. 3;

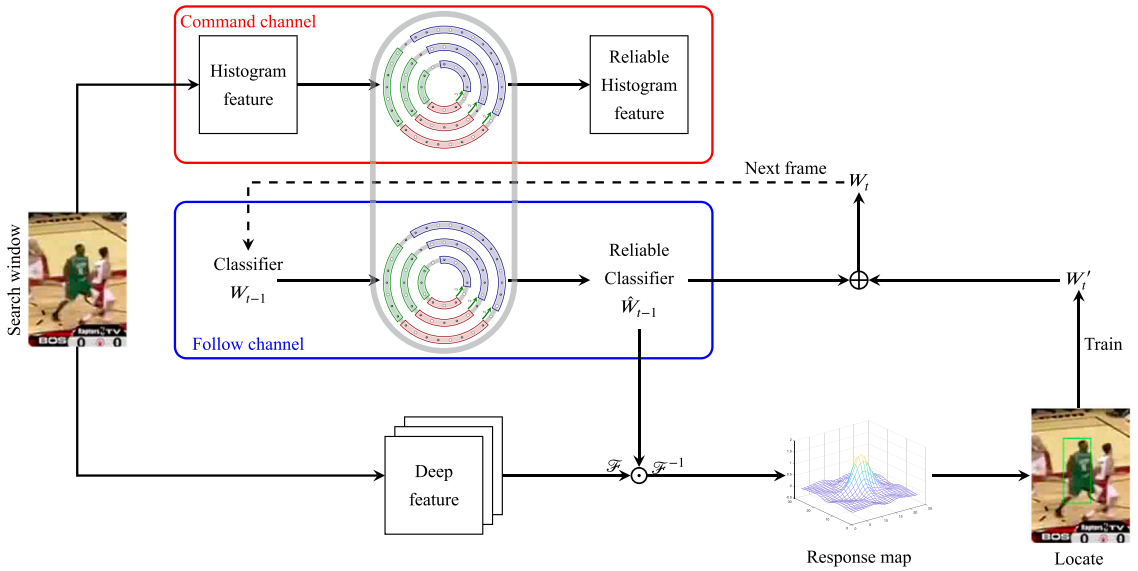

FIGURE 3
Pipeline of the MRM-based CF Tracker, the MRM model in the command channel gets the memory information update rule, and the follow channel updates the classifier in the CF tracker according to the rule, thereby improving the performance of the classifier.

TABLE 1 Parameter settings of the MRM model.

	Outer ring	Middle ring	Inner ring
Number of data storage	20	15	10
Rotation speed	2	1	1
Input window size	5	3	2
Observation window size	6	5	3
Output window size	5	5	3

(4) Classifier training: Train the classifier to obtain the new classifier of the tth frame image W_t, as shown in Eqss 5, 6.

5 Experiment

5.1 Experiment setup

A PC (Intel (R) Xeon E5-2620 (2.10 GHz) × 2 CPU, NVIDIA Quadro P2000 GPU, 64 GB memory) is used to carry out a comparative experiment of the proposed tracker.

The comparative experiment is based on the OTB50 [8] dataset, including 50 image sequences, each of which has different attributes. These image sequence attributes are factors that easily occur in the tracking process and affect the tracking accuracy. There are 11 types, namely: Illumination Variation (IV), Out-of-Plane Rotation (OPR), Scale Variation (SV), Occlusion (OCC), Deformation (DEF), Motion Blur (MB), Fast Motion (FM), In-Plane Rotation (IPR), Out-of-View (OV), Background Clutter (Background Clutter, BC) and Low Resolution (LR). In addition, the specific parameter settings of the memory space of each layer in the comparison experiment are shown in Table 1, and the tolerance distance in the algorithm is set to 0.35.

The tracking precision and success rate were evaluated by precision plot and success plot, respectively.

The tracking precision is the percentage of frames whose estimated locations lie in a given threshold distance to ground-truth centers. By setting a series of different thresholds, the corresponding tracking precision values can be calculated to generate a curve, i.e., a precision plot. Generally, the value obtained when the threshold is 20 pixels is treated as the tracking precision of the tracker.

As for the success rate, let $a$xdenote the area of the tracking box and $b$ydenote the ground truth. An Overlap Score (OS) can be defined by OS = $|a \cap b|/|a \cup b|$OS = $|x \cap y|/|x \cup y|$where ∩ and ∪ are the intersection and union of two regions, and |X| counts the number of pixels in the corresponding area X. Afterward, a frame whose OS is larger than a certain threshold is referred to as a successful frame, and the ratios of successful frames at the thresholds ranging from 0 to one are plotted in success plots. Generally, the value when the threshold is 0.5 is used as the tracking success rate of the tracker.

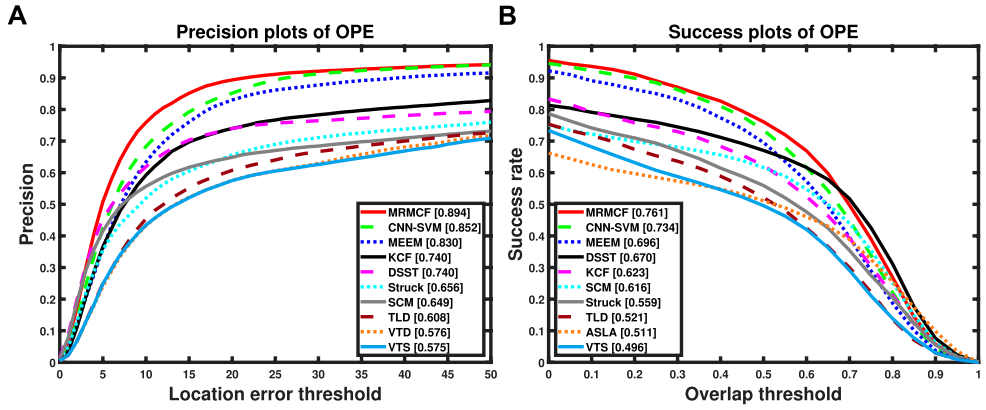

FIGURE 4
OPE comparison results of the proposed tracker and the comparison methods on OTB50. **(A)** Precision plots, **(B)** Success plots.

5.2 Results

5.2.1 Overall performance

The proposed MRMCF is compared with 18 trackers, including CNN-SVM [37], MEEM [20], KCF [13], DSST [28], Struck [38], SCM [39], TLD [40], VTD [41], VTS [42], CCT [43], ASLA [44], LSK [45], PCOM [46] etc.

Figure 4 is the overall comparison results under one pass evaluation (OPE). For readability, only the first 10 trackers are plotted. It can be seen that the tracking precision of the proposed MRMCF reaches 89.4%, and the tracking success rate reaches 76.1%, which is higher than comparison trackers, indicating that the proposed tracker has better tracking performance.

Figure 5 shows some of the tracking results of the proposed tracker and comparison trackers including sequences *coke*, *deer*, *football*, *freeman4*, *girl*, *lemming*, and *matrix* of the OTB50 [8]. In order to show the tracking boxes more clearly, only the top five trackers are shown in the figure.

Sequence *coke* has six attributes, including IV, OCC, FM, IPR, OPR, and BC. In the early stage of the tracking process (#0050 and #0116), the object keeps moving smoothly, so all five trackers are able to track the object steadily. Then, the object rotates in frame #0210, and the tracking boxes of DSST and MEEM drifted. Next, the object is blocked by a plant in frame #0260, and the tracking boxes of DSST and CNN-SVM drifted greatly. In the end, the object reappeared in frame #0270, while DSST, MEEM, and KCF could not find the object back;

Sequence *deer* has five attributes, including MB, FM, IPR, BC, and LR. Similarly, in the early stage, the five trackers all performed well (#0010). In the following tracking process, due to the fast movement of the object and the interference of similar objects, KCF lost the object in frames #0030, #0036, and #0050, DSST lost the object in frame #0030 and #0040, and the tracking box of MEEM has a small drift in #0040;

Sequence *football* has four attributes, including OCC, IPR, OPR and BC. In the beginning, all five trackers can track the object well (#0100). With the rapid movement of the object, the tracking boxes of DSST, MEEM, and KCF drifted (#0200). Due to the interference of similar objects, the tracking boxes of DSST, MEEM, CNN-SVM, and KCF have drifted (#0283 and #0290). Then, in frame #297, DSST, CNN-SVM, and KCF lost their targets, while the proposed MRMCF was not disturbed, maintaining good tracking performance.

Sequence *freeman4* has four attributes, including SV, OCC, IPR, OPR. Due to the object being occluded, object rotation, and other factors, the tracking boxes of the comparison trackers have drifted to different degrees. For example, in frame #0080, MEEM and KCF drifted, in frame #0150, DSST, CNN-SVM and KCF drifted, and MEEM drifted in a smaller range, and in frame #0270, all four comparison trackers drifted. Meanwhile, the proposed MRMCF maintained a good tracking result throughout the tracking process;

Sequence *girl* has four attributes, including SV, OCC, IPR and OPR. In the early stages, all the five trackers have good tracking performance, only DSST has a small range of drift (#0300 and #0420). When interfered with by a similar object, KCF, DSST, MEME, and CNN-SVM are affected. Among them, the tracking frame of KCF has a large drift, while DSST, MEME, and CNN-SVM have a small drift (#0438). With time, the tracking box of DSST also drifted widely (#0470 and #0490). In the whole process, the proposed MRMCF can achieve stable tracking without being disturbed by a similar object;

Sequence *lemming* has six attributes, including IV, SV, OCC, FM, OPR, and OV. Similarly, in the early stages of the tracking process, all five trackers perform well (#0200). When the object

FIGURE 5
Part of tracking results of the proposed tracker and comparison trackers on the OTB50.

rotates in frame #0370, the tracking boxes of DSST, MEEM, and KCF all drift in a small range. Later, as the object moved quickly, DSST and KCF lost the object, and the tracking boxes of CNN-SVM and MEEM also drifted (#0382 and #0776). In frame #1070, the posture and scale of the object changed, and the tracking boxes of the five trackers could not fully contain the object, while

TABLE 2 AUC values of success plot corresponding to each attribute (%), the highest values are highlighted in bold.

	IV	OPR	SV	OCC	DEF	MB	FM	IPR	OV	BC	LR
MRMCF	**60.3**	**59.5**	**55.5**	**58.7**	62.7	**58.5**	**57.0**	**58.6**	56.5	**64.1**	**49.4**
CNN-SVM	55.6	58.2	51.3	56.3	**64.0**	56.5	54.5	57.1	57.1	59.3	46.1
MEEM	53.3	55.8	49.8	55.2	56.0	54.1	55.3	53.5	**60.6**	56.9	36.0
DSST	56.1	53.6	54.6	53.2	50.6	45.5	42.8	56.3	46.2	51.7	40.8
KCF	49.3	49.5	42.7	51.4	53.4	49.7	45.9	49.7	55.0	53.5	31.2
SCM	47.3	47.0	51.8	48.7	44.8	29.8	29.6	45.8	36.1	45.0	27.9
Struck	42.8	43.2	42.5	41.3	39.3	43.3	46.2	44.4	45.9	45.8	37.2
LSK	37.1	40.0	37.3	40.9	37.7	30.2	32.8	41.1	43.0	38.8	23.5
VTD	42.0	43.4	40.5	40.3	37.7	30.9	30.2	43.0	44.6	42.5	17.7
TLD	39.9	42.0	42.1	40.2	37.8	40.4	41.7	41.6	45.7	34.5	30.9
VTS	42.9	42.5	40.0	39.8	36.8	30.4	30.0	41.6	44.3	42.8	16.8
CCT	28.6	36.4	33.5	37.8	34.5	31.2	33.1	35.5	46.7	38.5	18.9
FOT	28.6	36.4	33.5	37.8	34.5	31.2	33.1	35.5	46.7	38.5	18.9
PCOM	28.6	36.4	33.5	37.8	34.5	31.2	33.1	35.5	46.7	38.5	18.9
ASLA	42.9	42.2	45.2	37.6	37.2	25.8	24.7	42.5	31.2	40.8	15.7

the position of the tracking box of the proposed MRMCF is relatively accurate;

Sequence *matrix* has seven attributes, including IV, SV, OCC, FM, IPR, OPR, and BC. In frame #0021, DSST, CNN-SVM, and KCF lost the object, and MEEM drifted in a small range. In frame #0024, DSST, CNN-SVM, and KCF lost their targets. In frame #0047, CNN-SVM also lost the target, while DSST, MEEM, and KCF drifted in a small range. In frame #0084, all trackers lost the target due to the rapid movement of the object. While in the following frame #0086, the proposed MRMCF retrieved the object again.

In summary, for the above-mentioned typical sequences, the proposed MRMCF tracker shows better performance.

5.2.2 Attribute-based evaluation

For detailed analyses, an attribute-based evaluation in OTB50 is also conducted. The Area Under Curve (AUC) scores of MRMCF and the comparison trackers under 11 image sequence attributes are shown in Table 2. The results demonstrate that MRMCF performs well on most attributes, especially on occlusion, scale variation, illumination variation, background clutter, and out-of-plane rotation, etc.

5.3 Ablation studies

We performed an ablation analysis for different MRM structures. As shown in Figure 1, the proposed MRM consists

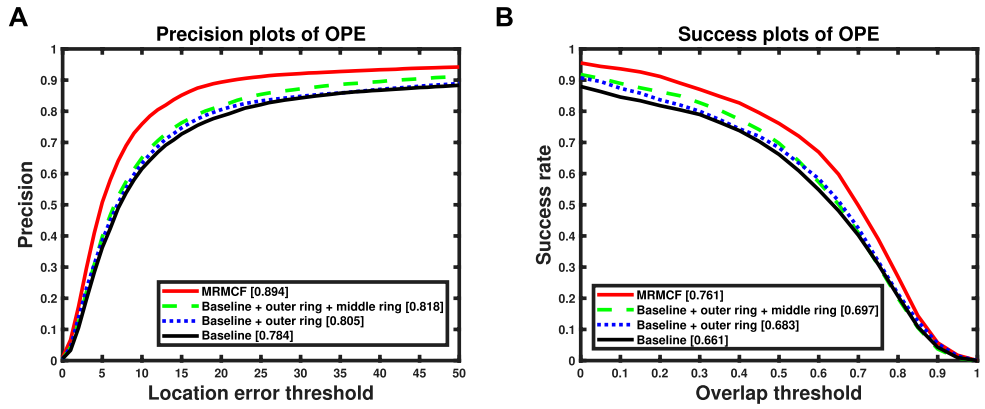

FIGURE 6
OPE comparison results of trackers with different configuration MRM models on OTB50. **(A)** Precision plots, **(B)** Success plots.

of three rings, representing the sensory, short-term and long-term memory space, respectively. In the ablation analysis, we take the CF tracker without the MRM model as the baseline tracker and compared it with three different MRM models with the following configurations: the MRM model including only the outer ring, the MRM model including the outer and middle rings and the MRM model including three rings (i.e. the proposed MRMCF), the results shown in Figure 6.

As shown in Figure 6, compared with the baseline tracker, the performance of the tracker incorporating the MRM model has improved. Moreover, the improvement of the tracker performance is limited by the incomplete MRM model, while the performance improvement of the tracker with the complete MRM model is very obvious.

5.4 generality analysis

The MRM model proposed in this paper is a relatively independent module in the whole tracker, which is mainly used to strengthen the connection with the previous classifier in the update process in the CF tracking framework. In most tracking-by-detection visual tracking methods, the classifier or object template update process is involved, so the proposed MRM model can be added to the update process of these trackers. Through reasonable parameter settings, performance improvement such as anti-occlusion similar to the tracker proposed in this paper can be finally achieved.

6 Conclusion

In this paper, an MRMCF tracker is proposed. Firstly, an MRM model based on the memory mechanism of HVS is established. By introducing the MRM model into the CF framework, the MRMCF tracker is formed, which realizes the dynamic update of CF classifier parameters. Under conditions such as occlusion or similar interferences, MRMCF can extract the reliable classifier parameters stored in the memory space of the MRM model to relocate the object, thereby achieving accurate object tracking. The experimental results based on the OTB50 show that compared with the comparison trackers, the proposed MRMCF has advantages in tracking precision and success rate, especially under various challenging conditions such as object occlusion and image clutter.

Data availability statement

Publicly available datasets were analyzed in this study. This data can be found here: http://cvlab.hanyang.ac.kr/tracker_benchmark/benchmark_v10.html.

Author contributions

YZ: Conceptualization, Methodology, Software, Validation, Writing-Original Draft. YS: Supervision, Project administration, Funding acquisition. GL: Supervision, Writing-review and editing, Investigation. LD: Software, Writing-review and editing, Visualization. YB: Data curation, Writing-review and editing. XW: Investigation.

Funding

This work was supported by the National Natural Science Foundation of China (NSFC) (81671787).

Conflict of interest

The authors declare that the research was conducted in the absence of any commercial or financial relationships that could be construed as a potential conflict of interest.

Publisher's note

All claims expressed in this article are solely those of the authors and do not necessarily represent those of their affiliated organizations, or those of the publisher, the editors and the reviewers. Any product that may be evaluated in this article, or claim that may be made by its manufacturer, is not guaranteed or endorsed by the publisher.

References

1. Zhang J, Xiao W, Coifman B, Mills JP. Vehicle tracking and speed estimation from roadside lidar. *IEEE J Sel Top Appl Earth Obs Remote Sens* (2020) 13:5597–608. doi:10.1109/jstars.2020.3024921

2. Wang Y, Zhu Y, Liu H. Research on unmanned driving interface based on lidar imaging technology. *Front Phys* (2022) 10. doi:10.3389/fphy.2022.810933

3. He S, Meng Y, Gong M. Active laser detection system for recognizing surveillance devices. *Opt Commun* (2018) 426:313–24. doi:10.1016/j.optcom.2018.05.069

4. Li H, Zhang X. Laser reflection characteristics calculation and detection ability analysis of active laser detection screen instrument. *IEEE Trans Instrum Meas* (2021) 71:1–11. doi:10.1109/tim.2021.3129223

5. Sahu RK. A review on application of laser tracker in precision positioning metrology of particle accelerators. *Precision Eng* (2021) 71:232–49. doi:10.1016/j.precisioneng.2021.03.015

6. Iñigo B, Ibabe A, Aguirre G, Urreta H, López de Lacalle LN. Analysis of laser tracker-based volumetric error mapping strategies for large machine tools. *Metals* (2019) 9:757. doi:10.3390/met9070757

7. Marvasti-Zadeh SM, Cheng L, Ghanei-Yakhdan H, Kasaei S. *Deep learning for visual tracking: A comprehensive survey*. IEEE Transactions on Intelligent Transportation Systems (2021).

8. Wu Y, Lim J, Yang MH. Online object tracking: A benchmark. In: Proceedings of the IEEE conference on computer vision and pattern recognition; Washington, DC, USA. IEEE (2013). p. 2411–8.

9. Zhang T, Ghanem B, Liu S, Ahuja N. Robust visual tracking via multi-task sparse learning. In: 2012 IEEE Conference on Computer Vision and Pattern Recognition; Washington, DC, USA. IEEE (2012). p. 2042–9.

10. Sevilla-Lara L, Learned-Miller E. Distribution fields for tracking. In: 2012 IEEE Conference on computer vision and pattern recognition; Washington, DC, USA. IEEE (2012). p. 1910–7.

11. Oron S, Bar-Hillel A, Levi D, Avidan S. Locally orderless tracking. *Int J Comput Vis* (2015) 111:213–28. doi:10.1007/s11263-014-0740-6

12. Zhang K, Zhang L, Liu Q, Zhang D, Yang MH. Fast visual tracking via dense spatio-temporal context learning. In: European conference on computer vision; Berlin, Heidelberg. Springer (2014). p. 127–41.

13. Henriques JF, Caseiro R, Martins P, Batista J. High-speed tracking with kernelized correlation filters. *IEEE Trans Pattern Anal Mach Intell* (2015) 37: 583–96. doi:10.1109/tpami.2014.2345390

14. Marvasti-Zadeh SM, Ghanei-Yakhdan H, Kasaei S. Adaptive exploitation of pre-trained deep convolutional neural networks for robust visual tracking. *Multimed Tools Appl* (2021) 80:22027–76. doi:10.1007/s11042-020-10382-x

15. Ma C, Huang JB, Yang X, Yang MH. Hierarchical convolutional features for visual tracking. In: Proceedings of the IEEE international conference on computer vision; Washington, DC, USA. IEEE (2015). p. 3074–82.

16. He K, Zhang X, Ren S, Sun J. Deep residual learning for image recognition. In: Proceedings of the IEEE conference on computer vision and pattern recognition; Washington, DC, USA. IEEE (2016). p. 770–8.

17. Simonyan K, Zisserman A. Very deep convolutional networks for large-scale image recognition. *Computer Sci* (2014).

18. Zhang K, Liu Q, Yi W, Yang MH. Robust visual tracking via convolutional networks without training. *IEEE Trans Image Process* (2016) 25:1779–92. doi:10.1109/tip.2016.2531283

19. Hare S, Golodetz S, Saffari A, Vineet V, Cheng MM, Hicks SL, et al. Struck: Structured output tracking with kernels. *IEEE Trans Pattern Anal Mach Intell* (2015) 38:2096–109. doi:10.1109/tpami.2015.2509974

20. Zhang J, Ma S, Sclaroff S. Meem: Robust tracking via multiple experts using entropy minimization. In: European conference on computer vision; Berlin, Heidelberg. Springer (2014). p. 188–203.

21. Wu Y, Lim J, Yang MH. Object tracking benchmark. *IEEE Trans Pattern Anal Mach Intell* (2015) 37:1834–48. doi:10.1109/tpami.2014.2388226

22. Ma C, Huang JB, Yang X, Yang MH. Adaptive correlation filters with long-term and short-term memory for object tracking. *Int J Comput Vis* (2018) 126: 771–96. doi:10.1007/s11263-018-1076-4

23. Wan X, Wang J, Kong Z, Zhao Q, Deng S. Multi-object tracking using online metric learning with long short-term memory. In: 2018 25th IEEE International Conference on Image Processing (ICIP); Washington, DC, USA. IEEE (2018). p. 788–92.

24. Mikami D, Otsuka K, Yamato J. Memory-based particle filter for face pose tracking robust under complex dynamics. In: 2009 IEEE Conference on Computer Vision and Pattern Recognition; Washington, DC, USA. IEEE (2009). p. 999–1006.

25. Li P, Wang D, Wang L, Lu H. Deep visual tracking: Review and experimental comparison. *Pattern Recognition* (2018) 76:323–38. doi:10.1016/j.patcog.2017.11.007

26. Bolme DS, Beveridge JR, Draper BA, Lui YM. Visual object tracking using adaptive correlation filters. In: 2010 IEEE computer society conference on computer vision and pattern recognition. IEEE (2010). p. 2544–50.

27. Danelljan M, Shahbaz Khan F, Felsberg M, Van de Weijer J. Adaptive color attributes for real-time visual tracking. In: Proceedings of the IEEE conference on computer vision and pattern recognition (2014). p. 1090–7.

28. Danelljan M, Häger G, Khan FS, Felsberg M. Accurate scale estimation for robust visual tracking. In: British Machine Vision Conference; Berlin, Heidelberg. Springer (2014).

29. Mueller M, Smith N, Ghanem B. Context-aware correlation filter tracking. In: Proceedings of the IEEE conference on computer vision and pattern recognition (2017). p. 1396–404.

30. Ma C, Yang X, Zhang C, Yang MH. Long-term correlation tracking. In: Proceedings of the IEEE conference on computer vision and pattern recognition (2015). p. 5388–96.

31. Bertinetto L, Valmadre J, Golodetz S, Miksik O, Torr PH. Staple: Complementary learners for real-time tracking. In: Proceedings of the IEEE conference on computer vision and pattern recognition (2016). p. 1401–9.

32. Kim HI, Park RH. Residual lstm attention network for object tracking. *IEEE Signal Process Lett* (2018) 25:1029–33. doi:10.1109/lsp.2018.2835768

33. Yang T, Chan AB. Recurrent filter learning for visual tracking. In: Proceedings of the IEEE International Conference on Computer Vision Workshops (2017). p. 2010–9.

34. Yang T, Chan AB. Learning dynamic memory networks for object tracking. Proceedings of the European conference on computer vision (ECCV) (2018), 152–67.

35. Atkinson RC, Shiffrin RM. Human memory: A proposed system and its control processes. *Psychol Learn Motiv* (1968) 2:89–195. doi:10.1016/s0079-7421(08)60422-3

36. Shiffrin RM, Atkinson RC. Storage and retrieval processes in long-term memory. *Psychol Rev* (1969) 76:179–93. doi:10.1037/h0027277

37. Hong S, You T, Kwak S, Han B. Online tracking by learning discriminative saliency map with convolutional neural network. *Computer Sci* (2015) 597–606.

38. Hare S, Saffari A, Torr PHS. Struck: Structured output tracking with kernels. In: International Conference on Computer Vision; Washington, DC, USA. IEEE (2011).

39. Wei Z. *Robust object tracking via sparsity-based collaborative model*. Washington, DC, USA: Computer Vision & Pattern RecognitionIEEE (2012).

40. Kalal Z, Matas J, Mikolajczyk K. Pn learning: Bootstrapping binary classifiers by structural constraints. In: 2010 IEEE Computer Society Conference on Computer Vision and Pattern Recognition; Washington, DC, USA. IEEE (2010). p. 49–56.

41. Kwon J, Lee KM. Visual tracking decomposition. In: 2010 IEEE Computer Society Conference on Computer Vision and Pattern Recognition; Washington, DC, USA. IEEE (2010). p. 1269–76.

42. Kwon J, Lee KM. Tracking by sampling and integratingmultiple trackers. *IEEE Trans Pattern Anal Mach Intell* (2013) 36:1428–41. doi:10.1109/TPAMI.2013.213

43. Danelljan M, Hager G, Shahbaz Khan F, Felsberg M. Convolutional features for correlation filter based visual tracking. In: Proceedings of the IEEE International Conference on Computer Vision Workshops; Washington, DC, USA. IEEE (2015). p. 58–66.

44. Jia X, Lu H, Yang MH. Visual tracking via adaptive structural local sparse appearance model. In: IEEE Conference on computer vision and pattern recognition; Washington, DC, USA. IEEE (2012). p. 1822–9.

45. Liu B, Huang J, Yang L, Kulikowsk C. *Robust tracking using local sparse appearance model and k-selection*. Washington, DC, USA: CVPR 2011IEEE (2011). p. 1313–20.

46. Dong W, Lu H. Visual tracking via probability continuous outlier model. In: IEEE Conference on computer vision and pattern recognition; Washington, DC, USA. IEEE) (2014).

frontiers | Frontiers in Physics

TYPE Original Research
PUBLISHED 23 September 2022
DOI 10.3389/fphy.2022.1028856

OPEN ACCESS

EDITED BY
Yufei Ma,
Harbin Institute of Technology, China

REVIEWED BY
Jin Li,
Northeastern University, China
Qiang Liu,
Northeastern University at Qinhuangdao, China

*CORRESPONDENCE
Zhiying Liu,
zyingliu@163.com

SPECIALTY SECTION
This article was submitted to Optics and Photonics, a section of the journal Frontiers in Physics

RECEIVED 26 August 2022
ACCEPTED 05 September 2022
PUBLISHED 23 September 2022

CITATION
Liu Z, Li H and Zhang Z (2022), Sagnac ring and photonic crystal fiber structure refractive index sensor with high birefringence and low temperature sensitivity.
Front. Phys. 10:1028856.
doi: 10.3389/fphy.2022.1028856

Sagnac ring and photonic crystal fiber structure refractive index sensor with high birefringence and low temperature sensitivity

Zhiying Liu[1]*, Hao Li[1] and Zhiwen Zhang[2]

[1]School of Opto-Electronic Engineering, Changchun University of Science and Technology, Changchun, China, [2]Heilongjiang Province Key Laboratory of Laser Spectroscopy Technology and Application, Harbin University of Science and Technology, Harbin, China

In this paper, a novel refractive index sensor based on photonic crystal fiber and Sagnac ring is studied. The sensor adopts Mach-Zehnder interference principle. The production and experimental steps are as follows: The first step is to fuse the single-mode fiber with the photonic crystal fiber to form a basic sensing unit. The second part uses the coupling birefringence effect of the tapered coupler to fold and fuse the single-mode fiber together to form the Sagnac interferometer. Through this structure, the sensor has the characteristics similar to the polished photonic crystal fiber sensor, while the fabrication complexity is greatly reduced. The refractive index sensing capability and temperature stability of the two structures are analyzed experimentally. Simulation results show that the structure has high birefringence effect. Experimental results show that the proposed photonic crystal fiber combined with Sagnac ring sensor has good sensing performance in the refractive index range of 1.3355–1.3560. Compared with the sensor structure without Sagnac ring, the performance is greatly improved, the maximum sensitivity is up to 234 nm/RIU, and it has good temperature stability. The sensor has the advantages of miniaturization, high integration and high sensitivity, and can be used in industry, chemical detection, agriculture and other fields.

KEYWORDS

photonic crystal fiber, Sagnac ring, refractive index sensor, high birefringence, temperature sensor

Introduction

Optical fiber sensor is different from traditional electrical sensor, the complex mechanical structure is replaced by optical fiber [1–3]. Fiber optic sensors are widely used in strain, temperature, refractive index and other parameters measurement because of their small size, anti-electromagnetic interference and high speed [4–6]. As one of the basic physical parameters, refractive index has important applications in the fields of medicine, biochemistry and life science [7–9]. Optical fiber refractive index sensor is the basis of optical fiber sensor. An excellent fiber refractive index sensor can be extended to other fields of sensing detection. If it is extended to the temperature detection field, only

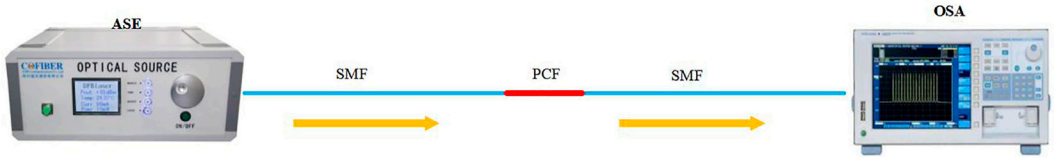

FIGURE 1
Single-mode fiber—PCF- Single-mode fiber structure diagram.

temperature-sensitive materials need to be coated in the sensing area. Extending to the field of humidity detection only requires coating the sensing area with moisture-sensitive material. Therefore, it is very important to propose a kind of fiber refractive index sensor with good performance [10–12].

At present, fiber optic devices used for sensing mainly include fiber Bragg grating, long period grating and Mach-Zehnder interferometer based on special fibers [13–16]. Vanita et al. designed a fiber refractive index sensor with a sensitivity of 197.33nm/RIU through malposition fusion mach-zehnder structure [17], but this structure has the disadvantage of low mechanical strength. In 2021, Zheng et al. proposed three kinds of fiber fusion interference structures, with the sensitivity reaching 101.996 nm/RIU [18]. But it is very difficult to manufacture. Abdul-jabbar et al. designed a fiber refractive index sensor in 2021 based on Fabry-Perot principle, with a sensitivity of 34.338nm/RIU [19]. However, due to the characteristics of the structure, it is greatly affected by temperature. PCF is also a hot topic in optical fiber sensing [20]. But at present, most photonic crystal fiber sensors are only studied in the simulation range [21]. In the research of photonic crystal fiber sensor, the performance of polished PCF sensor is higher than that of ordinary PCF sensor due to its high birefringence [22], but it is difficult to manufacture in practical experiment.

In order to solve the above problems, we put forward a new scheme. In this study, a Sagnac ring was added into the sensing structure of traditional single-mode fiber (SMF) and PCF, and a novel refractive index sensor was fabricated by using the cone-region coupling and the evanescent field superposition effect at the interference region of PCF. The Sagnac ring structure has a high birefringence characteristic even without polishing because the two beams travel in opposite directions and have inconsistent optical paths. The performance of Sagnac combined with PCF was compared with that of conventional SMF-PCF-SMF. The experimental results show that the sensitivity reaches 234.78252 nm/RIU in the refractive index 1.3355-1.3560 range.

Sensor manufacturing and principle analysis

SMF-PCF-SMF structure is a basic refractive index sensor unit that achieves Mach-Zehnder interference principle through fiber core mismatch. The structure is shown in Figure 1. In this paper, the refractive index sensing ability and temperature stability of SMF-PCF-SMF structure were measured first. The experimental device is shown in Figure 1. The two ends of single-mode fiber are respectively connected with broadband light source (ASE) and spectrum analyzer (OSA).

Next, we will remove the coating layer of the single-mode fiber on both sides, and stack them together, and put them into the fiber fusion taper platform. We operate a computer to control the length of the pull-out cone. In the pull-out process, the waveguides of two optical fibers are coupled and the light in one waveguide begins to affect the square distribution of the waveguides in the other fiber. A fused tapered Sagnac ring with a coupling length of 25 mm is formed and the tapered region is encapsulated. The structure of the Sagnac ring is shown in Figure 2, and which shows the instrument and method for manufacturing and testing. After the light signal is emitted by the broadband light source, the beam is evenly divided into two beams of equal intensity from both directions to the PCF by the fused tapered coupler. At this time, PCF and the pull cone area act together to form the sensing unit. Compared to Figure 1, there is an increased phase delay of $\pi/2$ when light passes through the coupler. In addition, due to the structure of PCF, the light source at PCF enters the cladding and produces interference, and the spectrum at this time can be measured by OSA.

Figure 3 shows the simulation results of mode refractive index and electric field distribution of the two parts of the structure used in this paper. Figure 3A part of photonic crystal fiber, Fig in the section for the refractive index of the two models, the red arrow for the direction of the electric field, electric field can be seen from the simulation results, under the condition of without considering manufacture error, we use the PCF structure of the odd and even mode refractive index are the same, there is no double refraction phenomenon. In Figure 3B, it can be seen that the refractive index values of the two modes in the pull-cone coupling part are different, indicating obvious birefringence phenomenon. It can be inferred that the proposed structure should have higher sensitivity than the simple PCF sensor.

Ignoring the insertion loss in the Sagnac ring, the transmittance T of the injected Sagnac interferometer is [23]:

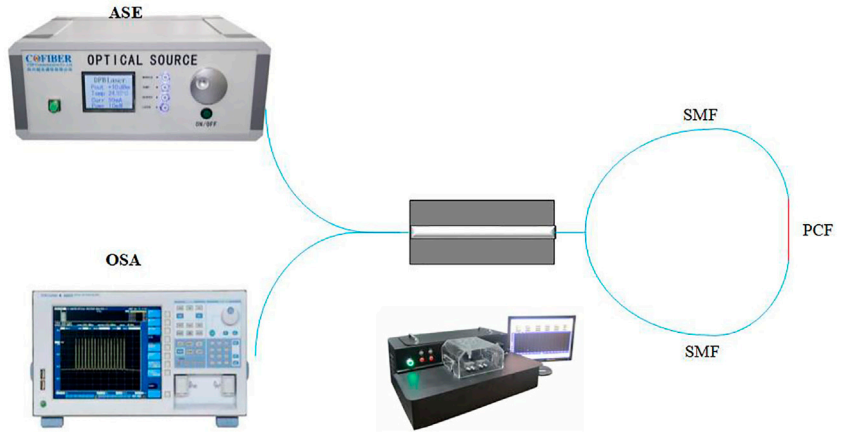

FIGURE 2
Sagnac interferometer sensor structure diagram.

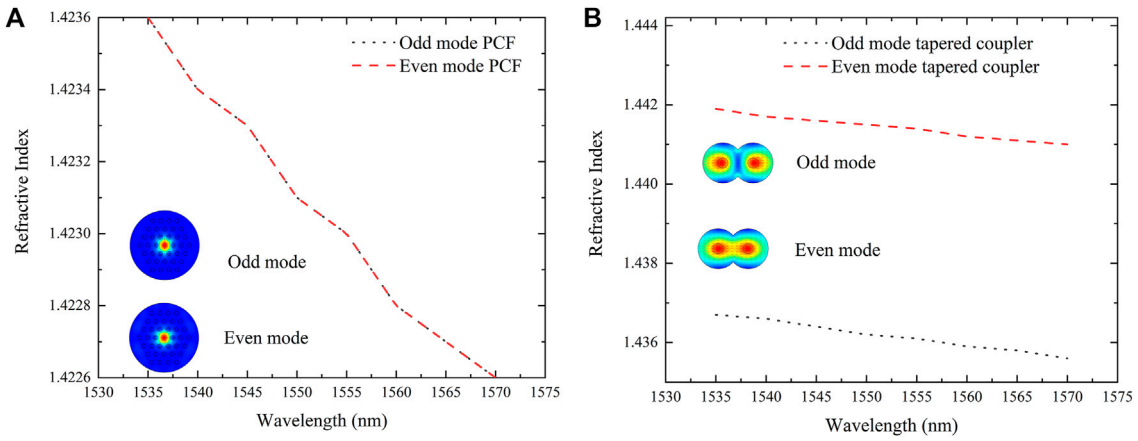

FIGURE 3
Optical fiber mode refractive index simulation and electric field diagram. **(A)** Partial refractive index simulation and electric field diagram of PCF. **(B)** Partial refractive index simulation and electric field diagram of tapered coupler.

$$T = [1 - \cos(\varphi)]/2 \tag{1}$$

In the experimental structure designed by us, light first excites even and odd modes through the cone region. Even mode and odd mode form interference in the coupling region of the taper. Due to the birefringence effect in the coupling region, the superposition of two interference spectra with different polarities and different interference periods can be obtained at the output end. At this point, the phase difference between even mode and odd mode can be expressed as [24]:

$$\varphi_{even} = \frac{2\pi L\left(n^x_{even} - n^y_{even}\right)}{\lambda} \tag{2}$$

$$\varphi_{odd} = \frac{2\pi L\left(n^x_{odd} - n^y_{odd}\right)}{\lambda} \tag{3}$$

Where, L is the length of the draw-cone 25mm, n_{even} and n_{odd} are the effective refractive index of even and odd modes. $B_{even} = n^x_{even} - n^y_{even}$, $B_{odd} = n^x_{odd} - n^y_{odd}$ represents the birefringence coefficients of even mode and odd mode in the waveguide respectively. The λ is the wavelength of incident light. Due to the structural characteristics of Sagnac ring, the two beams propagate in opposite directions, and the phase difference between even mode and odd mode is [25]:

$$\varphi = \frac{2\pi BL}{\lambda} \tag{4}$$

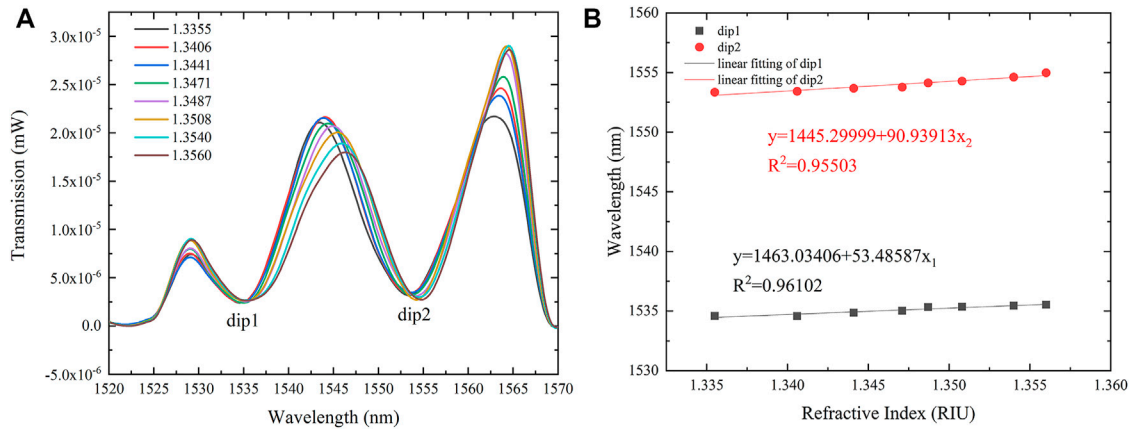

FIGURE 4
SMF-PCF-SMF Index sensor performance diagram. **(A)** Interference spectrum. **(B)** Fitting diagram.

Where, B is the birefringence coefficient, specifically, B = B_{odd}-B_{even}.

When the light beam reaches the mismatch region of PCF core, the light of the core is excited to the cladding layer, and the light in the cladding layer is coupled with the light in the core. When the external environment changes, the optical diameter difference between the cladding transmission light and the fiber core transmission light changes, and the phase difference is [26]:

$$\varphi_{PCF} = \frac{2\pi Z n_{eff}}{\lambda} \quad (5)$$

In this formula, x is the wavelength of the working light wave, Z is the total length of PCF, 20 mm in this paper, neff = N1-N2 is the refractive index of the fiber core, and N2 is the refractive index of the cladding. The total phase difference of the structure in Figure 2 is $\varphi_{all} = \varphi + \varphi_{PCF}$. In this paper, ethanol fusion deionized water (hereafter referred to as solution) was used as the test solution and the temperature stability of the structure in air was analyzed.

Experimental measurement and discussion of refractive index sensor

First of all, we carried out the fusion of single-mode fiber-PCF-single-mode fiber. After the fusion, a basic Machzand structure sensing unit was formed and tested.

We first put the sensor unit into solutions with different refractive indexes at room temperature of 24°C. For the accuracy of the experiment, eight solutions with different concentrations were conFigd for comparison. And after this measurement, the sensor unit is cleaned with deionized water and put into the next solution after drying. As can be seen from Figure 4A, with the increase of refractive index of solution (1.3355-1.3560), the spectrum appeared red-shift. The principle of this structure is the Mach-Zehnder interference caused by core mismatch caused by connecting single mode fiber and photonic crystal fiber. When the refractive index of solution changes, the coupling effect of single-mode fiber and PCF changes. The spectrum drifts. Subsequently, we performed a fitting analysis on dip1 and dip2 in Figure 4B, and it was clear that the sensitivities reached 53.48587nm/RIU and 90.93913nm/RIU, respectively, with R^2 saying 0.96102 and 0.95503. Experimental results show that the sensor using photonic crystal fiber has good refractive index sensitivity. However, when the refractive index of the solution increases further, the spectral shape changes, so we do not analyze the higher refractive index.

Next, we measured the temperature sensitivity of the sensor in the air, and the experimental device was a blast drying oven and a thermometer. In order to ensure the accuracy of measurement, we kept the same temperature for 20 min and then extracted the spectrum. It can be seen from Figure 5A that when the sensor unit detects the temperature in the air, the first trough of the spectrum becomes smaller, while the second trough remains unchanged. When the temperature rises (20–80°C), the wavelength is red-shifted, and we fit the dip. It can be clearly seen from Figure 5B that the temperature sensitivity of the sensing unit is 19.54 p.m./°C, and R^2 is 0.73366. The results show that the sensor is not suitable for temperature sensing, and the temperature sensitivity is far less than the refractive index sensitivity, which shows that the temperature stability of the sensor is very good.

Next, the two sides of single-mode fiber are fused and tapered to form Sagnac structure. The same refractive index and temperature sensing experiments were carried out. It can be seen from Figure 6A that when the refractive index of solution increases, the spectrum also occurs red shift. Different from the above structure, there are two Mach-Zehnder interferences in

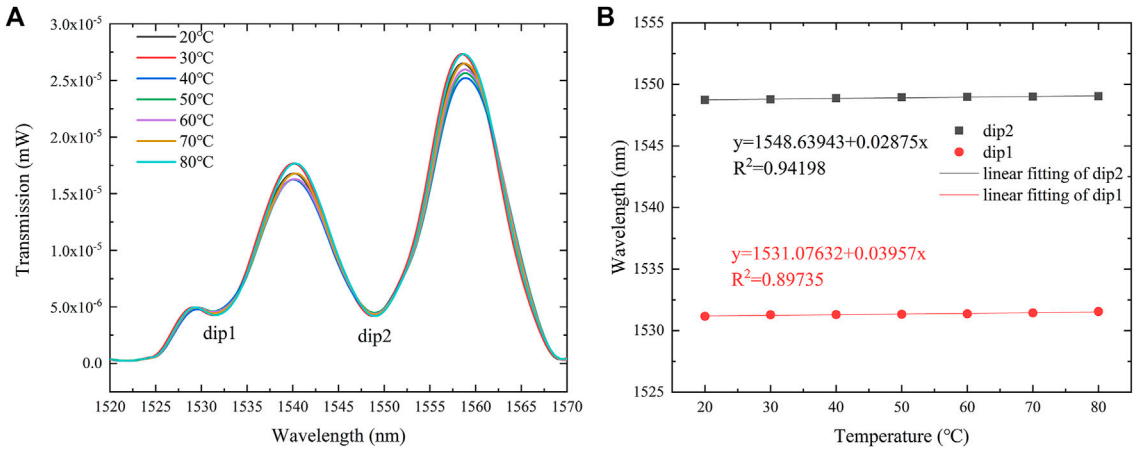

FIGURE 5
SMF-PCF-SMF Temperature sensor performance diagram. **(A)** Interference spectrum. **(B)** Fitting diagram.

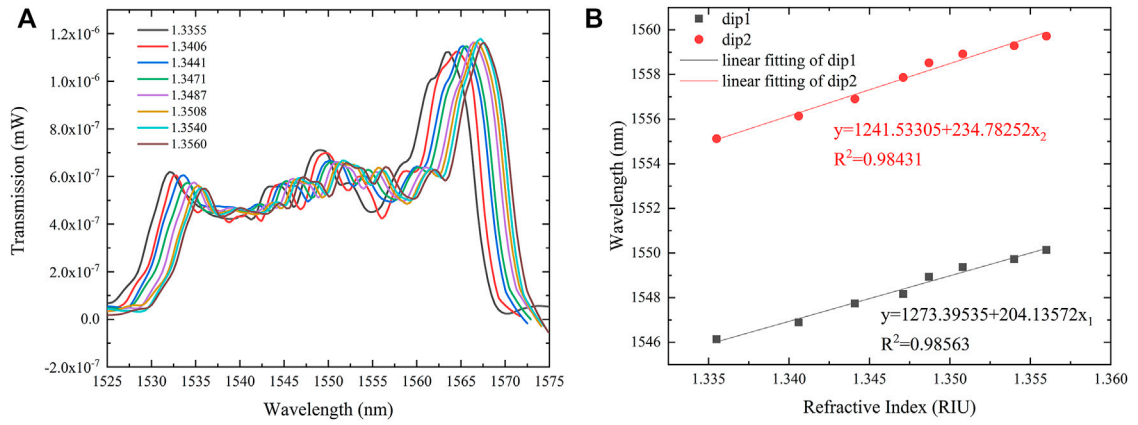

FIGURE 6
Sagnac interference structure refractive index sensor performance diagram. **(A)** Interference spectrum. **(B)** Fitting diagram.

this structure, respectively in the part of the tapered coupler and the part of the single mode and photonic crystal junction. In addition, light is split through the tapered coupler, and there is a certain optical path difference causing the second Mach-Zehnder interference with birefringence effect. Dip1 and dip2 are relatively obvious regions where wavelength drift can be distinguished. And it has good linearity. The peak on the side can also be used. In fact, there is little difference in sensitivity, but there is some deformation near the peak of high wavelength, so it is not possible to accurately judge which one is the correct peak. Dip is chosen for all. The fitting analysis of dip1 and dip2 shows that the refractive index sensitivity reaches 204.13572 nm/RIU and 234.78252 nm/RIU, respectively, which increases significantly compared to the sensor structure without Sagnac. And R^2 reached 0.98563 and 0.98431, respectively, proving that Sagnac structure of the sensor performance is superior.

Figure 7 shows the temperature sensing performance of Sagnac structure. It can be seen that when the object to be measured is room temperature, the spectrum becomes smooth. As the temperature rises, the spectrum also appears red shift, but the displacement amplitude is smaller than that of Sagnac free structure, which is contrary to the case of refractive index sensor. Through our analysis, this is because when the Sagnac ring is formed, the internal loss of the structure increases. Therefore, although the refractive

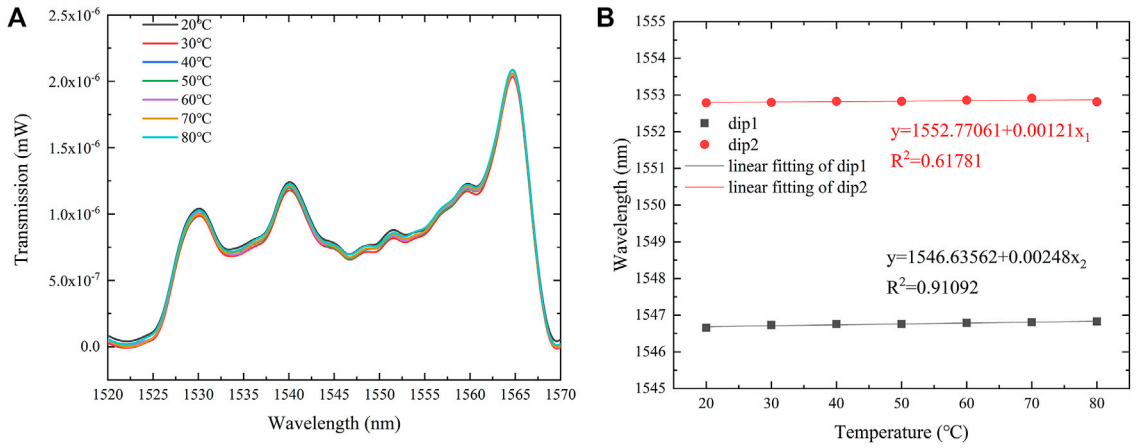

FIGURE 7
Temperature sensing performance diagram of Sagnac interference structure. **(A)** Interference spectrum. **(B)** Fitting diagram.

TABLE 1 Compared with the experimental data of optical fiber sensor published in recent years.

Structure	Sensing range	Sensing performance (nm/RIU)	Temperature deviation (pm/°C)	Year of publication
No core fiber	1.33–1.38	197.33	N/A	2017 [16]
Three kinds of fiber	1.3333–1.3794	101.996	4.9	2021 [18]
Fabry-Perot	1.3436–1.3481	34.338	N/A	2021 [19]
Polarization-maintaining fiber	1.3426–1.3492	48.3	N/A	2015 [27]
Dislocation PCF	1.339–1.347	169.63928	N/A	2021 [28]
Our work	1.3355–1.3560	234.78252	2.48	

index sensitivity increases, the temperature sensitivity with smaller change decreases due to the loss. Figure 7B shows that the temperature sensitivity of Sagnac structure is 2.48 p.m./°C and 1.21 p.m./°C, and R^2 is 0.91092 and 0.61781, respectively. The experimental results show that the structure is not suitable for temperature sensing because of its weak temperature sensing. It is also proved that the structure has high temperature stability.

As can be seen from the comparison in Table 1, the refractive index sensing ability of the sensor structure designed by us is better than that of some other optical fiber sensors published in recent years within similar sensing range, and is less affected by temperature. We selected and compared the experimental papers published in recent years, and the difficulty of the process is similar to this experiment. Some are difficult to verify by repeated experiments, require very high technological level and pure simulation sensors are not in the range of comparison. The structure is also less difficult to make. In general, it can be regarded as excellent among the experimental fiber sensor papers published in recent years.

Conclusion

This paper presents a PCF refractive index sensor with Sagnac ring structure. Through simulation analysis, it is proved that the structure has high birefringence effect and strong evanescent field, and it is speculated that it has higher sensing ability. We experimentally analyzed the sensitivity and temperature stability of refractive index measurement, and compared it with Single-Mode Fiber-PCF-Single-Mode Fiber. Experimental results show that Sagnac ring structure can enhance the refractive index sensitivity and reduce the influence of temperature on the sensor. The maximum refractive index sensitivity was 234.78252 nm/RIU in the refractive index range 1.3355–1.3560.

Data availability statement

The original contributions presented in the study are included in the article/supplementary material, further inquiries can be directed to the corresponding author.

Author contributions

Conceptualization, ZL and HL; methodology, ZZ; validation, ZL and ZZ; formal analysis, ZZ; investigation, ZL and ZZ; resources, ZL; data curation, ZZ; writing—original draft preparation, ZZ; writing—review and editing, ZL; visualization, HL; supervision, ZL; project administration, ZL; funding acquisition, ZL All authors have read and agreed to the published version of the manuscript.

Funding

This work was supported by the National Natural Science Foundation of China (grant number 52102164).

Conflict of interest

The authors declare that the research was conducted in the absence of any commercial or financial relationships that could be construed as a potential conflict of interest.

Publisher's note

All claims expressed in this article are solely those of the authors and do not necessarily represent those of their affiliated organizations, or those of the publisher, the editors and the reviewers. Any product that may be evaluated in this article, or claim that may be made by its manufacturer, is not guaranteed or endorsed by the publisher.

References

1. Li L, Wang Z, Ma Q, Wang M, Wu Q, Chen H, et al. Sagnac ring humidity sensor with a melting cone based on graphene properties. *IEEE Sens J* (2021) 21(14), 16061–5. doi:10.1109/jsen.2021.3075443

2. Barnes J, Li S, Goyal A, Abolmaesumi P, Mousavi P, Lock HP. Broadband vibration detection in tissue phantoms using a fiber fabry-perot cavity. *IEEE Trans Biomed Eng* (2018) 65(4):921–7. doi:10.1109/tbme.2017.2731663

3. Zhang Z, Zhang F, Xu B, Xie H, Fu B, Lu X, et al. High-sensitivity gas detection with air-lasing-assisted coherent Raman spectroscopy. *Ultrafast Sci* (2022) 2022: 1–8. doi:10.34133/2022/9761458

4. Li X, Zhang H, Qian C, Ou Y, Shen R, Xiao H. A new type of structure of optical fiber pressure sensor based on polarization modulation. *Opt Lasers Eng* (2020) 130: 106095. doi:10.1016/j.optlaseng.2020.106095

5. Chen Y, Wan H, Chen Q, Zhou Q, Zhang Z. High sensitivity optical fiber temperature sensor based on rare-earth-doped double-fiber peanut. 中国激光 (2020) 47:0110001. doi:10.3788/cjl202047.0110001

6. Pathak AK, Rahman ABM, Singh VK, Kumari S. Sensitivity enhancement of a concave shaped optical fiber refractive index sensor covered with multiple Au nanowires. *Sensors* (2019) 19(19):4210. doi:10.3390/s19194210

7. Eryurek M, Karadag Y, Ghafoor M, Bavili N, Cicek K, Kiraz A. Liquid refractometric sensors based on optical fiber resonators. *Sensors Actuators A: Phys* (2017) 265:161–7. doi:10.1016/j.sna.2017.08.019

8. Fan X, White IM, Shopova SI, Zhu H, Suter JD, Sun Y. Sensitive optical biosensors for unlabeled targets: A review. *Analytica Chim Acta* (2009) 620(1-2): 8–26. doi:10.1016/j.aca.2008.05.022

9. Baldini F, Brenci M, Chiavaioli F, Giannetti A, Trono C. Optical fibre gratings as tools for chemical and biochemical sensing. *Anal Bioanal Chem* (2012) 402(1): 109–16. doi:10.1007/s00216-011-5492-3

10. Duan L, Yang X, Lu Y, Yao J. Hollow-fiber-based surface plasmon resonance sensor with large refractive index detection range and high linearity. *Appl Opt* (2017) 56:9907–12. doi:10.1364/ao.56.009907

11. Gao X, Ning T, Zhang C, Xu J, Zheng J, Lin H, et al. A dual-parameter fiber sensor based on few-mode fiber and fiber Bragg grating for strain and temperature sensing. *Opt Commun* (2020) 454:124441. doi:10.1016/j.optcom.2019.124441

12. Fu Y, Cao J, Yamanouchi K, Xu H. Air-Laser-based standoff coherent Raman spectrometer. *Ultrafast Sci* (2022) 2022:1–9. doi:10.34133/2022/9867028

13. Ma YF, Feng W, Qiao SD, Zhao ZX, Gao SF, Wang YY. Hollow-core anti-resonant fiber based light-induced thermoelastic spectroscopy for gas sensing. *Opt Express* (2022) 30(11):18836–44. doi:10.1364/oe.460134

14. Polito D, Arturo Caponero M, Polimadei A, Saccomandi P, Massaroni C, Silvestri S, et al. A needle-like probe for temperature monitoring during laser ablation based on FBG: Manufacturing and characterization. *J Med Devices* (2015) 9(4):1590–4.

15. Poletti F, Petrovich MN, Richardson DJ. Hollow-core photonic bandgap fibers: Technology and applications. *Nanophotonics* (2013) 2:315–40. doi:10.1515/nanoph-2013-0042

16. Bhardwaj V, Kishor K, Vinod Kumar S. Experimental and theoretical analysis of connector offset optical fiber refractive index sensor. *Plasmonics* (2017) 12(6): 1999. doi:10.1007/s11468-016-0473-1

17. Qiao SD, Sampaolo A, Patimisco P, Spagnolo V, Ma YF. Ultra-highly sensitive HCl-LITES sensor based on a low-frequency quartz tuning fork and a fiber-coupled multi-pass cell. *Photoacoustics* (2022) 27:100381. doi:10.1016/j.pacs.2022.100381

18. Yuanyuan Z, Xiaozhan Y, Wenlin F, Wei F. Optical fiber refractive index sensor based on SMF-TCF-NCF-SMF interference structure. *Optik - Int J Light Electron Opt* (2021) 226:165900. doi:10.1016/j.ijleo.2020.165900

19. Nisreen A-J, Kadhim Shehab A, Naseef Intisar A. Characterization study of optical fiber refractive index sensor based on fabry-perot interferometer. *J Phys Conf Ser* (2021) 1963:1. doi:10.1088/1742-6596/1963/1/012052

20. Liu C, Su W, Wang F, Li X, Yang L, Sun T, et al. Theoretical assessment of a highly sensitive photonic crystal fibre based on surface plasmon resonance sensor operating in the near-infrared wavelength. *J Mod Opt* (2018) 66:1–6. doi:10.1080/09500340.2018.1508776

21. Zhang S, Li J, Li S. Design and numerical analysis of a novel dual-polarized refractive index sensor based on D-shaped photonic crystal fiber. *Metrologia* (2018) 55:828–39. doi:10.1088/1681-7575/aae757

22. Zhang ZW, Shen T, Wu HB, Feng Y, Wang X. Polished photonic crystal fiber refractive index sensor based on surface plasmon resonance. *J Opt Soc Am B* (2021) 38(12):F61–F68. doi:10.1364/josab.433726

23. Li X. G., Nguyen L. V., Zhao Y., Ebendorff-Heidepriem H., Warren-Smith S. C. High-sensitivity Sagnac-interferometer biosensor based on exposed core microstructured optical fiber. *Sensors Actuators B Chem[J]* (2018) 269:103–109. doi:10.1016/j.snb.2018.04.165

24. Hao JQ, Han BC. Highly sensitive tapered optical fiber coupler-based gas refractive index sensor enhanced by the Vernier effect. *Opt. Eng.* (2020) 59 (6): 066102. doi:10.1117/1.OE.59.6.066102

25. Yang F, Wu Y.J, Shi J, Yang K, Xu W, Guo C.J, et al. Curvature sensor based on fiber ring laser with Sagnac loop. *Opt Fiber Tech* (2020) 60:102341. doi:10.1016/j.yofte.2020.102341

26. Liu Q, Li S-G, Chen H. Enhanced sensitivity of temperature sensor by a PCF with a defect core based on Sagnac interferometer. *Sensors and Actuators B: Chemical[J]* (2018) 254. doi:10.1016/j.snb.2017.07.120

27. Zeng H, Shen C, Lu Y, Liu H, Dong X, Li C. Refractive index sensor based on polarization maintaining fiber Machzand interference combined with fiber Bragg grating [J]. *Chin J sensors actuators* (2015) 28(11):1727–31.

28. Gao P, Zheng X, Liu Y, Wang Z. *J Shenyang Normal Univ (Natural Science)* (2021) 39(06):506–10.

frontiers | Frontiers in Physics

TYPE Original Research
PUBLISHED 03 October 2022
DOI 10.3389/fphy.2022.1020376

OPEN ACCESS

EDITED BY
Yufei Ma,
Harbin Institute of Technology, China

REVIEWED BY
Zhenzhen Wang,
Xi'an Jiaotong University, China
Weiguang Ma,
Shanxi University, China

*CORRESPONDENCE
Shunchun Yao,
epscyao@scut.edu.cn

SPECIALTY SECTION
This article was submitted to Optics and Photonics,
a section of the journal
Frontiers in Physics

RECEIVED 16 August 2022
ACCEPTED 31 August 2022
PUBLISHED 03 October 2022

CITATION
Guo S, Yang Y, Shao G, Li Z, Ren W, Mo J, Lu Z and Yao S (2022), Correcting the light extinction effect of fly ash particles on the measurement of NO by TDLAS. *Front. Phys.* 10:1020376.
doi: 10.3389/fphy.2022.1020376

Correcting the light extinction effect of fly ash particles on the measurement of NO by TDLAS

Songjie Guo[1], Yan Yang[1], Guodong Shao[1], Zhenghui Li[1], Wei Ren[2], Juehui Mo[3], Zhimin Lu[1,4] and Shunchun Yao[1,4]*

[1]School of Electric Power Engineering, South China University of Technology, Guangzhou, China, [2]Department of Mechanical and Automation Engineering, The Chinese University of Hong Kong, Hong Kong, Hong Kong SAR, China, [3]Cntest Intelligent Scien-tech Co, LTD., Foshan, China, [4]Guangdong Province Key Laboratory of Efficient and Clean Energy Utilization, Guangzhou, China

The measurement of nitric oxide (NO) concentration in power plant flue gas by tunable diode laser absorption spectroscopy (TDLAS) is susceptible to fly ash particles. The presence of fly ash particles causes laser intensity fluctuations and leads to the second harmonic (2f) signal amplitude changes. In this manuscript, we analyzed the influence of particles on the 2f signal and corrected the measurement error of NO concentration by the wavelength modulation-second harmonic (WMS-2f) technique. Specifically, the 2f signal error caused by quartz sand and fly ash particles were measured, and the exponential function representing the peak-to-peak error of the 2f signal was obtained by fitting. Finally, the peak-to-peak value of the 2f signal and the NO concentration were corrected according to the exponential function. After correction, the NO concentration error under the fly ash influence (the particle size in the range of 10–200 μm and the mass concentration is less than 18.26 g/m^3) was no more than 2%. This correction method effectively improves the measurement accuracy of NO concentration by the WMS-2f technique in the fly ash environment.

KEYWORDS

TDLAS, wavelength modulation, particles, extinction effect, NO concentration, error correction

Introduction

Nitrogen oxide (NO_X) is an important air pollutant [1], and its primary source of emissions is coal-fired power plants. The main component of NOx in flue gas is nitric oxide (NO). Various optical techniques have been widely used in gas pollutant monitoring [2, 3]. In daily operation, the continuous emission monitoring system (CEMS) of flue gas is used to online monitor the NO emission concentration. Currently, the *in-situ* method is one of the primary forms of the CEMS system [4]. This method refers to directly measured in the flue, enables to obtain actual values more easily of flue gas concentrations, and has a short response time [5]. However, the environment in the flue is complex, and the mass concentration of fly ash is relatively high. The extinction effect caused by scattering and

absorption by fly ash particles will greatly influence the detection of NO and other components concentration by optical technique [6].

TDLAS is one of the main measurement techniques of NO concentration in flue gas at present [7], including direct absorption spectroscopy (DAS) and wavelength modulation spectroscopy (WMS). DAS is susceptible to interference from low-frequency noise, and its detection sensitivity is limited. WMS can effectively restrain low-frequency noise by superimposing a high-frequency modulation signal on the basic low-frequency scanning signal and demodulating it at high frequency [8–11]. WMS technique has a high detection sensitivity, which can reach 10^{-5}–10^{-6}. It is widely used for trace gas detection, such as in industrial process control [12], environmental monitoring [13], and pathology diagnosis [14]. The peak value of the second harmonic (2f) signal of demodulated WMS signal corresponds to the central frequency of the gas absorption line, and the 2f signal has a larger amplitude than the higher-order harmonics. Therefore, it is suitable for gas concentration inversion. It was demonstrated that when the absorption is small, the 2f signal amplitude changes approximately linearly with gas concentration at constant laser intensity, absorption path, and modulation parameters [15, 16]. The target gas concentration can be directly calculated by comparison with the 2f signal amplitude of the standard gas. This method is referred to as the wavelength modulation-second harmonic (WMS-2f) technique and was widely implemented in industrial equipment.

However, the stability of laser intensity must be guaranteed to calculate gas concentration using the WMS-2f technique reliably. If the laser intensity fluctuates, the amplitude of demodulated 2f signal accordingly changes. Attenuation of laser intensity by non-gas absorption introduces errors to the calculated values of gas concentration, which limits the application of the WMS-2f technique in environments with drastic laser intensity fluctuation [17]. In particular, the laser intensity is inevitably affected by the extinction effect of fly ash during the *in-situ* measurements in coal-fired power plants' flue, which results in small measurement values. Eliminating the influence of fly ash on calculated values of flue gas component concentrations is a difficult problem. Some researchers have proposed using a laser intensity reference signal to eliminate the effect of laser intensity fluctuation. The reference signals can be the filtered laser intensity signal or the first harmonic (1f) signal [18]. Although this method can somewhat eliminate the influence of laser intensity fluctuation, its calculation program is complicated. Moreover, drastic changes in laser intensity and electronic noise in the demodulation process can also result in some errors. Wang et al. discussed the effect of particles on the 2f signal based on the TDLAS technique. They used the transmitted laser intensity to calibrate the 2f signal to solve the problem of particle interference with gas measurements. A concentration of 20% carbon dioxide was measured, and the calibrated 2f peak error was less than 5% [19].

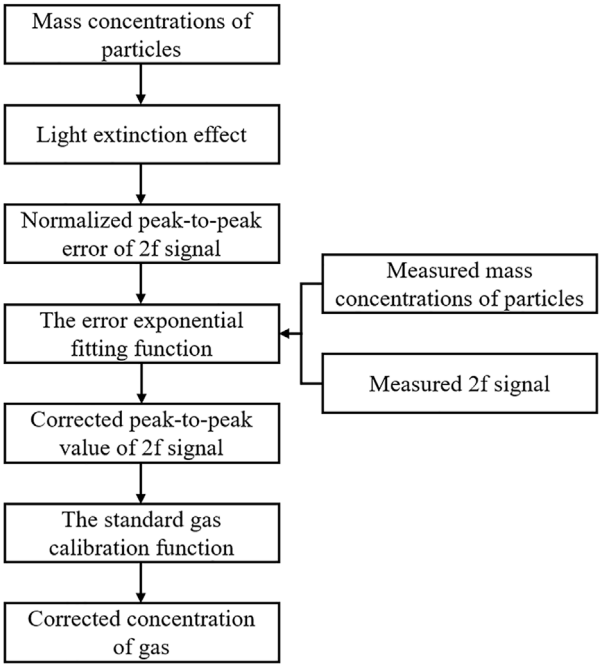

FIGURE 1
Correction flow chart of the peak-to-peak value of 2f signal and gas concentration.

In order to eliminate the particle's influence on the NO concentration measurement, we analyze the effect of particle mass concentration and particle size on the 2f signal. The law revealed can be used to correct NO concentration errors directly. This method is different from that of measuring laser reference intensity. Direct research on error sources can effectively improve the measurement accuracy of NO concentration in the particulate environment and simplify the computing system. The peak-to-peak error of the 2f signal caused by quartz sand and fly ash was measured in the manuscript. The error was normalized and fitted by the exponential function. Finally, the calculation error of NO concentration was corrected using the error exponential fitting function and the standard gas calibration function.

Correction method

As mentioned above, when measuring NO in the flue gas environment with particles, it is the fundamental guarantee for accurate measurement to determine the extinction effect of particles and correct the measurement signal. The correction flow chart is shown in Figure 1.

As shown in Figure 1, the error exponential fitting function needs to be obtained in advance before correction. In the online measurement, as long as we correct the error of the 2f signal and

the gas concentration according to the fitting function. The detailed principle is described as follows.

Due to scattering and absorption of particles, the laser intensity passing through a medium containing particles will attenuate. The attenuation degree is directly related to particles' mass concentration and particle size. According to the Beer-Lambert law, when a monochromatic parallel light with intensity I_0 is incident on a medium containing uniformly distributed particles, the relationship between the transmitted laser intensity I and I_0 is as follows [20]:

$$I = I_0 \exp\ (-\tau L), \tag{1}$$

where τ is the medium turbidity. In a simple model, if the scattering medium contains N spherical particles with a diameter D per unit volume, τ can be expressed as follows:

$$\tau = Nak_{ext} = \frac{\pi}{4} ND^2 k_{ext}, \tag{2}$$

where a is the light-facing area of a particle, k_{ext} is the extinction coefficient, and k_{ext} can be calculated according to the Mie scattering theory [21, 22], $k_{ext} = \frac{2}{\alpha^2}\sum_{n=0}^{\infty}(2n+1)(|a_n| + |b_n|)$, where $\alpha = \frac{\pi D}{\lambda}$ is called the dimensionless parameter, and a_n and b_n are the Mie coefficients, respectively. Substitution of Eq. 2 into Eq. 1 with subsequent transformation results in the following expression for the difference between the incident laser intensity and the transmitted one:

$$I_0 - I = I_0\left[1 - exp\left(-\frac{\pi}{4} ND^2 k_{ext} L\right)\right]. \tag{3}$$

For uniform particles of the same size, the relationship between their number concentration N and mass concentration W is expressed as $N = \frac{6W}{\pi\rho D^3}$, where ρ is the particle density. It can be seen from this expression that at constant values of particle density and average particle size, their mass concentration is proportional to the number concentration. Substituting N into Eq. 3 and normalizing by the incident laser intensity, the following expression for the difference of normalized light intensities to the particle mass concentration was obtained:

$$1 - \frac{I}{I_0} = 1 - exp\left(-\frac{6}{4\rho D} k_{ext} LW\right). \tag{4}$$

The effect of stable and uniformly distributed particles on the scattering and absorption of laser is constant. Therefore, the extinction effect caused by different mass concentrations of particles was measured through experiments and was fitted using Eq. 4. From this, the law describing the dependence of the extinction effect on particle mass concentration can be obtained. This law can be used to correct the measurement error of laser intensity at different mass concentrations of particles.

There are many ways to measure the laser intensity change, including direct and indirect measurements. Although the device for directly measuring the laser intensity is simple, it is necessary to keep the laser power stable, and it is difficult to avoid the interference of low-frequency noise, which will introduce significant errors [23]. TDLAS technique often measures gas concentration by scanning wavelength and also indirectly obtains the change in laser intensity. Noteworthily, correcting laser intensity changes can improve the TDLAS technique accuracy for measuring gas concentrations.

According to the Beer-Lambert law, when a laser beam of frequency ν and intensity I_0 passes through a gas sample, the transmitted laser intensity $I(\nu)$ can be expressed as follows [24]:

$$I(\nu) = I_0\, exp[-S(T)\Phi(\nu)PXL], \tag{5}$$

where $S(T)$ is the intensity of the characteristic spectral line of the gas, $\Phi(\nu)$ is the lineshape function of the absorbed spectral line, which is described here by the Voigt function, P is the total pressure of the gas, X is the volume concentration of the gas to be measured, and L is the transmission distance of laser in the gas medium, respectively. When the central laser frequency ν_0 is modulated by a sine wave with an angular frequency ω, the instantaneous laser frequency $\nu(t)$ can be expressed as follows [25, 26]:

$$\nu(t) = \nu_0 + d\cos\ (\omega t), \tag{6}$$

where d is the modulation amplitude. Taking into account the characteristics of distributed feedback laser (DFB), it is known that if the laser frequency is modulated, its intensity is modulated as well. The instantaneous laser intensity passing through the gas sample can be expressed by the cosine Fourier series of $I(\nu_0)$:

$$I(\nu_0, t) = \sum_{n=0}^{\infty} A_n(\nu_0)\cos(n\omega t), \tag{7}$$

where $A_n(\nu_0)$ are the different harmonic components, which can be measured by a lock-in amplifier:

$$A_n(\nu_0) = \frac{2}{\pi}\int_0^{\pi} I_0(\nu_0 + d\cos\theta)\, exp[- \sigma(\nu_0 + d\cos\theta)XL]cosn\theta d\theta. \tag{8}$$

Here, $\theta = \omega t$, and σ is the light absorption coefficient, respectively. For trace gases $\sigma XL \ll 1$, so Eq. 8 can be approximated as follows:

$$A_n(\nu_0) = \frac{2I_0 XL}{\pi}\int_0^{\pi} -\sigma(\nu_0 + d\cos\theta)cosn\theta d\theta. \tag{9}$$

It can be seen from Eq. 9 that each harmonic component is proportional to the gas concentration. In practical measurements, the gas concentration is often calculated using the peak-to-peak value of the 2f signal. At the same time, the 2f peak-to-peak value is proportional to the laser intensity. When the laser intensity decreases by non-gas absorption, the 2f peak-to-peak value also decreases. Eq. 4 can be further expressed as follows:

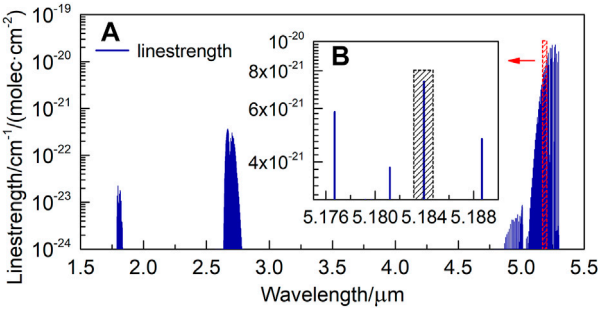

FIGURE 2
NO absorption lines distribution between **(A)** 1.5–5.5 μm. **(B)** 5.175–5.19 μm (From HITRAN Database).

$$1-\frac{V_{P-P}(2f)}{V_{P-P0}(2f)}=1-\exp\left(-\frac{6}{4\rho D}k_{ext}LW\right), \tag{10}$$

where $V_{P-P}(2f)$ and $V_{P-P0}(2f)$ are the 2f peak-to-peak values in the presence and absence of fly ash, respectively. Under the condition of known mass concentration of fly ash W, the reduction of 2f peak-to-peak value by fly ash extinction is expressed as $1-\frac{V_{P-P}(2f)}{V_{P-P0}(2f)}$. Assuming that the response of the 2f peak-to-peak value to the gas concentration in the absence of fly ash in a particular system is $V_{P-P0}(2f)=kX+b$, the actual gas concentration can be expressed as follows:

$$X=\frac{\left\{V_{P-P}(2f)+\left[1-\frac{V_{P-P}(2f)}{V_{P-P0}(2f)}\right]\right\}-b}{k}, \tag{11}$$

where k and b are the slope and the intercept of the linear response function of 2f peak-to-peak value to gas concentration, respectively. Using Eq. 11 to correct the gas concentration can eliminate the measurement error of gas concentration caused by the extinction of fly ash particles.

Experimental setup

In order to verify the feasibility and accuracy of the above correction method, we designed and built an experimental system. Firstly, we selected the absorption line of NO located at 1929.02 cm^{-1} as the target detection line, corresponding to a wavelength of 5.184 μm. Figure 2 shows the distribution of NO absorption lines between 1.5 and 5.5 μm. It can be seen that the absorption linestrength near 5–5.5 μm for NO is stronger. In particular, there are six very close absorption lines of NO at 5.184 μm, and they work together to produce a larger absorption peak, as shown in the black shaded area in Figure 2B.

The main components of the experimental system were the laser, the fly ash unit (as shown in the dashed box), the gas cell, and the signal processing section. A function generator was installed inside the lock-in amplifier (HPLIA, HEALTHY PHOTO), which generated a sawtooth signal with a frequency of 2 Hz and a sine wave signal with a frequency of 6 kHz. These signals were transmitted to the laser controller (HPTCD-Q, HEALTHY PHOTO) and controlled the current of a quantum cascade laser (HPQCL-Q, HEALTHY PHOTO). The modulation voltage was adjusted to keep the modulation coefficient at about 2.2. The QCL central wavelength is 5.184 μm. We used a self-designed fly ash unit system, which included a powder feeder, a fly ash pipe, a powder collector, and a vortex blower. Because the gas cell was closed and the fly ash pipe was open during measurements, it was inconvenient to combine them. Moreover, the effects of gas and fly ash on laser intensity could be considered independent, so we decided to separate them. In the experiment, the laser passed through the fly ash unit first and then through the gas cell. The powder feeder was located above the inlet of the fly ash pipe, so the fly ash reached the inlet of the fly ash pipe by free fall. The outlet of the fly ash pipe was connected to the powder collector and the vortex blower, and the suction force of the latter was used to suck the fly ash into the powder collector. This way, a stable flow fly ash environment was formed inside the fly ash pipe. In order to form a relatively stable gas-solid two-phase flow atmosphere, the fly ash pipe included two parts. The fly ash flowed into the second part of the pipe after being evenly mixed in the first part. In order to ensure the same effect distance between particles and NO on the laser, the length of the second part of the pipe was the same as that of the gas cell, both equal to 0.38 m. The laser beam passed through the second part of the pipe. The measurements were carried out on NO gas in the closed gas cell at the stable pressure of 0.99 atm. The laser beam passed through the gas cell once and entered the photodetector (HPPD-M-A, HEALTHY PHOTO). The laser intensity signal detected by the detector was input to the lock-in amplifier for demodulation to obtain the 2f signal. The latter was recorded and transmitted to the computer by a data acquisition card (USB-6363, NI). The experimental setup is schematically shown in Figure 3.

The particle amount was controlled by controlling the vibration frequency of the powder feeder. The particle mass concentration was calculated by measuring their mass per unit of time and the real-time volume of air in the vortex blower. When there were only fly ash particles smaller than 100 μm, agglomeration easily occurred in the powder feeder, and it was difficult to generate a uniform flow of fly ash. The intensity of the laser beam passed through the fly ash pipe considerably fluctuates, causing a measurement error. We first used quartz sand to simulate fly ash. The main component of fly ash is SiO_2, which is the same as quartz sand. However, the stacking density of quartz sand particles is slightly higher than that of fly ash, and their agglomeration is not easy to occur. Firstly, the mass concentration of quartz sand was measured and calculated by measuring the particle mass in the powder feeder per unit time (unit: g/h) and the air volume in the fly ash pipe in

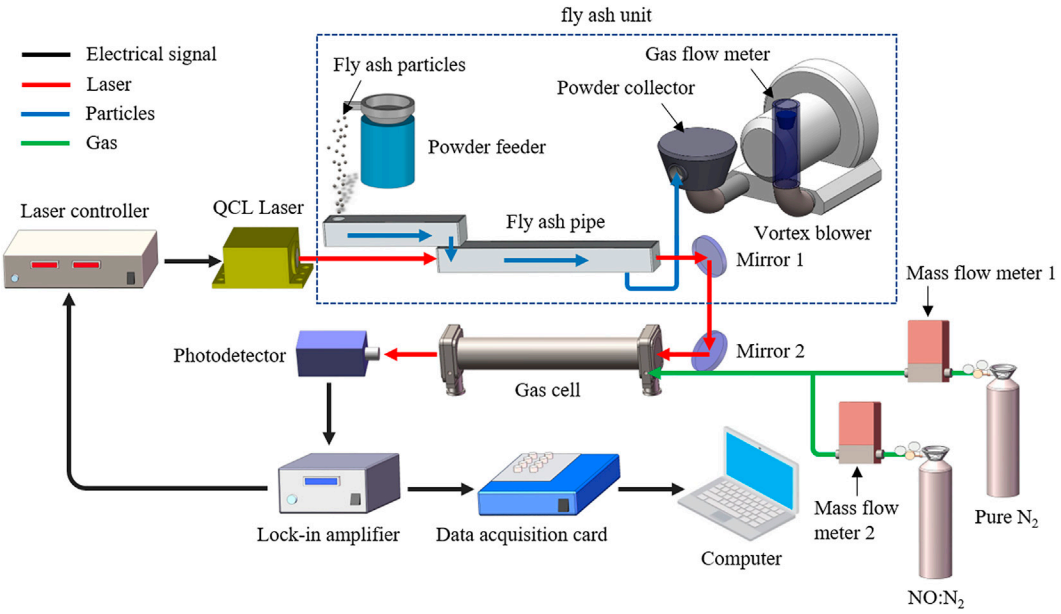

FIGURE 3
Schema of the experimental setup.

real-time. The air volume was measured using a gas flow meter installed at the outlet of the vortex blower. The air volume of the vortex blower was about 65 m^3/h in these experiments. The mass concentration of particles could be obtained by dividing the particle mass by the air volume. In this experiment, the effects of different mass concentrations of particles on the NO 2f signal were analyzed. A higher volume fraction of NO for the measurement was chosen to ensure that the 2f signal has a high amplitude. Firstly, the gas cell was filled with a gas mixture of NO and N_2, the volume fraction of the former being 9.06×10^{-5}. After particles flow in the fly ash pipe was stable, the NO 2f signal was recorded, and the experiment was repeated at different particle mass concentrations. Next, the gas cell was flushed with pure N_2. Then, five volume fractions of NO, namely 2×10^{-5}, 4×10^{-5}, 6×10^{-5}, 8×10^{-5}, and 1×10^{-4}, were formulated by NO standard gas of volume fraction 1×10^{-4} in order to quantify and calibrate the errors caused by different mass concentrations of fly ash on the measured values of NO concentration. Two mass flow meters (S48 32/HMT, HORIBA METRON) were used in this process. Finally, these five volume fractions of NO were injected into the gas cell, and their 2f signals were recorded.

Results and discussion

As we known, the fly ash particles produced by coal-fired power plants vary in size and have broad size distributions, usually ranging from several to two hundred microns. In order to study the influence of particle size on the NO 2f signal, we used quartz sand with different particle sizes for experiments. It was found after testing that the quartz sand particles smaller than 54 μm tend to agglomerate. Therefore, three particle sizes were chosen for the experiments, namely 54–76 μm, 97–105 μm, and 105–135 μm.

The measurement results of the NO 2f signal influenced by quartz sand with particle sizes of 54–76 μm are shown in Figure 4. Figure 4A presents the NO 2f signals with the removed background at different mass concentrations of particles. The 2f signal was averaged 10 times, and Figure 5, Figure 8 and Figure 10 were also operated in this way. According to Eq. 10, the 2f peak-to-peak value of NO corresponding to different mass concentrations of quartz sand particles was subtracted from the respective value obtained without quartz sand and normalized to obtain the 2f peak-to-peak error of NO. Figure 4A shows that the 2f peak-to-peak value of NO gradually decreased with the increased mass concentration of quartz sand particles. Then the 2f peak-to-peak error of NO and the mass concentration of quartz sand were fitted by an exponential function in the following form: $y = 1 - \exp(-x_t)$, where y was the 2f peak-to-peak error of NO, and x was the mass concentration of quartz sand, respectively. The fitting result is shown in Figure 4B. The fitting results concluded that the 2f peak-to-peak error of NO and the quartz sand mass concentration had a good exponential correlation with $R^2 = 0.999$. Therefore, this

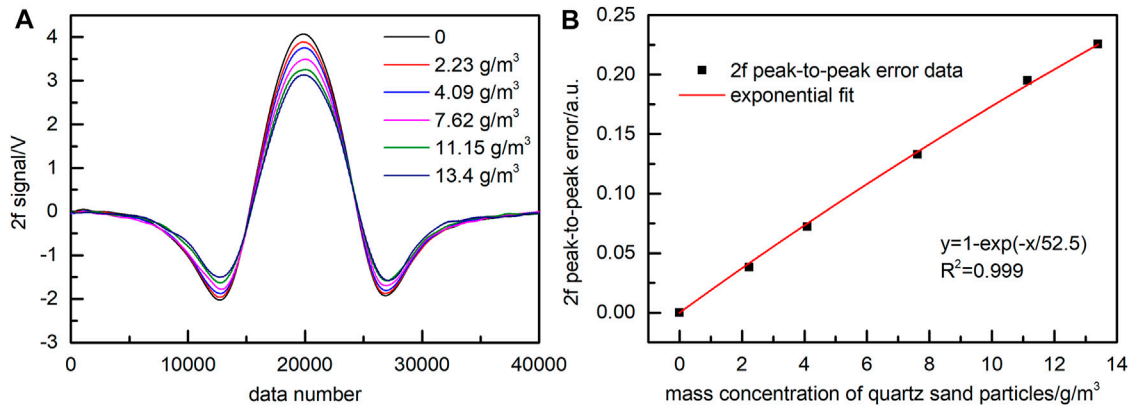

FIGURE 4
Effect of quartz sand (54–76 μm) on the NO 2f signal. **(A)** 2f signal with removed background. **(B)** Exponential fitting function of 2f peak-to-peak error.

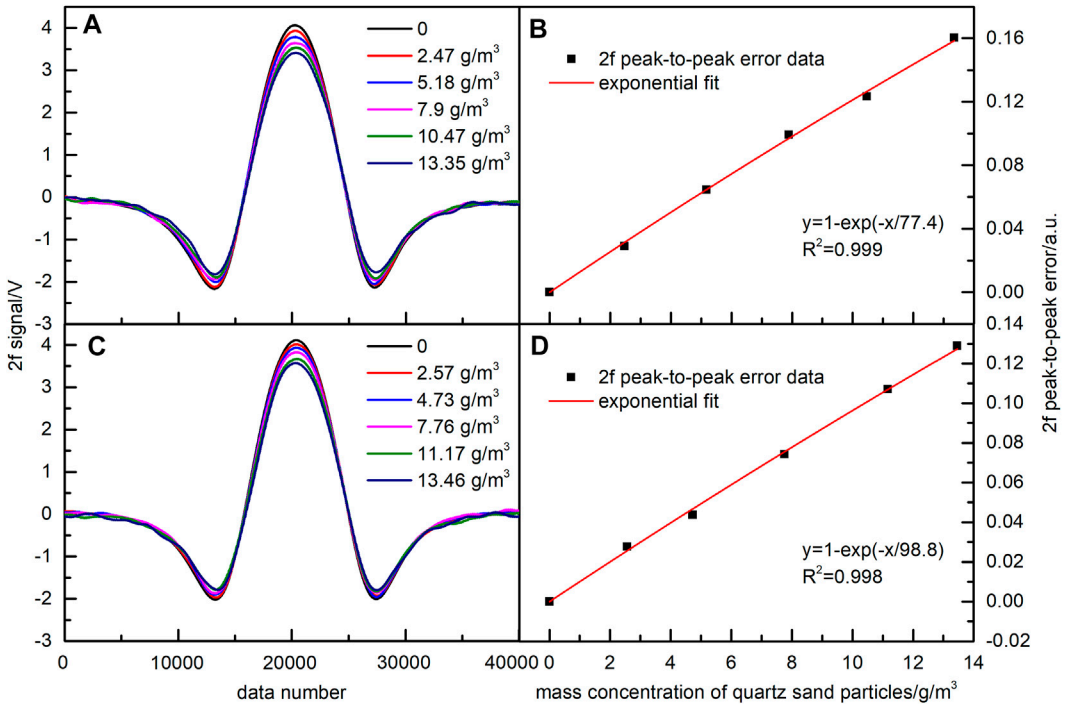

FIGURE 5
Effect of quartz sand on the NO 2f signal. **(A)** 2f signal with removed background (97–105 μm). **(B)** Exponential fitting function of 2f peak-to-peak error corresponding to Figure 5A. **(C)** 2f signal with removed background (105–135 μm). **(D)** Exponential fitting function of 2f peak-to-peak error corresponding to Figure 5C.

exponential function could be used to correct the 2f peak-to-peak value with subsequent correction of the NO concentration under the condition that the mass concentration of quartz sand particles was known.

In the same way, quartz sands with particle sizes of 97–105 and 105–135 μm were used for experiments. Obtained results are shown in Figure 5. Similar to the previous case, the 2f peak-to-peak errors of NO were fitted by exponential functions.

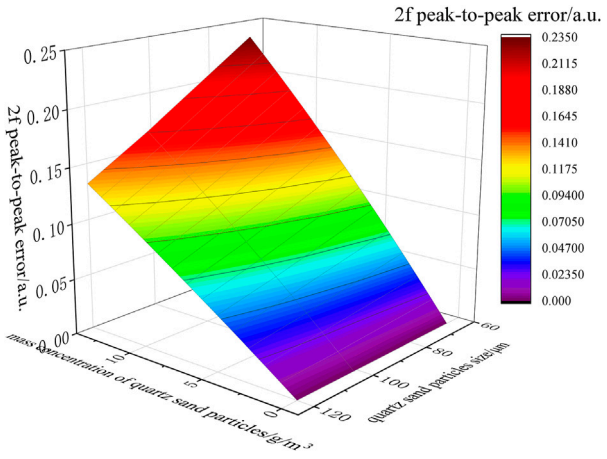

FIGURE 6
Relationship between the 2f peak-to-peak error of NO and the quartz sand mass concentration and size.

TABLE 1 Mass concentration of three particle sizes of quartz sand.

Particle sizes μm	Quartz sand mass concentration g/m³				
54–76	1.32	3.34	6.21	9.68	11.97
97–105	1.64	3.23	6.35	9.29	11.88
105–135	1.34	3.44	6.06	9.17	12.23

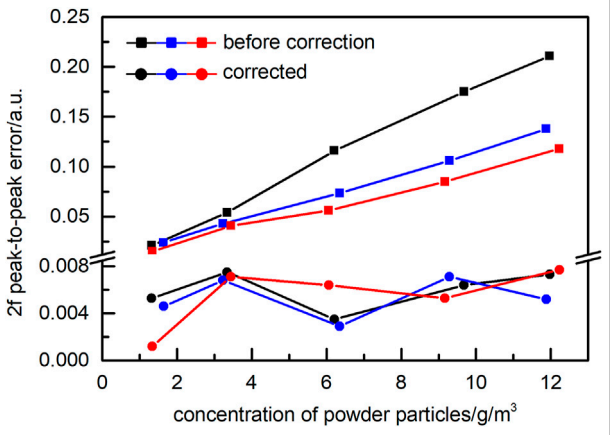

FIGURE 7
2f peak-to-peak errors and correction results.

The values of R^2 were 0.999 and 0.998. The obtained results demonstrated that for three different particle sizes, the 2f peak-to-peak error of the NO signal and the quartz sand mass concentration all satisfied a good exponential relationship. The mass concentration of quartz sand particles was calculated by their mass and the air volume of the vortex blower, and there were some differences in the particle amounts between the experiments. Therefore, the quartz sand mass concentrations in the three groups of particle sizes were not exactly the same.

The comparison of the 2f peak-to-peak error exponential fitting functions corresponding to three different sizes of quartz sand particles shown in Figure 4 and Figure 5 demonstrated different t-values for these functions. The t-values gradually increased with particle size, which was consistent with Eq. 10. It indicated that at a constant mass concentration of the same-material particles, the 2f signal error increased with the decrease of average particle size. The reason for this phenomenon was that for the particles with the same mass concentration, under the same action distance with the laser beam, the smaller the particle size, the stronger the extinction effect. Therefore, the laser transmittance and the peak-to-peak value of the 2f signal were also smaller, and the NO concentration error was more significant.

The relationship between the 2f peak-to-peak errors of NO and the mass concentration and particle size of quartz sand could be obtained from the error exponential fitting functions for quartz sand with three different particle sizes results are shown in Figure 6. For quartz sands with three particle sizes, the number of particles obeyed normal size distributions. Therefore, the median values of 65, 101, and 120 μm were taken as the representative ones of the particle size range. It can be seen from Figure 6 that there were some differences in the exponential fitting function of the 2f peak-to-peak error caused by different particle sizes of quartz sand. When the mass concentration of quartz sand was constant, the 2f peak-to-peak error of NO increased rapidly with the decrease of particle size, which is also consistent with Eq. 10.

Based on the error exponential fitting function of quartz sand with three particle sizes, the mass concentration of quartz sand was changed to make it different from the value in the error exponential fitting function. The changed mass concentrations are shown in Table 1. The 2f peak-to-peak error caused by them was measured again. The 2f peak-to-peak error was corrected with the error exponential fitting function obtained above, and the correction result is shown in Figure 7. Among them, the black line corresponds to the quartz sand of 54–76 μm, the blue line corresponds to the quartz sand of 97–105μm, and the red line corresponds to the quartz sand of 105–135 μm. The square represents the 2f peak-to-peak error before correction, and the circle represents the corrected value 2f peak-to-peak error. The corrected 2f peak-to-peak errors were all less than 0.8%, indicating that the correction effect was good.

To verify the applicability of the above conclusions to fly ash samples, we carried out the same experiments using real flue fly ash produced by a coal-fired power plant. The mass concentration of flue fly ash produced by domestic coal-fired

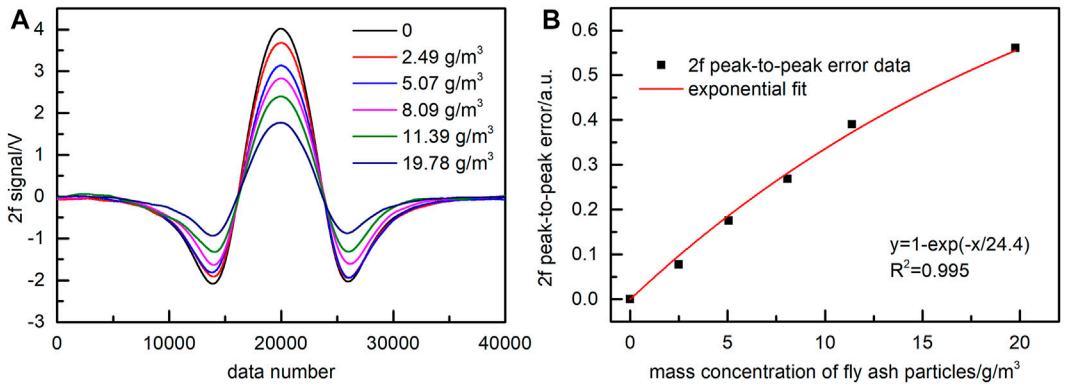

FIGURE 8
Effect of fly ash with particle sizes in the range of 10–200 μm on the NO 2f signal. **(A)** 2f signal with removed background. **(B)** Exponential fitting function of 2f peak-to-peak error.

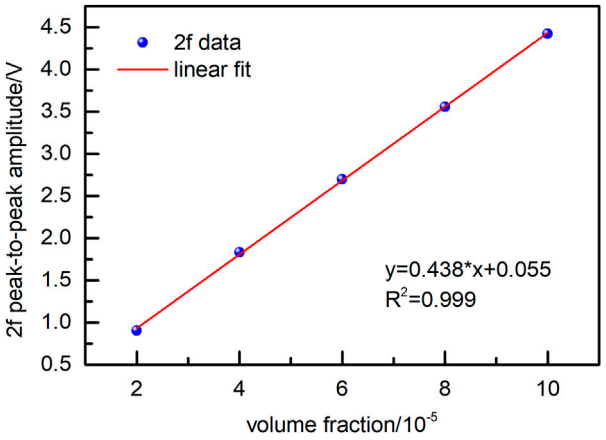

FIGURE 9
Relationship between 2f signal and volume fraction of NO.

power plants is usually between 10 and 20 g/m^3. The size range of fly ash particles used in the experiments was 10–200 μm. Similar to the quartz sand experiments described above, five fly ash mass concentrations were selected. The NO 2f signals corresponding to different mass concentrations were recorded, and the exponential function fitted the 2f peak-to-peak error data of NO. The fitting result shown in Figure 8 reveals the value of R^2 equal to 0.995.

The 2f signals of NO were measured for five volume fractions of 2×10^{-5}, 4×10^{-5}, 6×10^{-5}, 8×10^{-5}, and 1×10^{-4}. The relationship between the 2f peak-to-peak value and the volume fraction of NO was obtained by linear fitting of measurement data, as shown in Figure 9. It can be seen from Figure 9 that the 2f peak-to-peak value and the NO volume fraction satisfied a linear dependence, and the linearity R^2 reached 0.999.

To verify the accuracy of the determination of NO concentration using the described error correction method, the fly ash mass concentrations different from the five mass concentrations present in Figure 8 were selected. The values of these mass concentrations were 1.87, 3.95, 7.95, 15.8, and 18.26 g/m^3. The peak-to-peak value of the NO 2f signal was recorded at each fly ash mass concentration, and the NO concentration was calculated using the calibration function. After that, the NO concentration was corrected by Eq. 11 and using the 2f peak-to-peak error exponential fitting function presented in Figure 8B. The 2f peak-to-peak error and the NO concentration error caused by different mass concentrations of fly ash, together with the corrected results, are shown in Table 2. It can be seen from this table that the NO concentration error reached 54.6% at the fly ash mass concentration of 18.26 g/m^3. The maximum error of NO concentration after the correction was less than 2%, which indicated an effective improvement in measurement accuracy.

In order to compare with the method of measuring the laser reference intensity, we used a low-pass filter to filter the transmitted laser intensity to obtain the direct current (DC) signal. Then, the 2f/DC signal of NO sample gas with a volume fraction of 9.06×10^{-5} at the effect of fly ash was measured, and the results are shown in Figure 10. It can be seen that the 2f/DC signal peak value of the same NO concentration was still different at the effect of different concentrations of fly ash. The 2f/DC peak error became more significant as the fly ash concentration increased. At the same time, the 2f/DC signals of five groups of standard NO gases with volume fractions of 2×10^{-5}, 4×10^{-5}, 6×10^{-5}, 8×10^{-5}, and 1×10^{-4} were measured. The relationship between the peak value of the 2f/DC signal and the gas volume fraction was obtained by linear fitting, and the linearity was good, as shown in Figure 10B.

TABLE 2 2f peak-to-peak error and concentration error of NO before and after correction.

Fly ash mass concentration g/m^3	1.87 (%)	3.95	7.95	15.8	18.26
2f peak-to-peak error of NO before correction	5.6	15.4%	28.9%	48.9%	53.9%
Corrected 2f peak-to-peak error of NO	1.79	0.46%	1.1%	1.26%	1.19%
Concentration error of NO before correction	5.6	15.5%	29.2%	49.6%	54.6%
Corrected concentration error of NO	1.82	0.46%	1.12%	1.28%	1.2%
2f/DC peak error of NO	0.12	0.41%	1.07%	2.07%	4.21%
Concentration error of NO caused by 2f/DC	1.04	1.56%	0.27%	0.93%	3.02%

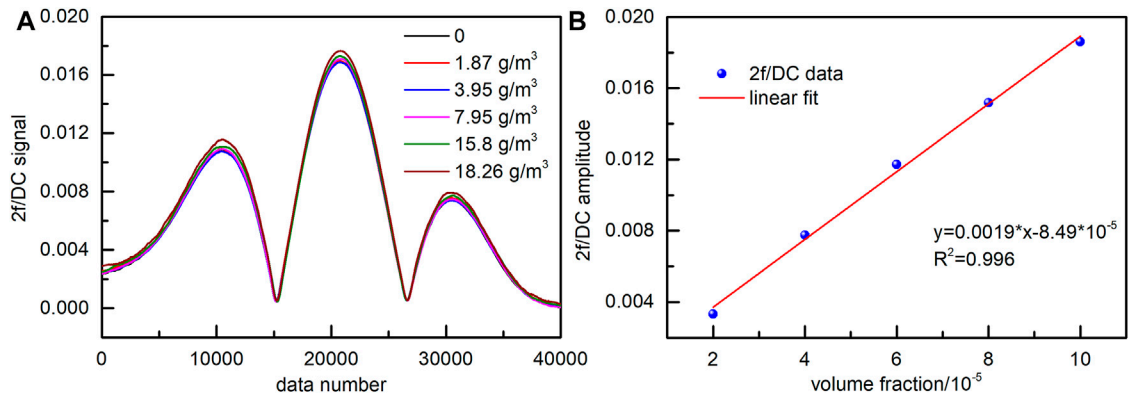

FIGURE 10
2f/DC signal of NO **(A)** Effect of fly ash (10–200 μm) on the 2f/DC signal. **(B)** Relationship between 2f/DC signal and volume fraction.

The 2f/DC peak error and the NO concentration error caused by different mass concentrations of fly ash are shown in the last two rows of Table 2. The maximum error of the 2f/DC peak value exceeded 4%, and the corresponding NO concentration error was 3.02%. It can be seen that compared with the method of measuring the laser reference intensity, the errors of the two methods were roughly equal when the mass concentration of fly ash was low. But if the mass concentration of fly ash was high, the corrected 2f peak-to-peak error was significantly smaller than the 2f/DC peak error. Therefore, without measuring the laser reference laser intensity, the WMS-2f signal could be directly corrected using the error exponential fitting function presented in the experiment.

Conclusion

In this paper, we analyzed the fly ash influence on the peak-to-peak value of the WMS-2f signal and the NO concentration. The study results are as follows: 1) The peak-to-peak value of the WMS-2f signal satisfied an exponential relationship with the mass concentration of uniformly distributed particles; 2) For the same kind of particles, different particle sizes had different effects on the peak-to-peak value of WMS-2f signal. At constant particle mass concentration, the 2f peak-to-peak error of NO was negatively correlated with the particle size. This conclusion also provided a new idea for obtaining fly ash particle size by optical techniques. The 2f peak-to-peak error and NO concentration error caused by fly ash particles were less than 2% after correction. Therefore, we could measure the exponential relationship between the 2f peak-to-peak error of NO and the fly ash mass concentration in advance. Then, the relationship was input into the calculation program of the gas concentration to introduce necessary corrections and to obtain the actual NO concentration. In conclusion, without measuring the laser reference laser intensity, the WMS-2f signal can be directly corrected by the error exponential fitting function presented in the paper. Such a procedure can effectively eliminate the fly ash influence on the flue gas concentration measurement. Obtained results provide a theoretical basis for fly ash error correction and flue gas concentration inversion in complex working environments.

Data availability statement

The raw data supporting the conclusion of this article will be made available by the authors, without undue reservation.

Author contributions

All authors listed have made a substantial, direct, and intellectual contribution to the work and approved it for publication.

Funding

The study was supported by the National Key R&D Program Intergovernmental International Science and Technology Innovation Cooperation Project (2019YFE0109700), the Science and Technology Project of Guangdong Province (2020A0505140001), the Natural Science Foundation of Guangdong Province-Outstanding Youth Project (2021B1515020071), the Fok Ying Tung Education Foundation 17th Foundation for Young Teachers in Higher Education (171,047), and Innovation and Technology Commission (MHP/049/19), Hong Kong SAR, China.

Conflict of interest

JM is employed by Cntest Intelligent scien-tech Co., LTD.

The remaining authors declare that the research was conducted in the absence of any commercial or financial relationships that could be construed as a potential conflict of interest.

Publisher's note

All claims expressed in this article are solely those of the authors and do not necessarily represent those of their affiliated organizations, or those of the publisher, the editors and the reviewers. Any product that may be evaluated in this article, or claim that may be made by its manufacturer, is not guaranteed or endorsed by the publisher.

References

1. Pan Y, Dong L, Yin X, Wu H. Compact and highly sensitive NO_2 photoacoustic sensor for environmental monitoring. *Molecules* (2020) 25:1201. doi:10.3390/molecules25051201

2. Zhang Z, Zhang F, Xu B, Xie H, Fu B, Lu X, et al.High-sensitivity gas detection with air-lasing-assisted coherent Raman spectroscopy. *Ultrafast Sci* (2022), 2022, 1–8. doi:10.34133/2022/9761458

3. Fu Y, Cao J, Yamanouchi K, Xu H. Air-laser-based standoff coherent Raman spectrometer. *Ultrafast Sci* (2022), 2022, 1–9. doi:10.34133/2022/9867028

4. Zheng H, Tang G. Developing Data Acquisition and Handling System for continuous emission monitoring system from coal-fired power plant. In: 2008 Chinese Control and Decision Conference; 02-04 July 2008; Yantai, China. p. 3616–9. doi:10.1109/CCDC.2008.4598004

5. Li J, Zhang C, Wei Y, Du Z, Sun F, Ji Y, et al.*In situ*, portable and robust laser sensor for simultaneous measurement of ammonia, water vapor and temperature in denitrification processes of coal fired power plants. *Sensors Actuators B: Chem* (2020) 305:127533. doi:10.1016/j.snb.2019.127533

6. Chao X, Jeffries JB, Hanson RK. Real-time, *in situ*, continuous monitoring of CO in a pulverized-coal-fired power plant with a 2.3 μm laser absorption sensor. *Appl Phys B* (2013) 110:359–65. doi:10.1007/s00340-012-5262-8

7. Wysocki G, Kosterev AA, Tittel FK. Spectroscopic trace-gas sensor with rapidly scanned wavelengths of a pulsed quantum cascade laser for *in situ* NO monitoring of industrial exhaust systems. *Appl Phys B* (2005) 80:617–25. doi:10.1007/s00340-005-1764-y

8. Peng Z, Du Y, Ding Y. Highly sensitive, calibration-free WM-DAS method for recovering absorbance-Part I: Theoretical analysis. *Sensors* (2020) 20:681. doi:10.3390/s20030681

9. Ma Y, Feng W, Qiao S, Zhao Z, Gao S, Wang Y. Hollow-core anti-resonant fiber based light-induced thermoelastic spectroscopy for gas sensing. *Opt Express* (2022) 30:18836–44. doi:10.1364/OE.460134

10. Pan Y, Zhao J, Lu P, Sima C, Zhang W, Fu L, et al.All-optical light-induced thermoacoustic spectroscopy for remote and non-contact gas sensing. *Photoacoustics* (2022) 27:100389. doi:10.1016/j.pacs.2022.100389

11. Qiao SD, Sampaolo A, Patimisco P, Spagnolo V, Ma YF. Ultra-highly sensitive HCl-LITES sensor based on a low-frequency quartz tuning fork and a fiber-coupled multi-pass cell. *Photoacoustics* (2022) 27:100381. doi:10.1016/j.pacs.2022.100381

12. Lackner M. Tunable diode laser absorption spectroscopy (TDLAS) in the process industries-A review. *Rev Chem Eng* (2007) 23:65–147. doi:10.1515/REVCE.2007.23.2.65

13. Li J, Deng H, Sun J, Yu B, Fischer H. Simultaneous atmospheric CO, N2O and H2O detection using a single quantum cascade laser sensor based on dual-spectroscopy techniques. *Sensors Actuators B: Chem* (2016) 231:723–32. doi:10.1016/j.snb.2016.03.089

14. Ghorbani R, Schmidt FM. ICL-based TDLAS sensor for real-time breath gas analysis of carbon monoxide isotopes. *Opt Express* (2017) 25:12743–52. doi:10.1364/OE.25.012743

15. Reid J, Labrie D. Second harmonic detection with tunable diode lasers comparison of experiment and theory. *Appl Phys B* (1981) 26:203–10. doi:10.1007/BF00692448

16. Li C, Dong L, Zheng C, Tittel FK. Compact TDLAS based optical sensor for ppb-level ethane detection by use of a 3.34μm room-temperature CW interband cascade laser. *Sensors Actuators B: Chem* (2016) 232:188–94. doi:10.1016/j.snb.2016.03.141

17. Sun K, Chao X, Sur R, Goldenstein CS, Jeffries JB, Hanson RK. Analysis of calibration-free wavelength-scanned wavelength modulation spectroscopy for practical gas sensing using tunable diode lasers. *Meas Sci Technol* (2013) 24:125203. doi:10.1088/0957-0233/24/12/125203

18. Rieker GB, Jeffries JB, Hanson RK. Calibration-free wavelength-modulation spectroscopy for measurements of gas temperature and concentration in harsh environments. *Appl Opt* (2009) 48:5546–60. doi:10.1364/ao.48.005546

19. Wang F, Cen K, Li N, Huang Q, Chao X, Yan J, et al.Simultaneous measurement on gas concentration and particle mass concentration by tunable diode laser. *Flow Meas Instrum* (2010) 21:382–7. doi:10.1016/j.flowmeasinst.2010.04.009

20. Uhlig EM, Hoyningen-Huene W. Correlation of the atmospheric extinction coefficient with the concentration of particulate matter for measurements in a polluted urban area. *Atmos Res* (1993) 30:181–95. doi:10.1016/0169-8095(93)90022-G

21. Wang RT, Hulst HC. Rainbows: Mie computations and the airy approximation. *Appl Opt* (1991) 30:106–17. doi:10.1364/AO.30.000106

22. Fu Q, Sun W. Mie theory for light scattering by a spherical particle in an absorbing medium. *Appl Opt* (2001) 40:1354–61. doi:10.1364/AO.40.001354

23. Mohammad IL, Anderson GT, Chen Y. Noise estimation technique to reduce the effects of 1/f noise in open path tunable diode laser absorption spectrometry (OP-TDLAS). *Proc SPIE* (2014) 9113:91130S. doi:10.1117/12.2063662

24. Zhu X, Yao S, Ren W, Lu Z, Li Z. TDLAS monitoring of carbon dioxide with temperature compensation in power plant exhausts. *Appl Sci (Basel)* (2019) 9:442. doi:10.3390/app9030442

25. Goldenstein CS, Spearrin RM, Jeffries JB, Hanson RK. Wavelength modulation spectroscopy near 2.5μm for H_2O and temperature in high-pressure and temperature gases. *Appl Phys B* (2014) 116:705–16. doi:10.1007/s00340-013-5754-1

26. Liu J, Zhou Y, Guo S, Hou J, Zhao G, Ma W. A novel methodology to directly pre-determine the relative wavelength response of DFB laser in wavelength modulation spectroscopy*Opt Express* (2019) 27:1249–61. doi:10.1364/OE.27.001249

frontiers | Frontiers in Physics

TYPE Original Research
PUBLISHED 17 October 2022
DOI 10.3389/fphy.2022.1036179

OPEN ACCESS

EDITED BY
Yufei Ma,
Harbin Institute of Technology, China

REVIEWED BY
Fei Liu,
Xidian University, China
Jinjia Guo,
Ocean University of China, China

*CORRESPONDENCE
Zhenzhen Wang,
zhenzhen-wang@xjtu.edu.cn

SPECIALTY SECTION
This article was submitted to Optics and Photonics,
a section of the journal
Frontiers in Physics

RECEIVED 04 September 2022
ACCEPTED 30 September 2022
PUBLISHED 17 October 2022

CITATION
Zhou W, Xu Z, Cui W, Wang Z, Chong D and Yan J (2022), Optimized CT-TDLAS reconstruction performance evaluation of least squares with the polynomial-fitting method.
Front. Phys. 10:1036179.
doi: 10.3389/fphy.2022.1036179

Optimized CT-TDLAS reconstruction performance evaluation of least squares with the polynomial-fitting method

Wangzheng Zhou[1], Zhekai Xu[1], Wei Cui[2], Zhenzhen Wang[1]*, Daotong Chong[1] and Junjie Yan[1]

[1]State Key Laboratory of Multiphase Flow in Power Engineering, School of Energy and Power Engineering, Xi'an Jiaotong University, Xi'an, China, [2]Science and Technology on Plasma Dynamics Laboratory, Air Force Engineering University, Xi'an, China

Computed tomography-tunable diode laser absorption spectroscopy (CT-TDLAS) has been widely used in the diagnosis of the combustion flow field. Several optimized CT reconstruction algorithms such as iteration methods, transformation methods, and nonlinear least squares were applied. Considering the industrial application background, the performances of algebraic iteration reconstruction with the simultaneous algebra reconstruction technique (SART), Tikhonov regularization, and least squares with the polynomial fitting method were discussed in this study. For the mentioned algorithm, identical simulated reconstruction parameters that contained 32-path laser structures, assumed temperature distribution, and absorption databases were adopted to evaluate the reconstruction performance including accuracy, efficiency, and measurement of environment applicability. In this study, different CT reconstruction algorithms were also used to calculate the temperature distribution of the Bunsen burner flame. The different reconstruction results were compared with thermocouple detection data. With the theoretically simulated and experimental analysis, the least squares with the polynomial fitting technique has advantages in reconstruction accuracy, calculation efficiency, and laser path applicability for the measurement condition. It will be helpful in enhancing CT-TDLAS technique development.

KEYWORDS

CT-TDLAS, SART, Tikhonov regularization, the polynomial fitting method, algorithm optimization

Introduction

Combustion is the most widely used chemical phenomenon, which is accompanied by a large amount of luminous heat. Since the industrial revolution, combustion has been applied in transportation, power generation, metallurgy, and aerospace. With the development of combustion research and application, the demands of combustion mechanism optimization and efficiency improvement could not be satisfied by the thermocouples and other traditional detection methods [1, 2]. A non-contract *in situ*

testing technique that will not destroy the combustion flow field is urgently needed, and it can obtain more different combustion parameters at the same time. Spectral analysis technology can perfectly satisfy all the aforementioned requirements, and it can also reproduce the flow field information on the combustion process as real as possible [3–9].

Tunable diode laser absorption spectroscopy (TDLAS) is one of the spectral analysis technologies which can measure the temperature and gas concentration parameters. TDLAS has several advantages including high sensitivity, high noise immunity, high repetition rate, and easy compatibility with communication fiber optic components [10–12]. It means the TDLAS system is easy to be integrated, and the cost is lower than that of other spectral analysis technologies [13, 14]. However, the most valuable superiority is that combined with computed tomography (CT), CT-TDLAS can achieve 2D/3D temperature and concentration distribution reconstruction using multiple intersecting laser paths [15–17]. Thus, time-resolved and *in situ* combustion temperature and gas concentration information will be gathered at the same time [18–20].

The accuracy of CT-TDLAS is decided by different CT algorithms. Common CT algorithms are the projection inversion method and the iterative method. Projection inversion requires the projection direction covered at 360° or at least 180°, and it needs a large number of laser paths, such as FBP and FDDI [21–23]. Another projection inversion Abel inversion [24, 25] is particularly aimed at an axisymmetric distributed flow field. Although these inversion methods can get quick, high accuracy, and high-resolution reconstruction results, the optical path arrangement is difficult to fit with large industrial field applications.

As for iterative methods, the inverse problem of CT-TDLAS is solving an inherently ill-posed equation set with a severe rank deficiency. It means the answers of the equation set are the indefinite solution. If the iteration's initial values are different, the different reconstruction results can be acquired, which will cause a serious error. This situation happens from time to time when we use the iterative algorithm, such as ART and MART [26–28]. Commonly, the ill-posedness of CT-TDLAS ill-conditioned equations can be reduced through an optimized laser path design method in two steps. First, four or more laser projection directions are applied in the measurement area. Second, the weights of different laser paths within the same mesh are corrected during iterative calculation [29]. However, this method will decrease the initial reconstruction resolution and needs a long iterative convergence time. Another solution is choosing machine learning or neural networks to establish an *a priori* model. After that, according to the computer training results, an optimized initial value is obtained to shorten reconstruction iterative steps, such as MBIR and PI-CNN-aided TDLAS [30–33]. This method can eliminate noise effects during measurement, but it needs a huge combustion simulation database for sample training before it is applied in new combustion environments.

Nowadays, regularization methods and least squares methods are applied in CT reconstruction [34, 35]. The most popular regularization method is Tikhonov regularization [25, 36], which adds a constant to the eigenvalue to improve the stability of the matrix. Tikhonov regularization can get accurate approximate solutions by matrix operations; thus, the calculation speed is much faster than iterative methods. Hyperspectroscopy [37, 38], as one of the least squares methods, considers extensive different spectral line information to improve CT reconstruction accuracy.

In this study, a CT algorithm named the polynomial fitting technique, which was based on nonlinear least squares, has been proposed and applied. First, the accuracy and the efficiency of different CT algorithms were discussed, which contain SART, Tikhonov regularization, and polynomial fitting with the same laser path structure and without optimizing the initial value. Second, Tikhonov regularization and the polynomial fitting method were used to calculate the temperature of the Bunsen burner flame. The simulation and experimental results of different CT algorithms were compared to discuss the priority of the polynomial fitting method.

CT algorithm

TDLAS is a spectral measurement method based on the principle of photon energy selective absorption by gas molecules. When the laser passes through the area to be measured, the laser energy will be absorbed by the gas molecules. The energy-changing relationship between the initial laser and the absorbed laser can be expressed by Beer–Lambert's law, as shown in Eq. 1:

$$\frac{I_\lambda}{I_{\lambda,0}} = \exp\{-A_\lambda\} = \exp\left\{-\sum_i \left(n_i L \sum_j S_{i,j}(T) G_{Vi,j}(n_i, T, P)\right)\right\}, \tag{1}$$

where λ—wavelength; $I_{\lambda,0}$—laser intensity without gas absorption; I_λ—laser intensity after gas absorption; A_λ—spectral integral; i—the type of measured gas; j—absorption line of gas; n_i—gas concentration; $S_{i,j}(T)$ — absorption line intensity; T—temperature; P—pressure; $G_{Vi,j}$—linear function; and L—laser path length.

The integral value of the linear function $G_{Vi,j}$ in the entire frequency domain is 1, so Eq. 1 can be transformed into Eq. 2

$$A_\lambda = \int -\ln\left(\frac{I_\lambda}{I_{\lambda,0}}\right) = n_i L S_i(T) P. \tag{2}$$

Because the temperature, pressure, gas concentration, and absorption path length are same at the same laser path, the temperature can be obtained through the ratio of the absorption

intensities between two different wavelength absorption lines, as shown in Eq. 3. The concentration can be calculated by Eq. 4.

$$T = \frac{\frac{hc}{K}\left(E_2'' - E_1''\right)}{\ln\left(\frac{A_1}{A_2}\right) + \ln\left(\frac{S_2(T_0)}{S_1(T_0)}\right) + \frac{hc}{K}\frac{\left(E_2'' - E_1''\right)}{T_0}}, \tag{3}$$

$$n_i = \frac{A_\lambda}{LS_i(T)P}, \tag{4}$$

where T_0—296K standard temperature; $S\ (T_0)$—spectrum intensity at the standard temperature; E''—low transition energy state energy; h—Planck's constant; K—Boltzmann constant; c—speed of light; υ_0—laser frequency; and spectral line intensity $S\ (T_0)$ can be queried in the HITRAN database.

Simultaneous algebra reconstruction technique (SART)

It can be considered that the temperature on each micro-length part is uniform when laser paths are divided into infinite micro-length parts. Thus, laser path absorption A can be calculated by Beer–Lambert's law, as shown in Eq. 5.

For different laser paths, the correction value is not completely the same. Because when two or more laser paths pass through a pixel grid at the same time, the same error correction of the pixel grid will cause additional noise. More iteration steps are needed to eliminate the noise effect to obtain high-precision reconstruction results. The SART algorithm takes into account the errors of all laser paths passing through the pixel grid during the iterative calculation of each pixel grid. This method can smooth out the influence of noise, and it can obtain relatively ideal reconstruction results. The formula of the SART is shown in Eq. 6:

$$\begin{cases} A_{\lambda,1} = \sum\limits_q L_{1,q}\alpha_{\lambda,1,q} = \sum\limits_q n_{1,q}L_{1,q}S_\lambda\left(T_{1,q}\right)G_{V\lambda}\left(n_{1,q}, T_{1,q}, P\right), \\ A_{\lambda,2} = \sum\limits_q L_{1,q}\alpha_{\lambda,2,q} = \sum\limits_q n_{2,q}L_{2,q}S_\lambda\left(T_{2,q}\right)G_{V\lambda}\left(n_{2,q}, T_{2,q}, P\right), \\ \quad\vdots \\ A_{\lambda,p} = \sum\limits_q L_{p,q}\alpha_{\lambda,p,q} = \sum\limits_q n_{p,q}L_{p,q}S_\lambda\left(T_{p,q}\right)G_{V\lambda}\left(n_{p,q}, T_{p,q}, P\right), \end{cases} \tag{5}$$

where q—mesh grid; L_q—laser length; and $\alpha_{\lambda,q}$—absorption coefficient.

$$\alpha_{\lambda,q}^{k+1} = \alpha_{\lambda,q}^{k} + \frac{\omega}{\sum_{p=1}^{m} L_{p,q}} \sum_{p=1}^{m} \left(\frac{A_{\lambda,p} - \sum_{q=1}^{n} \alpha_{\lambda,q} L_{p,q}}{\sum_{q=1}^{n} L_{p,q}} \right) \times L_{p,q}, \tag{6}$$

where m—number of all laser paths through the pixel grid and the relaxation factor ω should be $0<\omega \leq 1$.

Tikhonov regularization

Eq. 5 can be written in the matrix form as Eq. 7:

$$\begin{bmatrix} L_{1,1} & L_{1,2} & \cdots & L_{p,q} \\ L_{1,1} & L_{1,2} & \cdots & L_{p,q} \\ \vdots & \vdots & \ddots & \vdots \\ L_{1,1} & L_{1,2} & \cdots & L_{p,q} \end{bmatrix} \cdot \begin{bmatrix} \alpha_{\lambda,1,1} \\ \alpha_{\lambda,1,2} \\ \vdots \\ \alpha_{\lambda,p,q} \end{bmatrix} = \begin{bmatrix} A_{\lambda,1} \\ A_{\lambda,2} \\ \vdots \\ A_{\lambda,p+q} \end{bmatrix} \text{ or } L \cdot \alpha = A. \tag{7}$$

In the coefficient matrix L, there are lots of "0" because each mesh grid only contains limited laser paths. Non-negative least squares are directly used to solve Eq. 7, and unsatisfactory results will be obtained. Tikhonov regularization adds a regularization parameter η to improve the stability of the matrix, as shown in Eq. 8:

$$\alpha = \text{argmin}\left\{\|L\alpha - A\|_2^2 + \eta^2\|\alpha\|_2^2\right\}. \tag{8}$$

For different regularization parameters η, α_η is solved by Eq. 9. The L-curve method is used to find the fittest η, and α_η is used as the solution answer α.

$$\alpha_\eta = \left(L^{\mathrm{T}}L + \eta I\right)^{-1}L^{\mathrm{T}}A. \tag{9}$$

Polynomial fitting method

In the combustion flow field, parameter distribution is continuous. Taylor expansion can be carried out to temperature and concentration distribution functions $T\ (x, y)$ and $n\ (x, y)$, which are composed of a set of adaptation coefficients $a_{k,l}$ and $b_{k,l}$, as shown in Eqs. 10, 11.

$$T(x,y) = \sum_{k=0}^{m}\sum_{l=0}^{k} b_{k-l,l}x^{k-l}y^{l} = F_T\left(b_{k,l}\right), \tag{10}$$

$$n(x,y) = \sum_{k=0}^{m}\sum_{l=0}^{k} a_{k-l,l}x^{k-l}y^{l} = F_n\left(a_{k,l}\right). \tag{11}$$

For a certain laser path p, all points $(x_{p,1}, y_{p,1})$, $(x_{p,2}, y_{p,2})$, ... $(x_{p,q},\ y_{p,q})$, respectively, are substituted into Eqs. 10, 11:

$$\begin{bmatrix} 1 & x_{p,1} & y_{p,1} & x_{p,1}^2 & x_{p,1}y_{p,\cdot 1} & y_{p,1}^2 & \cdots & x_{p,1}^m & \ldots & y_{p,1}^m \\ 1 & x_{p,2} & y_{p,2} & x_{p,2}^2 & x_{p,2}y_{p,2} & y_{p,2}^2 & \cdots & x_{p,2}^m & \ldots & y_{p,2}^m \\ \vdots & \vdots & \vdots & \vdots & \vdots & \vdots & \cdots & \vdots & \cdots & \vdots \\ 1 & x_{p,q} & y_{p,3} & x_{p,q}^2 & x_{p,q}y_{p,q} & y_{p,q}^2 & \cdots & x_{p,q}^m & \cdots & y_{p,q}^m \end{bmatrix} \bullet \begin{bmatrix} b_{0,1} \\ b_{1,0} \\ \vdots \\ b_{0,m} \end{bmatrix} = \begin{bmatrix} T_{p,1} \\ T_{p,2} \\ \vdots \\ T_{p,q} \end{bmatrix}, \tag{12}$$

$$\begin{bmatrix} 1 & x_{p,1} & y_{p,1} & x_{p,1}^2 & x_{p,1}y_{p,.1} & y_{p,1}^2 & \cdots & x_{p,1}^m & \cdots & y_{p,1}^m \\ 1 & x_{p,2} & y_{p,2} & x_{p,2}^2 & x_{p,2}y_{p,2} & y_{p,2}^2 & \cdots & x_{p,2}^m & \cdots & y_{p,2}^m \\ \vdots & \vdots & \vdots & \vdots & \vdots & \vdots & \cdots & \vdots & \cdots & \vdots \\ 1 & x_{p,q} & y_{p,3} & x_{p,q}^2 & x_{p,q}y_{p,q} & y_{p,q}^2 & \cdots & x_{p,q}^m & \cdots & y_{p,q}^m \end{bmatrix} \bullet \begin{bmatrix} a_{0,1} \\ a_{1,0} \\ \vdots \\ a_{0,m} \end{bmatrix} = \begin{bmatrix} n_{p,1} \\ n_{p,2} \\ \vdots \\ n_{p,q} \end{bmatrix}. \quad (13)$$

According to Eqs. 5, 10, 11, the theoretical absorption summation of the laser path from 1 to p can be calculated, as shown in Eq. 14. Theoretical absorption summation is a function that is only related to the set of adaptation coefficients $a_{k,l}$ and $b_{k,l}$. When the *error* between A_{theory} and $A_{\text{experiment}}$ is minimum whose corresponding adaptation coefficients $a_{k,l}$ and $b_{k,l}$ are the temperature and concentration distribution function solution, respectively,

$$\left(A_{\lambda,p}\right)_{\text{theory}} = \sum_q L_{p,q} F_n\left(a_{k,l}\right) S_\lambda\left(F_T\left(b_{k,l}\right)\right) G_{V\lambda}\left(F_n\left(a_{k,l}\right), F_T\left(b_{k,l}\right), P\right), \quad (14)$$

$$error = \min\left\{ \sum_{\lambda,p} \left(A_{\lambda,p,theory} - A_{\lambda,p,\text{experiment}}\right)^2 \right\}. \quad (15)$$

In Eqs 10, 11, segments in the laser path q are decided by the initial CT resolution requirement, and the Taylor expansion series m is decided by the number of laser paths p and segments in the laser path q. Reconstruction accuracy can be improved by increasing m, but the CT accuracy will decrease when m is increased too much, which can cause overfitting. Like the "L-Curve" method in Tikhonov regularization, different Taylor expansion series "m" can be chosen for reconstruction calculation, and a fittest "m" value with a minimum deviation will be found. In this study, the value of m is 12 and q is 40. In solving Eq. 15, Levenberg–Marquardt, downhill simplex, and other nonlinear least squares methods can be chosen. Because the polynomial fitting temperature and concentration distribution functions are directly acquired, the initial reconstruction resolution of polynomial fitting is much higher than that of other CT algorithms without post-interpolation.

Experiment system

In this study, a CT-TDLAS system with a Bunsen burner flame was set up, and an *x-y-z* axis movable B-type thermocouple probe (BM-100-100-110) was used to verify the accuracy of the CT reconstruction algorithms. The laser wavelengths of H_2O absorption were 1388.139 nm, 1388.329 nm, 1388.454, and 1343.297 nm. The 1388-nm laser was mainly used in the detection of temperatures within 1000 K. For higher temperature situations, the 1343-nm laser signal should be added to the analysis.

The CT-TDLAS system, as shown in Figure 1, consisted of tunable diode lasers (NTT, NLK1E5GAAA, 1388 nm; NLK1B5EAAA, 1343 nm), fiber coupler (SL&PS, SBC-3655-2-50-2222-LLLL-1), laser driver (NTT, WL-100 -D-B-DFB-A), single-mode jumpers (P-55-R-22-C-F-2), fiber splitter (PLC-367020-0132-2), collimators (SL&PS, C-20-S-1-C-200-2-L-2-M), detectors (SL&PS, PD-16-1), amplifier (SL&PS, A-34ch-10 db-AC150DC2-IO1M50-SMAJ), AD unit (SL&PS, AD-35ch-10MHz-12bit-I1M-BNC), and a customized 32-path CT cell. The diameter of the CT measurement area was 60 mm. The customized 32-path CT cell was above the Bunsen burner nozzle by 100 mm and had four projection directions to increase the CT reconstruction accuracy, as shown in Figure 2. The diameter of the B-type thermocouple probe was 0.1 mm.

The flow rates of the Bunsen burner premixed gas consisted of 3.0 L/min methane (CH_4) and 3.0 L/min air. During the combustion process, there was 35 L/min compressed air surrounding the flame to make the premix flame steady. In the CT-TDLAS experiment, the water vapor mainly came from methane combustion. Some researchers usually used flat burner flame to verify the 2D temperature detection performance of the CT-TDLAS technique [15]. In this study, different from the flat burner, the diameter of the Bunsen burner nozzle was 10 mm, and the flame was difficult to fill all the CT measurement areas. Therefore, the H_2O concentration of the laser path located at the CT measurement edge area was extremely inadequate, and H_2O absorption was focused on the laser path that passed through the center area. This phenomenon was harmful to CT reconstruction accuracy. So the compressed air was fed into a humidifier before being inserted into the surrounding area of the Bunsen burner flame.

Before the CT-TDLAS experiment, steady flame combustion must be confirmed. At the center of the CT measurement area, five feature points were established in this study. Feature point 1 was the measurement center point. The other four feature points were, respectively, located at the $\pm X$ axis and $\pm Y$ axis, and the distance was all 5 mm. During steady flame confirmation, the temperature of five feature points was detected five times by the B-type thermocouple, while the Bunsen burner flame was rekindled 5 min each time. If the temperature was almost the same within confirmation of five times, it can be considered that the flame was in a steady combustion state.

When the flame was confirmed in the steady-combustion state, the B-type thermocouple probe was used to detect the temperature distribution of the center 40 mm × 40 mm area with 121 points, and the distance between each point was 4 mm. After that, the CT-TDLAS system was applied to record the 32-path 1388-nm laser, 1343-nm laser, and coupled laser signal information.

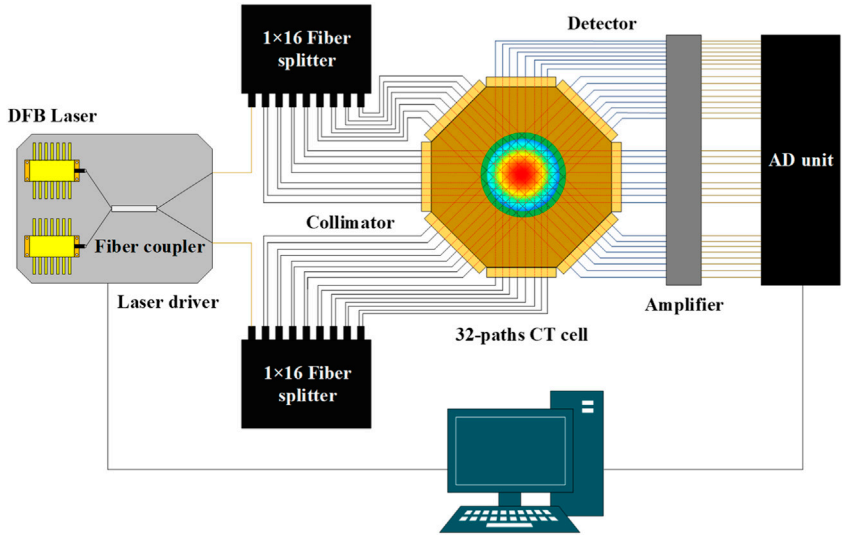

FIGURE 1
CT-TDLAS device connection.

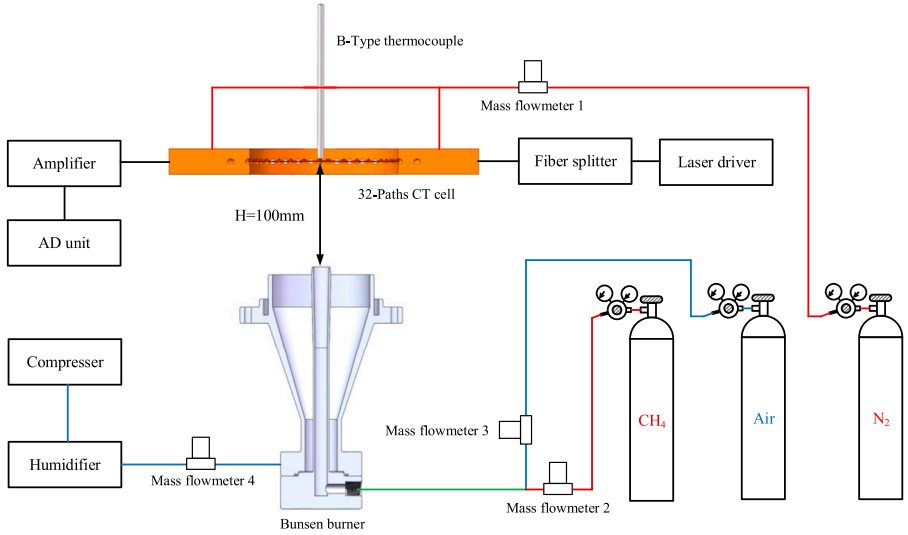

FIGURE 2
CT-TDLAS experiment system.

Results and discussion

In this section, the simulate reconstruction accuracy of two represented CT algorithms, SART and Tikhonov regularization, was compared with the performance of the polynomial fitting method. The reconstruction accuracy of the polynomial fitting method was obviously better than that of SART and Tikhonov regularization. SART and Tikhonov regularization had similar reconstruction accuracy, but Tikhonov regularization had an advantage in reconstruction efficiency. Thus, Tikhonov regularization and the polynomial fitting method were applied to the CT-TDLAS reconstruction of the Bunsen burner flame. The thermocouple detection results at the same flame condition were obtained to discuss the actual measurement accuracy of CT-TDLAS with Tikhonov regularization and the polynomial fitting method.

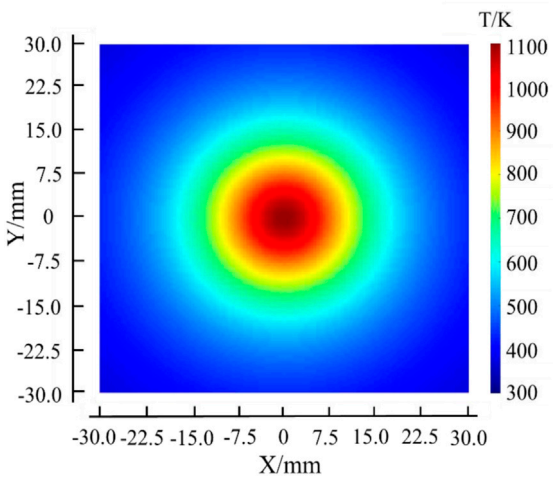

FIGURE 3
Assumed center-symmetric Cauchy–Lorentz temperature distribution.

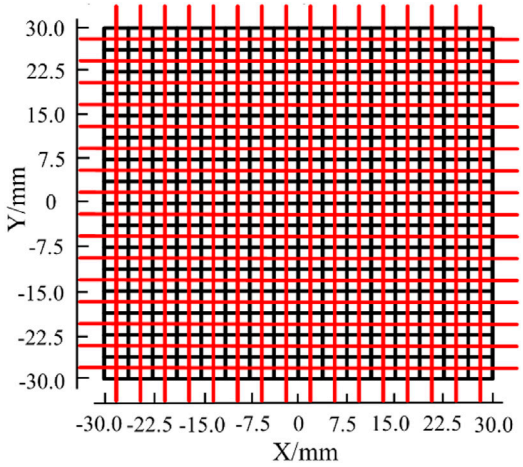

FIGURE 4
16 × 16 orthogonal simulated laser path structure.

Simulation analysis of CT algorithms' accuracy

To evaluate the accuracy and efficiency of CT reconstruction with three different CT algorithms, a unimodal and center-symmetric Cauchy–Lorentz temperature distribution was assumed. The assumed area was a 60-mm square. The water vapor concentration was 10%, and the maximum temperature in the center was 1100 K. The expression and image of the temperature distribution are shown in Eq. 16 and Figure 3, respectively. The simulated CT-TDLAS laser path was a 16 × 16 orthogonal structure, as shown in Figure 4. The distance between each laser path was 3.75 mm.

$$T = \frac{800 \times 13.5^2}{13.5^2 + x^2 + y^2} + 300. \tag{16}$$

The polynomial fitting method could receive a high-resolution reconstruction result. The CT reconstruction results of SART, Tikhonov regularization, and the polynomial fitting method are shown in Figure 5. The relaxation factor ω used in SART was 0.1, and the initial value of the absorbance used by each optical path during the iteration was set to 0. The resolutions of reconstructed results by SART and Tikhonov regularization were 16 × 16 pixels within a 60-mm square. This resolution was the highest result for these two algorithms to achieve. The reason was that each grid needed at least one laser path to go through. The resolution of the polynomial fitting method was decided by the Taylor expansion series m of the distribution function $T(x,y)$. In this simulate reconstruction, the polynomial fitting method obtained a 39 × 39 pixel resolution result. It was obvious that the polynomial fitting method had an advantage in initial reconstruction resolution. Benefitting from this, integral changes in the temperature gradient could be easily acquired.

The polynomial fitting method could receive a more accurate reconstruction result. Because of the central symmetry of the assumed temperature distribution, it was convenient to discuss the accuracy by analyzing the temperature deviation on the path "x = 0 mm". As shown in Figure 6, the reconstruction results of SART and Tikhonov regularization were almost the same. The mean relative error and maximum relative error of SART were 4.17% and 5.61%, respectively, while the mean relative error and maximum relative error of Tikhonov regularization were 4.22% and 5.58%, respectively. The polynomial fitting method was obviously much closer to the assumed distribution, and the mean relative error and maximum relative error were 1.23% and 1.63%, respectively, because the polynomial fitting method considered more residual terms during the calculation process.

The polynomial fitting method had the advantage of high resolution and reconstruction accuracy compared with the traditional CT algorithms. It was more suitable for complicated combustion flame detection.

Comparison of CT-TDLAS experimental results using different CT algorithms

According to the previous discussion, SART and Tikhonov regularization could get almost the same accuracy reconstruction results through the orthogonal laser path structure, which was easy to receive an ill-conditioned matrix with the ill-posed solution. However, SART needed a correct each grid absorption value individually during one iterative process, and it costs hours to converge. Tikhonov regularization could quickly

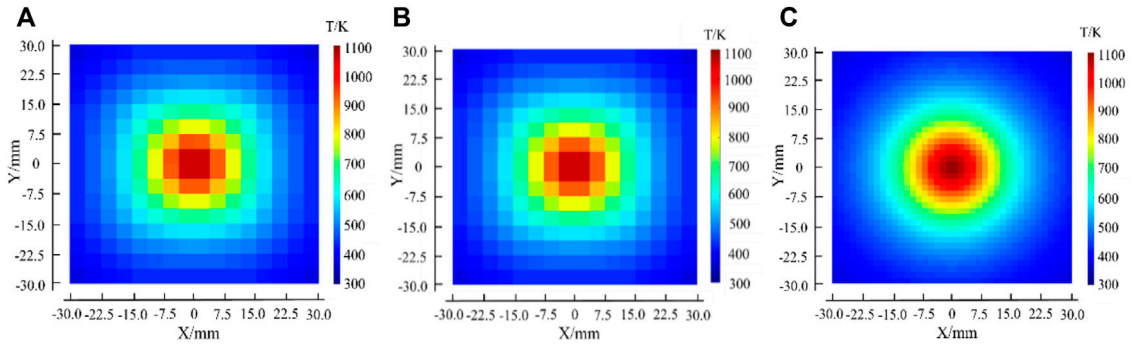

FIGURE 5
CT reconstruction results for assumed temperature distribution. **(A)** SART algorithm; **(B)** Tikhonov regularization; and **(C)** polynomial fitting method.

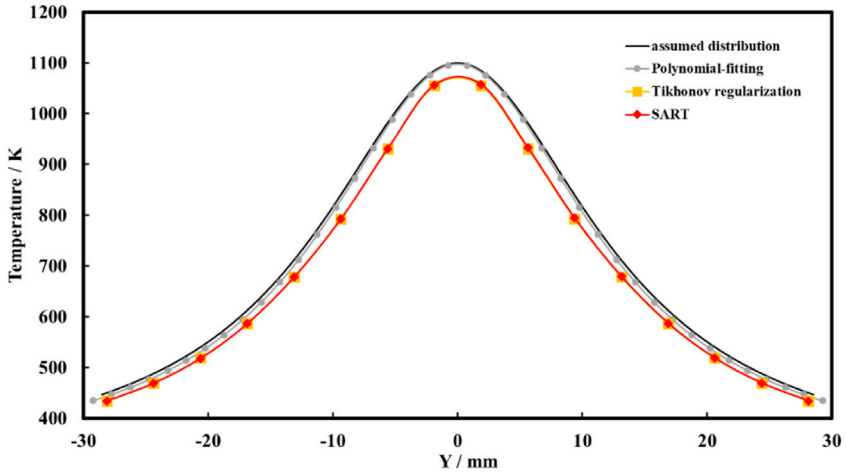

FIGURE 6
Temperature deviation by three CT algorithms on the path "x = 0 mm".

get solutions by simple matrix operations. So Tikhonov regularization and the polynomial fitting method were chosen to restructure the Bunsen burn flame.

The polynomial fitting method had significant advantages over actual flame detection. It got a clear and irregular temperature distribution result. In actual flame detection, the 16 × 16 orthogonal laser structure was not satisfied. As shown in Figure 1, the customized 32-path laser structure was divided into four projection directions to reduce the ill-posedness of CT-TDLAS ill-conditioned equations. Tikhonov regularization needed to guarantee that there was at least one laser path going through each grid. So the measurement area of the CT cell was set to a 10 × 10 grid mesh. However, the polynomial fitting method could still get a 39 × 39 pixel result, while the number of laser paths was not changing. The temperature distribution of the Bunsen burner flame has been shown in Figure 7. Because of the resolution limitation, Tikhonov regularization could only get a roughly presented temperature distribution trend. It could not display detailed information such as the gradient change of the flame temperature distribution. The actual combustion was complicated; according to the thermocouple result, the Bunsen burner flame section was not a regular symmetrical appearance, which was related to factors such as the horizontal inclination angle of the fixed Bunsen burner and the premixed gas flow emitted by a nozzle. It would enlarge the deviation when cubic spline interpolation is directly used without any reference to the increasing resolution. The polynomial fitting method could perfectly avoid these problems.

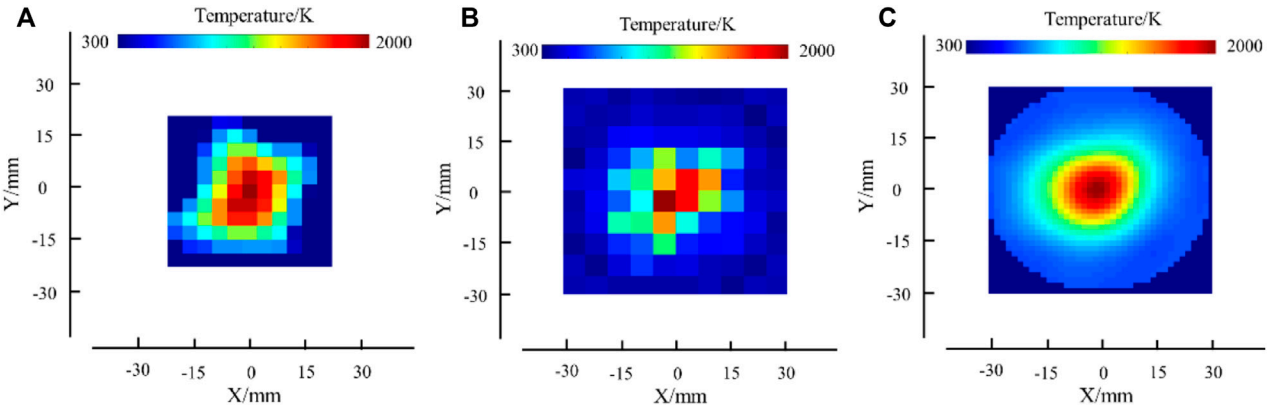

FIGURE 7
Temperature distribution of the Bunsen burner flame. **(A)** Thermocouple; **(B)** Tikhonov regularization; and **(C)** polynomial fitting method.

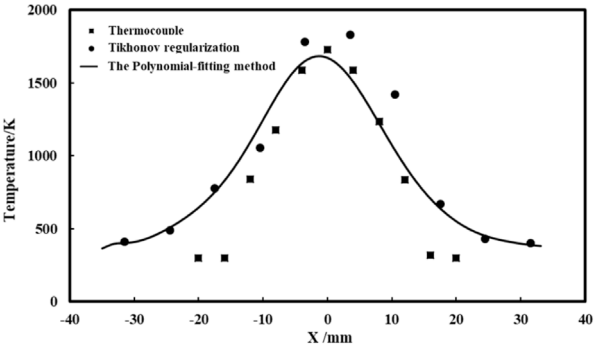

FIGURE 8
Temperature deviation on the path "Y = 0 mm."

In Figure 7C, more accurate and intuitive flame outline messages could be obtained.

The accuracy of the polynomial fitting method was convinced in the Bunsen burner flame experiment. The temperature on the path "Y = 0 mm" was compared, as shown in Figure 8. In the range of −10 to 10 mm, combustion was stable at the flame center, so the reconstruction results of the polynomial fitting method were consistent with the thermocouple. However, in the range of −20 to −10 mm and 10–20 mm, there was an obvious deviation between the polynomial fitting method and the thermocouple. In these areas, the unreacted methane gas and the reaction intermediates of the flame all reacted with the oxygen in the surrounding compressed air. The reaction process was complicated in these areas. It was impossible to ensure that the flame was always in the same combustion state during the thermocouple measurement. The constant slight disturbance of the flame would also cause deviation in the thermocouple reading. On the other hand, thermocouples could only collect the heat flux from convection and conduction. The heat radiation would be missed during the detection process. These two factors caused the deviation between the polynomial fitting method and the thermocouple. However, the resolution of the thermocouple measurement results was limited, and the best temperature detection range of the B-type thermocouple was 600–1700°C. In Figure 8, the results of CT-TDLAS with the polynomial fitting method and thermocouple are similar in the temperature range of 900–2000 K. The deviation of flame FWHM and peak temperature position between the polynomial fitting method and thermocouple was acceptable when the effect of calculation and experimental measurement error was considered. The temperature distribution trends of Tikhonov regularization and the polynomial fitting method reconstruction results were consistent, but there was a difference between the measurement center regions. This was due to the insufficient number of pixel grids in Tikhonov regularization.

According to the aforementioned comparison results, it could be considered that the polynomial fitting method could accurately reconstruct the two-dimensional temperature distribution of the combustion flame and displayed its temperature gradient change. At the same time, its ability to quickly complete reconstruction calculations had great advantages and potential in the field of industrial online measurement and diagnosis.

Conclusion

This study introduced two common CT algorithms of SART and Tikhonov regularization and proposed a new CT algorithm: the polynomial fitting method. First, compared to the accuracy and efficiency of different CT algorithms by an assumed unimodal and center-symmetric Cauchy–Lorentz temperature distribution and a

16 × 16 orthogonal laser path structure, the comparison results showed that SART and Tikhonov regularization could get almost the same accuracy reconstruction results, while Tikhonov regularization had a much higher computational efficiency. The polynomial fitting method showed more accuracy and higher resolution results. Second, a customized 32-path CT-TDLAS system was built. A Bunsen burner flame temperature distribution with 3.0L/min methane (CH_4) and 3.0 L/min air was reconstructed by the thermocouple, Tikhonov regularization, and the polynomial fitting method. The results exhibited that the polynomial fitting method could display detailed information such as the temperature gradient change, and it could also guarantee the reconstruction accuracy compared to the measured results using the thermocouple. CT-TDLAS with the polynomial fitting method had advantages in accuracy, reconstruction efficiency, resolution, and the adaptability of the laser path arrangement to the actual site environment. It was of great significance in the development of CT-TDLAS combustion diagnosis in practical industrial applications.

Data availability statement

The original contributions presented in the study are included in the article/Supplementary Material; further inquiries can be directed to the corresponding author.

Author contributions

WZ was responsible for all aspects of the study. ZX contributed to the CT-TDLAS experiment. WC was responsible for conceptualization and funding acquisition. ZW was responsible for CT reconstruction calculation and data analysis. DC and JY guided this research, revised, and edited the manuscript.

Conflict of interest

The authors declare that the research was conducted in the absence of any commercial or financial relationships that could be construed as a potential conflict of interest.

Publisher's note

References

1. Radajewski M, Decker S, Krueger L. Direct temperature measurement via thermocouples within an SPS/FAST graphite tool. *Measurement* (2019) 147:106863. doi:10.1016/j.measurement.2019.106863

2. Harada T, Watanabe H, Suzuki Y, Kamata H, Matsushita Y, Aoki H, et al. A numerical investigation of evaporation characteristics of a fuel droplet suspended from a thermocouple. *Int J Heat Mass Transfer* (2011) 54:649–55. doi:10.1016/j.ijheatmasstransfer.2010.08.021

3. Guo LB, Zhang D, Sun LX, Yao SC, Wang ZZ, et al. Development in the application of laser-induced breakdown spectroscopy in recent years: A review. *Front Phys (Beijing)* (2021) 16(2):22500. doi:10.1007/s11467-020-1007-z

4. Boeck LR, Mevel R, Fiala T, Hasslberger J, Sattelmayer T. High-speed OH-PLIF imaging of deflagration-to-detonation transition in H2–air mixtures. *Exp Fluids* (2016) 57:105. doi:10.1007/s00348-016-2191-z

5. Singh S, Musculus MP, Reitz RD. Mixing and flame structures inferred from OH-PLIF for conventional and low-temperature diesel engine combustion. *Combustion and Flame* (2009) 156:1898–908. doi:10.1016/j.combustflame.2009.07.019

6. Ma YF, Lewicki R, Razeghi M, Tittel FK. QEPAS based ppb-level detection of CO and N_2O using a high power CW DFB-QCL. *Opt Express* (2013) 21(1):1008–1019. doi:10.1364/oe.21.001008

7. Qiao SD, Sampaolo A, Patimisco P, Spagnolo V, Ma YF. Ultra-highly sensitive HCl-LITES sensor based on a low-frequency quartz tuning fork and a fiber-coupled multi-pass cell. *Photoacoustics* (2022) 27:100381. doi:10.1016/j.pacs.2022.100381

8. Fu Y, Cao JC, Yamanouchi K, Xu HL. Air-laser-based standoff coherent Raman spectrometer. *Ultrafast Sci* (2022) 2022:1–9. doi:10.34133/2022/9867028

9. Zhang ZH, Zhang FB, Xu B, Xie H, Fu B, Lu X, et al. High-sensitivity gas detection with air-lasing-assisted coherent Raman spectroscopy. *Ultrafast Sci* (2022) 2022:1–8. doi:10.34133/2022/9761458

10. Deng BT, Sima C, Xiao YF, Wang X, Ai Y, Li T, et al. Modified laser scanning technique in wavelength modulation spectroscopy for advanced TDLAS gas sensing. *Opt Lasers Eng* (2022) 151:106906. doi:10.1016/j.optlaseng.2021.106906

11. Weng WB, Larsson J, Bood J, Alden M, Li Z. Quantitative hydrogen chloride detection in combustion environments using tunable diode laser absorption spectroscopy with comprehensive investigation of hot water interference. *Appl Spectrosc* (2022) 76(2):207–15. doi:10.1177/00037028211060866

12. Yang XY, Peng ZM, Ding YJ, Du Y. Temperature and OH concentration measurements by ultraviolet broadband absorption of OH(X) in laminar methane/air premixed flames. *Fuel* (2021) 288:119666. doi:10.1016/j.fuel.2020.119666

13. Liu XN, Ma YF. Tunable diode laser absorption spectroscopy based temperature measurement with a single diode laser near 1.4 μm. *Sensors* (2022) 22:6095. doi:10.3390/s22166095

14. Liang TT, Qiao SD, Liu X, Ma YF. Highly sensitive hydrogen sensing based on tunable diode laser absorption spectroscopy with a 2.1 μm diode laser. *Chemosensors* (2022) 10:321. doi:10.3390/chemosensors10080321

15. Sun PS, Zhang ZR, Li Z, Guo Q, Dong F. A study of two dimensional tomography reconstruction of temperature and gas concentration in a combustion field using TDLAS. *Appl Sci (Basel)* (2017) 7(10):990. doi:10.3390/app7100990

16. Xia HH, Kan RF, Liu JG, Xu ZY, He YB. Analysis of algebraic reconstruction technique for accurate imaging of gas temperature and concentration based on tunable diode laser absorption spectroscopy. *Chin Phys B* (2016) 25(6):064205. doi:10.1088/1674-1056/25/6/064205

17. Liu C, Xu LJ, Chen JL, Cao Z, Lin Y, Cai W. Development of a fan-beam TDLAS-based tomographic sensor for rapid imaging of temperature and gas concentration. *Opt Express* (2015) 23(17):22494. doi:10.1364/oe.23.022494

18. Kamimoto T, Deguchi Y, Zhang N, Nakao R, Takagi T, Zhang JZ. Real-time 2D concentration measurement of CH4 in oscillating flames using CT tunable diode laser absorption spectroscopy. *J Appl Nonlinear Dyn* (2015) 4(3):295–303. doi:10.5890/jand.2015.09.009

19. Deguchi Y, Kamimoto T, Kiyota Y. Time resolved 2D concentration and temperature measurement using CT tunable laser absorption spectroscopy. *Flow Meas Instrumentation* (2015) 46:312–8. doi:10.1016/j.flowmeasinst.2015.06.025

20. Wang ZZ, Zhou WZ, Kamimoto T, Deguchi Y, Yan J, Yao S, et al. Two-dimensional temperature measurement in a high-temperature and high-pressure combustor using computed tomography tunable diode laser absorption spectroscopy (CT-TDLAS) with a wide-scanning laser at 1335–1375 nm. *Appl Spectrosc* (2020) 14(2):210–22. doi:10.1177/0003702819888214

21. Xia HH, Kan RF, Xu ZY, Liu J, He Y, Yang C, et al. Measurements of axisymmetric temperature and H_2O concentration distributions on a circular flat flame burner based on tunable diode laser absorption tomography. In: International Symposium on Hyperspectral Remote Sensing Applications/International Symposium on Environmental Monitoring and Safety Testing Technology; 9-11 May 2016; Beijing, China. Proc.SPIE (2016). p. 10156.

22. Han Y, Ye JC. Framing U-net via deep convolutional framelets: Application to sparse-view CT. *IEEE Trans Med Imaging* (2018) 37:1418–29. doi:10.1109/tmi.2018.2823768

23. Choo JY, Goo JM, Lee CH, Park CM, Park SJ, Shim MS. Quantitative analysis of emphysema and airway measurements according to iterative reconstruction algorithms: Comparison of filtered back projection, adaptive statistical iterative reconstruction and model-based iterative reconstruction. *Eur Radiol* (2014) 24(4):799–806. doi:10.1007/s00330-013-3078-5

24. Zhang GY, Wang GQ, Huang Y, Liu X. Reconstruction and simulation of temperature and CO2 concentration in an axisymmetric flame based on TDLAS. *Optik* (2018) 170:166–77. doi:10.1016/j.ijleo.2018.05.123

25. Guha A, Schoegl I. Tomographic laser absorption spectroscopy using Tikhonov regularization. *Appl Opt* (2015) 53(34):8095–8103. doi:10.1364/ao.53.008095

26. Choi DW, Jeon MG, Cho GR, Kamimoto T, Deguchi Y, Doh DH. Performance improvements in temperature reconstructions of 2-D tunable diode laser absorption spectroscopy (TDLAS). *J Therm Sci* (2016) 25(1):84–9. doi:10.1007/s11630-016-0837-z

27. Peng D, Jin Y, Zhai C, Yang J. Numerical simulations to improve the performance of tunable diode laser absorption tomography in a harsh combustion environment. *Spectrosc Lett* (2018) 51(1):7–16. doi:10.1080/00387010.2017.1399424

28. Shao J, Wang LM, Ying CF. Numerical investigation of the two-dimensional gas temperature distribution based on tunable diode laser absorption spectroscopy. *Optica Applicata* (2015) 45(2):183–198. doi:10.5277/oa150205

29. Busa KM, McDaniel JC, Brown MS. Implementation of maximum-likelihood expectation-maximization algorithm for tomographic reconstruction of TDLAT measurements. In: 52nd AIAA Aerospace Sciences Meeting; 2014, January 13-17; National Harbor, MD, USA. American Institute of Aeronautics and Astronautics (2014). p. 1–15.

30. Nadir Z, Brown MS, Comer ML, Bouman CA. A model-based iterative reconstruction approach to tunable diode laser absorption tomography. *IEEE Trans Comput Imaging* (2017) 3(4):876–90. doi:10.1109/tci.2017.2690143

31. Si J, Fu G, Zhang R, Rui Z, Godwin E, Liu C, et al. A quality-hierarchical temperature imaging network for TDLAS tomography. *IEEE Transcations Instrumentation Meas* (2022) 71:4500710. doi:10.1109/TIM.2022.3144211

32. Huang A, Cao Z, Wang CR, Wen J, Lu F, Xu L. An FPGA-based on-chip neural network for TDLAS tomography in dynamic flames. *IEEE Trans Instrum Meas* (2021) 70:4506911–11. doi:10.1109/tim.2021.3115210

33. Chen P, Kan LL, Song XM, Wang X, Jiang C. Application of VMD and Mahalanobis distance combination algorithm in TDLAS methane gas detection. *Optik* (2021) 728:166114. doi:10.1016/j.ijleo.2020.166114

34. Zhang S, Xia YS, Zou CZ. An adaptive regularization method for low-dose CT reconstruction from CT transmission data in Poisson-Gaussian noise. *Optik* (2019) 188:172–86. doi:10.1016/j.ijleo.2019.04.005

35. Gonzales B, Lalush D. Full-spectrum CT reconstruction using a weighted least squares algorithm with an energy-Axis penalty. *IEEE Trans Med Imaging* (2011) 30(2):173–83. doi:10.1109/tmi.2010.2048120

36. Liu C, Xu LJ, Cao Z. Measurement of nonuniform temperature and concentration distributions by combining line-of-sight tunable diode laser absorption spectroscopy with regularization methods. *Appl Opt* (2013) 52(20):4827–4842. doi:10.1364/ao.52.004827

37. Cai WW, Kaminski CF. Multiplexed absorption tomography with calibration-free wavelength modulation spectroscopy. *Appl Phys Lett* (2014) 104(15):154106. doi:10.1063/1.4871976

38. Ma L, Cai WW, Caswell AW, Kraetschmer T, Sanders ST, Roy S, et al. Tomographic imaging of temperature and chemical species based on hyperspectral absorption spectroscopy. *Opt Express* (2009) 17(10):8602–8613. doi:10.1364/oe.17.008602

frontiers | Frontiers in Physics

TYPE Original Research
PUBLISHED 19 October 2022
DOI 10.3389/fphy.2022.1048835

OPEN ACCESS

EDITED BY
Yufei Ma,
Harbin Institute of Technology, China

REVIEWED BY
Kaikai Liu,
Zhengzhou University, China
Xiaoyi Liu,
Soochow University, China

*CORRESPONDENCE
Bo Chen,
chenb@ciomp.ac.cn

SPECIALTY SECTION
This article was submitted to Optics and Photonics,
a section of the journal
Frontiers in Physics

RECEIVED 20 September 2022
ACCEPTED 03 October 2022
PUBLISHED 19 October 2022

CITATION
Ding G, Wu K, He L, Chen B and Liu F (2022), The flat-field method based on rotated images for FY-3E/X-EUVI. *Front. Phys.* 10:1048835. doi: 10.3389/fphy.2022.1048835

The flat-field method based on rotated images for FY-3E/X-EUVI

Guangxing Ding[1], Kun Wu[1], Lingping He[1], Bo Chen[1]* and Fei Liu[2]

[1]Changchun Institute of Optics, Fine Mechanics and Physics, Chinese Academy of Sciences (CAS), Changchun, China, [2]School of Optoelectronic Engineering, Xidian University, Xi'an, China

An algorithm to calculate the flat-field coefficient based on the series of rotated images captured by the solar X-ray and Extreme Ultraviolet Imager (X-EUVI) onboard the Fengyun-3E satellite is proposed in this article. The method includes determination of the solar disk centers and radiuses, calculation of the rotation angles, coordinate transformation to expand the solar disk into rectangles, and derivation of the flat matrix using the KLL algorithm. The accuracy of determination of the solar disk center and radius tested by the Hough gradient method and the least-squares method is at sub-pixel, and the precision of the calculated rotation angle based on the log-polar transform is less than 0.025°. Since the X-EUVI rotates relative to the Sun in real time, multiple rotating images can be obtained and used for flat-field calibration at any time, and the tested accuracy is estimated at 0.79–3.42%. This flat-field method will provide reference and support for solar image processing and research.

KEYWORDS

flat field, solar image, Hough gradient, KLL algorithm, canny operator

1 Introduction

The solar X-ray and Extreme Ultraviolet Imager (X-EUVI) are the first space solar observation equipment working in EUV and X-ray bands in China, which are loaded on the FY-3E satellite and rotating relative to the sun [1–4]. This article will expound how to use the solar rotation images observed by X-EUVI to calculate the flat field.

The flat field is the characterization of the non-uniformity of the response of the optical system to the incident light. The uneven responses may come from the inconsistency of the digital semiconductor detector pixels such as the charge-coupled device (CCD) and complementary metal-oxide semiconductor (CMOS), filters, reflector, and the mechanical structure. The observed images need to correct the non-uniformity of the detector response using the flat-field matrix to obtain the real observation image. Generally, the flat-field correction coefficient can be obtained by fitting the images observed under a uniform light source or stable light source with different exposure times.

However, sometimes both the uniform light source and the stable light source are difficult to obtain. In 1991, Kuhn et al proposed a method (KLL algorithm) to obtain a flat field by using relatively stable and non-uniform images [5]. On this basis, Chae improved the algorithm by liberalizing parameters such as solar images, light intensity change, and

the flat field in 2004 [6]. The KLL algorithm calculates the flat field using the solar images obtained at different positions on the detector. This method uses the observed solar image as the light source, by changing the direction of the telescope to obtain multiple solar images at different positions on the CCD or CMOS, and then calculates the flat field using the iterative method. Many instruments adopt the KLL method to derive the flat field, like the ground-based solar telescopes, such as the optical and near-infrared solar telescope (ONSET) [7], the Hα solar telescope of the Great Bear Lake Solar Observatory [8], and space-based solar observation equipment, like the Atmospheric Imaging Assembly (AIA) and the Helioseismic and Magnetic Imager (HMI) carried by the Solar Dynamics Observatory (SDO) [9–11]. Moreover, the solar telescopes with the local field of view also adopt the KLL method, such as the solar interface layer spectrometer (IRIS) and the magnetic field observation on the Great Bear Lake Solar Observatory [12, 13].

The FY-3E satellite was launched successfully in July 2021; due to the characteristics of the orbit, the solar images taken by X-EUVI rotate in real time. Combined with the characteristics of the rotated image and the requirements of the KLL algorithm, this article presents a flat-field calculation method based on the rotating image. The algorithm mainly includes determination of the solar disk center, calculation of the rotation angles, coordinate transformation to expand the solar disk into a rectangle, and derivation of the flat matrix using the KLL algorithm.

The article is arranged as follows: the data source and the general information of X-EUVI are introduced in Section 2. In Section 3, the calculation processes of the flat-field method are focused on, and finally, the conclusion, discussion of the results, and the source of error of the algorithm are presented in Section 4.

2 Data sets

Onboard the FY-3E satellite, the X-EUVI was launched in July 2021 successfully. So far, X-EUVI has observed and accumulated a large number of solar X-ray and EUV images. The FY-3E satellite operates in a polar-orbiting sun-synchronous dawn-dusk orbit at an altitude of ~840 km with ~99° inclination and with orbital periods near 102 min. X-EUVI tracks and images the sun in real time with the X-ray bands at 0.6–8.0 nm (X1 channel), 0.6–6.0 nm (X2 channel), 0.6–5.0 nm (X3 channel), 0.6–2.0 nm (X4 channel), 0.6–1.6 nm (X5 channel), and 0.6–1.2 nm (X6 channel), and the EUV bands at 19.5 nm. Due to the characteristics of the FY-3E orbit, the satellite rotates at a uniform rate relative to the Sun; therefore, the X-EUVI rotates relative to the Sun in real time; multiple rotating images can be used for flat-field calibration at any time, so that the high-quality solar X-ray and EUV images can be obtained.

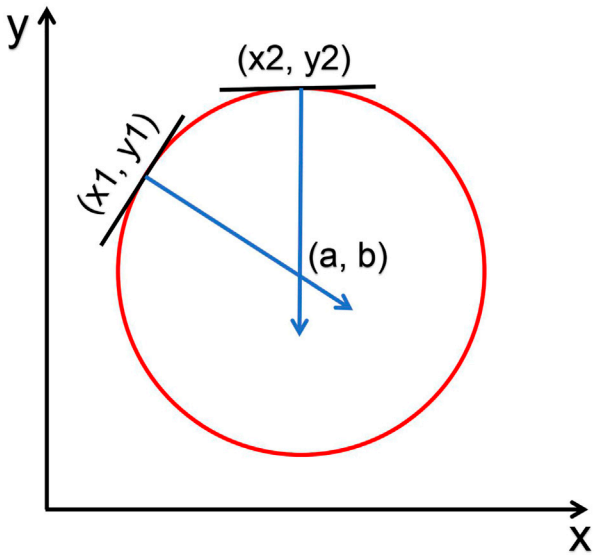

FIGURE 1
Schematic diagram of solar disk center detection.

3 Methods

The method to calculate the flat field can be divided into four steps, which include determination of the solar disk center, calculation of the rotation angles, coordinate transformation to expand the solar disk into a rectangle, and derivation of the flat matrix using the KLL algorithm. These calculation processes are described in detail.

3.1 Solar disk center

In this section, the Hough gradient method is used to detect the disk circle in the EUV solar image, and then the preliminary coordinates of the disk center and radius are obtained [14]. The optimal disk circle is selected by comparing the coefficient of the radius unit length of each circle. Also, in order to improve the accuracy of the center coordinates and radius, the least-squares method is finally used to realize the accurate fitting at the sub-pixel level. According to the input parameter threshold, the center and radius of the detection circle are screened with the Hough gradient method, and finally, the circle that initially meets the threshold conditions is obtained. The specific steps are as follows:

(1) The disk circle center (a, b) is detected in the solar image
   a) The original solar image is processed using CANNY edge detection to get the binary image.
   b) The Sobel operator is performed once on the original image to calculate the neighborhood gradient values of all pixels.

c) All disk center accumulators $N(a, b) = 0$ are initialized.
d) All non-zero pixels in the CANNY edge binary graph are tested, as shown in Figure 1. Lines are drawn along the gradient direction of the pixel edge (the vertical direction of the tangent line), and 1 is added to the accumulator of all pixel coordinates (a, b) that the line passes through, that is, $N(a, b) = N(a, b) + 1$.
e) The $N(a, b)$ are statistically sorted to obtain the possible disk circle center. The greater the $N(a, b)$, the more likely the corresponding pixel (a, b) is to be the center of the circle. If $N(a, b)$ is greater than the threshold T_1, then the corresponding pixel (a, b) is determined to be the center of the circle.

(2) For each detected circle center (a, b), the corresponding radius r is calculated.
a) The distance L between all non-zero points and the center (a, b) in the CANNY graph is calculated.
b) The radius accumulator $N(L) = 0$ is initialized.
c) The non-zero points in the CANNY graph are tested. If the distance from the point to the center is L, then $N(L) = N(L) + 1$. According to the input radius thresholds R_{min} and R_{max}, if L is between R_{min} and R_{max}, then L will be selected as the possible radius r.
d) The accumulator $N(R)$ of all possible radius r is counted to obtain the radius that meets the requirements of the threshold T_2. The greater the accumulator $N(R)$, the more likely r is to be the real radius value. According to the definition of the threshold, if $N(R)$ is greater than the threshold, then the R will be determined as the radius of the circle.

Threshold T_1 is the high threshold of CANNY edge detection, and the low threshold is automatically set to half of the high threshold. Threshold T_2 is the judgment threshold of whether a point on the accumulation plane is the center of the circle. The higher the T_2, the closer the detected circle is to the circle. R_{min} is the minimum value of the circle, and R_{max} is the maximum value of the circle. During the operation of the algorithm, if the distance between the centers of two circles is less than 1, the two circles will be regarded as the same circle.

The unit radius coefficients $K = N(r)/r$ of each circle tested by the Hough gradient method are calculated. The larger the coefficient K value, the more the image edge points in the circle will be contained within the unit radius. Therefore, it is determined that the circle with the largest K value is the best circle in the image. Since the accuracy of the solar disk center tested by the Hough gradient method is ± 1 pixel, the least-squares method to fit the center and radius will be used to further optimize the circle and improve the accuracy of the center and radius to sub-pixel. The least-squares circle fitting method is mainly based on statistics [15]. Even if the edge of the circular target in the image is missing due to the uneven illumination intensity, it will not affect the positioning of the center of the circle and the determination of the radius. Since the edge pixels on the optimal circle are known, the least-squares method can find the best function matching this group of pixels by minimizing the sum of squares of errors and fitting the final sub-pixel radius and circle center. The tested results of this method are shown in Figure 2. This solar EUV image was captured by X-EUVI at 00:02:05 UTC on 5 November 2021, and the red circle was the final determination of the solar disk edge on the CANNY graph.

3.2 Rotation angle

After the location of the image centroid is determined, the rotation angles between the sequence images need to be calculated. The method to calculate the rotation angle is developed from the log-polar transform. The image function in the plane rectangular coordinate system is represented as $f(x, y)$ and it can be represented as $f'(r, \theta)$ after the log-polar transformation. Through the transformation, the rotation transformation in the original image can be expressed as the circular translation along the θ axis direction in the polar coordinate system. The scale transformation in the original image can be expressed as the translation along the r-axis direction in the polar coordinate system. The log-polar transformation is often used to extract the rotation angle and the scale features in image matching. The processes are divided into three steps including extracting rays from the center of the image, calculating the sum of the gray values along the ray to obtain the polar gray curve, and determining the rotation angle between the sequence images based on two curves using the correlation algorithm [16, 17].

In Figure 3, the solar images were captured by X-EUVI on 5 November 2021: the time of 3a is 00:00:03 UTC, the time of 3b is 00:02:05 UTC, and the time of 3c is 00:04:06 UTC. Due to the instrument rotating around the earth with the satellite, there are rotation angles which exist between these three images. The gray curves of Figure 3 are given in Figure 4. The black curve corresponds to Figure 3A, the blue curve corresponds to Figure 3B, and the red curve corresponds to Figure 3C. The rotation angles calculated by the relevant algorithm are 7.200° between 3a and 3b and 7.200° between 3b and 3c. It is assumed that the sun is basically stable in the exposure time, and this assumption is reasonable because the time interval between two successive images is actually ~10s.

The experimental results show that the extraction accuracy of the algorithm is related to the number of lines from the image center. The higher the extraction accuracy, the more lines are set. In this article, the number of lines is selected as 14,400, and it can ensure that the error of the calculated rotation angle is less than 0.025°.

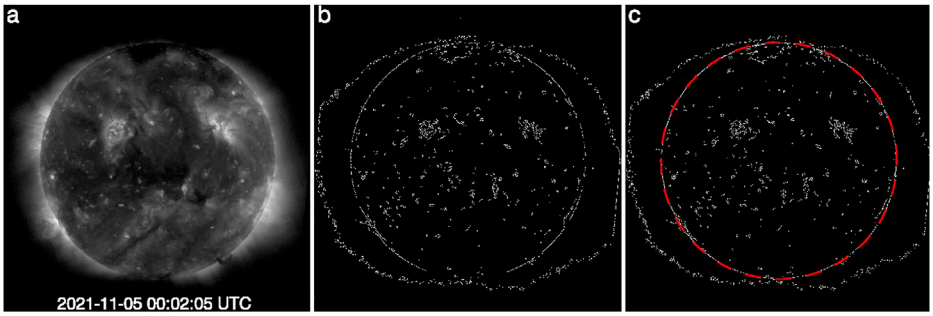

FIGURE 2
Tested solar image sample. **(A)** is the original image, **(B)** is CANNY edge detection, and the red curve in **(C)** is the optimal circle in the CANNY edge graph.

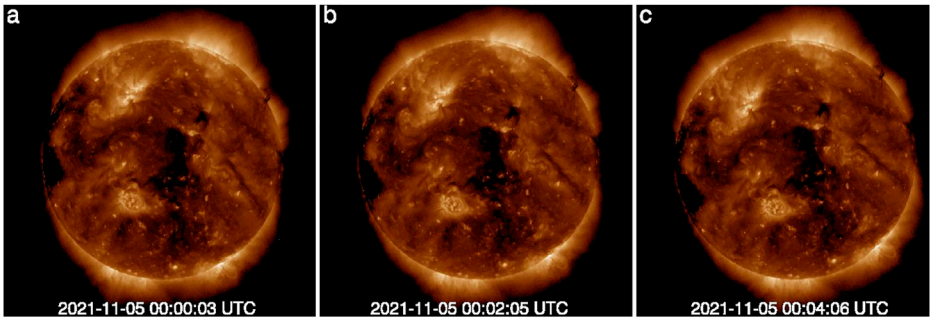

FIGURE 3
Solar images in 19.5 nm observed by X-EUVI on 5 November 2021. The time of 3a is 00:00:03 UTC, the time of 3b is 00:02:05 UTC, and the time of 3c is 00:04:06 UTC.

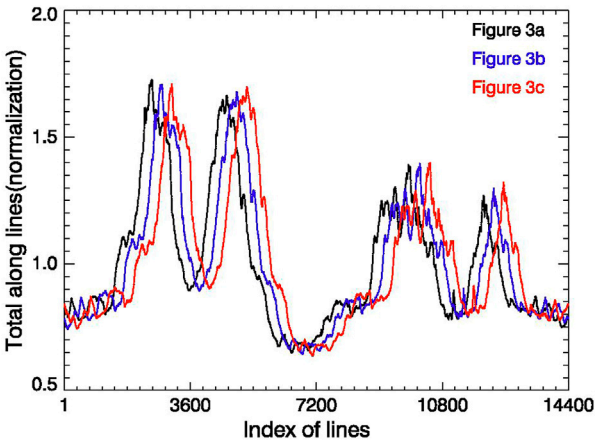

FIGURE 4
Gray curves of Figure 3. The black curve corresponds to Figure 3A, the blue curve corresponds to Figure 3B, and the red curve corresponds to Figure 3C. The abscissa represents the serial number of the line, and the ordinate represents the sum of gray values along the line.

3.3 Coordinate transformation and the KLL algorithm

After the solar image centers are determined, the Cartesian coordinate system is established with the center as the origin, and then, the solar images are expanded into rectangular shapes, as shown in Figure 5. The rotation angles of the images are converted into the translations in the X-direction in the rectangular images, and the displacements in the Y-direction are zero. Then, a series of expanded rectangular solar images and the corresponding rotation angles can be used to calculate the flat-field matrix.

The KLL algorithm is used to calibrate the spatial nonuniformity of an image-array based on a series of offset images, and the algorithm is robust and efficiently uses information from multiple data frames to determine pixel gain variations. Space-based solar observation instruments usually utilize the KLL algorithm to carry out flat-field calibration in orbit. The KLL algorithm does not rely on experimental equipment and directly uses the offset images to

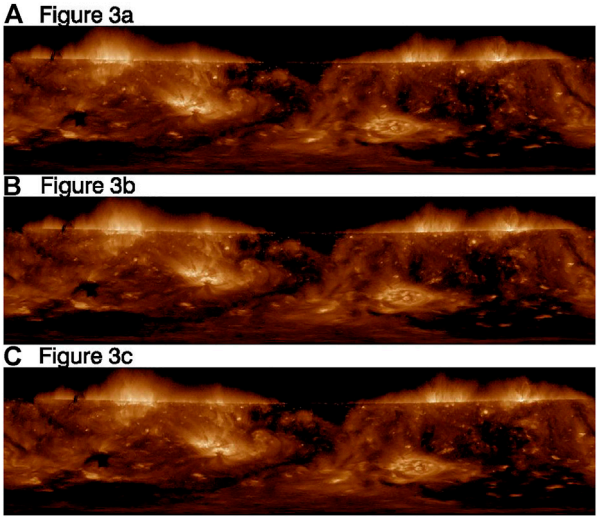

FIGURE 5
Solar images are in rectangular shape and, the original images are in Figure 3A, Figure 3B, and Figure 3C.

calculate the flat-field matrix of the imagers, which is widely used in SDO/AIA, SOHO/EIT, and other instruments.

It is assumed that the image-array detector can be calculated as a system, whose response is independent of the input intensity of the object, while depending on the optical sensitivity differences of each pixel element.

$$r(x) = o \cdot f(x). \tag{1}$$

Here, r and o are the actual inhomogeneous response and intensity of the object, respectively. F is the gain at an appointed position x.

We can also assume that the intensity of the object is stable and invariant when we take a series of shifted image samples. Let $R(x) = \ln(r(x))$ and $F(x) = \ln(f(x))$. The relationship between the gray value and response of each pixel in two images is given as formula (2), where displacements are described by a_i and a_j.

$$R_i(x + a_i) - R_j(x + a_j) - F_i(x + a_i) + F_j(x + a_j) = 0. \tag{2}$$

We can calculate a least-squares solution for the distribution of the gain if we build an oversampled, over-determined linear equation set about $r(x)$.

$$\sum_{i<j,x} \left[R_i(x + a_i) - R_j(x + a_j) - F_i(x + a_i) + F_j(x + a_j)\right]^2 = 0. \tag{3}$$

Differentiating Eq. 3 with $F(x)$ and setting the initial solution $F^0(x) = 0$, we arrived at an iterative solution:

$$F^{t+1}(x) = K(x) + \frac{1}{n(x)} \sum_{i<j} \left[F^t\left(x - a_i + a_j\right) - F^t\left(x - a_j + a_i\right)\right], \tag{4}$$

where

$$K(x) = \frac{1}{n(x)} \sum_{i<j} \left[R_i(x) - R_j(x - a_i + a_j)\right] + \left[R_j(x) - R_i(x - a_j + a_i)\right]. \tag{5}$$

This is the form of a solution to Poisson's equation. $n(x)$ counts the number that contributes to the sum. This model is useful where other models fail, especially when we cannot offer a proper uniform target in a short wavelength. Yet, the limitation is that the accuracy of the edge is too low to be accepted because of the internal vignetting and the boundary extraction process. That is why we proposed our method. The approximate optimal solution of this least-squares method is not unique. In order to avoid contingency and to improve credibility, the calibration result takes the average of multiple sets of data.

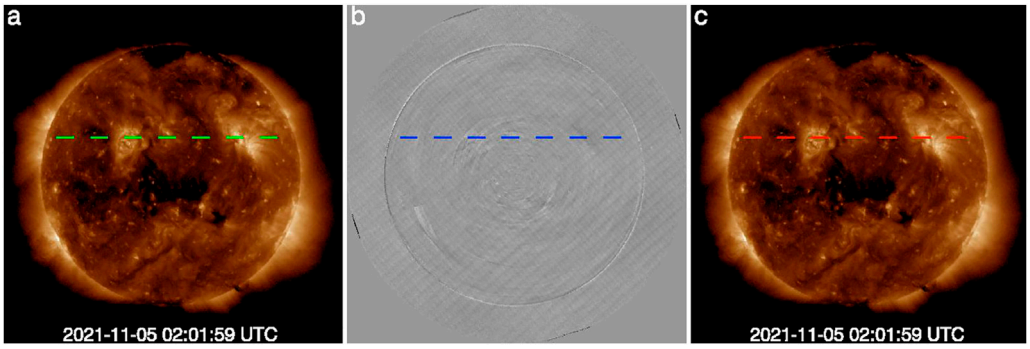

FIGURE 6
Original solar image **(A)**, flat-field matrix **(B)**, and the corrected image **(C)**. The solar image was captured by X-EUVI at 02: 01 on 05 November 2021.

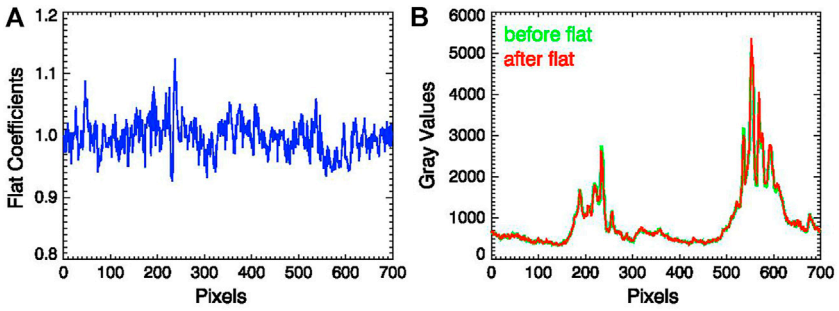

FIGURE 7
(A) is the flat-field coefficient along the blue line in Figure 6B. **(B)** is the comparison of the gray values along the green line in Figure 6A and the red line in Figure 6C.

The FY-3E satellite rotates relative to the Sun, and the solar images taken by X-EUVI are also rotated relative to the center of the field of view. Also, since the temporal resolution of X-EUVI is less than 10 s, it is reasonable to assume that the morphological features of the two adjacent solar images remain unchanged during the calculation; thus, only translation and rotation exist. Because of the characteristics of FY-3E satellite orbit, the solar images observed by X-EUVI are continually rotating, and the imager's flat-field matrix can be acquired at any time when the instrument is working. The flat-field matrix, the original solar image, and the corrected image using the flat-field matrix are shown in Figure 6. Figure 7 shows the flat-field coefficients' variation and the comparison of the gray values before and after flat.

4 Conclusion and discussion

The algorithm proposed in this article is used to calculate the flat field using the rotated solar EUV images from FY-3E/X-EUVI. The algorithm includes determination of the solar disk centers and radiuses, calculation of the rotation angles, coordinate transformation to expand the solar disk into rectangles, and derivation of the flat matrix using the KLL algorithm. The accuracy of the determination of the solar disk center tested by the Hough gradient method and the least-squares method is at sub-pixel, and the precision of the calculated rotation angle based on the log-polar transform is less than 0.025°. Since the X-EUVI rotates relative to the Sun in real time, multiple rotation images can be obtained and used for flat-field calibration at any time. Using this method, five flat fields were calculated to estimate the accuracy. The five flats were calculated using 61 rotated solar images that were obtained on September 23, September 29, October 2, October 4, and October 8 in 2021. The accuracy is (0.79–3.42) % estimated by the following method.

(1) Calculate the mean values and standard deviations of each pixel (five flats).
(2) Divide the standard deviation by the mean values to obtain a matrix (A).
(3) Calculate the mean value (B) and standard deviation (C) of matrix A.
(4) The accuracy of the flat can be estimated to be (B ± C) %.

The Sun is assumed to be stable in the calculation process of using a series of rotated images, but the solar radiation in the extreme ultraviolet band changes rapidly, so this assumption will introduce some errors. The calculated solar center still introduces errors to the final result since it is still difficult to determine the disk and the center of the EUV solar image due to the influence of the solar atmosphere. Moreover, the calculation of the rotation angle and the error of the KLL algorithm itself can introduce error in the final flat field.

Data availability statement

Publicly available datasets were analyzed in this study. These data can be found here: http://data.nsmc.org.cn/portalsite/default.aspx.

Author contributions

GD and LH contributed to the idea, method, and calculation of the flat-field method. GD and KW wrote the manuscript. BC contributed to the design of the X-EUVI and its observation and modified the writing. FL checked the algorithm program.

Funding

This work was supported by the National Science Foundation of China (Grant No. 42104166).

Acknowledgments

The authors would like to thank the X-ray and EUV optical technology laboratory in the Changchun Institute of Optics, Fine Mechanics and Physics (CIOMP) for supporting this research. Meanwhile, we would like to thank the ground application system at the National Satellite Meteorological Center, China Meteorological Administration (NSMC, CMA) for providing the X-EUVI raw data.

Conflict of interest

The authors declare that the research was conducted in the absence of any commercial or financial relationships that could be construed as a potential conflict of interest.

Publisher's note

All claims expressed in this article are solely those of the authors and do not necessarily represent those of their affiliated organizations, or those of the publisher, the editors, and the reviewers. Any product that may be evaluated in this article, or claim that may be made by its manufacturer, is not guaranteed or endorsed by the publisher.

References

1. Chen B, Ding GX, He LP. Solar X-ray and extreme ultraviolet imager(X-EUVI) loaded onto China's fengyun-3E satellite. *Light: Sci Appl* (2022) 11:29. doi:10.1038/s41377-022-00711-0

2. Zhang P, Hu XQ, Lu QF, Zhu AJ, Lin MY, Sun L, et al. FY-3E: The first operational meteorological satellite mission in an early morning orbit. *Adv Atmos Sci* (2022) 39(1):8. doi:10.1007/s00376-021-1304-7

3. Chen B, Chen SY, Gong Y. Design of a complex space soft X-ray and EUV telescope. *Opt Tech* (2004) 30(2):242–4. doi:10.3321/j.issn:1002-1582.2004.02.023

4. Chen B, Liu Z, Yang L, Gao L, He F, Wang XG, et al. Space solar telescope in soft X-ray and EUV band. *Sci China Ser G Phys Mech Astron* (2009) 52:1806–9. doi:10.1007/s11433-009-0250-7

5. Kuhn KR, Lin H, Loranz D. Gain Calibrating nonuniform image-array data using only the image data. *Publications Astronomical Soc Pac* (1991) 103:1097–108. doi:10.1086/132932

6. Chae J. Flat-Fielding of Solar Hα Observations using relativity shifted images. *Solar Phys* (2004) 221(1):1–14. doi:10.1023/B:SOLA.0000033357.72303.89

7. Fang C, Chen PF, Li Z, Ding MD, Dai Y, Zhang XY, et al. A new multi-wavelength solar telescope: Optical and near-infrared solar eruption tracer (ONSET). *Res Astron. Astrophys.* (2013) 13. doi:10.1088/1674-4527/13/12/011

8. Denker C, Johannesson A, Marquette W, Goode PR, Wang H, Zirin H. Synoptic Hα full-disk observations of the sun from big bear solar observatory – I. *Instrumentation, image processing, data products, and first results. Solar Phys* (1999) 184(1):87–102. doi:10.1023/A:1005047906097

9. Boerner P, Edwards C, Lemen J, Rausch A, Schrijver C, Shine R, et al. Initial calibration of the atmospheric imaging assembly (AIA) on the solar Dynamics observatory (SDO). *Solar Phys* (2012) 275(1):41–66. doi:10.1007/s11207-011-9804-8

10. Lemen JR, Title AM, Akin DJ, Boerner PF, Chou C, Drake JF, et al. The atmospheric imaging assembly (AIA) on the solar Dynamics observatory. *Solar Phys* (2012) 275:17. doi:10.1007/s11207-011-9776-8

11. Schou J, Scherrer PH, Bush RI, Wachter R, Couvidat S, Rabello-Soares MC, et al. Design and ground calibration of the helioseismic and magnetic imager (HMI) instrument on the solar Dynamics observatory (SDO). *Solar Phys* (2012) 275:229. doi:10.1007/s11207-011-9842-2

12. De Pontieu B, Title AM, Lemen JR, Kushner GD, Akin DJ, Allard B, et al. The interface region imaging spectrograph (IRIS). *Solar Phys* (2014) 289:2733. doi:10.1007/s11207-014-0485-y

13. Chae J. Flat-fielding of solar magnetograph observations using relatively shifted images. *Solar Phys* (2004) 221(1):15–21. doi:10.1023/B:SOLA.0000033359.96272

14. Djekoune AO, Messaoudi K, Amara K. Incremental circle hough transform: An improved method for circle detection. *Optik - Int J Light Electron Opt* (2017) 133:17–31. doi:10.1016/j.ijleo.2016.12.064

15. Liu D, Wang YT, Tang Z, Lu XQ. A robust circle detection algorithm based on top-down least-square fitting analysis. *Comput Electr Eng* (2014) 40(4):1415–28. doi:10.1016/j.compeleceng.2014.03.011

16. Qiao SD, Sampaolo A, Patimisco P, Spagnolo V, Ma YF. Ultra-highly sensitive HCl-LITES sensor based on a low-frequency quartz tuning fork and a fiber-coupled multi-pass cell. *Photoacoustics* (2022) 27:100381.

17. Liu XN, Ma YF. Tunable diode laser absorption spectroscopy based temperature measurement with a single diode laser near 1.4 μm. *Sensors* (2022) 22:6095.

frontiers | Frontiers in Physics

TYPE Original Research
PUBLISHED 02 November 2022
DOI 10.3389/fphy.2022.1055049

OPEN ACCESS

EDITED BY
Qun Hao,
Beijing Institute of Technology, China

REVIEWED BY
Zaijun Chen,
University of Southern California, United States
Ramy Abdlaty,
McMaster University, Canada
Qiang Liu,
Tsinghua University, China

*CORRESPONDENCE
Zhaoshuo Tian,
tianzhaoshuo@126.com
Qingcao Liu,
qingcao.liu@hit.edu.cn

SPECIALTY SECTION
This article was submitted to Optics and Photonics, a section of the journal Frontiers in Physics

RECEIVED 27 September 2022
ACCEPTED 18 October 2022
PUBLISHED 02 November 2022

CITATION
Che X, Tian Z, Sun F, Liu Q, Bi Z, Chen H and Cui Z (2022), Research on chemical oxygen demand based on laser Fluorescence-Raman spectroscopy. *Front. Phys.* 10:1055049. doi: 10.3389/fphy.2022.1055049

Research on chemical oxygen demand based on laser Fluorescence-Raman spectroscopy

Xiaohua Che, Zhaoshuo Tian*, Fenghao Sun, Qingcao Liu*, Zongjie Bi, Hao Chen and Zihao Cui

Institute of Marine Optoelectronic Equipment, Harbin Institute of Technology, Weihai, China

In this invited paper, a novel water chemical oxygen demand (COD) detection method based on laser spectroscopy is proposed, and the COD value is obtained according to the intensity ratio of laser Fluorescence-Raman signal produced by laser incident into water. Based on the laser Fluorescence-Raman ratio (LFRR) method, we design a portable water quality measurement system. In which, a 405 nm semiconductor laser is used as the light source. The laser is coupled into the delivering port of Y-type fiber and then transmitted into water. The generated Mie scattered light, water Raman light and corresponding fluorescence are received and transmitted into spectrometer through the detecting port of Y-type fiber, and the COD value can be obtained by analyzing the LFRR of water spectra. The mixed solution of sodium humate and glucose is used as the COD standard solution to calibrate the designed system. The experiment results show that the optimal volume ratio of the two solutions is 1:29. When the COD of standard solutions is in the 1–12 mg/L concentration range, a good linear relationship can be found between the COD value and LFRR value with a correlation coefficient of 0.974. In addition, the COD of natural water samples are measured with LFRR method, the results of which are consistent with COD values obtained by rapid digestion spectrophotometry. Meanwhile, experimental results prove that the COD detection method proposed in this paper has the advantages of high sensitivity, high precision, high detection speed and simplicity, which can be widely used in various water areas for real-time COD monitoring.

KEYWORDS

chemical oxygen demand, y-type fiber, spectroscopy, fluorescence, Raman laser, 405 nm laser

Introduction

Water quality analysis is an important task of environmental monitoring. The chemical oxygen demand (COD) describes the concentration of reducing substances in water, which is an important parameter for evaluating the organic pollution and quality of water [1–3]. Generally, there are two methods for measuring the COD: chemical

method and optical method. Currently, the method commonly used for determining COD is chemical method, which requires a long measurement period and a lot of chemical reagents that may lead to secondary pollution if the reagents are not handled properly [4]. Meanwhile, the chemical method cannot be used for real-time analysis of water quality. Compared to chemical method, optical method based on the material characteristic spectrum has been drew much attention in recent years for its rapid detection and pollution-free characteristics [4–10].

At present, the optical method mainly includes absorbance spectrophotometry, hyperspectral analysis [1, 2] and fluorescence spectroscopy. The absorbance spectrophotometry can be further divided into single-wavelength measurement method, double-wavelength measurement method, multi-wavelength measurement method and broad-spectrum measurement method. The essence of absorbance spectrophotometry is to measure the absorption of the organic matters at a certain wavelength to calculate the COD value of water, which is a common method for online COD measurement. However, this method has relatively poor sensitivity and may cause larger measurement errors when COD is lower than 20 mg/L [12]. The hyperspectral analysis method has the advantages of high spatial resolution, high spectral resolution and spectrum integration. However, the technical operation of this method is complicated and high cost [12]. The sensitivity of fluorescence measurement is typically 10–1,000 times that of absorbance spectrophotometry, and has received much attention in the field of water quality monitoring [14, 16]. Recently, some scientists have applied three-dimensional fluorescence spectrometry to water quality measurement [17–32]. In 2004, S. Lee used the fluorescence excitation-emission matrices (FEEM) to analyze various water quality parameters of domestic wastewater, and the results showed that there is a good linear relationship (r^2 = 0.914) between measured COD values by wet chemical method and that of FEEM [12]. In 2010, Hur used synchronous fluorescence spectra and its first derivatives to analyze the BOD and COD of wastewater samples collected in sewer systems in urban and non-urban areas, and the good correlation coefficients of 0.92 and 0.94 for BOD and COD can be obtained, respectively [18]. In 2011, Liu analyzed the absorption and fluorescence properties in a large subtropical reservoir and then used a chromophoric dissolved organic matter (CDOM) fluorescence monitoring sensor to predict several water quality parameters including the COD, dissolved organic nitrogen (DON), dissolved organic phosphorus (DOP) and dissolved organic matter (DOM). The significant correlations were found between the CDOM concentration and total nitrogen (TN), total phosphorus (TP), COD, dissolved organic carbon (DOC), and the maximum fluorescence intensity of humic-like component (C1), suggesting that the real-time monitoring of CDOM concentrations could be used to predict these water quality parameters [33]. In 2019, Goffin presented a method for measuring the soluble COD in raw sewage by means of three-dimensional fluorescence spectroscopy, and the results showed that the approach can be served as a guideline for purposes of implementing online wastewater monitoring and conducting environmentally friendly soluble COD measurements in the laboratory [20].

Generally, the advantages of three-dimensional fluorescence spectroscopy are mass spectral measurement data and high sensitivity but with the disadvantages of slow detection speed and complex operation, thus it is not suitable for on-line water quality analysis. Compared to three-dimensional fluorescence spectroscopy, two-dimensional fluorescence spectroscopy uses a single-wavelength laser or LED as the excitation light source, which simplifies the experimental design, and has a high analysis speed in water quality measurement since that only two-dimensional spectral data need to be analyzed. Therefore, many scholars begin to apply the two-dimensional fluorescence spectroscopy in water quality measurement. In 2015, Bridgeman designed a novel LED-based fluorescence instrument for the rapid assessment of potable water quality, and the results demonstrated that this device can provide an accurate *in situ* in real time assessment of water quality [34]. In 2022, Zheng proposed a water quality COD analysis method based on laser-induced fluorescence spectra, and used a single-wavelength semiconductor laser (wavelength of 405 nm) as the excitation light source and collected the emitted fluorescence spectra through a portable fiber optic spectrometer. PCA and PLS algorithms were used for data dimensionality reduction and model building, respectively. The results indicated that the COD prediction errors of this model for the test set are less than 20% [35].

At present, although two-dimensional fluorescence spectroscopy can measure COD parameter through the analysis of fluorescence intensity, the practical measurement accuracy is often influenced by some factors such as the interference of environmental light, water fluctuation, instrument vibration and laser-aging using [34–36]. In this paper, the development of a portable, laser spectroscopy-based system, capable of the real-time detection of COD parameter in water is described. The system adopts Y-type fiber as the transmission medium of optical signal, and uses the LFRR to calculate the COD value, which can reduce the influence caused by various factors to some extent. In experiment, we adopt the mixed solution of sodium humate and glucose as the COD standard solution of spectral method, and obtain the optimal mixing ratio of the two solutions through the detection and analysis of spectrum at different standard solution concentrations. In addition, the spectra of COD standard solutions within a certain range are detected, and significant positive correlation is found between COD value of standard solutions and LFRR.

Detection principal

A typical spectrum produced by a laser incident on water is shown in Figure 1, it can be seen that the whole spectra consists of [33] Rayleigh-scattered and Mie-scattered laser signal I_S generated by elastic scattering, water Raman signal I_R generated by inelastic scattering of the excitation light and DOM (dissolved organic matters) fluorescence signal I_F. In general, there are three

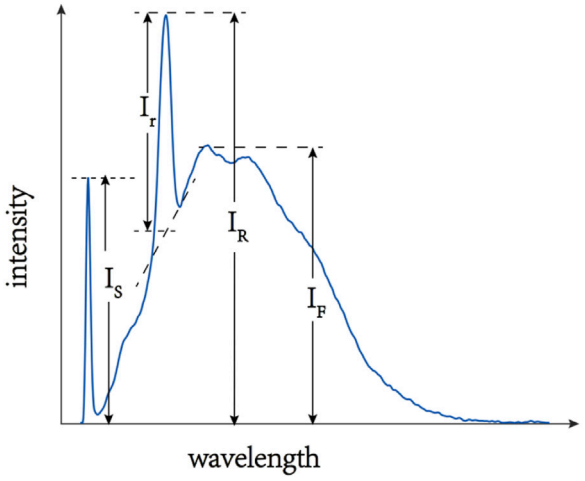

FIGURE 1
A typical spectrum produced by laser exciting water (I_S is Rayleigh-scattered and Mie-scattered laser signal generated by elastic scattering, I_r is the intensity of water Raman signal by deducting the fluorescence background, I_R is water Raman signal generated by inelastic scattering, I_F is DOM fluorescence signal.

significant water Raman peaks [37] with wavenumbers of 1,595 cm^{-1}, 3,120 cm^{-1} and 3,400 cm^{-1} when the water molecule is excited, and the 3400cm^{-1} can be excited to generate the strongest water Raman signal I_R since it has the highest Raman gain coefficient. When the laser incident into the water, the higher the concentration of organic matter in the water, the stronger the fluorescence signal is generated, thus it can be considered that the COD value is proportional to fluorescence intensity:

$$COD = K \times I_F + C \quad (1)$$

where the coefficient K and the limit of detection C are constant, which can be determined in experiment.

For the same water sample, the laser intensity fluctuations and environmental changes both have a major influence on the received fluorescence signal, which lead to instability of the measured COD value in practical application. To solve this problem, we measure the COD parameter of water quality using the LFRR method. In addition, since the spectral range of the fluorescence generated by organic matter is relatively large, the integrated-fluorescence-intensity I_T is adopted to calculate the COD value to obtain the fluorescence features of organic matters.

$$I_T = \int_{\lambda_1}^{\lambda_2} I_\lambda d\lambda / I_r \quad (2)$$

where λ_1 is the integrated starting wavelength, λ_2 is the integrated ending wavelength, I_λ is the intensity of optical signal at wavelengthλ, I_r is the intensity of water Raman signal by deducting the fluorescence background. In practical application, I_F can be replaced by I_T to achieve the accurate COD measurement.

Experimental setup

A schematic view of the experimental setup is shown in Figure 2, which is primarily composed of four parts: laser spectrum detection system, optical fiber transmission system, signal processing system and sample system. The laser spectrum detection system consists of laser emission unit, spectrum detection unit, and data acquisition unit. The laser emission unit is composed of a 405 nm semiconductor laser. The laser spectrum detection system includes a filter, optical splitting system, coupling lens, and CCD [38]. The spectrometer used in the experiment can measure light with wavelengths between 400 and 760 nm with a resolution of 2 nm. The fiber transmission system is a "8 + 1" Y-type fiber of 80 cm, which contains delivering port, receiving port, and detecting port. A semiconductor laser is coupled into the delivering port of a 400 μm-diameter single-core fiber. The receiving port is eight fibers bundle group with diameter of 200 μm which is connected to spectrometer. A computer is employed as signal processing system to control both laser emission and spectra reception, furthermore, it can process spectral data as well as calculate water quality parameters. The sample system consists of test tube, and water sample.

During the measurement period, output laser at 405 nm is firstly directed into the detecting port of Y-type fiber through the delivering port and then immersed into water sample vertically. Subsequently, optical signal excited by the laser is transmitted into receiving port of Y-type fiber through eight-core fiber of detecting port, and then input into the optical splitting system through the long-pass filter. Eventually, the optical signal is converted into electrical signal through CCD and then sent to a computer *via* a USB port. The computer is used to process data and calculate the COD with the corresponding software. In addition, the computer can adjust the exposure time of the CCD according to the intensity of the spectrum signal, and collect the spectrum of the water sample by controlling the power of the laser to turn on and off, so that the interference of the background light can be eliminated dynamically.

Results and discussion

The standard solution plays an important role in the calibration, adjustment and maintenance of instrument. Currently, potassium biphthalate and glucose are the commonly standard solutions used for potassium

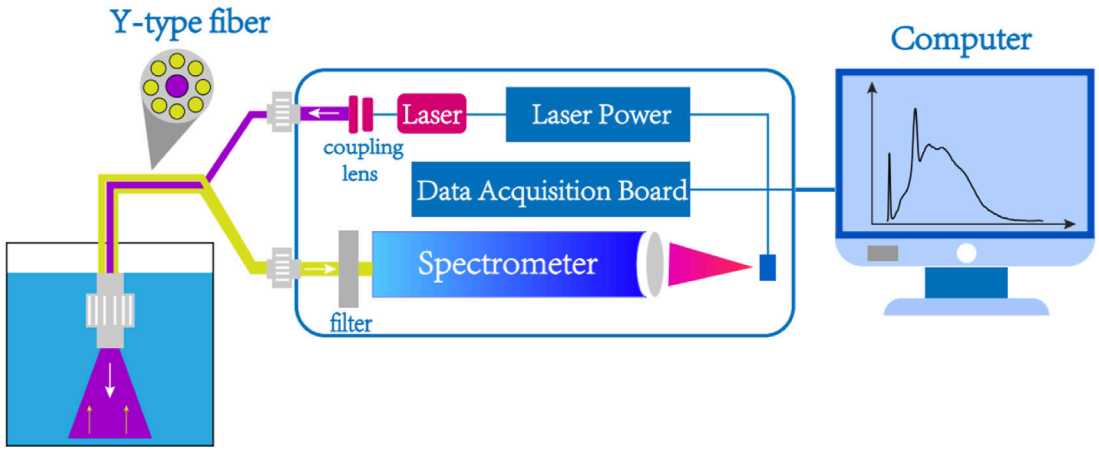

FIGURE 2
Experimental setup of the COD measurement.

permanganate oxidation (COD_{Mn}) and potassium dichromate oxidation (COD_{Cr}), respectively. In addition, absorbance spectrophotometry usually uses potassium biphthalate standard solution to calibrate the instrument when measuring water quality COD. Therefore, it is also necessary to select a suitable standard solution to accurately calibrate the experimental setup of COD measurement in "Experimental setup".

Preparation of standard solution

The organism in natural water is mainly composed of humic-like (estimated >50%) [39], protein-like, polysaccharide-like and polypeptide-like. For humic-like, it is vulnerable to generate the significant fluorescence when excited by UV laser, thus sodium humate can be employed as a substitute for humic-like in formulation of COD standard solution of laser spectroscopy. Since the fluorescence intensity in sodium humate solution is higher than that of natural water with same COD value, the mixed solution of no-fluorescence glucose solution and sodium humate solution is prepared as the COD standard solution. In the process, the ratio of sodium humate to glucose $R_{sg} = V_{sh}/V_g$ is adjusted to make the fluorescence intensity of the standard solution close to the natural water sample, where V_{sh} is the volume of sodium humate solution, V_g is the volume of glucose solution.

It is considered that the standard solution reaches the optimum ratio when standard solution and natural water have the same COD value detected by rapid digestion spectrophotometry and integrated-fluorescence-intensity calculated by spectra. In order to determine the optimum R_{sg}, the corresponding steps are as follows: firstly, we adopt the rapid digestion spectrophotometry to measure the COD value of natural water samples collected from Riyue lake in Harbin Institute of Technology (Weihai). Secondly, under the same identical COD as natural water, we formulate the standard solutions with different R_{sg}. Finally, the optimum R_{sg} can be obtained when the spectral integrated-fluorescence-intensity of natural water is same as that of standard solution.

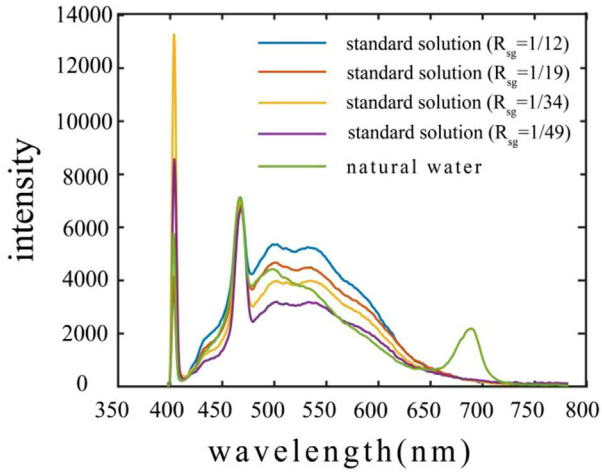

FIGURE 3
The spectra of standard solutions and natural water (vertical direction presents wavelength, horizontal direction presents spectral intensity, the green line presents natural water of COD = 8 mg/L collected from Riyue lake, and other color presents standard solutions under different ratios).

From the spectra of standard solutions and natural water (Figure 3), we can see that all spectra contain 405 nm

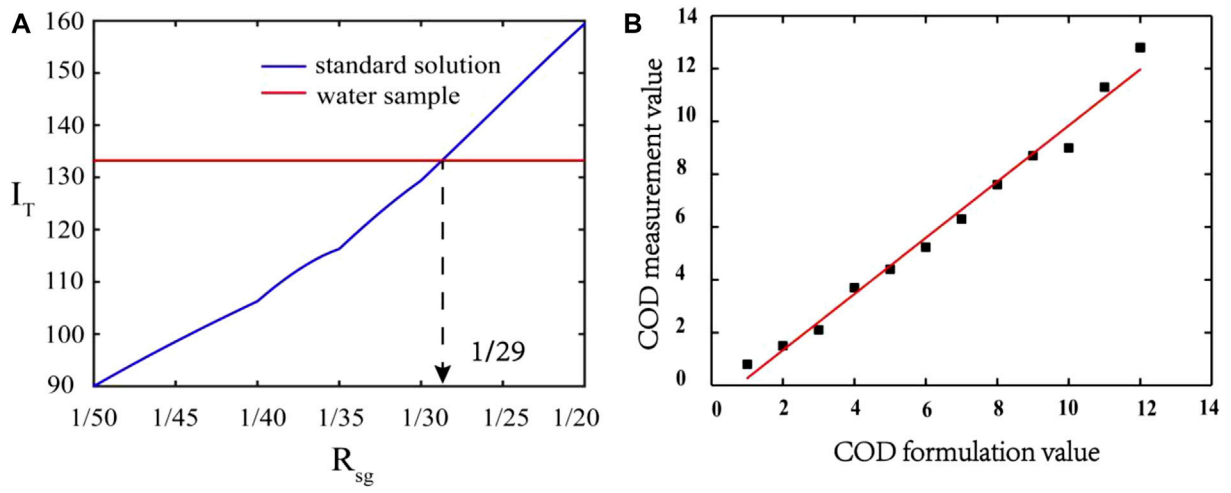

FIGURE 4
(A) The integrated-fluorescence-intensity of standard solution and natural water (red line is the result of natural water sample collected in Riyue lake, purple line is the result of standard solution) **(B)** The correlation between COD value of formulation and measurement (vertical direction presents COD formulation value, horizontal direction presents COD measurement value).

scattered light signal, 471 nm water-Raman signal, and fluorescence signal of organism, in addition, a 680 nm chlorophyll fluorescence signal can also be seen in spectrum of actual water. Overall, Under the identical laser power, the fluorescence intensity increases with the proportion of sodium humate in standard solution.

Excluding the effect of 405 nm scattered light signal and 680 nm chlorophyll fluorescence signal, the variation in integrated-fluorescence-intensity of standard solution with R_{sg} is shown in Figure 4A. It can be seen that the spectral integrated-fluorescence-intensity of the standard solution at the R_{sg} ranges of 1/50 to 1/20 increases with the increase of R_{sg}. This phenomenon can be explained that the sodium humate concentration in standard solution increases with R_{sg}, and results in the increase of fluorescence intensity and integrated-fluorescence-intensity. The crossing point (R = 1/29) of the two lines presents the optimum R_{sg} where the standard solution has same integrated-fluorescence-intensity as natural water.

To verify the accuracy of R = 1/29, rapid digestion spectrophotometry is employed to test the COD measurement value of standard solutions with different concentrations, and the detection of all water samples are repeated for three times. The correlation between the COD standard solution preparation value and the measurement value is established in Figure 4B. It can be seen that the correlation between the COD standard solution preparation value and the measurement value with a correlation coefficient of 0.986 is obtained. The experimental results show that the standard solution prepared at R = 1/29 can be used to simulate natural water.

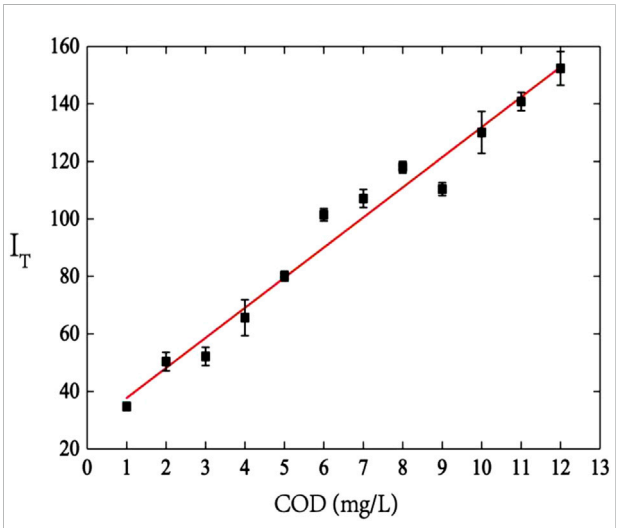

FIGURE 5
The correlation between COD value of standard solution and integrated-fluorescence-intensity (vertical direction presents COD value of standard solution, horizontal direction presents spectral integrated-fluorescence-intensity).

The correlation relationship between chemical oxygen demand value with integrated-fluorescence-intensity

Figure 5 shows the measured spectra from standard solutions (R = 1/29) of different concentrations, the integrated-fluorescence-intensity increases with COD value at 1–12 mg/L,

TABLE 1 COD measurement result of natural water samples.

Position	Laser spectroscopy/(mg/L)	Rapid digestion spectrophotometry/(mg/L)	Error/%
1	4.35	5.17	15.9
2	5.92	6	1.3
3	8.69	9.46	8.1

and a linear regression equation with a correlation coefficient r^2 = 0.974 is obtained:

$$\mathrm{COD} = 0.093 I_{\mathrm{T}} - 2.359 \quad (3)$$

In the practical application, we adopt a Y-type fiber to collect spectral signal, and calculate COD value from Eq 3.

The chemical oxygen demand measurement of natural water

To validate the accuracy of the system designed in this paper, a comparison of the COD measurement results of water samples collected at three different locations in Riyue lake for laser spectroscopy versus rapid digestion spectrophotometry is shown in Table 1. The error of two method is 15.9%, 1.3% and 8.1%, respectively. Overall, the result indicates that laser spectroscopy proposed in this paper can meet the demand on COD measurement of natural water with high accuracy.

Conclusion

In this paper, a novel water COD detection method based on laser Fluorescence-Raman ratio is proposed, and a small COD detection system is designed to realize the accurate COD measurement. In order to calibrate the instrument conveniently, the mixed solution of humic acid sodium and glucose is adopted as the standard solution for COD measuring by the laser spectroscopy method. The optimum ratio of sodium humate to glucose in standard solution is 1:29 in our experiment. Under this ratio, we detect the standard solution with COD value range of 1–12 mg/L, and establish the correlation between COD value with integrated-fluorescence-intensity. The linear correlation coefficient is r^2 = 0.974, and the empirical formula is COD = 0.093 I_{T}-2.359.

In the practical COD measurement, laser spectroscopy and rapid digestion spectrophotometry are used to detect the COD value of three natural water samples. The results of two methods have high consistency, and the measurement error in laser spectroscopy meets the COD detection requirement of natural water quality. The experimental results indicate that the system designed in this paper has the advantages of small probe volume, simplicity, high accuracy, high stability, and so on. Since the optimum ratio of standard solution may be different in different water area, the instrument should be calibrated again so as to achieve the accurate COD measurement in practical application.

Data availability statement

The raw data supporting the conclusion of this article will be made available by the authors, without undue reservation.

Author contributions

XC: Validation, investigation, methodology, and writing—original draft preparation, ZT: writing—review and editing, supervision. All authors contributed to the article and approved the submitted version.

Funding

This study was supported by the China National Key Research and Development Program under Grant 2020YFE0201500. Excellent Youth Science Foundation of Shandong Province (Overseas), Grant No. 2022HWYQ-073. Youth Program of National Natural Science Foundation of China, Grant No. 12204132.

Conflict of interest

The authors declare that the research was conducted in the absence of any commercial or financial relationships that could be construed as a potential conflict of interest.

Publisher's note

References

1 Zhou K P, Bi W H, Zhang Q H, Fu X, Wu G. Influence of temperature and turbidity on water COD detection by UV absorption spectroscopy. *Optoelectron Lett* (2016) 12(6):461–4. doi:10.1007/s11801-016-6178-z

2 Kolb M, Bahadir M, Teichgraber B. Determination of chemical oxygen demand (COD) using an alternative wet chemical method free of mercury and dichromate. *Water Res* (2017) 122:645–54. doi:10.1016/j.watres.2017.06.034

3 Ramona R, Valero F, Valle M D. Rapid determination of chemical oxygen demand using a focused microwave heating system featuring temperature control. *Analytica Chim Acta* (2003) 491:99–109. doi:10.1016/s0003-2670(03)00795-5

4 Ye S, Chen X, Dong D M, Wang J, Wang X, Wang F. Rapid determination of water COD using laserinducedbreakdown spectroscopy coupled with partial least-squares and random forest[J]. *Anal Methods* (2018) 10:4879–4885.

5 Chen B, Wu H, Li S F. Development of variable pathlength UV–vis spectroscopy combined with partial-least-squares regression for wastewater chemical oxygen demand (COD) monitoring. *Talanta* (2014) 120:325–30. doi:10.1016/j.talanta.2013.12.026

6 Rudnitskaya A, Kirsanov D, Legin A, Beullens K, Lammertyn J, Nicolai BM, et al. Analysis of apples varieties – comparison of electronic tongue with different analytical techniques. *Sensors Actuators B: Chem* (2006) 116(1):23–8. doi:10.1016/j.snb.2005.11.069

7 Zhang Z H, Zhang F B, Xu B, Xie H, Fu B, Lu X, et al. High-sensitivity Gas detection with Air-Lasing-Assisted Coherent Raman spectroscopy. *Ultrafast Sci* (2022) 2022:1–8. doi:10.34133/2022/9761458

8 Fu Y, Cao J C, Yamanouchi K R, Xu H. Air-laser-based Standoff Coherent Raman spectrometer. *Ultrafast Sci* (2022) 2022:1–9. doi:10.34133/2022/9867028

9 Liu X N, Ma Y F. Tunable diode laser absorption spectroscopy based temperature measurement with a single diode laser near 1.4 μm. *Sensors* (2022) 22:6095. doi:10.3390/s22166095

10 Qiao S D, Sampaolo A, Patimisco P, Spagnolo V, Ma Y. Ultra-highly sensitive HCl-LITES sensor based on a low-frequency quartz tuning fork and a fiber-coupled multi-pass cell. *Photoacoustics* (2022) 27:100381. doi:10.1016/j.pacs.2022.100381

11 Abdlaty R, Gobara M, Naiem I, Mokhtar M. Innovative technique for analysis of wastewater contaminants using hyperspectral imaging. *Environ Sci* (2020) 9:1–10.

12 Jay S, Guillaume M. Regularized estimation of bathymetry and water quality using hyperspectral remote sensing. *Int J Remote Sensing* (2016) 37(2):263–89. doi:10.1080/01431161.2015.1125551

13 Hang J G, Xiong R C. Quick evaluation of chemical oxygen demand based on spectrophotometric and multi-linear analysis[J]. *J Beijing University of Chem Technol* (2007) 34 (40):389–392.

14 Liu Y H, Hu J F, Song Y. Review of Research and Application of Environmental Monitoring System Based on Radio Frequency Technology[J]. *Technology Review* (2021) 27 (8):1–7.

15 Carstea E M, Bridgeman J, Baker A, Reynolds DM. Fluorescence spectroscopy for wastewater monitoring: A review. *Water Res* (2016) 95:205–219. doi:10.1016/j.watres.2016.03.021

16 Baker A. Fluorescence properties of some farm wastes: Implications for water quality monitoring. *Water Res* (2002) 36(1):189–195. doi:10.1016/s0043-1354(01)00210-x

17 Lee S., Ahn K H. Monitoring of COD as an organic indicator in waste water and treated effluent by fluorescence excitation-emission (FEEM) matrix characterization. *Water Sci Technology* (2004) 50(8):57–63. doi:10.2166/wst.2004.0488

18 Hur J, Lee B M, Lee T H, Park DH. Estimation of Biological oxygen demand and chemical oxygen demand for combined sewer systems using synchronous fluorescence spectra. *Sensors* (2010) 10:2460–71. doi:10.3390/s100402460

19 Chen W, Westerhoff P, Leenheer J A, Booksh K. Fluorescence excitation-emission matrix regional integration to quantify spectra for dissolved organic matter. *Environ Sci Technol* (2003) 37(24):5701–10. doi:10.1021/es034354c

20 Goffin A, Rechdaoui S G, Rocher V, Varrault G. An environmentally friendly surrogate method for measuring the soluble chemical oxygen demand in wastewater: Use of three-dimensional excitation and emission matrix fluorescence spectroscopy in wastewater treatment monitoring. *Environ Monit Assess* (2019) 191(7):421. doi:10.1007/s10661-019-7570-5

21 Lee S, Ahn K.H. Monitoring of COD as an organic indicator in waste water and treated effluent by fluorescence excitation-emission (FEEM) matrix characterization. *Water Sci Technol* (2004) 50:57–63. doi:10.2166/wst.2004.0488

22 Janhom T, Wattanachira S, Pavasant P. Characterization of brewery wastewater with spectrofluorometry analysis. *J Environ Manage* (2009) 90(2):1184–90. doi:10.1016/j.jenvman.2008.05.008

23 Stedmon C A, Sobecka B S, Hansen R B, Le Tallec N, Waul CK, Arvin E. A potential approach for monitoring drinking water quality from groundwater systems using organic matter fluorescence as an early warning for contamination events. *Water Res* (2011) 45(18):6030–8. doi:10.1016/j.watres.2011.08.066

24 Du S X, Wu Y Q, Yuan Z B. Detection of COD in the wastewater treatment process based on fluorescence excitation-emission matrix spectrometry. *Appl Mech Mater* (2012) 178-181:599–602. doi:10.4028/www.scientific.net/amm.178-181.599

25 Zepp R G, Sheldon W M, Moran M A. Dissolved organic fluorophores in southeastern US coastal waters: Correction method for eliminating Rayleigh and Raman scattering peaks in excitation–emission matrices. *Mar Chem* (2004) 89:15–36. doi:10.1016/j.marchem.2004.02.006

26 Yang L Y, Hur J, Zhuang W. Occurrence and behaviors of fluorescence EEM-PARAFAC components in drinking water and wastewater treatment systems and their applications: A review. *Environ Sci Pollut Res* (2015) 22(9):6500–10. doi:10.1007/s11356-015-4214-3

27 Bieroza M, Baker A, Bridgeman J. Classification and calibration of organic matter fluorescence data with multiway analysis methods and artificial neural networks: An operational tool for improved drinking water treatment. *Environmetrics* (2011) 22(3):256–70. doi:10.1002/env.1045

28 Hambly A C, Henderson R K, Storey M V, Baker A, Stuetz R, Khan S. Fluorescence monitoring at a recycled water treatment plant and associated dual distribution system – implications for cross-connection detection. *Water Res* (2010) 44:5323–33. doi:10.1016/j.watres.2010.06.003

29 Vallieres M, Donaldson D J. Fluorescence Quenching of chlorophyll by Sea water components. *ACS Earth Space Chem* (2020) 4:2378–83. doi:10.1021/acsearthspacechem.0c00247

30 Bridgeman J, Baker A, Carliell-marquet C, Carstea E. Determination of changes in wastewater quality through a treatment works using fluorescence spectroscopy. *Environ Technology* (2013) 34(23):3069–77. doi:10.1080/09593330.2013.803131

31 Old G H, Naden P S, Granger S J, Bilotta G, Brazier R, Macleod C, et al. A novel application of natural fluorescence to understand the sources and transport pathways of pollutants from livestock farming in small headwater catchments. *Sci Total Environ* (2012) 417-418(4):169–82. doi:10.1016/j.scitotenv.2011.12.013

32 Chen Q, Wang L F, Chen W, Wang YS, Liu XY, Jiang H, et al. Fluorescence approach for the determination of fluorescent dissolved organic matter. *Anal Chem* (2017) 89(7):4264–71. doi:10.1021/acs.analchem.7b00324

33 Liu X, Zhang Y, Shi K, Zhu G, Xu H, Zhu M. Absorption and fluorescence properties of chromophoric dissolved organic matter: Implications for the monitoring of water quality in a large subtropical reservoir. *Environ Sci Pollut Res* (2014) 21(24):14078–90. doi:10.1007/s11356-014-3319-4

34 Bridgeman J, Baker A, Boxall J, Brown D. Portable LED fluorescence instrumentation for the rapid assessment of potable water quality. *Sci Total Environ* (2015) 524-525:338–46. doi:10.1016/j.scitotenv.2015.04.050

35 Zheng P C, Yang C, Zhang H X, et al. Research on water quality COD detection method based on laser induced fluorescence[J]. *Laser J* (2022).

36 Dudelzak A E, Babichenko S M, Poryvkina L V, Saar KJ. Total luminescent spectroscopy for remote laser diagnostics of natural water conditions. *Appl Opt* (1991) 30:453. doi:10.1364/ao.30.000453

37 Maes T, Jessop R, Wellner N, Haupt K, Mayes AG. A rapid-screening approach to detect and quantify microplastics based on fluorescent tagging with Nile Red. *Sci Rep* (2017) 7:44501. doi:10.1038/srep44501

38 Tian Z S, Bi Z J, Wang Y W, Zhao H. Rapid evaluation method based on DOM for water quality by microlaser fluorescence spectrometer. *Appl Phys B* (2020) 126(9):150–5. doi:10.1007/s00340-020-07498-1

39 Dodd M C, Kohler H E, Gunten U V. Oxidation of Antibacterial Compounds by Ozone and Hydroxyl Radical: Elimination of Biological Activity during Aqueous Ozonation Processes. *Environ Sci Technol* (2009) 43:2498–504. doi:10.1021/es8025424

frontiers | Frontiers in Physics

TYPE Original Research
PUBLISHED 07 November 2022
DOI 10.3389/fphy.2022.1057519

OPEN ACCESS

EDITED BY
Yufei Ma,
Harbin Institute of Technology, China

REVIEWED BY
Jinbao Xia,
Shandong University, China
Chuanliang Li,
Taiyuan University of Science and Technology, China
Fupeng Wang,
Ocean University of China, China

*CORRESPONDENCE
Zhaowei Wang,
zw.wang@qlu.edu.cn
Wei Zhang,
zhang.wei@qlu.edu.cn

SPECIALTY SECTION
This article was submitted to Optics and Photonics,
a section of the journal
Frontiers in Physics

RECEIVED 29 September 2022
ACCEPTED 17 October 2022
PUBLISHED 07 November 2022

CITATION
Wang S, Gong W, Wang Z, Wei Y, Li Y, Zhang T, Zhang Q, Zhang L, Song F, Zhang W and Liu T (2022), Interference fringe suppression in tunable diode laser absorption spectroscopy based on CEEMDAN-WTD.
Front. Phys. 10:1057519.
doi: 10.3389/fphy.2022.1057519

Interference fringe suppression in tunable diode laser absorption spectroscopy based on CEEMDAN-WTD

Shoulin Wang[1], Weihua Gong[1], Zhaowei Wang[1]*, Yubin Wei[1], Yanfang Li[1], Tingting Zhang[1], Qinduan Zhang[1], Lin Zhang[1], Fugang Song[1], Wei Zhang[1]* and Tongyu Liu[1,2]

[1]Laser Institute, Qilu University of Technology (Shandong Academy of Sciences), Jinan, China, [2]Shandong Micro-Sensor Photonics Ltd., Jinan, China

Owing to interference fringes in the multireflective gas cell, the detection sensitivity of a system in tunable diode laser absorption spectroscopy (TDLAS) will decrease significantly. In this work, a combined scheme of complete ensemble empirical mode decomposition with adaptive noise (CEEMDAN) and wavelet threshold denoising (WTD) is proposed. Theoretical simulations were performed to validate the effects of the proposed algorithm, which was also verified *via* a CO_2 detection experiment. After CEEMDAN-WTD processing, the noisy intrinsic mode function (IMF), pure IMF, and residual components of the detection signal were identified and reconstructed successfully. Based on analysis of the simulations, CEEMDAN-WTD algorithm improved the signal-to-noise ratio by 1.87 times and decreased the root mean-squared error by 37.6% than the moving average algorithm. For the CO_2 detection system, R^2 = 0.999 was determined by the calibration experiment. Additionally, based on Allan variance analysis and a long-time experiment, the limit of detection was estimated to be 3.08 ppm for an average time of 148 s and measurement accuracy of 0.65%, respectively. The obtained results sufficiently validate that the CEEMDAN-WTD algorithm can effectively suppress interference fringe noise in TDLAS.

KEYWORDS

tunable diode laser absorption spectroscopy (TDLAS), complete ensemble empirical mode decomposition with adaptive noise (CEEMDAN), interference fringes, wavelet threshold denoising (WTD), carbon dioxide

Introduction

Carbon dioxide (CO_2) is considered to be the main component of greenhouse gases (GHGs). Anthropogenic excessive emissions of GHGs have caused severe climate and environmental problems, such as global warming, melting of glaciers, rising sea levels, and extreme weather incidents [1]. Recently, CO_2 emissions have increased annually owing to continuous developments with energy consumption and industrialization. Therefore,

accurate measurement of CO_2 emissions is of great significance for developing and implementing mitigation strategies [2–4]. Tunable diode laser absorption spectroscopy (TDLAS) is a gas detection technology that has been widely used in various fields [5]. It has the advantages of high sensitivity, real-time detection, fast response, and noncontact measurements [6, 7]. TDLAS mainly includes the direct absorption spectrum (DAS) [8] and wavelength modulation spectrum (WMS) [9]. The DAS can be established with a simple structure at very low cost; however, it is easily affected by noise, resulting in low detection sensitivity [10].

Detection equipment with both high accuracy and miniaturization ability have become new topics of research in certain application scenarios of TDLAS. One way to realize such equipment is to achieve long path lengths and compact gas sensors using multireflection gas absorption cells [11]. However, interference fringes caused by multiple reflections of the laser beam on the optical elements can lead to large deviations in the inversion of the concentration and severely affect the accuracy of the detection system. Therefore, suppression of the interference fringes of gas concentration signals has become a focus of current research. Luo et al. [12] proposed an adaptive harmonic feeding generative adversarial network as well as a novel adaptive weighting scheme for interference fringe suppression. They realized an average absolute oxygen concentration inversion of 0.57% for an actual pharmaceutical production line. Although neural networks are powerful tools, the learning time and training data required for the algorithms are considerable. Moreover, local convergence of the minimum value may lead to training failure. Zhou et al. [13] employed a multifrequency modulation method to suppress the interference fringe noise of a residual oxygen detection system in encapsulated pharmaceutical bottles, achieving a signal standard deviation of 2.96 and signal-to-noise ratio (SNR) of 36.979 dB. However, subtle differences in the diameters and thicknesses of different glass bottles can lead to significant variations in the interference demodulation amplitudes and spacing, thus limiting the application of their method to glasses with different parameters.

Kalman filter [14], wavelet transform [15], moving average [16], Wiener filter [17], and Gabor transform [18] have all been used to address noise suppression problems. Although these five methods reduce the influences of interference fringes on the detected signals, they are computationally intensive and not conducive to practical applications. Guo [19] and Yu [20] proposed approaches using empirical mode decomposition (EMD) and combined variable mode decomposition [21] with Savitzky–Golay denoising (VMD-SG), respectively; the computation times of these two methods were less than those of the Kalman and other methods. However, the EMD algorithm has problems with mode mixing and endpoint effects. Furthermore, the EMD algorithm directly removes the high-frequency intrinsic mode function (IMF), which can cause signal distortion upon reconstruction. To solve the mode-mixing problem of EMD, Huang [22] proposed ensemble empirical mode decomposition (EEMD); taking the characteristic that the mean value of white noise is zero, EEMD eliminates mode mixing by adding uniformly distributed Gaussian white noise in the decomposition process and averaging the decomposition results. However, the purity of the original signal in inevitably degraded in EEMD; to overcome this disadvantage, the complete ensemble empirical mode decomposition with adaptive noise (CEEMDAN) algorithm was first proposed in 2011 by Torres et al. [23]. The CEEMDAN algorithm is an improved modified version of EEMD, where white noise is added at each EMD stage and its specific residual is calculated to obtain each modal component; after decomposition, the reconstruction error is almost zero. Compared to EEMD, it overcomes mode mixing and effectively reduces reconstruction errors. However, it causes loss of useful high-frequency information during signal reconstruction. The wavelet threshold denoising (WTD) method applied in signal reconstruction is used to address this concern. Advantageously, WTD adapts to the requirements of time–frequency signal analysis to focus on arbitrary details of the signal. However, as the hard threshold function is not continuous at the threshold, the signal can easily fluctuate after hard-threshold-function processing. In contrast, the soft threshold function is coherent, but the signal loses a part of the high-frequency coefficients above the soft threshold.

In this work, a CEEMDAN and WTD combined algorithm is designed for application to direct absorption spectroscopy. The remainder of this paper is organized as follows. First, we discuss the causes of interference fringes, how to combine the two algorithms, and the methods for improvement. Then, the denoising ability of the combined algorithm is demonstrated *via* simulation analysis and comparisons with other filtering algorithms. Finally, we analyze the stability and detection limit of the CEEMDAN-WTD algorithm *via* calibration experiments and Allan variance analysis.

Theory of TDLAS

When a laser beam passes through a certain gas medium, the light intensity of the beam decays owing to partial absorption by the gas. The input and output light intensities (I_0 and I_t, respectively) satisfy Beer–Lambert law, and the output light intensity can be described as follows [24, 25]:

$$I_t = I_0 \, exp\left[- S(T)CPL\varphi(\nu - \nu_0)\right] \tag{1}$$

where $S(T)$ is the line strength of the spectral feature, C is the concentration of the gas to be measured, P is the pressure of the gas, L is the effective optical path length of the laser passing through the gas, and $\varphi(\nu\text{-}\nu_0)$ represents the gas absorption spectral line shape function.

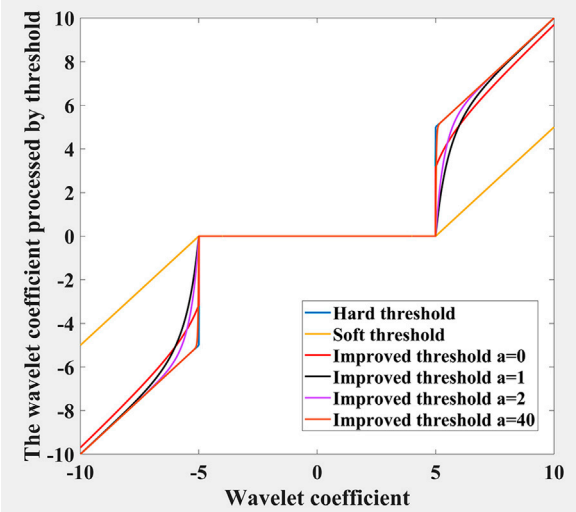

FIGURE 1
Comparison of different thresholding functions.

Almost all TDLAS systems show optical interference fringes that are caused by multiple reflections of the laser on the surface of the optical element; these fringes are also known as the etaloning effects. The transmitted light intensity can be calculated from the phase difference between multiple beams of light. According to the principle of the Fabry–Perot interferometer, the transmitted light intensity can be expressed as [26]

$$I_t = \frac{1}{1 + \frac{4R}{(1-R)^2} \cdot sin^2\left(\frac{\delta}{2}\right)} I_0 \tag{2}$$

Here, R is the interface reflectivity (assuming that the two interfaces have the same reflectivity), δ is the phase difference between the directly transmitted beam and that after secondary reflection. For the small surface reflectances of the lenses and transmission windows used in TDLAS systems, the transmitted light intensities sinusoidally vary with phase difference. Then, Eq. 2 can be simplified as

$$I_t = (1 + 2R\cos\delta - 2R)I_0 \tag{3}$$

The laser is assumed to be incident in a direction perpendicular to the parallel glass plate. Then, the distance between the two parallel interfaces is l, refractive index of the optical medium through which the laser passes is n, and laser wavelength is λ. The phase difference in Eq. 3 is given by

$$\delta = \frac{4\pi nl}{\lambda} \tag{4}$$

The transmitted light intensity can be calculated by combining Eqs. 3, 4 as

$$I_t = \left[1 + 2R\cos\left(\frac{4\pi nl}{\lambda}\right) - 2R\right] I_0 \tag{5}$$

Optical interfaces, such as laser windows, gas-cell windows, detector windows, and collimating lenses, are present in TDLAS systems, and all of these may cause optical interference fringes. The strength of the optical interference fringe is proportional to the reflectance of the interface in a direct absorption spectroscopy detection system. The reflectance of a typical optical quartz-glass surface is about 0.02 [27]. Theoretically, based on Eq. 3, the equivalent absorbance fluctuation due to the etalon effect is 0.04. Moreover, the equivalent absorbance corresponding to the gas detection limit in the current direct absorption spectroscopy detection system based on TDLAS is 10^{-3}, which is considerably less than 0.04. Therefore, to utilize the high accuracy and sensitivity of TDLAS, the direct absorption spectroscopy detection system needs to be optimized, and optical interference fringes need to be suppressed.

Principle of the CEEMDAN-WTD algorithm

CEEMDAN

The CEEMDAN algorithm decomposes a signal (original signal with Gaussian white noise) into finite IMFs and residual components [28]. The specific steps are as follows [29]:

1) Add i (i = 1,2,3,4 . . . I) sets of Gaussian white noise to the original signal, which is defined as $x(t)$ so that the signal to be processed is obtained as

$$x_i(t) = x(t) + \varepsilon e_i(t) \tag{6}$$

where ε is the amplitude (ratio of standard deviation of the amplitude of the white noise to that of the original signal), and $e_i(t)$ is the ith content N (0,1) of the added Gaussian white noise.

2) Decompose each $x_i(t)$ using EMD to obtain the first IMFs:

$$IMF_1 = \frac{1}{T}\sum_{i=1}^{T} IMF_1^i \tag{7}$$

The first residual is obtained by subtracting the first IMF from the original signal $x(t)$:

$$r_1(t) = x(t) - IMF_1 \tag{8}$$

3) Add i sets of white noise to $r_1(t)$ to compose a new signal to be processed:

$$R_1^i(t) = r_1(t) + \varepsilon e_i(t) \tag{9}$$

Decompose each $x_i(t)$ by EMD to extract the second mode as follows:

$$IMF_2 = \frac{1}{T}\sum_{i=1}^{T} IMF_2^i \tag{10}$$

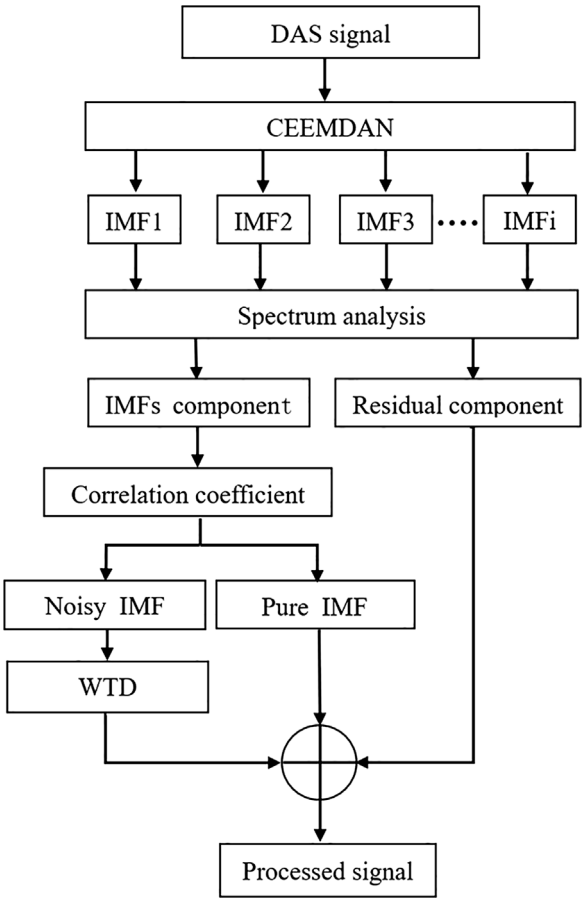

FIGURE 2
The flowchart of the CEEMDAN-WTD.

Additionally, the second residual is

$$r_2(t) = r_1(t) - IMF_2 \tag{11}$$

4) Repeat steps (1)–(3) until the resulting residual can no longer be decomposed. Finally, the k modal components, remaining residual $r_k(t)$, and original signal $x(t)$ can be expressed as

$$x(t) = r_k(t) + \sum_{i=1}^{k} IMF_i \tag{12}$$

WTD

WTD filters the signal to remove noise and extract the maximum useful signal; it is based on the principle that the selected wavelet basis function at different scales and a certain shift are applied by inner product with the original signal. Then, the result is mapped to the time and frequency domains. Owing to the different properties of the wavelet coefficients of the signal and noise, noise can be maximally filtered out by selecting a threshold value and reconstructing the signal.

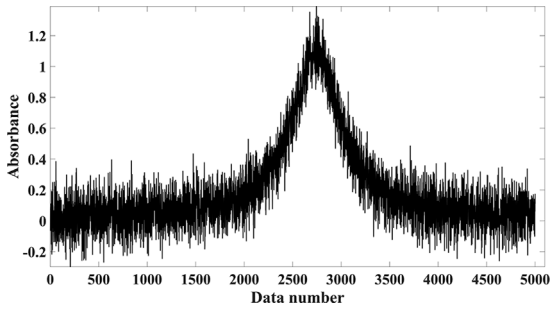

FIGURE 3
Simulation signal.

Threshold handling, including selection of both the threshold value and threshold function, is significant for WTD analysis [30]. The wavelet coefficients of the noise are analyzed to select a suitable threshold value that is greater than the maximum noise level. Hard and soft threshold functions are commonly used for this purpose, which are given in Eqs. 13, 14, respectively:

$$\omega_s = \begin{cases} \omega & |\omega| \geq \lambda_j \\ 0 & |\omega| < \lambda_j \end{cases} \tag{13}$$

$$\omega_s = \begin{cases} sgn(\omega)\left(|\omega| - \lambda_j\right) & |\omega| \geq \lambda_j \\ 0 & |\omega| < \lambda_j \end{cases} \tag{14}$$

Here, ω_s denotes the set of wavelet coefficients after decomposition, ω is the set of wavelet coefficients, and λ_j is the threshold value. However, both the hard and soft threshold functions have certain defects, and the denoising results are not ideal for complex signals. The hard threshold function preserves the local characteristics of the signal; however, as it is not continuous at the threshold value, the reconstructed signal can easily oscillate (pseudo-Gibbs phenomenon).

The soft threshold function is a continuous function; hence, the smoothness of its signal is better than that of the hard threshold function. Additionally, wavelet coefficients less than the threshold are set to 0. However, there is a constant deviation between the original wavelet coefficients and those after decomposition. Therefore, to overcome the shortcomings of the soft and hard threshold functions, we present an improved threshold function having the following expression:

$$\omega_s = \begin{cases} sgn(\omega) \cdot \left\{ |\omega| - \dfrac{\lambda_j}{|\omega| - \lambda_j + 1} \exp\left(|\omega| - \lambda_j\right)^a \right\} & |\omega| \geq \lambda_j \\ 0 & |\omega| \leq \lambda_j \end{cases} \tag{15}$$

where a is the adjustment factor. When $a = 0$, the improved threshold function is close to the semisoft threshold function.

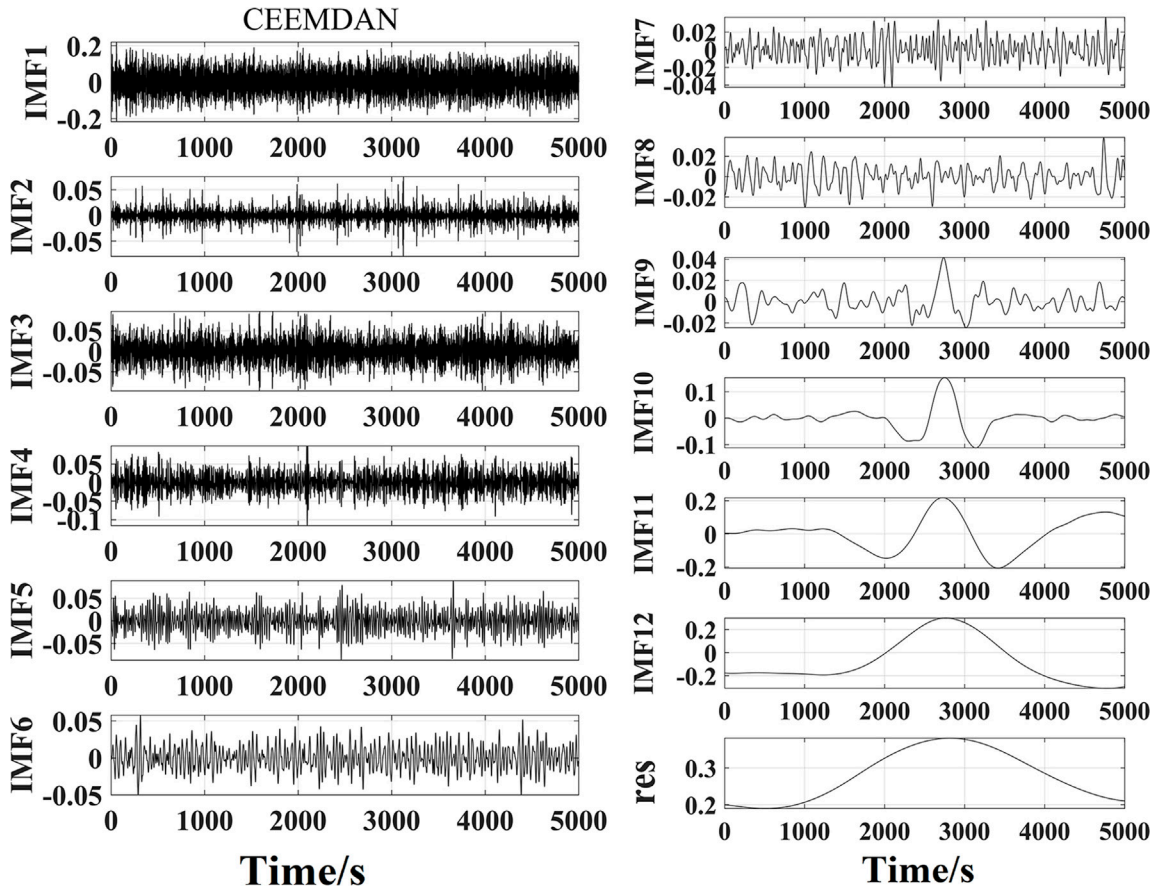

FIGURE 4
Decomposition diagram obtained IMF1-IMF12 using CEEMDAN.

When a tends to infinity, the new threshold function can be approximated to the hard threshold function. Unlike the hard threshold function, our proposed function is continuous. By changing the value of a to modify the properties of the threshold function, abrupt changes can be handled smoothly and the oversized wavelet coefficients are quantized such that they are close to the original values, thereby significantly preserving the true signal. A comparison of the different threshold functions is presented in Figure 1.

CEEMDAN-WTD

The flowchart of the CEEMDAN-WTD algorithm is given in Figure 2. CEEMDAN is first performed on the original signal to obtain multiple groups of IMFs. The correlation coefficient method is used to determine the IMF component that is dominated by noise. Then, this IMF component with noise is handled by WTD to improve the problem of loss of the real signal during the CEEMDAN process. Finally, the pure IMF component decomposed by CEEMDAN, noisy IMF component after wavelet processing, and residual component are reconstructed to obtain the processed signal.

Simulation and analysis

Simulation

Herein, a CO_2 detection system based on the DAS is employed to verify the CEEMDAN-WTD algorithm. The simulation parameters are as follows: standard atmospheric pressure, temperature T = 296 K, and effective absorption optical path length of the gas L = 200 cm. It is well known that the interference fringes are usually overlaid on real signals in the form of periodic sinusoidal functions to yield periodic fluctuations in the detected signal. Therefore, interference fringe noise is simulated by adding a sinusoidal signal with a certain amplitude to the simulated signal and random noise. Figure 3 displays this simulation signal.

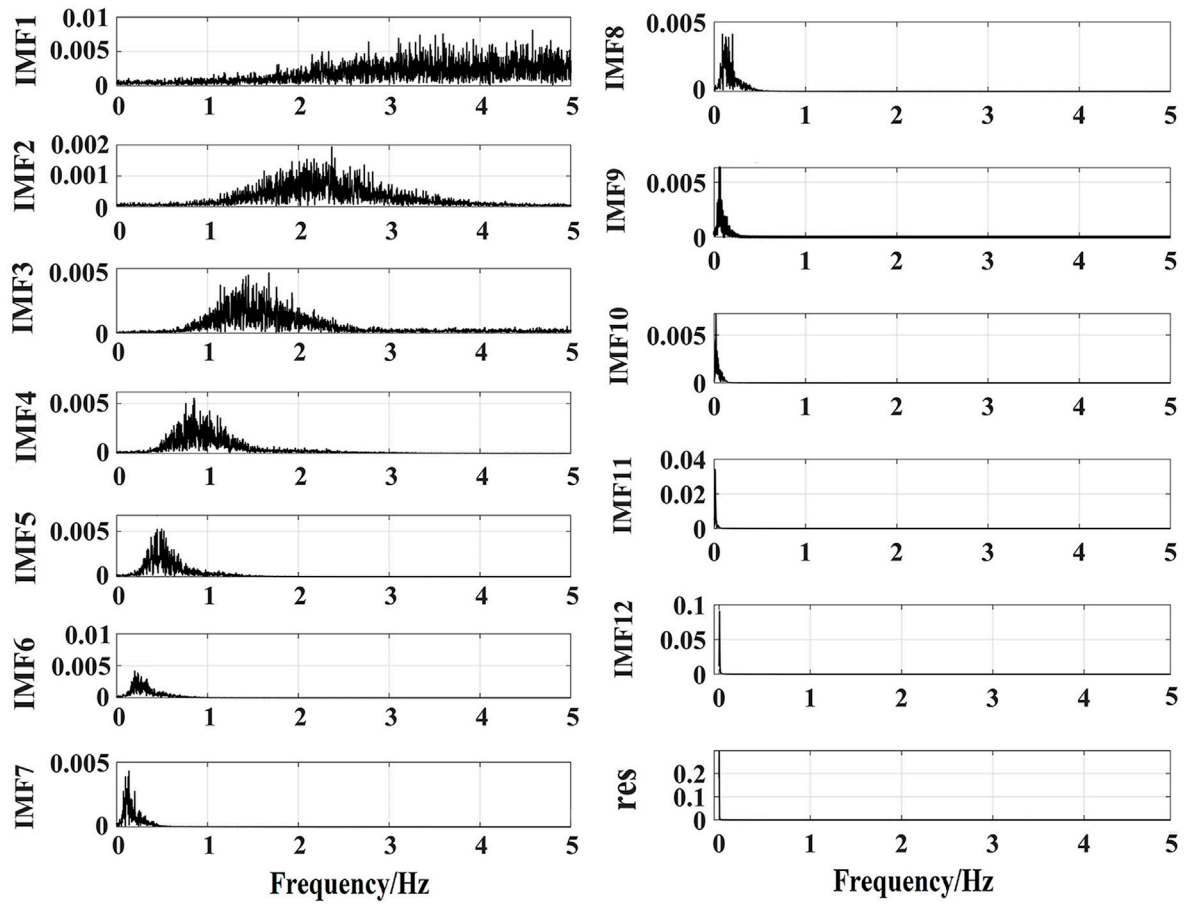

FIGURE 5
Frequency spectrum of IMF1-IMF12.

TABLE 1 Correlation coefficients between the IMF components and original signal.

IMF	Correlation coefficient	IMF	Correlation coefficient
IMF1	0.0280	IMF7	0.0512
IMF2	0.0186	IMF8	0.0715
IMF3	0.0182	IMF9	0.0906
IMF4	0.0152	IMF10	0.2417
IMF5	0.0113	IMF11	0.2503
IMF6	0.0470	IMF12	0.8708

Analysis of results

Before the signal is processed using the CEEMDAN algorithm, Gaussian white noise of amplitude *Nstd*, average number of signals *N*, and maximum number of iterations allowed Max_{iter} are selected. In this study, *Nstd* = 0.2, *N* = 100, and Max_{iter} = 2000. The 12 IMF components and the residuals are shown in Figure 4. Spectral analysis was performed for each IMF component. Figure 5 shows that the large-amplitude low-frequency mode components are decomposed precisely and that there is no confusion between the modes.

Generally, interference fringe noise is a high-frequency signal. For a signal with such noise, the signal energy is

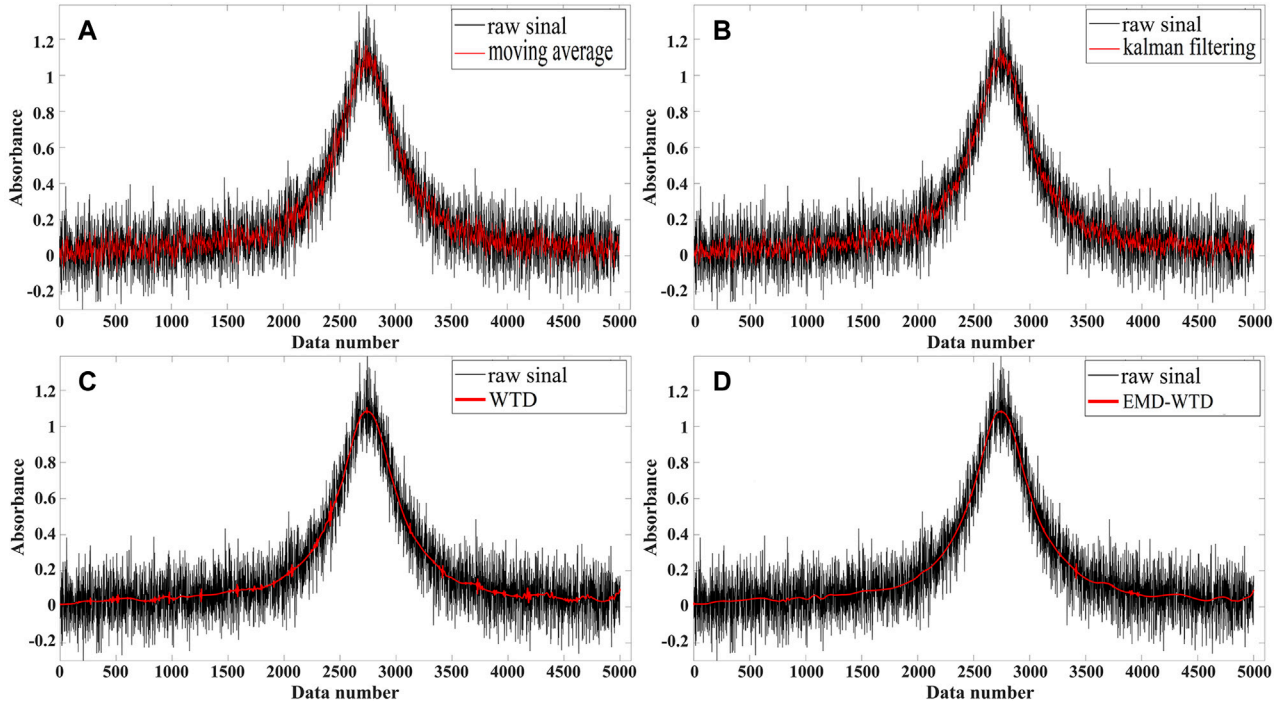

FIGURE 6
Comparison of moving average, Kalman filtering, WTD and EMD-WTD methods.

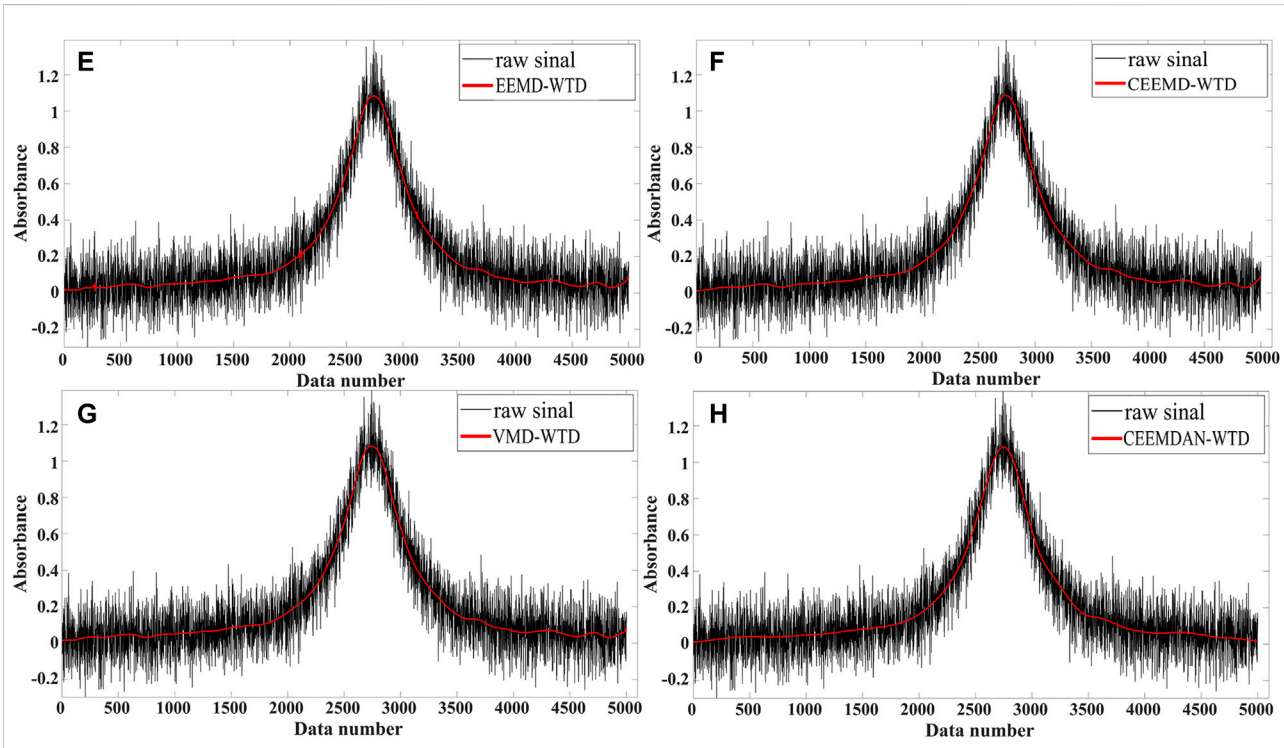

FIGURE 7
Comparison of EEMD-WTD, CEEMD-WTD, VMD-WTD and CEEMDAN-WTD methods.

TABLE 2 SNR and RMSE results after applying various denoising methods.

Denoising method	SNR/dB	RMSE
Moving average	17.4605	0.0456
Kalman filtering	19.7911	0.0348
WTD	30.6479	0.0100
EMD-WTD	32.0008	0.0091
EEMD-WTD	32.0653	0.0085
CEEMD-WTD	32.1497	0.0084
VMD-WTD	32.3638	0.0082
CEEMDAN-WTD	32.6050	0.0080

mostly concentrated in the IMF component with a relatively large order. To accurately discriminate the noisy IMF components, the correlation coefficient R is used herein to reflect the relationship between the IMF component and original signal to determine the IMF component with noise [31]. Table 1 presents the calculation results.

IMF1–IMF9 components are correlation coefficients less than 0.1, which are considered as components with noise [32]. These components are denoised using the improved WTD proposed in this work. The Daubechies wavelet (db10) was chosen as the wavelet basis, and the number of decomposition layers was set as 7. To verify the steps of the CEEMDAN-WTD algorithm, the denoising results were compared with those of the moving average, Kalman filter, WTD, EMD-WTD, EEMD-WTD, CEEMD-WTD, and VMD-WTD. The comparison shows that the CEEMDAN-WTD algorithm is significantly better than the other methods in terms of suppression of interference fringes and has equally excellent peak value extraction. The denoised results of the above methods are compared in Figure 6 and Figure 7.

SNR and root mean-squared error (RMSE) [33] are considered as two important bases for evaluating the processing effect; SNR and RMSE are determined using Eqs. 16, 17, respectively.

$$SNR = 10\lg\left[\sum_{i=1}^{N} X_i^2 \Big/ \sum_{i=1}^{N} (X_i - x_i)^2\right] \tag{16}$$

$$RMSE = \sqrt{\sum_{i=1}^{N} (X_i - x_i)^2 \Big/ N} \tag{17}$$

where X_i is the original signal, x_i the signal after processing, and N is the number of sampling points of the signal.

SNR represents the ratio of effective power of the signal to that of the noise; it is proportional to the denoising effect. RMSE reflects the deviation between the measured and actual values; it indicates the degree of signal distortion. Contrary to SNR, the smaller the RMSE, the smaller is the deviation between the two signals and more satisfactory is the denoising effect. The calculated SNR and RMSE results of the eight denoising methods are shown in Table 2. Among these methods, the SNR improvement of the signal is largest after CEEMDAN-WTD processing. The SNR improved by 1.87 times from 17.4605 to 32.6050 and RMSE reduced by 37.6% from 0.0456 to 0.0080 compared to the moving average approach; this indicates that CEEMDAN-WTD has the best denoising effect.

Experiments

Experimental setup

The experimentally acquired CO_2 concentration signal was processed using the CEEMDAN-WTD algorithm at temperature

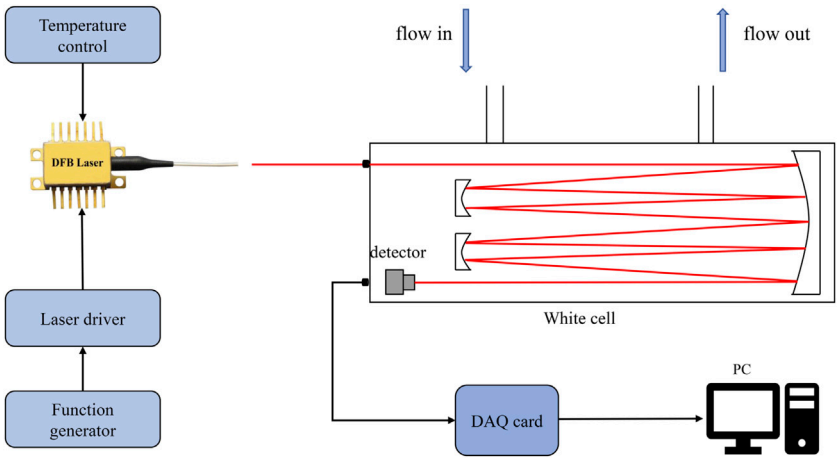

FIGURE 8
TDLAS experimental system structure.

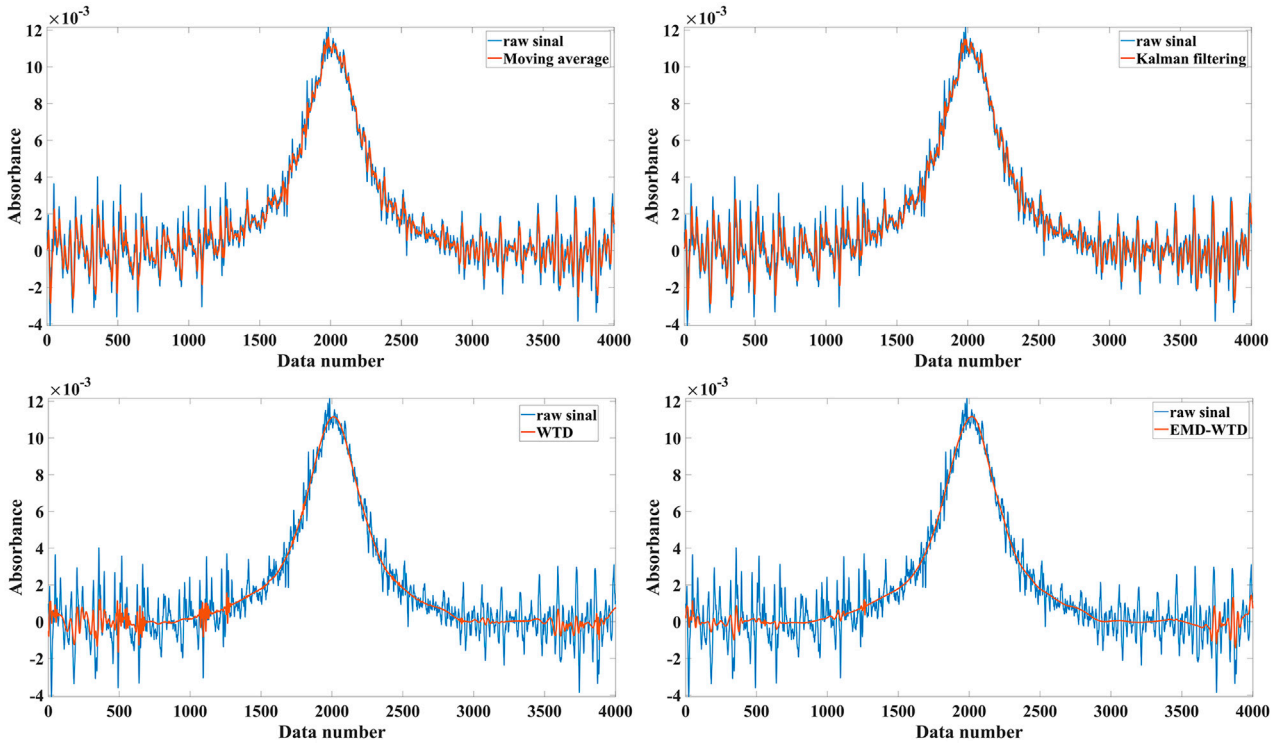

FIGURE 9
DAS signal of CO_2 detected in the experiment and the denoising result by using moving average, Kalman filtering, WTD and EMD-WTD.

T = 300 K, pressure P = 1 atm, and optical path length L = 200 cm. Figure 8 illustrates the detection principle of the CO_2 system. The source uses a distributed feedback (DFB) laser (DFB-2004-4.5-BF2-FC/APC, Nanosystems and Technologies GmbH, Germany) with a center frequency of 2004 nm. The laser output wavelength was controlled through a temperature controller and laser driver (LDC501, Stanford Research Systems, USA). The laser wavelength varied with current at a rate of 0.026 nm/mA. A signal generator (33210A, Keysight, USA) was used to generate a 10 Hz triangular wave signal that was applied to the laser driver to scan the center wavelength over the CO_2 absorption line. The collimated laser beam entered the gas absorption cell and reached the photodetector after multiple reflections. The gas absorption cell employed was a White cell with an effective absorption path length of 200 cm. The photoelectric detector converted the light signals containing the gas concentration information into electrical signals. The data acquisition card (DAQ) (PCL-4472, National Instruments, USA) captured the electrical signal and input it to the PC for analysis and processing.

Results and analysis of the calibration experiment

As shown in Figure 9 and Figure 10, the DAS signal of 300 ppm CO_2 was detected, and the results were processed using various methods. As shown in the figure, the original signal represented by the black curve was severely disturbed by noise; obvious interference fringe noise was present, which can result in errors in the detected absorption peak values. When using the traditional moving average method, the reconstructed signal still contained disturbances from the interference fringe noise. Further, the WTD and other methods were used for comparison, and the reconstructed DAS signal showed poor smoothness. In the results from CEEMDAN-WTD processing, the overall curve was smooth and the useful signal features were preserved well. From locally magnified images, we determined that the local signal did not mutate. In addition, the positions of the features remained unchanged, and the interference fringe noise was suppressed well. The results after denoising by various methods are shown in Table 3. The SNR and RMSE values of the proposed method are 14.3158 dB and 5.3093×10^{-4}, respectively.

We varied the CO_2 concentrations (50 ppm, 60 ppm, 70 ppm, 100 ppm, 200 ppm, and 300 ppm) under the same experimental conditions (P = 1 atm, T = 300 K, and L = 200 cm) and collected the absorption spectra of CO_2 [34]. The peaks of the absorption spectra were extracted using the noise reduction process proposed herein, and a straight line was

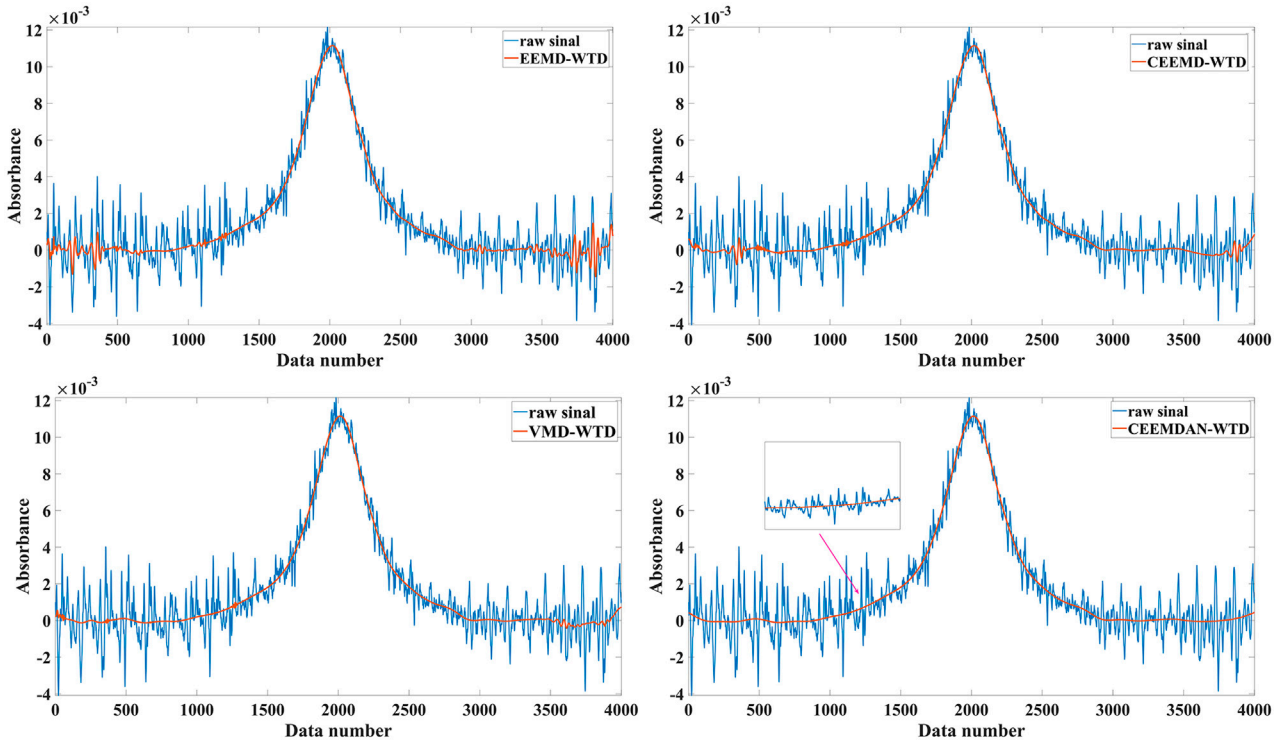

FIGURE 10
DAS signal of CO_2 detected in the experiment and the denoising result by using EEMD-WTD, CEEMD-WTD, VMD-WTD and CEEMDAN-WTD.

TABLE 3 SNR and RMSE results after denoising the DAS signal.

Denoising method	SNR/dB	RMSE
Moving average	8.4437	11.2696×10^{-4}
Kalman filtering	8.5577	11.1487×10^{-4}
WTD	11.7177	8.9817×10^{-4}
EMD-WTD	12.2558	8.4423×10^{-4}
EEMD-WTD	12.3671	8.3347×10^{-4}
CEEMD-WTD	12.4003	8.3029×10^{-4}
VMD-WTD	14.3158	6.6597×10^{-4}
CEEMDAN-WTD	16.2841	5.3093×10^{-4}

fitted based on the concentrations and peaks of the absorption spectra; the expression of the straight line is as follows [35]:

$$\gamma = 3.76 \times 10^{-5}x - 2.9 \times 10^{-4} \quad (18)$$

Figure 11 illustrates the fitting results, where the peak value of the DAS signal has a favorable linear relationship with the gas concentration. The determination coefficient (R^2) was calculated to be 0.999. This demonstrates the excellent linear concentration response of the CO_2 detection system with the CEEMDAN-WTD denoising algorithm.

Allan variance and system stability

Allan variance is an important tool for quantitatively analyzing various types of noise; it can be used to visually observe the variation patterns of noise with integration time as well as evaluate the sensitivity of the system [36]. In the experiment, 1000 data points of CO_2 at a concentration of 50 ppm were measured with a sampling period of 1 s. The signal amplitude was converted to concentration using Eq. 16. The 1000 data points were analyzed *via* Allan variance. Figure 12 shows the relationship between the Allan deviation and averaging time τ. From these, the lower limit of detection (LOD) of the system can be obtained [37]; when the averaging time was 1 s, the LOD was 7.82 ppm, and when the averaging time was 148 s, the LOD reached a minimum of 3.08 ppm.

Stability is an important indicator that affects the sensitivity of a detection system. Theoretically, a perfectly stable detection system can have extremely high detection sensitivity if the detected signals are infinitely averaged. However, various factors can cause system instabilities, such as changes in the laser wavelength due to ageing, temperature drift, white noise, and interference fringe noise from multiple reflections of the laser. Therefore, the actual experimental detection system is only stable for a limited

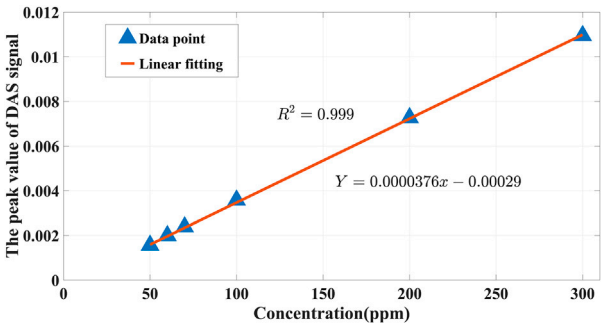

FIGURE 11
The fitting result in the calibration experiment.

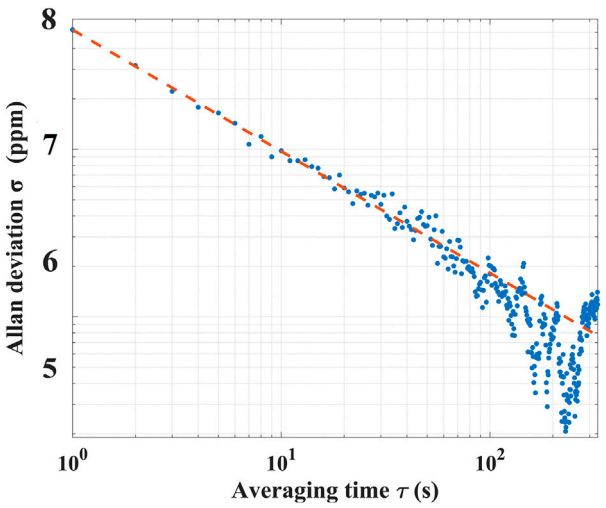

FIGURE 12
Allan variance plot for time series measurements of pure CO_2 and a slope indicating white behavior of the instrument.

period, which means that the system has an optimal averaging time. To further evaluate the stability of the system, a one-hour experiment was carried out in the lab for detecting 50 ppm of CO_2 gas continuously. The upper panels of Figure 13 show the time series of the measured concentrations of 50 ppm CO_2. The distribution histograms of deviations of the measured concentrations and the fitting curve of the probability distribution are depicted in the lower panels of Figure 13. From these, the half-width at half maximum (HWHM) was calculated as 0.326 ppm. Thus, it was confirmed that the precision of system measurement was better than 0.65%. The measured concentration data obviously resembled a Gaussian distribution. These results verify that the system has excellent precision and stability.

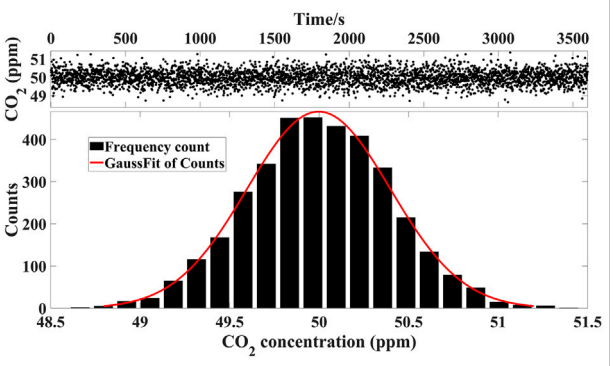

FIGURE 13
The measured CO_2 concentration data (top) and the distribution histograms of deviation (bottom). The red line depicts a Gaussian profile.

Conclusion

In summary, a signal processing algorithm combining CEEMDAN and WTD was proposed herein to suppress the interference fringe noise of the TDLAS system. Moreover, the equation and detection procedure of the proposed algorithm are given. The algorithm reduces large reconstruction errors and loss of useful signals that occur when using the EEMD algorithm. Furthermore, the proposed novel threshold function overcomes the shortcomings of the soft and hard threshold functions. The CEEMDAN-WTD algorithm was evaluated with both simulation and experimental signals. The results showed that the CEEMDAN-WTD algorithm achieved better interference fringe noise suppression performance than the moving average, Kalman filter, WTD, EMD-WTD, EEMD-WTD, CEEMD-WTD, and VMD-WTD algorithms. Additionally, it exhibited excellent peak value extraction performance. The CEEMDAN-WTD algorithm increased the SNR by 1.87 times and decreased the RMSE by 37.6% compared to the moving average algorithm; its R^2 was determined as 0.999 through calibration experiments. Allan variance analysis indicated that the proposed algorithm had a minimum system detection limit of 3.08 ppm for an averaging time of 148 s. From the long-time experiment, a measurement accuracy of 0.65% was verified.

Data availability statement

The raw data supporting the conclusions of this article will be made available by the authors without undue reservation.

Author contributions

SW: methodology and writing—original draft. WG: software. ZW: writing—review and editing. YW: validation. YL: formal

analysis. TZ: project administration and supervision. QZ: conceptualization. LZ: discussion and suggestions. FS: proofreading. WZ: resources. TL: funding acquisition.

Funding

This work was supported by the National Key Research and Development Program of China (Grant No. 2021YFB3201904), Natural Science Foundation of Shandong Province (Grant Nos. ZR2020QF098, ZR2020KC012, and ZR2022QF035), Innovation Team Program of Jinan (Grant Nos. 2020GXRC032 and 2021GXRC037), and Program from Qilu University of Technology (Grant Nos. 2022JBZ01-04, 2022GH001, 2022PX045, and 2022PT029).

Conflict of interest

TL was employed by Shandong Micro-Sensor Photonics Ltd. The remaining authors declare that this research was conducted in the absence of any commercial or financial relationships that could be construed as a potential conflict of interest.

Publisher's note

References

1. Zhao YT, Guo JJ, Bao C, Liang CY, Jain HK. Knowledge graph analysis of human health research related to climate change. *Int J Environ Res Public Health* (2020) 17(20):7395. doi:10.3390/ijerph17207395

2. Yu JN, Ming TK, Yin CK, Raima N, Sajid A, Wasim I. Role of solar-based renewable energy in mitigating CO_2 emissions: Evidence from quantile-on-quantile estimation. *Renew Energ* (2022) 182:216–26. doi:10.1016/J.RENENE.2021.10.002

3. Zhang ZH, Zhang FB, Xu B, Xie HQ, Fu BT, Lu X, et al. High-sensitivity gas detection with air-lasing-assisted coherent Raman spectroscopy. *Ultrafast Sci* (2022) 2022:1–8. doi:10.34133/2022/9761458

4. Fu Y, Cao JC, Yamanouchi K, Xu HL. Air-laser-based standoff coherent Raman spectrometer. *Ultrafast Sci* (2022) 2022:1–9. doi:10.34133/2022/9867028

5. Werle P. A review of recent advances in semiconductor laser based gas monitors. *Spectrochimica Acta A: Mol Biomol Spectrosc* (1998) 54(2):197–236. doi:10.1016/S1386-1425(97)00227-8

6. Ma YF. Recent advances in qepas and qepts based trace gas sensing: A review. *Front Phys* (2020) 8:268. doi:10.3389/FPHY.2020.00268

7. Liu XN, Ma YF. Tunable diode laser absorption spectroscopy-based temperature measurement with a single diode laser near 1.4 μm. *Sensors* (2022) 22(16):6095. doi:10.3390/s22166095

8. Razaa M, Ma LH, Yao C, Yang M, Wang Z, Wang Q, et al. MHz-rate scanned-wavelength direct absorption spectroscopy using a distributed Feedback diode laser at 2.3 μm. *Opt Laser Techn* (2020) 130:106344. doi:10.1016/j.optlastec.2020.106344

9. Rieker GB, Jeffries JB, Hanson RK. Calibration-free wavelength-modulation spectroscopy for measurements of gas temperature and concentration in harsh environments. *Appl Opt* (2009) 48(29):5546–60. doi:10.1364/AO.48.005546

10. Lin S, Chang J, Sun JC, Xu P. Improvement of the detection sensitivity for tunable diode laser absorption spectroscopy: A review. *Front Phys* (2022) 10:136. doi:10.3389/FPHY.2022.853966

11. Jiang J, Zhao MX, Ma GM, Song HT, Li CR, Han X, et al. TDLAS-based detection of dissolved methane in power transformer oil and field application. *IEEE Sens J* (2018) 18(6):2318–25. doi:10.1109/jsen.2017.2788871

12. Luo QW, Zhou J, Li WC, Yang CH, Gui WH. Interference fringe suppression for oxygen concentration measurement using adaptive harmonic feeding generative adversarial network. *IEEE Sens J* (2021) 22(3):2419–29. doi:10.1109/JSEN.2021.3133909

13. Zhou BX, Luo QW, Liu ZH, Yang CH. Multi-frequency modulation method for optical interference suppression in TDLAS system. In: Proceedings of the 32nd China Process Control Conference (2021). p. 1602. doi:10.26914/c.cnkihy.2021.047630

14. Leleux DP, Claps R, Chen W, Harman TL. Applications of Kalman filtering to real-time trace gas concentration measurements. *Appl Phys B: Lasers Opt* (2002) 74(1):85–93. doi:10.1007/s003400100751

15. Li CL, Guo XQ, Ji WH, Ma WG, Qiu X. Etalon fringe removal of tunable diode laser multi-pass spectroscopy by wavelet transforms. *Opt Quan Electron* (2018) 50(7):275–11. doi:10.1007/s11082-018-1539-4

16. Zou DB, Chen WL, Du ZF, Xu KX, Qi RB, Li HL, et al. Selection of digital filtering in the escaping ammonia monitoring with TDLAS. *Spectral Anal* (2012) 32(09):2322–6. doi:10.3964/j.issn.1000-0593(2012)09-2322-05

17. Kireev S, Kondrashov A, Shnyrev S. Application of the Wiener filtering algorithm for processing the signal obtained by the TDLAS method using the synchronous detection technique for the measurement problem of $^{13}CO_2$ concentration in exhaled air. *Laser Phys Lett* (2019) 16(8):085701. doi:10.1088/1612-202X/ab27b9

18. Zhang LF, Wang F, Wei H, Wang J, Cui HB, Zhao GJ. Denoising of digital filtering based on wavelength modulation spectroscopy. *Laser & Optoelectronics Progress* (2021) 58(7):0730001–402. doi:10.3788/LOP202158.0730001

19. Guo XQ, Qiu XB, Ji WH, Shao LG, Li CL Minimization of interference fringes in tunable diode laser absorption spectrum based on empirical mode decomposition. *Laser & Optoelectronics Progress* (2018) 55(11):113001–469. doi:10.3788/LOP55.113001

20. Liang Y, Liu TG, Liu K, Jiang JF, Li YF. Optimized gas detection method based on variational mode-decomposition algorithm. *Chinese Journal of Lasers* (2021) 48(7):0706003–144. doi:10.3788/CJL2021480706003

21. Dragomiretskiy K, Zosso D. Variational mode decomposition. *IEEE Trans Signal Process* (2014) 62(3):531–44. doi:10.1109/TSP.2013.2288675

22. Wu ZH, Norden EH. Ensemble empirical mode decomposition: A noise-assisted data analysis method. *Adv Adapt Data Anal* (2009) 1(1):1–41. doi:10.1142/S1793536909000047

23. Torres ME, Colominas MA, Schlotthauer G, Flandrin P. A Complete ensemble empirical mode decomposition with adaptive noise. In: Proceedings of the 2011 IEEE International Conference on Acoustics: Speech and Signal Processing (ICASSP) (2011). p. 4144–7. doi:10.1109/ICASSP.2011.5947265

24. Jia XN, Roels J, Baets R, Roelkens G. A miniaturised, fully integrated NDIR CO_2 sensor on-chip. *Sensors* (2021) 16:5347. doi:10.3390/s21165347

25. Abitan H, Bohr H, Buchhave P. Correction to the Beer-Lambert-Bouguer law for optical absorption. *Appl Opt* (2008) 47(29):5354–7. doi:10.1364/ao.47.005354

26. Werle P. Accuracy and precision of laser spectrometers for trace gas sensing in the presence of optical fringes and atmospheric turbulence. *Appl Phys B* (2011) 102(2):313–29. doi:10.1007/s00340-010-4165-9

27. He XY, Su Y. Machined surface microstructure of optical silica glasses. *J Wuhan Univ Techn* (2010) 32(13):34–7. doi:10.3963/j.issn.1671-4431.2010.13.009

28. Xu L, Cai DS. Research on signal processing of fiber optic gyroscope based on least square smooth filtering and CEEMDAN. *J Vibration Shock* (2020) 39(10):269–78. doi:10.13465/j.cnki.jvs.2020.10.037

29. Meng XM, Cai CC, Wang YQ, Wang QJ, Tan LL. Remaining useful life prediction of lithium-ion batteries using CEEMDAN and WOA-SVR model. *Front Energ Res* (2022) 10:1460. doi:10.3389/fenrg.2022.984991

30. Mou XJ, Li HL, Tuo XG. Research on improved wavelet threshold denoising algorithm and its simulation. *Process Automation Instrumentation* (2020) 41(08):46–50. doi:10.16086/j.cnki.issn1000-0380.2019070036

31. Xie MW. The relation of covariance, correlation coefficient and correlation. *J Appl Stat Manage* (2004) 03:33–6. doi:10.13860/j.cnki.sltj.2004.03.008

32. Fei HL, Liu M, Qu GJ, Gao Y. A method for blasting vibration signal denoising based on ensemble empirical mode decomposition-wavelet threshold. *Explosion and Shock Waves* (2018) 38(01):112–8. doi:10.11883/bzycj-2016-0148

33. Li GL, Zhang ZC, Zhang XN, Wu YH, Ma K, Jiao Y, et al. Performance of a mid-infrared sensor for simultaneous trace detection of atmospheric CO and N_2O based on PSO-kelm. *Front Chem* (2022) 10:930766. doi:10.3389/fchem.2022.930766

34. Qiao SD, Sampaolo A, Patimisco P, Spagnolo V, Ma YF. Ultra-highly sensitive HCl-LITES sensor based on a low-frequency quartz tuning fork and a fiber-coupled multi-pass cell. *Photoacoustics* (2022) 27:100381. doi:10.1016/j.pacs.2022.100381

35. Zhang L, Li YF, Wei YB, Wang ZW, Zhang TT, Gong WH, et al. SNR enhancement of direct absorption spectroscopy utilizing an improved particle swarm algorithm. *Photonics* (2022) 6:412. doi:10.3390/photonics9060412

36. Luo QW, Yang CH, Song C, Zhou J, Gui WH. TDLAS/WMS embedded system for oxygen concentration detection of glass vials with variational mode decomposition. *IFAC-PapersOnLine* (2020) 53(2):11626–31. doi:10.1016/J.IFACOL.2020.12.644

37. Lu HB, Zheng CT, Zhang L, Liu ZW, Song F, Li XY, et al. A remote sensor system based on TDLAS technique for ammonia leakage monitoring. *Sensors* (2021) 21(7):2448. doi:10.3390/S21072448

frontiers | Frontiers in Physics

TYPE Original Research
PUBLISHED 08 November 2022
DOI 10.3389/fphy.2022.1058733

OPEN ACCESS

EDITED BY
Yufei Ma,
Harbin Institute of Technology, China

REVIEWED BY
Qikun Pan,
Changchun Institute of Optics, Fine Mechanics and Physics (CAS), China
Kuijun Wu,
Yantai University, China

*CORRESPONDENCE
Qingsheng Xue,
xueqingsheng@ouc.edu.cn

SPECIALTY SECTION
This article was submitted to Optics and Photonics,
a section of the journal
Frontiers in Physics

RECEIVED 30 September 2022
ACCEPTED 12 October 2022
PUBLISHED 08 November 2022

CITATION
Xue Q, Li H, Lu F and Bai H (2022), Underwater hyperspectral imaging system for deep-sea exploration. *Front. Phys.* 10:1058733.
doi: 10.3389/fphy.2022.1058733

Underwater hyperspectral imaging system for deep-sea exploration

Qingsheng Xue*, Hui Li, Fengqin Lu and Haoxuan Bai

School of Physics and Optoelectronic Engineering, Department of Information Science and Engineering, Ocean University of China, Qingdao, China

As a technology that combines spectral technology and imaging technology, hyperspectral imaging technology can obtain the spectral and spatial information about the targets effectively. Hence, the underwater hyperspectral imaging technology has a fast development since it was first used underwater. Many kinds of hyperspectral imagers used for underwater detection at different depths were developed. However, the underwater hyperspectral imagers used at deep sea were rarely reported while the required detection depth increased. To satisfy the deep-sea exploration requirements, an underwater hyperspectral imaging system was designed. An optical system with a low F-number and a compact structure was first designed. The F-number of the system is 2.5. The focal length of the objective lens is 25 mm, and the field of view of the objective lens is 35.2°.The wavelength range of the system is from 400 to 1000 nm, and the spectral resolution of the spectrometer is better than 3 nm. The instrument cabin and other structures for waterproofing were designed. A minicomputer used for control communication, data acquisition, and processing was equipped in the actual system. The isolation performance and imaging quality were tested in the laboratory environment. According to the test result, the system has a good imaging quality and spectral detection capability. Also, the system can be used at 6000 m underwater, which may provide a new feasible technical scheme for deep-sea exploration.

KEYWORDS

deep-sea exploration, hyperspectral image, optical design, optical system, underwater hyperspectral imaging

Introduction

With the development of society, environmental and resource problems are becoming increasingly prominent at the global level. With the increasing abundance of land and space detection means [1–4], people have a deeper understanding of the land and the atmosphere. On the contrary, due to the limitation to detection technology, people have relatively little understanding of the ocean. Many kinds of detection methods, such as remote sensing [5] and acoustic detection [6], were developed to know the ocean. However, the rich information on underwater cannot be fully accessed because the methods mentioned previously were

limited by the resolution or detecting depth. Hence, the demand for deep-sea underwater detection with high resolution becomes urgent. As a combination of spectral technology and imaging technology, hyperspectral imaging technology can obtain the spectral and spatial information with high resolution and high efficiency, which can satisfy the demand mentioned previously [7]. So, the hyperspectral imaging technology was put into use for underwater detection by some researchers and developed fast.

The Norwegian University of Science and Technology (NTNU) has begun using underwater hyperspectral imaging technology since long time [8]. A prototype of the underwater hyperspectral imaging system was developed in April 2010 [8]; then, the prototype was mounted on different platforms to carry out the detection work. The system was mounted on a remote operated vehicle (ROV) to carry out the coral reef detection work in 2012. The detection depth reached was 80 m. Through the spectral imaging detection, different kinds of the coral reef can be classified by the spectrum obtained. In 2017, the system was mounted on an ROV and detected an underwater area at 4200 m depth [9]. By using the underwater spectral imaging detection method, manganese nodules in the area were detected successfully. At the same year, the system was mounted on a stationary platform and carried out detection work at 3500 m depth [10]. Different kinds of mineral materials were detected through this detection. In 2018, the system was mounted on an ROV and achieved the detection and recognition of different types of underwater cultural relics at 61 m depth [11]. The Max Planck Institute of Marine Microbiology in Germany has also started research on UHI detection technology since 2013. Two kinds of underwater hyperspectral imaging systems were designed and used in shallow water detection [12, 13]. The inversion of the chlorophyll concentration and classification of different kinds of materials were realized by processing the hyperspectral data obtained by the two systems. The Italian Institute of Marine Sciences has also started research on underwater hyperspectral imaging detection. In 2017, an underwater hyperspectral imager was mounted on the ROV by the Italian Institute of Marine Sciences. The system reached 200 m depth underwater and detected different kinds of materials [14].

According to the study mentioned previously, the detection depths of the underwater hyperspectral imaging detection systems change from shallow water to 4200 m. The systems which can reach deep water are rare. Although the maximal detection depth is deep, it may not be enough for further research in deep water. Hence, a line-scanning underwater hyperspectral imaging system used for deep-sea exploration was designed. Through the design of the optical system, mechanical structure, and electric control system, the underwater hyperspectral imaging system can be mounted on different underwater platforms to access the underwater hyperspectral data. The isolation performance and imaging quality were tested in a laboratory environment. According to the test result, the maximal detection depth of the system can reach 6000 m depth, and the system has a good imaging quality and spectral detection capability, which may provide a feasible plan for deep-sea exploration in the future.

Design of the system

Optical design of the system

The optical structure of the hyperspectral imaging system mainly includes three parts: the objective lens, spectrometer, and detector. Due to the severe light absorption of seawater at long wavelength [15], the main concerned detecting wavelength range of the system was from 400 to 700 nm. A detector (Basler Ac2040-90um, Germany) with high efficiency from 400 to 700 nm was first chosen. To have a relatively large field of view, the focal length of the objective length was determined as 25 mm. Because the system is used in deep sea where almost no natural light exists, the F-number of the whole system was determined as 2.5 to make full use of the light from the light source and have a relatively high signal-to-noise ratio. The objective lens of the system was designed to have a good imaging quality through focusing when the object distance changes. A prism-grating-prism structure was designed as the dispersion element so that the spectrometer can have a compact structure and small volume. The specification and value of the whole system are shown in Table 1. Simulation was performed by Zemax software, and part of the design result is shown in Figures 1, 2.

Design of the instrument cabin

The fixing structure of the optical elements and detector was first designed, which is shown in Figure 3A. Then,

TABLE 1 Design parameters of the optical system.

Parameter	Value
Focal length of the objective length/mm	25
Wavelength range/nm	400–1,000
Object distance/m	0.6–1.2
Field of view/°	35.2
F#	2.5
Silt size/mm	0.010 × 10
Detector size/pixel	2048 × 2048
Pixel size/micro	5.5 × 5.5
Digitalizing/bit	12
Maximal sample frame rate/fps	25
Spectral resolution of the whole system/nm	<3

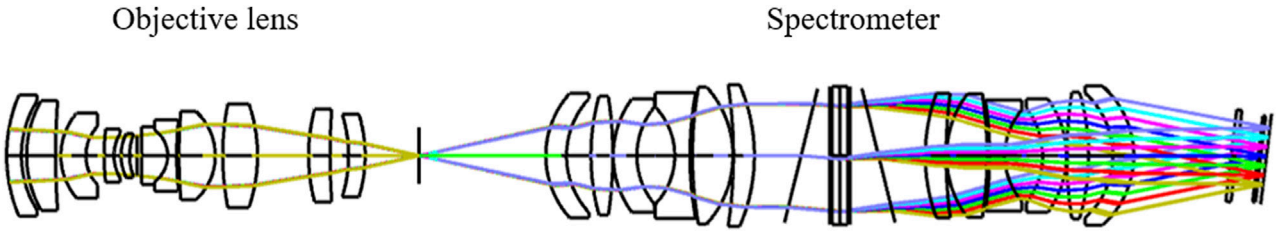

FIGURE 1
Optical structure of the whole underwater hyperspectral imaging system.

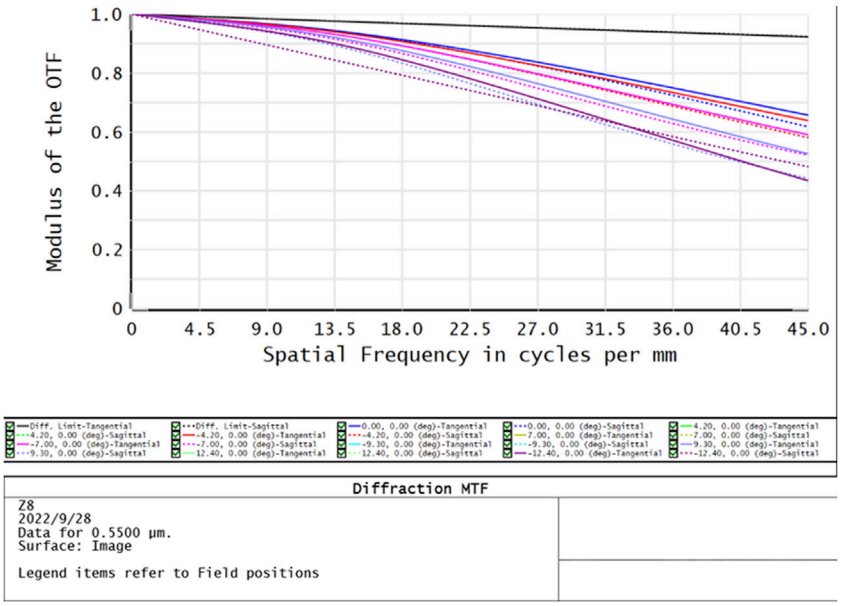

FIGURE 2
MTF curve of the whole system at the central wavelength.

according to the size of the optical and mechanical structure designed previously, an instrument cabin was designed to resist the water and pressure in deep sea. To have a good water and pressure resistance, the material of the cabin was chosen as TC4 titanium alloy. To have a better resistance of the sea flow and be easy to manufacture, the cabin was designed to be cylindrical. To accommodate the imaging system, the internal diameter of the cabin was determined as 90 mm.Then, the parameters of the cabin can be determined according to Eqs 1, 2 mentioned as follows. $\boldsymbol{D}$ is the internal diameter of the cabin, which was 90 mm. $\boldsymbol{K}$ is the safety parameter, which was 1.5 in this design. $\boldsymbol{\delta_b}$ is the tensile strength of the material, which was 800 MPa for TC4 titanium alloy. Then, the size of the cabin and its end cap can be calculated according to the formula [16]. The calculated result and design values are shown in Table 2. The design result of the whole mechanical structure is shown in Figure 3B. The front and bottom cap are shown in Figure 3C and Figure 3D. Three underwater connectors (SubConn, United States) were installed on the bottom cap to connect with the carrying platform for power supplement and data transmission. As is shown in Figure 3D, the port with 13 cores can supply system power and transmit data at about 100 Mb/s. The ports B and C are used for power supply and control the whole system. The overall length of the piece of equipment was 60 cm, the weight was 16kg, and the lighting mode was passive lighting.

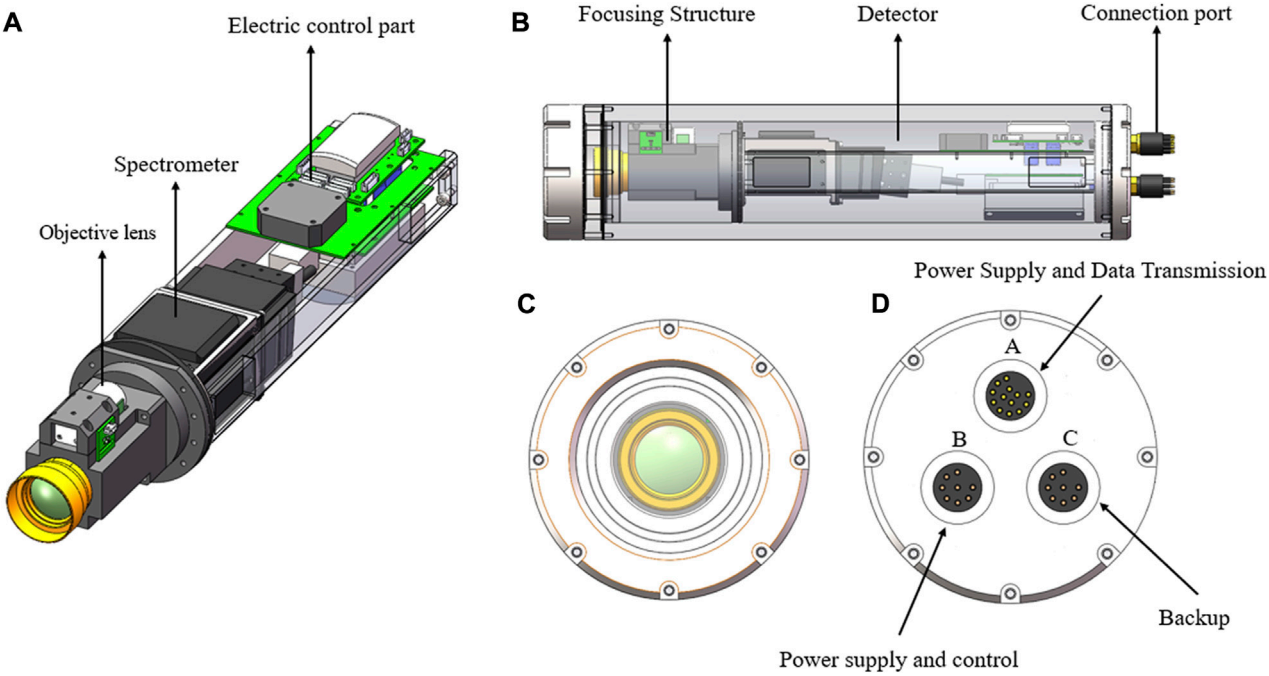

FIGURE 3
Mechanical structure design result. **(A)** Mechanical structure of the hyperspectral imaging system. **(B)** Mechanical structure of the instrument cabin. **(C)** Mechanical structure of the front cap of the instrument cabin. **(D)** Mechanical structure of the bottom cap.

TABLE 2 Design parameters of the cabin.

Value name	Calculated result/mm	Design value/mm
Thickness of the front cap	13.07	32
Thickness of the bottom cap	13.07	32
Thickness of the cabin wall	5.06	15

$$\delta_{lid} = 0.433D\sqrt{\frac{k.P_y}{\delta_b}}, \quad (1)$$

$$\delta_{wall} = \frac{P_y.D.k}{2\delta_b}. \quad (2)$$

Design of the electric control system

The frame of the electric control system is shown in Figure 4. The core part of the electric control system is TX2-IPC, which is a minicomputer used for controlling the hyperspectral imager and saving the data accessed by the hyperspectral imager. The detector used in the underwater hyperspectral imager connects with the minicomputer with a USB3.0 data transmission line. The power, command, and data can be transmitted between the minicomputer and camera through the line. The commands sent from the minicomputer are given by the upper computer by the four cores of the eight core ports. The power supply of the whole system was achieved by the two cores of the eight core ports. The remaining two cores connected with the computer, and the computer connected with a 485-communication module to control the focusing stepper motor. The port of the 13 cores was only used for data transmission above water by eight cores through a network cable put inside the cabin. In addition, two

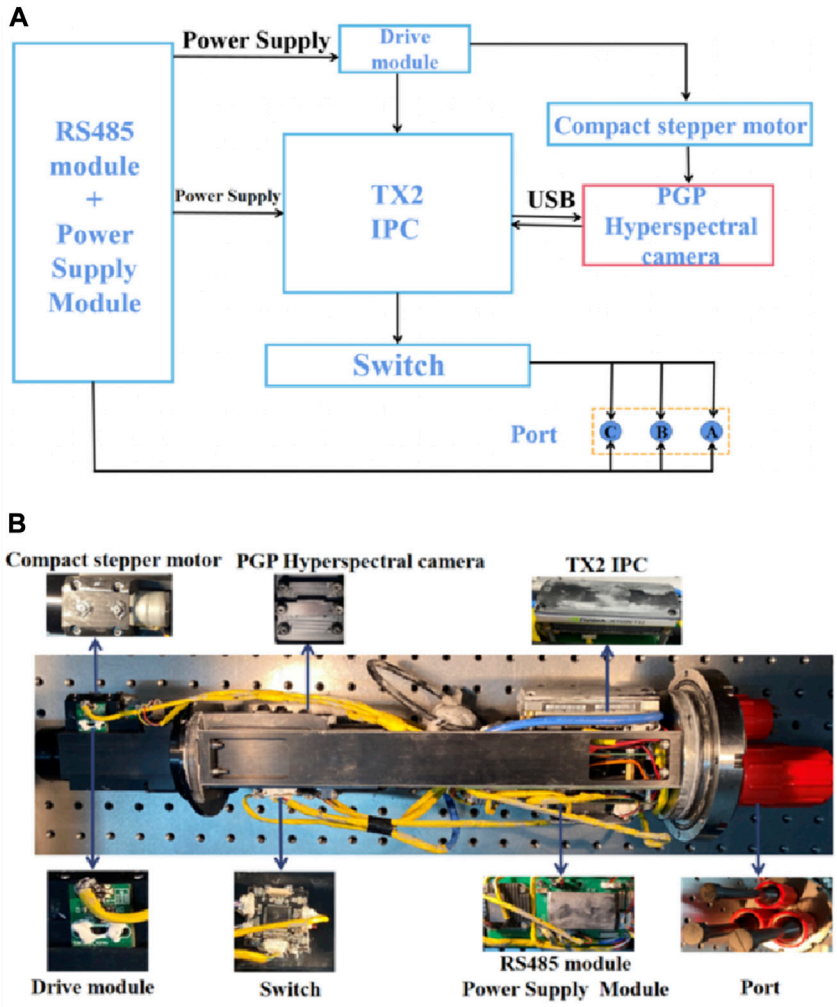

FIGURE 4
Design result of the electric control system. **(A)** Framework of the electric control system. **(B)** Actual structure of the electric control system.

cores of the 13 cores were used for power supply. A switch was used to share the data among the ports. Because the instrument works in the water environment, seawater can physically cool the instrument. To increase the safety factor, heat dissipation treatment of the instrument, the inside wall of the cabin, and the control system are coated with thermal silicone grease to ensure the instrument can work normally.

Instrument performance test

Watertight test of the instrument cabin

To verify the watertight performance of the instrument cabin, a watertight test was taken. The instrument cabin was sent to a watertight performance test organization, and the cabin was put into a special pressure tank. The pressure tank generates large pressure inside to test the watertight performance and pressure resistance. The pressure changes with time, and its value is shown in Figure 5. The maximal pressure in the pressure tank increased to 60 MPa and lasted for about an hour. Also, the instrument cabin was flawless, which means the instrument cabin can be used underwater 6000 m.

Spectral calibration of the optical system

To access the monochromatic image from the raw data obtained by the hyperspectral image, a spectral calibration is

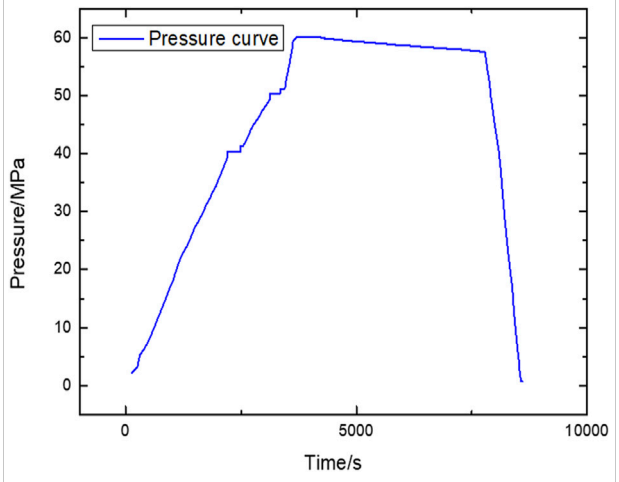

FIGURE 5
Pressure curve inside the pressure tank.

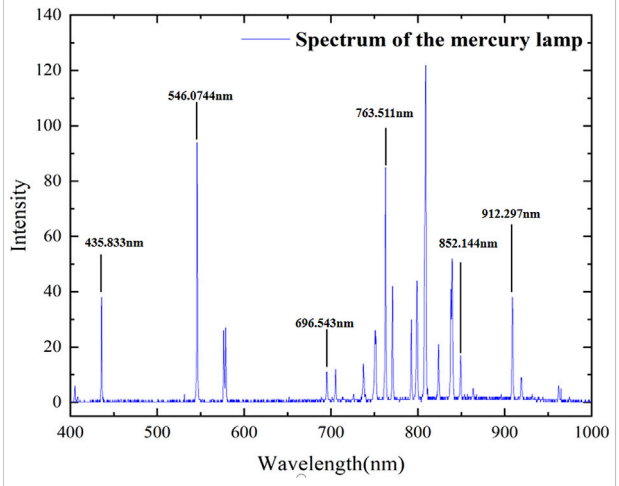

FIGURE 7
Spectrum of the mercury lamp obtained by the spectrometer.

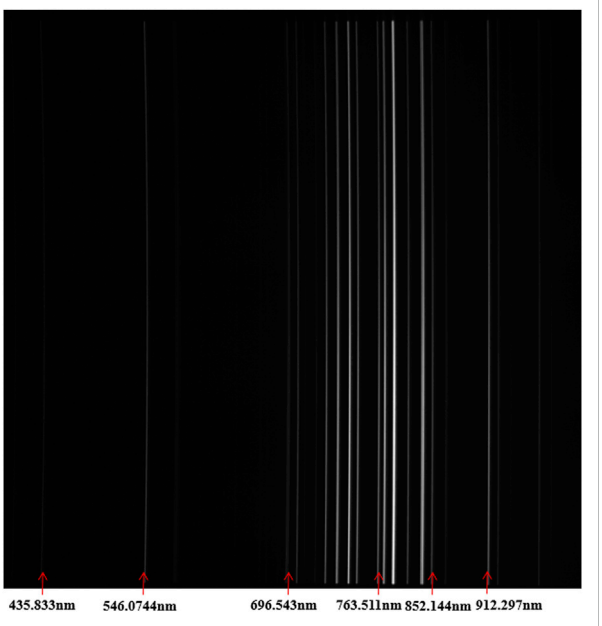

FIGURE 6
Raw data of the mercury lamp obtained by the spectrometer.

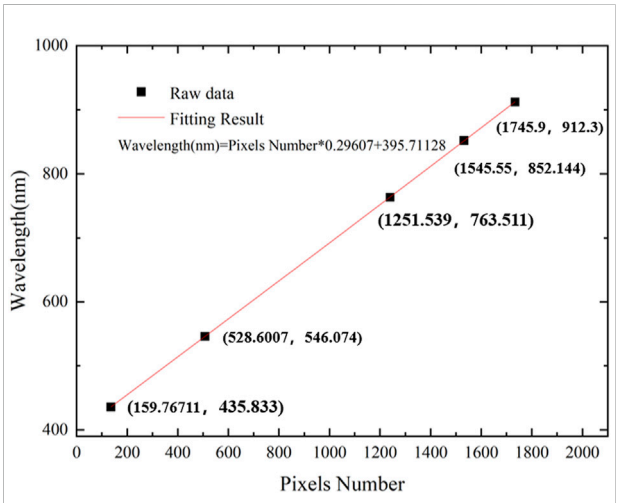

FIGURE 8
Linear fitting result of the calibration data.

necessary. A mercury lamp was used for spectral calibration, and the spectral resolution of the spectrometer at different peaks of the mercury lamp was calculated. The mercury lamp was placed in front of the slit of the spectrometer, and the raw data of the mercury lamp obtained by the spectrometer are shown in Figure 6. One row of the image is the spectrum of the mercury lamp, which is shown in Figure 7. A Gauss fitting method was used to determine the central position of the peaks of the mercury lamp and calculate the full width at half maxima (FWHM). According to the central position and peak wavelength, a linear fitting method was used to calculate the linear dispersion rate. Then, the spectral resolution can be calculated according to Eq. 3. The fitting result is shown in Figure 8. The spectral resolution calculated result is shown in Table.3.

TABLE 3 Calibration result of the spectrometer.

Central position	Wavelength/nm	FWHM/pixel	Spectral resolution/nm
135.731	435.840	3.125	0.925
507.425	546.080	3.143	0.930
1,239.960	763.511	3.682	1.090
1,531.969	852.144	4.441	1.315
1733.638	912.297	4.196	1.242

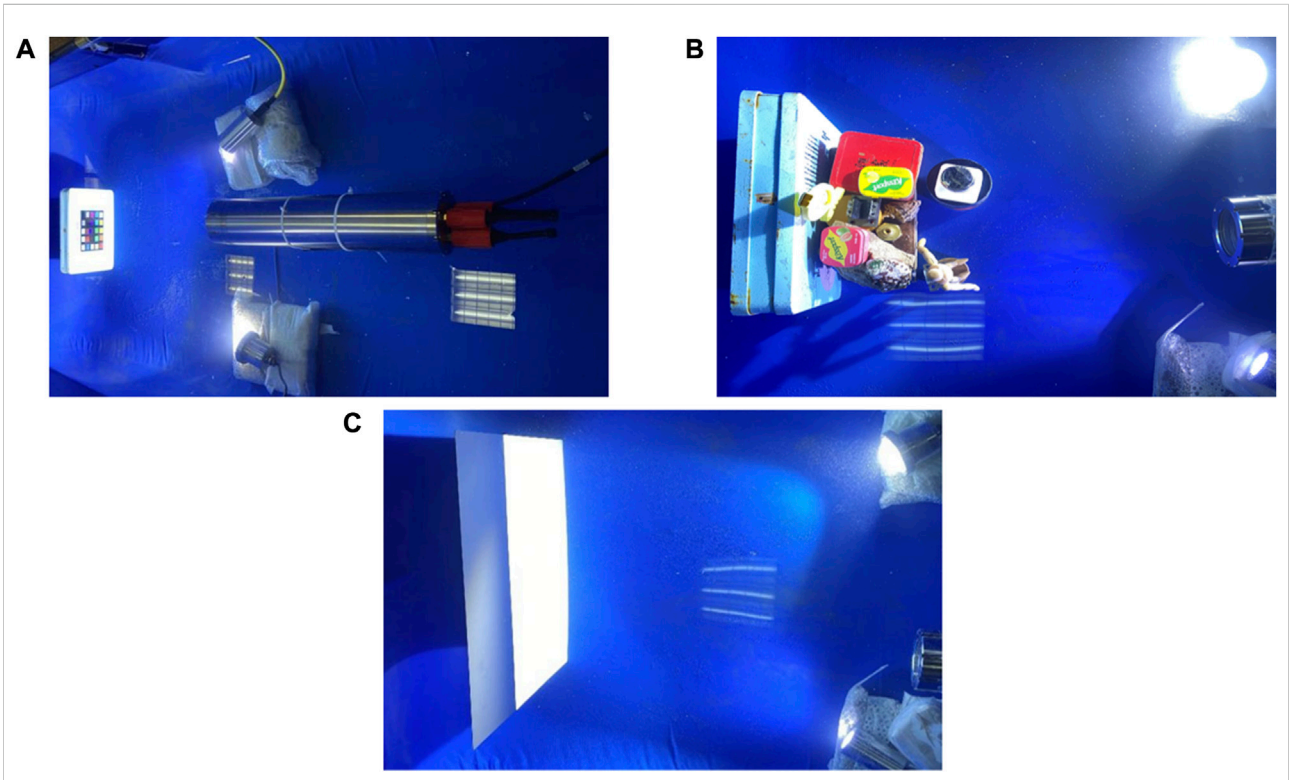

FIGURE 9
Underwater spectral imaging performance test. **(A)** Underwater hyperspectral imager scanning the color blocks. **(B)** Underwater hyperspectral imager scanning different objects. **(C)** Underwater hyperspectral imager scanning the standard whiteboard.

$$\delta_\lambda = \frac{d\lambda}{dpixel} FWHM_{pixels}. \quad (3)$$

Underwater hyperspectral imaging experiment

To test the imaging quality and spectral detection capability in the range of 400–700 nm, an underwater environment was established in the laboratory. In addition, two LED sources with 100 W power were placed beside the underwater hyperspectral imager. A mechanical rotating platform was used as the carrying platform to carry out the scanning imaging job. The experiment environment is shown in Figure 9.

A board with different color blocks was first detected to verify the spectral detection capability of the system. The monochromatic images of different wavelengths are shown in Figure 10. The spectrum of different color blocks is shown

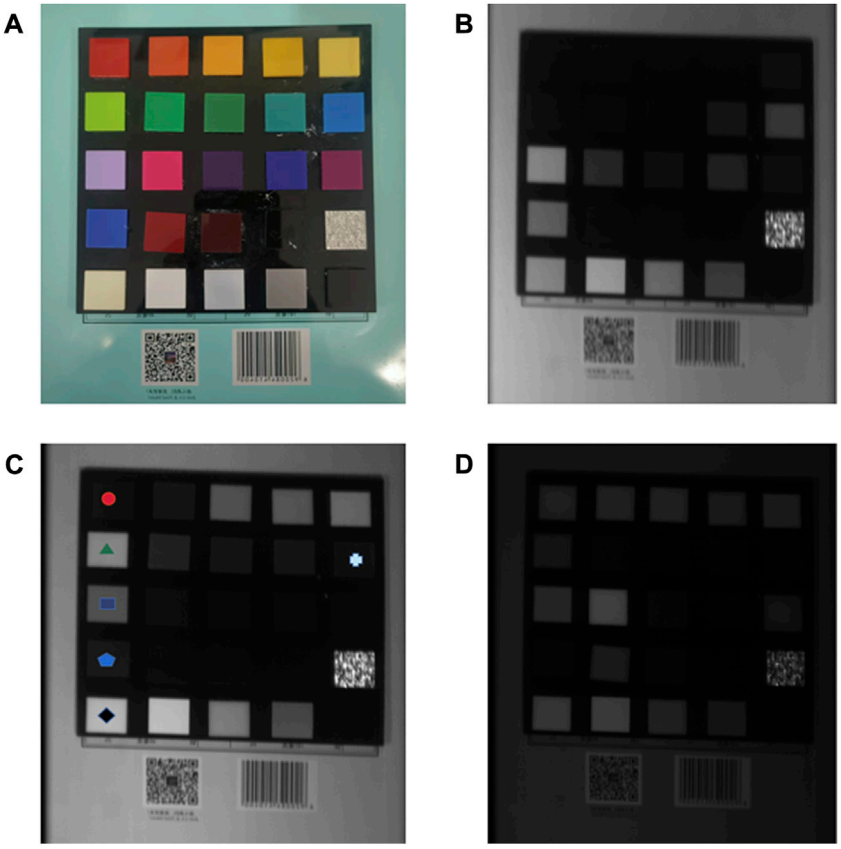

FIGURE 10
Monochromatic image obtained by the system. **(A)** Actual color blocks. **(B)** Monochromatic image of the color blocks at 455 nm. **(C)** Monochromatic image of the color blocks at 555 nm. **(D)** Monochromatic image of the color blocks at 655 nm.

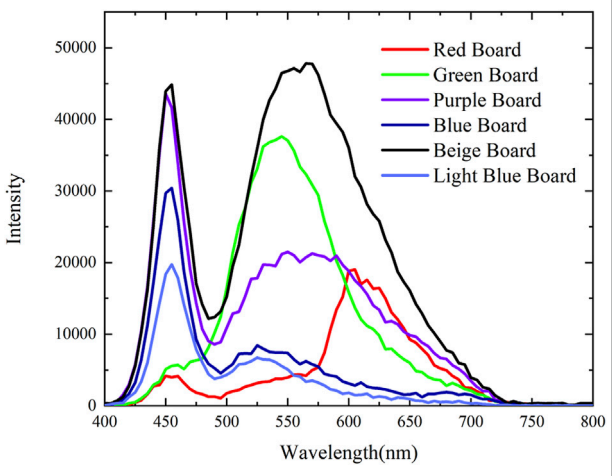

FIGURE 11
Spectrum of different color blocks.

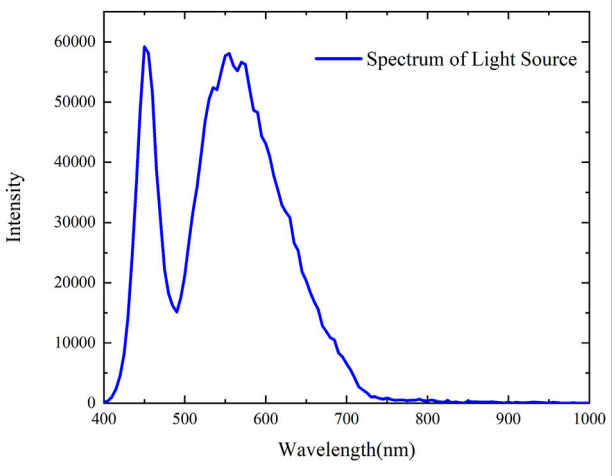

FIGURE 12
Spectrum of the standard light source.

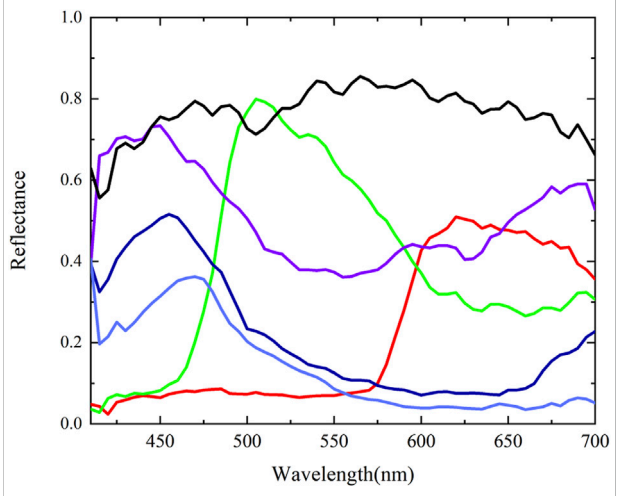

FIGURE 13
Reflectivity of different color blocks.

in Figure 11. A standard whiteboard was also used as the target to measure the standard spectrum of the light source. The spectrum of the light source is shown in Figure 12. The reflectivity of the different color blocks can be calculated according to the stand spectrum of the light source. The reflectivity curves of different color blocks are shown in Figure 13. The characteristics of the reflectivity curves are consistent with the wavelength range of different colors, which means that the system has a good spectral detection capability.

Different kinds of objects like metal boxes, plastic bottles, and some shells were used as the target. The monochromatic images of different wavelengths are shown in Figure 14. In addition, the spectrum and reflectivity of different objects are shown in Figures 15A,B. As shown in Figure 14, the system has a good imaging quality. Different objects can be classified according to the spectrum or reflectivity curves. According to the detecting results, the system has a good underwater detection capability, which may provide a feasible technical detecting plan for deep-sea exploration.

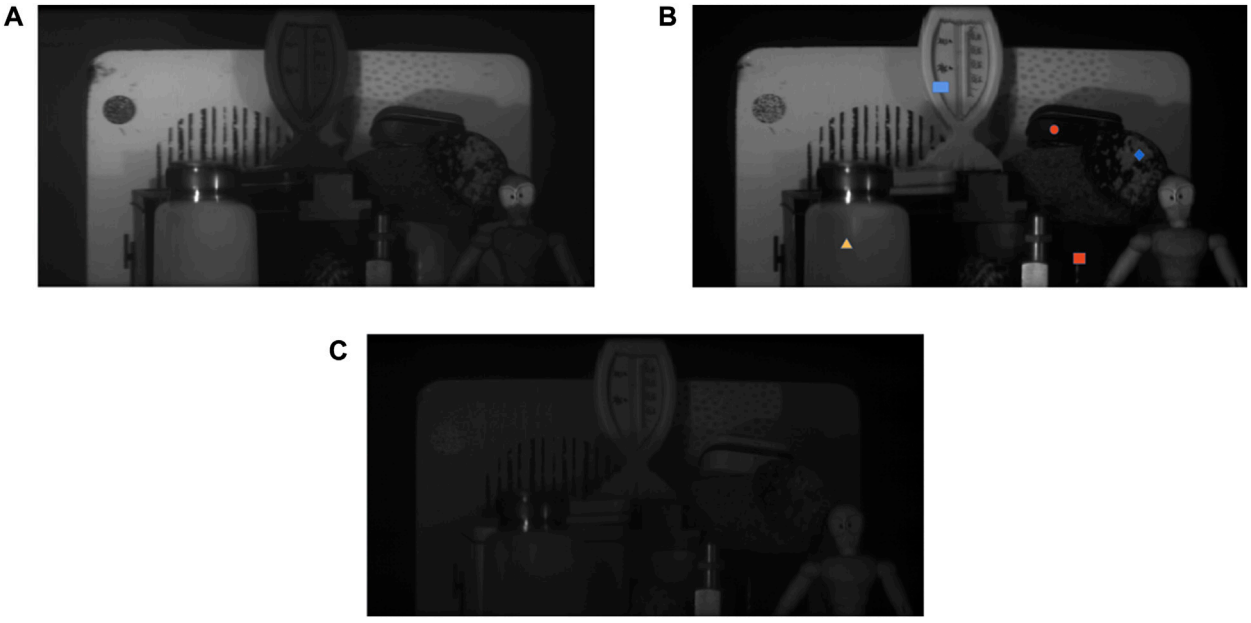

FIGURE 14
Monochromatic images of the different objects. **(A)** Monochromatic images of different objects at 455 nm. **(B)** Monochromatic images of different objects at 555 nm. **(C)** Monochromatic images of different objects at 655 nm.

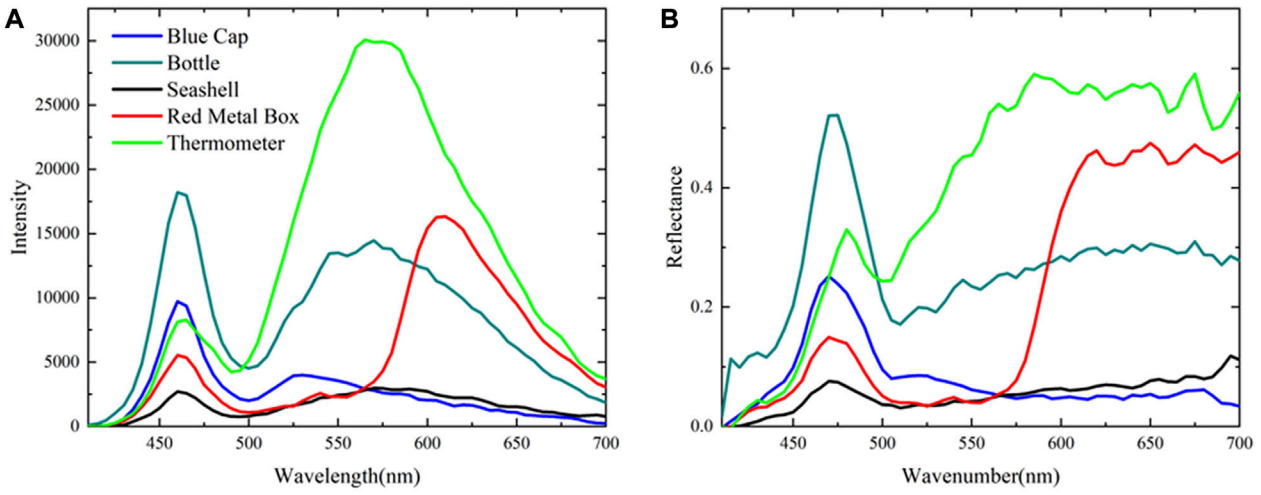

FIGURE 15
(A) Spectrum of different objects. **(B)** Reflectivity of different objects.

Conclusion

To make up the requirement for high-resolution deep-sea detection, an underwater hyperspectral imaging system was developed. The optical system was first designed according to deep-sea exploration requirements. Then, the mechanical structure and instrument cabin were designed. The electric control system was established. In addition, the communication with the upper computer, control of camera, and data transmission can be achieved by using the internal minicomputer. The multiple performances of the instrument have been tested in the laboratory environment. According to the test result, the spectral resolution of the spectrometer is better than 3 nm, and the system can work underwater 6000 m. Different underwater targets can be distinguished according to the spectrum accessed by the system. The system has a good underwater detection capability and may provide new feasible plans for future deep-sea exploration.

Data availability statement

The datasets presented in this article are not readily available because the complete dataset needs to be further collated. Requests to access the datasets should be directed to Qingsheng Xue, xueqingsheng@ouc.edu.cn.

Author contributions

QX: conceptualization and methodology. HL: experiment, simulation, and writing—original draft. FL: data processing. HB: data processing and writing—review and editing.

Funding

The study was funded by the Key Research and Development Program of Shandong Province (2020CXGC010706), the National Natural Science Foundation of China (U2006209 and 41575023), the National Natural Science Foundation of China (U2106210), the Scientific research funds of Taishan scholars (202105033008), the Excellent Researcher plan project (202112003), the Key deployment project of the Marine Science Research Centre of the Chinese Academy of Sciences (COMS2019J04), the National Key Research and Development Program of China (2019YFC1408300, 2019YFC1408301, and 2018YFF01011003), and the Consulting Research Project of the Chinese Academy of Engineering (2020-XZ-5-03).

Conflict of interest

The authors declare that the research was conducted in the absence of any commercial or financial relationships that could be construed as a potential conflict of interest.

Publisher's note

References

1. Qiao S, Sampaolo A, Patimisco P, Spagnolo V, Ma Y. Ultra-highly sensitive HCl-LITES sensor based on a low-frequency quartz tuning fork and a fiber-coupled multi-pass cell. *Photoacoustics* (2022) 27:100381. doi:10.1016/j.pacs.2022.100381

2. Ma Y, Feng W, Qiao S, Zhao Z, Gao S, Wang Y. Hollow-core anti-resonant fiber based light-induced thermoelastic spectroscopy for gas sensing. *Opt Express* (2022) 30(11):18836–44. doi:10.1364/OE.460134

3. Fu Y, Cao J, Yamanouchi K, Xu H. Air-laser-based standoff coherent Raman spectrometer. *Ultrafast Sci* (2022) 2022:1–9. doi:10.34133/2022/9867028

4. Kzhang Z, Zhang F, Xu B, Xie H, Fu B, Lu X, et al. High-sensitivity gas detection with air-lasing-assisted coherent Raman spectroscopy. *Ultrafast Sci* (2022) 2022:1–8. doi:10.34133/2022/9761458

5. Kratzer S, Harvey ET, Philipson P. The use of ocean color remote sensing in integrated coastal zone management—a case study from himmerfjärden, Sweden. *Mar Pol* (2014) 43:29–39. doi:10.1016/j.marpol.2013.03.023

6. Asada A, Ura T. Three dimensional synthetic and real aperture sonar technologies with Doppler velocity log and small fiber optic gyrocompass for autonomous underwater vehicle. In: *2012 oceans*. IEEE (2012). p. 1–5. doi:10.1109/OCEANS.2012.6405126

7. ElMasry G, Sun DW. *Principles of hyperspectral imaging technology// Hyperspectral imaging for food quality analysis and control*. Academic Press (2010). p. 3–43. doi:10.1016/B978-0-12-374753-2.10001-2

8. Johnsen G, Ludvigsen M, Sørensen A, Sandvik Aas LM. The use of underwater hyperspectral imaging deployed on remotely operated vehicles-methods and applications. *IFAC-PapersOnLine* (2016) 49(23):476–81. doi:10.1016/j.ifacol.2016.10.451

9. Dumke I, Nornes SM, Ludvigsen M. First hyperspectral survey of the deep seafloor: DISCOL area. In: *Peru basin//EGU general assembly conference abstracts* (2017). p. 4529.

10. Dumke I, Ludvigsen M, Ellefmo SL, Soreide F, Johnsen G, Murton BJ. Underwater hyperspectral imaging using a stationary platform in the Trans-Atlantic Geotraverse hydrothermal field. *IEEE Trans Geosci Remote Sens* (2018) 57(5):2947–62. doi:10.1109/TGRS.2018.2878923

11. Ødegård Ø, Mogstad AA, Johnsen G, Sorensen AJ, Ludvigsen M. Underwater hyperspectral imaging: A new tool for marine archaeology. *Appl Opt* (2018) 57(12):3214–23. doi:10.1364/AO.57.003214

12. Chennu A, Färber P, De'ath G, de Beer D, Fabricius KE. A diver-operated hyperspectral imaging and topographic surveying system for automated mapping of benthic habitats1-12. *Sci Repscientific Rep* (2017) 7(11):77122. doi:10.1038/s41598-017-07337-y

13. Chennu A, Färber P, Volkenborn N, Al-Najjar MAA, Janssen F, de Beer D, et al. Hyperspectral imaging of the microscale distribution and dynamics of microphytobenthos in intertidal sediments. *Limnol Oceanogr Methods* (2013) 11(10):511–28. doi:10.4319/lom.2013.11.511

14. Foglini F, Grande V, Marchese F, Bracchi VA, Prampolini M, Angeletti L, et al. Application of hyperspectral imaging to underwater habitat mapping, Southern Adriatic Sea. *Sensors* (2019) 19(10):2261. doi:10.3390/s19102261

15. Wozniak B, Dera J. *Light absorption by suspended particulate matter (SPM) in sea water*. New York: Springer (2007). doi:10.1007/978-0-387-49560-6_5

16. Wen BC. *Mechine design handbook*. Beijing: Mechanical Industry Press (2012). p. 22–249.

frontiers | Frontiers in Physics

TYPE Original Research
PUBLISHED 10 November 2022
DOI 10.3389/fphy.2022.1056639

OPEN ACCESS

EDITED BY
Yufei Ma,
Harbin Institute of Technology, China

REVIEWED BY
Dror Malka,
Holon, Institute of Technology (HIT), Israel
Chen Ming-Yang,
Jiangsu University, China

*CORRESPONDENCE
Hongjun Zheng,
370112418@qq.com

†These authors have contributed equally to this work

SPECIALTY SECTION
This article was submitted to Optics and Photonics, a section of the journal Frontiers in Physics

RECEIVED 29 September 2022
ACCEPTED 18 October 2022
PUBLISHED 10 November 2022

CITATION
Xing H, Su Y, Gao Y, Li X, Zheng H, Bai C, Hu W and Xu H (2022), A novel mode-division (de)multiplexer with degenerate modes output for MIMO-FREE applications.
Front. Phys. 10:1056639.
doi: 10.3389/fphy.2022.1056639

A novel mode-division (de) multiplexer with degenerate modes output for MIMO-FREE applications

Huadong Xing[1†], Yingqun Su[1†], Yan Gao[1], Xin Li[1], Hongjun Zheng[1*], Chenglin Bai[1], Weisheng Hu[2] and Hengying Xu[1]

[1]Shandong Provincial Key Laboratory of Optical Communication Science and Technology, School of Physics Science and Information Engineering, Liaocheng University, Liaocheng, China, [2]State Key Laboratory of Advanced Optical Communication Systems Networks, School of Electronic Information and Electrical Engineering, Shanghai Jiao Tong University, Shanghai, China

In this study, we propose a novel three-dimensional architecture mode (de)multiplexer with degenerate modes output using a pure silica FMF ring core transmission channel, which solves the problem caused by random mode rotation and can be used in multiple-input multiple-output free (MIMO-FREE) applications such as data center application in the future. By using the pure silica FMF ring core transmission channel and larger effective refractive index difference, the performance with low loss, high extinction ratio (ER) and low crosstalk is achieved. The main channel with a few-mode fiber (FMF) ring-core structure supports the modes LP01, LP11, and LP21, and the large effective refractive index difference between each mode in the core ensures low crosstalk characteristics between the modes. Using the pure silica core channel can effectively reduce propagation attenuation and fusion loss. Our proposed MUX/DEMUX with degenerate modes output is achieved when the degenerate modes LP11a/LP11b and LP21a/LP21b are transmitted as two independent mode signals, which can be used in MIMO-FREE applications. The extinction ratios (ERs) of the degenerate modes LP11 and LP21 are kept above 31.66 dB and 24.43 dB, respectively, and the ER of mode LP01 is kept above 38.72 dB in the C band. The coupling efficiency of mode LP01 is approximately 0 dB, which is almost unchanged with the increase of the wavelength. The coupling efficiency of LP11 is higher than −3.49 dB and that of LP21 is higher than −7.24 dB in the whole C-band. At 1550 nm, the coupling efficiencies of modes LP01, LP11, and LP21 are −0.002 dB, −0.052 dB, and −0.178 dB, respectively. The coupling efficiency and ER of LP01 mode are the best, and those of the degenerate mode LP11 are always better than those of mode LP21. Our proposed MUX/DEMUX achieves low crosstalk and high ER performance and solves the problem caused by the degenerate modes rotations during transmission.

KEYWORDS

mode-division multiplexing, mode-division multiplexer/demultiplexer, degenerate modes output, few-mode fiber ring-core, low crosstalk, low loss, MIMO-FREE

1 Introduction

In recent years, with the growth of communication services, the traffic of the transmission system has grown exponentially, and the traditional single-mode fiber (SMF) communication capacity has converged to the Shannon limit, which cannot meet the communication demand [1]. Space division multiplexing (SDM) is a novel technology developed after successful research and application of digital coherent communication technology, which is a system that can simultaneously transmit multiple independent channel signals in a single fiber. Mode division multiplexing (MDM), which is one of the SDMs, is widely considered an effective way to improve the capacity of communication systems and networks. Especially, the weak coupling method to suppress inter-mode crosstalk has attracted much attention [2, 3, 4, 5].

Few-mode fiber (FMF) and mode-division multiplexer/demultiplexer (MUX/DEMUX) are one of the key devices for the MDM. As the transmission carrier of the MDM system, the FMF is widely focused, which can break through the nonlinear Shannon limit of SMF's communication capacity [6, 7]. Several typical fibers reported in recent years include an elliptical-core FMF with low loss and low crosstalk for MIMO-FREE applications [8], a novel graded refractive index six-core supermode fiber [9], the polarization-maintaining elliptical ring-core fiber with four linearly polarized vector modes [10], undoped and N-doped-silica core PANDA fiber with different pulse times of radiation-induced absorption [11], low-loss four-mode-group ring-core FMFs that support only single-radial-order modes [12], low-index center and trench-assisted seven-ring-core five-mode-groups SDM fiber [13], and a 6-LP-mode ultralow-modal-crosstalk (1.49×10^{-3}) double-ring-core FMF for weakly-coupled MDM transmission [14]. The special design of the ring core with a high refractive index increases the effective refractive index difference between modes, which can greatly suppress the mode crosstalk between modes. The pure silica core can effectively reduce the attenuation and fusion loss in the fiber, which is widely used not only in SMF [15] [16] but also in the few-mode supermode fibers [9]. The advantages of the ring-core fiber are outstanding, and its application prospects are wide, which is our preliminary consideration to study and design a mode-division (de)multiplexing device with the FMF ring-core transmission channel.

A (de)multiplexer is a more important device for optical communications; for example, a RGB wavelength (de) multiplexer based on a polycarbonate multicore polymer optical fiber is important to use wavelength division multiplexing for visible light communication system [17, 18]. Similarly, a mode-division MUX/DEMUX is a key device for mode conversion and mode-division (de)multiplexing in the MDM optical communication system. It can multiplex different channel information into one fiber for mode signal transmission or demultiplex the transmission information from one fiber into other different transmission channels. Several different MUX/DEMUXs have been proposed in order to enable the signal to be multiplexed/demultiplexed the different modes. In the literature [19], the conversion of mode LP01 to mode LP11a/LP11b in a 36-core three-mode heterogeneous few-mode multicore fiber is accomplished using a phase-plate-based mode MUX. In the 108-channel (36-cores × three-mode) mode multiplexer, the insertion loss is about 6.3–6.9 dB for mode LP01 and 7.5–9.4 dB for modes LP11a/LP11b. The mismatch between the mode field of mode LP11 in the few-mode cores and the mode field of the long-tailed quasi-LP11 mode generated through the phase plates leads to lower coupling efficiency. Also, the MUX/DEMUX device is too large due to the size of the SMF collimator. In the literature [20], the mode-division multiplexing of five spatial modes with ten channels is accomplished using photonic lanterns, but complex MIMO DSP processing is needed. In the literature [21], an all-fiber mode MUX composed of a mode-selective coupler (MSC) based on an elliptical ring-core fiber structure is used to achieve high multiplexing efficiency of seven spatial modes by employing the directional coupling method, and the mode ERs in the C-band are all above 15 dB. The large size of the photonic lantern and phase-plate-based mode division MUX makes it difficult to miniaturize and integrate the mode division multiplexing system, while the mode division MUX/DEMUX based on the directional coupling method has the advantages of all-fiber structure, high mode selectivity, high coupling efficiency, high ER, low insertion loss and mode crosstalk, simple fabrication process, low cost, etc., which can be applied to the miniaturization and integration. The directional coupling method is one of the best solutions for weak coupling technology.

For multiplexing and demultiplexing mode signals in circular-core FMFs, it is common to separately process the degenerate non-circular symmetric polarization modes (e.g., LP11a/LP11b) with the same propagation constants. Due to the effect of random rotation of the degenerate modes caused by the non-circularity of fiber fabrication and fiber twist, detecting only one of the degenerate modes will lead to power fluctuation and rapid deterioration of the bit error rate (BER) [22]. In order to solve the problems caused by rotation of the degenerate modes, two solutions can be adopted, which can be applied in the MIMO-FREE scenarios to reduce the complexity of MIMO DSP, computation, cost, etc. One solution is to design non-circular symmetric fibers to break the mode degeneracy, such as the design of the elliptical core few-mode fiber [8]. The

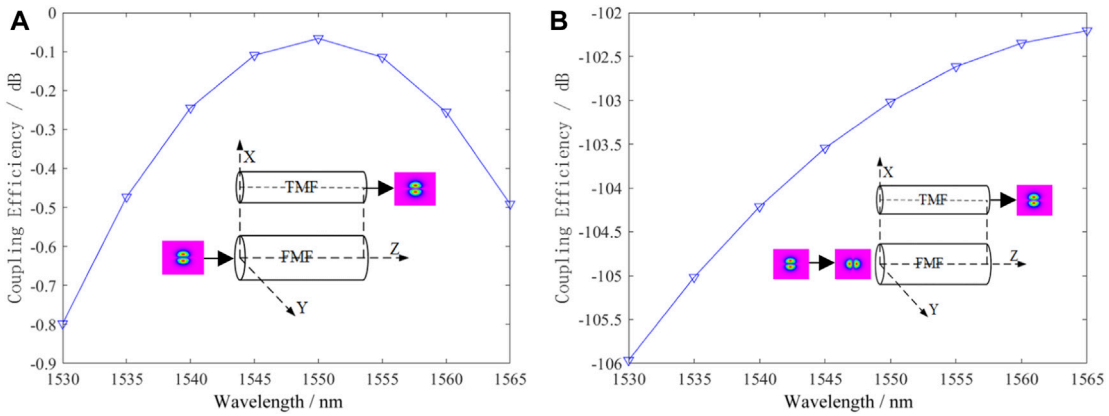

FIGURE 1
Mode rotation during the mode transmission leads to **(A)** the best coupling case with rotation angle of $\pm k\pi$, $k = 0, 1, 2, \ldots, .$) versus **(B)** the worst coupling case with $\frac{\pi}{2} \pm k\pi$, $k = 0, 1, 2, \ldots, .$

other is to use multiplexing and demultiplexing with degenerate modes output [23, 24]. The degenerate modes in one FMF can be separately coupled with a specific degenerate modes in another FMF where the modes meet the phase-matching condition [25, 26]. In addition, by carefully choosing the spacing between fiber cores and fiber length, a direction-insensitive fiber coupler with high coupling efficiency can be designed [26, 27]. Moreover, it is reasonable to use the two degenerate modes as one signal carrier for a single-channel transmission [28], which is compatible with conventional intensity modulation and direct detection (IM/DD) systems or MIMO-FREE applications. In the literature [29], the 4-LP mode MIMO-FREE transmission with the IM/DD is achieved by cascading the degenerate modes selective coupler (DMSC) for simultaneous detection of the degenerate mode, which effectively solves the problem caused by the degenerate mode rotation, but there is a large insertion loss of −10.5 dB for the LP21 mode and a large mode crosstalk of −14.6 dB (LP11 input and LP01 output) at 1550 nm.

In this study, combining the advantages of the pure silica core, FMF ring-core, directional coupling method, and degenerate modes output, we propose a novel three-dimensional architecture mode (de)multiplexer with degenerate modes output using the pure silica FMF ring core transmission channel, which solves the problem caused by random mode rotation and can be used in MIMO-FREE applications such as data center application in the future. By using pure silica cores, low loss performance is achieved, and the intrinsic loss of each mode is better than 0.164 dB/km. By employing the ring core transmission channel and larger effective refractive index difference, the high extinction ratio (ER) and good coupling efficiency are achieved. The coupling efficiency of each mode is better than −7.24 dB in the C-band and better than −0.178 dB at 1550 nm. The effective refractive index difference of each mode in the range of 1.50 μm–1.60 μm is higher than 4.18×10^{-3}, and the ER of each mode remains above 24.43 dB in the whole C-band and reaches above 31.60 dB at 1550 nm. We expect that the system based on our proposed (de) multiplexer can be applied in optical communication systems [30, 31, 32, 33], spectral detection and sensor systems [34, 35, 36, 37, 38] in the future, and so on.

2 (De)multiplexing principle of the degenerate modes output

2.1 Our proposed MUX/DEMUX with the degenerate modes output

Figure 1 shows that mode demultiplexing in two cases in the conventional mode demultiplexer occurs due to mode rotation during mode transmission. One case is (a) for the best coupling case with a rotation angle of $\pm k\pi$, $k = 0, 1, 2, \ldots, .$, and the other is (b) for the worst coupling one with a rotation angle of $\frac{\pi}{2} \pm k\pi$, $k = 0, 1, 2, \ldots, .$. In a conventional mode selective demultiplexer, there is only one mode coupling between two channels, as shown in the illustration in Figure 1. The FMF supports LP01, LP11a/LP11b, and LP21a/LP21b modes, and the TMF supports LP01 and LP11a/LP11b. Mode LP11b in the FMF is coupled to mode LP11b in the TMF, and thus mode LP11b is demultiplexed, while mode LP11a in the FMF cannot be demultiplexed into the TMF for a given length of the same transmission channel due to the coupling length of mode LP11a being very different from that of mode LP11b.

The spatial orientation of the mode may rotate randomly in the FMF during the mode transmission due to the non-circularity of fiber fabrication, fiber twist, and other factors. Figure 1A shows all modes are transmitted along the *Z*-axis, and both the channels are set in the XZ plane in parallel. It can be observed that the

mode coupling efficiency in the demultiplexed case is above −0.8 dB over the whole C-band, and the best value of −0.07 dB is achieved at 1550 nm. The aforementioned case is only a perfect transmission under ideal conditions. Although the mode demultiplexer remains unchanged, the demultiplexing transmission result is the worst, as shown in Figure 1B, when the mode direction is rotated by $\frac{\pi}{2} \pm k\pi$, $k = 0, 1, 2, \ldots$. The coupling efficiency of the mode demultiplexer is below −102 dB over the whole C-band, which indicates the mode demultiplexing function cannot be realized in this case. It shows that the conventional mode selective demultiplexer meets the problem of being unable to demultiplex or sharply reduce the bit error rate of demultiplexing due to the random mode rotation. In this study, we propose a novel MUX/DEMUX with the degenerate modes output, which can simultaneously multiplex/demultiplex the degenerate modes, solve the problems caused by the aforementioned random mode rotation, and can be used in MIMO-FREE applications.

2.2 (De)multiplexing principle of the degenerate modes output

Figure 2 shows the (de)multiplexing principle with the directional coupling method. Figure 2A is an illustration of the conventional MUX/DEMUX, and Figure 2B is that of our proposed MUX/DEMUX. Figure 2A shows the spatial orientation of the non-circular symmetric mode LP_{lm} ($l \neq 0$) in the FMF core is at an α angle to the horizontal line connecting the core axes [39]. It is proved that the coupling coefficient between the LP11 in the FMF core and the fundamental mode in a single-mode fiber has cos ($l\alpha$) dependence on the spatial orientation of the non-circular symmetric mode. The antisymmetry of the product of the electronic fields around the horizontal axis gives zero coupling coefficient for $\alpha = \pi/2l$, even though perfect phase matching is satisfied. No power of the higher-order mode can be coupled to the fundamental mode for $\alpha = \pi/2l$.

If the degenerate modes are simultaneously multiplexed/demultiplexed from fiber B into fiber A, then fiber A supports at least two spatial degrees of freedom. So, fiber A must be a FMF. However, the fiber B should not be the same as fiber A because all modes in the same fiber will satisfy the phase-matching condition at the same time, where the mode selectivity is lost. So, the best solution is that fiber A is designed as a TMF. As shown in Figure 2B, mode LPlma in the FMF B is coupled to mode LP11a in the TMF A, and mode LPlmb in the FMF B is coupled to mode LP11b in the TMF A at the same time, showing that mode multiplexing/demultiplexing with the degenerate modes output is achieved. The coupled-mode equations are as follows [29]:

$$\begin{bmatrix} \frac{dA^{A}_{11a}(z)}{dz} \\ \frac{dA^{B}_{lma}(z)}{dz} \end{bmatrix} = \begin{pmatrix} -j\beta_{11} & j\kappa_{a} \\ j\kappa_{a} & -j\beta_{lm} \end{pmatrix} \begin{bmatrix} A^{A}_{11a}(z) \\ A^{B}_{lma}(z) \end{bmatrix}, \tag{1}$$

where $A^{B}_{lma}(z)$ and $A^{B}_{lmb}(z)$ are the mode complex amplitudes of modes LPlma and LPlmb in the FMF B, respectively. $A^{A}_{11a}(z)$ and $A^{A}_{11b}(z)$ are the mode complex amplitudes of modes LP11a and LP11b in the TMF A, respectively. z is the axial distance along the coupler. β_{lm} is the propagation constant of modes LPlma and LPlmb in the FMF B. β_{11} is the propagation constant of modes LPlma and LPlmb in the TMF A. ka is the coupling coefficient between mode LPlma in the FMF B and mode LP11a in the TMF A. kb is the coupling coefficient between mode LPlmb in the FMF B and mode LP11b in the TMF A. Since the propagation constants of the degenerate modes are the same, mode LPlma in the FMF B and LP11a in the TMF A and mode LPlmb in the FMF B and LP11b in the TMF A should satisfy the phase matching condition at the same time, i.e., $\beta_{lm} = \beta_{11} = \beta$. Then, the complex amplitudes of LP11a/LP11b in the TMF A and LPlma/LPlmb in the FMF B are as follows:

$$\begin{bmatrix} \frac{dA^{A}_{11b}(z)}{dz} \\ \frac{dA^{B}_{lmb}(z)}{dz} \end{bmatrix} = \begin{pmatrix} -j\beta_{11} & j\kappa_{b} \\ j\kappa_{b} & -j\beta_{lm} \end{pmatrix} \begin{bmatrix} A^{A}_{11b}(z) \\ A^{B}_{lmb}(z) \end{bmatrix}, \tag{2}$$

$$\begin{bmatrix} A^{A}_{11a}(z) \\ A^{B}_{lma}(z) \end{bmatrix} = \begin{bmatrix} \cos(\kappa_{a}z) & j\sin(\kappa_{a}z) \\ j\sin(\kappa_{a}z) & \cos(\kappa_{a}z) \end{bmatrix} \times \begin{bmatrix} A^{A}_{11a}(0) \\ A^{B}_{lma}(0) \end{bmatrix} \exp(-j\beta z), \tag{3}$$

$$\begin{bmatrix} A^{A}_{11b}(z) \\ A^{B}_{lmb}(z) \end{bmatrix} = \begin{bmatrix} \cos(\kappa_{b}z) & j\sin(\kappa_{b}z) \\ j\sin(\kappa_{b}z) & \cos(\kappa_{b}z) \end{bmatrix} \times \begin{bmatrix} A^{A}_{11b}(0) \\ A^{B}_{lmb}(0) \end{bmatrix} \exp(-j\beta z). \tag{4}$$

Assuming no excitation power in the initial TMF A, the normalized power transfer functions for mode LP11a (LP11b) of the TMF A and mode LPlma (LPlmb) of the FMF B are obtained, respectively.

$$P_{11a}(z) = \frac{\left|A^{A}_{11a}(z)\right|^{2}}{\left|A^{B}_{lma}(0)\right|^{2}} = \sin^{2}(\kappa_{a}z), \tag{5}$$

$$P_{lma}(z) = \frac{\left|A^{A}_{lma}(z)\right|^{2}}{\left|A^{B}_{lma}(0)\right|^{2}} = \cos^{2}(\kappa_{a}z), \tag{6}$$

$$P_{11b}(z) = \frac{\left|A^{A}_{11b}(z)\right|^{2}}{\left|A^{B}_{lmb}(0)\right|^{2}} = \sin^{2}(\kappa_{b}z), \tag{7}$$

$$P_{lmb}(z) = \frac{\left|A^{A}_{lmb}(z)\right|^{2}}{\left|A^{B}_{lmb}(0)\right|^{2}} = \cos^{2}(\kappa_{b}z), \tag{8}$$

$$\kappa_{a}L = (2p+1)\frac{\pi}{2}, \tag{9}$$

$$\kappa_{b}L = (2q+1)\frac{\pi}{2}, \tag{10}$$

$$R_{ab} = \left|\frac{K_{1-l}\left(\frac{w_1 d}{a_1}\right) + K_{1+l}\left(\frac{w_1 d}{a_1}\right)}{K_{1-l}\left(\frac{w_1 d}{a_1}\right) - K_{1+l}\left(\frac{w_1 d}{a_1}\right)}\right| = \left|\frac{2p+1}{2q+1}\right|, \quad (11)$$

$$L = \frac{\pi(2p+1)}{2\kappa_a}. \quad (12)$$

The power of modes LPlma and LPlmb in the FMF B can be fully coupled to modes LP11a and LP11b in the TMF A when Eqs 9 and 10 are satisfied. L is the coupling length, p, q∈z. Eqs 9 and 10 show the phase-matching between the LPlm mode in the FMF and the LP11 mode in the TMF, which ensures maximum power transfer and mode selectivity. It is to be noted that the low-order LP mode of the FMF cannot match the LP01 mode of the TMF to avoid additional mode crosstalk. Eqs 11 and 12 ensure the simultaneous (de)multiplexing with the degenerate modes output. Generally, the phase-matching condition can be realized by choosing proper fibers or pre-tapering one fiber during the fabrication. Eqs 11 and 12 can be satisfied by tuning the core-to-core spacing and the coupling distance. That is to say, the (de)multiplexing principle of the degenerate modes output is based on phase-matching and transverse modal spatial distribution matching. The phase-matching is consistent with Eqs 9 and 10, which is the same as propagation constant matching and refractive index matching. The transverse modal spatial distribution matching consists of Eqs 11 and 12, which ensures simultaneous (de)multiplexing with the degenerate modes output.

The aforementioned results can also be verified using the beam-propagation method (BPM). We discuss the optimization of relevant parameters using the BPM. Figure 3 shows that the coupling efficiencies of the output modes LP11a/LP11b in the TMF1 at 1550 nm vary with the increase of the length of the fiber core channel in the case of the input modes LP11a/LP11b in the input FMF. The maximum power transfer and mode selectivity of the degenerate modes LP11a/LP11b are realized for phase-matching. The maximum power of the mode LP11a is well-consistent with that of LP11b by tuning the core-to-core spacing and the coupling distance, which ensures simultaneous (de)multiplexing with the output of the two degenerate modes. That is to say, Eqs 11 and 12 are satisfied by tuning the core-to-core spacing and the coupling distance, and the (de)multiplexing with the two degenerate modes output is achieved. In order to be convenient for the MUX/DEMUX fabrication, the maximum power of the mode LP11a can be basically consistent with that of LP11b by tuning the core-to-core spacing and the coupling distance. From Figure 3, the transmission channel length of the MUX/DEMUX can be L1 = 12.52 mm because the normalized coupling powers of the degenerate modes can reach the maximum in this case.

Figure 4 shows that the coupling efficiencies of the output modes LP11a/LP11b in the TMF2 at 1550 nm vary with the increase in the length of the fiber core channel in the case of the input modes LP21a/LP21b in the input FMF. From Figure 3, the transmission channel length of the MUX/DEMUX can be L2 = 8.95 mm because the normalized coupling powers of the degenerate modes can reach the maximum in this case.

2.3 Intrinsic loss of the transmission channel

The loss is one of the most important impairments that determine the capacity of fiber optic communication systems. The minimum loss of SMF is limited by two mechanisms, namely, Rayleigh scattering and infrared absorption loss.

Intrinsic loss of arbitrary transmission modes in optical fibers [40] α_{total},

$$\alpha_{total} = \alpha_R + \alpha_{IR} = \frac{A}{\lambda^4} + B\exp\left(-\frac{b}{\lambda}\right), \quad (13)$$

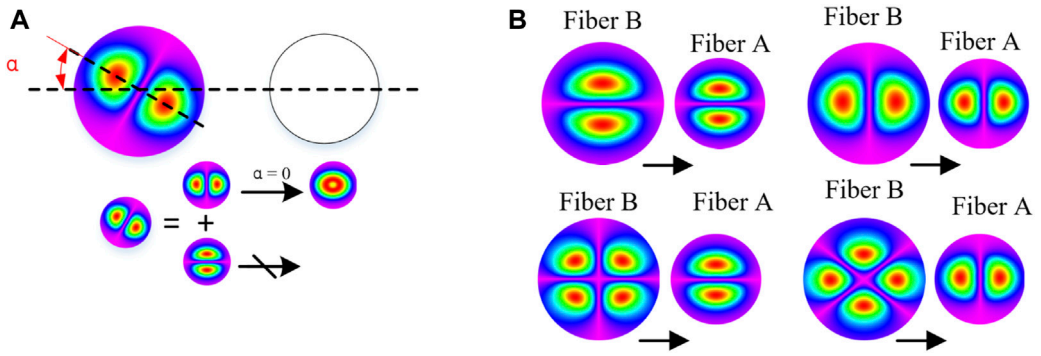

FIGURE 2
(De)multiplexing principle with the directional coupling method. **(A)** Illustration of conventional MUX/DEMUX. **(B)** Illustration of our proposed MUX/DEMUX.

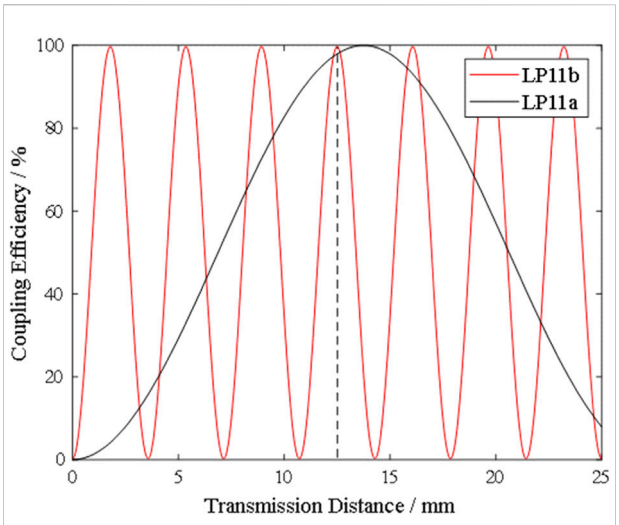

FIGURE 3
Variation of coupling efficiency of the output modes LP11a/LP11b in the TMF1 in the case of the input modes LP11a/LP11b in the FMF.

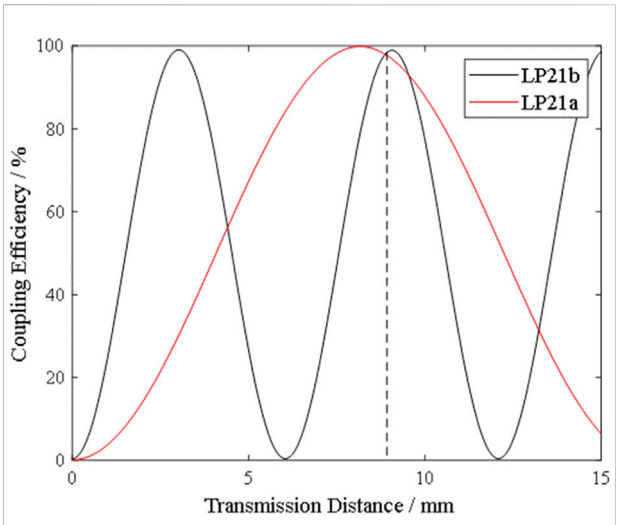

FIGURE 4
Variation of coupling efficiency of the output modes LP11a/LP11b in the TMF2 in the case of the input modes LP21a/LP21b in the FMF.

where α_R is the Rayleigh scattering loss, α_{IR} is the infrared absorption loss, A denotes the Rayleigh scattering coefficient, and B and b represent the correlation coefficients of the materials.

When the fiber is uniformly doped, the Rayleigh scattering loss can be expressed as

$$\alpha_R = \frac{1}{\lambda^4}\sum_i A_i(r)\Gamma_i \tag{14}$$

where $A_i(r)$ is the Rayleigh scattering coefficient in the fiber core or cladding, and the power limiting factor Γ_i is

$$\Gamma_{\text{core}} = \frac{\iint P_{\text{core}}(r,\theta)rdrd\theta}{\iint P_{\text{core}}(r,\theta)rdrd\theta + \iint P_{\text{clad}}(r,\theta)rdrd\theta} \tag{15}$$

$$\Gamma_{\text{clad}} = \frac{\iint P_{\text{clad}}(r,\theta)rdrd\theta}{\iint P_{\text{core}}(r,\theta)rdrd\theta + \iint P_{\text{clad}}(r,\theta)rdrd\theta} \tag{16}$$

$$\Gamma_{\text{core}} + \Gamma_{\text{clad}} = 1 \tag{17}$$

where $P_{\text{core}}(r,\theta)$ and $P_{\text{clad}}(r,\theta)$ are the modal power distributions in the fiber core and cladding, respectively.

The Rayleigh scattering coefficient of pure silica is $A_0 = 0.714\,(dB/km)\,(\mu m^4)$. The Rayleigh scattering coefficients of GeO_2-doped and F-doped are related to the difference of their refractive indices with respect to pure silica $|\Delta|$ related to

$$A_{Ge} = A_0(1 + 44|\Delta|) \tag{18}$$

$$A_F = A_0(1 + 41|\Delta|) \tag{19}$$

The infrared absorption loss of each mode supported by the FMF is the same as that of the fundamental mode in the SMF [40]:

$$\alpha_{IR} = B\exp\left(-\frac{b}{\lambda}\right) \tag{20}$$

where B and b are constants that depend only weakly on the doping level and λ is the wavelength. The parameters for pure silica cores and doped types of fibers are

$$B = 6\times10^{11}\text{dB/km}, b = 48\mu\text{m}\,(\text{pure silica fiber core}),$$
$$B = 7.81\times10^{11}\text{dB/km}, b = 48.48\mu\text{m}\,(GeO_2\text{ doped silica core}),$$
$$B = 6.5\times10^{11}\text{dB/km}, b = 49\mu\text{m}\,(\text{F}-\text{doped silica core}).$$

2.4 Coupling efficiency and extinction ratio of our proposed MUX/DEMUX

The coupling efficiency of the mode $LP_{lm}\,(l = 0, 1, 2;\ m = 1)$ is [27]

$$C_{LP_{lm}} = 10\cdot log_{10}\frac{P_{LP_{lm}}}{P_{in}}\,(l = 0, 1, 2; m = 1), \tag{21}$$

where P_{in} is the normalized input power of the main transmission channel and $P_{LP_{lm}}\,(l = 0, 1, 2;\ m = 1)$ is the normalized power of the modes LP01, LP11 (LP11a/LP11b), and LP21 (LP21a/LP12b) coupled into the TMF transmission channel.

The ER of the mode is [27]

$$ER = 10\cdot log_{10}\frac{P_{LP_{lm}}}{P_{LP_{others}}}\,(l = 0, 1, 2;\ m = 1), \tag{22}$$

where $P_{LP_{lm}}\,(l = 0, 1, 2; m = 1)$ are the normalized powers of the LP01, LP11, and LP21 modes coupled into the TMF transmission

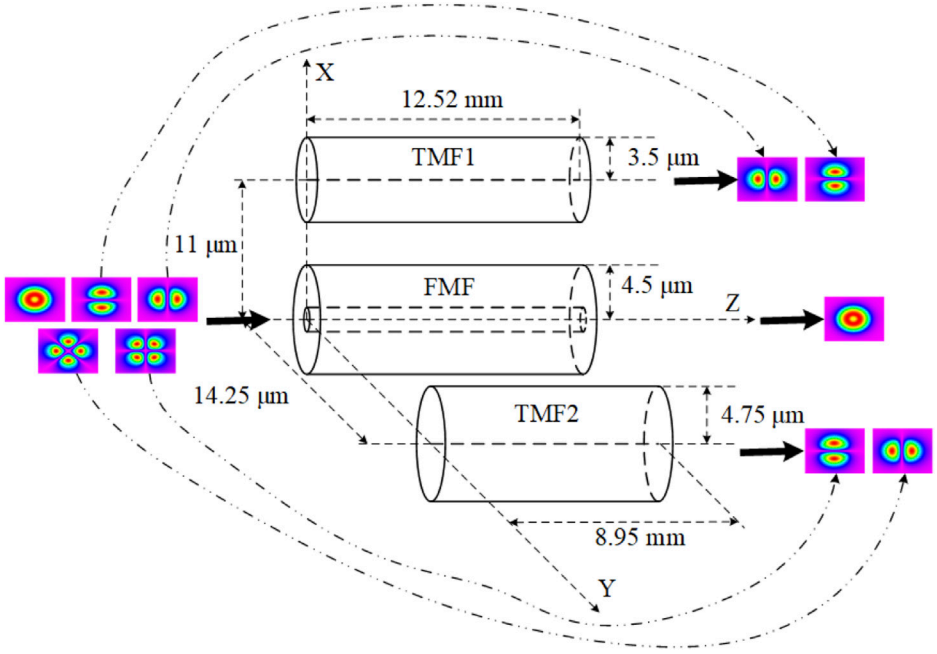

FIGURE 5
3D view of our proposed MUX/DEMUX.

channel, respectively. $P_{LP_{others}}$ is the sum of the other modes coupled into the TMF transmission channel.

Since the MUX/DEMUX can simultaneously multiplex/demultiplex two degenerate modes, its coupling efficiency and ER should be related to both the degenerate modes. Therefore, we normalize the experimental data of both the degenerate modes to characterize the MUX/DEMUX.

3 Structure and transmission characteristics of our proposed MUX/DEMUX

3.1 Architecture design of our proposed MUX/DEMUX

Three-dimensional (3D) mode-division MUX/DEMUX has the advantages of small size and easy integration compared to the traditional two-dimensional cascaded coupled mode-division MUX/DEMUX. We propose a mode-division MUX/DEMUX with degenerate modes output, as shown in Figure 5. As can be observed from Figure 5, our proposed MUX/DEMUX consists of three different FMF core transmission channels. We demonstrate the demultiplexing process of our proposed MUX/DEMUX as an example. The FMF ring-core is the main transmission channel of the MUX/DEMUX, supporting three modes, namely, LP01, LP11, and LP21. The FMF is placed on the z-axis, where the axis of the FMF coincides with the z-axis. Two different two-mode fiber (TMF) cores, namely, TMF1 and TMF2, which are made of the conventional single core, are placed in the x and y axes, respectively. The TMF_1 and TMF2 axes are parallel to the FMF axis from the x and y axes, respectively. The modes LP01, LP11, and LP21 are incident from the left end of the FMF core, which transmit and demultiplex along the z direction. We set that the mode LP01 is transmitted along the main transmission channel FMF from the left end to the right end. According to the coupling mode theory, the degenerate modes LP11a/LP11b are incident from the left end of the FMF, directly coupled to the modes LP11a/LP11b in the TMF1, respectively. That is to say, the demultiplexing of the modes LP11a/LP11b is achieved with the degenerate modes output. The degenerate modes LP21a/LP21b are incident from the left end of FMF, transformed and coupled into the modes LP11b/LP11a in TMF2, respectively. That is to say, the demultiplexing of the modes LP21a/LP21b is achieved with the degenerate modes output. So, the demultiplexing of three modes LP01, LP11, and LP21 is achieved from the main transmission channel FMF. The multiplexing process is inverse. If the degenerate modes LP01, LP11, and LP11 are incident from the left end of FMF, TMF1, and TMF2, respectively, the multiplexing with the degenerate modes output is achieved in the FMF along the z-direction.

According to the (de)multiplexing principle in Section 2.2, we optimize the relevant parameters of our proposed MUX/

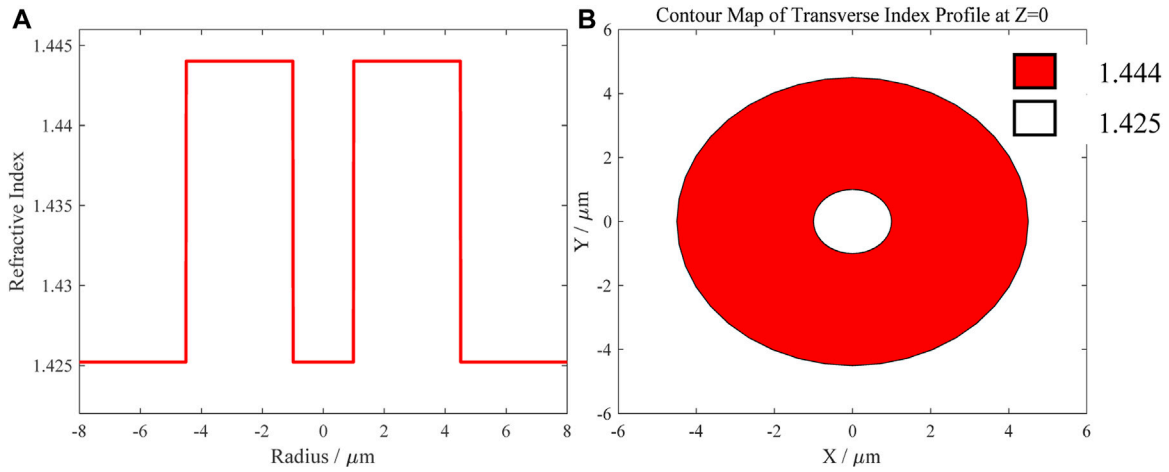

FIGURE 6
Refractive index distribution of FMF ring-core. **(A)** Refractive index distribution along the radial direction of the FMF ring-core. **(B)** Contour map of refractive index distribution along the cross-section of the FMF ring-core.

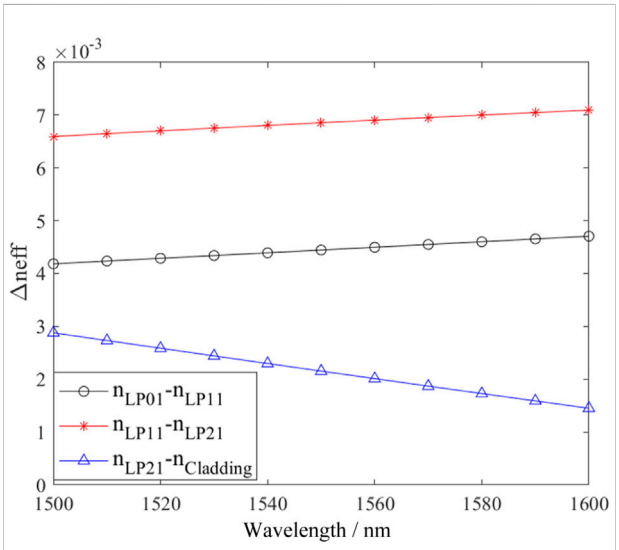

FIGURE 7
Effective refractive index difference between the modes in the FMF. The curve marked with the circles indicates the index difference between modes LP01 and LP11 $n_{LP01} - n_{LP11}$. The curve marked with the asterisks indicates the index difference between modes LP11 and LP21 $n_{LP11} - n_{LP21}$. The curve marked with the triangles indicates the index difference between mode LP21 and cladding $n_{LP21} - n_{Cladding}$.

DEMUX. The core diameter of TMF1 is 7 μm, the refractive index of the core is 1.4490, the TMF1 cladding is carried out with a F-doped silica of 1.4252, the axis distance between the two cores is 11 μm, and the transmission channel length of the TMF1 is L1 = 12.52 mm. The core diameter of TMF2 is 9.5 μm, the refractive index of the core is 1.4346, the TMF2 cladding and FMF cladding use the F-doped silica of 1.4252, the axis distance between the two cores is 14.25 μm, and the transmission channel length of the L2 = 8.95 mm. The FMF is the main transmission channel with ring core, where the part with 2 μm ≤ d ≤ 9 μm (the diameter d) is the ring core. The ring core is made of pure silica with a refractive index of n_1 = 1.4440, where the parts with d < 2 μm and d > 9 μm are the claddings with the F-doped silica refractive index of n_2 = 1.4252. Other parameters of the main transmission channel FMF are separately described in detail in the following sections due to their importance.

3.2 Refractive index distribution of the transmission channel of our MUX/DEMUX

The FMF core is an important transmission carrier to realize mode-division multiplexing technology. We propose a FMF ring-core with the step index distribution as the main transmission channel. This FMF ring-core supports three modes, LP01, LP11 (LP11b/LP11a), and LP21 (LP21a/LP21b). Figure 6 shows the refractive index distribution of the FMF ring-core, where plot (a) represents the refractive index distribution along the radial direction of the FMF ring-core and plot (b) represents the contour distribution along the cross-section of the FMF ring-core. The part with the diameter d < 2 μm is the inner cladding layer, which is made of F-doped silica with the refractive index n_2 = 1.4252. The part with 2 μm ≤ d ≤ 9 μm is the ring core, which is made of pure silica with the refractive index of n_1 = 1.4440. The part with d > 9 μm is the outer cladding, where the F-doped silica with the refractive index of n_2 = 1.4252 is used. The diameter of the outer cladding is 125 μm. The refractive index of the FMF

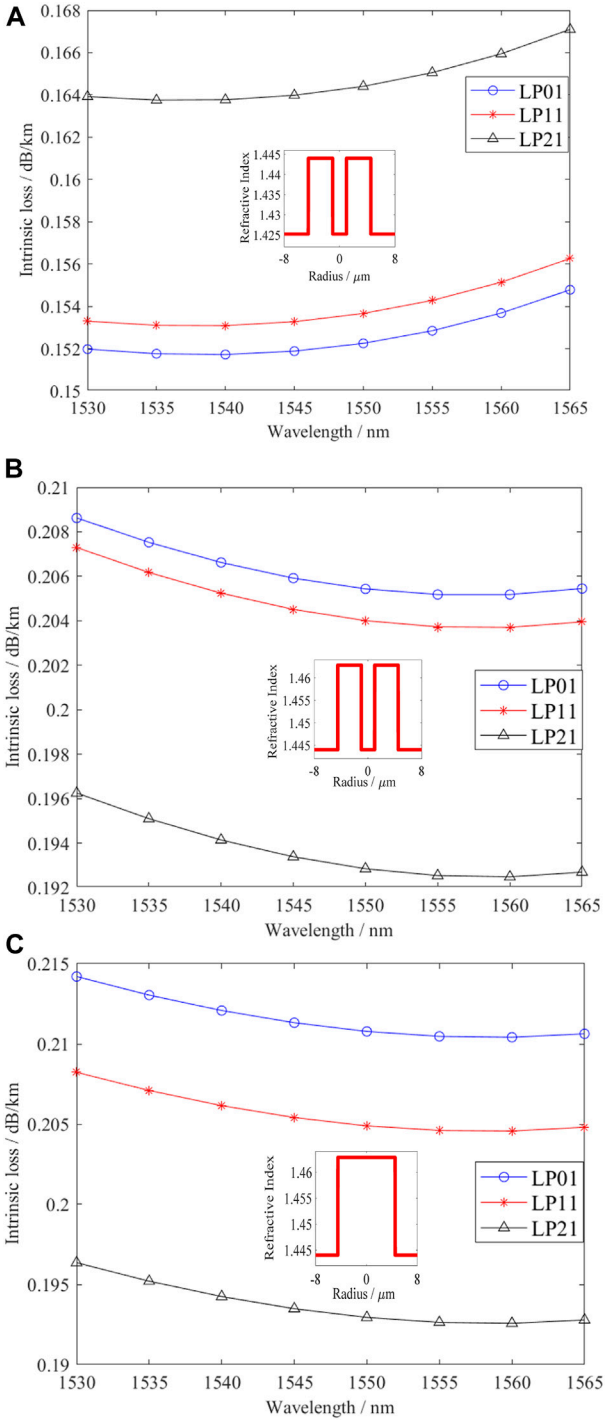

FIGURE 8
Intrinsic loss of the main transmission channel. **(A)** Intrinsic loss of pure silica FMF ring-core in our MUX/DEMUX. **(B)** Intrinsic loss of the equivalent FMF with GeO_2-doped ring-core. **(C)** Intrinsic loss of the equivalent FMF with the conventional GeO_2-doped single core.

ring-core is higher than that of the periphery, where the light is transmitted in the ring core. The mode field characteristics in the FMF ring-core can be changed by changing the size of the core, inner and outer cladding, and refractive index distribution. The use of pure silica ring-core effectively reduces fiber transmission loss and fusion loss.

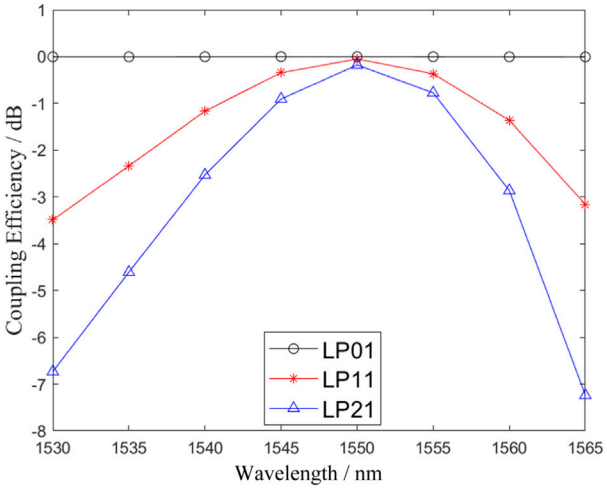

FIGURE 9
Coupling efficiency of each mode of our proposed MUX/DEMUX in the C-band.

Figure 7 shows the variations of the effective refractive index difference of the three modes, namely, LP01, LP11, and LP21, in the FMF ring-core in the wavelength range of 1500 nm–1600 nm, which are represented by the curves with the circles, asterisks, and triangles, respectively. Figure 7 shows that in the wavelength range of 1500 nm–1600 nm, the index difference between the mode LP01 and LP11 $n_{LP01} - n_{LP11}$ is greater than 4.18×10^{-3}, and it increases gradually with the increase of the wavelength. The index difference between modes LP11 and LP21 $n_{LP11} - n_{LP21}$ is greater than 6.59×10^{-3}, which gradually increases with the increase of the wavelength. The index difference between mode LP21 and the cladding $n_{LP21} - n_{Cladding}$ is greater than 1.45×10^{-3}, which gradually decreases with the increase of the wavelength. The index differences $n_{LP01} - n_{LP11}$ at 1540 nm and 1550 nm are 4.39×10^{-3} and 4.44×10^{-3}, respectively. Those of $n_{LP11} - n_{LP21}$ at 1540 nm and 1550 nm are 6.80×10^{-3} and 6.86×10^{-3}, respectively, and those of $n_{LP21} - n_{Cladding}$ at 1540 nm and 1550 nm are 2.30×10^{-3} and 2.15×10^{-3}, respectively. The low mode crosstalks of the transmission channels are achieved using the larger index difference.

3.3 Intrinsic loss of the transmission channel of our MUX/DEMUX

Using the method in the literature [40], we obtain the intrinsic loss of the main transmission channel of our MUX/DEMUX as follows. The reasons that the analysis of intrinsic loss is added in this study are as follows, first, our proposed (de)multiplexer is designed for the special transmission fiber, which is the same as our pure silica FMF ring-core transmission channel. The fusion loss between our (de)multiplexer and the transmission FMF is low due to their same transmission channel. Second, we can generally consider the (de) multiplexer and transmission FMF as a system. So, the intrinsic loss is suitable to be considered because the FMF length of the system is usually very long.

The results of the intrinsic losses of the main transmission channel are shown in Figure 8. Plot (a) represents the intrinsic loss of pure silica FMF ring-core in our proposed MUX/DEMUX, plot (b) shows the intrinsic loss of the equivalent FMF with GeO_2-doped ring-core, and plot (c) indicates the intrinsic loss of the equivalent FMF with the conventional GeO_2-doped single core. The inset shows the variation of the refractive index of the transmission channel with the radius. From Figure 8A, the intrinsic losses of all modes of the FMF ring-core transmission channel reach low values in the C-band. When the wavelength is 1540 nm, the intrinsic losses of the modes LP01, LP11, and LP21 are 0.152 dB/km, 0.153 dB/km, and 0.164 dB/km, respectively. At 1550 nm, the transmission loss of all three spatial modes is less than 0.164 dB/km, which is better than the 0.3 dB/km in the literature [41]. When the wavelength is less than 1540 nm, the intrinsic losses of the three modes increase with the decrease of the wavelength, mainly because the Rayleigh scattering losses become larger with the decrease of the wavelength. When the wavelength is larger than 1540 nm, the intrinsic losses of the three modes increase with the increase of the wavelength, mainly because the infrared losses become larger with the increase of the wavelength. Therefore, the optical loss is effectively reduced by using pure silica ring-core, and the crosstalk can be effectively reduced by using a large effective refractive index difference between the modes. This achieves the operation of low-loss and low-crosstalk, which further improves the performance of the transmission channel. Figure 8B shows that the intrinsic losses of all three modes in the FMF with GeO2-

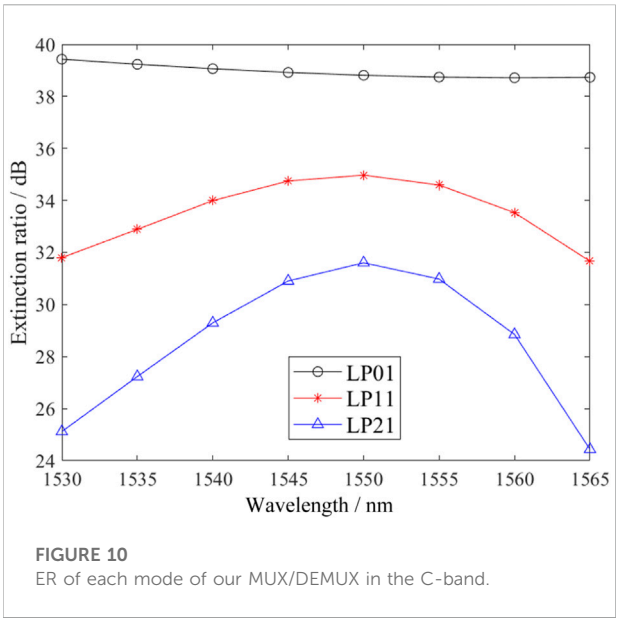

FIGURE 10
ER of each mode of our MUX/DEMUX in the C-band.

doped ring-core are larger than those of our proposed FMF with the pure silica ring-core. The lowest intrinsic losses of all three modes are achieved at 1560 nm with the lowest values of 0.205 dB/km, 0.204 dB/km, and 0.193 dB/km, respectively. The intrinsic losses of the three modes vary with the wavelength, which is similar to that in Figure 8A. From Figure 8C, it can be observed that the intrinsic losses of the three modes of the conventional FMF with GeO2-doped single core are greater than those of our proposed FMF ring core, where the variation of intrinsic losses with the wavelength is also similar to that in Figure 8A. The lowest intrinsic losses of the three modes are achieved at 1560 nm with 0.210 dB/km, 0.205 dB/km, and 0.193 dB/km, respectively, which are 38%, 34%, and 18% larger than those of the three modes in our proposed FMF ring core in Figure 8A.

Figure 8 shows that the variations of the intrinsic losses with the wavelength are similar in the three FMFs, and the intrinsic loss of our proposed FMF with the pure silica ring-core is very lower than those of other two equivalent FMFs with GeO2-doped core. This can induce the lowest optical transmission loss and fusion loss in our proposed FMF ring core and also avoid the power imbalance of the signal transmission amplification and detection caused by the very low loss difference between the modes.

3.4 Coupling efficiency and ER of our proposed MUX/DEMUX

Figure 9 gives the variation of the coupling efficiency of each spatial mode of our proposed MUX/DEMUX with the incident wavelength in the C-band. The coupling efficiencies of modes LP01, LP11, and LP21 are indicated by the curves with the circles, asterisks, and triangles, respectively. The coupling efficiency of mode LP11 is the average efficiency of the degenerate modes LP11a and LP11b, while that of mode LP21 is the average one of the degenerate modes LP21a and LP21b. The coupling efficiency of mode LP01 is approximately 0 dB, which is almost unchanged with the increase of the wavelength. At 1550 nm, the coupling efficiencies of modes LP01, LP11, and LP21 are −0.002 dB, −0.052 dB, and −0.178 dB, respectively. The coupling efficiencies of the degenerate modes LP11 and LP21 are decreased in the C-band on both sides of 1550 nm. The reason behind this is that the coupling period of each mode changes as the wavelength varies. Since the length of the transmission channel of our designed MUX/DEMUX is fixed, the maximum coupling efficiency of each wavelength cannot be reached simultaneously and changes with the wavelength. The coupling efficiency of LP11 is higher than −3.49 dB and that of LP21 is higher than −7.24 dB in the whole C-band. The coupling efficiency of LP01 mode is the best, while that of the degenerate mode LP11 is always better than that of mode LP21.

Figure 10 gives the variation of the mode ER of our MUX/DEMUX with the incident light wavelength. The ERs of the modes LP01, LP11, and LP21 are indicated by the curves with the circles, asterisks, and triangles, respectively. The ER of mode LP11 is the average ER of the degenerate modes LP11a and LP11b. The ER of mode LP21 is the average one of the degenerate modes LP21a and LP21b. The ER of mode LP11 can be maintained above 31.66 dB in the whole C-band, with a maximum value of 34.97 dB at 1550 nm. The ER of LP21 mode is above 24.43 dB, with a maximum value of 31.60 dB at 1550 nm. The ERs of modes LP21 and LP11 are decreased on both sides of 1550 nm. The ER of LP01 mode is the best, while that of the degenerate mode LP11 is always better than that of the mode LP21.

4 Conclusion

Combining the advantages of pure silica core, FMF ring-core, the directional coupling method, and the degenerate modes output, we use degenerate modes LP11a/LP11b and LP21a/LP21b as two independent channel signals and achieve the mode multiplexer/demultiplexer of LP01, LP11, and LP21 modes with the degenerate modes output, which can be used in MIMO-FREE applications. The pure silica core is used to achieve low loss performance, and the intrinsic loss of each mode can be better than 0.164 dB/km. Low crosstalk and high ER are achieved by using a ring core and a large effective refractive index difference. The coupling efficiency of mode LP01 is approximately 0 dB, which is almost unchanged with the increase of the wavelength. The coupling efficiency of LP11 is higher than −3.49 dB and that of LP21 is higher than −7.24 dB in the whole C-band. At 1550 nm, the coupling efficiencies of the

modes LP01, LP11, and LP21 are −0.002, −0.052 dB, and −0.178 dB, respectively. The effective refractive index difference of each mode within 1.50–1.60 μm is maintained at 4.18×10^{-3}, and the ER of each mode is maintained above 24.43 dB in the whole C-band and reaches above 31.60 dB at 1550 nm. The coupling efficiency and ER of LP01 mode are the best, while those of the degenerate mode LP11 are always better than those of the modes LP21. Our proposed MUX/DEMUX achieves low crosstalk and high ER performance and solves the problem caused by the degenerate modes rotations during transmission. It is expected to solve the challenges of the current research on the FMF MUX/DEMUX, which has important academic and application values.

Data availability statement

The raw data supporting the conclusion of this article will be made available by the authors, without undue reservation.

Author contributions

HX contributed to data curation, formal analysis, validation, writing—original draft, and software. YS contributed to data curation, formal analysis, validation, writing—original draft, and software. YG helped with data curation, formal analysis, validation, writing—original draft, and software. XL assisted with conceptualization, project administration, supervision, funding acquisition, investigation, and methodology. HZ contributed to conceptualization, project administration, supervision, writing—review editing, funding acquisition, investigation, and methodology. CB helped with supervision, funding acquisition, investigation, and methodology. WH involved in supervision, funding acquisition, investigation, and methodology. HX assisted with supervision, funding acquisition, investigation, and methodology.

Funding

This work is supported in part by the National Natural Science Foundation of China (Grant Nos 61671227 and 61431009), the Shandong Provincial Natural Science Foundation (ZR2020MF012 and ZR2011FM015), and the Taishan Scholar Research Fund of Shandong Province.

Conflict of interest

The authors declare that the research was conducted in the absence of any commercial or financial relationships that could be construed as a potential conflict of interest.

Publisher's note

References

1. Ellis AD, Zhao J, Cotter D. Approaching the non-linear Shannon limit. *J Lightwave Technol* (2010) 28(4):423–33. doi:10.1109/JLT.2009.2030693

2. Li G, Bai N, Zhao N, Xia C. Space-division multiplexing: The next frontier in optical communication. *Adv Opt Photon* (2014) 6(4):413–87. doi:10.1364/AOP.6.000413

3. Gao Y, Li Y, Xing H, Li X, Zheng H, Bai C, et al. Research on mode division multiplexing optical transmission. *J Liaocheng Univ (Nat Sci Ed* (2022) 35(1):30–56. doi:10.19728/j.issn1672-6634.2021040006

4. Du J, Shen W, Liu J, Chen Y, Chen X, He Z. Mode division multiplexing: From photonic integration to optical fiber transmission [invited]. *Chin Opt Lett* (2021) 19(9):091301. doi:10.3788/col202119.091301

5. Dong Q, Liu Y, Zheng H, Li X, Bai C, Hu W, et al. Research on mode (de) multiplexing technology for mode-division multiplexing system. *J Liaocheng Univ (Nat Sci Ed* (2020) 33(2):50–67. doi:10.19728/j.issn1672-6634.2020.02.008

6. Wang X, Zheng H, Li X, Liu Y, Yu R, Bai C, et al. Recent progresses on few mode fibers for mode-division multiplexing system. *J Liaocheng Univ (Nat Sci Ed* (2019) 32(2):69–79. doi:10.19728/j.issn1672-6634.2019.02.011

7. Zhang J, Wu X, Fan Q, Yi X, Tan Z, Li J, et al. High-capacity bi-directional full-duplex transmission based on fiber-eigenmode multiplexing over a FMF with 2×2 MIMO. *Opt Express* (2021) 29(19):30473. doi:10.1364/OE.433972

8. Gao Y, Li Y, Li X, Zheng H, Bai C, Hu W, et al. An elliptical-core few-mode fiber with low loss and low crosstalk for the MIMO-FREE applications. *Front Phys* (2022) 9. doi:10.3389/fphy.2021.796549

9. Li Y, Wang X, Zheng H, Li X, Bai C, Hu W, et al. A novel six-core few-mode fiber with low loss and low crosstalk. *Opt Fiber Tech* (2020) 57:102211. doi:10.1016/j.yofte.2020.102211

10. Nejad RM, Tavakoli F, Wang L, Guan X, LaRochelle S, Rusch LA. RoF data transmission using four linearly polarized vector modes of a polarization maintaining elliptical ring core fiber. *J Lightwave Technol* (2018) 36(17): 3794–801. doi:10.1109/JLT.2018.2851613

11. Tomashuk AL, Kashaykin PF, Semjonov SL, Filippov AV, Bychkova EA, Galanova SV, et al. Comparison study of radiation-resistant polarization-maintaining PANDA fibers with undoped- and N-Doped-Silica core. *J Lightwave Technol* (2020) 38(20):5817–24. doi:10.1109/JLT.2020.3002651

12. Jung Y, Kang Q, Zhou H, Zhang R, Chen S, Wang H, et al. Low-loss 25.3 km few-mode ring-core fiber for mode-division multiplexed transmission. *J Lightwave Technol* (2017) 35(8):1363–8. doi:10.1109/JLT.2017.2658343

13. Wang Z, Lu Q, Tu J, Xiao Q, Shen L, Lan X, et al. Design, fabrication, and characterization of a low-index center and trench-assisted 7-ring-core 5-mode-group fiber for dense space-division multiplexing. *Opt Express* (2022) 30(1):650–63. doi:10.1364/OE.447823

14. Ge D, Gao Y, Yang Y, Shen L, Li Z, Chen Z, et al. A 6-LP-mode ultralow-modal-crosstalk double-ring-core FMF for weakly-coupled MDM transmission. *Opt Commun* (2019) 451:97–103. doi:10.1016/j.optcom.2019.06.015

15. Hasegawa T, Yamamoto Y, Tamura Y, Hayashi T, "Advances in ultra-low loss silica fibers, " in, *Frontiers in Optics 2016, OSA Technical Digest (online) (Optica Publishing Group, 2016)*, 2016, Paper FTu2B.2. doi:10.1364/FIO.2016.FTu2B.2

16. Tamura Y, Sakuma H, Yamamoto Y, Hasegawa T. Ultra-low loss silica core fiber for long haul transmission. In: *Conference on lasers and electro-optics*. San Jose, California (2018). p. SF2K.3. doi:10.1364/CLEO_SI.2018.SF2K.3

17. Dadabayev R, Malka D. A visible light RGB wavelength demultiplexer based on polycarbonate multicore polymer optical fiber. *Opt Laser Technol* (2019) 116: 239–45. doi:10.1016/j.optlastec.2019.03.034

18. Gelkop B, Aichnboim L, Malka D. RGB wavelength multiplexer based on polycarbonate multicore polymer optical fiber. *Opt Fiber Tech* (2021) 61:102441. doi:10.1016/j.yofte.2020.102441

19. Sakaguchi J, Klaus W, Delgado Mendinueta JM, Puttnam BJ, Luis RS, Awaji Y, et al. Large spatial channel (36-core × 3 mode) heterogeneous few-mode multicore fiber. *J Lightwave Technol* (2016) 34(1):93–103. doi:10.1109/JLT.2015.2481086

20. Li Y, Hu Z, Benton DM, Ali A, Patel M, Ellis AD. Demonstration of 10-channel mode- and polarization-division multiplexed free-space optical transmission with successive interference cancellation DSP. *Opt Lett* (2022) 47(11):2742. doi:10.1364/OL.456235

21. Zhang H, Wang Z, Xi L, Du C, Zhang X, Li H, et al. All-fiber broadband multiplexer based on an elliptical ring core fiber structure mode selective coupler. *Opt Lett* (2019) 44(12):2994. doi:10.1364/OL.44.002994

22. Liu H, Wen H, Zacarias J, Antonio-Lopez J, Wang N, Sillard P, et al. Demonstration of stable 3x10 Gb/s mode group-multiplexed transmission over a 20 km few-mode fiber. In: *Optical fiber communication conference*. San Diego: California (2018). p. W4J.2. doi:10.1364/OFC.2018.W4J.2

23. Hu T, Li J, Ge D, Wu Z, Tian Y, Shen L, et al. Weakly-coupled 4-mode step-index FMF and demonstration of IM/DD MDM transmission. *Opt Express* (2018) 26(7):8356–63. doi:10.1364/OE.26.008356

24. Gasulla I, Kahn JM. Performance of direct-detection mode-group-division multiplexing using fused fiber couplers. *J Lightwave Technol* (2015) 33(9):1748–60. doi:10.1109/JLT.2015.2392255

25. Liu Y, Dong Q, Zheng H, Li X, Bai C, Hu W, et al. Research on a novel mode division multiplexer with low crosstalk, low loss and few mode ring-core transmission channel. *Opt Commun* (2020) 469:125778. doi:10.1016/j.optcom.2020.125778

26. Li J, Du J, Ma L, Li MJ, Jiang S, Xu X, et al. Coupling analysis of non-circular-symmetric modes and design of orientation-insensitive few-mode fiber couplers. *Opt Commun* (2017) 383:42–9. doi:10.1016/j.optcom.2016.08.051

27. Joseph T, John J. Two-core fiber-based mode converter and mode demultiplexer. *J Opt Soc Am B* (2019) 36:1987–94. doi:10.1364/JOSAB.36.001987

28. Zuo M, Ge D, Liu J, Gao Y, Shen L, Lan X, et al. Long-haul intermodal-MIMO-free MDM transmission based on a weakly coupled multiple-ring-core few-mode fiber. *Opt Express* (2022) 30(4):5868–78. doi:10.1364/OE.451971

29. Gao Y, Cui J, Jia J, Du C, Xia C, Liu Y, et al. A degenerate-mode-selective coupler for stable DSP-free MDM transmission. *J Lightwave Technol* (2019) 37(17): 4410–20. doi:10.1109/JLT.2019.2925116

30. Zheng H, Li X, Liu S, Hu W, Bai C. Generation and transmission of a High-bit-rate optical millimeter wave with an unrepeated long single-span using equalization amplification. *Opt Commun* (2015) 356:599–606. doi:10.1016/j.optcom.2015.08.062

31. Wen H, Zheng H, Mo Q, Velázquez-Benítez AM, Xia C, Huang B, et al. Few-mode fibre-optic microwave photonic links. *Light Sci Appl* (2017) 8(6):e17021–8. doi:10.1038/lsa.2017.21

32. Zheng H, Li X, Bai C. *Transmission of chirped pulse in optical fiber*. Beijing: Sci Press (2018). p. 1–184. (in Chinese).

33. Wang X, Zheng H, Zhu L, Li X, Bai C, Hu W, et al. A long single-span dispersion-decreasing-like fiber transmission system. *Opt Laser Technol* (2019) 116: 338–44. doi:10.1016/j.optlastec.2019.03.046

34. Zhang Z, Zhang F, Xu B, Xie H, Fu B, Lu X, et al. High-sensitivity gas detection with air-lasing-assisted coherent Raman spectroscopy. *Ultrafast Sci* (2022) 2022: 1–8. doi:10.34133/2022/9761458

35. Fu Y, Cao J, Yamanouchi K, Xu H. Air-Laser-based standoff coherent Raman spectrometer. *Ultrafast Sci* (2022) 2022:1–9. doi:10.34133/2022/9867028

36. Qiao SD, Sampaolo A, Patimisco P, Spagnolo V, Ma YF. Ultra-highly sensitive HCl-LITES sensor based on a low-frequency quartz tuning fork and a fiber-coupled multi-pass cell. *Photoacoustics* (2022) 27:100381. doi:10.1016/j.pacs.2022.100381

37. Liu XN, Ma YF. Tunable diode laser absorption spectroscopy based temperature measurement with a single diode laser near 1.4 μm. *Sensors* (2022) 22:6095. doi:10.3390/s22166095

38. Ma YF, Lewicki R, Razeghi M, Tittel FK. QEPAS based ppb-level detection of CO and N_2O using a high power CW DFB-QCL. *Opt Express* (2013) 21(1): 1008–19. doi:10.1364/OE.21.001008

39. Gao Y, Li J, Xia C, Liu Y, He Y, Chen Z, et al. Stable 4×10 Gb/s MIMO-free IM/DD MDM transmission enabled by Degenerate-mode-selective Couplers. In: Proceeding of the 2018 European Conference on Optical Communication (ECOC); September 2018; Rome, Italy. IEEE (2018). p. 3. doi:10.1109/ECOC.2018.8535512

40. Liu Y, Yang Z, Zhao J, Zhang L, Li Z, Li G. Intrinsic loss of few-mode fibers. *Opt Express* (2018) 26(2):2107. doi:10.1364/OE.26.002107

41. Liang J, Mo Q, Fu S, Tang M, Shum P, Liu D. Design and fabrication of elliptical-core few-mode fiber for MIMO-less data transmission. *Opt Lett* (2016) 41(13):3058. doi:10.1364/OL.41.003058

frontiers | Frontiers in Physics

TYPE Review
PUBLISHED 14 November 2022
DOI 10.3389/fphy.2022.1058475

OPEN ACCESS

EDITED BY
Yufei Ma,
Harbin Institute of Technology, China

REVIEWED BY
Xiaopeng Dong,
Xiamen University, China
Fupeng Wang,
Ocean University of China,
Xiaohu Zhao,
China University of Mining and Technology, China
Qiang Wang,
Changchun Institute of Optics, Fine Mechanics and Physics (CAS), China

*CORRESPONDENCE
Zhaowei Wang,
zw.wang@qlu.edu.cn
Tongyu Liu,
tongyu.liu@vip.iss-ms.com

†These authors have contributed equally to this work

SPECIALTY SECTION
This article was submitted to Optics and Photonics,
a section of the journal
Frontiers in Physics

RECEIVED 30 September 2022
ACCEPTED 27 October 2022
PUBLISHED 14 November 2022

CITATION
Gong W, Hu J, Wang Z, Wei Y, Li Y, Zhang T, Zhang Q, Liu T, Ning Y, Zhang W and Grattan KTV (2022), Recent advances in laser gas sensors for applications to safety monitoring in intelligent coal mines.
Front. Phys. 10:1058475.
doi: 10.3389/fphy.2022.1058475

Recent advances in laser gas sensors for applications to safety monitoring in intelligent coal mines

Weihua Gong[1†], Jie Hu[2†], Zhaowei Wang[1*], Yubin Wei[1], Yanfang Li[1], Tingting Zhang[1], Qinduan Zhang[1], Tongyu Liu[1,2*], Yanong Ning[2], Wei Zhang[1] and Kenneth T. V. Grattan[1,3]

[1]Laser Institute, Qilu University of Technology (Shandong Academy of Sciences), Jinan, China, [2]Shandong Micro-Sensor Photonics Ltd., Jinan, China, [3]School of Science and Technology, City University of London, London, United Kingdom

Due to the extremely complex working conditions, various health and safety hazards are present in underground coal mines, which cause economic losses and heavy casualties. Among these hazards, methane gas explosion and coal combustion are recognized as the two major hazards to miners. Traditional electronic sensors in mine safety monitoring systems have problems such as low precision, a large amount of maintenance, and monitoring dead zones. In the past decade, gas sensors based on tunable diode laser absorption spectroscopy (TDLAS) have been extensively studied and tailored for use in the coal mine industry because of their advantages of high sensitivity, high stability, fast response, intrinsic safety, and remote monitoring. This invited paper introduces the recent progress and typical applications of TDLAS-based methane sensors, carbon monoxide sensors, and multi-gas monitoring systems in coal mine gas monitoring, fire prevention, and early warning in intelligent coal mines.

KEYWORDS

coal mine safety, gas sensor, TDLAS, methane, carbon monoxide, multi-gas

Introduction

Currently, coal is one of the primary energy sources, and it will remain so in the near future. In 2021, 81.73 billion tons of coal were produced worldwide, which is 6.0% more than that in 2020. There are more than 5,000 coal mines in China, of which more than 95% are underground coal mines. Coal mine safety is a very serious issue. In the past decade, gas outbursts and explosions and coal combustion have been the two main hazards encountered in underground coal mines, among which gas explosions are the main cause of very serious accidents, where more than 10 people have died. With the rapid development of gas monitoring systems, coal mine safety has been consistently improved, which is signified by the decrease in casualties. In 2002, China produced 1.4 billion tons of coal with 6995 casualties [1]. In 2021, the casualties decreased to 178 and the production

increased to 4.13 billion tons, corresponding to an improvement of 111 times in terms of the casualty rate per million tons of coal production (from 4.9 in 2002 to 0.044 in 2021). To further reduce the number of casualties in coal mines and ensure the safety of life and property, all the hazardous gases present in the mines need to be monitored online to prevent the potential accidents. With the rapid development of the Internet of Things (IoT), 5G communication technology, big data, and other new technologies, mine safety IoT and intelligent mines have gradually become a new trend. Different types of mine sensors, especially for methane, carbon monoxide, and other environmental gases, provide the essential environmental information and data basis for constructing mine safety IoT or intelligent mines. Among the requirements of intelligent mines, one of the most important aims is to reduce the workload of miners and realize intelligent sensing, comprehensive monitoring, autonomous analysis, early warning, and effective control. However, the traditional electronic sensors employed in mine safety monitoring systems cannot meet the key requirements of intelligent mines due to problems such as low precision, poor reliability, large amounts of maintenance, and monitoring dead zones.

For methane detection, the main sensors employed in coal mines are catalytic combustion methane sensors [2–4]. However, they have some unavoidable disadvantages, such as easy poisoning, poor selectivity, and regular calibration, which inevitably increase the workload on coal miners and increase the risk of death and injury to workers. Another methane sensor is the infrared gas sensor, which adopts a broadband infrared light source and an optical filter for differential photoelectric detection [5]. However, it is easily affected by humidity and temperature. Therefore, its reliability and stability are poor in the complex environment of underground coal mines. Additionally, electronic sensors are also employed that cannot be used in special hazard areas, such as goaf, which lead to blind areas in monitoring. In the past decades, with the rapid progress in modern optoelectronic technology, the spectral technology has become the focus of research teams at home and abroad [6, 7]. There are many gas detection methods based on spectroscopy, including cavity-enhanced absorption spectroscopy (CEAS) [8], cavity ring-down spectroscopy (CRDS) [9], photoacoustic spectroscopy (PAS) [10], photothermal spectroscopy (PTS) [11], laser Raman spectroscopy (LRS) [12], and tunable diode absorption spectroscopy (TDLAS) [13]. Because of their better environmental adaptability and reliability, gas sensors based on TDLAS are more and more widely used in the field of gas detection [14, 15]. TDLAS-based gas sensors utilize lasers instead of current and voltage to realize information perception and use optical fibers instead of cables as the information transmission medium. Therefore, laser gas sensors are more suitable for flammable, explosive, and humid coal mine environments. TDLAS technology has the great advantage of *in situ* online monitoring, and it has become an irreplaceable detection technology in intelligent mines [16–18]. In 1981, Reid J et al. reported the measurement of gas concentrations based on the second harmonic detection technique, which greatly promoted the development of high-precision TDLAS equipment [19]. Since 2017, laser methane sensors have been gradually employed in coal mines [20]. The maintenance period of methane sensors is extended from 2 weeks for the conventional catalytic combustion methane sensor to 6 months for the laser methane sensor. Consequently, it has significantly reduced the number of underground coal miners and improved the intelligence level of coal mines.

Fire is one of the major hazards in coal mines. Coal spontaneous combustion stems from coal residues in the goaf being oxidized and heat being accumulated, which consequently accelerates the combustion and causes fire [21, 22]. The presence and increase of CO are typical characteristics during the early stages of oxidation. When the oxidation becomes severe, the temperature starts to increase, and C_2H_4 appears. C_2H_2 is the final warning indicator; its presence signifies that fire is imminent. Therefore, for the early detection of coal combustion, CO is the most important characteristic gas to monitor. Carbon dioxide (CO_2), ethylene (C_2H_4), acetylene (C_2H_2), and other landmark gases are also important for monitoring spontaneous combustion hazards. Typically, the required detection sensitivity for CO is 1 ppm, and for C_2H_4 and C_2H_2, it is 0.1 ppm. Conventional monitoring technology is based on tubing bundle gas sampling systems and chromatography-based gas monitoring instruments [23], which are typically located at the ground monitor center and suffer from long delay times, cumbersome maintenance, and inaccuracy due to possible tubing leakage.

Based on the demands of intelligent coal mines, our group has developed various gas sensors based on TDLAS technology, which have been successfully demonstrated and applied in the construction of mine safety IoT and intelligent coal mines. In this invited paper, the principle, advantages, applications, and recent progress in TDLAS-based gas sensors used for coal mine safety are comprehensively introduced.

Principles of laser absorption spectroscopy

The physical basis of TDLAS technology is the absorption of light energy of a specific frequency by gas molecules. When the frequency of incident light is the same as the vibration frequency inside a molecule, the two resonantly couple, and the molecule absorbs light energy and produces a transition. When the vibration level transits from the ground state to the first excited state, the absorption is the fundamental frequency absorption. When the molecular vibrational level transitions from the ground state to the second excited state and above, the resulting absorption is overtone absorption [24, 25]. The

absorption peaks have significant characteristics, which can be used as a basis for determining the molecular type or atomic group of gas and can be used for the qualitative and quantitative analyses of gas.

The intensity of infrared light absorbed by gas molecules is related to not only the optical path of light in the material but also the concentration of gas. The Beer–Lambert law of absorption is satisfied between the initial and outgoing light intensities [26]:

$$I_t(\nu) = I_0(\nu)\, exp[-\alpha(\nu)CL], \tag{1}$$

where $I_0(\nu)$ is the input light power, $I_t(\nu)$ is the outgoing light intensity, C is the volume concentration of the gas, L is the length of the gas absorption path, and $\alpha(\nu)$ is the gas absorption coefficient, which is affected by the temperature and pressure as gas is compressible and which satisfies

$$\alpha(\nu) = S(T)g(\nu, \nu_0)P, \tag{2}$$

where $S(T)$ is the temperature dependence of the absorption coefficient, P is the ambient pressure, and $g(\nu, \nu_0)$ is the line-shape function. The three commonly used line-shape functions are the Lorentzian function, the Gaussian function, and the Voigt function. In the measurement environment of coal mines, the collision broadening of gas molecules is dominant. Therefore, the Lorentzian function is selected to describe the line-shape function of the absorption spectrum, which satisfies

$$g(\nu, \nu_0) = \frac{1}{\pi} \frac{\frac{\Delta\nu}{2}}{(\nu - \nu_0)^2 + \left(\frac{\Delta\nu}{2}\right)^2}, \tag{3}$$

where ν_0 is the central frequency of the absorption spectrum line and $\Delta\nu$ is the full width at half height of the spectral line caused by collision widening. The integral value of the line-shape function $g(\nu, \nu_0)$ in the full frequency domain is 1 unit. By carrying out logarithm calculations on both sides of Eq. 1 followed by integration, we have

$$S(T)PCL = -\int_{-\infty}^{+\infty} \frac{I_0(\nu)}{I_t(\nu)} d\nu = A. \tag{4}$$

Then, the volume concentration of the gas can be expressed as follows:

$$C = \frac{-\int_{-\infty}^{+\infty} \frac{I_0(\nu)}{I_t(\nu)} d\nu}{S(T)PL} = \frac{A}{S(T)PL}. \tag{5}$$

TDLAS technology mainly uses the narrow line width and tunability of tunable semiconductor lasers to measure one or several close absorption lines of gas molecules. Gas sensors based on TDLAS technology are highly sensitive and stable due to the tunable semiconductor laser's narrow line width, controllable operating temperature, and optical power output, which is the reason for the rapid development of this technology.

Laser methane sensor and applications to on-line monitoring of coal mine gas

Laser methane sensor

Methane (CH_4) is the most important gas in coal mine safety monitoring. When CH_4 in the concentration range of 5%–16% meets an open flame, it will immediately explode. By pressurizing fresh air flow from the ground to the coal mine, O_2 can be supplied underground, and the CH_4 concentration can be reduced. Methane gas has absorption peaks around the 3.3 μm and 1.65 μm bands. However, the mid-infrared (MIR) laser is very expensive and needs to be cooled. The 1.65 μm band is similar to an optical fiber communication band, and the photoelectric device is mature and cheap. Therefore, laser methane sensors usually choose the absorption peak near 1.65 μm for detection. Direct absorption spectroscopy (DAS) and wavelength modulation spectroscopy (WMS) are two signal processing methods widely used in TDLAS [27, 28]. Direct absorption detection can be realized by scanning the gas absorption signal with sawtooth current modulation laser wavelength. When the laser passes through the target gas, a curve rising with the laser wavelength is detected using the photodetector. The curve has a depression at the corresponding absorption peak. The gas absorption characteristic line can be obtained by normalizing the detection curve. The DAS system inverts the gas concentration by directly monitoring the attenuation of light intensity, and its experimental device and scheme are relatively simple. For the WMS system, the high-frequency modulated signal is superimposed on the low-frequency scanning signal as the driving signal of the laser. Then, the harmonic signal of the absorption spectrum is obtained by using the phase-locked amplification technology, and the gas concentration is detected according to the peak value of the harmonic signal. Most of the background noise, especially the 1/f noise, has the characteristics of high intensity in the low-frequency band and is greatly reduced in the high frequency. Therefore, the WMS system can effectively suppress the background noise introduced into the spectrum by circuit systems, optical devices, and optical–mechanical systems. It can effectively extract weak signals from noise and improve the detection sensitivity of spectral signals. Inaba H et al. first used the spectral absorption method to conduct long-distance air pollution monitoring [29]. Uehara K and Tai H used a 1.6-μm single-mode distributed feedback laser (DFB-LD) to detect methane gas concentration at room temperature [30]. The system used the harmonic method with wavelength modulation, and its minimum detectable sensitivity is 20 ppm. The system achieved high detection sensitivity due to the combination of DFB-LD, wavelength modulation harmonic detection technology, and optical fiber technology. Zhang

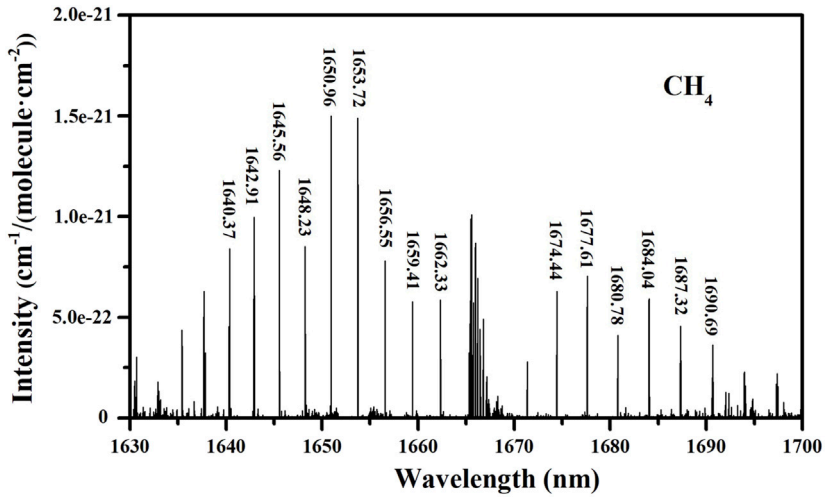

FIGURE 1
Absorption spectra of methane gas in the 1650 nm region.

et al. proposed a single-channel direct absorption methane measurement system with a 1.33-μm DFB-LD and an optical power meter with a response sensitivity of 1 nW [31]. They verified the linear relationship between the output electrical signal and the concentration when the concentration was less than 15%. Iseki et al. designed a portable methane telemetry sensor with a 1.65-μm DFB-LD and a measuring distance of 10 m and a measuring accuracy of 5 ppm [32]. The aforementioned studies greatly promoted the advancement of laser methane sensing technology.

Reducing the overall power consumption of laser methane sensors is important for application in underground coal mines. When the power consumption of a CH_4 sensor is too high, the number of sensors that can be supplied by an intrinsically safe power supply cannot meet the requirements of coal mine gas detection. Additionally, to meet the 6 km transmission distance requirement stipulated by the coal mine safety monitoring system, the sensor current and power consumption need to be reduced as much as possible to increase the detection distance between the sensor probe and the power supply substation. A vertical-cavity surface-emitting laser (VCSEL) has a considerably lower threshold current, operating current, and operating power consumption than the distributed feedback (DFB) laser [33, 34]. Generally, the current modulation regime of the DFB laser is about 10 p.m/mA and that of VCSEL is up to 400 p.m/mA. Thus, VCSEL has higher current-wavelength tuning characteristics than the DFB laser. Moreover, the wavelength modulation coefficient of VCSEL is smaller by temperature modulation and larger by current modulation [35]. With the development of long-wavelength VCSEL technology, the research on gas detection technology based on low-power VCSEL has become very attractive [36, 37].

In order to ensure that the laser output wavelength can lock the gas absorption peak stably, the conventional laser gas detection technology usually uses a semiconductor cooler to control the laser temperature within a certain range and uses the method of current trimming to measure the absorption spectrum line. The temperature control system of the laser increases the overall power consumption of the gas detection system. Our group developed a laser methane detection system based on VCSEL without a thermoelectric cooler (TEC). The system realized gas detection without a temperature control system, thus effectively reducing system power consumption. Based on the wide wavelength range of VCSEL, the multi-absorption peak intelligent tracking technology has been successfully developed. Figure 1 shows the absorption spectrum of methane gas in the near-infrared range. The wavelengths we selected to detect the absorption lines are 1642.9 nm, 1645.5 nm, 1650.9 nm, and 1653.7 nm. According to the absorption information of the reference gas chamber, the current feedback technology was used to control the laser to work on one of the aforementioned absorption peaks. According to the wavelength variation law of VCSEL with temperature, a dynamic adjustment relationship had been established between the gas detection absorption peak and temperature. The system realized methane detection by adaptively tracking the methane absorption line. Furthermore, the temperature and pressure characteristics of different absorption peaks have been studied. Subsequently, a laser methane-sensing module has been successfully developed with a power consumption of less than 100 mW at an ambient temperature of −20 to 60°C.

FIGURE 2
The developed laser methane sensor products.

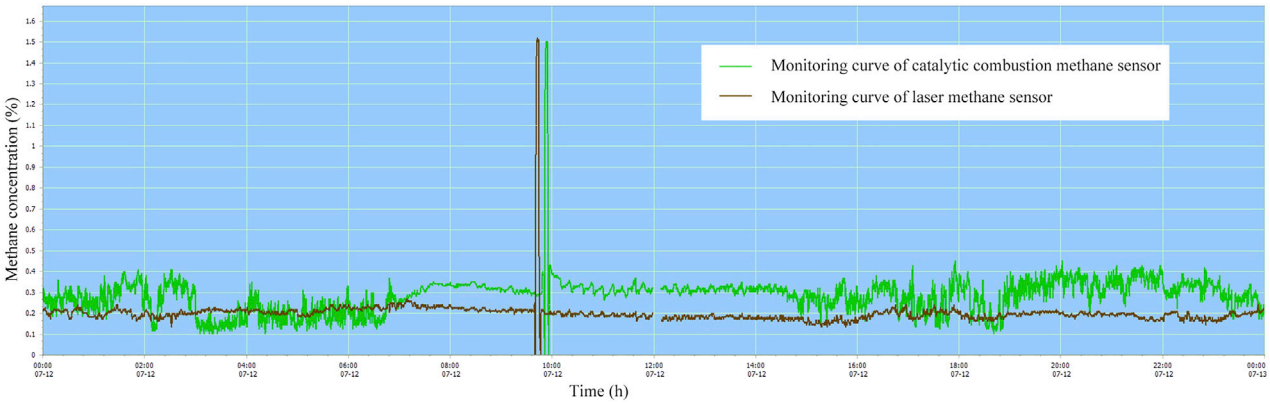

FIGURE 3
The methane monitoring data in 10307 working face.

Applications of the laser methane sensor in coal mine on-line monitoring

According to the safety regulations in coal mines, fixed or mobile methane sensors need to be installed in key areas of the mining face and return air roadways. When the methane concentration reaches 1.0%, a sound and light alarm will be set off, and when the methane concentration reaches 1.5%, power will be cut off for equipment in the related area [38]. Based on the high humidity and dust environment of coal mines, laser methane sensors need to conduct the engineering design of waterproof, dustproof, impact-resistant, anti-electromagnetic interference, and other necessary coal mine electrical equipment. Figure 2 displays the developed laser methane sensor products. These are the optical fiber methane sensor, the second-generation laser methane sensor, the latest miniaturization laser methane sensor, and the portable methane sensor. Currently, laser methane sensors are used in more than 1,000 coal mines in China. This application shows that their advantages, such as stability and moisture resistance, have been recognized by the coal mine industry. Laser methane sensors do not need to be recalibrated, which significantly reduces the workload of equipment maintenance personnel. With its low power consumption characteristics, the module can be used as a wireless sensor for remote detection in the upper corner of coal mines or gas drainage pipelines.

Figure 3 shows the continuous monitoring data of methane gas in 10,307 working faces of the Xinlongzhuang coal mine from 12 July to 13 July 2018. The results show that the monitoring curve of the laser methane sensor has a smaller fluctuation and a faster response than that of the traditional catalytic combustion methane sensor. Moreover, it verifies that the laser methane sensor is not easily affected by moisture, in contrast to the traditional catalytic element and infrared methane sensor, which are easily affected by moisture. Thus, laser methane sensors provide an effective way for methane monitoring in intelligent coal mines.

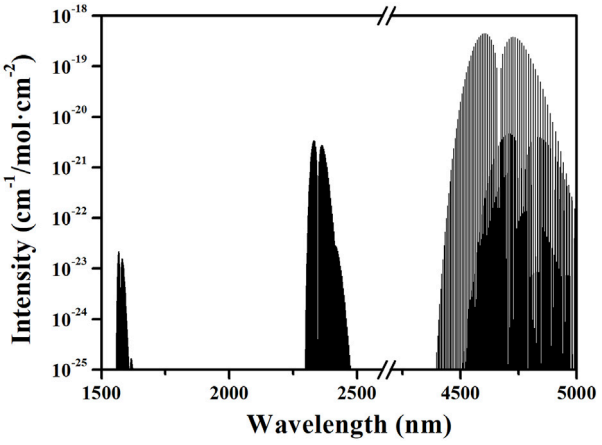

FIGURE 4
Absorption lines of CO from 1.5 μm to 5 μm.

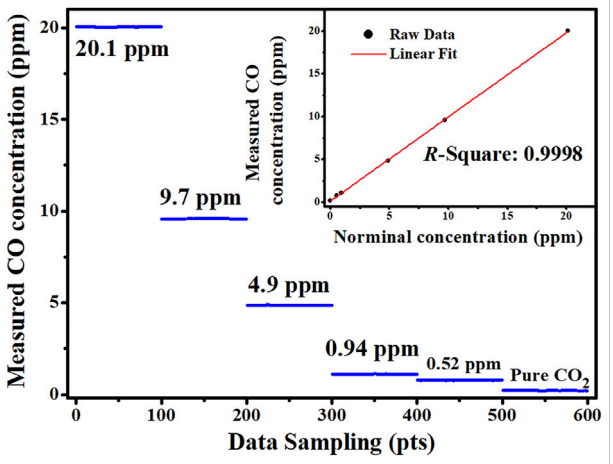

FIGURE 5
The typical measurement data of CO monitoring system.

Coal mine fire monitoring and early warning

In China, 95% of the coal mines are well coal mines, and more than 60% have a spontaneous combustion tendency. In goaf, coal can easily oxidize spontaneously and even develop into fire. In the early stage, the oxidation reaction mainly produces CO, and as the temperature increases, the oxidation reaction becomes violent and yields C_2H_4 and C_2H_2. Therefore, the presence of CO, C_2H_4, and C_2H_2 can be used for fire warning. Additionally, O_2, CH_4, and CO_2 are important gases that need to be monitored for the spontaneous combustion control of coal.

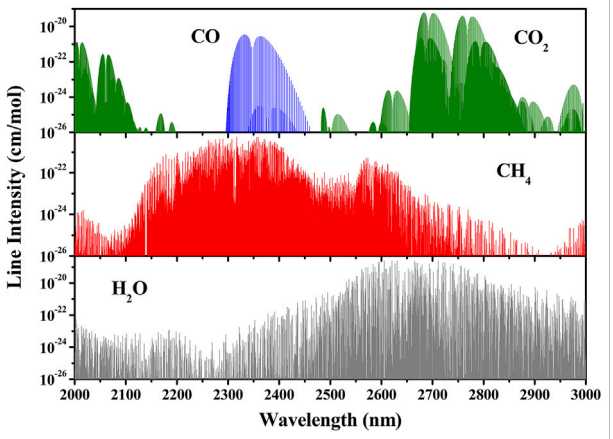

FIGURE 6
Absorption lines of CH_4, CO, CO_2, and H_2O at 2-3 μm.

Laser CO sensor

Accurate measurement of CO, the signature gas of early fire, is of decisive significance for the early diagnosis of fire and for providing sufficient time for prevention and control. The real-time monitoring of the CO concentration should be performed in coal seams that are prone to spontaneous combustion, such as return air lanes in mining areas, firewalls in closed fire areas, and spontaneous combustion observation points. The alarm trigger of the CO sensor is the CO concentration of 24 ppm. As depicted in Figure 4, CO affords absorption lines in the infrared region: the weak second overtone band (~1.56 μm), the first overtone band (~2.3 μm), and the strongest fundamental vibration band (~4.6 μm) [39]. According to the Beer–Lambert law, the performance of the laser CO sensors is closely related to the strength of the absorption lines. The figure shows that the near-infrared (NIR) absorption is about four magnitudes weaker than that around 4.6 μm. However, to use telecommunication laser devices and standard single-mode optical fibers, the harmonic absorption spectra in the NIR region are of interest. Xia et al. realized a detection sensitivity of 0.25 ppm in the 1566.6 nm band using the 56 m optical path and second harmonic technique [40]. Owing to the advantage of intrinsic safety, this sensor scheme can be successfully applied in coal mines. However, a long-path-length multi-pass gas cell must be employed in the developed NIR CO sensors. Therefore, complex structures and large volumes may be unavoidable for the NIR CO sensors.

As shown in Figure 4, the absorption lines of CO have coefficients of 3.47×10^{-21} (cm^{-1}/mol cm^{-2}) at 2.3 μm, which is about two magnitudes stronger than NIR absorption. Therefore, a highly sensitive CO sensor can be realized using a 2.3-μm laser. CO sensors with increasing sensitivity have been

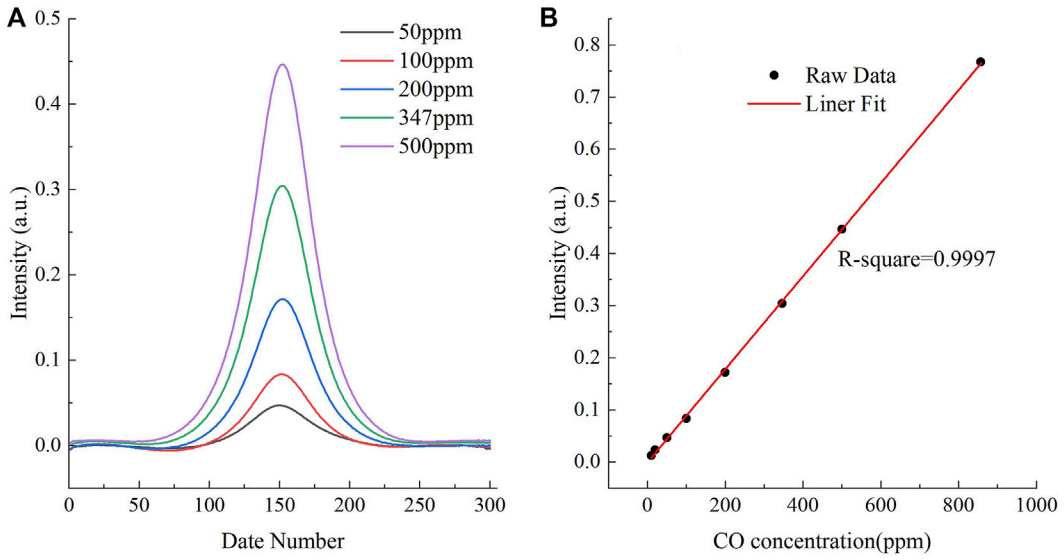

(a)Normalized absorption spectra of different concentration CO at 4.6 μm.

(b)The relation between the intensity(a.u.) and CO concentration.

FIGURE 7
The typical measurement data.

reported using a 2.3-μm laser diode. Dang et al. achieved a detection sensitivity of 0.06 ppm for CO monitoring with a 2334 nm absorption peak, which is therefore attractive for coal mining applications [41]. Chen et al. adopted a 2.3-μm VCSEL as the light source and realized the detection of trace CO using wavelength modulation and by introducing a reference chamber [42]. Wang et al. presented a stable and reliable CO monitoring system with high sensitivity for use in the mining industry in particular, tailoring the design specifically for forecasting spontaneous combustion [43]. Their results are shown in Figure 5.

The main difficulty in CO detection in underground coal mines is the elimination of the influence of CH_4, CO_2, and humidity on the measurement. The absorption lines of CH_4, CO, CO_2, and H_2O at 2–3 μm are shown in Figure 6. Therefore, the problem of multi-gas cross-interference in the practical application of sensors in underground coal mines needs to be analyzed and solved. In the 2.33 μm band, CH_4 has a serious effect on CO. Although it can be compensated by measuring the methane concentration, the compensation effect is limited due to the limitations of the methane measurement accuracy.

In the MIR band of 4.6 μm, several strong CO absorption peaks are present, which are not interfered by CH_4 and CO_2. With the rapid development of MIR laser technology, the TDLAS-based CO sensor has made a new breakthrough [44–46]. In recent years, compact CO sensors with ultra-high

TABLE 1 Measurement requirements of multi-gas monitoring.

Gas	Full-scale	Resolution		Unit
CO	0–1000	0–100	±4	10^{-6}
		100–500	±5% true value	
		500–1000	±6% true value	
CO_2	0–5	0–0.5	±0.1	%
		0.5–5	±(0.08 + 5% true value)	
C_2H_2	0–100	0–2	±0.5	10^{-6}
		2–5	±1	
		5–10	±2	
		10–20	±3	
		20–100	±(1 + 10% true value)	
C_2H_4	0–100	0–2	±0.5	
		2–5	±1	10^{-6}
		5–10	±2	
		10–20	±3	
		20–100	±(1 + 10% true value)	
CH_4	0–100	0–1	±0.1	%
		1–40	±10% true value	
		40–100	±10	

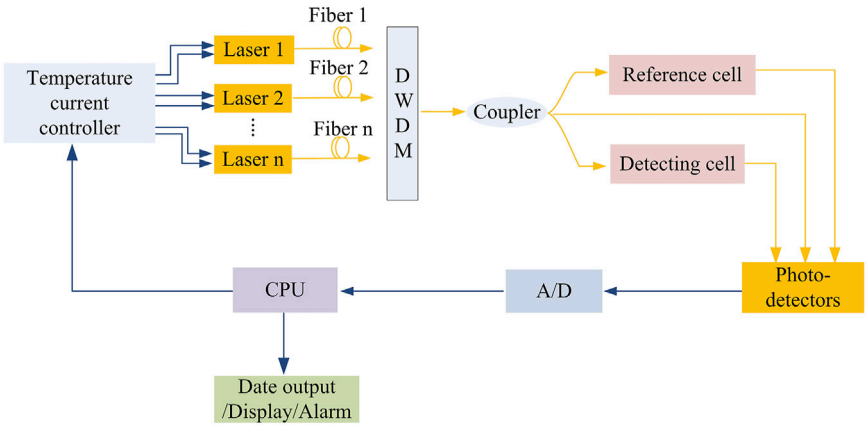

FIGURE 8
Block diagram of TDLAS-based multi-gas sensor system.

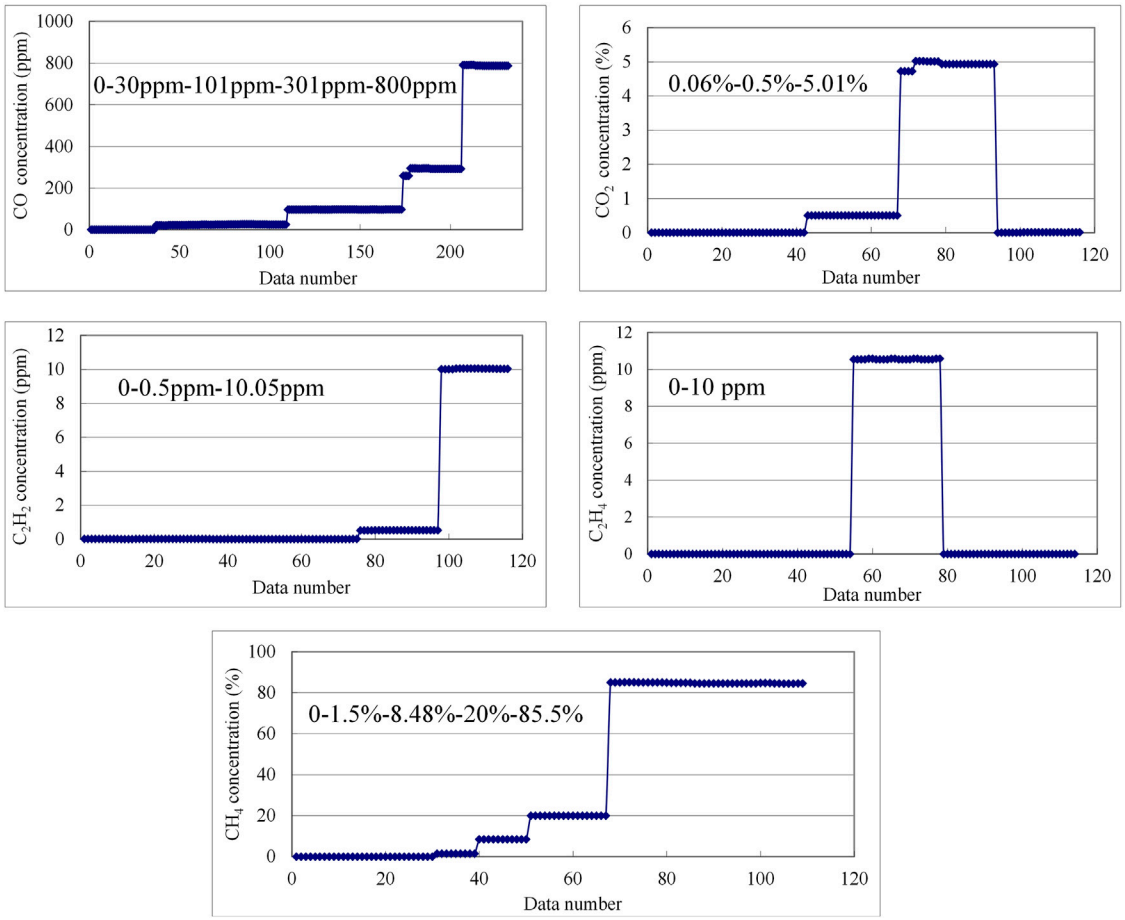

FIGURE 9
The test data of laser multi-gas monitoring system.

sensitivity have been reported using a room-temperature interband cascade laser or a quantum cascade laser (QCL) around 4.6 μm [47–49]. Our team developed a laser CO gas sensor with an optical path of 20 cm using a 4.6-μm QCL, and the measured results are shown in Figure 7. As shown in the figure, the detection sensitivity is greatly improved, even with short optical paths.

Multi-gas monitoring system

For early warning of coal spontaneous combustion, high precision and a wide dynamic detection range for the gas concentrations of CH_4, CO, CO_2, C_2H_4, and C_2H_2 as well as other markers are required. The typical measurement requirements for multi-gas monitoring are shown in Table 1.

In the recent years, considerable studies have been conducted on multi-gas monitoring [50–52]. Zhao et al. designed a detection system that can simultaneously detect CH_4, CO, and C_2H_2 by multiplexing 1653.72 nm, 2326.82 nm, and 1531.59 nm light sources [53]. However, the field application environment of coal mines has not been well studied. Based on the typical demand for coal mine fire monitoring and early warning, our group developed a laser multi-gas sensing system based on a multi-band semiconductor laser array. The schematic of the multi-gas sensing device is shown in Figure 8. The monitoring system solves the problem of the measurement error caused by the spectral overlap in a multi-component gas environment and realizes the simultaneous high-precision detection of trace gases and high-concentration gases. The test data on the laser multi-gas sensing device are shown in Figure 9. As an effective technical solution, the combination of the TDLAS-based multi-gas monitoring system and the fiber optic Raman-scattering-based distributed temperature sensor (DTS) provides early warning information about both the oxidation status and the hot zone location, which are increasingly used for goaf combustion monitoring in coal mines.

Conclusion

In the next few decades, coal will still occupy an important position in the energy structure. Therefore, the study on coal mine safety is of great significance. Multi-parameter monitoring in coal mines is challenging as the monitoring area is large, the environment is complex and harsh, and the number of objects to monitor is vast. With the advances in laser absorption spectroscopy, an increasing number of TDLAS-based gas sensors are being developed and applied in coal mines because of their unique advantages, including intrinsic safety, online detection, high precision, and reliability.

Coal mines have many hidden dangers, such as gas explosions and coal spontaneous ignition. Based on the monitoring needs of coal mine safety hazards, this invited paper focused on the research on laser methane sensors, CO sensors, multi-gas sensors and the application progress in gas monitoring and fire prevention. The laser methane sensor has realized full-range measurements with high precision, and field applications have shown that it has a significantly higher moisture resistance than infrared sensors. Since they do not require calibration, laser gas sensors can greatly reduce the maintenance workload, false alarm, and human fault. Aiming at the typical demand for multi-gas monitoring for coal mine fire monitoring and early warning, laser CO sensors and laser multi-gas sensing systems were demonstrated herein. With the rapid development of MIR laser technology, miniaturized laser trace gas sensors are gradually expected to be widely used in the coal mining industry.

With increasing coal mine safety, the emphasis has shifted toward mine safety IoT. For the monitoring and prevention of all hazards, mine safety IoT will be realized through the development of IoT and intelligent big data analysis. It is hoped that this invited paper can promote the application and technical progress of laser sensing technologies for mine safety and advance the rapid development of intelligent mines.

Author contributions

WG: methodology and writing—original draft. JH: methodology and writing—original draft. WG, JU, and ZW: writing—reviewing and editing. YW: validation. QZ: formal analysis. TZ: project administration and supervision. KG: conceptualization. YL: discussion and suggestions. TL: discussion and suggestions. WZ: proofreading. YN: resources.

Funding

This work was supported by the National Key Research and Development Program of China (Grant No. 2021YFB3201904), Natural Science Foundation of Shandong Province (Grant Nos. ZR2020QF098, ZR2020KC012, and ZR2022QF035), Innovation Team Program of Jinan (Grant Nos. 2020GXRC032 and 2021GXRC037), and Program from Qilu University of Technology (Grant Nos. 2022JBZ01-04, 2022GH001, 2022PX045, and 2022PT029).

Conflict of interest

JH, TL, and YN were employed by the company Shandong Micro-Sensor Photonics Ltd.

The remaining authors declare that the research was conducted in the absence of any commercial or financial relationships that could be construed as a potential conflict of interest.

Publisher's note

References

1. Wang WC, Qiao W, Wang RZ. Prediction research of annual death numbers and annual coal production in chinas coal industry based on simple linear regression. *Industry and Mine Automation* (2010) 36(12):27–9.

2. Su J, Cao L, Li L, Wei J, Li G, Yuan Y. Highly sensitive methane catalytic combustion micro-sensor based on mesoporous structure and nano-catalyst. *Nanoscale* (2013) 5(20):9720–5. doi:10.1039/c3nr02916f

3. Li Z, Ding X, Hu Y, Yu Y, Gao S. Research of methane measuring technique with full range by catalytic combustion. In: 2014 Fourth International Conference on Instrumentation and Measurement, Computer, Communication and Control; 18-20 September 2014; Harbin, China (2014). 671–4. doi:10.1109/IMCCC.2014.143

4. Wang Y, Tong MM, Zhang D, Gao Z. Improving the performance of catalytic combustion type methane gas sensors using nanostructure elements doped with rare Earth cocatalysts. *Sensors* (2010) 11(1):19–31. doi:10.3390/s110100019

5. Wu YZ, Chen DY, Guo AF. Development of non-dispersive infrared methane gas transducer. *J China Coal Soc* (2007) 32(11):1224–7. doi:10.3321/j.issn:0253-9993.2007.11.022

6. Bogue R. Detecting gases with light: A review of optical gas sensor technologies. *Sensor Rev* (2015) 35(2):133–40. doi:10.1108/SR-09-2014-696

7. Zhang Z, Zhang F, Xu B, Xie H, Fu B, Lu X, et al. High-sensitivity gas detection with air-lasing-assisted coherent Raman spectroscopy. *Ultrafast Sci* (2022) 2022: 11–8. doi:10.34133/2022/9761458

8. Amiot C, Aalto A, Ryczkowski P, Toivonen J, Genty G. Cavity enhanced absorption spectroscopy in the mid-infrared using a supercontinuum source. *Appl Phys Lett* (2017) 111(6):061103. doi:10.1063/1.4985263

9. Hu M, Hu M, Wang W, Wang Q. Wavelength-scanned all-fiber cavity ring-down gas sensing using an L-band active fiber loop. *Appl Phys B* (2022) 128(2):30–7. doi:10.1007/s00340-022-07757-3

10. Wang Z, Wang Q, Zhang H, Borri S, Galli I, Sampaolo A, et al. Doubly resonant sub-ppt photoacoustic gas detection with eight decades dynamic range. *Photoacoustics* (2022) 27:100387. doi:10.1016/j.pacs.2022.100387

11. Wang Q, Wang Z, Zhang H, Jiang S, Wang Y, Jin W, et al. Dual-comb photothermal spectroscopy. *Nat Commun* (2022) 13:2181. doi:10.1038/s41467-022-29865-6

12. Fu Y, Cao J, Yamanouchi K, Xu H. Air-laser-based standoff coherent Raman spectrometer. *Ultrafast Sci* (2022) 2022:1–9. doi:10.34133/2022/9867028

13. Lackner M. Tunable diode laser absorption spectroscopy (TDLAS) in the process industries–a review. *Rev Chem Eng* (2007) 23(2):65–147. doi:10.1515/REVCE.2007.23.2.65

14. Sun J, Chang J, Zhang Q, Xie Y, Zhang Z, Feng Y, et al. Recent progress in research on TDLAS fiber optical gas sensor performance improvement. *SPIE* (2019) 11068:138–43. doi:10.1117/12.2523562

15. Werle P, Slemr F, Maurer K, Kormann R, Mucke R, Janker B. Near- and mid-infrared laser-optical sensors for gas analysis. *Opt Lasers Eng* (2002) 37(2/3):101–14. doi:10.1016/S0143-8166(01)00092-6

16. Dinh TV, Choi IY, Son YS, Kim JC. A review on non-dispersive infrared gas sensors: Improvement of sensor detection limit and interference correction. *Sensors Actuators B: Chem* (2016) 231:529–38. doi:10.1016/j.snb.2016.03.040

17. Liu XN, Ma YF. Tunable diode laser absorption spectroscopy based temperature measurement with a single diode laser near 1.4 μm. *Sensors* (2022) 22:6095. doi:10.3390/S22166095

18. Qiao SD, Sampaolo A, Patimisco P, Spagnolo V, Ma YF. Ultra-highly sensitive HCl-LITES sensor based on a low-frequency quartz tuning fork and a fiber-coupled multi-pass cell. *Photoacoustics* (2022) 27:100381. doi:10.1016/J.PACS.2022.100381

19. Reid J, Labrie D. Second-harmonic detection with tunable diode lasers—comparison of experiment and theory. *Appl Phys B* (1981) 26(3):203–10. doi:10.1007/BF00692448

20. Wei Y, Hu J, Zhang T, Fu X, Yang B, Bi W, et al. Mine laser methane sensor and its application development. In: 2017 2nd International Conference for Fibre-optic and Photonic Sensors for Industrial and Safety Applications (OFSIS). IEEE; Jan 8-10; Brisbane,Australia (2017). 56–62. doi:10.1109/OFSIS.2017.15

21. Lang L, Fu-Bao Z. A comprehensive hazard evaluation system for spontaneous combustion of coal in underground mining. *Int J coal geology* (2010) 82(1-2):27–36. doi:10.1016/j.coal.2010.01.014

22. Deng J, Xu JC, Ruan GQ. Review of the prediction and forecasting techniques of coal self-heating both at home and abroad. *J Xi'an Mining Inst* (1999) 19(4): 293–7. doi:10.13800/j.cnki.xakjdxxb.1999.04.002

23. Cliff D. *The ability of current gas monitoring techniques to adequately detect spontaneous combustion*. Australia: University of Queensland (2005). 219–24. Available at: http://espace.library.uq.edu.au/view/UQ:102988.

24. Sonnenfroh DM, Allen MG. Absorption measurements of the second overtone band of NO in ambient and combustion gases with a 1.8-μm room-temperature diode laser. *Appl Opt* (1997) 36(30):7970–7. doi:10.1364/AO.36.007970

25. Claps R, Englich FV, Leleux DP, Richter D, Tittel FK, Curl RF. Ammonia detection by use of near-infrared diode-laser-based overtone spectroscopy. *Appl Opt* (2001) 40(24):4387–94. doi:10.1364/AO.40.004387

26. Abitan H, Bohr H, Buchhave P. Correction to the beer-lambert-bouguer law for optical absorption. *Appl Opt* (2008) 47(29):5354–7. doi:10.1364/AO.47.005354

27. Liang R, Wang F, Xue Q, Wang Q, Wu J, Cheng Y, et al. A Fourier-domain-based line shape recovery method used in direct absorption spectroscopy. *Spectrochimica Acta A: Mol Biomol Spectrosc* (2022) 275:121153. doi:10.1016/j.saa.2022.121153

28. Wang F, Liang R, Xue Q, Wang Q, Wu J, Cheng Y, et al. A novel wavelength modulation spectroscopy gas sensing technique with an ultra-compressed wavelength scanning bandwidth. *Spectrochimica Acta Part A: Mol Biomol Spectrosc* (2022) 280:121561. doi:10.1016/j.saa.2022.121561

29. Inaba H, Kobayasi T, Hirama M, Hamza M. Optical-fibre network system for air-pollution monitoring over a wide area by optical absorption method. *Electron Lett* (1979) 15:749–51. doi:10.1049/el:19790536

30. Uehara K, Tai H. Remote detection of methane with a 1.66-μm diode laser. *Appl Opt* (1992) 31(6):809–14. doi:10.1364/AO.31.000809

31. Zhang Y, Wang HY, Gao XN. Methane sensing system based on infrared absorption. *Piezoelectrics & Acoustooptics* (2008) 30(2):156–8. doi:10.3969/j.issn.1004-2474.2008.02.010

32. Iseki T, Tai H, Kimura K. A portable remote methane sensor using a tunable diode laser. *Meas Sci Technol* (2000) 11(6):594. doi:10.1088/0957-0233/11/6/302

33. Lytkine A, Jaeger W, Tulip J. Multi-species gas detection with long-wavelength VCSEL. *Proc SPIE* (2004) 5594:155–63. doi:10.1117/12.570059

34. Lytkine A, Lim A, Jaeger W, Tulip J. Tunable diode laser spectroscopy of benzene near 1684 nm with a low-temperature VCSEL. *Appl Phys B* (2010) 99(4): 825–32. doi:10.1007/s00340-010-4024-8

35. Li Y, Chang L, Zhao Y, Meng X, Wei Y, Wang X, et al. A fiber optic methane sensor based on wavelength adaptive vertical cavity surface emitting laser without thermoelectric cooler. *Measurement* (2016) 79:211–5. doi:10.1016/j.measurement.2015.09.044

36. Hangauer A, Chen J, Seemann K. Compact VCSEL based CO2 and H2O sensor with inherent wavelength calibration for safety and air-quality applications. In: Conference on Lasers and Electro-Optics: Applications; 16-21 May; San Jose,California (2010). JThB3. doi:10.1364/CLEO.2010.JThB3

37. Li YF, Yue JH, Meng H. Optic fiber sensing technology based safety monitoring system for coal mine gas drainage. *Shandong Sci* (2014) 27(3):51–6. doi:10.3976/j.issn.1002-4026.2014.03.010

38. Sun JP. Proposal of revision for monitoring, communication and video surveillance of coal mine safety regulation. *Industry and Mine Automation* (2014) 40(3):1–6. doi:10.13272/j.issn.1671-251x.2014.03.001

39. Rothman LS, Gordon IE, Babikov Y, Barbe A, Chris Benner D, Bernath P, et al. The HITRAN2012 molecular spectroscopic database. *J Quantitative Spectrosc Radiative Transfer* (2013) 130:4–50. doi:10.1016/j.jqsrt.2013.07.002

40. Xia H, Wu B, Zhang ZR, Pang T, Dong F-Z, Wang Y. Stability study on high sensitive CO monitoring in near-infrared. *Acta Phys Sin* (2013) 62(21):214208. doi:10.7498/aps.62.214208

41. Dang JM, Yu HY, Song F, Wang YD, Sun YJ. Development of a CO sensor for early fire detection. *Optics and Precision Engineering* (2018) 26(8):1876–81. doi:10.3788/OPE.20182608.1876

42. Chen J. *Compact laser-spectroscopic gas sensors using vertical-cavity surface-emitting lasers*. Munich: Technical University of Munich (2016).

43. Wang ZW, Li YF, Zhang TT, Hu J, Wei Y, Liu T, et al. A long-term stable monitoring system for atmospheric carbon monoxide based on 2.3 μm laser absorption. *J Phys : Conf Ser* (2018) 1065(25):252017. doi:10.1088/1742.6596/1065/25/252017

44. Li JS, Deng H, Sun J, Yu B, Fischer H. Simultaneous atmospheric CO N2O and H2O detection using a single quantum cascade laser sensor based on dual spectroscopy techniques. *Sensors Actuators B: Chem* (2016) 231:723–32. doi:10.1016/j.snb.2016.03.089

45. Shen F, Akil J, Wang G, Poupin C, Cousin R, Siffert S, et al. Real-time monitoring of N2O production in a catalytic reaction process using mid-infrared quantum cascade laser. *J Quantitative Spectrosc Radiative Transfer* (2018) 221:1–7. doi:10.1016/j.jqsrt.2018.09.022

46. Liu NW, Xu LG, Zhou S, Zhang L, Li J. Soil respiration analysis using a mid-infrared quantum cascade laser and calibration-free WMS-based dual-gas sensor. *Analyst* (2021) 146(12):3841–51. doi:10.1039/D1AN00503K

47. Ma Y, Lewicki R, Razeghi M, Tittel FK. QEPAS based ppb-level detection of CO and N_2O using a high power CW DFB-QCL. *Opt Express* (2013) 21(1):1008–19. doi:10.1364/OE.21.001008

48. Du Z, Zhang S, Li J, Gao N, Tong K. Mid-infrared tunable laser-based broadband fingerprint absorption spectroscopy for trace gas sensing: a review. *Appl Sci* (2019) 9(2):338. doi:10.3390/app9020338

49. Kosterev A, Wysocki G, Bakhirkin Y, So S, Lewicki R, Fraser M, et al. Application of quantum cascade lasers to trace gas analysis. *Appl Phys B* (2008) 90(2):165–76. doi:10.1007/s00340-007-2846-9

50. Sun J, Chang J, Wei Y, Zhang Z, Lin S, Wang F, et al. Dual gas sensor with innovative signal analysis based on neural network. *Sensors Actuators B: Chem* (2022) 373:132697. doi:10.1016/j.snb.2022.132697

51. Zhang T, Jiang T, Ning Y, Hu J, Liu T, Sun T, et al. High precision synchronous detection method for multi-gas detection using a single laser. *J Phys : Conf Ser* (2018) 1065(25):252013. doi:10.1088/1742-6596/1065/25/252013

52. Wang Z, Zhang H, Wang J, Jiang S, Gao S, Wang Y, et al. Photothermal multi-species detection in a hollow-core fiber with frequency-division multiplexing. *Sensors Actuators B: Chem* (2022) 369:132333. doi:10.1016/j.snb.2022.132333

53. Zhao XH, Sun PS, Zhang ZR. Wide-range multi-gas detection method based on wavelength modulation spectroscopy and direct absorption spectroscopy. *Infrared Laser Eng* (2022). doi:10.3788/IRLA20220248

frontiers | Frontiers in Physics

TYPE Original Research
PUBLISHED 14 November 2022
DOI 10.3389/fphy.2022.1057992

OPEN ACCESS

EDITED BY
Yufei Ma,
Harbin Institute of Technology, China

REVIEWED BY
Jun Dong,
Xi'an University of Posts and Telecommunications, China
Weizhen Liu,
Northeast Normal University, China
Ming Li Wang,
Yanshan University, China

*CORRESPONDENCE
Mei Liu,
liumei@sdnu.edu.cn
Chao Zhang,
czsdnu@126.com

†These authors have contributed equally to this work

SPECIALTY SECTION
This article was submitted to Optics and Photonics, a section of the journal Frontiers in Physics

RECEIVED 30 September 2022
ACCEPTED 17 October 2022
PUBLISHED 14 November 2022

CITATION
Liu M, Duan P, Shafi M, Liu W, Zhang W, Zhang C, Hu X, Gao J and Zhang C (2022), Surface-enhanced Raman spectroscopic activity study on topological ZnSe nanostructures. *Front. Phys.* 10:1057992. doi: 10.3389/fphy.2022.1057992

Surface-enhanced Raman spectroscopic activity study on topological ZnSe nanostructures

Mei Liu[1*†], Pengyi Duan[1†], Muhammad Shafi[1], Wenying Liu[1], Wenjie Zhang[1], Can Zhang[1], Xiaoxuan Hu[1], Jing Gao[2] and Chao Zhang[1*]

[1]School of Physics and Electronics, Shandong Normal University, Jinan, China, [2]Shandong Normal University Library, Shandong Normal University, Jinan, China

Topological nanomaterials generally exhibit different defect structures, high specific surface areas, and varying bandgaps. These special geometries, energy-level structures, and interfacial interaction properties provide possibilities to explore interesting properties in the surface-enhanced Raman scattering (SERS). Such properties offer unexplored possibilities for exploring interesting physics and materials science in the field of SERS physical property research and further enhancing substrate materials' SERS activity. In this paper, the ZnSe topological nanowire crystallite structure was grown using the chemical vapor deposition method, twin defects were introduced, and a topological branched structure that caused the corresponding changes in SERS activity was systematically investigated. On topological ZnSe nanowires, rhodamine 6G (R6G), methylene blue (MB), and crystalline violet (CV) molecules were detected using Raman spectroscopy. The Raman signal enhancement of MB on topological branched nanowires was about 1.9 times that of the trunk nanowires. Finally, the national standard measurement of malachite green (MG) content in water bodies were realized. The results suggest that semiconductor ZnSe topographical nanowires are an emerging class of SERS substrates, and a thorough investigation into the relationship between material structure and SERS performance in specific topological regions will provide new evidence for the principle of chemical enhancement of SERS, as well as recommendations for developing precisely functionalized SERS substrate nanomaterials.

KEYWORDS

surface-enhanced Raman scattering, growth defect nanowires, topological nanostructure, energy-level matching, charge transfer

1 Introduction

Recently, surface-enhanced Raman scattering (SERS) is an accurate and reliable molecular fingerprint technology widely used in biological medicine, environmental monitoring, disease diagnosis, chemical reagent detection and homeland security [1–5]. The scattering enhancement observed in SERS mainly has two mechanisms: electromagnetic (EM) and

chemical (CM) enhancement mechanism [6–8]. EM is mainly based on surface plasmon resonance generated by the interaction between the laser source and the SERS active substrate [9, 10]. With the ultra-high SERS enhanced factor up to 10^{12}, noble metal nanomaterials (such as gold, silver, and copper) enhanced *via* this mechanism enable ultra-sensitive molecular detection [6, 11]. However, because their local surface plasmon resonance covers the majority of visible and near-infrared wavelengths, their selectivity to target molecules is not strong. Meanwhile, the high cost, poor biocompatibility, and poor spectral stability seriously limit their practical applications [12, 13]. The CM-SERS activity mainly comes from the charge transfer (CT) between the substrate and probe molecules. With the development of materials science, various semiconductor materials have been introduced into the research of SERS and CM-SERS has played an important role [14, 15]. The study found that when semiconductor nanomaterials are used as SERS substrates, many parameters such as exciton Bohr radius, band structure, doping type, electron density, chemical stability, stoichiometry, geometric metrology, and crystallinity are controlled. Meanwhile, semiconductor substrates' spectral stability and repeatability are better than metal substrates.

For semiconductors, doping elements and constructing new structural morphologies can contribute to the improvement of SERS performance [16–18]. One-dimensional nanomaterials exhibit special properties, such as lateral quantum confinement and high specific surface area, resulting in severe uncoordinated surface atoms, providing more active sites for adsorbed molecules. The surface-trapped state of a surface-modified $W_{48}O_{19}$ nanowire provides an intermediate energy level for charge transfer to further improve the SERS performance of the substrate [19]. A self-assembly superstructured CuO_2 with a large number of copper vacancies demonstrates that defect states facilitate the resonant coupling of charge-transfer complexes with incident light and enhance the Raman scattering of target molecules [20]. Constructing the topological structure of one-dimensional materials and studying the SERS performance of topological branches will establish the connection between topological materials and SERS research.

ZnSe is a SERS active semiconductor compound with a bandgap of 2.7 eV at room temperature, which is a kind of short-wave optoelectronic device material with wide application prospects [21–23]. At room temperature, ZnSe is a SERS activity semiconductor compound with a bandgap of 2.7 eV [24]. ZnSe nanomaterials tend to have point defects (such as Zn vacancy, Zn interstitial and Se vacancy) and bulk phase defects (dislocation, stacking faults and twins) when growing in a stoichiometric atmosphere, thus introducing new energy levels. Studies have revealed that the SERS properties of ZnSe nanowires can be changed by the crystal structure and modulation bandgap of ZnSe [25]. The special structural characteristics of ZnSe itself make it easy to produce topological defects at the location where twins are formed in the growth process. These defects promote the formation of more active sites in the secondary topological structure so that the energy level of the whole secondary topological structure changes. It is helpful for studying the SERS properties of topological ZnSe branched nanowires.

Here, we focused on the SERS activity of ZnSe nanowires with a topological branched structure. The relationship between the geometry, defects, electronic energy-level structure, interfacial interaction, and SERS activity of topological ZnSe nanowires was examined. The unique Se vacancy donor defects of the topological branched nanowires provide a proper bandgap for electron–hole separation and good matches with the energy band of the probe molecules. Therefore, the common probe and environmental pollutant molecules have a better enhancement effect on the topological branched nanostructures. On topological branches, the signal of methylene blue (MB) molecules is up to 1.9 times greater than that on the trunk. The results will help us to further investigate the enhancement mechanism of topological semiconductor nanostructures represented by ZnSe in SERS and design and develop some new potent SERS device application platforms.

2 Experiment section

2.1 Synthesis of topological ZnSe nanowires

To prepare Ni-catalyzed ZnSe nanowires, the nickel catalyst (99.99% purity) was deposited on the surface of the substrate with a thickness of about 3 nm using a thermal evaporation method. The ZnSe powder (30 mg, 100 mesh, and 99.99% purity) was deposited in a ceramic boat in the center of the tubular furnace heating zone. Downstream the airflow, SiO_2/Si substrates coated with Ni particles were placed 12 cm away from the central source powder as the substrate. In the growth, a high purity argon with a flow rate of 30 standard cubic centimeters per minute (sccm) was used to keep the growth environment close to atmospheric pressure. The pressure was about 96–100 kPa. The growth temperature of ZnSe was 850°C for 1 h, and then the samples were cooled to room temperature naturally.

2.2 SERS activity

The SERS activity of topological ZnSe nanowires with various position was measured using the probe molecules: rhodamine 6G (R6G), MB and crystalline violet (CV). In the experiment, R6G, MB, and CV aqueous solutions were prepared with a concentration of 10^{-5} M. In addition, we configured malachite green (MG) aqueous solution (1×10^{-6} M to 5×10^{-4} M) for the practical application of the substrate assay. In SERS measurements, 2 μL of molecule solution with different concentrations was deposited on the fabricated sample surface. The samples were tested after drying in the air for 30 min. For Raman and SERS measurements, some individual

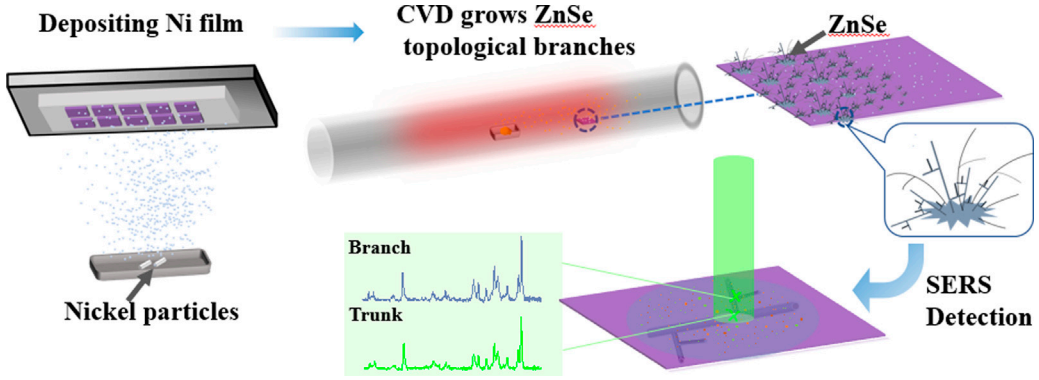

FIGURE 1
Diagram of the preparation of a ZnSe topological branched nanowire SERS substrate and the detection of SERS performance.

nanowires which were not tangled or disjointed with other wires were chosen to obtain the signal.

2.3 Characterization

The Zeiss Sigma 500 scanning electron microscope (SEM, Sigma 500, Zeiss, Germany) was equipped with an energy-dispersive spectrometer (EDS) to investigate the microstructure. Using an X-ray diffractometer (XRD, Ultima, Rigaku, Japan) with voltage: 40 kV, current: 40 mA, scan step: 0.02°, scan speed: 4°/min, and scan range: 10–60°, the crystal structure of topologically branched ZnSe nanowires was detected. The structure of the topological ZnSe nanowires was characterized using high-resolution transmission electron microscopy (HRTEM, JEM-2100, JEOL Ltd., Japan) with an accelerating voltage of 200 kV. All Raman spectra and photoluminescence (PL) were measured using an HR Evolution instrument produced by HORIBA Scientific, equipped with a 532 nm (Raman and SERS) and 325 nm (PL) laser. The spectrometer grating of 600 g/mm, the laser spot diameter of 2 μm, and the signal acquisition time of 4 s were chosen. A ×50 objective lens and a laser excitation energy of 48 mW and 12 mW were used for Raman and SERS measurements, respectively. A ×40 objective lens and a laser excitation energy of 6.25 mW were used for PL measurements. The resulting spectra are the average of the spectral signal intensity obtained from 20 locations in the same sample. All the measurements were performed at room temperature.

3 Results and discussion

Figure 1 shows a schematic diagram of the preparation of topological branched nanowires and the probe molecular detection. Figure 2 shows the SEM and EDS images of a topological grading tree-like structure of ZnSe nanowires. The diameters of the secondary branch (marked as B) and trunk (marked as T) are about 300 nm and 1200 nm, respectively. The branch is narrower than the trunk. Most of the branch nanowires are concentrated on the surface of the substrate. A crystal ball can be seen at the tip of the nanowires. The EDS results showed that the tip of the nanowires has little Zn element, but the dominant elements are Se and Ni. ZnSe topological nanostructures are grown by a vapor–liquid–solid (VLS) mechanism. The nanowire compositions are ZnSe with no detectable traces of other elements, except for the weak C and O signals originating from the substrate. The component proportion of the trunk and the topological branch differed under the same conditions. In the trunk, the atomic ratio of Zn and Se is closer to the stoichiometric ratio. The component ratio of Zn and Se is different along the growth direction of the topological branch and Se is a lesser element.

XRD further characterized the crystal structure of the ZnSe nanowires as shown in Figure 3A. The strong signal at 2 θ = 33.0° was attributed substrate (JCPDS 44-1394). The two characteristic peaks at 2 θ = 27.2° and 45.2° of the topological branched nanowire sample were ascribed to the (111) and (220) lattice planes of the ZnSe zinc-blende structure (JCPDS 37–1463). Two weak peaks appearing at 2θ = 29.6° and 40.4° correspond to the (101) and (102) lattice planes of hexagonal wurtzite-ZnSe structure (JCPDS 15-0105). As shown in Figure 3B, the lattice spacings on both the trunk and topological branches of ZnSe nanowires correspond to the zinc-blende (200) plane and wurtzite (102) plane, respectively. At the position where the topological branched nanowires start to extend, twinning defects appear in the intact single crystals on the trunk, extending the secondary nanowire branches. The lattice spacing parallel to the trunk nanowire direction in Figure 3C corresponds to the (200) lattice plane of the zinc blende. It shows that the trunk is growing

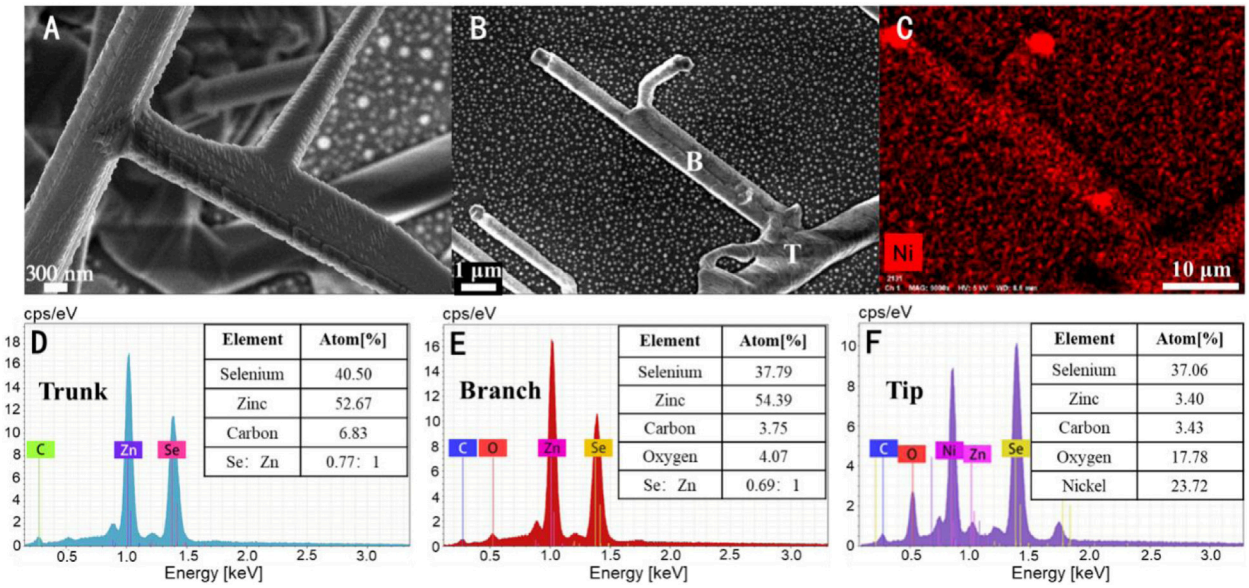

FIGURE 2
(A) SEM image of topological ZnSe nanowires. **(C)** EDS mapping scan of the image **(B)**. **(D–F)** Spectra of EDS scanning on the trunk, topological branch, and top of nanowires, respectively. The table in the upper right corner of each image corresponds to the elements and their proportions in each test position.

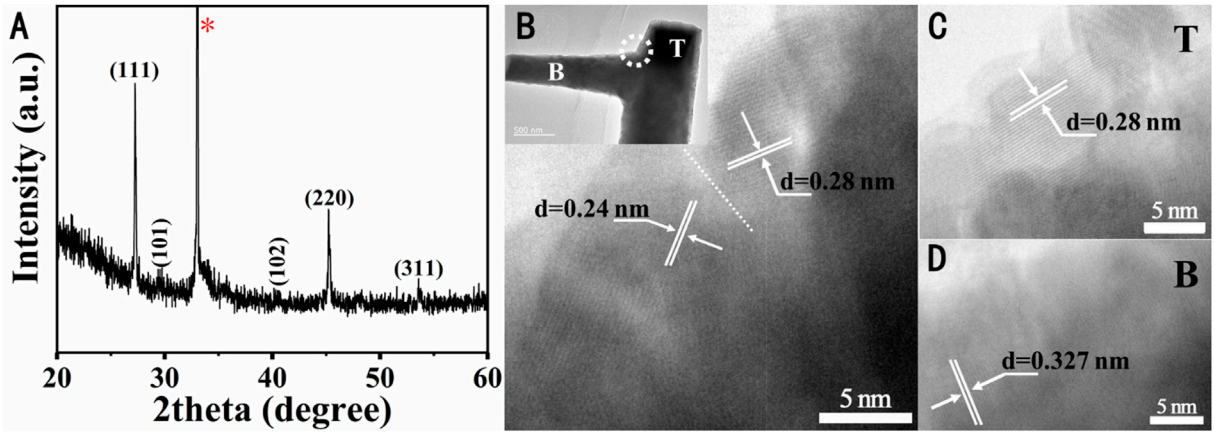

FIGURE 3
(A) XRD spectra of ZnSe nanowires, labeled with diffraction plane of the zinc blende-, wurtzite-ZnSe crystal structure. **(B)** HRTEM of the junction of the trunk and topological branch of the topological branched nanowires, and the inset in the upper left corner shows the full view of this position. HRTEM of the **(C)** trunk and **(D)** topological branched nanowires.

in a direction parallel to the (100) plane. The lattice spacing in Figure 3D corresponds to the (002) lattice plane of the wurtzite, and the growth direction of the topological branch is along the (001) plane. These results show that the secondary branched nanowires grow mainly on the (100) lattice surface of the zinc-blende structure's trunk. However, the lattice at the interface between the trunk and the topological branch is irregular and exhibits a twinned crystal delineation interface, indicating the presence of defects. The topological branches grow at the defective positions.

Under the low dissolution temperature, Se ions are evaporated firstly from the source powder during the growth

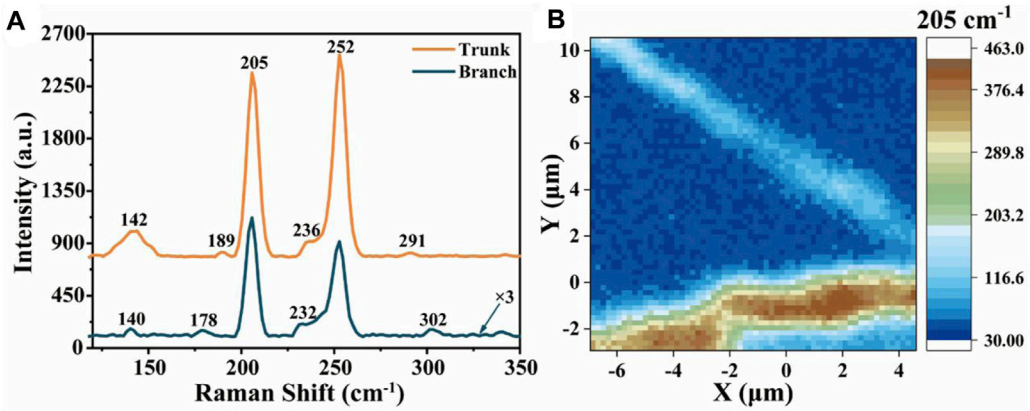

FIGURE 4
(A) Raman spectra of ZnSe nanowires (the ordinate of topological branches is ×3 times for the result) and **(B)** corresponding mapping at 205 cm^{-1}.

process. The Se atoms were transported from the evaporation source to the growth zone downstream and combined with the Ni nanoparticles on the substrate to form a Ni-Se solid solution alloy, which plays a nucleation role in the growth of ZnSe nanowires. The Zn ions are combined with the Se-Ni solid solution. When the number of these atoms exceeds the equilibrium concentration in the liquid phase, the crystallized ZnSe nanowires precipitate underneath the alloy droplet, while the alloy remains at the tip of the nanowires. At the initial stage of nanowire growth, sufficient source powder can make nanowires with fewer Se defects. The topological branched nanowires precipitate at the side of the trunk, as shown in Figure 2A. During the growth of ZnSe nanowires, the atomic binding energy varies with pressure and temperature, resulting in defects. Ni particles not involved in the nucleation initiation stage can move on the substrate surface at a certain temperature. The Ni catalyst will be absorbed in the defects of the first-formed ZnSe nanowires, which will lower the surface energy and result in the sprouting of subnanowires from the defects and the formation of secondary topological nanostructures.

Furthermore, the Ni droplets remaining at the trunk defects are smaller than the clustered droplets on the SiO_2/Si substrate. Hence, the diameter of the grown topological branched nanowires is narrower. Simultaneously, a large amount of Se was consumed with the extension of growth time, and the Ni particles of the grown catalysts melted and mixed with Zn and Se. Se element of the topological branch is less than that of the trunk. In addition, some Se atoms still were re-evaporated in the deposition, so the amount of Se element is less than that of Zn both in trunks and branches. Based on the VLS growth mode, the V, L, and S phases are closely coupled, and changes in the gas phase may affect the solid phase. It is difficult to obtain complete stoichiometry of ZnSe and many other II-VI semiconductors [26].

Figure 4A shows the Raman peaks of the trunk and the topological branches of the ZnSe nanowires, respectively. Raman peaks at 205 cm^{-1} and 252 cm^{-1} can be found in the trunk and topological branches, which are corresponding to the scattering of transverse optical (ω_{TO}) and longitudinal optical (ω_{LO}) phonon modes of ZnSe, respectively [27]. The trunk also has weak peaks at 142 cm^{-1}, 189 cm^{-1}, 236 cm^{-1} and 291 cm^{-1}. The peak at 142 cm^{-1} corresponds to the two-phonon transverse acoustic (2 ω_{TA}) mode, which presents the defective states in the ZnSe nanowire structure. Peaks at 189 cm^{-1} and 291 cm^{-1} correspond to double-phonon excitation [189 cm^{-1}: 2 ω_{TA}(K) and 291 cm^{-1}: ω_{TA}(X, K) + ω_{LA}(X)] [28]. The 236 cm^{-1} peak corresponds to the surface phonon mode, a characteristic feature of small-sized nanostructures. A significant contribution to the Raman scattering of this peak comes from LO phonons propagating in the surface loss layer [29]. The peak at 232 cm^{-1} of the branch shows a redshift compared with that of the trunk, which corresponds to the decreasing of the diameter of the nanowire. The peaks at 178 cm^{-1} and 302 cm^{-1} on the topological branches are different from those on the trunk. The peak at 302 cm^{-1} is attributed to ω_{LO}(X) + ω_{TA}(X, K) vibrational modes [30]. The peak at 178 cm^{-1} may be the contribution of two-phonon scattering from phonons in the directions near the K symmetry point or the contribution from the disorderly activated band-edge LA phonons [31]. The mapping diagram at 205 cm^{-1} is obtained to characterize the Raman signals of the trunk and the topological branches of the nanowires, as shown in Figure 4B. The high Raman signal of the trunk indicates that a good quality of the trunk for ZnSe nanowires.

Figure 5 shows the PL spectra of the trunk, and the topological branched nanostructures of ZnSe measured in the

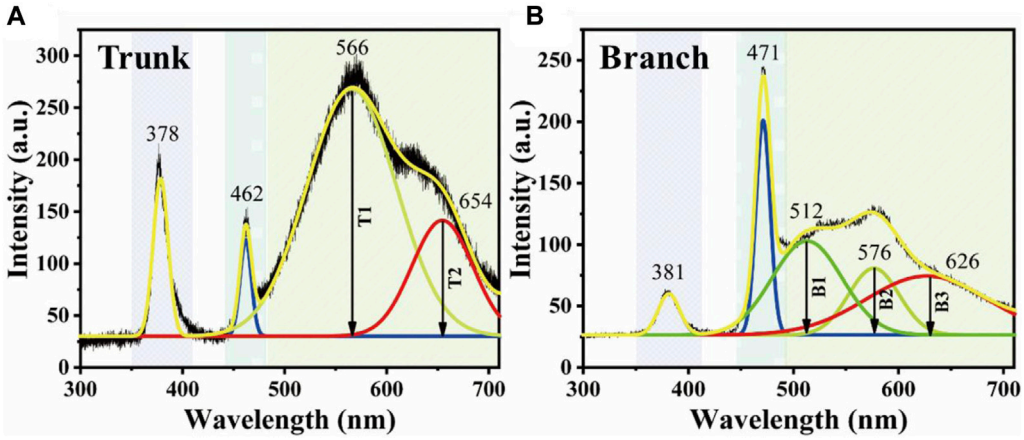

FIGURE 5
PL spectrum of ZnSe nanowires with the **(A)** trunk and **(B)** the topological branch.

wavelength range of 300–700 nm to investigate the optical properties of ZnSe nanostructures. The PL spectra of both the trunk and topological branched nanowires consist of three emission bands: a peak at about 380 nm, a narrow half-width ratio near-band edge (BE) peak at 460–470 nm, and a broad half-width ratio deep-defect (DD) band at 500–750 nm. In the trunk, the peak at 378 nm (3.28 eV) is the exciton emission peak generated by the direct recombination of electron–hole pairs, and the peak at 462 nm (2.68 eV) belongs to the intrinsic peak of ZnSe material. The DD broad emission band of the trunk can be divided into two peaks centered at 566 nm (T1) and 654 nm (T2) by fitting a Gaussian function. The emission at 566 nm is attributed to deep-defect-related emission, ascribed to the recombination of a donor–acceptor pair involving Zn vacancies and interstitials and surface emission [32–34]. A single local level mainly determines the characteristic peak at 654 nm (1.89 eV) to confirm that the recombination emission peak is caused by the direct transition of the Zn interstitial electron donor to the valence band and the higher emission intensity is caused by the higher Zn_i concentration excited by more Se ions [35]. The DD peaks on the topological branches can be fitted to three sub-bands centered at 512 nm (B1), 576 nm (B2), and 626 nm (B3) by the Gaussian function in the PL spectra for topological branches, and the peaks at 381 nm, 471 nm, and 576 nm are similar to the trunk. The emission peak at 512 nm (2.43 eV), which is different from the trunk peak, is derived from the surface trap state. The emission wavelength is caused by the conduction band (CB) to the single negatively charged Zn-vacancy (V_{Zn}^-) due to the high surface volume ratio [36]. Another unique PL peak at 626 nm (1.98 eV) of the topological branches corresponds to a donor–acceptor pair, charged Zn-vacancy (V_{Zn}^-) from V_{Se}.

According to the PL spectra of ZnSe nanowires, BE emission peak intensity on the trunk is weaker than DD emission peak intensity. In contrast, BE peak intensity on the topological branches is stronger than DD peak intensity. This is related to the growth conditions. The growth may introduce inherent point defect Zn interstitial when the Se content is rich in the early growth stage, which may cause the strong DD emission in the trunk. The lower concentration of Zn vacancy leads to the lower intensity of the DD emission peak on the topological branches when the nanowires grow under zinc-rich conditions at the later growth stage due to the lower melting point of Se in the source powder, longer growth time and higher Se activity [33]. According to the aforementioned evidence, there are emission peaks caused by different structural defects in the PL spectra of the trunk and topological branches. Therefore, different defect levels generated by the two have different effects on charge transfer, which may affect SERS results.

R6G and CV have a large Raman scattering cross section. The absorption peak of R6G is near 532 nm [37]. The excitation wavelength in the absorption region will lead to molecular resonance and cause a strong resonance Raman effect [38]. The maximum absorption wavelengths of CV and MB are 590 nm and 664 nm, respectively, and there is no resonance Raman effect under 532 nm excitation light [39]. CV is a cationic industrial dye with a complex structure and hard degradation [40]. It is widely used in the area of aquaculture disease prevention and control. MB is often used to localize sentinel lymph nodes in medical and prevent black spot disease for fish in aquaculture [41]. However, R6G, CV and MB dyes pose a hazard to the environment and animals, plants and human health [42]. Focusing on the SERS activity of the topological structure of ZnSe nanowires on these three dye molecules can help us study the topological structure's effect on the SERS activity and analyze the

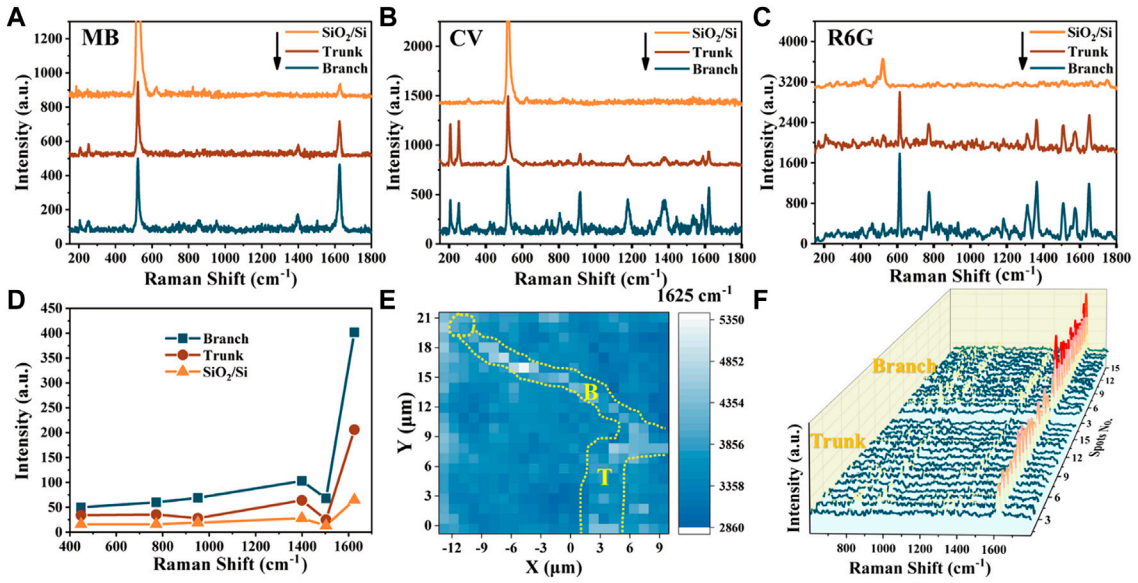

FIGURE 6
Raman spectra of **(A)** MB, **(B)** CV, and **(C)** R6G deposited on trunks and topological branches of ZnSe nanowire substrates; all concentration is 10^{-5} M. **(D)** Intensities of the peaks of MB (10^{-5} M) deposited on the trunks, topological branches, and blank SiO_2/Si substrate. **(E)** Spatial mapping of the SERS intensity at 1625 cm^{-1} of MB probe molecules on ZnSe SERS substrates over an area larger than 21 μm × 21 μm. **(F)** SERS peak values of MB (10^{-5} M) were taken from 15 random positions on the trunk and branch of the topological nanowire SERS substrate.

generality of the SERS activity based on topological nanowires of different chemical molecules. The SERS results of MB, CV and R6G molecules shown in Figure 6 indicate that the enhanced Raman signals of MB, CV and R6G absorbed on the topological branches are better than those absorbed on the trunks of ZnSe nanowires. Among them, the Raman peak intensity of the MB molecules at 1625 cm^{-1} is about 1.9 times higher than that of the trunk, and the peak of the CV molecules at 1622 cm^{-1} is about 3.2 times higher than that of the trunk. The relative intensity of the 1651 cm^{-1} peaks of R6G molecules on the topological branches reached 1.5 times higher than that on the trunk. For the Raman enhancement of R6G molecule, the contribution of resonance excitation is much greater than that of charge transfer. Therefore, the differences in the relative peak intensities of R6G molecules on the trunk and branches are the smallest among the three probe molecules.

The SERS signals of different peaks of MB molecules with a concentration of 10^{-5} M were further analyzed to obtain the different enhancement mechanisms of the trunk and topological branches of ZnSe nanowires. The weak peaks at 448, 772, 951, and 1502 cm^{-1} of MB molecules correspond to skeletal deformation of C-N-C, in-plane bending of C-H, in-plane bending of C-H, and asymmetrical stretching of C-C, respectively. Two prominent peaks at 1397 cm^{-1} and 1625 cm^{-1} are attributed to symmetrical stretching of C-N and ring stretching of the C–C vibration mode, respectively [43]. The intensities of Raman peaks of MB on the different positions of ZnSe nanowires were compared to those on the empty substrate and are shown in Figure 6D. The enhancement of the peak at 1625 cm^{-1} is the largest. The different enhancement of different vibration modes inhibits some surface molecular vibration due to the coupling binding effect of substrate and probe molecules [44, 45].

Figure 6E shows that the mapping scans of the peak at 1625 cm^{-1} of MB (concentration of 10^{-5} M) adsorbed on different positions of ZnSe nanowires. At the tip of the nanowires, there is almost no enhancement of the signal of the MB molecule, which indicates that the catalyst nickel metal particles do not contribute to the enhancement of the Raman signal of the probe molecule. The areas and boundaries of the enhancement of the Raman signal exhibited a higher relative peak intensity around the topological branched nanowires than around the trunk nanowires. The relative peak intensities in the SERS mapping of MB molecules on the topological branches and trunks are opposite to the results presented in the Raman mapping of the sample. We collected 15 points arbitrarily at different locations on the substrate as SERS spectra of MB, as shown in Figure 6F. It can be observed that the average peak intensity on the branch is higher than that on the trunk, indicating that the topological nanowires on the SERS substrate have high repeatability.

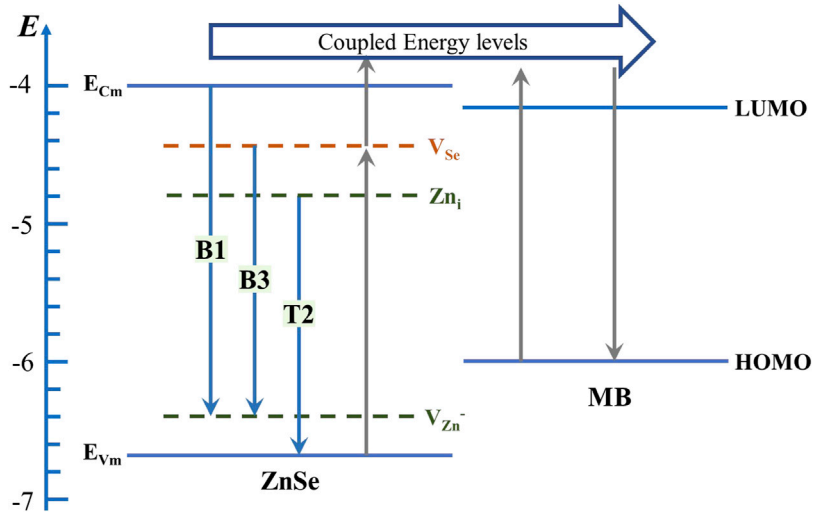

FIGURE 7
Energy-level diagram presenting the SERS ability mechanism on ZnSe microstructures using methylene blue. Abbreviation: V_{Zn}^{-} = monoionized zinc vacancy defect; Zn_i = zinc interstitial monodionized donor defect; V_{Se} = monoionized selenium vacancy defect.

It is generally known that chemical enhancement consists of three main contributions: 1) molecular resonance due to laser excitation; 2) Raman enhancement due to electrostatic charge transfer caused by the substrate–molecule interaction; and 3) charge transfer resonance between the molecule and substrate. Figure 7 shows the energy levels of CB, VB, and defect states of ZnSe and the highest occupied molecular orbital (HOMO) and the lowest unoccupied molecular orbital (LUMO) of MB molecules. This plot is based on the PL spectrum of the topological branched nanowires [46]. When the photon energy is high enough, electrons are excited from the VB of the substrate to higher energy levels in the CB of the substrate coupled to the molecular energy levels above LUMO during charge transfer between ZnSe nanostructures and MB-adsorbed molecules. These excited state electrons (except those leaping to the valence band to be recombined) are transferred to the molecular energy levels above LUMO *via* vibrational coupling of the energy levels, causing the molecular polarization tensor to amplify, giving rise to the SERS effect or electrons are excited from the HOMO of the molecule to higher levels of the LUMO of the molecule that are coupled to the energy levels above the substrate conduction band and transferred to the CB by vibrational coupling. New defect energy levels are also introduced by a defect during growth. The relative energy of the Se vacancy energy level to the VB of ZnSe is about 2.24 eV, very close to the energy of the excitation light (2.3 eV) since there are more Se vacancy donor defects on the topological branches than on the trunk. After absorbing the incident light energy, the electrons on the branch valence band are more easily excited to the defect level and then jump to the coupling level above the CB level and then inject into the LUMO of MB through vibration coupling so that the polarization tensor of the MB probe molecule becomes larger, and the SERS signal becomes stronger. Moreover, the special structural properties of ZnSe itself make it easy to produce topological structure defects at the sites where twinning occurs during the growth of nanowires. The generation of these defects induces more active sites in the secondary topological dendritic structure, which causes energy-level changes in the entire secondary topology and facilitates the further enhancement of the SERS activity.

To present the practical application of this SERS active substrate, MG were tested. MG is an ingredient contained in the "potent drug" used in aquaculture to fight against water mold disease in fish and water mold disease in fish eggs, which can be carcinogenic when used in excessive amounts for a long time and is prohibited in the field of pollution-free aquaculture. Figures 8A,B show the concentration gradient detection of MG by the branch and trunk as active substrates, respectively. The branch showed a better detection performance with a limit of detection of 5×10^{-6} M (the limit of detection of the trunk was 1×10^{-5} M). Both were lower than the newly revised national use standard of 6.85×10^{-5} M in the Food Safety Law. Figure 8C shows the detection at the trunk and branch of the topological ZnSe nanowires and the obvious linear relationship between the concentration of MG and the peak intensity at 1616 cm^{-1}, and the R^2 values of the trunk and branch are above 0.93, showing good SERS performance and quantitative detection results.

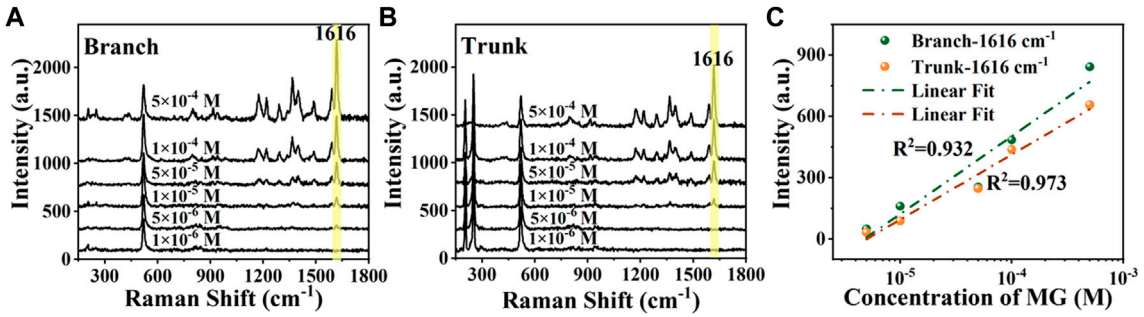

FIGURE 8
(A,B) Raman peaks in the range of 5×10^{-4} M–10^{-6} M for MG concentration on the branch and trunk of the ZnSe topological branched SERS substrate, respectively. **(C)** SERS spectra at 1616 cm^{-1} on trunk and branch substrates *versus* different MG concentrations on a logarithmic scale.

4 Conclusion

In conclusion, physical vapor deposition prepared topological ZnSe nanostructures on silicon substrates. The growth mechanism for the formation of such topological branched structures is discussed. The defects caused by the different structures developed independently are characterized. It is also examined that it leads to different enhancement effects when used as an SERS active substrate. It is shown that the formation of topological nanostructures of ZnSe nanowires in the absence of metal addition enhances surface Raman scattering in which the Se vacancy donor defects in the branches have a prominent contribution to SERS. The nanobranched active ZnSe substrates were identified better than nanotrunks when the enhancement was tested with several probe molecules. In the detection of toxic substances, MG reflected good quantitative detection results, the detection limit of MG reached 5×10^{-6} M. Studying the SERS activity of ZnSe topological nanostructures offer suggestions for using semiconductors in optoelectronic materials and active substrates to improve molecular detection and show great potential applications in different fields.

Data availability statement

The original contributions presented in the study are included in the article/Supplementary Material; further inquiries can be directed to the corresponding authors.

Author contributions

PD: investigation and writing—original draft preparation. MS: methodology. WL and WZ: data curation. CZ and XH: software. JG: search, collect and synthesize the related literatures. ML and CZ: project administration and funding acquisition.

Funding

All the authors were grateful for financial assistance from the National Natural Science Foundation of China (NSFC), under Grant Nos. 12074229 and 12174229.

Conflict of interest

The authors declare that the research was conducted in the absence of any commercial or financial relationships that could be construed as a potential conflict of interest.

Publisher's note

All claims expressed in this article are solely those of the authors and do not necessarily represent those of their affiliated organizations, or those of the publisher, the editors, and the reviewers. Any product that may be evaluated in this article, or claim that may be made by its manufacturer, is not guaranteed or endorsed by the publisher.

References

1. Bharati M. S., Soma V. R. Flexible SERS substrates for hazardous materials detection: Recent advances. *Opto-electron Adv* (2021) 4:210048–8. doi:10.29026/oea.2021.210048

2. Ji C., Lu J., Shan B., Li F., Zhao X., Yu J.,. The origin of Mo2C films for surface-enhanced Raman scattering analysis: Electromagnetic or chemical enhancement? *J Phys Chem Lett* (2022) 13:8864–71. doi:10.1021/acs.jpclett.2c02392

3. Zhao Y. Y., Ren X. L., Zheng M. L., Jin F., Liu J., Dong X. Z.,. Plasmon-enhanced nanosoldering of silver nanoparticles for high-conductive nanowires electrodes. *Opto-electron Adv* (2021) 4:200101–1. doi:10.29026/oea.2021.200101

4. Hao Q., Huang H., Fan X., Yin Y., Wang J., Li W.,. Controlled patterning of plasmonic dimers by using an ultrathin nanoporous Alumina membrane as a shadow mask. *ACS Appl Mater Inter* (2017) 9:36199–205. doi:10.1021/acsami.7b11428

5. Zhang C., Li Z., Qiu S., Lu W., Shao M., Ji C.,. Highly ordered arrays of hat-shaped hierarchical nanostructures with different curvatures for sensitive SERS and plasmon-driven catalysis. *Nanophotonics* (2021) 11:33–44. doi:10.1515/nanoph-2021-0476

6. Shafi M., Liu R., Zha Z., Li C., Du X., Wali S.,. Highly efficient SERS substrates with different Ag interparticle nanogaps based on hyperbolic metamaterials. *Appl Surf Sci* (2021) 555:149729. doi:10.1016/j.apsusc.2021.149729

7. Otto A. The 'chemical' (electronic) contribution to surface-enhanced Raman scattering. *J Raman Spectrosc* (2005) 36:497–509. doi:10.1002/jrs.1355

8. Zha Z., Liu R., Gao J., Yang W., Shafi M., Liu C.,. Graphene-covered Silver nanoisland array coupling with hyperbolic metamaterials for SERS sensing. *ACS Appl Nano Mater* (2022) 5:6618–26. doi:10.1021/acsanm.2c00665

9. Tian Z. Q., Ren B., Wu D. Y. Surface-enhanced Raman scattering: From noble to transition metals and from rough surfaces to ordered nanostructures. *J Phys Chem B* (2002) 106:9463–83. doi:10.1021/jp0257449

10. Guo L., Cao H., Cao L., Yang Y., Wang M., SERS study of wheat leaves substrates with two different structures. *Opt Commun* (2022) 510:127921. doi:10.1016/j.optcom.2022.127921

11. Dieringer J. A., Wustholz K. L., Masiello D. J., Camden J. P., Kleinman S. L., Schatz G. C., Surface-enhanced Raman excitation spectroscopy of a single rhodamine 6G molecule. *J Am Chem Soc* (2009) 131:849–54. doi:10.1021/ja8080154

12. Fu Y., Cao J., Yamanouchi K., Xu H. Air-laser-based standoff coherent Raman spectrometer. *Ultrafast Sci* (2022) 2022:9867028–9. doi:10.34133/2022/9867028

13. Zhang Z., Zhang F., Xu B., Xie H., Fu B., Lu X.,. High-sensitivity gas detection with air-lasing-assisted coherent Raman spectroscopy. *Ultrafast Sci* (2022) 2022:1–8. doi:10.34133/2022/9761458

14. Zhang Y., Shi Y., Wu M., Zhang K., Man B., Liu M. Synthesis and surface-enhanced Raman scattering of ultrathin SnSe(2) nanoflakes by chemical vapor deposition. *Nanomaterials (Basel)* (2018) 8:8070515. doi:10.3390/nano8070515

15. Liu M., Shi Y., Wu M., Tian Y., Wei H., Sun Q.,. UV surface-enhanced Raman scattering properties of SnSe2 nanoflakes. *J Raman Spectrosc* (2020) 51:750–5. doi:10.1002/jrs.5846

16. Zheng Z., Cong S., Gong W., Xuan J., Li G., Lu W., et al. Semiconductor SERS enhancement enabled by oxygen incorporation. *Nat Commun* (2017) 8:1993. doi:10.1038/s41467-017-02166-z

17. Lombardi J. R., Birke R. L., Theory of surface-enhanced Raman scattering in semiconductors. *J Phys Chem C* (2014) 118:11120. doi:10.1021/jp5020675

18. Yang L., Peng Y., Yang Y., Liu J., Huang H., Yu B., et al. A novel ultra-sensitive semiconductor SERS substrate boosted by the coupled resonance effect. *Adv Sci (Weinh)* (2019) 6:1900310. doi:10.1002/advs.201900310

19. Gu L. J., Ma C. L., Zhang X. H., Zhang W., Cong S., Zhao Z. G. Populating surface-trapped electrons towards SERS enhancement of W18O49 nanowires. *Chem Commun (Camb)* (2018) 54:6332–5. doi:10.1039/c8cc03880e

20. Lin J., Shang Y., Li X., Yu J., Wang X., Guo L. Ultrasensitive SERS detection by defect engineering on single Cu2O superstructure particle. *Adv Mater* (2017) 29:1604797. doi:10.1002/adma.201604797

21. Qiao S., Sampaolo A., Patimisco P., Spagnolo V., Ma Y. Ultra-highly sensitive HCl-LITES sensor based on a low-frequency quartz tuning fork and a fiber-coupled multi-pass cell. *Photoacoustics* (2022) 27:100381. doi:10.1016/j.pacs.2022.100381

22. Liu X., Ma Y. Tunable diode laser absorption spectroscopy based temperature measurement with a single diode laser near 1.4 μm. *Sensors (Basel)* (2022) 22:166095. doi:10.3390/s22166095

23. Ma Y., Lewicki R., Razeghi M., Tittel F. K., QEPAS based ppb-level detection of CO and N_2O using a high power CW DFB-QCL. *Opt Express* (2013) 21:1008–19. doi:10.1364/OE.21.001008

24. Zhang Q., Li H., Ma Y., Zhai T. ZnSe nanostructures: Synthesis, properties and applications. *Prog Mater Sci* (2016) 83:472–535. doi:10.1016/j.pmatsci.2016.07.005

25. Wang G., Wei H., Tian Y., Wu M., Sun Q., Peng Z.,. Twin-ZnSe nanowires as surface enhanced Raman scattering substrate with significant enhancement factor upon defect. *Opt Express* (2020) 28:18843–58. doi:10.1364/OE.388439

26. Zhang X. T., Liu Z., Ip K. M., Leung Y. P., Li Q., Hark S. K. Luminescence of ZnSe nanowires grown by metalorganic vapor phase deposition under different pressures. *J Appl Phys* (2004) 95:5752–5. doi:10.1063/1.1699497

27. Shan C. X., Liu Z., Zhang X. T., Wong C. C., Hark S. K. Wurtzite ZnSe nanowires: Growth, photoluminescence, and single-wire Raman properties. *Nanotechnology* (2006) 17:5561–4. doi:10.1088/0957-4484/17/22/006

28. Wu H., Dittmer J. J., Alivisatos A. P. Hybrid nanorod-polymer solar cells. *Science* (2002) 295:2425–7. doi:10.1126/science.1069156

29. Irmer G., Monaico E., Tiginyanu I. M., Gärtner G., Ursaki V. V., Kolibaba G. V.,. Fröhlich vibrational modes in porous ZnSe studied by Raman scattering and Fourier transform infrared reflectance. *J Phys D: Appl Phys* (2009) 42:045405. doi:10.1088/0022-3727/42/4/045405

30. Irwin J. C., LaCombe J. Second-order Raman spectrum of ZnSe. *Can J Phys* (1970) 48:2499–506. doi:10.1139/p70-314

31. Monaico E., Ursaki V. V., Tiginyanu I. M., Dashevsky Z., Kasiyan V., Boyd R. W. Porosity-induced blueshift of photoluminescence in CdSe. *J Appl Phys* (2006) 100:053517. doi:10.1063/1.2338833

32. Geng B. Y., Du Q. B., Liu X. W., Ma J. Z., Wei X. W., Zhang L. D. One-step synthesis and enhanced blue emission of carbon-encapsulated single-crystalline ZnSe nanoparticles. *Appl Phys Lett* (2006) 89:033115. doi:10.1063/1.2227964

33. Philipose U., Xu T., Yang S., Sun P., Ruda H. E., Wang Y. Q.,. Enhancement of band edge luminescence in ZnSe nanowires. *J Appl Phys* (2006) 100:084316. doi:10.1063/1.2362930

34. Geng J., Liu B., Xu L., Hu F. N., Zhu J. J. Facile route to Zn-based II-VI semiconductor spheres, hollow spheres, and core/shell nanocrystals and their optical properties. *Langmuir* (2007) 23:10286–93. doi:10.1021/la701299w

35. Makhnii V. P., Tkachenko I. V. Mechanism for forming the red emission band of ZnSe<Te> scintillation crystals. *J Opt Technol* (2003) 70:665–8. doi:10.1364/jot.70.000665

36. Masalov A. A., Seminko V. V., Kononets N. V., Maksimchuk P. O., BespalovaII, Voloshina L. I.,. ZnSe nanocrystals obtained in pores of SiO2 matrix with temperature stable green luminescence. *J Lumin* (2017) 181:337–44. doi:10.1016/j.jlumin.2016.09.043

37. Vogel R., Meredith P., Harvey M. D., Rubinsztein-Dunlop H. Absorption and fluorescence spectroscopy of rhodamine 6G in titanium dioxide nanocomposites. *Spectrochimica Acta A: Mol Biomol Spectrosc* (2004) 60:245–9. doi:10.1016/s1386-1425(03)00218-x

38. Wu H., Wang H., Li G. Metal oxide semiconductor SERS-active substrates by defect engineering. *Analyst* (2017) 142:326–35. doi:10.1039/c6an01959e

39. Deneme I., Liman G., Can A., Demirel G., Usta H., Enabling three-dimensional porous architectures via carbonyl functionalization and molecular-specific organic-SERS platforms. *Nat Commun* (2021) 12:6119. doi:10.1038/s41467-021-26385-7

40. Cañamares M. V., Chenal C., Birke R. L., Lombardi J. R., DFT, SERS, and single-molecule SERS of crystal violet. *J Phys Chem C* (2008) 112:20295–300. doi:10.1021/jp807807j

41. Fengzhang T., Huimei Y., Zhuguang L., Lanlan C., Liang Z. Study on adsorption properties and mechanism of methylene blue on coal fly ash by spectrophotometry. *Chin J Spectrosc Lab* (2010) 27:1116–21. doi:10.1145/1722024.1722072

42. Shanmugam S., Ulaganathan P., Sivasubramanian S., Esakkimuthu S., Krishnaswamy S., Subramaniam S. Trichoderma asperellum laccase mediated crystal violet degradation-Optimization of experimental conditions and characterization, *Journal of Environmental Chemical Engineering* 5 (2017). p. 222–31. doi:10.1016/j.ibiod.2017.08.001

43. Li C., Huang Y., Lai K., Rasco B. A., Fan Y. Analysis of trace methylene blue in fish muscles using ultra-sensitive surface-enhanced Raman spectroscopy. *Food Control* (2016) 65:99–105. doi:10.1016/j.foodcont.2016.01.017

44. Creighton J. A. Surface Raman electromagnetic enhancement factors for molecules at the surface of small isolated metal spheres: The determination of adsorbate orientation from sers relative intensities. *Surf Sci* (1983) 124:209–19. doi:10.1016/0039-6028(83)90345-x

45. Moskovits M., Suh J. S. Surface geometry change in 2-naphthoic acid adsorbed on silver. *J Phys Chem* (2002) 92:6327–9. doi:10.1021/j100333a030

46. Pham T. T., Vu X. H., Trang T. T., Ca N. X., Dien N. D., Van Hai P.,. Enhance Raman scattering for probe methylene blue molecules adsorbed on ZnO microstructures due to charge transfer processes. *Opt Mater (Amst)* (2021) 120:111460. doi:10.1016/j.optmat.2021.111460

Frontiers in Physics

Investigates complex questions in physics to understand the nature of the physical world

Addresses the biggest questions in physics, from macro to micro, and from theoretical to experimental and applied physics.

Discover the latest Research Topics

See more →

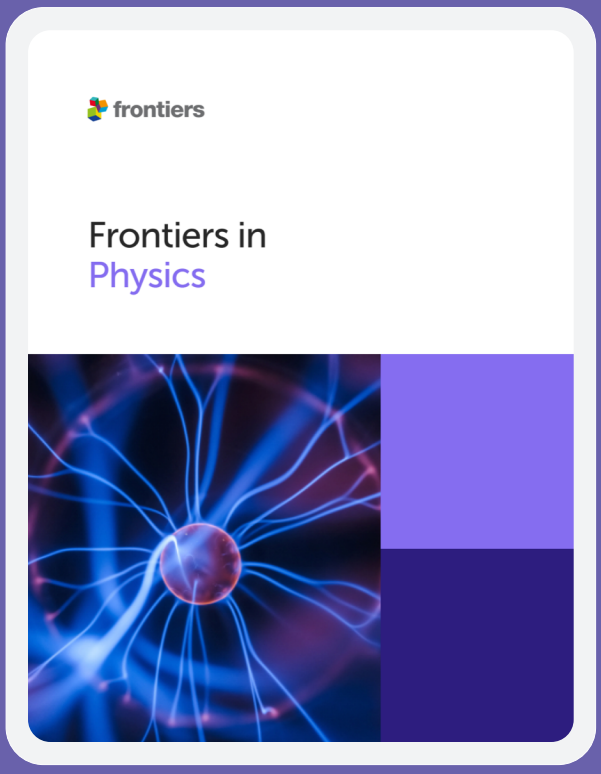

Frontiers

Avenue du Tribunal-Fédéral 34
1005 Lausanne, Switzerland
frontiersin.org

Contact us

+41 (0)21 510 17 00
frontiersin.org/about/contact